

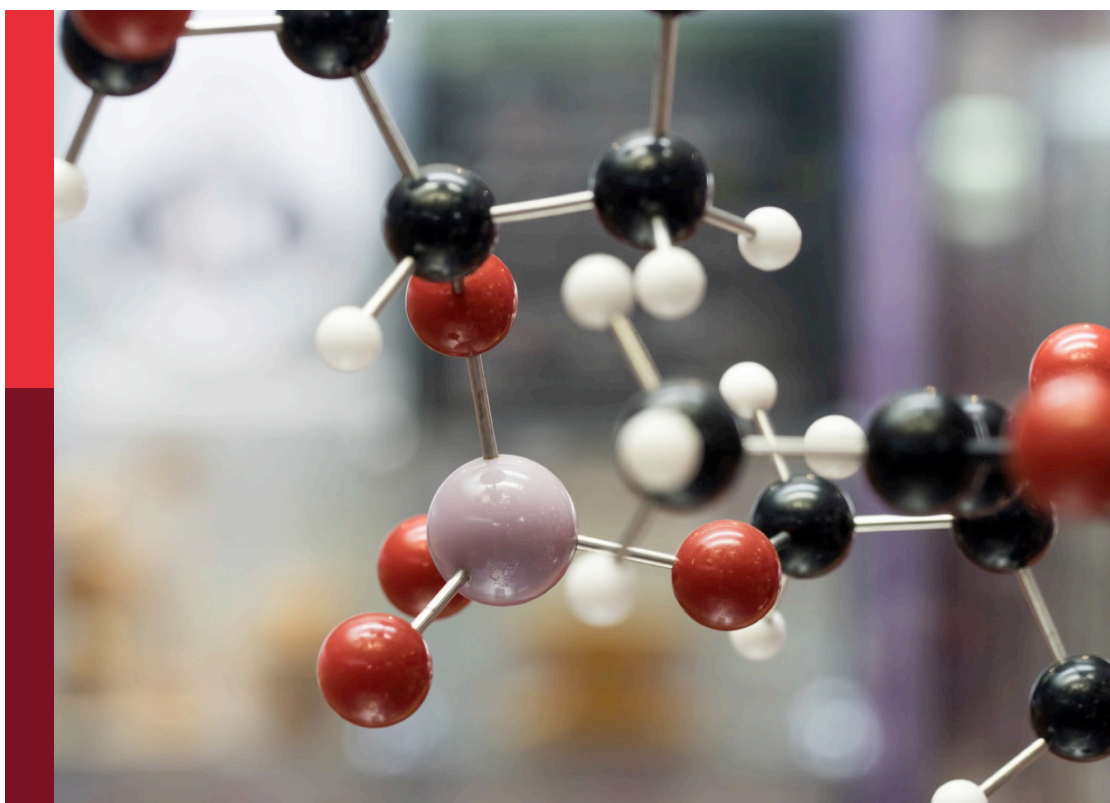
# Reviews in chemistry

**Edited by**

Omotayo Ademola Arotiba, Xiao Xiao, Mohammad Mansoob Khan,  
Jun Chen, Nan-Fu Chiu, Kang Xiao and Tingchao He

**Published in**

Frontiers in Chemistry



## FRONTIERS EBOOK COPYRIGHT STATEMENT

The copyright in the text of individual articles in this ebook is the property of their respective authors or their respective institutions or funders. The copyright in graphics and images within each article may be subject to copyright of other parties. In both cases this is subject to a license granted to Frontiers.

The compilation of articles constituting this ebook is the property of Frontiers.

Each article within this ebook, and the ebook itself, are published under the most recent version of the Creative Commons CC-BY licence. The version current at the date of publication of this ebook is CC-BY 4.0. If the CC-BY licence is updated, the licence granted by Frontiers is automatically updated to the new version.

When exercising any right under the CC-BY licence, Frontiers must be attributed as the original publisher of the article or ebook, as applicable.

Authors have the responsibility of ensuring that any graphics or other materials which are the property of others may be included in the CC-BY licence, but this should be checked before relying on the CC-BY licence to reproduce those materials. Any copyright notices relating to those materials must be complied with.

Copyright and source acknowledgement notices may not be removed and must be displayed in any copy, derivative work or partial copy which includes the elements in question.

All copyright, and all rights therein, are protected by national and international copyright laws. The above represents a summary only. For further information please read Frontiers' Conditions for Website Use and Copyright Statement, and the applicable CC-BY licence.

ISSN 1664-8714  
ISBN 978-2-8325-4236-1  
DOI 10.3389/978-2-8325-4236-1

## About Frontiers

Frontiers is more than just an open access publisher of scholarly articles: it is a pioneering approach to the world of academia, radically improving the way scholarly research is managed. The grand vision of Frontiers is a world where all people have an equal opportunity to seek, share and generate knowledge. Frontiers provides immediate and permanent online open access to all its publications, but this alone is not enough to realize our grand goals.

## Frontiers journal series

The Frontiers journal series is a multi-tier and interdisciplinary set of open-access, online journals, promising a paradigm shift from the current review, selection and dissemination processes in academic publishing. All Frontiers journals are driven by researchers for researchers; therefore, they constitute a service to the scholarly community. At the same time, the *Frontiers journal series* operates on a revolutionary invention, the tiered publishing system, initially addressing specific communities of scholars, and gradually climbing up to broader public understanding, thus serving the interests of the lay society, too.

## Dedication to quality

Each Frontiers article is a landmark of the highest quality, thanks to genuinely collaborative interactions between authors and review editors, who include some of the world's best academicians. Research must be certified by peers before entering a stream of knowledge that may eventually reach the public - and shape society; therefore, Frontiers only applies the most rigorous and unbiased reviews. Frontiers revolutionizes research publishing by freely delivering the most outstanding research, evaluated with no bias from both the academic and social point of view. By applying the most advanced information technologies, Frontiers is catapulting scholarly publishing into a new generation.

## What are Frontiers Research Topics?

Frontiers Research Topics are very popular trademarks of the *Frontiers journals series*: they are collections of at least ten articles, all centered on a particular subject. With their unique mix of varied contributions from Original Research to Review Articles, Frontiers Research Topics unify the most influential researchers, the latest key findings and historical advances in a hot research area.

Find out more on how to host your own Frontiers Research Topic or contribute to one as an author by contacting the Frontiers editorial office: [frontiersin.org/about/contact](https://frontiersin.org/about/contact)



# Reviews in chemistry

## Topic editors

Omotayo Ademola Arotiba — University of Johannesburg, South Africa

Xiao Xiao — University of California, Los Angeles, United States

Mohammad Mansoob Khan — Universiti Brunei Darussalam, Brunei

Jun Chen — University of California, Los Angeles, United States

Nan-Fu Chiu — National Taiwan Normal University, Taiwan

Kang Xiao — University of Chinese Academy of Sciences, China

Tingchao He — Shenzhen University, China

## Citation

Arotiba, O. A., Xiao, X., Khan, M. M., Chen, J., Chiu, N.-F., Xiao, K., He, T., eds. (2024).

*Reviews in chemistry*. Lausanne: Frontiers Media SA.

doi: 10.3389/978-2-8325-4236-1

## Table of contents

- 05 **Review of Thin Film Nanocomposite Membranes and Their Applications in Desalination**  
Jegatha Nambi Krishnan, Kaarthick Raaja Venkatachalam, Oindrila Ghosh, Krutarth Jhaveri, Advait Palakodeti and Nikhil Nair
- 27 **Chemical Modification of Hyaluronan and Their Biomedical Applications**  
Vera Hintze, Matthias Schnabelrauch and Sandra Rother
- 47 **Fermentative Lactic Acid Production From Lignocellulosic Feedstocks: From Source to Purified Product**  
Dragomir Yankov
- 81 **Structure-Property Relationship for Different Mesoporous Silica Nanoparticles and its Drug Delivery Applications: A Review**  
Parya Kazemzadeh, Khalil Sayadi, Ali Toolabi, Jalil Sayadi, Malihe Zeraati, Narendra Pal Singh Chauhan and Ghasem Sargazi
- 92 **A Perspective on Perovskite Solar Cells: Emergence, Progress, and Commercialization**  
Pengyu Zhang, Menglin Li and Wen-Cheng Chen
- 101 **Recent Progress in Fluorescent Probes For Metal Ion Detection**  
Luanjing Li, Jiahe Wang, Shihan Xu, Chunxia Li and Biao Dong
- 116 **Recent Progress on Carbon Quantum Dots Based Photocatalysis**  
Hwapyung Jung, Vijay S. Sapner, Arindam Adhikari, Bhaskar R. Sathe and Rajkumar Patel
- 144 **Electrocatalytic Water Oxidation: An Overview With an Example of Translation From Lab to Market**  
Rakesh Sen, Supriya Das, Aritra Nath, Priyanka Maharana, Pradipta Kar, Francis Verpoort, Pei Liang and Soumyajit Roy
- 168 **Two-Photon Absorption: An Open Door to the NIR-II Biological Window?**  
Paige A. Shaw, Ewan Forsyth, Fizza Haseeb, Shufan Yang, Mark Bradley and Maxime Klausen
- 201 **Key Considerations in Targeted Protein Degradation Drug Discovery and Development**  
Liena Qin, Han Dai and Junfeng Wang
- 216 **Perspective: Morphology and ion transport in ion-containing polymers from multiscale modeling and simulations**  
Zhenghao Zhu and Stephen J. Paddison
- 240 **Comprehensive review of  $\alpha$ -carboline alkaloids: Natural products, updated synthesis, and biological activities**  
Deping Li, Renze Yang, Jun Wu, Bin Zhong and Yan Li

- 264 **Recent advances in functionalized quinoline scaffolds and hybrids—Exceptional pharmacophore in therapeutic medicine**  
Oluwadunni F. Elebiju, Olayinka O. Ajani, Gbolahan O. Oduselu, Temitope A. Ogunnupebi and Ezekiel Adebisi
- 282 **Recent advances in enhanced polymer gels for profile control and water shutoff: A review**  
Siyu Lu, Qiwei Bo, Guang Zhao, Azizullah Shaikh and Caili Dai



# Review of Thin Film Nanocomposite Membranes and Their Applications in Desalination

Jegatha Nambi Krishnan<sup>1\*</sup>, Kaarthick Raaja Venkatachalam<sup>1</sup>, Oindrila Ghosh<sup>1</sup>, Krutarth Jhaveri<sup>2†</sup>, Advait Palakodeti<sup>3†</sup> and Nikhil Nair<sup>1</sup>

<sup>1</sup>Department of Chemical Engineering, Birla Institute of Technology and Science Pilani, K.K. Birla Goa Campus, Zuarinagar, India,

<sup>2</sup>Strategic Engagement and Analysis Group, Rocky Mountain Institute, Boulder, CO, United States, <sup>3</sup>Process and Environmental Technology Lab, Department of Chemical Engineering, KU Leuven, Leuven, Belgium

## OPEN ACCESS

### Edited by:

Pellegrino Musto,  
National Research Council (CNR), Italy

### Reviewed by:

Yanhu Zhan,  
Liaocheng University, China  
Ehsan Nazarzadeh Zare,  
Damghan University, Iran  
Giuseppe Scherillo,  
University of Naples Federico II, Italy

### \*Correspondence:

Jegatha Nambi Krishnan  
jegathak@goa.bits-pilani.ac.in

<sup>†</sup>These authors have contributed  
equally to this work

### Specialty section:

This article was submitted to  
Polymer Chemistry,  
a section of the journal  
Frontiers in Chemistry

Received: 22 September 2021

Accepted: 03 January 2022

Published: 28 January 2022

### Citation:

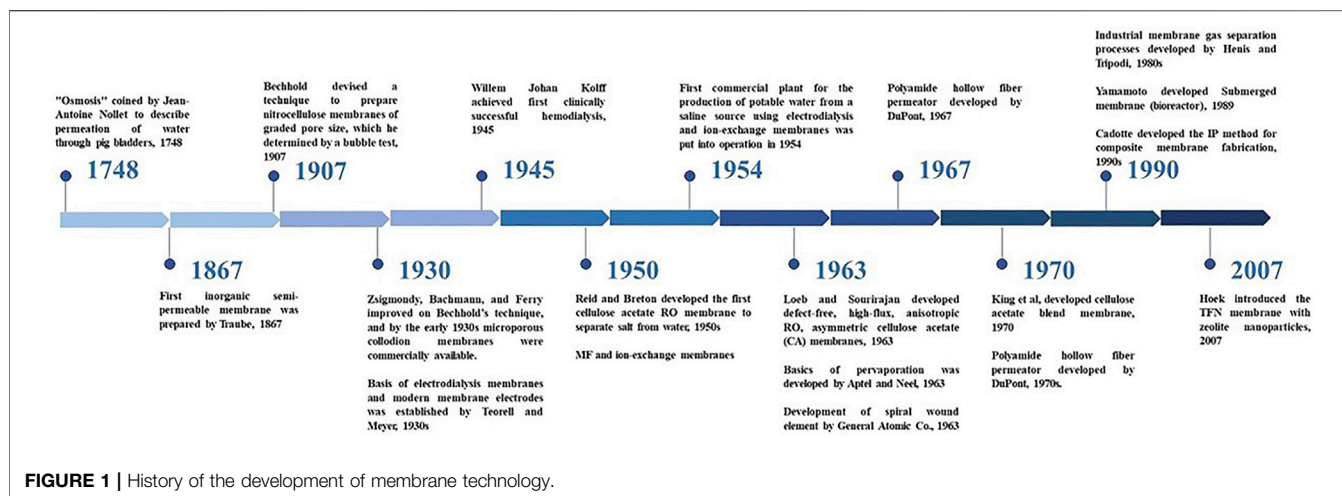
Nambi Krishnan J, Venkatachalam KR,  
Ghosh O, Jhaveri K, Palakodeti A and  
Nair N (2022) Review of Thin Film  
Nanocomposite Membranes and Their  
Applications in Desalination.  
Front. Chem. 10:781372.  
doi: 10.3389/fchem.2022.781372

All over the world, almost one billion people live in regions where water is scarce. It is also estimated that by 2035, almost 3.5 billion people will be experiencing water scarcity. Hence, there is a need for water based technologies. In separation processes, membrane based technologies have been a popular choice due to its advantages over other techniques. In recent decades, sustained research in the field of membrane technology has seen a remarkable surge in the development of membrane technology, particularly because of reduction of energy footprints and cost. One such development is the inclusion of nanoparticles in thin film composite membranes, commonly referred to as Thin Film Nanocomposite Membranes (TFN). This review covers the development, characteristics, advantages, and applications of TFN technology since its introduction in 2007 by Hoek. After a brief overview on the existing membrane technology, this review discusses TFN membranes. This discussion includes TFN membrane synthesis, characterization, and enhanced properties due to the incorporation of nanoparticles. An attempt is made to summarize the various nanoparticles used for preparing TFNs and the effects they have on membrane performance towards desalination. The improvement in membrane performance is generally observed in properties such as permeability, selectivity, chlorine stability, and antifouling. Subsequently, the application of TFNs in Reverse Osmosis (RO) alongside other desalination alternatives like Multiple Effect Flash evaporator and Multi-Stage Flash distillation is covered.

**Keywords:** reverse osmosis, thin film nanocomposite membrane, desalination, interfacial polymerization, chlorine resistance, antifouling, permeability

## 1 INTRODUCTION

The United Nations World Water Development Report 2020: Water and Climate Change states that in accordance with a study conducted by the 2030 Water Resources Group (WRG), the world will have only 60% of the water it needs by 2030, if it continues on its current trajectory (UNESCO, 2020). This scarcity has risen out of the ever growing gap between the overwhelming demand, through agriculture, industries, urbanization, rapidly rising population; and the worryingly low supply of consumable water. This is where the importance of recycling water and converting the abundantly available seawater to usable form by the process of desalination becomes critical. Over the previous decade, membrane based technologies have developed significantly (The World Bank, 2007; Lind et al., 2009a; Li et al., 2013) and the growth in total desalination capacity across the world has been staggering. Among the different



desalination techniques such as electrodialysis, Mechanical Vapor Compression (MVC) and Nano-Filtration (NF), Reverse Osmosis (RO) is the most popularly used technique. Energy consumption of RO membranes in 2013 was 1.8 k Wh, which makes the process much less energy intensive than the other available options, such as MSF (multi-stage flash distillation) and MEF (multiple effect flash distillation) (Buonomenna, 2013). Over 60% of today's desalinated water comes through RO technology.

For the purpose of desalination and other similar applications, various kinds of membranes are fabricated like thin film composite membranes (TFCs) and thin film nanocomposite membranes (TFNs). TFNs are a modification of the existing TFCs prepared through interfacial polymerization (IP). The modification is in the form of nanoparticles being incorporated into a thin polyamide (PA) dense layer at the top of the TFC membrane, aimed at improving its performance (Jeong et al., 2007). This enhancement could be varied such as in the form of improved water permeability and solute rejection.

The TFN membrane was introduced by Hoek (Jeong et al., 2007) in which TFNs were synthesized by embedding zeolite NaA nanoparticles (0.004–0.4% w/v) in the PA layer. The PA layer of the composite membrane was made of m-phenyldiamine (MPD) and trimesoyl chloride (TMC). This new concept showed a significant enhancement in the membrane flux while maintaining a comparable solute rejection to the traditionally prepared TFC membrane. This improvement in permeability due to the super-hydrophilic molecular sieve nanoparticle pores which provide distinct channels for the flow is ascribed (Jeong et al., 2007). The following section discusses the evolution of membrane technology from its first instance of application in a water separation process in 1748 to the currently produced more advanced TFNs.

## 2 BACKGROUND AND HISTORY

The application of membranes for separation of small solute particles from water was first reported in 1748 by Jean-Antoine Nollet (Williams, 2003). However, it was only in the 1850s that

Traube and Pfeffer became the first to study osmosis using ceramic membranes. In 1959, the first cellulose acetate RO membrane capable of separating salt from water was developed by C. E. Reid and E. J. Breton (Williams, 2003). These membranes had a very low flux due to the excess thickness a free standing membrane was required. It was in 1962 that a major advancement was made by Loeb and Sourirajan, who developed an anisotropic cellulose acetate membrane. It had a thin layer on top of a highly porous and thick substrate (Williams, 2003). This made RO a practical desalting process exhibiting salt rejection values of about 99.5%. Subsequently, different types of designs such as tubular, hollow fiber, and spiral wound were developed as shown in **Figure 1** to utilize the membranes on a commercial scale (Li and Wang, 2013).

The Loeb-Sourirajan membrane became an industry standard until the 1970s, when the IP method for composite membrane fabrication was developed by John Cadotte of Dow FilmTec (Li and Wang, 2013). This involved placing an ultra-thin aromatic top layer on a porous ultrafiltration membrane via the IP process. The aromatic structure made it highly durable making it the technologically most advanced membrane at that time. The applications of these membranes have been extended to the removal of other dissolved solutes from various feed waters (Ex. FT-30 membrane developed by Cadotte at Dow FilmTec). Modifications in membrane design, configuration, and introduction of pre-treatment and post-processes allowed the energy consumption of RO desalination to be reduced from six k Wh/m<sup>3</sup> (in the 1980s) to 1.8 k Wh/m<sup>3</sup> (Li and Wang, 2013). The FilmTec membranes continued to dominate the US market till Hoek introduced the first TFN membrane for brackish water reverse osmosis (BWRO) membranes in 2007. In that work, the membrane had zeolite nanoparticles dispersed in the organic solution of an interfacial polymerization reaction. This was commercialized in 2011 through a start-up called NanoH<sub>2</sub>O (NanoH<sub>2</sub>O and Inc. InterNano, 2021). Since then, TFNs have been at the center of attention in membrane technology. The following section delves deeper into the structure and synthesis of TFCs along with its limitations that make TFNs a better choice in most applications.



### 3 THIN FILM COMPOSITE MEMBRANES

TFC membranes are the precursors to TFNs. Composite membranes are a type of asymmetrical membranes that have a dense top layer and a porous support made of different materials. Commercial RO membranes were initially obtained from two kinds of membranes: Polyamide (PA) and Cellulose Acetate (CA) (Li and Wang, 2010; Rana T. M. D. et al., 2011). PA TFCs have two layers; a porous substrate layer (usually made of polysulfone) and a thin layer made of polyamide formed on it (Li and Wang, 2010). The top layer is concerned with permeation properties of the membrane, while the sub-layer, which is porous, provides mechanical strength and support. The advantage of having the two layers made of different chemicals is that each layer can be individually synthesized or customized so as to optimize the overall performance of the membrane (Louie et al., 2006). Compared to CA membranes, TFCs exhibit better salt rejection, water flux and resistance to biological attacks, apart from being able to operate at wider range of pH (varying from 1–11) and temperatures (varying from 0–45°C) (Li and Wang, 2010). The following subsection discusses the techniques involved in the fabrication of TFCs.

#### 3.1 Synthesis of TFCs

The methods of fabrication include techniques such as IP, solution mixing and polymer melt blending (Kim and Deng, 2011) of which IP has been the most common since its introduction in 2007 (Jeong et al., 2007). Generally an asymmetric membrane prepared through phase inversion is the support layer (Ghosh and Hoek, 2009). Polymers generally used to form the support layers are polysulfone (PSF), polyimide (PI), polyethersulfone (PES), polyacrylonitrile (PAN), and polypropylene (PP) (Ghosh and Hoek, 2009). Various techniques can be used to deposit a thin layer on a porous sub-layer one of these is IP. The traditional synthesis technique requires the dissolution of a difunctional amine in water and a trifunctional acid halide in an organic solvent. The solvent is usually chosen such that water and the solvent are immiscible. The support membrane (usually PSF) is initially immersed in the aqueous solution and, after saturation, is then immersed into the organic phase. Upon immersing in the organic phase, there is a polymerization reaction between the monomers to form the thin layer (Ghosh and Hoek, 2009). Alternatively, there is another method of IP known as the SIM method. In this method, the organic phase is poured over the membrane as it already has amines present on it due to phase inversion. This method is more efficient as there is more complete wetting, which results in a more homogenous, defect-free layer as compared to the traditional methods (Hermans et al., 2014).

TFCs have been a boon to membrane based technologies. However, they do have some limitations. These have been discussed in sub Section 3.2.

#### 3.2 Limitations of TFCs

One of the biggest advantages of a TFC is that one can control and optimize each layer individually to improve its function. A high solvent flux can be obtained without compromising on the salt

rejection. In addition, they are also much stronger and more stable (Petersen, 1993). However, in spite of the above advantages, TFCs have a few limitations which cannot be neglected.

One of the main drawbacks is its low resistance to chlorine (Lau et al., 2012). Chlorination of the main group present in the PA layer increases the hydrophobic nature of the membrane, which in turn decreases flux (Hermans et al., 2015). Chlorine is abundantly present in waters to be treated as chlorination is an important disinfection and pre-treatment step. Therefore, this is a significant performance inhibitor. TFCs are also very susceptible to fouling over time by microorganisms or organic compounds which leads to decline or deterioration of membrane performance. The process of de-fouling increases costs and energy consumption. In addition, high temperatures can also cause collapsing or compactness of pores in the membrane (Hermans et al., 2015).

To overcome these limitations, various methods were developed with the intent to improve the fouling resistance and chlorine resistance of TFCs thereby increasing their performance. This can primarily be done through modifications in the substrate. The following subsection discusses this aspect in details.

#### 3.3 Methods of Membrane Modification

##### 3.3.1 Modifications in the Substrate

Polysulfones are very commonly used as a substrate for the fabrication of TFCs. In recent years, substantial research work has been conducted with the aim to enhance membrane performance by modifying the substrate layer, either by the inclusion of organic solvents such as *n*-methyl pyrrolidone in precipitation, or by addition of hydrophilic agents such as polyethylene glycol (Zhou et al., 2009). Methods that have been reported to increase the fouling resistance and chlorine stability have been discussed in the subsequent sub sections.

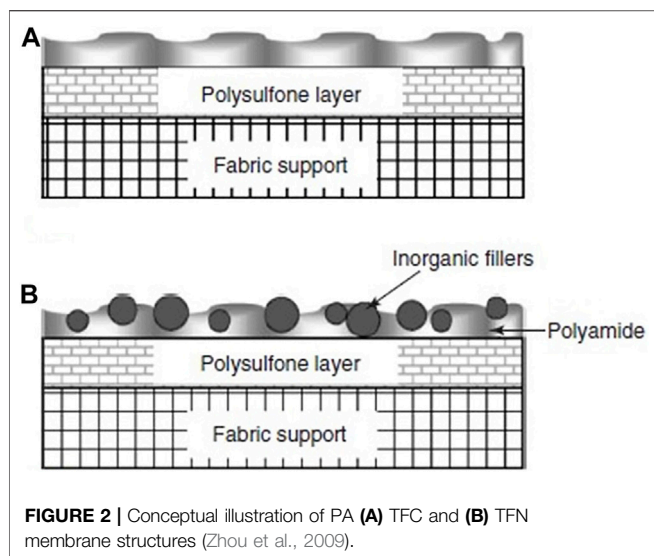
##### 3.3.2 Increase in the Fouling Resistance

The fouling of the membrane can lead to decreased water flux, which in turn leads to increased energy consumption to pump water through membranes. TFCs can be modified by physical or chemical methods so as to reduce fouling (Li and Wang, 2010). Physical methods include applying a coating on the surface of the membrane without interfering with the chemical structure of the material. Polyvinyl alcohol and polyethyleneimine are some of the polymers that have been used in this manner in recent studies (Kim et al., 2004; Louie et al., 2006; Zhou et al., 2009). As an example, polyethyleneimine can invert surface charges on polyamide membranes so as to reduce fouling by cationic substances by electrostatic repulsion (Zhou et al., 2009).

Chemical modification methods can also be used to increase fouling resistance. Monomers can be covalently attached to the monomers on membrane surfaces by radiation or redox grafting methods. This modification of the surface of membranes can lead to a decrease in contaminant adsorption for certain polymers (Li and Wang, 2010).

##### 3.3.3 Increase in Chlorine Stability

The chlorine resistance of the PA layer of the membranes depends upon the chemical nature of the diamine structure.



Chlorine resistance will be high if the amino groups have the following structures: i) aromatic diamines that have a mono methyl or chlorine substitutes at the ortho position of the amino groups; or with amino groups at ortho-position, compared with those at meta- and para-position; ii) aliphatic or cycloaliphatic diamines that possess a secondary amino group or a short methylene chain length between end amino groups; iii) secondary aromatic diamines (Li and Wang, 2010).

Chlorine resistance can also be increased by the addition of certain types of monomers. For example, membranes produced via IP by introducing -OH functional group containing monomers such as m-aminophenol and bisphenol-A show greater chlorine resistance than MPD-TMC polyamide membranes (Li and Wang, 2010). Another method is incorporating ester linkages by substituting aromatic amines, as this reduces the number of available sites for chlorine attack (Li and Wang, 2010).

Incorporation of nanoparticles in TFCs results in TFNs. These have a large number of preferable characteristics. The details of TFNs have been discussed in Section 4 starting with the processes developed for the synthesis of the same.

## 4 SYNTHESIS OF TFNS

TFNs can be synthesized by IP, solution mixing or polymer melt blending (Kim and Deng, 2011). One of the more commonly used techniques is IP (Jeong et al., 2007). Preparation of TFNs takes place in almost the same manner as TFCs, except for a step which involves the addition of fillers. Figure 2 illustrates PA in both TFC and TFN membrane structures (Li and Wang, 2010).

The fillers can be added to aqueous or organic phase (Figure 3) based on the properties of the nanoparticle fillers used. The membranes can be dipped into a nanoparticle solution (Shenvi et al., 2015). Once the nanoparticles are embedded in one of the phases, IP is carried out as per standard procedure (Figure 4). In IP, an aqueous amine solution is first used to

impregnate a microporous film. This is followed by a treatment using a multivalent cross linking agent that has been dissolved in a organic fluid, that is immiscible with water, for example, hexane. As a result, a thin polymer film is obtained at the interface of the two solutions. Table 1 summarizes the methods of synthesis and the important properties of various TFNs reported in literature (Petersen, 1993; Kim et al., 2004; Louie et al., 2006; Ghosh and Hoek, 2009; Jadav and Singh, 2009; Zhou et al., 2009; Park K. T. et al., 2010; Li and Wang, 2010; Fathizadeh et al., 2011; Kim and Deng, 2011; Rana T. M. D. et al., 2011; Zhang et al., 2011; Lau et al., 2012; Huang et al., 2013; Kim E. S. et al., 2013; Alam et al., 2013; Baroña et al., 2013; Chan et al., 2013; Pendergast et al., 2013; Shen et al., 2013; Hermans et al., 2014; Zhao et al., 2014; Ghanbari et al., 2015; Hermans et al., 2015; Safarpour et al., 2015; Shenvi et al., 2015).

### 4.1 Position of Fillers

It is difficult to regulate the position of the filler in TFNs. It has been reported that when NaA nanoparticles are dissolved in the aqueous phase, they are more concentrated near the porous sublayer as compared to near the surface of thin film. On the other hand, when NaA nanoparticles were dissolved in the organic phase, they were found to be homogeneously distributed with equal concentrations near the surface and the sublayer (Huang et al., 2013b). It has been reported that the position of the fillers in the membrane can be tuned by selecting an appropriate type of nanoparticle.

Additive nanomaterials have been demonstrated to improve the performance of TFNs. This has been discussed in the following section.

## 5 NEW FUNCTIONALITIES INTRODUCED BY ADDITIVE NANOMATERIALS

The addition of nanoparticles (NPs) provides significant improvements to the membrane performance (Liao et al., 2021). Moreover, the year wise publication status for TFN membranes is also shown in Figure 5. The various NPs that are added in order to aid the adsorption, photocatalysis and antimicrobial properties of TFNs have been discussed in the following subsections.

### 5.1 Adsorption

Membranes can be enabled to adsorb heavy metals from water by the incorporation of NPs inside the polymer matrix. Daraei developed a method to remove copper from aqueous solutions by incorporating PANI/Fe<sub>3</sub>O<sub>4</sub> NPs inside the PES matrix through PI method (Daraei et al., 2012). Elsewhere, Fe-Mn binary oxide (FMBO) is used to remove As (III) (Jamshidi Gohari et al., 2013). These highlight the possibility of nanocomposite membranes being incorporated with adsorbents for removal of contaminants.

### 5.2 Photocatalysis

TiO<sub>2</sub> has been known for its photocatalytic properties and as a result has been used for applications such as water splitting,

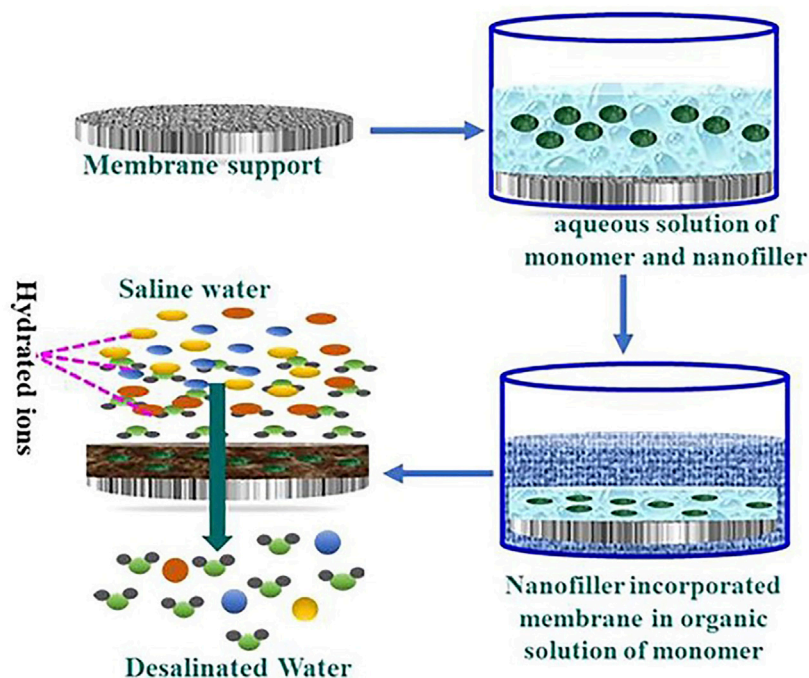


**FIGURE 3** | Diagrammatic representation of manufacturing TFN membrane through interfacial polymerization in the presence of nanofillers (Kumar et al., 2020).

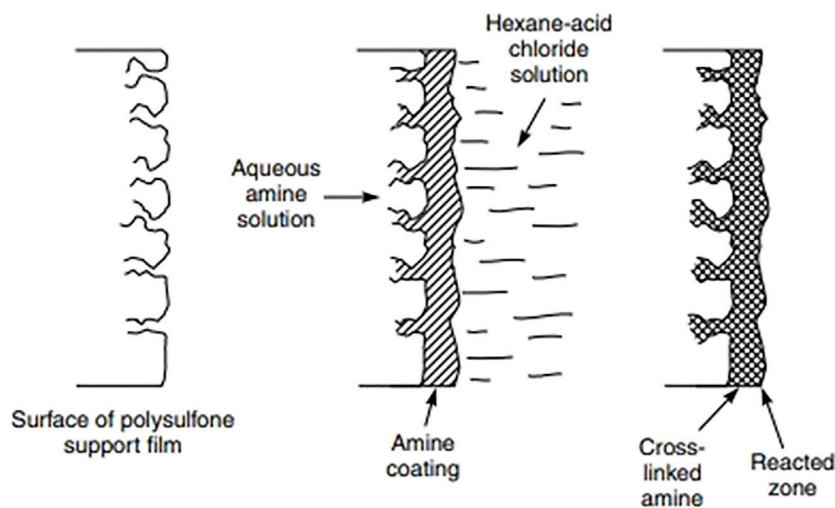


**FIGURE 4** | Schematic of the interfacial polymerization process (Kim and Deng, 2011).

treatment of water and self-cleaning of surfaces. Its stability, ease of preparation and commercial availability add to its functionality (Mills and Le Hunte, 1997; Paz, 2010). Rahimpour found that UV-irradiated  $\text{TiO}_2$ /PES nanocomposite membranes had higher flux and improved fouling resistance compared to ordinary nanocomposite membranes, attributing the improvement to the photocatalysis and high hydrophilicity of  $\text{TiO}_2$  under UV irradiation (Rahimpour et al., 2008).

### 5.3 Antimicrobial Activity

Membrane biofouling, which is caused by microbial growth, has been a major challenge to membrane technology (Zhu et al., 2010). It increases energy costs, decreases permeability, and reduces permeate quality. Hence, developing antimicrobial membranes can result in significant enhancement in efficiency of the separation process. Silver (Ag), due to its impressive biocidal properties, is a highly explored antimicrobial agent and has proven applications in avenues such as antimicrobial coatings, plastics, and wound dressings (Liu

**TABLE 1 | Synthesis and properties of TFNs** (Petersen, 1993; Kim et al., 2004; Louie et al., 2006; Ghosh and Hoek, 2009; Jadav and Singh, 2009; Zhou et al., 2009; Park K. T. et al., 2010; Li and Wang, 2010; Fathizadeh et al., 2011; Kim and Deng, 2011; Rana T. M. D. et al., 2011; Zhang et al., 2011; Lau et al., 2012; Huang et al., 2013a; Kim E. S. et al., 2013; Alam et al., 2013; Baroña et al., 2013; Chan et al., 2013; Pendergast et al., 2013; Shen et al., 2013; Hermans et al., 2014; Zhao et al., 2014; Ghanbari et al., 2015; Hermans et al., 2015; Safarpour et al., 2015; Shenvi et al., 2015).

Polymer matrix	Nanoparticle	Synthesis method	Properties	References
Polyamide(MPD—TMC)	Zeolite A (NaA) (50–150 nm)	IP with zeolite LTA in TMC hexane	Smoother, more hydrophilic, higher water permeability with equivalent salt rejection	Li and Wang, (2010)
Polyamide(MPD—TMC)	Zeolite A (NaA) (100,200,300 nm)	IP with zeolite LTA in TMC-isoparaffin	More permeable, negatively charged, thicker than PA TFC films	Li and Wang, (2010)
Polyamide(MPD—TMC)	Zeolite A(NaA or AgA) (140 nm)	IP with zeolite A in TMC isoparaffin	High water permeability, smooth interface, limited bactericidal activity for AgA membranes	Li and Wang, (2010)
Polyamide(MPD—TMC)	Zeolite A(NaA) 250 nm	IP with zeolite A in TMC-isoparaffin	Different post treatment changing the molecular structure, commercially relevant RO separation	Li and Wang, (2010)
Polyamide(MPD—TMC)	Commercial Silica nanoparticles LUDOX HS-40(16 nm) and TEOS hydrolyzed silican(3 nm)	IP with adding silican in MPD aqueous solution	Tunable pore radius, increasing number of pores, higher thermal stability, high water flux and low salt rejection	Li and Wang, (2010)
Polyamide (MPD-BTC)	Commercial silver nanoparticles (50–100 nm)	IP with adding silver in BTC-HCFC	Slightly lower flux and higher rejection, higher antibiofouling effect	Li and Wang, (2010)
Polyamide(MPD—TMC)	Synthesized TiO <sub>2</sub> (≤ 10 nm)	Self assembly of TiO <sub>2</sub> on the neat MPD-TMC TFC surface	Higher salt rejection and lower flux, higher photocatalytic bactericidal efficiency under UV light	Li and Wang, (2010)
Polyamide(MPD—TMC)	Commercial TiO <sub>2</sub> (30 nm)	IP with adding TiO <sub>2</sub> in TMC-HCFC	Enhanced surface hydrophilicity, comparable water flux and higher salt rejection with limited amount of TiO <sub>2</sub>	Li and Wang, (2010)
Polyamide(MPD—TMC)	Commercial MWCNT(dia: 9–12 nm; length: 10–15 um)	IP with adding MWCNTs in MPD aq. solution	Slightly lower salt rejection and flux; improved chlorine resistance with increase in MWCNT loading	Zhang et al. (2011)
Polyamide(MPD—TMC)	250 nm Linde Type-A zeolite	IP with adding Zeolite A in aq. solution of MPD, TEA, CSA, SLS, IPA	(1) Smoother, more hydrophilic surfaces (2) higher water permeability and salt rejection, and (3) improved resistance to physical compaction	Pendergast et al. (2013)
Sulfonated poly(arylene ether sulfone)—polyamide (MPD-TMC) copolymer	Synthesized mesoporous silica nanoparticles (100 nm)	Interfacial polymerization with adding SiO <sub>2</sub> in TMC-cyclohexane	High water flux and similar salt rejection	Park K. T. et al. (2010)
Polyamide(MPD—TMC)	Polyamide single walled aluminosilicate nanotubes	Ip followed by reacting different imogolite concentrations in 0.01% (w/v) TMC-hexane solution with the top surface of the MPD-soaked membrane	The hydrophilicity was increased as observed in the enhancement in water flux and pure water permeance, due to the presence of hydrophilic nanotubes. With the incorporation of the single-walled aluminosilicate nanotubes, higher permeate flux was achieved while sustaining high rejection of monovalent and divalent ions	Baroña et al. (2013)
Polyamide(MPD—TMC)	Nanozeolite NaX	IP over PES support. Immersed in aq MPD and then n-hexane soln of TMC	The results showed improvement of surface properties such as RMS roughness, contact angle and solid-liquid interfacial free energy, a decrease in film thickness and an increase in pore size and water flux	Fathizadeh et al. (2011)
Polyamide(MPD—TMC)	HNT	IP by pouring MPD over PES Support. TMC solutions in cyclohexane then added to the substrate	Shows increase in hydrophilicity, surface roughness and water flux. Higher loading of HNT results in increase in flux, but decrease in salt rejection	Ghanbari et al. (2015)
Polyamide(MPD - TMC)	silicalite-1 nanozeolite	IP carried out between semi-aligned functionalised CNTs over PES support. Immersed in aq MPD and non aq TMC.	Excellent permeability and chemical stability	Huang et al. (2013a)
Polyamide(MPD—TMC)	zwitterion functionalized CNT	IP over PES support. Immersed in aq MPD and then n-hexane soln of TMC	Increased salt rejection and flux	Chan et al. (2013)
Polyamide(MPD—TMC)	Modified carboxy-functionalized MWNT	IP over PES support. Immersed in aq MPD and then n-hexane soln of TMC	Increasing loading showed increase in flux without significant decrease in salt rejection. Improvement in antifouling and antioxidative properties	Zhao et al. (2014)

(Continued on following page)



**TABLE 1 |** (Continued) Synthesis and properties of TFNs (Petersen, 1993; Kim et al., 2004; Louie et al., 2006; Ghosh and Hoek, 2009; Jadav and Singh, 2009; Zhou et al., 2009; Park K. T. et al., 2010; Li and Wang, 2010; Fathizadeh et al., 2011; Kim and Deng, 2011; Rana T. M. D. et al., 2011; Zhang et al., 2011; Lau et al., 2012; Huang et al., 2013a; Kim E. S. et al., 2013; Alam et al., 2013; Baroña et al., 2013; Chan et al., 2013; Pendergast et al., 2013; Shen et al., 2013; Hermans et al., 2014; Zhao et al., 2014; Ghanbari et al., 2015; Hermans et al., 2015; Safarpour et al., 2015; Shenvi et al., 2015).

Polymer matrix	Nanoparticle	Synthesis method	Properties	References
Polyamide(MPD—TMC)	Reduced graphene oxide/TiO <sub>2</sub>	IP over PES support. Immersed in aq MPD and then n-hexane soln of TMC	Improved water permeability, salt rejection, antifouling property, and chlorine resistance by increasing hydrophilicity, negative surface charge and roughness of PA layer	Safarpour et al. (2015)
Polyamide(PIP-TMC)	PMMA-MWNTs	IP over PES support. Immersed in aq PIP and then toluene soln of TMC	—	Shen et al. (2013)
NMP-PES	nano-Fe <sub>3</sub> O <sub>4</sub>	Solution dispersion blending process and PI	—	Alam et al. (2013)
aPES/HBP	HBP-g-silica	—	enhanced the chlorine resistance of the RO membrane, improved water permeability	Kim K. S. et al. (2013)

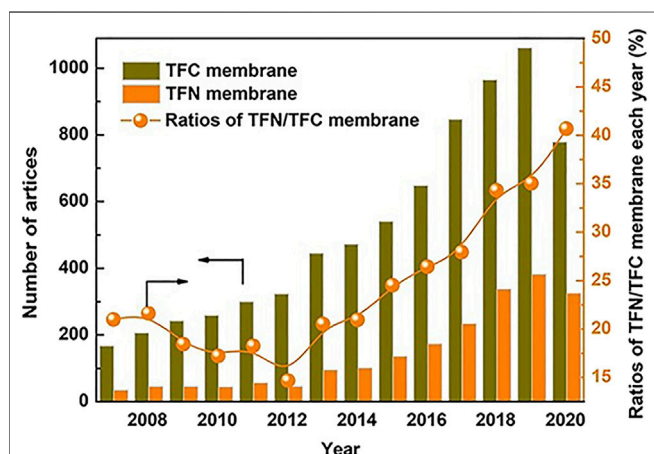


**FIGURE 5 |** Year wise Publication status of TFNs (Liao et al., 2021).

et al., 2008; Lind et al., 2009b). Addition of Ag<sub>2</sub>O nanoparticles not only acts as biocidal agent but also improves the desalination performance of the membrane (Al-Hobaib et al., 2015). Chou used Ag NPs in CA matrix and Zodrow incorporated Ag NPs into PSU matrix to improve biofouling resistance (Chou et al., 2005; Zodrow et al., 2009). **Table 2** provides a summary of the variety of nanoparticles that are used in TFNs (Mills and Le Hunte, 1997; Chou et al., 2005; Liu et al., 2008; Rahimpour et al., 2008; Zodrow et al., 2009; Paz, 2010; Zhu et al., 2010; Daraei et al., 2012; Kim E. S. et al., 2013; Huang S. G. et al., 2013; Jamshidi Gohari et al., 2013; Duan et al., 2015a). The various performance parameters that are utilized in order to characterize TFNs have been discussed in detail in **Section 6**.

## 6 TFN MEMBRANE PERFORMANCE CHARACTERISTICS

Salt rejection and water flux are the two most important parameters that are used to judge the performance of

TFNs. Some of the most important membrane performance parameters have been discussed in the following subsections. These parameters depend upon many factors, some of which are surface roughness, hydrophilicity, surface charge density (Lu et al., 2013; Safarpour et al., 2015). The performance TFNs can be tailored as required by using different nanoparticles as fillers in the thin film, or by even using different methods to synthesize the membrane (Safarpour et al., 2015). **Table 3** lists the different types of nanoparticles used as fillers in TFN membranes reported in literature. For each TFN, the water flux and salt rejection at a particular percentage loading of nanoparticles and the polymer matrix for the membrane is also reported. The last two membranes in **Table 3** are exceptions, as they are not synthesized by IP method. Each of the following subsections deals with commonly used performance parameters.

### 6.1 Water Flux

The measurement of water flux in thin film nanocomposite membranes was performed using a cross-flow membrane module. The water flux was calculated using **Equation 1**:

$$F = V / (At), \quad (1)$$

Where F is the pure water flux, V is total volume of permeated pure water, A is area of the membrane, and t is the operation time (Wu et al., 2010).

Nanoparticles in the thin film membrane can lead to an increase in hydrophilic nature and decrease in cross-linking of the membrane which consequently contributes to high flux of water through the membrane. Increased water flux can also depend upon the structure of the nanoparticle used. For example, MCM-41 silica nanoparticles are porous in nature (Yin et al., 2012). These pores inside the nano-particles present in the thin film membrane can act as short pathways for preferential passage of water molecules through the nanoparticle (Yin et al., 2012). Water tends to move faster through hydrophobic porous particles than hydrophilic non-porous particles (Duan et al., 2015b). The nanomaterials



**TABLE 2 |** Summary of nanoparticles used in TFNs (Fathizadeh et al., 2011; Daraei et al., 2012; Huang et al., 2013a; Kim E. S. et al., 2013; Alam et al., 2013; Baroña et al., 2013; Huang et al., 2013b; Chan et al., 2013; Shen et al., 2013; Zhao et al., 2014; Ghanbari et al., 2015; Safarpour et al., 2015).

Nanoparticle	Aqueous phase	Salt in feed	Applied pressure(psi)
multiwalled cnt; <8 nm diameter	MPD 2%wt	NaCl 1,000 ppm	100
halogen reactive, nitrogen from amines, imides, sulfonamides	MPD 4%wt	—	—
Zeolite A (0.4% w/v) (in organic phase)	MPD 2%wt	NaCl 2,000 ppm	180
Linde type A(LTA) zeolite nanocrystals	MPD(2–3% w/v) TEACSA(6% w/v) SLS(0.02% w/v) IPA (0–29% w/v)	NaCl 2,000 ppm	224.8
TiO <sub>2</sub> (in organic phase)	MPD (2%wt) NaOH(0.05wt%)	MgSO <sub>4</sub> 2,000 ppm	87
Ag nanoparticles	MPD(2%wt) NaOH	MgSO <sub>4</sub> 2,000 ppm	125–250
0.2 w/w% zeolite-A nanoparticles in the TMC solution	MPD(2% w/v) TEA(2%)CSA(4% w/v) SLS(0.02% w/v) IPA (10% w/v)	NaCl 10 mM soln	225
Polyhedral Oligomeric Silsesquioxane(POSS) (in organic phase)	MPD(2wt%)	NaCl 2,000 ppm	225
Oxidized MWNT	—	NaCl and MgSO <sub>4</sub> 2,000 ppm each	—
AluminoSilicate SWNT	—	—	—
nanozeolite NaX	MPD	—	175
HNT	MPD 2% w/v	NaCl 2,000 ppm	218
silicalite-1 nanozeolites	MPD 2% w/v	—	—
zwitterion functionalised CNT	MPD 2% w/v	NaCl 1,000 ppm	530
Modified carboxy-functionalised MWNT	MPD 2% w/v	NaCl 2,000 ppm	232
Reduced graphene oxide/TiO <sub>2</sub>	MPD 2%wt	NaCl 2,000 ppm	218
PMMA-MWNTs	PIP	NaCl 2,000 ppm	145
nano Fe <sub>3</sub> O <sub>4</sub>	NMP	—	—
mesoporous SiO <sub>2</sub> nano-particles	sulfonated poly(arylene ether sulfone)	NaCl 2,000 ppm	225
HBP-g-silica	aPES-MPDA-TEA	—	—
nano ZnO	MPD(2%)-TMC(0.1%)	—	—

possess high surface porosity resulting in improved salt rejection capacity and reduced macro void formation.

Carbon nanotubes also facilitate high flux of water, as they act like channels for transportation of water (Safarpour et al., 2015). This reduces the water transport route as the water molecules can enter into part of the multiwalled carbon nanotubes (MWCNTs) instead of passing through the entire PA film. Aggregation of these nanoparticles might also lead to the formation of a network inter-connected with other pores in the membrane leading to a higher increase in water flux (Zhang et al., 2011).

## 6.2 Salt Rejection

For all the data reported, salt rejection is calculated using the formula:

$$R = 1 - C_p / C_f, \quad (2)$$

Where R is salt rejection,  $C_p$  is concentration of salt in the permeate solution, and  $C_f$  is concentration of salt in the feed solution (Wu et al., 2010).

Salt rejection is governed by factors such as defects and molecular sieving. Also, it is known that for transport of ions of different valences through carbon channels with negatively charged functional groups, ion exclusion depends more upon electrostatic interactions (Donnan exclusion) rather than steric hindrance (Shen et al., 2013). It is also known that high crosslinking in the MPD-TMC (m-phenylene diamine—trimesoyl chloride) layer causes higher salt rejection and lower NaCl permeance (Duan et al., 2015b).

As reported by Safarpour, increase in rGo/TiO<sub>2</sub> loading in thin film membrane leads to decrease in roughness of membrane (Safarpour et al., 2015). This is due to the increase in hydrogen bonding between the hydrophilic nanoparticles and polyamide layer. It was also observed that increase in nanoparticle loading causes decrease in contact angle with water, which is an indication of increasing hydrophilicity of membrane. This can be understood based on the increase of surface charge density. Another trend observed is how the pure water flux increases with the increase in nanoparticle loading. This is expected as an increase in hydrophilicity leads to increased flux (Safarpour et al., 2015).

## 6.3 Selectivity Versus Permeability

Permeability and selectivity are two major performance factors for membrane technology. In improving the performance of membranes, there is always a trade-off between these two factors. In an attempt to achieve high levels of water flux, a decrease in salt rejection is obtained. For example, work done by Jun Yin shows a large trade-off between flux and salt rejection (Yin et al., 2012). Pure water flux increases with percentage loading of MWCNTs, from 20 LMH at zero loading of MWCNTs to 71 LMH at 0.1% w/v of MWCNTs. Salt rejection is observed to decrease with increase in loading of MWCNTs, from 94% at zero loading of MWCNTs to 82% at 0.1% w/v of MWCNTs.

The incorporation of nanomaterials could alter the physicochemical properties of the membrane such as cross

**TABLE 3 |** Water flux and NaCl rejection at given loading of nanoparticle fillers in TFN membranes (Fathizadeh et al., 2011; Daraei et al., 2012; Huang et al., 2013a; Kim E. S. et al., 2013; Alam et al., 2013; Baroña et al., 2013; Huang et al., 2013b; Chan et al., 2013; Shen et al., 2013; Zhao et al., 2014; Ghanbari et al., 2015; Safarpour et al., 2015).

Filler	Polymer matrix(for membranes manufactured by IP)	% Loading	Water flux (L/m <sup>2</sup> .h)	Salt rejection (%)	Salt solution	Pressure psi
Zeolite particles(NaA)	MPD-TMC	0.4(w/v)	0.95	92.0 ± 1.9	NaCl 2,000 ppm	179
Linde type A-1 (NaA)	MPD-TMC	0.2(w/v)	66.6	92.0 ± 0.5	NaCl 2,000 ppm	224.8
AgA	MPD-TMC	0.4 (w/v)	42.5 ± 1	93.5 ± 1	NaCl 2,000 ppm	225
MWNT (conventional process)	TEOA-TMC	0.05(w/v)	2.6 ± 0.1	Not reported	N/A	87
MWNT (improved process)	TEOA-TMC	0.05(w/v)	4.5 ± 0.5	Not reported	N/A	87
Ag2O (max - flux condition)	MPD-TMC	0.03(wt)	40.43 ± 3	99 ± 0.1	NaCl 2,000 ppm	225
Ag2O (max - rejection condition)	MPD-TMC	0.03(wt)	40.43 ± 3	99 ± 0.1	NaCl 2,000 ppm	225
MgTiO <sub>3</sub>	MPD-TMC	0.1(wt)	45	98	NaCl 2,000 ppm	225
Al <sub>2</sub> O <sub>3</sub>	MPD-TMC	1 wt	5	88	NaCl 2,000 ppm	145
Aluminosilicate single walled nanotubes	MPD-TMC	0.59 wt	24.6	96.24	0.034 M	232
HNT (max flux)	MPD-TMC	0.1(w/v)	48 ± 3	80 ± 3	NaCl 2,000 ppm	218
HNT (max rejection)	MPD-TMC	0.05(w/v)	36 ± 2	95 ± 2	NaCl 2,000 ppm	218
CNT	MPD-TMC	0.1(w/v)	28.05	90	NaCl 2,000 ppm	232
Silica (mcm-41) nanoparticles (max flux)	MPD-TMC	0.05(wt)	46.6	97.9	NaCl 2,000 ppm	290
Silica (mcm-41) nanoparticles (max rejection)	MPD-TMC	0.1(wt)	46	98.9 ± 3	NaCl 2,000 ppm	305
non porous spherical silica nps (max flux)	MPD-TMC	0.1(wt)	36 ± 2	97.6 ± 2	NaCl 2,000 ppm	319
non porous spherical silica nps (max rejection)	MPD-TMC	0.05(wt)	35 ± 2	98.1 ± 2	NaCl 2,000 ppm	334
Zwitter ion functionalised CNTs (max flux)	MPD-TMC	20 wt	28.5	98.6	NaCl 1,000 ppm	530
Carboxy functionalised MWNTs (max flux)	MPD-TMC	0.1(wt)	28 ± 2	90	NaCl 2,000 ppm	232
Reduced graphene oxide/TiO <sub>2</sub>	MPD-TMC	0.02(wt)	51.3	99.45	NaCl 2,000 ppm	218
PMMA-MWNT	PIP-TMC	0.67 g/L	5	44.1	NaCl 2,000 ppm	145
POSS-1 (max flux)	MPD-TMC	0.4 w/v	33. ± 3	98.2 ± 0.3	NaCl 2,000 ppm	225
POSS-2 (max flux)	MPD-TMC	0.4 w/v	27.1 ± 1.1	98.9 ± 0.2	NaCl 2,000 ppm	225
POSS-3 (max flux)	MPD-TMC	0.4 w/v	33.4 ± 1.1	98.6 ± 0.3	NaCl 2,000 ppm	225
POSS-4 (max flux)	MPD-TMC	0.4 w/v	3.2 ± 0.7	95.9 ± 0.6	NaCl 2,000 ppm	225
ZIF-8 (max flux)	MPD-TMC	0.4 (w/v)	51.92 ± 1.1	98.5 ± 0.3	NaCl 2,000 ppm	225
ZIF-8 (max rejection)	MPD-TMC	0.1 (w/v)	36 ± 1.2	99.2 ± 0.4	NaCl 2,000 ppm	225
acidified MWCNT (max flux)	MPD-TMC	0.1 (w/v)	71	82	NaCl 2,000 ppm	232
acidified MWCNT (max salt rejection)	MPD-TMC	0.1 (w/v)	20	94	NaCl 2,000 ppm	232
Nano-ZnO	MPD-TMC	0.5 wt%	32	98	Not reported	225
nano-Fe <sub>3</sub> O <sub>4</sub> (max flux condition)	PES dissolved in NMP (not by IP)	15(wt)	280 ± 3	39	NaCl 2,000 ppm	145
nano-Fe <sub>3</sub> O <sub>4</sub> (max rejection condition)	PES dissolved in NMP (not by IP)	10(wt)	75 ± 3	68	NaCl 2,000 ppm	145

linkage, charge density and hydrophilicity. This provides specific water pathways that could conquer the permeability-selectivity trade-off. These facts are evident by the advantage of polydopamine coating that provides ZIF-8 nanoparticles with dispersibility in water (You et al., 2021) and other recent works on TFN membranes (Jeon and Lee, 2020; Saleem and Zaidi, 2020; Siew Khoo et al., 2021). Such TFN membranes exhibited improved permeability in desalination.

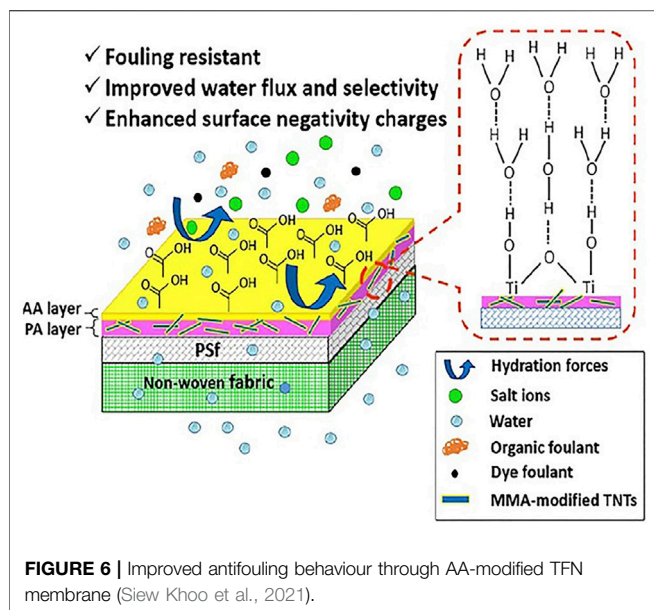
Almost all studies that used hydrophilic nanofillers showed a decreased contact angle in the TFNs, proving improved surface hydrophilicity. With increase in zeolite loading from 0 to 0.4% (w/v) the contact angle of zeolite-PA TFN membrane has been seen to decrease from around 70° to 40° (Jeong et al., 2007). Other examples of oxidized MWNTs-PA TFN membranes and silica-PA TFN membranes have also displayed a significant reduction in contact angle with increase in loading up to certain specific values (Zhang et al., 2011; Yin et al., 2012). This indicates enhanced water permeability with an increase in nanofiller loading.

Two possible explanations have been proposed for the decrease in the contact angle due to the nanoparticles (NPs). The first ascribes the increased surface hydrophilicity to the hydrolysis of acyl chloride resulting in the generation of

carboxylic acid functional groups. This phenomenon occurs due to increased count of surface acyl chloride groups in TMC that remain without reacting with the dimethyl pimelimidate's (DMP) amine group as a result of NPs hydrating and releasing heat when in contact with the MPD aqueous solution (Kim et al., 2000; Ghosh et al., 2008). The second suggests that the presence of embedded hydrophilic NPs on the membrane surface offers larger number of hydrophilic functional groups to the surface.

Along with hydrophilicity, the thickness and the cross-linkage condition of the thin-film layer are key factors in determining the water permeability and selectivity (Ghosh et al., 2008). Generally, a lesser extent of cross-linking and thinner films offer higher permeability. Incorporation of NPs in the PA matrix could reduce cross-linking in the thin-film layer by disrupting the reaction between amine groups and acyl chloride groups. Lind showed through FTIR and XPS results that the cross linking in all their TFN membranes were less compared to the corresponding TFC membranes (Lind et al., 2010). However, it was put forward that molecular sieving or defects could have played an important part in the performance.

Furthermore, the inclusion of NPs may also produce additional channels for the flow of water while excluding the



solutes. A higher value of water flux with constant salt rejection in zeolite-A NP TFNs was reported by Jeong (Jeong et al., 2007). The hydrophilic molecular sieving NPs may provide preferential flow paths for water molecules. Yin showed that mesoporous silica NPs with highly ordered hexagonal pores exhibit higher permeability compared to nonporous silica NPs (Yin et al., 2012). The nonporous silica NPs resulted in cross linking thereby increasing permeability compared to regular TFCs. The increase in permeability was even higher for the mesoporous silica NP TFNs.

It is desired to significantly improve permeability while maintaining the same salt rejection. However, in order to exploit the favorable properties of the NPs, it is necessary to optimize the internal structure, size and surface properties while ensuring suitable interfacial interactions with the polymer.

## 6.4 Antifouling

Extensive research has been conducted on incorporating nanoparticles that reduce the fouling of membranes, hence prolonging the duration for which the membrane can be used. It is known that the antifouling ability is related to the hydrophilic nature, negative charge and smoothness of the membrane (Shen et al., 2013). The anti-fouling performance of membranes can be evaluated by conducting filtration experiments. The membrane is first compacted using distilled water. This ensures that an almost constant permeate flux is obtained. This is necessary as the initial flux affects the extent of fouling. A protein solution, for example BSA (bovine serum albumin) that possesses synergistic fouling effects, is then taken in the reservoir in order to conduct the permeating experiment for a definite time period. The fouling capacity is measured based on the decline in the flux with time (Shen et al., 2013).

The incorporation of hydrophilic NPs into the PA structure has been shown to increase hydrophilicity of the surface and usually helps diminish surface fouling. Long term fouling tests

with silica particles, chloroform, and sodium humate have shown TFN membranes to have a much lower flux reduction when compared to TFC membranes (Rana D. et al., 2011). Extensive research work has been conducted to investigate the antifouling ability of TFNs shown in Figure 6 (Safarpour et al., 2015; Siew Khoo et al., 2021). In order to compare the antifouling properties, water flux through a pristine RO membrane was compared to flux through a TFN with 0.02 % wt. loading of rGo/TiO<sub>2</sub> under the same applied pressure. The flux through the former dropped to 49% of its value whilst the flux through later decreased to 75% of its value after 180 min of filtration (Safarpour et al., 2015). Hence the presence of fillers in thin film membrane leads to better antifouling resistance. Similarly, recent reports show how the introduction of carboxyl-functionalized MWCNTs reduces fouling (Zhao et al., 2014). This has been attributed to the negative surface charge and greater surface hydrophilicity (Lau et al., 2015).

## 6.5 Chlorine Resistance

Polyamide (PA) based membranes do not have a good resistance to continuous exposure of oxidizing agents. Chlorine is widely used as disinfectant in water treatment (Park et al., 2008). However, chlorine is also a strong oxidizing agent and feed water coming to membrane units from disinfection plants contains chlorine. PA membranes cannot tolerate water having chlorine even in the order of few parts per billion, and the chlorine treatment is required to check the development of biofilms on the membrane. Removing the chlorine from water is an undesired option as this will increase the number of treatment steps, and the overall cost of water treatment. Hence there is a need to increase the resistance of membranes to chlorine (Lau et al., 2015). In order to study the chlorine resistance of a membrane, it is subjected to a high concentration of free chlorine for a short time, which is essentially analogous to the exposure of the membrane for a long time to free chlorine of low concentration (Shen et al., 2013). In order to conduct this study, chlorinate solution is prepared and, the water flux and salt rejection of the required membrane, before and after chlorination is measured and compared (Shen et al., 2013).

As reported by Safarpour et al. (2015), salt rejections before and after exposure to sodium hypochlorite for pristine membrane and TFN were compared to study the chlorine resistance (Safarpour et al., 2015). The bare membrane (without any modifications) showed a decrease in salt rejection from 95.4 to 65.38%, while the TFN membrane with 0.02% loading of rGo/TiO<sub>2</sub> showed decrease from 99.45 to 96.4% (Safarpour et al., 2015).

Exposure to chlorine can cause ring-chlorination and N-chlorination reactions which disrupt the symmetry of the PA layer converting it from a crystalline state to an amorphous one (Safarpour et al., 2015). This leads to larger free volumes and flexibility of the PA layer that allow salt molecules to pass through easily. On the other hand, the intermolecular hydrogen bonds are amplified by interaction between rGo/TiO<sub>2</sub> particles and membrane active layer (Safarpour et al., 2015). This can provide obstruction to the substitution of hydrogen with chlorine on the amide groups of

**TABLE 4 |** Summary of TFNs and their composition, performance, fabrication and applications.

TFN		Particle size	Loading wt%(best performance)	Fabrication method	Application	Performance	References
Filler	Polymer						
Oxidized MWNTs	Pebax 1074 or PVA	OD:20–40 nm; L:5–15 $\mu$ m	0–20% of polymer(10% of PVA)	Coating + solvent evaporation	Water/oil emulsion separation	Under 100 psi, optimal water flux is 330 L/m <sup>2</sup> h, organic solute rejection is 99.8%; Fouling resistance $\uparrow$	Wang et al. (2005)
Zeolite(NaA)	PA	50–150 nm	0.004–0.4% (w/v) in organic phase	IP	RO	Surface hydrophilicity $\uparrow$ ; Pw $\uparrow$ ; Salt rejection no change; New concept: TFN	Jeong et al. (2007)
Ag NPs	PA	50–100 nm	10% of polymer in organic phase	IP	NF	Water flux and salt rejection no change; Good antibiofouling property	Lee et al. (2007)
TiO <sub>2</sub> (P25)	PA	30 nm	1.0–9.0% (5.0%) organic phase	IP	NF	Under 87 psi, optimal water flux is 9.1 L/m <sup>2</sup> h, MgSO <sub>4</sub> rejection (95%, 2000 mg/L)	Lee et al. (2008)
Silica(LUDOX HS-40)	PA	13.2 nm	5–28% of PA	IP	Dioxane solution filtration	Pw $\uparrow$ ; Solute rejection $\downarrow$	Singh and Aswal, (2008)
Zeolite (NaA and AgA)	PA	50–250 nm	0.4% (w/v) in organic phase	IP	RO	Pw $\uparrow$ ; Salt rejection no change; AgA-TFN membranes exhibited more hydrophilic and smooth surfaces	Duan et al. (2015a)
Zeolite	PA	97, 212–286 nm	0.2% (w/v) in organic phase	IP	RO	Smaller NPs produced higher permeability enhancements, but larger NPs produced more surface properties change	Li et al. (2013)
Silica	PA	3–16 nm	0–0.4% (3 nm) and 0–0.5% (16 nm) in aqueous phase	IP	RO	Pw $\uparrow$ ; NaCl rejection $\nearrow$ ; Thermal stability $\uparrow$	Jadav and Singh, (2009)
Oxidized MWNT's	PVA	OD:8–15 nm; L: 10–50 $\mu$ m	10% of PVA	Coating + Cross-linking	UF of oil/water emulsion	Pw $\uparrow$ ; Solute rejection slightly decreased;	Ma et al. (2010)
Cellulose Nanofibers		OD: 5 nm; L < 10 $\mu$ m	0.25 and 1.25% of PVA			Suggested the presence of directional water channels through the interface between filler and PVA matrix	
Carboxylic MWNTs	Polyester	OD < 8 nm; L = 10–30 $\mu$ m	0.05%(w/v) in aqueous phase	Modified IP; O/ A/O	NF	Pw $\uparrow$ ; Na <sub>2</sub> SO <sub>4</sub> rejection $\uparrow$ ; Immerse support layer into organic phase before conventional IP process improved TFN performance	Wu et al. (2010)
MWNTs	PA	OD = 9–12 nm; L = 10–15 $\mu$ m	0.1, 0.5, 1, 5% (w/v) in aqueous phase	IP	RO	Surfactant (Triton X-100) was used to facilitate the dispersion of MWNTs; Chlorine resistance $\uparrow$	Park J. et al. (2010)
Zeolite (LTA)	PA	~250 nm	0.2% in organic phase	IP	Seawater RO	Under 800 psi, optimal permeate flux is around 42 L/m <sup>2</sup> h, NaCl rejection (99.4%, 32,000 mg/L); Defects and molecular-sieving largely govern transport through zeolite-TFN membrane	Lind et al. (2010)
Functionalized Silica	PA	—	0.04, 0.4% in aqueous phase	IP	RO; PV	Small-angle neutron scattering (SANS) was used to study the dispersion of silica NPs in thin-film layer; Thermal	Jadav et al. (2010)

(Continued on following page)

**TABLE 4 |** (Continued) Summary of TFNs and their composition, performance, fabrication and applications.

TFN		Particle size	Loading wt%(best performance)	Fabrication method	Application	Performance	References
Filler	Polymer						
Functionalized MWNTs	PA	OD = ~ 30 nm; L1 = 10–30 µm; L2 = 0.5–2.0 µm	0.01–0.06% in aqueous or organic phase	IP	NF	stability ↑; Pw ↑; NaCl rejection ↓ Pw ↑; Solute rejection no change; Nanogaps around the external surface of fillers provide a low resistance solvent pathway	Roy et al. (2011)
Oxidized; MWNTs	PA	—	0–0.2% (w/v) in aqueous phase	IP	RO	Surface hydrophilicity ↑; Pw ↑; NaCl rejection ↓	Zhang et al. (2011)
Metal alkoxide (TTIP, BTESE, PhTES)	PA	—	0–5% in organic phase	IP	NF/RO	Pore size ↑; Pw ↑; With PhTES, Pw ↑, NaCl rejection no change	Kong et al. (2011)
Zeolite (NaX)	PA	40–150 nm	0.004, 0.01, 0.04, 0.2% (w/v) in organic phase (0.2%)	IP	RO	Thermal stability ↑; Hydrophilicity ↑; Pw ↑; NaCl rejection no change	Fathizadeh et al. (2011)
Hydrophilized ordered mesoporous carbon (OMC)	PA	—	0–10% in aqueous phase (5%)	IP	NF	Hydrophilicity ↑; Protein adsorption ↓; Pw ↑; NaCl rejection ↓; Na2SO4 rejection slightly ↓	Kim and Deng, (2011)
Hydrophilic macromolecules + Ag+	PA	11,000 Da	0.25% of (MDI + PEG) in organic phase; 0.25% of AgNO <sub>3</sub> in aqueous phase	IP	Seawater RO	Good seawater desalination performance; Fouling resistance ↑; Biofouling resistance ↑	Rana D. et al. (2011)
Ag NPs	PA	Several nanometers	Dispersed in aqueous phase Finally, 10% in PA	IP	NF	Surface hydrophilicity ↑; Pw ↑; Salt rejection no change; Biofouling resistance ↑	Kim et al. (2012)
Mesoporous silica (MCM-41) and nonporous silica	PA	~100 nm; ~ 100 nm	0–0.1% in organic phase (0.05%)	IP	RO	Surface hydrophilicity ↑; Pw ↑; Salt rejection no change; Under 300 psi, optimal permeate flux is 46.6 L/m2h, NaCl rejection (97.9, 2000 mg/L); Porous structures of filler contributed significantly to the water flux enhancement	Yin et al. (2012)
Proteoliposome with aquaporin	PA	<150 nm	10 mg/ml in aqueous phase	IP	RO	Pw ↑; Salt rejection no change; Under 72.5 psi, water flux is 20 L/m2h, NaCl rejection (~97%, 584.4 mg/L)	Zhao et al. (2012)
Aluminosilicate SWNTs	PVA	OD = 2.7 nm; L > 200 nm	0–20% (v/v) in PVA solution	Coating + Cross-linking	NF	Surface hydrophilicity ↑; Roughness ↓; Pw ↑; Salt rejection ↑	Baroña et al. (2012)
Zeolite (NaY)	PA	40–150 nm	0–0.4% (w/v) in organic phase (0.1%)	IP	FO	Pw ↗↘; NaCl rejection ↘↗; Surface roughness ↗↘	Ma et al. (2012)
Alumina NPs	PA	~14 nm	1% in organic phase	IP	NF	Surface hydrophilicity ↑; Pw ↑; Salt rejection no change	Saleh and Gupta, (2012)
Oxidized MWNTs	PA	OD = 5–10 nm; L = 10–30 µm	5% of PA	IP	Oil sand process-affected water treatment	Water flux ↑; Organic fraction rejection ↑; Fouling resistance ↑	Kim S. G. et al. (2013)
Zwitterion functionalized CNTs	PA	OD = 1.5 nm; L = 1 µm	0, 9, 20% of PA (20%)	Deposition + IP	RO	Water flux and salt rejection ↑; Under 530 psi, optimal water flux is 48.8 L/m2h, NaCl rejection (98.6%, 2,542 mg/L)	Chan et al. (2013)
Carboxylic MWNTs	PA			Deposition + IP	RO		

(Continued on following page)



**TABLE 4 |** (Continued) Summary of TFNs and their composition, performance, fabrication and applications.

TFN		Particle size	Loading wt%(best performance)	Fabrication method	Application	Performance	References
Filler	Polymer						
		OD < 8 nm; L = 10–30 μm	3 mg per membrane sample			High electrical conductivity (~400 S/m), NaCl rejection (>95%, 1000 mg/L), high water flux; Biofouling resistance ↑ under electric potential	de Lannoy et al. (2013)
Oxidized MWNTs	PVA	OD = 10–30 nm; L = 0.5–2 μm	0, 5, 10, 15% of PVA	Electrospinning + Cross-linking	UF	Water flux ↑; Organic fraction rejection (99.5%); Good mechanical properties	You et al. (2013)
PMMA modified MWNTs	PA	OD = 20–30 nm; L < 50 μm	0–5.4 g/L in organic phase (0.67 g/L)	IP	NF	Pw and selectivity ↑	Shen et al. (2013)
PMMA modified MWNTs	PA	OD = 20–30 nm; L < 10 μm	0.67, 1.33, 2.0 g/L in organic phase (0.67)	IP	NF	Under 145 psi, optimal water flux is 69.7 L/m2h, Na2SO4 rejection (99.0%, 2000 mg/L)	Yu et al. (2013)
Carboxylic MWNTs	PA	OD < 8 nm; L = 10–30 μm	0–2.0 mg/ml in aqueous phase (0.5)	Modified IP; O/ A/O	NF	Pw↗↘; Hydrophilicity↗↘; Under 87 psi, optimal water flux is 21.2 L/m2h, Na2SO4 rejection (>70%, 5 mmol/L)	Wu et al. (2013a)
Amine functionalized MWNTs	PA	OD = ~ 5 nm; L = ~ 50 μm	0.01, 0.05, 0.1% in aqueous phase	IP	FO	Hydrophilicity ↑; S value ↓; Pw and salt rejection ↑ in both AL-FS and AL-DS modes	Amini et al. (2013)
Zeolite (Silicalite-1)	PA	—	0–0.2% in organic phase	IP	RO	Pw, hydrophilicity, and acid stability ↑; Silicalite-1 is superior to NaA in fabricating TFN	Huang et al. (2013a)
Zeolite (NaA)	PA	—	0–0.2%(w/v) in organic phase	IP	RO	Water flux and salt rejection ↑	Huang et al. (2013b)
Aminated Zeolite	PA	≤ 100 nm	0.02% in aqueous solution	IP	RO	Pw ↑; Chlorine resistance ↑; Under 800 psi, water flux is 37.8 L/m2h, NaCl rejection is 98.8% (32,000 mg/L)	Kim S. G. et al. (2013)
Zeolite A	PA	250 nm	0.2% in organic phase	IP	RO	Pw and salt rejection ↑; Resistance to physical compaction ↑	Pendergast et al. (2013)
Modified mesoporous silica	PA	~100 nm	0–0.07% in aqueous phase (0.03%)	IP	NF	Under 87 psi, optimal water flux is 32.4 L/m2h, Na2SO4 rejection (> 80%, 5 mmol/L)	Wu et al. (2013b)
Mesoporous silica	PA	~164 nm	0–0.1% (w/v) in organic phase (0.1)	IP	RO	Pw and hydrophilicity ↑; Under 232 psi, optimal water flux is 53 L/m2h, NaCl rejection (>96%, 2,000 mg/L)	Bao et al. (2013)
Aminated hyper branched silica	PA	~7 nm	0.02% in aqueous solution	IP	RO	Pw ↑; Chlorine resistance ↑; Under 800 psi, water flux is 34.5 L/m2h, NaCl rejection is 97.7% (32,000 mg/L)	Kim K. S. et al. (2013)
Silica	Fluoropolyamide	—	0–1.0% (w/v) in aqueous phase (0.1)	IP	NF	Pw ↑; Na2SO4 rejection↗↘; Under 87 psi, optimal water flux is 15.2 L/m2h, Na2SO4 rejection (85.0%, 2000 mg/L)	Hu et al. (2013)
	PA						

(Continued on following page)

**TABLE 4 |** (Continued) Summary of TFNs and their composition, performance, fabrication and applications.

TFN		Particle size	Loading wt%(best performance)	Fabrication method	Application	Performance	References
Filler	Polymer						
Aluminosilicate SWNT		OD = ~ 2.7 nm; L = 150 nm	0.05, 0.1, 0.2% (w/v) in organic phase	IP (single pass flow)	Low pressure RO	Pw and salt rejection ↑; Resistance to physical compaction ↑	Baroña et al. (2013)
Aminosilanized TiO <sub>2</sub>	PA	~21 nm	0.005, 0.05, 0.1% in aqueous solution (0.005%)	IP	NF	Pw and selectivity ↑; Thermal stability ↑; Under 110 psi, optimal water flux is 12.3 L/m <sup>2</sup> h, NaCl rejection is 54% (2,000 mg/L)	Rajaeian et al. (2013)
Organoclay (Cloisite 15A and 30B)	Chitosan	—	0.5, 1, 2% in casting solution	Coating on PVDF substrate	NF for dye removal	Dye removal ↑; Adsorption is the dominating removal mechanism	Daraei et al. (2013)
Proteoliposome containing Aquaporin Z	PEI	~ 107.8 nm	0, 50, 200, 400 in Lipid-to-protein ratio (200)	PEI crosslinking	NF	Under 14.5 psi, optimal water flux is 36.6 L/m <sup>2</sup> h MgCl <sub>2</sub> rejection (95%, 100 mg/L)	Li et al. (2014)
Carboxylic MWNTs	PA	OD = 20–40 nm; L = 1–5 μm	0–0.1% in MPD solution	IP	RO	Hydrophilicity ↑; Water flux ↑; Solute rejection no change; Better antifouling and antioxidative properties	Zhao et al. (2014)

IP, interfacial polymerization; PA:polyamide; PV, pervaporation; Pw, water permeability.

the aromatic polyamide membranes resulting in an increase in the chlorine resistance of the membrane. TFNs having carboxyl-functionalized MWCNTs as fillers have also been known to show high chlorine resistance (Park J. et al., 2010). Interactions between the carboxyl group and amide layer is understood to be the reason causing this behavior. **Table 4** attempts to summarize a majority of the TFNs reported in literature (Petersen, 1993; Mills and Le Hunte, 1997; Kim et al., 2000; Williams, 2003; Kim et al., 2004; Chou et al., 2005; Wang et al., 2005; Louie et al., 2006; Jeong et al., 2007; Lee et al., 2007; Ghosh et al., 2008; Lee et al., 2008; Liu et al., 2008; Park et al., 2008; Rahimpour et al., 2008; Singh and Aswal, 2008; Ghosh and Hoek, 2009; Jadav and Singh, 2009; Lind et al., 2009b; Zhou et al., 2009; Zodrow et al., 2009; Jadav et al., 2010; Li and Wang, 2010; Lind et al., 2010; Ma et al., 2010; Park K. T. et al., 2010; Park J. et al., 2010; Paz, 2010; Wu et al., 2010; Zhu et al., 2010; Rana D. et al., 2011; Rana T. M. D. et al., 2011; Roy et al., 2011; Kim and Deng, 2011; Kong et al., 2011; Pendergast and Hoek, 2011; Zhang et al., 2011; Baroña et al., 2012; Daraei et al., 2012; Kim et al., 2012; Lau et al., 2012; Ma et al., 2012; Saleh and Gupta, 2012; Yin et al., 2012; Zhao et al., 2012; Alam et al., 2013; Amini et al., 2013; Bao et al., 2013; Baroña et al., 2013; Chan et al., 2013; Daraei et al., 2013; de Lannoy et al., 2013; Hu et al., 2013; Huang et al., 2013a; Huang et al., 2013b; Jamshidi Gohari et al., 2013; Kim S. G. et al., 2013; Kim E. S. et al., 2013; Kim S. G. et al., 2013; Li and Wang, 2013; Lu et al., 2013; Li et al., 2014; Pendergast et al., 2013; Rajaeian et al., 2013; Shen et al., 2013; Wu et al., 2013b; You et al., 2013; Yu et al., 2013; Wu et al., 2013a; Hermans et al., 2014; Subramani et al., 2014; Zhao et al., 2014; Al-Hobaib et al., 2015; Duan et al., 2015a; Duan et al., 2015b; Ghanbari et al., 2015; Hermans et al., 2015; Lau et al., 2015; Safarpour et al., 2015; Shenvi et al., 2015; NanoH<sub>2</sub>O and Inc. InterNano, 2021). The arrows under the application column denote the performance of

the TFN membrane as compared to the parent TFC membrane. For example, in the first row, the fouling resistance of the membrane with Oxidized MWNT nano-fillers increases when compared with the fouling resistance of the TFC membrane without the nano-fillers.

The following section discusses various desalination processes and the use of TFNs along with specific modifications to improve the desalination performance of the same in detail.

## 7 DESALINATION

It is estimated that only 0.8% of the water on Earth is freshwater, while the seas and oceans constitute almost 96% of the water on Earth (Greenlee et al., 2009). To address the increasingly troublesome problem of water shortage around the world, it is important to develop desalination technologies to make use of the salty water from oceans and groundwater aquifers.

The feed water for desalination plants ranges from 10,000 ppm TDS to 60,000 ppm TDS (Mickley, 2001). The concentration of the feed water is the basis upon which desalination plants are designed. Desalination process, energy costs, product recovery and waste management are some of the design choices that are made feed water in mind (Greenlee et al., 2009).

Desalination can be broadly classified into two basic methods; thermal processes and membrane processes (Greenlee et al., 2009). Thermal processes include MED and MFD. MED involves heat transfer between feed water and steam over multiple stages with the aim to desalinate water (Kesime et al., 2013). The process is optimized with the aim to produce the highest amount of fresh water with the least input of energy. MSF is a commonly used technique which involves passing the

feed water through a series of flash chambers to heat the feed seawater, after which the condensate is collected separately (Van der Bruggen and Vandecasteele, 2002). Even though MSF is easier and more reliable than MED, it is more expensive and energy-intensive (Sagle and Freeman, 2004).

Electrodialysis is a type of membrane process, where the water is passed through a series of parallel cationic and anionic membranes, and an electric current is passed through the seawater to cause separation. This method is suitable only for waters having low concentrations, like brackish water (Reahl, 2004). NF is another membrane based process, but cannot be used as a treatment step on its own as it is not able to bring the water down to drinking water standards (Bohdziewicz et al., 1999). Therefore NF is used in association with RO. RO is one of the most popular membrane based processes, achieving salt rejections of greater than 99% (Bates and Cuozzo, 2000). RO membranes can be used for both seawater and brackish waters (Greenlee et al., 2009).

The other methods of desalination are Capacitive Deionization (CDI) and MVC (Bates and Cuozzo, 2000; Van der Bruggen and Vandecasteele, 2002). CDI is an electrochemical method in which the ions are separated by electrosorption onto a porous charged electrode (Zhao, 2013). While CDI has advantages like easy cleaning, low cost and good mechanical properties, there is not enough data for implementation on a large scale (Zhao, 2013). MVC follows the same steps as MED or MFD, except that the vapor is condensed into water using mechanical methods. The energy produced by this is then in turn used to heat the feed. Although this process has a high efficiency, it has some drawbacks like that it is difficult to control and complex and so it is used only in small-scale plants (Sagle and Freeman, 2004).

The following subsections compared the major desalination techniques based on factors like energy demand and cost.

## 7.1 Energy Demands

Energy demand is one of the most important considerations that need to be taken into account for desalination. RO consumes the least amount of energy among MED, MSF and RO (Wade, 1993; Wade, 2001). For RO membranes, energy is consumed in pumping water across the membranes while in MSF and MED energy is consumed in converting water to steam and for running pumps (Sagle and Freeman, 2004). Energy consumption is also affected by the salinity of the feed water (Ettouney et al., 2002). Higher concentration of salt in feed water leads to larger osmotic pressure. Larger osmotic pressure means a larger *trans*-membrane pressure needs to be applied which in turn means larger pressure needs to be applied by the pumps, leading to an increase in the energy consumption (Sagle and Freeman, 2004). The energy consumption of TFNs are improved compared to TFCs for the separation process requirement (Subramani et al., 2014).

While MED and MSF require thermal and electrical energy, RO requires only electrical energy. Assuming water production of 290,000 m<sup>3</sup>/day, average total energy consumption (ATEC) in MW (Mega Watt) for the three processes is graphically shown in Figure 7A.

## 7.2 Cost

Figure 7B allows us to compare the three desalination technologies: MED, MSF and RO, based on the energy consumption and the water cost. The energy cost calculations are based on a plant capacity of a volume 32,000 m<sup>3</sup>/day; and a total dissolved solids (TDS) concentration of 42,000 mg/L. The energy cost used is \$0.053/kWh. The specific heat consumption (abbreviated as SHC in the figure) is expressed in kW<sub>th</sub> h/m<sup>3</sup> and the specific electricity consumption (abbreviated as SEC in the figure) is expressed in kW<sub>e</sub> h/m<sup>3</sup>. The water cost (abbreviated as WC in the figure) calculations are based on a plant capacity of volume 31,822 m<sup>3</sup>/day and a TDS concentration of 37,000 mg/L. Energy costs are expressed in \$1.5/m<sup>3</sup> (Sagle and Freeman, 2004).

It can be seen that RO has the lowest cost per unit volume. RO membranes have a higher initial cost, but the end result is a higher production rate as compared to MED and MSF (Ettouney et al., 2002; Sagle and Freeman, 2004; Kesieme et al., 2013). In fact, it has been concluded by Kesieme that even with the inclusion of carbon tax in Australia, RO continues to be the most cost effective of the discussed desalination processes (Kesieme et al., 2013).

RO is the predominant technology used for desalination. Figure 8 shows the (global) cumulative desalination capacity trends (Zhao et al., 2020) and forecast up to 2030 (Shahzad et al., 2019). It is a common practice to improve parameters like salt rejection and permeate flux using various kinds of NPs. The following subsection discusses such modifications that have been reported in the recent times in detail.

## 7.3 Improvement in Desalination Performance of TFNs

It is possible to improve the desalination performance of TFNs by incorporating NPs like functionalized silica nanoparticles (SNs) into the membrane. SNs can be synthesized in various sizes and with differing surface functionalities like epoxy, amine and hydroxyl. The chemistry, surface hydrophilicity and morphology of TFNs are affected by the various factors like size, concentration and surface functionality of the used SNs resulting in an increase in the permeate flux without any drastic change in the salt rejection. Similarly, it is possible to incorporate various other kinds of NPs in order to improve the desalination performance of TFNs (Zargar et al., 2017).

A polyamide TFN has also been reported that has been incorporated with multiwalled carbon nanotubes-titania nanotubes hybrids (MWCNT-TN). The use of acid treated MWCNT-TN as a filler in the PA membrane results in improvement in the surface properties of the membrane (surface charge, contact angle and roughness) resulting in an increase in the water permeability with negligible change in the salt rejection (Wan Azelee et al., 2017).

ZnO nanostructures like nanorods (R-ZnO), nanoflowers (F-ZnO) and nanospheres (S-ZnO) have been shown to improve the hydrophilicity of the TFN membrane with increase in the ZnO loading. Amongst three nanostructures, S-ZnO has the largest surface area and smaller size. TFNs with S-ZnO incorporated in them were seen to possess the highest

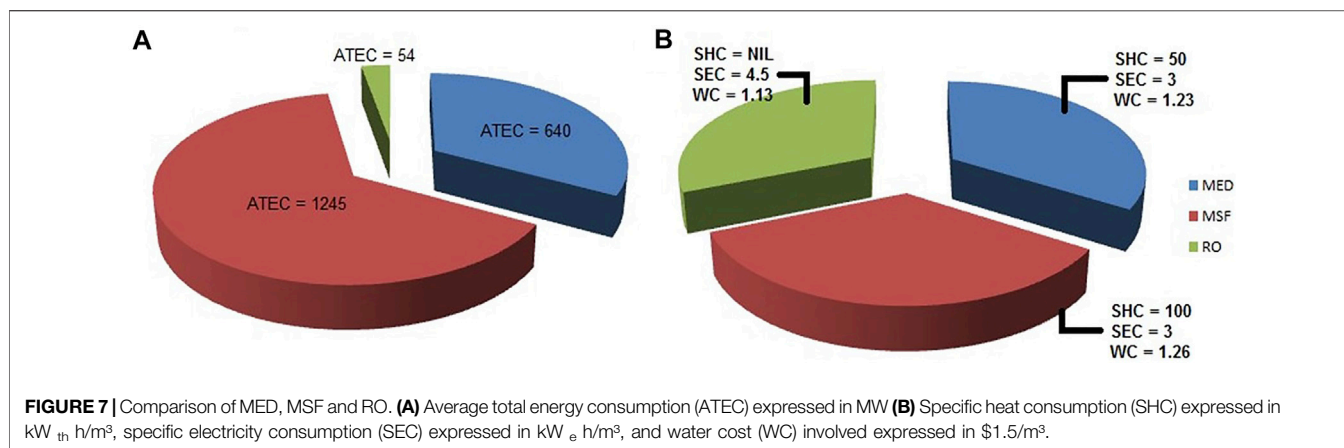


**FIGURE 7 |** Comparison of MED, MSF and RO. **(A)** Average total energy consumption (ATEC) expressed in MW **(B)** Specific heat consumption (SHC) expressed in  $\text{kW}_{\text{th}}/\text{h}/\text{m}^2$ , specific electricity consumption (SEC) expressed in  $\text{kW}_{\text{e}}/\text{h}/\text{m}^2$ , and water cost (WC) involved expressed in  $\$/1.5/\text{m}^3$ .

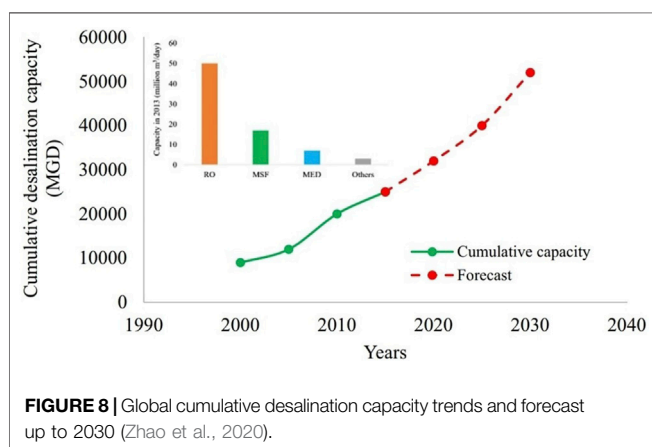


**FIGURE 8 |** Global cumulative desalination capacity trends and forecast up to 2030 (Zhao et al., 2020).

permeate flux with good salt rejection, out of three types of ZnO nanostructures (Rajakumaran et al., 2020).

Similarly, Na + functionalized carbon quantum dot (Na-CQD) incorporated into the PA layer, resulting in a TFN hollow fiber membrane has been shown to possess a much larger effective surface area, a larger number of hydrophilic O-containing groups in the PA layer and a less thickness of the PA layer. These results in a better permeate flux of water enabling use in the desalination of brackish water (Gai et al., 2019).

Another research work done on amino-phenyl modified mesoporous silica NP based TFNs reported a 21.6% increase in water permeability with a marginal decrease in salt rejection (0.29%) compared to pure PA membrane under optimum AMSN dosage of 0.25 g/L (Wang et al., 2019).

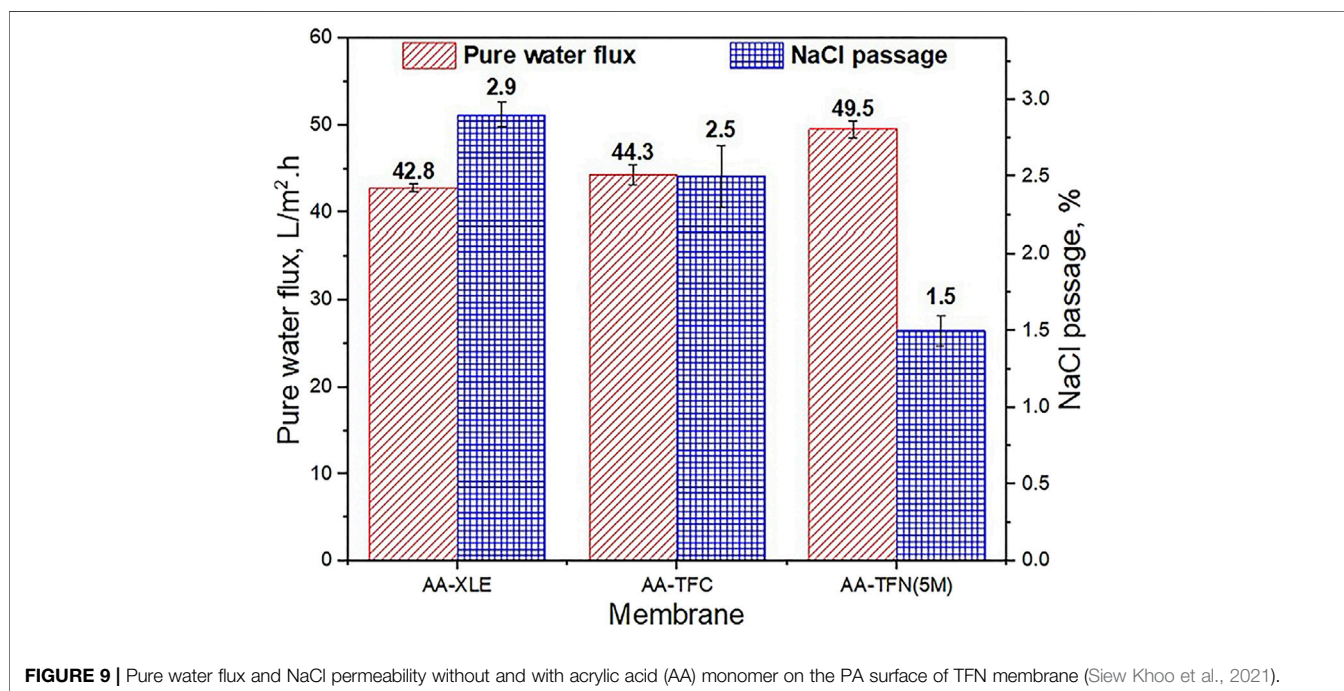


**FIGURE 9 |** Pure water flux and NaCl permeability without and with acrylic acid (AA) monomer on the PA surface of TFN membrane (Siew Khoo et al., 2021).



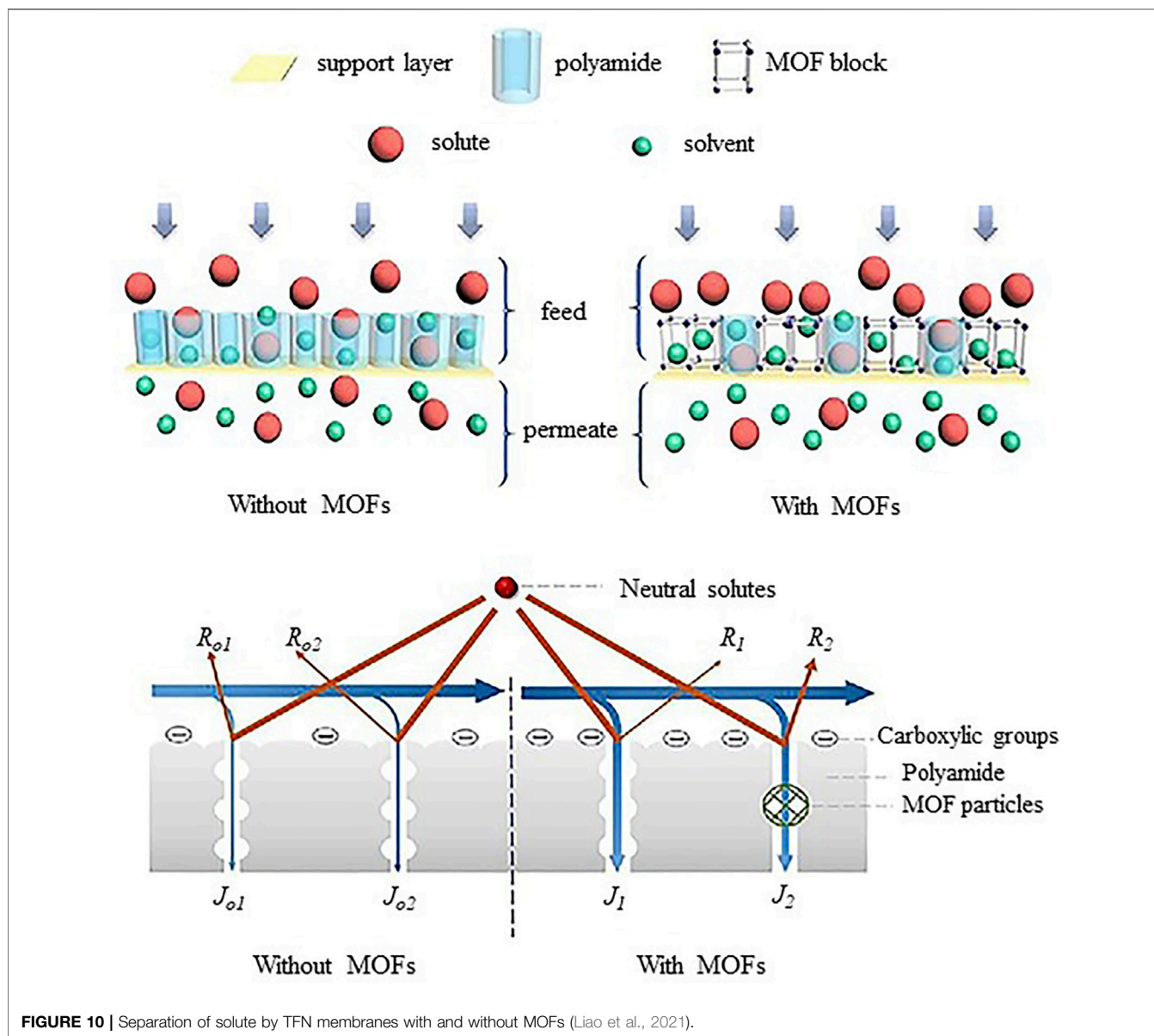


FIGURE 10 | Separation of solute by TFN membranes with and without MOFs (Liao et al., 2021).

TFC membranes modified with Cu-Al layered double hydroxide nanofillers were found to be less negative than the usual TFC membranes and a substantial improvement in the anti-fouling properties was observed indicated by an improvement in water flux by 14% (Tajuddin et al., 2019).

Biopolymer based nanocomposite films, which consist of single dimensional palygorskite (PAL) nanorods and double dimensional montmorillonite (MMT) nanoplatelets in the sodium alginate (SA) film resulted in an enhancement in the tensile stress and the capacity of water resistance of the film (Huang et al., 2018).

All of these above examples showcase some of the numerous recently developed mechanisms to enhance the applicability of thin film nanocomposites in desalination applications by improving the various properties like water permeability and salt rejection of the membrane (Figure 9). However, TFNs

continue to have some limitations, especially those concerning the adverse effects of desalination processes on the environment. Some of these concerns have been discussed in Section 7.4.

## 7.4 Environmental Concerns

Thermal emissions, brine discharge and chemicals used in the process all contribute towards environmental pollution (Van der Bruggen and Vandecasteele, 2002). Thermal emissions are directly related to the electric power consumption in the process. Therefore, RO membranes show the least amount of thermal emissions (Van der Bruggen and Vandecasteele, 2002). The impact of brine discharge on the environment can be determined by the temperature and salinity of the waste stream (Van der Bruggen and Vandecasteele, 2002). Brine released at high temperatures in fresh water bodies can decrease the oxygen content of the water hence harming the



microorganisms present in the water. Since RO process does not involve heating up the water like in MED or MSF, it causes less harm to the environment in this aspect. When evaluating the environmental impact, all chemical additives that have been added to the water have to be considered (Van der Bruggen and Vandecasteele, 2002). Chemicals that might be used to reduce fouling or scaling, enter fresh water bodies, causing water pollution (Van der Bruggen and Vandecasteele, 2002). Taking all factors into account, it can be seen that RO is the least destructive to surroundings (Sagle and Freeman, 2004).

However, as seen in the previous section, RO involves water wastage. In addition, the demineralized water obtained is unhealthy and the process requires energy input. RO also tends to make the water acidic and is unable to remove chlorine, chloramines, volatile organic compounds (VOCs) and pharmaceuticals. In fact, all conventional methods of water treatment have drawbacks. Ultrafiltration is incapable of removing dissolved inorganic components and involves high energy costs. In microfiltration, fouling is a very serious issue and requires regular cleaning. Similarly, in nanofiltration, membrane fouling results in these membranes having a very limited lifetime. Pre-treatment is often a necessity in the case of nanofiltration (Das et al., 2014).

It has been suggested that CNT membranes possess various favorable properties like anti-fouling function, low energy consumption and self-cleaning functions (Das et al., 2014). This makes them a good alternative to conventional water treatment technologies and they might help in eradicating the fresh water crisis very soon (Das et al., 2014). In the following **Section 7.5**, the future scope of thin film nanocomposite membrane and their requisite for design and development towards commercialization for various applications is elucidated.

## 7.5 Future Perspective

Hoek introduced thin film nanocomposite (TFN) RO membranes by incorporating nanoparticles in polyamide layer in 2007 (Jeong et al., 2007). Since then, the new nanoparticles and nanocomposites were researched. The TFN membranes exhibited greater potential in overcoming trade-off between permeability and selectivity. The TFN membranes provided improvement in chlorine resistance and antifouling properties (Wang et al., 2011). Despite such unique properties, dispersion of hydrophilic nanoparticles and leaching of nanoparticles into retentate and permeate has raised the environmental concerns and need further research. As the world is facing shortage of freshwater, thin film nanocomposite (TFN) membranes are anticipated to accelerate desalination industry and it can be extended as selective membranes for CO<sub>2</sub> separation (Wong et al., 2016). The incorporation of functionalized fillers such as GO, CNT, TiO<sub>2</sub>, Ag-TiO<sub>2</sub>, MOFs (**Figure 10**) or organic fillers for specific applications has the potential to enhance membrane performance (Kumar et al., 2020). Recently, an interlayer of nanomaterials (TFNi) membranes showed extraordinary improvement in water flux and selectivity that can be used for the removal of heavy metals and micropollutants at a large scale

(Yang et al., 2020). In the near future, high impact TFN membranes with antifouling and biofouling properties, chemical resistance, improved mechanical strength and thermal stability need to be produced by either predisposition of new types of functionalized nanofillers or organic fillers compatible with selective layers of respective membranes. Such design and development of TFN membranes may pave way for more robust membrane systems with increased performance and long term durability providing precise solutions for various commercial water treatment challenges.

## 8 CONCLUSION

The utilization of nanotechnology in different environments has upgraded the present day environmental engineering and science together with a fresh set of technology that emerged from nanotechnology. The emerged technology at nanoscale has stimulated the advanced utilization of innovative and low-cost techniques that are effective for separation techniques. TFNs are obtained as modifications of TFCs. This modification is in the form of nanoparticles being incorporated into a thin polyamide (PA) dense layer at the top of the TFC membrane, aimed at improving its performance. In particular for desalination, specific modifications are generally made such that the permeate flux increases with negligible changes in the salt rejection upon nanomaterials incorporation. The full potential of a material development is on its performance and feasibility. Both these parameters are being answered in the PA nanocomposites development. The TFNs are used diversely in all membrane based desalination techniques. The transport properties of the penetrants are highly modified with addition of nanoparticles. The functionality of the membrane surface is targeted on specific membrane foulants. A specific kind of requirement is always being supported with a nanocomposites preparation. One of the main limitations of the TFNs is the amount of loading of nanomaterials and effective means for its distribution and dispersion on the whole polymer matrix. The liberty to functionalize the nanomaterials using several chemical groups could also improve their homogenization inside the polymer matrix. It appears that the choice of membrane materials for future RO processes would depend largely on the desired permselectivity and the targeted foulants. This review has focused on a variety TFNs prepared and their enhanced properties for addressing specified desalination requirements. The feasibility of such robust technology specifically meeting environmental impact and energy demands is widely discussed in this review paving way for the progress in research towards the development of new thin film nanocomposite membrane synthesis and manufacturing methods for desalination applications.

## AUTHOR CONTRIBUTIONS

JK contributed conception and design of research, manuscript editing and final submission. KRV contributed analysis, research

and collection of references. OG wrote sections of the manuscript and developed database. KJ and AP contributed early research and analysis. KJ performed statistical analysis. AP organized database. NN wrote sections of manuscript and performed comparative analysis of Data.

## REFERENCES

- Al-Hobaib, A. S., Al-Sheetan, K. M., Shaik, M. R., Al-Andis, N. M., and Al-Suhbani, M. S. (2015). Characterization and Evaluation of Reverse Osmosis Membranes Modified with Ag<sub>2</sub>O Nanoparticles to Improve Performance. *Nanoscale Res. Lett.* 10, 1–13. doi:10.1186/s11671-015-1080-3
- Alam, J., Dass, L. A., Ghasemi, M., and Alhoshan, M. (2013). Synthesis and Optimization of PES-Fe<sub>3</sub>O<sub>4</sub> Mixed Matrix Nanocomposite Membrane: Application Studies in Water Purification. *Polym. Compos.* 34, 1870–1877. doi:10.1002/pc.22593
- Amini, M., Jahanshahi, M., and Rahimpour, A. (2013). Synthesis of Novel Thin Film Nanocomposite (TFN) Forward Osmosis Membranes Using Functionalized Multi-Walled Carbon Nanotubes. *J. Membr. Sci.* 435, 233–241. doi:10.1016/j.memsci.2013.01.041
- Bao, M., Zhu, G., Wang, L., Wang, M., and Gao, C. (2013). Preparation of Monodispersed Spherical Mesoporous Nanosilica-Polyamide Thin Film Composite Reverse Osmosis Membranes via Interfacial Polymerization. *Desalination* 309, 261–266. doi:10.1016/j.desal.2012.10.028
- Baroña, G. N. B., Choi, M., and Jung, B. (2012). High Permeate Flux of PVA/PSf Thin Film Composite Nanofiltration Membrane with Aluminosilicate Single-Walled Nanotubes. *J. Colloid Interf. Sci.* 386, 189–197. doi:10.1016/j.jcis.2012.07.049
- Baroña, G. N. B., Lim, J., Choi, M., and Jung, B. (2013). Interfacial Polymerization of Polyamide-Aluminosilicate SWNT Nanocomposite Membranes for Reverse Osmosis. *Desalination* 325, 138–147. doi:10.1016/j.desal.2013.06.026
- Bates, W. T., and Cuozzo, R. (2000). *Integrated Membrane Systems*. Oceanside, CA: Hydranautics, Nitto Group Company. Available from: [http://www.membranes.com/docs/papers/01\\_ims.pdf](http://www.membranes.com/docs/papers/01_ims.pdf)
- Bohdziewicz, J., Bodzek, M., and Wąsik, E. (1999). The Application of Reverse Osmosis and Nanofiltration to the Removal of Nitrates from Groundwater. *Desalination* 121, 139–147. doi:10.1016/s0011-9164(99)00015-6
- Buonomenna, M. G. (2013). Nano-enhanced Reverse Osmosis Membranes. *Desalination* 314, 73–88. doi:10.1016/j.desal.2013.01.006
- Chan, W.-F., Chen, H.-y., Surapathi, A., Taylor, M. G., Shao, X., Marand, E., et al. (2013). Zwitterion Functionalized Carbon Nanotube/Polyamide Nanocomposite Membranes for Water Desalination. *ACS Nano* 7, 5308–5319. doi:10.1021/nn4011494
- Chou, W.-L., Yu, D.-G., and Yang, M.-C. (2005). The Preparation and Characterization of Silver-Loading Cellulose Acetate Hollow Fiber Membrane for Water Treatment. *Polym. Adv. Technol.* 16, 600–607. doi:10.1002/pat.630
- Daraei, P., Madaeni, S. S., Ghaemi, N., Salehi, E., Khadivi, M. A., Moradian, R., et al. (2012). Novel Polyethersulfone Nanocomposite Membrane Prepared by PANI/Fe<sub>3</sub>O<sub>4</sub> Nanoparticles with Enhanced Performance for Cu(II) Removal from Water. *J. Membr. Sci.* 415–416, 250–259. doi:10.1016/j.memsci.2012.05.007
- Daraei, P., Madaeni, S. S., Salehi, E., Ghaemi, N., Ghari, H. S., Khadivi, M. A., et al. (2013). Novel Thin Film Composite Membrane Fabricated by Mixed Matrix Nanoclay/chitosan on PVDF Microfiltration Support: Preparation, Characterization and Performance in Dye Removal. *J. Membr. Sci.* 436, 97–108. doi:10.1016/j.memsci.2013.02.031
- Das, R., Ali, M. E., Hamid, S. B. A., Ramakrishna, S., and Chowdhury, Z. Z. (2014). Carbon Nanotube Membranes for Water Purification: A Bright Future in Water Desalination. *Desalination* 336, 97–109. doi:10.1016/j.desal.2013.12.026
- de Lannoy, C.-F., Jassby, D., Gloe, K., Gordon, A. D., and Wiesner, M. R. (2013). Aquatic Biofouling Prevention by Electrically Charged Nanocomposite Polymer Thin Film Membranes. *Environ. Sci. Technol.* 47, 2760–2768. doi:10.1021/es3045168
- Duan, J., Litwiller, E., and Pinnau, I. (2015a). Preparation and Water Desalination Properties of POSS-Polyamide Nanocomposite Reverse Osmosis Membranes. *J. Membr. Sci.* 473, 157–164. doi:10.1016/j.memsci.2014.09.022
- Duan, J., Pan, Y., Pacheco, F., Litwiller, E., Lai, Z., and Pinnau, I. (2015b). High-performance Polyamide Thin-Film-Nanocomposite Reverse Osmosis Membranes Containing Hydrophobic Zeolitic Imidazolate Framework-8. *J. Membr. Sci.* 476, 303–310. doi:10.1016/j.memsci.2014.11.038
- Ettouney, H. M., El-Sessouky, H. T., Faibish, R. S., and Gowin, P. J. (2002). Evaluating the Economics of Desalination. *Chem. Eng. Prog.* 98 (46), 32–39.
- Fathzadeh, M., Aroujalian, A., and Raisi, A. (2011). Effect of Added NaX Nano-Zeolite into Polyamide as a Top Thin Layer of Membrane on Water Flux and Salt Rejection in a Reverse Osmosis Process. *J. Membr. Sci.* 375, 88–95. doi:10.1016/j.memsci.2011.03.017
- Gai, W., Zhao, D. L., and Chung, T.-S. (2019). Thin Film Nanocomposite Hollow Fiber Membranes Comprising Na<sup>+</sup>-Functionalized Carbon Quantum Dots for Brackish Water Desalination. *Water Res.* 154, 54–61. doi:10.1016/j.watres.2019.01.043
- Ghanbari, M., Emadzadeh, D., Lau, W. J., Matsuura, T., and Ismail, A. F. (2015). Synthesis and Characterization of Novel Thin Film Nanocomposite Reverse Osmosis Membranes with Improved Organic Fouling Properties for Water Desalination. *RSC Adv.* 5, 21268–21276. doi:10.1039/c4ra16177g
- Ghosh, A. K., and Hoek, E. M. V. (2009). Impacts of Support Membrane Structure and Chemistry on Polyamide-Polysulfone Interfacial Composite Membranes. *J. Membr. Sci.* 336, 140–148. doi:10.1016/j.memsci.2009.03.024
- Ghosh, A. K., Jeong, B.-H., Huang, X., and Hoek, E. M. V. (2008). Impacts of Reaction and Curing Conditions on Polyamide Composite Reverse Osmosis Membrane Properties. *J. Membr. Sci.* 311, 34–45. doi:10.1016/j.memsci.2007.11.038
- Greenlee, L. F., Lawler, D. F., Freeman, B. D., Marrot, B., and Moulin, P. (2009). Reverse Osmosis Desalination: Water Sources, Technology, and Today's Challenges. *Water Res.* 43, 2317–2348. doi:10.1016/j.watres.2009.03.010
- Hermans, S., Bernstein, R., Volodin, A., and Vankelecom, I. F. J. (2015). Study of Synthesis Parameters and Active Layer Morphology of Interfacially Polymerized Polyamide-Polysulfone Membranes. *Reactive Funct. Polym.* 86, 199–208. doi:10.1016/j.reactfunctpolym.2014.09.013
- Hermans, S., Mariën, H., Dom, E., Bernstein, R., and Vankelecom, I. F. J. (2014). Simplified Synthesis Route for Interfacially Polymerized Polyamide Membranes. *J. Membr. Sci.* 451, 148–156. doi:10.1016/j.memsci.2013.10.005
- Hu, D., Xu, Z.-L., and Wei, Y.-M. (2013). A High Performance Silica-Fluoropolyamide Nanofiltration Membrane Prepared by Interfacial Polymerization. *Separat. Purif. Techn.* 110, 31–38. doi:10.1016/j.seppur.2013.03.001
- Huang, D., Zhang, Z., Ma, Z., and Quan, Q. (2018). Effect of Natural Nanostructured Rods and Platelets on Mechanical and Water Resistance Properties of Alginate-Based Nanocomposites. *Front. Chem.* 6. doi:10.3389/fchem.2018.00635
- Huang, H., Qu, X., Ji, X., Gao, X., Zhang, L., Chen, H., et al. (2013a). Acid and Multivalent Ion Resistance of Thin Film Nanocomposite RO Membranes Loaded with Silicalite-1 Nanozeolites. *J. Mater. Chem. A* 1, 11343. doi:10.1039/c3ta12199b
- Huang, H., Qu, X., Dong, H., Zhang, L., and Chen, H. (2013b). Role of NaA Zeolites in the Interfacial Polymerization Process towards a Polyamide Nanocomposite Reverse Osmosis Membrane. *RSC Adv.* 3, 8203. doi:10.1039/c3ra09606k
- Jadav, G. L., Aswal, V. K., and Singh, P. S. (2010). SANS Study to Probe Nanoparticle Dispersion in Nanocomposite Membranes of Aromatic Polyamide and Functionalized Silica Nanoparticles. *J. Colloid Interf. Sci.* 351, 304–314. doi:10.1016/j.jcis.2010.07.028
- Jadav, G. L., and Singh, P. S. (2009). Synthesis of Novel Silica-Polyamide Nanocomposite Membrane with Enhanced Properties. *J. Membr. Sci.* 328, 257–267. doi:10.1016/j.memsci.2008.12.014
- Jamshidi Gohari, R., Lau, W. J., Matsuura, T., and Ismail, A. F. (2013). Fabrication and Characterization of Novel PES/Fe-Mn Binary Oxide UF Mixed Matrix Membrane for Adsorptive Removal of As(III) from Contaminated Water Solution. *Separat. Purif. Techn.* 118, 64–72. doi:10.1016/j.seppur.2013.06.043

## FUNDING

This work was supported by the Early Career Research Award (DST-SERB), India ECR/2015/000014 and the Grant of OPERA Award from BITS Pilani FR/SCM/290513/CHEG.

- Jeon, S., and Lee, J. (2020). Rationally Designed *In-Situ* Fabrication of Thin Film Nanocomposite Membranes with Enhanced Desalination and Anti-biofouling Performance. *J. Membr. Sci.* 615, 118542. doi:10.1016/j.memsci.2020.118542
- Jeong, B.-H., Hoek, E. M. V., Yan, Y., Subramani, A., Huang, X., Hurwitz, G., et al. (2007). Interfacial Polymerization of Thin Film Nanocomposites: A New Concept for Reverse Osmosis Membranes. *J. Membr. Sci.* 294, 1–7. doi:10.1016/j.memsci.2007.02.025
- Kesime, U. K., Milne, N., Aral, H., Cheng, C. Y., and Duke, M. (2013). Economic Analysis of Desalination Technologies in the Context of Carbon Pricing, and Opportunities for Membrane Distillation. *Desalination* 323, 66–74. doi:10.1016/j.desal.2013.03.033
- Kim, C. K., Kim, J. H., Roh, I. J., and Kim, J. J. (2000). The Changes of Membrane Performance with Polyamide Molecular Structure in the Reverse Osmosis Process. *J. Membr. Sci.* 165, 189–199. doi:10.1016/s0376-7388(99)00232-x
- Kim, E.-S., and Deng, B. (2011). Fabrication of Polyamide Thin-Film Nanocomposite (PA-TFN) Membrane with Hydrophilized Ordered Mesoporous Carbon (H-OMC) for Water Purifications. *J. Membr. Sci.* 375, 46–54. doi:10.1016/j.memsci.2011.01.041
- Kim, E.-S., Hwang, G., Gamal El-Din, M., and Liu, Y. (2012). Development of Nanosilver and Multi-Walled Carbon Nanotubes Thin-Film Nanocomposite Membrane for Enhanced Water Treatment. *J. Membr. Sci.* 394–395, 37–48. doi:10.1016/j.memsci.2011.11.041
- Kim, I. C., Ka, Y. H., Park, J. Y., and Lee, K. H. (2004). Preparation of Fouling Resistant Nanofiltration and Reverse Osmosis Membranes and Their Use for Dyeing Wastewater Effluent. *J. Ind. Eng. Chem.* 10, 115–121.
- Kim, S. G., Chun, J. H., Chun, B.-H., and Kim, S. H. (2013). Preparation, Characterization and Performance of Poly(arylene Ether Sulfone)/modified Silica Nanocomposite Reverse Osmosis Membrane for Seawater Desalination. *Desalination* 325, 76–83. doi:10.1016/j.desal.2013.06.017
- Kim, E.-S., Liu, Y., and Gamal El-Din, M. (2013). An *In-Situ* Integrated System of Carbon Nanotubes Nanocomposite Membrane for Oil Sands Process-Affected Water Treatment. *J. Membr. Sci.* 429, 418–427. doi:10.1016/j.memsci.2012.11.077
- Kim, S. G., Hyeon, D. H., Chun, J. H., Chun, B.-H., and Kim, S. H. (2013). Nanocomposite Poly(arylene Ether Sulfone) Reverse Osmosis Membrane Containing Functional Zeolite Nanoparticles for Seawater Desalination. *J. Membr. Sci.* 443, 10–18. doi:10.1016/j.memsci.2013.03.065
- Kong, C., koushima, A., Kamada, T., Shintani, T., Kanezashi, M., Yoshioka, T., et al. (2011). Enhanced Performance of Inorganic-Polyamide Nanocomposite Membranes Prepared by Metal-Alkoxide-Assisted Interfacial Polymerization. *J. Membr. Sci.* 366, 382–388. doi:10.1016/j.memsci.2010.10.026
- Kumar, M., Khan, M. A., and Ararat, H. A. (2020). Recent Developments in the Rational Fabrication of Thin Film Nanocomposite Membranes for Water Purification and Desalination. *ACS Omega* 5, 3792–3800. doi:10.1021/acsomega.9b03975
- Lau, W. J., Gray, S., Matsuura, T., Emadzadeh, D., Paul Chen, J., and Ismail, A. F. (2015). A Review on Polyamide Thin Film Nanocomposite (TFN) Membranes: History, Applications, Challenges and Approaches. *Water Res.* 80, 306–324. doi:10.1016/j.watres.2015.04.037
- Lau, W. J., Ismail, A. F., Misdan, N., and Kassim, M. A. (2012). A Recent Progress in Thin Film Composite Membrane: A Review. *Desalination* 287, 190–199. doi:10.1016/j.desal.2011.04.004
- Lee, H. S., Im, S. J., Kim, J. H., Kim, H. J., Kim, J. P., and Min, B. R. (2008). Polyamide Thin-Film Nanofiltration Membranes Containing TiO<sub>2</sub> Nanoparticles. *Desalination* 219, 48–56. doi:10.1016/j.desal.2007.06.003
- Lee, S. Y., Kim, H. J., Patel, R., Im, S. J., Kim, J. H., and Min, B. R. (2007). Silver Nanoparticles Immobilized on Thin Film Composite Polyamide Membrane: Characterization, Nanofiltration, Antifouling Properties. *Polym. Adv. Technol.* 18, 562–568. doi:10.1002/pat.918
- Li, D., and Wang, H. (2010). Recent Developments in Reverse Osmosis Desalination Membranes. *J. Mater. Chem.* 20, 4551. doi:10.1039/b924553g
- Li, D., and Wang, H. (2013). “Thin Film Nanocomposite Membranes for Water Desalination,” in *Functional Nanostructured Materials and Membranes for Water Treatment*. Editors M. Duke, D. Zhao, and R. Semiat (Weinheim, Germany: Wiley-VCH Verlag GmbH & Co. KGaA). doi:10.1002/9783527668502.ch7
- Li, D., and Wang, H. (2013). “Thin Film Nanocomposite Membranes for Water Desalination,” in *Functional Nanostructured Materials and Membranes for Water Treatment*, 163–194. doi:10.1002/9783527668502.ch7
- Li, X., Wang, R., Wicaksana, F., Tang, C., Torres, J., and Fane, A. G. (2014). Preparation of High Performance Nanofiltration (NF) Membranes Incorporated with Aquaporin Z. *J. Membr. Sci.* 450, 181–188. doi:10.1016/j.memsci.2013.09.007
- Liao, Z., Zhu, J., Li, X., and Van Der Bruggen, B. (2021). Regulating Composition and Structure of Nanofillers in Thin Film Nanocomposite (TFN) Membranes for Enhanced Separation Performance: A Critical Review. *Separat. Purif. Techn.* 266, 118567. doi:10.1016/j.seppur.2021.118567
- Lind, M. L., Eumine Suk, D., Nguyen, T.-V., and Hoek, E. M. V. (2010). Tailoring the Structure of Thin Film Nanocomposite Membranes to Achieve Seawater RO Membrane Performance. *Environ. Sci. Technol.* 44, 8230–8235. doi:10.1021/es101569p
- Lind, M. L., Ghosh, A. K., Jawor, A., Huang, X., Hou, W., Yang, Y., et al. (2009a). Influence of Zeolite Crystal Size on Zeolite-Polyamide Thin Film Nanocomposite Membranes. *Langmuir* 25, 10139–10145. doi:10.1021/la900938x
- Lind, M. L., Jeong, B.-H., Subramani, A., Huang, X., and Hoek, E. M. V. (2009b). Effect of mobile Cation on Zeolite-Polyamide Thin Film Nanocomposite Membranes. *J. Mater. Res.* 24, 1624–1631. doi:10.1557/jmr.2009.0189
- Liu, Y., Wang, X., Yang, F., and Yang, X. (2008). Excellent Antimicrobial Properties of Mesoporous Anatase TiO<sub>2</sub> and Ag/TiO<sub>2</sub> Composite Films. *Microporous Mesoporous Mater.* 114, 431–439. doi:10.1016/j.micromeso.2008.01.032
- Louie, J. S., Pinnau, I., Ciobanu, L., Ishida, K. P., Ng, A., and Reinhard, M. (2006). Effects of Polyether-Polyamide Block Copolymer Coating on Performance and Fouling of Reverse Osmosis Membranes. *J. Membr. Sci.* 280, 762–770. doi:10.1016/j.memsci.2006.02.041
- Lu, M. (2013). in *Functional Nanostructured Materials and Membranes for Water Treatment*. Editors M. Duke, D. Zhao, and R. Semiat (Weinheim, Germany: Wiley-VCH Verlag GmbH & Co. KGaA).
- Ma, H., Yoon, K., Rong, L., Shokralla, M., Kopot, A., Wang, X., et al. (2010). Thin-Film Nanofibrous Composite Ultrafiltration Membranes Based on Polyvinyl Alcohol Barrier Layer Containing Directional Water Channels. *Ind. Eng. Chem. Res.* 49, 11978–11984. doi:10.1021/ie100545k
- Ma, N., Wei, J., Liao, R., and Tang, C. Y. (2012). Zeolite-polyamide Thin Film Nanocomposite Membranes: Towards Enhanced Performance for Forward Osmosis. *J. Membr. Sci.* 405–406, 149–157. doi:10.1016/j.memsci.2012.03.002
- Mickley, M. C. (2001). *Membrane Concentrate Disposal: Practices and Regulation*. Denver, Colorado US Department of the Interior, Bureau of Reclamation, Technical Service Center, Water Treatment Engineering and Research Group. Final Report.
- Mills, A., and Le Hunte, S. (1997). An Overview of Semiconductor Photocatalysis. *J. Photochem. Photobiol. A: Chem.* 108, 1–35. doi:10.1016/s1010-6030(97)00118-4
- NanoH<sub>2</sub>O, Inc. InterNano (2021). Internano.org. Available at: <https://www.internano.org/node/1516> (Accessed May 22, 2021).
- Park, H. B., Freeman, B. D., Zhang, Z.-B., Sankir, M., and McGrath, J. E. (2008). Highly Chlorine-Tolerant Polymers for Desalination. *Angew. Chem. Int. Edition* 47, 6019–6024. doi:10.1002/anie.200800454
- Park, K. T., Kim, S. G., Chun, B.-H., Bang, J., and Kim, S. H. (2010). Sulfonated Poly(arylene Ether Sulfone) Thin-Film Composite Reverse Osmosis Membrane Containing SiO<sub>2</sub> Nano-Particles. *dwt* 15, 69–75. doi:10.5004/dwt.2010.1669
- Park, J., Choi, W., Kim, S. H., Chun, B. H., Bang, J., and Lee, K. B. (2010). Enhancement of Chlorine Resistance in Carbon Nanotube Based Nanocomposite Reverse Osmosis Membranes. *Desalination Water Treat.* 15, 198–204. doi:10.5004/dwt.2010.1686
- Paz, Y. (2010). Application of TiO<sub>2</sub> Photocatalysis for Air Treatment: Patents’ Overview. *Appl. Catal. B: Environ.* 99, 448–460. doi:10.1016/j.apcatb.2010.05.011
- Pendergast, M. M., Ghosh, A. K., and Hoek, E. M. V. (2013). Separation Performance and Interfacial Properties of Nanocomposite Reverse Osmosis Membranes. *Desalination* 308, 180–185. doi:10.1016/j.desal.2011.05.005
- Pendergast, M. M., and Hoek, E. M. V. (2011). A Review of Water Treatment Membrane Nanotechnologies. *Energy Environ. Sci.* 4, 1946. doi:10.1039/c0ee00541j
- Petersen, R. J. (1993). Composite Reverse Osmosis and Nanofiltration Membranes. *J. Membr. Sci.* 83, 81–150. doi:10.1016/0376-7388(93)80014-o
- Rahimpour, A., Madaeni, S. S., Taheri, A. H., and Mansourpanah, Y. (2008). Coupling TiO<sub>2</sub> Nanoparticles with UV Irradiation for Modification of



- Polyethersulfone Ultrafiltration Membranes. *J. Membr. Sci.* 313, 158–169. doi:10.1016/j.memsci.2007.12.075
- Rajaeian, B., Rahimpour, A., Tade, M. O., and Liu, S. (2013). Fabrication and Characterization of Polyamide Thin Film Nanocomposite (TFN) Nanofiltration Membrane Impregnated with TiO<sub>2</sub> Nanoparticles. *Desalination* 313, 176–188. doi:10.1016/j.desal.2012.12.012
- Rajakumaran, R., Kumar, M., and Chetty, R. (2020). Morphological Effect of ZnO Nanostructures on Desalination Performance and Antibacterial Activity of Thin-Film Nanocomposite (TFN) Membrane. *Desalination* 495, 114673. doi:10.1016/j.desal.2020.114673
- Rana, D., Kim, Y., Matsuura, T., and Arafat, H. A. (2011). Development of Antifouling Thin-Film-Composite Membranes for Seawater Desalination. *J. Membr. Sci.* 367, 110–118. doi:10.1016/j.memsci.2010.10.050
- Rana, T. M. D., Qtaishat, M. R., and Singh, G. (2011). "Recent Advances in Membrane Science and Technology in Seawater Desalination—With Technology Development in the Middle East and Singapore," in *Water and Water Treatment Technologies, Encyclopedia of Life Support Systems (EOLSS), Developed under the Auspices of the UNESCO* (Oxford, UK: Eolss Publishers).
- Reahl, E. R. (2004). *Half a Century of Desalination with Electrodialysis*. New York, NY: General Electric Company.
- Roy, S., Ntini, S. A., Mitra, S., and Sirkar, K. K. (2011). Facile Fabrication of superior Nanofiltration Membranes from Interfacially Polymerized CNT-Polymer Composites. *J. Membr. Sci.* 375, 81–87. doi:10.1016/j.memsci.2011.03.012
- Safarpour, M., Khataee, A., and Vatanpour, V. (2015). Thin Film Nanocomposite Reverse Osmosis Membrane Modified by Reduced Graphene oxide/TiO<sub>2</sub> with Improved Desalination Performance. *J. Membr. Sci.* 489, 43–54. doi:10.1016/j.memsci.2015.04.010
- Sagle, A., and Freeman, B. (2004). Fundamentals of Membranes for Water Treatment. *Future desalination Tex.* 2, 137–154.
- Saleem, H., and Zaidi, S. J. (2020). Nanoparticles in Reverse Osmosis Membranes for Desalination: A State of the Art Review. *Desalination* 475, 114171. doi:10.1016/j.desal.2019.114171
- Saleh, T. A., and Gupta, V. K. (2012). Synthesis and Characterization of Alumina Nanoparticles Polyamide Membrane with Enhanced Flux Rejection Performance. *Separat. Purif. Techn.* 89, 245–251. doi:10.1016/j.seppur.2012.01.039
- Shahzad, M. W., Burhan, M., and Ng, K. C. (2019). A Standard Primary Energy Approach for Comparing Desalination Processes. *Npj Clean. Water* 2, 1. doi:10.1038/s41545-018-0028-4
- Shen, J. n., Yu, C. c., Ruan, H. m., Gao, C. j., and Van der Bruggen, B. (2013). Preparation and Characterization of Thin-Film Nanocomposite Membranes Embedded with Poly(methyl Methacrylate) Hydrophobic Modified Multiwalled Carbon Nanotubes by Interfacial Polymerization. *J. Membr. Sci.* 442, 18–26. doi:10.1016/j.memsci.2013.04.018
- Shenvi, S. S., Isloor, A. M., and Ismail, A. F. (2015). A Review on RO Membrane Technology: Developments and Challenges. *Desalination* 368, 10–26. doi:10.1016/j.desal.2014.12.042
- Siew Khoo, Y., Jye Lau, W., Yeow Liang, Y., Karaman, M., Gürsoy, M., and Fauzi Ismail, A. (2021). Eco-friendly Surface Modification Approach to Develop Thin Film Nanocomposite Membrane with Improved Desalination and Antifouling Properties. *J. Adv. Res.*, 1–27. doi:10.1016/j.jare.2021.06.011
- Singh, P. S., and Aswal, V. K. (2008). Characterization of Physical Structure of Silica Nanoparticles Encapsulated in Polymeric Structure of Polyamide Films. *J. Colloid Interf. Sci.* 326, 176–185. doi:10.1016/j.jcis.2008.07.025
- Subramani, A., Voutchkov, N., and Jacangelo, J. G. (2014). Desalination Energy Minimization Using Thin Film Nanocomposite Membranes. *Desalination* 350, 35–43. doi:10.1016/j.desal.2014.07.011
- Tajuddin, M. H., Yusof, N., Wan Azelee, I., Wan Salleh, W. N., Ismail, A. F., Jaafar, J., et al. (2019). Development of Copper-Aluminum Layered Double Hydroxide in Thin Film Nanocomposite Nanofiltration Membrane for Water Purification Process. *Front. Chem.* 7. doi:10.3389/fchem.2019.00003
- The World Bank (2007). *IDA at Work: Water Resources - Improving Services for the Poor*. Washington DC.
- UNESCO (2020). *The United Nations World Water Development Report 2020: Water and Climate Change*. Paris.
- Van der Bruggen, B., and Vandecasteele, C. (2002). Distillation vs. Membrane Filtration: Overview of Process Evolutions in Seawater Desalination. *Desalination* 143, 207–218. doi:10.1016/s0011-9164(02)00259-x
- Wade, N. M. (2001). Distillation Plant Development and Cost Update. *Desalination* 136, 3–12. doi:10.1016/s0011-9164(01)00159-x
- Wade, N. M. (1993). Technical and Economic Evaluation of Distillation and Reverse Osmosis Desalination Processes. *Desalination* 93, 343–363. doi:10.1016/0011-9164(93)80113-2
- Wan Azelee, I., Goh, P. S., Lau, W. J., Ismail, A. F., Rezaei-DashtArzhandi, M., Wong, K. C., et al. (2017). Enhanced Desalination of Polyamide Thin Film Nanocomposite Incorporated with Acid Treated Multiwalled Carbon Nanotube-Titania Nanotube Hybrid. *Desalination* 409, 163–170. doi:10.1016/j.desal.2017.01.029
- Wang, J., Wang, Q., Gao, X., Tian, X., Wei, Y., Cao, Z., et al. (2019). Surface Modification of Mesoporous Silica Nanoparticle with 4-triethoxysilylaniline to Enhance Seawater Desalination Properties of Thin-Film Nanocomposite Reverse Osmosis Membranes. *Front. Environ. Sci. Eng.* 14. doi:10.1007/s11783-019-1185-5
- wang, L. K., Chen, J. P., Hung, Y. – T., and Shammas, N. K. (2011). *Handbook of Environmental Engineering : Membrane and Desalination Technologies*. New York, NY: Springer Science+ Business Media, LLC, 13, 1–699. doi:10.1007/978-1-59745-278-6\_1
- Wang, X., Chen, X., Yoon, K., Fang, D., Hsiao, B. S., and Chu, B. (2005). High Flux Filtration Medium Based on Nanofibrous Substrate with Hydrophilic Nanocomposite Coating. *Environ. Sci. Technol.* 39, 7684–7691. doi:10.1021/es050512j
- Williams, M. E. (2003). *A Brief Review of Reverse Osmosis Membrane Technology*. EET Corporation and Williams Engineering Services Company Inc.
- Wong, K. C., Goh, P. S., and Ismail, A. F. (2016). Thin Film Nanocomposite: the Next Generation Selective Membrane for CO<sub>2</sub> Removal. *J. Mater. Chem. A.* 4, 15726–15748. doi:10.1039/c6ta05145f
- Wu, H., Tang, B., and Wu, P. (2010). MWNTs/Polyester Thin Film Nanocomposite Membrane: An Approach to Overcome the Trade-Off Effect between Permeability and Selectivity. *J. Phys. Chem. C* 114, 16395–16400. doi:10.1021/jp107280m
- Wu, H., Tang, B., and Wu, P. (2013a). Optimization, Characterization and Nanofiltration Properties Test of MWNTs/polyester Thin Film Nanocomposite Membrane. *J. Membr. Sci.* 428, 425–433. doi:10.1016/j.memsci.2012.10.042
- Wu, H., Tang, B., and Wu, P. (2013b). Optimizing Polyamide Thin Film Composite Membrane Covalently Bonded with Modified Mesoporous Silica Nanoparticles. *J. Membr. Sci.* 428, 341–348. doi:10.1016/j.memsci.2012.10.053
- Yang, Z., Sun, P.-F., Li, X., Gan, B., Wang, L., Song, X., et al. (2020). A Critical Review on Thin-Film Nanocomposite Membranes with Interlayered Structure: Mechanisms, Recent Developments, and Environmental Applications. *Environ. Sci. Technol.* 54, 15563–15583. doi:10.1021/acs.est.0c05377
- Yin, J., Kim, E.-S., Yang, J., and Deng, B. (2012). Fabrication of a Novel Thin-Film Nanocomposite (TFN) Membrane Containing MCM-41 Silica Nanoparticles (NPs) for Water Purification. *J. Membr. Sci.* 423–424, 238–246. doi:10.1016/j.memsci.2012.08.020
- You, H., Li, X., Yang, Y., Wang, B., Li, Z., Wang, X., et al. (2013). High Flux Low Pressure Thin Film Nanocomposite Ultrafiltration Membranes Based on Nanofibrous Substrates. *Separat. Purif. Techn.* 108, 143–151. doi:10.1016/j.seppur.2013.02.014
- You, H., Zhang, X., Zhu, D., Yang, C., Chammingkwan, P., and Taniike, T. (2021). Advantages of Polydopamine Coating in the Design of ZIF-8-Filled Thin-Film Nanocomposite (TFN) Membranes for Desalination. *Colloids Surf. A: Physicochemical Eng. Aspects* 629, 127492. doi:10.1016/j.colsurfa.2021.127492
- Yu, C. C., Yu, H. W., Chu, Y. X., Ruan, H. M., and Shen, J. N. (2013). Preparation Thin Film Nanocomposite Membrane Incorporating PMMA Modified MWNT for Nanofiltration. *Kem* 562–565, 882–886. doi:10.4028/www.scientific.net/kem.562-565.882
- Zargar, M., Hartanto, Y., Jin, B., and Dai, S. (2017). Understanding Functionalized Silica Nanoparticles Incorporation in Thin Film Composite Membranes: Interactions and Desalination Performance. *J. Membr. Sci.* 521, 53–64. doi:10.1016/j.memsci.2016.08.069
- Zhang, L., Shi, G.-Z., Qiu, S., Cheng, L.-H., and Chen, H.-L. (2011). Preparation of High-Flux Thin Film Nanocomposite Reverse Osmosis Membranes by Incorporating Functionalized Multi-Walled Carbon Nanotubes. *Desalination Water Treat.* 34, 19–24. doi:10.5004/dwt.2011.2801

- Zhao, D. L., Japip, S., Zhang, Y., Weber, M., Maletzko, C., and Chung, T.-S. (2020). Emerging Thin-Film Nanocomposite (TFN) Membranes for Reverse Osmosis: A Review. *Water Res.* 173, 115557. doi:10.1016/j.watres.2020.115557
- Zhao, H., Qiu, S., Wu, L., Zhang, L., Chen, H., and Gao, C. (2014). Improving the Performance of Polyamide Reverse Osmosis Membrane by Incorporation of Modified Multi-Walled Carbon Nanotubes. *J. Membr. Sci.* 450, 249–256. doi:10.1016/j.memsci.2013.09.014
- Zhao, R. (2013). *Theory and Operation of Capacitive Deionization Systems*. Weinheim: Wiley-VCH Verlag GmbH & C. KGaA.
- Zhao, Y., Qiu, C., Li, X., Vararattanavech, A., Shen, W., Torres, J., et al. (2012). Synthesis of Robust and High-Performance Aquaporin-Based Biomimetic Membranes by Interfacial Polymerization-Membrane Preparation and RO Performance Characterization. *J. Membr. Sci.* 423–424, 422–428. doi:10.1016/j.memsci.2012.08.039
- Zhou, Y., Yu, S., Gao, C., and Feng, X. (2009). Surface Modification of Thin Film Composite Polyamide Membranes by Electrostatic Self Deposition of Polycations for Improved Fouling Resistance. *Separat. Purif. Techn.* 66, 287–294. doi:10.1016/j.seppur.2008.12.021
- Zhu, X., Bai, R., Wee, K.-H., Liu, C., and Tang, S.-L. (2010). Membrane Surfaces Immobilized with Ionic or Reduced Silver and Their Anti-biofouling Performances. *J. Membr. Sci.* 363, 278–286. doi:10.1016/j.memsci.2010.07.041
- Zodrow, K., Brunet, L., Mahendra, S., Li, D., Zhang, A., Li, Q., et al. (2009). Polysulfone Ultrafiltration Membranes Impregnated with Silver Nanoparticles Show Improved Biofouling Resistance and Virus Removal. *Water Res.* 43, 715–723. doi:10.1016/j.watres.2008.11.014
- Conflict of Interest:** The authors declare that the research was conducted in the absence of any commercial or financial relationships that could be construed as a potential conflict of interest.
- Publisher's Note:** All claims expressed in this article are solely those of the authors and do not necessarily represent those of their affiliated organizations, or those of the publisher, the editors and the reviewers. Any product that may be evaluated in this article, or claim that may be made by its manufacturer, is not guaranteed or endorsed by the publisher.
- Copyright © 2022 Nambi Krishnan, Venkatachalam, Ghosh, Jhaveri, Palakodeti and Nair. This is an open-access article distributed under the terms of the Creative Commons Attribution License (CC BY). The use, distribution or reproduction in other forums is permitted, provided the original author(s) and the copyright owner(s) are credited and that the original publication in this journal is cited, in accordance with accepted academic practice. No use, distribution or reproduction is permitted which does not comply with these terms.





# Chemical Modification of Hyaluronan and Their Biomedical Applications

Vera Hintze<sup>1\*</sup>, Matthias Schnabelrauch<sup>2\*</sup> and Sandra Rother<sup>3\*</sup>

<sup>1</sup>Institute of Materials Science, Max Bergmann Center of Biomaterials, Technische Universität Dresden, Dresden, Germany,

<sup>2</sup>Biomaterials Department, INNOVENT e. V., Jena, Germany, <sup>3</sup>School of Medicine, Center for Molecular Signaling (PZMS), Saarland University, Homburg, Germany

Hyaluronan, the extracellular matrix glycosaminoglycan, is an important structural component of many tissues playing a critical role in a variety of biological contexts. This makes hyaluronan, which can be biotechnologically produced in large scale, an attractive starting polymer for chemical modifications. This review provides a broad overview of different synthesis strategies used for modulating the biological as well as material properties of this polysaccharide. We discuss current advances and challenges of derivatization reactions targeting the primary and secondary hydroxyl groups or carboxylic acid groups and the *N*-acetyl groups after deamidation. In addition, we give examples for approaches using hyaluronan as biomedical polymer matrix and consequences of chemical modifications on the interaction of hyaluronan with cells via receptor-mediated signaling. Collectively, hyaluronan derivatives play a significant role in biomedical research and applications indicating the great promise for future innovative therapies.

**Keywords:** hyaluronan, glycosaminoglycan, synthesis, interaction, signaling, degradation

## OPEN ACCESS

### Edited by:

Jianrong Steve Zhou,  
Peking University, China

### Reviewed by:

Gloria Huerta-Angeles,  
Contipro Inc., Czechia  
Changchun Zhou,  
Sichuan University, China

### \*Correspondence:

Vera Hintze  
Vera.Hintze@tu-dresden.de  
Matthias Schnabelrauch  
ms@innovent-jena.de  
Sandra Rother  
sandra.rother@uks.eu

### Specialty section:

This article was submitted to  
Organic Chemistry,  
a section of the journal  
Frontiers in Chemistry

**Received:** 07 December 2021

**Accepted:** 10 January 2022

**Published:** 11 February 2022

### Citation:

Hintze V, Schnabelrauch M and  
Rother S (2022) Chemical Modification  
of Hyaluronan and Their  
Biomedical Applications.  
Front. Chem. 10:830671.  
doi: 10.3389/fchem.2022.830671

## INTRODUCTION

Hyaluronan (HA, formerly named hyaluronic acid) is an ionic, non-branched and multifunctional heteropolysaccharide. Together with other low- or medium-sulfated representatives (heparan sulfate, chondroitin sulfate, dermatan sulfate, keratan sulfate) and the high-sulfated heparin, the non-sulfated HA belongs to the family of naturally occurring glycosaminoglycan (GAG) biomacromolecules, the so called mucopolysaccharides. GAG are found throughout the body, often in mucus and joint fluids, and as components of the extracellular matrix (ECM) and tissues of vertebrates and invertebrates. GAG are localized also inside and on the surface of all cells. They are involved in various biochemical processes such as cell adhesion, growth and proliferation, cell surface binding, wound healing, or tumor metastasis (Dicker et al., 2014).

Compared to sulfated GAG, HA is a structurally uniform natural macromolecule and due to established biotechnological production processes it is readily available in higher quantities (Badri et al., 2018). Despite the progress achieved in the total synthesis of complex oligomeric carbohydrates (DeAngelis et al., 2013; Mende et al., 2016; Fittolani et al., 2021), HA represents an ideal starting material for the chemical conversion into other hardly accessible, mainly high-sulfated GAG or carbohydrate-analogous polymeric molecules mimicking their function, e.g., in the interactions with proteins like mediator molecules (e.g. cytokines).

There are two main features of HA that have contributed to its attractiveness as a biomaterial. Firstly HA can act as a passive structural molecule. Due to its macromolecular size, the marked hygroscopicity and viscoelasticity, HA is able to modulate tissue hydration, and to act as an osmotic

balance. As a component of the ECM, HA can provide an extracellular space, where cells and various other ECM compounds like collagen or elastin fibers are firmly maintained. In an active way, HA is able to act as signaling molecule interacting with various receptor proteins, namely extracellular and cellular hyaloadherins (Fallacara et al., 2018). In this function HA is involved in angiogenesis, cell migration and motility, and tissue organization. It also plays a role in inflammation and stimulation of cytokine activity.

Secondly, HA can be functionalized and chemically modified to present a range of physical characteristics with wide-ranging solubility and even mechanical properties. HA is highly soluble in aqueous media, especially at low pH, and it has a high rate of turnover in human tissue. At higher concentrations HA forms physically crosslinked gels of often unsatisfactory mechanical stability.

Both, the relatively rapid degradability of HA in living tissues and its low mechanical stability are often a challenge for the broad applicability of HA in the clinic as a versatile biomaterial. Classical applications of HA include currently injections into joint spaces for the treatment of osteoarthritis or into the eye to increase the viscosity of the vitreous humor as well as wound carrier materials based on HA-esters or crosslinked HA derivatives.

The synthesis of new HA derivatives should take into account the multifunctionality of the HA molecule by selecting highly regioselective syntheses applying mild reaction conditions. Special attention should also be paid to the properties of native HA as its excellent biocompatibility, adjustable biodegradability, and mucoadhesivity.

Based on the structural peculiarities and the multifunctional character of the high molecular-weight HA molecule, recent advancements in the selective chemical functionalization of HA are presented in the following. These selectively modified derivatives are intended, on the one hand, to mimic more complex GAG or GAG derivatives that can be synthesized only in time-consuming multi-step syntheses and high personal efforts. On the other hand, significant contributions to the detailed understanding of important interaction processes between GAG and their different reaction partners like ECM proteins, intracellular proteins or specific growth factors (Grosskopf et al., 2021) are expected.

## OCCURRENCE, BIOSYNTHESIS, AND DEGRADATION

GAG occur as the constituents of so-called proteoglycans (all GAG members except HA) forming a large heterogeneous family of macromolecules consisting of a central protein backbone to which one or more unbranched GAG chains are covalently linked (Pomin and Mulloy, 2018). In case of cell surface proteoglycans, the protein core is membrane-spanning or lipid-bound, while ECM proteoglycans are predominantly secreted. HA is widely distributed in both prokaryotic and eukaryotic cells. Adult humans contain about 15 g of HA (Fallacara et al., 2018), mostly occurring in skin, vitreous body of the eye, umbilical

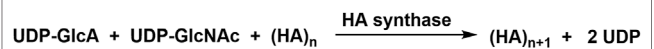


**FIGURE 1** | Overall reaction of the chain elongation step during HA biosynthesis.

cord, synovial fluid of articular joints, intervertebral disks, and embryonic mesenchymal tissues. In addition, it is present in further tissues such as heart valves, lungs, tendon sheaths, bursas aorta, and prostate (Valachová and Šoltés, 2021).

Biosynthesis of HA occurs in eukaryotic cells at the inner surface of the plasma membrane catalyzed by a class of integral membrane proteins, the HA synthases (HAS1, HAS2, HAS3; Vigetti et al., 2014). These enzymes which contain both GlcNAc ( $\beta$ -1  $\rightarrow$  4) and GlcA ( $\beta$ -1  $\rightarrow$  3) transferase activities, elongate HA at its reducing end by repeatedly adding nucleotide [uridine-diphosphate (UDP)]-activated GlcA and UDP-GlcNAc to the nascent polysaccharide (Hascall and Esko, 2009). The overall reaction scheme is given in **Figure 1** (Schnabelrauch et al., 2013). Finally, the synthesized HA is extruded through the plasma membrane into the extracellular space. A comparable pathway to produce HA is used by bacteria leading to HA with identical structural features (DeAngelis, 2012).

The first pharmaceutically pure HA was produced from rooster combs using the extraction and purification method by Balazs (Balazs, 1979). Currently, industrial production of HA mainly occurs by microbial fermentation (Boeriu et al., 2013) using at first *Streptococci* strains A and C, and more recently, various commercially available strains like *Streptococcus equi*, or *Streptococcus zooepidemicus* and even genetically modified bacterial strains (Moradali and Rehm, 2020; Manfrão-Netto et al., 2021). Even though high amounts of HA occur within the glycocalyx of all cells and in the ECM, the plasma HA levels are usually low due to the rapid clearance of HA in the kidney and liver (Fraser et al., 1997). About one-third of the total HA amounts in the human body are subject to daily turnover. HA degradation is mainly achieved by the activity of hyaluronidases, which catalyze the hydrolysis of disaccharides at hexosaminidic ( $\beta$ -1  $\rightarrow$  4) linkages. In most tissues, among the six identified hyaluronidases, HYAL1 and HYAL2 are the dominating ones. Cell surface bound HYAL2 degrades high-molecular-weight HA into HA fragments of around 50 disaccharide units (about 20 kDa), which stimulate angiogenic and inflammatory signaling pathways (Stern, 2004). After internalization of these fragments into endosomes and transport to lysosomes, HYAL1 cleaves the HA fragments into small oligosaccharides before further degradation by exoglycosidases (Stern et al., 2006).

## GENERAL STRUCTURE AND PROPERTIES

HA is a negatively charged, unbranched and multi-functional polysaccharide formed by repeating disaccharide units of D-N-acetylglucosamine (GlcNAc) and D-glucuronic acid (GlcA) linked by alternating ( $\beta$ -1 $\rightarrow$ 3) and ( $\beta$ -1 $\rightarrow$ 4) glycosidic bonds. In contrast to the other members of the GAG family, HA is not

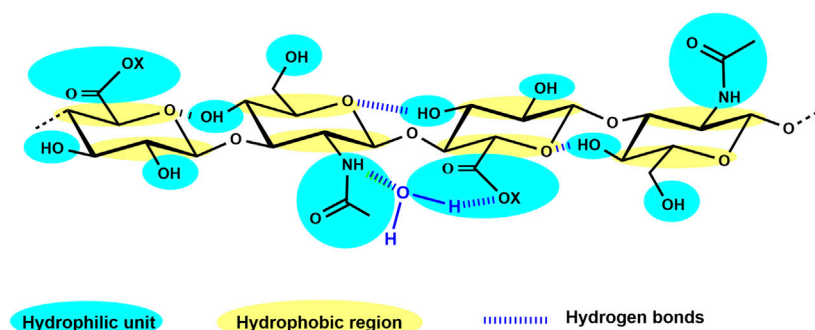


**FIGURE 2** | HA tetrasaccharide unit schematically showing the hydrophilic moieties (in blue) and the hydrophobic regions (in yellow), while hydrogen bonds are represented by dark blue dashed lines (adapted from Fallacara et al., 2018, 10, 701).

sulfated. At physiological pH (around 7.4), most carboxyl groups are deprotonated and, therefore, HA ( $pK \approx 3.2$ ) is negatively charged. In solution and at physiological pH value, the negative charge of HA is balanced with different cations (e.g.,  $Na^+$ ,  $K^+$ ,  $Ca^{2+}$ , and  $Mg^{2+}$ ). Furthermore, HA can chelate and neutralize iron and copper ions, which are required for the Fenton reaction and are responsible to form the most deleterious reactive oxygen species (ROS) (Gligorovski et al., 2015). In the absence of iron and copper ions, the formation of these hydroxyl radicals is suppressed. Moreover, HA can also neutralize ROS around leukocytes and protect neighboring cells (Litwiniuk et al., 2016).

Concluded from experimental findings and supported by various spectroscopic analyses and first data from energy calculations as well as computer simulations at the beginning of the 1990s, a twofold helix for HA was hypothesized to be present in aqueous solution (Heatley and Scott, 1988; Scott et al., 1991). The formed double helix is probably driven by interactions between large hydrophobic patches on alternate sides of the tape-like polymer and additionally by hydrogen bonding, forming stable aggregates at biological temperatures in water (Scott, 1992). This interplay of hydrophilic nature, hydrophobic portions, and a strong network of hydrogen bonds (Figure 2) results in the generation of an unstable  $\beta$ -sheet tertiary structure (Amorim et al., 2021). Although rather simply structured, compared to the other GAG, HA shows remarkable physico-chemical and biological properties (Bohaumilitzky et al., 2017). It is a very hygroscopic macromolecule able to tightly bind 15 water molecules per disaccharide repeating unit (Jouon et al., 1995) and has a great ability to retain water. Furthermore, HA shows a very high and shear-dependent viscoelasticity, resulting in the role of HA as an extracellular lubricant (Laurent et al., 1996). These remarkable hydrodynamic properties are essential for the biological function of HA to maintain tissue hydration, tension, and integrity.

The molecular weight of HA is a fundamental molecular parameter that has to be determined with high accuracy. Especially, the biological properties of HA and its synthesized derivatives largely depend on its molecular weight. Gel permeation chromatography (GPC), a special form of size exclusion chromatography (SEC), equipped with a multiangle laser light scattering (MALLS) detection system is the most

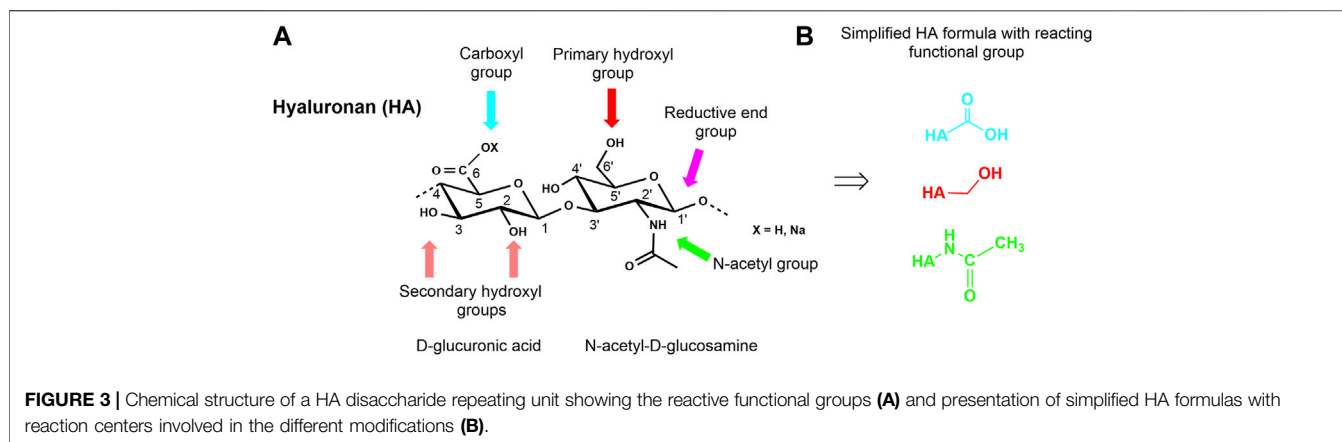
commonly used analytical technique for determining the average molecular weight and molecular weight distribution (Botha et al., 2018; Schnabelrauch et al., 2021).

Depending on the biological source, HA may possess a very high molecular weight of about  $10^7$  Dalton, e.g. as component in articular cartilage or of the synovial fluid in healthy joints (Fraser et al., 1997). In the physiological situation, there is a rapid HA turnover resulting in the constant presence of distinct forms of HA of various molecular weight (Bohaumilitzky et al., 2017). High-molecular weight HA (HMW-HA with molecular weights ranging from 1,000–5,000 kDa) possesses anti-inflammatory, anti-proliferative, anti-angiogenic, and immunosuppressive properties (Dovedytis et al., 2020). Besides providing water homeostasis, it modulates cell proliferation and differentiation, and participates in several other important biological processes, e.g. tissue regeneration, wound healing, epithelial integrity, embryogenesis, plasma protein distribution, and matrix structuring (Valachová and Šoltés, 2021).

## CHEMICAL MODIFICATION OF HA

### General Remarks

HA, like the other GAG, is a multifunctional macromolecule bearing primary and secondary hydroxyl, carboxyl, and N-acetyl groups within each anhydrodisaccharide repeating unit and a reducing sugar end group at the HA chain terminus (Figure 3A). The carboxylate group is responsible for the anionic character of the polysaccharide and makes HA soluble in aqueous solutions. However, the presence of the ionic functionality in combination with an intra- and intermolecular hydrogen-bonding network makes HA insoluble in conventional organic solvents. Nevertheless, it is possible to transform the sodium salt or the acidic form of HA into tertiary or quaternary ammonium salts of HA rendering such salts soluble or at least highly swellable in aprotic solvents like N,N-dimethyl formamide (DMF) or dimethyl sulfoxide (DMSO). These solvents usually allow esterification reactions under nearly homogeneous reaction conditions (Moeller et al., 2012). Some other solvent systems like ionic liquids (Zakrzewska et al., 2010) have already been used to modify other non-GAG polysaccharides or have been used for



the extraction of GAG- and ECM-containing proteins as supercritical carbon dioxide (Wang et al., 2017). Another aspect that must be considered when chemically manipulating HA and other GAG is their sensitivity to oxidative agents as well as to thermal stress.

Overall, the multi-functionality of HA (Figure 3B) combined with its limited solubility in organic solvents and its sensitivity to enzymatic and thermal degradation make the discovery of selective chemical reactions a challenge for the synthetic chemist.

In principle, HA can be modified by two different methods, crosslinking, and conjugation. Both methods are based on the same chemical reaction and differ in the fact that conjugation is characterized by grafting a single bond onto a HA chain whereas crosslinking means that different HA chains are linked together by two or more bonds (Schanté et al., 2011). Crosslinking is a well-known method to improve the mechanical, swelling, and rheological properties of HA. In this way, the degradation time of HA materials is slowed down and their residence time at the respective application site is enhanced. Covalent crosslinking provides the opportunity to provide hydrogels or cryogels, sponges, and other solid forms as scaffolds and drug carriers whilst maintaining biological functionality over an adjustable period of time (Williams, 2014).

Conjugation involves a variety of chemical modifications, such as the introduction of special functional units including ether, ester or amide groups, the attachment of bioactive as well as prodrug moieties, and last but not least the incorporation of marker molecules like specific dyes. Often an approach to chemically modify HA, contains both conjugation and cross-linking processes.

In recent years, the introduction of additional anionic groups, especially sulfate half-ester groups in HA has received much attention. Such highly-sulfated HA derivatives are able, similar to heparin and heparan sulfate, but in contrast to unsulfated HA, to interact with biological mediator molecules (e.g., growth factors) and positively influence biochemical processes, e.g. wound healing (for a detailed discussion, please see one of the next chapters on interaction of chemically modified HA with biological mediator proteins). Another example is the grafting of long hydrophobic chains onto HA. Amphiphilic HA polymers

of this type can form strong physical interactions which are broken when submitted to high shear forces (Huini-Amargier et al., 2005). Compared to native HA, the shear-thinning behaviour of these HA derivatives is much more marked. An important property of native HA is its mucoadhesivity. Maintaining or improving mucoadhesive properties of HA derivatives is initially important for the development of effective drug release systems. Through thiolation of HA not only mucoadhesiveness can be improved, but also properties as swelling capacity, stability, enzyme inhibition properties, and biocompatibility can be enhanced (Griesser et al., 2018).

## Controlled Degradation to Provide Suitable Starting Hyaluronans for Chemical Modification

The high solution viscosity of native HA in aqueous or organic solvents necessitates homogeneous reaction conditions as complete solubility and good miscibility. Therefore, the controlled degradation of HMW-HA to starting materials with molecular weights of 500–20 kDa prior to chemical modification reactions might often be an advantage (Schnabelrauch et al., 2021). Retaining the original macromolecular structure in form of a degraded material free of undesired side products especially without non-saturated or oxidized moieties is essential. Further, there is another critical point concerning the degradation as well as the medical use of HA products. It is well accepted that HA can modulate many biological processes including cell adhesion, cell migration, morphogenesis, tumorigenesis, cell survival, apoptosis, and inflammation and that these biological effects can (and often do) differ depending on the HA molecular weight (Cyphert et al., 2015; Fallacara et al., 2018). The mentioned complications to ensure largely homogeneous chemical HA modifications and the increasing application of HA as a component of artificial matrices and in bioengineering for tissue scaffolding, makes it necessary to develop procedures leading to HA starting materials with a controlled range of molecular weight and a narrow dispersity.

In the human body the degradation of HA is either specifically mediated by a group of endoglycosidases, the so-called

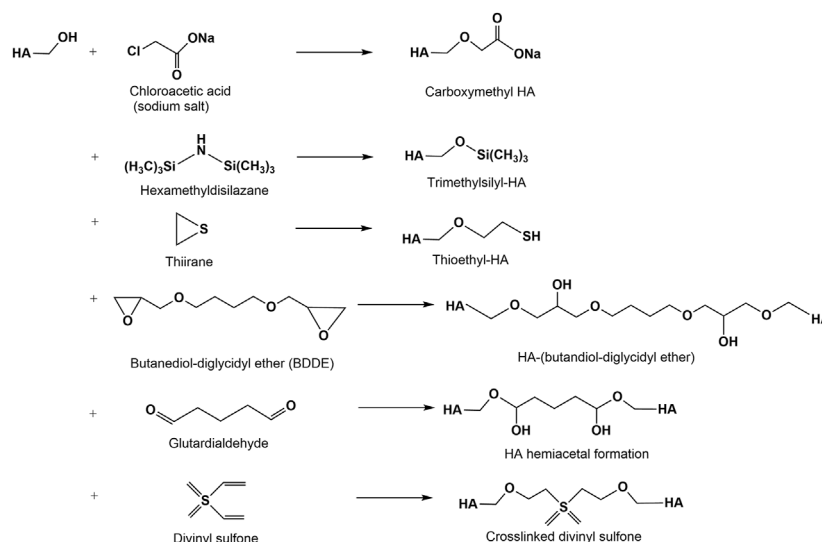


**FIGURE 4 |** Alkylation and bis-alkylation (crosslinking) of hydroxyl groups of HA.

hyaluronidases or non-specifically by oxidative damage due to initiation of reactive oxidative species (ROS) (Stern et al., 2007; Fallacara et al., 2018). In recent years, several enzymatic processes have been established to provide purified and structurally characterized HA oligosaccharides in up to milligram-/gram-scale quantities (Tawada et al., 2002; Blundell et al., 2006; Koehling et al., 2016). Degradation processes for HMW-HA have also been developed under largely controlled laboratory conditions by means of oxidative processes (Duan and Kasper, 2011). As oxidation agents mainly ozone (Yue 2012; Rother et al., 2015) or chlorine dioxide (Wyrwa et al., 2012) have been used. In recent years, intensive studies have been performed about acidic degradation of HA (Smejkalová et al., 2012a; Cožíková et al., 2017). Degraded HA with very narrow dispersity ( $M_w/M_n < 1.23$ ) covering a broad range of differently sized products (420–3 kDa) could thus be obtained prior fractionation on a preparative scale. Based on earlier work on the thermal stability (Bothner et al., 1988; Lowry and Beavers, 1994), a simple thermal degradation process for HA was recently established (Kunze et al., 2010). Starting with a HA of weight-average molecular weight ( $M_w$ ) of 1,000 kDa the final  $M_w$ -value of low molecular weight HA (LMW-HA) can be adjusted by choosing the processing time between 30 and 240 min resulting in  $M_w$  from 500 to 6 kDa (Schnabelrauch et al., 2021). Furthermore, automated solid-phase synthesis was used to produce HA oligosaccharides from monosaccharide building blocks, however, only in low amounts (Walvoort et al., 2012).

## Functionalization of the HA Hydroxyl Group

### Alkylation Reactions

The modification of hydroxyl group containing biopolymers with mono- and dialkylating agents to form ethers is a classical reaction for many polysaccharides (Heinze et al., 2018). In the

HA chemistry this reaction is especially used for crosslinking reactions resulting in hydrogels or scaffold materials (Figure 4). The synthesis of HA ethers is limited to a few examples due to harsh reaction conditions (pH 13–14) often necessary for the etherification reaction. Water soluble alkyl derivatives of HA have been prepared by reaction of HA with 2-alkyloxymethyloxirane in DMSO under slightly alkaline conditions (Mlbochová et al., 2007). Another approach to HA ethers described the tosylation of the primary hydroxyl group of HA followed by exchange of the more reactive tosylate functionality by hydrophobic hexyl- and pentadecyl ether groups, resp. (Lapcik et al., 2010). Carboxymethylated HA (CM-HA) can be synthesized in analogy to other carboxymethylated polysaccharides (Yang et al., 2010) by reacting HA with monochloroacetic acid under alkaline conditions (Moeller et al., 2012). Degrees of carboxymethylation ( $DS_{CM}$ ) for HMW- and LMW-HA ranging between 0.2 and 0.5 are obtained after a single carboxymethylation step. A repeated carboxymethylation gave a slight increase of the  $DS_{CM}$ -values to about 0.6–0.8. As shown by <sup>13</sup>C-NMR studies, carboxymethylation mainly took place at the primary OH-group of HA. Molecular weight determinations employed by GPC of the products confirmed a remarkable decrease after both alkylation steps. A thioethyl ether derivative was synthesized by reaction of ethylene sulfide (thiiran) to the hydroxyl groups of HA under alkaline conditions followed by addition of dithiothreitol (Serban et al., 2008). This derivative shows a radical scavenger activity.

Silylation of polysaccharides has been recognized as an effective method to prepare organic soluble derivatives and to improve their hydrophobicity (Heinze and Liebert, 2001). Silylation of HA has been reported to occur in a homogeneous salt complex of HA with cetyltrimethylammonium bromide (Scott, 1962). The silylation was performed in this salt complex homogeneously using hexamethyldisilazane (HMDS) and DMSO as solvents (Zhang and James, 2005a) resulting in



silylated HA materials characterized by high degree of substitution (DS) values (above 2.5), relatively low molecular weight loss, and solubility in non-polar organic solvents. Furthermore, the silylated cetyltrimethylammonium HA can be used as intermediate in an exchange reaction with aliphatic acid chloride (from hexanoyl to stearoyl acid chloride) to prepare HA esters (Zhang and James, 2005b). Trimethylsilyl chloride is formed as leaving group. The HA esters are soluble in non-polar solvents like xylenes.

Several difunctional agents have been used to crosslink hydroxyl groups of HA via ether linkages (**Figure 4**) forming hydrogels (Schanté et al., 2011; Collins and Birkinshaw, 2013; Khunmanee et al., 2017). Among diepoxy compounds used for the crosslinking of HA are butanediol-diglycidyl ether (Xue et al., 2020), ethylene glycol-diglycidyl ether (Oelschlaeger et al., 2016), polyethylene glycol diglycidyl ether (Calles et al., 2013), polyglycerol polyglycidyl ether (Yui et al., 1992) and 1,2,7,8 diepoxyoctane (Zhao, 2006). At present, BDDE represents the most promising diepoxide due to its easy availability and the capability to degrade into non-cytotoxic fragments (De Boule et al., 2013). Numerous studies showed that crosslinking can be performed by hemiacetal bonds using glutardialdehyde in an acetone-water medium catalyzed at acidic conditions (Collins and Birkinshaw, 2007). However, under the same conditions, the hemiacetals can be hydrolyzed recovering the starting materials (Schanté et al., 2011). HA crosslinking is also performed with divinyl sulfone in alkaline solution (Collins and Birkinshaw, 2007; Shimojo et al., 2015).

## Esterification Reactions

The esterification of the hydroxyl groups of HA is often a problem due to the incomplete solubility of HA in solvents suitable for acylation reactions and the lower reactivity of the

secondary hydroxyl groups. Often more drastic conditions with regard to increased reaction temperature and time are needed, and in many cases only the primary hydroxyl groups are involved into the reaction. This was documented in earlier experiments on the esterification of HA with fatty acid chlorides in DMF/pyridine (Kawaguchi et al., 1992; Kawaguchi et al., 1995). In a later study HA was esterified with hexanoic anhydride under homogeneous reaction conditions at room temperature for 2 h (Smejkalová et al., 2012b). For this reason, the sodium salt of HA was previously converted into the acid form to perform the acylation in a completely dissolved state. Under the same reaction conditions, the sodium salt was esterified in a DMSO/water solution. The formed HA esters were elucidated by means of nuclear magnetic resonance (NMR) spectroscopy, and mass spectrometry. It was found that acylation in DMSO regioselectively took place at the primary hydroxyl group of the C-6 position whereas acylation in a DMSO/water solvent was carried out both at the primary C-6 position, but also at the secondary hydroxyl group of the C-4 position of the N-acetyl-D-glucosamine unit.

The anhydrides of haloacetic acids have also been used to prepare bromo- and iodoacetates of HA which are versatile precursors for the formation of HA-based hydrogels (Serban and Prestwich, 2008).

In further studies, often highly reactive acylation components like imidazole-conjugated acids (Picotti et al., 2013) or mixed anhydrides (Huerta-Angeles et al., 2014) have been used as reactive intermediates. In a similar manner, it was also possible to graft acid-activated synthetic oligo-esters derived from polylactides and poly (3-hydroxyalkanoates), resp., to the primary hydroxyl group of HA (Pravata et al., 2008; Huerta-Angeles et al., 2017). In a simple approach using an octenyl succinate half-ester as

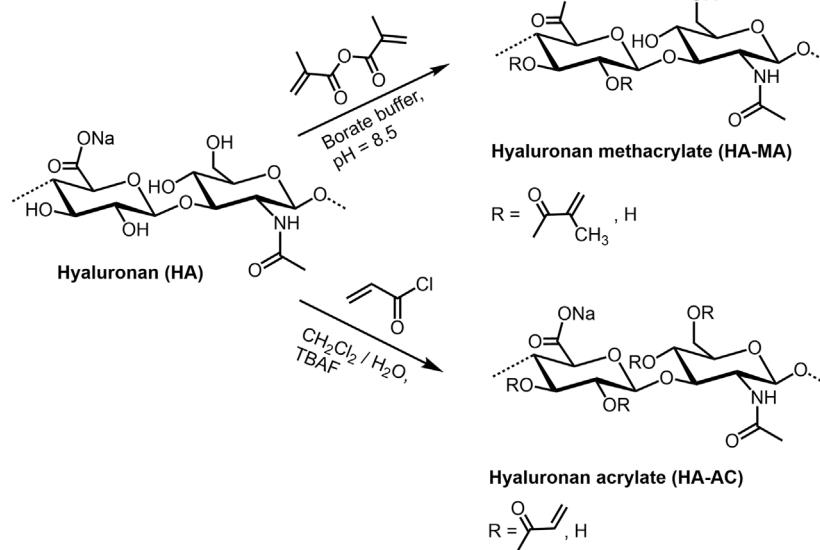


**FIGURE 5 |** (Meth)acrylation of HA.

reactive acylating reagent, an amphiphilic HA could be synthesized in aqueous media (Eenschooten et al., 2010).

Unsaturated HA esters serve as promising building blocks for the generation of novel supramolecular hydrogel networks with potential applications in regenerative, cell-based research and therapies (Highley et al., 2016; D'Amora et al., 2019; Kotla et al., 2021).

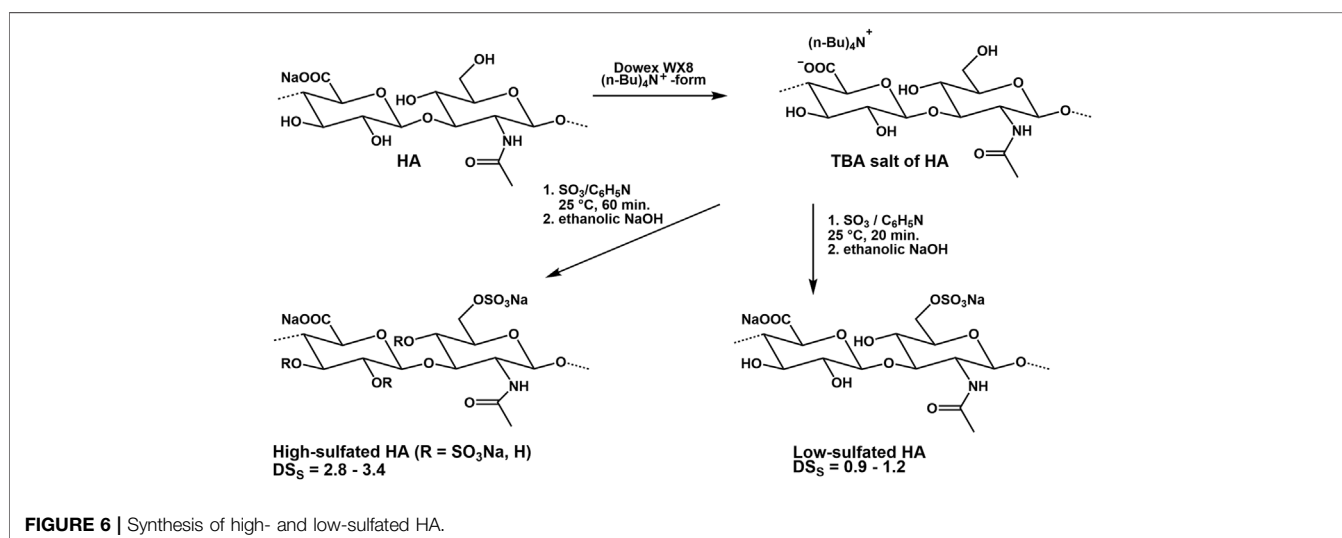
HA (meth)acrylates (**Figure 5**) are versatile macromers to generate functional coatings, and photopolymerizable scaffolds (Schnabelrauch et al., 2021). They can be prepared in a classical way by reaction of HA with methacrylic anhydride under pH values of 8–11 and ice cooling (Smeds et al., 2001; Burdick et al., 2005; Seidlits and al., 2010). The corresponding HA acrylate could be synthesized with acryloyl chloride both as mentioned above in a dichloromethane/water mixture (Qin et al., 2014), and with addition of tetra-*n*-butylammonium fluoride as phase-transfer catalyst (Becher et al., 2013). In analogy to non-derivatized HA, the sulfated derivatives with different degree of sulfation (DS: 0.9–1.4) can be (meth)acrylated in the same manner (Rother et al., 2017a). Further, HA esters of unsaturated carboxylic acids as pentenoates (Mergy et al., 2012) and maleates (Vasi et al., 2014) are available by treating HA with the corresponding acid anhydrides (see for example Smejkalova et al., 2014). A series of HA vinyl esters, able to be microstructured by two-photon lithography, have been synthesized by lipase-catalyzed transesterification (Qin et al., 2014).

## Sulfate and Phosphate Esters

The biological properties of sulfated GAG are influenced to a considerable extent by the degree of sulfation and the sulfate group distribution within the disaccharide repeating units. In particular, the higher sulfated GAG can only be isolated to a limited extent with structural uniformity from biological sources and they are accessible by total synthesis only at extremely high time expenditure. For this reason, the stepwise and regioselective sulfation of HA is a time- and cost-efficient approach mimicking important biological

features of high-sulfated GAG (Scharnweber et al., 2015; Townley and Bülow, 2018).

Experiments on the sulfation of HA were already carried out in the 1950s (Balazs et al., 1951). In these early experiments, sulfuric acid or chlorosulfonic acid were used as sulfating agents (Bedini et al., 2017; Caputo et al., 2019). These relatively drastic reaction conditions did not result in a complete sulfation of all free OH-groups but caused a partial degradation of the polymer chain. Therefore, in more recent attempts, complexes of SO<sub>3</sub> with organic amines, especially triethylamine (Satoh et al., 2004), trimethylamine (Nagira et al., 2007), and pyridine (Magnani et al., 1996) or amides like DMF (Crescenzi et al., 2002a) were used. The SO<sub>3</sub>-complexes are relatively mild reagents causing less polymer degradation. Due to their different reactivities in aprotic solvents, the sulfation of HA and other GAG is adjustable to a range between 0 and 4. Preferentially, the sulfation is performed in aprotic solvents like DMF after transformation of HA in its tributyl ammonium salt (Magnani et al., 1998, **Figure 6**). Studies on regioselectivity of this reaction proved that the primary hydroxyl group reacts preferably. As shown by <sup>13</sup>C-NMR, a sulfation of secondary hydroxyl groups was detected in HA sulfates only at a degree of sulfation (DS<sub>S</sub>) above 1.0 (Hintze et al., 2009). In addition to regioselective sulfation reactions, there exist two other pathways for directing sulfate groups into specific positions of HA hydroxyl moieties, namely 1) de-sulfation reactions and 2) the use of protecting groups (Bedini et al., 2016; Bedini et al., 2017). Following the former route, desulfation of a high-sulfated HA (DS<sub>S</sub> = 3.1) by means of silylating agents like *N*-methyl-*N*-(trimethylsilyl)-trifluoroacetamide (MSTFA) or *N*,*O*-bis(trimethylsilyl)acetamide (BTSA) resulted in HA sulfates with DS<sub>S</sub> values of 1.5 and 1.6, resp., bearing the sulfate groups mainly at the secondary hydroxyl groups as shown by <sup>13</sup>C-NMR (Becher et al., 2010). In this context, it was found that the benzoyl ester group is suitable to protect the primary hydroxyl group of HA and subsequent sulfation leads to a sulfated benzoylated HA (Becher et al., 2010). Cleavage of the benzoate group under mild alkaline conditions resulted in a HA sulfate with DS<sub>S</sub> values



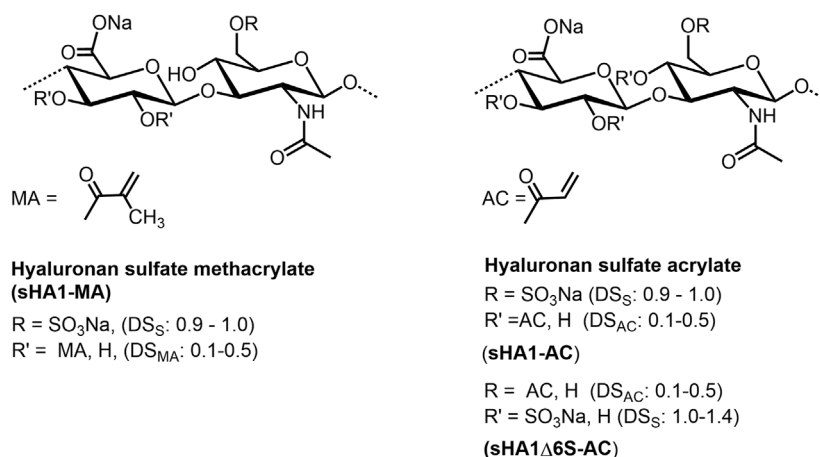


**FIGURE 7 |** Sulfated methacrylates, and sulfated acrylates of HA.

between 2.0 and 3.0.  $^{13}\text{C}$ -NMR confirmed a complete sulfation of the secondary hydroxyl groups and a free primary hydroxyl group. A subsequent esterification of the differently sulfated HA, for example, with (meth)acrylate groups result in mixed HA derivatives bearing both sulfate and (meth)acrylate units in different positions of the disaccharide repeating unit (Rother et al., 2017a; Becher et al., 2012, **Figure 7**). The introduction of a phosphate group into HA could be attractive for their application to biochemical systems via mediation of GAG-protein interactions. Although the phosphorylation of polysaccharides is reported in several reviews (Xu et al., 2019; Zhou and Huang, 2021), only few studies describe the phosphorylation of HA and give detailed characterization data of synthesized HA phosphates (Dulong et al., 2004; Leone et al., 2012; Bojarski et al., 2019). Phosphorylation is associated with several challenges that have not yet been satisfactorily solved. For example, the reactivity of conventional phosphorylating agents is significantly lower compared to sulfating agents, which requires harsher reaction conditions. At the same time, the tendency to crosslinking is much more pronounced with phosphorylation than with

sulfation and hinders homogeneous reaction control. Chemical phosphorylation of HA and other GAG remains a challenge for the preparative polysaccharide chemistry.

### Oxidation

Common oxidation reactions of polysaccharides have recently been reviewed (Palhares et al., 2021). The periodate oxidation, also called Malaprade oxidation acting on *cis*-diols which changes the polysaccharide backbone, and leads to the cleavage of the sugar ring forming corresponding carbonyl moieties (Kristiansen et al., 2010, **Figure 8**). Another typical regioselective oxidation of the primary hydroxyl group is mediated by the 2,2,6,6-tetramethyl-piperidiny-1-oxy radical (Crescenzi et al., 2001; Pierre et al., 2017). The secondary hydroxyl groups and hence the sugar ring form are left unaffected. The actual oxidant in this reaction is the nitroxyl radical in form of a nitrosonium cation, which is continuously regenerated by another oxidant present in the reaction mixture. The oxidation can thus proceed to a high yield with only a catalytic amount of TEMPO (Jiang et al., 2000). In an improved

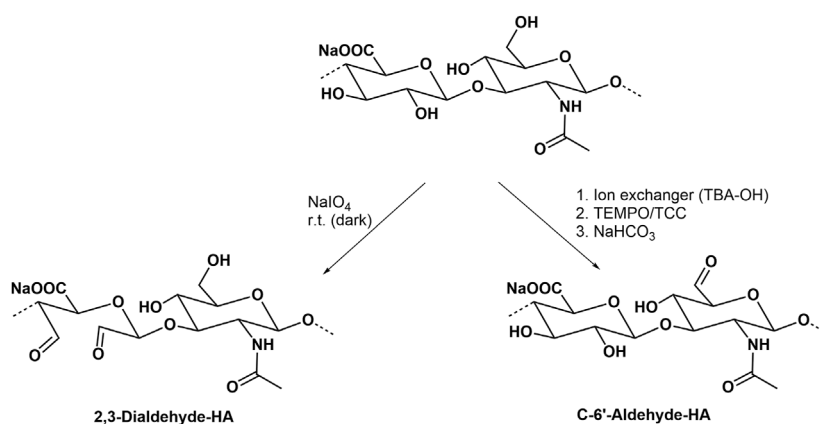


**FIGURE 8 |** Selective oxidation of hydroxyl groups of HA.

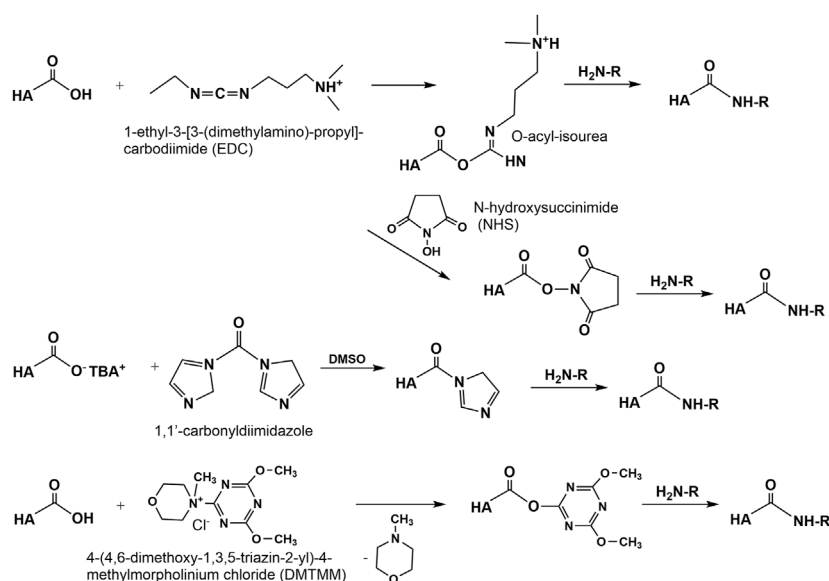


**FIGURE 9 |** Activation of the HA carboxyl group to perform HA amidation.

version, trichloroisocyanuric acid (TCC) is used as a secondary oxidation reagent (**Figure 8**), both to activate and regenerate TEMPO (Shan et al., 2021). Oxidized HA derivatives resulting from both types of oxidation can serve as precursors for the formation of drug releasing hydrogels (Zhang et al., 2011) or the conjugation of proteins (Mero and Campisi, 2014).

Besides TEMPO, also periodinane (also called Dess-Martin periodinane) can be used as a relatively mild oxidation agent which similar to TEMPO is able to transform primary hydroxyl groups from HA to aldehyde functions (Durana et al., 2006; Šedová et al., 2013). Aldehyde-containing HA derivatives have recently shown a high potential to prepare

conjugates with different amines in drug delivery (Buffa et al., 2018).

## Functionalization of the HA Carboxyl Group

### Esterification

Strategies for the modification of the carboxyl group of HA also involve esterification and amidation reactions. Well-known biomaterials synthesized in this context are the family of HYAFF materials, especially the benzyl (HYAFF 11) and the ethyl ester (HYAFF 7) of HA (Benedetti et al., 1990; Benedetti et al., 1993). The HA esters have been prepared from the

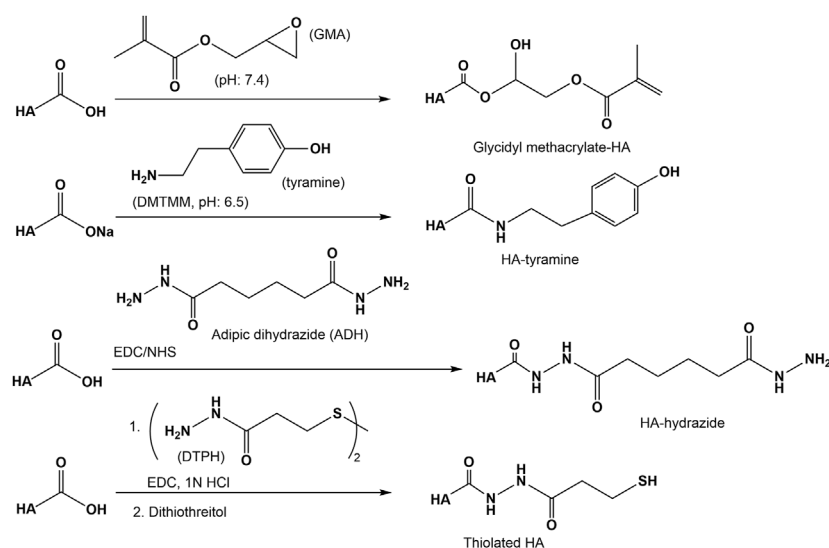


**FIGURE 10 |** Reactions of the HA carboxyl group with epoxides, amines, and hydrazides.

corresponding alcohols after dissolution of the quaternary HA in an aprotic solvent (Campoccia et al., 1998).

The reaction of epoxides with the carboxyl group of HA is in particular reported for the reaction with glycidyl methacrylate to generate methacrylate ester under aqueous conditions with catalytic amounts of triethylamine (Baier Leach et al., 2003; Moeller et al., 2007). As shown by  $^{13}\text{C}$ -NMR studies (Bencherif et al., 2008) at pH 7.4 two reactions occur simultaneously, namely an irreversible ring-opening conjugation through the HA carboxylic group toward the highest substituted carbon of the epoxide and a reversible transesterification through the primary hydroxyl group of HA.

## Amidation

Amidation of the carboxyl group of HA with amines, hydrazines, and hydrazides is one of the most widely used method in the synthesis of new HA amides (Schanté et al., 2011), the design of novel delivery systems (Oh et al., 2010), and also in HA carboxy-based network formation (Burdick and Prestwich, 2011). To initiate amidation, normally the carboxyl group of HA has to be activated. Typical activation agents used are water-soluble carbodiimides like 1-ethyl-3-[3-(dimethylamino)-propyl]-carbodiimide (EDC), often used in combination with 1-hydroxybenzotriazole (HOBt) or N-hydroxysulfosuccinimide (sulfo-NHS) (Bulpitt and Aeschlimann, 1999). Further activating agents are 1,1'-carbonyldiimidazole (D'Este et al., 2012), 2-chloro-1-methylpyridinium iodide (Magnani et al., 2000), 2-chloro-dimethoxy-1,3,5-triazine (Bergman et al., 2007), and 4-(4,6-dimethoxy-1,3,5-triazin-2-yl)-4-methylmorpholinium chloride (D'Este et al., 2014, **Figure 9**). The advantages of DMETMM conjugation, as a powerful tool to synthesize tyramine modified HA hydrogels, which are bio-orthogonally crosslinked with horseradish peroxidase (HRP) and hydrogen peroxide ( $\text{H}_2\text{O}_2$ ) have also been demonstrated (Loebel et al., 2015).

A versatile chemical methodology that allows attachment of therapeutic drugs, reporter groups, crosslinking units, and other bioactive moieties to HA was developed in the Prestwich lab. Several mono-, bis-, and polyhydrazides have been attached at pH 4.0–4.75 in the presence of a water-soluble carbodiimide (EDC) to HA (Prestwich et al., 1998). Under similar conditions dithio-containing hydrazides like 3,3'-dithiobis (propanoic hydrazide) (DTP) were attached to the carboxylic HA group (Shu et al., 2002, **Figure 10**). In the subsequent reaction step, the corresponding HA thiols are formed by addition of DTT. This disulfide cross-linked HA hydrogel can be prepared under physiological conditions without the addition of cross-linking agents and without the production of byproducts.

Another approach to attach thiol groups to HA consist in the reaction of the HA carboxyl group with cystamine in the presence of EDC/NHS at pH 4–5 followed by cleavage of the disulfide using DTT (Jin et al., 2010, **Figure 10**). Using this method, also cysteine was attached via an amide linkage to the HA carboxyl group (Kafedjiiski et al., 2007). As recently shown, such thiolated HA derivatives are known for their mucoadhesive properties as well as enzyme inhibitory, permeation enhancing effects in drug delivery systems (Griesser et al., 2018).

Recently, a disulfide-based protecting group strategy for *in situ* formation of stable HA hydrogels has been developed (Ossipov et al., 2010). In this work a central divalent protecting group, 2,2'-dithiobis (ethoxycarbonyl), which links two identical molecules, was used. The designed reagents allow mild and highly controlled functionalization of HA with various types of nucleophilic chemoselective groups (Ossipov et al., 2010). The used strategy has been applied in later studies for the preparation of *in situ* forming HA gels hybridized with nanoparticles (Kheirabadi et al., 2015) or interpenetrating double HA-fibrin networks as an injectable and biodegradable scaffold for cell proliferation and differentiation (Zhang et al., 2016).

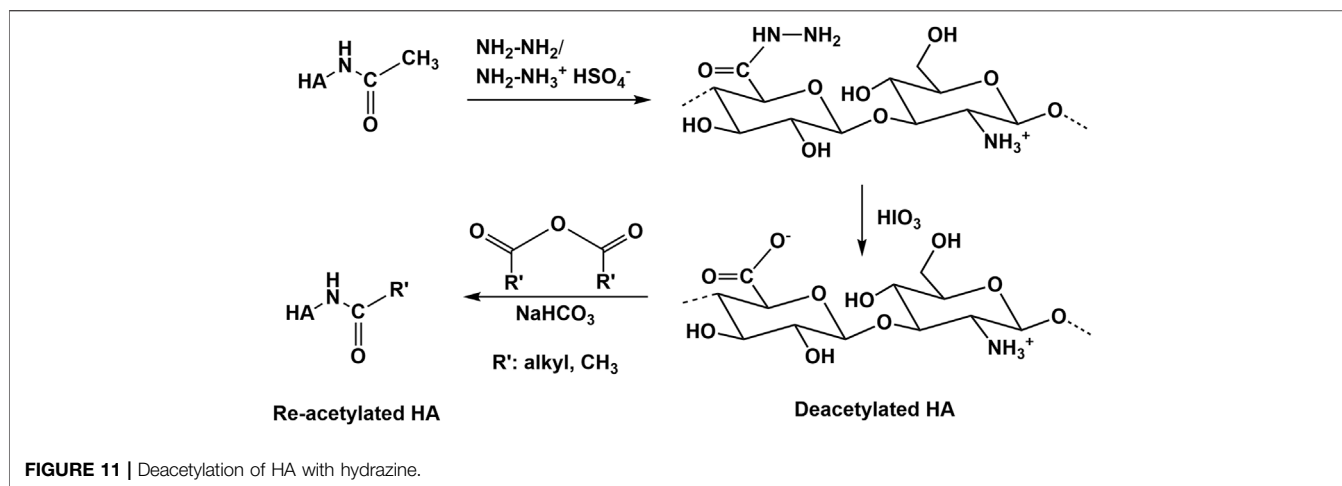
## Modification of the N-Acetyl Group of HA

Deacetylation recovering the free amino group is the main reaction type performed at the N-acetyl group of HA (Sedláček et al., 2020). Usually, deacetylation of HA occurs with hydrazine sulfate at increased temperatures over several days (Dahl et al., 1988; Crescenzi et al., 2002b). Recently, an advanced procedure, using a hydrazine/hydrazine sulfate mixture for deacetylation followed by the addition of iodic acid was described (Zhang et al., 2013; Babasola et al., 2014, **Figure 11**). In addition, partial deacetylation is also possible by treatment of HA with NaOH (Wada et al., 1994). In all these cases a substantial molecular weight decrease occurs. In contrast to chemical methods of N-deacetylation, enzymatic processes of N-deacetylation (Chen et al., 2009; Kim and Kim, 2011) occur at mild conditions without massive molecular weight changes (Sedláček et al., 2020). However, this process requires enzymes (HA-N-deacetylases) which are at present not well described and commercially not available. Future progress in enzyme technology will help to prepare deacetylated HA without using hazardous and HA degrading chemicals. Several subsequent reactions of the amino group of deacetylated HA including reacylation (Babasola et al., 2014) or Ugi-reaction to form novel HA derivatives and hydrogels (Crescenzi et al., 2002b) have been described.

## Conjugation of HA by Reducing End Group Functionalization

Advanced screening applications e.g., as microarrays, functional molecular and cellular assays, as well as biosensors require the attachment of HA to surfaces or other biomaterial scaffolds. In this regard, specific conjugation of active molecules like markers through the reducing end is desirable, as it effectively mimics the cell surface presentation of HA motifs and avoids alteration of HA-peptide interactions by chemical modifications along the biopolymer chain, or by surface-imposed conformational or spatial constraints. The most frequently used techniques for this type of GAG functionalization are currently hydrazone (Altgård et al., 2013; Peerboom et al., 2017) and oxime (Novoa-Carballal and Müller, 2012; Thakar et al., 2014) ligation chemistry. Another procedure uses reductive amination with e.g., ethylenediamine dihydrochloride and sodium cyanoborohydride (Clauder et al., 2020). Examples of conjugation reactions are presented in **Figure 12**.





HA functionalization at the reducing end can also be performed with a thiol group, enabling direct immobilization on gold and other metal surfaces and coupling to marker molecules as biotin. The end group functionalization is performed treating HA with cysteamine and using sodium cyanoborohydride as reductive agent (Minsky et al., 2016).

## Interaction of Chemically Modified Hyaluronan With Biological Mediator Proteins

The interaction analyses of sulfated and carboxymethylated GAG derivatives with the biological mediator proteins transforming growth factor- $\beta$ 1 (TGF- $\beta$ 1), bone morphogenetic protein-2 and -4 (BMP-2 and -4) and osteoprotegerin (OPG) were previously reviewed (Schnabelrauch et al., 2013; Scharnweber et al., 2015) and are briefly summarized here. For these interactions, sulfation degree and patterns as well as the structure of the sugar backbone were identified as major determinants for binding strength as revealed by combining immunobiochemical methods and surface plasmon resonance (SPR) with molecular modelling (Hintze et al., 2009; Hintze et al., 2012; Salbach-Hirsch et al., 2013; Hintze et al., 2014). Using the complementary experimental methods, ELISA and SPR, with either the GAG or the proteins immobilized it could be shown that the derived GAG binding profiles match in general, excluding effects due to immobilization of one interaction partner. HA derivatives were found to interact stronger than the corresponding CS derivatives with the same sulfation degree (Hintze et al., 2009; Hintze et al., 2012; Hintze et al., 2014). Since the natural CS used for sulfation contained 70% chondroitin-4-sulfate and 30% chondroitin-6-sulfate, differences in the sulfation degree of the C-4 position, next to different geometries of the sugar backbone, were identified as possible reasons for this effect. Further, the additional carboxymethylation of the high-sulfated sHA3 was detrimental for the binding strength towards TGF- $\beta$ 1, which was attributed to possible differences in the C-4 and C-6 sulfation due to carboxymethylation preceding the sulfation reaction (Hintze et al., 2012).

In case of BMP-2 and OPG the biological relevance of the GAG/mediator protein interaction was further investigated by including cell receptors or other natural interaction partners in the SPR interaction studies, i.e. BMP-2 receptor-IA/Fc chimera or receptor activator NF- $\kappa$ B ligand (RANKL) (Salbach-Hirsch et al., 2013; Hintze et al., 2014). Here, the latter were immobilized on the sensor surface and studied for their interaction with the mediator proteins pre-incubated with HA derivatives. In both cases, this resulted in a concentration- and sulfation-dependent decrease of the binding response indicating that HA derivatives interfere with the complexation of these natural interaction partners and thus reduce the biological activity of the respective biological mediators. For OPG, SPR findings on the biological relevance were supported in a RANKL-induced *in vitro* osteoclastogenesis model demonstrating a rescued osteoclast formation after pre-incubation of OPG with sulfated GAG (Salbach-Hirsch et al., 2013). In both cases, the integration of computational methods revealed how sHA derivatives influence the interplay of these mediators with their natural interaction partners up to the atomic level.

This approach was subsequently applied on further biological systems to gain a broader understanding of the structure-function relationship of GAG in their interaction with mediator proteins relevant to the healing process in bone and skin and the biological consequences of these interactions.

The biological relevance of the GAG/TGF- $\beta$ 1 interaction was further investigated by including its natural receptors TGF- $\beta$  receptor-I (T $\beta$ R-I) and -II (T $\beta$ R-II) (Koehler et al., 2017). As for BMP-2 and OPG, sHA blocked binding of TGF- $\beta$ 1 to its receptors in a concentration- and sulfation-dependent manner, supporting a previous publication showing an impaired TGF- $\beta$ 1 driven differentiation of dermal fibroblasts due to TGF- $\beta$ 1 interaction with sHA derivatives (van der Smitten et al., 2013).

The capability of GAG derivatives to modulate canonical Wnt signaling, in particular the activity of the extracellular inhibitors sclerostin (SOST) and Dickkopf (Dkk-1) that promote osteoclastogenesis and bone resorption, was evaluated utilizing a combination of the abovementioned complementary methods

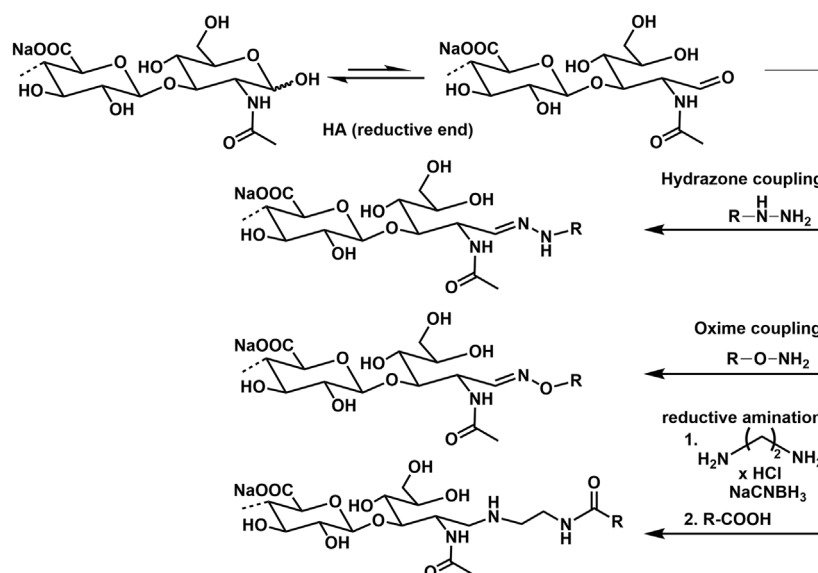


**FIGURE 12 |** Conjugation of amino group containing molecules at the reducing end of HA.

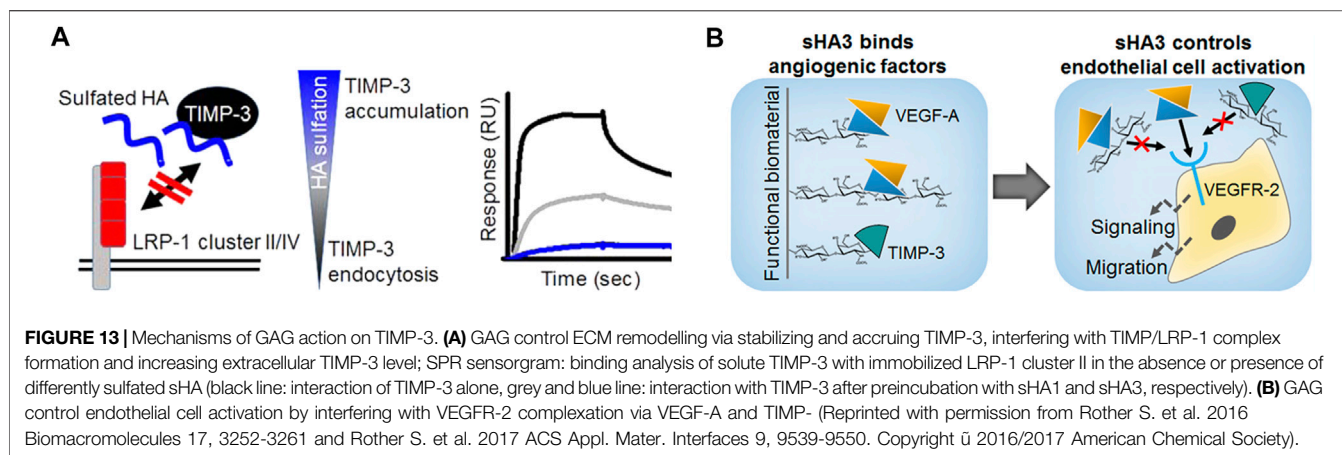
(Salbach-Hirsch et al., 2015; Gronbach et al., 2020). SPR revealed that GAG interact with SOST in a concentration- and sulfation-dependent manner, with sHA3 being the strongest binder, while high-sulfated CS (sCS3) and heparin demonstrated significantly weaker binding (Salbach-Hirsch et al., 2015). In contrast, HA binding was found to be marginal. The biological relevance was verified in an LRP5/SOST interaction study and in an *in vitro* model of Wnt activation showing a sulfation- and concentration-dependent reduction in bioactivity due to the SOST/GAG interaction via interference with sclerostin/LRP5/6 complex formation.

The sulfation-dependent interaction of sHA3 with Dkk-1 was demonstrated by SPR analysis (Gronbach et al., 2020). Further, binding affinity was found to be comparable for those derivatives containing an ATTO-565 fluorescent label to non-labeled sHA3, while non-sulfated ATTO-labeled GAG showed negligible binding responses towards Dkk-1. This result was in line with findings of the same study on a macromer-based film covalently decorated with ATTO-labeled sHA3 efficiently scavenging Dkk-1 and displaying pro-osteogenic effects with SaOS-2 cells and primary human mesenchymal stem cells (hMSC).

The interaction of polymeric and oligomeric GAG derivatives with heparin-binding EGF-like growth factor (HB-EGF), a major factor activating keratinocytes and dermal fibroblasts in skin wound healing, was analyzed via SPR and molecular modeling (Thönes et al., 2019). While there was no binding detected for non-sulfated HA, CS and sHA1 were found to interact with HB-EGF. Interestingly, heparin displayed the same binding strength as sHA1 albeit a higher sulfation degree. This indicated that next to sulfation degree, the sulfation pattern and/or the structure of the sugar-backbone might play a role. This was supported by the interaction profiles of HA oligosaccharides with immobilized HB-EGF demonstrating an interaction for those molecules with at least one sulfate group at the C4 or C6 position of the

N-acetylglucosamine unit. In this case, the binding strength of sHA tetrasaccharides increased with the degree of sulfation. Importantly, the interaction strength of a persulfated hexasaccharide was found to be lower than for its tetrasaccharide counterpart, highlighting an additional effect of chain length. These findings provided a rational for the development of sHA1-containing HA/collagen hydrogels that were found to improve wound healing processes *in vitro* and in a porcine skin organ culture model by the sustained release of biologically active HB-EGF.

A particular striking example of how biophysical/biochemical interaction analyses in combination with computational methods and *in vitro* cell culture models move forward insights into the mechanism of GAG action, are a compendium of studies regarding the tissue inhibitor of metalloproteinases-3 (TIMP-3). First of all, the molecular interplay of polymeric and oligomeric GAG derivatives with TIMP-3 was demonstrated by SPR, molecular modeling and hydrogen/deuterium exchange mass spectrometry (Rother et al., 2016a). Interestingly, unlike for previously investigated mediators, the interaction of sHA derivatives was found to be of comparable strength than for the corresponding sCS derivatives with the same sulfation degree. Importantly, this interaction did not limit the capacity of TIMP-3 to inhibit matrix metalloproteinase-1/-2 (MMP-1/-2) in enzyme kinetics, since no overlap of the binding sites was revealed. These observations pointed towards a novel strategy for controlling ECM remodelling by GAG, e.g. in chronic wound situations, via stabilizing and accruing TIMP-3, while maintaining its inhibitory activity towards MMP activity. This hypothesis was further corroborated by the observation that TIMP-3 directly interacts with clusters of the endocytic receptor low-density lipoprotein receptor-related protein (LRP-1) (Rother et al., 2016b; **Figure 13A**). GAG were shown to interfere with this TIMP-3/LRP-1 complex formation in a sulfation-dependent



manner. Further, sHA1 was found to increase the extracellular TIMP-3 level of hMSC. Thus, sHA-containing biomaterials might be promising to interfere with pathological matrix degradation and thereby encourage wound healing. Finally, a novel mechanism was identified by which GAG might control angiogenic processes (Rother et al., 2017b; **Figure 13B**), which could be of interest in angiogenesis-related diseases. By blocking the binding of both, VEGF-A and the angiogenic inhibitor TIMP-3, to the VEGF-A receptor VEGFR-2, GAG reduce the biological activity in a sulfation-dependent manner. When TIMP-3/sHA complexes were simultaneously forming, VEGF-A/VEGFR-2 signaling was partially rescued. While labeling sHA3 with an ATTO-565 fluorescent label did not change the binding characteristics of sHA3 with immobilized Dkk-1 as mentioned above (Gronbach et al., 2020), acrylation significantly reduced binding strength of the low sulfated HA derivatives, sHA1 and sHA1Δ6s, towards immobilized VEGF-A in SPR analysis as well as in molecular docking and dynamics (MD) simulations (Rother et al., 2021). This was supported by a solid-phase binding assays with immobilized GAG demonstrating a significantly negative effect of acrylation for sHA1Δ6s suggesting that the presence of acrylate groups alter the accessibility of the sulfate groups and/or have a detrimental effect on the optimal carbohydrate conformation. When translated to sHA-containing acrylated HA/collagen hydrogels, this led to biomaterials releasing biologically active VEGF-A in a defined manner depending on the substitution pattern of the sulfated GAG. In turn angiogenic processes like endothelial cell proliferation and the formation of an extended morphology, indicating sprouting, could be controlled. Together with the findings of Thönes et al., it can be concluded that multivalent carbohydrate-based hydrogels containing acrylated sHA derivatives are promising for reaching distinct growth factor delivery profiles, increasing the healing capacity of vascularized tissues.

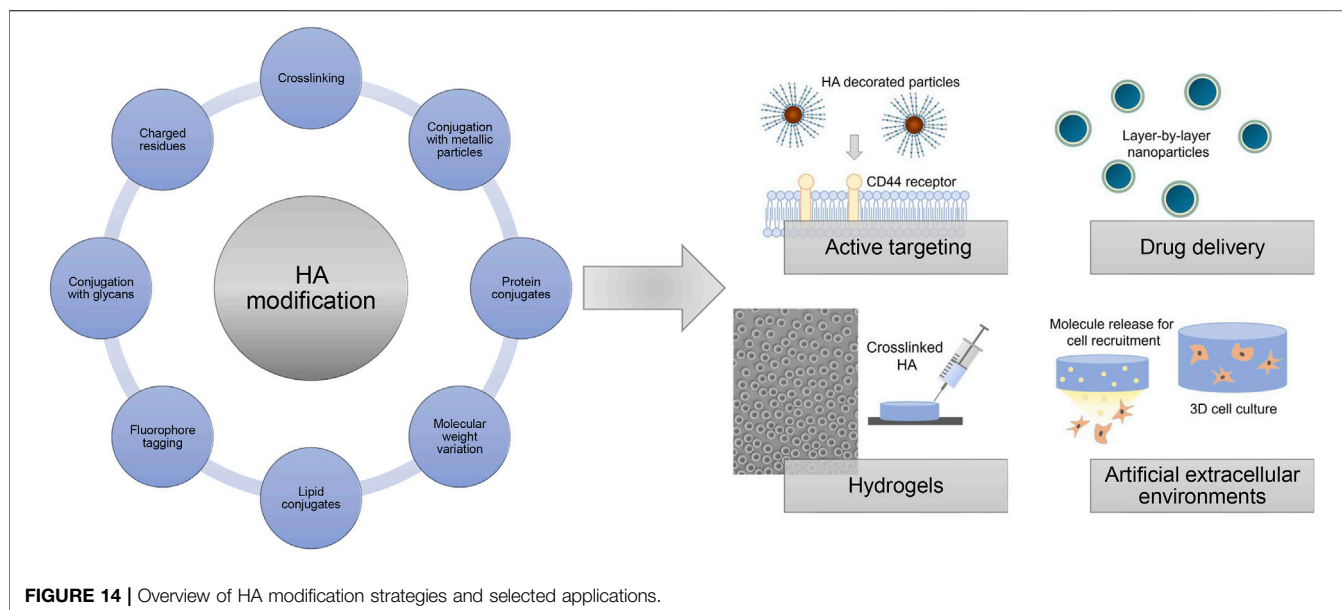
## HA AS BIOMEDICAL POLYMER MATRIX

Native HA is biofunctional and forms viscoelastic biocompatible and degradable polymer networks making it an interesting

material for medical and pharmacological applications. However, modifying HA is especially favorable to overcome certain limitations of native HA such as the quick enzymatic degradation and rapid dissolution in water (Smejkalová et al., 2012b). A higher enzymatic resistance as well as tunable solvation profiles are often prerequisites for biomedical applications. The simplest usage of HA is in form of solutions in physiological buffers, where different properties are achieved by varying the concentration as well as the molecular weight of HA (Nicholls et al., 2018). Hybrid complexes composed of thermally treated HMW-HA and LMW-HA based on biophysical interactions between hydrogen bonds of HA chains are explored as injectable polymer matrix especially for the treatment of osteoarthritis (Stellavato et al., 2019; La Gatta et al., 2021).

Chemical modification strategies targeting the preponderantly present carboxylic acid groups, or primary and secondary hydroxyl groups and, after deamidation, the *N*-acetyl groups, give rise to HA derivatives with altered biological as well as material properties (**Figure 14**). The introduction of hydrophobic groups allows to encapsulate for example, hydrophobic drugs in amphiphilic HA, which was used for active targeting and drug delivery (Smejkalová et al., 2012b; Huerta-Angeles et al., 2014; Kwag et al., 2014; Huerta-Angeles et al., 2016). Achieving tailored HA properties depends on precise and effective synthesis strategies. In this regard, functionalized HA can be used to generate films and hydrogels after crosslinking with different mechanical properties as sprays, wound dressings, scaffolds for tissue engineering approaches or as anti-adhesive materials (Eng et al., 2010; Gebe et al., 2017; reviewed in Burdick and Prestwich, 2011).

In addition, HA derivatives conjugated with metallic particles, like gold nano particles, are explored for targeted treatment of infected and cancer cells (Lee et al., 2012; Sanfilippo et al., 2020). HA-protein conjugates using for example, growth factors have been produced to mask the protein activity and to extend the protein stability (Ferguson et al., 2010; Altiok et al., 2016). Commercially available degradation assays use immobilized biotin-tagged HA as substrate to determine hyaluronidase activities (Krupkova et al., 2020). Another way to use HA for mimicking the native cell microenvironment is by physically



entrapment of HA of different molecular weights within a polymer network like collagen fibers (Rother et al., 2015; Unnikandam Veetil et al., 2021).

The negative charge of HA allows for non-specific adsorption on cationic surfaces such as poly (L-lysine)-coated substrates and layer-by-layer approaches (Dreaden et al., 2014; Kocourková et al., 2021). Bisphosphonate-functionalized HA was used as injectable non-covalently self-assembling hydrogel with reversible calcium binding properties (Nejadnik et al., 2014). Surfaces coated with HA-binding proteins like aggrecan globular domain 1 (HA binding protein, HABP) or HA binding peptides allow for a more selective capturing of HA, which can be used for potential interaction studies e.g. in form of enzyme-linked immunosorbent assays and GAG-protein microarrays (Yuan et al., 2013; Faust et al., 2018). HA derivatives with introduced negatively charged residues like sulfate groups and networks composed of HA covalently linked to sulfated GAG derivatives like chondroitin sulfate are also exploited as platforms with tunable growth factor presentation and release to direct cellular behavior (Ni et al., 2015; Thönes et al., 2019). Furthermore, HA derivatives with covalently attached fluorophores are widely applied as tools studying the potential association and translocation of HA in biological contexts (AlKhouri et al., 2020). Overall, modified HA derivatives are widely used and explored in different biomedical fields and applications repeatedly indicating the great promise for future customized therapies.

Due to its transparency and its lubricating and hydrophilic properties, HA solutions are often used during ophthalmic surgery and for ophthalmic preparations such as eye drops treating the dry eye syndrome (Huerta Angeles and Nesporova, 2021). Furthermore, HA is widely applied as part of contact lenses, for surface modifications of medical lenses and for sustained drug release to treat eye-related diseases (Chang

et al., 2021). Subcutaneous injections of HA solutions and *in situ* forming hydrogels are applied in aesthetic dermatology for reducing wrinkles, folds, and augmenting for example, lips (Rah, 2011). In addition, viscosupplementation with HA formulations is often used to treat osteoarthritis in the knee and in other joints by reducing the mechanical stress on the joints (Henrotin et al., 2015).

## PERSPECTIVES AND CONCLUDING REMARKS

In the last decades, the development of HA as a biomaterial has been a major success due to the good industrial availability of pure HA and its properties including an excellent biocompatibility, an adjustable biodegradability, mucoadhesiveness and viscoelasticity.

This review aims to provide a short overview about known and suitable chemical methods to modify the natural GAG, HA, which is of particular interest in the field of tissue regeneration and regenerative medicine. Due to the mentioned challenges of limited HA solubility in organic solvents and its sensitivity to more drastic chemical reaction conditions with regard to oxidative or thermal stress, and both strong acidic or alkaline environment, the controlled chemical modification of this multifunctional polysaccharide is still a challenging task. Nevertheless, during the last decade, numerous regioselective syntheses routes could be elaborated, which proceed with high control of regioselectivity regarding the degree and the position of substitution along the HA chain as well as with largely preservation of the HA molecular weight. At last, this could also be achieved by the advancement of modern polymer analytics, especially high-resolution NMR-spectroscopy. A current trend is the combination of conjugation and cross-linking processes using bioactive molecules for applications in



regenerative medicine, pharmaceuticals and bioengineering, including cell and bioactive molecule delivery combined with tissue engineering scaffolds (Knopf-Marques et al., 2016; Fallacara et al., 2017). Although HA displays a great number of potential applications, further studies and technological advancement are necessary as there are still some open questions to be answered. The key mechanisms that control the molecular weight of HA during biotechnological synthesis has to be clarified to develop methods for the production of defined HA with uniform size (Fallacara et al., 2018). Also the reproducibility of the preparation of HA derivatives during scale-up processes has to be improved as a basis for their successful commercialization.

A wide range of biological activities has been investigated using modified HA derivatives and some of these applications are highlighted in this paper. HA has a broad scientific capability and especially the role of sulfated HA in viral infections, and the potential of HA and other GAG to address numerous medical and biotechnological challenges is becoming without any doubt the focus of renewed attention.

## REFERENCES

- AlKhoury, H., Hautmann, A., Erdmann, F., Zhou, G., Stojanović, S., Najman, S., et al. (2020). Study on the Potential Mechanism of Anti-inflammatory Activity of Covalently Immobilized Hyaluronan and Heparin. *J. Biomed. Mater. Res. A* 108, 1099–1111. doi:10.1002/jbm.a.36885
- Altgård, N., Nilebäck, E., de Battice, L., Pashkuleva, I., Reis, R. L., Becher, J., et al. (2013). Probing the Biofunctionality of Biotinylated Hyaluronan and Chondroitin Sulfate by Hyaluronidase Degradation and Aggrecan Interaction. *Acta Biomater.* 9, 8158–8166. doi:10.1016/j.actbio.2013.05.031
- Altiok, E. I., Santiago-Ortiz, J. L., Svedlund, F. L., Zbinden, A., Jha, A. K., Bhatnagar, D., et al. (2016). Multivalent Hyaluronic Acid Bioconjugates Improve sFlt-1 Activity *In Vitro*. *Biomaterials* 93, 95–105. doi:10.1016/j.biomaterials.2016.03.017
- Amorim, S., Reis, C. A., Reis, R. L., and Pires, R. A. (2021). Extracellular Matrix Mimics Using Hyaluronan-Based Biomaterials. *Trends Biotechnol.* 39, 90–104. doi:10.1016/j.tibtech.2020.06.003
- Babasola, O., Rees-Milton, K. J., Bebe, S., Wang, J., and Anastasiades, T. P. (2014). Chemically Modified N-Acylated Hyaluronan Fragments Modulate Proinflammatory Cytokine Production by Stimulated Human Macrophages. *J. Biol. Chem.* 289, 24779–24791. doi:10.1074/jbc.M113.515783
- Badri, A., Asher Williams, A., Robert J Linhardt, R. J., and Koffas, M. A. G. (2018). The Road to Animal-free Glycosaminoglycan Production: Current Efforts and Bottlenecks. *Curr. Opin. Biotechnol.* 53, 85–92. doi:10.1016/j.copbio.2017.12.018
- Baier Leach, J., Bivens, K. A., Patrick, C. W., Jr., and Schmidt, C. E. (2003). Photocrosslinked Hyaluronic Acid Hydrogels: Natural, Biodegradable Tissue Engineering Scaffolds. *Biotechnol. Bioeng.* 82, 578–589. doi:10.1002/bit.10605
- Balazs, E. A. (1979). "Ultrapure Hyaluronic Acid and the Use There of". U.S. Patent No. 4,141,973,27.
- Balazs, E. A., Högborg, B., and Laurent, T. C. (1951). The Biological Activity of Hyaluron Sulfuric Acid. *Acta Physiol. Scand.* 23, 168–178. doi:10.1111/j.1748-1716.1951.tb00806.x
- Becher, J., Moeller, S., and Schnabelrauch, M. (2013). Phase Transfer-Catalyzed Synthesis of Highly Acrylated Hyaluronan. *Carbohydr. Polym.* 93, 438–441. doi:10.1016/j.carbpol.2012.12.056
- Becher, J., Moeller, S., Weiss, D., Schiller, J., and Schnabelrauch, M. (2010). Synthesis of New Regioselectively Sulfated Hyaluronans for Biomedical Application. *Macromol. Symp.* 296, 446–452. doi:10.1002/masy.201051060
- Becher, J., Möller, S., Riemer, T., Schiller, J., Hintze, V., Bierbaum, S., et al. (2012). Sulfated Glycosaminoglycan Building Blocks for the Design of Artificial Extracellular Matrices. *ACS Symp. Ser.* 1107, 315–328. doi:10.1021/bk-2012-1107.ch017
- Bedini, E., Laezza, A., and Iadonisi, A. (2016). Chemical Derivatization of Sulfated Glycosaminoglycans. *Eur. J. Org. Chem.* 2016, 3018–3042. doi:10.1002/ejoc.201600108
- Bedini, E., Laezza, A., Michelangelo Parrilli, M., and Iadonisi, A. (2017). A Review of Chemical Methods for the Selective Sulfation and Desulfation of Polysaccharides. *Carbohydr. Polym.* 174, 1224–1239. doi:10.1016/j.carbpol.2017.07.017
- Bencherif, S. A., Srinivasan, A., Horkay, F., Hollinger, Matyjaszewski, J. O. K., and Washburn, N. R. (2008). Influence of the Degree of Methacrylation on Hyaluronic Acid Hydrogels Properties. *Biomaterials* 29, 1739–1749. doi:10.1016/j.biomaterials.2007.11.047
- Benedetti, L., Cortivo, R., Berti, T., Berti, A., Pea, F., Mazza, M., et al. (1993). Biocompatibility and Biodegradation of Different Hyaluronan Derivatives (Hyaff) Implanted in Rats. *Biomaterials* 14, 1154–1160. doi:10.1016/0142-9612(93)90160-4
- Benedetti, L. M., Topp, E. M., and Stella, V. J. (1990). Microspheres of Hyaluronic Acid Esters - Fabrication Methods and *In Vitro* Hydrocortisone Release. *J. Controlled Rel.* 13, 33–41. doi:10.1016/0168-3659(90)90072-2
- Bergman, K., Elvingson, C., Hilborn, J., Svensk, G., and Bowden, T. (2007). Hyaluronic Acid Derivatives Prepared in Aqueous Media by Triazine-Activated Amidation. *Biomacromolecules* 8, 2190–2195. doi:10.1021/bm0701604
- Blundell, C. D., Michelle Reed, M. A. C., and Almond, A. (2006). Complete Assignment of Hyaluronan Oligosaccharides up to Hexasaccharides. *Carbohydr. Res.* 341, 2803–2815. doi:10.1016/j.carres.2006.09.023
- Boeriu, C. G., Springer, J., Kooy, F. K., van den Broek, L. A. M., and Eggink, G. (2013). Production Methods for Hyaluronan. *Int. J. Carbohydr. Chem.* 2013, 624967. doi:10.1155/2013/624967
- Bohaumilitzky, L., Huber, A.-K., Stork, E. M., Wengert, S., Woelfl, F., and Boehm, H. (2017). A Trickster in Disguise: Hyaluronan's Ambivalent Roles in the Matrix. *Front. Oncol.* 7, 242. doi:10.3389/fonc.2017.00242
- Bojarski, K. K., Becher, J., Riemer, T., Lemmertz, K., Möller, S., Schiller, J., et al. (2019). Synthesis and *In Silico* Characterization of Artificially Phosphorylated Glycosaminoglycans. *J. Mol. Struct.* 1197, 401–416. doi:10.1016/j.molstruc.2019.07.064
- Botha, C., Kuntz, J.-F., Moire, C., Farcet, C., Pfuikwa, H., and Pasch, H. (2018). Molar Mass Analysis of Hydrophobically Modified Hyaluronic Acid by SEC-MALLS: Facing the Challenges of Amphiphilic Biomacromolecules. *Macromol. Chem. Phys.* 219, 1800233. doi:10.1002/macp.201800233

## AUTHOR CONTRIBUTIONS

VH: Wrote the chapter "Interaction of Chemically Modified Hyaluronan With Biological Mediator Proteins," prepared the respective figure and revised the complete manuscript critically. SR: Wrote the abstract, the chapter "HA as Biomedical Polymer Matrix" and parts of "Occurrence, Biosynthesis, and Degradation," prepared the respective figure and revised the complete manuscript critically. MS: Wrote all other chapters of the manuscript, and prepared the respective figures. All authors substantially contributed to the conception of this review, and revised the complete manuscript critically. All authors agree to be accountable for the content of the work.

## FUNDING

Authors VH and MS acknowledge funding by the Deutsche Forschungsgemeinschaft (DFG, project number 59307082—TRR67, subprojects Z3, A3).



- Bothner, H., Waaler, T., and Wik, O. (1988). Limiting Viscosity Number and Weight Average Molecular Weight of Hyaluronate Samples Produced by Heat Degradation. *Int. J. Biol. Macromol.* 10, 287–291. doi:10.1016/0141-8130(88)90006-2
- Buffa, R., Odstrčilová, L., Šedová, P., Basarabová, I., Novotný, J., and Velebný, V. (2018). Conjugates of Modified Hyaluronic Acid with Amino Compounds for Biomedical Applications. *Carbohydr. Polym.* 189, 273–279. doi:10.1016/j.carbpol.2018.02.048
- Bulpitt, P., and Aeschlimann, D. (1999). New Strategy for Chemical Modification of Hyaluronic Acid: Preparation of Functionalized Derivatives and Their Use in the Formation of Novel Biocompatible Hydrogels. *J. Biomed. Mater. Res.* 47, 152–169. doi:10.1002/(SICI)1097-4636(199911)47:2<152::AID-JBM5>3.0.CO;2-I
- Burdick, J. A., Chung, C., Jia, X., Randolph, M. A., and Langer, R. (2005). Controlled Degradation and Mechanical Behavior of Photopolymerized Hyaluronic Acid Networks. *Biomacromolecules* 6, 386–391. doi:10.1021/bm049508a
- Burdick, J. A., and Prestwich, G. D. (2011). Hyaluronic Acid Hydrogels for Biomedical Applications. *Adv. Mater.* 23, H41–H56. doi:10.1002/adma.201003963
- Calles, J. A., Tártara, L. I., Lopez-García, A., Diebold, Y., Palma, S. D., and Vallés, E. M. (2013). Novel Bioadhesive Hyaluronan–Itaconic Acid Crosslinked Films for Ocular Therapy. *Int. J. Pharmaceut.* 455, 48–56. doi:10.1016/j.ijpharm.2013.07.063
- Campoccia, D., Doherty, P., Radice, M., Brun, P., Abatangelo, G., and Williams, D. F. (1998). Semisynthetic Resorbable Materials from Hyaluronan Esterification. *Biomaterials* 19, 2101–2127. doi:10.1016/S0142-9612(98)00042-8
- Caputo, H. E., Straub, J. E., and Grinstaff, M. W. (2019). Design, Synthesis, and Biomedical Applications of Synthetic Sulphated Polysaccharides. *Chem. Soc. Rev.* 48, 2338–2365. doi:10.1039/C7CS00593H
- Chang, W. H., Liu, P. Y., Lin, M. H., Lu, C. J., Chou, H. Y., Nian, C. Y., et al. (2021). Applications of Hyaluronic Acid in Ophthalmology and Contact Lenses. *Molecules* 26, 2485. doi:10.3390/molecules26092485
- Chen, F., Kakizaki, I., Yamaguchi, M., Kojima, K., Takagaki, K., and Endo, M. (2009). Novel Products in Hyaluronan Digested by Bovine Testicular Hyaluronidase. *Glycoconj. J.*, 26, 559–566. doi:10.1007/s10719-008-9200-2
- Clauder, F., Moeller, S., Köhling, S., Bellmann-Sickert, K., Rademann, J., Schnabelrauch, M., et al. (2020). Peptide-mediated Surface Coating for the Release of Wound-Healing Cytokines. *J. Tissue Eng. Regen. Med.* 14, 1738–1748. doi:10.1002/term.3123
- Collins, M. N., and Birkinshaw, C. (2007). Comparison of the Effectiveness of Four Different Crosslinking Agents with Hyaluronic Acid Hydrogel Films for Tissue-Culture Applications. *J. Appl. Polym. Sci.* 104, 3183–3191. doi:10.1002/app.25993
- Collins, M. N., and Birkinshaw, C. (2013). Hyaluronic Acid Based Scaffolds for Tissue Engineering—A Review. *Carbohydr. Polym.* 92, 1262–1279. doi:10.1016/j.carbpol.2012.10.028
- Cožiková, D., Šilová, T., Moravcová, V., Smejkalová, D., Pepeliaev, S., Velebný, V., et al. (2017). Preparation and Extensive Characterization of Hyaluronan with Narrow Molecular Weight Distribution. *Carbohydr. Polym.* 160, 134–142. doi:10.1016/j.carbpol.2016.12.045
- Crescenzi, V., Francescangeli, A., Renier, D., and Bellini, D. (2002a). New Cross-Linked and Sulfated Derivatives of Partially Deacetylated Hyaluronan: Synthesis and Preliminary Characterization. *Biopolymers* 64, 86–94. doi:10.1002/bip.10131
- Crescenzi, V., Francescangeli, A., Renier, D., and Bellini, D. (2001). New Hyaluronan Chemical Derivatives. Regioselectively C(6) Oxidized Products. *Macromolecules* 34, 6367–6372. doi:10.1021/ma0102363
- Crescenzi, V., Francescangeli, A., Segre, A. L., Capitani, D., Mannina, L., Renier, D., et al. (2002b). NMR Structural Study of Hydrogels Based on Partially Deacetylated Hyaluronan. *Macromol. Biosci.* 2, 272–279. doi:10.1002/1616-5195(200208)2:6<272::AID-MABI272>3.0.CO;2-V
- Cyphert, J. M., Trempus, C. S., and Garantziotis, S. (2015). Size Matters: Molecular Weight Specificity of Hyaluronan Effects in Cell Biology. *Int. J. Cell Biol.* 2015, 1–8. doi:10.1155/2015/563818
- Dahl, L. B., Laurent, T. C., and Smedsrod, B. (1988). Preparation of Biologically Intact Radioiodinated Hyaluronan of High Specific Radioactivity: Coupling of <sup>125</sup>I-Tyramine-Cellobiose to Amino Groups after Partial N-Deacetylation. *Analyt. Biochem.* 175, 397–407. doi:10.1016/0003-2697(88)90563-5
- D'Amora, U., Ronca, A. A., Raucci, M. G., Dozio, S. M., Lin, H. H., Fan, Y. Y., et al. (2019). *In Situ* sol-gel Synthesis of Hyaluronan Derivatives Bio-Nanocomposite Hydrogels. *Regen. Biomater.* 6, 249–258. doi:10.1093/rb/rbz029
- De Boule, K., Glogau, R., Kono, T., Nathan, M., Tezel, A., Roca-Martinez, J. X., et al. (2013). A Review of the Metabolism of 1,4-Butanediol Diglycidyl Ether–Crosslinked Hyaluronic Acid Dermal Fillers. *Dermatol. Surg.* 39, 1758–1766. doi:10.1111/dsu.12301
- DeAngelis, P. L. (2012). Glycosaminoglycan Polysaccharide Biosynthesis and Production: Today and Tomorrow. *Appl. Microbiol. Biotechnol.* 94, 295–305. doi:10.1007/s00253-011-3801-6
- DeAngelis, P. L., Liu, J., and Linhardt, R. J. (2013). Chemoenzymatic Synthesis of Glycosaminoglycans: Re-creating, Re-modeling and Re-designing Nature's Longest or Most Complex Carbohydrate Chains. *Glycobiology* 23, 764–777. doi:10.1093/glycob/cwt016
- D'Este, M., Eglina, D., and Alini, M. (2014). A Systematic Analysis of DMTMM vs EDC/NHS for Ligation of Amines to Hyaluronan in Water. *Carbohydr. Polym.* 108, 239–246. doi:10.1016/j.carbpol.2014.02.070
- D'Este, M., Alini, M., and Eglina, D. (2012). Single Step Synthesis and Characterization of Thermoresponsive Hyaluronan Hydrogels. *Carbohydr. Polym.* 90, 1378–1385. doi:10.1016/j.carbpol.2012.07.007
- Dicker, K. T., Gurski, L. A., Pradhan-Bhatt, S., Witt, R. L., Farach-Carson, M. C., and Jia, X. (2014). Hyaluronan: A Simple Polysaccharide with Diverse Biological Functions. *Acta Biomater.* 10, 1558–1570. doi:10.1016/j.copbio.2017.12.018
- Dovedytis, M., Liu, Z. J., and Bartlett, S. (2020). Hyaluronic Acid and its Biomedical Applications: A Review. *Engin. Regen.* 1, 102–113. doi:10.1016/j.engreg.2020.10.001
- Dreaden, E. C., Morton, S. W., Shpowsitz, K. E., Choi, J. H., Deng, Z. J., Cho, N. J., et al. (2014). Bimodal Tumor-Targeting from Microenvironment Responsive Hyaluronan Layer-By-Layer (LbL) Nanoparticles. *ACS Nano* 8 (8), 8374–8382. doi:10.1021/nn502861t
- Duan, J., and Kasper, D. L. (2011). Oxidative Depolymerization of Polysaccharides by Reactive Oxygen/nitrogen Species. *Glycobiology* 21, 401–409. doi:10.1093/glycob/cwq171
- Dulong, V., Lack, S., Le Cerf, D., Picton, L., Vannier, J. P., and Muller, G. (2004). Hyaluronan-based Hydrogels Particles Prepared by Crosslinking with Trisodium Trimetaphosphate. Synthesis and Characterization. *Carbohydr. Polym.* 57, 1–6. doi:10.1016/j.carbpol.2003.12.006
- Durana, R., Lacik, I., Paulovicova, E., and Bystricky, S. (2006). Functionalization of Mannans from Pathogenic Yeasts by Different Means of Oxidations – Preparation of Precursors for Conjugation Reactions with Respect to Preservation of Immunological Properties. *Carbohydr. Polym.* 63, 72–81. doi:10.1016/j.carbpol.2005.08.003
- Eenschooten, C., Guillaumie, F., Kontogeorgis, G. M., Stenby, E. H., and Schwach-Abdellouki, K. (2010). Preparation and Structural Characterisation of Novel and Versatile Amphiphilic Octenyl Succinic Anhydride–Modified Hyaluronic Acid Derivatives. *Carbohydr. Polym.* 79, 597–605. doi:10.1016/j.carbpol.2009.09.011
- Eng, D., Caplan, M., Preul, M., and Panitch, A. (2010). Hyaluronan Scaffolds: a Balance between Backbone Functionalization and Bioactivity. *Acta Biomater.* 6 (7), 2407–2414. doi:10.1016/j.actbio.2009.12.049
- Fallacara, A., Baldini, E., Manfredini, S., and Vertuani, S. (2018). Hyaluronic Acid in the Third Millennium. *Polymers* 10, 701. doi:10.3390/polym10070701
- Fallacara, A., Manfredini, S., Durini, E., and Vertuani, S. (2017). Hyaluronic Acid Fillers in Soft Tissue Regeneration. *Facial Plast. Surg.* 33, 87–96. doi:10.1055/s-0036-1597685
- Faust, H. J., Sommerfeld, S. D., Rathod, S., Rittenbach, A., Ray Banerjee, S., Tsui, B. M. W., et al. (2018). A Hyaluronic Acid Binding Peptide-Polymer System for Treating Osteoarthritis. *Biomaterials* 183, 93–101. doi:10.1016/j.biomaterials.2018.08.045
- Ferguson, E. L., Alshame, A. M., and Thomas, D. W. (2010). Evaluation of Hyaluronic Acid-Protein Conjugates for Polymer Masked-Unmasked Protein Therapy. *Int. J. Pharm.* 402 (1–2), 95–102. doi:10.1016/j.ijpharm.2010.09.029
- Fittolani, G., Tyrikos-Ergas, T., Vargová, D., Chaube, M. A., and Delbianco, M. (2021). Progress and Challenges in the Synthesis of Sequence Controlled

- Polysaccharides. *Beilstein J. Org. Chem.* 17, 1981–2025. doi:10.3762/bjoc.17.129
- Fraser, J. R. E., Laurent, T. C., and Laurent, U. B. G. (1997). Hyaluronan: its Nature, Distribution, Functions and Turnover. *J. Intern. Med.* 242, 27–33. doi:10.1046/j.1365-2796.1997.00170.x
- Gebe, J. A., Yadava, K., Ruppert, S. M., Marshall, P., Hill, P., Falk, B. A., et al. (2017). Modified High-Molecular-Weight Hyaluronan Promotes Allergen-specific Immune Tolerance. *Am. J. Respir. Cel. Mol. Biol.* 56, 109–120. doi:10.1165/rmb.2016-0111OC
- Gligorovski, S., Strekowski, R., Barbati, S., and Vione, D. (2015). Environmental Implications of Hydroxyl Radicals ( $\bullet\text{OH}$ ). *Chem. Rev.* 115, 13051–13092. doi:10.1021/cr500310b
- Griesser, J., Hetényi, G., and Bernkop-Schnürch, A. (2018). Thiolated Hyaluronic Acid as Versatile Mucoadhesive Polymer: From the Chemistry behind to Product Developments—What Are the Capabilities. *Polymers* 10, 243. doi:10.3390/polym10030243
- Gronbach, M., Mitrach, F., Lidzba, V., Müller, B., Möller, S., Rother, S., et al. (2020). Scavenging of Dickkopf-1 by Macromer-Based Biomaterials Covalently Decorated with Sulphated Hyaluronan Displays Pro-osteogenic Effects. *Acta Biomater.* 114, 76–89. doi:10.1016/j.actbio.2020.07.017
- Grosskopf, H., Vogel, S., Mueller, C. D., Köhling, S., Duerig, J.-N., Moeller, S., et al. (2021). Identification of Intracellular Glycosaminoglycan-Interaction Proteins by Affinity Purification Mass Spectrometry. *Biol. Chem.* 402, 1427–1440. doi:10.1515/hsz-2021-0167
- Hascall, V., and Esko, J. D. (2009). “Hyaluronan,” in *Essentials of Glycobiology*. Editors A. Varki, R.D. Cummings, J.D. Esko, H.H. Freeze, P. Stanley, C.R. Bertozzi, et al. (Cold Spring Harbor: Spring Harbor Laboratory Press), 219–227.
- Heatley, F., and Scott, J. E. (1988). A Water Molecule Participates in the Secondary Structure of Hyaluronan. *Biochem. J.* 254, 489–493. doi:10.1042/bj2540489
- Heinze, T., El Seoud, O. A., and Koschella, A. (2018). “Etherification of Cellulose,” in *Cellulose Derivatives: Synthesis, Structure, and Properties*. Editors Heinze, T., El Seoud, O. A., and Koschella, A. (Cham: Springer), p. 293–427.
- Heinze, T., and Liebert, T. (2001). Unconventional Methods in Cellulose Functionalization. *Progr. Polym. Sci.* 26, 1689–1762. doi:10.1016/S0079-6700(01)00022-3
- Henrotin, Y., Raman, R., Richette, P., Bard, H., Jerosch, J., Conrozier, T., et al. (2015). Consensus Statement on Viscosupplementation with Hyaluronic Acid for the Management of Osteoarthritis. *Semin. Arthritis Rheum.* 45, 140–149. doi:10.1016/j.semarthrit.2015.04.011
- Highley, C. B., Prestwich, G. D., and Burdick, J. A. (2016). Recent Advances in Hyaluronic Acid Hydrogels for Biomedical Applications. *Curr. Opin. Biotechnol.* 40, 35–40. doi:10.1016/j.copbio.2016.02.008
- Hintze, V., Miron, A., Moeller, S., Schnabelrauch, M., Wiesmann, H. P., Worch, H., et al. (2012). Sulfated Hyaluronan and Chondroitin Sulfate Derivatives Interact Differently with Human Transforming Growth Factor-Beta 1 (TGF-Beta 1). *Acta Biomater.* 8 (6), 2144–2152. doi:10.1016/j.actbio.2012.03.021
- Hintze, V., Moeller, S., Schnabelrauch, M., Bierbaum, S., Viola, M., Worch, H., et al. (2009). Modifications of Hyaluronan Influence the Interaction with Human Bone Morphogenetic Protein-4 (hBMP-4). *Biomacromolecules* 10, 3290–3297. doi:10.1021/bm9008827
- Hintze, V., Samsonov, S. A., Anselmi, M., Moeller, S., Becher, J., Schnabelrauch, M., et al. (2014). Sulfated Glycosaminoglycans Exploit the Conformational Plasticity of Bone Morphogenetic Protein-2 (BMP-2) and Alter the Interaction Profile with its Receptor. *Biomacromolecules* 15 (8), 3083–3092. doi:10.1021/bm5006855
- Huerta Angeles, G., and Nesporova, K. (2021). Hyaluronan and its Derivatives for Ophthalmology: Recent Advances and Future Perspectives. *Carbohydr. Polym.* 259, 117697. doi:10.1016/j.carbpol.2021.117697
- Huerta-Angeles, G., Brandejsová, M., Kulhánek, J., Pavlík, V., Šmejkalová, D., Vágnerová, H., et al. (2016). Linolenic Acid Grafted Hyaluronan: Process Development, Structural Characterization, Biological Assessing, and Stability Studies. *Carbohydr. Polym.* 152, 815–824. doi:10.1016/j.carbpol.2016.07.030
- Huerta-Angeles, G., Bobek, M., Příkopová, E., Šmejkalová, D., and Velebný, V. (2014). Novel Synthetic Method for the Preparation of Amphiphilic Hyaluronan by Means of Aliphatic Aromatic Anhydrides. *Carbohydr. Polym.* 111, 883–891. doi:10.1016/j.carbpol.2014.05.035
- Huerta-Angeles, G., Brandejsová, M., Nigmatullin, R., Kopecká, K., Vágnerová, H., Šmejkalová, D., et al. (2017). Synthesis of Graft Copolymers Based on Hyaluronan and Poly(3-Hydroxyalkanoates). *Carbohydr. Polym.* 171, 220–228. doi:10.1016/j.carbpol.2017.05.011
- Huin-Amargier, C., Marchal, P., Payan, E., Netter, P., and Dellacherie, E. (2005). New Physically and Chemically Crosslinked Hyaluronate (HA)-based Hydrogels for Cartilage Repair. *J. Biomed. Mater. Res.* 76A, 416–424. doi:10.1002/jbm.a.30536
- Jiang, B., Drouet, E., Milas, M., and Rinaudo, M. (2000). Study on TEMPO-Mediated Selective Oxidation of Hyaluronan and the Effects of Salt on the Reaction Kinetics. *Carbohydr. Res.* 327, 455–461. doi:10.1016/S0008-6215(00)00059-8
- Jin, R., Moreira Teixeira, L. S., Krouwels, A., Dijkstra, P. J., van Blitterswijk, C. A., Karperien, M., et al. (2010). Synthesis and Characterization of Hyaluronic Acid-Poly(ethylene Glycol) Hydrogels via Michael Addition: An Injectable Biomaterial for Cartilage Repair. *Acta Biomater.* 6, 1968–1977. doi:10.1016/j.actbio.2009.12.024
- Jouan, N., Rinaudo, M., Milas, M., and Desbrihes, J. (1995). Hydration of Hyaluronic Acid as a Function of the Counterion Type and Relative Humidity. *Carbohydr. Polym.* 26, 69–73. doi:10.1016/0144-8617(95)98837-7
- Kafedjiiski, K., Jetti, R. K. R., Foger, F., Hoyer, H., Werle, H., Hoffer, M., et al. (2007). Synthesis and *In Vitro* Evaluation of Thiolated Hyaluronic Acid for Mucoadhesive Drug Delivery. *Int. J. Pharmaceut.* 343, 48–58. doi:10.1016/j.ijpharm.2007.04.019
- Kawaguchi, Y., Matsukawa, K., Gama, Y., and Ishigami, Y. (1992). The Effects of Polysaccharide Chain-Length in Coating Liposomes with Partial Palmitoyl Hyaluronates. *Carbohydr. Polym.* 18, 139–142. doi:10.1016/0144-8617(92)90136-E
- Kawaguchi, Y., Matsukawa, K., and Ishigami, Y. (1995). The Relation between the Adsorption Behavior at the Interface and the Conformational Changes in Hyaluronates Partially Modified with Various Acyl Chains. *Carbohydr. Polym.* 26, 149–154. doi:10.1016/0144-8617(94)00089-C
- Kheirabadi, M., Shi, L., Bagheri, R., Kabiri, K., Hilborn, J., and Ossipov, D. A. (2015). *In Situ* forming Interpenetrating Hydrogels of Hyaluronic Acid Hybridized with Iron Oxide Nanoparticles. *Biomater. Sci.* 3, 1466–1474. doi:10.1039/C5BM00150A
- Khunmanee, S., Jeong, Y., and Park, H. (2017). Crosslinking Method of Hyaluronic-Based Hydrogel for Biomedical Applications. *J. Tiss. Eng.* 8, 1–16. doi:10.1177/2041731417726464
- Kim, C.-H., and Kim, J.-I. (2011). “Deacetylation Hydrolase of Hyaluronic Acid, Hyaluronic Acid Deacetylated by Same and Derivative Thereof”. U.S. Patent 13/703,619.
- Knopf-Marques, H., Pravda, M., Wolfova, L., Velebný, V., Schaaf, P., Vrana, N. E., et al. (2016). Hyaluronic Acid and its Derivatives in Coating and Delivery Systems: Applications in Tissue Engineering, Regenerative Medicine and Immunomodulation. *Adv. Healthc. Mater.* 5, 2841–2855. doi:10.1002/adhm.201600316
- Kocourková, K., Musilová, L., Smolka, P., Mráček, A., Humeník, M., and Minařík, A. (2021). Factors Determining Self-Assembly of Hyaluronan. *Carbohydr. Polym.* 254, 117307. doi:10.1016/j.carbpol.2020.117307
- Koehler, L., Samsonov, S., Rother, S., Vogel, S., Köhling, S., Moeller, S., et al. (2017). Sulfated Hyaluronan Derivatives Modulate TGF- $\beta$ 1:Receptor Complex Formation: Possible Consequences for TGF- $\beta$ 1 Signaling. *Sci. Rep.* 7, 1210. doi:10.1038/s41598-017-01264-8
- Koehling, S., Kunze, G., Lemmnitz, K., Bermudez, M., Wolber, G., Schiller, J., et al. (2016). Chemoenzymatic Synthesis of Nonsulfated Tetrahyaluronan with a Paramagnetic Tag for Studying its Complex with Interleukin-10. *Chem. Eur. J.* 22, 563–5574. doi:10.1002/chem.201504459
- Kotla, N. G., Bonam, S. R., Rasala, S., Wankar, J., Bohara, R. A., Bayry, J., et al. (2021). Recent Advances and Prospects of Hyaluronan as a Multifunctional Therapeutic System. *J. Controlled. Rel.* 336, 598–620. doi:10.1016/j.jconrel.2021.07.002
- Kristiansen, K. A., Potthast, A., and Christensen, B. E. (2010). Periodate Oxidation of Polysaccharides for Modification of Chemical and Physical Properties. *Carbohydr. Res.* 345, 1264–1271. doi:10.1016/j.carres.2010.02.011
- Krupkova, O., Greutert, H., Boos, N., Lemcke, J., Liebscher, T., and Wuertz-Kozak, K. (2020). Expression and Activity of Hyaluronidases HYAL-1, HYAL-2 and

- HYAL-3 in the Human Intervertebral Disc. *Eur. Spine J.* 29, 605–615. doi:10.1007/s00586-019-06227-3
- Kunze, R., Rösler, M., Möller, S., Schnabelrauch, M., Riemer, T., Hempel, U., et al. (2010). Sulfated Hyaluronan Derivatives Reduce the Proliferation Rate of Primary Rat Calvarial Osteoblasts. *Glycoconj. J.* 27, 151–158. doi:10.1007/s10719-009-9270-9
- Kwak, D. S., Oh, K. T., and Lee, E. S. (2014). Facile Synthesis of Multilayered Polysaccharidic Vesicles. *J. Controlled Rel.* 187, 83–90. doi:10.1016/j.jconrel.2014.05.032
- La Gatta, A., Stellavato, A., Vassallo, V., Di Meo, C., Toro, G., Iolascon, G., et al. (2021). Hyaluronan and Derivatives: An *In Vitro* Multilevel Assessment of Their Potential in Viscosupplementation. *Polymers* 13, 3208. doi:10.3390/polym13193208
- Lapcik, L., Jr., Benesova, K., Lapcik, L., De Smedt, S., and Lapcikova, B. (2010). *Chem. Modification Hyaluronic Acid: Alkylation. Int. J. Polym. Anal. Charact.* 15, 486–496. doi:10.1080/1023666X.2010.520904
- Laurent, T. C., Laurent, U. B. G., and Fraser, J. R. E. (1996). The Structure and Function of Hyaluronan: An Overview Immunol. *Cell Biol.* 74, A1–A7. doi:10.1038/icb.1996.32
- Lee, M. Y., Yang, J. A., Jung, H. S., Beack, S., Choi, J. E., Hur, W., et al. (2012). Hyaluronic Acid–Gold Nanoparticle/interferon  $\alpha$  Complex for Targeted Treatment of Hepatitis C Virus Infection. *ACS Nano* 6, 9522–9531. doi:10.1021/nn302538y
- Leone, G., Consumi, M., Lamponi, S., and Magnani, A. (2012). New Hyaluronan Derivative with Prolonged Half-Life for Ophthalmological Formulation. *Carbohydr. Polym.* 88, 799–808. doi:10.1016/j.carbpol.2011.12.047
- Litwiniuk, M., Krejner, A., and Grzela, T. (2016). Hyaluronic Acid in Inflammation and Tissue Regeneration. *Wounds* 28, 78–88.
- Loebel, C., D'Estea, M., Alinia, M., Zenobi-Wong, M., and Eglin, D. (2015). Precise Tailoring of Tyramine-Based Hyaluronan Hydrogel Properties Using DMTMM Conjugation. *Carbohydr. Polym.* 115, 325–333. doi:10.1016/j.carbpol.2014.08.097
- Lowry, K. M., and Beavers, E. M. (1994). Thermal Stability of Sodium Hyaluronate in Aqueous Solution. *J. Biomed. Mater. Res.* 28, 1239–1244. doi:10.1002/jbm.820281014
- Magnani, A., Albanese, A., Lamponi, S., and Barbucci, R. (1996). Blood-interaction Performance of Differently Sulphated Hyaluronic Acids. *Thromb. Res.* 81, 383–395. doi:10.1016/0049-3848(96)00009-6
- Magnani, A., Lamponi, S., Rappuoli, R., and Barbucci, R. (1998). Sulphated Hyaluronic Acids: a Chemical and Biological Characterization. *Polym. Int.* 46, 225–240. doi:10.1002/(SICI)1097-0126(199807)46:3<225::AID-PI45>3.0.CO;2-I
- Magnani, A., Rappuoli, R., Lamponi, S., and Barbucci, R. (2000). Novel Polysaccharide Hydrogels: Characterization and Properties. *Polym. Adv. Technol.* 11, 488–495. doi:10.1002/1099-1581(200008/12)11:8/12<488::AID-PAT995>3.0.CO;2-5
- Manfrão-Netto, J. H. C., Queiroz, E. B., de Oliveira Junqueira, A. C., Gomes, A. M. V., Gusmão de Moraes, D., Costa Paes, H., et al. (2021). Genetic Strategies for Improving Hyaluronic Acid Production in Recombinant Bacterial Culture. *J. Appl. Microbiol.* in press. doi:10.1111/jam.15242
- Mende, M., Bednarek, C., Wawryszyn, M., Sauter, P., Biskup, M. B., Schepers, U., et al. (2016). Chemical Synthesis of Glycosaminoglycans. *Chem. Rev.* 116, 8193–8255. doi:10.1021/acs.chemrev.6b00010
- Mergy, J., Fournier, A., Hachet, E., and Auzely-Velty, R. (2012). Modification of Polysaccharides via Thiol-Ene Chemistry: A Versatile Route to Functional Biomaterials. *J. Polym. Sci. Part. A: Polym. Chem.* 50, 4019–4028. doi:10.1002/pola.26201
- Mero, A., and Campisi, M. (2014). Hyaluronic Acid Bioconjugates for the Delivery of Bioactive Molecules. *Polymers* 6, 346–369. doi:10.3390/polym6020346
- Minsky, B. B., Antoni, C. H., and Boehm, H. (2016). Controlled Immobilization Strategies to Probe Short Hyaluronan-Protein Interactions. *Sci. Rep.* 6, 21608. doi:10.1038/srep21608
- Mrbochová, P., Hájková, V., Steiner, B., Bystrický, S., Koón, M., Medová, M., et al. (2007). Preparation and Characterization of Biodegradable Alkylether Derivatives of Hyaluronan. *Carbohydr. Polym.* 69, 344–352. doi:10.1016/j.carbpol.2006.10.015
- Moeller, S., Schmidtke, M., Weiss, D., Schiller, J., Pawlik, K., Wutzler, P., et al. (2012). Synthesis and Antihyperthermic Activity of Carboxymethylated and Sulfated Hyaluronan Derivatives. *Carbohydr. Polym.* 90, 608–615. doi:10.1016/j.carbpol.2012.05.085
- Moeller, S., Weisser, J., Bischoff, S., and Schnabelrauch, M. (2007). Dextran and Hyaluronan Methacrylate Based Hydrogels as Matrices for Soft Tissue Reconstruction. *Biomol. Eng.* 24, 496–504. doi:10.1016/j.bioeng.2007.08.014
- Moradali, M. F., and Rehm, B. H. A. (2020). Bacterial Biopolymers: from Pathogenesis to Advanced Materials. *Nat. Rev.* 18, 195–210. doi:10.1038/s41579-019-0313-3
- Nagira, T., Nagahata-Ishiguro, M., and Tsuchiya, T. (2007). Effects of Sulfated Hyaluronan on Keratinocyte Differentiation and Wnt and Notch Gene Expression. *Biomaterials* 28, 844–850. doi:10.1016/j.biomaterials.2006.09.041
- Nejadnik, M. R., Yang, X., Bongio, M., Alghamdi, H. S., van den Beucken, J. J., Huysmans, M. C., et al. (2014). Self-healing Hybrid Nanocomposites Consisting of Bisphosphonated Hyaluronan and Calcium Phosphate Nanoparticles. *Biomaterials* 35, 6918–6929. doi:10.1016/j.biomaterials.2014.05.003
- Ni, Y., Tang, Z., Cao, W., Lin, H., Fan, Y., and Guo, L. (2015). Tough and elastic hydrogel of hyaluronic acid and chondroitin sulfate as potential cell scaffold materials. *Int. J. Biol. Macromol.* 74, 367–375. doi:10.1016/j.ijbiomac.2014.10.058
- Nicholls, M., Manjoo, A., Shaw, P., Niazi, F., and Rosen, J. A. (2018). Comparison between Rheological Properties of Intra-articular Hyaluronic Acid Preparations and Reported Human Synovial Fluid. *Adv. Ther.* 35, 523–530. doi:10.1007/s12325-018-0688-y
- Novoa-Carballal, R., and Müller, A. H. E. (2012). Synthesis of Polysaccharide-B-PEG Block Copolymers by Oxime Click. *Chem. Commun.* 48, 3781–3783. doi:10.1039/c2cc30726j
- Oelschlaeger, C., Bossler, F., and Willenbacher, N. (2016). Synthesis, Structural and Micromechanical Properties of 3D Hyaluronic Acid-Based Cryogel Scaffolds. *Biomacromolecules* 17, 580–589. doi:10.1021/acs.biomac.5b01529
- Oh, E. J., Park, K., Kim, K. S., Kim, J., Yang, J.-A., Kong, J.-H., et al. (2010). Target Specific and Long-Acting Delivery of Protein, Peptide, and Nucleotide Therapeutics Using Hyaluronic Acid Derivatives. *J. Controlled Rel.* 141, 2–12. doi:10.1016/j.jconrel.2009.09.010
- Ossipov, D. A., Piskounova, S., Varghese, O. P., and Hilborn, J. (2010). Functionalization of Hyaluronic Acid with Chemoselective Groups via a Disulfide-Based Protection Strategy for *In Situ* Formation of Mechanically Stable Hydrogels. *Biomacromolecules* 11, 2247–2254. doi:10.1021/bm1007986
- Palhares, L. C. G. F., London, J. A., Kozłowski, A. M., Esposito, E., Chavante, S. F., Ni, M., et al. (2021). Chemical Modification of Glycosaminoglycan Polysaccharides. *Molecules* 26, 5211. doi:10.3390/molecules26175211
- Peerboom, N., Block, S., Altgarde, N., Wahlsten, O., Moeller, S., Schnabelrauch, M., et al. (2017). Binding Kinetics and Lateral Mobility of HSV-1 on End-Grafted Sulfated Glycosaminoglycans. *Biophysical J.* 113, 1223–1234. doi:10.1016/j.bpj.2017.06.028
- Picotti, F., Fabbian, M., Gianni, R., Sechi, A., Stucchi, L., and Bosco, M. (2013). Hyaluronic Acid Lipote: Synthesis and Physicochemical Properties. *Carbohydr. Polym.* 93, 273–278. doi:10.1016/j.carbpol.2012.04.009
- Pierre, G., Punta, C., Delattre, C., Melone, L., Dubessay, P., Fiorati, A., et al. (2017). TEMPO-mediated Oxidation of Polysaccharides: An Ongoing Story. *Carbohydr. Polym.* 165, 71–85. doi:10.1016/j.carbpol.2017.02.028
- Pomin, V. H., and Mulloy, B. (2018). Glycosaminoglycans and Proteoglycans. *Pharmaceuticals* 11, 27. doi:10.3390/ph11010027
- Pravata, L., Braud, C., Boustta, M., El Ghzaoui, A., Tømmeraaas, K., Guillaumie, F., et al. (2008). New Amphiphilic Lactic Acid Oligomer-Hyaluronan Conjugates: Synthesis and Physicochemical Characterization. *Biomacromolecules* 9, 340–348. doi:10.1021/bm700843m
- Prestwich, G. D., Marecek, D. M., Marecek, J. F., Vercruysse, K. P., and Ziebell, M. R. (1998). Controlled Chemical Modification of Hyaluronic Acid: Synthesis, Applications, and Biodegradation of Hydrazide Derivatives. *J. Controlled. Rel.* 53, 93–103. doi:10.1016/S0168-3659(97)00242-3
- Qin, X.-H., Gruber, P., Markovic, M., Plochberger, B., Klotzsch, E., Stampfl, et al. (2014). Enzymatic Synthesis of Hyaluronic Acid Vinyl Esters for Two-Photon Microfabrication of Biocompatible and Biodegradable Hydrogel Constructs. *Polym. Chem.* 5, 6523. doi:10.1039/c4py00792a
- Rah, M. J. (2011). A Review of Hyaluronan and its Ophthalmic Applications. *Optometry* 82, 38–43. doi:10.1016/j.optm.2010.08.003



- Rother, S., Galianzo, V. D., Kilian, D., Fiebig, K. M., Becher, J., Moeller, S., et al. (2017a). Hyaluronan/collagen Hydrogels with Sulfated Hyaluronan for Improved Repair of Vascularized Tissue Tune the Binding of Proteins and Promote Endothelial Cell Growth. *Macromol. Biosci.* 17, 1700154. doi:10.1002/mabi.201700154
- Rother, S., Ruiz-Gómez, G., Koehler, L., Balamurugan, K., Fiebig, K. M., Galianzo, V. D., et al. (2021). Hyaluronan/collagen Hydrogels with Sulfated Glycosaminoglycans Maintain VEGF<sub>165</sub> Activity and fine-tune Endothelial Cell Response. *ACS Appl. Bio Mater.* 4 (1), 494–506. doi:10.1021/acsabm.0c01001
- Rother, S., Salbach-Hirsch, J., Moeller, S., Seemann, T., Schnabelrauch, M., Hofbauer, L. C., et al. (2015). Bioinspired Collagen/Glycosaminoglycan-Based Cellular Microenvironments for Tuning Osteoclastogenesis. *ACS Appl. Mater. Inter.* 7, 23787–23797. doi:10.1021/acsami.5b00849
- Rother, S., Samsonov, S. A., Hempel, U., Vogel, S., Moeller, S., Blaszkiewicz, J., et al. (2016b). Sulfated Hyaluronan Alters the Interaction Profile of TIMP-3 with the Endocytic Receptor LRP-1 Clusters II and IV and Increases the Extracellular TIMP-3 Level of Human Bone Marrow Stromal Cells. *Biomacromolecules* 17, 3252–3261. doi:10.1021/acs.biomac.6b00980
- Rother, S., Samsonov, S. A., Hofmann, T., Blaszkiewicz, J., Köhling, S., Moeller, S., et al. (2016a). Structural and Functional Insights into the Interaction of Sulfated Glycosaminoglycans with Tissue Inhibitor of Metalloproteinase-3-A Possible Regulatory Role on Extracellular Matrix Homeostasis. *Acta Biomater.* 45, 143–154. doi:10.1016/j.actbio.2016.08.030
- Rother, S., Samsonov, S. A., Moeller, S., Schnabelrauch, M., Rademann, J., Blaszkiewicz, J., et al. (2017b). Sulfated Hyaluronan Alters Endothelial Cell Activation *In Vitro* by Controlling the Biological Activity of the Angiogenic Factors Vascular Endothelial Growth Factor-A and Tissue Inhibitor of Metalloproteinase-3. *ACS Appl. Mater. Inter.* 9, 9539–9550. doi:10.1021/acsami.7b01300
- Salbach-Hirsch, J., Samsonov, S. A., Hintze, V., Hofbauer, C., Picke, A. K., Rauner, M., et al. (2015). Structural and Functional Insights into Sclerostin-Glycosaminoglycan Interactions in Bone. *Biomaterials* 67, 335–345. doi:10.1016/j.biomaterials.2015.07.021
- Salbach-Hirsch, J., Kraemer, J., Rauner, M., Samsonov, S., Pisabarro, M. T., Moeller, S., et al. (2013). The Promotion of Osteoclastogenesis by Sulfated Hyaluronan through Interference with Osteoprotegerin and Receptor Activator of NF- $\kappa$ B Ligand/osteoprotegerin Complex Formation. *Biomaterials* 34, 7653–7661. doi:10.1016/j.biomaterials.2013.06.053
- Sanfilippo, V., Caruso, V. C. L., Cucci, L. M., Inturri, R., Vaccaro, S., and Satriano, C. (2020). Hyaluronan-Metal Gold Nanoparticle Hybrids for Targeted Tumor Cell Therapy. *Int. J. Mol. Sci.* 21, 3085. doi:10.3390/ijms21093085
- Satoh, T., Nagahata, M., Teramoto, A., Hatimori, A., Abe, K., and Im, S. S. (2004). The Basic Research on Physiological Property of Functionalized Hyaluronan—I. Effect of Hyaluronan and Sulfated Hyaluronan on Cell Proliferation of Human Epidermal Keratinocytes. *Polym. Adv. Technol.* 15, 329–334. doi:10.1002/pat.468
- Schanté, C. E., Zuber, G., Herlin, C., and Vandamme, T. F. (2011). Chemical Modifications of Hyaluronic Acid for the Synthesis of Derivatives for a Broad Range of Biomedical Applications. *Carbohydr. Polym.* 85, 469–489. doi:10.1016/j.carbpol.2011.03.019
- Scharnweber, D., Hübner, L., Rother, S., Hempel, U., Anderegg, U., Samsonov, S. A., et al. (2015). Glycosaminoglycan Derivatives: Promising Candidates for the Design of Functional Biomaterials. *J. Mater. Sci. Mater. Med.* 26, 232. doi:10.1007/s10856-015-5563-7
- Schnabelrauch, M., Scharnweber, D., and Schiller, J. J. (2013). Sulfated Glycosaminoglycans as Promising Artificial Extracellular Matrix Components to Improve the Regeneration of Tissues. *Curr. Med. Chem.* 20, 2501–2523. doi:10.2174/0929867311320200001
- Schnabelrauch, M., Schiller, J., Möller, S., Scharnweber, D., and Vera Hintze, V. (2021). Chemically Modified Glycosaminoglycan Derivatives as Building Blocks for Biomaterial Coatings and Hydrogels. *Biol. Chem.* 402, 1385–1395. doi:10.1515/hsz-2021-0171
- Scott, J. E. (1962). The Precipitation of Polyanions by Long-Chain Aliphatic Ammonium Salts. 6. The Affinity of Substituted Ammonium Cations for the Anionic Groups of Some Biological Polymers. *Biochem. J.* 84, 270–275. doi:10.1042/bj0840270
- Scott, J. E., Cummings, C., Brass, A., and Chen, Y. (1991). Secondary and Tertiary Structures of Hyaluronan in Aqueous Solution, Investigated by Rotary Shadowing-Electron Microscopy and Computer Simulation. Hyaluronan Is a Very Efficient Network-Forming Polymer. *Biochem. J.* 274, 699–705. doi:10.1042/bj2740699
- Scott, J. E. (1992). Supramolecular Organization of Extracellular Matrix Glycosaminoglycans, *In Vitro* and in the Tissues. *FASEB J.* 6, 2639–2645. doi:10.1096/fasebj.6.9.1612287
- Sedláček, J., Hermannová, M., Šatinský, D., and Velebný, V. (2020). Current Analytical Methods for the Characterization of N-Deacetylated Hyaluronan: A Critical Review. *Carbohydr. Polym.* 249, 116720. doi:10.1016/j.carbpol.2020.116720
- Šedová, P., Buffa, R., Kettou, S., Huerta-Angeles, G., Hermannová, M., Leierová, V., et al. (2013). Preparation of Hyaluronan Polyaldehyde—A Precursor of Biopolymer Conjugates. *Carbohydr. Res.* 371, 8–15. doi:10.1016/j.carres.2013.01.025
- Seidlits, S. K., Khaing, Z. Z., Petersen, R. R., Nickels, J. D., Vanscoy, J. E., Shear, J. B., et al. (2010). The Effects of Hyaluronic Acid Hydrogels with Tunable Mechanical Properties on Neural Progenitor Cell Differentiation. *Biomaterials* 31, 3930–3940. doi:10.1016/j.biomaterials.2010.01.125
- Serban, M. A., and Prestwich, G. D. (2008). Synthesis of Hyaluronan Haloacetates and Biology of Novel Cross-linker-free Synthetic Extracellular Matrix Hydrogels. *Biomacromolecules* 8, 2821–2828. doi:10.1021/bm700595s
- Serban, M. A., Yang, G., and Prestwich, G. D. (2008). Synthesis, Characterization and Chondroprotective Properties of a Hyaluronan Thioethyl Ether Derivative. *Biomaterials* 29, 1388–1399. doi:10.1016/j.biomaterials.2007.12.006
- Shan, J., Böck, T., Keller, T., Forster, L., Blunk, T., Groll, J., et al. (2021). TEMPO/TCC as a Chemo Selective Alternative for the Oxidation of Hyaluronic Acid. *Molecules* 26, 5963. doi:10.3390/molecules26195963
- Shimojo, A. A. M., Pires, A. M. B., Lichy, R., and Santana, M. H. A. (2015). The Performance of Crosslinking with Divinyl Sulfone as Controlled by the Interplay between the Chemical Modification and Conformation of Hyaluronic Acid. *J. Braz. Chem. Soc.* 26, 506–512. doi:10.5935/0103-5053.20150003
- Shu, X. Z., Liu, Y., Luo, Y., Roberts, M. C., and Prestwich, G. D. (2002). Disulfide Cross-Linked Hyaluronan Hydrogels. *Biomacromolecules* 3, 1304–1311. doi:10.1021/bm025603c
- Smeds, K. A., Pfister-Serres, A., Miki, D., Dastgheib, K., Inoue, M., Hatchell, D. L., et al. (2001). Photocrosslinkable Polysaccharides for *In Situ* Hydrogel Formation. *J. Biomed. Mater. Res.* 54, 115–121. doi:10.1002/1097-4636(200101)54:1<115::AID-JBM14>3.0.CO;2-Q
- Smejkalová, D., Hermannová, M., Buffa, R., Coziková, D., Vistejnová, L., Matulková, Z., et al. (2012a). Structural Characterization and Biological Properties of Degradation Byproducts from Hyaluronan after Acid Hydrolysis. *Carbohydr. Polym.* 88, 1425–1434. doi:10.1016/j.carbpol.2012.02.031
- Smejkalová, D., Hermannová, M., Suláková, R., Prusová, A., Kucerík, J., and Velebný, V. (2012b). Structural and Conformational Differences of Acylated Hyaluronan Modified in Protic and Aprotic Solvent System. *Carbohydr. Polym.* 87, 1460–1465. doi:10.1016/j.carbpol.2011.09.057
- Smejkalová, D., Nešporová, K., Huerta-Angeles, G., Syrovátka, J., Jiráček, D., Gáliková, A., et al. (2014). Selective *In Vitro* Anticancer Effect of Superparamagnetic Iron Oxide Nanoparticles Loaded in Hyaluronan Polymeric Micelles. *Biomacromolecules* 15, 4012–4020. doi:10.1021/bm501065q
- Stellavato, A., Vassallo, V., La Gatta, A., Pirozzi, A. V. A., De Rosa, M., Balato, G., et al. (2019). Novel Hybrid Gels Made of High and Low Molecular Weight Hyaluronic Acid Induce Proliferation and Reduce Inflammation in an Osteoarthritis *In Vitro* Model Based on Human Synoviocytes and Chondrocytes. *Biomed. Res. Int.* 23, 4328219. doi:10.1155/2019/4328219
- Stern, R. (2004). Hyaluronan Catabolism: a New Metabolic Pathway. *Eur. J. Cell Biol.* 83, 317–325. doi:10.1078/0171-9335-00392
- Stern, R., Asari, A. A., and Sugahara, K. N. (2006). Hyaluronan Fragments: an Information-Rich System. *Eur. J. Cell Biol.* 85, 699–715. doi:10.1016/j.ejcb.2006.05.009
- Stern, R., Kogan, G., Jedrzejewski, M. J., and Šoltés, L. (2007). The many Ways to Cleave Hyaluronan. *Biotechnol. Adv.* 25, 537–557. doi:10.1016/j.biotechadv.2007.07.001
- Tawada, A., Masa, T., Oonuki, Y., Watanabe, A., Matsuzaki, Y., and Asari, A. (2002). Large-scale Preparation, Purification, and Characterization of Hyaluronan Oligosaccharides from 4-mers to 52-mers. *Glycobiology* 12, 421–426. doi:10.1093/glycob/cwf048

- Thakar, D., Migliorini, E., Coche-Guerente, L., Sadir, R., Lortat-Jacob, H., Boturyn, D., et al. (2014). A Quartz crystal Microbalance Method to Study the Terminal Functionalization of Glycosaminoglycans. *Chem. Commun.* 50, 15148–15151. doi:10.1039/c4cc06905f
- Thönes, S., Rother, S., Wippold, T., Blaszkiewicz, J., Balamurugan, K., Moeller, S., et al. (2019). Hyaluronan/collagen Hydrogels Containing Sulfated Hyaluronan Improve Wound Healing by Sustained Release of Heparin-Binding EGF-like Growth Factor. *Acta Biomater.* 86, 135–147. doi:10.1016/j.actbio.2019.01.029
- Townley, R. A., and Bülow, H. E. (2018). Deciphering Functional Glycosaminoglycan Motifs in Development. *Curr. Opin. Struct. Biol.* 50, 144–154. doi:10.1016/j.sbi.2018.03.011
- Unnikandam Veetil, S. R., Hwang, D., Correia, J., Bartlett, M. D., and Schneider, I. C. (2021). Cancer Cell Migration in Collagen-Hyaluronan Composite Extracellular Matrices. *Acta Biomater.* 130, 183–198. doi:10.1016/j.actbio.2021.06.009
- Valachová, K., and Šoltés, L. (2021). Hyaluronan as a Prominent Biomolecule with Numerous Applications in Medicine. *Int. J. Mol. Sci.* 22, 7077. doi:10.3390/ijms22137077
- van der Smissen, A., Samsonov, S., Hintze, V., Scharnweber, D., Moeller, S., Schnabelrauch, M., et al. (2013). Artificial Extracellular Matrix Composed of Collagen I and Highly Sulfated Hyaluronan Interferes with TGFβ-1 Signaling and Prevents TGFβ1-Induced Myofibroblast Differentiation. *Acta Biomater.* 9, 7775–7786. doi:10.1016/j.actbio.2013.04.023
- Vasi, A.-M., Popa, M. I., Butnaru, M., Dodi, G., and Verestiuc, L. (2014). Chemical Functionalization of Hyaluronic Acid for Drug Delivery Applications. *Mater. Sci. Eng. C* 38, 177–185. doi:10.1016/j.msec.2014.01.052
- Vigetti, D., Viola, M., Karousou, E., De Luca, G., and Passi, A. (2014). Metabolic Control of Hyaluronan Synthases. *Matrix Biol.* 35, 8–13. doi:10.1016/j.matbio.2013.10.002
- Wada, T., Chirachanchai, S., Izawa, N., Inaki, Y., and Takemoto, K. (1994). Synthesis and Properties of Hyaluronic Acid Conjugated Nucleic Acid Analogs—I: Synthesis of Deacetylhyaluronan and Introduction of Nucleic Acid Bases. *J. Bioact. Compat. Polym.* 9, 429–447. doi:10.1177/088391159400900405
- Walvoort, M. T., Volbeda, A. G., Reintjens, N. R., van den Elst, H., Plante, O. J., Overkleef, H. S., et al. (2012). Automated Solid-phase Synthesis of Hyaluronan Oligosaccharides. *Org. Lett.* 14, 3776–3779. doi:10.1021/ol301666n
- Wang, J. K., Luo, B., Guneta, V., Li, L., Min Foo, S. E., Dai, Y., et al. (2017). Supercritical Carbon Dioxide Extracted Extracellular Matrix Material from Adipose Tissue. *Mater. Sci. Engin. C* 75, 349–358. doi:10.1016/j.msec.2017.02.002
- Williams, D. (2014). *Essential Biomaterials Science*. Cambridge: Cambridge University Press, 537–539.
- Wyrwa, R., Schnabelrauch, M., and Becher, J. (2012). “Process for the Degradation of Polysaccharides Selected from the Groups of Substances of the Glycosaminoglycans and Derivatives Thereof and Alginates”. German Patent No. 10, 2012,009,593.
- Xu, Y., Wu, Y., Sun, P., Zhang, F., Linhardt, R. J., and Zhang, A. (2019). Chemically Modified Polysaccharides: Synthesis, Characterization, Structure Activity Relationships of Action. *Int. J. Biol. Macromol.* 132, 970–977. doi:10.1016/j.ijbiomac.2019.03.213
- Xue, Y., Chen, H., Xu, C., Yu, D., Xu, H., and Hu, Y. (2020). Synthesis of Hyaluronic Acid Hydrogels by Crosslinking the Mixture of High-Molecular-Weight Hyaluronic Acid and Low-Molecular-Weight Hyaluronic Acid with 1,4-butanediol Diglycidyl Ether. *RSC Adv.* 10, 7206–7213. doi:10.1039/C9RA09271D
- Yang, S., Guo, Z., Miao, F., Xue, Q., and Qin, S. (2010). The Hydroxyl Radical Scavenging Activity of Chitosan, Hyaluronan, Starch and Their O-Carboxymethylated Derivatives. *Carbohydr. Polym.* 82, 1043–1045. doi:10.1016/j.carbpol.2010.06.014
- Yuan, H., Tank, M., Alsofyani, A., Shah, N., Talati, N., LoBello, J. C., et al. (2013). Molecular Mass Dependence of Hyaluronan Detection by sandwich ELISA-like Assay and Membrane Blotting Using Biotinylated Hyaluronan Binding Protein. *Glycobiology* 23, 1270–1280. doi:10.1093/glycob/cwt064
- Yue, W. (2012). Preparation of Low-Molecular-Weight Hyaluronic Acid by Ozone Treatment. *Carbohydr. Polym.* 89, 709–712. doi:10.1016/j.carbpol.2012.03.081
- Yui, N., Okano, T., and Sakurai, Y. (1992). Inflammation Responsive Degradation of Crosslinked Hyaluronic Acid Gels. *J. Controlled Rel.* 22, 105–116. doi:10.1016/0168-3659(92)90195-W
- Zakrzewska, M. E., Bogel-Lukasik, E., and Bogel-Lukasik, R. (2010). Solubility of Carbohydrates in Ionic Liquids. *Energy Fuels* 24, 737–745. doi:10.1021/ef901215m
- Zhang, M., and James, S. P. (2005a). Silylation of Hyaluronan to Improve Hydrophobicity and Reactivity for Improved Processing and Derivatization. *Polymer* 46, 3639–3648. doi:10.1016/j.polymer.2005.03.022
- Zhang, M., and James, S. P. (2005b). Synthesis and Properties of Melt-Processable Hyaluronan Esters. *J. Mater. Sci. Mater. Med.* 40, 2937–2943. doi:10.1007/s10853-005-2432-7
- Zhang, R., Huang, Z. B., Xue, M. Y., Yang, J., and Tan, T. W. (2011). Detailed Characterization of an Injectable Hyaluronic Acid-Polyaspartylhydrazide Hydrogel for Protein Delivery. *Carbohydr. Polym.* 85, 717–725. doi:10.1016/j.carbpol.2011.02.014
- Zhang, W., Mu, H., Zhang, A., Cui, G., Chen, H., and Duan, J. (2013). A Decrease in Moisture Absorption-Retention Capacity of N-Deacetylation of Hyaluronic Acid. *Glycoconj. J.* 30, 577–583. doi:10.1007/s10719-012-9457-3
- Zhang, Y., Heher, P., Hilborn, J., Redl, H., and Ossipov, D. A. (2016). Hyaluronic Acid-Fibrin Interpenetrating Double Network Hydrogel Prepared *In Situ* by Orthogonal Disulfide Cross-Linking Reaction for Biomedical Applications. *Acta Biomater.* 38, 23–32. doi:10.1016/j.actbio.2016.04.041
- Zhao, X. (2006). Synthesis and Characterization of a Novel Hyaluronic Acid Hydrogel. *J. Biomater. Sci. Polym.* 17, 419–433. doi:10.1163/156856206776374115
- Zhou, S., and Huang, G. (2021). Preparation, Structure and Activity of Polysaccharide Phosphate Esters. *Biomed. Pharmacotherap.* 144, 112332. doi:10.1016/j.biopha.2021.112332

**Conflict of Interest:** The authors declare that the research was conducted in the absence of any commercial or financial relationships that could be construed as a potential conflict of interest.

**Publisher’s Note:** All claims expressed in this article are solely those of the authors and do not necessarily represent those of their affiliated organizations, or those of the publisher, the editors and the reviewers. Any product that may be evaluated in this article, or claim that may be made by its manufacturer, is not guaranteed or endorsed by the publisher.

Copyright © 2022 Hintze, Schnabelrauch and Rother. This is an open-access article distributed under the terms of the Creative Commons Attribution License (CC BY). The use, distribution or reproduction in other forums is permitted, provided the original author(s) and the copyright owner(s) are credited and that the original publication in this journal is cited, in accordance with accepted academic practice. No use, distribution or reproduction is permitted which does not comply with these terms.





# Fermentative Lactic Acid Production From Lignocellulosic Feedstocks: From Source to Purified Product

Dragomir Yankov\*

Chemical and Biochemical Reactors Laboratory, Institute of Chemical Engineering, Bulgarian Academy of Sciences, Sofia, Bulgaria

## OPEN ACCESS

### Edited by:

Svilen Simeonov,  
Institute of Organic Chemistry with  
Centre of Phytochemistry (BAS),  
Bulgaria

### Reviewed by:

Paripok Phitsuan,  
King Mongkut's University of  
Technology Thonburi, Thailand  
Yu-Cai He,  
Changzhou University, China

### \*Correspondence:

Dragomir Yankov  
yanpe@bas.bg

### Specialty section:

This article was submitted to  
Green and Sustainable Chemistry,  
a section of the journal  
Frontiers in Chemistry

**Received:** 26 November 2021

**Accepted:** 21 January 2022

**Published:** 04 March 2022

### Citation:

Yankov D (2022) Fermentative Lactic  
Acid Production From Lignocellulosic  
Feedstocks: From Source to  
Purified Product.  
Front. Chem. 10:823005.  
doi: 10.3389/fchem.2022.823005

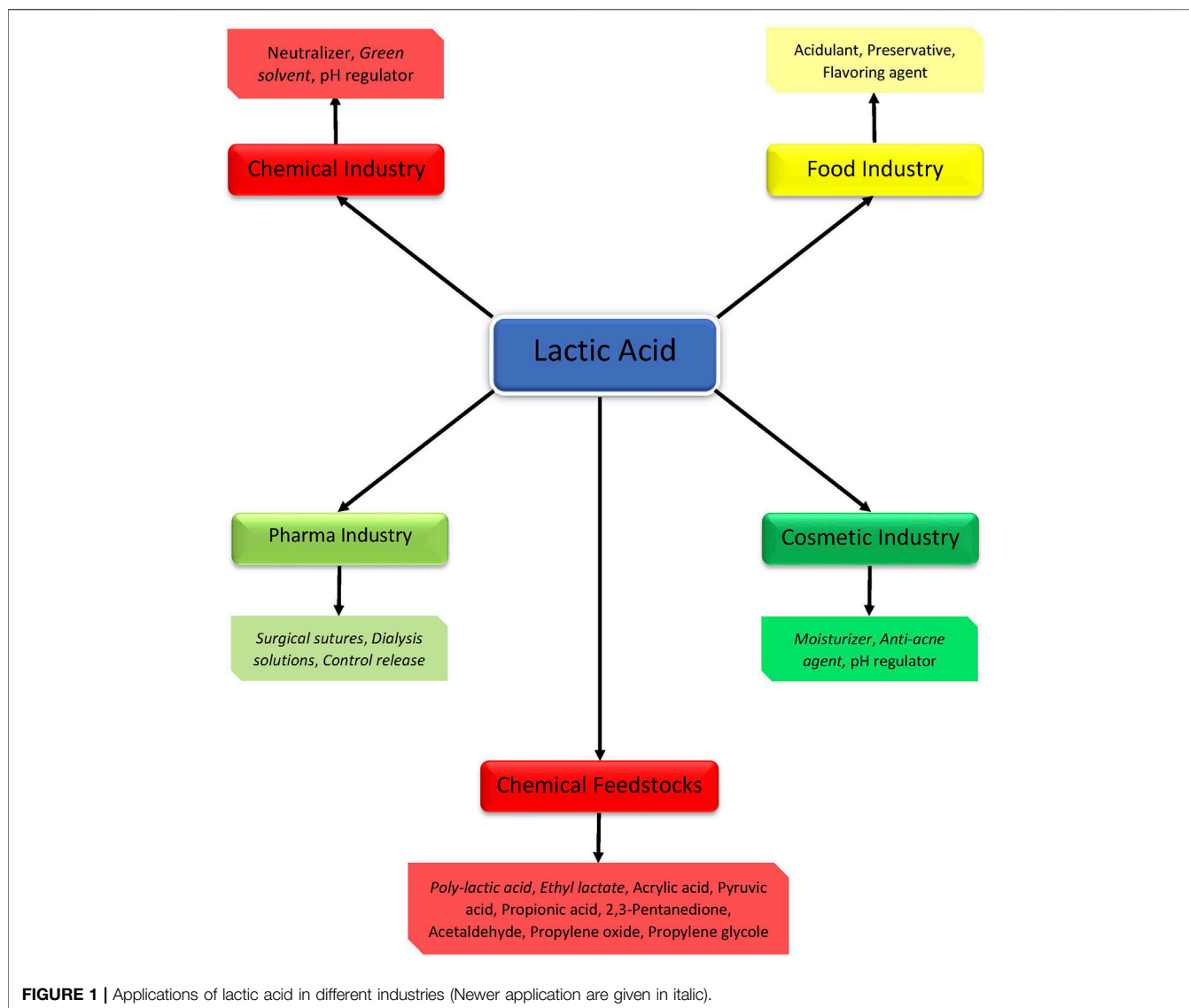
The second (lignocellulosic biomass and industrial wastes) and third (algal biomass) generation feedstocks gained substantial interest as a source of various value-added chemicals, produced by fermentation. Lactic acid is a valuable platform chemical with both traditional and newer applications in many industries. The successful fractionation, separation, and hydrolysis of lignocellulosic biomass result in sugars' rich raw material for lactic acid fermentation. This review paper aims to summarize the investigations and progress in the last 5 years in lactic acid production from inexpensive and renewable resources. Different aspects are discussed—the type of raw materials, pretreatment and detoxification methods, lactic acid-producers (bacteria, fungi, and yeasts), use of genetically manipulated microorganisms, separation techniques, different approaches of process organization, as well as main challenges, and possible solutions for process optimization.

**Keywords:** lignocellulosic biomass, lactic acid, pretreatment, fermentation, separation

## 1 INTRODUCTION

The intensive economic growth during the past century is accompanied by high energy consumption. Nowadays fossil fuels (coal, petroleum, and natural gas) are still the main energy source and raw material for the production of various chemicals. The fossil fuels were formed and stored underground for millions of years and their extensive use has led to the situation where the present vegetation on Earth cannot treat the emitted carbon dioxide by photosynthesis (Damyanova and Beschkov 2020). As a consequence, the strong emissions of carbon dioxide and greenhouse gases affect and change the climate. One of the ways to cope with this global problem is to close the natural carbon cycle using renewable sources as a platform for biofuels and chemicals production, and thus enabling recycling of the biological sources and consumption of the resulting carbon dioxide by photosynthesis (Beschkov et al., 2020).

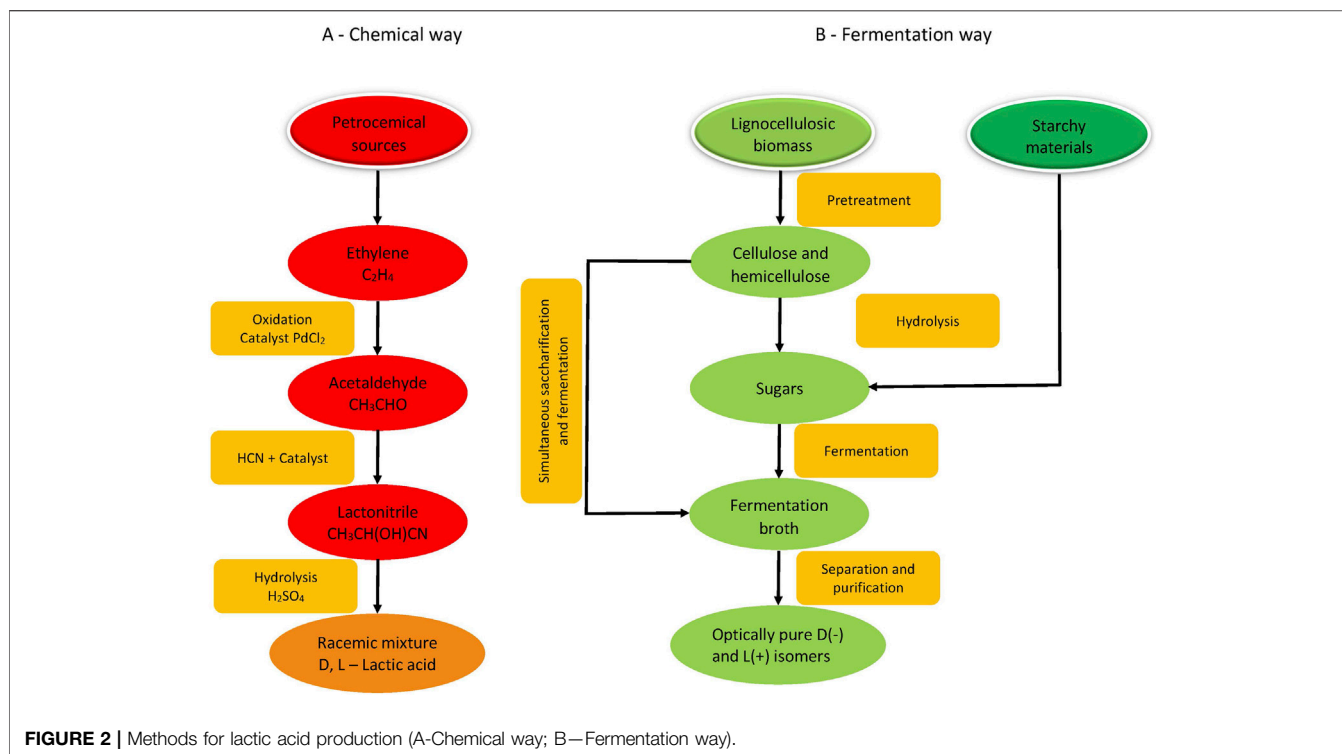
A major step in the development of a sustainable, industrial society will be the shift from dependence on oil to the use of renewable resources. In the prospect of environmental sustainability, the utilization of agro-industrial waste residues as feedstock for the production of both biofuels and basic synthetic chemicals in biorefineries has gained widespread attention (Yaashikaa et al., 2022). In the long run, oil use can be eliminated and gas emissions reduced. The market share of biotechnological processes for the production of various chemical products is expected to increase in the coming years from 5 to 20%. Organic acids are a key group of chemicals that can be produced microbiologically. Functional groups that need to be introduced through an expensive multistage oil oxidation process are present in plant materials such as carbohydrates.



Cellulosic biomass is an abundant and sustainable source of valuable chemicals that are truly unique for making various organic products. It includes agricultural wastes (corn stover, spent grains, and sugarcane bagasse), some municipal solid wastes (waste paper), wastes from forestry residues (mill wastes and sawdust), herbaceous (switchgrass), and woody (poplar trees) crops. Such materials are plentiful and accessible in many regions of the world and can be competitive in price with petroleum and thus opening up a new route to manufacturing organic fuels and chemicals. Despite the high availability, the degradation of biomass is a substantial challenge. Hence, it is necessary to integrate several unit processes such as biochemical, thermochemical, physical, and catalytic conversion to produce a wide range of bio-based products (Velvizhi et al., 2022).

Lignocellulosic biomass is composed of cellulose linear chains formed from glucose units. Cellulose fibers are held

together with hemicellulose (branched heteropolymer formed by various hexoses and pentoses) and lignin (complex heteropolymer built from phenylpropanoid units). The specific structure of lignocellulose restricts the access of enzymes to cellulose and hemicellulose fibers and hinders effective hydrolysis. In view of converting lignocellulose to valuable chemicals by fermentation, this structure must be destroyed by some pretreatment. The purpose of the pretreatment is to decrease the crystallinity of cellulose and degree of polymerization, destruct hydrogen bonds between fibers, and thus increase the area accessible for the enzymes' action. The lignin should be at least partially removed and cellulose and hemicellulose efficiently hydrolyzed to fermentable sugars. Various pretreatment techniques have been used with the goal of breakdown the lignocellulosic complex and liberating sugars for further use.



Lignocellulosic biomass of various sources can be used for the production of different chemicals such as fuels (ethanol, methane, hydrogen), enzymes (cellulases, amylase, protease), high-value chemicals (hydroxycinnamic acid, lactic acid, xylitol), etc.

The present review aims to summarize in-depth the latest achievements in the field of fermentative lactic acid production from renewable sources –various substrates, microorganisms including gene manipulated, as well as process organization and downstream techniques.

## 2 LACTIC ACID

Lactic (2-hydroxypropanoic) acid (LA) is a valuable platform chemical with both traditional and newer applications (**Figure 1**). It was widely used as a neutralizer, preservative, or acidulant in food and beverage, cosmetic, pharmaceutical, and other industries. Recently, lactic acid is applied as the building block for various biodegradable polymers or precursor for environmentally friendly solvents. The annual global market of lactic acid in 2020 is valued at USD 1.1 billion with an increasing tendency to double till 2025 (Lactic Acid Market by Application (Biodegradable Polymers, Food & Beverages, Pharmaceutical Products) 2020). The global market for lactic acid was 750.00 kilotons in 2017 and is projected to reach 1,845.00 kilotons by 2022 (Global Lactic Acid Market 2017-2025 - Growth Trends, Key Players, Competitive Strategies and Forecasts - Research and Market 2017).

Nowadays, lactic acid is produced by chemical or fermentation way. In the chemical route (**Figure 2A**), lactic acid is produced from petrochemical sources by a multistep reaction scheme. It includes catalytic oxidation of ethylene, conversion of obtained acetaldehyde to lactonitrile end its hydrolysis to a racemic mixture of D (-) and L (+) lactic acid. Of course, there are other methods for the chemical synthesis of lactic acid like oxidation of propylene or propylene glycol, hydrolysis of chloropropionic acid, but they are not economically and technically feasible (Krishna et al., 2018). Fermentative production of lactic acid is based on the conversion of different sugars (glucose, lactose), starchy or lignocellulosic hydrolysates by different microorganisms, mainly lactobacilli (**Figure 2B**). Factors affecting lactic acid fermentation (pH, temperature, nutrients, substrate, product concentrations, etc.) are discussed in the review of Rawoof et al. (Rawoof et al., 2021).

- *pH*—for most lactobacilli the optimum value for effective lactic acid production is between 5 and 7. Unfortunately, accumulation of the lactic acid leads to decreasing pH, even outside the optimum value, leading to a decrease in microorganisms' growth and lactic acid production. Additionally, high lactic acid concentration inhibits cellular metabolism. A decrease in pH could be overcome by neutralization with strong bases like sodium, ammonium, or calcium hydroxide, or low molecular mass water-soluble amines. Another way is *in-situ* product removal during fermentation. Discovering or engineering the acid-tolerant strains is a challenge. This will permit to decrease the

product inhibition, and overall cost of the process, eliminating the use of neutralizers.

- *Temperature*—the temperature is an important factor for bacterial growth and lactic acid production. Most of the lactobacilli are mesophilic (25–40°C). An increase in the operational temperature will result in decreasing contamination and increasing substrate hydrolysis. Very often, the optimal temperature for microbial growth differs from that for maximal lactic acid production. The selection of strains capable to grow at thermophilic (40–65°C) or extreme thermophilic (65–80°C) conditions will be very favorable.
- *Media composition*—the complexity of the fermentation media (carbon and nitrogen sources, minerals, vitamins) is a factor increasing the cost of lactic acid production. Carbon is an indispensable element and the replacement of costly individual sugars with cheap agricultural and industrial wastes is a step towards decreasing the total cost. Nitrogen is a major component in the anabolic and catabolic processes. Usually, complex nitrogen sources like peptone, yeast extract, and meat extract are used. Alternatives for cheap nitrogen sources are corn steep liquor, hydrolysate of fish waste, and wheat bran extract. DDGS (about 30% protein) is an attractive alternative because its hydrolysis results in carbon sources and nitrogen at a time. The ratio between carbon and nitrogen (C/N) also is very important. An optimal C/N ratio results in a positive effect on lactic acid fermentation. Usually, the optimal C/N ratio is between 3 and 7 (Gómez-Gómez et al., 2015), (Gilver Rosero Chasoy et al., 2020), (Mejia-Gomez and Balcazar 2020).
- *Sugars concentration*—at a high initial substrate concentration some problems such as longer lag phase, decreased activity, cellular lysis, and osmotic stress could occur, resulting in reduced substrate consumption and low lactic acid production. The effect of substrate inhibition can be diminished by adding osmo-protective substances, fed-batch fermentation mode, developing high sugars tolerant strains. Substrates originating from lignocellulosic sources usually are a mix of pentoses and hexoses. Lactic acid bacteria possess a hierarchical pattern of sugar utilization—glucose is utilized first and then other sugars. This leads to carbon catabolite repression, a decrease in fermentation efficiency, and low product concentration. The problem can be solved by using pentoses and hexoses utilizing strains in co-fermentation mode. Another way is isolating or engineering strains with increased carbon catabolic repression resistance.
- *Effect of end- and by-product accumulation*—the effect of product accumulation and subsequences were discussed above. Glucose and xylose are the main constituents of agrocellulosic hydrolysates. While glucose undergoes conversion to lactic acid mainly by homo-fermentation, xylose is converted by the hetero-fermentative pathway, leading to the formation of by-products like ethanol and acetic acid. The accumulation of by-products leads to a decrease in lactic acid yield and an increase in the cost of product recovery. Again, the selection of novel strains and genetically modifying the existing strains to follow the desired pathway is the possible solution to the problem.

- *Sensitivity to toxic compounds*—most of the pretreatment methods lead to the formation of inhibitory compounds—furfural, 5-hydroxymethyl furfural, levulinic acid, formic acid, *p*-coumaric acid, ferulic acid, etc. These compounds exhibit an inhibitory effect on the enzyme's action, cellular growth, and lactic acid production. Different approaches can be used for elimination of inhibitory effect—use of pretreatment methods leading to less liberation of inhibitors, chemical or biological neutralization of the inhibitors, use of adaptive evaluated, inhibitor-tolerant, or engineered strains.

Some bottlenecks hinder effective lactic acid production. The major one is product inhibition. Accumulation of the lactic acid leads to a fast drop in the medium pH, outside of the optimum value for the producer strain. This results in low substrate conversion and low final product concentration. The problem may be overcome either by *in situ* product removal or by using acid-tolerant bacteria. The cost of raw material and nutritional additives are with the major contribution to the overall cost of lactic acid. Usually, the pure sugars used as a substrate for lactic acid fermentation are very costly and take part in the human food chain. According to S. Tejayadi and M. Cheryan in the case of lactic acid production from whey permeate, the cost of whey (including transportation) was 35% and for yeast extract—38% of the total cost (Tejayadi and Cheryan 2005). Akerberg and Zacchi reported that the major operational costs (raw material, saccharification, fermentation, and electrodialysis) contributed about 80% to the total cost in case of lactic acid production from wheat flour (Akerberg and Zacchi 2000). For using starch or other natural polymers, like inulin, it is necessary either to hydrolyze it to individual sugars or use lactic acid-producing bacteria with relevant enzyme activity. In recent years, a new process for lactic acid production attract the interest of researchers in the field—catalytic conversion of lignocellulosic biomass. The process is led in the presence of homogeneous and heterogeneous catalysts at lower temperatures or under subcritical conditions. For example, lactic acid production from empty fruit palm oil bunch under hydrothermal conditions in the presence of metal salts was described (Sitompul et al., 2014) and (Chin et al., 2016). In an extensive and comprehensive review, Mäki-Arvela et al. (2014) describe the research since 2000 on the production of lactic acid from biomass and its transformation to commodity chemicals. The mechanisms in the production of lactic acid and its derivatives in the presence of homogeneous and heterogeneous catalysts were described, as well as reaction conditions, catalysts' properties, stability, and reuse. The authors also discussed some reactor technologies and kinetic modeling of the processes in hydrogenation and esterification of lactic acid.

In any case, it is clear that finding a cheap, abundant, and easily accessible raw material is a key factor for an effective and economically profitable method for fermentative lactic acid production. Lignocellulosic biomass especially forest biomass, waste, and inedible plant materials, as well as various agricultural crop residues, seems to be a promising substrate for an effective and economically profitable method for fermentative lactic acid production which non-competes with

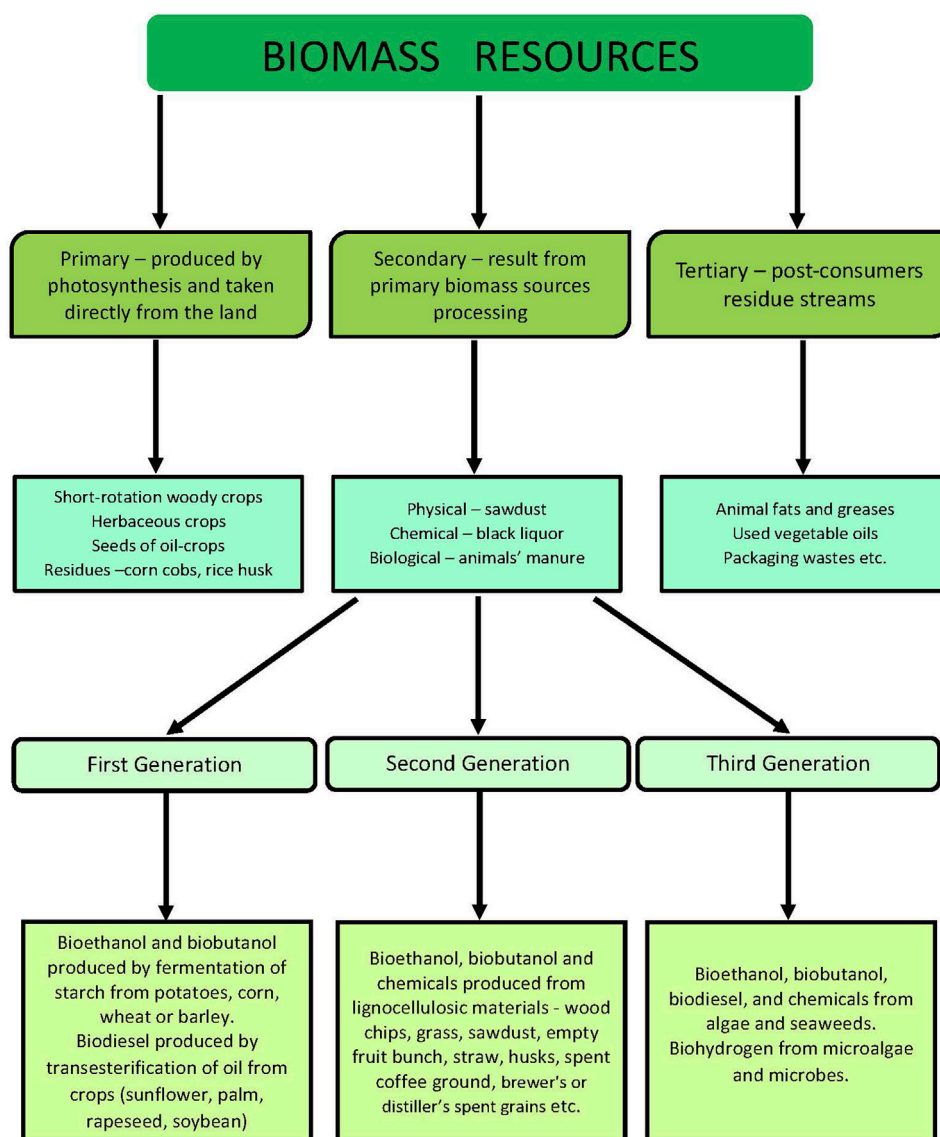


FIGURE 3 | Classification of biomass resources.

the human food chain. Recently, several review papers concerning lignocellulosic biomass utilization as a source for bio-based chemicals production have been published. (Tišma et al., 2021; Banu et al., 2021; Haldar and Purkait 2020; Usmani et al., 2021; Nwamba et al., 2021).

Regarding lactic acid production from lignocellulosic biomass, there are some reviews published in the last 2 years considering different aspects of the issue—microorganisms (Abedi and Hashemi 2020), sources (Lopez-Gomez et al., 2020; Ajala et al., 2020), pretreatment methods (Huang et al., 2021; Mankar et al., 2021), separation (De Oliveira et al., 2020; Li et al., 2021), techno-economic analysis (Li et al., 2021; Manandhar and Shah 2020; Daful and Görgen 2017), etc. Thygesen et al. (2021) summarized recent data on the

valorization of municipal organic waste into purified lactic acid - pretreatment, enzymatic hydrolysis, LA fermentation, and downstream processing.

## 2.1 Problems and Obstacles in Fermentative Lactic Acid Production From Lignocellulosic Biomass

In every step of lactic acid production by fermentation from lignocellulosic feedstocks, from pretreatment to separation, there are various bottlenecks, which must be overcome for the realization of an effective and low-cost process.

Regardless of the undoubted advantages of using lignocellulosic biomass as raw material for lactic acid



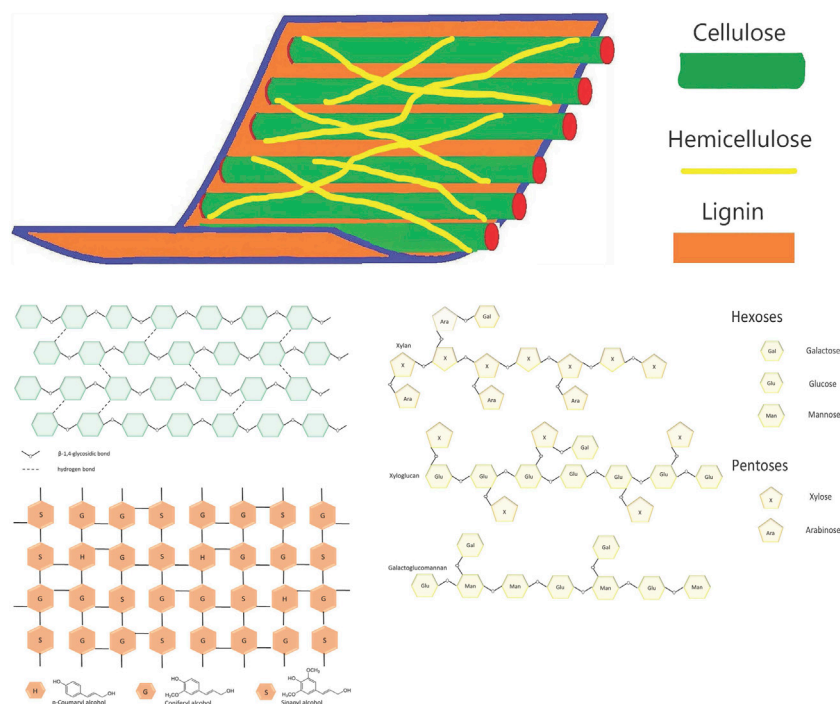


**FIGURE 4 |** Sketch of lignocellulose structure.

production, like low cost and global availability, main problems can be summarized as follows:

- in pretreatment step—i) resistant nature of biomass and difficulties in full separation of lignin from cellulose and hemicellulose; ii) energy consumption, toxicity, and environmental problems of some used chemicals; iii) release of inhibitory compounds; iv) high cost of hydrolytic enzymes and their product inhibition.
- in fermentation step—i) nutritional requirements of lactic acid bacteria; ii) carbon catabolite repression; iii) product and substrate inhibition; iv) by-product formation in hetero-fermentation.
- in separation and purification step—i) low concentration of feeding stream; ii) more complex composition of fermentation broth in comparison with first-generation LA production; iii) high cost of downstream processes; iv) not all separation methods are tested on second-generation LA; v) ecological problems connected with classical precipitation separation.

More details for different problems and possible solutions are given in (Cubas-Cano et al., 2018; Tan et al., 2018; Grewal et al., 2020).

### 3 LIGNOCELLULOSIC FEEDSTOCKS

The term biomass generally includes the mass of organic material in all living organisms on Earth (microorganisms, algae, plants,

and animals). The main building elements of biomass are carbon, hydrogen, oxygen, and nitrogen, and similarly to fossil feedstocks, the biomass can be used for various chemicals production. Biomass is abundant and renewable and can be divided into three groups (**Figure 3**). Primary resources are produced directly by photosynthesis and taken from the land; secondary resources result from the processing of primary sources and tertiary—post-consumers residue streams. The greater part of plant biomass consists of lignocellulose—a complex of three polymers (cellulose, hemicellulose, and lignin) and a small number of extractives, pectin, and ash. A sketch of lignocellulose structure is given in **Figure 4**.

Cellulose is a linear polysaccharide comprising D-glucose units, linked by  $\beta$  (1–4)-glycoside bonds (in contrast to  $\alpha$  (1–4) bonds in starch amylose). Cellulosic molecules are located in parallel, forming primary fibrils, stabilized by hydrogen bonds. The sections with a strictly parallel arrangement and additional hydrogen bonding, are referred to as crystalline, in contrast, to those in which such arrangement is missing. The latter are called amorphous. The cellulose fibrils can further interact to form cellulose fibers. The cellulose is very stable and insoluble in water, diluted acids, and the majority of common solvents, but is soluble in concentrated acids, and alkali bases (for DP smaller than 100).

Hemicellulose is a branched polymer built from different saccharides—pentoses (xylose, arabinose), hexoses (glucose, mannose, galactose) as well as some uronic acids (glucuronic,

**TABLE 1** | Composition of different lignocellulosic feedstocks.

Lignocellulosic biomass	Cellulose%	Hemicellulose %	Lignin %	Reference
Softwood chips (pine)	46.7	23.5	28.1	Wu et al., (2020)
Softwood pellets (spruce, pine, and fir)	42.4	21.6	27.5	
Hardwood (aspen) chips	46	19	28	Wu et al. (2019)
Softwood (Lodgepole pine) chips	46.7	23.5	28.1	Wu et al., (2020)
Softwood (spruce, pine and fir) pellets	42.4		27.5	
<i>Sophora flavescens</i> root	46.6	19.5	20.2	Ma et al. (2020)
Sugar palm trunk	40.1	16.5	27.2	Erlana et al. (2020)
Pine sawdust	24.9	31.5	36.6	Rapado et al. (2021)
Oil Palm Empty Fruit Bunch	29.4	14.4	22.7	Aini et al. (2018)
Date palm wastes				
Leaves	59.1	16.7	16.1	Alrumman (2016)
Leaf bases	51.5	24.4	18.5	
Fibrous material	43.2	12.8	24.1	
Pulp mill residue	80.9	16.2	1.7	Moraes et al. (2016)
Orange peel waste	19.1	14.8	6.2	Bustamante et al. (2020)
Pressed recycled paper sludge	34.1	7.9	20.4	Marques et al. (2017)
Cassava bagasse	13.5	5.8	2.8	Chen et al. (2020)
Sugarcane bagasse	34.7	25.2	19.2	Wischral et al. (2019)
	47.4	9.7	5.4	Oliveira et al. (2019)
	41.4	32.4	8.3	Zheng et al. (2021)
	13.5	26.0	22.5	Chen et al. (2020)
	47.2	5.8	2.8	Baral et al. (2021)
	43.8	19.6	27.7	Grewal and Khare (2018)
	34.5	32.7	23.2	González-Leos et al. (2020)
	36.6	16.0	32.1	Nalawade et al. (2020)
	45.5	20.8	22.1	Nalawade et al. (2020)
	33.0	22.3	29.9	Li et al. (2021)
	39.6	26.2	23.4	Pin et al. (2019)
	27.9	25.6	2.8	Azaizah et al. (2020)
Bagasse sulphite pulp	73.8	14.3	5.9	Zhou et al. (2016)
Sweet sorghum bagasse	38.5	23.4	21.4	Wang et al. (2016)
Banana peel	14.0	13.0	17.0	Martínez-Trujillo et al. (2020)
Banan peel	12.2	10.2	2.9	Redondo-Gómez et al. (2020)
Banana rachis	23.0	11.2	10.8	
Banana penduncle	35.8	20.7	6.16	Azaizah et al. (2020)
Carob biomass	19.0	0.35	28.4	Azaizah et al. (2020)
Brewers spent grains	16.8	28.4	27.8	Mussatto and Roberto (2006)
	21.7	19.3	19.4	Meneses et al. (2013)
	25.3	41.9	16.9	Silva et al. (2004)
	21.9	29.6	20.6	Carvalho et al. (2004)
Corn stover	41.2	30.1	19.4	Rahman et al. (2020)
	37.1	29.6	20.8	Zhang et al., 2020
	31.3	26.9	16.4	Sun et al. (2021)
	32.6	26.4	31.0	Cheng et al. (2018)
	31.2	22.3	20.8	Han et al. (2019)
	38.8	23.6	18.4	Ma et al. (2016)
	45.0	21.0	17.0	He et al. (2016)
	43.6	19.2	22.6	Zhang et al. (2021)
	33.0	26.9	20.8	Wei et al. (2018)
	40.1	15.1	18.3	Chen et al. (2020)
	34.7	21.3	21.7	Shi et al. (2021)
Corn cob	37.0	34.3	16.4	Lin et al. (2020)
	70.0	9.7	16.2	Alhafiz et al. (2020)
	36.7	30.0	23.3	Sánchez et al. (2012)
	32.6	31.7	16.9	He et al. (2017)
Wheat straw	41.1	37.5	13.5	Grewal and Khare (2018)
	40.5	26.1	18.1	Cubas-Cano et al. (2019)
Rye straw	38.0	25.5	27.1	Schroedter et al. (2021)
Digestate of energy corn silage	29.3	22.4	33.5	Schroedter et al. (2021)
Sorghum straw	25.0	27.5	20.2	Wu et al. (2021)
Rice straw	33.3	23.3	17.5	Yao et al. (2007)
	44.6	29.0	12.4	Jaichakan et al. (2021)
	32.2	18.9	24.0	Younas et al. (2016)

(Continued on following page)

**TABLE 1 |** (Continued) Composition of different lignocellulosic feedstocks.

Lignocellulosic biomass	Cellulose%	Hemicellulose %	Lignin %	Reference
	34.2	17.2	21.4	Chen et al. (2019)
	35.0	18.0	15.0	Yadav et al. (2021)
	34.5	21.3	13.3	Tu et al. (2019)
Rice husk	47.6	19.1	19.3	Jaichakan et al. (2021)
Soybean hulls	35.8	23.1	9.1	Rojas et al. (2014)
Chestnut shell	27.6	15.7	27.5	He et al. (2016)
	28.1	16.7	23.2	He et al. (2016)
Pecan nutshell	28.7	8.8	27.1	Qin et al. (2017)
Deoiled cottonseed cake	24.4	14.3	5.2	Grewal and Khare (2018)
Spent coffee grounds	24.3	24.8	13.5	Giroto et al. (2018)
	10.8	28.3	10.7	Cruz-Lopes et al. (2017)
	12.4	39.1	23.9	Ballesteros et al. (2014)
	7.0	43.0	37.0	Koo et al. (2019)
Distillery stillage - Rye	16.8	29.6	15.6	Mikulski and Kłosowski (2018)
Wheat	18.6	34.1	9.5	
Corn	32.2	20.9	3.2	
Distillers spent grain -wheat	11.1	20.3	2.0	Zaini et al. (2019)

galacturonic acid). For example, the main components in softwood hemicelluloses are built from hexoses and those of hardwood from pentoses. The polymerization degree of hemicelluloses is smaller than in cellulose. Hemicellulosic polysaccharides are soluble in bases (10% KON or 18% NaOH), dimethylsulphoxide, and in rare cases in hot water.

Lignin is a highly branched amorphous phenolic polymer composed mainly of p-coumarin alcohol (H unit), coniferyl alcohol (G unit), and sinapyl alcohol (S unit). Lignin is a highly cross-linked polymer with long chains. The structure of lignin differs considerably from its source (type of plant, and even different parts of the same plant), for example, the lignin, derived from softwood is built predominantly of G units, hardwood lignin is mostly comprised of G and S units, while lignin from grass contains all three units.

Cellulose fibers are stacked together by hydrogen bonds with hemicellulose and pectin. Lignin interacts with cellulose and hemicellulose not only by hydrogen bonding but with covalent bonds and thus forming a rigid complex structure difficult for chemical or biochemical degradation.

Lignocellulosic biomass differs considerably depending on its origin. In general, the composition is cellulose 30–60%, hemicellulose 20–40%, and lignin 15–25% (Norrrahim et al., 2021). Reshmy et al. (2022) discussed the selection of lignocellulosic sources, advanced pretreatment methods for various types of cellulose for use in cost-effective bio-refineries for future industrial application. A short description of major platform chemicals and biomaterials as well as different biofuels such as biomethane, bioethanol, and biohydrogen, is given. In **Table 1** data for different lignocellulosic feedstocks composition are summarized.

In what follows a brief data for the most used lignocellulosic feedstocks are given.

### 3.1 Corn Residues

The world corn production for 2020/2021 is estimated at around 1.125 billion metric tons (Shahbandeh, 2021a). It is

estimated that for each bushel of shelled corn 50 pounds of corn residue (cobs, leaves, stalks, and husks) are also produced (McCutcheon and Samples 2002). It means that an enormous amount of corn residues are available for converting into value-added products.

### 3.2 Brewer's Spent Grains

Brewer's spent grains (BSG) are the major by-product in the brewing industry. The quantity of residue material in beer production is about 24.4 kg per 100 L of beer produced (about 85% of total generated by-products are brewer's spent grains or approximately 20 kg per 100 L of beer (Reinold 1997)). The worldwide beer production in the last decade is around 1.93 billion hectoliters (Conway 2021).

### 3.3 Sugarcane Bagasse

Sugarcane is a perennial grass mainly used for sugar production. Annually around 1,89 billion tonnes of sugarcane are produced worldwide and 250–270 kg of sugarcane bagasse are generated from each ton of sugarcane (Wischnal et al., 2019).

### 3.4 Spent Coffee Grounds

Coffee is surely one of the most popular beverages consumed in the world. The volume of world coffee production in 2019/2020 is estimated to be 163.7 million 60-kg bags (Shahbandeh, 2021b). Approximately half (in dry weight bases) of the coffee is separated in the form of spent coffee grounds during the preparation of coffee beverages or the manufacturing of instant coffee or instant coffee-making process (Kim et al., 2019). According to (Mussatto et al., 2011) 650 kg of Spent Coffee Grounds (SCG) are generated from each ton of green coffee.

### 3.5 Distillery's Dried Grains With Solubles

Distillery's Dried Grains With Solubles (DDGS) represent the most important by-product in bioethanol production. After ethanol distillation, the thin stillage from the fermentation

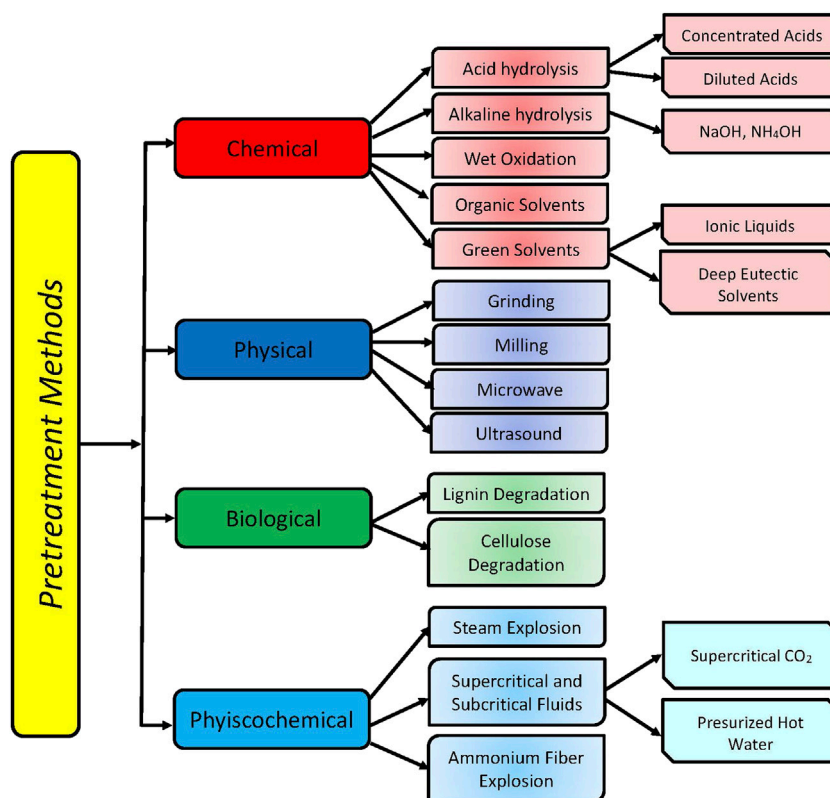


**FIGURE 5** | Classification of biomass pretreatment methods.

broth was decanted, and the solid is dried to produce DDGS. The world bioethanol production (from sugarcane, wheat, corn, and other feedstocks) in 2020 was estimated at around 100 billion liters (Bio-ethanol market-growth, trends, covid-19 impact, and forecasts (2021 - 2026) 2021). The production of the first generation of ethanol is almost strictly differentiated by countries (mainly from corn in the United States and sugarcane in Brazil). Taking into account that from bushel (25.4 kg) grains about 8.2 kg of ethanol is produced, releasing about 7.7 kg of DDGS (Jacques et al., 2003) it is easy to calculate that about 73 million of tonnes DDGS are produced annually.

From the data presented above, it is seen that lignocellulosic sources are released in enormous quantities and can be used as a substrate for fermentative production of various value-added chemicals after individual sugars liberating.

## 4 PRETREATMENT METHODS

The specific structure of the lignocellulose restricts the access of enzymes to cellulose and hemicellulose fibers and hinders effective hydrolysis. In view to converting lignocellulose to fermentable sugars, the lignocellulosic biomass must be subjected to some pretreatment. The purpose of the pretreatment is to break down the structure of lignocellulose,

destruct hydrogen bonds between fibers, remove at least partially the lignin, decrease the crystallinity of cellulose, and degree of polymerization, and thus increase the area accessible for the enzymes' action, as well as efficiently hydrolyze cellulose and hemicellulose. Different methods have been applied for the pretreatment of lignocellulosic biomass (Norrahim et al., 2021). In general, they can be classified into four main groups—physical, chemical, physicochemical, and biological methods (Figure 5). When the main goal of lignocellulosic biomass processing is obtaining maximum fermentable sugars as a substrate for fermentative production of value-added products, pretreatment is an inevitable step. Usually, each method results in different effects (delignification, hemicellulose dissolution, etc.). The most important is that there is no universal method for lignocellulosic biomass pretreatment. This is due to the different compositions of lignocellulosic biomass (ratio of main components and degree of crystallinity of cellulose) from different sources (soft- and hard-wood, agricultural, or industrial wastes). The compositional differences influence the efficacy of pretreatment. The severity of treatment (pressure, temperature, and acid or alkali concentration) also lead to differences in the composition of obtained hydrolysates as well as in the concentration of inhibitors of enzyme hydrolysis and fermentation. Recently Zhao et al. (2022) summarized the current state and the latest advances of

lignocellulose pretreatment technologies and described several new strategies for overcoming pretreatment bottlenecks for the realization of highly efficient lignocellulose bioconversion.

In view to choosing an “optimal” pretreatment method, one needs broad knowledge about the chemical composition of the feedstock, but also the final aim of pretreatment. For example, in case the fermentation step is done by an industrial strain non-converting pentoses—lignin, and hemicellulose should be separated from biomass before cellulose hydrolysis. In the case of using a strain capable to convert pentoses or co-fermentation removal of lignin should be enough. Usually, a combination of two or more methods is used before the enzymatic hydrolysis of lignocellulosic biomass.

## 4.1 Physical Methods

The main purpose of these methods is to reduce the particle size of biomass, the crystallinity of cellulose, and the degree of polymerization of cellulose and hemicellulose and thus increasing surface area accessible for enzymes and biomass biodegradability. Physical methods do not use any chemicals and include different types of chipping, milling, and grinding, as well as gamma- or microwave irradiation, and ultrasound treatment. The main disadvantage of physical methods is high energy requirements, especially on a large scale.

## 4.2 Chemical Methods

This group includes several methods, based on reactions between lignocellulose biomass and various chemicals in the water phase. This is the most applied group of methods and its main goal is to reduce the amount of lignin and hemicellulose content in the biomass.

### 4.2.1 Acid and Alkaline Hydrolysis

These methods are relatively cheap and easy to perform. Acid hydrolysis of biomass can be done using diluted (0.5–5%) or concentrated (10–60%) acids. Sulphuric and hydrochloric acids are most employed. Smits et al. (2019) developed a fast method for screening of optimal acid-pretreatment conditions in the conversion of wood lignocellulose to sugar. Luo et al. (2021) developed an artificial neural network model to simultaneously predict the derived feature of phenolic compounds content and glucose yield in lignocellulosic biomass hydrolysate from dilute inorganic acid pretreatment and enzymatic hydrolysis. Also, there are attempts to use some organic acids to avoid problems with the corrosive action of the acids. While hydrolysis with concentrated acids can be realized at low temperature and normal pressure, dilute acid hydrolysis require elevated temperatures and pressure.

Hydroxides like NaOH, KOH,  $\text{NH}_4\text{OH}$ ,  $\text{Ca}(\text{OH})_2$ . Hydroxides are less corrosive in comparison to acids and can be applied at moderate temperatures and ambient pressure when the alkali concentration is about 10–20%. At low concentrations higher temperatures and elevated pressure are necessary. These methods are considered better in delignification compared to acid hydrolysis methods, whereas cellulose remains mostly intact, and hemicellulose is affected depending on the severity of treatment.

Another successful method for lignin separation is so-called solvolysis. This technique uses some low boiling alcohols (methanol, ethanol) or high boiling alcohols, like glycerol, ethylene glycol, and butanol. Some ketones—acetone, methyl isobutyl ketone, and organic acids (formic, acetic, oxalic) are also utilized. Methods applying low boiling chemicals require high temperatures (150–250°C) and pressure. After solvolysis pretreatment, the lignocellulosic biomass separates into three fractions—precipitated lignin, solid cellulosic pulp, and liquid phase, containing hemicellulosic sugars (Goh et al., 2011). Sidiras et al. (2022) reviewed organosolv pretreatment methods and the optimization of feedstock delignification, sugars production, enzymatic digestibility of the cellulose fraction, and quality of lignin.

### 4.2.2 Oxidative Pretreatment

Oxidative pretreatment methods involve biomass processing with air, pure oxygen, hydrogen peroxide, or ozone in the water phase. In the case of ozone, the process can be conducted at ambient conditions, while other oxidizers demand high temperatures (150–250°C) and pressure—10–20 bar for short periods—10–15 min. During pretreatment, the lignin is converted to carboxylic acids, carbon dioxide, and water. The presents of acids in the solution facilitate the solubilization of the hemicellulose and increase the cellulose content.

### 4.2.3 Ionic Liquids and Deep Eutectic Solvents

In the last 20 years, the application of ionic liquids (IL) and deep eutectic solvents (DES) in biomass pretreatment gains more and more the attention of researchers. Ionic liquids are composed of a large organic cation and a small anion. They are liquid at room temperature with low vapor pressure, which facilitates their almost full recovery and thus somehow overcomes the main drawback of using IL—their high cost. Deep eutectic solvents are easily prepared by heating (60–80°C, for 4–8 h) a hydrogen bond donor (urea, acetamide, glycerol, some acids—lactic, oxalic, and sugars—glucose, maltose) and a hydrogen bond acceptor (different quaternary ammonium salts—choline chloride, tetramethylammonium chloride, etc.). The compounds forming DES are linked through hydrogen bonds and the formed eutectic mixture has a lower melting temperature than the initial components. The main advantages of DES are their ease of synthesis, biodegradability, and low cost. It is accepted that IL and DES are more effective in the separation of lignin and hemicellulose than acid and alkali treatment. Xu et al. (2021) analyzed the influence of different hydrogen bond donors on the lignocellulosic biomass pretreatment with choline chloride-based DES. The authors defined the most important among 42 key process factors—HBD hydrophilic ability, HBD polarity, HBD acidity, HBD ability to form hydrogen bonds, the molar ratio of HBD to choline chloride, and pretreatment severity (Xu et al., 2021). Yadav et al. (2020) have screened some lactic acid bacteria for their stability in ionic liquids. Recent reviews published by Usmani et al. (2020) and Halder et al. (2019) describe recent developments in using techniques applying ionic liquids in biomass pretreatment—breakdown mechanism, process parameters, the impact of cation and anion groups, and the



advantages of IL on the further processing of the fractionated biomass.

### 4.3 Physicochemical Methods

These methods combine physical forces with the action of chemicals to modify the lignocellulosic biomass structure. Steam explosion, ammonia fiber expansion (AFEX), and supercritical fluids treatment take part in this group. The treatment can be done with pure water or water steam at elevated pressure and temperatures (hydrothermal treatment) or in the presence of some chemicals acting as a catalyst. Depending on temperature and pressure (below or above the critical point of the solvent) methods can be divided into two groups—subcritical and supercritical. As a result of physicochemical pretreatment dissolution of hemicellulose, changes in lignin structure and decreasing degree of polymerization and cellulose crystallinity are observed. Duque et al. (2016) described the fundamentals of steam explosion methods, their advantages and disadvantage, and technological advancements made in the last years.

#### 4.3.1 Steam Explosion

In this method the biomass is subject to high temperature (150–250°C) for a short time (from certain seconds to a few minutes) in the presence of saturated steam, followed by a quick release of the pressure. Sometimes a two-step method is applied—in the first step, the biomass is heated to 180°C in view to solubilize and remove hemicellulose, and then the temperature is elevated to 240°C to modify cellulose and lignin. The method is environmentally friendly with advantages like low energy consumption and low cost. The drawback is the formation of some fermentation inhibitors.

#### 4.3.2 Pressurized Hot Water

Similarly to steam explosion the biomass is heated to 150–250°C at pressure 3–5 MPa, but without quick decompression, which permits to realize the process in a flow-through reactor. The method is cost-effective, does not use toxic chemicals, and is possible to control the release of inhibitors by controlling pH values between 4 and 7.

#### 4.3.3 Ammonia Fiber Expansion

The method uses liquid or gaseous ammonia (usually at 1:1 ratio) under high pressure (15–30 bar) and moderate temperatures (60–100°C) for 5–10 min. The moderate temperatures, as well as the possibility of recovering and reuse of the ammonia, reduce the cost of the process. The method is not very effective in treating biomass with high lignin content (higher the 20%) and also does not fully dissolve the hemicellulose. Recently, a new method called extractive ammonia is investigated. It is characterized by a higher ratio of ammonia to biomass (up to 6:1). The method is very effective in lignin removal (about 45% in corn stover) leaving almost all carbohydrates (more than 90%) in the solid phase (Avci et al., 2019).

#### 4.3.4 Supercritical Fluid Pretreatment

Supercritical fluids are characterized by their unique properties—they have a density like a liquid and viscosity and

diffusivity like gases. Carbon dioxide is the most widely used chemical in supercritical conditions. While the biomass pretreatment with sec carbon dioxide is not enough effective, the presence of moisture ameliorates changes in the biomass structure significantly. In the presence of moisture, CO<sub>2</sub> forms carbonic acid which augments hemicellulose hydrolysis. Supercritical CO<sub>2</sub> can be used also with co-solvents (methanol or ethanol) and thus enhance digestibility. The main advantages of this method are low cost, easy recovery of CO<sub>2</sub>, no release of toxic compounds, non-inflammability of CO<sub>2</sub>, and reduced environmental impact. Supercritical water is also used for biomass pretreatment. In contrast to supercritical CO<sub>2</sub>, in the case of water, much higher temperatures and pressures are applied. Short reaction times (1–2 s) result in high sugars yield, whereas long reaction times decrease the yield.

### 4.4 Biological Methods

These methods involve the use of enzymes or enzymatic systems of whole microorganisms (mainly fungi and bacteria. Depending on their goal, the methods can be divided into two groups—delignification and saccharification methods. Fungi (white-, brown and soft-rot) possess in their enzymatic system enzymes like lignin peroxidases, manganese peroxidases, laccases, glyoxal, and alcohol oxidases and are capable to degrade lignin. Some fungi degrade selectively lignin (mainly white-rot), while others attack also cellulose and hemicellulose (Rouches et al., 2016). Except for fungi, there are many bacterial strains (*Bacillus* sp., *Streptomyces* sp., *Clostridium* sp., *Thermomonospora* sp., *Cellulomonas* sp., etc.), producing enzymes capable to degrade various lignocellulosic biomasses (Sharma et al., 2019). Besides using an individual strain in biomass pretreatment, very often consortia of different microorganisms are applied. Working with consortia can provide process robustness, higher stability, and productivity of the treatment. Recently, the application of lignin-degrading enzymes instead of using whole organisms gains considerable interest among researchers. The most utilized enzymes belong to cellulases, ligninases, and xylanases. Different enzymes like laccase, versatile peroxidase, manganese peroxidase, and lignin peroxidase are effective in lignin degradation (Kumar and Chandra 2020). Cellulases are multienzyme complexes comprising mainly three components: endo-  $\beta$  1–4—glucanase, exo-  $\beta$  1–4—glucanase, and  $\beta$ -glucosidase. Endo-  $\beta$  1–4—glucanase hydrolyzes internal links in cellulose chains to short-chain cellobioses. Exo-  $\beta$  1–4—glucanase cleaves cellobiose from the non-reducing end of the chains, and  $\beta$ -glycosidase hydrolyzes cellobiose units to glucose units (Shuddhodana et al., 2016). Regarding the heteropolysaccharide structure of hemicellulose, different enzymes are needed to hydrolyze it to monomeric sugars. Endo-xylanases and endo-mannanases randomly attack the inner bonds in xylan and mannan, while  $\beta$ -xylosidase and  $\beta$ -mannosidase hydrolyze oligosaccharides to xylose and mannose. For hydrolysis of the lateral groups (arabinose, acetyl, galactose, and glucose) linked to the main polysaccharide chain supplementary enzymes are necessary— $\alpha$ -glucuronidase, acetyl xylan esterase, acetyl mannan esterase, ferulic acid esterase, etc. (Laca et al., 2019).

Biological methods of lignocellulosic materials degradation have advantages, such as low energy cost, environmental

**TABLE 2 |** Advantages and disadvantages of different pretreatment methods.

Pretreatment methods	Process	Advantages	Disadvantages
Physical	Milling Grinding Chipping Gamma-or microwave irradiation Ultrasound treatment	No chemicals use; no inhibitory compounds or byproducts formation; Reduce biomass size, degree of polymerization; and crystallinity of cellulose; short operation time. Increase surface area for enzymatic hydrolysis	Low sugar yield; High-energy requirements; No lignin degradation  Special equipment design; High costs in large scale
	Chemical	Acid  Alkaline  Oxidative  Organosolv  Ionic liquids (IL) and deep eutectic solvents (DES)	High reaction rate and relatively short time; Remove hemicellulose and partly lignin; Increase surface area for enzymatic hydrolysis; High yield of sugars after enzymatic hydrolysis  Moderate reaction conditions; Less corrosive than acids; Delignification; Hemicellulose is affected depending on severity of treatment; Decrease degree of polymerization; and crystallinity of cellulose  Lignin degradation; Hemicellulose solubilization; Low inhibitors formation; Possibility of working at ambient conditions  Lignin and hemicellulose solubilization; Lignin recovery; High sugars yield; Increase surface area for enzymatic hydrolysis  Mild conditions; Very good lignin separation; High biomass loading; High cellulose solubilization; DES are biodegradable and biocompatible; No toxic product formation  High cost; Inhibitors formation, Need of anticorrosive equipment and neutralization; Sugar losses  High costs; Salts formation; Relatively long reaction time  Elevated cost when using ozone or hydrogen peroxide; Some oxidants are toxic or corrosive  Expensive; Energy consuming; Need for solvents regeneration; Inhibitors generation; Explosion and fire dangers  Need for recovery and recycle; Possible enzyme inhibition; High IL cost
Physicochemical	Steam explosion	Environmentally friendly; Low energy consumption; Cost effective; Short process time; High sugars yield in two step method	High pressure and temperatures; Special equipment; Toxic and inhibitory compounds formation; Partial hemicellulose degradation; Less effective at high lignin content
	Pressurized hot water	Cost-effective; No use of toxic chemicals; Possibility to control inhibitors release by controlling pH; Low or no inhibitors release	Long residence time; High temperatures and pressure; Special equipment; Less effective at lignin removal
	Supercritical CO <sub>2</sub>	Non-toxic chemicals used; Increases accessible surface area for enzyme hydrolysis, High solid load; No inhibitors formation	High pressure; High equipment cost; Does not modify lignin; Less effective at high lignin content
	AFEX	Short process time; Possibility of recovering and reuse of the ammonia; Efficient removal of lignin; Low formation of inhibitors	Less efficient for biomass with high lignin content; partial dissolution of hemicellulose; Large amount of used ammonia
Biological	Microbial Enzymatic	Low energy consumption; Mild reaction conditions; No chemicals use; No formation of inhibitors; Efficient lignin and hemicellulose degradation; Environmentally friendly	Slow reaction rate; Long process time; High cost of enzymes; Necessity of strict and sterile conditions

friendliness, low capital investment cost, no reagent dependence, and no production of fermentation inhibitors. Still, long reaction time and low reaction rate, and the relatively high price of the enzymes are the main limitations, preventing the successful implementation of the biological methods in the industry.

Recent trends in lignocellulosic biomass pretreatment methods, their advantages, and disadvantages and the role of various key factors that affect the separation of lignocellulose constituents are discussed in Baruah et al. (2018) and Mankar et al. (2021). It is worth mentioning that the use of only one pretreatment method is not effective and usually a combination of two or more methods are applied. It seems that the use of a mechanical method for reducing the size of the biomass particles and enzyme hydrolysis of hemicellulose and cellulose to fermentable sugars is inevitable.

The most important is that there is no universal method (or combination of methods) for lignocellulosic biomass pretreatment. This is due to the different compositions of lignocellulosic biomass (ratio of main components and degree of crystallinity of cellulose) from different sources (soft and hardwood, agricultural or industrial wastes). The compositional differences influence the efficacy of pretreatment. The severity of treatment (pressure, temperature, and acid or alkali concentration) also lead to differences in the composition of obtained hydrolysates as well as in the concentration of inhibitors of enzyme hydrolysis and fermentation. In view to choosing an “optimal” pretreatment method, one needs broad knowledge about the chemical composition of the feedstock, but also the final aim of pretreatment. For example, in case the fermentation step is

**TABLE 3 |** Pretreatment methods and conditions of different lignocellulosic biomasses.

Pretreatment method	Lignocellulosic biomass	Conditions	Reference
Ionic liquids pretreatment			
[EMIM][Ac] 1-Ethyl-3-ethylimidazolium-acetate	Cottonseed cake Wheat straw Sugarcane bagasse	Biomass to IL ratio of 1:2 (w/w); at 120°C for 2 h	Grewal and Khare (2018)
[EMIM][OAc] 1-Ethyl-3-methyl-imidazolium-acetate	Rice straw	2:1, 1:1, 1:2, 1:3 Biomass to IL ratios at 120°C for 2 h	Yadav et al. (2021)
[(Emim)][Ac] 1-Ethyl-3-methylimidazolium Acetate	Wheat straw Barley straw Grape stem	Biomass to IL ratios of 1:1, 1:3, and 1:5, 120°C for 120 min	Marin-Batista et al. (2021)
Pyridiniumhydrogensulphate	Wheat straw	Lignin extraction—60°C, 2 h, with 5% biomass loading Reducing sugars—100°C, 2 h with 5% biomass loading	Asim et al. (2021)
Deep eutectic solvents			
Triethylbenzyl ammonium chloride/lactic acid Ethylammonium chloride/ethylene glycol—enzymatic	Wheat straw Oil palm trunk	Solid:liquid ratio—1:15, 100°C for 10 h 100°C, 48 h Celluclast 1.5 L—53 FPU/ml Novozyme 188—122 CBU/ml, 50°C, 24, pH 4.8	Liu et al. (2019) Zulkefli et al. (2017)
Choline chloride/glycerol with salts—enzymatic hydrolysis	<i>Pennisetum</i> biomass	Five times at 120°C for 6 h Cellic CTec2, pH 4.8, 15 FPU/ml, 72 h	Wang et al. (2020)
Choline chloride/glycerol	Coffee silverscin	150°C, 3 h, biomass:solvent ratio 1:32	Procentese and Rehmann (2018) Pin et al. (2019)
2-aminoethanol, 2-(methylamino)ethanol, 2-(ethylamino)ethanol, diethylamine, triethylamine and butan-1-amine with sulphuric and acetic acid	Sugarcane bagasse	IL:H <sub>2</sub> O ratio 5:1, 160°C, 3 h	Loow et al. (2018)
Sequential pretreatment choline chloride:urea (1:2 ratio) and divalent inorganic salt (CuCl <sub>2</sub> )	Oil palm fronds	Solid:liquid ratio 1:10 120°C, 4 h CuCl <sub>2</sub> 120°C, 30 min	
Chemical pretreatment			
Sulfuric acid Sulfuric acid/enzymatic hydrolysis	Exhausted sugar beet pulp Wheat straw	Solid/liquid ratio 1:20, 1%, 120°C, 20 min 0.5% H <sub>2</sub> SO <sub>4</sub> at 180°C for 4 min Cellic-HTec2 and Megazyme 40°C, pH 5.5 for 72 h	Marzo et al. (2021) Cubas-Cano et al. (2019)
Sulfuric acid or enzymatic hydrolysis	Wheat straw	4% H <sub>2</sub> SO <sub>4</sub> at 120°C for 30 min 40°C, pH 5.5 for 24 h	Cubas-Cano et al. (2019)
HCl treatment/cellulose hydrolysis	Corn straw	6% HCl at 90°C for 1 h, cellulase complex-solid-liquid ratio 1:20 at 50°C for 48 h	Si et al. (2020)
Sulfuric acid/enzymatic hydrolysis Sulfuric acid/enzymatic hydrolysis	Corn stover Distillers' dried grains with solubles	2% sulfuric acid at 130°C, 8 min 3 M H <sub>2</sub> SO <sub>4</sub> at 110°C for 24 h 1% enzyme solution, 60°C, 48 h	Utrilla et al. (2016) Krull et al. (2020)
Sulfuric acid hydrolysis	Sugarcane bagasse	2% sulfuric acid at 121°C; 1.5 h; 2:1 liquid:solid ratio	Utrilla et al. (2016)
Sulfuric acid hydrolysis	Sugarcane bagasse	2% sulfuric acid at 122°C for 24 min, solid:liquid ratio of 1:8	González-Leos et al. (2020)
Sulfuric acid hydrolysis	Rice straw	1% sulfuric acid at 180°C for 1 min, 40% solid content	Tu et al. (2019)
Sulfuric acid hydrolysis	Microalgae <i>Chlorella vulgaris</i> ESP-31	4% H <sub>2</sub> SO <sub>4</sub> , 120°C, 20 min, continuous fermentation, PVA immobilized cells	Nandini et al. (2020)
Sulfuric acid hydrolysis	Green seaweed <i>Enteromorpha prolifera</i>	0.5 M H <sub>2</sub> SO <sub>4</sub> at 120°C for 2 h	Hwang et al. (2012)
Sulfuric acid hydrolysis Sulfuric acid hydrolysis	Spent coffee grounds Corn stover	1% H <sub>2</sub> SO <sub>4</sub> at 121°C for 30 min 7.2% H <sub>2</sub> SO <sub>4</sub> at 175°C for 5 min solid/liquid ratio -2:1	Kim et al. (2019) Wei et al. (2018)
Sulfuric acid hydrolysis	Corn stover	2% H <sub>2</sub> SO <sub>4</sub> at 160°C for 60 min 10% solid loading	Jiang et al. (2016)
Oxalic acid hydrolysis	Corn cob	5% oxalic acid, 25°C for 30 min 1:10 solid: liquid ratio	Alhafiz et al. (2020)
Acid-catalyzed steam-exploded hydrolysis Liquid hot water hydrolysate Sulfite hydrolysis	Corn stover Corn stover Corn stover	1.29% H <sub>2</sub> SO <sub>4</sub> at 175°C for 5 min 180°C for 40 min, 1:10 solid:liquid ratio 4% (Mg(HSO <sub>3</sub> ) <sub>2</sub> ) at 160°C for 60 min, 1:6 solid:liquid ratio	Jiang et al. (2016) Jiang et al. (2016) Jiang et al. (2016)

(Continued on following page)

**TABLE 3 |** (Continued) Pretreatment methods and conditions of different lignocellulosic biomasses.<sup>a</sup>

Pretreatment method	Lignocellulosic biomass	Conditions	Reference
Sulfuric acid/enzymatic hydrolysis	Spent coffee grounds	27 g/L H <sub>2</sub> SO <sub>4</sub> , 121°C, 40 min 4 vol% of Celluclast 1.5 L, 0.4% β-glucosidase, 0.4% Viscozyme L 50°C, 48 h	Hudeckova et al., (2018)
Sulfuric acid/enzymatic hydrolysis	Wheat straw	1.5% sulfuric acid for 40 min at 160°C, solid-liquid ratio 1:10 Cellulase Cellic Ctec2, 5 FPU/g cellulose, 150°C, pH 5.5, 150 rpm for 72 h	Ouyang et al. (2020)
Hydrochloric acid hydrolysis	Sugarcane bagasse	(v/v) of HCl, at 140°C, for 15 min, 10% solid load of	Oliveira et al. (2019)
HCl/cellulase hydrolysis	Marine algae <i>Gracilaria</i> sp., <i>Sargassum siliquosum</i> , <i>Ulva lactuca</i>	0.4 N HCl, 30 min at 121°C; 7.6 U/mL cellulase at 37°C for 48 h	Lin et al. (2020)
Acid pressurized hydrolysis	Rice husks	175°C (58.8 bar), 46 min, 0.8% HCl or 2.2% H <sub>2</sub> SO <sub>4</sub>	Montipo et al. (2016)
Phosphoric acid/enzymatic hydrolysis	Agave bagasse	75–80% phosphoric acid, 50–75°C, ratio 1:3	Schroedter et al. (2021)
	Rye straw	15–45 min	
	Digestate of energy corn silage	Cellic <sup>®</sup> CTec 2, 0.4 ml/g, 11.2% total solids, 50°C, 24 h	Hu et al. (2016)
NaOH/cellulase hydrolysis	Corn Stover	5% NaOH, 75°C for 3 h, 20% solid loading	
NaOH/cellulase hydrolysis	Sweet sorghum bagasse	Cellic CTec2 118°C for 80 min 2% (w/v) NaOH at a 10% (w/v) loading	Wang et al. (2016)
		Cellulase—25 FPU/g	
NaOH/cellulase hydrolysis	Sugarcane bagasse	0.5 M NaOH at 80°C; 120 min	Nalawade et al. (2020)
NaOH/cellulase hydrolysis	Corn stover	Cellulase—50°C, 24 h	Zhang et al., (2020)
		5% NaOH at 75°C for 3 h at a 20% solid loading	
NaOH/cellulase hydrolysis	Corn stover	Cellic CTec2 2% NaOH, solid:liquid ratio 10% at 118°C for 1 h	Chen et al. (2020)
		Cellulase 20 U/g solid in SSF	
NaOH/cellulase hydrolysis	DDGS	5% NaOH at 121°C for 15 min at 10% DDGS loading	Zaini et al. (2019)
		Cellulase-Accellerase <sup>®</sup> 1,500 ratio enzyme: cellulose 3:1 at 50°C	
NaOH/cellulase hydrolysis	<i>Sophora flavescens</i> root	1.5% NaOH, 120°C, 2 h, solid/liquid ratio 1:10.25 FPU/g, 50°C 72 h	Ma et al. (2020)
Alkaline peroxide/cellulase hydrolysis	Corn stover	NaOH solution, and 33.3 g H <sub>2</sub> O <sub>2</sub> (30%), solid: liquid ratio 1:20 for 1 day	Akao et al. (2016)
		Cellulase—Meiselase 60 U/g during SSF	
Alkaline/cellulase hydrolysis	Date palm wastes	2N NaOH, 50°C, 48 h	Alrumman (2016)
		4% substrate, 30 FPU/g, pH 5.0	
Alkaline/peroxide	Corn stover	3% NH <sub>2</sub> OH for 2 days, 5% H <sub>2</sub> O <sub>2</sub> for 7 days at room temperature	Liu et al., (2020)
		Solid/liquid ratio 1:20, 1% hydrogen peroxide, pH 11.5, 30°C, 24 h	
Alkaline/Hydrogen Peroxide	Exhausted sugar beet pulp		Marzo et al. (2021)
KOH/enzyme hydrolysis	Spend coffee grounds	35 g/L of KOH, 121°C, 60 min Viscozyme L -2%, 55°C, 7 days	Koo et al. (2019)
KOH/enzyme hydrolysis	Spend coffee grounds	3% KOH, 75°C, 2.8 h cellulase, cellobiase, and mannanase—3% solid loading, 50°C, 96 h	Lee et al. (2021)
Ammonia/enzyme hydrolysis	Corn stover	15% ammonia, 0.3 wt% polyDADMAC, solid/liquid ratio 1:9, 160°C, 1 h 5 FPU/g- Cellic <sup>®</sup> C-Tec2, 50°C, and 200 rpm, 120 h	Shi et al. (2021)
Acid, alkali, and enzyme hydrolysis	Sugarcane bagasse	solid:liquid ratio of 1:2.8, 1% sulfuric acid at 121°C, 27 min 4% sodium hydroxide at 121°C, 30 min, solid: liquid ratio 1:20 Enzymatic hydrolysis at 50°C, pH 5.0, 24 h with a commercial enzyme cocktail	Wischral et al. (2019)
Hydrothermal pretreatment with magnetic carbon-based solid acid followed by enzyme hydrolysis	Sugarcane bagasse	sugarcane bagasse, catalyst and water in ratio s 1:1:25 (g:g:mL), 170°C for 10 min Cellulase—at 50°C for 72 h	Lu et al. (2021)
Wet explosion and enzyme hydrolysis	Corn stover	190°C, 30 min, oxygen loading- 7.5% Cellic <sup>®</sup> CTec2-50°C, pH 5.0, 4 days	Ahring et al. (2016)
Hydrothermal pretreatment with ethylenediamine	Rice straw	80–200°C, solid; liquid ratio 1:10 for 1 h	Chen et al. (2019)

(Continued on following page)

**TABLE 3 |** (Continued) Pretreatment methods and conditions of different lignocellulosic biomasses.

Pretreatment method	Lignocellulosic biomass	Conditions	Reference
Ethanolysis	Corn stover	Ethanol:H <sub>2</sub> O (1:1) co-solvent 0.050 M oxalic acid at 140°C for 1 h	He et al. (2016)
Acid-organosolv	Sugar palm trunk	0.2 M H <sub>2</sub> SO <sub>4</sub> solid:liquid ratio 1:5, 120°C 40 min	Erlana et al. (2020)
Biological pretreatment			
Enzyme hydrolysis α-amylase glucoamylase cellulase	Microalga <i>Arthrospira platensis</i>	2 h at 90°C 2 h at 60°C 40 h at 50°C	Werlang et al. (2020)
Enzyme hydrolysis α-amylase, glucoamylase, cellulase	Cassava bagasse	60 min at 105°C Glucoamylase and cellulase are added during SSF	Chen et al. (2020)
Enzyme hydrolysis α-amylase, glucoamylase, cellulase	Brewer's spent grain	Termamyl SC <sup>®</sup> (α-amylase), 1 h at 90°C, SAN Super 240 L <sup>®</sup> (amyloglucosidase, α-amylases), 1 h at 55°C Celluclast 1.5 L <sup>®</sup> (cellulase) 10 h at 45°C	Pejin et al. (2017)
Enzyme hydrolysis	Corn stover	Crude lignocellulolytic enzyme system 50°C, pH 5.0, 72 h	Ma et al. (2016)
Enzyme hydrolysis	Rice straw	Cellic CTec2 (20 units/1 g), 7.5%, pH 5), at 50°C, 24 h	Verma and Subudhi (2021)
Enzyme hydrolysis—Celluclast 1.5; Novozym188; Pectinex Ultra SP-L	Orange peel	pH 5.2; 50°C, for 26 h	de la Torre et al. (2017)
Enzyme hydrolysis—Celluclast 1.5; Novozym188; Pectinex Ultra SP-L	Orange peel waste	pH 5.2; 50°C, for 26 h	Bustamante et al. (2020)
Enzyme hydrolysis—Cellic <sup>®</sup> CTec2	Pulp mill residue	Solid:liquid ratio 1:4, 25 FPU/g, pH 5.0; 50°C 26 h	Moraes et al. (2016)
Enzyme hydrolysis—Cellic <sup>®</sup> CTec2	Date pulp waste	150 g/L total solids, pH 5.0–5.5, 50°C, 72	Ahmad et al. (2021)
Solid state fermentation with <i>Aspergillus awamori</i> 2B.361 U2/1	Exhausted sugar beet pulp	Moisture content 70%, 30°C, 8 days	Marzo et al. (2021)
Enzyme hydrolysis Viscozyme <sup>®</sup> and Ultraflo <sup>®</sup> Max	Sugar beet pulp	12% pulp, Viscozyme <sup>®</sup> : Ultraflo <sup>®</sup> Max—1:1, 37°C, 16 h	Berlowska et al. (2016)
Enzyme hydrolysis commercial and fabricated cellulases (1:1)	Paper sludge	2.4 FPU/g, pH 6.0, 40°C, 144 h	Dhandapani et al. (2021)
Physical pretreatment			
Microwave-assisted autohydrolysis/cellulase (Ctec2) hydrolysis	Macroalgae <i>Eucheuma denticulatum</i>	120°C and 50 min/pH 4.8 at 50°C for 72 h	Chai et al. (2021)
Mechanical screw press	Sweet sorghum	Chopping <20 mm and pressure of 5 bar	Olszewska-Widdrat et al. (2019)
Physicochemical pretreatment			
Steam explosion	Corn stover	Solid/liquid ratio 2:1, 1.6 MPa, 201°C, 5 min	Han et al. (2021)
Steam explosion	Beech wood chips	230°C, 15 min	Shahab et al. (2018)
Organosolv	Wheat straw	80°C, 70% formic and acetic acids 1:1, 30 min	Tsegaye et al. (2021)
Supercritical CO <sub>2</sub>	Cyanobacterium <i>Arthrospira platensis</i>	450 bar, 40°C, CO <sub>2</sub> flow 4 g/min	Esquivel-Hernández et al. (2021)

done by a strain not converting pentoses—lignin and hemicellulose should be separated from biomass before enzyme hydrolysis. In case of using a strain capable to convert pentoses or co-fermentation removal of lignin should be enough. In general, an “ideal” lignocellulose pretreatment method should provide 1) full degradation and removal of the lignin presented; 2) utterly separation of cellulose and hemicellulose; 3) possibility of complete liberation of fermentative mono sugars; 4) minimal or no release of fermentation inhibitory compounds.

Recently Shen and Sun described three strategies for lignocellulosic biomass pretreatment, depending on the final goal, namely cellulose-first, hemicellulose-first, and lignin-first strategies together with most appropriated methods. These strategies possess unique advantages, permitting a component

of lignocellulose to be selectively fractioned for value-added application (Shen and Sun 2021).

**Table 2** summarizes the advantages and disadvantages of different pretreatment methods and **Table 3**—the methods used in lignocellulosic biomass pretreatment for lactic acid production.

## 5 DETOXIFICATION

As was mentioned above, the majority of pretreatment methods generated some products that can hinder subsequent hydrolysis and fermentation. The inhibitory compounds are a result of the degradation of lignin and sugars from cellulose and hemicellulose



and represent different carboxylic acids and also furanic and phenolic compounds. Hexoses from cellulose and hemicellulose can be transformed during pretreatment to 5-hydroxymethyl furfural (HMF), which further dehydration leads to levulinic and formic acid formation. Various inhibitory products like furan aldehydes, sugar acids, and aliphatic acids are produced upon hemicellulose pretreatment. Acetic, formic, acrylic, and levulinic acids are detected in hemicellulose hydrolysates, but furfural is the most strong and abundant inhibitor. Various phenolic compounds are liberated during lignin pretreatment. The concentration and type of these compounds depend on biomass source and H/G/S group ratio in the lignin structure. The most important lignin-degradation products are *p*-coumaric acid, ferulic acid, 4-hydroxybenzoic acid, vanillic acid, syringic acid, 4-hydroxybenzaldehyde, syringaldehyde, vanillin, etc. In a recent review paper, Kumar et al. summarized various inhibitory compounds produced during lignocellulosic biomass pretreatment and different methods for hydrolysates detoxification and inhibitors removal (Kumar et al., 2020). Vanmarcke et al. (2021) also have described the inhibitor composition of different lignocellulose hydrolysates resulting from different pretreatment methods and investigated individual inhibitor effects in the case of ethanol fermentation.

Van der Pol et al. (2016) developed a small-scale rapid screening method to identify inhibitory effects of single and combined by-products from acid and alkaline hydrolysates on the growth of lactic acid-producing microorganisms. Five lactic acid-producing strains were tested—*Lactobacillus casei*, *Lactobacillus delbrueckii*, *Lactococcus lactis*, *Bacillus coagulans*, and *Bacillus smithii*. While in the presence of alkaline treatment by-products, *L. casei* was least affected (depending on the inhibitor's concentration), in the case of acid treatment—only growth of *L. casei* and *L. lactis* was not fully inhibited. The synergy between formic acid, acetic acid, and coumaric acid was found as a key inhibitory parameter in alkaline pretreated lignocellulose, while in the case of acid pretreated lignocellulose, furfural was the major inhibitor (van der Pol et al. (2016)). Cola et al. (2020) investigated the influence of an inhibitory cocktail (acetic acid, HMF, furfural, and *p*-coumaric acid) on the growth of four *Saccharomyces cerevisiae* and four *Lactobacillus paracasei* strains. Whilst all yeast strains were unable to grow in the presence of inhibitory compounds from sugarcane-based lignocellulosic hydrolysates, bacteria preserved an average of roughly 50% of their growth rates.

In view of reducing the content of inhibitory compounds, different approaches have been used. Various physicochemical methods like adsorption, ion exchange, extraction, membrane separation, overliming, etc. are applied. Other strategies involve biological treatment of the hydrolysates, gene manipulation of the microorganisms to improve their tolerance in regards to inhibitors, or plant improvement to decrease lignin content. Biological detoxification can be mediated by microorganisms or enzymes like laccase (Bhatia et al., 2020). Tramontina et al. (2020) reviewed enzyme-mediated detoxification methods for the removal of inhibitory compounds from lignocellulosic hydrolysates and described some novel strategies using classical enzymes such as laccases and peroxidases, as well as

more advanced strategies using prooxidant, antioxidant, and detoxification enzymes, i.e., superoxide dismutases.

Ludwig et al. (2013) investigated detoxification of organosolv pretreated wheat straw by using free and immobilized laccase. Laccase was immobilized on Sepabeads (modified methacrylic polymer) ion-exchange resin. Free laccase was capable to remove up to 82% of phenolic compounds, while immobilized laccase could remove also HMF and acids not only by enzyme action but by the polymerization and *in-situ* product removal. Phenolic compounds precipitated onto the carrier surface and could be easily removed. In all cases, enzyme treatment improved the fermentability of pretreated wheat straw hydrolysate (Ludwig et al., 2013).

Liu et al. (2019) have isolated three strains (*Enterococcus faecalis* B101, *Acinetobacter calcoaceticus* C1, and *Pseudomonas aeruginosa* CS) capable to utilize some phenolics from ammonia pretreated corn stover (vanillin, 4-hydroxybenzaldehyde, or syringaldehyde) as a sole carbon source. Lactic acid production from 50 g/L ammonia pretreated corn stover was increased nearly twofold [from 16.98 g/L to 31.35 g/L LA (0.63 g/g corn stover)] by inoculating phenolic degrading bacteria mentioned above and lactic acid bacteria *Lactobacillus pentosus* FL0421 (Liu et al., 2019). In another paper, Liu et al. (2020) cultivated *Trichoderma viride* R16 on alkaline/peroxide pretreated corncob as the substrate in a fed-batch SSF process, and the produced enzymes were used in LA production by *Bacillus coagulans* LA204. Because of the high capacity of inhibitors' degradation by *Trichoderma viride* R16 enzymes compared to some commercial ones the lactic acid production was increased by 24% (Liu et al., 2020).

Giacon et al. (2021) have studied the influence of two inhibitors furfural and HMF on the growth of five homofermentative (*Lactobacillus plantarum* CECT 221, *Lactobacillus delbrueckii*, *Lactobacillus plantarum* ESALQ 4, *Lactobacillus paracasei* LAB 4, *Lactobacillus paracasei* LAB 5) and seven (*Lactobacillus fermentum* DSM 20391, *Lactobacillus reuteri* ATCC 23272, *Lactobacillus fermentum* ESALQ 3, *Lactobacillus fermentum* ESALQ 5, *Lactobacillus fermentum* 1L-6-MRS, *Lactobacillus fermentum* 3L-2-M17, *Lactobacillus paracasei* LAB 2) heterofermentative lactic acid bacteria and have found that the effect of HMF and furfural on the growth rate of lactic acid bacteria (LAB) depended on the metabolic pathway. The growth kinetics in the presence of these compounds is enhanced for heterofermentative LAB, whereas is inhibitory to homofermentative LAB. The heterofermentative bacterium presented the ability to decrease the concentrations of furfural and HMF in the fermentation medium, with simultaneous lactic acid production. Low concentrations of these compounds present in the sugarcane bagasse hemicellulosic liquor did not have inhibitory effects on lactic acid production (Giacon et al., 2021).

Liu et al. (2013) compared the possibility for lactic acid production from glucose by three *Pediococcus* strains in the presence of inhibitors generated by acid hydrolysis of lignocellulosic biomass and reported that the strain *Pediococcus acidilactici* DQ2 could produce high concentrations of lactic acid from glucose in the presence of acetic acid, furfural, HMF, and vanillin in concentration range presented in acid pretreated biomass.

Oliveira et al. (2018) investigated the lactic acid production from sugarcane bagasse hydrolysates by *Lactobacillus plantarum* in the presence of furfural and HMF. The strain was capable to assimilate the inhibitors simultaneously with lactic acid production. A decrease of 86% for HMF and 98% for furfural was observed, together with 34.5 g/L lactic acid production. This approach could decrease the cost of the process eliminating the need for detoxification before fermentation (Oliveira et al., 2018).

Zhang et al. (2016) identified the inhibitory compounds generated during corn stover and corn cob pretreatment and investigated the toxicity limits of individual chemicals in the fermentation of hydrolysates to lactic acid by *Rhizopus oryzae*. They found that HMF and furfural were toxic at 0.5–1.0 g/L, while the carboxylic acid (formic, acetic, and levulinic) were non-toxic at concentrations less than 4 and 10 g/L. Among the phenolic *trans*-cinnamic acid and syringaldehyde had the highest toxicity at 1 g/L, while ferulic, *p*-coumaric, and syringic acids were not toxic. Although the concentrations in the hydrolysates were much lower than the toxicity levels of individual inhibitors, the lactic acid fermentation was considerably affected, suggesting possible synergistic action. The authors observed that while cell growth, lactate dehydrogenase, and lactic acid production were strongly inhibited, alcohol dehydrogenase and ethanol production were less or not affected. For the first time, this study showed that the inhibitors shifted the metabolic pathway from lactic acid to ethanol biosynthesis (Zhang et al., 2016).

Kunasundari et al. (2017) studied lactic acid production from oil palm sap by *B. coagulans* 191 strain and reported 53% conversion in case of non-treated sap, 54–74% when the sap was treated with charcoal, and up to 88% by acid and 92% for alkaline precipitation.

Cubas-Cano et al. (2020) investigated lactic acid production by three *B. coagulans* strains in defined media with inhibitors mixtures at high concentrations and hemicellulosic gardening hydrolysate pretreated by steam explosion. One of the isolates (A162) demonstrated high lactic acid productivity (up to 2.4 g L<sup>-1</sup> h<sup>-1</sup>), even in presence of 5 g L<sup>-1</sup> of furans and phenols (Cubas-Cano et al., 2020).

Zhang et al. used dry acid pretreated corn stover for LA production. The hydrolysate was neutralized by 20% Ca(OH)<sub>2</sub> and bio-detoxified by solid-state fermentation with *Amorphotheca resinae* ZN1. The furfural and HMF content were fully degraded, and an increase of lactic acid production in simultaneous saccharification and co-fermentation (SSCF) of corn stover hydrolysate was observed (Han et al., 2018).

## 6 MICROORGANISMS

Different groups of microorganisms (bacteria, fungi, yeasts, and algae) are capable to produce lactic acid from various substrates. Although many bacteria have been extensively used for lactic acid production as a primary or secondary end-product, the term lactic acid bacteria (LAB) is used for several genera. The recently reclassified genus *Lactobacillus* (into 25 new genera) (Zheng et al., 2020), *Lactococcus*, *Enterococcus*, and *Pediococcus*, have been proven as the main producers. LAB are divided into

two main groups - homo - and heterofermentative strains. Homofermentative LAB operate via Embden-Meyerhof-Parnas (EMP) pathway, expressing the aldolase enzyme with LA being the major product. They convert one molecule of glucose to two molecules of LA generating two molecules of ATP (Grewal et al., 2020). Some homofermentative strains metabolize sugars via the pentose phosphate (PP) pathway, producing 1.67 molecules LA from pentoses and hexoses and generating either 1.67 molecules (from hexose) or 0.67 (from pentose) ATP. Hetero-fermentative LAB are classified as obligate and facultative. Obligate LAB use exclusively the phosphoketolase (PK) pathway to convert one molecule of glucose or xylose to one molecule of LA and one molecule of ethanol or acetic acid and generate one molecule of ATP. Facultative heterofermentative LAB convert hexoses *via* EMP pathway and pentose *via* PK pathway (Cubas-Cano et al., 2018). Homofermentative strains producing optically pure L (+) or D (-) LA are preferred for industrial application due to the higher yield and easier downstream processing (Juturu and Wu 2016). Bacteria of genus *Bacillus* sp. (*B. subtilis*, *B. coagulans*, *B. stearothermophilus*, *B. licheniformis*, *B. licheniformis*), *Corynebacterium glutamicum*, and *Escherichia coli* are also capable to produce lactic acid. Filamentous fungi are another important microbial producer of LA. Various representatives of the genus *Rhizopus* (*R. oryzae* and *R. arrhizus*) are utilized in free and immobilized form. The main advantages of using fungi for LA production are their amylolytic properties, simple medium requirements, their facilitate separation from the fermentation broth, and capacity to assimilate complex substrates like different lignocellulosic biomass. Numerous yeasts also can produce LA. Yeasts can tolerate low pH in comparison with LABs and thus minimizing the use of the neutralizing agent. The main disadvantage of yeasts is the low final LA concentration, but the use of engineered yeasts can overcome this drawback. The most important representatives of LA producing yeasts are *Candida* sp. (*C. sonorensis*, *C. boidinii*, and *C. utilis*), *Kluyveromyces* sp. (*K. lactis*, *K. marxianus*), *Pichia* sp. (*P. stipidis*, *P. pastoris*) as well as *Saccharomyces cerevisiae*. Other LA-producing species are algae and cyanobacteria. They are photosynthetic microorganisms, which can grow at minimal feed medium almost anywhere with a short growth cycle.

In a detailed review paper, Abedi and Hashemi listed almost all LA producing microorganisms together with their substrates, final LA concentration, LA yield, and productivity (Abedi and Hashemi 2020).

In Table 4 microorganisms capable of lactic acid production from lignocellulosic materials are summarized.

### 6.1 Metabolic Engineered Microorganisms for High Lactic Acid Production

Normally, lactobacilli can not ferment pentose sugars, which is an obstacle to the effective utilization of hemicellulosic hydrolysates as a substrate. On the one hand, some of the highly productive strains produce a racemic mixture of D- and L-lactic acid. On the other hand, in hetero-fermentative lactic acid production, by-products are formed, which decrease the effectiveness of the process and increase the cost of pure lactic acid production.

**TABLE 4 |** Microorganisms, substrates, and lactic acid yield and productivity from different feedstocks.

Microorganism	Substrate	Optical isomer	Process organization	Lactic acid, g/l	Yield, g/g sugar	Productivity, g/l.h	Reference
<i>Lactobacillus plantarum</i> 23	<i>Chlorella vulgaris</i> ESP-31 hydrolysate	L (+)-LA	Batch	42.34	0.93	7.56	Chen et al. (2020)
<i>Lactobacillus pentosus</i> ATCC 8041	Sugarcane bagasse	N/D	Continuous	39.72	0.99	9.93	Wischral et al. (2019)
<i>Lactobacillus pentosus</i> CECT-4023T (ATCC-8041)	Sugarcane bagasse	N/D	Batch	65.0	0.93	1.01	González-Leos et al. (2020)
<i>Lactobacillus pentosus</i> CECT 4023 T	Wheat straw hydrolysate	N/D	Batch	55.44	0.72	0.43	Cubas-Cano et al. (2019)
<i>Lactobacillus pentosus</i> (TBRC)	Sugarcane bagasse	N/D	Fed-batch SSF	12.58	0.55	0.22	Unrean (2018)
<i>Lactobacillus pentosus</i> FL0421	Corn stover	N/D	Fed-batch SSF	72.75	0.61	1.01	Hu et al. (2016)
<i>Lactobacillus sakei</i> 25, <i>Weissella paramesenteroides</i> 24	40 g/L Green algae <i>Ulwa</i> sp. acid hydrolysate	N/D	Batch	92.30	0.66	1.92	Nagarajan et al. (2022)
<i>Lactobacillus plantarum</i> 23				25.14	0.78	6.79	
<i>Lactobacillus rhamnosus</i>				24.98	0.73	6.25	
				28.79	0.81	7.20	
				30.93	0.85	7.53	
<i>Lactobacillus sakei</i> 25, <i>Lactobacillus plantarum</i> 23, <i>Lactobacillus rhamnosus</i> , <i>Weissella</i> sp. 28, <i>Weissella paramesenteroides</i> 24	40 g/L Red algae <i>Gracilaria</i> sp. acid hydrolysate	N/D	Batch	28.45	0.84	3.56	Nagarajan et al. (2022)
<i>Weissella cibaria</i> 27				31.49	0.80	3.93	
				33.82	0.83	4.23	
				22.50	0.79	1.88	
				32.12	0.90	4.39	
				27.15	0.89	2.26	
<i>Lactobacillus sakei</i> 25, <i>Weissella paramesenteroides</i> 24, <i>Lactobacillus plantarum</i> 23, <i>Lactobacillus rhamnosus</i> , <i>Weissella cibaria</i> 27, <i>Weissella</i> sp. 28	15 g/L Brown algae <i>Sargassum cristaefolium</i> acid hydrolysate	N/D	Batch	10.97	0.87	2.19	Nagarajan et al. (2022)
				10.38	0.87	2.08	
				11.65	0.89	2.53	
				10.80	0.88	2.15	
				9.90	0.86	1.65	
				9.02	0.83	1.51	
<i>Lactobacillus rhamnosus</i> LA-04-1	Cassava bagasse	N/D	SSCF	31.0	0.94	1.94	Chen et al. (2020)
<i>Bacillus coagulans</i> LA-15-2	enzyme hydrolysate			30.0	0.91	1.50	
mixed culture				112.5	0.88	2.74	
<i>Lactobacillus rhamnosus</i> ATCC 7469	Forest and marginal lands lignocellulosic biomass	L (+)-LA	SHF	57.8	1.0	0.81	Pontes et al. (2021)
			SSF	61.7	1.0	1.4	
<i>Lactobacillus rhamnosus</i> ATCC 7469	Pressed recycled paper sludge enzyme hydrolysate	N/D	SHF	63.5	0.74	0.38	Marques et al. (2017)
			SSF	73.2	0.76	0.44	
			Pulsed SSF	108.2	0.62	0.9	
<i>Lactobacillus acidophilus</i> BCRC 10695 and <i>Lactobacillus plantarum</i> BCRC 12327	<i>Microalgae Gracilaria</i> sp. HCl and enzyme hydrolysate	N/D	Batch	19.32	0.65	-	Lin et al. (2020)
<i>Lactobacillus</i> sp. L47	Corn straw hydrolysate	L (+)-LA	pH controlled batch	99.8	0.67	-	Si et al. (2020)
<i>Lactobacillus</i> sp. TERI-D3	Rice straw hydrolysate	N/D	Batch	11.16	0.96	-	Verma and Subudhi (2021)
<i>Lactobacillus plantarum</i> 23	<i>Chlorella vulgaris</i> ESP-31 acid hydrolysate	N/D	Batch	40.30	0.97	6.72	Nandini et al. (2020)
			Continuous	37.76	0.91	12.59	
<i>Lactobacillus plantarum</i>	Rice straw hydrolysate	N/D	SSF	65.6	0.38	0.45	Tu et al. (2019)
<i>Lactobacillus rhamnosus</i> ATCC 7469	Brewer's spent grain hydrolysate	L (+)-LA	pH-controlled batch	39.38	0.91	1.69	Pejin et al. (2017)
<i>Lactobacillus rhamnosus</i> ATCC 7469	Brewer's spent grain hydrolysate	L (+)-LA	Batch	28.43	0.93	1.04	Radosavljevic et al. (2020)
<i>Lactobacillus rhamnosus</i> ATCC 7469	Waste bread stillage	L (+)-LA	Batch	50.59	0.91	1.40	Djukic-Vukovic et al. (2016)
	Waste potato stillage			46.21	0.81	1.28	
	Brewer's spent grain hydrolysate			17.22	0.34	0.48	
<i>Lactobacillus rhamnosus</i> CCM 1825	Spent coffee grounds hydrolysate	N/D	Batch	25.69	0.98	0.35	Hudeckova et al., (2018)
<i>Lactobacillus rhamnosus</i> + <i>Lactobacillus brevis</i>	Sugar palm trunk pretreated enzyme hydrolysate	N/D	Batch	33.29	-	0.69	Erlana et al. (2020)
<i>Lactobacillus casei</i> ATCC 393	Distillers' dried grains with solubles	L (+)-LA	Batch	101.7	0.84	3.9	Krull et al. (2020)
<i>Lactobacillus rhamnosus</i> ATCC 10863	Spent coffee grounds hydrolysate	N/D	SHF	24.95	0.91	0.59	Koo et al. (2019)
		N/D	SHF	6.5	0.56	0.54	Lee et al. (2021)

(Continued on following page)

**TABLE 4 |** (Continued) Microorganisms, substrates, and lactic acid yield and productivity from different feedstocks.

Microorganism	Substrate	Optical isomer	Process organization	Lactic acid, g/l	Yield, g/g sugar	Productivity, g/l.h	Reference
<i>Lactobacillus parabuchneri</i> ATCC 49374	Spent coffee grounds hydrolysate						
<i>Lactobacillus brevis</i> ATCC 8287	Spent coffee grounds hydrolysate	N/D	SHF	4.6	0.40	0.38	Lee et al. (2021)
<i>Lactobacillus delbrueckii</i> ssp. <i>delbrueckii</i> CECT286	Orange peel wastes hydrolysate	D (-)-LA	SHF	-	0.95	6.72	de la Torre et al. (2019)
<i>Lactobacillus delbrueckii</i> ssp. <i>delbrueckii</i> CECT286	Orange peel wastes hydrolysate	D (-)-LA	Batch				de la Torre et al. (2020)
			Resting cells	81.5	0.76	2.60	
			Growing cells	99.8	0.83	1.57	
<i>Lactobacillus delbrueckii</i> ssp. <i>delbrueckii</i> CECT 286	Orange peel wastes hydrolysate	D (-)-LA	SHF	45	0.86	0.63	Bustamante et al. (2020)
<i>Lactobacillus delbrueckii</i> ssp. <i>bulgaricus</i> CECT 5037	Orange peel wastes hydrolysate	D (-)-LA	SHF	39	0.84	0.55	Bustamante et al. (2020)
<i>Lactobacillus delbrueckii</i> subsp. <i>lactis</i>	Date palm waste hydrolysate	N/D	SHF	27.8	0.76	0.39	Alrumman (2016)
<i>Lactobacillus coryniformis</i>	Alkali pretreated DDGS	D (-)-LA	SHF	24.1	0.73	1.3	Zaini et al. (2019)
			SSF	27.9	0.85	1.5	
			Fed-batch	34.0	0.76	0.7	
			SSF(11 g/L)				
			SSF(22 g/L)	38.1	0.70	0.8	
<i>Lactobacillus coryniformis</i> subsp. <i>torquens</i>	Pulp mill residue enzyme hydrolysate	D (-)-LA	Batch SHF	57	0.97	2.8	Moraes et al. (2016)
<i>Sporolactobacillus inulinus</i> DSM 20,348	Corn gluten acid hydrolysate	D (-)-LA	Fed batch	81	-	3.85	Brock et al. (2019)
	DDGS acid hydrolysate			107	-	3.44	
	Sunflower meal acid hydrolysate			103	-	3.27	
	Rapeseed meal enzyme hydrolysate			221	0.96	1.55	
<i>Bacillus coagulans</i>	Paper mill sludge	L (+)-LA	SSCF	82.6	0.83	0.69	Li et al. (2021)
<i>Bacillus coagulans</i> ATCC 7050	Macroalgae <i>Eucheuma denticulatum</i>	L (+)-LA	SSF	14.0	0.99	-	Chai et al. (2021)
<i>Bacillus coagulans</i> NCIM 5648	Alkali and enzyme pretreated sugarcane bagasse	L (+)-LA	SHF	69.2	0.55	2.88	Baral et al. (2020)
<i>Bacillus coagulans</i> DSM ID 14–300	Concentrated sugarcane bagasse HCl hydrolysate	L (+)-LA	Batch	55.99	0.87	1.7 g	Oliveira et al. (2019)
<i>Bacillus coagulans</i> CC17	Bagasse sulfite pulp enzyme hydrolysate	L (+)-LA	SHF	32.22	0.5	-	Zhou et al. (2016)
			SSF	50.20	0.84		
			Fed-batch SSF	110	0.72		
<i>Bacillus coagulans</i> CC17A	Wheat straw dilute acid and enzyme hydrolysate	L (+)-LA	SSCF	26.30	0.71	0.25	Ouyang et al. (2020)
<i>Bacillus coagulans</i> LA1507	Sweet sorghum bagasse, NaOH hydrolysate	L (+)-LA	SSF	111	0.73	1.59	Wang et al. (2016)
<i>Bacillus coagulans</i> NCIM 5648	Alkali and enzyme pretreated sugarcane bagasse	L (+)-LA	SHF				Nalawade et al. (2020)
			54.7 g/L glucose	50.4	0.92	2.4	
			62.7 g/L glucose	51.24	0.81	1.75	
<i>Bacillus coagulans</i> AD	Corn stover—wet explosion and enzyme hydrolysis	L (+)-LA	Continuous	22.3–35.2	0.95	3.69	Ahring et al. (2016)
<i>Bacillus coagulans</i> NBRC 12714	Corn stover hydrolysate	L (+)-LA	Batch	98.3	0.95	3.28	Ma et al. (2016)
			Repeated batch	93.8	0.93	3.80	
			Continuous	92.0	0.92	13.8	
<i>Bacillus coagulans</i> strain H-1	Corn cob hydrolysate	L (+)-LA	Batch	68.0–36 h	0.85	1.8	Jiang et al. (2019)
				79.1–84 h	0.76	0.94	
<i>Bacillus coagulans</i> LA-15–2	Rice straw hydrolysate	L (+)-LA	Batch	63.5	0.3	3.18	Chen et al. (2019)
			Fed-batch	92.50	0.58	2.01	
<i>Bacillus coagulans</i>	Coffee mucilage	L (+)-LA	Batch	45.3 with yeast extract	0.77	4.4	Neu et al. (2016)

(Continued on following page)

**TABLE 4 |** (Continued) Microorganisms, substrates, and lactic acid yield and productivity from different feedstocks.

Microorganism	Substrate	Optical isomer	Process organization	Lactic acid, g/l	Yield, g/g sugar	Productivity, g/l.h	Reference
				43.3 without yeast extract	0.70	1.5	
<i>Bacillus coagulans</i>	Pretreated corn cob	N/D	Batch	77.34	0.82	1.61	Alhafiz et al. (2020)
<i>Bacillus coagulans</i> JCM 2258 and JCM 9076	Alkaline peroxide pretreated corn stover	L (+)-LA	SSF	-	0.33	-	Akao et al. (2016)
<i>Bacillus coagulans</i> GKN316	Corn stover diluted acid hydrolysate	L (+)-LA	Batch	35.37	0.83	0.91	Jiang et al. (2016)
	Acid-catalyzed steam-exploded hydrolysate			45.39			
	Acid-catalyzed liquid hot water hydrolysate			16.83			
	Acid-catalyzed sulfite hydrolysate			18.71			
<i>Bacillus coagulans</i> LA204	NH <sub>3</sub> -H <sub>2</sub> O <sub>2</sub> pretreated corn stover	N/D	Batch SSF	33.62	0.42	0.23	Liu et al., (2020)
			Fed-batch SSF	64.95	0.54	0.57	
<i>Bacillus coagulans</i> 14–300	Rye straw (RS)		SHF			1.73	Schroedter et al. (2021)
	Digestate of energy corn silage		RS	31.1	0.84	1.72	
	hydrolysates (DCS)		DCS	21.1	0.84		
			SSF				
			RS	39.3	-	0.82	
			DCS	15.7	-	0.58	
<i>Bacillus coagulans</i> A-35	Sweet sorghum juice	L (+)-LA	Batch				Olszewska-Widdrat et al. (2019)
			Lab. scale	78.75	0.78	1.77	
			Pilot plant	73.0	0.70	1.47	
<i>Pediococcus acidilactici</i> ZY271	Detoxified dry acid pretreated corn stover enzyme hydrolysate	L (+)-LA	Batch	61.6	0.87	2.34	Han et al. (2019)
<i>Pediococcus acidilactici</i> PA204	NaOH pretreated corn stover	N/D	Fed-batch SSF	25.92 (4% stover)	0.65	0.54	Zhang et al. (2020)
				92.01 (12% stover)	0.77	1.28	
				104.11 (15% stover)	0.69	1.24	
<i>Pediococcus acidilactici</i> ZY271	H <sub>2</sub> SO <sub>4</sub> pretreated corn stover	L (+)-LA	SSCF with <i>Amorphotheca resinae</i> ZN1	130.3	-	1.81	Wei et al. (2018)
<i>Pediococcus acidilactici</i> ZY15	H <sub>2</sub> SO <sub>4</sub> pretreated corn stover	D (-)-LA	SSCF with <i>Amorphotheca resinae</i> ZN1	124.8		1.73	Wei et al. (2018)
<i>Bacillus coagulans</i> L-LA 1507	NaOH pretreated corn stover	L (+)-LA	Fed-batch SSF	92.5	0.39	1.25	Chen et al. (2020)
<i>Rhizopus oryzae</i> NLX-M-1	XOS waste residue d from alkali-pretreated corncobs	L (+)-LA	SHF	34.0	0.34	0.71	Zhang et al. (2016)
			SSF	60.3	0.6	1.0	
<i>Rhizopus oryzae</i> 3.819	<i>Sophora flavescens</i> root	N/D	SHF	30.6	-	0.23	Ma et al. (2020)
			SSF	46.8	0.33	0.97	
<i>Rhizopus oryzae</i> MTCC5384	Paper sludge	N/D	SSF	27.0	0.36	1.19	Dhandapani et al. (2021)
<i>Escherichia coli</i> JU15	<i>Arthrospira platensis</i> hydrolysate	D (-)-LA	SHF	25.5	0.86	2.8	Werlang et al. (2020)
<i>Escherichia coli</i> JU15	Cassava bagasse hydrolysate	D (-)-LA	Batch	57.8	1.11	0.98	Utrilla et al. (2016)
<i>Escherichia coli</i> AV03	Corn stover hydrolysate			65.2	1.11	1.21	
<i>Enterococcus hirae</i> ds10	Sugar beet molasse	N/D	Batch	36.79	0.91	1.02	Abdel-Rahman et al. (2021)
			High cell density batch	49.49	0.91	0.41	
			fed-batch	61.76	0.97	2.06	
<i>Enterococcus mundtii</i> DSM 4838	Spent sulfite liquor	L (+)-LA	Fed-batch	87.9	1.0	3.25	Hoheneder et al. (2021)
		N/D	SSF	43.73	0.50	0.32	Sun et al. (2021)

(Continued on following page)



**TABLE 4 |** (Continued) Microorganisms, substrates, and lactic acid yield and productivity from different feedstocks.

Microorganism	Substrate	Optical isomer	Process organization	Lactic acid, g/l	Yield, g/g sugar	Productivity, g/l.h	Reference
<i>Enterococcus</i> (97.6%) dominated microbial consortia	Acid pretreated corn stover						
<i>Saccharomyces cerevisiae</i>	Spent coffee grounds	N/D	SSF	11.15	0.11	0.46	Kim et al. (2019)
<i>Trichoderma reesei</i> / <i>Lactobacillus pentosus</i>	Steam pretreated beech wood	N/D	SSCF	19.8	0.83	0.1	Shahab et al. (2018)

SHF, separate hydrolysis and fermentation; SSF, simultaneous saccharification and fermentation; SSCF, simultaneous saccharification and co-fermentation; N/D—not described.

Metabolic engineering is a powerful tool finding increased application for overcoming some bottlenecks in lactic acid production from lignocellulosic biomass—low yield, substrate specificity, optical purity, acid tolerance, etc. Obtaining genetically modified strains by adding genes for pentoses assimilation, deleting undesirable branches in the metabolic pathway, or deleting one of the lactate dehydrogenase genes will help in using lignocellulosic feedstocks for pure lactic acid isomers production. Wu et al. (2021) summarized the advances in techniques of genome manipulation for engineering lactobacilli and future development of genetic tools for obtaining recombinant lactic acid bacteria.

The main approaches for obtaining high-performing strains LAB are adaptive evolution, mutagenesis screening, and metabolic engineering. Each of these methods has its own advantages and disadvantages. High-throughput screening techniques can be introduced into the post-mutagenesis screening process, but still relies heavily on random mutation and is time-consuming. In contrast, both metabolic engineering and adaptive evolution approaches targeted compensating shortcomings of mutagenesis screening. Currently, commonly used methods for the gene editing and metabolic engineering of LAB are plasmid-based homologous recombination, Red/RecET-mediated double-stranded DNA recombination, and single-stranded DNA recombination. Recently emerged CRISPR/Cas9 gene-editing technique is characterized by simple operation, efficiency, and precision (Tian et al., 2021). The gene manipulation tools of lactic acid bacteria are also discussed in Borner et al. (2019), Plavec and Berlec (2020), and Cho et al. (2020).

Upadhyaya et al. (2014) highlighted four main challenges (purity of lactic acid, acid tolerance of lactic acid bacteria, carbon sources, and parameters for industrial production) and summarized metabolic engineering solutions for lactic acid production.

Mazzoli (2020) outlined two main strategies in metabolic engineering of microorganisms for consolidated lactic acid production from lignocellulosic biomass—recombinant cellulolytic strategy, consisting in introducing cellulase systems in native producers of LA, and native cellulolytic strategy, aiming at improving LA production in natural cellulolytic microorganisms.

Cubas-Cano et al. (2019) applied adaptive laboratory evolution to improve the xylose fermentation capacity of a *Lactobacillus pentosus* strain. In sequential batch cultivation

the ratio xylose: glucose was increased gradually from 15: 5 to 20: 0. When an improvement in bacterial growth and xylose consumption was detected the xylose content in media was increased. Clones were isolated from the final population of cells at different working conditions and that showed best performance was selected for further experiments. The selected strain (MAX2) showed up to 2-fold more xylose consumption and lactic acid production in comparison with the parental strain. The strain possessed high acidic tolerance and was capable to convert mixed sugars presented in a wheat straw hydrolysate (Cubas-Cano et al., 2019).

Other microorganisms were also been engineered for high lactic acid production. Yang et al. (2013) engineered *Thermoanaerobacterium aotearoense* by blocking the acetic acid formation pathway. The observed maximum L-lactic acid yield with the engineered strain was 0.93 g/g glucose, 0.79 g/g xylose, and 0.32 g/g xylan as a sole carbon source without any pretreatment. The obtained optical purity of L-lactic acid was 99.3% and the engineered strain was capable of high production in non-sterile fermentation (Yang et al., 2013).

Kong et al. (2019) described the genetic manipulation of a yeast strain *Kluyveromyces marxianus* for effective LA production from corncob. Introduction of heterologous lactate dehydrogenase gene (from *Plasmodium falciparum* or *Bacillus subtilis*) and the proton-coupled monocarboxylate transporter gene from *Saccharomyces cerevisiae* together with disruption of putative D-lactate dehydrogenase in *Kluyveromyces marxianus* led to production of 103.00 g/L L-lactic acid with optical purity of 99.5% from 180.00 g/L corncob residue via simultaneous saccharification and co-fermentation (Kong et al., 2019).

Kuo et al. (2015) isolated twenty-six strains from soil and putrid fruits and tested the ability of 11 of them to ferment wood hydrolysate. *Lactobacillus paracasei* 7B showed high lactic acid productivity and high tolerance to inhibitors was chosen for further gene manipulation by interruption of *ldhD* gene. The resulting strain was able to ferment glucose and lignocellulosic hydrolysates of wood and rice straw without detoxification and achieved high yields—215 g/L in fed-batch glucose fermentation, 99 g/L from the undetoxified and 102 g/L from the detoxified hydrolysate (Kuo et al., 2015).

Turner et al. (2016) constructed a recombinant *Saccharomyces cerevisiae* strain capable of assimilating cellobiose and xylose and producing lactic acid. Different

genes (*cdt-1*, *gh1-1*, *XYL1*, *XYL2*, *XYL3*, and *ldhA*) coding cellobiose transporter,  $\beta$ -glucosidase, xylose reductase, xylitol dehydrogenase, xylulokinase, and lactate dehydrogenase were integrated into the *S. cerevisiae*. In the engineered strain native pyruvate decarboxylase (*pdh*) and alcohol dehydrogenase (*adh*) genes were not deleted, but still, almost no ethanol was produced when fermenting a cellobiose and xylose mixture. The engineered strain produced 83 g/L of lactic acid with a yield of 0.66 g/g sugar from a cellulosic sugar mixture (10 g/L glucose, 40 g/L xylose, and 80 g/L cellobiose) (Turner et al., 2016).

Kim et al. (2019) engineered *Saccharomyces cerevisiae* SR8 to produce lactic acid and ethanol from pretreated spent coffee grounds. The pRS41N-Cas9 plasmid was introduced and expression of the lactate dehydrogenase gene was confirmed (Kim et al., 2019).

Using helium-based atmospheric and room temperature plasma mutation and evolution Jiang et al. (2016) adapted *Bacillus coagulans* NL01 strain to overcome the inhibitors' action in corn stover hydrolysates. The mutant strain *Bacillus coagulans* GKN316 was capable to convert different hydrolysates to lactic acid with high inhibitor tolerance. The individual inhibitory effect of furfural, 5-hydroxymethylfurfural, vanillin, syringaldehyde, and *p*-hydroxybenzaldehyde was also studied and was found that the syringyl compound was most toxic. The strain *B. coagulans* GKN316 could effectively convert these inhibitors to the less toxic corresponding alcohols (Jiang et al., 2016).

Most of the microorganisms producing lactic acid ferment sugars to L-lactic acid and there are only a few capable to produce D-lactic acid. In recent years, the demand for D-lactic acid has increased, especially for the production of polylactic blends (stereo-complex polylactic acid, composed of both L and D-lactic acid) which is characterized by a high melting point. Therefore, the interest in D-lactic acid-producing strains, including genetically manipulated also increases.

Zhang et al. investigated d-lactic production from glucose, xylose, and alkaline corn stover hydrolysate by an L-lactate deficient strain of *Lactobacillus plantarum* in which xylose-assimilating genes encoding xylose isomerase and xylulokinase were successfully cloned. The engineered strain produced 19.7 g/L d-lactic from 40 g/L xylose in a batch experiment. In a fed-batch mode production of 30.1 g/L of d-lactic was achieved. When a mixture of glucose and xylose (2:1 ratio) was used as a substrate, 47.2 g/L d-lactic was produced, with a lactic acid yield of 0.84 g/g. The experiments with corn stover were carried out in two modes—separate saccharification and fermentation (SHF) and simultaneous saccharification and fermentation (SSF). In the first case, 19.4 g/L D-lactic acid was produced, while in the second—26.8 g/L when the hydrolysate was supplemented with yeast extract and 29.4 g/L when soybean meal extract was added. Finally, in a fed-batch experiment with corn stover hydrolysate in SSF mode production of 61.3 g/L D-lactic acid was achieved. The production of acetic acid was observed in all experiments (Zhang et al., 2016). In other work, the authors constructed and compared an L-lactate-deficient mutant strain *Lactobacillus plantarum* NCIMB 8826 *ldhL1* and

its derivative harboring a xylose assimilation plasmid (*DldhL1-pCU-PxylAB*). Recombinant *DldhL1-pCU-PxylAB* used xylose to produce high yields of D-lactic acid and was able to ferment xylose and glucose simultaneously which is an important advantage when using lignocellulosic biomass as a substrate for producing lactic acid. As substrates for D-lactic acid production, corn stover and sorghum stalk hydrolysates were successfully used. *DldhL1-pCUPxylAB* produces 20% more D-lactic acid than *DldhL1* from lignocellulosic biomass. In the SSCF process the yield increased about 38%, and productivity—almost three-fold when compared with SHF process (Zhang et al., 2016).

In a series of three papers, Kondo and coworkers studied the possibility of d-lactic production with engineered *Lactobacillus plantarum* strains. Firstly, they engineered an L-lactate dehydrogenase-deficient *Lactobacillus plantarum* strain for D-lactic acid production from cellulosic materials. When an endoglucanase-secreting plasmid was introduced into *L. plantarum* 1.27 g/L D-lactic acid was produced with 2 g/L cellohexaose as substrate and 1.47 g/L with barley  $\beta$ -glucan as substrate. Although anaerobic conditions partially suppressed this conversion of d-lactic to acetic acid, the final product was predominantly acetic acid (Okano et al., 2010). In another paper, the xylose assimilating operon from *Lactobacillus pentosus* was introduced into an L-lactate dehydrogenase deficient *Lactobacillus plantarum* to achieve efficient D-lactic acid fermentation from a mixture of xylose and glucose. Successful homo-D-lactic acid production was achieved 41.0 g/L lactic acid (88% g/g xylose yield and 98.7% optical purity) from 50 g/L xylose. In the case of a mixture of xylose and glucose (1:3 ratio) 74.2 g/L of lactic acid was produced with 0.78 g/g sugar yield with D-lactic acid optical purity of 99.5%. Finally, a mixture of three sugars—xylose, glucose, and arabinose (5:10:1 ratio) and 61.2 g/L of lactic acid was produced with a yield of 0.80 g/g sugar consumed and 99.5% optical purity was produced from 80 g/L sugars. Simultaneous sugars utilization was achieved without carbon catabolite repression (Yoshida et al., 2011). The last paper was focused on the D-lactic acid production from delignified hardwood pulp. The previously described *Lactobacillus plantarum* mutant (Yoshida et al., 2011) was used for D-lactic acid production from both glucose and xylose in a simultaneous saccharification and fermentation (SSF) process. The SSF resulted in 55.2–84.6 g/L lactic acid, depending on the load (5–15%) after 72 h. To improve the enzymatic saccharification at high-load, short-term pulverization of pulp was conducted. The pretreatment significantly ameliorated saccharification and suppressed the formic acid by-product formation. In this case, SSF resulted in a lactic acid production of 102.3 g/(0.88 g/g-sugars yield) and optical purity of 99.2%. (Hama et al., 2015).

Zunar et al. (2020) manipulated a wild strain *Lactobacillus gasseri* JCM 1131T firstly by transforming with plasmids carrying additional copies for each of the three lactate dehydrogenases that the wild type encodes for. Secondly, each of the three endogenous genes for lactate dehydrogenases was inactivated using the plasmid *pHBintE*, which was used for the first time to inactivate genes in lactobacilli. Transformation of *L. gasseri* with plasmids carrying additional genes for L- or D-lactate dehydrogenases didn't affect the ratio of produced

stereoisomers, but inactivation of the endogenous genes created strains which yielded 0.96 g/g glucose of either L- or D-lactate. Constructed strains efficiently fermented wheat straw hydrolysate and produced 0.37–0.42 g of lactate/g wheat straw (Žunar et al., 2020).

Prasad et al. (2020) described the application of an evolutionary engineered thermo-tolerant strain of *Lactobacillus bulgaricus* strain in D-lactic acid production from rice straw. The engineered strain was capable to work at 45°C and thus be used in an SSF process enzyme significantly reducing the enzyme loading. The powdered rice straw biomass was pretreated by dilute acid followed by steam explosion. The rice straw was soaked with 0.2% w/v H<sub>2</sub>SO<sub>4</sub> for 24 h and then heated to 175°C for 30 min followed by rapid decompression to atmospheric pressure. The pretreated rice straw contained 45.84% cellulose and 4.63% xylan and was used in further experiments after enzymatic hydrolysis with commercial cellulase complex (SacchariSEB C6L Plus). SHF and batch and fed-batch SSF mode of fermentation were carried out. In batch SSF experiments 11.8–32.4 g/l D-lactic acid was produced, depending on the enzyme and total solid loading, while in fed-batch SSF the final obtained lactic acid concentration was 108.6 g/L (Prasad et al., 2020).

Tian et al. (2021) developed through the CRISPR-Cas9 gene-editing platform a high optical purity L-lactic acid producing strains. Further, by adaptive evolution a high-performance strain (NCBIO01-M2-*ldhL1-HT*) was obtained, that could efficiently produce L-lactic acid at a high temperature (45°C). The strain was capable of producing 221.0 g/L of L-lactic acid in open fermentation. The productivity and yield were above 7.5 g/L/h and 0.96 g/g respectively, and the optical purity of L-lactic acid exceeded 99.1% (Tian et al., 2021).

A lactogenic *Escherichia coli* strain JU15 (MG1655,  $\Delta pflB$ ,  $\Delta adhE$ ,  $\Delta frdA$ ,  $\Delta xylFGH$ ,  $gatC$ -S184L,  $\Delta midarPA$ , and  $\Delta reg$  27.3 kb) was used and modified to produce D-lactic acid from sugarcane bagasse and corn stover hydrolysates. The strain JU15 was additionally genetically modified by deleting the pathways for the production of L-lactic acid and acetic acid, thus leading to a new strain - AV03 (JU15,  $\Delta poxB$ ,  $\Delta ackA-pta$ ,  $\Delta mgsA$ ). While JU15 showed sequential sugars assimilation and acetic acid production, AV03 showed simultaneous sugars consumption no acetic acid production, with a minimal nutrient addition in pH-controlled fermentation. The D-lactic acid yield in all cases was close to 0.95 g/g sugars (Utrilla et al., 2016).

Werlang et al. (2020) have also used the recombinant *Escherichia coli* strain JU15 for D-lactic acid production from algal biomass pretreated by acid and enzyme hydrolysis. The strain was capable of producing 25.5 g/L D-lactate (86% of the theoretical conversion of glucose to lactate) after 9 h of fermentation with 0.255 g/g of dried *A. platensis* biomass (Werlang et al., 2020).

## 6.2 Immobilized Microorganisms in Lactic Acid Production From Lignocellulosic Biomass

Cells immobilization offers undoubted advantages in a fermentation process such as the possibility of realization of fed-batch or continuous process; high cells concentration;

increased stability of the biocatalyst and reduced influence of substrate and product inhibition; easier separation of biocatalyst from fermentation broth; and higher fermentation rate. Different immobilization methods were used in lactic acid production from biomass—adhesion, encapsulation, gel entrapment, etc.

Radosavljevic et al. (2021) used *L. rhamnosus* cells immobilized by encapsulation in polyvinyl alcohol cryogel for LA production from brewer's spent grain (BSG) and malt rootlets (MR) hydrolysates. For hydrolysate production, dry BSG and MR in ratio 4:1 were sequentially mixed with Termamyl SC (amylase), SAN Super 240 L (glucoamylase), and Cellic CTec2 (cellulase) enzymes. After enzymatic hydrolysis, the obtained hydrolysate was separated from solids and vacuum concentrated to 5.5% reducing sugars content before was used in LA fermentations. Application of 10% PVA in BSG and MR hydrolysate throughout 12 consecutive batch fermentations resulted in high LA yield and volumetric productivity of 97.1% and 2.1 g/L h<sup>-1</sup>, respectively (Radosavljevic et al., 2021).

*Lactobacillus bifermentans* cells were immobilized in Calcium alginate gel for lactic acid production from the wheat bran hemicellulosic hydrolysate. Cells entrapped in calcium alginate beads can consume all glucose and arabinose and 75% of xylose in one step. The maximum values of lactic acid yield, productivity, and percent sugar utilization were 0.83 g/g, 1.17 g/L/h, and 76%, respectively, at temperature 42°C and pH 7.5 (Givry et al., 2008).

Mladenovic et al. (2018) have used *Lactobacillus paracasei* immobilized by adhesion onto agro-industrial residues—sunflower seed hull, brewer's spent grain, and sugar beet pulp for lactic acid production from distillery waste potato stillage remaining after bioethanol production. The immobilized preparations were stable at least in five consecutive cycles and a maximal LA concentration of 80.1 g/L with an average yield coefficient of 0.97 g/g was achieved using sugar beet pulp. The LA productivity was 1.48 g/L/h. In a later paper (Mladenovic et al., 2019) extended their research on the possibility of simultaneous production of LA and probiotic enriched livestock feed on a combined substrate based on molasses and potato stillage. The highest total LA concentration of 399 g/L and overall productivity of 1.27 g/L/h was achieved in five repeated fermentation batches.

Shi et al. (2012) investigated the production of L-lactic acid by immobilizing *Lactococcus lactis* cells in a fibrous bed bioreactor system. The substrate was *Jerusalem artichoke* hydrolysate and the immobilization was done by adhesion in a column packed with spiral wound cotton towel. Using the fed-batch strategy, 142 g/L lactic acid was produced. Subsequent repeated-batch fermentations further exhibited the persistence and stability of the system for the high production of L-lactic acid in a long term.

*Lactobacillus plantarum* 23 immobilized in polyvinyl alcohol beads was tested for LA production from renewable feedstocks (Nagarajan et al., 2020). Sugarcane bagasse, cheese whey, and microalgal biomass of *Chlorella vulgaris* and *Ulva* sp. were used as substrates after pretreatment. Sugarcane bagasse was hydrolyzed by two steps—phosphoric acid hydrolysis to remove the lignin fraction and obtain bagasse cellulose, followed by sulfuric acid hydrolysis to hydrolyze the cellulose. Microalgal biomass was subjected to a combined acid/thermal pretreatment (4% H<sub>2</sub>SO<sub>4</sub>, 120°C, 20 min). Lactic

acid fermentation was carried out in batch and continuous mode. The best results were obtained with sugarcane bagasse—41–42 g/L LA and 0.98–1.0 g/g sugars and microalgal biomass—37.9 g/L and 0.91 g/g sugars. In another publication (Chen et al., 2020) extended the research on LA production from *Chlorella vulgaris* biomass with PVA immobilized *Lactobacillus plantarum*, including *in-situ* LA removal by ion exchange. Optimal conditions of fermentation were determined and a substantial increase in LA yield (72%) was observed in the case fed-batch coupled with ion exchange. Continuous fermentation using immobilized *L. plantarum* with high productivity was demonstrated (14.22 g/l.h from glucose and 9.93 g/l.h from algal biomass) and immobilized beads could be used for 4 months without loss of activity.

Thakur et al. (2019) investigated lactic acid production from sugarcane molasses by calcium alginate immobilized *Lactobacillus casei* MTCC 1423 cells. Different process parameters (bead diameter, bead coating, biomass concentration, shaking speed, substrate concentration, nitrogen content, temperature, incubation time, and pH) were optimized. The immobilized cells were stable between 4 and 9 cycles depending on the bead coating method. At optimal conditions, 128.45 g/L lactic acid was achieved (Thakur et al., 2019).

## 7 PROCESS ORGANIZATION

All well-known biotechnological fermentation methods are also applicable in lactic acid fermentation from lignocellulosic and industrial wastes. Batch fermentation is the widely used and simplest method. The fermentation medium is seeded with the appropriate microorganism and no product is extracted or substrate is added to the end of the process. High final LA concentration and low risk of contamination are the main advantages of this fermentation mode, while low cell densities, low productivity, and substrate and/or product inhibition are the main disadvantages. The substrate inhibition can be overcome by fed-batch—substrate is added in portions and no product is withdrawn, but still, product inhibition is the major obstacle. In repeated batch (semicontinuous), fermentation a part or all of the cells from a previous run are inoculated into the next run. The semicontinuous mode can assure a decrease in time, energy costs, and increased LA productivity. Continuous fermentation is realized by steadily fresh medium feeding and fermentation broth withdrawal. The dilution rate (the velocity of substrate feeding and product withdrawal) must be carefully chosen, so no cell washing or product accumulation is accomplished. The main disadvantages of this process organization are incomplete substrates utilization and low LA concentration. High cell density fermentation using cell recycling is an efficient strategy for enhancing sugar consumption. The cells retention by ultrafiltration permits separation and recirculation. Cells immobilization can resolve the problem with retention of the cells into the system and facilitate continuous process realization. Different reactor types—continuous stirred tank, packed bed, and fibrous bed were utilized.

The necessity of individual sugars production by hydrolysis of cellulose and hemicellulose in pretreated lignocellulosic biomass leads to the use of enzymes like amylases and cellulases. Separate hydrolysis and fermentation (SHF) and simultaneous saccharification and fermentation (SSF) are the main strategies for lignocellulosic and waste biomass utilization. An asset of SHF is that hydrolysis and fermentation are separately performed under their optimal conditions. Usually, hydrolysis and fermentation have different optimal conditions (temperature and pH). The drawback is that during enzymatic hydrolysis, the sugars released might lead to an increase of the inhibition and suppress enzyme activity. On the other hand, SSF offers more advantages than SHF—the possibility of a one-pot process, reducing time and cost of fermentation, and reducing inhibition. The mentioned above difference in optimal temperatures and pH for both hydrolysis and fermentation is the main drawback of SSF. A possible way of overcoming this discrepancy lies in using microorganisms releasing cellulitic enzymes during so-called simultaneous saccharification and co-fermentation (SSCF). Tarraran and Mazzoli (2018) reviewed recent research in co-fermentation of LAB with native cellulolytic microorganisms, as well as the construction of recombinant cellulolytic LAB by metabolic engineering, for direct fermentation of plant biomass for reducing the high cost of exogenous cellulase supplementation. Zaini et al. (2019) compared SHF and SSF approaches for D-lactic acid production from DDGS by *Lactobacillus coryniformis*. They reported that SSF demonstrated better fermentation characteristics compared to SHF [Zaini, Chatzifragkou and Charalampopoulos, Microbial production of D-lactic acid from Dried Distillers Grains with Solubles (DDGS) 2019]. An additional plus offers the possibility of such microorganisms to grow in the presence of inhibitors released during pretreatment. Some of them use the inhibitors as a carbon source and thus decreasing their concentration and negative effect on LA fermentation. Examples of using different modes of fermentation are listed in Table 4.

Integration of fermentation and separation steps *in situ* extractive fermentation gives the possibility of increasing productivity and decreasing energy consumption. Different methods are proposed for lactic acid removal—ion exchange (Othman et al., 2018), membrane bioreactors (Gössi et al., 2020), liquid-liquid extraction (Lan et al., 2019). Although process integration is well documented in the case of lactic acid production from sugars (M. Othman et al., 2017), there are no published results for second-generation biomass.

Some advantages and drawbacks of different process organizations are presented in Table 5.

## 8 SEPARATION

Downstream processing (separation, purification, and recovery) is a very important step in lactic acid production and its cost can reach up to 50% of the total price of the final product. In general, separation and purification methods of second-generation LA (from lignocellulosic feedstocks) don't differ from these applied



**TABLE 5 |** Advantages and drawbacks of different process organizations.

Fermentation mode	Advantages	Disadvantages
Batch	Ease of operation; Low risk of contamination High cell concentration	Substrate and product inhibition Low yield
Fed batch	Less substrate inhibition; Increase cell concentration	Product inhibition; Difficulties of maintaining process conditions
Repeated batch	Short process time; Increased cells growth	Decreasing productivity with increasing batch number; Problems with cells viability and stability
Continuous	Controlled growth; High productivity	Incomplete substrate utilization; Possible cells washing or product accumulation
Separate hydrolysis and fermentation	Each process is performed at optimal condition; Increased productivity; Low enzyme intake	Higher risk of contamination; Increased inhibition; Requires more equipment
Simultaneous saccharification and fermentation	Shorter time; Reduced reactor volume; Reduced inhibition; Low cost	Difficulties in matching of optimal conditions for both processes
Separate hydrolysis and co-fermentation	Both processes are performed at optimal conditions; Increased product yield	Increased risk of contamination; Increased enzyme requirements; Increased inhibition
Simultaneous saccharification and co-fermentation	Lower risk of contamination; Lower costs; Shorter time	Increased enzyme requirements; Difficulties in matching of optimal conditions for both processes

for first-generation LA. Having in mind that the use of pretreated biomass for LA production can result in a more complex fermentation broth, containing more impurities (unfermented pentoses and hexoses, inhibitory substances, lignin, protein, pigments, and salts), a more complex and expensive downstream process will be needed. Therefore, searching for a highly effective, improving LA yield, low-cost, and environmentally friendly method is of great importance. It is well known that LA fermentation is characterized by relatively low final concentration and low production rate, due on one hand, to the change of pH caused by acid accumulation and, on the other hand, to the product inhibition. Hence, neutralization of the broth or *in situ* removal of the product and thus increasing productivity is necessary. Sodium hydroxide, ammonia  $\text{Ca}(\text{OH})_2$ , or  $\text{CaCO}_3$  are used as neutralizing agents.

Conventionally, industrially produced by fermentation LA is removed by precipitation with  $\text{Ca}(\text{OH})_2$ . The method suffers from many drawbacks—precipitated calcium lactate has considerable water solubility [5–20%, depending on temperature (10–50°C)], additional steps have to be applied for converting lactate to free lactic acid—filtration, acidification with  $\text{H}_2\text{SO}_4$  (generates a large amount of  $\text{CaSO}_4$ ), activated carbon purification and decolorization, concentration by evaporation and crystallization. In the case of lignocellulosic biomass-derived substrates, the separation process is additionally complicated by other simultaneously precipitated.

Because of numerous disadvantages of the precipitation method, different techniques have been investigated as an alternative to the traditional recovery process. These include liquid-liquid extraction (including liquid membranes), electrodialysis, ion exchange, membrane separation, aqueous two-phase systems, etc.

Liquid-liquid extraction is a separation method based on different solubility of the target compound in water and immiscible organic solvent (hydrocarbons or alcohols with high molecular mass). For increasing the partition a chemical called extractant is added to the organic phase. The target compound (lactic acid) forms a complex with the extractant with an increased affinity towards the organic phase.

Different membrane-based separation techniques (micro-, ultra-, nano-filtration, reverse osmosis, and pervaporation) can be successfully used as a preliminary step for lactic acid purification. These methods are environmentally friendly and easily scaled up. Usually, they are employed for the separation of cells, proteins, and sugars.

Adsorption is a powerful method for bioseparation with easy regeneration, low energy consumption, and high selectivity. Neutral (activated carbon) or ion exchange adsorbents can be used. Din et al. (2021) analyzed in-depth second-generation lactic acid separation and recovery from fermentation broth by ion exchange. The authors highlighted different factors influencing the process and briefly discussed other methods for LA separation.

Electrodialysis is a method facilitating salt ions transport through an ion-exchange membrane from one to another solution by applying an electric field. Mono- and bipolar electrodialysis are widely used for lactic acid separation.

Aqueous two-phase systems (ATPS) are formed when two water-soluble polymers (or a polymer and a salt) are mixed in a common solution. Because of the incompatibility of the constituents, the system is separated into two phases. ATPS are extensively used in the separation of various bioproducts. Zhou et al. (2021) investigated the separation of lactic acid from simulated and actual lignocellulosic (from SSCF of dilute acid-pretreated corn stover) fermentation broth. In a three-stage ionic liquid-based sugaring-out extraction from the filtered and unfiltered fermentation broth, the total recovery of LA was 89.5 and 89.4%, respectively (Zhou et al., 2021).

Other methods like molecular distillation, short path evaporation, salting-out extraction, emulsion liquid membranes are also tested for lactic acid separation. There are numerous papers concerning lactic acid separation from the fermentation broth, but the majority of them are devoted to lactic acid produced of sugars or starchy materials (first generation LA), and data for the separation of lactic acid obtained from lignocellulosic biomass are scarce. Several review papers summarize recent progress in lactic acid separation by different methods (Kumar et al., 2019; Li et al.,



2021; Yankov 2020). De Oliveira et al. (2020) discussed current state-of-the-art on the separation and purification methods of lactic acid derived from the fermentation of second-generation feedstocks.

Baral et al. (2021) investigated lactic acid separation from the broth after sugarcane bagasse hydrolysate fermentation. Various extractants (tripropylamine, trihexylamine, trioctylamine, triisooctylamine, and tributylphosphate) and diluents (chloroform, dodecane, ethyl acetate, MIBK, hexane, and 1-octanol) were screened for choosing the best extractant-diluent pair. Tributylphosphate and ethyl acetate were selected because of their higher extraction efficiency— $59.63 \pm 1.28\%$ . Different salts—calcium chloride, ammonium sulfate, sodium dihydrogen phosphate, and di-potassium hydrogen phosphate were used in the view to enhance extraction. Salting-out extraction with 60% ammonium sulfate increased the lactic acid extraction efficiency to  $85.95 \pm 0.44\%$ . About 80% salt recovery was achieved using chilled acetone (Baral et al., 2021).

Demmelmayr and Kienberger (2022) studied reactive extraction of lactic acid from sweet sorghum silage press juice. Different extractants (dioctylamine, trioctylamine, and Aliquat 336) and diluents/modifiers (octanol, decanol, hexane, nonane, and undecane) were used in various ratios. Stripping of the loaded organic phase was done by sodium hydroxide. The extraction efficiency of 41.1% was reached using system DOA/ALIQUAT: 1-octanol:n-nonane (35:35; 15:15) with a stripping efficiency of 98.2% (Demmelmayr and Kienberger 2022).

Hu et al. (2017) explored lactic acid recovery from fermentation broths of food waste and bakery waste hydrolysates by continuous ultrasonic solvent extraction. They compared the extraction efficiency of six organic solvents and chose ethyl acetate (EA) as the best option. The extraction into ethyl acetate (LA:EA ratio 1:2) by sonication at pH 2 under room temperature resulted in 82–84% yield and 98% purity (Hu et al., 2017).

Lan et al. (2019) compared two methods for lactic acid extraction from corn stover hemicellulose-derived liquor (HDL). In the first one, 10% trioctylamine in octanol was used with 50.8% extraction efficiency. An additional salting-out extraction step was included before TOA extraction. The salting-out extraction was done in THF/NaCl system. The overall efficiency of 83% was achieved in the two-step extraction of an activated carbon-treated HDL. The process provided stable LA removal during five consecutive extraction/stripping cycles (Lan et al., 2019).

Xu et al. (2018) studied salting-out extraction of lactic acid in systems composed of  $\text{Na}_2\text{SO}_4$  and organic solvent (1,4-dioxane, THF,  $\gamma$ -butyrolactone, and  $\gamma$ -valerolactone). Best results were obtained with the system  $\text{Na}_2\text{SO}_4$ /1,4-dioxane, and the conditions for LA extraction were further optimized. In the case of 13.5%  $\text{Na}_2\text{SO}_4$ /28% 1,4-dioxane, at low pH (1.68) 91% extraction efficiency was achieved in the case of model LA solution and 90% from real mixture directly derived from the chemical catalytic conversion of corn stover (Xu et al., 2018).

Chen et al. (2020) realized a combined process for LA production and separation. After fermentation of corn cob hydrolysate, the fermentation broth was fed into an

ultrafiltration cell and retentate, containing mainly cellulase was recycled. The permeate was acidified to liberate free acid from calcium lactate and the liquid fraction was transferred in a nanofiltration unit. The permeate was further purified by distillation for pure lactic acid production, while the retentate, containing mainly residual sugars was transferred back in the fermentor. A total of six cycles of fed-batch SSF were performed (Chen et al., 2020).

Short-path evaporation of lactic acid from hemicellulose hydrolysate after acid hydrolysis of sugarcane bagasse was investigated by De Oliveira et al. (2020). During the fermentation pH of the broth was maintained by  $\text{Ca}(\text{OH})_2$ . At the end of fermentation, the broth was treated with sulphuric acid for calcium lactate destroying and then filtered and centrifuged. The clear liquid was evaporated and a concentration of 3 times (from 27.85 g/L to 86.69 g/L) was obtained at 120°C evaporator temperature of, 13°C condenser temperature of, and 8.27 ml/min feed flow rate. The authors mentioned a more difficult process than the separation of LA from sugars (Oliveira et al., 2019).

Garrett et al. (2015) realized an *in situ* extractive fermentation of lactic acid from corn stover sugars. The corn stover was pretreated by a wet explosion followed by enzyme hydrolysis. The resulting sugar solution was fermented by a mixed culture, dominated by a *Bacillus coagulans* strain. A weak base resin Amberlite IRA-67 was used for LA removal during fermentation. The base eluted resin was able to maintain stable fermentation over 108-days, during which the average loading of lactic and acetic acids was 112.2 and 19.6 mg acid/g resin, respectively (Garrett et al., 2015).

Oonkhanond et al. (2017) used pretreated sugarcane bagasse in an integrated system with *ex-situ* nanofiltration. The first step fractionation was carried out using acid ethanolsis (5N  $\text{H}_2\text{SO}_4$  in 50% v/v ethanol) at 90°C for 4 h. In the second step, the neutralized solid part was treated with an alkaline/peroxide reaction at 4.5% wt  $\text{H}_2\text{O}_2$  at pH 11.5 for 24 h at 60°C. and finally was hydrolyzed by Accellerase 1,500 at pH 5.0, 50°C for 96 h. Using nanofiltration with a low flux membrane, lactic acid was efficiently separated from the fermentation broth, and after vacuum distillation, a lactic acid solution with 80% purity was achieved (Oonkhanond et al., 2017).

Alexandri et al. (2018) carried out a pilot-scale LA production using a defined medium with glucose, acid whey, sugar bread, and crust bread, coupled with membrane technologies. Microfiltration and nanofiltration were successfully used to separate lactic acid from the majority of the other fermentation components, leading to a more than 10% improvement of lactic acid's purity (Alexandri et al., 2018).

Neu et al. (2016) explored different methods for downstream processing of a lactic acid stream obtained after fermentation of coffee mucilage. Micro- and nanofiltration, electro-dialysis, ion-exchange, and distillation result in a 930 g/L lactic acid solution with 99.8% purity (Neu et al., 2016).

Olszewska-Widdrat et al. (2019) investigated complex method combining various technics in LA separation from sweet sorghum juice—filtration and ultra-filtration, chelating resin, mono- and bipolar electrodialysis, followed by chromatography and vacuum evaporation were

subsequently carried out producing a 905.8 g/L lactic acid solution, with an optical purity of 98.9% (Olszewska-Widdrat et al., 2019).

Prado-Rubio et al. (2020) presented a techno-economic assessment of lactic acid (produced from sugarcane feedstock) separation. The evaluation of three separation methods (reactive distillation, reactive extraction, and electrodialysis) was made based on a LA/water stream in mass ratio 0.3038/0.6962. The calculations were made using a specific methodology design for each separation technique applying Aspen Plus, Matlab, and their combination. Taking reactive distillation as a base, other methods showed a significant reduction in total annual cost—reactive extraction—44% and electrodialysis—55% (Prado-Rubio et al., 2020).

Mandegari et al. (2017) investigated four scenarios for ethanol and/or lactic acid production in lignocellulose biorefineries annexed to a typical sugar mill using Aspen Plus simulator. Economic evaluation, energy assessment, and environmental life cycle assessment (LCA) were carried out. The LCA suggested that all LA producing scenarios introduced environmental burdens (Mandegari et al., 2017).

## 9 CONCLUSION AND PERSPECTIVES

In the way of decreasing dependence on petroleum-based production of valuable chemicals, considerable efforts are concentrated on the investigation of different lignocellulosic feedstocks as raw materials for fermentative production of various chemical products. Fermentative lactic acid production from first-generation biomass is an example of a growing production process. High cost of the substrates and enzymes, some environmental issues, food competition, and waste generation are the factors hindering the industrial process implementation. Second and third-generation sources present an attractive alternative for lactic acid production. From the summarized here research during the last 5 years, the most employed feedstock is corn stover and the most used pretreatment method—acid and enzyme hydrolysis. Nevertheless, there are numerous challenges in the route

towards a cost-effective process—separation of lignin from cellulose and hemicellulose; release of inhibitory compounds during pretreatment; product and substrate inhibition; and by-product formation in fermentation; the more complex composition of fermentation broth in and ecological problems connected with classical precipitation separation, etc. However, there are some encouraging signs of developing an economically effective and environmentally friendly method for lactic acid production from renewable resources. First of all, is the progress in using green solvents like ionic liquids, capable of being more effective and producing fewer inhibitors during lignocellulose dissolution. What is more, ionic liquids have very tunable characteristics and can be easily tailored for different feedstocks. Secondly, developing genetically modified microorganisms with high productivity and adapted to inhibitors. Finally, process integration—elaboration of different SSF processes with different microorganisms, as well as *in situ* extraction, both leading to minimization of the substrate and product inhibition and thus increasing the yield and decreasing the total cost.

In general, the development of such innovative, sustainable, and cost-effective method with high yield and purity of lactic acid is still on the horizon. The most promising method for lactic acid production from lignocellulosic feedstocks seems to be pretreatment with DES, followed by SSF (or SSCF) in fed-batch or continuous mode.

## AUTHOR CONTRIBUTIONS

DY contributed to the conceptualization, the literature research, the writing of the manuscript, and the design of the figures.

## ACKNOWLEDGMENTS

The author is thankful to the National Science Fund of Bulgaria for the financial support by the contract KP-06-Russia-10/2020, which made this study possible.

## REFERENCES

- Abdel-Rahman, M. A., Hassan, S. E.-D., Alrefaey, H. M. A., El-Belely, E. F., Elsakhaw, T., Fouda, A., et al. (2021). Subsequent Improvement of Lactic Acid Production from Beet Molasses by *Enterococcus Hirae* Ds10 Using Different Fermentation Strategies. *Bioresour. Technol. Rep.* 13, 100617. doi:10.1016/j.biteb.2020.100617
- Abedi, E., and Hashemi, S. M. B. (2020). Lactic Acid Production - Producing Microorganisms and Substrates Sources-State of Art. *Heliyon* 6, e04974. doi:10.1016/j.heliyon.2020.e04974
- Ahmad, A., Banat, F., and Taher, H. (2021). Comparative Study of Lactic Acid Production from Date Pulp Waste by Batch and Cyclic-Mode Dark Fermentation. *Waste Manage.* 120, 585–593. doi:10.1016/j.wasman.2020.10.029
- Ahring, B. K., Traverso, J. J., Murali, N., and Srinivas, K. (2016). Continuous Fermentation of Clarified Corn stover Hydrolysate for the Production of Lactic Acid at High Yield and Productivity. *Biochem. Eng. J.* 109, 162–169. doi:10.1016/j.bej.2016.01.012
- Ajala, E. O., Olonade, Y. O., Ajala, M. A., and Akinpelu, G. S. (2020). Lactic Acid Production from Lignocellulose - A Review of Major Challenges and Selected Solutions. *ChemBioEng Rev.* 7 (2), 38–49. doi:10.1002/cben.201900018
- Akao, S., Nagare, H., Maeda, M., Kondo, K., and Fujiwara, T. (2016). Non-sterile Simultaneous Saccharification and Fermentation of Corn Leaves and Stalks to L-Lactic Acid without External Nutrient Addition. *J. Mater. Cycles Waste Manag.* 18, 208–214. doi:10.1007/s10163-015-0390-y
- Åkerberg, C., and Zacchi, G. (2000). An Economic Evaluation of the Fermentative Production of Lactic Acid from Wheat Flour. *Bioresour. Technol.* 75, 119–126. doi:10.1016/S0960-8524(00)00057-2
- Alexandri, M., Schneider, R., and Venus, J. (2018). Membrane Technologies for Lactic Acid Separation from Fermentation Broths Derived from Renewable Resources. *Membranes* 8, 94. doi:10.3390/membranes8040094
- Alhafiz, H. A., Isa, M. T., Sallau, A. B., and O Ameh, A. (2020). Delignification of Corn Cob for the Synthesis of Lactic Acid. *J. Niger. Soc. Chem. Eng.* 35 (1), 64–70.
- Alrumman, S. A. (2016). Enzymatic Saccharification and Fermentation of Cellulosic Date palm Wastes to Glucose and Lactic Acid. *Braz. J. Microbiol.* 47, 110–119. doi:10.1016/j.bjm.2015.11.015

- Alves de Oliveira, R., Komesu, A., Vaz Rossell, C. E., Wolf Maciel, M. R., and Maciel Filho, R. (2019). Concentrating Second-Generation Lactic Acid from Sugarcane Bagasse via Hybrid Short Path Evaporation: Operational Challenges. *Separat. Purif. Technol.* 209, 26–31. doi:10.1016/j.seppur.2018.07.012
- Alves de Oliveira, R., Schneider, R., Vaz Rossell, C. E., Maciel Filho, R., and Venus, J. (2019). Polymer Grade L-Lactic Acid Production from Sugarcane Bagasse Hemicellulosic Hydrolysate Using *Bacillus Coagulans*. *Bioresour. Technol. Rep.* 6, 26–31. doi:10.1016/j.biteb.2019.02.003
- Alves de Oliveira, R., Vaz Rossell, C. E., Venus, J., Cândida Rabelo, S., and Maciel Filho, R. (2018). Detoxification of Sugarcane-Derived Hemicellulosic Hydrolysate Using a Lactic Acid Producing Strain. *J. Biotechnol.* 278, 56–63. doi:10.1016/j.jbiotec.2018.05.006
- Asim, A. M., Uroos, M., Naz, S., and Muhammad, N. (2021). Pyridinium Protic Ionic Liquids: Effective Solvents for Delignification of Wheat Straw. *J. Mol. Liquids* 325, 115013. doi:10.1016/j.molliq.2020.115013
- Avci, U., Zhou, X., Pattathil, S., da Costa Sousa, L., Hahn, M. G., Dale, B., et al. (2019). Effects of Extractive Ammonia Pretreatment on the Ultrastructure and Glycan Composition of Corn Stover. *Front. Energ. Res.* 7, 85. doi:10.3389/fenrg.2019.00085
- Azaiz, H., Abu Tayeh, H. N., Schneider, R., Klongklaew, A., and Venus, J. (2020). Production of Lactic Acid from Carob, Banana and Sugarcane Lignocellulose Biomass. *Molecules* 25, 2956. doi:10.3390/molecules25132956
- Ballesteros, L. F., Teixeira, J. A., and Mussatto, S. I. (2014). Chemical, Functional, and Structural Properties of Spent Coffee Grounds and Coffee Silverskin. *Food Bioproc. Technol.* 7, 3493–3503. doi:10.1007/s11947-014-1349-z
- Banu, J. R., Preethi, S. K., Kavitha, S., Tyagi, V. K., Gunasekaran, M., Karthikeyan, O. P., et al. (2021). Lignocellulosic Biomass Based Biorefinery: A Successful Platform towards Circular Bioeconomy. *Fuel* 302, 121086. doi:10.1016/j.fuel.2021.121086
- Baral, P., Munagala, M., Shastri, Y., Kumar, V., and Agrawal, D. (2021). Cost Reduction Approaches for Fermentable Sugar Production from Sugarcane Bagasse and its Impact on Techno-Economics and the Environment. *Cellulose* 28, 6305–6322. doi:10.1007/s10570-021-03940-5
- Baral, P., Pundir, A., Kumar, V., Kurmi, A. K., and Agrawal, D. (2020). Expeditious Production of Concentrated Glucose-Rich Hydrolysate from Sugarcane Bagasse and its Fermentation to Lactic Acid with High Productivity. *Food Bioprocess Process.* 124, 72–81. doi:10.1016/j.fbp.2020.08.005
- Baral, P., Pundir, A., Kurmi, A., Singh, R., Kumar, V., and Agrawal, D. (2021). Salting-out Assisted Solvent Extraction of L (+) Lactic Acid Obtained after Fermentation of Sugarcane Bagasse Hydrolysate. *Separat. Purif. Technol.* 269, 118788. doi:10.1016/j.seppur.2021.118788
- Baruah, J., Nath, B. K., Sharma, R., Kumar, S., Deka, R. C., Baruah, D. C., et al. (2018). Recent Trends in the Pretreatment of Lignocellulosic Biomass for Value-Added Products. *Front. Energ. Res.* 6, 141. doi:10.3389/fenrg.2018.00141
- Berlowska, J., Cieciora, W., Borowski, S., Dudkiewicz, M., Binczarski, M., Witonska, I., et al. (2016). Simultaneous Saccharification and Fermentation of Sugar Beet Pulp with Mixed Bacterial Cultures for Lactic Acid and Propylene Glycol Production. *Molecules* 21, 1380. doi:10.3390/molecules21101380
- Beschkov, V., Razkazova-Velkova, E., and Liutskanov, L. (2020). Carbon Dioxide Recycling for Fuels and Chemical Products. *Prog. Petrochemical Sci.* 3 (5), 376–379. doi:10.31031/pp.2020.03.000572
- Bhatia, S. K., Jagtap, S. S., Bedekar, A. A., Bhatia, R. K., Patel, A. K., Pant, D., et al. (2020). Recent Developments in Pretreatment Technologies on Lignocellulosic Biomass: Effect of Key Parameters, Technological Improvements, and Challenges. *Bioresour. Technol.* 300, 122724. doi:10.1016/j.biortech.2019.122724
- Bio-ethanol market-growth, trends, covid-19 impact, and forecasts (2021 - 2026) (2021). Bio-ethanol Market-Growth, Trends, Covid-19 Impact, and Forecasts (2021 - 2026). Available at: <https://www.mordorintelligence.com/industry-reports/bio-ethanol-market> (Accessed October 27, 2021).
- Börner, R. A., Kandasamy, V., Axelsen, A. M., Nielsen, A. T., and Bosma, E. F. (2019). Genome Editing of Lactic Acid Bacteria: Opportunities for Food, Feed, Pharma and Biotech. *FEMS Microbiol. Lett.* 366, fny291. doi:10.1093/femsle/fny291
- Brock, S., Kuenz, A., and Prüße, U. (2019). Impact of Hydrolysis Methods on the Utilization of Agricultural Residues as Nutrient Source for D-Lactic Acid Production by *Sporolactobacillus Inulinus*. *Fermentation* 5 (12), 5010012. doi:10.3390/fermentation5010012
- Bustamante, D., Tortajada, M., Ramón, D., and Rojas, A. (2020). Production of D-Lactic Acid by the Fermentation of Orange Peel Waste Hydrolysate by Lactic Acid Bacteria. *Fermentation* 6, 1.
- Carvalho, F., Esteves, M. P., Parajo, J. C., Pereira, H., and Girio, F. M. (2004). Production of Oligosaccharides by Autohydrolysis of Brewery's Spent Grain. *Bioresour. Technol.* 91 (1), 93–100. doi:10.1016/S0960-8524(03)00148-2
- Chai, C. Y., Tan, I. S., Foo, H. C. Y., Lam, M. K., Tong, K. T. X., and Lee, K. T. (2021). Sustainable and green Pretreatment Strategy of *Eucheuma Denticulatum* Residues for Third-Generation L-Lactic Acid Production. *Bioresour. Technol.* 330, 124930. doi:10.1016/j.biortech.2021.124930
- Chen, H., Chen, B., Su, Z., Wang, K., Wang, B., Wang, Y., et al. (2020). Efficient Lactic Acid Production from Cassava Bagasse by Mixed Culture of *Bacillus Coagulans* and *Lactobacillus Rhamnosus* Using Stepwise pH Controlled Simultaneous Saccharification and Co-fermentation. *Ind. Crops Prod.* 146, 112175. doi:10.1016/j.indcrop.2020.112175
- Chen, H., Huo, W., Wang, B., Wang, Y., Wen, H., Cai, D., et al. (2019). L-lactic Acid Production by Simultaneous Saccharification and Fermentation of Dilute Ethylenediamine Pre-treated rice Straw. *Ind. Crops Prod.* 141, 111749. doi:10.1016/j.indcrop.2019.111749
- Chen, H., Su, Z., Wang, Y., Wang, B., Si, Z., Lu, J., et al. (2020). Lactic Acid Production from Pretreated Corn stover with Recycled Streams. *Process Biochem.* 91, 132–140. doi:10.1016/j.procbio.2019.12.004
- Chen, P.-T., Hong, Z.-S., Cheng, C.-L., Ng, I.-S., Lo, Y.-C., Nagarajan, D., et al. (2020). Exploring Fermentation Strategies for Enhanced Lactic Acid Production with Polyvinyl Alcohol-Immobilized *Lactobacillus Plantarum* 23 Using Microalgae as Feedstock. *Bioresour. Technol.* 308, 123266. doi:10.1016/j.biortech.2020.123266
- Cheng, Q., Shi, X., Liu, Y., Liu, X., Dou, S., Ning, C., et al. (2018). Production of Nisin and Lactic Acid from Corn stover through Simultaneous Saccharification and Fermentation. *Biotechnol. Biotechnological Equipment* 32 (2), 420–426. doi:10.1080/13102818.2017.1420425
- Chin, S. X., Tasirin, S. M., Chan, C. H., Chia, C. H., Chook, S. W., Zakaria, S., et al. (2016). Catalytic Conversion of Empty Fruit Bunch (EFB) Fibres into Lactic Acid by Lead (II) Ions. *BioResources* 11 (1), 2186–2201. doi:10.15376/biores.11.1.2186-2201
- Cho, S. W., Yim, J., and Seo, S. W. (2020). Engineering Tools for the Development of Recombinant Lactic Acid Bacteria. *Biotechnol. J.* 15, 1900344. doi:10.1002/biot.201900344
- Cola, P., Procópio, D. P., Alves, A. T. d. C., Carnevali, L. R., Sampaio, I. V., da Costa, B. L. V., et al. (2020). Differential Effects of Major Inhibitory Compounds from Sugarcane-Based Lignocellulosic Hydrolysates on the Physiology of Yeast Strains and Lactic Acid Bacteria. *Biotechnol. Lett.* 42, 571–582. doi:10.1007/s10529-020-02803-6
- Conway, J. (2021). Global Beer Production 1998–2020. October 15. Available at: <https://www.statista.com/statistics/270275/worldwide-beer-production/>.
- Cruz-Lopes, L., Domingos, I., Ferreira, J., and Esteves, B. (2017). *J. Int. Scientific Publications* 5, 85–93.
- Cubas-Cano, E., González-Fernández, C., Ballesteros, M., and Tomás-Pejó, E. (2018). Biotechnological Advances in Lactic Acid Production by Lactic Acid Bacteria: Lignocellulose as Novel Substrate. *Biofuels, Bioprod. Bioref.* 12 (2), 290–303. doi:10.1002/bbb.1852
- Cubas-Cano, E., González-Fernández, C., Ballesteros, M., and Tomás-Pejó, E. (2019). *Lactobacillus Pentosus* CECT 4023 T Co-utilizes Glucose and Xylose to Produce Lactic Acid from Wheat Straw Hydrolysate: Anaerobiosis as a Key Factor. *Biotechnol. Prog.* 35 (1), e2739. doi:10.1002/btpr.2739
- Cubas-Cano, E., González-Fernández, C., and Tomás-Pejó, E. (2019). Evolutionary Engineering of *Lactobacillus Pentosus* Improves Lactic Acid Productivity from Xylose-Rich media at Low pH. *Bioresour. Technol.* 288, 121540. doi:10.1016/j.biortech.2019.121540
- Cubas-Cano, E., Venus, J., González-Fernández, C., and Tomás-Pejó, E. (2020). Assessment of Different *Bacillus Coagulans* Strains for L-Lactic Acid Production from Defined media and Gardening Hydrolysates: Effect of Lignocellulosic Inhibitors. *J. Biotechnol.* 323, 9–16. doi:10.1016/j.jbiotec.2020.07.017
- Damyanova, S., and Beschkov, V. (2020). "Biogas as a Source of Energy and Products," in *Biorefinery Concepts, Energy and Products* (London: IntechOpen Ltd), 17–30.

- de la Torre, I., Acedos, M. G., Ladero, M., and Santos, V. E. (2019). On the Use of Resting *L. Delbrueckii* Spp. *Delbrueckii* Cells for D-Lactic Acid Production from orange Peel Wastes Hydrolysates. *Biochem. Eng. J.* 145, 162–169. doi:10.1016/j.bej.2019.02.012
- de la Torre, I., Ladero, M., and Santos, V. E. (2020). D-lactic Acid Production from orange Waste Enzymatic Hydrolysates with *L. Delbrueckii* Cells in Growing and Resting State. *Ind. Crops Prod.* 146, 112176. doi:10.1016/j.indcrop.2020.112176
- de la Torre, I., Ravelo, M., Segarra, S., Tortajada, M., Santos, V. E., and Ladero, M. (2017). Study on the Effects of Several Operational Variables on the Enzymatic Batch Saccharification of orange Solid Waste. *Bioresour. Technol.* 245, 906–915. doi:10.1016/j.biortech.2017.08.094
- de Oliveira Moraes, A., Ramirez, N. I. B., and Pereira, N. (2016). Evaluation of the Fermentation Potential of Pulp Mill Residue to Produce D(–)-Lactic Acid by Separate Hydrolysis and Fermentation Using *Lactobacillus Coryniformis* Subsp. *Torquens*. *Appl. Biochem. Biotechnol.* 180, 1574–1585. doi:10.1007/s12010-016-2188-3
- De Oliveira, R. A., Alexandri, M., Komesu, A., Venus, J., Vaz Rossell, C. E., and Maciel Filho, R. (2020). Current Advances in Separation and Purification of Second-Generation Lactic Acid. *Separat. Purif. Rev.* 49 (2), 159–175. doi:10.1080/15422119.2019.1590412
- Demmelmayr, P., and Kienberger, M. (2022). Reactive Extraction of Lactic Acid from Sweet Sorghum Silage Press Juice. *Separat. Purif. Technol.* 282, 120090. doi:10.1016/j.seppur.2021.120090
- Dhandapani, B., Vishnu, D., Murshid, S., A. R. P., R. M., D. P., et al. (2021). Production of Lactic Acid from Industrial Waste Paper Sludge Using *Rhizopus Oryzae* MTCC5384 by Simultaneous Saccharification and Fermentation. *Chem. Eng. Commun.* 208 (6), 822–830. doi:10.1080/00986445.2019.1657422
- Din, N. A. S., Lim, S. J., Maskat, M. Y., Mutalib, S. A., and Zaini, N. A. M. (2021). Lactic Acid Separation and Recovery from Fermentation Broth by Ion-Exchange Resin: A Review. *Bioresour. Bioproc.* 8, 31. doi:10.1186/s40643-021-00384-4
- Djukic-Vukovic, A., Mladenovic, D., Radosavljevic, M., Kocic-Tanackov, S., Pejcin, J., and Mojovic, L. (2016). Wastes from Bioethanol and Beer Productions as Substrates for L(+) Lactic Acid Production – A Comparative Study. *Waste Manage.* 48, 478–482.
- Duque, A., Manzanares, P., Ballesteros, I., and Ballesteros, M. (2016). “Steam Explosion as Lignocellulosic Biomass Pretreatment,” in *Biomass Fractionation Technologies for a Lignocellulosic Feedstock-Based Biorefinery*. Editor S. I. Mussatto (Amsterdam: Elsevier), 349–368. doi:10.1016/b978-0-12-802323-5.00015-3
- Erliana, W. H., Widjaja, T., Altway, A., and Pudjiastuti, L. (2020). Synthesis of Lactic Acid from Sugar palm Trunk Waste (*Arenga Pinnata*): Preliminary Hydrolysis and Fermentation Studies. *Biodiversitas* 21 (5), 2281–2288. doi:10.13057/biodiv/d210559
- Esquivel-Hernández, D. E., Pennacchio, A., Torres-Acosta, M. A., Parra-Saldivar, R., de Souza Vandenbergh, L. P., and Faraco, V. (2021). Multi-product Biorefinery from *Arthrospira Platensis* Biomass as Feedstock for Bioethanol and Lactic Acid Production. *Scientific Rep.* 11, 19309.
- Garrett, B. G., Srinivas, K., and Ahning, B. K. (2015). Performance and Stability of Amberlite IRA-67 Ion Exchange Resin for Product Extraction and pH Control during Homolactic Fermentation of Corn stover Sugars. *Biochem. Eng. J.* 94, 1–8. doi:10.1016/j.bej.2014.11.004
- Gezae Dafu, A., and Görgens, J. F. (2017). Techno-economic Analysis and Environmental Impact Assessment of Lignocellulosic Lactic Acid Production. *Chem. Eng. Sci.* 162, 53–65. doi:10.1016/j.ces.2016.12.054
- Giacon, T. G., Cunha, G. G. G., Eliodório, K. P., Oliveira, R. P. S., and Basso, T. O. (2021). Homo- and Heterofermentative *Lactobacilli* Are Differently Affected by Lignocellulosic Inhibitory Compounds. *bioRxiv* 2021.01.18.427060. doi:10.1101/2021.01.18.427060
- Gilver Rosero Chasoy, G. R., Chairez, I., and Durán-Páramo, E. (2020). Carbon/nitrogen Ratio and Initial pH Effects on the Optimization of Lactic Acid Production by *Wulfenia* J. 27 (10), 37–59.
- Giroto, F., Pivato, A., Cossu, R., Nkeng, G. E., and Lavagnolo, M. C. (2018). The Broad Spectrum of Possibilities for Spent Coffee Grounds Valorisation. *J. Mater. Cycles Waste Manag.* 20, 695–701. doi:10.1007/s10163-017-0621-5
- Givry, S., Prevot, V., and Duchiron, F. (2008). Lactic Acid Production from Hemicellulosic Hydrolyzate by Cells of *Lactobacillus Bifermentans* Immobilized in Ca-Alginate Using Response Surface Methodology. *World J. Microbiol. Biotechnol.* 24, 745–752. doi:10.1007/s11274-007-9534-0
- Global Lactic Acid Market 2017–2025 - Growth Trends, Key Players, Competitive Strategies and Forecasts - Research and Market (2017). Global Lactic Acid Market 2017–2025 - Growth Trends, Key Players, Competitive Strategies and Forecasts - Research and Market. Available at: <https://www.businesswire.com/news/home/20170621005594/en/Global-Lactic-Acid-Market-2017-2025-Growth-Trends-Key-Players-Competitive-Strategies-and-Forecasts-Research-and-Markets>.
- Goh, C. S., Tan, H. T., Lee, K. T., and Brosse, N. (2011). Evaluation and Optimization of Organosolv Pretreatment Using Combined Severity Factors and Response Surface Methodology. *Biomass and Bioenergy* 35 (9), 4025–4033. doi:10.1016/j.biombioe.2011.06.034
- Gómez-Gómez, J. A., Giraldo-Estrada, C., Habeych, D., and Baena, S. (2015). Evaluation of Biological Production of Lactic Acid in a Synthetic Medium and in Aloe Vera (L.) Burm. F. Processing By-Products. *Universitas Scientiarum* 20 (3), 369–385.
- González-Leos, A., Bustos-Vázquez, M. G., Rodríguez-Castillejos, G. C., Rodríguez-Durán, L. V., and Del Ángel-Del Ángel, A. (2020). Kinetics of Lactic Acid Fermentation from Sugarcane Bagasse by *Lactobacillus Pentosus*. *Revista Mexicana de Ingeniería Química* 19 (1), 377–386.
- Gössi, A., Burgener, F., Kohler, D., Urso, A., Kolvenbach, B. A., Riedl, W., et al. (2020). *In-situ* Recovery of Carboxylic Acids from Fermentation Broths through Membrane Supported Reactive Extraction Using Membrane Modules with Improved Stability. *Separat. Purif. Technol.* 241, 116694.
- Grewal, J., and Khare, S. K. (2018). One-pot Bioprocess for Lactic Acid Production from Lignocellulosic Agro-Wastes by Using Ionic Liquid Stable *Lactobacillus Brevis*. *Bioresour. Technol.* 251, 268–273. doi:10.1016/j.biortech.2017.12.056
- Grewal, J., Sadaf, A., Yadav, N., and Khare, S. K. (2020). “Agroindustrial Waste Based Biorefineries for Sustainable Production of Lactic Acid,” in *Waste Biorefinery: Integrating Biorefineries for Waste Valorisation*. Editors T. Bhaskar, A. Pandey, E. Rene, and D. Tsang (Amsterdam, Netherlands: Elsevier), 125–153. doi:10.1016/b978-0-12-818228-4.00005-8
- Haldar, D., and Purkait, M. K. (2020). Lignocellulosic Conversion into Value-Added Products: A Review. *Process Biochem.* 89, 110–133. doi:10.1016/j.procbio.2019.10.001
- Halder, P., Kundu, S., Patel, S., Setiawan, A., Atkin, R., Parthasarthy, R., et al. (2019). Progress on the Pre-treatment of Lignocellulosic Biomass Employing Ionic Liquids. *Renew. Sustain. Energ. Rev.* 105, 268–292. doi:10.1016/j.rser.2019.01.052
- Hama, S., Mizuno, S., Kihara, M., Tanaka, T., Ogino, C., Noda, H., et al. (2015). Production of D -lactic Acid from Hardwood Pulp by Mechanical Milling Followed by Simultaneous Saccharification and Fermentation Using Metabolically Engineered *Lactobacillus Plantarum*. *Bioresour. Technol.* 187, 167–172. doi:10.1016/j.biortech.2015.03.106
- Han, X., Dong, W., and Bao, J. (2021). Upgrading Steam Pretreatment by Converting Water-Soluble Carbohydrates into Lactic Acid Prior to Pretreatment. *Biomass Conv. Bioref.* doi:10.1007/s13399-020-01183-1
- Han, X., Hong, F., Liu, G., and Bao, J. (2018). An Approach of Utilizing Water-Soluble Carbohydrates in Lignocellulose Feedstock for Promotion of Cellulosic L-Lactic Acid Production. *J. Agric. Food Chem.* 66, 10225–10232. doi:10.1021/acs.jafc.8b03592
- Han, X., Li, L., Wei, C., Zhang, J., and Bao, J. (2019). Facilitation of L-Lactic Acid Fermentation by Lignocellulose Biomass Rich in Vitamin B Compounds. *J. Agric. Food Chem.* 67, 7082–7086. doi:10.1021/acs.jafc.9b02297
- He, T., Jiang, Z., Wu, P., Yi, J., Li, J., and Hu, C. (2016). Fractionation for Further Conversion: from Raw Corn stover to Lactic Acid. *Sci. Rep.* 6, 38623. doi:10.1038/srep38623
- He, Y.-C., Liu, F., Di, J.-H., Ding, Y., Zhu, Z.-Z., Wu, Y.-Q., et al. (2016). Effective Enzymatic Saccharification of Dilute NaOH Extraction of Chestnut Shell Pretreated by Acidified Aqueous Ethylene Glycol media. *Ind. Crops Prod.* 81, 129–138. doi:10.1016/j.indcrop.2015.11.079
- He, Y.-C., Liu, F., Gong, L., Di, J.-H., Ding, Y., Ma, C.-L., et al. (2016). Enzymatic *In Situ* Saccharification of Chestnut Shell with High Ionic Liquid-Tolerant Cellulases from *Galactomyces* Sp. CCZU11-1 in a Biocompatible Ionic Liquid-Cellulase media. *Bioresour. Technol.* 201, 133–139. doi:10.1016/j.biortech.2015.11.034



- He, Y., Ding, Y., Ma, C., Di, J., Jiang, C., and Li, A. (2017). One-pot Conversion of Biomass-Derived Xylose to Furfuralcohol by a Chemo-Enzymatic Sequential Acid-Catalyzed Dehydration and Bioreduction. *Green. Chem.* 19, 3844–3850. doi:10.1039/c7gc01256j
- Hoheneder, R., Fitz, E., Bischof, R. H., Russmayer, H., Ferrero, P., Peacock, S., et al. (2021). Efficient Conversion of Hemicellulose Sugars from Spent Sulfite Liquor into Optically Pure L-Lactic Acid by *Enterococcus Mundtii*. *Bioresour. Technol.* 333, 125215. doi:10.1016/j.biortech.2021.125215
- Hu, J., Lin, Y., Zhang, Z., Xiang, T., Mei, Y., Zhao, S., et al. (2016). High-titer Lactic Acid Production by *Lactobacillus Pentosus* FL0421 from Corn stover Using Fed-Batch Simultaneous Saccharification and Fermentation. *Bioresour. Technol.* 214, 74–80. doi:10.1016/j.biortech.2016.04.034
- Hu, Y., Kwan, T. H., Daoud, W. A., and Lin, C. S. K. (2017). Continuous Ultrasonic-Mediated Solvent Extraction of Lactic Acid from Fermentation Broths. *J. Clean. Prod.* 145, 142–150. doi:10.1016/j.jclepro.2017.01.055
- Huang, C., Liu, J., Geng, W., Tang, W., and Yong, Q. (2021). A Review of Lignocellulosic Biomass Pretreatment Technologies. *Paper Biomater.* 6 (3), 61–76.
- Hudeckova, H., Neureiter, M., Obruca, S., Frühauf, S., and Marova, I. (2018). Biotechnological Conversion of Spent Coffee Grounds into Lactic Acid. *Lett. Appl. Microbiol.* 66, 306–312. doi:10.1111/lam.12849
- Hwang, H. J., Kim, S. M., Chang, J. H., and Lee, S. B. (2012). Lactic Acid Production from Seaweed Hydrolysate of *Enteromorpha Prolifera* (Chlorophyta). *J. Appl. Phycol.* 24, 935–940. doi:10.1007/s10811-011-9714-z
- Jacques, K. A., Lyons, T. P., and Kelsall, D. R. (2003). *The Alcohol Textbook*. 4th edition. Nottingham: Nottingham University Press.
- Jaichakan, P., Nakphaichit, M., Rungchang, S., Weerawatanakorn, M., Phongthai, S., and Klangpetch, W. (2021). Two-stage Processing for Xylooligosaccharide Recovery from rice By-Products and Evaluation of Products: Promotion of Lactic Acid-Producing Bacterial Growth and Food Application in a High-Pressure Process. *Food Res. Int.* 147, 110529. doi:10.1016/j.foodres.2021.110529
- Jiang, S., Xu, P., and Tao, F. (2019). L-Lactic Acid Production by *Bacillus* Coagulans through Simultaneous Saccharification and Fermentation of Lignocellulosic Corn cob Residue. *Bioresour. Technol. Rep.* 6, 131–137. doi:10.1016/j.biteb.2019.02.005
- Jiang, T., Qiao, H., Zheng, Z., Chu, Q., Li, X., Yong, Q., et al. (2016). Lactic Acid Production from Pretreated Hydrolysates of Corn Stover by a Newly Developed *Bacillus* Coagulans Strain. *PLoS ONE* 11 (2), e0149101. doi:10.1371/journal.pone.0149101
- Juturu, V., and Wu, J. C. (2016). Microbial Production of Lactic Acid: the Latest Development. *Crit. Rev. Biotechnol.* 36 (6), 967–977. doi:10.3109/07388551.2015.1066305
- Kim, J.-w., Jang, J. H., Yeo, H. J., Seol, J., Kim, S. R., and Jung, Y. H. (2019). Lactic Acid Production from a Whole Slurry of Acid-Pretreated Spent Coffee Grounds by Engineered *Saccharomyces cerevisiae*. *Appl. Biochem. Biotechnol.* 189, 206–216. doi:10.1007/s12010-019-03000-6
- Kong, X., Zhang, B., Hua, Y., Zhu, Y., Li, W., Wang, D., et al. (2019). Efficient L-Lactic Acid Production from Corn cob Residue Using Metabolically Engineered Thermo-Tolerant Yeast. *Bioresour. Technol.* 273, 220–230. doi:10.1016/j.biortech.2018.11.018
- Koo, J.-R., Min Park, H., Kyung Kim, S., and Shik Yun, H. (2019). Lactic Acid Fermentation from Coffee Ground Waste Hydrolysate by *Lactobacillus Rhamnosus*. *J. Renew. Mater.* 7 (4), 365–372. doi:10.32604/jrm.2019.04170
- Krishna, B. S., Nikhilesh, G. S. S., Tarun, B., Narayana, K. V. S., and Gopinadh, R. (2018). Industrial Production of Lactic Acid and its Applications. *Int. J. Biotech Res.* 1 (1), 42–54.
- Krull, S., Brock, S., Prüße, U., and Kuenz, A. (2020). Hydrolyzed Agricultural Residues-Low-Cost Nutrient Sources for L-Lactic Acid Production. *Fermentation* 6, 97. doi:10.3390/fermentation6040097
- Kumar, A., and Chandra, R. (2020). Ligninolytic Enzymes and its Mechanisms for Degradation of Lignocellulosic Waste in Environment. *Heliyon* 6, e03170. doi:10.1016/j.heliyon.2020.e03170
- Kumar, A., Thakur, A., and Panesar, P. S. (2019). Lactic Acid and its Separation and Purification Techniques: A Review. *Rev. Environ. Sci. Biotechnol.* 18, 823–853. doi:10.1007/s11157-019-09517-w
- Kumar, V., Yadav, S. K., Kumar, J., and Ahluwalia, V. (2020). A Critical Review on Current Strategies and Trends Employed for Removal of Inhibitors and Toxic Materials Generated during Biomass Pretreatment. *Bioresour. Technol.* 299, 122633. doi:10.1016/j.biortech.2019.122633
- Kunasundari, B., Arai, T., Sudesh, K., Hashim, R., Sulaiman, O., Stalin, N. J., et al. (2017). Detoxification of Sap from Felled Oil Palm Trunks for the Efficient Production of Lactic Acid. *Appl. Biochem. Biotechnol.* 183, 412–425. doi:10.1007/s12010-017-2454-z
- Kuo, Y.-C., Yuan, S.-F., Wang, C.-A., Huang, Y.-J., Guo, G.-L., and Hwang, W.-S. (2015). Production of Optically Pure L-Lactic Acid from Lignocellulosic Hydrolysate by Using a Newly Isolated and D-Lactate Dehydrogenase Gene-Deficient *Lactobacillus Paracasei* Strain. *Bioresour. Technol.* 198, 651–657. doi:10.1016/j.biortech.2015.09.071
- Laca, A., Laca, A., and Díaz, M. (2019). “Hydrolysis: From Cellulose and Hemicellulose to Simple Sugars,” in *Second and Third Generation of Feedstocks* (Amsterdam: Elsevier), 213–240. doi:10.1016/b978-0-12-815162-4.00008-2
- Lactic Acid Market by Application (Biodegradable Polymers, Food & Beverages, Pharmaceutical Products) (2020). Lactic Acid Market by Application (Biodegradable Polymers, Food & Beverages, Pharmaceutical Products). Available at: <https://www.marketsandmarkets.com/Market-Reports/poly-lactic-acid-387.html>.
- Lan, K., Xu, S., Li, J., and Hu, C. (2019). Recovery of Lactic Acid from Corn Stover Hemicellulose-Derived Liquor. *ACS Omega* 4, 10571–10579. doi:10.1021/acsomega.9b00794
- Lee, K. H., Jang, Y. W., Lee, J., Kim, S., Park, C., and Yoo, H. Y. (2021). Statistical Optimization of Alkali Pretreatment to Improve Sugars Recovery from Spent Coffee Grounds and Utilization in Lactic Acid Fermentation. *Processes* 9, 494. doi:10.3390/pr9030494
- Li, C., Gao, M., Zhu, W., Wang, N., Ma, X., Wu, C., et al. (2021). Recent Advances in the Separation and Purification of Lactic Acid from Fermentation Broth. *Process Biochem.* 104, 142–151. doi:10.1016/j.procbio.2021.03.011
- Li, J., Shi, S., Wang, Y., and Jiang, Z. (2021). Integrated Production of Optically Pure L-Lactic Acid from Paper Mill Sludge by Simultaneous Saccharification and Co-fermentation (SSCF). *Waste Manage.* 129, 35–46. doi:10.1016/j.wasman.2021.05.008
- Li, Q., Ma, C.-L., Zhang, P.-Q., Li, Y.-Y., Zhu, X., and He, Y.-C. (2021). Effective Conversion of Sugarcane Bagasse to Furfural by Coconut Shell Activated Carbon-Based Solid Acid for Enhancing Whole-Cell Biosynthesis of Furfurylamine. *Ind. Crops Prod.* 160, 113169. doi:10.1016/j.indcrop.2020.113169
- Li, Y., Bhagwat, S. S., Cortés-Peña, Y. R., Ki, D., Rao, C. V., Jin, Y.-S., et al. (2021). Sustainable Lactic Acid Production from Lignocellulosic Biomass. *ACS Sustain. Chem. Eng.* 9, 1341–1351. doi:10.1021/acssuschemeng.0c08055
- Lin, H.-T. V., Huang, M.-Y., Kao, T.-Y., Lu, W.-J., Lin, H.-J., and Pan, C.-L. (2020). Production of Lactic Acid from Seaweed Hydrolysates via Lactic Acid Bacteria Fermentation. *Fermentation* 6 (1), 37. doi:10.3390/fermentation6010037
- Lin, Q., Yan, Y., Liu, X., He, B., Wang, X., Wang, X., et al. (2020). Production of Xylooligosaccharide, Nanolignin, and Nanocellulose through a Fractionation Strategy of Corn cob for Biomass Valorization. *Ind. Eng. Chem. Res.* 59, 17429–17439. doi:10.1021/acs.iecr.0c02161
- Liu, J., Cai, Y., Liu, L., Zhan, R., Zhao, S., Liang, Y., et al. (2020). Enhanced Lactic Acid Production by *Bacillus* Coagulans through Simultaneous Saccharification, Biodegradation, and Fermentation. *Biofuels, Bioprod. Bioref.* 14, 533–543. doi:10.1002/bbb.2086
- Liu, L., Cai, Y., Li, H., Zhao, S., He, M., Hu, G.-q., et al. (2019). Bio-detoxification Bacteria Isolated from Dye-Polluted Soils Promote Lactic Acid Production from Ammonia Pretreated Corn Stover. *Appl. Biochem. Biotechnol.* 189, 129–143. doi:10.1007/s12010-019-02993-4
- Liu, Y., Ashok, S., Seol, E., Bao, J., and Park, S. (2013). Comparison of Three *Pediococcus* Strains for Lactic Acid Production from Glucose in the Presence of Inhibitors Generated by Acid Hydrolysis of Lignocellulosic Biomass. *Biotechnol. Bioproc. E* 18, 1192–1200. doi:10.1007/s12257-013-0360-y
- Liu, Y., Zheng, J., Xiao, J., He, X., Zhang, K., Yuan, S., et al. (2019). Enhanced Enzymatic Hydrolysis and Lignin Extraction of Wheat Straw by Triethylbenzyl Ammonium Chloride/Lactic Acid-Based Deep Eutectic Solvent Pretreatment. *ACS Omega* 4 (22), 19829–19839. doi:10.1021/acsomega.9b02709
- Loow, Y.-L., Wu, T. Y., Yang, G. H., Ang, L. Y., New, E. K., Siow, L. F., et al. (2018). Deep Eutectic Solvent and Inorganic Salt Pretreatment of Lignocellulosic Biomass for Improving Xylose Recovery. *Bioresour. Technol.* 249, 818–825. doi:10.1016/j.biortech.2017.07.165



- López-Gómez, J. P., Pérez-Rivero, C., and Venus, J. (2020). Valorisation of Solid Biowastes: The Lactic Acid Alternative. *Process Biochem.* 99, 222–235. doi:10.1016/j.procbio.2020.08.029
- Lu, S., Wang, Q., Liang, Z., Wang, W., Liang, C., Wang, Z., et al. (2021). Saccharification of Sugarcane Bagasse by Magnetic Carbon-Based Solid Acid Pretreatment and Enzymatic Hydrolysis. *Ind. Crops Prod.* 160, 113159. doi:10.1016/j.indcrop.2020.113159
- Ludwig, D., Amann, M., Hirth, T., Rupp, S., and Zibek, S. (2013). Development and Optimization of Single and Combined Detoxification Processes to Improve the Fermentability of Lignocellulose Hydrolyzates. *Bioresour. Technol.* 133, 455–461. doi:10.1016/j.biortech.2013.01.053
- Luo, H., Gao, L., Liu, Z., Shi, Y., Xie, F., Bilal, M., et al. (2021). Prediction of Phenolic Compounds and Glucose Content from Dilute Inorganic Acid Pretreatment of Lignocellulosic Biomass Using Artificial Neural Network Modeling. *Bioresour. Bioproc.* 8, 134. doi:10.1186/s40643-021-00488-x
- Ma, K., Hu, G., Pan, L., Wang, Z., Zhou, Y., Wang, Y., et al. (2016). Highly Efficient Production of Optically Pure L-Lactic Acid from Corn Stover Hydrolysate by Thermophilic *Bacillus Coagulans*. *Bioresour. Technol.* 219, 114–122. doi:10.1016/j.biortech.2016.07.100
- Ma, X., Gao, M., Yin, Z., Zhu, W., Liu, S., and Wang, Q. (2020). Lactic Acid and Animal Feeds Production from *Sophora Flavescens* Residues by *Rhizopus Oryzae* Fermentation. *Process Biochem.* 92, 401–408. doi:10.1016/j.procbio.2020.01.030
- Manandhar, A., and Shah, A. (2020). Techno-Economic Analysis of Bio-Based Lactic Acid Production Utilizing Corn Grain as Feedstock. *Processes* 8, 199. doi:10.3390/pr8020199
- Mandegari, M. A., Farzad, S., van Rensburg, E., and Görgens, J. F. (2017). Multi-criteria Analysis of a Biorefinery for Co-production of Lactic Acid and Ethanol from Sugarcane Lignocellulose. *Biofuels, Bioprod. Bioref.* 11 (6), 971–990. doi:10.1002/bbb.1801
- Mankar, A. R., Pandey, A., Modak, A., and Pant, K. K. (2021). Pretreatment of Lignocellulosic Biomass: A Review on Recent Advances. *Bioresour. Technol.* 334, 125235. doi:10.1016/j.biortech.2021.125235
- Marin-Batista, J. D., Mohedano, A. F., and de la Rubia, A. (2021). Pretreatment of Lignocellulosic Biomass with 1-Ethyl-3-Methylimidazolium Acetate for its Eventual Valorization by Anaerobic Digestion. *Resources* 10, 118. doi:10.3390/resources10120118
- Marques, S., Gírio, F. M., Santos, J. A. L., and Roseiro, J. C. (2017). Pulsed Fed-Batch Strategy towards Intensified Process for Lactic Acid Production Using Recycled Paper Sludge. *Biomass Conv. Bioref.* 7, 127–137. doi:10.1007/s13399-016-0211-0
- Martínez-Trujillo, M. A., Bautista-Rangel, K., García-Rivero, M., Martínez-Estrada, A., and Cruz-Díaz, M. R. (2020). Enzymatic Saccharification of Banana Peel and Sequential Fermentation of the Reducing Sugars to Produce Lactic Acid. *Bioproc. Biosyst. Eng.* 43, 413–427.
- Marzo, C., Díaz, A. B., Caro, I., and Blandino, A. (2021). Effect of Several Pretreatments on the Lactic Acid Production from Exhausted Sugar Beet Pulp. *Foods* 10, 2414. doi:10.3390/foods10102414
- Mazzoli, R. (2020). Metabolic Engineering Strategies for Consolidated Production of Lactic Acid from Lignocellulosic Biomass. *Biotechnol. Appl. Biochem.* 67 (1), 61–72. doi:10.1002/bab.1869
- Mäki-Arvela, P., Simakova, I. L., Salmi, T., and Murzin, D. Yu. (2014). Production of Lactic Acid/Lactates from Biomass and Their Catalytic Transformations to Commodities. *Chem. Rev.* 114, 1909–1971.
- McCutcheon, J., and Samples, D. (2002). *Grazing Corn Residue*. Columbus, OH ANR-10-02: The Ohio State University Extension. Available at: [https://www.agrireseau.net/bovinsboucherie/documents/0010\[1\].pdf](https://www.agrireseau.net/bovinsboucherie/documents/0010[1].pdf)
- Mejia-Gomez, C. E., and Balcázar, N. (2020). Isolation, Characterisation and Continuous Culture of *Lactobacillus* Spp. And its Potential Use for Lactic Acid Production from Whey. *Food Sci. Technol.* 40 (4), 1021–1028. doi:10.1590/fst.29619
- Meneses, N. G. T., Martins, S., Teixeira, J. A., and Mussatto, S. I. (2013). Influence of Extraction Solvents on the Recovery of Antioxidant Phenolic Compounds from brewer's Spent Grains. *Separat. Purif. Technol.* 108, 152–158. doi:10.1016/j.seppur.2013.02.015
- Mikulski, D., and Klosowski, G. (2018). Efficiency of Dilute Sulfuric Acid Pretreatment of Distillery Stillage in the Production of Cellulosic Ethanol. *Bioresour. Technol.* 268, 424–433. doi:10.1016/j.biortech.2018.08.005
- Mladenovic, D., Djukic-Vukovic, A., Stankovic, M., Milasinovic-Seremesic, M., Radosavljevic, M., Pejic, J., et al. (2019). Bioprocessing of Agro-Industrial Residues into Lactic Acid and Probiotic Enriched Livestock Feed. *J. Sci. Food Agric.* 99, 5293–5302.
- Mladenović, D., Pejic, J., Kocić-Tanackov, S., Radovanović, Ž., Djukić-Vuković, A., and Mojević, L. (2018). Lactic Acid Production on Molasses Enriched Potato Stillage by *Lactobacillus Paracasei* Immobilized onto Agro-Industrial Waste Supports. *Ind. Crops Prod.* 124, 142–148.
- Montipó, S., Pedroso, G. B., Bevilacqua, D. B., Prestes, O. D., Corona-González, R. I., and Martins, A. F. (2016). Building Block Lactic Acid from Rice Husks and Agave Bagasse. *Waste Biomass Valor.* 7, 1495–1507. doi:10.1007/s12649-016-9554-9
- Mussatto, S. I., Machado, E. M. S., Martins, S., and Teixeira, J. A. (2011). Production, Composition, and Application of Coffee and its Industrial Residues. *Food Bioproc. Technol.* 4, 661–672. doi:10.1007/s11947-011-0565-z
- Mussatto, S. I., and Roberto, I. C. (2006). Chemical Characterization and Liberation of Pentose Sugars from brewer's Spent Grain. *J. Chem. Technol. Biotechnol.* 81, 268–274. doi:10.1002/jctb.1374
- Nagarajan, D., Nandini, A., Dong, C.-D., Lee, D.-J., and Chang, J.-S. (2020). Lactic Acid Production from Renewable Feedstocks Using Poly(vinyl Alcohol)-Immobilized *Lactobacillus Plantarum* 23. *Ind. Eng. Chem. Res.* 59, 17156–17164. doi:10.1021/acs.iecr.0c01422
- Nagarajan, D., Oktarina, N., Chen, P.-T., Chen, C.-Y., Lee, D.-J., and Chang, J.-S. (2022). Fermentative Lactic Acid Production from Seaweed Hydrolysate Using *Lactobacillus* Sp. And *Weissella* Sp. *Bioresour. Technol.* 344, 126166. doi:10.1016/j.biortech.2021.126166
- Nalawade, K., Baral, P., Patil, S., Pundir, A., Kurmi, A. K., Konde, K., et al. (2020). Evaluation of Alternative Strategies for Generating Fermentable Sugars from High-Solids Alkali Pretreated Sugarcane Bagasse and Successive Valorization to L (+) Lactic Acid. *Renew. Energ.* 157, 708–717. doi:10.1016/j.renene.2020.05.089
- Nandini, A., Nagarajan, D., and Chang, J.-S. (2020). Production of Lactic Acid from Microalgal Biomass *Chlorella Vulgar* ESP-31 as a Feedstock Using PVA Immobilized Bacteria *L. Plantarum* 23. *NST Proc.* 2020, 165–169. doi:10.11594/nstp.2020.0525
- Neu, A.-K., Pleissner, D., Mehlmann, K., Schneider, R., Puerta-Quintero, G. I., and Venus, J. (2016). Fermentative Utilization of Coffee Mucilage Using *Bacillus Coagulans* and Investigation of Down-Stream Processing of Fermentation Broth for Optically Pure L(+)-lactic Acid Production. *Bioresour. Technol.* 211, 398–405. doi:10.1016/j.biortech.2016.03.122
- Norrahim, M. N. F., Ilyas, R. A., Nurazzi, N. M., Rani, M. S. A., Atikah, M. S. N., and a Shazleen, S. S. (2021). Chemical Pretreatment of Lignocellulosic Biomass for the Production of Bioproducts: An Overview. *Appl. Sci. Eng. Prog.* 14 (4), 588–605. doi:10.14416/j.asep.2021.07.004
- Nwamba, M. C., Sun, F., Mukasekuru, M. R., Song, G., Harindintwali, J. D., Boyi, S. A., et al. (2021). Trends and Hassles in the Microbial Production of Lactic Acid from Lignocellulosic Biomass. *Environ. Technol. Innovation* 21, 101337. doi:10.1016/j.eti.2020.101337
- Okano, K., Zhang, Q., Yoshida, S., Tanaka, T., Ogino, C., Fukuda, H., et al. (2010). D-Lactic Acid Production from Cellooligosaccharides and  $\beta$ -glucan Using L-LDH Gene-Deficient and Endoglucanase-Secreting *Lactobacillus Plantarum*. *Appl. Microbiol. Biotechnol.* 85, 643–650. doi:10.1007/s00253-009-2111-8
- Olszewska-Widdrat, A., Alexandri, M., López-Gómez, J. P., Schneider, R., Mandl, M., and Venus, J. (2019). Production and Purification of L-Lactic Acid in Lab and Pilot Scales Using Sweet Sorghum Juice. *Fermentation* 5 (2), 36. doi:10.3390/fermentation5020036
- Oonkhanond, B., Jonglertjunya, W., Srimarut, N., Bunpachart, P., Tantinukul, S., Nasongkla, N., et al. (2017). Lactic Acid Production from Sugarcane Bagasse by an Integrated System of Lignocellulose Fractionation, Saccharification, Fermentation, and Ex-Situ Nanofiltration. *J. Environ. Chem. Eng.* 5, 2533–2541. doi:10.1016/j.jece.2017.05.004
- Othman, M., Ariff, A. B., Kapri, M. R., Rios-Solis, L., and Halim, M. (2018). Growth Enhancement of Probiotic *Pediococcus Acidilactici* by Extractive Fermentation of Lactic Acid Exploiting Anion-Exchange Resin. *Front. Microbiol.* 9, 2554. doi:10.3389/fmicb.2018.02554
- Othman, M., Ariff, A. B., Rios-Solis, L., and Halim, M. (2017). Extractive Fermentation of Lactic Acid in Lactic Acid Bacteria Cultivation: A Review. *Front. Microbiol.* 8, 2285. doi:10.3389/fmicb.2017.02285

- Ouyang, S., Zou, L., Qiao, H., Shi, J., Zheng, Z., and Ouyang, J. (2020). One-pot Process for Lactic Acid Production from Wheat Straw by an Adapted *Bacillus* Coagulans and Identification of Genes Related to Hydrolysate-Tolerance. *Bioresour. Technol.* 315, 123855. doi:10.1016/j.biortech.2020.123855
- Pedro Silva, J., Sousa, S., Rodrigues, J., Antunes, H., Porter, J. J., Gonçalves, I., et al. (2004). Adsorption of Acid orange 7 Dye in Aqueous Solutions by Spent Brewery Grains. *Separat. Purif. Technol.* 40, 309–315. doi:10.1016/j.seppur.2004.03.010
- Pejin, J., Radosavljević, M., Kocić-Tanackov, S., Djukić-Vuković, A., and Mojović, L. (2017). Lactic Acid Fermentation of brewer's Spent Grain Hydrolysate by *Lactobacillus Rhamnosus* with Yeast Extract Addition and pH Control. *J. Inst. Brew.* 123, 98–104. doi:10.1002/jib.403
- Pin, T. C., Nakasu, P. Y. S., Mattedi, S., Rabelo, S. C., and Costa, A. C. (2019). Screening of Protic Ionic Liquids for Sugarcane Bagasse Pretreatment. *Fuel* 235, 1506–1514. doi:10.1016/j.fuel.2018.08.122
- Plavec, T. V., and Berlec, A. (2020). Safety Aspects of Genetically Modified Lactic Acid Bacteria. *Microorganisms* 8, 297. doi:10.3390/microorganisms8020297
- Pontes, R., Romaní, A., Michelin, M., Domingues, L., Teixeira, J., and Nunes, J. (2021). L-lactic Acid Production from Multi-Supply Autohydrolyzed Economically Unexploited Lignocellulosic Biomass. *Ind. Crops Prod.* 170, 113775. doi:10.1016/j.indcrop.2021.113775
- Prado-Rubio, O. A., Gasca-González, R., Fontalvo, J., Gómez-Castro, F. I., Pérez-Cisneros, E. S., and Morales-Rodríguez, R. (2020). Design and Evaluation of Intensified Downstream Technologies towards Feasible Lactic Acid Bioproduction. *Chem. Eng. Process. - Process Intensification* 158, 108174. doi:10.1016/j.cep.2020.108174
- Procentese, A., and Rehmann, L. (2018). Fermentable Sugar Production from a Coffee Processing By-Product after Deep Eutectic Solvent Pretreatment. *Bioresour. Technol. Rep.* 4, 174–180. doi:10.1016/j.biteb.2018.10.012
- Puspita Aini, A., Lee, H. W., Parningotan Sitompul, J., and Rasrendra, C. B. (2018). Production of Lactic Acid from Empty Fruit Bunch of Palm Oil Using Catalyst of Barium Hydroxide. *MATEC Web Conf.* 156, 06004. doi:10.1051/mateconf/201815606004
- Qin, L., Qian, H., and He, Y. (2017). Microbial Lipid Production from Enzymatic Hydrolysate of Pecan Nutshell Pretreated by Combined Pretreatment. *Appl. Biochem. Biotechnol.* 183 (4), 1336–1350. doi:10.1007/s12010-017-2501-9
- Radosavljevic, M., Levic, S., Belovic, M., Pejin, J., Djukic-Vukovic, A., Mojovic, L., et al. (2021). Encapsulation of *Lactobacillus Rhamnosus* in Polyvinyl Alcohol for the Production of L-(+)-Lactic Acid. *Process Biochem.* 100, 149–160.
- Radosavljevic, M., Pejin, J., Pribic, M., Kocić-Tanackov, S., Mladenovic, D., Djukic-Vukovic, A., et al. (2020). Brewing and Malting Technology By-Products as Raw Materials in L-(+)-lactic Acid Fermentation. *J. Chem. Technol. Biotechnol.* 95, 339–347.
- Rahman, M. S., H. Mondal, M. I., Yeasmin, M. S. S., Sayeed, M. A., Hossain, M. A., and Ahmed, M. B. (2020). Conversion of Lignocellulosic Corn Agro-Waste into Cellulose Derivative and its Potential Application as Pharmaceutical Excipient. *Processes* 8, 711. doi:10.3390/pr8060711
- Rapado, P., Faba, L., and Ordóñez, S. (2021). Influence of Delignification and Reaction Conditions in the Aqueous Phase Transformation of Lignocellulosic Biomass to Platform Molecules. *Bioresour. Technol.* 321, 124500. doi:10.1016/j.biortech.2020.124500
- Rawoof, S. A. A., Kumar, P. S., Vo, D.-V. N., Devaraj, K., Mani, Y., Devaraj, T., et al. (2021). Production of Optically Pure Lactic Acid by Microbial Fermentation: a Review. *Environ. Chem. Lett.* 19, 539–556. doi:10.1007/s10311-020-01083-w
- Redondo-Gómez, C., Quesada, M. R., Astúa, S. V., Zamora, J. P. M., Lopretti, M., and Vega-Baudrit, J. R. (2020). Biorefinery of Biomass of Agro-Industrial Banana Waste to Obtain High-Value Biopolymers. *Molecules* 25, 3829.
- Reinold, M. R. (1997). *Manual pratico de cervejaria*. first edition. São Paulo: ADEN Editora e Comunicações Ltda.
- Reshmy, R., Philip, E., Madhavan, A., Sirohi, R., Pugazhendhi, A., Binod, P., et al. (2022). Lignocellulose in Future Biorefineries: Strategies for Cost-Effective Production of Biomaterials and Bioenergy. *Bioresour. Technol.* 344, 126241. doi:10.1016/j.biortech.2021.126241
- Rojas, M. J., Siqueira, P. F., Miranda, L. C., Tardioli, P. W., and Giordano, R. L. C. (2014). Sequential Proteolysis and Cellulytic Hydrolysis of Soybean Hulls for Oligopeptides and Ethanol Production. *Ind. Crops Prod.* 61, 202–210. doi:10.1016/j.indcrop.2014.07.002
- Rouches, E., Zhou, S., Steyer, J. P., and Carrere, H. (2016). White-rot Fungi Pretreatment of Lignocellulosic Biomass for Anaerobic Digestion: Impact of Glucose Supplementation. *Process Biochem.* 51, 1784–1792. doi:10.1016/j.procbio.2016.02.003
- Sánchez, C., Egués, I., García, A., Llano-Ponte, R., and Labidi, J. (2012). Lactic Acid Production by Alkaline Hydrothermal Treatment of Corn Cobs. *Chem. Eng. J.* 181–182, 655–660.
- Schroedter, L., Streffer, F., Streffer, K., Unger, P., and Venus, J. (2021). Biorefinery Concept Employing *Bacillus* Coagulans: LX-Lignin and L-(+)-Lactic Acid from Lignocellulose. *Microorganisms* 9, 1810. doi:10.3390/microorganisms9091810
- Shahab, R. L., Luterbacher, J. S., Brethauer, S., and Studer, M. H. (2018). Consolidated Bioprocessing of Lignocellulosic Biomass to Lactic Acid by a Synthetic Fungal-Bacterial Consortium. *Biotechnol. Bioeng.* 115, 1207–1215. doi:10.1002/bit.26541
- Shahbandeh, M. (2021a). Coffee Production Worldwide from 2003/04 to 2019/20 (In Million 60 Kilogram Bags). March 4. Available at: <https://www.statista.com/statistics/263311/worldwide-production-of-coffee/> (Accessed October 26, 2021).
- Shahbandeh, M. (2021b). Corn Industry Worldwide - Statistics & Facts. July 23. Available at: <https://www.statista.com/topics/7169/corn-industry-worldwide/#dossierKeyfigures>.
- Sharma, H. K., Xu, C., and Qin, W. (2019). Biological Pretreatment of Lignocellulosic Biomass for Biofuels and Bioproducts: An Overview. *Waste Biomass Valor.* 10, 235–251. doi:10.1007/s12649-017-0059-y
- Shen, X., and Sun, R. (2021). Recent Advances in Lignocellulose Prior-Fractionation for Biomaterials, Biochemicals, and Bioenergy. *Carbohydr. Polym.* 261, 117884. doi:10.1016/j.carbpol.2021.117884
- Shi, S., Guan, W., Blerch, D., and Li, J. (2021). Improving the Enzymatic Digestibility of Alkaline-Pretreated Lignocellulosic Biomass Using polyDADMAC. *Ind. Crops Prod.* 162, 113244. doi:10.1016/j.indcrop.2021.113244
- Shi, Z., Wei, P., Zhu, X., Cai, J., Huang, L., and Xu, Z. (2012). Efficient Production of L-Lactic Acid from Hydrolysate of Jerusalem Artichoke with Immobilized Cells of *Lactococcus Lactis* in Fibrous Bed Bioreactors. *Enzyme Microb. Technol.* 51, 263–268. doi:10.1016/j.enzmictec.2012.07.007
- Shuddhodana, D. M., Mohnot, D., Biswas, R., and Bisaria, V. S. (2016). “Enzymatic Hydrolysis of Lignocellulosic Residues,” in *Biomass Fractionation Technologies for a Lignocellulosic Feedstock Based Biorefinery* (Amsterdam: Elsevier), 543–560. doi:10.1016/b978-0-12-802323-5.00023-2
- Si, H., Liang, X., Liu, S., Xu, M., Wang, J., and Hua, D. (2020). Efficient Production of L-Lactic Acid from Corn Straw Hydrolysate. *IOP Conf. Ser. Earth Environ. Sci.* 514, 052049. doi:10.1088/1755-1315/514/5/052049
- Sidiras, D., Politi, D., Giakoumakis, G., and Salapa, I. (2022). Simulation and Optimization of Organosolv Based Lignocellulosic Biomass Refinery: A Review. *Bioresour. Technol.* 343, 126158. doi:10.1016/j.biortech.2021.126158
- Sitompul, J. P., Simangunsong, R. F., Asrizal, A. A., Alisyahbana, H., Lee, H. W., and Rasrendra, C. B. (2014). Catalytic Conversion of Empty Fruit Bunch of Palm Oil for Producing Lactic Acid. *Proced. Chem.* 9, 88–93. doi:10.1016/j.proche.2014.05.011
- Smits, J., Bevers, L., van Haastert, M., Wiertz, R., and Kroon, H. (2019). Fast Screening of Optimal Acid-Pretreatment Conditions in the Conversion of wood to Lignocellulosic Sugars. *Bioresour. Technol. Rep.* 5, 220–229. doi:10.1016/j.biteb.2019.01.016
- Sun, Y., Li, X., Wei, C., Qi, W., and Xiu, Z. (2021). An Aptly Industrialized Bioprocess for Lactic Acid Production from Corn stover Using Thermotolerant Microbial Consortia. *Bioproc. Biosyst Eng* 44, 2445–2454. doi:10.1007/s00449-021-02616-5
- Tan, J., Abdel-Rahman, M. A., and Sonomoto, K. (2018). Biorefinery-Based Lactic Acid Fermentation: Microbial Production of Pure Monomer Product. *Adv. Polym. Sci.* 279, 27–66.
- Tarraran, L., and Mazzoli, R. (2018). Alternative Strategies for Lignocellulose Fermentation through Lactic Acid Bacteria: the State of the Art and Perspectives. *FEMS Microbiol. Lett.* 365 (15), fny126. doi:10.1093/femsle/fny126
- Tejayadi, S., and Cheryan, M. (2005). Lactic Acid from Cheese Whey Permeate. Productivity and Economics. *Appl. Microbiol. Biotechnol.* 43, 242–248.
- Thakur, A., Panesar, P. S., and Saini, M. S. (2019). L-(+)-Lactic Acid Production by Immobilized *Lactobacillus Casei* Using Low Cost Agro-Industrial Waste as Carbon and Nitrogen Sources. *Waste Biomass Valor.* 10, 1119–1129. doi:10.1007/s12649-017-0129-1

- Thygesen, A., Tsapekos, P., Alvarado-Morales, M., and Angelidaki, I. (2021). Valorization of Municipal Organic Waste into Purified Lactic Acid. *Bioresour. Technol.* 342, 125933. doi:10.1016/j.biortech.2021.125933
- Tian, X., Liu, X., Zhang, Y., Chen, Y., Hang, H., Chu, J., et al. (2021). Metabolic Engineering Coupled with Adaptive Evolution Strategies for the Efficient Production of High-Quality L-Lactic Acid by *Lactobacillus Paracasei*. *Bioresour. Technol.* 323, 124549. doi:10.1016/j.biortech.2020.124549
- Tišma, M., Bucić-Kojić, A., and Planinić, M. (2021). Bio-based Products from Lignocellulosic Waste Biomass: A State of the Art. *Chem. Biochem. Eng. Q.* 35 (2), 139–156.
- Tramontina, R., Brenelli, L. B., Sodr , V., Franco Cairo, J. P., Trav lia, B. M., Egawa, V. Y., et al. (2020). Enzymatic Removal of Inhibitory Compounds from Lignocellulosic Hydrolysates for Biomass to Bioproducts Applications. *World J. Microbiol. Biotechnol.* 36, 166. doi:10.1007/s11274-020-02942-y
- Tsegaye, B., Gupta, P., Balomajumder, C., and Roy, P. (2021). Optimization of Organosolv Pretreatment Conditions and Hydrolysis by *Bacillus* Sp. BMP01 for Effective Depolymerization of Wheat Straw Biomass. *Biomass Conv. Bioref.* 11 (6), 2747–2761. doi:10.1007/s13399-020-00691-4
- Tu, W.-L., Hsu, T.-C., Wang, C.-A., Guo, G.-L., and Chao, Y. (2019). Using Novel *Lactobacillus Plantarum* to Produce Lactic Acid from Lignocellulosic Biomass in an Integrated Simultaneous Saccharification and Fermentation Process. *BioResources* 14 (2), 3873–3885.
- Turner, T. L., Zhang, G.-C., Oh, E. J., Subramaniam, V., Adiputra, A., Subramaniam, V., et al. (2016). Lactic Acid Production from Cellobiose and Xylose by engineered *Saccharomyces Cerevisiae*. *Biotechnol. Bioeng.* 113, 1075–1083. doi:10.1002/bit.25875
- Unrean, P. (2018). Optimized Feeding Schemes of Simultaneous Saccharification and Fermentation Process for High Lactic Acid Titer from Sugarcane Bagasse. *Ind. Crops Prod.* 111, 660–666. doi:10.1016/j.indcrop.2017.11.043
- Upadhyaya, B. P., DeVeaux, L. C., and Christopher, L. P. (2014). Metabolic Engineering as a Tool for Enhanced Lactic Acid Production. *Trends Biotechnol.* 32 (12), 637–644. doi:10.1016/j.tibtech.2014.10.005
- Usmani, Z., Sharma, M., Awasthi, A. K., Lukk, T., Tuohy, M. G., Gong, L., et al. (2021). Lignocellulosic Biorefineries: The Current State of Challenges and Strategies for Efficient Commercialization. *Renew. Sustain. Energy Rev.* 148, 111258. doi:10.1016/j.rser.2021.111258
- Usmani, Z., Sharma, M., Gupta, P., Karpichev, Y., Gathergood, N., Bhat, R., et al. (2020). Ionic Liquid Based Pretreatment of Lignocellulosic Biomass for Enhanced Bioconversion. *Bioresour. Technol.* 304, 123003. doi:10.1016/j.biortech.2020.123003
- Utrilla, J., Vargas-Tah, A., Trujillo-Martinez, B., Gosset, G., and Martinez, A. (2016). Production of D-Lactate from Sugarcane Bagasse and Corn stover Hydrolysates Using Metabolic Engineered *Escherichia coli* Strains. *Bioresour. Technol.* 220, 208–214. doi:10.1016/j.biortech.2016.08.067
- van der Pol, E. C., Vaessen, E., Weusthuis, R. A., and Eggink, G. (2016). Identifying Inhibitory Effects of Lignocellulosic By-Products on Growth of Lactic Acid Producing Micro-organisms Using a Rapid Small-Scale Screening Method. *Bioresour. Technol.* 209, 297–304. doi:10.1016/j.biortech.2016.03.037
- Vanmarcke, G., Demeke, M. M., Foulqui -Moreno, M. R., and Thevelein, J. M. (2021). Identification of the Major Fermentation Inhibitors of Recombinant 2G Yeasts in Diverse Lignocellulose Hydrolysates. *Biotechnol. Biofuels* 14, 92. doi:10.1186/s13068-021-01935-9
- Velvizhi, G., Balakumar, K., Shetti, N. P., Ahmad, E., Kishore Pant, K., and Aminabhavi, T. M. (2022). Integrated Biorefinery Processes for Conversion of Lignocellulosic Biomass to Value Added Materials: Paving a Path towards Circular Economy. *Bioresour. Technol.* 343, 126151. doi:10.1016/j.biortech.2021.126151
- Verma, D., and Subudhi, S. (2021). 'Lactobacillus Sp. Strain TERI-D3', as Microbial Cell Factory for Fermentative Production of Lactic Acid'. *Curr. Res. Green Sustain. Chem.* 4, 100059. doi:10.1016/j.crgsc.2021.100059
- Vishnu Prasad, J., Sahoo, T. K., Naveen, S., and Jayaraman, G. (2020). Evolutionary Engineering of *Lactobacillus Bulgaricus* Reduces Enzyme Usage and Enhances Conversion of Lignocellulosics to D-Lactic Acid by Simultaneous Saccharification and Fermentation. *Biotechnol. Biofuels* 13, 171. doi:10.1186/s13068-020-01812-x
- Wang, Y., Wang, M., Cai, D., Wang, B., Wang, Z., Qin, P., et al. (2016). Efficient L-Lactic Acid Production from Sweet Sorghum Bagasse by Open Simultaneous Saccharification and Fermentation. *RSC Adv.* 6, 35771–35777. doi:10.1039/c6ra04538c
- Wang, Z.-K., Li, H., Lin, X.-C., Tang, L., Chen, J.-J., Mo, J.-W., et al. (2020). Novel Recyclable Deep Eutectic Solvent Boost Biomass Pretreatment for Enzymatic Hydrolysis. *Bioresour. Technol.* 307, 123237. doi:10.1016/j.biortech.2020.123237
- Wei, C., Liu, G., Zhang, J., and Bao, J. (2018). Elevating Fermentation Yield of Cellulosic Lactic Acid in Calcium Lactate Form from Corn stover Feedstock. *Ind. Crops Prod.* 126, 415–420. doi:10.1016/j.indcrop.2018.10.041
- Werlang, E. B., Ibarra, E. S., Neves, F. d. F., Julich, J., Martinez, A., and Schneider, R. d. C. d. S. (2020). D-lactate Production from *Spirulina* (*Arthrospira Platensis*) Biomass Using Lactogenic *Escherichia coli*. *Bioresour. Technol. Rep.* 12, 100598. doi:10.1016/j.biteb.2020.100598
- Wischnal, D., Arias, J. M., Modesto, L. F., de Fran a Passos, D., and Pereira, N., Jr. (2019). Lactic Acid Production from Sugarcane Bagasse Hydrolysates by *Lactobacillus Pentosus* : Integrating Xylose and Glucose Fermentation. *Biotechnol. Prog.* 35 (1), e2718. doi:10.1002/btpr.2718
- Wu, J., Chandra, R., Takada, M., Del Rio, P., Kim, K. H., Kim, C. S., et al. (2020). Alkaline Sulfonation and Thermomechanical Pulping Pretreatment of Softwood Chips and Pellets to Enhance Enzymatic Hydrolysis. *Bioresour. Technol.* 315, 123789. doi:10.1016/j.biortech.2020.123789
- Wu, J., Xin, Y., Kong, J., and Guo, T. (2021). Genetic Tools for the Development of Recombinant Lactic Acid Bacteria. *Microb. Cel Fact* 20, 118. doi:10.1186/s12934-021-01607-1
- Wu, M., Gong, L., Ma, C., and He, Y.-C. (2021). Enhanced Enzymatic Saccharification of Sorghum Straw by Effective Delignification via Combined Pretreatment with Alkali Extraction and Deep Eutectic Solvent Soaking. *Bioresour. Technol.* 340, 125695. doi:10.1016/j.biortech.2021.125695
- Wu, J., Chandra, R., and Saddler, J. (2019). Alkali-oxygen Treatment Prior to the Mechanical Pulping of Hardwood Enhances Enzymatic Hydrolysis and Carbohydrate Recovery through Selective Lignin Modification. *Sustain. Energy Fuels* 3 (1), 227–236. doi:10.1039/c8se00452h
- Xu, H., Kong, Y., Peng, J., Song, X., Liu, Y., Su, Z., et al. (2021). Comprehensive Analysis of Important Parameters of Choline Chloride-Based Deep Eutectic Solvent Pretreatment of Lignocellulosic Biomass. *Bioresour. Technol.* 319, 124209. doi:10.1016/j.biortech.2020.124209
- Xu, S., Lan, K., Li, J., He, T., and Hu, C. (2018). Separation of Lactic Acid from Synthetic Solutions and the Mixture Directly Derived from Corn stover by Aqueous Two Phase Extraction. *Separat. Purif. Technol.* 204, 281–289. doi:10.1016/j.seppur.2018.04.086
- Yaashikaa, P. R., Senthil Kumar, P., and Varjani, S. (2022). Valorization of Agro-Industrial Wastes for Biorefinery Process and Circular Bioeconomy: a Critical Review. *Bioresour. Technol.* 343, 126126. doi:10.1016/j.biortech.2021.126126
- Yadav, N., Nain, L., and Khare, S. K. (2021). One-pot Production of Lactic Acid from rice Straw Pretreated with Ionic Liquid. *Bioresour. Technol.* 323, 124563. doi:10.1016/j.biortech.2020.124563
- Yadav, N., Pranaw, K., and Khare, S. K. (2020). Screening of Lactic Acid Bacteria Stable in Ionic Liquids and Lignocellulosic By-Products for Bio-Based Lactic Acid Production. *Bioresour. Technol. Rep.* 11, 100423. doi:10.1016/j.biteb.2020.100423
- Yang, X., Lai, Z., Lai, C., Zhu, M., Li, S., Wang, J., et al. (2013). Efficient Production of L-Lactic Acid by an Engineered *Thermoanaerobacterium Aotearoense* with Broad Substrate Specificity. *Biotechnol. Biofuels* 6, 124. doi:10.1186/1754-6834-6-124
- Yankov, D. (2020). Aqueous Two-phase Systems as a Tool for Bioreseparation - Emphasis on Organic Acids. *Phys. Sci. Rev.* 5 (9), 20180067. doi:10.1515/psr-2018-0067
- Yao, R., Qi, B., Deng, Sh., Liu, N., Peng, Sh., and Cui, Q. (2007). Use of Surfactants in Enzymatic Hydrolysis of rice. *BioResources* 2 (3), 389–398.
- Yoshida, S., Okano, K., Tanaka, T., Ogino, C., and Kondo, A. (2011). Homo-D-lactic Acid Production from Mixed Sugars Using Xylose-Assimilating Operon-Integrated *Lactobacillus Plantarum*. *Appl. Microbiol. Biotechnol.* 92, 67–76. doi:10.1007/s00253-011-3356-6
- Younas, R., Zhang, S., Zhang, L., Luo, G., Chen, K., Cao, L., et al. (2016). Lactic Acid Production from rice Straw in Alkaline Hydrothermal Conditions in Presence of NiO Nanoplates. *Catal. Today* 274, 40–48. doi:10.1016/j.cattod.2016.03.052
- Zaini, N. A. B. M., Chatzifragkou, A., and Charalampopoulos, D. (2019). Alkaline Fractionation and Enzymatic Saccharification of Wheat Dried

- Distillers Grains with Solubles (DDGS). *Food Bioproducts Process.* 118, 103–113. doi:10.1016/j.fbp.2019.09.006
- Zaini, N. A. B. M., Chatzifragkou, A., and Charalampopoulos, D. (2019). Microbial Production of L-Lactic Acid from Dried Distiller's Grains with Solubles. *Eng. Life Sci.* 19, 21–30. doi:10.1002/elsc.201800077
- Zhang, F., Lan, W., Li, Z., Zhang, A., Tang, B., Wang, H., et al. (2021). Co-production of Functional Xylo-Oligosaccharides and Fermentable Sugars from Corn stover through Fast and Facile ball Mill-Assisted Alkaline Peroxide Pretreatment. *Bioresour. Technol.* 337, 125327. doi:10.1016/j.biortech.2021.125327
- Zhang, L., Li, X., Yong, Q., Yang, S.-T., Ouyang, J., and Yu, S. (2016). Impacts of Lignocellulose-Derived Inhibitors on L-Lactic Acid Fermentation by *Rhizopus Oryzae*. *Bioresour. Technol.* 203, 173–180. doi:10.1016/j.biortech.2015.12.014
- Zhang, Y., Kumar, A., Hardwidge, P. R., Tanaka, T., Kondo, A., and Vadlani, P. V. (2016). D-Lactic Acid Production from Renewable Lignocellulosic Biomass via Genetically modified *Lactobacillus Plantarum*. *Biotechnol. Prog.* 32 (2), 271–278. doi:10.1002/btpr.2212
- Zhang, Y., Vadlani, P. V., Kumar, A., Hardwidge, P. R., Govind, R., Tanaka, T., et al. (2016). Enhanced D-Lactic Acid Production from Renewable Resources Using Engineered *Lactobacillus Plantarum*. *Appl. Microbiol. Biotechnol.* 100, 279–288. doi:10.1007/s00253-015-7016-0
- Zhang, Z., Li, Y., Zhang, J., Peng, N., Liang, Y., and Zhao, S. (2020). High-Titer Lactic Acid Production by *Pediococcus Acidilactici* PA204 from Corn Stover through Fed-Batch Simultaneous Saccharification and Fermentation. *Microorganisms* 8, 1491. doi:10.3390/microorganisms8101491
- Zhao, L., Sun, Z.-F., Zhang, C.-C., Nan, J., Ren, N.-Q., Lee, D.-J., et al. (2022). Advances in Pretreatment of Lignocellulosic Biomass for Bioenergy Production: Challenges and Perspectives. *Bioresour. Technol.* 343, 126123. doi:10.1016/j.biortech.2021.126123
- Zheng, J., Wittouck, S., Salvetti, E., Franz, C. M. A. P., Harris, H. M. B., Mattarelli, P., et al. (2020). A Taxonomic Note on the Genus *Lactobacillus*: Description of 23 Novel Genera, Emended Description of the Genus *Lactobacillus* Beijerinck 1901, and union of *Lactobacillaceae* and *Leuconostocaceae*. *Int. J. Syst. Evol. Microbiol.* 70, 2782–2858. doi:10.1099/ijsem.0.004107
- Zheng, X., Xian, X., Hu, L., Tao, S., Zhang, X., Liu, Y., et al. (2021). Efficient Short-Time Hydrothermal Depolymerization of Sugarcane Bagasse in One-Pot for Cellulosic Ethanol Production without Solid-Liquid Separation, Water Washing, and Detoxification. *Bioresour. Technol.* 339, 125575. doi:10.1016/j.biortech.2021.125575
- Zhou, J., Ouyang, J., Xu, Q., and Zheng, Z. (2016). Cost-effective Simultaneous Saccharification and Fermentation of L-lactic Acid from Bagasse Sulfite Pulp by *Bacillus Coagulans* CC17. *Bioresour. Technol.* 222, 431–438. doi:10.1016/j.biortech.2016.09.119
- Zhou, X., Sun, Y., Zhan, H., Liu, H., Wang, X., Xu, Y., et al. (2021). Ionic Liquid-Based Multi-Stage Sugaring-Out Extraction of Lactic Acid from Simulated Broth and Actual Lignocellulosic Fermentation Broth. *Bioresour. Bioproc.* 8, 123. doi:10.1186/s40643-021-00481-4
- Zulkefli, S., Abdulmalek, E., and Abdul Rahman, M. B. (2017). Pretreatment of Oil palm Trunk in Deep Eutectic Solvent and Optimization of Enzymatic Hydrolysis of Pretreated Oil palm Trunk. *Renew. Energ.* 107, 36–41. doi:10.1016/j.renene.2017.01.037
- Žunar, B., Trontel, A., Svetec Miklenić, M., Prah, J. L., Štafa, A., Mardetko, N., et al. (2020). Metabolically Engineered *Lactobacillus Gasserii* JCM 1131 as a Novel Producer of Optically Pure L- and D-Lactate. *World J. Microbiol. Biotechnol.* 36, 111. doi:10.1007/s11274-020-02887-2

**Conflict of Interest:** The author declares that the research was conducted in the absence of any commercial or financial relationships that could be construed as a potential conflict of interest.

**Publisher's Note:** All claims expressed in this article are solely those of the authors and do not necessarily represent those of their affiliated organizations, or those of the publisher, the editors and the reviewers. Any product that may be evaluated in this article, or claim that may be made by its manufacturer, is not guaranteed or endorsed by the publisher.

Copyright © 2022 Yankov. This is an open-access article distributed under the terms of the Creative Commons Attribution License (CC BY). The use, distribution or reproduction in other forums is permitted, provided the original author(s) and the copyright owner(s) are credited and that the original publication in this journal is cited, in accordance with accepted academic practice. No use, distribution or reproduction is permitted which does not comply with these terms.





# Structure-Property Relationship for Different Mesoporous Silica Nanoparticles and its Drug Delivery Applications: A Review

Parya Kazemzadeh<sup>1</sup>, Khalil Sayadi<sup>2</sup>, Ali Toolabi<sup>3</sup>, Jalil Sayadi<sup>4</sup>, Malihe Zeraati<sup>5</sup>, Narendra Pal Singh Chauhan<sup>6\*</sup> and Ghasem Sargazi<sup>7\*</sup>

<sup>1</sup>Department of Chemistry, Lorestan University, Khorramabad, Iran, <sup>2</sup>Department of Chemistry, Young Researchers Society, Shahid Bahonar University of Kerman, Kerman, Iran, <sup>3</sup>Department of Environmental Health Engineering, School of Public Health, Bam University of Medical Sciences, Bam, Iran, <sup>4</sup>Department Environmental Engineering, University of Zabol, Zabol, Iran, <sup>5</sup>Department of Materials Engineering, Shahid Bahonar University of Kerman, Kerman, Iran, <sup>6</sup>Department of Chemistry, Faculty of Science, Bhupal Nobles' University, Udaipur, India, <sup>7</sup>Noncommunicable Diseases Research Center, Bam University of Medical Sciences, Bam, Iran

## OPEN ACCESS

### Edited by:

Sudip Mukherjee,  
Rice University, United States

### Reviewed by:

Ravindra Pratap Singh,  
Indira Gandhi National Tribal  
University, India  
Vijay Sagar Madamsetty,  
Mayo Clinic Florida, United States

### \*Correspondence:

Ghasem Sargazi  
g.sargazi@gmail.com  
Narendra Pal Singh Chauhan  
narendrapalsingh14@gmail.com

### Specialty section:

This article was submitted to  
Nanoscience,  
a section of the journal  
Frontiers in Chemistry

**Received:** 29 November 2021

**Accepted:** 25 January 2022

**Published:** 14 March 2022

### Citation:

Kazemzadeh P, Sayadi K, Toolabi A, Sayadi J, Zeraati M, Chauhan NPS and Sargazi G (2022) Structure-Property Relationship for Different Mesoporous Silica Nanoparticles and its Drug Delivery Applications: A Review. *Front. Chem.* 10:823785. doi: 10.3389/fchem.2022.823785

Mesoporous silica nanoparticles (MSNs) are widely used as a promising candidate for drug delivery applications due to silica's favorable biocompatibility, thermal stability, and chemical properties. Silica's unique mesoporous structure allows for effective drug loading and controlled release at the target site. In this review, we have discussed various methods of MSNs' mechanism, properties, and its drug delivery applications. As a result, we came to the conclusion that more *in vivo* biocompatibility studies, toxicity studies, bio-distribution studies and clinical research are essential for MSN advancement.

**Keywords:** mesoporous, silica, nanoparticles, properties, drug delivery

## INTRODUCTION

One of the most important purposes pursued by nanotechnology is the production of nanoparticles that have the desired distribution of drug in the body (El-Boubbou, 2018; Tandel et al., 2018). Over the past two decades, researchers have concluded that a vital step in the development of drugs is to focus on designing new drug delivery systems (NDDS) (Martínez-Ortega et al., 2019). Ideally, all new systems should improve the stability, absorption, drug concentration, and long-term release of the drug in the target tissue. In addition (Djekic et al., 2019), reducing the number of drug injections to increase patient comfort (Reibaldi et al., 2019), advanced drug delivery systems (Bhatia, 2016), pharmacokinetics of proteins (Turner and Balu-Iyer, 2018), and peptides (Hughes, 2005) that are usually low in half-time should be considered. The ultimate goal of the drug research is to safely transfer the drug to the suitable location in the body at the right time (Jahangirian et al., 2017; Yin and Zhang, 2020). However, for many drugs, these ideals are often impossible. For example, the oral method is usually the best way to use a drug due to non-invasiveness, but peptides and proteins will be absorbed and effectiveness will be reduced due to the acidic properties of the stomach, as well as the effects of the first transfer of the liver, such as drug loss due to metabolic processes prior to systemic rotation and resistance by the intestine (Ahmed and Aljaeid, 2016; Khadair et al., 2016). Finally, its accessibility will be greatly diminished. Nanotechnology, with the elimination of many problems with traditional drugs, allows the application of oral drugs that were previously not usable. In some cases, co-administration of the drug with nanoparticles can increase the



bioavailability of the drug in a way that is useful for oral use (Chen et al., 2018). Nanoparticles protect the drugs that are susceptible to degradation in the body and give more durability to the drug's presence in the blood, attach the drug to the target tissue, release the drug in the target site, and increase the efficacy of the drug several times over (McClements, 2018; Paunovska et al., 2018). The main roles of the preparation of nano-drug delivery systems are to control particle size (Cooley et al., 2018), surface properties (Banerjee et al., 2016) and release of the drug in a good therapeutic dose (Kamaly et al., 2016). Generally, by fabricating silica, the micelles self-assemble around a template and then remove the template using a suitable method such as calcination. The design and manufacture of controlled drug release systems can be very helpful in cancer drug therapies. So far, many substances have been introduced as drug release systems, among which biodegradable polymer materials (Goetjen et al., 2020), ceramic materials such as hydroxyapatite (Martínez-Vázquez et al., 2015), and calcium phosphates (Kapoor et al., 2015) can be mentioned. Recently, mesoporous materials have attracted the most attention in this regard. In fact, the porosity of silica mesoporous materials allows biologically active molecules of different sizes to locate in the cavities of these materials (Vallet-Regí et al., 2007). Also, the regular porosity of these materials makes it possible to achieve a convenient loading and release rate (Anglin et al., 2008). Conversely, as the adsorption of molecules into mesoporous (Manzano and Vallet-Regí, 2019) is a surface phenomenon and the specific surface of these materials also results in the absorption of more active biological molecules (Manzano and Vallet-Regí, 2019). What is important in designing a drug release system is biocompatibility and biodegradability (Jindal et al., 2019). Recent research is based on the development of drug delivery systems that are stable in structure and capable of carrying large volumes of drugs without the problem of early release to target tissues or even small intracellular organs (Manzano and Vallet-Regí, 2019). Among many of the materials that have been investigated in terms of their stable structure for drug delivery, silica mesoporous nanomaterials are known to be biocompatible with defined structures and certain surface specific properties (Dudarko et al., 2019). Silica mesoporous is known as a selective material for the biological applications of inorganic nanoparticles. Typically, silica meso-nanostructure coated with semiconductor quantum dots, such as high-stability cadmium sulfide and selenide (Sharma et al., 2019; Tarrahi et al., 2019), has the potential for chemical change and high biocompatibility that can be used for many diagnostic biomedical applications. In addition, meso silica nanoparticle can be applied to increase the biocompatibility of several drug delivery systems, such as magnetic nanoparticles (Vallet-Regí et al., 2018), biopolymers (Nairi et al., 2018) and micelles (Zhang et al., 2019). In this article, we have reviewed and studied the introduction of various types of silica mesostructure and their application in various drug delivery processes, the advantages of the application of

silica nanoparticles in drug delivery systems, and biocompatibility and mechanism reception by the host cell.

## MESOPOROUS SILICA MATERIALS AND ITS SYNTHETIC METHOD

In general, the porous nanoparticles are divided into three groups according to their size: Microporous (pore size: <2 nm), mesoporous (pore size: 2–50 nm) and macroporous (pore size: >50 nm) (Vallet-Regí, 2012). The mesoporous silica was produced in two steps: first, the micelles self-assembled around a template and then the template was removed *via* calcination (**Figure 1**). Mesoporous nanomaterials with a well-defined architecture have a high density of silanol (Si-OH) functional groups at their surface that can be modified with a wide range of organic groups to stabilize biomolecules and other applications (Wang, 2009).

Chen and coworkers developed the “DOX@MSNs-CAIX” targeted and redox-responsive drug delivery system, in which MSNs were used as the vehicle for loading chemotherapeutic drug doxorubicin (DOX) and CAIX grafted on MSNs by disulfide bonds. MSNs-CAIX are a promising medication delivery method for cancer treatment with a specific target (Meynen et al., 2009).

In some cases, additional functional groups penetrate into the mesoporous nanoparticles due to fill the silica walls, and consequently reducing the size of the pore and drug loading, despite the fact that this controls drug release. Modification of the nanoparticles surface with a variety of functional groups can cause changes in electrostatic forces, hydrophilic or hydrophobic forces, and internal reactions of the drug and the matrix (Meynen et al., 2009). Various methods for producing silica mesoporous nanomaterials have been reported that show, with sufficient knowledge of preparation methods, pore size engineering, morphological control, and structural properties, that these materials can be of good quality. In addition, the manufacturing of these materials by modifying different of agents, such as a diversity of surfactants, acquires the specific mechanism and the internal reaction of silica with template molecules (Wang et al., 2016; Yi, 2021). For example, through direct reaction of  $S^{+}I^{-}$ , they occur between a positively charged molecular based organized system (MOS) activating surface ion by and a negatively charged silicate source. Two kinds of mechanisms including liquid crystal templating, self-assembly mechanisms have been proposed for mesoporous synthesis (Meynen et al., 2009). **Figure 2** presents an overview of possible pathways for their synthesis.

These materials can also be manufactured using surface activators called polymeric based organized systems (POS) through the indirect reaction of template with a silicate source in an acidic media. Conversely, the interaction between the MOS and the inorganic silicate source ( $S^{0}I^{0}$ ) leads to the formation of hollow mesoporous silica (HMS) materials (Meynen et al., 2009). Many factors such as pH, salts, inflammasome, co-solvents, co-surfactants, concentration, specific silicate source, solvent, and temperature are involved in the organization of mesopores (Zhao et al., 2000). In a typical method of preparation of mesosilica

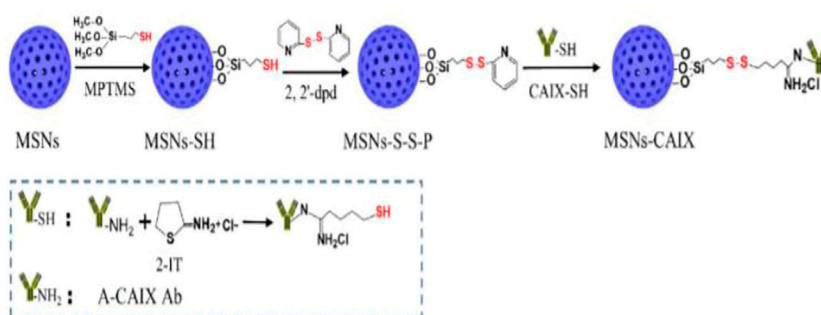


**FIGURE 1** | Preparation route for CAIX guided mesoporous silica nanoparticles (Chen et al., 2020).

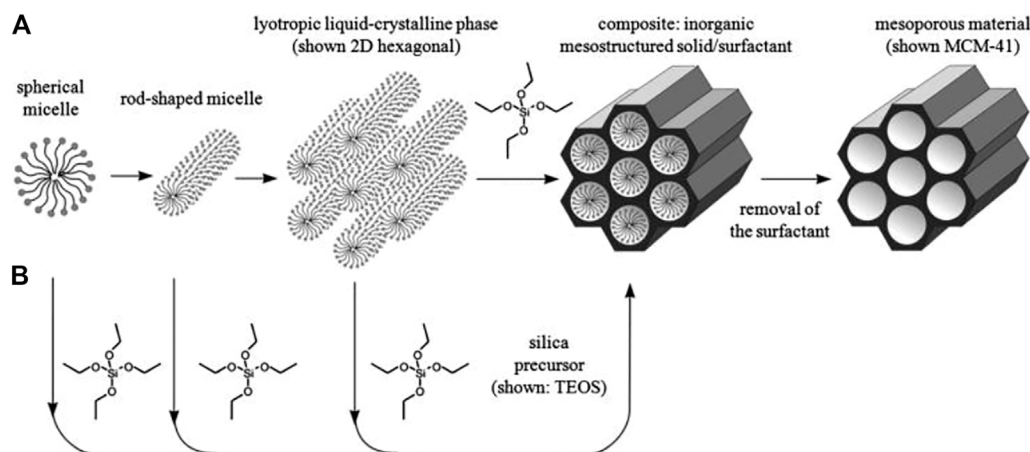


**FIGURE 2** | Possible pathways for the synthesis of mesoporous materials (A) Liquid crystal templating and (B) self-assembly.

materials, the dissolution of template molecules in the solvent and the addition of a silicate source such as tetraethoxy ortho silane (TEOS), meta silicate ( $\text{Na}_2\text{SiO}_3$ ), and gaseous silica are performed. After some time at a certain temperature, the hydrolysis and condensation processes begin. Finally, the resulting product is washed and dried, and by removing the mold using calcining, the silica mesoporous is obtained (Kim et al., 2000).

Mesoporous silica nanoparticles have shown to have excellent properties for biomedical applications. These properties include porous ordered and well aligned structure, which shows fine control of drug delivery and release kinetics; larger surface area and pore volume, which shows high potential for molecule loading and dissolution enhancement; tunable particle size in between 50 and 300 nm which is suitable for facile endocytosis by living cells; and silanol-contained surfaces have two functional surfaces with cylindrical pore surface, exhibit better control over drug loading and release; and have excellent biocompatibility.

The oral route is the most popular route for drug delivery, despite the fact that many medicines, particularly highly pH- and/or enzymatic biodegradable peptide substances, are extremely difficult to manufacture and obtain efficient intestine absorption. Only if the drug 1) is substantially present as a solution in the

gastrointestinal tract, 2) is able to penetrate through the intestinal mucus, 3) overcomes the various gastrointestinal barriers, and 4) provides an effective therapeutic dose that is efficient for systematic absorption of an active substance, is oral ingestion possible. As a result, improving the oral bioavailability of poorly soluble medications is still a major challenge for the pharmaceutical industry. Despite the fact that several traditional drug carriers have solved some of the problems associated with the oral delivery of poorly soluble medicines, only a few have fulfilled commercialization requirements. Due to these limitations, scientists have begun to rethink their methods for targeted drug delivery systems and researchers have begun looking for alternate vectorized carriers (Florek et al., 2017).

Lee et al. synthesized MSNs with varying concentrations of positive surface charges (Lee et al., 2008). The positive surface charge was achieved by directly co-condensing a TA-silane and tetraethoxysilane (TEOS) in the presence of a base as a catalyst and inserting trimethylammonium (TA) functional groups into the framework of MSN (MSN-TA). These MSN-TA samples have well-defined hexagonal structures with an average particle diameter of 100 nm, pore size of 2.7 nm, and surface area of about  $1,000 \text{ m}^2 \text{ g}^{-1}$ . Anionic drug molecules, Orange II (a fluorescent tracing molecule), and sulfasalazine (an anti-inflammatory

prodrug used for bowel disorders) were successfully loaded into these MSN-TA samples and persisted within the MSN-TA in an acidic environment (pH 2–5) (Li et al., 2021;1196). Guha and others developed poly (methacrylic acid-co-vinyl triethoxysilane) coated MSN with better hypoglycemic effect for insulin delivery (Guha et al., 2016). Ang and coworkers have reported the synthesis of MCM-41 nanoparticles using sol-gel method for oral delivery of MCC7433 and pretomanid and its surface was modified with phosphonate and amino groups (Ang et al., 2021). The impact of various structural features of MSNs on protein loading, protection, and delivery performance have been reviewed by Xu and coworkers. They also discussed the current state of MSN research in enzyme mobilization, catalysis, intracellular delivery, extracellular delivery, and antimicrobial protein delivery (Xu et al., 2019). Janjua and coworkers have developed a room temperature procedure for synthesizing ultra-small silica nanoparticles with large pore sizes that can load high amounts of chemotherapeutic medicines and attach a targeting moiety to their surface for the first time. To accomplish additional active targeting, the nanoparticles were coupled with lactoferrin (>80 kDa), whose receptors are overexpressed by both the blood-brain barrier and glioblastoma (Janjua et al., 2021).

Meka et al. studied the solubility, permeability, and anti-cancer activity of vorinostat encapsulated within MSNs with various functional groups. When vorinostat was encapsulated in pristine MSNs, its solubility was increased by 2.6 fold when compared to the free drug (MCM-41-VOR). When MSNs were treated with silanes with amino (3.9 fold) or phosphonate (4.3 fold) terminal functional groups and solubility were increased even further. Also, MSN-based formulations considerably improved vorinostat permeability into Caco-2 human colon cancer cells, particularly MSNs modified with an amino functional group (MCM-41-NH<sub>2</sub>-VOR), where it increased by fourfold (Meka et al., 2018).

## TYPES OF SILICA MESOPOROUS SYSTEMS

The meso-silica, due to their high thermal stability, chemical stability, high surface area, and good compatibility with other materials meso-silica systems, they have found wide applications in adsorption, enzyme stabilization and particularly drug delivery. These structures are MCM (Mobile Composition of Matter), SBA (Santa Barbara Amorphous), TUD (Technische Universiteit Delft), HMS (Hollow Mesoporous Silica) and MCF (Meso Cellular Form) (Yue et al., 2000; Heikkilä et al., 2007; Martínez-Edo et al., 2018; Wang et al., 2018).

### Mobile Composition of Matter

These adsorbents are the first material in the mesopores generation that were synthesized in 1992, which was the first step in the design of novel silica meso-carriers (Vadia and Rajput, 2011). The two groups identified from this family are MCM-41 (Chen et al., 1993) and MCM-48 (Kim et al., 2010). The synthesis of these materials is based on the creation of a liquid crystalline mesophase of surfactants that takes place in an acidic or base

media (Janicke et al., 1999). Their appearance, shape, and pore size can be changed by manipulating pH and adding co-solvent. During the synthesis of MCM, from CTAB (Cetyl trimethyl ammonium Bromide) cationic surfactant, which is strongly stirred in a high-temperature in a basic solution are apply. TEOS is then added and the resulting solution is heated at high temperature to be stirred for 2 h. After the reaction is complete, the product is filtered, rinsed with water and ethanol and then dried under vacuum. The surfactant is then removed by acid wash (**Figure 3**) (Janicke et al., 1999).

Depending on the synthesis conditions, inorganic silica templates can be hexagonal, irregular, cubic, and so on. The first case was reported in the release of silica porous mesoporous to carriers of MCM-41 with ibuprofen (Salonen et al., 2008). Kavallaro et al. used Al Si- MCM-41 mesoporous silica for drugs such as difflonisal and its sodium salt and naproxen. Qiu and et al. investigated the Si-MCM-41 system as carrier of the drug captopril in water. They obtained a cavity size of 4.3 nm and a loading of 32.5%, while Kavrallio et al. obtained a cavity size of 2.79 nm and a total of 15.6% loading. The lower drug loading for Al Si-MCM-41 is presence of Al and Si metals of loaded in the MCM-41 pores, so if the size of the pore is less, the amount of drug loading is increases (Cavallaro et al., 2004).

Zeng et al. synthesized MCM-41 with the organic group of aminopropyl as carriers of aspirin and the results showed its release properties were influenced by the amount and distribution of aminopropyl groups in the pores wall and their regular structure (Zeng et al., 2005). MCM-48 is another mesoporous carrier from MCM group that has the three-dimensional shape group and cubic cavities, and the delayed release of the erythromycin antibiotic from this adsorbent was observed (Izquierdo-Barba et al., 2005). Izquierdo-Barba et al. conducted synthesis of MCM-48/erythromycin and MCM-48/ibuprofen nanocarriers. They illustrate that both have good release (Izquierdo-Barba et al., 2005). Also, these matters have been reported to increase the dissolution rate of piroxicam analgesic (Patil et al., 2019).

### Santa Barbara Amorphous

In 1998, silica materials with regular meso pores synthesized in acidic conditions using non-ionic copolymers were synthesized with high amounts of polyethylene oxide and polypropylene oxide such as F-127 and P-123 pluronic (Speybroeck et al., 2009). The naming of these batches is based on their shape, such that the SBA-1 has a cage shape with cube circular pores (Che et al., 2001), SBA-11 (cubic) (Che et al., 2001), SBA-3 has a six-sided cylindrical porosity shape (Chen et al., 2004), SBA-14 (sheet) (Yu et al., 2018), SBA-15 has a two-dimensional hexagon shape (Margolese et al., 2000) and SBA-16 has a cubic cage structure (Rivera-Muñoz and Huirache-Acuña, 2010). Among these mesostructures, the SBA-15, followed by the SBA-16, quickly became the focus of attention. Because they have desirable surfaces, physicochemical properties such as low toxicity, biocompatibility, biodegradability, low-cost sources for synthesis, and are widespread their daily applications (Speybroeck et al., 2009). The SBA mesoporous pore wall is thicker than the MCM; although their specific surface area and

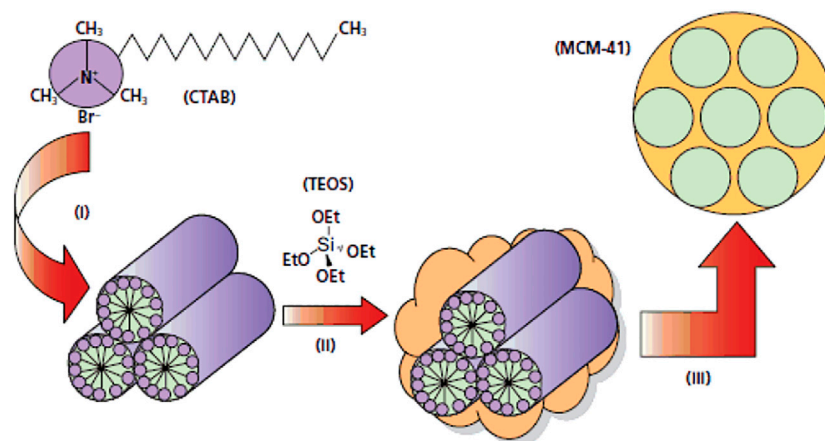


**FIGURE 3** | Synthesis of MCM-41 in basic media (Janicke et al., 1999).

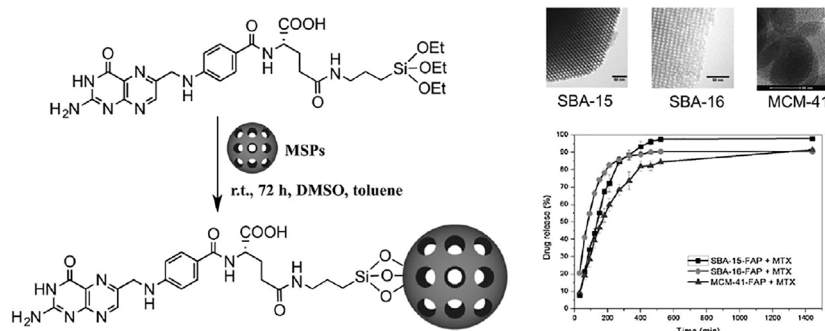


**FIGURE 4** | Loading of folic acid into SBA-15/NH<sub>2</sub>.

pore volume are smaller than the MCM group, but they have a high mechanical and thermal stability (Speybroeck et al., 2009). Recently, the use of SBA-15 as a drug carrier has been evaluated and proven to have a structural shape and pore size effect on atenolol release. The appearance of the properties can be changed by altering the synthesis temperature. It also appears that SBA-15 is leading to the slow release of drugs (Speybroeck et al., 2009). Wang et al. showed that the choice of aqueous and non-aqueous solvents for loading into the SBA-15 had a significant effect on the rate of drug dissolution (Wang, 2009). An acceptable therapeutic target of hybrid porous mesoporous silica to which amine functional groups were added was also observed in folic acid loading (**Figure 4**) (Freitas et al., 2016).

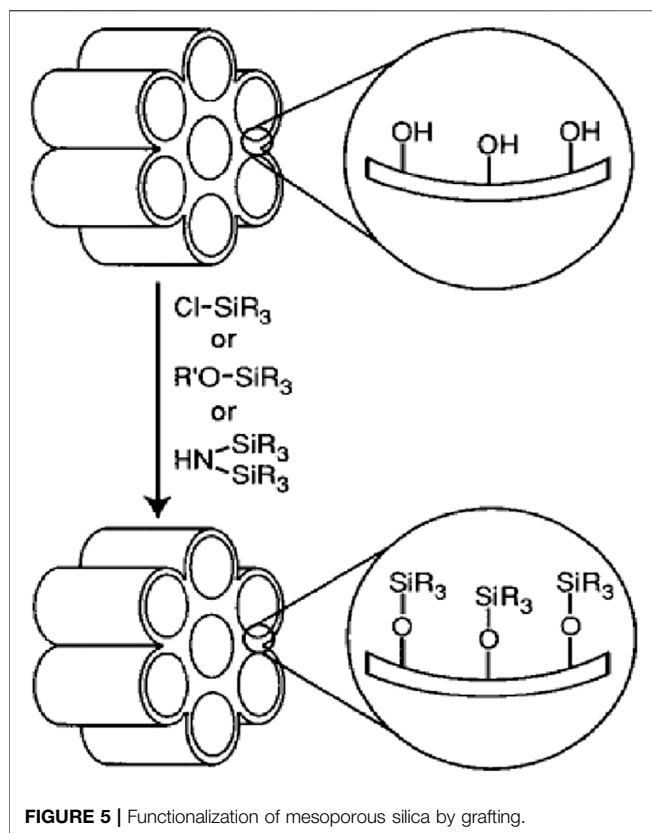
Melaerts et al. locate itraconazole, a low-soluble antifungal drug in porous SBA-15, which increased its release. Zelenak et al. stabilized two  $Zn_3(\text{benzoate})_6(\text{nicotinamide})_2$  ZnNIA and  $Zn(\text{benzoate})_2(3\text{-pyridinemethanol})_2$  ZnPCB antibacterial drug complexes on SBA-16 and examined their release (Zelenák et al., 2005).

## Other Silica Mesopores

TUD-1 is similar to foam because of its three-dimensional structure, where ibuprofen loading has led to improved drug release rates. Its synthesis conditions are slightly different from that of porous silica nanoparticles and the manufacturing process is carried out without the presence of surfactants, which is essential in terms of toxicity reduction and economic feasibility. It has a high absorption capacity and is suitable for loading water-soluble drugs (Heikkilä et al., 2007). HMS has been reported as another meso-silica with a porous structure, the central part of which is hollow, which has given it the potential to load the drug as a nano-carrier (Zhu et al., 2005). The loading of ibuprofen and vancomycin by MCFs has been reported to have resulted in their dissolution rate increasing and as a good candidate for drug delivery (Zhu et al., 2009).

The incorporation of magnetic nanoparticles with mesoporous nanoparticles with a particle diameter of about 150 nm and pore size of 4 nm also showed slow drug release, similar to ibuprofen (Kim et al., 2006).





## FUNCTIONALIZATION OF MESOPOROUS SILICA

Modification of the surface of the porous silica nanoparticles is carried out to enhance their different physical and chemical attributes. As mentioned, porous silica materials have an unusually broad surface area. Their surface is covered with silanol groups, which makes their cavities surface functional to be adjustable, which dramatically enhances the various physical and chemical properties (Kim et al., 2006). For example, the mesoporous surface of the silica can be modified by sulfonic acid groups derived from oxidized mercapto. Modified mesosilica can also be obtained with the aldehyde functional group by reaction with the amine and glutaraldehyde functional groups. Therefore, the various groups are capable of generating internal reactions such as hydrogen bonding, electrostatic adsorption, and covalent bonding with host molecules. Also, an organoalkoxy silane can be replaced with the cyano group present in the mesoporous surface, and the modified groups in the presence of sulfuric acid as catalysts were varied through hydrolysis by acidic groups.

### Post-synthesis Grafting

Grafting is a type of post-fabrication process used to modify the surface of pre-fabricated porous silica material which bonds the functional groups connected to their surface after removing the surfactant (Zhang et al., 2004; Lesaint et al., 2005). The abundant silanol groups present on the surface of the silica

porous material are applied as suitable junctions for functionalization with organic functional groups (Figure 5) (Barczak, 2019).

After removal of the surfactant, the organosilanes can be attached to the silanol channels using trichloro organosilanes or trialkoxy organosilanes (Barczak, 2019). A series of organosilanes including amine (Aguado et al., 2009), thiol (Li et al., 2011), chloride (Han et al., 2003), cyano (Prouzet et al., 1999), ester (Prouzet et al., 1999), aldehyde (Yin et al., 2020), epoxy (Yeganeh et al., 2019), anhydride (Park et al., 2019), isocyanate (Ratirotjanakul et al., 2019), phosphor (Yamada et al., 2019), imidazole (Nuri et al., 2019), ammonium (Lagarde et al., 2019), acryl (Xiao Song et al., 2019), alkyl (Nuntang et al., 2019), and phenyl (Gao et al., 2019) are available for application in the grafting procedure. The grafting is done by silicification so that the reaction is carried out on free (Si-OH) and attached silanol (HO-Si-OH) groups (Barczak, 2019). To diversify the surface or cavity walls of silica nanoparticles, silanol groups bonded hydrogen have limited access because they form hydrophilic networks between themselves (Barczak, 2019). It is worth noting that the main structure of the mesoporous does not change after applying the grafting procedure (Zhang et al., 2004). Silica mesostructures have two inner and exterior parts. Functional groups on the outer part will be more accessible than the inner part but the presence of these patches will diminish the use of pores space (Lesaint et al., 2005). To minimize the barriers of the outer surface in reaction and selective optimization, the outer surfaces may be coated to reduce chemical reactions before the functionalization of the inner surfaces occurs (Zhang et al., 2004; Lesaint et al., 2005). It is also possible to modify the surface in a controlled manner through site-selective grafting methods. Thus, in the first step, the cavities are filled with surfactants, and the exterior modification is accomplished by the proximity of the template to a solution such as a trimethylsilyl chloride (Lesaint et al., 2005). Then, template and finally the interior pore surfaces, for example, are functionalized with the phenyl propyl dimethyl chlorosilane sample (Zhang et al., 2004).

### Co-Condensation

The co-condensation matter is, in fact, sol-gel chemistry between tetraalkoxysilanes and one or more of the organoalkoxy silanes with Si-C bonds (Gao et al., 2019). In its mechanism of operation, silica precursor with a organotrialkoxy silanes ( $R'(Si(OR)_3)$  precursor in neutral, acidic media that the organosilane precursor plays two important roles in silica-based skeletal formation and binding of an organic group to the skeleton (Hamoudi and Kaliaguine, 2002). Due to the presence of organic groups in the synthesized nanoparticles, template removal should be performed under appropriate conditions in terms of temperature and pH (Wu et al., 2013). Template removal is generally preferred by chemical extraction, and depending on the nature of the template and the manufacturing process, chemical extraction of the surfactant molecules is carried out by refluxing with ethanol or ethanol/HCl under highly acidic  $H_2SO_4$  conditions. Functional groups such as



polypropylene glycol, trimethylbenzene and tetradecane can also be used to achieve modified ordered mesoporous (Diagboya and Dikio, 2018). One of the advantages of this method, compared to the post-synthesis grafting, is the applicability of a wide range of organoalkoxy silanes (Jeelani et al., 2020) suitable for a wide range of reaction conditions (Fukuda and Yoshitake, 2019), homogeneous coverage of functional groups (Putz et al., 2019), and high loading of functional groups without destructing the regular structure of the pores (Nguyen et al., 2019).

## SILICA MESOPOROUS FOR DRUG DELIVERY

The use of nanosilica materials for controlled drug delivery and release has been reported since the beginning of 1983 (He and Shi, 2011). To date, silica nanoparticles are widely used as drug carriers due to their easy compatibility and formulation with drugs (Yamada et al., 2019). Advantages of using mesoporous silica to transport bioactive molecules include protecting cargo from physiological destruction of controlled release of drugs (Tang et al., 2012), longer durability in the bloodstream (Privett et al., 2011), improving targeted drug delivery (Wang et al., 2010), and reduction of side effects to healthy tissues (Zhou et al., 2017). In recently years, non-steroidal Analgesics (NSA) have been considered. Non-steroidal painkillers, which are analgesic (Aiello et al., 2002), fever-inducing (N et al., 2019), and platelet-inhibiting (Brogan et al., 2019), are one of the most widely used medical drugs whose biological target is the cyclooxygenase (COX) enzyme (Voiriot et al., 2019). These drugs actually suppress prostaglandins, which are chemical messengers for pain, fever, and inflammation (Mahalanobish et al., 2019). Their strategy of action is to inactivate the performance of the COX, which has the potential to convert fatty acid to prostaglandin, or in other words, overcome the production of prostaglandin by COX (FitzGerald, 2003). In addition to the advantages of these drugs, they have side effects, including excessive body retention (Marsh et al., 1972) and low solubility (Rives et al., 2013), which disrupt the treatment. As a result, in recent years, silica porous nanoparticles have been proposed to address these problems. Increasing the solubility of NSA drugs can be justified by the size of the cavities (Mellaerts et al., 2008), easy dispersion, indirect transfer of the drug into the aqueous media (Li et al., 2007), utilization of surfactants (Chen et al., 2010), and long durability in the body by biodegradable coatings such as polyethylene glycol (PEG) (Morelli et al., 2011). Research has reported the release of a number of drugs such as ibuprofen (Charnay et al., 2004), diclofenac (Barczak, 2018), melasamine (Mes) (Tiwari et al., 2019), naproxen (Halamová et al., 2010), piroxicam (Ambrogi et al., 2007), celecoxib (Zhao et al., 2012) and mefenamic acid (Mustafa and Hodali, 2015) and etc.

Yoncheva et al. synthesized MCM-41/carbopol/indomethacine nanocarrier. They reported that this meso-carrier showed little cytotoxicity due to carbopol coating (Tzankov et al., 2013). Naproxen (Nap) is a potent Cox enzyme inhibitor that reduces

prostaglandin production and exhibits analgesic and anti-inflammatory effects (Lejal et al., 2013). Therefore, Halamova et al. two mesostructures used amine- non-amine functionalized hexagonal MCM-41 to release Nap. Comparison of these two carriers showed that after 72 h, the efficiency of release of MCM-41/Nap was 95% and with MCM-41/amine/Nap 90%, respectively. Their groups' research also showed that the release of the Nap using SBA-15 with a larger cavity size was less than MCM-41 with a smaller cavity size (Halamová and Zelenák, 2012). The preparation of SBA-15 decorated by glycidyl methacrylate (GMA) as nanocarrier for release of ibuprofen and Mes was carried out by Rehman and coworkers. Copper was modified with hydrophobic ligands to slow and adjust the release of the two drugs and increase the ibuprofen and Mes- SBA-15 interaction. The impact of pH in their research revealed interesting results. The *in vitro* release rate from the functionalized SBA-15 was slow in simulated gastric fluid where pH = 1.2 was less than 10% of Mes and ibuprofen was released in initial time 8 h, while comparatively high release rates were observed in simulated intestinal (pH = 6.8) and simulated body fluids (pH = 7.2) (Rehman et al., 2016).

## CONCLUSION AND CLINICAL TRANSLATION

MSNs are one-of-a-kind nanoparticles that combine the chemical and physical stability of silica with the potential of the mesoporous structure's network of cavities. MSNs' unique properties, such as pore-volume, their great loading capability, their controllable particle size and shape, and their high drug loading capacity, make them an excellent carrier for nano-drug delivery systems. MSNs can be anchored with many polymers, proteins, enzymes and due to their ease of functionalization, make them a good candidate for drug delivery applications.

Standardization of manufacturing techniques is vital for achieving reproducibility in MSN synthesis. It is also critical that the generated nanoparticles have the proper stability, dispersibility; and any surface functionalization method should be standardized before reaching the clinic. More importantly, additional MSN biodistribution studies on various animal models should be conducted to be certain of the MSNs' ultimate fate. From a broad view, it is clear that significant progress has been made in the design and development of MSNs for biological applications. However, much more work needs to be done before clinical translation can be accomplished.

Based on their efficacy in clinical studies, silica nanoparticles are developing as a viable diagnostic and delivery platform, and might play a crucial role in the development of next-generation theranostics, nanovaccines, and formulations to orally transport peptides and proteins. However, establishing safety from chronic exposure, establishing long-term toxicological profiles from various routes of administration, investigating reliable scale-up methods, and synthesizing reproducible silica nanoparticles with minimal batch-to-batch variation, are all major obstacles that must be overcome before silica nanoparticles can be used in clinical trials. Furthermore, only solid silica nanoparticles with no or small pores have been clinically evaluated to date. These

nanoparticles have a low cargo-loading capacity which is particularly problematic for nucleic-acid-based medicines.

## AUTHOR CONTRIBUTIONS

KS: writing—original draft methodology, software, validation, formal analysis, data curation, visualization JS: writing—original draft methodology, software, validation, formal analysis, data curation. AT: writing—original draft

## REFERENCES

- Aguado, J., Arsuaga, J. M., Arencibia, A., Lindo, M., and Gascón, V. (2009). Aqueous Heavy Metals Removal by Adsorption on Amine-Functionalized Mesoporous Silica. *J. Hazard. Mater.* 163, 213–221. doi:10.1016/j.jhazmat.2008.06.080
- Ahmed, T., and Aljaeid, B. (2016). Preparation, Characterization, and Potential Application of Chitosan, Chitosan Derivatives, and Chitosan Metal Nanoparticles in Pharmaceutical Drug Delivery. *Dddt* 10, 483. doi:10.2147/dddt.s99651
- Aiello, R., Cavallaro, G., Giammona, G., Pasqua, L., Pierro, P., and Testa, F. (2002). “Mesoporous Silicate as Matrix for Drug Delivery Systems of Non-steroidal Antinflammatory Drugs,” in *Studies in Surface Science and Catalysis* (Elsevier), 1165–1172. doi:10.1016/s0167-2991(02)80276-2
- Ambrogio, V., Perioli, L., Marmottini, F., Giovagnoli, S., Esposito, M., and Rossi, C. (2007). Improvement of Dissolution Rate of Piroxicam by Inclusion into MCM-41 Mesoporous Silicate. *Eur. J. Pharm. Sci.* 32, 216–222. doi:10.1016/j.ejps.2007.07.005
- Ang, C. W., Tan, L., Qu, Z., West, N. P., Cooper, M. A., Popat, A., et al. (2021). *Mesoporous Silica Nanoparticles Improve Oral Delivery of Antitubercular Bicyclic Nitroimidazoles*. Washington, DC: ACS biomaterials science & engineering.
- Anglin, E., Cheng, L., Freeman, W., and Sailor, M. (2008). Porous Silicon in Drug Delivery Devices and Materials☆. *Adv. Drug Deliv. Rev.* 60, 1266–1277. doi:10.1016/j.addr.2008.03.017
- Banerjee, A., Qi, J., Gogoi, R., Wong, J., and Mitragotri, S. (2016). Role of Nanoparticle Size, Shape and Surface Chemistry in Oral Drug Delivery. *J. Controlled Release* 238, 176–185. doi:10.1016/j.jconrel.2016.07.051
- Barczak, M. (2019). Functionalization of Mesoporous Silica Surface with Carboxylic Groups by Meldrum's Acid and its Application for Sorption of Proteins. *J. Porous Mater.* 26, 291–300. doi:10.1007/s10934-018-0655-7
- Barczak, M. (2018). Synthesis and Structure of Pyridine-Functionalized Mesoporous SBA-15 Organosilicas and Their Application for Sorption of Diclofenac. *J. Solid State. Chem.* 258, 232–242. doi:10.1016/j.jssc.2017.10.006
- Bhatia, S. (2016). “Nanoparticles Types, Classification, Characterization, Fabrication Methods and Drug Delivery Applications,” in *Natural Polymer Drug Delivery Systems* (Springer), 33–93. doi:10.1007/978-3-319-41129-3\_2
- Brogan, S. E., Mandym, S., and Odell, D. W. (2019). “Nonopioid Analgesics,” in *Pharmacology and Physiology for Anesthesia* (Elsevier), 369–389. doi:10.1016/b978-0-323-48110-6.00019-3
- Cavallaro, G., Pierro, P., Palumbo, F. S., Testa, F., Pasqua, L., and Aiello, R. (2004). Drug Delivery Devices Based on Mesoporous Silicate. *Drug Deliv.* 11, 41–46. doi:10.1080/10717540490265252
- Charnay, C., Bégu, S., Tourné-Péteilh, C., Nicole, L., Lerner, D. A., and Devoisselle, J. M. (2004). Inclusion of Ibuprofen in Mesoporous Templated Silica: Drug Loading and Release Property. *Eur. J. pharmaceutical biopharmaceutics* 57, 533–540. doi:10.1016/j.ejpb.2003.12.007
- Che, S., Sakamoto, Y., Terasaki, O., and Tatsumi, T. (2001). Control of crystal Morphology of SBA-1 Mesoporous Silica. *Chem. Mater.* 13, 2237–2239. doi:10.1021/cm010297f
- Chen, C.-Y., Li, H.-X., and Davis, M. E. (1993). Studies on Mesoporous Materials. *Microporous Mater.* 2, 17–26. doi:10.1016/0927-6513(93)80058-3
- Chen, F.-H., Zhang, L.-M., Chen, Q.-T., Zhang, Y., and Zhang, Z.-J. (2010). Synthesis of a Novel Magnetic Drug Delivery System Composed of Doxorubicin-Conjugated

methodology, software, validation, MZ: writing—original draft methodology, software, validation, formal analysis, visualization NC: conceptualization, methodology, software, validation, formal analysis, investigation, resources, data curation, writing—original draft, review and editing, visualization. GS: conceptualization, methodology, software, validation, formal analysis, investigation, resources, data curation, writing—original draft, review and editing, visualization, supervision, project administration.

- Fe3O4 Nanoparticle Cores and a PEG-Functionalized Porous Silica Shell. *Chem. Commun.* 46, 8633–8635. doi:10.1039/c0cc02577a
- Chen, F., Xu, X.-J., Shen, S., Kawi, S., and Hidajat, K. (2004). Microporosity of SBA-3 Mesoporous Molecular Sieves. *Microporous mesoporous Mater.* 75, 231–235. doi:10.1016/j.micromeso.2004.07.028
- Chen, M., Hu, J., Wang, L., Li, Y., Zhu, C., Chen, C., et al. (2020). Targeted and Redox-Responsive Drug Delivery Systems Based on Carbonic Anhydrase IX-Decorated Mesoporous Silica Nanoparticles for Cancer Therapy. *Sci. Rep.* 10, 14447–14512. doi:10.1038/s41598-020-71071-1
- Chen, X. J., Zhang, X. Q., Liu, Q., Zhang, J., and Zhou, G. (2018). Nanotechnology: a Promising Method for Oral Cancer Detection and Diagnosis. *J. Nanobiotechnology* 16, 52–17. doi:10.1186/s12951-018-0378-6
- Cooley, M., Sarode, A., Hoore, M., Fedosov, D. A., Mitragotri, S., and Sen Gupta, A. (2018). Influence of Particle Size and Shape on Their Margination and wall-adhesion: Implications in Drug Delivery Vehicle Design across Nano-To-Micro Scale. *Nanoscale* 10, 15350–15364. doi:10.1039/c8nr04042g
- Diagboya, P. N. E., and Dikio, E. D. (2018). Silica-based Mesoporous Materials; Emerging Designer Adsorbents for Aqueous Pollutants Removal and Water Treatment. *Microporous Mesoporous Mater.* 266, 252–267. doi:10.1016/j.micromeso.2018.03.008
- Djekic, L., Martinović, M., Dobričić, V., Čalića, B., Medarević, Đ., and Primorac, M. (2019). Comparison of the Effect of Bioadhesive Polymers on Stability and Drug Release Kinetics of Biocompatible Hydrogels for Topical Application of Ibuprofen. *J. Pharm. Sci.* 108, 1326–1333. doi:10.1016/j.xphs.2018.10.054
- Dudarko, O. A., Sliesarenko, V. V., Tomin, O. O., Pamin, K., Serwicka, E. M., and Zub, Y. L. (2019). “Mesoporous Surface-Functionalized Silicas and Their Application in Sorption and Catalysis,” in *Biocompatible Hybrid Oxide Nanoparticles for Human Health* (Elsevier), 51–65. doi:10.1016/b978-0-12-815875-3.00004-7
- El-Boubbou, K. (2018). Magnetic Iron Oxide Nanoparticles as Drug Carriers: Preparation, Conjugation and Delivery. *Nanomedicine* 13, 929–952. doi:10.2217/nnm-2017-0320
- FitzGerald, G. A. (2003). COX-2 and beyond: Approaches to Prostaglandin Inhibition in Human Disease. *Nat. Rev. Drug Discov.* 2, 879–890. doi:10.1038/nrd1225
- Florek, J., Caillard, R., and Kleitz, F. (2017). Evaluation of Mesoporous Silica Nanoparticles for Oral Drug Delivery - Current Status and Perspective of MSNs Drug Carriers. *Nanoscale* 9, 15252–15277. doi:10.1039/c7nr05762h
- Freitas, L. B. d. O., Bravo, I. J. G., Macedo, W. A. d. A., and de Sousa, E. M. B. (2016). Mesoporous Silica Materials Functionalized with Folic Acid: Preparation, Characterization and Release Profile Study with Methotrexate. *J. Sol-gel Sci. Technol.* 77, 186–204. doi:10.1007/s10971-015-3844-8
- Fukuda, K., and Yoshitake, H. (2019). Alternating Copolymerization of Functionalized Silica Nanoparticles. *Polymer* 165, 133–141. doi:10.1016/j.polymer.2019.01.036
- Gao, P., Liang, Z., Zhao, Z., Wang, W., Yang, C., Hu, B., et al. (2019). Enhanced Adsorption of Steroid Estrogens by One-Pot Synthesized Phenyl-Modified Mesoporous Silica: Dependence on Phenyl-Organosilane Precursors and pH Condition. *Chemosphere* 234, 438–449. doi:10.1016/j.chemosphere.2019.06.089
- Goetjen, T. A., Liu, J., Wu, Y., Sui, J., Zhang, X., Hupp, J. T., et al. (2020). Metal-organic Framework (MOF) Materials as Polymerization Catalysts: a Review and Recent Advances. *Chem. Commun.* 56, 10409–10418. doi:10.1039/d0cc03790g
- Guha, A., Biswas, N., Bhattacharjee, K., Sahoo, N., and Kuotsu, K. (2016). pH Responsive Cylindrical MSN for Oral Delivery of Insulin-Design, Fabrication

- and Evaluation. *Drug Deliv.* 23, 3552–3561. doi:10.1080/10717544.2016.1209796
- Halamová, D., Badaničová, M., Zelenák, V., Gondová, T., and Vainio, U. (2010). Naproxen Drug Delivery Using Periodic Mesoporous Silica SBA-15. *Appl. Surf. Sci.* 256, 6489–6494. doi:10.1016/j.apsusc.2010.04.044
- Halamová, D., and Zelenák, V. (2012). NSAID Naproxen in Mesoporous Matrix MCM-41: Drug Uptake and Release Properties. *J. Incl. Phenom. Macrocycl. Chem.* 72, 15–23. doi:10.1007/s10847-011-9990-x
- Hamoudi, S., and Kaliaguine, S. (2002). Periodic Mesoporous Organosilica from Micellar Oligomer Template solution Electronic Supplementary Information (ESI). *Chem. Commun.*, 2118–2119. doi:10.1039/b207134g
- Han, S., Hou, W., Dang, W., Xu, J., Hu, J., and Li, D. (2003). Synthesis of Rod-like Mesoporous Silica Using Mixed Surfactants of Cetyltrimethylammonium Bromide and Cetyltrimethylammonium Chloride as Templates. *Mater. Lett.* 57, 4520–4524. doi:10.1016/s0167-577x(03)00355-0
- He, Q., and Shi, J. (2011). Mesoporous Silica Nanoparticle Based Nano Drug Delivery Systems: Synthesis, Controlled Drug Release and Delivery, Pharmacokinetics and Biocompatibility. *J. Mater. Chem.* 21, 5845–5855. doi:10.1039/c0jm03851b
- Heikkilä, T., Salonen, J., Tuura, J., Hamdy, M., Mul, G., Kumar, N., et al. (2007). Mesoporous Silica Material TUD-1 as a Drug Delivery System. *Int. J. Pharmaceutics* 331, 133–138. doi:10.1016/j.ijpharm.2006.09.019
- Hughes, G. A. (2005). Nanostructure-mediated Drug Delivery. *Nanomedicine: nanotechnology, Biol. Med.* 1, 22–30. doi:10.1016/j.nano.2004.11.009
- Izquierdo-Barba, I., Martínez, Á., Doadrio, A. L., Pérez-Pariente, J., and Vallet-Regí, M. (2005). Release Evaluation of Drugs from Ordered Three-Dimensional Silica Structures. *Eur. J. Pharm. Sci.* 26, 365–373. doi:10.1016/j.ejps.2005.06.009
- Jahangirian, H., Ghasemian lemraski, E., Webster, T. J., Rafiee-Moghaddam, R., and Abdollahi, Y. (2017). A Review of Drug Delivery Systems Based on Nanotechnology and green Chemistry: green Nanomedicine. *Ijn* Vol. 12, 2957–2978. doi:10.2147/ijn.s127683
- Janick, M. T., Landry, C. C., Christiansen, S. C., Birtalan, S., Stucky, G. D., and Chmelka, B. F. (1999). Low Silica MCM-41 Composites and Mesoporous Solids. *Chem. Mater.* 11, 1342–1351. doi:10.1021/cm981135v
- Janjua, T. I., Ahmed-Cox, A., Meka, A. K., Mansfeld, F. M., Forgham, H., Ignacio, R. M. C., et al. (2021). Facile Synthesis of Lactoferrin Conjugated Ultra Small Large Pore Silica Nanoparticles for the Treatment of Glioblastoma. *Nanoscale* 13, 16909–16922. doi:10.1039/d1nr03553c
- Jeelani, P. G., Mulay, P., Venkat, R., and Ramalingam, C. (2020). Multifaceted Application of Silica Nanoparticles. A Review. *Silicon* 12, 1337–1354. doi:10.1007/s12633-019-00229-y
- Jindal, A., Juneja, S., Bakshi, M., Chaudhuri, P., and Bhattacharya, J. (2019). Mesoporous Zinc Silicate Bio-Composite: Preparation, Characterization and *In Vitro* Evaluation. *Microporous Mesoporous Mater.* 277, 124–131. doi:10.1016/j.micromeso.2018.10.025
- Kamaly, N., Yameen, B., Wu, J., and Farokhzad, O. C. (2016). Degradable Controlled-Release Polymers and Polymeric Nanoparticles: Mechanisms of Controlling Drug Release. *Chem. Rev.* 116, 2602–2663. doi:10.1021/acs.chemrev.5b00346
- Kapoor, D. N., Bhatia, A., Kaur, R., Sharma, R., Kaur, G., and Dhawan, S. (2015). PLGA: a Unique Polymer for Drug Delivery. *Ther. Deliv.* 6, 41–58. doi:10.4155/tde.14.91
- Khdair, A., Hamad, I., Alkhatib, H., Bustanji, Y., Mohammad, M., Tayem, R., et al. (2016). Modified-chitosan Nanoparticles: Novel Drug Delivery Systems Improve Oral Bioavailability of Doxorubicin. *Eur. J. Pharm. Sci.* 93, 38–44. doi:10.1016/j.ejps.2016.07.012
- Kim, J., Lee, J. E., Lee, J., Yu, J. H., Kim, B. C., An, K., et al. (2006). Magnetic Fluorescent Delivery Vehicle Using Uniform Mesoporous Silica Spheres Embedded with Monodisperse Magnetic and Semiconductor Nanocrystals. *J. Am. Chem. Soc.* 128, 688–689. doi:10.1021/ja0565875
- Kim, J. M., Han, Y.-J., Stucky, G. D., and Chmelka, B. F. (2000). One-step Synthesis of Ordered Mesocomposites with Non-ionic Amphiphilic Block Copolymers: Implications of Isoelectric point, Hydrolysis Rate and Fluoride. *Chem. Commun.*, 2437–2438. doi:10.1039/b005608l
- Kim, T.-W., Chung, P.-W., and Lin, V. S.-Y. (2010). Facile Synthesis of Monodisperse Spherical MCM-48 Mesoporous Silica Nanoparticles with Controlled Particle Size. *Chem. Mater.* 22, 5093–5104. doi:10.1021/cm1017344
- Lagarde, F., Srour, H., Berthet, N., Oueslati, N., Bousquet, B., Nunes, A., et al. (2019). Investigating the Role of SBA-15 Silica on the Activity of Quaternary Ammonium Halides in the Coupling of Epoxides and CO<sub>2</sub>. *J. CO<sub>2</sub> Utilization* 34, 34–39. doi:10.1016/j.jcou.2019.05.023
- Lee, C.-H., Lo, L.-W., Mou, C.-Y., and Yang, C.-S. (2008). Synthesis and Characterization of Positive-Charge Functionalized Mesoporous Silica Nanoparticles for Oral Drug Delivery of an Anti-inflammatory Drug. *Adv. Funct. Mater.* 18, 3283–3292. doi:10.1002/adfm.200800521
- Lejal, N., Tarus, B., Bouguyon, E., Chenavas, S., Bertho, N., Delmas, B., et al. (2013). Structure-based Discovery of the Novel Antiviral Properties of Naproxen against the Nucleoprotein of Influenza A Virus. *Antimicrob. Agents Chemother.* 57, 2231–2242. doi:10.1128/aac.02335-12
- Lesaint, C., Frébault, F., Delacôte, C., Lebeau, B., Marichal, C., Walcarius, A., et al. (2005). “Synthesis and Characterization of Mesoporous Silicas Functionalized by Thiol Groups, and Application as Sorbents for Mercury (II),” in *Studies in Surface Science and Catalysis* (Elsevier), 925–932. doi:10.1016/s0167-2991(05)80305-2
- Li, G., Zhao, Z., Liu, J., and Jiang, G. (2011). Effective Heavy Metal Removal from Aqueous Systems by Thiol Functionalized Magnetic Mesoporous Silica. *J. Hazard. Mater.* 192, 277–283. doi:10.1016/j.jhazmat.2011.05.015
- Li, X.-Y., Song, Y., Zhang, C.-X., Zhao, C.-X., and He, C. (2021). Inverse CO<sub>2</sub>/C<sub>2</sub>H<sub>2</sub> Separation in a Pillared-Layer Framework Featuring a Chlorine-Modified Channel by Quadrupole-Moment Sieving. *Sep. Purif. Tech.* 279, 119608. doi:10.1016/j.seppur.2021.119608
- Li, X., Zhang, L., Dong, X., Liang, J., and Shi, J. (2007). Preparation of Mesoporous Calcium Doped Silica Spheres with Narrow Size Dispersion and Their Drug Loading and Degradation Behavior. *Microporous Mesoporous Mater.* 102, 151–158. doi:10.1016/j.micromeso.2006.12.048
- Mahalanobish, S., Saha, S., Dutta, S., Ghosh, S., and Sil, P. C. (2019). “Anti-inflammatory Efficacy of Some Potentially Bioactive Natural Products against Rheumatoid Arthritis,” in *Discovery and Development of Anti-inflammatory Agents from Natural Products* (Elsevier), 61–100. doi:10.1016/b978-0-12-816992-6.00003-6
- Manzano, M., and Vallet-Regí, M. (2019). Ultrasound Responsive Mesoporous Silica Nanoparticles for Biomedical Applications. *Chem. Commun.* 55, 2731–2740. doi:10.1039/c8cc09389j
- Margolese, D., Melero, J. A., Christiansen, S. C., Chmelka, B. F., and Stucky, G. D. (2000). Direct Syntheses of Ordered SBA-15 Mesoporous Silica Containing Sulfonic Acid Groups. *Chem. Mater.* 12, 2448–2459. doi:10.1021/cm0010304
- Marsh, A., Kim, D. N., Lee, K. T., Reiner, J. M., and Thomas, W. A. (1972). Cholesterol Turnover, Synthesis, and Retention in Hypercholesterolemic Growing Swine. *J. lipid Res.* 13, 600–615. doi:10.1016/s0022-2275(20)39366-4
- Martínez-Edo, G., Balmori, A., Pontón, I., Martí del Río, A., and Sánchez-García, D. (2018). Functionalized Ordered Mesoporous Silicas (MCM-41): Synthesis and Applications in Catalysis. *Catalysts* 8, 617. doi:10.3390/catal8120617
- Martínez-Ortega, L., Mira, A., Fernández-Carvajal, A., Mateo, C. R., Mallavia, R., and Falco, A. (2019). Development of a New Delivery System Based on Drug-Loadable Electrospun Nanofibers for Psoriasis Treatment. *Pharmaceutics* 11, 14. doi:10.3390/pharmaceutics11010014
- Martínez-Vázquez, F. J., Cabañas, M. V., Paris, J. L., Lozano, D., and Vallet-Regí, M. (2015). Fabrication of Novel Si-Doped Hydroxyapatite/gelatin Scaffolds by Rapid Prototyping for Drug Delivery and Bone Regeneration. *Acta Biomater.* 15, 200–209. doi:10.1016/j.actbio.2014.12.021
- McClements, D. J. (2018). Encapsulation, protection, and Delivery of Bioactive Proteins and Peptides Using Nanoparticle and Microparticle Systems: A Review. *Adv. Colloid Interf. Sci.* 253, 1–22. doi:10.1016/j.cis.2018.02.002
- Meka, A., Jenkins, L., Dávalos-Salas, M., Pujara, N., Wong, K., Kumeria, T., et al. (2018). Enhanced Solubility, Permeability and Anticancer Activity of Vorinostat Using Tailored Mesoporous Silica Nanoparticles. *Pharmaceutics* 10, 283. doi:10.3390/pharmaceutics10040283
- Mellaerts, R., Mols, R., Jammaer, J. A. G., Aerts, C. A., Annaert, P., Van Humbeek, J., et al. (2008). Increasing the Oral Bioavailability of the Poorly Water Soluble Drug Itraconazole with Ordered Mesoporous Silica. *Eur. J. Pharmaceutics Biopharmaceutics* 69, 223–230. doi:10.1016/j.ejpb.2007.11.006
- Meynen, V., Cool, P., and Vansant, E. F. (2009). Verified Syntheses of Mesoporous Materials. *Microporous mesoporous Mater.* 125, 170–223. doi:10.1016/j.micromeso.2009.03.046
- Morelli, C., Maris, P., Sisci, D., Perrotta, E., Brunelli, E., Perrotta, I., et al. (2011). PEG-templated Mesoporous Silica Nanoparticles Exclusively Target Cancer Cells. *Nanoscale* 3, 3198–3207. doi:10.1039/c1nr10253b



- Mustafa, F. M., and Hodali, H. A. (2015). "Use of Mesoporous Silicate Nanoparticles as Drug Carrier for Mefenamic Acid," *IOP Conf. Ser. Mater. Sci. Eng.*, 92, 012018. doi:10.1088/1757-899x/92/1/012018
- N, P., Ss, A., and Pv, M. (2019). Comprehensive Biology of Antipyretic Pathways. *Cytokine* 116, 120–127. doi:10.1016/j.cyt.2019.01.008
- Nairi, V., Medda, S., Piludu, M., Casula, M. F., Vallet-Regi, M., Monduzzi, M., et al. (2018). Interactions between Bovine Serum Albumin and Mesoporous Silica Nanoparticles Functionalized with Biopolymers. *Chem. Eng. J.* 340, 42–50. doi:10.1016/j.cej.2018.01.011
- Nguyen, T. L., Choi, Y., and Kim, J. (2019). Mesoporous Silica as a Versatile Platform for Cancer Immunotherapy. *Adv. Mater.* 31, 1803953. doi:10.1002/adma.201803953
- Nuntang, S., Yousatit, S., Yokoi, T., and Ngamcharussrivichai, C. (2019). Tunable Mesoporosity and Hydrophobicity of Natural Rubber/hexagonal Mesoporous Silica Nanocomposites. *Microporous Mesoporous Mater.* 275, 235–243. doi:10.1016/j.micromeso.2018.09.004
- Nuri, A., Mansoori, Y., and Bezaatpour, A. (2019). N-heterocyclic carbene-Palladium(II) Complex Supported on Magnetic Mesoporous Silica for Heck Cross-coupling Reaction. *Appl. Organometal Chem.* 33, e4904. doi:10.1002/aoc.4904
- Park, J., Park, S. S., Jo, N.-J., and Ha, C.-S. (2019). Folic Acid-Polyethyleneimine Functionalized Mesoporous Silica Nanoparticles as a Controlled Release Nanocarrier. *J. nanosci. nanotechnol.* 19, 6217–6224. doi:10.1166/jnn.2019.17054
- Patil, L. D., Verma, U., Patil, U. D., Naik, J. B., and Narkhede, J. S. (2019). Inclusion of Aceclofenac in Mesoporous Silica Nanoparticles: Drug Release Study and Statistical Optimization of Encapsulation Efficiency by Response Surface Methodology. *Mater. Tech.* 34, 751–763. doi:10.1080/10667857.2019.1624301
- Paunovska, K., Gil, C. J., Lokugamage, M. P., Sago, C. D., Sato, M., Lando, G. N., et al. (2018). Analyzing 2000 *In Vivo* Drug Delivery Data Points Reveals Cholesterol Structure Impacts Nanoparticle Delivery. *ACS nano* 12, 8341–8349. doi:10.1021/acsnano.8b03640
- Privett, B. J., Youn, J., Hong, S. A., Lee, J., Han, J., Shin, J. H., et al. (2011). Antibacterial Fluorinated Silica Colloid Superhydrophobic Surfaces. *Langmuir* 27, 9597–9601. doi:10.1021/la201801e
- Prouzet, E., Cot, F., Nabias, G., Larbot, A., Kooyman, P., and Pinnavaia, T. J. (1999). Assembly of Mesoporous Silica Molecular Sieves Based on Nonionic Ethoxylated Sorbitan Esters as Structure Directors. *Chem. Mater.* 11, 1498–1503. doi:10.1021/cm9810281
- Putz, A.-M., Almásy, L., Len, A., and Ianași, C. (2019). Functionalized Silica Materials Synthesized via Co-condensation and post-grafting Methods. *Fullerenes, Nanotubes and Carbon Nanostructures* 27, 323–332. doi:10.1080/1536383x.2019.1593154
- Ratirotnanakul, W., Suteewong, T., Polpanich, D., and Tangboriboonrat, P. (2019). Amino Acid as a Biodegradation Accelerator of Mesoporous Silica Nanoparticles. *Microporous Mesoporous Mater.* 282, 243–251. doi:10.1016/j.micromeso.2019.02.033
- Rehman, F., Rahim, A., Airoidi, C., and Volpe, P. L. O. (2016). Preparation and Characterization of Glycidyl Methacrylate Organo Bridges Grafted Mesoporous Silica SBA-15 as Ibuprofen and Mesalamine Carrier for Controlled Release. *Mater. Sci. Eng. C* 59, 970–979. doi:10.1016/j.msec.2015.11.005
- Reibaldi, M., Avitabile, T., Bandello, F., Longo, A., Bonfiglio, V., Russo, A., et al. (2019). The Effectiveness of 0.6% Povidone Iodine Eye Drops in Reducing the Conjunctival Bacterial Load and Needle Contamination in Patients Undergoing Anti-VEGF Intravitreal Injection: a Prospective, Randomized Study. *J. Clin. Med.* 8, 1031. doi:10.3390/jcm8071031
- Rivera-Muñoz, E. M., and Huirache-Acuña, R. (2010). Sol Gel-Derived SBA-16 Mesoporous Material. *Ijms* 11, 3069–3086. doi:10.3390/ijms11093069
- Rives, V., Del Arco, M., and Martín, C. (2013). Layered Double Hydroxides as Drug Carriers and for Controlled Release of Non-steroidal Antiinflammatory Drugs (NSAIDs): a Review. *J. Controlled Release* 169, 28–39. doi:10.1016/j.jconrel.2013.03.034
- Salonen, J., Kaukonen, A. M., Hirvonen, J., and Lehto, V.-P. (2008). Mesoporous Silicon in Drug Delivery Applications. *J. Pharm. Sci.* 97, 632–653. doi:10.1002/jps.20999
- Sharma, R., Kumar, V., and Kumar, R. (2019). Distribution of Phytoliths in Plants: A Review. *Geology. Ecology, Landscapes* 3, 123–148. doi:10.1080/24749508.2018.1522838
- Speybroeck, M. V., Barillaro, V., Thi, T. D., Mellaerts, R., Martens, J., Humbeek, J. V., et al. (2009). Ordered Mesoporous Silica Material SBA-15: a Broad-Spectrum Formulation Platform for Poorly Soluble Drugs. *J. Pharm. Sci.* 98, 2648–2658. doi:10.1002/jps.21638
- Tandel, H., Bhatt, P., Jain, K., Shahiwal, A., and Misra, A. (2018). *In-Vitro* and *In-Vivo* Tools in Emerging Drug Delivery Scenario: Challenges and Updates. *chapter*, 1–24. doi:10.1201/b22448-1
- Tang, F., Li, L., and Chen, D. (2012). Mesoporous Silica Nanoparticles: Synthesis, Biocompatibility and Drug Delivery. *Adv. Mater.* 24, 1504–1534. doi:10.1002/adma.201104763
- Tarrahi, R., Movafeghi, A., Khataee, A., Rezaeejad, F., and Gohari, G. (2019). Evaluating the Toxic Impacts of Cadmium Selenide Nanoparticles on the Aquatic Plant *Lemna Minor*. *Molecules* 24, 410. doi:10.3390/molecules24030410
- Tiwari, A., Verma, A., Panda, P. K., Saraf, S., Jain, A., and Jain, S. K. (2019). "Stimuli-responsive Polysaccharides for colon-targeted Drug Delivery," in *Stimuli Responsive Polymeric Nanocarriers for Drug Delivery Applications* (Elsevier), 547–566. doi:10.1016/b978-0-08-101995-5.00022-2
- Turner, M. R., and Balu-Iyer, S. V. (2018). Challenges and Opportunities for the Subcutaneous Delivery of Therapeutic Proteins. *J. Pharm. Sci.* 107, 1247–1260. doi:10.1016/j.xphs.2018.01.007
- Tzankov, B., Yoncheva, K., Popova, M., Szegedi, A., Momekov, G., Mihály, J., et al. (2013). Indometacin Loading and *In Vitro* Release Properties from Novel Carboxypol Coated Spherical Mesoporous Silica Nanoparticles. *Microporous mesoporous Mater.* 171, 131–138. doi:10.1016/j.micromeso.2012.12.037
- Vadia, N., and Rajput, S. (2011). Mesoporous Material, MCM-41: a New Drug Carrier. *Asian J. Pharm. Clin. Res.* 4, 44–53.
- Vallet-Regi, M., Balas, F., and Arcos, D. (2007). Mesoporous Materials for Drug Delivery. *Angew. Chem. Int. Edition* 46, 7548–7558.
- Vallet-Regi, M., Colilla, M., Izquierdo-Barba, I., and Manzano, M. (2018). Mesoporous Silica Nanoparticles for Drug Delivery: Current Insights. *Molecules* 23, 47.
- Vallet-Regi, M. (2012). Mesoporous Silica Nanoparticles: Their Projection in Nanomedicine. *Int. Scholarly Res. Notices*, 2012. doi:10.5402/2012/608548
- Voiriot, G., Philippot, Q., Elabbadi, A., Elbm, C., Chalumeau, M., and Fartoukh, M. (2019). Risks Related to the Use of Non-steroidal Anti-inflammatory Drugs in Community-Acquired Pneumonia in Adult and Pediatric Patients. *Jcm* 8, 786. doi:10.3390/jcm8060786
- Wang, L.-S., Wu, L.-C., Lu, S.-Y., Chang, L.-L., Teng, I.-T., Yang, C.-M., et al. (2010). Biofunctionalized Phospholipid-Capped Mesoporous Silica Nanoshuttles for Targeted Drug Delivery: Improved Water Susceptibility and Decreased Nonspecific Protein Binding. *ACS nano* 4, 4371–4379. doi:10.1021/nn901376h
- Wang, S. (2009). Ordered Mesoporous Materials for Drug Delivery. *Microporous mesoporous Mater.* 117, 1–9. doi:10.1016/j.micromeso.2008.07.002
- Wang, X., Zhang, Y., Luo, W., Elzatahy, A. A., Cheng, X., Alghamdi, A., et al. (2016). Synthesis of Ordered Mesoporous Silica with Tunable Morphologies and Pore Sizes via a Nonpolar Solvent-Assisted Stöber Method. *Chem. Mater.* 28, 2356–2362. doi:10.1021/acs.chemmater.6b00499
- Wang, Y.-P., Zhou, P., Luo, S.-Z., Liao, X.-P., Wang, B., Shao, Q., et al. (2018). Controllable Synthesis of Monolayer Poly(acrylic Acid) on the Channel Surface of Mesoporous Alumina for Pb(II) Adsorption. *Langmuir* 34, 7859–7868. doi:10.1021/acs.langmuir.8b00789
- Wu, S.-H., Mou, C.-Y., and Lin, H.-P. (2013). Synthesis of Mesoporous Silica Nanoparticles. *Chem. Soc. Rev.* 42, 3862–3875. doi:10.1039/c3cs35405a
- Xiao Song, X., Hu, L., Pang, X., and Li, S. (2019). Synthesis of a Novel Mesoporous Carbon Nanocube@Mesoporous Silica@Poly(acrylic Acid) Composite and Application as Potential Drug Carriers. *Russ. J. Phys. Chem.* 93, 1349–1356. doi:10.1134/s003602441907029x
- Xu, C., Lei, C., and Yu, C. (2019). Mesoporous Silica Nanoparticles for Protein protection and Delivery. *Front. Chem.* 7, 290. doi:10.3389/fchem.2019.00290
- Yamada, S., Shang, Y., Yamada, I., and Tagaya, M. (2019). Synthesis of Phosphonate-Containing Mesoporous Silica Spheres under Basic Condition. *Adv. Powder Tech.* 30, 1116–1119. doi:10.1016/j.apt.2019.02.021
- Yeganeh, M., Asadi, N., Omid, M., and Mahdavian, M. (2019). An Investigation on the Corrosion Behavior of the Epoxy Coating Embedded with Mesoporous



- Silica Nanocontainer Loaded by Sulfamethazine Inhibitor. *Prog. Org. Coat.* 128, 75–81. doi:10.1016/j.porgcoat.2018.12.022
- Yi, H. (2021). *Secure Social Internet of Things Based on post-quantum Blockchain*. Piscataway, NJ, United States: IEEE transactions on Network Science and Engineering.
- Yin, L., and Zhang, X. (2020). Green and Quality Development of Service Industry in West Coast Economic Zone. *J. Coastal Res.* 103, 1158–1161. doi:10.2112/si103-242.1
- Yin, W., Liu, L., Zhang, H., Tang, S., and Chi, R. (2020). A Facile Solvent-free and One-step Route to Prepare Amino-Phosphonic Acid Functionalized Hollow Mesoporous Silica Nanospheres for Efficient Gd(III) Removal. *J. Clean. Prod.* 243, 118688. doi:10.1016/j.jclepro.2019.118688
- Yu, J., Cao, J., Du, L., Wei, Y., Wang, T., and Tian, H. (2018). Enhancement of Diethyl Malonate Hydrogenation to 1,3-propanediol Using Mesoporous Cu/SBA-15 as Catalyst. *Appl. Catal. A: Gen.* 555, 161–170. doi:10.1016/j.apcata.2018.02.020
- Yue, Y.-H., Gédéon, A., Bonardet, J.-L., d'Espinose, J. B., Melosh, N., and Fraissard, J. (2000). "Direct Incorporation of Al in SBA Mesoporous Materials: Characterization, Stability and Catalytic Activity," in *Studies in Surface Science and Catalysis* (Elsevier), 209–218. doi:10.1016/s0167-2991(00)80216-5
- Zečević, V., Hornebecq, V., and Llewellyn, P. (2005). Zinc (II)-benzoate Complexes Immobilised in Mesoporous Silica Host. *Microporous mesoporous Mater.* 83, 125–135.
- Zeng, W., Qian, X.-F., Zhang, Y.-B., Yin, J., and Zhu, Z.-K. (2005). Organic Modified Mesoporous MCM-41 through Solvothermal Process as Drug Delivery System. *Mater. Res. Bull.* 40, 766–772. doi:10.1016/j.materresbull.2005.02.011
- Zhang, W., Zheng, N., Chen, L., Xie, L., Cui, M., Li, S., et al. (2019). Effect of Shape on Mesoporous Silica Nanoparticles for Oral Delivery of Indomethacin. *Pharmaceutics* 11, 4. doi:10.3390/pharmaceutics11010004
- Zhang, W.-H., Lu, X.-B., Xiu, J.-H., Hua, Z.-L., Zhang, L.-X., Robertson, M., et al. (2004). Synthesis and Characterization of Bifunctionalized Ordered Mesoporous Materials. *Adv. Funct. Mater.* 14, 544–552. doi:10.1002/adfm.200305001
- Zhao, D., Sun, J., Li, Q., and Stucky, G. D. (2000). Morphological Control of Highly Ordered Mesoporous Silica SBA-15. *Chem. Mater.* 12, 275–279. doi:10.1021/cm9911363
- Zhao, P., Jiang, H., Jiang, T., Zhi, Z., Wu, C., Sun, C., et al. (2012). Inclusion of Celecoxib into Fibrous Ordered Mesoporous Carbon for Enhanced Oral Bioavailability and Reduced Gastric Irritancy. *Eur. J. Pharm. Sci.* 45, 639–647. doi:10.1016/j.ejps.2012.01.003
- Zhou, S., Wu, D., Yin, X., Jin, X., Zhang, X., Zheng, S., et al. (2017). Intracellular pH-Responsive and Rituximab-Conjugated Mesoporous Silica Nanoparticles for Targeted Drug Delivery to Lymphoma B Cells. *J. Exp. Clin. Cancer Res.* 36, 24–34. doi:10.1186/s13046-017-0492-6
- Zhu, S., Zhang, D., and Yang, N. (2009). Hydrophobic Polymers Modification of Mesoporous Silica with Large Pore Size for Drug Release. *J. Nanopart. Res.* 11, 561–568. doi:10.1007/s11051-007-9325-4
- Zhu, Y., Shi, J., Chen, H., Shen, W., and Dong, X. (2005). A Facile Method to Synthesize Novel Hollow Mesoporous Silica Spheres and Advanced Storage Property. *Microporous Mesoporous Mater.* 84, 218–222. doi:10.1016/j.micromeso.2005.05.001

**Conflict of Interest:** The authors declare that the research was conducted in the absence of any commercial or financial relationships that could be construed as a potential conflict of interest.

**Publisher's Note:** All claims expressed in this article are solely those of the authors and do not necessarily represent those of their affiliated organizations, or those of the publisher, the editors and the reviewers. Any product that may be evaluated in this article, or claim that may be made by its manufacturer, is not guaranteed or endorsed by the publisher.

Copyright © 2022 Kazemzadeh, Sayadi, Toolabi, Sayadi, Zeraati, Chauhan and Sargazi. This is an open-access article distributed under the terms of the Creative Commons Attribution License (CC BY). The use, distribution or reproduction in other forums is permitted, provided the original author(s) and the copyright owner(s) are credited and that the original publication in this journal is cited, in accordance with accepted academic practice. No use, distribution or reproduction is permitted which does not comply with these terms.



# A Perspective on Perovskite Solar Cells: Emergence, Progress, and Commercialization

Pengyu Zhang<sup>1,2</sup>, Menglin Li<sup>1\*</sup> and Wen-Cheng Chen<sup>3\*</sup>

<sup>1</sup>School of Materials Science and Engineering, Beijing Institute of Technology, Beijing, China, <sup>2</sup>Beijing JAYU New Energy Technology Development Co., Ltd., JAYU Group, Beijing, China, <sup>3</sup>School of Chemical Engineering and Light Industry, Guangdong University of Technology, Guangzhou, China

## OPEN ACCESS

### Edited by:

Wenwu Qin,  
Northeast Normal University, China

### Reviewed by:

Miaoqiang Lyu,  
The University of Queensland,  
Australia  
Alaa El-Din Bekhit,  
University of Otago, New Zealand  
Wenlian Li,  
Changchun Institute of Optics, Fine  
Mechanics and Physics (CAS), China

### \*Correspondence:

Menglin Li  
menglinli90@bit.edu.cn  
Wen-Cheng Chen  
wencchen@gdut.edu.cn

### Specialty section:

This article was submitted to  
Solid State Chemistry,  
a section of the journal  
Frontiers in Chemistry

**Received:** 27 October 2021

**Accepted:** 17 February 2022

**Published:** 11 April 2022

### Citation:

Zhang P, Li M and Chen W-C (2022) A  
Perspective on Perovskite Solar Cells:  
Emergence, Progress,  
and Commercialization.  
Front. Chem. 10:802890.  
doi: 10.3389/fchem.2022.802890

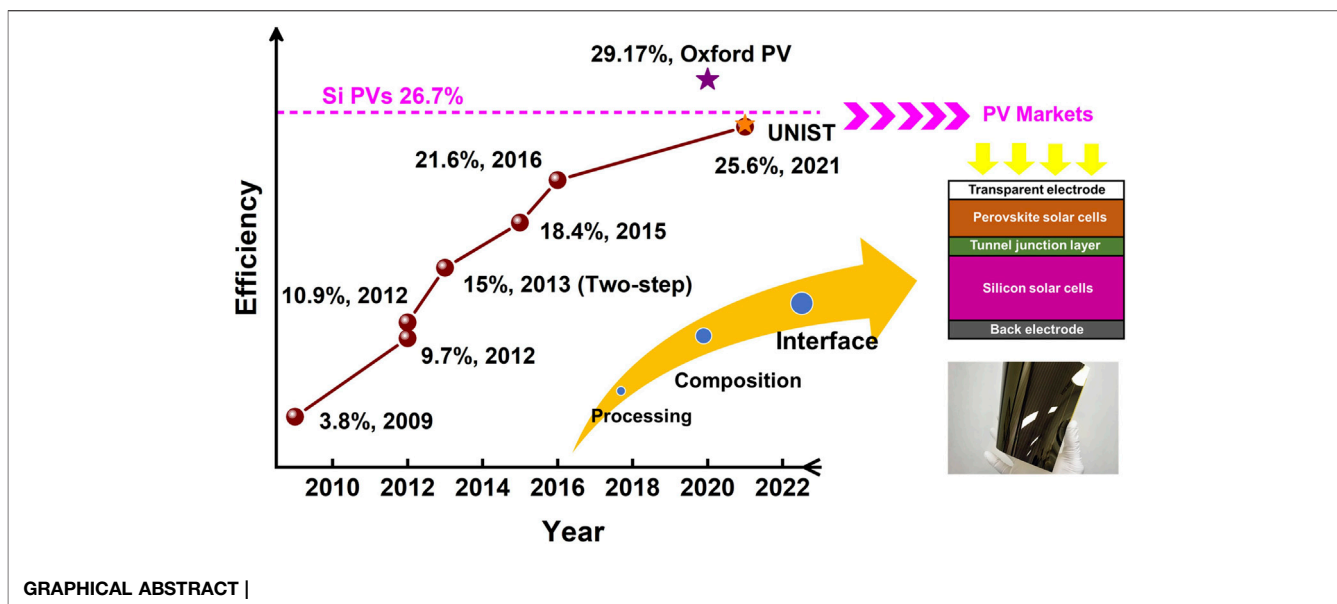
With rapid progress in light-to-electric conversion efficiencies, perovskite solar cells (PSCs) have exhibited great potential as next-generation low-cost, efficient photovoltaic technology. In this perspective, we briefly review the development of PSCs from discovery to laboratory research to commercializing progress. The past several decades have witnessed great achievement in device efficiency and stability due to tremendous research efforts on compositional, process, and interfacial engineering. Regarding commercial applications, we expound the merits and disadvantages of PSCs compared to the existing silicon photovoltaic technologies. Although PSCs promise solution processability and low manufacturing cost, their limited stability and element toxicity should be addressed on the path to commercialization. Finally, we provide future perspectives on commercialization of PSCs in the photovoltaic marketplace. It is suggested that PSCs will be more promising in low-cost modules and tandem configurations.

**Keywords:** perovskite, solar cells, composition engineering, process engineering, interfacial engineering, industrial progress, commercialization

## EMERGENCE OF PEROVSKITE SOLAR CELLS

Metal halide perovskites (MHPs) have attracted intensive attention as promising photovoltaic materials during the last few decades. The term of “Perovskite” is employed to describe a class of materials with the same crystal structure as the mineral calcium titanate ( $\text{CaTiO}_3$ ), which was firstly discovered in the Ural Mountains of Russia in 1839 and named after Lev Perovski, a renowned Russian mineralogist (Chakhmouradian and Woodward, 2014). Now, MHPs have developed into a broad range of materials with the general formula  $\text{ABX}_3$ , where A and B are monovalent and divalent cations, respectively and X stands for anions. Besides, MHPs have been widely used as active materials in various optical and electronic applications, such as photovoltaic devices (PV) (Kojima et al., 2009; Kim et al., 2012; Lee et al., 2012; Jeong et al., 2021), light-emitting diode (Cho et al., 2015; Cao et al., 2018; Lin et al., 2018), photodetector (Li et al., 2020a; Li et al., 2020b), laser (Sutherland and Sargent, 2016; Wei et al., 2019), sensor (Zaza et al., 2019; George et al., 2020), biomedicine (Fang et al., 2021; Zhang et al., 2021; Fang et al., 2022) etc.

The first demonstration of the photovoltaic effect on perovskite materials dates back to 2009 by Miyasaka and his co-works, but the power conversion efficiency (PCE) was only 3.8% (Kojima et al., 2009). Although the performance of perovskite solar cells (PSCs) was low at that time, the strong optical absorption of perovskite materials attracted widespread attention in academic circles. However, these cells suffered from



rapid degradation of perovskite materials in the liquid electrolyte. In 2012, important breakthroughs in PSCs were realized by (Kim et al., 2012; Lee et al., 2012). In these works, all-solid device configurations were reported with Spiro-MeOTAD [2,2',7,7'-tetrakis (N,N-di-p-methoxyphenylamine)-9,9'-spirobifluorene] as the hole transport layer to solve the instability problem in liquid electrolytes. The PCEs of about 10% have been reported with improved operation stability. Now, the most recent world record for single-junction PSCs has reached 25.6%, claimed by researchers at South Korea's Ulsan National Institute of Science and Technology (UNIST) (Jeong et al., 2021). As demonstrated in **Figure 1**, the laboratory efficiency of PSCs is comparable to that of the first-generation monocrystalline silicon solar cell that takes about 40 years for this level.

In addition, perovskites have been demonstrated as promising candidates in multi-junction cells due to their easily tunable bandgap through constituents (Al-Ashouri et al., 2020; Chen

et al., 2021; Chen et al., 2022; Lin et al., 2022; Qin et al., 2022). The state-of-the-art perovskite-on-silicon tandem solar cell has achieved a PCE of 29.52% in Oxford PV on approximately  $30 \times 30 \text{ cm}^2$  device area (Al-Ashouri et al., 2020). More recently, the all-perovskite tandem solar cell with a certified efficiency of 26.4% has also been reported by (Lin et al., 2022).

Perovskite materials are excellent light absorbers with outstanding optoelectronic properties such as high light absorption coefficient, long carrier diffusion length (exceeding 1 mm), low non-radiative recombination loss and high defect tolerance (Stranks et al., 2013; Xing et al., 2013; Eperon et al., 2014; Green et al., 2014). The theoretical limit of single-junction PSCs is about 33%, and that of tandem solar cells can reach over 40%. Along with ease of accessibility through low-cost solution processes, there is no doubt that PSCs have become one of the most promising photovoltaic technologies. Since reported in 2009, it was rated as one of the ten scientific breakthroughs by *Science*. Next year, it was elected as one of the most anticipated scientific and technological breakthroughs by *Nature*. In the World Economic Forum of 2016, PSCs were honored as one of the top 10 emerging technologies that would break the limitations of silicon-based photovoltaics. In a world, perovskite materials have become a hot topic in both academic and industrial fields.

## RESEARCH PROGRESS

Since reported in 2009, intensive research efforts have been made to improve the efficiency of PSCs, including compositional, process and interfacial engineering. Perovskite photovoltaic materials are ionic compounds in the general formula of  $\text{ABX}_3$ , as shown in **Figure 2A**. The crystallographic structure can be deduced by the Goldschmidt tolerance factor ( $t = (R_A + R_X)/\sqrt{2}(R_B + R_X)$ ) and the octahedral factor ( $\mu = R_B/R_X$ ) (Li et al., 2008). For applications in solar cells,

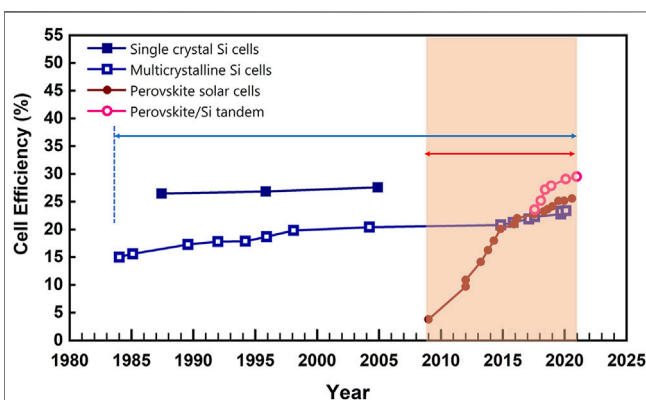


**FIGURE 1** | Progress of cell efficiency in single crystal and multicrystalline Si cells, perovskite solar cells, perovskite/Si tandem according to Best Research-Cell Efficiency chart from National Renewable Energy Laboratory (NREL, 2020).

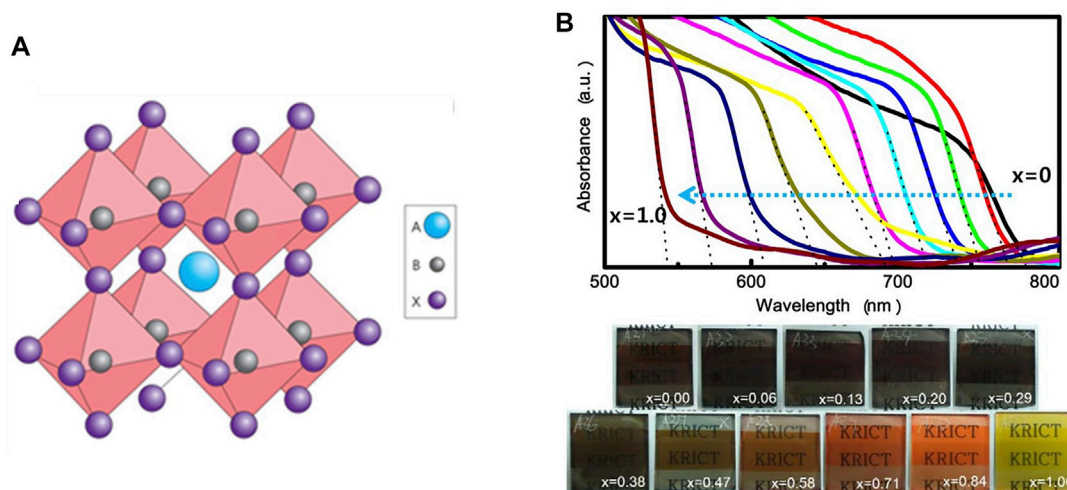


**FIGURE 2 | (A)** Cubic perovskite structure with ABX<sub>3</sub>. Adapted from Green et al. (2014) with permission from Nature springer. **(B)** UV-vis absorption spectra of PSCs with mixing halide ions and corresponding colorful films. Adapted from Noh et al. (2013) with permission from American Chemical Society.

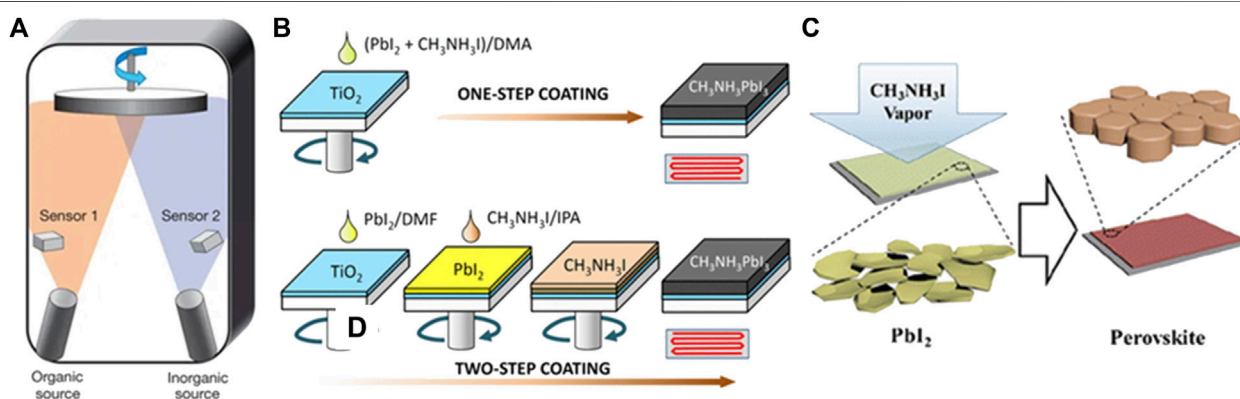


**FIGURE 3 | (A)** Dual-source thermal evaporation. Adapted from Liu et al. (2013) with permission from Nature springer. **(B)** One-step and two-step solution process for perovskite film growth. Adapted from Im et al. (2014) with permission from Nature springer. **(C)** Perovskite film formation through vapor-assisted deposition. Reproduced from Chen et al. (2014) with permission from American Chemical Society.

MHPs commonly are obtained with  $t$  and  $\mu$  in the range of 0.81–1.1 and 0.44–0.9, respectively. Despite these constraints, a broad range of ions enables good results. For example, cation A has methylammonium MA<sup>+</sup>, formamidinium FA<sup>+</sup> and cesium (Cs<sup>+</sup>) and other long-chain organic cations, metallic cation B has universally been Pb<sup>2+</sup> or Sn<sup>2+</sup> and anion X is halide ions (Cl<sup>−</sup>, Br<sup>−</sup>, I<sup>−</sup>) or Pseudo-halide ions.

The optoelectronic properties of MHPs are strongly correlated with ion species. Firstly, the bandgap can be continuously tuned in the range of almost the whole visible spectrum by X-site halide mixing (Noh et al., 2013; Eperon et al., 2014). As shown in **Figure 2B**, the absorption edge moves from 786 to 544 nm with the substitution of I with Br ions, corresponding to the bandgap increasing from 1.58 to 2.28 eV. The bandgap engineering by halide ions provides an effective strategy to design wide-bandgap perovskites into tandem solar cells. Another significant ion

substitution is replacing the MA<sup>+</sup> by FA<sup>+</sup>. Due to the larger ion size of FA<sup>+</sup>, the replacement expands the perovskite crystal and shortens the Pb–I bond distance, resulting in the reduced bandgap of 1.47 eV. The use of FA<sup>+</sup> as the A-site cation in MHPs further increases photocurrents. Unfortunately, phase stability of FAPbI<sub>3</sub> still depends on the following chemical management according to Goldschmidt rule. At the ambient conditions, the photoactive  $\alpha$ -FAPbI<sub>3</sub> is unstable and easily transforms into the yellow  $\delta$  phase, which seriously deteriorates the device performance. To solve this problem, new strategies are needed for stabilizing the  $\alpha$ -phase in FA-based PSCs. Seok and co-workers firstly stabilized  $\alpha$ -phase FAPbI<sub>3</sub> by incorporation of MAPbBr<sub>3</sub> and achieved a PCE of more than 18% PCE (Jeon et al., 2015). Later on, A site cation was further optimized as a “cation cascade” by mixing FA<sup>+</sup>, MA<sup>+</sup> and Rb<sup>+</sup> to eliminate the residual  $\delta$ -phase by Saliba and his co-workers (Saliba et al., 2016). By this



method, FA-based PSCs can deliver a stabilized PCE of over 21% and a long shelf lifetime of over 1,000 h. However, the use of  $\text{MA}^+$ ,  $\text{Rb}^+$  and  $\text{Br}^-$  into  $\text{FAPbI}_3$  perovskites can inevitably widen the bandgap, limiting the device performance. Instead, an anion engineering was introduced to stabilize pure phase  $\text{FAPbI}_3$  with the pseudo-halide anion ( $\text{HCOO}^-$ ) passivating the I-vacancy defects. The resulting solar cells have world-record efficiency of 25.6% and long-term stability over 450 h (Jeong et al., 2021).

The prerequisite for high-efficiency device is to fabricate high-quality perovskite films with a flat and compact morphology. To date, numerous processing techniques have been developed to prepare high-quality perovskite films, including vacuum deposition, one-step solution deposition (antisolvent dripping, solvent-assisted annealing, and precursor engineering), two-step sequential deposition and vapor-assisted deposition. Among these methods, solution processes are promising with low temperature and cost, compatible with flexible electronics. Furthermore, scaling-up methods (slot-die coating, roll-to-roll, and inkjet printing) have also been developed for the industrial manufacturing of PSCs in the future.

## Vacuum Deposition

The vacuum deposition method was firstly reported by Mitzi and co-workers, in which organic-inorganic compounds were rapidly heated to sublimate, then deposited on the substrate (Mitzi et al., 1999). This technique allows facile control over the film composition and thickness with high reproducibility. With the rapid development of PSCs, Snaith et al. employed dual-source co-evaporation to deposit a uniform  $\text{MAPbI}_{3-x}\text{Cl}_x$  perovskite layer and a PCE of 15% was reported (Figure 3A) (Liu et al., 2013). The perovskite films fabricated by vacuum deposition were proven to be high-quality with excellent film uniformity. Although the vacuum deposition requires expensive equipment, it still holds the advantages of fabricating large-area films without using toxic solvents. This makes it very promising in the production of the perovskite module. Recently, vacuum deposition has witnessed further progress in the perovskites materials including mixed halide (Longo et al., 2018), narrow-bandgap (Igual-Muñoz et al., 2020), and formamidine based perovskite solar cells (Chiang et al., 2020; Feng et al., 2021). The champion efficiency of 21.32% and 18.13% has been reported on the small-size cell (Feng et al., 2021) and mini-modules (effective device area  $21\text{ cm}^2$ ) (Li J. et al., 2020), respectively.

## One-Step Solution Deposition

One-step solution deposition is a commonly used method for fabricating perovskite films in labs. In this method, the precursor solutions are prepared by mixing precursors in solvents such as N, N-dimethylformamide (DMF), then spin-coated on the substrates, followed by thermal annealing to initialize the crystallization (Im et al., 2014). To obtain flat and compact films without pin-holes, antisolvents are usually used to induce homogenous nucleation, for example, toluene (Jeon et al., 2014), chlorobenzene (Bi et al., 2016), or diethyl ether (Li et al., 2017; Gao et al., 2018). One-step deposition is simple to conduct in labs and antisolvents can serve as the carriers for Lewis acid and base additives, which has been demonstrated as

an effective strategy for defect passivation. For example, Wu et al. achieved highly efficient inverted PSCs with a perovskite-fullerene graded heterojunction formed by dripping the antisolvent containing fullerenes (Wu et al., 2016). Subsequently, conjugated polymers dissolved in antisolvents were introduced in perovskite films to reduce trap states and non-radiative recombination loss (Rajagopal et al., 2017; Qin et al., 2018; Yang et al., 2018; Chen et al., 2019a; Wu et al., 2019).

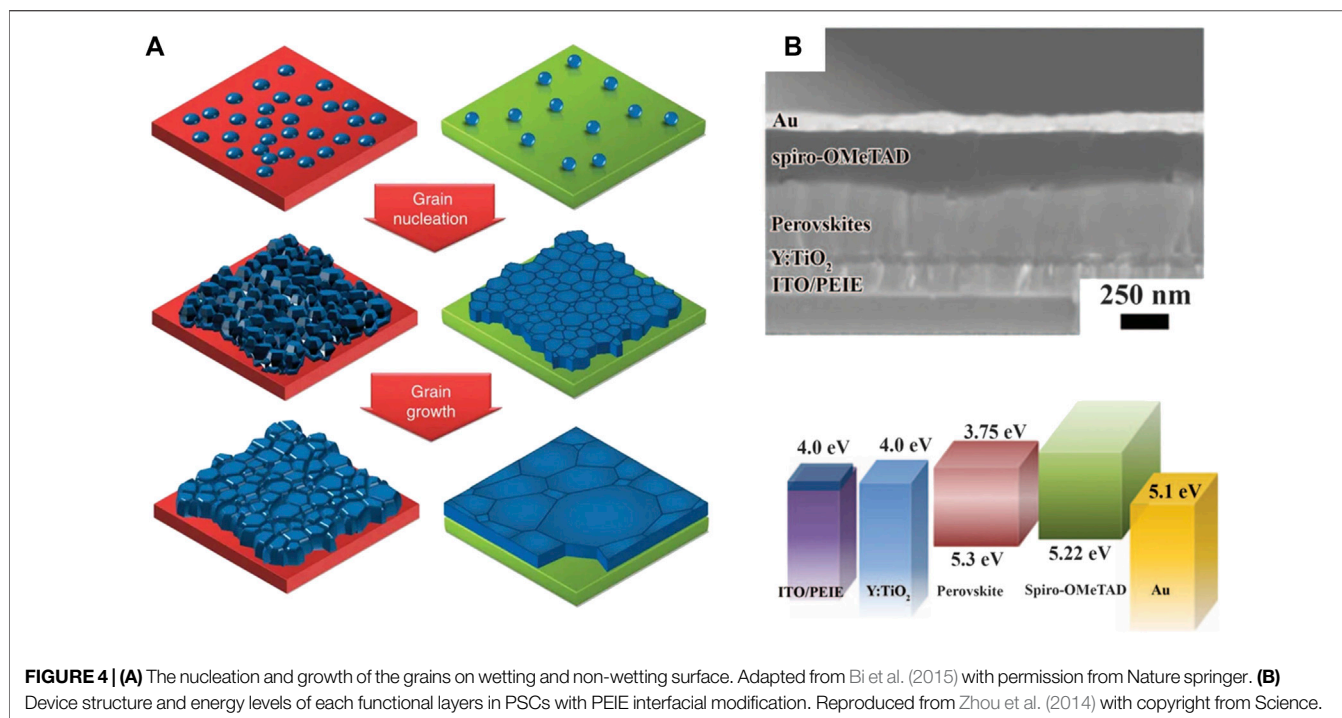
## Two-Step Solution Deposition

Besides one-step solution deposition, two-step sequential deposition is another commonly used method to obtain perovskite films with improved reproducibility (Burschka et al., 2013; Im et al., 2014). As firstly reported by Burschka et al.,  $\text{PbI}_2$  was spin-coated on the substrates followed by sequential deposition of MAI, then the formation of the perovskite was accomplished by thermal annealing, as depicted in Figure 3B. Compared with one-step solution deposition, two-step deposition has better control over the film morphology by relieving effects from the surrounding environment. However, the conversion of  $\text{PbI}_2$  to the perovskite remains a major challenge to achieve highly efficient and stable devices (Zhang et al., 2015; Chen, 2017; Chiang et al., 2017; Xu et al., 2019). The residual  $\text{PbI}_2$  at the interfaces was suggested to impede the carrier transportation and induce severe degradation PSCs (Jiang et al., 2016).

## Vapor-Assisted Deposition

This method was firstly proposed by Chen et al. in which *in-situ* reaction between the as-deposited  $\text{PbI}_2$  (solid) and MAI vapor was adopted to obtain perovskite films with full coverage and smooth surface, as schematically illustrated in Figure 3C (Chen et al., 2014). The vapor-assisted process is a facile low-temperature method with the slowdown in nucleation and film growth, which delivers increasing grain size and high reproducibility. In addition, vapor-assisted deposition provides the possibility of growing high-quality perovskites on curvature or textured substrates. Zou et al. demonstrated a high-quality perovskite film grown on a fibrous substrate by the improved vapor-assisted deposition and the fiber-shaped perovskite solar cell with a PCE of 10.79% was obtained (Dong et al., 2019).

For commercializing PSCs, the large-scale process method has attracted more attention in recent years. With the development of large-area coating methods, including blade, slot-die and spray coating, the roll-roll (R2R) printed process has been suggested to realize the upscaling of PSCs with low cost and high-throughput (Yang et al., 2021). At first, a sequential slot-die method was developed to fabricate large-area PSCs with a PCE up to 11.96% (Hwang et al., 2015). The process was demonstrated to be incorporated into R2R printing. During the past few years, some researchers tried to produce PSCs by the R2R printed process, but only partial processes were reported at laboratory scale (Dou et al., 2018; Galagan et al., 2018; Kim J. E. et al., 2019; Kim Y. Y. et al., 2019). More recently, Kim et al. demonstrated the fully R2R manufacturing of PSCs with PCEs of 23.5% and 19.1% on planar and flexible substrates, respectively. This work suggested the gravure R2R printed process as a promising



method to upscaling PSCs in the near future (Kim et al., 2020; Yang et al., 2021).

Besides compositional and process engineering, interfacial engineering has also contributed to the rapid progress in the efficiency and stability of PSCs. Interfacial engineering mainly focuses on charge transport layers (CTLs) together with interfacial modifications. CTLs play important roles in PSCs, which can not only promote the photogenerated carrier extraction but also suppress the non-radiative recombination. An effective CTL should meet the following requirements: first, matched energy level for the charge extraction from perovskite layer; second, high transparency to avoid energy loss of solar light; and finally, high hole/electron mobility, and the blocking ability of the counter carrier (Ouyang et al., 2019).

Mesoporous TiO<sub>2</sub> and small molecule Spiro-MeOTAD were used as effective electron transport layer (ETL) and hole transport layer (HTL) in the pioneering works (Kim et al., 2012; Lee et al., 2012). Significantly, the use of Spiro-MeOTAD solved the corrosive problem of liquid electrolytes, making all-solid cells. However, Spiro-MeOTAD remains far inferior to commercial photovoltaic cells. Under continuous illumination, doped lithium salt tends to cause aggregation of Spiro-MeOTAD, leading to a rapid decrease in the device efficiency (Abate et al., 2013). On the other side, mesoporous TiO<sub>2</sub> induces fast decay due to exposed oxygen vacancies under ultraviolet light (Leijtens et al., 2013). Therefore, more stable CTLs with effective charge extraction are still required to address the stability issue. Up till now, a great number of CTLs have been studied to deliver more efficient and stable PSCs, including small molecules, polymers and inorganic materials. In terms of long-term operational stability, inorganic materials would be more

suitable for the commercialization of PSCs due to chemical inertness and low cost. You et al. demonstrated air-stable PSCs with p-type NiO<sub>x</sub> and n-type ZnO as HTL and ETL, respectively. The all-metal-oxide devices retain about 90% of the initial efficiency after 60 days of storage at room temperature (You et al., 2016). Fullerene-derived carbon materials such as PCBM and C60 have been developed as promising ETLs in inverted planar structures (Jeng et al., 2013). Besides, a broad range of metal oxides [ZnO (Liu and Kelly, 2014; Cheng et al., 2015), SnO<sub>2</sub> (Jiang et al., 2016; Jiang et al., 2018), Zn<sub>2</sub>SnO<sub>4</sub> (Shin et al., 2015) as ETLs and NiO<sub>x</sub> (Jiang et al., 2015; Kim et al., 2015; Zhang et al., 2016), NiCo<sub>2</sub>O<sub>4</sub> (Ouyang et al., 2018), CuGaO<sub>2</sub> (Chen et al., 2018) as HTLs] are used in PSCs and deliver improved efficiency and stability.

An important aspect of interfacial engineering is the impact of CTLs on perovskite formation. According to the Gibbs free energy [ $\Delta G_{\text{het}} = \Delta G_{\text{hom}} \times f(\theta)$ ], nucleation is determined by the interfacial free energy  $\Delta G$  and wetting angle  $\theta$ . Adjusting surface energy can control the nucleation and growth process of perovskite materials. Generally, hydrophilic CTLs lead to homogenous nucleation, resulting in perovskite films with high coverage and uniformity. On the contrary, hydrophobic surfaces reduce the nucleation, favoring the growth of large grain size. Huang et al. reported the growth of perovskite grains on non-wetting surfaces (Bi et al., 2015). The large-size perovskite grain featured a high grain size/thickness aspect ratio reaching 2.3–7.9, surpassing the limitation of the film thickness (Figure 4A).

The interfaces between CTLs and perovskite layers are crucial for PSCs, but imperfect with various trap states, which gives rise to intensive research on interfacial modifications. As early as 2014, Zhou et al. demonstrated that the electron extraction

process was improved by modifying the interface with polyethyleneimine ethoxylated (Zhou et al., 2014), as shown in **Figure 4B**. These modifications led to a maximum cell efficiency of over 19%. Furthermore, deep trap states at the interfaces need to be suppressed to reduce interfacial non-radiative recombination loss. Chen et al. proposed that interfacial chlorine avoided the formation of deep delocalized states at the  $\text{TiO}_2$ /perovskite interface (Tan et al., 2017). The interfacial recombination was mitigated by the contact passivation strategy. A similar effect was also observed on alkali chloride treated  $\text{NiO}_x$ /perovskite interfaces that delivered improved ordering and reduced defect density (Chen et al., 2019b).

## INDUSTRIAL PROGRESS OF PSCS

In 2022, the perovskite-on-silicon tandem solar cell hits the world-record efficiency of 29.5% in Oxford Photovoltaics (Oxford PV), which has been certified by National Renewable Energy Laboratory (NREL) (Al-Ashouri et al., 2020). This not only refreshes the record of 28.0% previously reported by this company but also breaks the performance record of 29.2% in the Helmholtz Zentrum Berlin (HZB). Instead of replacing silicon solar cells, the perovskite-on-silicon tandem configuration provides a more accessible strategy to develop PSCs in the existing photovoltaic market, which has been considered as very promising in the industrial process of PSCs. Oxford PV that was established in 2010 from the University of Oxford, is one of the first photovoltaic companies focusing on the commercialization of perovskite based photovoltaic technology. The mainstream perovskite-on-silicon tandem solar cell technology allows breaking the previous performance limit of cell modules. The perovskite-based tandem technology has shown great potential to be compatible with the current photovoltaic industry with predicted over 30% combined cell efficiency and the ease of integration.

At the same time, photovoltaic companies in China have been devoted to the scale-up production of PSCs. Hangzhou Microquanta Co. Ltd.'s firstly established the production line of 20 MW with 200–800 cm perovskite solar cell modules and achieved 11.98% PCE, breaking the previous world record held by Toshiba. In 2019, Suzhou GCL Nano Technology Co., Ltd. (GCL Nano), a subsidiary of GCL group, built a 10 MW production line for large-area perovskite modules, and completed the material synthesis and manufacturing process. Later, GCL announced to develop the product line of 100 MW production line and planned to realize the commercial production of perovskite modules. GCL Nano announced to achieve the PCE of 15.21% on an effective area of  $1,241.16 \text{ cm}^2$ . Besides, the Jayu Group and its subsidiary Jayu Solar Energy Technology Co., Ltd. also pay considerable attention to the commercialization of the third-generation perovskite photovoltaic technology, and plan a new layout in their future production bases.

With the target of carbon neutrality in 2060, it is scheduled that non-fossil energy should account for 25% in 2030, and renewable energy capacity should increase to 1.2 billion KW or more. Next decade, the photovoltaic industry should reach 70–90 million KW per year compared with 50 million per year in the past 5 years.

## MERITS AND FUTURE CHALLENGES

Perovskite materials have advantages as photovoltaics such as light absorption coefficient up to  $10^4 \text{ cm}^{-1}$ , long carrier diffusion length and solution processability. For example,  $\text{MAPbI}_3$  perovskites have covered a wide solar light range up to 800 nm with high light absorption coefficient. The use of  $\text{FA}^+$  cation extends the absorption edge to 840 nm, leading to remarkable photocurrent comparable to silicon solar cells (Jena et al., 2019; Min et al., 2019). The manufacturing of PSCs can be conducted through simple solution processes with low-cost earth-abundant elements such as C, H, Pb, I. It is estimated that the manufacturing cost of PSCs is only half of that of silicon solar cells (Meng et al., 2018). Compared with other commercial photovoltaic semiconductors, perovskites also exhibit higher defect tolerance (Ball and Petrozza, 2016), which delivers good reproducibility and reduces production requirements even in a module of 30 W. This merit is extremely desirable in the solution processes of films. In the large-scale integration, perovskite modules can adopt traditional rectangular photovoltaic modules that can be flexible, allowing to be intensively used on building roofs. Due to these advantages, the time horizon of PSCs is expected to be shorter than that of crystalline silicon photovoltaics.

However, there are still limitations that impede the commercialization of PSCs, for example, lead toxicity and long-term stability. Light-induced degradation of perovskites under operating conditions including moisture, oxygen, heat and current stress has become the major concern for outdoor applications of PSCs (Leijtens et al., 2015), even though crystal Si cells face similar problems when exposed to moisture and oxygen. However, the environmental impact can be resolved at the utmost by standard encapsulation technique. The future of PSCs should be bright in consideration of the history of copper indium gallium selenide (CIGS), which is first found to be unstable in the presence of water but has been widely used with long-term stability. Another instability issue is the use of organic interfacial layers such as PEDOT:PSS, Spiro-OMeTAD and so on. To solve these problems, many laboratories have been devoted to developing alternative inorganic interlayers with efficient carrier extraction. It is fortunate to see that, like the rapid development of cell efficiency, the long-term stability of PSCs has also increased a lot in the past several years. This can be attributed to the reduction in the intrinsic degradation of perovskites and the use of various CTLs with good stability. Nowadays, life-cycle assessment (LCA) of PSCs has reached more than 1,000 h (Industrial Standard for New Photovoltaic Technology), even as long as 10,000 h (Shi et al., 2020).

Another concern with perovskite-based photovoltaic technology is the toxicity of lead. Although it has been proposed that one of the main reasons for excellent optoelectronic properties in perovskite materials is the orbital overlap of Pb and I ions, the actual content of lead in PSCs is still lower than that in commercial modules. It is estimated that a perovskite cell module only contains 2 g of lead, while the value of a crystalline silicon cell module is 16 g. Furthermore, encapsulation and recycling techniques have been developed to prevent lead

pollution. Obviously, the use of lead inevitably causes the risk of environmental pollution and increases the additional cost in the recycling process. Scientists have always been looking for ideal elements to replace lead in perovskite materials. Tin (Sn) is one of the potential elements to avoid the use of lead, but it is accompanied by the instability issue because of the oxidation of  $\text{Sn}^{2+}$  to  $\text{Sn}^{4+}$ .

## FUTURE PROSPECTS OF THE COMMERCIALIZATION

In the past several years, the manufacturing costs of silicon solar cells have dropped significantly that makes it possible to use photovoltaics as the large-scale clean energy supply to replace the fossil fuels. Many studies suggest that the solar energy can completely compete with conventional plants when the cost is below than 32 cents/W in well-equipped regions with sufficient solar light. However, the silicon based photovoltaic technology has approached its cost-effective limit due to thermalization loss, low absorption coefficient, and high material requirements. PSCs provides opportunities to go well beyond silicon based photovoltaic technology. Compare with silicon based photovoltaic technology that requires highly pure raw materials (99.999%), PSCs can be manufactured with relatively low purity ( $> 99\%$ ). More importantly, perovskite films are fabricated by low temperature solution routes that result into less power assumption and environmental pollution. Although the second-generation gallium arsenide thin-film solar cell has higher PCEs of about 30%, the cost is extremely high. It is expected that the manufacturing cost of perovskite modules would be 50% lower than that of monocrystalline silicon. However, it is difficult to

displace silicon solar cells in photovoltaic market due to the lack of demonstrated production line. Alternatively, the perovskite-on-silicon tandem configuration should be one of promising technological routes in industrial progress of PSCs. The ease of tuning the bandgap of perovskites and compatible processes make them ideal wide-bandgap materials in the silicon based multi-junction solar cells, although there are some challenges in the transparent conductive layers, tunnel junctions, and light utilization (Li and Zhang, 2020). In the commercialization of PSCs, the supply chain for manufacturing is shorter, and large-scale coating equipment can be developed rapidly. The key technologies for large-area flexible perovskite solar photovoltaic cells will be achieved in about 3 years. The pathways of PSCs from the laboratory to market are emerging with numerous the efforts in academic and industrial field. The commercialization of PSCs is estimated to give rise to at least 100 billion in the photovoltaic market.

## AUTHOR CONTRIBUTIONS

PZ organized the database and wrote the first draft of the manuscript. ML and W-CC contributed conception and design of the study and revised the whole manuscript.

## FUNDING

This work was supported by the National Natural Science Foundation of China (No. 52003058), Guangdong Basic and Applied Basic Research Foundation (No. 2021A1515010607).

## REFERENCES

- Abate, A., Leijtens, T., Pathak, S., Teuscher, J., Avolio, R., Errico, M. E., et al. (2013). Lithium Salts as "redox Active" P-type Dopants for Organic Semiconductors and Their Impact in Solid-State Dye-Sensitized Solar Cells. *Phys. Chem. Chem. Phys.* 15 (7), 2572–2579. doi:10.1039/C2CP44397J
- Al-Ashouri, A., Köhnen, E., Li, B., Magomedov, A., Hempel, H., Caprioglio, P., et al. (2020). Monolithic Perovskite/Silicon Tandem Solar Cell with  $>29\%$  Efficiency by Enhanced Hole Extraction. *Science* 370 (6522), 1300–1309. doi:10.1126/science.abd4016
- Ball, J. M., and Petrozza, A. (2016). Defects in Perovskite-Halides and Their Effects in Solar Cells. *Nat. Energ.* 1 (11), 16149. doi:10.1038/nenergy.2016.149
- Bi, C., Wang, Q., Shao, Y., Yuan, Y., Xiao, Z., and Huang, J. (2015). Non-Wetting Surface-Driven High-Aspect-Ratio Crystalline Grain Growth for Efficient Hybrid Perovskite Solar Cells. *Nat. Commun.* 6 (1), 7747. doi:10.1038/ncomms8747
- Bi, D., Yi, C., Luo, J., Décoppet, J.-D., Zhang, F., Zakeeruddin, S. M., et al. (2016). Polymer-Templated Nucleation and Crystal Growth of Perovskite Films for Solar Cells with Efficiency Greater Than 21%. *Nat. Energ.* 1 (10), 16142. doi:10.1038/nenergy.2016.142
- Burschka, J., Pellet, N., Moon, S.-J., Humphry-Baker, R., Gao, P., Nazeeruddin, M. K., et al. (2013). Sequential Deposition as a Route to High-Performance Perovskite-Sensitized Solar Cells. *Nature* 499 (7458), 316–319. doi:10.1038/nature12340
- Cao, Y., Wang, N., Tian, H., Guo, J., Wei, Y., Chen, H., et al. (2018). Perovskite Light-Emitting Diodes Based on Spontaneously Formed Submicrometre-Scale Structures. *Nature* 562 (7726), 249–253. doi:10.1038/s41586-018-0576-2
- Chakhmouradian, A. R., and Woodward, P. M. (2014). Celebrating 175 Years of Perovskite Research: A Tribute to Roger H. Mitchell. *Phys. Chem. Minerals* 41 (6), 387–391. doi:10.1007/s00269-014-0678-9
- Chen, H. (2017). Two-Step Sequential Deposition of Organometal Halide Perovskite for Photovoltaic Application. *Adv. Funct. Mater.* 27 (8), 1605654. doi:10.1002/adfm.201605654
- Chen, Q., Zhou, H., Hong, Z., Luo, S., Duan, H.-S., Wang, H.-H., et al. (2014). Planar Heterojunction Perovskite Solar Cells via Vapor-Assisted Solution Process. *J. Am. Chem. Soc.* 136 (2), 622–625. doi:10.1021/ja411509g
- Chen, W., Li, D., Chen, X., Chen, H., Liu, S., Yang, H., et al. (2021). Surface Reconstruction for Stable Monolithic All-Inorganic Perovskite/Organic Tandem Solar Cells with over 21% Efficiency. *Adv. Funct. Mater.* 32 (5), 2109321. doi:10.1002/adfm.202109321
- Chen, W., Wang, Y., Pang, G., Koh, C. W., Djurišić, A. B., Wu, Y., et al. (2019a). Conjugated Polymer-Assisted Grain Boundary Passivation for Efficient Inverted Planar Perovskite Solar Cells. *Adv. Funct. Mater.* 29 (27), 1808855. doi:10.1002/adfm.201808855
- Chen, W., Zhou, Y., Chen, G., Wu, Y., Tu, B., Liu, F. Z., et al. (2019b). Alkali Chlorides for the Suppression of the Interfacial Recombination in Inverted Planar Perovskite Solar Cells. *Adv. Energ. Mater.* 9 (19), 1803872. doi:10.1002/aenm.201803872
- Chen, W., Zhu, Y., Xiu, J., Chen, G., Liang, H., Liu, S., et al. (2022). Monolithic Perovskite/Organic Tandem Solar Cells with 23.6% Efficiency Enabled by Reduced Voltage Losses and Optimized Interconnecting Layer. *Nat. Energ.* doi:10.1038/s41560-021-00966-8
- Chen, Y., Yang, Z., Wang, S., Zheng, X., Wu, Y., Yuan, N., et al. (2018). Design of an Inorganic Mesoporous Hole-Transporting Layer for Highly Efficient and Stable Inverted Perovskite Solar Cells. *Adv. Mater.* 30 (52), 1805660. doi:10.1002/adma.201805660



- Cheng, Y., Yang, Q.-D., Xiao, J., Xue, Q., Li, H.-W., Guan, Z., et al. (2015). Decomposition of Organometal Halide Perovskite Films on Zinc Oxide Nanoparticles. *ACS Appl. Mater. Inter.* 7 (36), 19986–19993. doi:10.1021/acsami.5b04695
- Chiang, C.-H., Nazeeruddin, M. K., Grätzel, M., and Wu, C.-G. (2017). The Synergistic Effect of H<sub>2</sub>O and DMF towards Stable and 20% Efficiency Inverted Perovskite Solar Cells. *Energy Environ. Sci.* 10 (3), 808–817. doi:10.1039/C6EE03586H
- Chiang, Y.-H., Anaya, M., and Stranks, S. D. (2020). Multisource Vacuum Deposition of Methylammonium-Free Perovskite Solar Cells. *ACS Energy Lett.* 5 (8), 2498–2504. doi:10.1021/acsenerylett.0c00839
- Cho, H., Jeong, S.-H., Park, M.-H., Kim, Y.-H., Wolf, C., Lee, C.-L., et al. (2015). Overcoming the Electroluminescence Efficiency Limitations of Perovskite Light-Emitting Diodes. *Science* 350 (6265), 1222–1225. doi:10.1126/science.aad1818
- Dong, B., Hu, J., Xiao, X., Tang, S., Gao, X., Peng, Z., et al. (2019). High-Efficiency Fiber-Shaped Perovskite Solar Cell by Vapor-Assisted Deposition with a Record Efficiency of 10.79%. *Adv. Mater. Tech.* 4 (7), 1900131. doi:10.1002/admt.201900131
- Dou, B., Whitaker, J. B., Bruening, K., Moore, D. T., Wheeler, L. M., Ryter, J., et al. (2018). Roll-to-Roll Printing of Perovskite Solar Cells. *ACS Energy Lett.* 3 (10), 2558–2565. doi:10.1021/acsenerylett.8b01556
- Eperon, G. E., Stranks, S. D., Menelaou, C., Johnston, M. B., Herz, L. M., and Snaith, H. J. (2014). Formamidinium lead Trihalide: A Broadly Tunable Perovskite for Efficient Planar Heterojunction Solar Cells. *Energy Environ. Sci.* 7 (3), 982–988. doi:10.1039/C3EE43822H
- Fang, F., Yuan, Y., Wan, Y., Li, J., Song, Y., Chen, W. C., et al. (2022). Near-Infrared Thermally Activated Delayed Fluorescence Nanoparticle: A Metal-Free Photosensitizer for Two-Photon-Activated Photodynamic Therapy at the Cell and Small Animal Levels. *Small* 18 (6), 2106215. doi:10.1002/smll.202106215
- Fang, F., Zhu, L., Li, M., Song, Y., Sun, M., Zhao, D., et al. (2021). Thermally Activated Delayed Fluorescence Material: An Emerging Class of Metal-Free Luminophores for Biomedical Applications. *Adv. Sci.* 8 (24), 2102970. doi:10.1002/advs.202102970
- Feng, J., Jiao, Y., Wang, H., Zhu, X., Sun, Y., Du, M., et al. (2021). High-Throughput Large-Area Vacuum Deposition for High-Performance Formamidinium-Based Perovskite Solar Cells. *Energy Environ. Sci.* 14 (5), 3035–3043. doi:10.1039/D1EE00634G
- Galagan, Y., Di Giacomo, F., Gortler, H., Kirchner, G., de Vries, I., Andriessen, R., et al. (2018). Roll-to-Roll Slot Die Coated Perovskite for Efficient Flexible Solar Cells. *Adv. Energy Mater.* 8 (32), 1801935. doi:10.1002/aenm.201801935
- Gao, Y., Yang, L., Wang, F., Sui, Y., Sun, Y., Wei, M., et al. (2018). Anti-Solvent Surface Engineering via Diethyl Ether to Enhance the Photovoltaic Conversion Efficiency of Perovskite Solar Cells to 18.76%. *Superlattices Microstruct.* 113, 761–768. doi:10.1016/j.spmi.2017.12.015
- George, J. J. K., Halali, V. V., C. G., S., Suvina, V., Sakar, M., and Balakrishna, R. G. (2020). Perovskite Nanomaterials as Optical and Electrochemical Sensors. *Inorg. Chem. Front.* 7 (14), 2702–2725. doi:10.1039/D0QI00306A
- Green, M. A., Ho-Baillie, A., and Snaith, H. J. (2014). The Emergence of Perovskite Solar Cells. *Nat. Photonics* 8, 506. doi:10.1038/nphoton.2014.134
- Hwang, K., Jung, Y.-S., Heo, Y.-J., Scholes, F. H., Watkins, S. E., Subbiah, J., et al. (2015). Toward Large Scale Roll-To-Roll Production of Fully Printed Perovskite Solar Cells. *Adv. Mater.* 27 (7), 1241–1247. doi:10.1002/adma.201404598
- Igual-Muñoz, A. M., Ávila, J., Boix, P. P., and Bolink, H. J. (2020). FAPb<sub>0.5</sub>Sn<sub>0.5</sub>I<sub>3</sub>: A Narrow Bandgap Perovskite Synthesized through Evaporation Methods for Solar Cell Applications. *Sol. RRL* 4 (2), 2070024. doi:10.1002/solr.202070024
- Im, J.-H., Kim, H.-S., and Park, N.-G. (2014). Morphology-Photovoltaic Property Correlation in Perovskite Solar Cells: One-Step versus Two-Step Deposition of CH<sub>3</sub>NH<sub>3</sub>PbI<sub>3</sub>. *APL Mater.* 2 (8), 081510. doi:10.1063/1.4891275
- Jena, A. K., Kulkarni, A., and Miyasaka, T. (2019). Halide Perovskite Photovoltaics: Background, Status, and Future Prospects. *Chem. Rev.* 119 (5), 3036–3103. doi:10.1021/acs.chemrev.8b00539
- Jeng, J.-Y., Chiang, Y.-F., Lee, M.-H., Peng, S.-R., Guo, T.-F., Chen, P., et al. (2013). CH<sub>3</sub>NH<sub>3</sub>PbI<sub>3</sub>/Perovskite/Fullerene Planar-Heterojunction Hybrid Solar Cells. *Adv. Mater.* 25 (27), 3727–3732. doi:10.1002/adma.201301327
- Jeon, N. J., Noh, J. H., Kim, Y. C., Yang, W. S., Ryu, S., and Seok, S. I. (2014). Solvent Engineering for High-Performance Inorganic-Organic Hybrid Perovskite Solar Cells. *Nat. Mater.* 13 (9), 897–903. doi:10.1038/nmat4014
- Jeon, N. J., Noh, J. H., Yang, W. S., Kim, Y. C., Ryu, S., Seo, J., et al. (2015). Compositional Engineering of Perovskite Materials for High-Performance Solar Cells. *Nature* 517 (7535), 476–480. doi:10.1038/nature14133
- Jeong, J., Kim, M., Seo, J., Lu, H., Ahlawat, P., Mishra, A., et al. (2021). Pseudo-Halide Anion Engineering for  $\alpha$ -FAPbI<sub>3</sub> Perovskite Solar Cells. *Nature* 592 (7854), 381–385. doi:10.1038/s41586-021-03406-5
- Jiang, F., Choy, W. C. H., Li, X., Zhang, D., and Cheng, J. (2015). Post-Treatment-Free Solution-Processed Non-Stoichiometric NiOx Nanoparticles for Efficient Hole-Transport Layers of Organic Optoelectronic Devices. *Adv. Mater.* 27 (18), 2930–2937. doi:10.1002/adma.201405391
- Jiang, Q., Zhang, L., Wang, H., Yang, X., Meng, J., Liu, H., et al. (2016). Enhanced Electron Extraction Using SnO<sub>2</sub> for High-Efficiency Planar-Structure HC(NH<sub>2</sub>)<sub>2</sub>PbI<sub>3</sub>-based Perovskite Solar Cells. *Nat. Energy* 2 (1), 16177. doi:10.1038/nenergy.2016.177
- Jiang, Q., Zhang, X., and You, J. (2018). SnO<sub>2</sub>: A Wonderful Electron Transport Layer for Perovskite Solar Cells. *Small* 14 (31), 1801154. doi:10.1002/smll.201801154
- Kim, H. S., Lee, C. R., Im, J. H., Lee, K. B., Moehl, T., Marchioro, A., et al. (2012). Lead Iodide Perovskite Sensitized All-Solid-State Submicron Thin Film Mesoscopic Solar Cell with Efficiency Exceeding 9%. *Sci. Rep.* 2 (1), 591. doi:10.1038/srep00591
- Kim, J. E., Kim, S. S., Zuo, C., Gao, M., Vak, D., and Kim, D. Y. (2019a). Humidity-Tolerant Roll-to-Roll Fabrication of Perovskite Solar Cells via Polymer-Additive-Assisted Hot Slot Die Deposition. *Adv. Funct. Mater.* 29 (26), 1809194. doi:10.1002/adfm.201809194
- Kim, J. H., Liang, P.-W., Williams, S. T., Cho, N., Chueh, C.-C., Glaz, M. S., et al. (2015). High-Performance and Environmentally Stable Planar Heterojunction Perovskite Solar Cells Based on a Solution-Processed Copper-Doped Nickel Oxide Hole-Transporting Layer. *Adv. Mater.* 27 (4), 695–701. doi:10.1002/adma.201404189
- Kim, Y. Y., Yang, T.-Y., Suhonen, R., Kemppainen, A., Hwang, K., Jeon, N. J., et al. (2020). Roll-to-roll Gravure-Printed Flexible Perovskite Solar Cells Using Eco-Friendly Antisolvent Bathing with Wide Processing Window. *Nat. Commun.* 11 (1), 5146. doi:10.1038/s41467-020-18940-5
- Kim, Y. Y., Yang, T. Y., Suhonen, R., Välimäki, M., Maaninen, T., Kemppainen, A., et al. (2019b). Gravure-Printed Flexible Perovskite Solar Cells: Toward Roll-to-Roll Manufacturing. *Adv. Sci.* 6 (7), 1802094. doi:10.1002/advs.201802094
- Kojima, A., Teshima, K., Shirai, Y., and Miyasaka, T. (2009). Organometal Halide Perovskites as Visible-Light Sensitizers for Photovoltaic Cells. *J. Am. Chem. Soc.* 131 (17), 6050–6051. doi:10.1021/ja809598r
- Lee, M. M., Teuscher, J., Miyasaka, T., Murakami, T. N., and Snaith, H. J. (2012). Efficient Hybrid Solar Cells Based on Meso-Superstructured Organometal Halide Perovskites. *Science* 338 (6107), 643–647. doi:10.1126/science.1228604
- Leijtens, T., Eperon, G. E., Noel, N. K., Habisreutinger, S. N., Petrozza, A., and Snaith, H. J. (2015). Stability of Metal Halide Perovskite Solar Cells. *Adv. Energy Mater.* 5 (20), 1500963. doi:10.1002/aenm.201500963
- Leijtens, T., Eperon, G. E., Pathak, S., Abate, A., Lee, M. M., and Snaith, H. J. (2013). Overcoming Ultraviolet Light Instability of Sensitized TiO<sub>2</sub> with Meso-Superstructured Organometal Tri-halide Perovskite Solar Cells. *Nat. Commun.* 4 (1), 2885. doi:10.1038/ncomms3885
- Li, C., Lu, X., Ding, W., Feng, L., Gao, Y., and Guo, Z. (2008). Formability of ABX<sub>3</sub> (X = F, Cl, Br, I) Halide Perovskites. *Acta Crystallogr. Sect B* 64 (6), 702–707. doi:10.1107/s0108768108032734
- Li, C., Ma, Y., Xiao, Y., Shen, L., and Ding, L. (2020a). Advances in Perovskite Photodetectors. *InfoMat* 2 (6), 1247–1256. doi:10.1002/inf2.12141
- Li, C., Wang, H., Wang, F., Li, T., Xu, M., Wang, H., et al. (2020b). Ultrafast and Broadband Photodetectors Based on a Perovskite/organic Bulk Heterojunction for Large-Dynamic-Range Imaging. *Light Sci. Appl.* 9 (1), 31. doi:10.1038/s41377-020-0264-5
- Li, H., and Zhang, W. (2020). Perovskite Tandem Solar Cells: From Fundamentals to Commercial Deployment. *Chem. Rev.* 120 (18), 9835–9950. doi:10.1021/acs.chemrev.9b00780
- Li, J., Wang, H., Chin, X. Y., Dewi, H. A., Vergeer, K., Goh, T. W., et al. (2020c). Highly Efficient Thermally Co-Evaporated Perovskite Solar Cells and Mini-Modules. *Joule* 4 (5), 1035–1053. doi:10.1016/j.joule.2020.03.005
- Li, Y., Wang, J., Yuan, Y., Dong, X., and Wang, P. (2017). Anti-Solvent Dependent Device Performance in CH<sub>3</sub>NH<sub>3</sub>PbI<sub>3</sub> Solar Cells: The Role of Intermediate Phase Content in the As-Prepared Thin Films. *Sustain. Energy Fuels* 1 (5), 1041–1048. doi:10.1039/C7SE00125H

- Lin, K., Xing, J., Quan, L. N., de Arquer, F. P. G., Gong, X., Lu, J., et al. (2018). Perovskite Light-Emitting Diodes with External Quantum Efficiency Exceeding 20 Per Cent. *Nature* 562 (7726), 245–248. doi:10.1038/s41586-018-0575-3
- Lin, R., Xu, J., Wei, M., Wang, Y., Qin, Z., Liu, Z., et al. (2022). All-perovskite Tandem Solar Cells with Improved Grain Surface Passivation. *Nature*. doi:10.1038/s41586-021-04372-8
- Liu, D., and Kelly, T. L. (2014). Perovskite Solar Cells with a Planar Heterojunction Structure Prepared Using Room-Temperature Solution Processing Techniques. *Nat. Photon* 8 (2), 133–138. doi:10.1038/nphoton.2013.342
- Liu, M., Johnston, M. B., and Snaith, H. J. (2013). Efficient Planar Heterojunction Perovskite Solar Cells by Vapour Deposition. *Nature* 501 (7467), 395–398. doi:10.1038/nature12509
- Longo, G., Momblona, C., La-Placa, M.-G., Gil-Escrig, L., Sessolo, M., and Bolink, H. J. (2018). Fully Vacuum-Processed Wide Band Gap Mixed-Halide Perovskite Solar Cells. *ACS Energ. Lett.* 3 (1), 214–219. doi:10.1021/acsenenergylett.7b01217
- Meng, L., You, J., and Yang, Y. (2018). Addressing the Stability Issue of Perovskite Solar Cells for Commercial Applications. *Nat. Commun.* 9 (1), 5265. doi:10.1038/s41467-018-07255-1
- Min, H., Kim, M., Lee, S.-U., Kim, H., Kim, G., Choi, K., et al. (2019). Efficient, Stable Solar Cells by Using Inherent Bandgap of  $\alpha$ -phase Formamidinium lead Iodide. *Science* 366 (6466), 749–753. doi:10.1126/science.aay7044
- Mitzi, D. B., Prikas, M. T., and Chondroudis, K. (1999). Thin Film Deposition of Organic-Inorganic Hybrid Materials Using a Single Source Thermal Ablation Technique. *Chem. Mater.* 11 (3), 542–544. doi:10.1021/cm9811139
- Noh, J. H., Im, S. H., Heo, J. H., Mandal, T. N., and Seok, S. I. (2013). Chemical Management for Colorful, Efficient, and Stable Inorganic-Organic Hybrid Nanostructured Solar Cells. *Nano Lett.* 13 (4), 1764–1769. doi:10.1021/nl400349b
- NREL (2020). Best Research-Cell Efficiency Chart [Online]. NREL. Available: <https://www.nrel.gov/pv/cell-efficiency.html> (Accessed April 19, 2021).
- Ouyang, D., Huang, Z., and Choy, W. C. H. (2019). Solution-Processed Metal Oxide Nanocrystals as Carrier Transport Layers in Organic and Perovskite Solar Cells. *Adv. Funct. Mater.* 29 (1), 1804660. doi:10.1002/adfm.201804660
- Ouyang, D., Xiao, J. Y., Ye, F., Huang, Z. F., Zhang, H., Zhu, L., et al. (2018). Strategic Synthesis of Ultrasmall NiCo<sub>2</sub>O<sub>4</sub> NPs as Hole Transport Layer for Highly Efficient Perovskite Solar Cells. *Adv. Energy Mater.* 8 (16), 1702722. doi:10.1002/aenm.201702722
- Qin, P.-L., Yang, G., Ren, Z.-W., Cheung, S. H., So, S. K., Chen, L., et al. (2018). Stable and Efficient Organo-Metal Halide Hybrid Perovskite Solar Cells via  $\pi$ -Conjugated Lewis Base Polymer Induced Trap Passivation and Charge Extraction. *Adv. Mater.* 30 (12), 1706126. doi:10.1002/adma.201706126
- Qin, S., Lu, C., Jia, Z., Wang, Y., Li, S., Lai, W., et al. (2022). Constructing Monolithic Perovskite/Organic Tandem Solar Cell with Efficiency of 22.0% via Reduced Open-Circuit Voltage Loss and Broadened Absorption Spectra. *Adv. Mater.*, 2108829. doi:10.1002/adma.202108829
- Rajagopal, A., Liang, P.-W., Chueh, C.-C., Yang, Z., and Jen, A. K.-Y. (2017). Defect Passivation via a Graded Fullerene Heterojunction in Low-Bandgap Pb-Sn Binary Perovskite Photovoltaics. *ACS Energ. Lett.* 2 (11), 2531–2539. doi:10.1021/acsenenergylett.7b00847
- Saliba, M., Matsui, T., Seo, J.-Y., Domanski, K., Correa-Baena, J.-P., Nazeeruddin, M. K., et al. (2016). Cesium-containing Triple Cation Perovskite Solar Cells: Improved Stability, Reproducibility and High Efficiency. *Energ. Environ. Sci.* 9 (6), 1989–1997. doi:10.1039/C5EE03874J
- Shi, L., Bucknall, M. P., Young, T. L., Zhang, M., Hu, L., Bing, J., et al. (2020). Gas Chromatography-mass Spectrometry Analyses of Encapsulated Stable Perovskite Solar Cells. *Science* 368 (6497), eaba2412. doi:10.1126/science.aba2412
- Shin, S. S., Yang, W. S., Noh, J. H., Suk, J. H., Jeon, N. J., Park, J. H., et al. (2015). High-performance Flexible Perovskite Solar Cells Exploiting Zn<sub>2</sub>SnO<sub>4</sub> Prepared in Solution below 100 °C. *Nat. Commun.* 6 (1), 7410. doi:10.1038/ncomms8410
- Stranks, S. D., Eperon, G. E., Grancini, G., Menelaou, C., Alcocer, M. J. P., Leijtens, T., et al. (2013). Electron-Hole Diffusion Lengths Exceeding 1 Micrometer in an Organometal Trihalide Perovskite Absorber. *Science* 342 (6156), 341–344. doi:10.1126/science.1243982
- Sutherland, B. R., and Sargent, E. H. (2016). Perovskite Photonic Sources. *Nat. Photon* 10 (5), 295–302. doi:10.1038/nphoton.2016.62
- Tan, H., Jain, A., Voznyy, O., Lan, X., García de Arquer, F. P., Fan, J. Z., et al. (2017). Efficient and Stable Solution-Processed Planar Perovskite Solar Cells via Contact Passivation. *Science* 355 (6326), 722–726. doi:10.1126/science.aai9081
- Wei, Q., Li, X., Liang, C., Zhang, Z., Guo, J., Hong, G., et al. (2019). Recent Progress in Metal Halide Perovskite Micro- and Nanolasers. *Adv. Opt. Mater.* 7 (17), 1900080. doi:10.1002/adom.201900080
- Wu, T., Wang, Y., Li, X., Wu, Y., Meng, X., Cui, D., et al. (2019). Efficient Defect Passivation for Perovskite Solar Cells by Controlling the Electron Density Distribution of Donor- $\pi$ -Acceptor Molecules. *Adv. Energ. Mater.* 9 (17), 1803766. doi:10.1002/aenm.201803766
- Wu, Y., Yang, X., Chen, W., Yue, Y., Cai, M., Xie, F., et al. (2016). Perovskite Solar Cells with 18.21% Efficiency and Area over 1 cm<sup>2</sup> Fabricated by Heterojunction Engineering. *Nat. Energ.* 1 (11), 16148. doi:10.1038/nenergy.2016.148
- Xing, G., Mathews, N., Sun, S., Lim, S. S., Lam, Y. M., Grätzel, M., et al. (2013). Long-Range Balanced Electron- and Hole-Transport Lengths in Organic-Inorganic CH<sub>3</sub>NH<sub>3</sub>PbI<sub>3</sub>. *Science* 342 (6156), 344–347. doi:10.1126/science.1243167
- Xu, X., Li, M., Xie, Y.-M., Ma, Y., Ma, C., Cheng, Y., et al. (2019). Porous and Intercrossed PbI<sub>2</sub>-CsI Nanorod Scaffold for Inverted Planar FA-Cs Mixed-Cation Perovskite Solar Cells. *ACS Appl. Mater. Inter.* 11 (6), 6126–6135. doi:10.1021/acsaami.8b20933
- Yang, G., Qin, P., Fang, G., and Li, G. (2018). A Lewis Base-Assisted Passivation Strategy towards Highly Efficient and Stable Perovskite Solar Cells. *Sol. RRL* 2 (8), 1800055. doi:10.1002/solr.201800055
- Yang, T.-Y., Kim, Y. Y., and Seo, J. (2021). Roll-to-roll Manufacturing toward Lab-To-Fab-Translation of Perovskite Solar Cells. *APL Mater.* 9 (11), 110901. doi:10.1063/5.0064073
- You, J., Meng, L., Song, T.-B., Guo, T.-F., Yang, Y., Chang, W.-H., et al. (2016). Improved Air Stability of Perovskite Solar Cells via Solution-Processed Metal Oxide Transport Layers. *Nat. Nanotech* 11 (1), 75–81. doi:10.1038/nnano.2015.230
- Zaza, F., Pallozzi, V., and Serra, E. (2019). Optimization of Working Conditions for Perovskite-Based Gas Sensor Devices by Multiregression Analysis. *J. Nanotechnol* 2019, 4628765. doi:10.1155/2019/4628765
- Zhang, H., Cheng, J., Lin, F., He, H., Mao, J., Wong, K. S., et al. (2016). Pinhole-Free and Surface-Nanostructured NiO<sub>x</sub> Film by Room-Temperature Solution Process for High-Performance Flexible Perovskite Solar Cells with Good Stability and Reproducibility. *ACS Nano* 10 (1), 1503–1511. doi:10.1021/acsnano.5b07043
- Zhang, H., Mao, J., He, H., Zhang, D., Zhu, H. L., Xie, F., et al. (2015). A Smooth CH<sub>3</sub>NH<sub>3</sub>PbI<sub>3</sub> Film via a New Approach for Forming the PbI<sub>2</sub> Nanostructure Together with Strategically High CH<sub>3</sub>NH<sub>3</sub>I Concentration for High Efficient Planar-Heterojunction Solar Cells. *Adv. Energ. Mater.* 5 (23), 1501354. doi:10.1002/aenm.201501354
- Zhang, Y., Gao, X., Wu, Y., Gui, J., Guo, S., Zheng, H., et al. (2021). Self-powered Technology Based on Nanogenerators for Biomedical Applications. *Exploration* 1 (1), 90–114. doi:10.1002/EXP.10.1002/exp.20210152
- Zhou, H., Chen, Q., Li, G., Luo, S., Song, T.-b., Duan, H.-S., et al. (2014). Interface Engineering of Highly Efficient Perovskite Solar Cells. *Science* 345 (6196), 542–546. doi:10.1126/science.1254050

**Conflict of Interest:** Author PZ is employed by the Beijing JAYU New Energy Technology Development Co., Ltd.

The remaining authors declare that the research was conducted in the absence of any commercial or financial relationships that could be construed as a potential conflict of interest.

**Publisher's Note:** All claims expressed in this article are solely those of the authors and do not necessarily represent those of their affiliated organizations, or those of the publisher, the editors and the reviewers. Any product that may be evaluated in this article, or claim that may be made by its manufacturer, is not guaranteed or endorsed by the publisher.

Copyright © 2022 Zhang, Li and Chen. This is an open-access article distributed under the terms of the Creative Commons Attribution License (CC BY). The use, distribution or reproduction in other forums is permitted, provided the original author(s) and the copyright owner(s) are credited and that the original publication in this journal is cited, in accordance with accepted academic practice. No use, distribution or reproduction is permitted which does not comply with these terms.



# Recent Progress in Fluorescent Probes For Metal Ion Detection

Luanjing Li<sup>1</sup>, Jiahe Wang<sup>2</sup>, Shihan Xu<sup>3</sup>, Chunxia Li<sup>4</sup> and Biao Dong<sup>2\*</sup>

<sup>1</sup>Sdu-Anu Joint Science College, Shandong University, Weihai, China, <sup>2</sup>State Key Laboratory on Integrated Optoelectronics, College of Electronic Science and Engineering, Jilin University, Changchun, China, <sup>3</sup>Department of Bioengineering, University of Washington, Seattle, WA, United States, <sup>4</sup>Institute of Frontier and Interdisciplinary Science, Shandong University, Qingdao, China

All forms of life have absolute request for metal elements, because metal elements are instrumental in various fundamental processes. Fluorescent probes have been widely used due to their ease of operation, good selectivity, high spatial and temporal resolution, and high sensitivity. In this paper, the research progress of various metal ion ( $\text{Fe}^{3+}$ ,  $\text{Fe}^{2+}$ ,  $\text{Cu}^{2+}$ ,  $\text{Zn}^{2+}$ ,  $\text{Hg}^{2+}$ ,  $\text{Pb}^{2+}$ ,  $\text{Cd}^{2+}$ ) fluorescent probes in recent years has been reviewed, and the fluorescence probes prepared with different structures and materials in different environments are introduced. It is of great significance to improve the sensing performance on metal ions. This research has a wide prospect in the application fields of fluorescence sensing, quantitative analysis, biomedicine and so on. This paper discusses about the development and applications of metal fluorescent probes in future.

**Keywords:** fluorescent probes, metal ions, cell imaging, sensors, quantum dots

## OPEN ACCESS

### Edited by:

Shusheng Zhang,  
Linyi University, China

### Reviewed by:

Gang Wei,  
Qingdao University, China  
Jianqiang Liu,  
Guangdong Medical University, China

### \*Correspondence:

Biao Dong  
dongb@jlu.edu.cn

### Specialty section:

This article was submitted to  
Analytical Chemistry,  
a section of the journal  
Frontiers in Chemistry

**Received:** 15 February 2022

**Accepted:** 28 March 2022

**Published:** 13 April 2022

### Citation:

Li L, Wang J, Xu S, Li C and Dong B  
(2022) Recent Progress in Fluorescent  
Probes For Metal Ion Detection.  
Front. Chem. 10:875241.  
doi: 10.3389/fchem.2022.875241

## 1 INTRODUCTION

Metal cations and anions play an important role in the versatile physiological and pathological processes, including metabolism, osmotic regulation, catalysis and so on. It is well known that normal biological events can be adversely affected by maladjustment on the levels of certain ions in organisms (Park et al., 2020). It is because of these ions has certain pathophysiological significance, so we explore how these ions detection in biological systems of sensitive and selective is important.

In order to detect and quantify ions, researchers are committed to developing appropriate chemical sensors. Fluorescence in combination with appropriate probes is a good way to measure metal ions, because fluorescence has certain advantages, such as being faster, less destructive and more sensitive, which can present information about the location and quantity of the target (Li et al., 2017). Fluorescence probe method means that the photophysical properties of probe molecules change obviously before and after the specific binding between probe and analyte, so as to detect the change of fluorescence signal, realizing the detection of different molecular or ion content in the organism or the environment (Xu et al., 2016). In general, for the fluorometric determination of cations or anions, the sensor must consist of two components: a fluorescent carrier and an ionic carrier, which may be independent species or covalently linked on a molecule.

Fluorescent probes can be combined with bioluminescence imaging technology to achieve *in vivo* detection at the cellular level or animal level, which is considered to be the most potential tool for studying different components in the organisms. Fluorescent probe for metal ions, therefore, carries on the synthesis and design gradually become the research hot spot. It is of great significance in chemistry, biology, clinical medicine and agriculture to search for novel organic molecular recognition carriers with high selectivity and to design a novel fluorescent probe for metal ion detection (Xu and Xu, 2016). To have an extensive overview of present studies, we summarized popular fluorescent probes from literatures, classified them according to the types of ions being

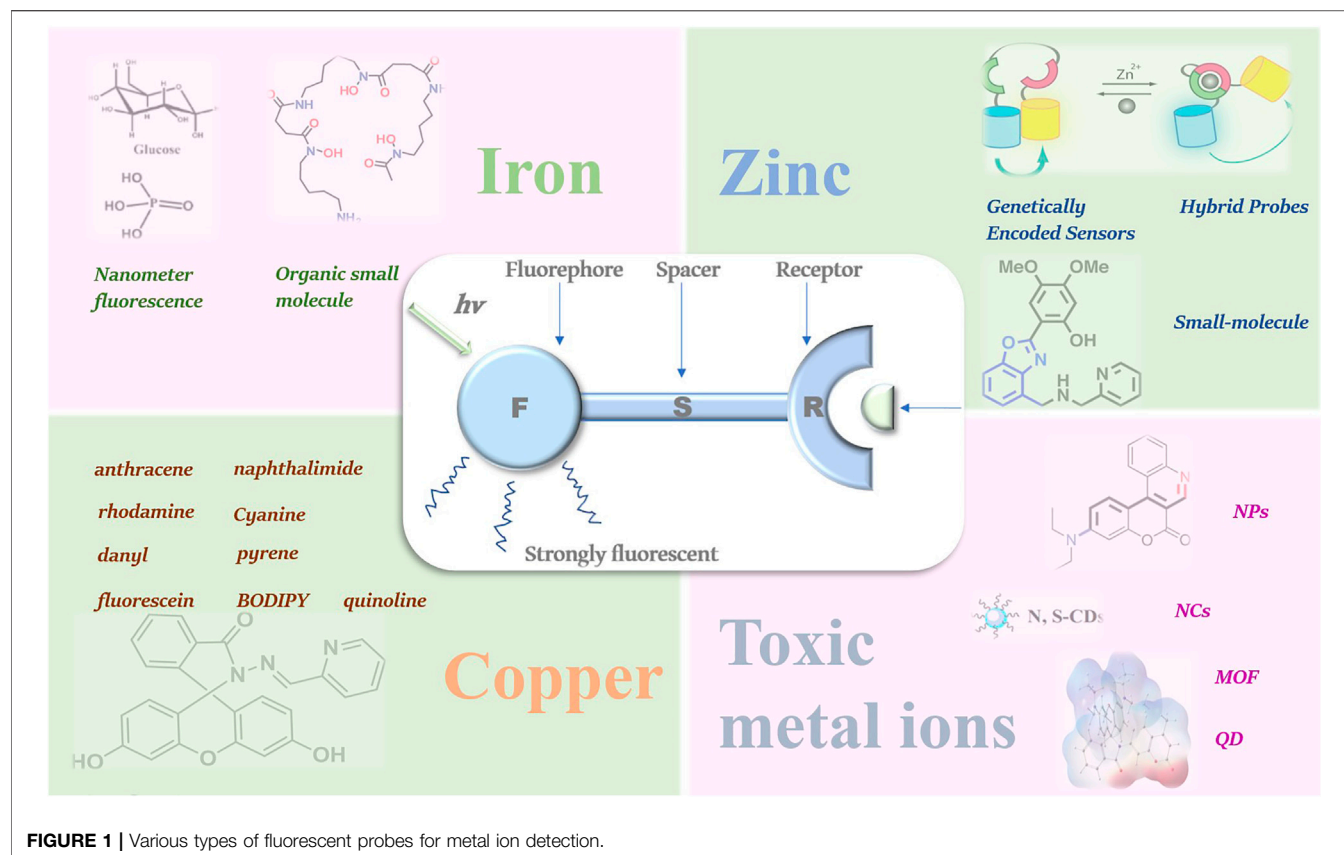


**FIGURE 1** | Various types of fluorescent probes for metal ion detection.

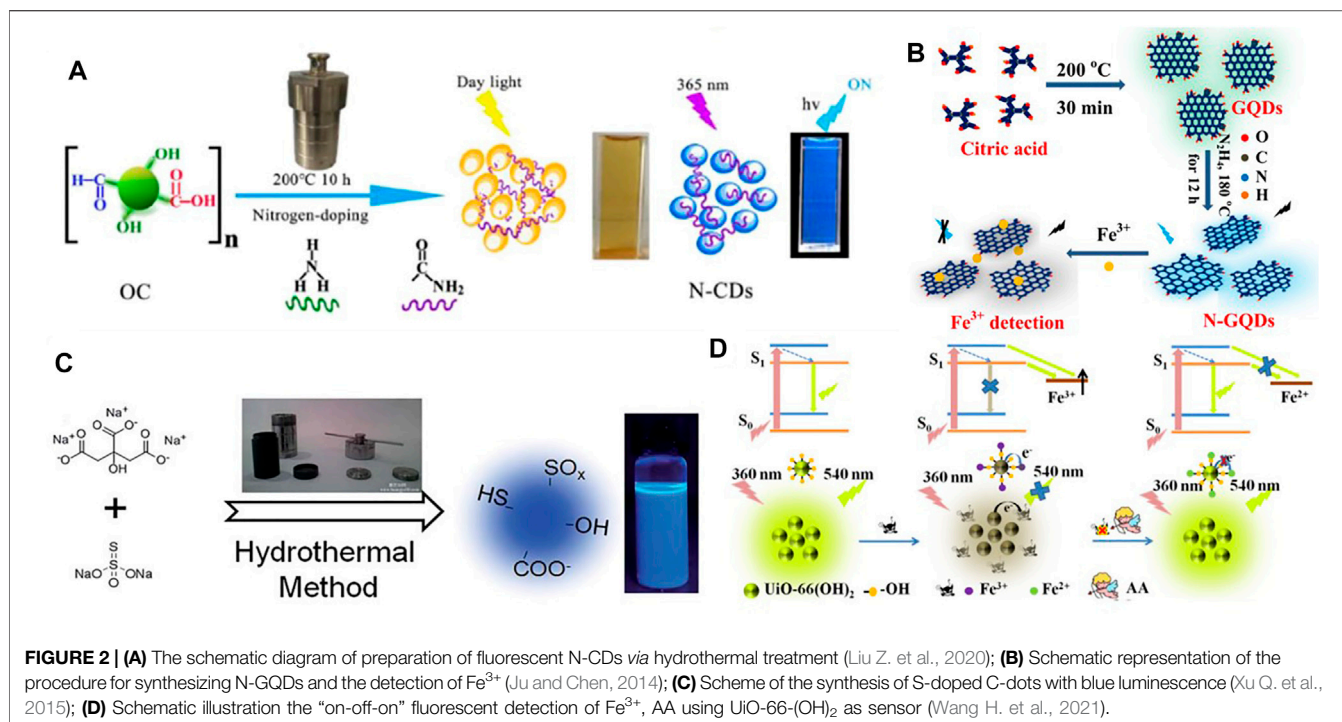
**TABLE 1** | List of methods of fluorescent probe detection of metal ions.

Target	Probe	LOD/ $\mu\text{M}$	Real Sample	Ref.
$\text{Fe}^{3+}$	N, P-CDs	$1.8 \times 10^{-3}$	Human Serum, Living Cells	8
	N-CDs	1.14	Vero cells	9
	Phe-CDs	0.72	water samples	11
	KN-CDs	0.85	—	12
	N-GQDs	$9 \times 10^{-2}$	aqueous media	13
	TPC	$0.2 \times 10^3$	water samples	24
	LaOBr/DAT	0.3	living cells	25
$\text{Fe}^{2+}$	CDs	—	living cells	27
	MOFs	—	aqueous environments	28
	ACQ	—	living cells	30
	FeP1	$1.8 \times 10^{-2}$	living cells, physiological saline	33
	P FeaD	0.46	Live cells, cosmetics	34
$\text{Cu}^{2+}$	turn-on red-emitting	$4 \times 10^{-3}$	living plant tissues, living zebrafish	40
	DCM-Cu	$2.54 \times 10^{-2}$	living MCF-7 cells	41
	CdTe/ QDs	20	real samples	42
	CQDs	5	living cells	43
	BTTPA	0.506	real samples (tea, fish, crab meat)	49
$\text{Zn}^{2+}$	UCNPs	—	real biological samples	61
	NR-Zn	0.131	Hela cells	69
$\text{Hg}^{2+}$	N,S-CDs	0.083	living cells	83
$\text{Pb}^{2+}$	MNPs	$5.7 \times 10^3$	tea and waste water	90
$\text{Cd}^{2+}$	6-(dimethylamino)	0.515	in living cells	112

detected, and presented their structures and strategies. In addition, we focus on numerous strategies to improve the selectivity of fluorescent probes, including metal-organic

backbones, central hydrophilic external hydrophobic strategies, etc., which will provide additional insights for biomedicine.





In this review, the latest research progress of fluorescent probes for iron, copper, zinc, mercury, lead, chromium and other metal ions are summarized (Figure 1), and the development trend and application prospect of this field are also discussed. Basic information on the fluorescent probes for the detection of various ions is listed in Table 1.

## 2 PROBES FOR IRON

### 2.1 Probes For Detecting $\text{Fe}^{3+}$

$\text{Fe}^{3+}$  is considered among the most important metal ions in biological systems and exerts an unparalleled role in many biological processes one of the most vital metal ions in biological systems, such as RNA and DNA synthesis, metabolism and so on. To develop new fluorescent probes having low levels of cellular toxicity, good biocompatibility and high solubility in water is becoming more and more important and urgent.

Lytton and co-workers (Lytton et al., 1992) put forward the earliest reported about an iron fluorescent sensor, which is on the basis of the iron carrier desferrioxamine B (DFO) model, connect to the fluorescent carrier 7-nitrobenz-2-oxa-1, 3-diazole (NBD). By detecting and monitoring  $\text{Fe}^{3+}$  performance in solution, the NBD-DFO model proves its advantage in monitoring iron under various conditions of iron imbalance diseases. For the past few years, various fluorescent probes developed for selective detection of  $\text{Fe}^{3+}$  can be divided into four categories according to the fluorescence signal processing: Turn-Off, Turn-on, ratiometric and chemodosimeters.

#### 2.1.1 Nanometer Fluorescence Probes

For the exploration of the iron ion, nano fluorescent probe plays an important role. Among them, one of the most well-studied materials is semiconductor nanoparticles, also known as quantum dots. In recent years, carbon dots (CDs) are widely used in fluorescent biological imaging and sensing (Zhu et al., 2013). However, the low quantum yield (QY) of CDs severely restricts its development and application. Chemically doped heteroatoms can effectively adjust electron density to improve the QY value of CDs. Therefore, the photochemical and physicochemical properties of carbon dots (CDs) can be efficiently regulated by chemical doping heteroatoms (Guo et al., 2015).

Shi et al. (Shi et al., 2016) synthesized N, P-CDs multi heteroatom (nitrogen and phosphorus co-doped carbon nanodots) fluorescence sensor, which has low cytotoxicity and high photostability, and measured its sensitivity to  $\text{Fe}^{3+}$ . Liu et al. (Liu Z. et al., 2020) synthesized the non-toxic nitrogen-doped fluorescent carbon dots (N-CDs) that can detect ferric ions, at the same time can be used for fluorescent probe of Vero cell biological imaging (Figure 2A). Du et al. (Du et al., 2021) demonstrated that off-on switch fluorescent probe based on yellow emission carbon dots (y-CDs) provides a highly sensitive and selective method for the detection of ferric ions. Pu et al. (Pu et al., 2020) proposed a static quenching mechanism about the phenylalanine carbon dots (Phe-CDs), which kept its outstanding fluorescence intensity despite its extreme pH values. Atchudan et al. (Atchudan et al., 2021) reported that they synthesized fluorescent carbon dots (KN-CDs) by hydrothermal carbonization method as a good fluorescence sensor of  $\text{Fe}^{3+}$  based on the closing sensor of Fe (III)

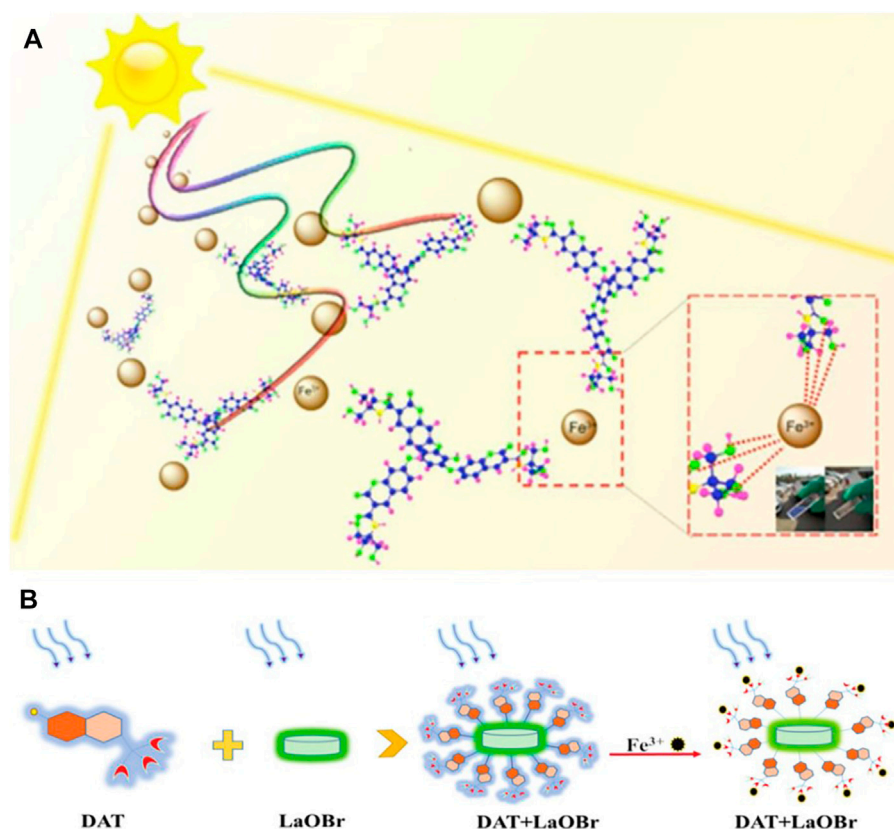


**FIGURE 3 | (A)** The trimeric phenolic coumarin (TPC) designed through the internal hydrophobic-external hydrophilic strategy achieves greatly enhanced  $\text{Fe}^{3+}$  sensing performance, and can be used for naked eye detection with sunlight excitation (Liu J. et al., 2020); **(B)** A schematic diagram showing the preparation of the LaOBr/DAT [N-(2-hydroxy-1,1-bis(hydroxymethyl)ethyl)-7-hydroxycoumarin-3-carboxamide] composite and the mechanism of  $\text{Fe}^{3+}$  sensing (Sun et al., 2020).

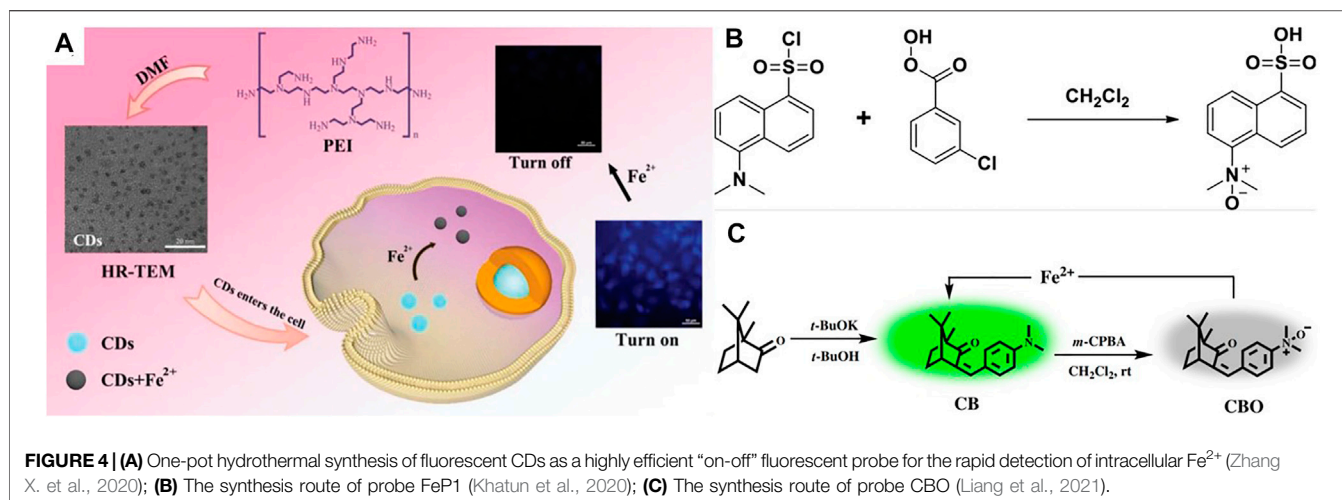
ions. Ju *et al.* (Ju and Chen, 2014) synthesized environmentally friendly nitrogen-doped graphene quantum dots (N-GQDs) for the unlabeled  $\text{Fe}^{3+}$  ions detection in various actual water (Figure 2B). Qi *et al.* (Qi et al., 2019) designed and demonstrated the promise of nitrogen-doped carbon quantum dots (N-CQDs) as probes for iron ions. Zhang *et al.* (Zhang Y. et al., 2021) obtained  $\text{B}_1\text{N}_2\text{CQDs}$  (core-shell carbon quantum dots), which has been proved that its detection of  $\text{Fe}^{3+}$  can be applied to both endocellular scenarios in biological system and river water samples due to its high stability and fluorescence quantum yield. Xu *et al.* (Xu Q. et al., 2015) synthesized Sulfur-doped carbon dots (S-doped C-dots), which can also be used to detect iron ions efficiently (Figure 2C).

Qu *et al.* (Qu et al., 2013) took advantage of dopamine for light source synthetic photoluminescence carbon nanoparticles (CNPs), which can be used as a very powerful fluorescence sensitive stage and has been successfully applied to iron ion detection in some water samples. Based on hydroxy functional metal organic skeleton (MOF)  $\text{UiO-66-(OH)}_2$ , Wang *et al.* (Wang H. et al., 2021) also proposed a “on—off—on” fluorescent switch nano probe (Figure 2D). Dong *et al.* (Dong et al., 2021) synthesized the NIR PL of GSH-capped gold nanoclusters (GSH-AuNCs), which exhibits excellent sensing performance.

### 2.1.2 Organic Small Molecules

Xu and co-workers (Xu H. et al., 2015) obtained a owns two one-dimensional channel unparalleled of three-dimensional TB - BTB (benzene-1, 3, 5-tribenzoate) framework for high sensitivity detection of  $\text{Fe}^{3+}$ . Using an EuL3 ( $\text{L} = 4'-(4\text{-carboxyphenyl})-2, 2':6', 2''\text{-tripyridine}$ ) fluorescence sensor, Zheng and co-workers (Zheng et al., 2013) designed a portable daily life iron ion test paper. Azmi *et al.* (Al-Azmi and John, 2021) produced a tricyanofuran hydrazone (TCFH) optical probe for better recognition of Fe (III) ions in the hydro environment. Zhang (Zhang et al., 2018) reported a new fluorescence and specific color probe containing both deoxycholic acid and rhodamine molecules and used the spectrum to achieve the measurement of iron ions.

In order to achieve better sensing performance and water-solubility of organic molecular probes, Liu *et al.* (Liu J. et al., 2020) proposed a method with great potential and development space. They linked the inner hydrophobic molecule tribromophenol with the outer hydrophobic molecule coumarin on the basis of the original iron fluorescence probe (Figure 3A). Besides, in view of the water-soluble dilemma of organic small molecules, Sun *et al.* (Sun et al., 2020) also adopted a similar structural strategy, and developed a unique vanilloid fluorescent probe for the assay of



iron ions by increasing the nucleophilic substitution reaction of  $\text{LaOBr}$  (Figure 3B). Designing composite materials is of great significance to the change of the water solubility of organic small molecules, and it can also improve the probe's sensitivity to ions.

High levels of trivalent iron ions can cause many diseases, including cancer, organ disorders of the heart, liver and pancreas, hepatitis, Parkinson's disease, Alzheimer's disease, etc. Therefore, the development of fluorescent probes for iron ions has greatly facilitated biomedical imaging in human cells and has contributed to disease diagnosis.

In last several years, lots of researchers have designed different methods of novel iron (III) fluorescence sensors, and successfully synthesized sensors for monitoring the concentration of environmental iron and studying iron migration in various microbial species. Most sensors are derived from the principle of fluorescence quenching, so future probes should be preferentially designed for absorption at longer wavelength to avoid the internal filtering effect of iron (III) absorption in the UV-vis region.

## 2.2 Probes For Detecting $\text{Fe}^{2+}$

Although the iron in the cells has two forms of  $\text{Fe}^{2+}$  and  $\text{Fe}^{3+}$ , it mainly exists with the form of  $\text{Fe}^{2+}$  because of the reductive microenvironment of cells (Ma et al., 2021). On the one hand, it is difficult to establish a highly specific probe for the detection of  $\text{Fe}^{2+}$ , because the different oxidation states of  $\text{Fe}^{2+}$  and  $\text{Fe}^{3+}$  vary with each other. On the other hand, due to the strong force between paramagnetic  $\text{Fe}^{2+}$  and fluorophore, fluorescence quenching is usually induced, resulting in part of the constructed probes being “on-off” type, which is not easy to observe due to the influence of spontaneous fluorescence of organisms (Wei et al., 2020). Currently, the  $\text{Fe}^{2+}$  fluorescent probes mainly include N-oxides, nitroxyl radicals, endoperoxides, bionic ligands, heavy metals, imines and so on.

In order to achieve high-efficiency sensing of  $\text{Fe}^{2+}$ , Yan et al. (Yan, 2017) proposed a dual-correspondence luminescence probe with optimized metal-Organic Framework (MOF) as the main body. The special feature of this probe is the use of various luminescent substances, such as lanthanide ions, carbon quantum

dots, etc. Xu et al. (Xu and Yan, 2015) also synthesized a layer similar to MOF [ $\text{MIL-124}$ , or  $\text{Ga}_2(\text{OH})_4(\text{C}_9\text{O}_6\text{H}_4)$ ], and further designed and developed a probe to detect  $\text{Fe}^{2+}$  ions. For  $\text{Fe}^{2+}$  detection, Yang et al. (Yang et al., 2021) reported on the aggregation-induced emission (AIE) based probe named QM-Fe, and verified the feasibility of  $\text{Fe}^{2+}$  detection in viable cells. Zhang et al. (Zhang D. et al., 2021) gained a new spiropyran-based fluorescent probe to detect  $\text{Fe}^{2+}$  ion. The results show that the addition of  $\text{Fe}^{2+}$  with the probe solution improved the magnetic intensity of fluorescence by 6-fold. Wei et al. (Wei et al., 2020) developed a “on-off” fluorescent probe based on a carbon point (CDs), which has been efficiently used to detect  $\text{Fe}^{2+}$  in BSA solution, tap water and living cells (Figure 4A). In order to realize real-time detection of unstable ferric divalent ions in living systems, Long et al. (Long et al., 2018) designed a fluorescent probe of coumarin by using a unique cyclization reaction. Gao et al. (Gao et al., 2020) constructed a practical and novel  $\text{Fe}^{2+}$  fluorescent probe via a unique strategy with  $\text{Fe}^{2+}$ -induced reducing reaction, which can act in different monitoring of the environment, such as living cells. Khatun et al. (Khatun et al., 2020) developed a kind of “Turn-On” probe P-Fe (II), which is used to measure the exact amount of ferrous ion ( $\text{Fe}^{2+}$ ) in cosmetics or living cells (Figure 4B). Liang et al. (Liang et al., 2021) developed a new camphor-based fluorimetric probe (CBO) with a natural monoterpene ketone camphor as a base material for the detection of  $\text{Fe}^{2+}$  and it can be easily observed by fluorescence of  $\text{Fe}^{2+}$  ions in some animals and in plant cells  $\text{Fe}^{2+}$  imaging (Figure 4C).

By stimulating the two-photon microscope fluorescence imaging at 680 nm, Yang et al. (Yang et al., 2019) reported for the first time a novel intramolecular charge transfer (ICT) based two-photon, near-infrared (NIR) -enabled fluorescent probe for detecting  $\text{Fe}^{2+}$ , and applied to the actual living cells. In view of the test organisms or the ferrous ions in aqueous environment, Zhang et al. (Zhang X. et al., 2020) on the basis of nitrogen oxides reduction reaction, invented and created a new kind of “off-on” fluorescent probes the NT-Fe (4-Amino-1, 8-naphthalimide), which greatly improved the efficiency of  $\text{Fe}^{2+}$  detection in zebrafish.



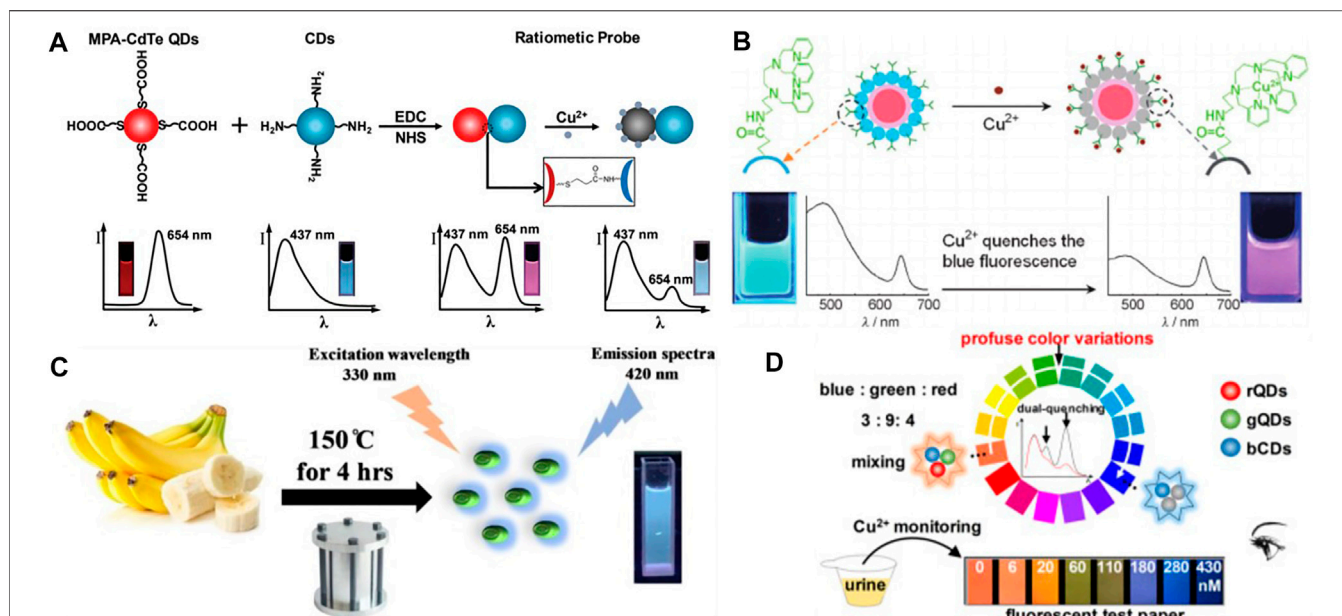


**FIGURE 5 | (A)** Schematic illustration of the formation of the dual-emission ratiometric fluorescence probe and the visual detection principle for copper ions (Wang et al., 2016); **(B)** Dual-emission fluorescent sensing of Cu<sup>2+</sup> ions based on a CdSe@C-TPEA nanohybrid (Zhu et al., 2012); **(C)** Schematic representation of NS-CQDs synthesis synthesizing NS-CQDs from banana juice (Chaudhary et al., 2020); **(D)** Schematic illustration of the visual detection principle for Cu<sup>2+</sup> using the tricolor probe (Cai et al., 2018).

During recent years, although there are not numerous reports on the detection of Fe<sup>2+</sup> by the methods of fluorescent probes, some progress has been made. It can be roughly divided into “off-on” type Fe<sup>2+</sup> fluorescent probes, “on-off” type Fe<sup>2+</sup> fluorescent probes, ratio type and other types of Fe<sup>2+</sup> fluorescent probes. These in-depth exploration and research will be of great significance for in-depth understanding of the specific functions of Fe<sup>2+</sup> in organisms and the mechanism of action on diseases.

### 3 PROBES FOR DETECTING COPPER

As we all know, copper ion (Cu<sup>2+</sup>) is another heavy metal ion found in very high concentrations in our people’s body. As a cofactor of many enzymes, copper ion is inseparable from various enzymatic catalysis and electron transfer processes, and it occupies a unique and key position in various physiological processes. Therefore, if copper homeostasis is out of whack, it can lead to a lot of neurodegenerative diseases that we don’t expect. In order to achieve an optimal measurement performance for copper ions, small polymer fluorescent probes have been extensively used in the procedure of microscopic image analysis due to their certain uniqueness.

So far, methods about the Cu<sup>2+</sup> ions’ detection using small molecular fluorescent probes have generally included the UV-to-O-NIR regions of anthracene, danyl, pyrene, quinazoline, cyanine dyes, naphthalimide, quinoline, rhodamine, fluorescein, BODIPY and so on (Sivaraman et al., 2018). However, many significant properties of fluorescent probes

used in living cells and *in vivo* still need to be improved, such as slow response speed, high detection limit and poor selectivity (Kar et al., 2013).

Recently, Zhou et al. (Zhou et al., 2021) designed an open red fluorescent probe that can be used well and efficiently to detect copper ions (Cu<sup>2+</sup>) in some food samples and live zebrafish. Besides, Copper (Cu) has also been found to be indispensable and extremely important in the process of oxygen-containing photosynthesis in biological systems. Li et al. (Li et al., 2021) developed a novel “turn on” NIR probe DCM-Cu whose basic is DCM for the detection of copper ion (II). Due to its wonderful sensitivity and low cytotoxicity toward Cu<sup>2+</sup> with a Stokes shift of 140 nm, the probe has been widely used by scholars. What’s more, by covalently linking carboxylate-modified red fluorescent cadmium telluride (CdTe) quantum dots (QDs) with fluorescent blue carbon nanodots functionalized with amino groups (CDs), Wang et al. (Wang et al., 2016) developed a ratio fluorescence nanosensor with good performance for Cu<sup>2+</sup> detection (Figure 5A). In addition, Zhu et al. (Zhu et al., 2012) also adopted a ratio fluorescence detection method for copper ions, in particular, the CdSe@C quantum dots (QDs) with different fluorophore dual-emission were selected. This probe ion recognition higher and better stability (Figure 5B). Lin et al. (Lin et al., 2014) successfully designed a new type of high-fluorescence metal-organic structure (MOFs) for the determination of copper ion content in water in the environment. This strategy utilized a branched chain polyethylamine encapsulated carbon quantum dot material, thus improving the fluorescence quantum yield and detection effect. By using mesoporous silica (MS) spheres as the material of



nanometer reactors, Zong *et al.* (Zong *et al.*, 2014) improved the fluorescence probe of carbon point (CDs), and made a contribution to the detection of copper ions by synthesizing CDs as fluorescence probe by “off-on” method. Wang *et al.* (Wang L. *et al.*, 2020) implemented the chemical probe formation of the copper (II) complex L-  $\text{Cu}^{2+}$  as a dual-channel recognition probe, allowing one to identify dramatic changes in color with the naked eye. Yao *et al.* (Yao *et al.*, 2013) designed a ratiometric fluorescent probe based on hybridized dual-emission quantum dots (QDs) and demonstrated that it can visualize real-time monitoring of copper ions in natural environmental water sources, greatly improving efficiency. Ye *et al.* (Ye *et al.*, 2015) first reported the use of a cadmium pamoate metal-organic framework as a bifunctional fluorescent sensor for the detection of trace amounts of 2, 4, 6-Trinitrophenol (TNP) and  $\text{Cu}^{2+}$ , a study that greatly improved the sensitivity of the fluorescent probe for the recognition of copper ions. For the detection of copper ions in actual samples, Tang *et al.* (Tang *et al.*, 2020) developed a pyridine amide (BTPPA) with aggregation-induced emission (AIE) properties as a probe, which achieved by aggregating switching strategies, through “on-off-on” variation of emissions.

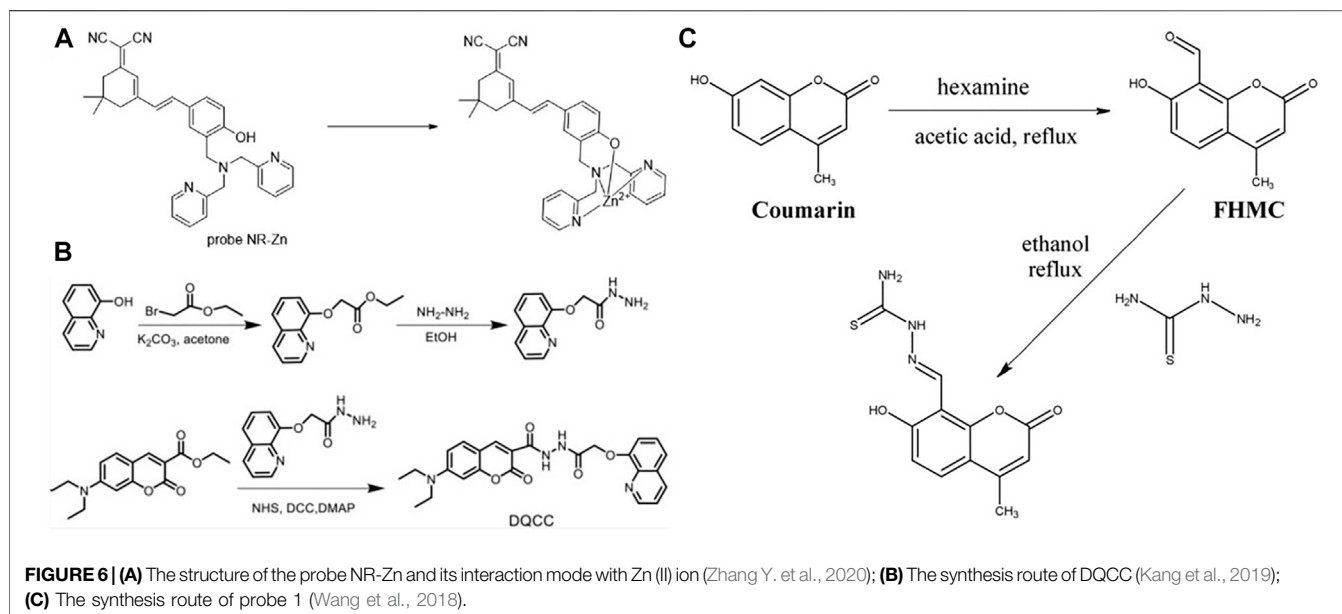
Fluorescent probes for the detection of Cu(II) in water samples are also accessible from natural sources, such as Chaudhary *et al.* (Chaudhary *et al.*, 2020)'s synthesized and published highly fluorescent N,S co-doped CQD (NS-CQD) at an excitation wavelength of 330 nm with an enhanced quantum yield (32%) (Figure 5C). For monitoring and identifying  $\text{Cu}^{2+}$ , Wang *et al.* (Wang Z.-G. *et al.*, 2020) developed a novel colorimetric/fluorescent probe (7-(diethylamino)-2-oxo-2H-chromen-3-yl)methylene-4-(dimethylamino) benzohydrazide (HL). Furthermore, in order to improve the continuity of the process when detecting copper ions, Mohammadi *et al.* (Mohammadi and Ghasemi, 2020) developed a novel pyrimidine-based chemosensor (PyrCS) and was able to achieve an intuitive vivid colorimetric response for observation in a specific pH range. Song *et al.* (Song *et al.*, 2018) designed a dual emission ratio fluorescence sensing membrane for copper ion detection. This double emission film managed to fabricate the chitosan, graphite carbonitride ( $\text{G-C}_3\text{N}_4$ ) and Gold nanoclusters (Au NCs). The film has high sensitivity and portability, which opens up a new way for the detection of copper ions in the environment. Rane *et al.* (Rane *et al.*, 2018) synthesized quinoline based novel fluorescent probes for the selectivity and sensitivity of detecting  $\text{Cu}^{2+}$  ions. Kumar *et al.* (Gujuluva Gangatharan *et al.*, 2018) synthesized an easily available and portable “off-off” colorimetric and fluorescent probe with excellent results in the application of trace  $\text{Cu}^{2+}$  ions in real water samples. Cai *et al.* (Cai *et al.*, 2018) reported a fluorescent test paper probe consisting of three different emitting quantum dots including blue (bCDs), green (gQDs), and red (rQDs), which enables a simple and rapid detection of  $\text{Cu}^{2+}$  ions in human urine by observing the color of the filter paper (Figure 5D). Abnormal levels of copper ions in living organisms can also cause many neurological related diseases, and therefore it is of great importance for biomedicine to have a variety of copper ion fluorescent probes for use in living cells.

## 4 PROBES FOR DETECTING ZINC

Zinc is the next most prevalent of the transition metal ions in the human body. In small amounts,  $\text{Zn}^{2+}$  is beneficial to people's health, but at higher concentrations, it appears toxic. Zinc imbalances have been linked to serious neurological diseases, such as Alzheimer's and Parkinson's (Xu *et al.*, 2012). So far, people have developed a variety of  $\text{Zn}^{2+}$  fluorescent sensors, and successfully applied in living cells, hippocampal slices, and  $\text{Zn}^{2+}$  imaging in zebrafish, especially Lippard and Nagano. In more recent years, zinc ion fluorometric probes have been arranged under different columns of fluorescent architecture, including unquinoline, rhodamine, naphthalene, coumarin, naphthalimide, pyrene, luciferin, derivatives of phenol and several other fluorophore groups (Wang F. *et al.*, 2021).

Walkup *et al.* (Walkup *et al.*, 2000) first prepared a novel, highly affinity, selective, membrane permeable  $\text{Zn}^{2+}$  fluorescence sensor. Roy *et al.* (Roy *et al.*, 2007) investigated a DFP based sensor for the first time, which can be used as a fluorescent probe for the detection of zinc ions and applied under certain physiological conditions. Peng *et al.* (Peng *et al.*, 2015) designed and synthesized a chromophore-based up-conversion nanoparticle (UCNPs) nano system as a fluorescent probe for  $\text{Zn}^{2+}$  by combining chromophore groups and lanthanide-doped UCNPs together. This method was demonstrated to significantly improve the efficiency of divalent Zn ion detection in specific animals, such as zebrafish. Kim *et al.* (Kim *et al.*, 2013) reported a unique fluorogenic  $\text{Zn}^{2+}$  chemosensor based on a cap-typed tripodal Schiffbase. Zhou *et al.* (Zhou *et al.*, 2010) designed a hydrazone-pyrene-based fluorescent probe with simplicity and efficiency in order to improve the selectivity of the fluorescent probe for Zn ions. Then they further expanded the application scenario of the probe and verified the feasibility of detecting  $\text{Zn}^{2+}$  ions in pancreatic  $\beta$ -cells, which made a contribution to the biomedical field. Hagimori *et al.* (Hagimori, 2013) reported that novel fluorescent probes based on pyridine-pyridone possess low molecular weight for zinc ion detection. Price *et al.* (Price *et al.*, 2018) reported AQA-F, a fluorescent probe that can be used to detect zinc ions in prostate and prostate cancer cell lines *in vitro*. Zhang (Zhang *et al.*, 2012) developed a pyrazoline based fluorescent probe and verified that this probe showed 40-fold enhanced fluorescence for  $\text{Zn}^{2+}$  compared to other metal ions, i.e., good selectivity for Zn ions, and that it could be well applied in living neuronal cells.

Zhang *et al.* (Zhang *et al.*, 2016) reported two near-infrared fluorescent probes based on the fluorophore platform corresponding to Rhodol functionalized by dimethylamine Zn (II) binding groups, and this probe enables the detection of Zn (II) ions produced by intracellular metalloproteins. In addition to this, Fang *et al.* (Fang *et al.*, 2016) similarly synthesized and studied two NIR fluorescent probes (A and B), but chose different material bases. One is a semicyano structure attached to dimethylamine (DPA) and the other is a dimethylamine derivative with pyridine substituted by pyrazine, which are very effective in detecting zinc ions in living cells. Among the various near-infrared fluorescence (NIR) probes, Zhang *et al.* (Zhang Y. *et al.*, 2020) synthesized a near-infrared fluorescence



(NIR) probe NR-Zn consisting of a dicyanoisophorone derivative and a dimethylamine molecule in a structure (**Figure 6A**). So far, this probe has proved to be successfully applicable for zinc ion recognition in Hela cells. Kang *et al.* (Kang et al., 2019) designed a sophisticated fluorescent probe test paper in the acyl hydrazine linkage mode that allows copper ion detection based on color change according to a 365 nm UV lamp (**Figure 6B**). In some specific scenarios, such as the detection of  $\text{Zn}^{2+}$  ions in  $\text{CH}_3\text{CN}$ /HEPES solution (1/1, 10.0 mM, pH = 7.0), a Schiff base fluorescent probe (L) designed by Chang *et al.* (Chang et al., 2020) can efficiently achieve this purpose. Wang *et al.* (Wang et al., 2018) devised and synthesized a novel coumarin based dual chemosensor (probe 1), which was observed by fluorescent cell imaging as a bio-imaging fluorescent sensor for detecting  $\text{Zn}^{2+}$  in human cancer cells (**Figure 6C**).

## 5 PROBES FOR SENSING TOXIC METAL IONS

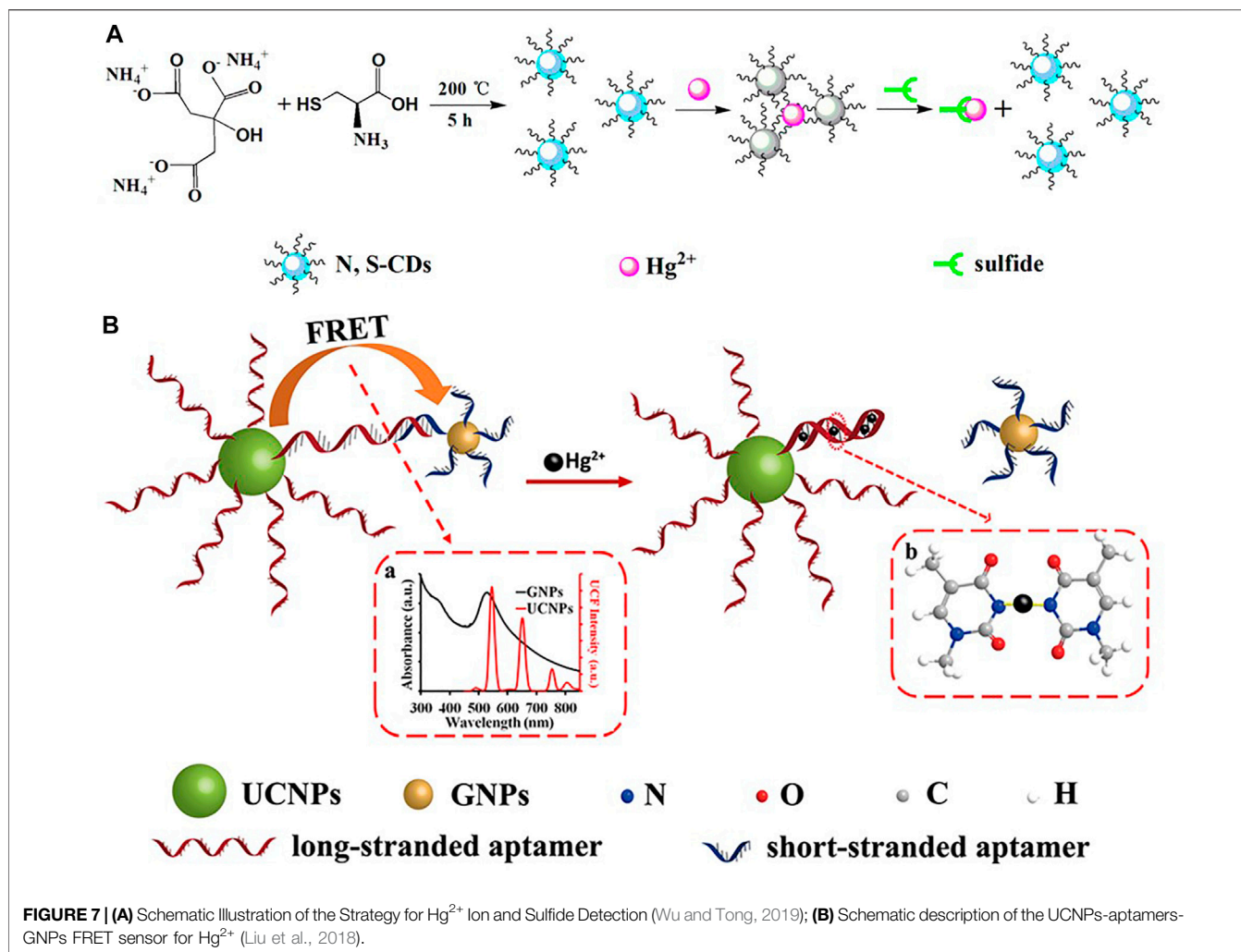
Among all kinds of heavy metal ions, lead, cadmium and mercury ions do great harm to the environment and human beings because of their dangerous properties. Since its high toxicity directly or indirectly affect human health, it has been widely concerned in the world. These three heavy metal ions are not biodegradable and can therefore accumulate in the environment, leading to food and water contamination. Heavy metal ions and proteins (or enzymes) can have a strong interaction in the human body, so that the protein inactivity, resulting in chronic poisoning (He and Lu, 2001). People exposed to even very low amount of lead, cadmium and mercury ions can lead to diseases of various systems of the human body. Therefore, a reliable, and convenient method to detect heavy metal ions, especially  $\text{Hg}^{2+}$ ,  $\text{Pb}^{2+}$  and  $\text{Cd}^{2+}$ , has generated a lot of interest in recent years, which is of

great significance not only in environmental research, but also in food research and industry and agriculture (Kim et al., 2012).

### 5.1 Probes For Detecting $\text{Hg}^{2+}$

The detection of mercury ions is of great importance due to their high toxicity and wide distribution in the environment, through which they can enter the food chain and then have an impact on human life and health (Staudinger and Borisov, 2015). Therefore, there is an urgent need for simple, inexpensive and reliable mercury detection methods with high selectivity and sensitivity. In recent years, fluorescence probes used to detect mercury ions are classified according to the changes of fluorescence signal, including signal attenuation fluorescence probes, signal enhancement fluorescence probes and ratio fluorescence probes (Wang Y. et al., 2021). The applications of mercury ion probes can be broadly divided into two areas: environmental and biological.

In purpose of detecting ions in the environment, Lu *et al.* (Lu et al., 2012) reported for the first time a water-soluble fluorescent carbon nanoparticles (CPs) and used to detect  $\text{Hg}^{2+}$  in natural environmental lakes, a method that is environmentally friendly, economical and simple with greater universality. In addition, in order to detect  $\text{Hg}^{2+}$  in real lake water, Zhang *et al.* (Zhang and Chen, 2014) also tried another method, where they obtained nitrogen-doped carbon quantum dots (N-CQDs) using folic acid as the carbon and nitrogen sources, which proved to be highly luminescent with a detection limit of 0.23  $\mu\text{M}$ . Wang *et al.* (Wang S. et al., 2021) synthesized thioctic acid-carbon dots (SCDs), which was used as an “off-on” type fluorescent probe in the detection of  $\text{Hg}^{2+}$ . Xu *et al.* (Xu et al., 2018) expected to identify  $\text{Hg}^{2+}$  by changes in fluorescence spectra and fabricated a colorimetric long-wavelength type fluorescent probe Hg-P to obtain higher selectivity. Tao *et al.* (Tao et al., 2020) synthesized a fluorescent probe based on a simple coumarin



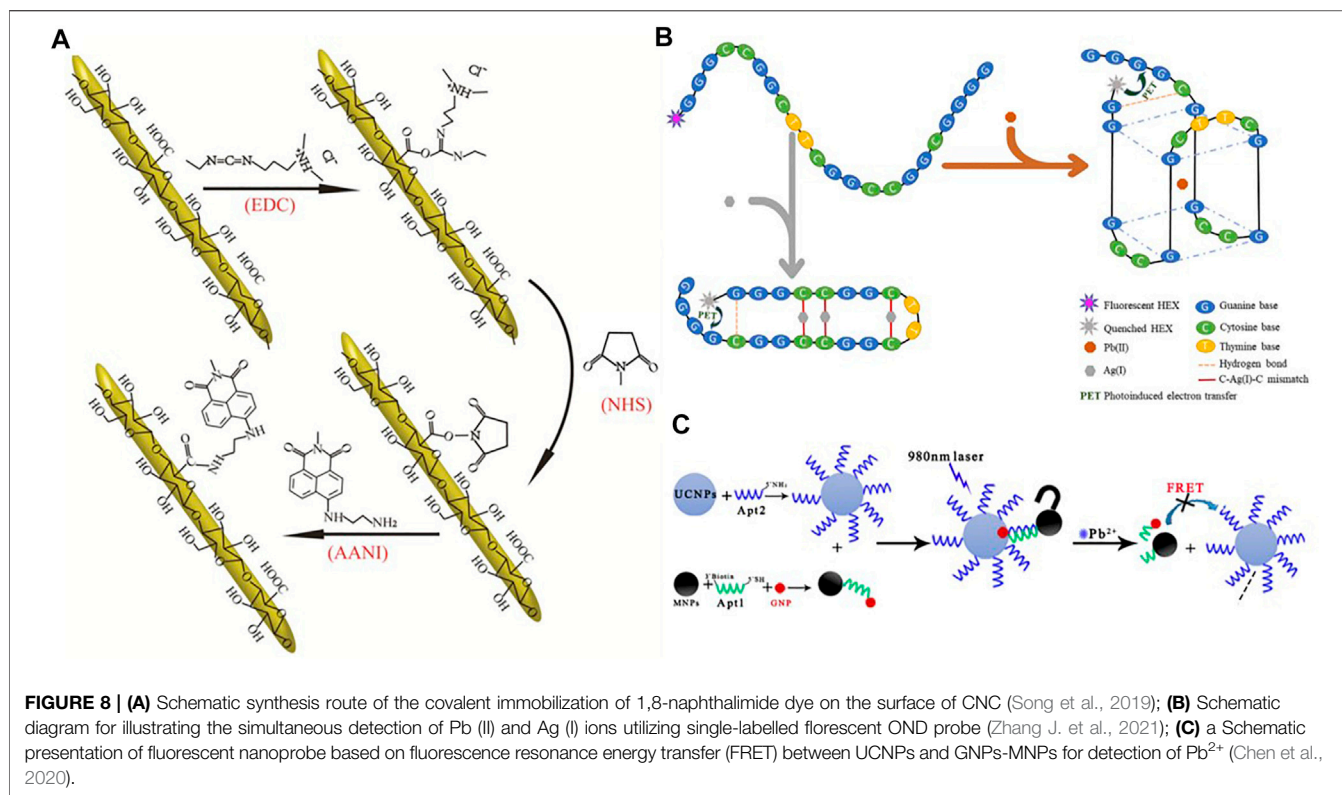
derivative, which could recognize mercury  $\text{Hg}^{2+}$  selectively in aqueous solution.

In the field of biology, in order to identify  $\text{Hg}^{2+}$  in living cells, fluorescent probes with less cytotoxicity and better biocompatibility are needed, therefore Li *et al.* (Li et al., 2015) designed nitrogen-sulphur co-doped carbon dots (N,S/C-dots) and demonstrated their high fluorescence quantum yield (FLQY, 25%) and good practical application. Wu *et al.* (Wu and Tong, 2019) synthesized a nitrogen-sulfur co-doped carbon dots (N,S-CDs) as a fluorescent probe with good luminescence properties and high fluorescence quantum yield (16.1%), and achieved good results in  $\text{Hg}^{2+}$  ion recognition detection in HepG2 cells (Figure 7A). Li *et al.* (Liu et al., 2018) have done some research on nano sensors by developing a turn-on nanoprobe, which was prepared based on the principle of fluorescence resonance energy transfer (FRET) between long-chain inducer-functionalized upconversion nanoparticles (UCNPs) and short-chain inducer-functionalized gold nanoparticles (GNPs) (Figure 7B).

Pan *et al.* (Pan et al., 2018) reported the first reaction-based fluorescent probe (ATC-Hg) that detects Hg (II), which was

designed based on the “covalent assembly” principle and is now used to enable the detection of Hg ions in *E. coli*. Chen *et al.* (Chen et al., 2019) synthesized a reactive fluorescent probe PIC based on peramidine group, this probe is very high in selectivity due to the fluorescence can be enhanced by 42-fold and is a promising method for the determination of mercury ions. Zhou *et al.* (Zhou et al., 2017) designed and synthesized a novel small molecule ratiometric fluorescent probe P-Hg using the ESIPT/ICT mechanism, which can be better used to identify  $\text{Hg}^{2+}$ . This probe can be applied to capture mercury ions both in the natural environment and in biological systems.

Given the diversity of both environmental conditions and biological environments, the field of innovative fluorescent probes for the selective detection of  $\text{Hg}^{2+}$  faces challenges such as endogenous active substance interference, leaky cells, and photostability. Fluorescent probes are generally constructed from organic molecular framework with poor stability.  $\text{Hg}^{2+}$ , as a kind of toxic heavy metal ion, seriously disrupts the natural physiological activities of living organisms. It is of great significance to design powerful probe tools to study the effects of  $\text{Hg}^{2+}$  on the health of organisms (Wang Y. et al., 2021).



## 5.2 Probes For Detecting Pb<sup>2+</sup>

Lead is a highly toxic substance used in batteries, gasoline and paints. Lead contamination is a chronic concern that creates a lasting threat to our human health and the environment in which we live. Even very small amounts of lead can cause serious damage to various neurological and reproductive systems in our bodies, and can even cause hypertension, lower IQ and slower reactions. According to a large study of scholars, fluorescence and colorimetric sensors were well used, and roughly divided into several categories according to its receptors, including chemical sensor based on nanoparticles, polymer, small molecules, naphthalimide and nanoparticles (Kim et al., 2012).

A number of nanoparticle-based sensing systems have been investigated. Song *et al.* (Song et al., 2019) designed a fluorescent ion probe for achieving the measurement of lead ions in aquatic solutions using covalent binding fluorescence of 1, 8-naphthylamine dyes with cellulose nanocrystals (CNCs) (Figure 8A). Zhang *et al.* (Zhang J. et al., 2021) designed a new dual-functional oligonucleotide (OND) probe for the trace Pb(II) detection, in which the 5' end is a single fluorescent moiety using HEX labeling (Figure 8B). Chen *et al.* (Chen et al., 2020) developed a fluorometric nanoprobe for the determination of Pb(II) based on up-converted nanoparticles (UCNPs) and on magnetic Fe<sub>3</sub>O<sub>4</sub>-modified (MNPs) gold nanoparticles (GNPs) (Figure 8C).

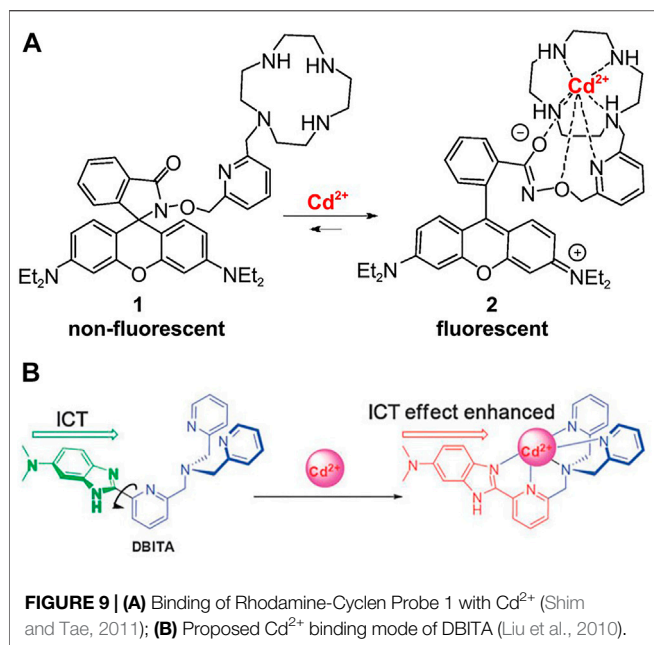
Several sensing systems based on polymers and small molecule particles have been developed. Chini *et al.* (Chini et al., 2019) reported a polymodal sensing method consisting of a highly

fluorescent dansyl-labeled copolymer P (MMA-co-Dansyl-Ala-HEMA) (DCP) and a small molecule diketopyrrolopyrrole (DPP) for the assay of the heavy metal lead (Pb<sup>2+</sup>). Liu *et al.* (Liu J. et al., 2013) reported a highly selective Pb<sup>2+</sup> fluorescent probe that is consisted of a BODIPY fluorescent moiety and a polyamide receptor. Anand *et al.* (Anand et al., 2015) synthesized a *de novo* probe 5-[(anthracene-9-methylene) amino] quinolin-10-ol (ANQ) on the anthracene platform. What's more, Liu *et al.* (Liu et al., 2015) reported a fluorescent turn-on probe of an oxadiazole derivative (OXD) that is based on the Schiff base molecule and was used to detect lead ions.

Fluorescent sensors based on naphthalimide are also an essential structure. Jiang *et al.* (Jiang et al., 2021) prepared a chemical fluorescent probe by attaching thiocarbamate to a naphthylamine derivative and applied it for Pb<sup>2+</sup> recognition in specific chemical reagents. Un *et al.* (Un et al., 2014) successfully developed a good performance naphthylamino fluorescent probe named NPA with Pb<sup>2+</sup> recognition.

Other sensors based on receptors are still available for the detection of lead ions. Recently, Bi and co-workers (Bi et al., 2017) rationally designed and developed a unique near-infrared fluorescent probe (NIR-PbP) and verified the capability of probing Pb(II) ions in both solution and live cells. Mei *et al.* (Mei et al., 2020) designed a newly available fluorescent probe L for Pb<sup>2+</sup> based phenanthroline derivative. Khandare *et al.* (Khandare et al., 2014) developed a fluorescent sensor based on aggregation-induced emission (AIE) using the intense affinity of lead ions for phosphate residues. Zhao *et al.* (Zhao et al., 2016) developed a fluorescent biosensor to detect Pb<sup>2+</sup> that utilized a





water-soluble derivative of cationic perylene (compound 1) with the characteristics of simplicity, label-free and high speed.

### 5.3 Probes For Detecting $\text{Cd}^{2+}$

$\text{Cd}$  ions are also toxic to cells, while there are few fluorescent tools to study  $\text{Cd}^{2+}$  toxicity. Due to the very similar binding properties of  $\text{Cd}^{2+}$  and  $\text{Zn}^{2+}$ , this poses a great challenge and difficulty for the development of  $\text{Cd}^{2+}$  probes. The first HK-2 intracellular fluorescent probe for  $\text{Cd}^{2+}$  was a Liu Cd-1 consisting of fluorescein and thiocarbamate (Carter et al., 2014). Nowadays, various methods have been well developed for the determination of  $\text{Cd}^{2+}$ , such as simultaneous radiation X-ray spectrometry, synchrotron X-ray spectrometry and atomic absorption chromatography. In recent years, researches on  $\text{Cd}^{2+}$  ion fluorescent probes include the following categories: Quinolone-based, coumarin-, benzothiazole based, rhodamine-based, dansyl based, and diarylethylene based  $\text{Cd}^{2+}$  fluorescent sensor. There are also other small organic molecules based  $\text{Cd}^{2+}$  sensor and nanosensor-based  $\text{Cd}^{2+}$  fluorescent sensor. In addition, fluorescence and colorimetric nano  $\text{Cd}^{2+}$  sensors, such as metal-organic framework (MOF), quantum dots (QD), nanoclusters (NCs) and nanoparticles (NPs), have also made good progress in recent years (Shi et al., 2021).

First, due to the ease of synthesis and precise control of the active site (Abdollahi et al., 2020), the synthesis and design of metal-organic framework (MOF) have been applied to the design of neutral architectures for anion recognition (Esrafil et al., 2020) and the selective capture of heavy metal ions (Esrafil et al., 2021). To detect  $\text{Cd}^{2+}$  in alkaline solutions, Hao et al. (Hao and Yan, 2015) reported the one of the first fluorescent probes for  $\text{Cd}^{2+}$  on the basis of lanthanide structure of functionalized metal-organic framework (MOF), and this sensor has the advantage of a high sensitivity. Liu et al. (Liu Q. et al., 2013) designed a kind of new fluorescent probe  $\text{DQCd}_2$  for  $\text{Cd}^{2+}$  based on 4-

piperidinylquinoline by utilizing the ratiometric reaction in phosphate buffered saline solution (PBS) buffer, and its emission intensity was significantly enhanced. Tsukamoto et al. (Tsukamoto et al., 2016) a highly practical naphthalenyl  $\text{Cd}^{2+}$  fluorescent probe, which allows a good selectivity and is suitable for a range of pH values since this method has almost no background reaction. Furthermore, Shim et al. (Shim and Tae, 2011) also developed a rhodamine-hydroxylamine platform-based fluorescent probe consisting of a picolinic and a cycloalkene-binding unit (Figure 9A). Xin et al. (Xin et al., 2013) synthesized the first fluorescent probe on the basis of difluoroborane dibenzoyl for the determination of  $\text{Cd}^{2+}$ . Liu et al. (Liu et al., 2010) developed DBITA, a ratiofluorescent sensor that can be used for the recognition of  $\text{Cd}^{2+}$  in live cells or aqueous media, with a  $\text{Cd}^{2+}$ -induced emission redshift of 53 nm (Figure 9B). Sun et al. (Sun et al., 2016) reported a ratio-measured and reversible fluorescent probe for the recognition of  $\text{Cd}^{2+}$  in living cells that was based on a 6-(dimethylamino) quinaldine derivative. For  $\text{Cd}^{2+}$  in living human cells, Jiang et al. (Jiang et al., 2014) developed a novel fluorescence probe (L) for C-3-symmetric Schiff alkaloids on the basis of 8-hydroxy-2-methylquinoline. Liu et al. (Liu et al., 2014) synthesized a well-performing organic salt probe in the determination of  $\text{Cd}^{2+}$  based on bis-1, 3, 4-oxadiazole derivatives and BAPTA. Liu et al. (Liu et al., 2012) developed and synthesized a novel two-photon excited cadmium fluorescent probe (named TPCd) based on o-phenylenediamine derivatives and Prodan (6-acetyl-2-methoxynaphthalene) derivatives by a two-photon approach, and demonstrated that  $\text{Cd}^{2+}$  detection in organisms is feasible and versatile. Therefore, this is a very meaningful study.

## 6 CONCLUSION

In summary, the identification and detection of biologically and environmentally critical species is already an important area of research in the field of the chemosensor. Fluorometry in combination with suitable probes is the preferred and excellent method of measuring these analytes due to the fast, nondestructive and sensitive nature of fluorometry measurements, and important progress has been realized in the definition and composition of fluorescent chemosensors predicated on various platforms. More and more researchers are engaged in this field, and have accumulated a lot of theoretical and practical experience in the development, synthesis and application of probes, accelerating further development of new fluorescent probes.

In this paper, the research progress of fluorescent probes for metal ion detection is reviewed. These fluorescent probes are mainly divided into organic small molecule probes and nano fluorescent probes. For different metal ions, different materials are selected to design and synthesize fluorescent probes, such as quantum dots, coumarin derivatives, benzene derivatives, etc. The development of sensing mechanisms plays an important role in improving the sensing

performance of metal ions. For example, the solar excited naked eye  $\text{Fe}^{3+}$  detection is realized by improving the luminescence efficiency based on the central hydrophobic/external hydrophilic strategy (Sun et al., 2020). So far, the main efforts have been devoted to the study of new sensing mechanisms, strategies to expand the range of detected metal ions, and methods to improve sensitivity and selectivity. However, there are still limitations and unparalleled challenges in the practical application of fluorescent probes. The variation of pH, temperature and probe behavior in different environments, as well as the accompanying fluorescence burst effect in some fluorescent sensors, have raised high requirements for the design of fluorescent probes. Therefore, in future, lots of aspects need to be further improved, including compatibility of probes in organisms and accuracy of fluorescent probe sensing, etc., so they can be applicable to more complex detection environments. We believe that fluorescent probes

will become a very powerful tool in the biomedical field and make great contributions to biology in future.

## AUTHOR CONTRIBUTIONS

All authors listed have made a substantial, direct and intellectual contribution to the work, and approved it for publication. All authors conducted literature compilation and discussion. LL and JW wrote this article. BD, SX, and CL checked and reviewed this article.

## FUNDING

This work was supported by the Major Basic Research Projects of Shandong Natural Science Foundation (ZR2020ZD36) and the National Natural Science Foundation of China (82073475).

## REFERENCES

- Abdollahi, N., Akbar Razavi, S. A., Morsali, A., and Hu, M.-L. (2020). High Capacity  $\text{Hg(II)}$  and  $\text{Pb(II)}$  Removal Using MOF-Based Nanocomposite: Cooperative Effects of Pore Functionalization and Surface-Charge Modulation. *J. Hazard. Mater.* 387, 121667. doi:10.1016/j.jhazmat.2019.121667
- Al-Azmi, A., and John, E. (2021). Synthesis and Characterization of Novel Tricyanofuran Hydrazone Probe: Solvatochromism, Density-functional Theory Calculation and Selective Fluorescence, and Colorimetric Determination of Iron (III). *Luminescence* 36 (5), 1220–1230. doi:10.1002/bio.4047
- Anand, T., Sivaraman, G., Mahesh, A., and Chellappa, D. (2015). Aminoquinoline Based Highly Sensitive Fluorescent Sensor for Lead(II) and Aluminum(III) and its Application in Live Cell Imaging. *Analytica Chim. Acta* 853, 596–601. doi:10.1016/j.aca.2014.11.011
- Atchudan, R., Edison, T. N. J. I., Perumal, S., Vinodh, R., Sundramoorthy, A. K., Babu, R. S., et al. (2021). Leftover Kiwi Fruit Peel-Derived Carbon Dots as a Highly Selective Fluorescent Sensor for Detection of Ferric Ion. *Chemosensors* 9 (7), 166. doi:10.3390/chemosensors9070166
- Bi, J., Fang, M., Wang, J., Xia, S., Zhang, Y., Zhang, J., et al. (2017). Near-infrared Fluorescent Probe for Sensitive Detection of  $\text{Pb(II)}$  Ions in Living Cells. *Inorg. Chim. Acta* 468, 140–145. doi:10.1016/j.ica.2017.06.044
- Cai, Y., You, J., You, Z., Dong, F., Du, S., and Zhang, L. (2018). Profuse Color-Evolution-Based Fluorescent Test Paper Sensor for Rapid and Visual Monitoring of Endogenous  $\text{Cu}^{2+}$  in Human Urine. *Biosens. Bioelectron.* 99, 332–337. doi:10.1016/j.bios.2017.07.072
- Carter, K. P., Young, A. M., and Palmer, A. E. (2014). Fluorescent Sensors for Measuring Metal Ions in Living Systems. *Chem. Rev.* 114 (8), 4564–4601. doi:10.1021/cr400546e
- Chang, Y., Li, B., Mei, H., Xu, K., Xie, X., and Yang, L. (2020). A Novel Reversible Fluorescent Probe for Zinc(II) Ion and Bioimaging in Living Cells. *Supramolecular Chem.* 32 (7), 393–402. doi:10.1080/10610278.2020.1749627
- Chaudhary, N., Gupta, P. K., Eremin, S., and Solanki, P. R. (2020). One-step green Approach to Synthesize Highly Fluorescent Carbon Quantum Dots from Banana Juice for Selective Detection of Copper Ions. *J. Environ. Chem. Eng.* 8 (3), 103720. doi:10.1016/j.jece.2020.103720
- Chen, C.-G., Vijay, N., Thirumalaivasan, N., Velmathi, S., and Wu, S.-P. (2019). Coumarin-based  $\text{Hg}^{2+}$  Fluorescent Probe: Fluorescence Turn-On Detection for  $\text{Hg}^{2+}$  Bioimaging in Living Cells and Zebrafish. *Spectrochimica Acta A: Mol. Biomol. Spectrosc.* 219, 135–140. doi:10.1016/j.saa.2019.04.048
- Chen, M., Hassan, M., Li, H., and Chen, Q. (2020). Fluorometric Determination of Lead(II) by Using Aptamer-Functionalized Upconversion Nanoparticles and Magnetite-Modified Gold Nanoparticles. *Microchim. Acta* 187 (1), 9. doi:10.1007/s00604-019-4030-4
- Chini, M. K., Kumar, V., Maiti, B., De, P., and Satapathi, S. (2019). A Dual "Turn-on/Turn-Off" "FRET" Sensor for Highly Sensitive and Selective Detection of lead and Methylene Blue Based on Fluorescent Dansyl Tagged Copolymer and Small Molecule Diketopyrrolopyrrole. *Polym. Test.* 79, 105997. doi:10.1016/j.polymertesting.2019.105997
- Dong, W., Yu, J., Gong, X., Liang, W., Fan, L., and Dong, C. (2021). A Turn-Off-On Near-Infrared Photoluminescence Sensor for Sequential Detection of  $\text{Fe}^{3+}$  and Ascorbic Acid Based on Glutathione-Capped Gold Nanoclusters. *Spectrochimica Acta Part A: Mol. Biomol. Spectrosc.* 247, 119085. doi:10.1016/j.saa.2020.119085
- Du, J., Yang, Y., Shao, T., Qi, S., Zhang, P., Zhuo, S., et al. (2021). Yellow Emission Carbon Dots for Highly Selective and Sensitive OFF-ON Sensing of Ferric and Pyrophosphate Ions in Living Cells. *J. Colloid Interf. Sci.* 587, 376–384. doi:10.1016/j.jcis.2020.11.108
- Esrifili, L., Firuzabadi, F. D., Morsali, A., and Hu, M.-L. (2021). Reuse of Predesigned Dual-Functional Metal Organic Frameworks (DF-MOFs) after Heavy Metal Removal. *J. Hazard. Mater.* 403, 123696. doi:10.1016/j.jhazmat.2020.123696
- Esrifili, L., Morsali, A., Hu, M.-L., Azhdari Tehrani, A., Carlucci, L., Mercandelli, P., et al. (2020). Size-Selective Urea-Containing Metal-Organic Frameworks as Receptors for Anions. *Inorg. Chem.* 59 (22), 16421–16429. doi:10.1021/acs.inorgchem.0c02215
- Fang, M. X., Xia, S., Bi, J. H., Wigstrom, T. P., Valenzano, L., Wang, J. B., et al. (2016). Detecting  $\text{Zn(II)}$  Ions in Live Cells with Near-Infrared Fluorescent Probes. *Molecules* 24 (8), 1592. doi:10.3390/molecules24081592
- Gao, G., Wang, X., Wang, Z., Jin, X., Ou, L., Zhou, J., et al. (2020). A Simple and Effective Dansyl Acid Based "Turn-On" Fluorescent Probe for Detecting Labile Ferrous Iron in Physiological saline and Live Cells. *Talanta* 215, 120908. doi:10.1016/j.talanta.2020.120908
- Gujuluva Gangatharan, V. K., Mookkandi Palsamy, K., Gandhi, S., Jamespandi, A., Kandasamy, A., Arunachalam, T., et al. (2018). Reversible NIR Fluorescent Probes for  $\text{Cu}^{2+}$  Ions Detection and its Living Cell Imaging. *Sensors Actuators B: Chem.* 255, 3235–3247. doi:10.1016/j.snb.2017.09.150
- Guo, R., Zhou, S., Li, Y., Li, X., Fan, L., and Voelcker, N. H. (2015). Rhodamine-Functionalized Graphene Quantum Dots for Detection of  $\text{Fe}^{3+}$  in Cancer Stem Cells. *ACS Appl. Mater. Inter.* 7 (43), 23958–23966. doi:10.1021/acsami.5b06523
- Hagimori, M. (2013). Development of  $\text{Zn}^{2+}$  Selective Fluorescent Probes for Biological Applications. *Yakugaku Zasshi* 133 (10), 1087–1092. doi:10.1248/yakushi.13-00192
- Hao, J.-N., and Yan, B. (2015). A Water-Stable Lanthanide-Functionalized MOF as a Highly Selective and Sensitive Fluorescent Probe for  $\text{Cd}^{2+}$ . *Chem. Commun.* 51 (36), 7737–7740. doi:10.1039/C5CC01430A
- He, W., and Lu, J. (2001). Distribution of Cd and Pb in a Wetland Ecosystem. *Sc. China Ser. B-chem.* 44 (1), 178–184. doi:10.1007/BF02884825

- Jiang, C., Yang, I., Li, P., Liu, Y., Li, S., Fu, Y., et al. (2021). A Simple and Rapid Fluorescent Approach for Pb<sup>2+</sup> Determination and Application in Water Samples and Living Cells. *Spectrochimica Acta Part A: Mol. Biomol. Spectrosc.* 263, 120168. doi:10.1016/j.saa.2021.120168
- Jiang, X.-J., Li, M., Lu, H.-L., Xu, L.-H., Xu, H., Zang, S.-Q., et al. (2014). A Highly Sensitive C3-Symmetric Schiff-Base Fluorescent Probe for Cd<sup>2+</sup>. *Inorg. Chem.* 53 (24), 12665–12667. doi:10.1021/ic501279y
- Ju, J., and Chen, W. (2014). Synthesis of Highly Fluorescent Nitrogen-Doped Graphene Quantum Dots for Sensitive, Label-free Detection of Fe (III) in Aqueous media. *Biosens. Bioelectron.* 58, 219–225. doi:10.1016/j.bios.2014.02.061
- Kang, T., Wang, H., Wang, X., and Feng, L. (2019). A Facile Zn(II) Probe Based on Intramolecular Charge Transfer with Fluorescence Red-Shift. *Microchemical J.* 148, 442–448. doi:10.1016/j.microc.2019.05.035
- Kar, C., Adhikari, M. D., Ramesh, A., and Das, G. (2013). NIR- and FRET-Based Sensing of Cu<sup>2+</sup> and S<sup>2-</sup> in Physiological Conditions and in Live Cells. *Inorg. Chem.* 52 (2), 743–752. doi:10.1021/ic301872q
- Khandare, D. G., Joshi, H., Banerjee, M., Majik, M. S., and Chatterjee, A. (2014). An Aggregation-Induced Emission Based "Turn-On" Fluorescent Chemodosimeter for the Selective Detection of Pb<sup>2+</sup> Ions. *RSC Adv.* 4 (87), 47076–47080. doi:10.1039/C4RA09451D
- Khatun, S., Biswas, S., Binoy, A., Podder, A., Mishra, N., and Bhuniya, S. (2020). Highly Chemoselective Turn-On Fluorescent Probe for Ferrous (Fe<sup>2+</sup>) Ion Detection in Cosmetics and Live Cells. *J. Photochem. Photobiol. B: Biol.* 209, 111943. doi:10.1016/j.jphotobiol.2020.111943
- Kim, H. N., Ren, W. X., Kim, J. S., and Yoon, J. (2012). Fluorescent and Colorimetric Sensors for Detection of lead, Cadmium, and Mercury Ions. *Chem. Soc. Rev.* 41 (8), 3210–3244. doi:10.1039/C1CS15245A
- Kim, K. B., Kim, H., Song, E. J., Kim, S., Noh, I., and Kim, C. (2013). A Cap-type Schiff Base Acting as a Fluorescence Sensor for Zinc(II) and a Colorimetric Sensor for Iron(II), Copper(II), and Zinc(II) in Aqueous media. *Dalton Trans.* 42 (47), 16569–16577. doi:10.1039/c3dt51916c
- Li, J., Yim, D., Jang, W.-D., and Yoon, J. (2017). Recent Progress in the Design and Applications of Fluorescence Probes Containing crown Ethers. *Chem. Soc. Rev.* 46 (9), 2437–2458. doi:10.1039/c6cs00619a
- Li, L., Yu, B., and You, T. (2015). Nitrogen and Sulfur Co-doped Carbon Dots for Highly Selective and Sensitive Detection of Hg (II) Ions. *Biosens. Bioelectron.* 74, 263–269. doi:10.1016/j.bios.2015.06.050
- Li, Z., Xu, Y., Xu, H., Cui, M., Liu, T., Ren, X., et al. (2021). A Dicyanomethylene-4h-Pyran-Based Fluorescence Probe with High Selectivity and Sensitivity for Detecting Copper (II) and its Bioimaging in Living Cells and Tissue. *Spectrochimica Acta Part A: Mol. Biomol. Spectrosc.* 244, 118819. doi:10.1016/j.saa.2020.118819
- Liang, Y., Zhang, Y., Li, M., Meng, Z., Gao, Y., Yin, J., et al. (2021). A Highly Effective "Turn-On" Camphor-Based Fluorescent Probe for Rapid and Sensitive Detection and its Biological Imaging of Fe<sup>2+</sup>. *Anal. Bioanal. Chem.* 413 (25), 6267–6277. doi:10.1007/s00216-021-03581-4
- Lin, X., Gao, G., Zheng, L., Chi, Y., and Chen, G. (2014). Encapsulation of Strongly Fluorescent Carbon Quantum Dots in Metal-Organic Frameworks for Enhancing Chemical Sensing. *Anal. Chem.* 86 (2), 1223–1228. doi:10.1021/ac403536a
- Liu, J., Guo, Y., Dong, B., Sun, J., Lyu, J., Sun, L., et al. (2020). Water-soluble Coumarin Oligomer Based Ultra-sensitive Iron Ion Probe and Applications. *Sensors Actuators B: Chem.* 320, 128361. doi:10.1016/j.snb.2020.128361
- Liu, J., Wu, K., Li, S., Song, T., Han, Y., and Li, X. (2013). A Highly Sensitive and Selective Fluorescent Chemosensor for Pb<sup>2+</sup> Ions in an Aqueous Solution. *Dalton Trans.* 42 (11), 3854–3859. doi:10.1039/c2dt32531d
- Liu, Q., Feng, L., Yuan, C., Zhang, L., Shuang, S., Dong, C., et al. (2014). A Highly Selective Fluorescent Probe for Cadmium Ions in Aqueous Solution and Living Cells. *Chem. Commun.* 50 (19), 2498–2501. doi:10.1039/C3CC48668K
- Liu, Q. Q., Li, G.-P., Zhu, D.-J., Xue, L., and Jiang, H. (2013). Design of Quinoline-Based Fluorescent Probe for the Ratiometric Detection of Cadmium in Aqueous media. *Chin. Chem. Lett.* 24 (6), 479–482. doi:10.1016/j.ccl.2013.04.002
- Liu, W., Wu, G., Gu, X., Yuan, X., Li, J., and Wang, H. (2015). Synthesis of Schiff Base-Based 1,2,4-Oxadiazole Derivative as Fluorescence Turn-On Sensor for High Selectivity of Pb<sup>2+</sup>. *J. Fluoresc.* 25 (3), 557–561. doi:10.1007/s10895-015-1534-0
- Liu, Y., Dong, X., Sun, J., Zhong, C., Li, B., You, X., et al. (2012). Two-photon Fluorescent Probe for Cadmium Imaging in Cells. *Analyst* 137 (8), 1837–1845. doi:10.1039/c2an16254g
- Liu, Y., Ouyang, Q., Li, H., Chen, M., Zhang, Z., and Chen, Q. (2018). Turn-On Fluorescence Sensor for Hg<sup>2+</sup> in Food Based on FRET between Aptamers-Functionalized Upconversion Nanoparticles and Gold Nanoparticles. *J. Agric. Food Chem.* 66 (24), 6188–6195. doi:10.1021/acs.jafc.8b00546
- Liu, Z. Z., Chen, M., Guo, Y., Zhou, J., Shi, Q., and Sun, R. (2020). Oxidized Nanocellulose Facilitates Preparing Photoluminescent Nitrogen-Doped Fluorescent Carbon Dots for Fe<sup>3+</sup> Ions Detection and Bioimaging. *Chem. Eng. J.* 384, 123260. doi:10.1016/j.cej.2019.123260
- Liu, Z., Zhang, C., He, W., Yang, Z., Gao, X., and Guo, Z. (2010). A Highly Sensitive Ratiometric Fluorescent Probe for Cd<sup>2+</sup> Detection in Aqueous Solution and Living Cells. *Chem. Commun.* 46 (33), 6138–6140. doi:10.1039/c0cc00662a
- Long, L., Wang, N., Han, Y., Huang, M., Yuan, X., Cao, S., et al. (2018). A Coumarin-Based Fluorescent Probe for Monitoring Labile Ferrous Iron in Living Systems. *Analyst* 143 (11), 2555–2562. doi:10.1039/C8AN00556G
- Lu, W., Qin, X., Liu, S., Chang, G., Zhang, Y., Luo, Y., et al. (2012). Economical, Green Synthesis of Fluorescent Carbon Nanoparticles and Their Use as Probes for Sensitive and Selective Detection of Mercury(II) Ions. *Anal. Chem.* 84 (12), 5351–5357. doi:10.1021/ac3007939
- Lytton, S. D., Mester, B., Libman, J., Shanzer, A., and Ioav Cabantchik, Z. (1992). Monitoring of Iron(III) Removal from Biological Sources Using a Fluorescent Siderophore. *Anal. Biochem.* 205 (2), 326–333. doi:10.1016/0003-2697(92)90443-B
- Ma, S., Yu, Q., Lu, L., Li, L., Liu, W., Wu, Z., et al. (2021). Recent Progress in Fluorescent Probes for the Detection of Ferrous Ion. *Chin. J. Org. Chem.* 41 (1), 229–240. doi:10.6023/cjoc202006003
- Mei, H., Yang, M., Liu, X., Tian, Y., and Xu, K. (2020). A Novel Phenanthroline-Based Fluorescent Probe for Pb(II). *Chin. J. Org. Chem.* 40 (8), 2508–2512. doi:10.6023/cjoc202004037
- Mohammadi, A., and Ghasemi, Z. (2020). A Simple Pyrimidine Based Colorimetric and Fluorescent Chemosensor for Sequential Detection of Copper (II) and Cyanide Ions and its Application in Real Samples. *Spectrochimica Acta Part A: Mol. Biomol. Spectrosc.* 228, 117730. doi:10.1016/j.saa.2019.117730
- Pan, S.-L., Li, K., Li, L.-L., Li, M.-Y., Shi, L., Liu, Y.-H., et al. (2018). A Reaction-Based Ratiometric Fluorescent Sensor for the Detection of Hg(II) Ions in Both Cells and Bacteria. *Chem. Commun.* 54 (39), 4955–4958. doi:10.1039/C8CC01031E
- Park, S.-H., Kwon, N., Lee, J.-H., Yoon, J., and Shin, I. (2020). Synthetic Ratiometric Fluorescent Probes for Detection of Ions. *Chem. Soc. Rev.* 49 (1), 143–179. doi:10.1039/c9cs00243j
- Peng, J., Xu, W., Teoh, C. L., Han, S., Kim, B., Samanta, A., et al. (2015). High-Efficiency *In Vitro* and *In Vivo* Detection of Zn<sup>2+</sup> by Dye-Assembled Upconversion Nanoparticles. *J. Am. Chem. Soc.* 137 (6), 2336–2342. doi:10.1021/ja5115248
- Price, T. W., Firth, G., Eling, C. J., Kinnon, M., Long, N. J., Sturge, J., et al. (2018). A 18F Radiolabelled Zn(ii) Sensing Fluorescent Probe. *Chem. Commun.* 54 (26), 3227–3230. doi:10.1039/c8cc00687c
- Pu, Z.-F., Wen, Q.-L., Yang, Y.-J., Cui, X.-M., Ling, J., Liu, P., et al. (2020). Fluorescent Carbon Quantum Dots Synthesized Using Phenylalanine and Citric Acid for Selective Detection of Fe<sup>3+</sup> Ions. *Spectrochimica Acta Part A: Mol. Biomol. Spectrosc.* 229, 117944. doi:10.1016/j.saa.2019.117944
- Qi, H., Teng, M., Liu, M., Liu, S., Li, J., Yu, H., et al. (2019). Biomass-derived Nitrogen-Doped Carbon Quantum Dots: Highly Selective Fluorescent Probe for Detecting Fe<sup>3+</sup> Ions and Tetracyclines. *J. Colloid Interf. Sci.* 539, 332–341. doi:10.1016/j.jcis.2018.12.047
- Qu, K., Wang, J., Ren, J., and Qu, X. (2013). Carbon Dots Prepared by Hydrothermal Treatment of Dopamine as an Effective Fluorescent Sensing Platform for the Label-free Detection of Iron(III) Ions and Dopamine. *Chem. Eur. J.* 19 (22), 7243–7249. doi:10.1002/chem.201300042
- Ranee, S. J., Sivaraman, G., Pushpalatha, A. M., and Muthusubramanian, S. (2018). Quinoline Based Sensors for Bivalent Copper Ions in Living Cells. *Sensors Actuators B: Chem.* 255, 630–637. doi:10.1016/j.snb.2017.08.111
- Roy, P., Dhara, K., Manassero, M., Ratha, J., and Banerjee, P. (2007). Selective Fluorescence Zinc Ion Sensing and Binding Behavior of 4-Methyl-2,6-Bis((phenylmethyl)imino)methylphenol: Biological Application. *Inorg. Chem.* 46 (16), 6405–6412. doi:10.1021/ic700420w



- Shi, B., Su, Y., Zhang, L., Huang, M., Liu, R., and Zhao, S. (2016). Nitrogen and Phosphorus Co-doped Carbon Nanodots as a Novel Fluorescent Probe for Highly Sensitive Detection of Fe<sup>3+</sup> in Human Serum and Living Cells. *ACS Appl. Mater. Inter.* 8 (17), 10717–10725. doi:10.1021/acsami.6b01325
- Shi, C.-t., Huang, Z.-y., Wu, A.-b., Hu, Y.-x., Wang, N.-c., Zhang, Y., et al. (2021). Recent Progress in Cadmium Fluorescent and Colorimetric Probes. *RSC Adv.* 11 (47), 29632–29660. doi:10.1039/D1RA05048F
- Shim, S.-Y., and Tae, J.-S. (2011). Rhodamine Cyclen-Based Fluorescent Chemosensor for the Detection of Cd<sup>2+</sup>. *Bull. Korean Chem. Soc.* 32 (8), 2928–2932. doi:10.5012/bkcs.2011.32.8.2928
- Sivaraman, G., Iniya, M., Anand, T., Kotla, N. G., Sunnapu, O., Singaravadevel, S., et al. (2018). Chemically Diverse Small Molecule Fluorescent Chemosensors for Copper Ion. *Coord. Chem. Rev.* 357, 50–104. doi:10.1016/j.ccr.2017.11.020
- Song, R., Zhang, Q., Chu, Y., Zhang, L., Dai, H., and Wu, W. (2019). Fluorescent Cellulose Nanocrystals for the Detection of lead Ions in Complete Aqueous Solution. *Cellulose* 26 (18), 9553–9565. doi:10.1007/s10570-019-02760-y
- Song, S., Wang, C., Zhao, Y., Hu, T., Zhou, X., Zhao, T., et al. (2018). Gold-Cluster-Based Dual-Emission Nanocomposite Film as Ratiometric Fluorescent Sensing Paper for Specific Metal Ion. *Part. Part. Syst. Charact.* 35 (4), 1700471. doi:10.1002/ppsc.201700471
- Staudinger, C., and Borisov, S. M. (2015). Long-wavelength Analyte-Sensitive Luminescent Probes and Optical (Bio)sensors. *Methods Appl. Fluoresc.* 3 (4), 042005. doi:10.1088/2050-6120/3/4/042005
- Sun, L., Liu, J., Xu, S., Dong, B., Lv, J., Hu, S., et al. (2020). High Fluorescence LaOBr/coumarin Organic-Inorganic Composite Nanomaterials for Ultra-sensitive Fe<sup>3+</sup> Sensing, Fluorescence Imaging and Water-Based Ink Anti-counterfeiting Applications. *J. Mater. Chem. C* 8 (39), 13733–13742. doi:10.1039/D0TC03354E
- Sun, Z.-G., Li, Z., Yuan, D.-d., Gao, J.-F., Lin, L., Lin, J., et al. (2016). A Quinoline-Based Ratiometric and Reversible Fluorescent Probe for Cadmium Imaging in Living Cells. *Chem. Pharm. Bull.* 64 (1), 27–33. doi:10.1248/cpb.c15-00579
- Tang, L., Xia, J., Zhong, K., Tang, Y., Gao, X., and Li, J. (2020). A Simple AIE-Active Fluorogen for Relay Recognition of Cu<sup>2+</sup> and Pyrophosphate through Aggregation-Switching Strategy. *Dyes Pigm.* 178, 108379. doi:10.1016/j.dyepig.2020.108379
- Tao, P., Chen, D., Xu, Z., Song, Y., Li, H., and Xian, C. (2020). A Fluorescent Probe for the Dual Detection of Mercury Ions and Thiols Based on a Simple Coumarin Derivative. *Coloration Technol.* 136 (1), 75–86. doi:10.1111/cote.12447
- Tsukamoto, K., Shimabukuro, S., Mabuchi, M., and Maeda, H. (2016). A Naphthalimide-Based Cd<sup>2+</sup>-Fluorescent Probe with Carbamoylmethyl Groups Working as Chelators and PET-Promoters under Neutral Conditions. *Chem. Eur. J.* 22 (25), 8579–8585. doi:10.1002/chem.201600556
- Un, H.-I., Huang, C.-B., Huang, J., Huang, C., Jia, T., and Xu, L. (2014). A Naphthalimide-Based Fluorescence "Turn-On" Probe for the Detection of Pb<sup>2+</sup> in Aqueous Solution and Living Cells. *Chem. Asian J.* 9 (12), 3397–3402. doi:10.1002/asia.201402946
- Walkup, G. K., Burdette, S. C., Lippard, S. J., and Tsien, R. Y. (2000). A New Cell-Permeable Fluorescent Probe for Zn<sup>2+</sup>. *J. Am. Chem. Soc.* 122 (23), 5644–5645. doi:10.1021/ja000868p
- Wang, F., Wang, K., Kong, Q., Wang, J., Xi, D., Gu, B., et al. (2021). Recent Studies Focusing on the Development of Fluorescence Probes for Zinc Ion. *Coord. Chem. Rev.* 429, 213636. doi:10.1016/j.ccr.2020.213636
- Wang, H., Wang, X., Kong, R.-M., Xia, L., and Qu, F. (2021). Metal-organic Framework as a Multi-Component Sensor for Detection of Fe<sup>3+</sup>, Ascorbic Acid and Acid Phosphatase. *Chin. Chem. Lett.* 32 (1), 198–202. doi:10.1016/j.ccl.2020.10.017
- Wang, L., Li, W., Zhi, W., Huang, Y., Han, J., Wang, Y., et al. (2018). A New Coumarin Schiff Based Fluorescent-Colorimetric Chemosensor for Dual Monitoring of Zn<sup>2+</sup> and Fe<sup>3+</sup> in Different Solutions: An Application to Bio-Imaging. *Sensors Actuators B: Chem.* 260, 243–254. doi:10.1016/j.snb.2017.12.200
- Wang, L., Wei, Z.-L., Chen, Z.-Z., Liu, C., Dong, W.-K., and Ding, Y.-J. (2020). A Chemical Probe Capable for Fluorescent and Colorimetric Detection to Cu<sup>2+</sup> and CN<sup>-</sup> Based on Coordination and Nucleophilic Addition Mechanism. *Microchemical J.* 155, 104801. doi:10.1016/j.microc.2020.104801
- Wang, S., Chen, H., Xie, H., Wei, L., Xu, L., Zhang, L., et al. (2021). A Novel Thioctic Acid-Carbon Dots Fluorescence Sensor for the Detection of Hg<sup>2+</sup> and Thiophanate Methyl via S-Hg Affinity. *Food Chem.* 346, 128923. doi:10.1016/j.foodchem.2020.128923
- Wang, Y., Zhang, C., Chen, X., Yang, B., Yang, L., Jiang, C., et al. (2016). Ratiometric Fluorescent Paper Sensor Utilizing Hybrid Carbon Dots-Quantum Dots for the Visual Determination of Copper Ions. *Nanoscale* 8 (11), 5977–5984. doi:10.1039/C6NR00430J
- Wang, Y., Zhang, L., Han, X., Zhang, L., Wang, X., and Chen, L. (2021). Fluorescent Probe for Mercury Ion Imaging Analysis: Strategies and Applications. *Chem. Eng. J.* 406, 127166. doi:10.1016/j.cej.2020.127166
- Wang, Z.-G., Ding, X.-J., Huang, Y.-Y., Yan, X.-J., Ding, B., Li, Q.-Z., et al. (2020). The Development of Coumarin Schiff Base System Applied as Highly Selective Fluorescent/colorimetric Probes for Cu<sup>2+</sup> and Tumor Biomarker Glutathione Detection. *Dyes Pigm.* 175, 108156. doi:10.1016/j.dyepig.2019.108156
- Wei, S., Tan, L., Yin, X., Wang, R., Shan, X., Chen, Q., et al. (2020). A Sensitive "ON-OFF" Fluorescent Probe Based on Carbon Dots for Fe<sup>2+</sup> Detection and Cell Imaging. *Analyst* 145 (6), 2357–2366. doi:10.1039/C9AN02309G
- Wu, H., and Tong, C. (2019). Nitrogen- and Sulfur-Codoped Carbon Dots for Highly Selective and Sensitive Fluorescent Detection of Hg<sup>2+</sup> Ions and Sulfide in Environmental Water Samples. *J. Agric. Food Chem.* 67 (10), 2794–2800. doi:10.1021/acs.jafc.8b07176
- Xin, L., Chen, Y.-Z., Niu, L.-Y., Wu, L.-Z., Tung, C.-H., Tong, Q.-X., et al. (2013). A Selective Turn-On Fluorescent Probe for Cd<sup>2+</sup> Based on a boron Difluoride  $\beta$ -dibenzoyl Dye and its Application in Living Cells. *Org. Biomol. Chem.* 11 (18), 3014–3019. doi:10.1039/c3ob40376a
- Xu, H., Hu, H.-C., Cao, C.-S., and Zhao, B. (2015). Lanthanide Organic Framework as a Regenerable Luminescent Probe for Fe<sup>3+</sup>. *Inorg. Chem.* 54 (10), 4585–4587. doi:10.1021/acs.inorgchem.5b00113
- Xu, J., Wang, Z., Liu, C., Xu, Z., Wang, N., Cong, X., et al. (2018). A Highly Selective Colorimetric and Long-Wavelength Fluorescent Probe for the Detection of Hg<sup>2+</sup>. *Luminescence* 33 (6), 1122–1127. doi:10.1002/bio.3518
- Xu, Q., Pu, P., Zhao, J., Dong, C., Gao, C., Chen, Y., et al. (2015). Preparation of Highly Photoluminescent Sulfur-Doped Carbon Dots for Fe(III) Detection. *J. Mater. Chem. A* 3 (2), 542–546. doi:10.1039/C4TA05483K
- Xu, W., Zeng, Z., Jiang, J.-H., Chang, Y.-T., and Yuan, L. (2016). Discerning the Chemistry in Individual Organelles with Small-Molecule Fluorescent Probes. *Angew. Chem. Int. Ed.* 55 (44), 13658–13699. doi:10.1002/anie.201510721
- Xu, X.-Y., and Yan, B. (2015). Eu(III)-Functionalized MIL-124 as Fluorescent Probe for Highly Selectively Sensing Ions and Organic Small Molecules Especially for Fe(III) and Fe(II). *ACS Appl. Mater. Inter.* 7 (1), 721–729. doi:10.1021/am5070409
- Xu, Z., Liu, X., Pan, J., and Spring, D. R. (2012). Coumarin-derived Transformable Fluorescent Sensor for Zn<sup>2+</sup>. *Chem. Commun.* 48 (39), 4764–4766. doi:10.1039/c2cc30963g
- Xu, Z., and Xu, L. (2016). Fluorescent Probes for the Selective Detection of Chemical Species inside Mitochondria. *Chem. Commun.* 52 (6), 1094–1119. doi:10.1039/c5cc09248e
- Yan, B. (2017). Lanthanide-Functionalized Metal-Organic Framework Hybrid Systems to Create Multiple Luminescent Centers for Chemical Sensing. *Acc. Chem. Res.* 50 (11), 2789–2798. doi:10.1021/acs.accounts.7b00387
- Yang, L., Chen, Q., Gan, S., Guo, Q., Zhang, J., Zhang, H., et al. (2021). An Activatable AIEgen Probe for *In-Situ* Monitoring and Long-Term Tracking of Ferrous Ions in Living Cells. *Dyes Pigm.* 190, 109271. doi:10.1016/j.dyepig.2021.109271
- Yang, X., Wang, Y., Liu, R., Zhang, Y., Tang, J., Yang, E.-b., et al. (2019). A Novel ICT-Based Two Photon and NIR Fluorescent Probe for Labile Fe<sup>2+</sup> Detection and Cell Imaging in Living Cells. *Sensors Actuators B: Chem.* 288, 217–224. doi:10.1016/j.snb.2019.02.123
- Yao, J., Zhang, K., Zhu, H., Ma, F., Sun, M., Yu, H., et al. (2013). Efficient Ratiometric Fluorescence Probe Based on Dual-Emission Quantum Dots Hybrid for On-Site Determination of Copper Ions. *Anal. Chem.* 85 (13), 6461–6468. doi:10.1021/ac401011r
- Ye, J., Zhao, L., Bogale, R. F., Gao, Y., Wang, X., Qian, X., et al. (2015). Highly Selective Detection of 2,4,6-Trinitrophenol and Cu<sup>2+</sup>-Ions Based on a Fluorescent Cadmium-Pamoate Metal-Organic Framework. *Chem. Eur. J.* 21 (5), 2029–2037. doi:10.1002/chem.201405267



- Zhang, D., Qi, Y., Li, Y., Song, Y., Xian, C., Li, H., et al. (2021). A New Spiropyran-Based Fluorescent Probe for Dual Sensing of Ferrous Ion and pH. *J. Fluoresc.* 31 (4), 1133–1141. doi:10.1007/s10895-021-02741-0
- Zhang, J., Ma, X., Chen, W., Bai, Y., Xue, P., Chen, K., et al. (2021). Bifunctional Single-Labelled Oligonucleotide Probe for Detection of Trace Ag(I) and Pb(II) Based on cytosine-Ag(I)-cytosine Mismatches and G-Quadruplex. *Analytica Chim. Acta* 1151, 338258. doi:10.1016/j.aca.2021.338258
- Zhang, R., and Chen, W. (2014). Nitrogen-doped Carbon Quantum Dots: Facile Synthesis and Application as a "Turn-Off" Fluorescent Probe for Detection of Hg<sup>2+</sup> Ions. *Biosens. Bioelectron.* 55, 83–90. doi:10.1016/j.bios.2013.11.074
- Zhang, S., Adhikari, R., Fang, M., Dorh, N., Li, C., Jaishi, M., et al. (2016). Near-Infrared Fluorescent Probes with Large Stokes Shifts for Sensing Zn(II) Ions in Living Cells. *ACS Sens.* 1 (12), 1408–1415. doi:10.1021/acssensors.6b00490
- Zhang, X., Chen, Y., Cai, X., Liu, C., Jia, P., Li, Z., et al. (2020). A Highly Sensitive Rapid-Response Fluorescent Probe for Specifically Tracking Endogenous Labile Fe<sup>2+</sup> in Living Cells and Zebrafish. *Dyes Pigm.* 174, 108065. doi:10.1016/j.dyepig.2019.108065
- Zhang, Y., Qin, H., Huang, Y., Zhang, F., Liu, H., Liu, H., et al. (2021). Highly Fluorescent Nitrogen and boron Doped Carbon Quantum Dots for Selective and Sensitive Detection of Fe<sup>3+</sup>. *J. Mater. Chem. B* 9 (23), 4654–4662. doi:10.1039/D1TB00371B
- Zhang, Y., Yuan, B., and Ma, D. (2020). Selective Recognition of Zn(II) Ions in Live Cells Based on Chelation Enhanced Near-Infrared Fluorescent Probe. *Inorg. Chim. Acta* 508, 119640. doi:10.1016/j.ica.2020.119640
- Zhang, Z., Deng, C., Zou, Y., and Chen, L. (2018). A Novel Fluorescent and Colorimetric Probe for cascade Selective Detection of Fe(III) and Pyrophosphate Based on a Click Generated Cyclic Steroid-Rhodamine Conjugate. *J. Photochem. Photobiol. A: Chem.* 356, 7–17. doi:10.1016/j.jphotochem.2017.12.023
- Zhang, Z., Wang, F.-W., Wang, S.-Q., Ge, F., Zhao, B.-X., and Miao, J.-Y. (2012). A Highly Sensitive Fluorescent Probe Based on Simple Pyrazoline for Zn<sup>2+</sup> in Living Neuron Cells. *Org. Biomol. Chem.* 10 (43), 8640–8644. doi:10.1039/c2ob26375k
- Zhao, X.-H., Gong, L., Wu, Y., Zhang, X.-B., and Xie, J. (2016). Cationic-erylene-G-quadruplex Complex Based Fluorescent Biosensor for Label-free Detection of Pb<sup>2+</sup>. *Talanta* 149, 98–102. doi:10.1016/j.talanta.2015.11.038
- Zheng, M., Tan, H., Xie, Z., Zhang, L., Jing, X., and Sun, Z. (2013). Fast Response and High Sensitivity Europium Metal Organic Framework Fluorescent Probe with Chelating Terpyridine Sites for Fe<sup>3+</sup>. *ACS Appl. Mater. Inter.* 5 (3), 1078–1083. doi:10.1021/am302862k
- Zhou, Y., He, X., Chen, H., Wang, Y., Xiao, S., Zhang, N., et al. (2017). An ESIPT/ICT Modulation Based Ratiometric Fluorescent Probe for Sensitive and Selective Sensing Hg<sup>2+</sup>. *Sensors Actuators B: Chem.* 247, 626–631. doi:10.1016/j.snb.2017.03.085
- Zhou, Y., Kim, H. N., and Yoon, J. (2010). A Selective 'Off-On' Fluorescent Sensor for Zn<sup>2+</sup> Based on Hydrazone-Pyrene Derivative and its Application for Imaging of Intracellular Zn<sup>2+</sup>. *Bioorg. Med. Chem. Lett.* 20 (1), 125–128. doi:10.1016/j.bmcl.2009.11.028
- Zhou, Z., Tang, H., Chen, S., Huang, Y., Zhu, X., Li, H., et al. (2021). A Turn-On Red-Emitting Fluorescent Probe for Determination of Copper(II) Ions in Food Samples and Living Zebrafish. *Food Chem.* 343, 128513. doi:10.1016/j.foodchem.2020.128513
- Zhu, A., Qu, Q., Shao, X., Kong, B., and Tian, Y. (2012). Carbon-Dot-Based Dual-Emission Nanohybrid Produces a Ratiometric Fluorescent Sensor for *In Vivo* Imaging of Cellular Copper Ions. *Angew. Chem. Int. Ed.* 51 (29), 7185–7189. doi:10.1002/anie.201109089
- Zhu, S., Meng, Q., Wang, L., Zhang, J., Song, Y., Jin, H., et al. (2013). Highly Photoluminescent Carbon Dots for Multicolor Patterning, Sensors, and Bioimaging. *Angew. Chem. Int. Ed.* 52 (14), 3953–3957. doi:10.1002/anie.201300519
- Zong, J., Yang, X., Trinch, A., Hardin, S., Cole, I., Zhu, Y., et al. (2014). Carbon Dots as Fluorescent Probes for "Off-On" Detection of Cu<sup>2+</sup> and L-Cysteine in Aqueous Solution. *Biosens. Bioelectron.* 51, 330–335. doi:10.1016/j.bios.2013.07.042

**Conflict of Interest:** The authors declare that the research was conducted in the absence of any commercial or financial relationships that could be construed as a potential conflict of interest.

**Publisher's Note:** All claims expressed in this article are solely those of the authors and do not necessarily represent those of their affiliated organizations, or those of the publisher, the editors and the reviewers. Any product that may be evaluated in this article, or claim that may be made by its manufacturer, is not guaranteed or endorsed by the publisher.

Copyright © 2022 Li, Wang, Xu, Li and Dong. This is an open-access article distributed under the terms of the Creative Commons Attribution License (CC BY). The use, distribution or reproduction in other forums is permitted, provided the original author(s) and the copyright owner(s) are credited and that the original publication in this journal is cited, in accordance with accepted academic practice. No use, distribution or reproduction is permitted which does not comply with these terms.



# Recent Progress on Carbon Quantum Dots Based Photocatalysis

Hwapyung Jung<sup>1</sup>, Vijay S. Sapner<sup>2</sup>, Arindam Adhikari<sup>3</sup>, Bhaskar R. Sathe<sup>2\*</sup> and Rajkumar Patel<sup>4\*</sup>

<sup>1</sup>Nano Science and Engineering, Integrated Science and Engineering Division (ISED), Underwood International College, Yonsei University, Incheon, South Korea, <sup>2</sup>Department of Chemistry, Dr. Babasaheb Ambedkar Marathwada University Aurangabad, Seoul, South Korea, <sup>3</sup>Aadarsh Innovations, Pune, India, <sup>4</sup>Energy and Environmental Science and Engineering (ESEE), Integrated Science and Engineering Division (ISED), Underwood International College, Yonsei University, Incheon, South Korea

As a novel carbon allotrope, carbon quantum dots (CQDs) have been investigated in various fields, including photocatalysis, bioimaging, optoelectronics, energy and photovoltaic devices, biosensing, and drug delivery owing to their unique optical and electronic properties. In particular, CQDs' excellent sunlight harvesting ability, tunable photoluminescence (PL), up-conversion photoluminescence (UCPL), and efficient photo-excited electron transfer have enabled their applications in photocatalysis. This work focuses on the recent progress on CQDs-related materials' synthesis, properties, and applications in photocatalysis.

## OPEN ACCESS

### Edited by:

Hanfeng Liang,  
Xiamen University, China

### Reviewed by:

Jie Chen,  
Xi'an Jiaotong University, China  
Hao Wu,  
Shandong University, China

### \*Correspondence:

Bhaskar R. Sathe  
bhaskarsathe@gmail.com  
Rajkumar Patel  
rajkumar@yonsei.ac.kr

### Specialty section:

This article was submitted to  
Photocatalysis and Photochemistry,  
a section of the journal  
Frontiers in Chemistry

Received: 22 February 2022

Accepted: 07 March 2022

Published: 25 April 2022

### Citation:

Jung H, Sapner VS, Adhikari A,  
Sathe BR and Patel R (2022) Recent  
Progress on Carbon Quantum Dots  
Based Photocatalysis.  
Front. Chem. 10:881495.  
doi: 10.3389/fchem.2022.881495

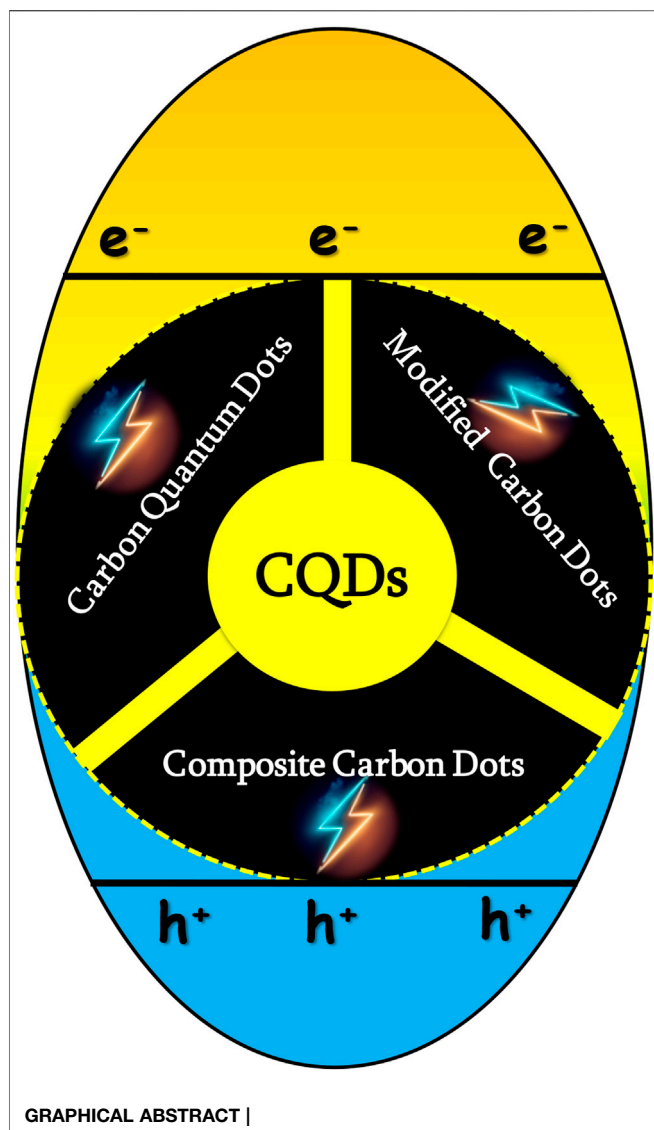
**Keywords:** carbon quantum dots (CQDs), photocatalysis, modified quantum dots, composite quantum dots, energy and environmental remediation, photovoltaic devices

## 1 INTRODUCTION

A new kind of carbon allotrope, carbon quantum dots (CQDs), carbon dots (CDs, C-dots, or C<sub>Dots</sub>), or carbon nanodots (Liu et al., 2016) are quasi-spherical, monodisperse carbon nanoparticles with a diameter below 10 nm. Graphene quantum dots (GQDs) are a kind of CQDs with relatively high crystallinity over other allotropic forms (Li et al., 2015). CQDs possess both electronic properties of carbon materials and optical properties of quantum dots (Yu et al., 2016). They were discovered in 2004 (Xu et al., 2004) and got their name in 2006 (Sun et al., 2006). CQDs have been researched in various fields such as photocatalysis (Hu et al., 2013a; Han et al., 2013; Hou et al., 2015; Fang et al., 2016), bioimaging (Ray et al., 2009; Antaris et al., 2013; Bhunia et al., 2013), optoelectronics (Guo et al., 2012; Chen Q.-L. et al., 2013; Bourlinos et al., 2013; Ma et al., 2015), photovoltaic devices (Zhang et al., 2013; Suzuki et al., 2015), biosensing (Kleinauskas et al., 2013; Zhu et al., 2013), and drug delivery (Tang J. et al., 2013; Feng et al., 2016).

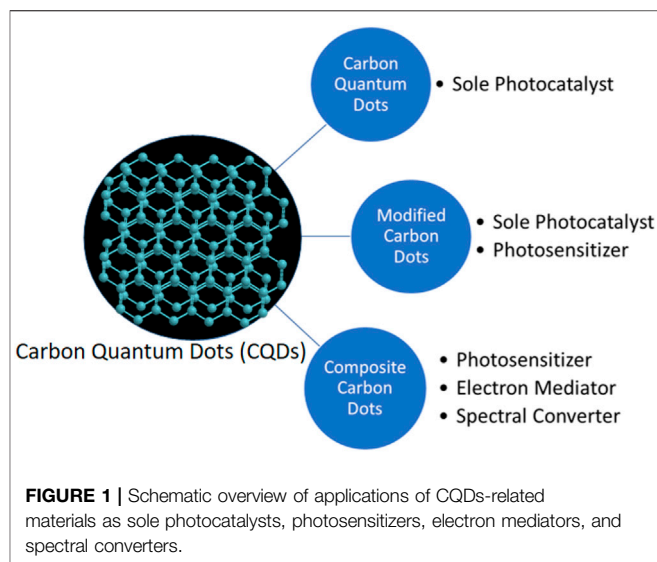
CQDs have an amorphous or nanocrystalline core, which is mainly sp<sup>2</sup> carbon, with the lattice spacings of graphite and oxygenic functional groups (5–50 wt%) on the surface, which give water solubility and the possibility of further functionalization (Yang et al., 2009a; Yang et al., 2009b; Baker and Baker, 2010). This structure gives CQDs having unique properties, including excellent sunlight harvesting ability, tunable photoluminescence (PL), up-converted photoluminescence (UCPL), and efficient photo-excited electron transfer. Depending on synthesis methods, functional groups on the surface can be modified to further tune the PL of CQDs. By introducing electron donor and/or electron acceptor, PL of CQDs can be quenched (Wang et al., 2009; Basit et al., 2022; Chang et al., 2022).

The unique properties of CQDs enable their applications in photocatalysis (Murali et al., 2021; Syed et al., 2021; Yao et al., 2022), where photogenerated electrons and holes do the job. The UCPL of CQDs makes the use of the full spectrum of solar light possible to increase the light absorption and



thus the photogenerated electrons and holes (Wang and Hu, 2014; Farshbaf et al., 2018; An et al., 2022; Preethi et al., 2022; Saeidi et al., 2022; Su et al., 2022). The efficient photo-excited electron transfer of CQDs retard the recombination of electron-hole pairs to increase the lifetime of photogenerated electrons and holes (Liang et al., 2021; Liu et al., 2021; Mahmood et al., 2021). Hence, CQDs can be used in photocatalysis. CQDs can act as a sole photocatalyst or enhance the photocatalytic activity of other photocatalysts as an electron mediator, a photosensitizer, and/or a spectral converter (**Figure 1**).

This work focuses on recent progress on CQDs-related materials' synthesis, properties, and applications in photocatalysis. Subsequently, **Sections 2–4** will be about carbon quantum dots, modified carbon dots, and composite carbon dots, respectively. In each section, the synthesis methods, characterization, and photocatalysis of corresponding materials will be introduced. The synthesis of those materials and



the pollutants they photodegrade are summarized in **Table 1**, and **Section 5** will present the conclusion.

## 2 SYNTHESIS METHODS OF CQDS

Xu et al. discovered fluorescent CQDs by coincidence while purifying single-walled carbon nanotubes (SWCNTs) from arc-discharged soot that they came up with the idea to publish their findings in *Science* (Xu et al., 2004). There have now been other alternative synthesis strategies for producing CQDs that have been found and refined. This research is primarily concerned with easy, cost-effective, size adjustable, and large-scale methodologies for synthesizing CQDs that have improved functions and can be produced in a wide range of compositions and structural arrangements. “Top-down” and “bottom-up” strategies are often used in the production of CQDs, and they may be separated from one another by the direction in which the size expansion of the implemented materials takes place: “top-down” and “bottom-up” procedures schematic representation in **Figure 2**.

Top-down techniques use treatments including arc discharge, laser ablation, electrochemical oxidation, chemical oxidation, and ultrasonic synthesis to create CQDs from macroscopic carbon structures such as graphite, activated carbon, and carbon nanotubes (Zhou et al., 2007; Yang et al., 2009a; Peng and Travas-Sejdic, 2009; Tian et al., 2009; Li X. et al., 2011; Tang D. et al., 2013; Hu et al., 2013b). Bottom-up procedures use microwave synthesis, thermal decomposition, hydrothermal treatment, template-based routes, and plasma treatment to make CQDs from molecular precursors such as citric acid, sucrose, and glucose (Zhu et al., 2009; Li et al., 2012; Tang et al., 2012; Chen B. et al., 2013; Qu et al., 2013; Bian et al., 2014; Ma et al., 2015).

**TABLE 1 |** CQDs-based materials' synthesis and application in photocatalytic pollution control processes.

CQDs catalytic system	Source	Method	Pollutants	CQDs	References
Graphene quantum dots	Citric acid	Pyrolysis	New fuchsin dye	Sole	(Roushani et al., 2015)
Carbon dots	<i>Elettariacardamomum</i>	Solution extraction	Congo red and methylene blue dyes	Photocatalyst	(Zaib et al., 2021)
Carbon dots	Bitter apple peel	Carbonization	Crystal violet dye	Photosensitizer	(Aggarwal et al., 2020)
Carbon dots	Pear juice	Hydrothermal treatment	Methylene blue dye		(Das et al., 2019)
Nitrogen doped carbon dots	<i>Cocciniagrandidis</i>	Hydrothermal treatment	Methyl orange dye		(Chandrasekaran et al., 2020)
Nitrogen doped carbon dots	<i>Citrus grandis</i>	Hydrothermal treatment	Methylene blue dye		(Ramar et al., 2018)
Nitrogen doped carbon dots	Empty fruit bunches	Hydrothermal treatment	Methylene blue and malachite green dyes		(Rani et al., 2021)
Nitrogen doped carbon dots	<i>Azadirachtaindica</i>	Hydrothermal treatment	Safranin-O dye		(Dhanush and Sethuraman, 2020)
Nitrogen doped carbon dots and chlorine doped carbon dots	Aqua mesophase pitch	Hydrothermal treatment	Rhodamine B, methylene blue and indigo carmine dyes		(Cheng et al., 2019)
Nitrogen and magnesium co-doped carbon dots	<i>Bougainvillea</i> leaves	Carbonization	Methylene blue dye		(Bhati et al., 2018)
Nitrogen and cobalt co-doped carbon dots	Vitamin B12	Pyrolysis	Rhodamine B dye		(Wang et al., 2020)
Sulfur and chlorine co-doped carbon dots	Palm powder	Hydrothermal treatment	Rhodamine B and methylene blue dyes		(Zhu et al., 2020)
Phosphorus doped carbon dots	D-glucose anhydrous	Hydrothermal treatment	Methylene blue dye		(Mathew et al., 2020)
Boron doped carbon dots	Citric acid	Hydrothermal treatment	Rhodamine B and methylene blue dyes	Photosensitizer	(Peng et al., 2020)
Phenylhydrazine modified carbon dots	Maltitol	Thermal decomposition	Methylene blue dye	Electron Mediator	(Han et al., 2020)
TiO <sub>2</sub> -wsCQDs	Lemon peel	Hydrothermal treatment	Methylene blue dye		(Tyagi et al., 2016)
CQDs/TNTs	Citric acid	Hydrothermal treatment	Methylene blue dye		(Zhao et al., 2018)
CDs/N-TiO <sub>2</sub>	Ascorbic acid	Hydrothermal treatment	Rhodamine B dye		(Zhang J. et al., 2020)
Active blend functionalized TiO <sub>2</sub>	Sodium alginate	Microwave digestion	Methylene blue, crystal violet and methyl orange dyes and pharmaceuticals like diclofenac and tetracaine		(Vassalini et al., 2020)
N-CDs/TiO <sub>2</sub>	Citric acid	Hydrothermal treatment	Rhodamine B dye		(Ouyang et al., 2020)
NCQDs/TiO <sub>2</sub>	Citric acid	Microwave assisted method			(Li et al., 2018)
NP-CQDs/TiO <sub>2</sub>	Citric acid	Thermal treatment	Methylene blue dye		(Guo et al., 2018)
cl-Ch-p(VI)/TiO <sub>2</sub> NPs-CDs	Sugar cane juice	Microwave assisted method	Reactive Blue 4 and Reactive Red 15 dyes and toxic compound 2,4-dichlorophenol		(Midya et al., 2020)
CDs/P25/Rgo	Citric acid	Hydrothermal treatment	Rhodamine B, methylene blue and methyl orange dyes	Photosensitizer	(Zhu et al., 2021b)
CQDZ	Ammonium citrate	Thermal treatment	Methylene blue dye	Electron Mediator	(Ratnayake et al., 2019)
CDs_BZO	Citric acid	Hydrothermal treatment	Methylene blue dye	Special Converter	(Patra et al., 2018)
N,Fe-CDs/G-WO <sub>3</sub>	Folic acid	Hydrothermal treatment	Rhodamine B and methylene blue dyes and pharmaceuticals like ciprofloxacin, tetracycline hydrochloride and oxytetracycline		(Ni et al., 2020)
WO <sub>3</sub> /GO/NCQDs	Citric acid	Hydrothermal treatment	Methyl orange dye		(Jamila et al., 2020a)
ZnO/C-dots	Glucose and copra oil	Solvothermal treatment	Methylene blue dye		(Velumani et al., 2020)
ZnO-CDs	Grounded coffee	Hydrothermal treatment	Methylene blue dye		(Omer et al., 2018)
C <sub>Dots</sub> /ZnO <sub>2</sub>	D-glucose	Microwave assisted method	Methyl orange, methylene blue and Rhodamine B dyes		(El-Shamy, 2020b)
PVA/CZnO <sub>2</sub>	D-glucose	Microwave assisted method	Methylene blue dye		(El-Shamy, 2020a)

(Continued on following page)



**TABLE 1 |** (Continued) CQDs-based materials' synthesis and application in photocatalytic pollution control processes.

CQDs catalytic system	Source	Method	Pollutants	CQDs	References
PVA/CQDs	D-glucose	Solution casting method	Methylene blue dye		(El-Shamy and Zayied, 2020)
PVP-CD	Lemon juice	Hydrothermal treatment	Rhodamine B, malachite green, crystal violet and Eosin Y dyes		(Nayak et al., 2020)
CDs/CeO <sub>2</sub>	Wood powder and citric acid	Hydrothermal treatment	Methylene blue dye		(Gong et al., 2019)
CuO/NCQDs	Citric acid	Hydrothermal treatment	Methyl orange dye	Photosensitizer	(Jamila et al., 2020b)
CQDs/KNbO <sub>3</sub>	L-ascorbic acid	Hydrothermal treatment	Crystal violet dye	Electron Mediator	(Qu et al., 2018)
Pd@CD-CONH	Citric acid	Hydrothermal treatment	Rhodamine B dye	Special Converter	(Selim et al., 2020)
MIL-53(Fe)/CQDs/MNPs	Wood based activated carbon	HNO <sub>3</sub> treatment	Rhodamine B, malachite green and methylene blue dyes and Cr(VI)		(He et al., 2021)
CCN	Citric acid	Hydrothermal treatment	Methylene blue and Rhodamine B dyes		(Zhang L. et al., 2020)
NCQD/g-C <sub>3</sub> N <sub>4</sub>	Citric acid	Hydrothermal treatment	Methylene blue dye		(Seng et al., 2020)
GA-CQDs/CNN	EDTA-2Na•2H <sub>2</sub> O	Hydrothermal treatment	Methyl orange dye		(He et al., 2018a)
g-C <sub>3</sub> N <sub>4</sub> /Ag <sub>3</sub> PO <sub>4</sub> /NCDs	Citric acid	Solution process	Methylene blue and Rhodamine B dyes and refractory pollutant phenol		(Miao et al., 2018a)
Ag <sub>3</sub> PO <sub>4</sub> /GO/NCD	Citric acid	Hydrothermal treatment	Methylene blue and Rhodamine B dyes and refractory pollutant phenol		(Miao et al., 2018b)
CDC-dye	Citric acid	Microwave assisted method			(Jana et al., 2020)
N-CDs/m-TiO <sub>2</sub>	Citric acid		Methylene blue dye		(Zhang et al., 2021)
CDs/g-C <sub>3</sub> N <sub>4</sub> /SnO <sub>4</sub>	Quanidiniumhydrochloride	Thermal polymerization method	Indomethacin (IDM)		(Li et al., 2021)
ZnO/CQDs		Hydrothermal treatment	Benzene and Methanol		(Yu et al., 2012)
CDs/NiCO <sub>2</sub> O <sub>4</sub>		Hydrothermal treatment	Photocatalytic HER and OER		(Nie et al., 2021)
Au/CQDs			Cyclohexane		(Liu et al., 2014)
L-CQDs/ZnO		Hydrothermal treatment	Phenol		(Liang et al., 2020)
ZnO/CQDs/AuNPs	D-lactose	Hydrothermal treatment	Methylene blue dye		(Bozetine et al., 2021)
CQDs/Au/BMO	Citric acid	Hydrothermal treatment	Phenol		(Zhao et al., 2021)
CQDs/BIOCOOH/uCN	Citric acid	Hydrothermal treatment	Sulfathiazole (STZ)		(Hu et al., 2021)
N-CQDs/BiOI <sub>x</sub> Br <sub>1-x</sub>	Citric acid	Co-precipitation method	Phenol		(Gao et al., 2021)

## 2.1 Top-Down

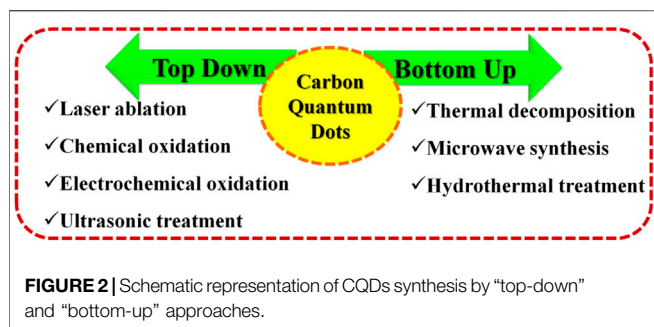
### 2.1.1 Laser Ablation

Recent trends in CQD preparation favor laser ablation, which can easily control morphology and manufacture a variety of nanostructures. Laser ablation is an excellent process for creating CQDs with a limited size distribution, good water solubility, and fluorescence properties, among other qualities. However, it is not widely used because of its intricate operation and high cost (Hu et al., 2009; Cui et al., 2020).

In two different configurations, a batch configuration and a flow jet configuration, Donate-Buendia et al. synthesized CQDs by laser irradiation of glassy carbon particles suspended in polyethylene glycol 200 (Doñate-Buendia et al., 2018).

### 2.1.2 Chemical Oxidation

Chemical oxidation is a cost-effective and convenient method for large-scale production that does not require sophisticated devices. Tan et al. made CQDs *via* oxidation (Tan et al., 2019). In a 100 ml round-bottom flask, 50 ml of concentrated HNO<sub>3</sub>, and HClO<sub>4</sub> were combined 1:1 with 2.00 g coconut shell activated carbon. Oxidation was carried out for 120 min at 100°C with 500 rpm magnetic stirring (500 rpm). The dark suspension was cooled and then separated using a 1,000 Da ultrafiltration membrane in an MSC300 ultrafiltration apparatus. The filtrate was concentrated in vacuo and dialyzed for 3 days to remove inorganic ions to create CODs.



### 2.1.3 Electrochemical Oxidation

In the production of CQDs, electrochemical oxidation is the most often used technique. This approach has the benefits of high purity, cheap cost, high yield, ease of size modification, and excellent repeatability (Zhou et al., 2021). Zhou et al. reported the first electrochemical generation of CQDs from multiwalled carbon nanotubes (MWCNTs) (Zhou et al., 2007). Li et al. described the direct electrochemical production of 3–5 nm green luminous GQDs (Li Y. et al., 2011).

### 2.1.3 Ultrasonic Synthesis

Although it is widely established that ultrasound can generate alternate low-pressure and high-pressure waves in liquids, the development and collapse of small vacuum bubbles are not well understood (Liang et al., 2013; Lu and Zhou, 2019; Wu et al., 2019; Rosiles-Perez et al., 2020).

Qi et al. synthesized CQDs by ultrasonic synthesis 60 ml L-glutamic acid aqueous (0.45 M) introduced to the reaction kettle through an ultrasonic transducer. The ultrasonic generator remained at 50% power during the reaction. The solution was heated to a particular temperature and then cooled to room temperature when it became yellow and no visible precipitation occurred, indicating the CQDs were formed (Qi et al., 2021).

## 2.2 Bottom-Up

### 2.2.1 Thermal Decomposition

The thermal breakdown has been utilized in the past to produce various semiconductor and magnetic nanomaterials, among other things. Recent research has demonstrated that external heat can contribute to the dehydration and carbonization of organic materials, resulting in the formation of CQDs. The advantages of this process include ease of operation, a solvent-free approach, a wide range of precursor tolerance, a fast reaction time, a low cost, and the ability to scale up production (Chen et al., 2018; Ghosh et al., 2021; Kang et al., 2022; Đorđević et al., 2022).

Tang et al. created R-CQDs by heat treatment wine lees, which served as the carbon source (Tang et al., 2021). By an open beaker, 100 ml of wine lees was heated for 0.5–2 h on a heating platform at 300°C to get the reactants, and then 100 ml of ethanol solution was poured into the beaker once the reactants had cooled. For regulating CQD size and homogeneity, the supernatant was post-treated using column chromatography or dialysis followed with evaporation of ethanol yields CQDs.

### 2.2.2 Microwave Synthesis

Microwaves are a form of electromagnetic wave with a broad wavelength range of 1 mm to 1 m, and they can deliver massive amounts of energy to a substrate, allowing it to be broken apart chemically. Therefore, the microwave approach may be used to significantly reduce reaction time while also providing homogenous heating, which results in a more consistent distribution of quantum dots in the final product (Yang et al., 2018; Zhu J. et al., 2021).

Yu et al. prepared CQDs by a microwave synthesis method (Yu et al., 2018). In a 100 ml beaker, phthalic acid (2 g) and triethylenediamine hexahydrate (1 g) were dissolved in 3 ml deionized water. The beaker was then cooked for 60 s on the revolving plate of a household MW oven (700 W). After cooling, the crude products were dialyzed for 24 h against 500 ml deionized water to make powdered CQDs. Basoglu et al. synthesized CQDs by the microwave-assisted pyrolysis of the roasted chickpeas (Başoğlu et al., 2020). In total, 2 g of roasted chickpeas were digested in 40 ml ultra-pure water. This mixture was transferred to a 250 ml beaker and microwaved for 2 min. 15 min at 3,000 rpm centrifuged the cooled solution. The Allegra X-30R was utilized (Beckman Coulter). The cream solid was extracted from the supernatant. The liquid was filtered using 0.45 and 0.2 mm syringe membranes. The solution was centrifuged for 15 min at 12,000 rpm to remove the aggregates. The liquid CQD was blended. Solute was chilled at 4°C to make CQDs.

### 2.2.3 Hydrothermal Treatment

Hydrothermal carbonization produces innovative carbon-based compounds from saccharides, organic acids, juice, or discarded peels. Generally, an organic precursor solution is enclosed and heated in a hydrothermal reactor.

Das et al. fabricated green-emissive carbon quantum dots (CQDs) from pear juice in a simple and scalable hydrothermal route (Das et al., 2019). In order to make the CQDs, the pear juice was held in a Teflon-lined autoclave at 180°C for 36 h and filtered with a 0.22 µm filter. Chandrasekaran et al. prepared nitrogen-doped carbon dots (N-CDs) from *Coccinia grandis* extract by a simple hydrothermal method (Chandrasekaran et al., 2020). The *Coccinia grandis* extract and aqueous ammonia were held in a Teflon-lined autoclave for 12 h at 180°C, filtered with Whatman 40 filter paper, and centrifuged at 1,000 rpm for 1 h to make N-CDs.

## 3 PROPERTIES OF CQDS

### 3.1 Optical Absorbance

For the most part, the optical absorption peaks of CQDs in the UV visible region are interpreted as being caused by the  $sp^2$  conjugated carbon p-p transition and the n-p transition caused by the hybridization with heteroatoms such as N, S, and P, among others. Surface passivation or modification processes can be used to control the absorption property of the surface. He et al. synthesized CODs from lemon juice using a simple hydrothermal treatment at low temperatures and short time

(He M. et al., 2018). The CQDs have good optical and material qualities. Under UV or blue light irradiation, they produce strong blue-green fluorescent light. According to He et al., CQDs can image plant cells. These critical insights can help us learn more about CQDs and investigate their potential applications.

### 3.2 Fluorescence

PL is one of the most intriguing characteristics of CQDs, both from a basic and an application-oriented standpoint. **Section 4** describes how to modify the PL features of CQDs to get the desired result. Raj et al. (2021) synthesized water-dispersible and fluorescence-stable carbon quantum dots (CQDs) at a gram scale. Their optical and fluorescent properties were studied in depth. Aqueous dispersion emits intense yellow light in UV lamps (365 nm). As a nano-probe CQDs can detect heavy metal ions like  $\text{Cr}^{3+}$ ,  $\text{Fe}^{3+}$ , and  $\text{Cu}^{2+}$  in aqueous media at neutral pH by quenching their fluorescence. The LOD of 100 nM for each of these ions of CQDs. These fluorescence-stable CQDs are easily manufactured and maintained for sensing applications.

### 3.3 Phosphorescence

CQDs have recently been discovered to have phosphorescence capabilities (Tan et al., 2016a, Tan et al., 2016b; Chen et al., 2019; Yuan et al., 2022). It has been possible to develop a pure organic room temperature phosphorescent (RTP) material based on water-soluble CQDs, and the phosphorescent lifetime of this material has been increased to the sub-second order (380 ms). It was possible to witness clear phosphorescence at room temperature when the CQDs were dispersed in a polyvinyl alcohol (PVA) matrix when the PVA matrix was activated with UV light (Deng et al., 2013). Preliminary research revealed that the phosphorescence was caused by triplet excited states of aromatic carbonyls on the surface of the CQDs, which was supported by the results of the experiments. The hydrogen bonding between the matrixes PVA molecules can successfully preserve the triplet excited state energy from rotational or vibrational loss by rigidifying the groups that make up the triplet excited state. **Section 4** discussed more related literature on CODs.

### 3.4 Chemiluminescence

The chemiluminescence (CL) of CQDs was initially observed when they were mixed with oxidants such as potassium permanganate ( $\text{KMnO}_4$ ) and Cerium (IV) (Lin et al., 2012). EPR shows that oxidants such as  $\text{KMnO}_4$  and Cerium (IV) may insert holes into CQDs. This increases the population of holes in CQDs and speeds up electron-hole annihilation, leading to CL emission. Moreover, the CL intensity was dependent on CQD concentration. The thermal equilibrium of electron dispersion in CQDs also discovered that increasing temperature had a beneficial influence on CL. The fact that the surface groups of this system's CL characteristics can be changed is intriguing (Teng et al., 2014). The CL of CQDs offers new possibilities for their use in reductive substance determination (Lin et al., 2011; Zhao et al., 2013; Wang et al., 2019; Shen et al., 2020).

### 3.5 Photoluminescence

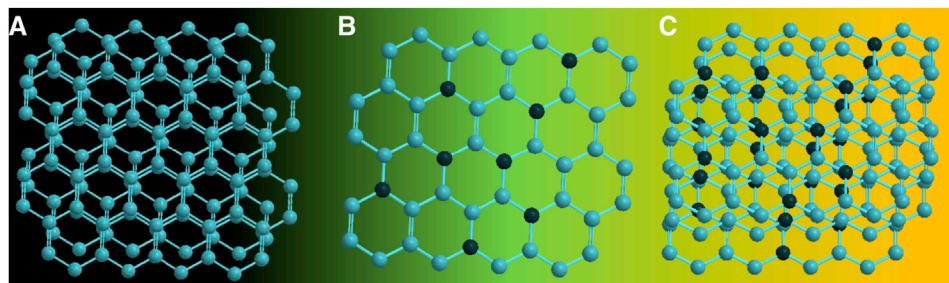
There has been a significant increase in recent years in the amount of research being done on the PL of CQDs, which is one of the most exciting characteristics of CQDs and has been used in the field of photocatalysis (Chen et al., 2022; Peng et al., 2022). The PL emission pattern is similar to the Stokes type emission pattern in that the PL emission wavelength is longer than the excitation wavelength of the laser. Many publications have been published on the observation of PL emissions in CQDs from diverse sources (Cao et al., 2022; Liang et al., 2022; Pooremaeil et al., 2022; Yu et al., 2022; Zhang et al., 2022). A detailed look at the spectroscopic aspects of the emissions and the underlying structural characteristics reveals that most recorded PL emissions fall into one of two groups. One is related to band gap transitions corresponding to conjugated p-domains, while the other is due to defects in graphene structures. The two groups are often interrelated since the exploitation or manipulation of graphene sheet defects creates or inducts p-domains. Many investigations examined the relationship between PL emission and CQD excitation wavelength discussed in **Section 4**.

## 4 PHOTOCATALYTIC APPLICATIONS OF CQDS

There are some advantages to using CQDs in photocatalysis. CQDs are superior to other typical photocatalysts in terms of water solubility, chemical stability, and low toxicity (e.g.,  $\text{ZnO}$ ,  $\text{TiO}_2$ , and  $\text{CdS}$ ). After surface modification, CQDs display outstanding and tunable optical characteristics of absorbance and PL. UCPL of CQDs, in particular, may greatly increase the sunlight absorption of wide band gap semiconductors into the visible and near-infrared regions. Photoinduced CQDs are also good electron donors and acceptors, allowing for efficient electron-hole separation. Thus, CQDs can be used as electron mediators, photosensitizers, spectral converters, and sole photocatalysts. In fact, these many impacts often occur concurrently. CQD-based photocatalyst systems are summarized in this section.

### 4.1 Carbon Quantum Dots (CQDs)

Roushani et al. fabricated graphene quantum dots (GQDs) by pyrolyzing citric acid (CA) as a source of carbon (Roushani et al., 2015). The CA was held in a beaker on a heating mantle at  $200^\circ\text{C}$  for 30 min and then neutralized with NaOH to make GQDs. According to the photoluminescence (PL) spectrum, the GQDs showed an emission peak at 460 nm with an excitation wavelength of 362 nm, indicating that GQDs are fluorescent in nature. The TEM result demonstrated that the GQDs had an average diameter of 15 nm. The zeta potential of the GQDs was  $-24.6$  mV, indicating that the GQDs had a negatively charged surface. The Raman spectrum confirmed the presence of G-band and D-band at  $1,600$  and  $1,377\text{ cm}^{-1}$ , respectively. The  $I_D/I_G$  value of GQDs was as high as 1.03, indicating GQDs have a crystal structure with some  $\text{sp}^2$  defects caused by smaller clusters. The GQDs were used as photocatalysts for the degradation of New Fuchsin (NF) dye under visible light. The effects of GQDs, initial NF concentration, pH of dye, and contacting time on the degradation



**SCHEME 1** | Schematics of (A) unmodified, (B) modified, and (C) composite carbon quantum dots (CQDs).

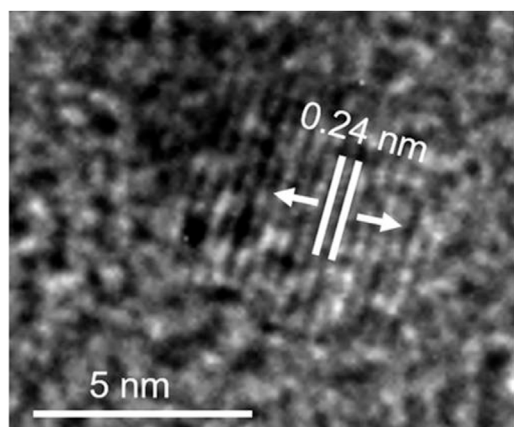


**FIGURE 3** | High resolution transmission electron microscopic (H-TEM) image of a single CQD showing graphitic spacing. (Reproduced from Das et al., 2019, Springer Nature).

efficiency were investigated. The rate constant and degradation efficiency were rarely affected by NF concentration and only decreased slightly when the initial NF concentration increased.

Zaib et al. synthesized carbon dots (CDs) from *Elettaria cardamomum* in an eco-friendly way by the facile sonication method (Zaib et al., 2021). The *Elettaria cardamomum* leaves were ultra-sonicated for 45 min, centrifuged at 4,500 rpm for 15 min, and filtered with 0.22  $\mu\text{m}$  membrane filter to make CDs. In the XRD result, the peak at  $22.9^\circ$  confirmed the existence of amorphous phase carbon in the synthesized CDs. The Raman spectroscopic result showed a G-band at  $1,575\text{ cm}^{-1}$ , which represents a graphitic band of carbon, and a weaker D-band at  $1,365\text{ cm}^{-1}$ , which represents a disordered band of carbon. According to the photoluminescence spectroscopic result, when the excitation wavelength was 514 nm, CDs showed two emission peaks at 520 and 850 nm, respectively, indicating that CDs are fluorescent. The CDs were used as photocatalysts for the degradation of methylene blue (MB) and congo red (CR) under visible light irradiation. At the optimal condition (4 pH, 5 ppm CR, and 5 ml CDs), CR degradation took 50 min. However, when the dye was changed to MB with a similar concentration and at 8 pH, degradation took just 5 min more than CR.

Aggarwal et al. prepared photoactive carbon dots (CDs) through a facile, green, and scalable method by charring bitter apple peel (Aggarwal et al., 2020). Dried peel was carbonized at around  $300^\circ\text{C}$  in a muffle furnace for 2 h to generate carbon dots. XPS study showed the elemental composition of CDs to be 60.3, 37.47, and 2.23% for C, N, and O, respectively. The presence of graphitic G-band and disordered D-band at  $1,571$  and  $1,355\text{ cm}^{-1}$  was confirmed by Raman spectroscopy. H-TEM studies showed the presence of graphitic fringes in CDs. The photoactive CDs were used as photocatalysts for the degradation of crystal violet (CV) under solar light. The photoactive CDs degraded 20 ppm of CV in  $\sim 90$  min, much faster than the degradation in the dark. According to the active species scavenging experiment, the most important active species engaged in the degradation reactions were photogenerated electrons and holes. The degradation of CV, from aromatic compound to little aliphatic pieces, was confirmed by NMR spectroscopy.

Das et al. fabricated green-emissive carbon quantum dots (CQDs) from pear juice in a simple and scalable hydrothermal route (Das et al., 2019) and H-TEM analysis shows the high crystallinity of CQDs in Figure 3. According to XPS results, the elemental composition of CQDs was 71% and 29% for C and O, respectively. The photoluminescence (PL) results revealed that the CQDs showed excitation-dependent emission. As the excitation wavelength increased from 380 to 600 nm, emission wavelength increased from 470 to 650 nm with gradually decreasing emission intensity. The CQDs were used as photocatalysts for the degradation of methylene blue (MB) under visible light. 99.5% of MB was degraded within 130 min. The excellent photocatalytic performance was due to efficient transfer and separation of photogenerated charge and good light-harvesting capability. Besides, the CQDs were used as selective sensors for Fe (III) and ascorbic acid (AA). The CQDs stopped emitting fluorescence when they were bound to Fe (III) and began to emit fluorescence again when AA was added. Accordingly, Scheme 1 demonstrates the various types of CQDs Scheme 1A Unmodified, Scheme 1B Modified and Scheme 1C Composite Carbon Quantum Dots (CQDs).

## 4.2 Modified Carbon Quantum Dots (CQDs)

Chandrasekaran et al. prepared nitrogen-doped carbon dots (N-CDs) from *Coccinia grandis* extract by a simple hydrothermal method (Chandrasekaran et al., 2020).



According to H-TEM results, N-CDs had spherical shapes with a diameter of 3.3 nm. The EDS result demonstrated that N-CDs had a composition of C (91.55%), N (2.12%), and O (5.48%). In XRD results, the peak at  $28.5^\circ$  confirmed the existence of amorphous carbon in N-CDs. N-CDs were used as catalysts for the reduction of methyl orange (MO) with  $\text{NaBH}_4$ . The MO reduction rate constant was  $0.1263 \text{ min}^{-1}$ , which was higher than that of using pure  $\text{NaBH}_4$ .

Ramar et al. (2018) synthesized undoped carbon quantum dots (UCQDs) and N-doped carbon quantum dots (NCQDs) using Pomelo juice *via* a simple and eco-friendly hydrothermal process. The Pomelo juice was held in a Teflon-lined autoclave at  $200^\circ\text{C}$  for 7 h and centrifuged for 30 min at 12,000 rpm to make UCQDs. The Pomelo juice and ammonium bicarbonate were held in a Teflon-lined autoclave at  $200^\circ\text{C}$  for 7 h and centrifuged for 30 min at 12,000 rpm to make NCQDs. In the XRD results, the peak at  $22.4^\circ$  and the peaks at  $12.6^\circ$  and  $28.2^\circ$  confirmed the presence of amorphous carbon in UCQDs and NCQDs, respectively. According to TEM results, UCQDs and NCQDs had average diameters of 3 and 70 nm, respectively. The Raman spectroscopy demonstrated that the D-band, corresponding to disordered carbon, was shifted from  $1,354$  to  $1,335 \text{ cm}^{-1}$ , and the G-band, corresponding to graphitic carbon, was shifted from  $1,571$  to  $1,563 \text{ cm}^{-1}$  when CQDs were N-doped. Both CQDs acted as good photocatalysts for the degradation of methylene blue (MB) under solar light, which followed pseudo-first-order kinetics. CQDs showed brilliant photocatalytic performance because they have high transfer efficiency of photoinduced electrons and remarkable sunlight absorption abilities.

Rani et al. (2021) synthesized N-doped carbon quantum dots (NCQDs) from empty fruit bunches (EFB) by a green hydrothermal method. The lignin extracted from EFB, urea, and deionized water was held in a Teflon-lined autoclave for 8 h at  $180^\circ\text{C}$  and filtered with 20–25  $\mu\text{m}$  filter paper to make NCQDs. The EDX result showed that the elemental composition of NCQDs was 60.76, 9.01, 20.38, 5.92, and 3.93% for C, N, O, Na, and Cl, respectively. According to the TEM analysis, the NCQDs had diameters of 3.6 nm. The zeta potential of NCQDs was  $-20.35 \pm 0.52 \text{ mV}$ , indicating that the NCQDs had a negatively charged surface. With NCQDs, 97% of methylene blue (MB) and 98% of malachite green (MG) were degraded in 180 and 120 min under solar light. Without NCQDs, only 59% of MB and MG were degraded. The excellent photocatalytic activity of NCQDs was because of the separation of photogenerated charge and suppressed electron-hole recombination. The photocatalytic activity of NCQDs was superior to that of CQDs owing to the good fluorescent properties gained from N-doping. The NCQDs could be used at least ten times without significant performance decrease due to their high stability.

Dhanush et al. prepared fluorescent phyto-derived nitrogen-doped carbon dots (PDNCDs) from neem seeds using a green hydrothermal method (Dhanush and Sethuraman, 2020). The neem seeds and aqueous ammonia were held in an autoclave with Teflon lining for 12 h at  $180^\circ\text{C}$ , filtered with Whatman 40 filter paper, and centrifuged to make PDNCDs. According to H-TEM results, PDNCDs had diameters of 2.5 nm. In the XRD result, the

peak at  $28.47^\circ$  confirmed the existence of amorphous carbon in PDNCDs. The Raman spectroscopic result showed a G-band at  $1,606 \text{ cm}^{-1}$ , which represents a disordered band of carbon, and a weaker D-band at  $1,369 \text{ cm}^{-1}$ , which represents a graphitic band of carbon. The properties of PDNCDs could be precisely tuned using different solvents. PDNCDs were used as catalysts for the reduction of Safranin-O dye with  $\text{NaBH}_4$ . Safranin-O was reduced in 6 min, which was better than that of pure  $\text{NaBH}_4$  and undoped CDs. The catalytic activity of PDNCDs came from their ability to transfer electrons from  $\text{NaBH}_4$  to Safranin-O.

Cheng et al. synthesized fluorescent nitrogen-doped carbon quantum dots (N-CQDs) and chlorine-doped carbon quantum dots (Cl-CQDs) from aqua mesophase pitch (AMP) through a hydrothermal process (Cheng et al., 2019). The AMP solution was held in a polytetrafluoroethylene-lined autoclave at 120, 150, and  $180^\circ\text{C}$  for 12, 24, and 48 h, respectively, and centrifuged for 10 min at 8,000 rpm to make CQDs. Then, the CQDs held at  $120^\circ\text{C}$  for 24 h (CQDs-120-24) and ammonia were kept for 12 h at  $120^\circ\text{C}$  in the autoclave and kept for 0.5 h at  $80^\circ\text{C}$  in an open space to make N-CQDs. CQDs-120-24 and thionyl chloride went through the same procedure to make Cl-CQDs. The CQDs, N-CQDs, and Cl-CQDs had diameters of 2.8, 4.5, and 4.2 nm, respectively, according to the TEM results. Furthermore, the PL results demonstrate that CQDs had a quantum yield (QY) of 27.6%, while N-CQDs and Cl-CQDs had lower quantum yields. In the H-TEM results of CQDs, N-CQDs, and Cl-CQDs, interlayer spacing was 0.33 nm, corresponding to the (002) spacing of graphitic carbon. XPS results demonstrated that the CQDs contained C and O; N-CQDs contained C, N, and O; and Cl-CQDs contained C, Cl, and O. The CQDs, N-CQDs, and Cl-CQDs were used as photocatalysts for the degradation of rhodamine-B (Rh B), methylene blue (MB), and indigo carmine (IC) under sunlight. The N-CQDs exhibited the highest Rh B degradation efficiency of 97% in 4 h and a rate constant of  $0.02463 \text{ min}^{-1}$ . The degradation efficiency was maintained at 93% during five degradation cycles. The Cl-CQDs displayed the highest MB and IC degradation efficiency of 56% and 60%, respectively. The photocatalytic performances of N-CQDs and Cl-CQDs were better than that of pristine CQDs because the electric field was generated in N-CQDs and Cl-CQDs.

Bhati et al. prepared red-emitting-magnesium-nitrogen-embedded carbon dots (r-Mg-N-CD) in an eco-friendly way (Bhati et al., 2018). Bougainvillea leaves extract was carbonized in a 1400 W microwave oven for 15 min, sonicated, and centrifuged for 30 min at 7,000 rpm to make r-Mg-N-CD. The H-TEM results showed in (Figure 4) the graphitic fringes of r-Mg-N-CD. According to the photoluminescence (PL) results, the r-Mg-N-CD showed excitation-independent emissions at  $\sim 678 \text{ nm}$ , a high quantum yield of  $\sim 40\%$ , and high photostability. According to XPS results, the elemental composition of r-Mg-N-CD was 76.7, 11.4, 6.9, and 5.0% for C, O, N, and Mg, respectively. The r-Mg-N-CD was used as a cheap photocatalyst for aqueous phase photodegradation of a pollutant dye, methylene blue (MB), under sunlight. The photodegradation under sunlight was about six times faster than that under visible light from the artificial tungsten bulb, which only took  $\sim 120 \text{ min}$ .

Wang et al. developed single cobalt atoms anchored carbon dots (CoSAS@CD) (Wang et al., 2020). Vitamin B<sub>12</sub> was held in a quartz boat for 2 h at 250°C; was hydrolyzed with NaOH for 24 h at 80°C; and went through filtration, dialysis for 3 days, and freeze-drying to make CoSAS@CD. The TEM results showed that CoSAS@CD were spheres with the size of 9.0 nm. According to XRD results, the broad peak at 22° confirmed that CoSAS@CD was slightly graphitic. XPS results revealed that the elemental composition of CoSAS@CD was 64.73, 9.05%, 22.03%, and 4.19% for C, N, O, and Co, respectively. The photoluminescence (PL) results demonstrated that CoSAS@CD exhibited the strongest emission at 415 nm when the excitation wavelength was 300 nm. The CoSAS@CD was used as a photocatalyst for three oxidation reactions under visible light irradiation. The CoSAS@CD exhibited high oxygen evolution rate of 168 μmol/h/g during the water oxidation reaction, high conversion of ~90%, and high selectivity over 99% in imine formation reaction and oxidation degradation time of 10 min against RhB. The excellent photocatalytic activity of the CoSAS@CD came from improved visible light-harvesting ability and enhanced photoinduced charge transfer and separation.

Zhu et al. fabricated S/Cl co-doped biomass-based CDs (Bio-CDs) using palm powders through the hydrothermal process (Zhu et al., 2020). Palm powders and thionyl chloride were held in a Teflon-lined autoclave for 7 h at 200°C, filtered with a 0.22 μm syringe filter, and went through dialysis for 2 days, with freeze-drying to make Bio-CDs. According to the HTEM results, the Bio-CDs were spherical, had diameters of 3.54 nm, and displayed graphitic fringes. XPS result showed that the elemental composition of Bio-CDs was 42.20%, 43.36%, 10.02%, and 4.3% for C, O, S, and Cl, respectively. According to photoluminescence (PL) spectroscopy results, Bio-CDs showed excitation-dependent blue fluorescence with the strongest emission at 425 nm when the excitation wavelength was 340 nm. The Bio-CDs were used as photocatalysts for the degradation of rhodamine B (RhB) and methylene blue (MB) under visible light irradiation. The Bio-CDs displayed high RhB and MB degradation efficiency of ~71.7% and ~94.2%, respectively. The excellent photocatalytic activity was due to S/Cl co-doping and quantum confinement effect.

Mathew et al. fabricated carbon nano-dots (CD) and P-doped carbon nano-dots (P-CD) from D-glucose anhydrous *via* hydrothermal treatment (Mathew et al., 2020). Glucose was held in an autoclave with Teflon lining for 6 h at 150°C, filtered, and centrifuged at 5,000 rpm to make CD. Glucose and orthophosphoric acid were held in a Teflon-lined autoclave for 6 h at 110°C, neutralized with NaOH, filtered, and centrifuged at 5,000 rpm to make P-CD. The HTEM image showed that P-CD was quasi-spherical and had a radius of 2.19 nm. According to XPS result, the elemental composition of P-CD was 37%, 51.43%, 4.49%, and 7.08% for C, O, P, and Na, respectively. The photoluminescence (PL) spectra showed that P-CD exhibited the strongest emission at 524 nm at the excitation wavelength of 420 nm. The P-CD and CD were used as photocatalysts for the degradation of methylene blue (MB) under solar light. The P-CD and CD exhibited degradation rate constants of 0.02736 and 0.01645 min<sup>-1</sup>, which were

much higher than the self-degradation rate constant of MB. The P-CD degraded about 85% of MB in 180 min. The enhanced photocatalytic activity of P-CD was due to the large surface area coming from the small size of P-CD.

Peng et al. synthesized “B-doped” carbon dots (C-dots) through a hydrothermal treatment (Peng et al., 2020). Citric acid, 1, 2-diboranyethane, and anhydrous dimethylformamide were held in a Teflon-lined autoclave for 6 h at 160°C, centrifuged at 3,000 rpm for 15 min, and subjected to dialysis for 3 days to make “B-doped” C-dots. In the TEM result, the absence of noticeable lattices showed that the “B-doped” C-dots were amorphous, not graphitic. The zeta potential of “B-doped” C-dots was -11.6 mV, indicating that the “B-doped” C-dots were negatively charged. According to photoluminescence (PL) results, the “B-doped” C-dots exhibited excitation-dependent emission, with the strongest emission at 450 nm when the excitation wavelength was 360 nm. The XPS results confirmed that the elemental composition of “B-doped” C-dots was 75.8%, 19.1%, and 5.1% for C, O, and N, respectively. The “B-doped” C-dots were used as photocatalysts for the degradation of rhodamine B (RhB) and methylene blue (MB) under visible light irradiation. RhB and MB were completely degraded in 170 min. The rate constants for RhB and MB degradation were  $1.8 \times 10^{-2}$  and  $2.4 \times 10^{-2}$  min<sup>-1</sup>. The “B-doped” C-dots showed good photocatalytic activity, which was better than other C-dots photocatalysts and comparable to metal-containing photocatalysts.

Han et al. prepared carbon quantum dots (CQDs) by a simple and scalable method (Han et al., 2020). Maltitol and hydrogen peroxide were held in a glass petri dish for 20 min at 200°C and centrifuged for 20 min at 13,000 rpm to make CQDs. Phenylhydrazine (PH), HCl, CHCl<sub>3</sub>, and CQDs were stirred for 36 h and filtered. Then, the precipitate was washed with CHCl<sub>3</sub> and dried at 40°C in a vacuum for 24 h to make CQDs modified with PH (CQDs-PH). XPS result revealed that the elemental composition of CQDs was 57.6% and 42.4% for C and O, respectively. Raman spectroscopy confirmed the presence of a D-band at 1,354 cm<sup>-1</sup> and a G-band at 1,595 cm<sup>-1</sup>, corresponding to disordered graphitic carbons, respectively. HTEM result demonstrated the presence of lattice fringes of graphene in CQDs. According to photoluminescence (PL) spectroscopy results, CQDs exhibited the strongest emission at 452 nm when the excitation wavelength was 360 nm. The CQDs/peroxymonosulfate (PMS) system was used in the photo-degradation of dyes under visible light irradiation and showed good photocatalytic activity and high stability. The alkaline condition was preferred in dye degradation because the alkaline condition promoted the separation of charge. CQDs modified with phenylhydrazine (CQDs-PH) displayed the strongest photocatalytic PMS activation for methylene blue (MB) degradation, showing a degradation time of ~5 min. By radical quenching tests, the MB degradation mechanism was revealed. Photogenerated electrons were reacted with PMS to produce O<sub>2</sub><sup>•-</sup>. Then, O<sub>2</sub><sup>•-</sup> and photogenerated h<sup>+</sup> degraded MB.

### 4.3 Composite Carbon Dots

Tyagi et al. prepared water-soluble carbon quantum dots (wsCQDs) from lemon peel *via* a simple and cheap

hydrothermal method (Tyagi et al., 2016). The lemon peel was held in a Teflon-lined autoclave for 12 h at 200°C, washed with dichloromethane, centrifuged for 30 min at 10,000 rpm, and dried at 100°C to make wsCQDs. According to TEM images, the wsCQDs were spherical and had diameters of 1–3 nm. XPS result demonstrated that the wsCQDs contained C and O. The photoluminescence (PL) spectra showed that the wsCQDs had photoluminescent properties with a quantum yield of ~14%. As excitation wavelength increased from 300 to 540 nm, emission wavelength also increased. The emission intensity was highest when the excitation wavelength was 360 nm. The wsCQDs were used as sensitive and selective fluorescent probes for  $\text{Cr}^{6+}$  ions and showed a detection limit of ~73 nM. Polyvinyl pyrrolidone solution and titanium isopropoxide solution were mixed, made into nanofibers with a syringe, and calcined in a muffle furnace for 2 h at 500°C to make  $\text{TiO}_2$  nanofibers.  $\text{TiO}_2$  nanofibers were functionalized with 6-aminohexanoic acid and were mixed with wsCQDs solution to make  $\text{TiO}_2$ -wsCQDs nanocomposite.  $\text{TiO}_2$ -wsCQDs nanocomposite was used as a photocatalyst for the degradation of methylene blue (MB) under visible light. The  $\text{TiO}_2$ -wsCQDs nanocomposite displayed degradation efficiency that was about 2.5 times higher than that of  $\text{TiO}_2$  nanofibers. The photocatalytic performance was enhanced because wsCQDs promoted charge separation.

Zhao et al. developed a carbon quantum dots/ $\text{TiO}_2$  nanotubes (CQDs/TNTs) nanocomposite by an enhanced hydrothermal method by anchoring CQDs onto the outer surface of TNTs (Zhao et al., 2018).  $\text{TiO}_2$  nanoparticles and NaOH were held in a Teflon-lined autoclave for 36 h at 135°C, treated with HCl, stirred overnight, neutralized with DI water, and dried for 24 h at 80°C to make TNTs. Citric acid and ethylene diamine were held in the autoclave for 5 h at 150°C and subjected to dialysis for 2 days to make CQDs. TNTs were dispersed in CQDs solution and stirred for 24 h, centrifuged for 30 min at 10,000 rpm, and dried for 12 h at 70°C to make CQDs/TNTs. HTEM image showed (101) plane of  $\text{TiO}_2$  and (100) plane of CQDs. Energy dispersive spectroscopy (EDS) revealed that the elements weight of CQDs/TNTs was 20.3%, 63.31%, and 16.39% for Ti, O, and C, respectively. XRD pattern of CQDs/TNTs exhibited characteristic peaks of  $\text{TiO}_2$  at 25.1°, 28.2°, 39.39°, and 48.42°. The CQDs/TNTs nanocomposite was used as a photocatalyst for the degradation of 30 mg/L methylene blue (MB) under visible light irradiation. The CQDs/TNTs-0.2 (0.2 g of TNTs) showed the highest MB degradation efficiency of 91.3% in 50 min, which was two times higher than that of pristine TNTs. The photocatalytic performance was improved because the up-conversion photoluminescence (UCPL) properties of CQDs enabled more efficient use of visible light. Furthermore, the photoinduced electrons of TNTs were transferred to CQDs, and the electron-hole recombination was delayed. The  $\pi$ - $\pi$  stacking between CQDs and dyes enhanced the adsorption ability of the CQDs/TNTs nanocomposite.

Zhang et al. constructed a carbon quantum dots/nitrogen doping  $\text{TiO}_2$  (CDs/N- $\text{TiO}_2$ ) nanocomposite (Zhang J. et al., 2020). Ascorbic acid and ethanol were held in a high-pressure reactor for 3 h at 160°C to make CDs. The mixture of tetrabutyl titanate, anhydrous ethanol, nitric acid, and urea was held in a

high-pressure reactor at 240°C for 10 h, dried at 110°C, and calcined at 200°C for 6 h to make N- $\text{TiO}_2$ . N- $\text{TiO}_2$  and CDs were stirred for 1 h, centrifuged, washed with distilled water, and dried overnight at 90°C to make CDs/N- $\text{TiO}_2$ . The XRD pattern of CDs/N- $\text{TiO}_2$  showed peaks at 25.3°, 37.8°, 48.0°, 53.9°, 55.1°, 62.7°, and 75.0°, representing the (101), (004), (200), (105), (211), (204), and (215) planes of anatase phase. HTEM images confirmed the (101) plane of the anatase and (100) plane of the graphene carbon. According to XPS results, the CDs/N- $\text{TiO}_2$  contained C, O, N, and Ti. Photoluminescence (PL) spectra revealed that 30CDs/N- $\text{TiO}_2$  exhibited the lowest PL intensity, indicating the lowest recombination rate of charge carriers, which are used for photocatalytic degradation. The CDs/N- $\text{TiO}_2$  nanocomposite was used as a photocatalyst for the degradation of 10 mg/L rhodamine B (RhB) under visible light and the reduction of 20 mg/L Cr (VI) under sunlight. The 30CDs/N- $\text{TiO}_2$  (30  $\mu\text{L}$  of CDs) nanocomposite displayed RhB degradation efficiency of 99.8% in 5 min, which was higher than that of  $\text{TiO}_2$  (6.66%) and N- $\text{TiO}_2$  (19.97%). The 30CDs/N- $\text{TiO}_2$  nanocomposite exhibited kinetic constants of RhB degradation 85.52 and 25.40 times higher than those of  $\text{TiO}_2$  and N- $\text{TiO}_2$ . With the 30CDs/N- $\text{TiO}_2$  nanocomposite, Cr (VI) reduction took only 4 min. The photocatalytic activity was enhanced because N doping shifted absorption range to visible light range and made  $\text{TiO}_2$  behave like a p-type semiconductor to transfer photogenerated electrons to CDs more easily. Moreover, CDs stored received electrons to promote the photo-induced charge separation.

Vassalini et al. synthesized an active blend consisting of carbon-based nanoparticles, alginate, and organic acids in an eco-friendly way (Vassalini et al., 2020). Sodium alginate solution was sonicated for 15 min and held in a digester at 200°C for 15 min to make the active blend. The photoluminescence (PL) spectrum showed that the active blend emitted blue PL when the excitation wavelength was 365 nm. Raman spectroscopy confirmed the presence of D-band at 1,370  $\text{cm}^{-1}$ , corresponding to disordered carbons, and G-band at 1,550  $\text{cm}^{-1}$ , corresponding to graphite carbons. TEM image demonstrated that nanoparticles were successfully introduced to the active blend. Sodium alginate, sodium citrate, and  $\text{TiO}_2$  nanopowder were sonicated for 30 min and added dropwise into the mixture of  $\text{CaCl}_2 \cdot 2\text{H}_2\text{O}$ , water, and ethanol to make  $\text{TiO}_2$  macro beads. The mixture of oxide beads and the active blend was stirred for 1 h and dried in air overnight to make oxide beads functionalized with the active blend. Alginate-based  $\text{TiO}_2$  macro beads, a photocatalyst for degradation of cationic pollutants, functionalized with the active blend showed better photocatalytic effect and adsorptive ability in mild conditions than the oxide beads functionalized with each component of the active blend or carbon dots prepared through energy-consuming hydrothermal synthesis. Functionalized  $\text{TiO}_2$  macro beads showed methylene blue (MB) dye adsorption capability of 82% and completely degraded MB in 30 min.

Ouyang et al. fabricated a nitrogen-doped carbon quantum dots/ $\text{TiO}_2$  (N-CDs/ $\text{TiO}_2$ ) composite from urea and tetrabutyl titanate (TBT) through hydrothermal treatment (Ouyang et al., 2020). The mixture of citric acid, urea, tetrabutyl titanate,



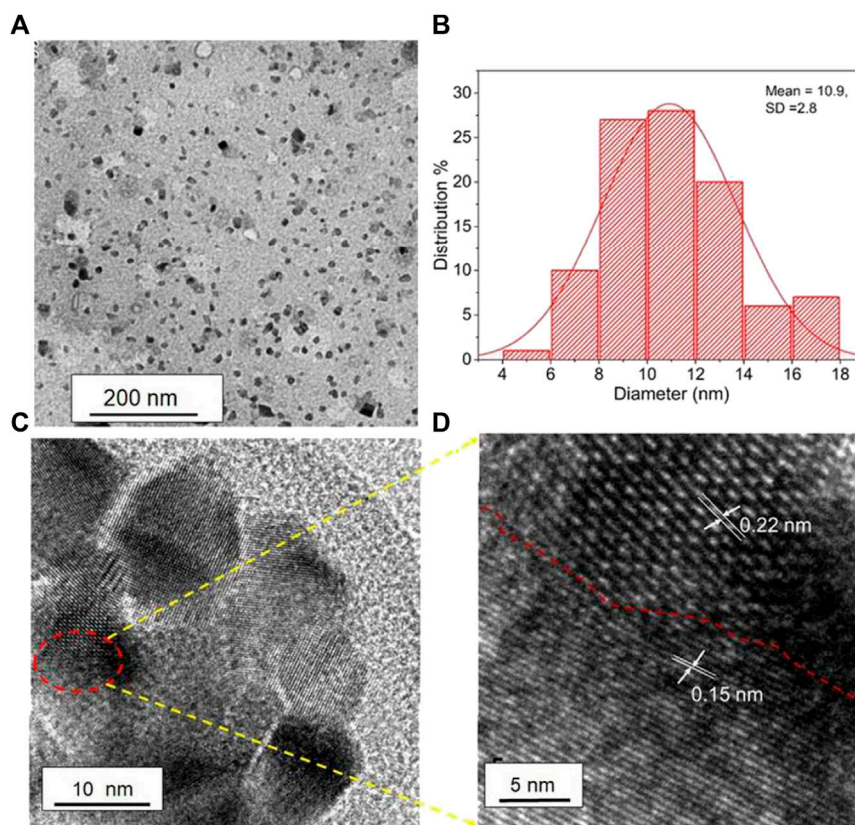


**FIGURE 4 |** Different magnification (A) TEM image of r-Mg-N-CD and (B) its corresponding size distribution; (C) HRTEM image of r-Mg-N-CD and (D) zoomed image of (C). (Reproduced with permission from Bhati et al., 2018, Copyright © 2018, American Chemical Society).

ethylene glycol, and acetic acid was held in a Teflon-lined autoclave for 24 h at 200°C, centrifuged, washed with distilled water and ethanol, dried for 12 h at 60°C, and calcined for 1 h at 450°C in air to make N-CDs/TiO<sub>2</sub>. According to XRD results, (110) and (101) crystal facets of rutile appeared as N-CDs content increased. The SEM images showed that, as N-CDs content increased, the morphology of the N-CDs/TiO<sub>2</sub> composite changed from nano sphere agglomerations, honeycomb, to empty spheres ((A) 4). The XPS result revealed that the elemental composition of N-CDs/TiO<sub>2</sub>-6 (mass ratio of urea to TBT = 6) was 71.96%, 2.6%, 18%, and 7.44% for C, N, O, and Ti, respectively. The photoluminescence (PL) spectra demonstrated that emission intensity decreased as N-CDs content increased. The N-CDs/TiO<sub>2</sub> composite was used as a photocatalyst for the degradation of rhodamine B (RhB) under visible light. N-CDs/TiO<sub>2</sub>-1 degraded RhB in 120 min, which was 11.42 times better than pristine TiO<sub>2</sub>.

Li et al. prepared nitrogen and sulfur-containing carbon quantum dots (NCQDs)/TiO<sub>2</sub> nanocomposites in a simple and eco-friendly way by depositing NCQDs onto TiO<sub>2</sub> nanosheets (Li et al., 2018). Citric acid and thiourea were transferred to a Teflon-lined vial, heated in an 800 W microwave oven for 7 min, and subjected to dialysis for 1 day to make NCQDs. The TiO<sub>2</sub> and NCQDs solution was sonicated for 30 min, stirred for 12 h at

80°C, washed with deionized water and ethanol, and lyophilized overnight to make NCQDs/TiO<sub>2</sub>. XRD pattern of NCQDs/TiO<sub>2</sub> nanocomposite showed (101) peak of anatase and (110) peak of rutile. H-TEM images revealed that NCQDs/TiO<sub>2</sub> nanocomposite exhibited (101) crystal planes of anatase, (111) crystal plane of rutile, and (101) plane of carbon. XPS result demonstrated that NCQDs/TiO<sub>2</sub> nanocomposite contained C, O, N, S, and Ti. According to photoluminescence (PL) spectra, emission intensity decreased as NCQDs content increased. The NCQDs/TiO<sub>2</sub> nanocomposite was used as a photocatalyst for the photoreduction of CO<sub>2</sub> under simulated sunlight. The maximum amounts of CH<sub>4</sub> and CO produced by the CO<sub>2</sub> photoreduction using the nanocomposite in 1 h were 0.769 and 1.153 μmol, respectively, which were 7.79 and 7.61 times higher than those using only TiO<sub>2</sub>. The nanocomposite showed improved photocatalytic activity because NCQDs sensitized TiO<sub>2</sub> to have enhanced light absorption.

Guo et al. prepared N and P co-doped carbon quantum dots (NP-CQDs) by simple heat treatment (Guo et al., 2018). Citric acid and phosphorylethanolamine were held in an autoclave with Teflon lining for 12 h at 200°C, centrifuged for 15 min at 10,000 rpm, and subjected to dialysis in a cellulose ester dialysis membrane for 1 day to make NP-CQDs. According to the TEM image, NP-CQDs had an average size of 3.03 ± 1.01 nm.



The XPS result demonstrated that NP-CQDs contained C, O, N, and P. According to the photoluminescence (PL) spectroscopy, when 365 nm light is illuminated, the NP-CQDs solution emitted intense blue-green light with maxima at 475 nm. The NP-CQDs displayed high stability in saline conditions, quantum yield of 8.45%, and brilliant photostability. The NP-CQDs were used as sensitive and selective fluorescent probes for  $\text{Fe}^{3+}$ . The NP-CQDs exhibited detection range from 0.05 to 200  $\mu\text{M}$ . NP-CQDs and titanium butoxide were held in a Teflon-lined autoclave for 1 day at 160°C, centrifuged, washed with ethanol and water, and dried for 1 day at 60°C to make NP-CQDs/ $\text{TiO}_2$  nanocomposite. The NP-CQDs/ $\text{TiO}_2$  nanocomposite was used as a photocatalyst for the degradation of methylene blue (MB) under simulated solar light. The NP-CQDs/ $\text{TiO}_2$  nanocomposite had a degradation time of 15 min, which was shorter than pristine  $\text{TiO}_2$ .

Midya et al. constructed titania nanoparticles ( $\text{TiO}_2$  NPs) and carbon dots (CDs) deposited polyvinyl imidazole cross-linked chitosan (cl-Ch-p (VI)/ $\text{TiO}_2$ NPs-CDs) (Midya et al., 2020). The mixture of chitosan, acetic acid, potassium persulphate, 1-vinylimidazole, and diurethane dimethacrylate was held in a 600 W microwave oven for 2 min at 75°C to make cl-Ch-p (VI). The cl-Ch-p (VI) and titanium isopropoxide solution was held in the 750 W microwave oven for 2 min at 75°C to make cl-Ch-p (VI)/ $\text{TiO}_2$ NPs. The reaction mixture and sugar cane juice solution were treated with microwave for 4 min, precipitated using acetone, filtered using vacuum filtration, washed with acetone, and dried under vacuum at 50°C to make cl-Ch-p (VI)/ $\text{TiO}_2$ NPs-CDs. XRD pattern of cl-Ch-p (VI)/ $\text{TiO}_2$ NPs-CDs showed a peak at 24.1°, corresponding to (002) plane of carbon and (101) plane of anatase  $\text{TiO}_2$ , and peaks at 37.5°, 47.7°, 53.9°, 62.6°, and 74.5°, corresponding to (004), (200), (105), (204), and (215) planes of crystalline  $\text{TiO}_2$  NPs, respectively. TEM image revealed that CDs and  $\text{TiO}_2$  NPs were introduced to the polymer matrix. XPS result demonstrated that cl-Ch-p (VI)/ $\text{TiO}_2$ NPs-CDs contained C, N, O, and Ti. The cl-Ch-p (VI)/ $\text{TiO}_2$ NPs-CDs nanocomposite was used as a photocatalyst for the degradation of organic materials under solar light. The cl-Ch-p (VI)/ $\text{TiO}_2$ NPs-CDs nanocomposite showed degradation efficiency of ~98.6%, ~95.8%, and ~98.2% for 2,4-dichlorophenol, reactive blue 4, and reactive red 15, respectively, which were better than those of cl-Ch-p (VI)/ $\text{TiO}_2$ NPs and cl-Ch-p (VI)/CDs composites. The improved photocatalytic activity was due to the synergistic effects of CDs and  $\text{TiO}_2$  NPs and narrowed band gap.

Zhu et al. prepared a multiplecore@shells clustered carbon dots (CDs)/ $\text{TiO}_2$ (P25)/reduced graphene oxide (rGO) nanocomposite through a simple hydrothermal process (Zhu W. et al., 2021). Citric acid and aphen were held in a Teflon-lined autoclave for 7 h at 200°C, centrifuged, dialyzed for 3 days, and subjected to freeze-drying under vacuum to make CDs. The mixture of P25, GO, and CDs solution was stirred for 12 h, held in the autoclave for 3 h at 120°C, washed with deionized water and absolute ethanol, and dried at 60°C overnight to make CDs/P25/rGO. XRD pattern of CDs/P25/rGO showed peaks at 25.3° and 27.5°, corresponding to (101) plane of anatase P25 and (110) plane of rutile P25 and a broad peak at 24.5°, indicating an intense interface interaction between components of CDs/P25/rGO.

HTEM image of CDs/P25/rGO exhibited the (101) plane of P25. According to photoluminescence (PL) spectra, CDs/P25/rGO displayed a strong excitation-independent emission at 430 nm and a weak emission at 630 nm when the excitation wavelength was below 400 nm. EDS result revealed that the elemental composition of CDs/P25/rGO was 5.17%, 0.73%, 62.86%, and 31.24% for C, N, O, and Ti, respectively. Raman spectroscopy demonstrated D- and G-band at ~1,361 and ~1,601  $\text{cm}^{-1}$ , corresponding to disordered/defective and graphitic carbons, respectively. The CDs/P25/rGO nanocomposite was used as a high stability photocatalyst for the degradation of rhodamine-B (RhB), methylene blue (MB), and methyl orange (MO), and antibacterial performance under visible light. The 2% CDs/0.5% rGO/P25 composite showed the best photocatalytic activity. The rate constant of 2% CDs/0.5% rGO/P25 for Rh-B degradation was 29, 2.8, and 1.3 times higher than that of P25, rGO/P25, and CDs/P25, respectively. The CDs/P25/rGO nanocomposite displayed enhanced photocatalytic activity because CDs improved visible light-harvesting ability and promoted photogenerated charge separation.

Ratnayake et al. synthesized carbon-quantum-dot-decorated  $\text{ZrO}_2$  nanoparticles (CQDZ) by a simple method (Ratnayake et al., 2019). The colloids formed in the mixture of  $\text{ZrOCl}_2 \cdot 8\text{H}_2\text{O}$  and ammonia were calcined for 4 h at 800°C to make  $\text{ZrO}_2$  nanoparticles. Ammonium citrate was held in a petri dish for 3 h at 180°C to make CQDs. Suspension of CQDs in absolute ethanol and 40 nm sized  $\text{ZrO}_2$  nanoparticles were mixed under sonication for 5 min and dried in air overnight to synthesize CQDZ. The TEM results showed that  $\text{ZrO}_2$  nanoparticles were mostly spherical with some rod-like particles. They also demonstrated that spherical CQDs were successfully adsorbed to  $\text{ZrO}_2$  nanoparticles. According to the XRD pattern, CQDZ exhibited peaks at 24.32°, 28.30°, and 34.52°, corresponding to (110), (020), and (120) planes of  $\text{ZrO}_2$  nanoparticles. The Raman spectrum of CQDZ confirmed the presence of G- and D-bands at 1,550 and 1,356  $\text{cm}^{-1}$ , corresponding to graphitic carbon and disordered carbon, respectively. CQDZ was used as a photocatalyst for the elimination of a dye, methylene blue (MB), in water under UV light. Using CQDZ, 95% of MB was eliminated after 1 h. Using pristine  $\text{ZrO}_2$  nanoparticles, however, only 34% of MB was eliminated after 1 h. The enhanced photocatalytic activity of CQDZ might be due to the CQDs effect of slowing down the electron-hole recombination.

Patra et al. prepared carbon dots\_ $\text{BaZrO}_{3-\delta}$  (CDs\_BZO) hybrid nanomaterials by loading CDs on BZO hollow nanospheres, which were both hydrothermally synthesized (Patra et al., 2018). Citric acid and ethylene diamine were held in a jacket for 5 h at 200°C, filtered with a 0.4  $\mu\text{m}$  syringe filter, dialyzed with a dialysis bag against Milli-Q water for 1 day, and dried overnight at 80°C to make CDs.  $\text{KOH}$ ,  $\text{BaCl}_2 \cdot 2\text{H}_2\text{O}$ , and  $\text{ZrOCl}_2 \cdot 8\text{H}_2\text{O}$  were held in an autoclave for 24 h at 200°C; centrifuged; washed with water, dilute acetic acid, and ethanol; and dried overnight in an electric oven at 100°C to make BZO. CDs and BZO were dispersed in ethanol for 2 h at 45°C by sonication to make CDs-BZO. Raman spectroscopy results exhibited D-band and G-band at 1,325 and 1,548  $\text{cm}^{-1}$ , corresponding to disordered carbon and graphitic carbon,

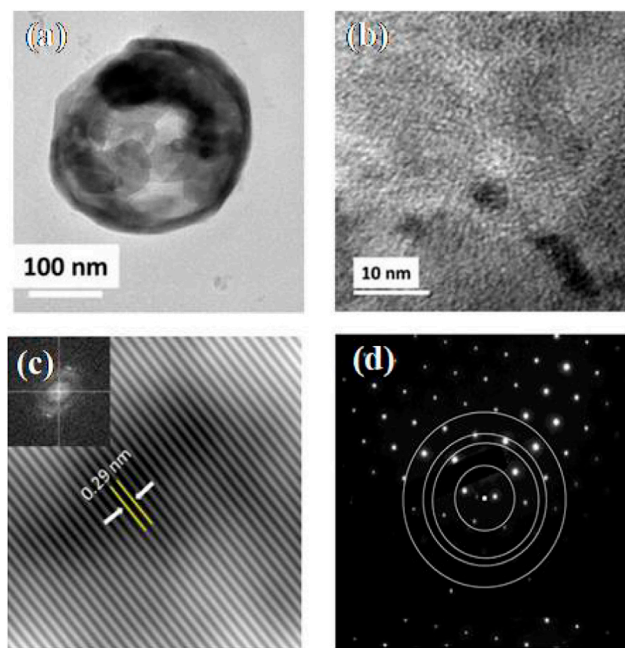


**FIGURE 5 |** Field-emission transmission electron microscopic image of **(A)** BZO hollow nanospheres and **(B)** high-resolution transmission electron microscopic image of BZO hollow spheres. The inset to **(C)** is the fast Fourier transformed image of the highlighted portion in image **(B)**, **(C)** shows the inverse fast Fourier transformed image of the masked fast Fourier transformed image shown in the inset to **(C)**, **(D)** shows the selected area electron diffraction patterns of BZO. (Reproduced from Patra et al., 2018, American Chemical Society).

respectively. According to the photoluminescence (PL) spectrum, CDs\_BZO displayed a strong emission at 460 nm when the excitation wavelength was 340 nm. The FETEM images revealed that BZO were hollow spheres, and CDs were spheres with diameters of  $\sim 2\text{--}7$  nm shown in **Figure 5**. XPS result demonstrated that CDs\_BZO contained C, N, O, Ba, and Zr. The CDs\_BZO hybrid nanomaterial was used as a photocatalyst for  $\text{H}_2$  generation and methylene blue (MB) dye degradation under UV-visible light. The CDs\_BZO with 3 wt% CDs had the highest hydrogen generation efficiency of  $670 \mu\text{mol/h/g}$  with apparent quantum yield (AQY) of  $\sim 4\%$ , which was higher than AQY of BZO ( $\sim 2\%$ ). It also showed the highest MB degradation efficiency of  $\sim 90\%$ . Here, the defect states and oxygen vacancies generated by hydrothermal synthesis enable visible light absorption of the photocatalyst, and CDs improve the light absorption of the photocatalyst.

Ni et al. synthesized nitrogen and iron co-doped carbon dots/gear-shaped  $\text{WO}_3$  (N,Fe-CDs/G- $\text{WO}_3$ ) composite by simple hydrothermal synthesis (Ni et al., 2020).  $\text{Na}_2\text{WO}_4 \cdot 2\text{H}_2\text{O}$  solution was held in a Teflon-lined autoclave for 12 h at  $180^\circ\text{C}$ , washed with deionized water and ethanol, and dried for 6 h in an oven at  $80^\circ\text{C}$  to make G- $\text{WO}_3$ . Folic acid and  $\text{FeCl}_3 \cdot 6\text{H}_2\text{O}$  were held in the autoclave for 4 h at  $200^\circ\text{C}$ , filtered with  $0.22 \mu\text{m}$  aqueous microporous membranes, dialyzed for 6 h, and subjected to freeze-drying to make N,Fe-CDs. N,Fe-CDs and G- $\text{WO}_3$  were held in the autoclave for 8 h at  $190^\circ\text{C}$ , centrifuged, and dried at  $80^\circ\text{C}$  to make the N,Fe-CDs/

G- $\text{WO}_3$  composite in **Scheme 2**. SEM and TEM images of G- $\text{WO}_3$  showed in **Figures 6A–F** the 3-D gear-like structure consisting of a plate with many protruding nanorods on its surface. The particle diameters was N,Fe-CDs ranged from 3.5 to 13.5 nm, with an average diameter of 6.5 nm. HTEM images showed that G- $\text{WO}_3$  exhibited lattice fringe with a lattice spacing of 0.39 nm and N,Fe-CDs exhibited lattice fringe with a lattice spacing of 0.32 nm. The XRD pattern of N,Fe-CDs/G- $\text{WO}_3$  revealed peaks at  $13.8^\circ$ ,  $22.6^\circ$ ,  $28.0^\circ$ ,  $36.3^\circ$ , and  $49.7^\circ$ , corresponding to the hexagonal crystalline phase of G- $\text{WO}_3$ . XPS result demonstrated that N,Fe-CDs/G- $\text{WO}_3$  contained C, N, O, W, and Fe. According to the photoluminescence (PL) spectrum, PL intensity of N,Fe-CDs/G- $\text{WO}_3$  was reduced after loading of N,Fe-CDs. The N,Fe-CDs/G- $\text{WO}_3$  composite was used as a photocatalyst for degradation of rhodamine B (RhB) under UV-vis-NIR light. 81.4%, 97.1%, and 75% of RhB were degraded in 2 h under UV, visible, and NIR light, respectively, which were better than those of commercial  $\text{WO}_3$ , G- $\text{WO}_3$ , and N-CDs/G- $\text{WO}_3$  composites. The composite was also used for the degradation of methylene blue (MB), ciprofloxacin (CIP), tetracycline hydrochloride (TCH), and oxytetracycline (OTC) under visible light. 91.1%, 70.5%, 54.5%, and 47.8% of respective materials were degraded in 3 h. According to the radical trapping experiments, the conversion between Fe (III) and Fe (II) is the most important factor in photocatalysis. The photocatalytic activity was improved because N,Fe-CDs enhanced light absorption ability, and the gear shape of the  $\text{WO}_3$  increased light reflections.

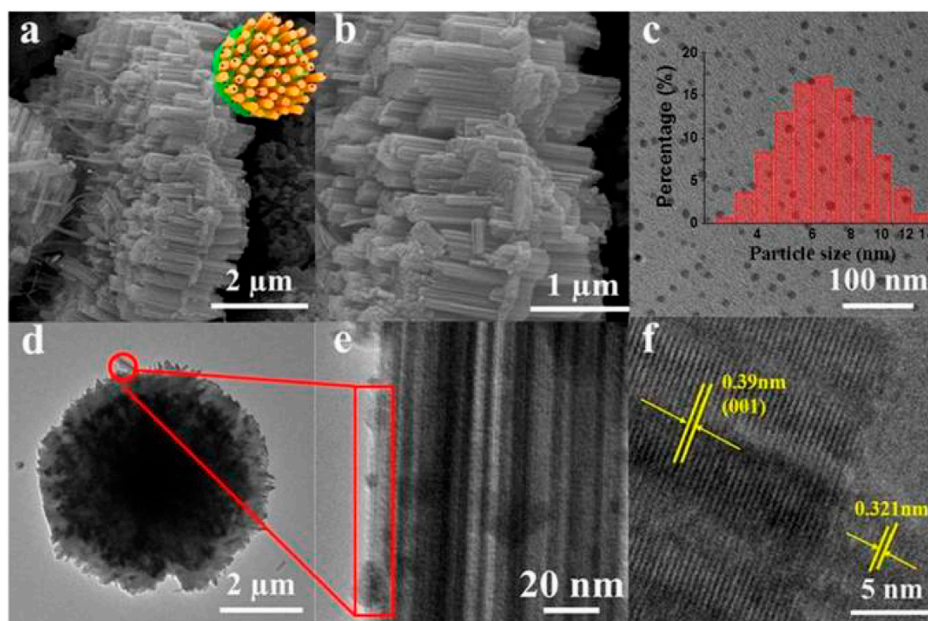
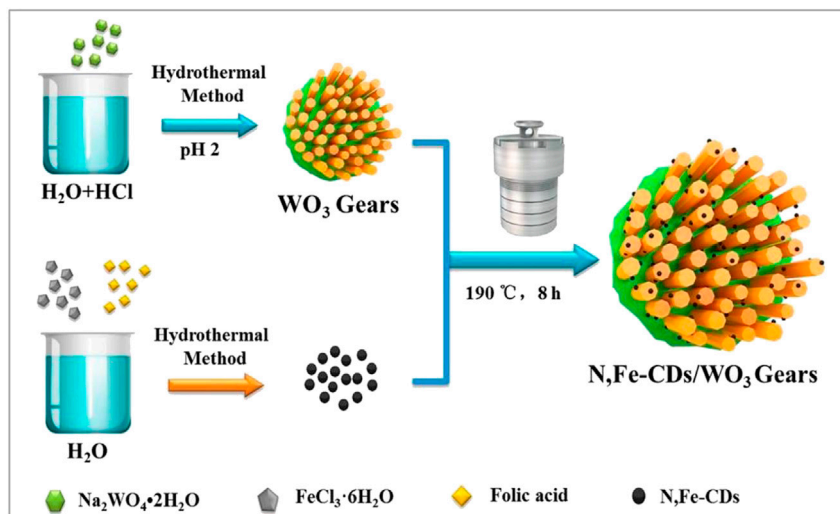


**FIGURE 6** | SEM and TEM of N,Fe-CDs; N,Fe-CDs/G-WO<sub>3</sub>-0.6 composite. **(A,B)** SEM of N,Fe-CDs/G-WO<sub>3</sub>-0.6; **(C)** TEM of N,Fe-CDs with the inset for the size distribution; **(D)** TEM of N,Fe-CDs/G-WO<sub>3</sub>-0.6; **(E,F)** HRTEM of N,Fe-CDs/G-WO<sub>3</sub>-0.6. (Reproduced from Ni et al., 2020, MDPI).



**SCHEME 2** | A schematic illustration of the fabrication of the gear-shaped WO<sub>3</sub> (G-WO<sub>3</sub>) and N, Fe-CDs/G-WO<sub>3</sub>. (Reproduced from Ni et al., 2020, MDPI).

Jamila et al. constructed a WO<sub>3</sub>/graphene oxide/N-doped carbon quantum dots (WO<sub>3</sub>/GO/NCQDs) composite by introducing NCQDs to GO modified WO<sub>3</sub> nanosheets (Jamila et al., 2020a). Graphite powder, sodium nitrate, concentrated sulfuric acid, potassium permanganate, and H<sub>2</sub>O<sub>2</sub> were stirred with a magnetic stirrer, filtered, washed with HCl, centrifuged, and dried at 60°C in an oven to make GO. Sodium tungstate and nitric acid were mixed under magnetic stirring for 10 min, kept for 6 h at 40°C, washed using distilled water and ethanol, dried at

60°C, and calcined for 4 h at 600°C to make WO<sub>3</sub>. Citric acid and urea were held in a Teflon-lined autoclave for 4 h at 160°C and NCQDs. TEM image revealed that GO and NCQDs were fixed on WO<sub>3</sub> nanosheets. EDAX result demonstrated that the elemental composition of WO<sub>3</sub>/GO/NCQDs was 9.50, 43.03, 30.04, and 17.43% for W, O, C, and N, respectively. Photoluminescence (PL) intensity of WO<sub>3</sub>/GO/NCQDs decreased when NCQDs content increased. According to Raman spectroscopy, WO<sub>3</sub>/GO/NCQDs displayed D- and G-band at 1,435 and 1,575 cm<sup>-1</sup>, corresponding



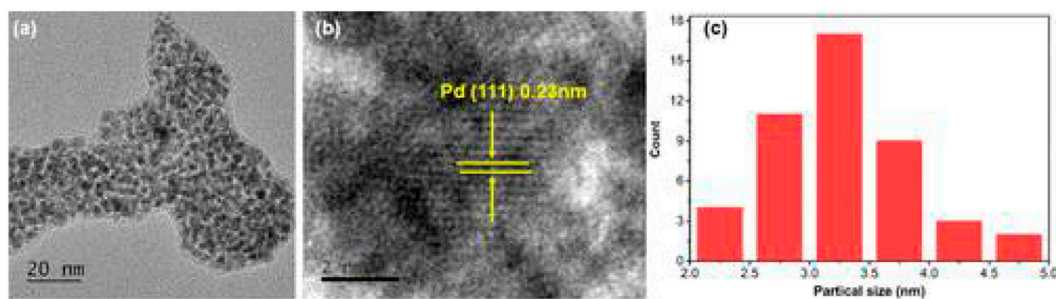


**FIGURE 7 | (A)** TEM and **(B)** HR-TEM images of Pd@CD-CONH and **(C)** histogram. (Reproduced from Selim et al., 2020, American Chemical Society).

to disordered carbon and graphitic carbon, respectively. The  $\text{WO}_3/\text{GO}/\text{NCQDs}$  composite was used as a photocatalyst for the degradation of methyl orange (MO) under visible light irradiation. The  $\text{WO}_3/\text{GO}/\text{NCQDs}$  composite with 1.5 ml NCQDs showed the best degradation efficiency of 86%. The  $\text{WO}_3/\text{GO}/\text{NCQDs}$  composite exhibited better photocatalytic activity than  $\text{WO}_3/\text{GO}$  composite and  $\text{WO}_3$ . The photocatalytic effect was improved because NCQDs extended the absorption region to the visible light region, increased active sites, and promoted charge separation.

Velumani et al. constructed carbon quantum dots supported ZnO hollow spheres (ZnO/C-dots) by a solvothermal process (Velumani et al., 2020). Glucose and urea were added to 250°C copra oil, and the mixture was stirred for 3 min. Chloroform was added to the solution, and the upper oil layer was removed by a separation funnel to make C-dots. Zinc acetate dihydrate, urea, polyethylene glycol-400, and C-dots solution were magnetically stirred at room temperature for 90 min, held in a Teflon-lined autoclave for 15 h at 180°C, centrifuged, washed with ethanol and deionized water, and dried at 80°C in an oven for 12 h to make ZnO/C-dots. The photoluminescence (PL) spectra showed that ZnO/C-dots exhibited the strongest emission when the excitation wavelength was 345 nm. PXRD pattern of ZnO/C-dots revealed peaks at 31.8°, 34.4°, 36.3°, 47.5°, 56.6°, 62.9°, and 68.0° corresponding to (100), (002), (101), (102), (110), (103), and (112) planes of ZnO, respectively. According to the TEM result, ZnO/C-dots were spheres with the size of 500 nm. The ZnO/C-dots nanocomposite was used as a photocatalyst for the degradation of methylene blue (MB) under UV-vis light. Using the ZnO/C-dots nanocomposite, 96% of MB was degraded in 30 min. However, using pristine ZnO, only 63% of MB was degraded in 30 min. The photocatalytic effect was improved because C-dots slowed down the photogenerated electron-hole pairs' recombination rate and enhanced visible light absorption. The nanocomposite could be used for five cycles, showing high stability.

Omer et al. prepared a ZnO-phosphorous and nitrogen co-doped carbon quantum dots (CDs) nanocomposite in an eco-friendly way (Omer et al., 2018).  $\text{Zn}(\text{CH}_3\text{COO})_2 \cdot 2\text{H}_2\text{O}$  in methanol was adjusted to pH 8 using NaOH, held in a Teflon-lined autoclave for 6 h at 200°C, washed with methanol,

filtered, and dried at 60°C in an oven to make the ZnO nanoparticles. Grounded coffee and concentrated phosphoric acid were kept in a water bath for 30 min at 90–95°C, filtered, centrifuged for 30 min at 14,000 rpm, adjusted to pH 1–3, and dialyzed with dialysis membrane for 5 h to make CDs. ZnO and CDs were stirred for 2 h to make the ZnO-CDs nanocomposite. The TEM result showed that CDs and ZnO had diameters of 3–4 nm and 15–20 nm. The XRD pattern of ZnO-CDs nanocomposite displayed characteristic peaks of both ZnO and CDs. According to the XPS result, CDs contained C, O, N, and P.

The excitation-independent fluorescence of CDs centered around 480 nm was confirmed by fluorescence spectrum. The ZnO-CDs nanocomposite was used as a photocatalyst for the degradation of organic materials under energy-efficient weak LED light (visible-NIR light) irradiation. The ZnO-CDs nanocomposite exhibited methylene blue (MB) degradation efficiency of 80% in 10 h, which was much higher than that of pristine ZnO (10%). The photocatalytic activity was enhanced because CDs promoted photogenerated charge separation and transfer, and CDs' up-conversion properties improved light absorption.

El-Shamy et al. developed a carbon quantum dots/zinc peroxide ( $\text{C}_{\text{Dots}}/\text{ZnO}_2$ ) composite by introducing  $\text{C}_{\text{Dots}}$  to  $\text{ZnO}_2$  nanoparticles (El-Shamy A.g., 2020). D-Glucose solution was heated in a 500 W microwave oven for 7 min and centrifuged to make  $\text{C}_{\text{Dots}}$ . Zinc acetate solution, 30%  $\text{H}_2\text{O}_2$ , NaOH, and ethanol were heated in a 400 W microwave oven for 3h, filtered, washed using DI water, and dried at 60°C in an oven overnight to make  $\text{ZnO}_2$ . The mixture of  $\text{C}_{\text{Dots}}$  solution and  $\text{ZnO}_2$  solution was stirred for 30 min at room temperature, centrifuged, washed using ethanol, and air-dried to make  $\text{C}_{\text{Dots}}/\text{ZnO}_2$  composite. The XRD result of  $\text{C}_{\text{Dots}}/\text{ZnO}_2$  composite showed a hump at 23°, corresponding to the (002) plane of graphitic carbon, and peaks corresponding to (111), (200), (220), and (311) planes of crystalline  $\text{ZnO}_2$ . The TEM image of  $\text{C}_{\text{Dots}}/\text{ZnO}_2$  composite revealed the (110) plane of graphitic  $\text{C}_{\text{Dots}}$  and (111) plane of  $\text{ZnO}_2$ . The energy dispersive spectroscopy (EDS) result demonstrated that  $\text{C}_{\text{Dots}}/\text{ZnO}_2$  composite contained C, O, and Zn. According to the up-conversion photoluminescence (PL) spectra,  $\text{C}_{\text{Dots}}$  absorb NIR light and emit light with a shorter wavelength. The  $\text{C}_{\text{Dots}}/\text{ZnO}_2$  composite was used as a



photocatalyst for the degradation of methyl orange (MO), methylene blue (MB), and rhodamine B (RhB) under UV-A light irradiation. The  $C_{\text{Dots}}/\text{ZnO}_2$  composite exhibited better degradation efficiencies for MO ( $91 \pm 2\%$  in 60 min), MB ( $99 \pm 1\%$  in 50 min), and RhB ( $99 \pm 1\%$  in 80 min) than  $\text{ZnO}_2$ ,  $\text{TiO}_2$ , and  $C_{\text{Dots}}/\text{TiO}_2$  due to promoted charge separation by  $C_{\text{Dots}}$  and  $\text{ZnO}_2$ , electron capturing and up-conversion photoluminescence by  $C_{\text{Dots}}$ , and the  $C_{\text{Dots}}/\text{ZnO}_2$  structure advantageous to charge transfer and separation. The  $C_{\text{Dots}}/\text{ZnO}_2$  composite could be used five times without any decrease in photocatalytic performance.

El-Shamy et al. developed polyvinyl alcohol/carbon dot-decorated zinc peroxide (PVA/CZnO<sub>2</sub>) films by introducing CZnO<sub>2</sub> to PVA (El-Shamy A. G., 2020). The microwave irradiation method was used to make carbon dots. The mixture of  $\text{Zn}(\text{CH}_3\text{COO})_2 \cdot 2\text{H}_2\text{O}$ , triple-distilled water,  $\text{H}_2\text{O}_2$ , NaOH, and ethanol was held in a 400 W microwave oven for 3 h at 180°C, filtered, washed with water, and dried for 1 day at 60°C in an oven to make  $\text{ZnO}_2$ .  $\text{ZnO}_2$  solution and carbon dot solution were mechanically stirred for 1 h, centrifuged, filtered, washed with ethanol, and dried in air to make CZnO<sub>2</sub>. PVA and triple-distilled water were stirred at  $67 \pm 3^\circ\text{C}$  for 2 h, transferred to glass dishes, and air-dried for 3 days at ambient temperature to make PVA. CZnO<sub>2</sub> was dispersed in PVA solution, transferred to glass dishes, and air-dried for 3 days to make PVA/CZnO<sub>2</sub>. XRD pattern of PVA/CZnO<sub>2</sub> exhibited a peak at  $19.5^\circ$  for (101) plane of PVA and peaks of  $\text{ZnO}_2$ . FE-SEM images showed that CZnO<sub>2</sub> particles were uniformly dispersed on PVA matrix.

According to Brunauer–Emmett–Teller (BET) analysis, the PVA/CZnO<sub>2</sub> nanocomposite had a large surface area of  $241.04 \text{ m}^2 \text{ g}^{-1}$ , larger than the PVA/ $\text{ZnO}_2$  nanocomposite ( $167.17 \text{ m}^2 \text{ g}^{-1}$ ). The PVA/CZnO<sub>2</sub> nanocomposite with 4 wt% CZnO<sub>2</sub> exhibited an adsorption capacity of  $1,972 \pm 40 \text{ mg/g}$  against methylene blue (MB), which was higher than that of the PVA/ $\text{ZnO}_2$  nanocomposite with 4 wt%  $\text{ZnO}_2$  ( $1,831 \pm 20 \text{ mg/g}$ ). At pH = 6, room temperature, with low ionic strength, 40 mg of PVA/CZnO<sub>2</sub> nanocomposite eliminated 98% of 2,000 mg/L MB in 60 min. The enhanced adsorption ability came from improved electrical conductivity, crystallinity, pore size, and mechanical properties. A solution with pH = 1 removed 75% of MB from the nanocomposite, and the nanocomposite could be used five times with only a slight decrease in adsorption efficiency (~2%).

El-Shamy et al. constructed polyvinyl alcohol/carbon quantum dots (PVA/CQDs) nanocomposite films using the solution casting method (El-Shamy and Zayied, 2020). PVA and bi-distilled water were mechanically stirred at  $65 \pm 3^\circ\text{C}$  for 2 h, transferred to a petri-dish, and air-dried for 3 days to make PVA films. The mixture of D-glucose, acetone, and bi-distilled water was heated in a 700 W microwave oven for 13 min and centrifuged to make CQDs. The mixture of PVA solution and CQDs solution was mechanically stirred and dried for 3 days at ambient temperature to make PVA/CQDs. XRD pattern of PVA/CQDs showed a broad peak at  $19.5^\circ$ , corresponding to the crystalline part of semi-crystalline PVA. According to photoluminescence (PL) spectra, as CQDs content increased, PL intensity increased and PL peak exhibited red shift

behavior. FE-SEM images revealed that, as CQDs content increased, the surface area of PVA/CQDs increased. The PVA/CQDs nanocomposite films were used for the elimination of methylene blue (MB) from waste water by adsorption at room temperature. The 80 mg of (PVA/CQDs 2 wt%) film eliminated  $97 \pm 1\%$  of 30 mg/L MB in 40 min at pH = 12. In the basic environment, -OH groups in PVA and -OH groups or -COOH groups in CQDs were ionized, making the composite surface more negatively charged. This made the composite more easily adsorb cationic MB. The PVA/CQDs nanocomposite films could be used five times after ethanol treatment without any photocatalytic activity decrease.

Nayak et al. fabricated carbon quantum dots cross-linked polyvinyl pyrrolidone (PVP-CD) hydrogels (Nayak et al., 2020). Lemon juice and cysteamine were evaporated in a beaker at  $90^\circ\text{C}$ , held in a Teflon-lined autoclave for 6 h at  $150^\circ\text{C}$ , diluted with water, centrifuged at 10,000 rpm, and filtered by a  $0.2 \mu\text{m}$  syringe filter to make CD. PVP was treated with NaOH under reflux condition at  $140^\circ\text{C}$  for 2 days, further treated with formaldehyde for 1 h at  $0^\circ\text{C}$  and pH 9, finally treated with  $\text{NaBH}_4$  under stirring at ambient temperature for 1.5 h, and dialyzed for 6 h to make carboxylate-PVP. The mixture of carboxylate-PVP, EDC, MES buffer, and NHS was dialyzed with water for 18 h, concentrated at  $60^\circ\text{C}$  in a vacuum, treated with water, and held in an air oven at  $75^\circ\text{C}$  to make PVP-CD. For PVP-CD, storage modulus was higher than loss modulus, indicating the elasticity of PVP-CD. PVP-CD emitted blue fluorescence when UV light was illuminated. The SEM image showed that cross-linking with CD has increased the surface area of PVP-CD. 50 mg of PVP-CD hydrogel adsorbed ~2 mg of malachite green (MG), crystal violet (CV), and eosin Y in 12 h, which followed pseudo-second-order kinetics. The good adsorptive ability came from hydrogen bonding, inductive effect, and  $\pi$ - $\pi$  interaction of both CD and the PVP backbone. The PVP-CD hydrogel also showed excellent photodegradative capability of dyes under solar light by degrading them in 30 min, which followed pseudo-first-order kinetics. The PVP-CD hydrogel killed gram-positive and gram-negative bacteria in 10 min under solar light. The degradation of dyes and bacterial elimination were all carried out by reactive oxygen species generated from CD. The PVP-CD hydrogel could be used four times when washed with dilute acid.

Gong et al. fabricated carbon quantum dots (CDs) from wood powder *via* hydrothermal process (Gong et al., 2019). The mixture of wood powder, citric acid, ethanediamine, and deionized water was sonicated for 20 min, magnetically stirred for 30 min, held in a Teflon-lined autoclave for 6 h at  $200^\circ\text{C}$ , vacuum-filtrated, heated for 12 h at  $30^\circ\text{C}$ , washed using anhydrous ethanol, dried for 12 h at  $30^\circ\text{C}$ , dissolved in deionized water, and filtrated with membrane to make CDs. The XPS result showed that CDs contained C, O, and N. The CDs were environment-friendly, nontoxic, and water-soluble. According to photoluminescence (PL) spectra, the CDs solution emitted blue light under UV light irradiation with a quantum yield of 47.4%. Furthermore, the CDs solution was used as a fluorescent stamp-pad and pen ink, showing its possibility in anti-counterfeit applications. The mixture of cerium nitrate,

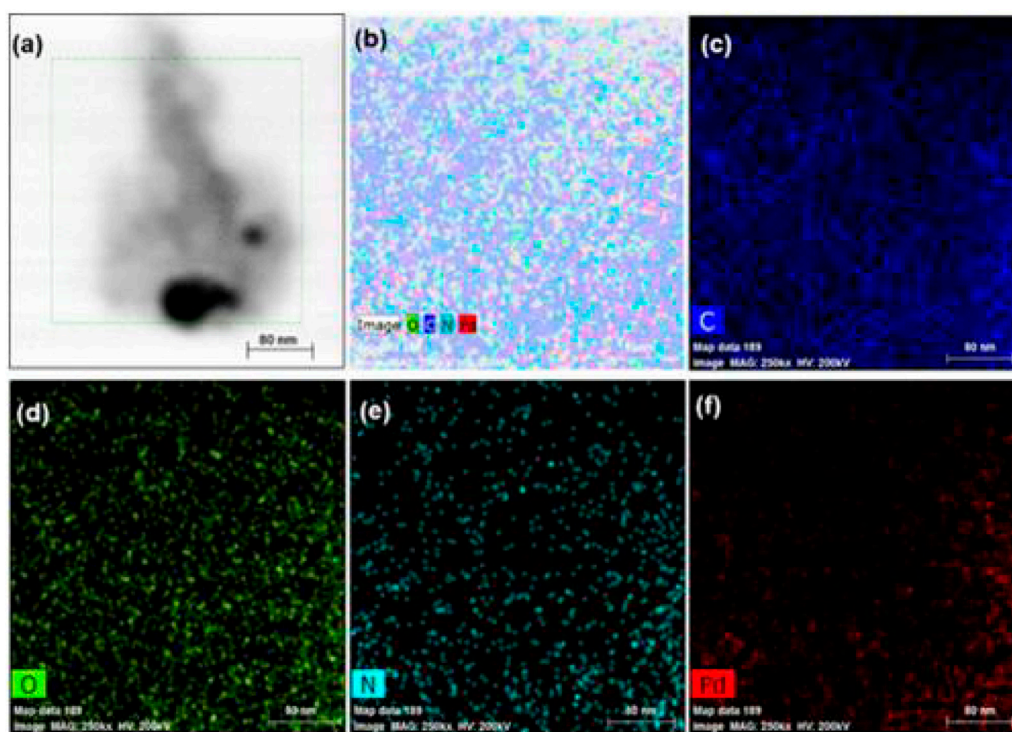


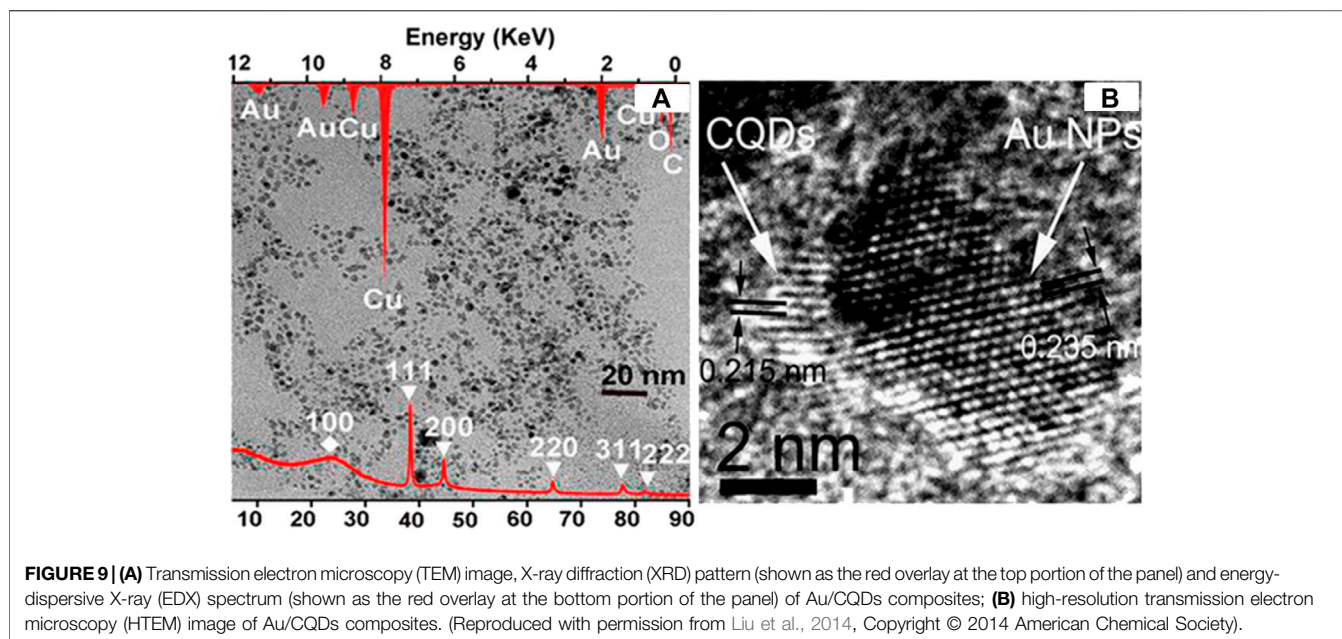
**FIGURE 8 | (A)** TEM images of Pd@CD-CONH, **(B)** EDAX mapping of some areas of the catalyst, **(C)** C, **(D)** O, **(E)** N, and **(F)** Pd. (Reproduced from Selim et al., 2020, American Chemical Society).

deionized water, and dilute ammonia was held in an autoclave for 4 h at 150°C, centrifuged for 5 min at 8,000 rpm, washed by ethanol and deionized water, dried for 1 day at 80°C, and calcined for 4 h at 450°C to make CeO<sub>2</sub>. CDs solution, CeO<sub>2</sub> powder, and deionized water were magnetically stirred for 10 h, centrifuged, washed by ethanol and water, and dried for 12 h at 90°C to make CDs/CeO<sub>2</sub> composite. The HTEM image revealed that CDs were successfully incorporated into CDs/CeO<sub>2</sub> composite. The XRD patterns demonstrated peaks at 28.5, 33.2, 47.5, 56.3, and 59.1° corresponding to <111>, <200>, <220>, <311>, and <400> planes of cubic fluorite CeO<sub>2</sub>. Raman spectroscopy showed an F2g mode of fluorite phase at 430 cm<sup>-1</sup>, a D-band at 1,410 cm<sup>-1</sup>, corresponding to lattice defect of carbon, and a G-band at 1,580 cm<sup>-1</sup>, corresponding to graphitic carbon. CDs/CeO<sub>2</sub> composite was used as a photocatalyst for the degradation of methylene blue (MB) under visible light. The reaction constant of CDs/CeO<sub>2</sub> composite was much higher than that of CeO<sub>2</sub>.

Jamila et al. prepared copper oxide/N-doped carbon quantum dots (CuO/NCQDs) by introducing NCQDs into CuO nanoleaves (Jamila et al., 2020b). Copper nitrate, distilled water, and NaOH were stirred, washed with distilled water, centrifuged, dried at 60°C, and calcined for 2 h at 500°C to make CuO. Citric acid, deionized water, and urea were held in an autoclave for 4 h at 180°C and centrifuged for 10 min at 4,000 rpm to make NCQDs. CuO, distilled water, and NCQDs were magnetically stirred and dried at 60°C in an oven to make

CuO/NCQDs. XRD pattern of CuO/NCQDs exhibited peaks at 32.3°, 35.2°, 38.3°, 48.8°, 53.2°, 57.9°, 61.3°, 66.0°, 67.9°, and 75.2° corresponding to (110), ( $\bar{1}11$ ), (111), ( $\bar{2}02$ ), (020), (202), ( $\bar{1}13$ ), (022), (220), and (203) planes of CuO and a broad carbon peak around 30°. According to the TEM image of CuO/NCQDs, NCQDs were dispersed on slightly distorted CuO nanoleaves. The EDAX result demonstrated that the elemental composition of CuO/NCQDs was 34.31%, 50.45%, 6.22%, and 9.02% for Cu, O, C, and N, respectively. According to PL results, the CuO/NCQDs had lower photoluminescence intensity than CuO, showing decreased electron-hole recombination. The CuO/NCQDs were used as a photocatalyst for the degradation of methyl orange (MO) under sunlight. The CuO/NCQDs with 1.5 ml of NCQDs displayed the highest degradation efficiency (92.0%). The CuO/NCQDs exhibited better degradation efficiency than pristine CuO because NCQDs increased charge separation efficiency and visible light-harvesting capacity.

Qu et al. fabricated a carbon quantum dots (CQDs)/KNbO<sub>3</sub> composite in mixed-calcination and hydrothermal routes by anchoring CQDs on KNbO<sub>3</sub> (Qu et al., 2018). The mixture of distilled water, Nb<sub>2</sub>O<sub>5</sub>, and KOH was held in a Teflon-lined autoclave for 12 h at 160°C, washed by ethanol and distilled water, dried overnight at 80°C, and calcined for 1 h at 400°C to make KNbO<sub>3</sub> particles. The mixture of triple-distilled water, L-ascorbic acid, and glycol was held in the autoclave for 70 min at 160°C to make CQDs. KNbO<sub>3</sub> particles were dispersed in CQDs solution, stirred for 30 min at ambient temperature, and dried for 8 h at



80°C to make CQDs/ $\text{KNbO}_3$  composite. According to photoluminescence (PL) spectra, when excitation wavelength was 400–500 nm, CQDs exhibited down-conversion PL. When excitation wavelength was 500–600 nm, CQDs exhibited up-conversion PL. The TEM result showed that CQDs were well dispersed on the surface of  $\text{KNbO}_3$  particles. EDX result revealed that the elemental composition of CQDs/ $\text{KNbO}_3$  composite was 19.40%, 23.26%, 21.89%, and 35.45% for C, Nb, K, and O, respectively. The CQDs/ $\text{KNbO}_3$  composite was used as a photocatalyst for the degradation of crystal violet dye and hydrogen evolution under visible light. When the mass ratio was CQDs:  $\text{KNbO}_3$  = 1.5:0.5, the dye degradation efficiency and hydrogen evolution rate were 70.00% and 468.72  $\mu\text{mol/h/g}$ , which were higher than those of pristine  $\text{KNbO}_3$  (41.50% and 245.52  $\mu\text{mol/h/g}$ ). The photocatalytic performance was enhanced because CQDs converted visible light to UV light, which could activate  $\text{KNbO}_3$ , and captured electrons to help the separation of electron-hole pairs. The CQDs/ $\text{KNbO}_3$  composite could be used four times without a significant decrease in performance.

Selim et al. synthesized a Pd-doped hybrid nanocatalyst (Pd@CD-CONH) by cross-linking carbon dots (CDs) with benzene-1,4-diamine (BDA) and doping the resulting polymer with palladium nanoparticles (Pd NPs) (Selim et al., 2020). The mixture of CD-COCl, dry THF,  $\text{Et}_3\text{N}$ , and BDA was dried at 40°C under vacuum; transferred to a sintered funnel; washed with water, hexane, and diethyl ether; dissolved in methanol, and dried again at 40°C under vacuum to make CD-CONH. The mixture of CD-CONH, ethanol, and  $\text{PdCl}_2$  was dried at 40°C under vacuum, transferred to a sintered funnel, washed with water, and dried for 12 h at 60°C in a vacuum oven to make Pd@CD-CONH. The PXRD patterns showed peaks corresponding to (100), (111), (200), (220), (311), and (222) planes of Pd NPs. According to the HRTEM result, Pd@CD-CONH exhibited lattice fringes of the (111) plane

(Figure 7). The Pd peak is observed in the EDX mapping of Pd@CDCONH along with C, N, and O, indicated that the Pd NPs have been clearly homogeneously distributed throughout the entire CD polymer (Figure 8). The XPS result revealed that Pd@CD-CONH contained C, N, and Pd. The Pd@CD-CONH was used as a recyclable sonocatalyst for degrading rhodamine B dye in water without using any light. With Pd@CD-CONH, 99% of rhodamine B dye was degraded in 5 min in dark, which was faster than other catalysts. Mechanistic studies indicate that reactive oxygen species (ROS) produced with the help of CDs and Pd NPs enhance the sonocatalytic effect.

He et al. synthesized a MIL-53(Fe)/carbon quantum dots/noble metal (MIL-53(Fe)/CQDs/MNPs) photocatalyst in a simple way (He et al., 2021). The mixture of water, MIL-53(Fe), and CQDs was stirred for 10 min at 500 rpm, centrifuged, washed, and dried in a vacuum for 1 day at 60°C to make MIL-53(Fe)/CQDs.  $\text{HAuCl}_4$ ,  $\text{AgNO}_3$ , or  $\text{H}_2\text{PdCl}_4$  was added to the mixture of water, ethanol, and MIL-53(Fe)/CQDs, illuminated with 300 W xenon lamp for 60 min, treated with  $\text{N}_2$ , washed with ethanol, and blow-dried by  $\text{N}_2$  to make MIL-53(Fe)/CQDs/MNPs. The zeta potential of CQDs (−14.8 mV) indicated a negative charge, and the zeta potential of MIL-53(Fe) (4.6 mV) indicated a positive charge. Therefore, CQDs and MIL-53(Fe) were combined readily by electrostatic attraction. XRD pattern of MIL-53(Fe)/CQDs/Au showed peaks corresponding to MIL-53(Fe), a weak peak at 26° corresponding to carbon, and a weak peak at 38.1° corresponding to (111) crystal planes of Au. TEM images revealed that noble metal particles were dispersed on MIL-53(Fe)/CQDs. XPS result demonstrated that MIL-53(Fe)/CQDs/MNPs contained C, O, Fe, and noble metal. With the MIL-53(Fe)/CQDs/2%Au (mass ratio of Au to MIL-53(Fe)/CQDs = 2%) photocatalyst, almost 100% of Cr (VI) was reduced in 20 min under visible light irradiation. The MIL-53(Fe)/CQDs/2%Au displayed a rate constant of 0.1820  $\text{min}^{-1}$ ,



which was about 7.4, 2.76, 1.77, and 1.47 times higher than that of MIL-53(Fe), MIL-53(Fe)/CQDs, MIL-53(Fe)/CQDs/2%Ag, and MIL-53(Fe)/CQDs/2%Pd. It was revealed that the MIL-53(Fe)/CQDs/2%Au could also eliminate Cr (VI) and dyes at the same time. The enhanced photocatalytic activity came from increased light absorption, the high electrical conductivity of CQDs and gold, and the surface plasmon resonance effect of gold.

Zhang et al. prepared carbon quantum dots (CQDs) modified graphitic carbon nitride (CCN) in a simple way (Zhang L. et al., 2020). Citric acid was heated for 20 min at 180°C, treated with NaOH, sonicated for 20 min, centrifuged for 10 min at 8,000 rpm, and dialyzed for 2 days using a dialysis bag to make CQDs. The mixture of urea and CQDs solution was held in an alumina crucible for 2 h at 550°C, stripped in HNO<sub>3</sub> solution for 1 h at 80°C, diluted using deionized water, treated with NaOH, centrifuged for 5 min at 8,000 rpm, and washed with water to make CCN. The SEM images with element mapping showed that CQDs were uniformly distributed on graphitic carbon nitride. XRD pattern of CCN exhibited peaks at 13.1° and 27.5°, corresponding to <002> and <100> crystal planes of graphite. XPS result revealed that CCN contained C, N, and O. The CCN was used as a photocatalyst for the degradation of methylene blue (MB) and rhodamine B (RhB) and hydrogen evolution under visible light irradiation. The 4CCN (0.98 wt% CQDs) showed the shortest MB degradation time of 20 min and the highest hydrogen evolution rate of 1,291 μmol/h/g. The CCN had better performance than pristine graphitic carbon nitride because CQDs increased visible light absorption and promoted photogenerated charge separation and transfer.

Seng et al. developed a nitrogen-doped carbon quantum dots-decorated 2D graphitic carbon nitride (NCQD/g-C<sub>3</sub>N<sub>4</sub>) composite through a hydrothermal method (Seng et al., 2020). The mixture of distilled water, citric acid, and urea was held in a Teflon-lined autoclave for 4 h at 150°C, centrifuged for 20 min at 12,000 rpm, and dried at 90°C overnight in an oven to make bulk NCQDs. Urea was held in a covered porcelain crucible for 3 h at 550°C and ground into powder to make bulk g-C<sub>3</sub>N<sub>4</sub>. g-C<sub>3</sub>N<sub>4</sub> exfoliated by sonication and NCQDs solution were vigorously stirred for 30 min at ambient temperature, held in the autoclave for 4 h at 120°C, filtered by vacuum filter, washed by distilled water, and dried at 70°C in an oven overnight to make NCQD/g-C<sub>3</sub>N<sub>4</sub>. According to the TEM result, the morphology of g-C<sub>3</sub>N<sub>4</sub> did not change after the addition of NCQDs. EDX result showed that the elemental composition of NCQD/g-C<sub>3</sub>N<sub>4</sub> was 31%, 18.85%, 0.58%, and 49.5% for C, N, O, and Si, respectively. The XRD pattern of NCQD/g-C<sub>3</sub>N<sub>4</sub> exhibited peaks at 13.2° and 27.4°, corresponding to (100) and (002) planes of graphite. Photoluminescence (PL) spectrum revealed that PL intensity of NCQD/g-C<sub>3</sub>N<sub>4</sub> decreased after NCQDs loading. The NCQD/g-C<sub>3</sub>N<sub>4</sub> composite was used as a photocatalyst for the degradation of methylene blue (MB) under LED light. The 1 wt% NCQD/g-C<sub>3</sub>N<sub>4</sub> (1 wt% NCQD) exhibited the highest MB degradation efficiency of 54.6%, which was 2.6 times higher than that of pristine g-C<sub>3</sub>N<sub>4</sub>. The 1 wt% NCQD/g-C<sub>3</sub>N<sub>4</sub> displayed an MB degradation rate constant of  $5.061 \times 10^{-3} \text{ min}^{-1}$ , which was 3.85 times higher than that of pure g-C<sub>3</sub>N<sub>4</sub>. The improved photocatalytic activity was due to increased speed of charge

transfer, suppressed electron-hole recombination, and optimized heterojunction interface between g-C<sub>3</sub>N<sub>4</sub> and NCQD. When the 1 wt% NCQD/g-C<sub>3</sub>N<sub>4</sub> was used for three times, the degradation efficiency was 91.2% of original efficiency, showing high stability of the composite.

He et al. constructed a 3D graphene oxide- (GO-) carbon quantum dots/g-C<sub>3</sub>N<sub>4</sub> nanosheet (GA-CQDs/CNN) aerogel by a simple hydrothermal method (He H. et al., 2018). EDTA-2Na•2H<sub>2</sub>O was held in a quartz boat for 2 h at 350°C, dissolved in ethanol, centrifuged for 30 min at 12,000 rpm, and freeze-dried overnight to make CQDs. Dicyandiamide underwent thermal polycondensation to make bulk g-C<sub>3</sub>N<sub>4</sub>. The mixture of deionized water, bulk g-C<sub>3</sub>N<sub>4</sub>, and H<sub>2</sub>SO<sub>4</sub> was sonicated for 8 h and washed by distilled water to make CNN. Graphite powder underwent modified Hummers' method to make GO. The mixture of CQDs and CNN was held in an autoclave for 4 h at 180°C, mixed with ultrasonic GO, stirred for 1 h, heated again for 6 h at 180°C, washed by distilled water, and freeze-dried overnight to make GA-CQDs/CNN. The XRD patterns of GA-CQDs/CNN exhibited peaks at 27.85° and 13.29°, corresponding to (002) and (100) planes of pristine CNN. XPS result showed that GA-CQDs/CNN contained C, O, and N. HTEM image revealed a distinguished interface between reduced GO and CNN. According to photoluminescence (PL) spectra, GA-CQDs/CNN displayed the PL quenching phenomenon. The GA-CQDs/CNN was used as a photocatalyst for the degradation of methyl orange (MO) under visible light irradiation. The GA-CQDs/CNN-24% (mass ratio of GO to CNN = 24%) exhibited MO degradation efficiency of 91.1%, which was 7.6 times higher than that of bulk g-C<sub>3</sub>N<sub>4</sub>. The GA-CQDs/CNN also displayed high adsorption capacity. The photocatalytic and adsorptive performance was improved because the large specific surface area of the porous structure was advantageous for light absorption and material adsorption. Moreover, the large planar interface between CNN and GO promoted photoexcited charge transfer and separation, and CQDs enhanced light absorption and charge separation. The GA-CQDs/CNN could be used for four cycles without a significant decrease in performance.

Miao et al. synthesized an all-solid-state Z-scheme graphitic carbon nitride (g-C<sub>3</sub>N<sub>4</sub>)/Ag<sub>3</sub>PO<sub>4</sub>/nitrogen-doped carbon dots (NCDs) photocatalyst by a simple solution process by anchoring NCDs onto g-C<sub>3</sub>N<sub>4</sub>/Ag<sub>3</sub>PO<sub>4</sub> photocatalyst (Miao et al., 2018a). The mixture of water, citric acid, and ethylene diamine was held in a Teflon-lined autoclave for 5 h at 200°C, dialyzed for 1 day, freeze-dried, and dispersed in water to make NCDs dispersion. Urea was held in a covered alumina crucible at 250°C for 1 h, 350°C for 1 h, and 550°C for 2 h and calcined for 2 h at 600°C to make g-C<sub>3</sub>N<sub>4</sub> nanosheets. The mixture of DI water, g-C<sub>3</sub>N<sub>4</sub>, AgNO<sub>3</sub>, and Na<sub>2</sub>HPO<sub>4</sub> was centrifuged, washed with ethanol and DI water, vacuum-dried for 12 h at 45°C, and ground into powder to make g-C<sub>3</sub>N<sub>4</sub>/Ag<sub>3</sub>PO<sub>4</sub>. The mixture of g-C<sub>3</sub>N<sub>4</sub>/Ag<sub>3</sub>PO<sub>4</sub> and NCDs was centrifuged, washed with ethanol and DI water, and vacuum-dried for 12 h at 45°C to make g-C<sub>3</sub>N<sub>4</sub>/Ag<sub>3</sub>PO<sub>4</sub>/NCDs. XRD pattern of g-C<sub>3</sub>N<sub>4</sub>/Ag<sub>3</sub>PO<sub>4</sub>/NCDs showed characteristic peaks of the cubic phase Ag<sub>3</sub>PO<sub>4</sub>. According to the TEM result, Ag<sub>3</sub>PO<sub>4</sub> and NCDs particles



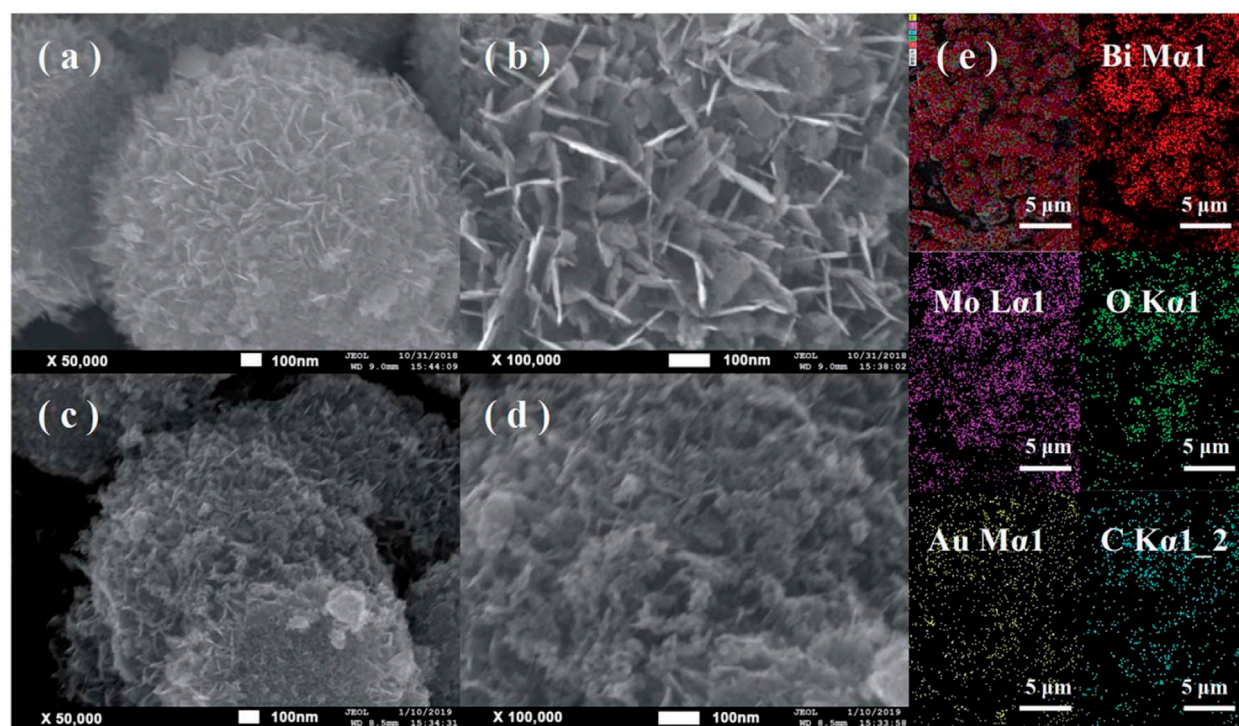


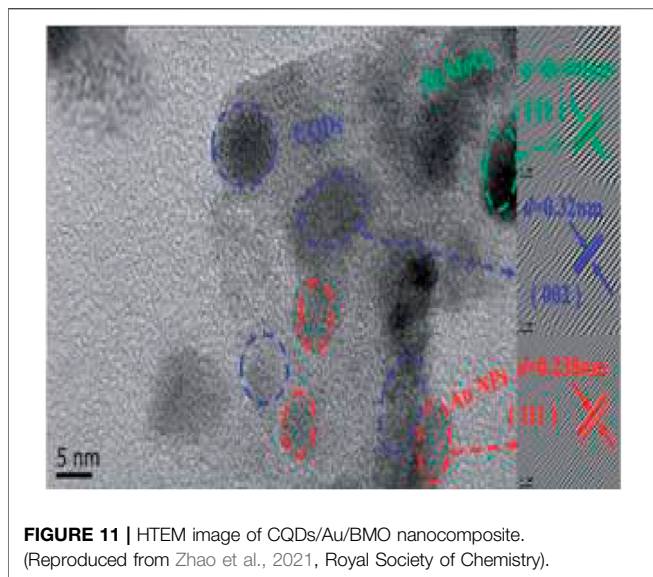
**FIGURE 10** | FE-SEM images of (A,B) hollow BMO microsphere and (C,D) CQDs/Au/BMO; (E) EDX spectrum of sample CQDs/Au/BMO showing the presence of Bi, Mo, O, Au and C elements. (Reproduced from Zhao et al., 2021, Royal Society of Chemistry).

were successfully loaded to g-C<sub>3</sub>N<sub>4</sub>. The XPS result revealed that g-C<sub>3</sub>N<sub>4</sub>/Ag<sub>3</sub>PO<sub>4</sub>/NCDs contained C, N, O, Ag, and P. The g-C<sub>3</sub>N<sub>4</sub>/Ag<sub>3</sub>PO<sub>4</sub>/NCDs photocatalyst was used for photodegradation of methylene blue (MB), rhodamine B (RhB), and phenol under visible light. 10 mg L<sup>-1</sup> MB solution and 10 mg L<sup>-1</sup> RhB solution were degraded in 20 and 15 min, respectively, and 64% of 50 mg L<sup>-1</sup> phenol solution was degraded in 80 min, much faster than other catalysts such as Ag<sub>3</sub>PO<sub>4</sub> and g-C<sub>3</sub>N<sub>4</sub>/Ag<sub>3</sub>PO<sub>4</sub>. The g-C<sub>3</sub>N<sub>4</sub>/Ag<sub>3</sub>PO<sub>4</sub>/NCDs photocatalyst showed enhanced performance because NCDs have increased molecular oxygen activation, promoted charge transfer, and improved light absorption capacity. The photocatalyst could be used up to four times without a significant decrease in performance, suggesting that the photocatalyst has high stability.

Miao et al. developed an all-solid-state Z-scheme Ag<sub>3</sub>PO<sub>4</sub>/graphene oxide (GO)/nitrogen-doped carbon dot (NCD) photocatalyst by depositing NCDs on Ag<sub>3</sub>PO<sub>4</sub>/GO composite (Miao et al., 2018b). The mixture of water, citric acid, and ethylene diamine was held in a Teflon-lined autoclave for 5 h at 200°C, dialyzed for 1 day, freeze-dried, and dispersed in water to make NCDs dispersion. The mixture of DI water, GO, AgNO<sub>3</sub>, and Na<sub>2</sub>HPO<sub>4</sub> was centrifuged, washed with ethanol and DI water, dried for 12 h at ambient temperature in the dark, and ground into powder to make Ag<sub>3</sub>PO<sub>4</sub>/GO. The mixture of DI water, Ag<sub>3</sub>PO<sub>4</sub>/GO, and NCDs was centrifuged, washed with ethanol and DI water, dried at ambient temperature in the dark, and ground into powder to make Ag<sub>3</sub>PO<sub>4</sub>/GO/NCD. The XRD

pattern of Ag<sub>3</sub>PO<sub>4</sub>/GO/NCD exhibited peaks corresponding to the cubic phase Ag<sub>3</sub>PO<sub>4</sub>. From Raman spectroscopy, the D-band and G-band of carbon at 1,370 and 1,600 cm<sup>-1</sup>, respectively, and Ag<sub>3</sub>PO<sub>4</sub> peaks at 905 and 1,000 cm<sup>-1</sup> were observed. TEM images showed that Ag<sub>3</sub>PO<sub>4</sub> and NCD particles were successfully incorporated with GO sheets. XPS result revealed that Ag<sub>3</sub>PO<sub>4</sub>/GO/NCD contained C, N, O, Ag, and P. According to photoluminescence (PL) spectra, Ag<sub>3</sub>PO<sub>4</sub>/GO/NCD exhibited lower PL intensity than its components. The Ag<sub>3</sub>PO<sub>4</sub>/GO/NCD photocatalyst was used for the degradation of methylene blue (MB), rhodamine B (RhB), and phenol under visible light. 10 mg L<sup>-1</sup> MB solution, 10 mg L<sup>-1</sup> RhB solution, and 50 mg L<sup>-1</sup> phenol solution were degraded in 2.5, 5, and 120 min, respectively, which were much faster than those of Ag<sub>3</sub>PO<sub>4</sub> and Ag<sub>3</sub>PO<sub>4</sub>/GO. The photocatalytic activity was improved because NCDs increased the oxygen activation, enhanced light absorption capacity, and suppressed photoinduced electron-hole pairs recombination. The Ag<sub>3</sub>PO<sub>4</sub>/GO/NCD photocatalyst could be used four times without a significant decrease in photocatalytic activity, showing the high stability of the photocatalyst.

Jana et al. prepared CuO-associated carbon dots (CDCs) in an eco-friendly way (Jana et al., 2020). The mixture of citric acid (CA), tetraethylenepentamine (TEPA), and copper sulfate pentahydrate was sonicated, heated in a microwave oven for 5 min, dissolved in water, centrifuged for 10 min at 10,000 rpm, and dialyzed for 12 h to make CDCs. The TEM result revealed



that CDCs had an average size of 5.16 nm. XRD pattern of CDCs exhibited a broad peak of around  $21^\circ$  corresponding to amorphous carbon. The XPS result showed that CDCs contained C, N, O, and Cu. The zeta potential of CDCs was +5.42 mV, indicating that CDCs had a positive surface charge. CDCs were incorporated with a cationic dye rhodamine B (RhB), an anionic dye alizarin red S (ArS), or a neutral dye fluorescein C (FlC) into CDC-dye systems exhibiting photoelectric conversion processes. The CDC-RhB system displayed the lowest energy transfer efficiency ( $\eta$ ) of 6.03% because the repulsion between positively charged CDCs and cationic RhB decreased the energy transfer. A positively charged surfactant cetyltrimethylammonium bromide (CTAB) and a negatively charged surfactant sodium dodecyl sulfate (SDS) were used to enhance  $\eta$  of the CDC-RhB system, and the negatively charged surfactant enhanced  $\eta$  more, showing FRET efficiency  $\eta_{FRET}$  of 14.7%.

Zhang et al. prepared a first-time novel synergistic catalyst (N-CDs/m-TiO<sub>2</sub>) by compounding m-TiO<sub>2</sub> with N-CDs (Zhang and Dai, 2016). The mixture of citric acid (CA), urea (U), and N,N-dimethylformamide (DMF) ultrasonication and held on PTFE autoclave in microwave vessel at  $108^\circ\text{C}$  for 20 min, temperature elevating range of  $15^\circ\text{C min}^{-1}$ , dialyzed for 48 h, freeze-dried this N-CDs/m-TiO<sub>2</sub> were carried out for the preparation of N-CDs. The mixture of PS sphere and m-TiO<sub>2</sub> heated at  $70^\circ\text{C}$  for 12 h in an oven further sintered in a muffle furnace at a setting temperature of  $500^\circ\text{C}$  for 2 h for removing PS sphere to make macro porous TiO<sub>2</sub> (m-TiO<sub>2</sub>). The mixture N-CDs and m-TiO<sub>2</sub> was transferred into the heating mantle at a set temperature of  $60^\circ\text{C}$  for 12 h by the thermal deposition technique. XRD of N-CDs/m-TiO<sub>2</sub> exhibited peaks at  $25.3^\circ$ ,  $48.1^\circ$ ,  $53.8^\circ$ ,  $55.2^\circ$ , and  $62.8^\circ$ , corresponding to (101), (200), (105), (211), and (204), respectively for the anatase TiO<sub>2</sub>. For the FTIR spectra of N-CDs/m-TiO<sub>2</sub>, the additional peak appears at  $1,050\text{ cm}^{-1}$ , corresponding to bending vibration of C-NH-C, and the absorption peak appears between  $3,600$  and  $3,300\text{ cm}^{-1}$  for the TiO<sub>2</sub> NPs and m-TiO<sub>2</sub> for a fact at N-CDs use capable of

enhancing charge transfer rate as well as CQDs beneficial for promotion photocatalytic efficiency of TiO<sub>2</sub>. The N<sub>2</sub> adsorption-desorption isotherm of N-CDs/m-TiO<sub>2</sub> demonstrates the hysteresis loops at relative pressure 0.2 with type IV adsorption-desorption having uniform pore size distribution. For the UV-DRS spectra of N-CDs/m-TiO<sub>2</sub>, the threshold wavelength ( $\lambda_g$ ) of N-CDs/m-TiO<sub>2</sub> was 511.49 nm and band gap energy ( $E_g$ ) was 2.42 eV. The N-CDs/m-TiO<sub>2</sub> shows the higher photo-anode, photocurrent intensity. There was a higher photochemical activity of N-CDs/m-TiO<sub>2</sub> due to its unique porous structure and sensitization of N-CDs. The N-CDs/m-TiO<sub>2</sub> shows excellent photovoltaic conversion efficiency and stability.

The photocatalytic performance of N-CDs/m-TiO<sub>2</sub> was examined by using MB as a target pollutant under UV light irradiation. For N-CDs/m-TiO<sub>2</sub> to enhanced degradation efficiency, the decolorization ratio at MB over N-CDs/m-TiO<sub>2</sub> still shows excellent recycling ability of the N-CDs/m-TiO<sub>2</sub> photocatalyst. During photocatalytic degradation of MB to determine the major oxidant, that is, ethylene diamine tetraacetic acid (EDTA), tert-butanol (TBA), and p-benzoquinone (BQ) were employed as  $h^+$ ,  $OH^\cdot$ , and  $O_2$  scavengers, respectively. The luminescence property of N-CDs/m-TiO<sub>2</sub> significantly enhanced photocatalytic performance due to the synergistic effect between N-CDs sensitization and the unique porous structure of m-TiO<sub>2</sub>. In MB containing aromatic ring is responsible for the  $\pi$ - $\pi$  conjugated structure with the  $\pi$  orbitals of N-CDs, and hence enhancing the photocatalytic activity of N-CDs/m-TiO<sub>2</sub> on the MB surface.

Li et al. synthesized carbon dots modified g-C<sub>3</sub>N<sub>4</sub>/SnO<sub>2</sub> photocatalyst (CDs/g-C<sub>3</sub>N<sub>4</sub>/SnO<sub>2</sub>) using the thermal polymerization method (Li et al., 2021). Preparation of g-C<sub>3</sub>N<sub>4</sub> using guanidinium hydrochloride heated in a muffle furnace at  $550^\circ\text{C}$  for 12 h with a ramp rate of  $2^\circ\text{C min}^{-1}$ . Herein to make SnO<sub>2</sub> nanoparticles; SnCl<sub>4</sub>·H<sub>2</sub>O dissolved in DI water followed with 17 h ultrasonication and the mixture is transferred into stainless steel autoclave and processed further at  $180^\circ\text{C}$  for 12 h. The mixture further rinsed with ethanol and DI water dried at  $60^\circ\text{C}$  for 24 h. The mixture of CN and SnO<sub>2</sub> was dissolved in ethanol heated at  $60^\circ\text{C}$  to remove the ethanol mixture calcined at  $400^\circ\text{C}$  for 2 h with a ramp rate of  $2^\circ\text{C min}^{-1}$ . CDs were prepared by using a mixture of citric acid (CA), urea (U), and DI water held in a Teflon-lined stainless steel autoclave at  $180^\circ\text{C}$  for 5 h. CDs/CN/SnO<sub>2</sub> was prepared using CSn<sub>20</sub> and CDs with ethanol heated at  $60^\circ\text{C}$  for evaporating ethanol and then heated at  $300^\circ\text{C}$  for 3 h. CDs/CN (CCN) and CDs/SnO<sub>2</sub> (CSnO<sub>2</sub>) were prepared by the same method to make 0.5 CCSn20. The TEM, HTEM, and FPT pattern clearly shows the hexagonal crystalline structure of CDs (Figures 9B,C), confirming that the CDs dispersed in g-C<sub>3</sub>N<sub>4</sub> and SnO<sub>2</sub> assigned (110) planes. XRD spectra of 0.5 CCSn20 show that a high purity crystalline state of materials was synthesized. The N<sub>2</sub> adsorption-desorption isotherms of 0.5 CCSn20 photocatalysts showed a higher specific surface area ( $53.717\text{ m}^2/\text{g}$ ). XPS spectra reveal that 0.5 CCSn20 contains C, N, O, and Sn3d. UV-vis DRS for 0.5 CCSn20 increased light absorption capacity more than its components. According to photoluminescence (PL) spectra, 0.5 CCSn20



exhibited lower PL intensity than its components. The 0.5 CCSn20 photocatalyst was used for the degradation of indomethacin (IDM) under visible light. The photocatalytic IDM degradation rate of 0.5 CCSn20 was higher by 70.3% than CN (32.0%).

Yu et al. prepared ZnO/CQDs nanocomposites for the one-step hydrothermal reaction method (Yu et al., 2012). The mixture of Zn ( $\text{AC}_2$ )  $2\text{H}_2\text{O}$  and the alcoholic solution of CQDs was held in a Teflon-lined stainless steel autoclave heated at  $100^\circ\text{C}$  for 8 h washed with DI water and ethanol and then vacuum-dried at  $60^\circ\text{C}$  for 24 h. XRD of ZnO/CQDs shows the successful formation of ZnO/CQDs diffraction peak at ZnO corresponding to wurtzite ZnO phase (JCPDS-36-1451). Raman spectrum shows prepared ZnO/CQDs nanocomposites are composed at CQDs and ZnO. FTIR spectra results showed CQDs are successfully attached to ZnO nanoparticles. UV-Vis ZnO/CQDs nanocomposites showed higher photocatalytic activity than other components. SEM showed small uniform nanoparticles with a size of 20–30 nm of ZnO/CQDs. HTEM and TEM of ZnO/CQDs formation of carbon layer due to the addition of CQDs are shown in **Figures 10A,B**. EDS gives the elements present in ZnO/CQDs nanocomposites Zn, O, and C. The ZnO/CQDs nanocomposite was used as the photocatalytic ability for photodegradation of gas-phase benzene under visible light carried out at room temperature. The photocatalytic degradation efficiency of gas-phase benzene and gas-phase methanol was found at 86% and 82% using ZnO/CQDs higher than that of ZnO at 26%, 22%, and N-doped  $\text{TiO}_2$  (N- $\text{TiO}_2$ ) at 60% and 55%, respectively. The CODs were loaded on the ZnO surface to the main function for the enhanced photocatalytic activity of ZnO/CQDs because ZnO/CQDs had better performance than ZnO due to CQDs increased photocatalytic activity toward degradation of toxic gas (benzene and methanol) under visible light at RT.

Nie et al. synthesized CDs/ $\text{NiCo}_2\text{O}_4$  photocatalyst (Nie et al., 2021). Nickel nitrate, cobalt nitrate, and DI water were stirred; CDs were added in different wt% into the mixture, sonicated, and stirred, and then the solution was moved to porcelain crucible. Mixtures of the solution were then heated at  $400^\circ\text{C}$  for 2 h in a muffle furnace, washed with water and ethanol, and then dried at  $70^\circ\text{C}$  in a vacuum oven to make CDs/ $\text{NiCo}_2\text{O}_4$ . TEM and H-TEM images reveal that the CDs/ $\text{NiCo}_2\text{O}_4$  exhibits irregular spherical shapes, and the interplanar spacing of 0.21 and 0.24 nm is associated with the (100) spacing of CDs and (311) spacing of  $\text{NiCo}_2\text{O}_4$  shown in **Figures 10C,D**. The XRD pattern of CDs/ $\text{NiCo}_2\text{O}_4$  perfectly matches with (JCPDS No. 73-1702) card. XPS result confirmed that CDs/ $\text{NiCo}_2\text{O}_4$  nanocomposite contained Ni, Co, C, and O. Electrochemical band structure of the CDs/ $\text{NiCo}_2\text{O}_4$  photocatalyst reveals that helps photocatalytic overall water decomposition. According to TPV, the measurement of CDs/ $\text{NiCo}_2\text{O}_4$  showed greater photocurrent intensity, and *in situ* TPV measurement study during the reaction of photocatalytic HER and OER further enhanced the reaction rate after being supported with CDs. The EIS spectra of CDs/ $\text{NiCo}_2\text{O}_4$  demonstrates is having lower charge transfer resistance, and hence it showed better photocurrent intensity, and higher overall water decomposition reaction activity. The CDs/ $\text{NiCo}_2\text{O}_4$  showed the best possible hydrogen (oxygen evolution) production is up to

$62\ \mu\text{mol h}^{-1}\text{g}^{-1}$  ( $29\ \mu\text{mol h}^{-1}\text{g}^{-1}$ ). The CDs/ $\text{NiCo}_2\text{O}_4$  is still stable toward  $\text{H}_2$  production. According to the TPV test, the CDs enhanced the interface electron extraction by about 0.09 ms, while the maximum electron storage time by CDs is up to 0.7 ms, concluding that CDs enhanced the photocatalytic water decomposition activity.

Liu et al. prepared metal nanoparticles/carbon quantum dot composite photocatalyst using Au and CQDs (Liu et al., 2014). CQDs were prepared by electrochemical ablation of graphite. Two graphite rods were placed in an ultrapure water electrolyte solution, applying static potential 15–60 V by both electrodes using direct current for 10 days, with stirring then centrifuged to make CODs.  $\text{HAuCl}_2$  and CQDs solution stirred dark environments at room temperature for 2 h overnight, centrifuged, washed DI water, and ethanol-dried for 6 h at  $25$ – $60^\circ\text{C}$  to make Au/CQDs. EDX results demonstrated the elemental composition of Au, C, and O from AuNPs and CQDs. XRD pattern of Au/CQDs exhibited planes (111), (200), (220), (311), and (222) for AuNPs and a strong peak at  $20^\circ$  for carbon. The TEM image showed the successful formation of Au/CQDs (**Figure 9**). UV-Vis absorption spectra of Au/CQDs showed both UV-Vis absorption peaks at 230 nm and 490–590 nm for CQDs and AuNPs, respectively. Raman of Au/CQDs composites showed a higher  $I_D/I_G$  ratio than AuNPs and CQDs. Photocatalytic oxidation of cyclohexane to cyclohexanone with Au/CQDs composites under visible light is increased could be due to a similar combination and interaction of CQDs and AuNPs. According to PL spectra, CQDs were excellent, as they were quenched by either an electron donor or an electron acceptor. Electrocatalytic studies on Au/CODs composite toward hydrogen peroxide decomposition shows excellent activity under visible-light irradiation than that absence of light irradiation. Au/CQDs composite exhibited high photocatalytic activity selective for oxidation of cyclohexane to cyclohexanone using hydrogen peroxide as oxidant solvent-free. Electrochemical study reveals that visible light enhanced catalytic reaction.

Liang et al. prepared ZnO sensitized by carbon quantum dots (L-CQDs/ZnO) by a combination of L-CQDs and ZnO using the hydrothermal method (Liang et al., 2020). Zinc oxide, ammonia water, and ammonium bicarbonate were mixed together, filtered, and stirred for 4 h. The supernatant was steamed at  $90 \pm 2^\circ\text{C}$ , filtrated, washed, dried in a vacuum oven at  $120 \pm 2^\circ\text{C}$ , and then annealed at  $500 \pm 2^\circ\text{C}$  for 4 h to make ZnO. ZnO was added into 120 ml L-CQDs aqueous solutions, stirred for 2 h, held into stainless steel autoclave heated air dry oven at  $120 \pm 2^\circ\text{C}$  for 2 h, cooled, filtrated, washed with water dried at  $60 \pm 2^\circ\text{C}$  for 12 h, and dried at vacuum oven to make L-CQDs/ZnO. TEM result demonstrated that the L-CQD had average diameter of  $2.1 \pm 0.4$  nm (**Figures 12A,B**). FTIR spectra demonstrated the strong absorption peak at  $400$ – $800\text{ cm}^{-1}$  of L-CQDs/ZnO, which confirmed strong physical interaction between carbon and zinc atoms. According to XPS results, L-CQDs/ZnO contained Zn, C, O with peaks appears at 1,021.1 eV ( $\text{Zn}_{2p_{3/2}}$ ) and 1,044.2 eV ( $\text{Zn}_{2p_{1/2}}$ ), 284.8 eV, 288.3 eV (C1s) and 531.8 eV, 532.6 eV (O1s). UV-Vis DRS results demonstrated that the L-CQDs/ZnO showed better photocatalytic activity. According to PL results, the L-CQDs/ZnO had lower photogenerated electron-hole pair recombination.

The result demonstrated the efficient electron transport caused by the  $\pi$  bond conjugate system of L-CQDs. The L-CQDs/ZnO was used as a photocatalyst for the degradation of phenol under sunlight. The L-CQDs/ZnO's highest degradation efficiency (60%) completely degrades phenol at 5.5 h compared to ZnO. The L-CQDs/ZnO exhibited better degradation efficiency than ZnO because wt% of CQDs increased charge separation efficiency.

Bozetine et al. developed ZnO/CQDs/AgNPs by the green approach of the *in situ* hydrothermal method (Bozetine et al., 2021). D-Lactose source of carbon and NaOH solution held in Teflon-beaker heated at 80°C for 15 min for the synthesis of CQD. Further to this CQD dispersion added  $\text{Zn}(\text{CH}_3\text{COO})_2$  at RT and adjusted pH-10 by addition of 8 M NaOH dropwise with constant stirring for 15 min. The mixture was heated at 80°C for 2 h and added drop-wise silver nitrate under stirring at 80°C for 1 h to make ZnO/CQDs/AgNPs. The XRD pattern of ZnO/CQDs/AgNPs exhibited a peak at 30°, 44.5°, and 64.6°, corresponding to (111), (200), and (220) planes Ag. According to SEM results, ZnO/CQDs/AgNPs had particles size (<50 nm). The EDX results demonstrated that chemical composition consisted of Zn, C, O, and Ag elements. XPS results demonstrated that ZnO/CQDs/AgNPs contained Zn, O, C, and Ag.  $\text{N}_2$  adsorption-desorption isotherms of ZnO/CQDs/AgNPs ternary achieved the highest surface area compared to the composite of ZnO, Ag, and binary of CQDs. UV-Vis spectra of ZnO/CQDs/AgNPs achieved band gap at 3.22 eV to generate electron-hole pairs. The ZnO/CQDs/AgNPs composite was used for photocatalysis of MB dye under UV-light irradiation. The photodegradation efficiency of MB dye was 98.6% for ZnO/CQDs/AgNPs. ZnO/CQDs/AgNPs photocatalyst achieved higher photocatalytic activity under UV-light irradiation due to the AgNPs, and CQDs reduced the recombination rate of the photogenerated electron-hole pairs and enhanced photocatalytic reactions.

Zhao et al. synthesized carbon quantum dots and Au nanoparticles with  $\text{Bi}_2\text{MoO}_6$  by simple hydrothermal method (CQDs/Au/BMO) (Zhao et al., 2021). Citric acid and urea were held in a Teflon-lined autoclave for 5 h at 180°C, centrifuged for 30 min, and subjected to vacuum drying for 3 h at 80°C to make CQDs.  $\text{Bi}(\text{NO}_3)_3 \cdot 5\text{H}_2\text{O}$  and  $\text{Na}_2\text{MoO}_4 \cdot 2\text{H}_2\text{O}$  were added in ethylene glycol, and ethanol stirring was held in an autoclave for 12 h at 2016°C, centrifuged, washed with water and alcohol, and dried overnight in an electric oven at 60°C to make BMO. BMO,  $\text{HAuCl}_4$ , and lysine were added in DI water, maintained pH with added NaOH and  $\text{NaBH}_4$ , centrifuged, washed with water, and dried overnight in an oven at 60°C to make Au/BMO. CDs and Au/BMO were dispersed in ethanol using ultrasonic treatment followed by drying and calcination 2 h at 250°C to make CQDs/Au/BMO. XRD pattern of CQDs/Au/BMO showed peaks at 38.2° and 44.3° corresponding to (111) and (200) planes for Au NPs for Au/BMO and CQDs/Au/BMO. The XPS result demonstrated that CQDs/Au/BMO contained Bi, Mo, O, Au, and C elements. The morphology and EDX of BMO possesses a hierarchical microsphere with an average diameter was about 1–2  $\mu\text{m}$ , CQDs/Au/BMO are similar to that of BMO, EDX indicated that all the elements are uniformly distributed (Figures 10A–E). According to the H-TEM result, CQDs/Au/BMO revealed (131), (002), and (111) planes for BMO, CQDs, and Au, respectively (Figure 11). EPR spectra showed

the oxygen vacancies in BMO and CQDs/Au/BMO. The CQDs/Au/BMO was used as a photocatalyst for the degradation of phenol under visible light. The phenol degradation rate constant of 7% CQDs/Au/BMO was  $228.21 \times 10^{-4} \text{ min}^{-1}$ . The 7% CQDs/Au/BMO exhibited the highest phenol degradation efficiency of 94%, which was higher than that of BMO-SOVs (24%), Au/BMO (45%), and CQDs/BMO (51%). According to PL and EIS spectra, 7% CQDs/Au/BMO showed higher photocatalytic activity due to the interaction of CQDs and Au NPs on the surface of BMO. The EIS result confirmed that CQDs/Au/BMO showed the strongest ability to separate and transfer photogenerated  $e^-/h^+$  and enhanced photocatalytic activity.

Hu et al. developed carbon dots-decorated  $\text{BiO}(\text{COOH})/\text{ultrathin } g\text{-C}_3\text{N}_4$  nanosheets (CQDs/ $\text{BiO}(\text{COOH})/\text{uCN}$ ) photocatalyst by the simple method (Hu et al., 2021). Melamine was calcined for 4 h at 550°C to make bulk  $g\text{-C}_3\text{N}_4$ . The bulk  $g\text{-C}_3\text{N}_4$  was held in an aluminum crucible and thermally exploited in uCN for 2 h at 500°C to make uCN. Citric acid and ethylene diamine were held in a Teflon-lined autoclave for 5 h at 200°C and dialyzed for 24 h to make CQDs. The mixture of uCN,  $\text{HCOONa}$  and  $\text{Bi}(\text{NO}_3)_3 \cdot 5\text{H}_2\text{O}$  is taken in water and stirred for 30 min followed by added CQDs solution. Furthermore the solution was transfer into Teflon lined autoclave and heated at 150°C for 10 h to make CQDs/ $\text{BiO}(\text{COOH})/\text{uCN}$ . The SEM image of CQDs/ $\text{BiO}(\text{COOH})/\text{uCN}$  showed a flower-like structure. EDS of CQDs/ $\text{BiO}(\text{COOH})/\text{uCN}$  contained Bi, O, N, and C elements. HTEM of CQDs/ $\text{BiO}(\text{COOH})/\text{uCN}$  demonstrated that the lattice stripes and planes ((102) (110)), (101), and (002)) for  $\text{BiO}(\text{COOH})$ , graphitic carbon, and uCN. XRD pattern of CQDs/ $\text{BiO}(\text{COOH})/\text{uCN}$  exhibited peaks at 13.1° and 27.4°, corresponding to (100) and (002) for uCN and broad peak 25° for the disorder of carbon. XPS spectra revealed that CQDs/ $\text{BiO}(\text{COOH})/\text{uCN}$  contained C, N, Bi, and O elements. The photoluminescence (PL) spectra showed that CQDs/ $\text{BiO}(\text{COOH})/\text{uCN}$  exhibited the strongest emission when the excitation wavelength was 460 nm. The CQDs/ $\text{BiO}(\text{COOH})/\text{uCN}$  was used as a photocatalyst for the degradation of sulfathiazole (STZ) under LED lamp irradiation. Using the CQDs/ $\text{BiO}(\text{COOH})/\text{uCN}$  showed higher photocatalytic activity compared to its composites. The photocatalytic effect was improved because of the formation of heterojunction. Photodegradation efficiencies of STZ at various pH values were studied up to 98%, and the 4-CQDs/ $\text{BiO}(\text{COOH})/\text{uCN}$  showed excellent photocatalytic activity, both acidic and alkaline. The degradation efficiency of STZ was checked by adding natural organic matter and inorganic anions, which revealed CQDs/ $\text{BiO}(\text{COOH})/\text{uCN}$  was an attractive material for both NOM and IA. The CQDs/ $\text{BiO}(\text{COOH})/\text{uCN}$  showed better photocatalyst activity.

Gao et al. prepared N-CQDs/ $\text{BiOI}_x\text{Br}_{1-x}$  by the one-step *in situ* co-precipitation method (Gao et al., 2021). Citric acid and urea ultrasonication 2 h were mixture held in a Teflon-lined stainless steel autoclave for 5 h at 180°C, dialyzed for 24 h, and dried for 12 h at 60°C to make N-CQDs. The  $\text{Bi}(\text{NO}_3)_3 \cdot 5\text{H}_2\text{O}$  in glycol is ultrasonicated for better dispersion and added N-CQDs under stirring for next 2 h to make N-CQDs/ $\text{BiOI}_x\text{Br}_{1-x}$ . The XRD spectra of N-CQDs/ $\text{BiOI}_x\text{Br}_{1-x}$  exhibited a characteristic peak at  $2\theta = 26^\circ$  to  $35^\circ$ . According to SEM images, the N-CQDs/ $\text{BiOI}_x\text{Br}_{1-x}$  were nanosheets thickness of about 23 nm. HTEM results demonstrated the presence of lattice fringes and an average



diameter of about 7 nm. XPS result demonstrated that N-CQDs/BiOxBr1-x contained Bi, O, I, Br, C, and N elements. According to the Brunauer–Emmett–Teller (BET) analysis of N-CQDs/BiOxBr1-x, the large specific surface area was 20.97 m<sup>2</sup>/g. The N-CQDs/BiOxBr1-x was used as a photocatalyst for the degradation of phenol under visible light irradiation. The photocatalytic phenol degradation rate of N-CQDs/BiOxBr1-x was higher 98.7% than its composites. The enhancement of the photocatalytic activity of N-CQDs/BiOxBr1-x was due to the scattering of light and layered BiOxBr1-x, as well as the internal electric field from N-CQD to BiOxBr1-x.

## 5 CONCLUSION

After CQDs were discovered in 2004, there have been many investigations on their synthesis, properties, modifications, and applications due to their distinctive optical and electronic properties. This work focuses on recent progress on CQDs-related materials' synthesis, properties, and applications in photocatalysis. Many simple, low-cost, and scalable synthesis routes of CQDs-related materials have been devised. CQDs exhibited excellent sunlight harvesting ability, tunable PL, UCPL, and efficient photoexcited electron transfer. CQDs can act as a sole photocatalyst or enhance the photocatalytic activity of other photocatalysts as an electron mediator, a photosensitizer, and/or a spectral converter.

Despite significant improvement over the previous decade, various issues still require much investigation. Defects in CQDs modify their optical and electrical characteristics dramatically. Despite this, there are no established methodologies or tactics for dealing with CQD issues.

## REFERENCES

- Aggarwal, R., Saini, D., Singh, B., Kaushik, J., Garg, A. K., and Sonkar, S. K. (2020). Bitter Apple Peel Derived Photoactive Carbon Dots for the Sunlight Induced Photocatalytic Degradation of crystal Violet Dye. *Solar Energy* 197, 326–331. doi:10.1016/j.solener.2020.01.010
- An, M., Li, L., Wu, Q., Yu, H., Gao, X., Zu, W., et al. (2022). CdS QDs Modified Three-Dimensional Ordered Hollow Spherical ZnTiO<sub>3</sub>-ZnO-TiO<sub>2</sub> Composite with Improved Photocatalytic Performance. *J. Alloys Compounds* 895, 162638. doi:10.1016/j.jallcom.2021.162638
- Antaris, A. L., Robinson, J. T., Yaghi, O. K., Hong, G., Diao, S., Luong, R., et al. (2013). Ultra-Low Doses of Chirality Sorted (6,5) Carbon Nanotubes for Simultaneous Tumor Imaging and Photothermal Therapy. *ACS Nano* 7, 3644–3652. doi:10.1021/nn4006472
- Baker, S. N., and Baker, G. A. (2010). Luminescent Carbon Nanodots: Emergent Nanolights. *Angew. Chem. Int. Edition* 49, 6726–6744. doi:10.1002/anie.200906623
- Basit, M. A., Raza, F., Ali, G., Parveen, A., Khan, M., and Park, T. J. (2022). Nanoscale Modification of Carbon Fibers with CdS Quantum-Dot Sensitized TiO<sub>2</sub>: Photocatalytic and Photothermal Evaluation under Visible Irradiation. *Mater. Sci. Semiconductor Process.* 142, 106485. doi:10.1016/j.mssp.2022.106485
- Başoğlu, A., Ocak, Ü., and Gümrükçioğlu, A. (2020). Synthesis of Microwave-Assisted Fluorescence Carbon Quantum Dots Using Roasted-Chickpeas and its Applications for Sensitive and Selective Detection of Fe<sup>3+</sup> Ions. *J. Fluoresc.* 30, 515–526. doi:10.1007/s10895-019-02428-7
- Bhati, A., Anand, S. R., Gunture, G., Garg, A. K., Khare, P., and Sonkar, S. K. (2018). Sunlight-Induced Photocatalytic Degradation of Pollutant Dye by Highly
- Further research on CQD structure synthesis using dense and precise stages is required. CQD modification has sparked much interest in the scientific community. Many applications can benefit from better PL control and efficiency by readily functionalizing and doping CQDs. In the future, the mechanisms of CQD-associated phenotypes will be investigated. The UCPL mechanism of CQDs, for example, is currently unknown. As a result, additional research is needed to determine the photogenerated electron transfer route in the UCPL process. Due to UV absorption, photocatalytic CQDs have a low light-harvesting capability. CQDs that can be triggered in the visible or even in the near-infrared range can be created. This will aid heterogeneous photocatalysts in making use of the solar spectrum. Few studies have been conducted on the photostability of CQD-based nanocomposites, which are difficult to fabricate. The presence of oxygen groups on CQD surfaces may affect photocatalytic activity. The loss of oxygenic functional groups during photocatalysis doubts the photostability of CQD-based photocatalysts. As a result, CQDs will play a significant role in future photocatalytic devices. Innovative, cost-effective, and simple synthetic methodologies, as well as innovative photocatalytic applications for CQDs, will be developed.

## AUTHOR CONTRIBUTIONS

HJ and VS wrote the first draft of the review. AA, BS, and RP proposed and supervised the whole project and assisted in the writing process.

Fluorescent Red-Emitting Mg-N-Embedded Carbon Dots. *ACS Sustainable Chem. Eng.* 6, 9246–9256. doi:10.1021/acssuschemeng.8b01559

Bhunia, S. K., Saha, A., Maity, A. R., Ray, S. C., and Jana, N. R. (2013). Carbon Nanoparticle-Based Fluorescent Bioimaging Probes. *Sci. Rep.* 3, 1473. doi:10.1038/srep01473

Bian, J., Huang, C., Wang, L., Hung, T., Daoud, W. A., and Zhang, R. (2014). Carbon Dot Loading and TiO<sub>2</sub> Nanorod Length Dependence of Photoelectrochemical Properties in Carbon Dot/TiO<sub>2</sub> Nanorod Array Nanocomposites. *ACS Appl. Mater. Inter.* 6, 4883–4890. doi:10.1021/am4059183

Bourlinos, A. B., Karakassides, M. A., Kouloumpis, A., Gournis, D., Bakandritsos, A., Papagiannouli, I., et al. (2013). Synthesis, Characterization and Non-linear Optical Response of Organophilic Carbon Dots. *Carbon* 61, 640–643. doi:10.1016/j.carbon.2013.05.017

Bozentine, H., Meziane, S., Aziri, S., Berkane, N., Allam, D., Boudinar, S., et al. (2021). Facile and green Synthesis of a ZnO/CQDs/AgNPs Ternary Heterostructure Photocatalyst: Study of the Methylene Blue Dye Photodegradation. *Bull. Mater. Sci.* 44, 64. doi:10.1007/s12034-021-02353-1

Cao, A., Sang, L., Yu, Z., Zhao, Y., Wang, X., Wang, C., et al. (2022). Investigation of the Local Photothermal Effects by Fabricating a CQDs/Au/TiO<sub>2</sub> Photoelectrode in a PEC Water Splitting System. *Catal. Sci. Technol.* 2022. doi:10.1039/D1CY02113C

Chandrasekaran, P., Arul, V., and Sethuraman, M. G. (2020). Ecofriendly Synthesis of Fluorescent Nitrogen-Doped Carbon Dots from Coccinia Grandis and its Efficient Catalytic Application in the Reduction of Methyl Orange. *J. Fluoresc.* 30, 103–112. doi:10.1007/s10895-019-02474-1

Chang, B., Guo, Y., Liu, H., Li, L., and Yang, B. (2022). Engineering a Surface Defect-Rich Ti<sub>3</sub>C<sub>2</sub> Quantum Dots/mesoporous C<sub>3</sub>N<sub>4</sub> Hollow Nanosphere

- Schottky junction for Efficient N<sub>2</sub> Photofixation. *J. Mater. Chem. A* 10, 3134–3145. doi:10.1039/D1TA09941H
- Chen, B., Li, F., Li, S., Weng, W., Guo, H., Guo, T., et al. (2013a). Large Scale Synthesis of Photoluminescent Carbon Nanodots and Their Application for Bioimaging. *Nanoscale* 5, 1967. doi:10.1039/c2nr32675b
- Chen, H.-R., Meng, W.-M., Wang, R.-Y., Chen, F.-L., Li, T., Wang, D.-D., et al. (2022). Engineering Highly Graphitic Carbon Quantum Dots by Catalytic Dehydrogenation and Carbonization of Ti<sub>3</sub>C<sub>2</sub>T<sub>x</sub>-MXene Wrapped Polystyrene Spheres. *Carbon* 190, 319–328. doi:10.1016/j.carbon.2022.01.028
- Chen, Q.-L., Wang, C.-F., and Chen, S. (2013b). One-step Synthesis of Yellow-Emitting Carbogenic Dots toward white Light-Emitting Diodes. *J. Mater. Sci.* 48, 2352–2357. doi:10.1007/s10853-012-7016-8
- Chen, Q., Sheth, S., Zhao, Y., and Song, Q. (2019). A Novel Cyclometallated Iridium(III) Complex Based Dual-Mode Phosphorescent Probe for Detection of Acidity and Bovine Serum Albumin. *Anal. Methods* 11, 3033–3040. doi:10.1039/C9AY00878K
- Chen, X., Gao, H., Yang, M., Dong, W., Huang, X., Li, A., et al. (2018). Highly Graphitized 3D Network Carbon for Shape-Stabilized Composite PCMs with superior thermal Energy Harvesting. *Nano Energy* 49, 86–94. doi:10.1016/j.nanoen.2018.03.075
- Cheng, Y., Bai, M., Su, J., Fang, C., Li, H., Chen, J., et al. (2019). Synthesis of Fluorescent Carbon Quantum Dots from Aqua Mesophase Pitch and Their Photocatalytic Degradation Activity of Organic Dyes. *J. Mater. Sci. Technology* 35, 1515–1522. doi:10.1016/j.jmst.2019.03.039
- Cui, L., Ren, X., Wang, J., and Sun, M. (2020). Synthesis of Homogeneous Carbon Quantum Dots by Ultrafast Dual-Beam Pulsed Laser Ablation for Bioimaging. *Mater. Today Nano* 12, 100091. doi:10.1016/j.mtnano.2020.100091
- Das, G. S., Shim, J. P., Bhatnagar, A., Tripathi, K. M., and Kim, T. (2019). Biomass-derived Carbon Quantum Dots for Visible-Light-Induced Photocatalysis and Label-free Detection of Fe(III) and Ascorbic Acid. *Sci. Rep.* 9, 1–9. doi:10.1038/s41598-019-49266-y
- Deng, Y., Zhao, D., Chen, X., Wang, F., Song, H., and Shen, D. (2013). Long Lifetime Pure Organic Phosphorescence Based on Water Soluble Carbon Dots. *Chem. Commun.* 49, 5751. doi:10.1039/c3cc42600a
- Dhanush, C., and Sethuraman, M. G. (2020). Influence of Phyto-Derived Nitrogen Doped Carbon Dots from the Seeds of *Azadirachta indica* on the NaBH<sub>4</sub> Reduction of Safranin-O Dye. *Diamond Relat. Mater.* 108, 107984. doi:10.1016/j.diamond.2020.107984
- Doñate-Buendia, C., Torres-Mendieta, R., Pyatenko, A., Falomir, E., Fernández-Alonso, M., and Mínguez-Vega, G. (2018). Fabrication by Laser Irradiation in a Continuous Flow Jet of Carbon Quantum Dots for Fluorescence Imaging. *ACS Omega* 3, 2735–2742. doi:10.1021/acsomega.7b02082
- Dordević, L., Arcudi, F., Cacioppo, M., and Prato, M. (2022). A Multifunctional Chemical Toolbox to Engineer Carbon Dots for Biomedical and Energy Applications. *Nat. Nanotechnol.* 17, 112–130. doi:10.1038/s41565-021-01051-7
- El-Shamy, A. G. (2020a). An Efficient Removal of Methylene Blue Dye by Adsorption onto Carbon Dot @ Zinc Peroxide Embedded Poly Vinyl Alcohol (PVA/CZnO<sub>2</sub>) Nano-Composite: A Novel Reusable Adsorbent. *Polymer* 202, 122565. doi:10.1016/j.polymer.2020.122565
- El-Shamy, A. G. (2020b). New Carbon Quantum Dots Nano-Particles Decorated Zinc Peroxide (Cdots/ZnO<sub>2</sub>) Nano-Composite with superior Photocatalytic Efficiency for Removal of Different Dyes under UV-A Light. *Synth. Met.* 267, 116472. doi:10.1016/j.synthmet.2020.116472
- El-Shamy, A. G., and Zayied, H. S. S. (2020). New Polyvinyl Alcohol/carbon Quantum Dots (PVA/CQDs) Nanocomposite Films: Structural, Optical and Catalysis Properties. *Synth. Met.* 259, 116218. doi:10.1016/j.synthmet.2019.116218
- Fang, S., Xia, Y., Lv, K., Li, Q., Sun, J., and Li, M. (2016). Effect of Carbon-Dots Modification on the Structure and Photocatalytic Activity of G-C<sub>3</sub>N<sub>4</sub>. *Appl. Catal. B: Environ.* 185, 225–232. doi:10.1016/j.apcatb.2015.12.025
- Farshbaf, M., Davaran, S., Rahimi, F., Annabi, N., Salehi, R., and Akbarzadeh, A. (2018). Carbon Quantum Dots: Recent Progresses on Synthesis, Surface Modification and Applications. *Artif. Cell Nanomedicine, Biotechnol.* 46, 1331–1348. doi:10.1080/21691401.2017.1377725
- Feng, T., Ai, X., An, G., Yang, P., and Zhao, Y. (2016). Charge-Convertible Carbon Dots for Imaging-Guided Drug Delivery with Enhanced *In Vivo* Cancer Therapeutic Efficiency. *ACS Nano* 10, 4410–4420. doi:10.1021/acsnano.6b00043
- Gao, K., Gao, X., Zhu, W., Wang, C., Yan, T., Fu, F., et al. (2021). The Hierarchical Layered Microsphere of BiO<sub>1-x</sub>Br<sub>1-x</sub> Solid Solution Decorated with N-Doped CQDs with Enhanced Visible Light Photocatalytic Oxidation Pollutants. *Chem. Eng. J.* 406, 127155. doi:10.1016/j.cej.2020.127155
- Ghosh, D., Sarkar, K., Devi, P., Kim, K.-H., and Kumar, P. (2021). Current and Future Perspectives of Carbon and Graphene Quantum Dots: From Synthesis to Strategy for Building Optoelectronic and Energy Devices. *Renew. Sustainable Energy Rev.* 135, 110391. doi:10.1016/j.rser.2020.110391
- Gong, X., Gao, X., Du, W., Zhang, H., Zhang, S., Nguyen, T. T., et al. (2019). Wood Powder-Derived Quantum Dots for CeO<sub>2</sub> Photocatalytic and Anti-counterfeit Applications. *Opt. Mater.* 96, 109302. doi:10.1016/j.optmat.2019.109302
- Guo, X., Wang, C.-F., Yu, Z.-Y., Chen, L., and Chen, S. (2012). Facile Access to Versatile Fluorescent Carbon Dots toward Light-Emitting Diodes. *Chem. Commun.* 48, 2692–2694. doi:10.1039/c2cc17769b
- Guo, Y., Cao, F., and Li, Y. (2018). Solid Phase Synthesis of Nitrogen and Phosphor Co-doped Carbon Quantum Dots for Sensing Fe<sup>3+</sup> and the Enhanced Photocatalytic Degradation of Dyes. *Sensors Actuators B: Chem.* 255, 1105–1111. doi:10.1016/j.snb.2017.08.104
- Han, W., Li, D., Zhang, M., Ximin, H., Duan, X., Liu, S., et al. (2020). Photocatalytic Activation of Peroxymonosulfate by Surface-Tailored Carbon Quantum Dots. *J. Hazard. Mater.* 395, 122695. doi:10.1016/j.jhazmat.2020.122695
- Han, X., Han, Y., Huang, H., Zhang, H., Zhang, X., Liu, R., et al. (2013). Synthesis of Carbon Quantum dots/SiO<sub>2</sub> Porous Nanocomposites and Their Catalytic Ability for Photo-Enhanced Hydrocarbon Selective Oxidation. *Dalton Trans.* 42, 10380. doi:10.1039/c3dt51165k
- He, H., Huang, L., Zhong, Z., and Tan, S. (2018a). Constructing Three-Dimensional Porous Graphene-Carbon Quantum Dots/g-C<sub>3</sub>N<sub>4</sub> Nanosheet Aerogel Metal-free Photocatalyst with Enhanced Photocatalytic Activity. *Appl. Surf. Sci.* 441, 285–294. doi:10.1016/j.apsusc.2018.01.298
- He, M., Zhang, J., Wang, H., Kong, Y., Xiao, Y., and Xu, W. (2018b). Material and Optical Properties of Fluorescent Carbon Quantum Dots Fabricated from Lemon Juice via Hydrothermal Reaction. *Nanoscale Res. Lett.* 13, 175. doi:10.1186/s11671-018-2581-7
- He, Z., Liang, R., Zhou, C., Yan, G., and Wu, L. (2021). Carbon Quantum Dots (CQDs)/noble Metal Co-decorated MIL-53(Fe) as Difunctional Photocatalysts for the Simultaneous Removal of Cr(VI) and Dyes. *Separation Purif. Technology* 255, 117725. doi:10.1016/j.seppur.2020.117725
- Hou, J., Cheng, H., Yang, C., Takeda, O., and Zhu, H. (2015). Hierarchical Carbon Quantum Dots/hydrogenated-γ-TaON Heterojunctions for Broad Spectrum Photocatalytic Performance. *Nano Energy* 18, 143–153. doi:10.1016/j.nanoen.2015.09.005
- Hu, S.-L., Niu, K.-Y., Sun, J., Yang, J., Zhao, N.-Q., and Du, X.-W. (2009). One-step Synthesis of Fluorescent Carbon Nanoparticles by Laser Irradiation. *J. Mater. Chem.* 19, 484–488. doi:10.1039/B812943F
- Hu, S., Tian, R., Dong, Y., Yang, J., Liu, J., and Chang, Q. (2013a). Modulation and Effects of Surface Groups on Photoluminescence and Photocatalytic Activity of Carbon Dots. *Nanoscale* 5, 11665. doi:10.1039/c3nr03893a
- Hu, S., Tian, R., Wu, L., Zhao, Q., Yang, J., Liu, J., et al. (2013b). Chemical Regulation of Carbon Quantum Dots from Synthesis to Photocatalytic Activity. *Chem. Asian J.* 8, 1035–1041. doi:10.1002/asia.201300076
- Hu, Z., Xie, X., Li, S., Song, M., Liang, G., Zhao, J., et al. (2021). Rational Construct CQDs/BiO<sub>2</sub>COOH/uCN Photocatalyst with Excellent Photocatalytic Performance for Degradation of Sulfathiazole. *Chem. Eng. J.* 404, 126541. doi:10.1016/j.cej.2020.126541
- Jamila, G. S., Sajjad, S., Leghari, S. A. K., and Long, M. (2020a). Nitrogen Doped Carbon Quantum Dots and GO Modified WO<sub>3</sub> Nanosheets Combination as an Effective Visible Photo Catalyst. *J. Hazard. Mater.* 382, 121087. doi:10.1016/j.jhazmat.2019.121087
- Jamila, G. S., Sajjad, S., Leghari, S. A. K., and Mahmood, T. (2020b). Role of Nitrogen Doped Carbon Quantum Dots on CuO Nano-Leaves as Solar Induced Photo Catalyst. *J. Phys. Chem. Sol.* 138, 109233. doi:10.1016/j.jpcs.2019.109233
- Jana, J., Yoo, I. K., Chung, J. S., and Hur, S. H. (2020). Effect of Surfactant Surface Nature on the Energy Transfer Efficiency (η) of a Carbon Dot-Dye System. *Curr. Appl. Phys.* 20, 1058–1065. doi:10.1016/j.cap.2020.06.019
- Kang, C., Tao, S., Yang, F., and Yang, B. (2022). Aggregation and Luminescence in Carbonized Polymer Dots. *Aggregate* 2022, e169. doi:10.1002/AGT2.169

- Kleinauskas, A., Rocha, S., Sahu, S., Sun, Y.-P., and Juzenas, P. (2013). Carbon-core Silver-Shell Nanodots as Sensitizers for Phototherapy and Radiotherapy. *Nanotechnology* 24, 325103. doi:10.1088/0957-4484/24/32/325103
- Li, D., Huang, J., Li, R., Chen, P., Chen, D., Cai, M., et al. (2021). Synthesis of a Carbon Dots Modified G-C<sub>3</sub>N<sub>4</sub>/SnO<sub>2</sub> Z-Scheme Photocatalyst with superior Photocatalytic Activity for PPCPs Degradation under Visible Light Irradiation. *J. Hazard. Mater.* 401, 123257. doi:10.1016/j.jhazmat.2020.123257
- Li, H., Kang, Z., Liu, Y., and Lee, S.-T. (2012). Carbon Nanodots: Synthesis, Properties and Applications. *J. Mater. Chem.* 22, 24230. doi:10.1039/c2jm34690g
- Li, M., Wang, M., Zhu, L., Li, Y., Yan, Z., Shen, Z., et al. (2018). Facile Microwave Assisted Synthesis of N-Rich Carbon Quantum Dots/dual-phase TiO<sub>2</sub> Heterostructured Nanocomposites with High Activity in CO<sub>2</sub> Photoreduction. *Appl. Catal. B: Environ.* 231, 269–276. doi:10.1016/j.apcatb.2018.03.027
- Li, X., Rui, M., Song, J., Shen, Z., and Zeng, H. (2015). Carbon and Graphene Quantum Dots for Optoelectronic and Energy Devices: A Review. *Adv. Funct. Mater.* 25, 4929–4947. doi:10.1002/adfm.201501250
- Li, X., Wang, H., Shimizu, Y., Pyatenko, A., Kawaguchi, K., and Koshizaki, N. (2011a). Preparation of Carbon Quantum Dots with Tunable Photoluminescence by Rapid Laser Passivation in Ordinary Organic Solvents. *Chem. Commun.* 47, 932–934. doi:10.1039/C0CC03552A
- Li, Y., Hu, Y., Zhao, Y., Shi, G., Deng, L., Hou, Y., et al. (2011b). An Electrochemical Avenue to Green-Luminescent Graphene Quantum Dots as Potential Electron-Acceptors for Photovoltaics. *Adv. Mater.* 23, 776–780. doi:10.1002/adma.201003819
- Liang, C., Wang, C., Xu, K., He, H., Li, Q., Yang, C., et al. (2022). N-CQDs Act as Electronic Warehouse in N-CQDs/CdS Regulate Adsorption Energy to Promote Photocatalytic Selective Oxidation of Aromatic Alcohols. *Colloids Surf. A: Physicochemical Eng. Aspects* 641, 128559. doi:10.1016/j.colsurfa.2022.128559
- Liang, H., Tai, X., Du, Z., and Yin, Y. (2020). Enhanced Photocatalytic Activity of ZnO Sensitized by Carbon Quantum Dots and Application in Phenol Wastewater. *Opt. Mater.* 100, 109674. doi:10.1016/j.optmat.2020.109674
- Liang, Q., Ma, W., Shi, Y., Li, Z., and Yang, X. (2013). Easy Synthesis of Highly Fluorescent Carbon Quantum Dots from Gelatin and Their Luminescent Properties and Applications. *Carbon* 60, 421–428. doi:10.1016/j.carbon.2013.04.055
- Liang, Y., Xu, W., Fang, J., Liu, Z., Chen, D., Pan, T., et al. (2021). Highly Dispersed Bismuth Oxide Quantum Dots/graphite Carbon Nitride Nanosheets Heterojunctions for Visible Light Photocatalytic Redox Degradation of Environmental Pollutants. *Appl. Catal. B: Environ.* 295, 120279. doi:10.1016/j.apcatb.2021.120279
- Lin, Z., Xue, W., Chen, H., and Lin, J.-M. (2012). Classical Oxidant Induced Chemiluminescence of Fluorescent Carbon Dots. *Chem. Commun.* 48, 1051–1053. doi:10.1039/C1CC15290D
- Lin, Z., Xue, W., Chen, H., and Lin, J.-M. (2011). Peroxynitrous-Acid-Induced Chemiluminescence of Fluorescent Carbon Dots for Nitrite Sensing. *Anal. Chem.* 83, 8245–8251. doi:10.1021/ac202039h
- Liu, R., Huang, H., Li, H., Liu, Y., Zhong, J., Li, Y., et al. (2014). Metal Nanoparticle/Carbon Quantum Dot Composite as a Photocatalyst for High-Efficiency Cyclohexane Oxidation. *ACS Catal.* 4, 328–336. doi:10.1021/cs400913h
- Liu, W., Li, C., Ren, Y., Sun, X., Pan, W., Li, Y., et al. (2016). Carbon Dots: Surface Engineering and Applications. *J. Mater. Chem. B* 4, 5772–5788. doi:10.1039/C6TB00976j
- Liu, Y., Zhu, C., Sun, J., Ge, Y., Song, F., Wang, G., et al. (2021). Efficient Photocatalytic Degradation of Volatile Organic Compounds over Carbon Quantum Dots Decorated Bi<sub>2</sub>WO<sub>6</sub> under Visible Light. *Environ. Sci. Pollut. Res.* 28, 25949–25958. doi:10.1007/s11356-020-12273-y
- Lu, M., and Zhou, L. (2019). One-step Sonochemical Synthesis of Versatile Nitrogen-Doped Carbon Quantum Dots for Sensitive Detection of Fe<sup>2+</sup> Ions and Temperature. *In Vitro. Mater. Sci. Eng. C* 101, 352–359. doi:10.1016/j.msec.2019.03.109
- Ma, C.-B., Zhu, Z.-T., Wang, H.-X., Huang, X., Zhang, X., Qi, X., et al. (2015). A General Solid-State Synthesis of Chemically-Doped Fluorescent Graphene Quantum Dots for Bioimaging and Optoelectronic Applications. *Nanoscale* 7, 10162–10169. doi:10.1039/C5NR01757B
- Mahmood, A., Shi, G., Wang, Z., Rao, Z., Xiao, W., Xie, X., et al. (2021). Carbon Quantum Dots-TiO<sub>2</sub> Nanocomposite as an Efficient Photocatalyst for the Photodegradation of Aromatic Ring-Containing Mixed VOCs: An Experimental and DFT Studies of Adsorption and Electronic Structure of the Interface. *J. Hazard. Mater.* 401, 123402. doi:10.1016/j.jhazmat.2020.123402
- Mathew, R. M., John, J., Zachariah, E. S., Jose, J., Titus, T., Abraham, R., et al. (2020). Metal Free, Phosphorus Doped Carbon Nanodot Mediated Photocatalytic Reduction of Methylene Blue. *Reac. Kinet. Mech. Cat* 129, 1131–1143. doi:10.1007/s11144-020-01724-9
- Miao, X., Yue, X., Ji, Z., Shen, X., Zhou, H., Liu, M., et al. (2018a). Nitrogen-doped Carbon Dots Decorated on G-C<sub>3</sub>N<sub>4</sub>/Ag<sub>3</sub>PO<sub>4</sub> Photocatalyst with Improved Visible Light Photocatalytic Activity and Mechanism Insight. *Appl. Catal. B: Environ.* 227, 459–469. doi:10.1016/j.apcatb.2018.01.057
- Miao, X., Yue, X., Shen, X., Ji, Z., Zhou, H., Zhu, G., et al. (2018b). Nitrogen-doped Carbon Dot-Modified Ag<sub>3</sub>PO<sub>4</sub>/GO Photocatalyst with Excellent Visible-Light-Driven Photocatalytic Performance and Mechanism Insight. *Catal. Sci. Technol.* 8, 632–641. doi:10.1039/c7cy01883e
- Midya, L., Sarkar, A. N., Das, R., Maity, A., and Pal, S. (2020). Crosslinked Chitosan Embedded TiO<sub>2</sub> NPs and Carbon Dots-Based Nanocomposite: An Excellent Photocatalyst under Sunlight Irradiation. *Int. J. Biol. Macromolecules* 164, 3676–3686. doi:10.1016/j.ijbiomac.2020.08.230
- Murali, G., Modigunta, J. K. R., Park, S., Lee, S., Lee, H., Yeon, J., et al. (2021). Enhancing Light Absorption and Prolonging Charge Separation in Carbon Quantum Dots via Cl-Doping for Visible-Light-Driven Photocharge-Transfer Reactions. *ACS Appl. Mater. Inter.* 13, 34648–34657. doi:10.1021/acsami.1c01879
- Nayak, S., Prasad, S. R., Mandal, D., and Das, P. (2020). Carbon Dot Cross-Linked Polyvinylpyrrolidone Hybrid Hydrogel for Simultaneous Dye Adsorption, Photodegradation and Bacterial Elimination from Waste Water. *J. Hazard. Mater.* 392, 122287. doi:10.1016/j.jhazmat.2020.122287
- Ni, T., Li, Q., Yan, Y., Wang, F., Cui, X., Yang, Z., et al. (2020). N,fe-doped Carbon Dot Decorated Gear-Shaped Wo<sub>3</sub> for Highly Efficient UV-VIS-NIR-Driven Photocatalytic Performance. *Catalysts* 10, 416. doi:10.3390/catal10040416
- Nie, H., Liu, Y., Li, Y., Wei, K., Wu, Z., Shi, H., et al. (2021). *In-situ* Transient Photovoltage Study on Interface Electron Transfer Regulation of Carbon dots/ NiCo<sub>2</sub>O<sub>4</sub> Photocatalyst for the Enhanced Overall Water Splitting Activity. *Nano Res.* 15, 1786–1795. doi:10.1007/s12274-021-3723-2
- Omer, K. M., Mohammad, N. N., and Baban, S. O. (2018). Up-Conversion Fluorescence of Phosphorous and Nitrogen Co-doped Carbon Quantum Dots (CDs) Coupled with Weak LED Light Source for Full-Spectrum Driven Photocatalytic Degradation via ZnO-CDs Nanocomposites. *Catal. Lett.* 148, 2746–2755. doi:10.1007/s10562-018-2459-4
- Ouyang, H., Huang, H., Wang, H., and Zheng, X. (2020). The Morphology Evolution of Nitrogen-Doped Carbon Quantum Dots/hollow TiO<sub>2</sub> Composites and Their Applications in Photocatalysis. *J. Mater. Sci.* 55, 976–989. doi:10.1007/s10853-019-03991-x
- Patra, A. S., Gogoi, G., and Qureshi, M. (2018). Ordered-Disordered BaZrO<sub>3</sub>- $\delta$  Hollow Nanosphere/Carbon Dot Hybrid Nanocomposite: A New Visible-Light-Driven Efficient Composite Photocatalyst for Hydrogen Production and Dye Degradation. *ACS Omega* 3, 10980–10991. doi:10.1021/acsomega.8b01577
- Peng, H., and Travas-Sejdic, J. (2009). Simple Aqueous Solution Route to Luminescent Carbogenic Dots from Carbohydrates. *Chem. Mater.* 21, 5563–5565. doi:10.1021/cm901593y
- Peng, P., Chen, Z., Li, X., Wu, Y., Xia, Y., Duan, A., et al. (2022). Biomass-Derived Carbon Quantum Dots Modified Bi<sub>2</sub>mo<sub>6</sub>/Bi<sub>2</sub>s<sub>3</sub> Heterojunction for Efficient Photocatalytic Removal of Organic Pollutants and Cr(VI). *SSRN J.* 2022. doi:10.2139/ssrn.4028414
- Peng, Z., Zhou, Y., Ji, C., Pardo, J., Mintz, K. J., Pandey, R. R., et al. (2020). Facile Synthesis of "Boron-Doped" Carbon Dots and Their Application in Visible-Light-Driven Photocatalytic Degradation of Organic Dyes. *Nanomaterials* 10, 1560–1617. doi:10.3390/nano10081560
- Pooremaeil, M., Namazi, H., and Salehi, R. (2022). Dual Anticancer Drug Delivery of D-Galactose-Functionalized Stimuli-Responsive Nanogels for Targeted Therapy of the Liver Hepatocellular Carcinoma. *Eur. Polym. J.* 167, 111061. doi:10.1016/j.eurpolymj.2022.111061
- Preethi, M., Viswanathan, C., and Ponpandian, N. (2022). A Metal-free, Dual Catalyst for the Removal of Rhodamine B Using Novel Carbon Quantum Dots from Muskmelon Peel under Sunlight and Ultrasonication: A green Way to Clean the Environment. *J. Photochem. Photobiol. A: Chem.* 426, 113765. doi:10.1016/j.jphotochem.2021.113765



- Qi, C., Wang, H., Yang, A., Wang, X., and Xu, J. (2021). Facile Fabrication of Highly Fluorescent N-Doped Carbon Quantum Dots Using an Ultrasonic-Assisted Hydrothermal Method: Optical Properties and Cell Imaging. *ACS Omega* 6, 32904–32916. doi:10.1021/acsomega.1c04903
- Qu, D., Zheng, M., Du, P., Zhou, Y., Zhang, L., Li, D., et al. (2013). Highly Luminescent S, N Co-doped Graphene Quantum Dots with Broad Visible Absorption Bands for Visible Light Photocatalysts. *Nanoscale* 5, 12272. doi:10.1039/c3nr04402e
- Qu, Z., Wang, J., Tang, J., Shu, X., Liu, X., Zhang, Z., et al. (2018). Carbon Quantum dots/KNbO<sub>3</sub> Hybrid Composites with Enhanced Visible-Light Driven Photocatalytic Activity toward Dye Waste-Water Degradation and Hydrogen Production. *Mol. Catal.* 445, 1–11. doi:10.1016/j.mcat.2017.11.002
- Raj, S. K., Rathod, N. H., Tripathi, B., Patidar, R., and Kulshrestha, V. (2021). Fluorescence Properties of Yellow Light Emitting Carbon Quantum Dots and Their Application for Effective Recognition of Heavy Metal Ions in Aqueous Medium. *Nano Select* 2, 2432–2439. doi:10.1002/nano.202100127
- Ramar, V., Moothattu, S., and Balasubramanian, K. (2018). Metal Free, Sunlight and white Light Based Photocatalysis Using Carbon Quantum Dots from Citrus Grandis: A green Way to Remove Pollution. *Solar Energy* 169, 120–127. doi:10.1016/j.solener.2018.04.040
- Rani, U. A., Ng, L. Y., Ng, C. Y., Mahmoudi, E., Ng, Y.-S., and Mohammad, A. W. (2021). Sustainable Production of Nitrogen-Doped Carbon Quantum Dots for Photocatalytic Degradation of Methylene Blue and Malachite green. *J. Water Process Eng.* 40, 101816. doi:10.1016/j.jwpe.2020.101816
- Ratnayake, S. P., Mantilaka, M. M. M. G. P. G., Sandaruwan, C., Dahanayake, D., Murugan, E., Kumar, S., et al. (2019). Carbon Quantum Dots-Decorated Nano-Zirconia: A Highly Efficient Photocatalyst. *Appl. Catal. A: Gen.* 570, 23–30. doi:10.1016/j.apcata.2018.10.022
- Ray, S. C., Saha, A., Jana, N. R., and Sarkar, R. (2009). Fluorescent Carbon Nanoparticles: Synthesis, Characterization, and Bioimaging Application. *J. Phys. Chem. C* 113, 18546–18551. doi:10.1021/jp905912n
- Rosiles-Perez, C., Serrano-Estrada, M. A., Sidhik, S., Alatorre-Ordaz, A., Torres-Castro, A., Vallejo, M. A., et al. (2020). Synthesis of High Quality PbS Colloidal Quantum Dots by Ultrasonic bath as Photosensitizers in a TiO<sub>2</sub> Solar Cell. *J. Solid State. Chem.* 292, 121720. doi:10.1016/j.jssc.2020.121720
- Roushani, M., Mavaei, M., and Rajabi, H. R. (2015). Graphene Quantum Dots as Novel and green Nano-Materials for the Visible-Light-Driven Photocatalytic Degradation of Cationic Dye. *J. Mol. Catal. A: Chem.* 409, 102–109. doi:10.1016/j.molcata.2015.08.011
- Saeidi, S., Rezaei, B., and Ensafi, A. A. (2022). Fabrication and Characterization of Upconversion N-Doped Graphene Quantum Dots for Improving Photoelectrocatalytic Performance of Rutile Hierarchical TiO<sub>2</sub> Nanowires under Visible and Near-Infrared Light Irradiations. *Mater. Today Chem.* 23, 100742. doi:10.1016/j.mtchem.2021.100742
- Selim, A., Kaur, S., Dar, A. H., Sartaliya, S., and Jayamurugan, G. (2020). Synergistic Effects of Carbon Dots and Palladium Nanoparticles Enhance the Sonocatalytic Performance for Rhodamine B Degradation in the Absence of Light. *ACS Omega* 5, 22603–22613. doi:10.1021/acsomega.0c03312
- Seng, R. X., Tan, L.-L., Lee, W. P. C., Ong, W.-J., and Chai, S.-P. (2020). Nitrogen-doped Carbon Quantum Dots-Decorated 2D Graphitic Carbon Nitride as a Promising Photocatalyst for Environmental Remediation: A Study on the Importance of Hybridization Approach. *J. Environ. Manage.* 255, 109936. doi:10.1016/j.jenvman.2019.109936
- Shen, C.-L., Lou, Q., Liu, K.-K., Dong, L., and Shan, C.-X. (2020). Chemiluminescent Carbon Dots: Synthesis, Properties, and Applications. *Nano Today* 35, 100954. doi:10.1016/j.nantod.2020.100954
- Su, Y., Xu, X., Li, R., Luo, X., Yao, H., Fang, S., et al. (2022). Design and Fabrication of a CdS QDs/Bi<sub>2</sub>WO<sub>6</sub> Monolayer S-Scheme Heterojunction Configuration for Highly Efficient Photocatalytic Degradation of Trace Ethylene in Air. *Chem. Eng. J.* 429, 132241. doi:10.1016/j.cej.2021.132241
- Sun, Y.-P., Zhou, B., Lin, Y., Wang, W., Fernando, K. A. S., Pathak, P., et al. (2006). Quantum-Sized Carbon Dots for Bright and Colorful Photoluminescence. *J. Am. Chem. Soc.* 128, 7756–7757. doi:10.1021/ja062677d
- Suzuki, K., Malfatti, L., Carboni, D., Loche, D., Casula, M., Moretto, A., et al. (2015). Energy Transfer Induced by Carbon Quantum Dots in Porous Zinc Oxide Nanocomposite Films. *J. Phys. Chem. C* 119, 2837–2843. doi:10.1021/jp510661d
- Syed, N., Huang, J., and Feng, Y. (2021). CQDs as Emerging Trends for Future prospect in Enhancement of Photocatalytic Activity. *Carbon Lett.* 32, 81–97. doi:10.1007/s42823-021-00282-x
- Tan, C., Zuo, S., Zhao, Y., and Shen, B. (2019). Preparation of Multicolored Carbon Quantum Dots Using HNO<sub>3</sub>/HClO<sub>4</sub> Oxidation of Graphitized Carbon. *J. Mater. Res.* 34, 3428–3438. doi:10.1557/jmr.2019.261
- Tan, J., Zhang, J., Li, W., Zhang, L., and Yue, D. (2016a). Synthesis of Amphiphilic Carbon Quantum Dots with Phosphorescence Properties and Their Multifunctional Applications. *J. Mater. Chem. C* 4, 10146–10153. doi:10.1039/C6TC03027K
- Tan, J., Zou, R., Zhang, J., Li, W., Zhang, L., and Yue, D. (2016b). Large-scale Synthesis of N-Doped Carbon Quantum Dots and Their Phosphorescence Properties in a Polyurethane Matrix. *Nanoscale* 8, 4742–4747. doi:10.1039/C5NR08516K
- Tang, D., Zhang, H., Huang, H., Liu, R., Han, Y., Liu, Y., et al. (2013a). Carbon Quantum Dots Enhance the Photocatalytic Performance of BiVO<sub>4</sub> with Different Exposed Facets. *Dalton Trans.* 42, 6285. doi:10.1039/c3dt50567g
- Tang, J., Kong, B., Wu, H., Xu, M., Wang, Y., Wang, Y., et al. (2013b). Carbon Nanodots Featuring Efficient FRET for Real-Time Monitoring of Drug Delivery and Two-Photon Imaging. *Adv. Mater.* 25, 6569–6574. doi:10.1002/adma.201303124
- Tang, J., Zhang, J., Zhang, W., Xiao, Y., Shi, Y., Kong, F., et al. (2021). Modulation of Red-Light Emission from Carbon Quantum Dots in Acid-Based Environment and the Detection of Chromium (III) Ions. *J. Mater. Sci. Technology* 83, 58–65. doi:10.1016/j.jmst.2020.11.072
- Tang, L., Ji, R., Cao, X., Lin, J., Jiang, H., Li, X., et al. (2012). Deep Ultraviolet Photoluminescence of Water-Soluble Self-Passivated Graphene Quantum Dots. *ACS Nano* 6, 5102–5110. doi:10.1021/nn300760g
- Teng, P., Xie, J., Long, Y., Huang, X., Zhu, R., Wang, X., et al. (2014). Chemiluminescence Behavior of the Carbon Dots and the Reduced State Carbon Dots. *J. Lumin.* 146, 464–469. doi:10.1016/j.jlumin.2013.09.036
- Tian, L., Ghosh, D., Chen, W., Pradhan, S., Chang, X., and Chen, S. (2009). Nanosized Carbon Particles from Natural Gas Soot. *Chem. Mater.* 21, 2803–2809. doi:10.1021/cm900709w
- Tyagi, A., Tripathi, K. M., Singh, N., Choudhary, S., and Gupta, R. K. (2016). Green Synthesis of Carbon Quantum Dots from Lemon Peel Waste: Applications in Sensing and Photocatalysis. *RSC Adv.* 6, 72423–72432. doi:10.1039/c6ra10488f
- Vassalini, I., Gjipalaj, J., Crespi, S., Gianoncelli, A., Mella, M., Ferroni, M., et al. (2020). Alginate-Derived Active Blend Enhances Adsorption and Photocatalytic Removal of Organic Pollutants in Water. *Adv. Sustainable Syst.* 4, 1900112. doi:10.1002/adsu.201900112
- Velumani, A., Sengodan, P., Arumugam, P., Rajendran, R., Santhanam, S., and Palanisamy, M. (2020). Carbon Quantum Dots Supported ZnO Sphere Based Photocatalyst for Dye Degradation Application. *Curr. Appl. Phys.* 20, 1176–1184. doi:10.1016/j.cap.2020.07.016
- Wang, D. M., Lin, K. L., and Huang, C. Z. (2019). Carbon Dots-Involved Chemiluminescence: Recent Advances and Developments. *Luminescence* 34, 4–22. doi:10.1002/bio.3570
- Wang, Q., Li, J., Tu, X., Liu, H., Shu, M., Si, R., et al. (2020). Single Atomically Anchored Cobalt on Carbon Quantum Dots as Efficient Photocatalysts for Visible Light-Promoted Oxidation Reactions. *Chem. Mater.* 32, 734–743. doi:10.1021/acs.chemmater.9b03708
- Wang, X., Cao, L., Lu, F., Mezzani, M. J., Li, H., Qi, G., et al. (2009). Photoinduced Electron Transfers with Carbon Dots. *Chem. Commun.* 2009, 3774–3776. doi:10.1039/b906252a
- Wang, Y., and Hu, A. (2014). Carbon Quantum Dots: Synthesis, Properties and Applications. *J. Mater. Chem. C* 2, 6921. doi:10.1039/C4TC00988F
- Wu, Y., Liu, Y., Yin, J., Li, H., and Huang, J. (2019). Facile Ultrasonic Synthesized NH<sub>2</sub>-carbon Quantum Dots for Ultrasensitive Co<sup>2+</sup> Ion Detection and Cell Imaging. *Talanta* 205, 120121. doi:10.1016/j.talanta.2019.120121
- Xu, X., Ray, R., Gu, Y., Ploehn, H. J., Gearheart, L., Raker, K., et al. (2004). Electrophoretic Analysis and Purification of Fluorescent Single-Walled Carbon Nanotube Fragments. *J. Am. Chem. Soc.* 126, 12736–12737. doi:10.1021/ja040082h
- Yang, P., Zhu, Z., Chen, M., Chen, W., and Zhou, X. (2018). Microwave-assisted Synthesis of Xylan-Derived Carbon Quantum Dots for Tetracycline Sensing. *Opt. Mater.* 85, 329–336. doi:10.1016/j.optmat.2018.06.034
- Yang, S.-T., Cao, L., Luo, P. G., Lu, F., Wang, X., Wang, H., et al. (2009). Carbon Dots for Optical Imaging *In Vivo*. *J. Am. Chem. Soc.* 131, 11308–11309. doi:10.1021/ja904843x



- Yang, S.-T., Wang, X., Wang, H., Lu, F., Luo, P. G., Cao, L., et al. (2009a). Carbon Dots as Nontoxic and High-Performance Fluorescence Imaging Agents. *J. Phys. Chem. C* 113, 18110–18114. doi:10.1021/jp9085969
- Yao, J., Yang, L., Huang, L., Wang, C., Liu, J., Huang, L., et al. (2022). Construction of a N-P Type Bi12O15Cl6@BiOI-CQDs junction with Core-Shell Structure for Boosting Photocatalytic Degradation and Antibacterial Performance. *Appl. Surf. Sci.* 578, 151913. doi:10.1016/j.apsusc.2021.151913
- Yu, H., Shi, R., Zhao, Y., Waterhouse, G. I. N., Wu, L.-Z., Tung, C.-H., et al. (2016). Smart Utilization of Carbon Dots in Semiconductor Photocatalysis. *Adv. Mater.* 28, 9454–9477. doi:10.1002/adma.201602581
- Yu, H., Zhang, H., Huang, H., Liu, Y., Li, H., Ming, H., et al. (2012). ZnO/carbon Quantum Dots Nanocomposites: One-step Fabrication and superior Photocatalytic Ability for Toxic Gas Degradation under Visible Light at Room Temperature. *New J. Chem.* 36, 1031. doi:10.1039/c2nj20959d
- Yu, J., Wang, X., Chen, L., Lu, G., Shi, G., Xie, X., et al. (2022). Enhanced Adsorption and Visible-Light Photocatalytic Degradation of Toluene by CQDs/UiO-66 MOG with Hierarchical Pores. *Chem. Eng. J.* 435, 135033. doi:10.1016/j.cej.2022.135033
- Yu, T., Wang, H., Guo, C., Zhai, Y., Yang, J., and Yuan, J. (2018). A Rapid Microwave Synthesis of green-emissive Carbon Dots with Solid-State Fluorescence and pH-Sensitive Properties. *R. Soc. Open Sci.* 5, 180245. doi:10.1098/rsos.180245
- Yuan, T., Meng, T., Shi, Y., Song, X., Xie, W., Li, Y., et al. (2022). Toward Phosphorescent and Delayed Fluorescent Carbon Quantum Dots for Next-Generation Electroluminescent Displays. *J. Mater. Chem. C* 10, 2333–2348. doi:10.1039/D1TC04271H
- Zaib, M., Akhtar, A., Maqsood, F., and Shahzadi, T. (2021). Green Synthesis of Carbon Dots and Their Application as Photocatalyst in Dye Degradation Studies. *Arab. J. Sci. Eng.* 46, 437–446. doi:10.1007/s13369-020-04904-w
- Zhang, J., Cao, Y., Zhao, P., Xie, T., Lin, Y., and Mu, Z. (2020). Visible-light-driven Pollutants Degradation with Carbon Quantum dots/N-TiO<sub>2</sub> under Mild Condition: Facile Preparation, Dramatic Performance and Deep Mechanism Insight. *Colloids Surf. A: Physicochemical Eng. Aspects* 601, 125019. doi:10.1016/j.colsurfa.2020.125019
- Zhang, J., and Dai, L. (2016). Nitrogen, Phosphorus, and Fluorine Tri-doped Graphene as a Multifunctional Catalyst for Self-Powered Electrochemical Water Splitting. *Angew. Chem. Int. Ed.* 55, 13296–13300. doi:10.1002/anie.201607405
- Zhang, K., Zhou, M., Yang, K., Yu, C., Mu, P., Yu, Z., et al. (2022). Photocatalytic H<sub>2</sub>O<sub>2</sub> Production and Removal of Cr (VI) via a Novel Lu<sub>3</sub>NbO<sub>7</sub>: Yb, Ho/CQDs/AgInS<sub>2</sub>/In<sub>2</sub>S<sub>3</sub> Heterostructure with Broad Spectral Response. *J. Hazard. Mater.* 423, 127172. doi:10.1016/j.jhazmat.2021.127172
- Zhang, L., Zhang, J., Xia, Y., Xun, M., Chen, H., Liu, X., et al. (2020). Metal-free Carbon Quantum Dots Implant Graphitic Carbon Nitride: Enhanced Photocatalytic Dye Wastewater Purification with Simultaneous Hydrogen Production. *Ijms* 21, 1052. doi:10.3390/ijms21031052
- Zhang, Y.-Q., Ma, D.-K., Zhang, Y.-G., Chen, W., and Huang, S.-M. (2013). N-doped Carbon Quantum Dots for TiO<sub>2</sub>-Based Photocatalysts and Dye-Sensitized Solar Cells. *Nano Energy* 2, 545–552. doi:10.1016/j.nanoen.2013.07.010
- Zhao, F., Rong, Y., Wan, J., Hu, Z., Peng, Z., and Wang, B. (2018). High Photocatalytic Performance of Carbon Quantum dots/TNTs Composites for Enhanced Photogenerated Charges Separation under Visible Light. *Catal. Today* 315, 162–170. doi:10.1016/j.cattod.2018.02.019
- Zhao, L., Di, F., Wang, D., Guo, L.-H., Yang, Y., Wan, B., et al. (2013). Chemiluminescence of Carbon Dots under strong Alkaline Solutions: a Novel Insight into Carbon Dot Optical Properties. *Nanoscale* 5, 2655. doi:10.1039/c3nr00358b
- Zhao, Q., Zhang, Z., Yan, T., Guo, L., Yang, C., Gao, G., et al. (2021). Synergism of Carbon Quantum Dots and Au Nanoparticles with Bi<sub>2</sub>MoO<sub>6</sub> for Activity Enhanced Photocatalytic Oxidative Degradation of Phenol. *RSC Adv.* 11, 28674–28684. doi:10.1039/D1RA05164D
- Zhou, J., Booker, C., Li, R., Zhou, X., Sham, T.-K., Sun, X., et al. (2007). An Electrochemical Avenue to Blue Luminescent Nanocrystals from Multiwalled Carbon Nanotubes (MWCNTs). *J. Am. Chem. Soc.* 129, 744–745. doi:10.1021/ja0669070
- Zhou, Q., Yuan, G., Lin, M., Wang, P., Li, S., Tang, J., et al. (2021). Large-scale Electrochemical Fabrication of Nitrogen-Doped Carbon Quantum Dots and Their Application as Corrosion Inhibitor for Copper. *J. Mater. Sci.* 56, 12909–12919. doi:10.1007/s10853-021-06102-x
- Zhu, H., Wang, X., Li, Y., Wang, Z., Yang, F., and Yang, X. (2009). Microwave Synthesis of Fluorescent Carbon Nanoparticles with Electrochemiluminescence Properties. *Chem. Commun.* 5118, 5118. doi:10.1039/b907612c
- Zhu, J., Wu, C., Cui, Y., Li, D., Zhang, Y., Xu, J., et al. (2021a). Blue-emitting Carbon Quantum Dots: Ultrafast Microwave Synthesis, Purification and strong Fluorescence in Organic Solvents. *Colloids Surf. A: Physicochemical Eng. Aspects* 623, 126673. doi:10.1016/j.colsurfa.2021.126673
- Zhu, S., Meng, Q., Wang, L., Zhang, J., Song, Y., Jin, H., et al. (2013). Highly Photoluminescent Carbon Dots for Multicolor Patterning, Sensors, and Bioimaging. *Angew. Chem.* 125, 4045–4049. doi:10.1002/ange.201300519
- Zhu, W., Mi, J., Fu, Y., Cui, D., and Lü, C. (2021b). Multiple-cores@shell Clustered Carbon dots/P25/rGO Nanocomposite as Robust Visible-Light Photocatalyst for Organic Pollutant Degradation and Water Disinfection. *Appl. Surf. Sci.* 538, 148087. doi:10.1016/j.apsusc.2020.148087
- Zhu, Z., Yang, P., Li, X., Luo, M., Zhang, W., Chen, M., et al. (2020). Green Preparation of palm Powder-Derived Carbon Dots Co-doped with Sulfur/chlorine and Their Application in Visible-Light Photocatalysis. *Spectrochimica Acta A: Mol. Biomol. Spectrosc.* 227, 117659. doi:10.1016/j.saa.2019.117659

**Conflict of Interest:** AA was employed by Aadarsh Innovations.

The remaining authors declare that the research was conducted in the absence of any commercial or financial relationships that could be construed as a potential conflict of interest.

**Publisher's Note:** All claims expressed in this article are solely those of the authors and do not necessarily represent those of their affiliated organizations or those of the publisher, the editors, and the reviewers. Any product that may be evaluated in this article, or claim that may be made by its manufacturer, is not guaranteed or endorsed by the publisher.

Copyright © 2022 Jung, Sapner, Adhikari, Sathe and Patel. This is an open-access article distributed under the terms of the Creative Commons Attribution License (CC BY). The use, distribution or reproduction in other forums is permitted, provided the original author(s) and the copyright owner(s) are credited and that the original publication in this journal is cited, in accordance with accepted academic practice. No use, distribution or reproduction is permitted which does not comply with these terms.



# Electrocatalytic Water Oxidation: An Overview With an Example of Translation From Lab to Market

Rakesh Sen<sup>1</sup>, Supriya Das<sup>1</sup>, Aritra Nath<sup>1</sup>, Priyanka Maharana<sup>1</sup>, Pradipta Kar<sup>2</sup>, Francis Verpoort<sup>2,3,4\*</sup>, Pei Liang<sup>2\*</sup> and Soumyajit Roy<sup>1,2\*</sup>

<sup>1</sup>Eco-Friendly Applied Materials Laboratory (EFAML), Department of Chemical Sciences, Materials Science Centre, Indian Institute of Science Education and Research- Kolkata, Kolkata, India, <sup>2</sup>Solaire Initiative Private Limited, Bhubaneswar and Kolkata, India, <sup>3</sup>State Key Laboratory of Advanced Technology for Materials Synthesis and Processing, Wuhan University of Technology, Wuhan, China, <sup>4</sup>Center for Environmental and Energy Research, Ghent University Global Campus, Incheon, South Korea

## OPEN ACCESS

### Edited by:

Zongyou Yin,  
Australian National University,  
Australia

### Reviewed by:

Cheng Tang,  
University of Adelaide, Australia  
Xiaoyong Xu,  
Yangzhou University, China

### \*Correspondence:

Francis Verpoort  
Francis.Verpoort@ghent.ac.kr  
Pei Liang  
liangpei0108@126.com  
Soumyajit Roy  
s.roy@iiserkol.ac.in

### Specialty section:

This article was submitted to  
Inorganic Chemistry,  
a section of the journal  
Frontiers in Chemistry

Received: 24 January 2022

Accepted: 30 March 2022

Published: 11 May 2022

### Citation:

Sen R, Das S, Nath A, Maharana P,  
Kar P, Verpoort F, Liang P and Roy S  
(2022) Electrocatalytic Water  
Oxidation: An Overview With an  
Example of Translation From Lab  
to Market.  
Front. Chem. 10:861604.  
doi: 10.3389/fchem.2022.861604

Water oxidation has become very popular due to its prime role in water splitting and metal–air batteries. Thus, the development of efficient, abundant, and economical catalysts, as well as electrode design, is very demanding today. In this review, we have discussed the principles of electrocatalytic water oxidation reaction (WOR), the electrocatalyst and electrode design strategies for the most efficient results, and recent advancement in the oxygen evolution reaction (OER) catalyst design. Finally, we have discussed the use of OER in the Oxygen Maker (OM) design with the example of OM REDOX by Solaire Initiative Private Ltd. The review clearly summarizes the future directions and applications for sustainable energy utilization with the help of water splitting and the way forward to develop better cell designs with electrodes and catalysts for practical applications. We hope this review will offer a basic understanding of the OER process and WOR in general along with the standard parameters to evaluate the performance and encourage more WOR-based profound innovations to make their way from the lab to the market following the example of OM REDOX.

**Keywords:** water oxidation reaction, oxygen evolution reactions, surface modification of electrodes, oxygen generator, industrial applications of water oxidation, lab to market

## INTRODUCTION

In 1671, scientist Robert Boyle first produced hydrogen gas by conducting the reaction between iron lings and dilute acids. Later, the research work of British Chemist Henry Cavendish and French Chemist Antoine Lavoisier led to the discovery of hydrogen gas in 1783. On the other hand, in 1771–1772, Swedish Chemist Carl Wilhelm Scheele first produced oxygen gas by heating mercuric oxide, potassium nitrate, and some other nitrates. In 1774, British chemist Joseph Priestly discovered oxygen independently, and later, in 1775–1780, Antoine Lavoisier explained the role of this gas in combustion and named it “Oxygen.” Both of these gases are very much important for our daily lives. In the last few decades, hydrogen has given importance as a potentially sustainable and renewable energy source to meet the rapidly increasing demand for energy due to the dramatic rise in world population, industrialization, and worldwide economic growth. Generally, carbon-based fossil fuels are used to meet such ever-increasing demand for energy, but these fuels are non-sustainable and have limited reserves. Massive fossil fuel combustion also causes a large amount of CO<sub>2</sub> and other greenhouse gas emissions. However, the burning of Hydrogen gas with oxygen in fuel cells almost leads to zero

emissions (Tang et al., 2021). That's why, for having high mass-energy density and for being an environment-friendly clean energy carrier, hydrogen gas has been considered as an alternative to fossil fuels. Similarly, for being a strong oxidizing agent, having an important role in respiration, combustion processes, oxygen has its broad application in different industries like chemical and petrochemical industry, metal industry, oil, and gas industry, and it is also used in fish farming, glass manufacture, waste management, and oxygen therapy. Especially, during the COVID-19 pandemic, we have realized the huge demand for oxygen for medical oxygen therapy to treat the patients having low oxygen saturation. Electrochemical water splitting is one of the most promising and widespread sustainable pollution-free approaches for producing hydrogen and oxygen. In the water electrolysis process, electrical power is used to dissociate water molecules into hydrogen gas at the cathode side and oxygen gas at the anode side. To overcome different activation barriers related to these reactions, excess energy in the form of "overpotential" is required for the electrocatalysis of pure water. That is why an electrolyte (an acid or a base or a salt) is added to it, and different electrocatalysts are used to increase the efficiency of water electrolysis by lowering the "overpotential." This electrochemical water splitting reaction has two components—Hydrogen Evolution Reaction (HER) and Oxygen Evolution Reaction (OER). HER is the reaction where hydrogen ( $H_2$ ) is generated *via* the reduction of either proton ( $H^+$ ) or  $H_2O$  at the cathode depending on the pH of the electrolyte, and OER is the reaction where oxygen ( $O_2$ ) is generated *via* the oxidation of either the hydroxyl ion ( $OH^-$ ) or  $H_2O$  at the anode depending on the pH of the electrolyte. Although the water splitting electrolysis is straightforward and environment-friendly, the large-scale application of this process for the production of hydrogen and oxygen is still absent today due to the low efficiency and high cost of production. Therefore, the development of efficient, low-cost, earth-abundant electrocatalysts suitable for different mediums (acidic, neutral, or alkaline) having high catalytic activity, long-term stability is highly desirable for efficient production of hydrogen and oxygen gas from water splitting to meet the commercial-scale demand of  $H_2$  and  $O_2$  since the electrocatalysts help to minimize the overpotentials for HERs and OERs. The performance of an electrocatalyst for electrochemical water oxidation depends on three key factors—1) Activity, 2) Stability, and 3) Efficiency. In this paper, the activity of electrocatalysts is explained in terms of overpotential, Tafel slope, and exchange current density. ECSA (Electrochemically Active Surface Area) is also another parameter that influences the catalytic activity of the electrocatalysts. Stability is one of the important parameters for describing the ability of an electrocatalyst to maintain its original activity over a long range of time. It can be assessed by recording the changes of the overpotential at a particular current density or by recording the variation of current density under a fixed applied overpotential, over a period of time. Another parameter that plays a significant role in evaluating the performance of an electrocatalyst is its efficiency, which is characterized by Faradaic efficiency and turn-over frequency. How these factors influence the performance of electrocatalysts are mentioned in the later section of this paper. The role of electrocatalysts in the electrochemical water-splitting

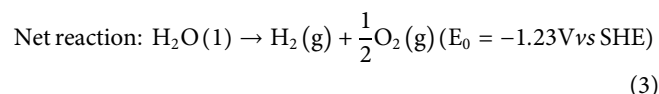
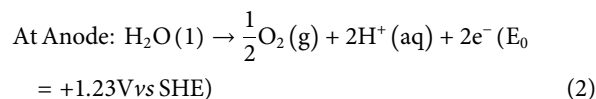
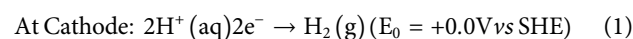
reaction is another focal point of this review. In this paper, we have discussed the design strategies and the catalytic properties of recently developed OER electrocatalysts that are suitable for different mediums (acidic, neutral, or alkaline). Along with the knowledge about several efficient electrocatalysts for water-splitting reactions, it is also very much important to know their practical applications. The applications of electrocatalytic water oxidation in several fields—oxygen generator, spacecraft, Fuel Cell Electric Vehicle (FCEV) technologies, nuclear submarines, etc.—are worth mentioning. Therefore, the discussion of design strategies, electrocatalytic properties, of such electrocatalysts in this review paper is expected to lead to new advances in developing active, stable, efficient, low-cost HER, and OER electrocatalysts for the mass commercialization of water splitting-based hydrogen and oxygen production. Finally, it refers to a product developed in our start-up by us: OM REDOX.

## PRINCIPLES OF ELECTROCATALYTIC WATER OXIDATION REACTION

From the thermodynamic point of view, the water splitting reaction is an endergonic process. However, this non-spontaneous reaction can be done by providing external energy to the system, such as electricity. That's why electrical power is needed for water electrolysis to dissociate water molecules into hydrogen gas at the cathode and oxygen gas at the anode. To overcome different activation barriers, excess energy in the form of "overpotential" is required for the electrocatalysis of pure water. The electrical conductivity of pure water is significantly less. Therefore, an electrolyte (an acid or a base or a salt) is added to it, and different electrocatalysts are used to increase the efficiency of water electrolysis by lowering the "overpotential."

In the acidic medium ( $pH < 7$ ), excess  $H^+$  ions, present in the solution, move towards the cathode and are reduced to hydrogen gas, while the water molecules are oxidized at the anode to form oxygen gas. Therefore, the water electrolysis process that occurs at the surface of the electrodes in an acidic medium can be described by the following half-cell reactions (Santos et al., 2013); (Figure 1):

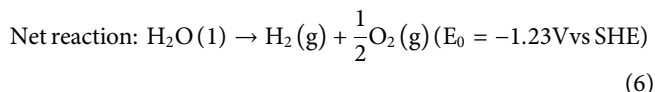
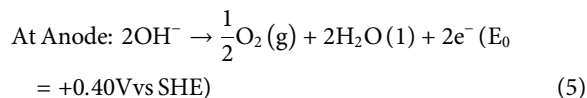
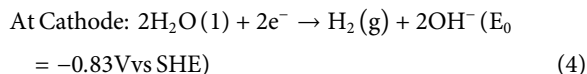
In acidic medium,



However, in an alkaline medium ( $pH > 7$ ), additional hydroxyl ions, present in the solution, release their electrons to anode during water electrolysis and get oxidized to form oxygen gas, while the water molecules are reduced at the cathode and generate hydrogen gas. The water electrolysis process that occurs at the surface of the electrodes

in an alkaline medium can be described by the following half-cell reactions (Santos et al., 2013); (**Figure 1**).

In an alkaline medium,



Under the standard condition (ambient temperature and pressure), the Gibbs free energy and the enthalpy of the water-splitting reaction are  $\Delta G^0 = 237 \text{ kJ mol}^{-1}$  and  $\Delta H^0 = 286 \text{ kJ mol}^{-1}$ , respectively. The thermodynamic standard cell potential for water-splitting reaction can be calculated by using the following equation:

$$\Delta G^0 = nFE^0 \quad (7)$$

In the above equation,  $\Delta G^0$  is the standard Gibbs free energy,  $n$  is the number of electrons,  $F$  is Faraday's constant, and  $E^0$  is the standard cell potential. Using **Equation 7**, the theoretical reversible voltage required for dissociating a water molecule into hydrogen and oxygen gas is calculated as 1.23 V at 25°C, in both acidic and alkaline mediums (Shinagawa and Takanabe, 2017). However, in practice, to overwhelm the activation barrier of reaction, more than 1.8 V is required. This substantial overpotential for the water-splitting reactions emerges because of the sluggish transfer kinetics of the four-electron transfer in the anodic oxidation reaction and the two-electron transfer in the cathode reduction reaction (Li et al., 2020). The Nernst equation of water electrolysis can be expressed as (Shen et al., 2011)

$$E_{\text{cell}}^0 = 1.23 - 0.9 \times 10^{-3} (T - 298) + \frac{RT}{4F} \ln \left( \frac{p_{\text{H}_2} \cdot p_{\text{O}_2}}{p_{\text{H}_2\text{O}}} \right). \quad (8)$$

In the above equation,  $p_{\text{H}_2}$ ,  $p_{\text{O}_2}$ , and  $p_{\text{H}_2\text{O}}$  are the partial pressures of hydrogen, oxygen, and water vapor, respectively, and  $T$  refers to the temperature in K (Shen et al., 2011). The Nernst equation enables us to determine the cell potential for water splitting reaction under non-standard conditions (at reaction condition). This water dissociation potential is influenced by the catalyst activity of electrodes. Moreover, the electrochemical properties of the electrodes influence the mechanism of the water-splitting reaction. The value of water dissociation potential depends on it (Shen et al., 2011). As mentioned earlier, high overpotential is one of the main reasons for the sluggish kinetics of the water-splitting reaction. This kinetic effect of water electrolysis can be expressed with the Butler–Volmer equation *via* the activation overpotential of the cathode and anode. This equation is as follows (Shen et al., 2011):

$$\begin{aligned} \eta_{\text{act},i} &= \frac{RT}{F} \sinh^{-1} \left( \frac{J}{2J_{0,i}} \right) \\ &= \frac{RT}{F} \ln \left[ \frac{J}{2J_{0,i}} + \sqrt{\left( \frac{J}{2J_{0,i}} \right)^2 + 1} \right], \text{ where } i = a, c \end{aligned} \quad (9)$$

In **Equation 9**,  $\eta_{\text{act}}$  is the activation overpotential of electrode  $i$  ( $i = a, c$ ), where “ $a$ ” and “ $c$ ” subscripts represent the anode and cathode, respectively,  $J$  is the operating current density,  $J_0$  is the exchange current density, and  $R$  is the ideal gas constant.

The exchange current density can be expressed as the following equation (Shen et al., 2011):

$$J_{0,i} = J_i^{\text{ref}} \exp \left( \frac{E_{\text{act},i}}{RT} \right), i = a, c, \quad (10)$$

where  $J_i^{\text{ref}}$  is the pre-exponential factors and  $E_{\text{act},i}$  is the activation energy.

Generally, in the electrochemical water oxidation process, the activation overpotentials of the cathode and anode are different from each other, which means that they have different catalytic activities. However, the ratio of electrochemical reaction rate on the cathode to the anode or the rate of product formation at both the electrodes does not depend on their catalytic activities. Rather, it depends on the stoichiometric ratio as the current passing through the cathode and anode is always the same in the electrolysis process. Therefore, the rate of production of hydrogen and oxygen can be expressed with **Equations 11, 12**, respectively (Shen et al., 2011),

$$N_{\text{H}_2} = \frac{JA}{2F} \quad (11)$$

$$N_{\text{O}_2} = \frac{JA}{4F} \quad (12)$$

The rate of hydrogen and oxygen gas production is also influenced by the efficiency of water electrolysis. The efficiency of electrolysis depends on several factors. It depends on the availability of the cations and anions in the solution, their mobility rate to reach the electrode, and the required activation energy to transfer electrons from the electrode to the electrolyte ions. In addition to these, the wettability of the electrocatalyst with electrolyte and the rapid desorption of the bubbles generated on the electrodes is very important to increase the efficiency of water-dissociation reactions. Because the breaking of the generated gas bubbles from the electrode surface sometimes becomes difficult, and as a result, the electrolyte cannot easily diffuse to access the interface of the electrolyte or catalyst. Therefore, hydrophilicity and aerophobicity are considered two important facets of electrodes to perform an efficient and stable water electrolysis process. Hence, developing efficient, low-cost, stable, earth-abundant electrocatalysts for water-splitting reactions is imperative (Li et al., 2020).



## ELECTRODE DESIGN IN ELECTROCATALYTIC REACTION INVOLVING WATER OXIDATION

The simplest electrochemical cells can consist of anode and cathode immersed in an electrolyte in a glass beaker, split *via* porous separator or membrane. With the increasing need, the complexity also increases and starts including a series of complex components, including electrode plates, housing, separators, and gaskets. The modern cells now comprise new features such as well-spaced threaded fastenings for compression (seen in the electrocell, the FM01-LC electrolyzer, and the microflow cell), wrenches, thumb screws for fixing and relaxing the frame (Ralph et al., 1999), inlet and outlet flow tubes ruling out the requirement for hand tools, electrode and membrane gaskets, membrane and separator, current collector, and rear and front plate assembly.

### Fabrication of Electrode Materials

Electrochemical cell components are prime candidates for 3D printers, either from polymer materials for it to be electrically insulating or stainless steel for functioning as a current collector. Diversity of materials including conducting polymers such as polypyrroles, polythiophenes (Campbell et al., 2007; de León et al., 2008), boron-doped diamond ceramics, and electrically conductive suboxides of titanium and Ebonex (Walsh and Wills, 2010) are used for electrode materials. Mature coating techniques were developed, such as plasma and vapor deposition, anodized, and electrodeposited finishes (Walsh et al., 2015). Carbon fiber polymer and metal-ceramic/polymer are also utilized as modern ceramic composites. The most widely used is a nanostructured surface on the electrode for their high activity and area properties.

Stacked cell designs require adequate distance between the cathode and anode to prevent electrical short circuits or product crossover. In this regard, porous polymer meshes and crushed glass frits are successfully applied for electrical separation.

Here, we highlight the techniques for the design of electrodes and their surface modification, but other complementary approaches also came into notice for the realization of modern electrochemical materials, such as electrospinning and electrostatic deposition. Composite fibers of carbon nanotubes and titanium nanotubes composing biomaterials like chitosan can be produced by electrospinning. Electrostatically deposited Pd/Ir catalyzed micro-fibrous carbon mats have been utilized for peroxide reduction as a 3D cathode in a borohydride fuel cell (Dechakiatkrai et al., 2009). The continued development of classical imaging tools such as scanning electron microscopy (SEM), transmission electron microscopy (TEM), atomic force microscopy (AFM), and advanced X-ray computed tomography (Arenas et al., 2018) has helped to realize the surface morphology of structured surfaces in a great extent.

### Choice of Electrolyte

In an electrochemical reaction, one should choose solvents and supporting electrolytes considering the full electrochemical mechanism and the overpotential window for the electrolyte and the solvent. Interaction between the electrolyte ions and the catalyst surface is also very important because strongly

absorbing species can reduce the reaction rate drastically by blocking the catalyst sites (Perry and Denuault, 2015). Strong pH dependence and the need for proton transfer often make aqueous solutions good options for many electrochemical systems. However, the solvent window is narrow for water compared to ionic liquids and organic media. Organic electrolytes and ionic liquids (room temperature) allow reactions through an intermediate that would otherwise be oxidized in aqueous media, thus presenting a wider window (Möhle et al., 2018). They can also stabilize high-energy radical intermediates for organic electrochemical synthesis (Wiebe et al., 2018). Ionic liquids are desirable from green and environmental perspective as these are recyclable. However, they are costly and their viscosities give low mass transport (Kathiresan and Velayutham, 2015).

### Types of Electrochemical Cells

In the 1960s, electrochemists developed engineering principles to design cells with a diverse range of electrode and cell geometries for laboratory and pilot-scale use in the 1970s (Goodridge and Scott, 2013). Such developments and principles till date are very relevant for any cell-related designing purposes. From using a diverse range of materials (e.g., metals, polymers, composites, etc.) to improving structural and surface designs (e.g., introducing nanostructures and hierarchical features or using techniques such as electrodeposition, anodizing, electrophoresis, electrospinning, etc.), several domains have been developed to improve the efficiency of electrodes for electrochemical reactions. 3D printing and lithographic techniques have been adopted for fast production and prototyping, which is aided by computer-simulated designs and a wide range of characterization techniques, from optical and SEM through to X-ray computed tomography and synchrotron radiation (catalyst) studies (Figure 2).

We have already understood that depending on the application, different types of electrodes and cell geometries are developed to optimize the conversion, current efficiency, electroactive area, mass transport, selectivity, energy transport, and efficiency. During the design, some considerations are necessary to realize their importance for the process. These are as follows: a) low-cost production by maintaining the simplicity; b) low operational cost as well as component costs such as an electrolyte and a separator; c) reliability for routine operations, cleaning and inspection; d) engineering of the reaction pathway for highest selectivity, production, mass transport, electroactive area, current and potential distribution, inter-electrode gap, and low overpotential (Fleischmann et al., 1980); e) low-pressure drop over the cell; f) ease of the product extraction; and so on.

Considering these points, some simple cell types are already available to aid the selection of particular electrode geometry and cell design (Walsh and de León, 2018). When used retrospectively, this approach is very beneficial to rationalize diverse cell designs by considering their significant characteristics.

- 1) Filter-press cell: There are two main types: Undivided cell and Divided cell. The divided cell can be further classified

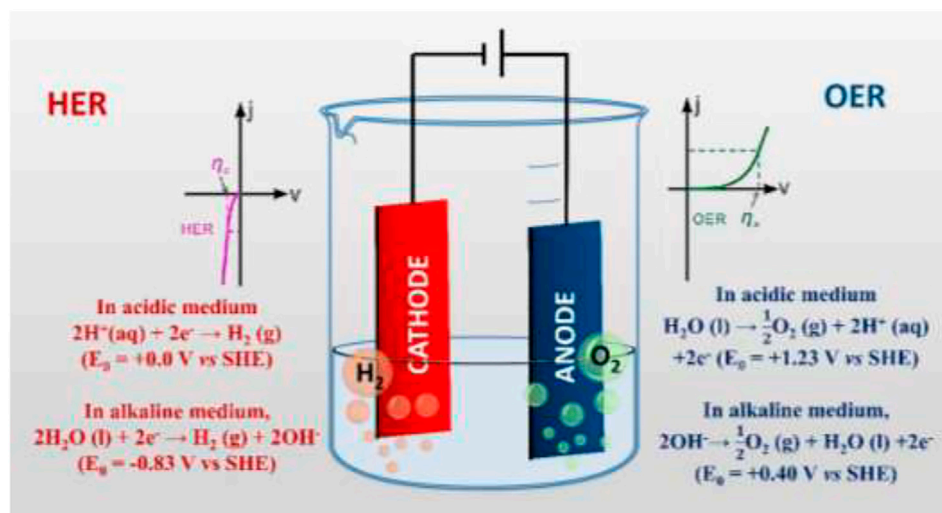


**FIGURE 1** | Schematic illustration of the electrochemical water-splitting reaction and related reaction kinetics.

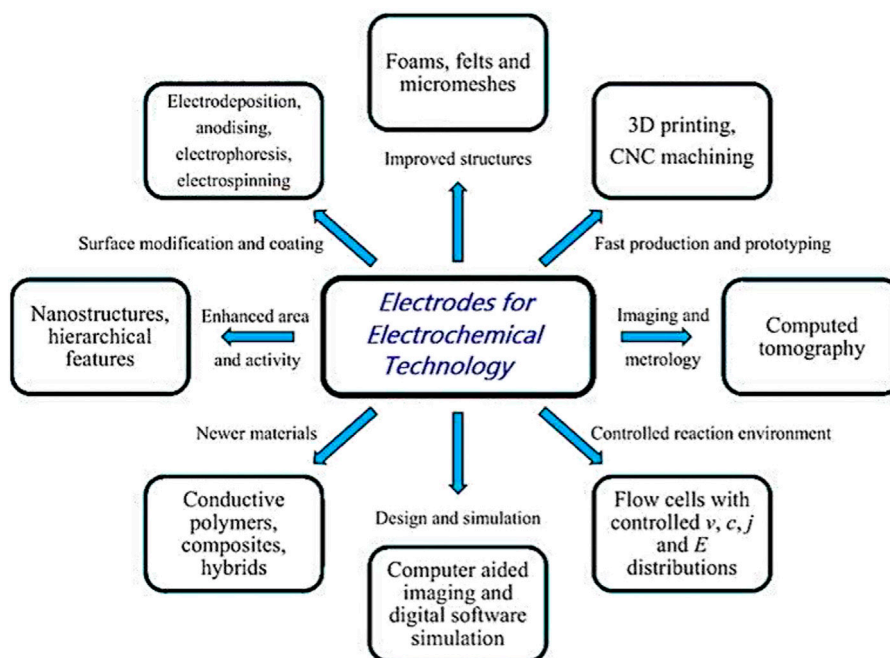


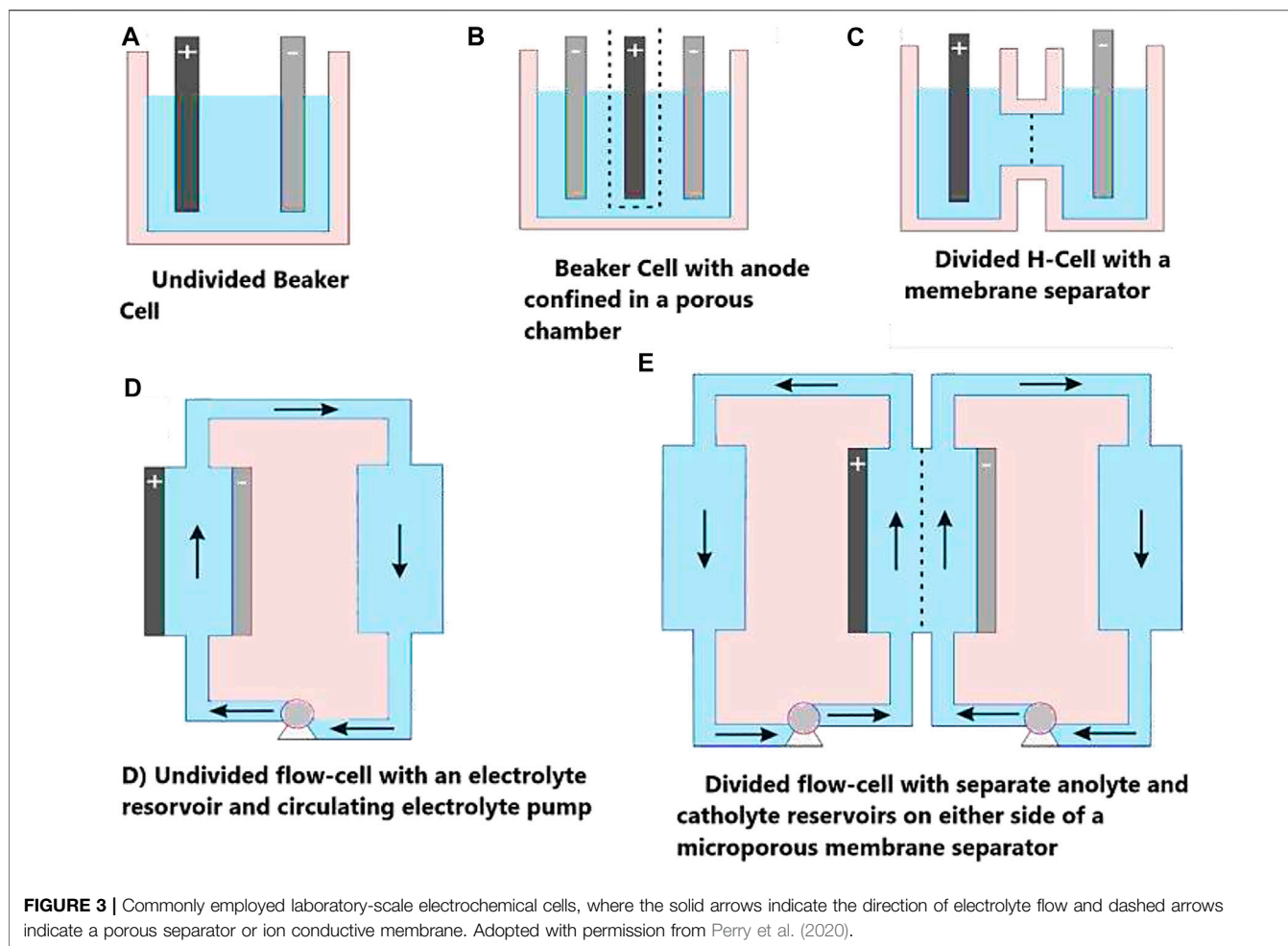
**FIGURE 2** | Various electrodes used in electrochemical technology, showing the diversity of materials, structures, coatings, shapes, manufacturing methods, and characterization techniques. Adopted with permission from Walsh et al. (2018).

into monopolar electrodes and bipolar electrodes. 2D electrodes and 3D electrodes are the two categories of bipolar electrodes. These two types of cells can be classified into commercial cells and in-house cells. Filter-press cells can also be divided into fast prototyping, such as 3D printing and conventional manufacturing by machining or molding. Both the types have applications as a commercial cell and an in-house cell.

- 2) More specialized cell: There are three main types: rotating electrode (e.g., rotating cylinder electrode reactor), porous electrode (e.g., packed bed or reticulated electrode reactor), and thin-film (e.g., bipolar trickle tower)

### Electrode Design: Structure and Form

The scope of electrochemistry is enormous, covering anywhere from electrocatalyst studies at atomic or molecular-sized species to



full-scale commercial cell rooms. The working electrodes play a critical role in determining the performance and greatly influence the reaction rate due to their different structures, conductivity, and access of the catalyst to the electrolyte. The electrode size can also be extremely diverse, laboratory electrodes ranging from  $1 \text{ mm}^2$  to  $10 \text{ cm}^2$  including microelectrodes, while pilot plant electrodes can be  $100\text{--}500 \text{ cm}^2$  (sometimes even  $1 \text{ m}^2$ ). Electrodes are designed for a particular use, such as electro-kinetics studies, bulk electrolysis, determination of limiting currents, or continuous reactor operation (Pletcher, 2019). The type of cell design is extensively considered elsewhere with respect to electrode shape, geometry, and electrolyte flow/electrical connections (Walsh and Reade, 1994a; b). Large scale reactions need the mass transport of reactants/products and heat transfer to/from the electrode. The design should improve sufficient mass transfer with the necessary reactants for efficient reaction progress. Thermal control is also very important as many redox reactions are exothermic in nature. Thermal control plays an important role in ensuring the stability and operational safety of the cell as active cooling may be needed in the form of heat exchange to get rid of the heat generated by the Joule effect. **Figure 3** demonstrates some commonly employed laboratory scale electrochemical cells.

General considerations regarding electrodes: A) Cost is always one of the main factors, so low-cost development is always economical. B) To make the electrodes cost-efficient, an adequate lifetime of the electrodes needs good mechanical, thermal, and chemical stability along with corrosion resistance. C) A high electrical conductivity gives a uniform current distribution and low ohmic losses. Choosing materials with very low resistivity is very important since the chemical resistance of the materials increases by the use of high surface area porous materials and 3D structures. D) Electrocatalysts should be modified for higher stability and yield by providing a low overpotential for the reaction.

One of the most important points of electrode activity is its surface area. We already know the importance of achieving a high current, but increasing the surface area is necessary for efficient activity if the current density is restricted. Porous materials and 3D surfaces can offer a low-pressure drop over the flow channel and moderate density. In the case of electrodeposited solids, suitable morphology and purity should be maintained for good current efficiency (Walsh, 2001). An increase in current with the electrode area will be accompanied by ohmic and kinetic losses, leading to a more negative cell potential, and will also result in a higher capacitance,

Cell potential difference  $U = U_e + \sum [\eta] + \sum j \cdot A \cdot R$ , where  $\eta$  = polarization,  $A$  = electrode area, and  $R$  = gas constant;

Mass transport limiting current  $I_L = z \cdot F \cdot c \cdot A \cdot k_m = K \cdot \nu^x$ , where  $z$  = no of electron transferred,  $F$  = Faraday's constant,  $c$  = concentration, and  $A$  = electrode area;

Charge transfer current  $I = z \cdot F \cdot A \cdot k \cdot c \exp(\frac{\alpha z F \eta}{R \cdot T})$ , where  $z$  = no of electron transferred,  $F$  = Faraday's constant,  $c$  = concentration,  $A$  = electrode area,  $\eta$  = overpotential,  $R$  = gas constant,  $T$  = absolute temperature, and  $\alpha$  = charge transfer coefficient;

Capacitance  $C = \frac{q}{\Delta E} = \frac{A \cdot \int l \cdot dt}{\Delta E}$ , where  $q$  = charge,  $\Delta E$  = change in potential,  $l$  = distance between the electrodes, and  $A$  = electrode area.

## Modification of Electrode Surface

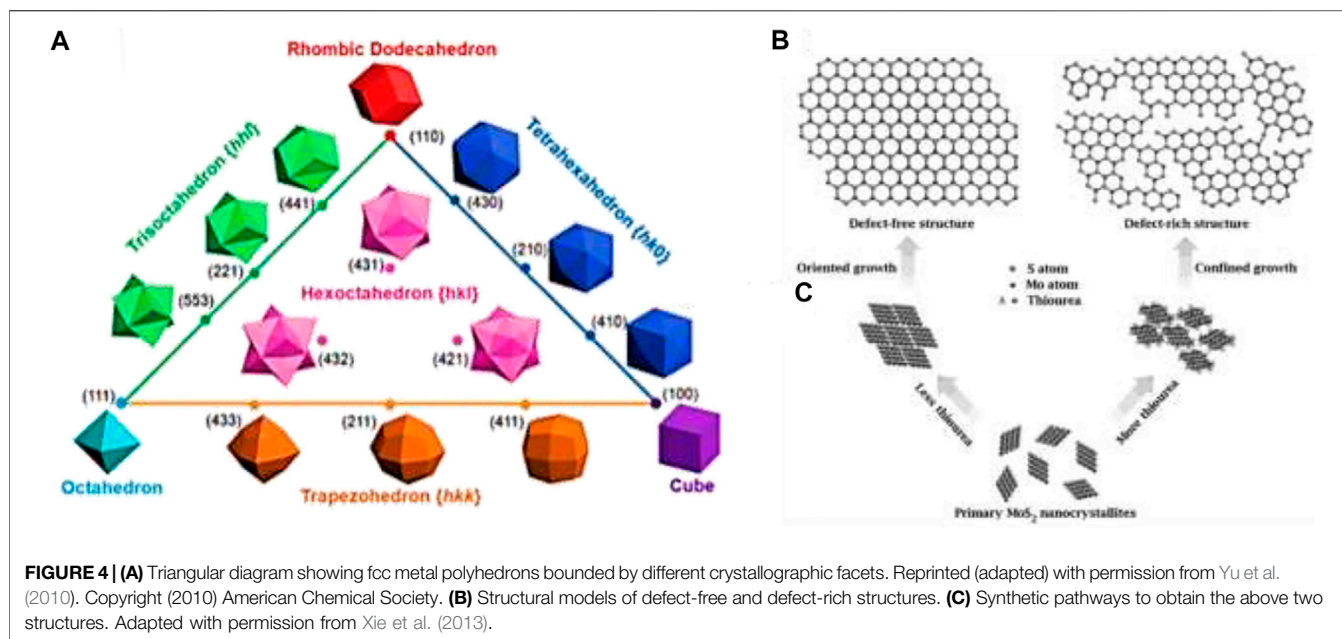
The surface area of the electrodes can be increased by using porous hybrids and 3D electrodes. Porous electrodes can be arranged in two configurations: flowthrough (Alkire and Gracon, 1975) and flow-by (Alkire and Ng, 1977), where the current and electrolyte flow run parallel and perpendicular to each other, respectively. In both cases, the electrodes face each other for uniform current distribution. Reticulated vitreous carbon (RVC) (Arenas et al., 2018), foam (Mustafa et al., 2019), and carbon felt (Castañeda et al., 2017) electrodes have been extensively used for the same purpose. The strategies for modifying the electrode surface include electro-depositing high surface area, combining foam with a fibrous structure and active nano-particles on the surface. The intricate surface of the 3D electrodes enhances the mass transport of the active species to the surface and creates different resistance between the opposite points of the electrodes. This geometric influence can affect their performance by changing the potential and current distribution. The geometry of the 3D electrodes can also increase the space-time yield of the electrochemical cells compared to 2D electrodes (Arenas et al., 2016). Here, mass transport can be correlated and controlled to the pressure drop and flow dispersion to evaluate the overall cost-benefit of the electrodes. The significance of 3D and porous architecture can be realized when structures such as nanorods, nanospheres, nano-onions, networks of nanowires and nanoflowers, micro-flowers, nano walls, etc., are manufactured on flat plate electrodes or inside already three-dimensional electrodes (Egorov and O'Dwyer, 2020). The electrochemical properties can be tailored by surface treatment or deposition of electrocatalysts. One such example is the electro-deposition of Pt on the Ti plate, felt, or meshes (Arenas et al., 2019). While depositing gold nanoparticle, by sputtering, onto a nano-porous array of TiO<sub>2</sub> on a Ti foil, felt or mesh surface, the hybrid surface nanostructure can be prepared by comprising "tubes within tubes" as in the incorporation of titanates via electrophoresis into an anodized microporous TiO<sub>2</sub> array on a Ti foil (Low et al., 2012). The hybrid surface nanostructure can be prepared by comprising "tubes within tubes" as in the incorporation of titanates *via* electrophoresis into an

anodized microporous TiO<sub>2</sub> array on a Ti foil (Low et al., 2012). The surface of the electrodes can always be modified for enhanced activity to incorporate nanoparticles into it by sol-gel coating, chemical reduction of metal salts, electroless deposition, and anodic or cathodic electrodeposition. The resulting surface had an average surface roughness of ca. 100 nm. By these techniques, examples of deposited materials include (a) precious metals such as Pt, Ru, etc., by galvanic reduction of metal salts (Walsh et al., 2006); (b) Ni, Co, Pt, Sn, etc., transition metals by immersion, electroless, and cathodic deposition (Walsh and Low, 2016); (c) metal oxides such as PbO<sub>2</sub> or MnO<sub>2</sub> by chemical and anodic deposition (Li et al., 2011); and (d) anodic and cathodic deposition of metal-metal, metal-polymer, and metal-ceramic composites (Walsh et al., 2015).

In recent years, cell design can be assisted by computer-aided design (CAD), and computer modeling of the reaction environment such as pressure drop, electrolyte hydrodynamics, and leakage currents flowing around the electrode rather than in the ordered fashion (shunt currents) together with concentration, current, and potential distribution. Digital designing is now a breakthrough for producing multiple, improved 3D electrodes by 3D printing, which are then tested in the laboratory. The development of technology has enabled 3D printers to assess a broader range of solid materials such as auxetic polymer foams having controlled pore shape, size, and density (Critchley et al., 2013). The advancement has been seen by the production of the fast prototype laboratory Zn-Ce redox flow battery (Arenas et al., 2015). Quickly modifying and manufacturing the cell resulted in a much faster development process. It was seen that high-resolution laser curing was a more suitable technique for printing electrochemical flow cell components because melting of polymer resulted in undesired porosity and deformation due to thermal stress. Developments of 3D printing have resulted the successful manufacture of 3D porous metal electrodes. Digital imaging software allowed visualization, simulation, and modification before manufacturing.

Now coming to some disadvantages, 3D electrodes can present uneven current and potential distributions, resulting in the asymmetric electrodeposition of catalyst particles and uneven final operations. Therefore, establishing the optimal electrode thickness ensures the electrochemical activity of the covered electrode surface. Not all the surface of the thicker electrodes has the same potential, so the catalyst distribution may not be homogeneous. That is why the electrodeposition technique is the most reliably used for such proposes. There is still possibility that parts of the electrode can be inactive if the electrode is too thick or if the electrolyte species has very low concentration. However, mathematical simulation can determine the optimal thickness, such as in conductive porous electrodes. A unidirectional potential distribution under limiting current conditions can be modeled assuming plug-flow conditions and that in excess of supporting electrolyte, the conductivity changes during electrolysis are negligible (Nava et al., 2008). In practice, the potential difference between the porous electrode surface and the





solutions should not be too large to ensure that hydrogen or oxygen evolution does not occur during reduction or oxidation, respectively.

Catalytic properties of nanostructure not only depend on the surface area but also on the surface facets. For a face-centered cubic (fcc) lattice structure, surface facets such as {111}, {100}, and {110} can be classified as low-index facets (**Figure 4A**). Nanocrystals usually form low index facets to minimize the surface energy. On the other hand, nanocrystals with high index planes show enhanced activities due to their higher surface energy and lower coordinated atoms. Thus, controlling the nucleation and growth process through synthesis can develop high index surfaces for valuable applications. As an example, the activities of high index facets of Pt, such as Pt (520), Pt (710), Pt (310), etc., with large density of atomic steps and dangling bonds, show a significantly higher formic acid oxidation rate than those of low index facets (Tian et al., 2007). Thus, the need formation of surface facets of a particular nanocrystal can be altered by introducing foreign species into the system and the absorption ability of the species on the metal surface can change the surface energy. As the particle size shows a strong correlation with the nanocrystal formation, the growth rates of various facets can be controlled by selecting appropriate surface capping reagents. Therefore, through capping agents, one can regulate the two rates (nucleation and growth rates) as well as two mechanisms (thermodynamic control and kinetic control) to obtain 1D or 2D nanostructures by inducing either anisotropic growth or epitaxial growth.

On a catalyst surface, not all sites are equally active. The active catalyst sites are regarded as low-coordinated surface atomic sites, including the low-coordinated atoms at terrace, steps, kinks, edges, corners, vertexes, vacancies, defects, holes, and pits that often favor catalytic reactions. Active sites can be strongly correlated with the surface roughness of the electrode and the number depends on the features of the surface and interface. A

metal surface can generally be of two types: 1) equilibrated metal surface (EMS), which is well embedded, predominant, and stable surface; and 2) metastable metal surface (MMS), which is protruding, low-population, and high-energy surface. The MMS atoms act as the surface-active sites in general because these are prone to undergo reactions with the involved species at low overpotentials (Lertanantawong et al., 2008). Active sites are intuitively associated with the surface facets of the nanocrystal. The metal surface is enclosed by different types of atoms whose coordination numbers follow the order of face > edge > vertex with the reverse order in terms of catalytic activity. For different well-defined shapes, the variation of the surface facets can alter the proportions of various surface atoms with various coordinated states, affecting the catalytic properties thereafter. Active sites are also related to surface defects and vacancies as well as on the surface area and the particle size. Breaking chemical bonds to endow atoms with low coordinated states is beneficial to create active sites. Defect or vacancy on the basal planes of the catalyst can increase the exposure of active sites by forming cracks on the surfaces, and as a result, the electrocatalytic activity may dramatically increase (Xie et al., 2013) (**Figures 4B,C**).

Interfaces are formed when different phases or objects contact each other. Thus, heterogeneous catalytic reactions can be regarded as various interfacial effects. Engineering the interface between the catalyst and electrode can potentially alter the geometrical structures, and interfacial compositions, electronic structure and electron transport, Fermi levels and band alignments, proton transfer and species exchange, coordination numbers and atomic arrangements, crystal structures and dangling bonds, and selective adsorption and desorption, which all have tunable and synergistic effects during the heterogeneous electrocatalysis at the active sites of the electrode catalysts (Xia et al., 2015). For instance, the Pt<sub>3</sub>Y nanostructure can modify the d-band depth, surface

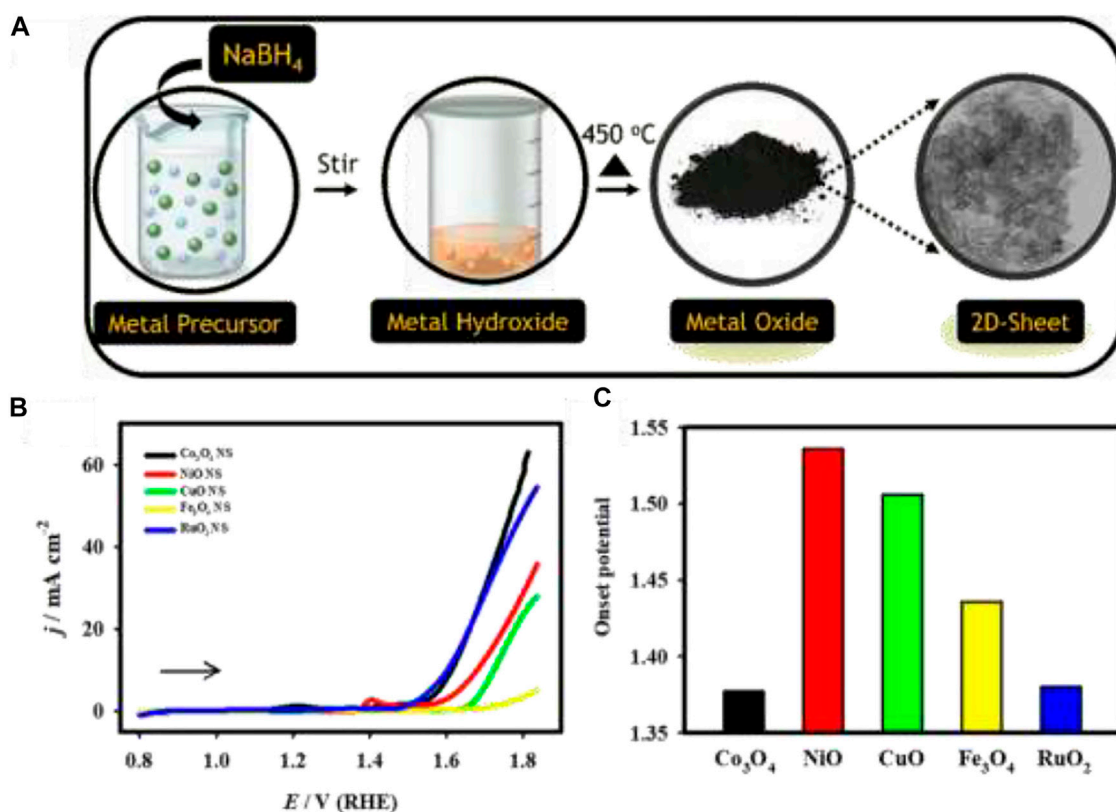


**FIGURE 5 | (A)** Schematic illustration of the synthesis of 2d-metal oxide nanosheets, **(B)** LSV curves of the  $\text{Co}_3\text{O}_4$  (black),  $\text{NiO}$  (red),  $\text{CuO}$  (green),  $\text{Fe}_3\text{O}_4$  (yellow), and  $\text{RuO}_2$  (blue) electrodes recorded in 1.0 M KOH at a scan rate of  $20 \text{ mV s}^{-1}$ . **(C)** Plot of the OER onset potential: Reprinted (adapted) with permission from Elakkiya and Maduraiveeran (2020). Copyright 2020 American Chemical Society.

adsorption ability, and electronic structure to improve the oxygen reduction reaction (ORR) performance (Hwang et al., 2012).

## Electrocatalyst Modified Electrodes

When an electrode such as a piece of Pt or carbon is dipped into a solution, its surface is then covered by a layer of water molecules or species present in the electrolyte solution. Such adsorbed species can often modify the electrochemical activity of the electrode. Now purposely modified electrode surfaces can produce electrodes with new and exciting properties that may form the basis of new applications of electrochemistry (Murray, 1980) as we have already discussed a bit in the case of electrolysis of water. In addition, many reactions that one would like to carry out in electrochemical cells do not occur readily at inexpensive electrode materials (e.g., carbon). Before the mid-1970s, electrochemistry was confined only with electrode materials such as C, Au, Pt, Hg, etc. Murray and co-workers initiated the field of chemically modified electrodes (CME) by taking the fundamental group transformation to  $\text{SnO}_2$  and Pt-OH (Murray et al., 1987). That is why catalysis is important to enhance the reaction rate by introducing suitable, stable layers to the electrode surface. By applying known chemical principles about the structure and reactivity, useful surface catalysts can be developed for individual reactions considering the cost-effectiveness and commercialization. One of such first

examples is the modification of a graphite surface by irreversible adsorption of a co-facial dicobalt porphyrin dimer which allowed the reduction of oxygen under conditions where reduction was not possible on the substrate itself. The path was sensitive to the detailed structure of the attached molecule. There are four main possible routes for preparing CMEs: sorption, covalently modified carbon, redox polymer coatings (uniform), and heterogeneous multilayers (non-uniform). Physical and chemical interaction properties are utilized for sorption-based modified electrodes. Easy surface modification and functional group attachment are the chief advantages of this approach. Thiols' self-assembled monolayer (SAM) of Au-chemisorbed is a well-known example of this aspect (Chaki and Vijayamohan, 2002). Using a specific functional group for covalent modification of the electrode surface is also very important. For example, the glassy carbon electrode (GCE) can form attachment with the  $>\text{C}=\text{O}$  and  $>\text{C}-\text{O}-$  functional groups and  $-\text{OH}$  groups from oxide electrodes (Downard, 2000). Polymer-based multilayer CMEs can resolve the lack of active components on the monolayer electrode surface. There are two ways to prepare these: homogeneous (uniform) and heterogeneous (non-uniform). Non-uniform systems are created on heterogeneous supports such as zeolite,  $\text{SiO}_2$  (sol-gel), clay, carbon paste, epoxy resin, phosphomolybdic acid ( $\text{PMo}_{12}$ ), and other polymeric systems (Sadakane and Steckhan, 1998; Walcarius, 2001a; Walcarius,

2001b; Kong et al., 2001). The uniform multilayer preparation includes ionomers, inorganic polymers, redox polymers, electrochemically deposition of mediators (metals or simple metal complexes), and mediator bearing monomers (pyrrole and amine containing complexes) (Murray, 1992).

Pure organic or organometallic complexes can be physisorbed on porous carbon bases such as vitreous carbon (VCE), graphite (GE), basal plane pyrolytic graphite (BPG), and ordinary pyrolytic graphite (OPG) for the preparation of sorption-based CMEs, by simply coating the electrodes with non-aqueous solution followed by droplet evaporation. For example, the pyridine solvent was used to modify cobalt phthalocyanine on VCE with a surface coverage of ca.  $3.1 \times 10^{-11} \text{ mol cm}^{-2}$  for nitrite oxidative detection (Caro et al., 2002). Carbon nanotubes (CNTs), having a honeycomb-like nano-lattice structure with cylindrical closed topology, has unique absorption abilities for special applications as catalysts, sensors, etc. (Baughman et al., 2002; Haddon, 2002). Clay modified electrodes are other CMEs that are prepared by dip-coating of the aqueous colloidal solution (Baughman et al., 2002). GCE is quite unstable for such coating due to its polished surface nature, and additional polymeric systems are required for stability improvement (Zen et al., 2002b). The stability problems of physisorbed systems can be overcome by the chemisorbed route. Due to the easy preparation procedure of the self-assembly monolayer (SAM)/Au-oriented system by simple soaking up the Au electrode in thiol ( $-\text{SH}$ ) and ethanol solutions, this kind of system carries great importance in the chemisorbed studies. Some recent progress in analytical chemistry using SAM/Au is cysteine for CO oxidation (Shi et al., 2001), disulfide derivatives of vitamin B<sub>12</sub> for ORR (Viana et al., 2002), etc.

The surface functional groups of the base electrode can be made to form covalent linkage either by controlling the oxidation/reduction potentials or by the synthetic route in a suitable medium. First examples of such functional group transformation on the electrode surface are  $\equiv\text{Sn}-\text{OH}$  and  $\equiv\text{Pt}-\text{OH}$ . The carbon surface has many alterable functionalities and is hence very suitable for covalent modification (Downard, 2000). Aryl diazonium (Allongue et al., 1997), aryl acetate, and amino (Deinhammer et al., 1994) are most viable for covalent modification than other organic entities. For example, the anthraquinone (AQ)-grafted GCE surface (GC-AQ) in coupling with the Au ring disk electrode was used for the ORR (Tammeveski et al., 2001). The GC-AQ has produced a defined potential at  $-0.9 \text{ V}$  (vs. SCE) in  $0.1 \text{ (M) KOH}$  with  $\Gamma_{\text{AQ}} = 2.5 \times 10^{-10} \text{ mol.cm}^{-2}$ . 4,5-dihydroxyAQ-2-carboxylic acid modified GCE was prepared by the simple potential electrochemical cycling method in  $\text{pH} = 3$  solution for its use in the reductive detection of hemoglobin at  $-0.2 \text{ V}$  (vs. Ag/AgCl) (Zhang et al., 2002). These were further modified by the solution phase synthetic method with exfoliating graphite (EC) powder to form covalently modified AQ-EC (Ramesh and Sampath, 2001).

Oyama and Anson first utilized the plan to modify poly (4-vinyl pyridine) (PVP) on the carbon surface for the ion exchange of ferrocyanide ions in acidic solutions (Oyama and Anson, 1980). Thus, the modification of specific ion-exchange membranes or polymers on the electrode surface is a very interesting branch in

electrochemical analysis, where the system allows the ionic species to incorporate as counterions inside the galleries. The cationic exchange membrane Tosflex was applied in analytical applications that have analog backbone like Nafion (Dunsch et al., 1990), as PVP and Nafion were extensively utilized for various applications. Selectivity is an essential criterion for sensors, and ionomeric systems can also be used for sensing charged species other than catalytic activity. Electrochemical depositions of monomeric units under potential cyclic conditions or by galvanostatic/potentiostatic methods opened another elegant way of preparing electrodes with homogeneous multilayer CMEs. A bare polymeric system or pure organic polymer without any metal and metal complex can successfully participate in the electron transfer reactions such as the formation of nitronium or oxonium radicals as a typical example. In this category, Nile blue was used for the ORR and oxidation of NADH (Ju and Shen, 2001). Electrochemical co-deposition is another popular area to utilize to form uniform multicomponent films. Besides organic sources as modifiers, simple metal plate electrodes can also be applicable for these applications. A disposable copper-plated screen-printed electrode (SPE) (i.e., CuSPE) was invented by Zen et al. for the detection of  $\text{H}_2\text{O}_2$  (Zen et al., 2000a), which was modified further with glucose oxidase for glucose sensing (Zen et al., 2002a). Inorganic polymers are also looked at with equal interest towards potentiometric and amperometric sensing. Prussian Blue (PB), known for more than 250 years, was first utilized in electrochemistry in 1978 for various applications (Karyakin, 2001).

In heterogeneous multilayer CMEs, the solid supports are deliberately combined with the mediator system in a non-uniform way. Carbon paste electrode (CPE) is prepared simply by mixing binder paste/graphite and redox mediator and it is the most convenient to make among others. This procedure can be utilized to make enzymatic clay and zeolite-modified electrodes. One such example of this utilization is the MB, methyl viologen (MV), and benzyl viologen (BV)-modified zirconium phosphate electrode for NADH oxidation (Munteanu et al., 2001). This approach is also suitable for preparing multiple integrated systems. Lev's group introduced carbon-ceramic composite electrodes (CCEs) as a modern technique to prepare stable multilayers (Tsionsky et al., 1994). Later, the CCE system was extremely introduced for analytical purposes (Wang et al., 1997). In the CCE preparation route, mediators were first mixed with  $\text{SiO}_2$  first in an appropriate ratio with alcohol and dilute HCl, sonicated for a couple of minutes after mixing it with carbon powder. Then it was converted into a suitable electrode by filling in a glass tube or by coating on conducting support. Other applications include making of an ethanol sensor out of alcohol oxidase enzyme (AOx) (Boujtita et al., 2000), a phenol sensor by the mixture of graphite, acetyl cellulose acetate (ACA) with ferrocene and *pseudomonas* bacteria (Skládal et al., 2002), an  $\text{H}_2\text{O}_2$  sensor by PVA, etc. (Wang and Dong, 2000). Industrially iron-enriched waste cinder ( $\text{CFe}^*$ ) was also reported as a useful host to form the stable hybrid  $\{\text{CFe}^* - \text{Fe}(\text{CN})\}$  derivatives directly inside the matrix by potential cycling with cyanometallate in  $\text{pH} = 2 \text{ KC/HCl}$  solutions (Zen et al., 2000b). Hence, from these chemical

modification types of the electrodes, we get to know the many potential applications already discovered for various analytical applications for multiple purposes and realized that this can play a key role for new inventions in the near future.

## SURFACE ENGINEERING FOR ELECTROCATALYTIC WATER OXIDATION

Hence, after all the discussions related to electrode materials, electrode designs and geometry, and the electrocatalysts, we can describe what the ideal electrode design should be for successful water oxidation and OER. As we already know, the working electrodes play a critical role in determining the performance and greatly influence the reaction rate due to their unique structure, degree of wettability, and access of catalyst to an electrolyte. For example, flat surface electrodes like glassy carbon allow the single-way penetration of the electrolyte that limits the catalysis only on the surface of the catalyst, whereas 3D electrodes like carbon cloth allow multiple pathways for electrolyte penetration from all sides of the catalyst and involve all the materials in the catalytic reaction (Dou et al., 2016; Tahir et al., 2017). They all have advantages and disadvantages like glassy carbon electrodes are easy to handle and widely used in the literature but offer only limited access to the catalyst. Thus, in this section, the discussion will be regarding the type of electrode surface morphology and catalyst property that will make water oxidation most feasible.

### Surface Area

Heterogeneous catalytic reactions, in general, occur on the surface of the electrode. Therefore, we already realized that a large surface area would be advantageous for catalytic reactions. We can apply four different methods to increase the surface area of a catalyst. Decreasing the size of the particle can dramatically boost the surface-to-volume ratio, thus increasing the effective surface area without altering the total electrode area. This is one of the most important reasons to widely use the size-control strategy in heterogeneous catalysis. If we can decrease the surface nanostructure size by 2 nm, their surface-to-volume ratio can be increased to 80%. The other approach is to synthesize catalysts into thin-layer 2D nanostructures (such as 2D nanosheets and 2D nanoplates). This also has the same effect to increase the surface-to-volume ratio of catalysts. Metal oxides and metal chalcogenides can be used for this specific purpose of 2D nanostructures for the optimized synthesis and design of the electrode, and these materials are proven to be useful to improve the surface area, active reaction sites, flexibility, and dispersion (Du et al., 2019; Elakkiya and Maduraiveeran, 2020); (Figure 5). Another approach is to increase the roughness of the catalyst surface nanostructures to form convex, concave, pilated, or cracking rough nanostructures. These types of unique structures with morphologies analogous to flowers, dendrites, tapers, multi-pods, stars, starfishes, islands, and cactuses can naturally promote the effective surface area for catalytic performance enhancement (McCrory et al., 2013). The last way is to manufacture hollow, porous, or mesoporous nanostructures (nanotubes, nano-frameworks, nanocages, nano-boxes, and metalorganic

framework) with porosities that not only can increase the number of active reaction sites and the specific surface areas but also efficiently accelerates the transportation and exchange of species of the catalyst surface (Lv et al., 2015; Wu et al., 2018). Besides all these means, 3D nano-porous structures of noble metals and their alloys can be prepared through the methods of electrodeposition, templating, annealing, de-alloying, *in-situ* synthesis, and galvanic replacement and modification for various electrocatalytic applications (Lu, 2019).

### Low-Index Facets

Surface facets influence the surface morphology and activity to a great extent due to different atomic arrangements of various facets. For example, in the case of an fcc noble-metal crystal, the low index facets generally are {111}, {100}, and {110} with their surface energies already stated as  $\gamma\{111\} < \gamma\{100\} < \gamma\{110\}$  (Fang et al., 2015). The activities of different surfaces depend on the reaction type and reaction media. For this purpose, to utilize here, we can use the acquisition of metal nanocrystals bound by different low-index facets with comparable sizes. This will allow us to investigate the facet-dependent effects free from size-effect interference. To give an example to illustrate, we can take Pd nano-crystals, which can be Pd nano-cubes enclosed by {100} facets and Pd octahedrons enclosed by {111} facets. The sizes of the nanostructures here can be controlled by applying etching techniques or reaction times. The Pd {100} surface can better activate oxygen species during reaction (Toyoshima et al., 2012); thus, this facet is significantly more active in electrode catalysis than the Pd {111} facet. Low-index facets can also be made catalytically active by tuning the particle sizes of nanocrystals on the electrode surface to alter the surface area. The size effect can influence the reaction rate, like with the shrinkage of the particle size, reaction rate and efficiency increase due to the boosted surface to volume ratio. The size control can provide an excellent platform for the investigation of size-dependent catalytic activities in various reactions for catalytic efficiency improvement, most of the times by reducing the particle size for a more exposed surface area.

Another evaluation of low-index facets includes assessing the effect of electrical contact between low-index facets and electrodes on electrocatalytic performance. Low contact resistance supports the electrode's high efficiency despite being consist of low-index facets. Sometimes this can even outperform high-index facets despite having higher surface energy. As an example, Pt multi-cubes with {100} facets (high coverage) achieve high catalytic activity (ORR), which can be comparable to Pt multi-pods with high-index {311} facets (Ma et al., 2015).

### High-Index Facets

We have already examined that high-index facets have much higher surface energy and catalytic activity than low-index facets, which usually act as distinct catalytic active sites for breaking chemical bonds. Electrocatalysts for metal electrodes can be synthesized with well-defined morphologies and high-index facets to exhibit significantly enhanced catalytic performance. These types of nano-crystals can be classified into monometallic and multi-metallic nano-crystals. For instance, unique Pt



nanocrystals with high-index facets (tetrahedrons/concave polyhedrons/concave nano cubes) show improved catalytic activity in many aspects (like ORR) (Luo et al., 2018). High-index facets possess a large number of steps, kinks, edges, corners, terraces, and vertexes, so they have more low-coordinated active sites on the surface to enable high electrocatalytic activities. Thus, the preparation of high-index facets can act as the solution to many electrocatalytic problems of metal nanocrystals. Oxidation etching can be used to introduce high-index facets with branched nanocrystals. The modification of etching strength can tailor several important parameters in the synthesis including, structure of seeds, the growth sites on the seeds, and the rate of atomic addition on the seeds (Xia et al., 2017). Therefore, tunable branched structures with tripods, tetrapods, hexapods, and octopods can be obtained. In the case of Pt, hexapods and octopods have higher active surface areas and roughness than those of Pt/C catalysts. Generally, these multi-pods have activity orders: octopods > hexapods > tetrapods > tripods (Ma et al., 2012). The superior electrocatalytic performance of octopods is ascribed to their high densities of stepped surfaces. Uneven anisotropic growth can also introduce high-index facets. The electrocatalytic performance of nanocrystals is usually increased in the order: octahedrons < nanowires < nanocubes < nanotapers. Nanotapers have the most densities of high-index facets, thus most active in electrochemical reactions (WANG et al., 2013a).

## Fabrication of Multi-Metallic Nanostructures

Electrocatalytic reactions can also occur at active sites on the interface besides the surface of the electrode. The interfaces are the sites relating to the species exchange, electronic structure, and charge transport. Thus, the interface design is crucial for good electrocatalytic performance. For exposed interfaces, these can also act as the active sites for the reactions. Now hybrid and alloys are two different types of multi-metallic nanostructures, having different electronic structures, atomic arrangements, functional sites, d-band depths, and compositions. By using this method, we can reduce the usage of costly metals like Pt by preparing multi-metallic nanostructures with similar or better activity (Zhang and Wöllner, 2018; Li et al., 2021). Now, we already know that hybrid materials possess high-index surfaces with high surface energy for effective catalytic activity. Thus, we can fabricate high-performance and low-cost catalytic electrodes through controllable growth of noble metals on the surface of the base electrode by simply modifying the surface and interface conditions. Alloying represents another approach to control the performance through tuning of atomic interfacing. Alloying can be used to prevent the oxidation of any metal nanostructure by mixing with it any passive metal. For example, Cu nanocrystals cannot survive from oxidation but alloying it with platinum to give  $\text{Cu}_x\text{Pt}_{100-x}$  improve the chemical stability, catalytic activity, and positive shifted the overpotential (Zhao et al., 2015).

## 2D Materials

2D materials may have prominent geometrical, thermal, mechanical, and electrical characteristics along with excellent solubility, adhesion, and dispersion altogether. Thus, graphene-like 2D materials can be used as support to fabricate unique hybrid structures to achieve optimized electrocatalytic performance (Zhao et al., 2019). These materials can also exhibit synergistic effects. Modified 2D hybrid materials can enhance electron conductivity, promote catalyst electrode adhesion, and suppress the agglomeration and oxidation erosion of catalysts (Fang et al., 2020). Through the fast development of 2D materials, the main challenge is to synthesize them properly and later stabilize them for the application, as metal atoms have strong preference to form-closed packed crystal structures in three dimensions. Recently, development has been made to synthesize nanosheets and nanoplates of Pd, Rh, Ru, Ag, Au, Pt-Cu, etc., with catalytic and optical applications, which has increased the possibility of fabricating 2D metal structures (Saleem et al., 2013; Fan et al., 2015).

## Interfacial Polarization

Charge on the surface can affect molecular adsorption on the surface and promotes species-catalyst charge transfer, and thus is a very important parameter in this regard. Polarization can tune the surface charge state of catalysts among the other approaches adopted. An example of this kind is graphene doped with nitrogen due to the electronegativity difference of N and C. polarization can be induced by external electrical field or ferroelectric substrates and charges accumulated at the interface can be extended to the surface, modifying the surface charge state of catalysts as a surface polarization (Shao et al., 2010; Wang et al., 2010). In a hybrid structure, the contact of two different metals has different work functions, which can cause a flow of electrons from one metal to another to equilibrate the electron Fermi distribution and induce polarization at the interface. Thereafter, reducing the distance between the polarized interface and reactive surface can cause accumulation of a particular charge on the surface, which may help in water oxidation. Thus, tuning the thickness to the effective level is very important to achieve effective surface polarization (Lin et al., 2018).

## Surface-State Passivation

The high density of surface states mainly due to crystalline defects is found in many semiconductor electrodes used for water oxidation. Although these may possess good charge transfer kinetics, the surface states are generally considered detrimental for OER electrodes because these may attract the movement of electrons toward the surface and act as traps for charge recombination at the surface. This can cause a shift in the overpotential value. Therefore, these are highly needed to be passivated in order to improve the OER performance. For example, CoPi, FeNiOx have been reported to effectively passivate the surface states of hematite for better water oxidation (Du et al., 2013; Thorne et al., 2016).

## Catalytic Efficiency Preservation

The conversion or deactivation of oxygen evolution catalysts can be the major concern for long-term operation. Moreover, depositing a thick layer of catalysts may not solve this problem but can give rise to the issue of catalyst overloading and slow down the reaction due to undesired charge recombination on the surface. This problem can be solved by *in-situ* catalyst regeneration to selectively deposit new catalyst where the catalytic activity decreases due to the loss of catalyst to preserve the high catalytic efficiency of the electrode. In combination with this corrosion inhibition property, more stability can be given by high-temperature annealing enabled by doping another metal into the base electrode metal. Life span and solar to hydrogen efficiency (STH) efficiency are the most important parameters affecting the economic feasibility and energy metrics (Sathre et al., 2014; Kuang et al., 2017). Many materials used for water oxidation are unstable for water oxidation due to their surface corrosion/dissolution. One such solution to this problem is to apply water oxidation catalysts to efficiently extract charges to reduce the probability of surface oxidation by the accumulated charges (Abe et al., 2010). We can also design the reaction in such a way as to change the catalytic pathways to suppress the generation of harmful products. Still, the working electrode is partially exposed to the solution because these electrodes are either made of scattered nanoparticles or porous films permeable to the electrolyte solution. A more effective solution is to protect the electrode surface by completely separating it from solutions using dense solid films. These protective layers should ideally not allow the permeation of electrolytes, conduct holes to facilitate charge transfer, and form good quality junctions with a large barrier height. These protective layers can be prepared by atomic layer deposition (ALD) and sputtering techniques (Hu et al., 2014; Mei et al., 2014; Hu et al., 2015; Kuang et al., 2017).

## RECENT ADVANCES IN IMPROVING OER CATALYSTS

Electrocatalysts are catalysts used in electrochemical reactions (reactions that include at least one outer-sphere electron transfer event for the occurrence of overall chemical transformation) to facilitate the reaction process. An electrocatalyst can either perform its functions on the electrode surface or act as the electrode itself (Suen et al., 2017). Without being consumed, electrocatalysts can increase the speed of the reactions by lowering the energy barrier for the electrochemical reactions. Generally, the main function of the electrocatalyst is to adsorb reactants on the surface to generate adsorbed intermediate. This process facilitates the charge transfer between the reactant and electrode (Suen et al., 2017). Thus, electrocatalysts reduce the potential required for electrochemical transformation.

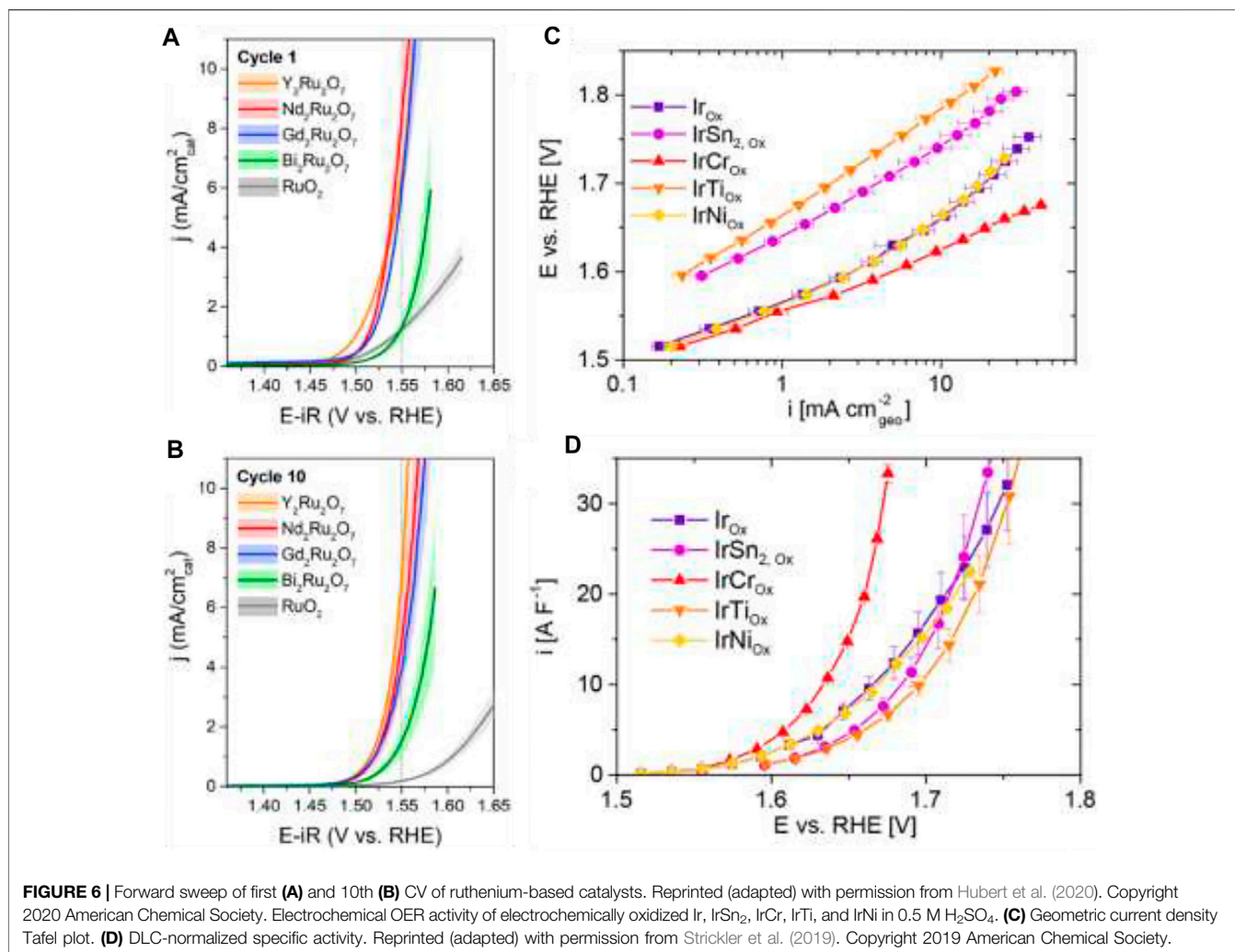
The performance of an electrocatalyst for electrochemical water oxidation can be evaluated based on three key factors—1) activity, 2) stability, and 3) efficiency. The activity of electrocatalysts can be explained in terms of overpotential, Tafel slope, and exchange current density. Polarization curves

help to know about these parameters. ECSA (Electrochemically Active Surface Area) is also another parameter that influences the catalytic activity of the electrocatalysts. Stability is one of the important parameters for describing the ability of an electrocatalyst to maintain its original activity over a long range of time. It can be assessed by recording the changes of the overpotential at a particular current density or by recording the variation of current density under a fixed applied overpotential, over a period of time. Another parameter that plays a significant role in evaluating the performance of an electrocatalyst is its efficiency, which is characterized by Faradaic efficiency and turn-over frequency.

Electrochemical water splitting is a clean and sustainable way to produce both hydrogen and oxygen through the use of renewable such as solar or wind (Debe, 2012), during which the OER takes place on anode through oxidation and HER takes place on the cathode through reduction. (Wang et al., 2019). In OER, molecular oxygen is produced *via* several proton/electron coupled procedures (Busch et al., 2016). The reaction can be very sensitive to pH. Two water molecules are oxidized into an oxygen molecule ( $O_2$ ) and four protons ( $H^+$ ) basically in acidic and neutral conditions, while  $H_2O$  and  $O_2$  are generated in the basic condition by the oxidation of hydroxyl groups ( $OH^-$ ). As we know, a potential difference of 1.23 V is required to drive the OER reaction, according to the Nernst equation; a unit shift in pH can shift the reaction potential approximately 59 mV. OER requires the transfer of four electrons, and a kinetically favorable OER process occurs through multi-step reactions with single electron transfer in each step. Therefore, the accumulation of energy of each step makes OER kinetics very sluggish that results in large overpotential for the process. This is where the need for electrocatalyst emerges again to overcome the energy barrier by increasing the electrode activity (Gorlin and Jaramillo, 2010; McCrory et al., 2013).

## Noble Metal-Based Materials

Molecular transition metal-based catalysts are of particular interest for water oxidation. Brudvig and co-workers specifically focused on Mn, Ru, Ir, Fe, and Co (Blakemore et al., 2015). Ru, Ir, Pd, and Pt also show good catalytic activity toward OER. Jaramillo and co-workers have also revolutionized the use of Ru- and Ir-based electrocatalysts for efficient oxygen evolution reactions (Seitz et al., 2016; Strickler et al., 2019; Hubert et al., 2020); (Figure 6). To decrease the usage of precious metals, it is very important to rationally design specific topological and electronic structures of catalysts to achieve satisfactory activity and stability (Xie et al., 2019). Noble metals and their alloys, oxides, and composites are among the most-studied catalysts for water oxidation for their excellent performance for OER. Experimental evidence shows that Ir and Ru are more active towards OER than Pt or Pd ( $Ru > Ir > Pd > Pt$ ) (Jiao et al., 2015). Ir and Ru are recognized as the state-of-the-art water oxidation electrocatalysts with relatively low overpotential and Tafel slope as well as superior stability (Danilovic et al., 2014), though Ru has comparative less stability. The 3D superstructure with Ir was recently developed containing ultrathin nanosheets, and the excellent catalytic activity of the electrode was seen in both



acidic and basic media, even better than Ir NPs (Pi et al., 2016). Considering the oxides, iridium oxide (IrO<sub>2</sub>) and ruthenium oxide (RuO<sub>2</sub>) are the most promising for OER (Ledendecker et al., 2019), though RuO<sub>2</sub> NPs have slightly higher intrinsic and mass OER activities than IrO<sub>2</sub>. Recently, the activity trends of noble metal-based materials have been identified: Ru > Ir ≈ RuO<sub>2</sub> > IrO<sub>2</sub>, while the dissolution trend is as follows: Ru >> Ir > RuO<sub>2</sub> >> IrO<sub>2</sub>. Thus, oxides have more potential applications with better stability and good activity here as metal dissolution is very much higher in both the acidic and basic medium. In spite of having substantial applications as efficient OER electrocatalysts, these materials suffer from high cost, unsatisfactory long-term stabilities, and limited compositions or morphologies that further calls for through investigation in designing robust noble metal-based materials for OER electrocatalysis (Shi et al., 2019).

## Earth-Abundant Transition Metals

Earth-abundant transition metal oxides have low costs, plentiful sources, and good corrosion resistance, and that is why their application has increased so much in the field of electrocatalysts (OER/HER/ORR). Their multivalent oxidation states

(M<sup>+2/+3/+4</sup>) make them excellent candidates for OER by providing the active sites for reaction (Risch et al., 2015). The OER activities of these materials are highly dependent on composition, oxidation state, morphology of the surface oxygen binding energy, the 3d electron number of transition metal ions, and the enthalpy for the lower- to higher-oxide transition (Yang et al., 2014). The intrinsic activity of individual active sites is dictated by their electronic structure. Cationic (e.g., Ni, Fe, Co, Sn) and anionic (e.g., O, S, OH) regulation is revealed to be a promising method for transition metal compounds to alter the electronic structure and generate high activity (Tang et al., 2018). During OER, phase conversions of Co-based materials, such as oxides to hydroxides or oxohydroxides, play a major role besides the multiple valence states. Wang et al. specified that the activity of Co<sub>3</sub>O<sub>4</sub> largely depends on the morphology, surface area, and oxidation state (Wang et al., 2014). Mesoporous Co<sub>3</sub>O<sub>4</sub> nanowires have a high surface area leading to more active sites, and the oxygen vacancies in it enhance the electrical conductivity due to the formation of new states through the delocalization of the Co–O bonds (Figures 7A,B).

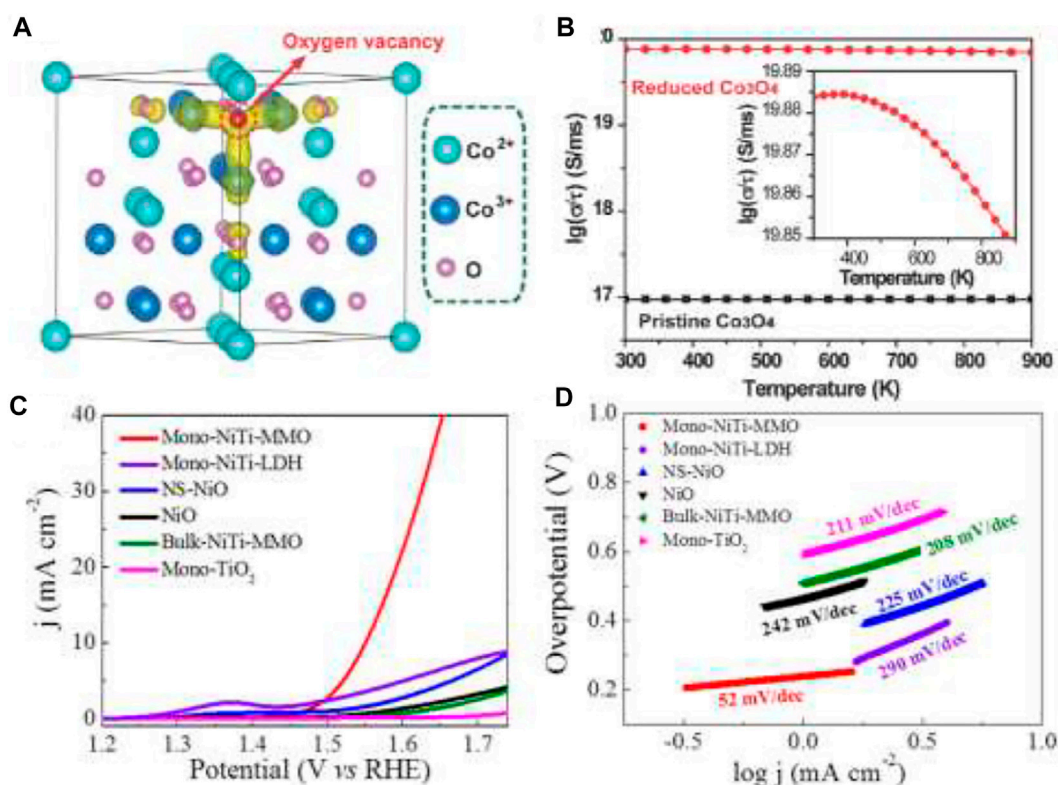


**FIGURE 7 | (A)** Partial charge density of the reduced  $\text{Co}_3\text{O}_4$ . The states of  $\text{Co}^{2+}$  are displayed in yellow. The iso-surface levels are  $0.037 \text{ e}^- \text{ \AA}^{-3}$ . **(B)** Calculated conductivity for the reduced  $\text{Co}_3\text{O}_4$  and the pristine  $\text{Co}_3\text{O}_4$ . Inset: An expansion of the plot of reduced  $\text{Co}_3\text{O}_4$  (Wang et al., 2014) OER performance; **(C)** linear sweep voltammetry (LSV) curves; **(D)** corresponding Tafel plots (Zhao et al., 2016).

Similar to cobalt oxide, great efforts have been made to improve the activity of NiO by tuning the particle size, surface area, and surface micro-structure (Han et al., 2016a) (**Figures 7C,D**).  $\text{Ni}^{3+}$  is very active as the higher oxidation state for OER. Ultra-small crystalline NiO NPs are fabricated using solvothermal reaction to form  $\text{Ni}^{3+}$  on the surface due to the small particle size of NiO. Therefore, the reactivity normally increases with the surface energy in the order  $\{101\} > \{113\} > \{100\}$  for NiO facets (Zhao et al., 2016). The oxides of manganese are other candidates to display excellent water oxidation activity. The catalytic activity again is dependable on the crystallographic structure, morphologies, pore structure, and chemical compositions. The good OER activity of manganese oxides in alkaline solution (Gorlin and Jaramillo, 2010) is mainly attributed to the nanostructured nature expediting the occurrence of suitable  $\text{Mn}_x\text{O}_y$  active sites at the related potentials. The order of activity of different crystal structures of manganese oxides is  $\alpha\text{-MnO}_2 > \text{amorphous MnO}_2 > \beta\text{-MnO}_2 > \alpha\text{-MnO}_2$  (Meng et al., 2014). Mixed metal oxides, like  $\text{NiCo}_2\text{O}_4$ , are very efficient for electrocatalysts for high electrical conductivity and excellent electrochemical activity. Hollow, porous, and complex 3D structures ( $\text{NiCo}_2\text{O}_4$ ) also have a very positive effect on the water oxidation activity (Han et al., 2016b) due to the penetration of the electrolyte and sufficient contact area between the electrolyte and reactants. Mixed Ni-Fe electrocatalysts are also widely studied for electrocatalytic

activity in alkaline solution (Görlin et al., 2016).  $\text{LiCoO}_2$  has also attracted considerable attention in OER for its stability and good activity, cubic NPs of which exhibit great water oxidation ability in neutral and basic electrolytes in all means (Chen et al., 2016).

## Hydroxides

Hydroxides generally have cationic brucite-like layers separated by charge balancing interlayer anions, and this open structure helps in fast diffusion with a rapid proton-coupled electron structure. Thus, the easy availability of catalytic active sites gives rise to a good electrocatalytic activity. The layered structure also allows the intercalation of water molecules and anions, providing better bulk redox activity. The typical hydroxide of water oxidation is  $\text{Ni}(\text{OH})_2\{\alpha \text{ and } \beta\}$ . For better stability and activity in alkaline solution,  $\alpha\text{-Ni}(\text{OH})_2$  is more suitable for this purpose than  $\beta\text{-Ni}(\text{OH})_2$ . Subbaraman et al. have found the following trend of 3d metal hydroxides with defined morphologies and stoichiometric ratio:  $\text{Mn} < \text{Fe} < \text{Co} < \text{Ni}$  (Subbaraman et al., 2012).

## Perovskites

Perovskites, having the general formula  $\text{ABO}_x$  with alkaline earth or rare earth metals (A) and transition metals (B) in their composition, are very important for OER due to flexibility in their composition and structure (Zhu et al., 2016).  $\text{CoSn}(\text{OH})_6$  perovskite nanocubes can be electrochemically carved in such a way to make it extremely active for



OER (Song et al., 2016). Crystal vacancies play a significant role in the construction of active catalysts. The activity of transition metals shows a volcano-shape necessity on the tendency of 3d electron and  $e_g$  symmetry in the oxide of the transition metal. The highest OER activity is expected at  $e_g$  occupancy very close to unity with high covalency of metal-oxygen bonds. Fabricated  $\text{Ba}_{0.5}\text{Sr}_{0.5}\text{Co}_{0.8}\text{Fe}_{0.2}\text{O}_{3-x}$  (BSCF) obtained higher OER activity than  $\text{IrO}_2$  in an alkaline medium (Suntivich et al., 2011).

## Metal Phosphides/Phosphates

Transition metal (Ni, Co, Mn) phosphates are more stable in oxidative environments than the oxides mainly because of their flexible structural natures as well as different orientations of the accessible phosphate groups in their crystals (Zhang et al., 2016). The main participant in this category is Co-based phosphates/phosphides ( $\text{CoP}$ ,  $\text{Li}_2\text{CoP}_2\text{O}_7$ ,  $\text{Na}_2\text{CoP}_2\text{O}_7$ ,  $\text{NaCoPO}_4$  and  $\text{LiCoPO}_4$ ). Serving as a working electrode, well-defined mesoporous CoP nanorod arrays on Ni foam display good OER activity (Zhu et al., 2015). The electrode is found to have excellent electric interconnection along with better mass transportation. Cations and anions significantly optimize the electrocatalytic activity by enlarging the active sites in the electrode and have important roles in overall water splitting (Duan et al., 2016). Thin films work more efficiently than pasting catalyst materials into electrodes or fabricating directly into some support such as Ni foam or carbon cloth because the deactivation by mechanical shredding or poisoning from the supporting materials can be prevented in this way. For example, Yang et al. made a diverse-phased porous Co phosphide/phosphate thin film that functionalizes directly as a working electrode. Similar to CoP, Mn and Ni based phosphides ( $\text{NiP}$ ,  $\text{Ni}_2\text{P}$ ,  $\text{MnP}$ ,  $\text{CoMnP}$ , etc.) are also studied for their water oxidation activities (Yang et al., 2015). Carbon-coated porous NiP (Yu et al., 2016) exhibits much better stability and excellent activity by improving the conductivity as well as charge transfer ability than MnP. In addition, MnP is not stable under oxidizing conditions due to the oxophilic nature of Mn. Recently, their performance are enhanced to much extent through the modulation of porosity, morphology, and combining with different materials (Stern et al., 2015). Furthermore, electrochemical studies show that oxygen evolution from Co-Pi prepared by electrodepositions from  $\text{Co}^{2+}$  solutions in phosphate electrolytes involves a turnover-limiting chemical step that is preceded by a one-electron, one-proton PCET equilibrium step (Surendranath et al., 2010).

## Carbonaceous Materials

Carbon-based materials, such as carbon nanotubes (CNTs), nanocarbons, graphenes, and mesoporous carbons, have been found very much active for electrocatalytic oxygen evolution reactions. They have a large specific surface area and excellent electrical conductivity along with good stability, making them perfect candidates for OER. Their performance can be further enhanced by shaping the geometrical and electrical structure of the electrode and doping materials such as N, S, P, B, O, etc., in the electrode material. Carbon atoms, bonding to electronegative oxygen or nitrogen, are positively charged. These positively charged carbon atoms adsorb  $\text{OH}^-$  through charge transfer and accelerate the recombination of intermediates such as  $\text{O}_2^-$  and  $\text{O}_2^{2-}$  to form oxygen gas and thus decrease the activation energy for the process.

Basically, the rational control of the electronic structure, strong chemical synergetic effect, and carbon defects prompted by the external carbon atoms enhance the activity (Yu X. et al., 2016). In nitrogen-doped carbon nanomaterials, Zhao et al. reported that the active sites for OER activities were pyridine and quaternary N (Zhao et al., 2013). Co-doping in carbon materials is another significant method, and Chen et al. reported the synthesis of N, O co-doped graphene carbon nanotube (NG-CNT) hydrogen film, which shows high OER activity overtaking  $\text{IrO}_2$  (Chen et al., 2014) with robust stability in alkaline and acidic solutions. Yu et al. conducted the experiment with N, S co-doped graphite foam (NSGF), which is directly used as an electrode without any polymeric binder. It showed fast kinetics and lower overpotential than N-doped graphite foam in alkaline solutions (Yu X. et al., 2016). Ma et al. designed the fabrication of g- $\text{C}_3\text{N}_4$  nanosheets-carbon nanotubes to have a strong composite for water oxidation possessing high nitrogen content, easily tailorable structure, and low cost (Ma et al., 2014a).

## Hybrid Nanostructure

The hybrid materials used for water oxidation include carbon material-based, Graphene-based, g- $\text{C}_3\text{N}_4$ -based, and many others for their high carrier mobility and long-term durability (Zhu et al., 2017). The interface should be strong between the catalyst materials and working electrode for high performance.  $\text{Co}_3\text{O}_4$  nanosheets are deposited on carbon paper ( $\text{Co}_3\text{O}_4$ -CP), which shows high catalytic activity towards water oxidation in 0.5 M  $\text{H}_2\text{SO}_4$  with an excellent overpotential of 370 mV and amazing stability. For increasing the interface-contact strength,  $\text{Co}_3\text{O}_4$ -carbon porous nanowire arrays are prepared through carbonization on the Cu foil (Ma et al., 2014b). Carbon-hybrid materials can also be made by layer double hydroxide, such as the fabrication of nanoplates of crystalline ultrathin Ni-Fe layered double hydroxide in multi-walled carbon nanotubes (Gorlin and Jaramillo, 2010). Nitrogen-doped hybrids based on phthalocyanines and porphyrins are also fabricated to boost the OER (Masa et al., 2014). High conductivity, large surface area, and atomic thinness make 2D carbon material graphene a fit substance to make composites with other transition metal oxides/hydroxides/sulfides for water oxidation OER. It can minimize the agglomeration of other nanoparticles to enhance the stability of the electrode. One such example of its use is crumpled graphene-cobalt oxide nanocrystal hybrids, which can fully utilize the catalytic surface area through the minimization of agglomeration of graphene sheets (Mao et al., 2014). Because of high nitrogen content and amazing stability together with graphene alike structure made g- $\text{C}_3\text{N}_4$  popular for hybrid OER electrocatalysts. Hybrid cobalt-hydroxide nanowires coated with graphitic carbon nitride nanosheets (Tahir et al., 2016) demonstrate a low overpotential of 320 mV at  $10 \text{ mA cm}^{-2}$  for water oxidation (Figure 8), showing better capabilities than  $\text{Co}(\text{OH})_2$ ,  $\text{IrO}_2$ ,  $\text{RuO}_2$ , and g- $\text{C}_3\text{N}_4$ . Core-branch hydroxysulfides like  $\text{Co}_2\text{NiS}_{2.4}(\text{OH})_{1.2}$  also exhibit superior OER performance, with a remarkably low overpotential (279 mV required for  $10.0 \text{ mA cm}^{-2}$ ), a low Tafel slope ( $52 \text{ mV dec}^{-1}$ ), and a favorable long-term stability (Wang et al., 2019). Spatially confined hybridization of nanometer-sized NiFe hydroxides into nitrogen-doped graphene frameworks is also found to exhibit superior OER activity (Tang et al., 2015).

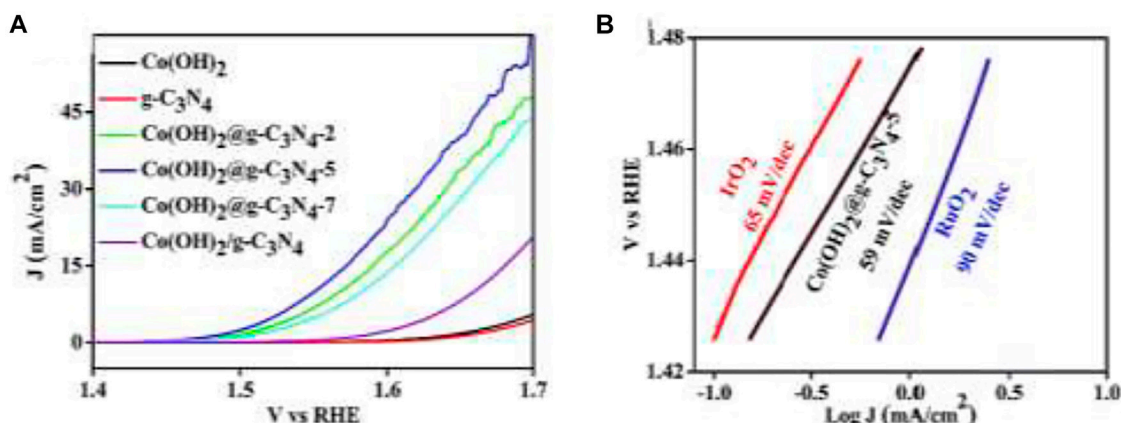


**FIGURE 8 | (A)** LSV curves of  $\text{g-C}_3\text{N}_4$ ,  $\text{Co(OH)}_2/\text{g-C}_3\text{N}_4$ ,  $\text{Co(OH)}_2$ , and  $\text{Co(OH)}_2/\text{g-C}_3\text{N}_4$  NWs and **(B)** Tafel slope of  $\text{Co(OH)}_2/\text{g-C}_3\text{N}_4-5$ ,  $\text{RuO}_2$ ,  $\text{IrO}_2$ , and Pt/C (Tahir et al., 2016).

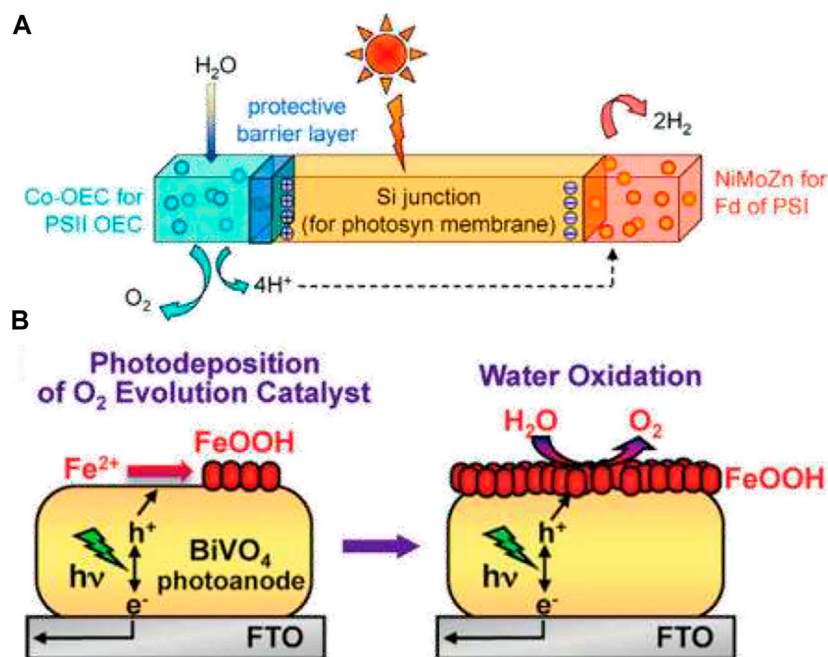


**FIGURE 9 | (A)** Construction of an artificial leaf. The photosynthetic membrane is replaced by a Si junction, which performs the light capture and conversion to a wireless current. The oxygen-evolving complex and ferredoxin reductase of the photosynthetic membrane are replaced by Co-OEC and NiMoZn OER and HER catalysts, respectively, to perform water splitting. Reprinted (adapted) with permission from (Nocera, 2012). Copyright (2012) American Chemical Society. **(B)** Photo-oxidation of water by a bismuth vanadate photoanode coupled with an iron oxyhydroxide oxygen evolution catalyst. Reprinted (adapted) with permission from Seabold and Choi (2012). Copyright (2012) American Chemical Society.

## Photochemical Water Oxidation

The earliest reported semiconducting material for this purpose is  $\text{TiO}_2$  for PEC water oxidation, which can stably oxidize water without any surface modification (Wang et al., 2013b), but it generally absorbs in the UV region, thus making its solar conversion efficiency insufficient for practical use. For water oxidation, most of the active electrocatalysts need an overpotential of around 0.2 V (McCrorry et al., 2013). Surface-active sites for hematite electrodes to produce  $\text{O}_2$  or  $\text{H}_2\text{O}_2$  depend on the surface hole density. Amorphous and

disordered catalysts, formed by electrodeposition or some low-temperature method, are more efficient for photocatalytic water oxidation due to their higher permissibility for the electrolyte. Dense catalysts form buried junctions, and the performance of the modified electrodes is then limited by Fermi-level pinning. Nocera et al. developed an electrodeposited “CoPi” catalyst for using it in various photoanodes due to the ease of deposition and high activity (Nocera, 2012); (Figure 9A). Fe doping in Co- and Ni-based OER electrocatalysts has emerged as the improved version for the problem

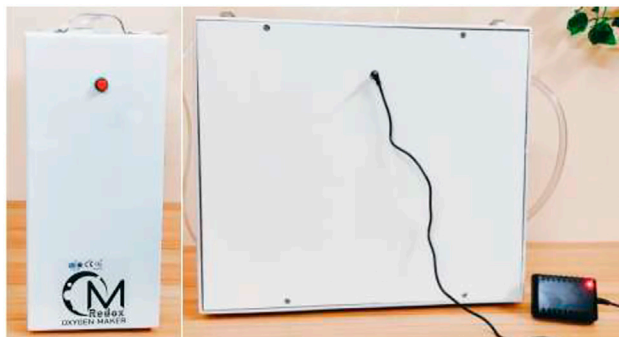


**FIGURE 10 |** Product oxygen maker, OM REDOX; the left and right sides present the front and side view of the prototype.

of the low-bias performance of  $\text{BiVO}_4$  electrodes (Morales-Guio et al., 2016). The PEC performance of photoanodes is sensitive to the thickness of the catalyst on the electrode surface if the catalyst is charged during decomposition for nanostructured electrodes with large surface areas.  $\text{FeOOH}$  provides an example to show much better stability for both planar and nanoporous  $\text{BiVO}_4$  electrodes than Co-based catalysts (Seabold and Choi, 2012); (Figure 9B) as a thick layer of catalyst can increase significantly the chance for the forward electron transfer of electrons, resulting in a severe surface charge recombination. The recently developed champion for electrochemical water oxidation is ternary  $\text{FeCoW}$  oxyhydroxide, and its high catalytic activity is ascribed to a synergistic interplay between tungsten, iron, and cobalt (Zhang et al., 2016). Some other promising materials for photoelectrochemical water splitting include  $\text{SnNb}_2\text{O}_6$ ,  $\text{Ta}_3\text{N}_5$ ,  $\text{BaTaO}_2\text{N}$ , Si, GaAs, CdTe, etc.

## TRANSLATING ACADEMIA TO INDUSTRY: OM-REDOX, AN OXYGEN GENERATING DEVICE BY SOLAIRE INITIATIVE PRIVATE LTD

In recent years, water oxidation reaction and, more specifically, oxygen evolution reaction have become a hot avenue for translating knowledge from academia to industry because of its widespread industrial applications in water splitting, rechargeable metal–air batteries, and fuel cells. Research is being performed to develop efficient electrocatalytic systems for these reactions, which can meet the industrial requirements of current densities of  $\geq 500 \text{ mA cm}^{-2}$  at overpotentials of  $\leq 300 \text{ mV}$  with long-term stability (Yu et al., 2021). Of late, water electrolysis has emerged as a reliable and eco-friendly way to produce high purity  $\text{H}_2$ , which is an environmentally benign energy carrier and feedstock for diverse applications, ranging from chemical industry to transportation, and power sectors. Over the past few decades, Ir- and Ru-based oxide electrocatalysts have been widely used in industrial proton-exchange membrane water electrolyzers (Li et al., 2020). However, their high cost, as well as limited supply, restricts their applications, which makes non-precious-metal-based

catalysts [e.g., oxides (Song et al., 2018) and (oxy) hydroxides (Yu et al., 2021) of first-row transition metals] great alternatives for the job. Among various electrochemical energy storage systems, metal–air battery presents very high theoretical energy density (e.g., the specific energy density of lithium–air battery is  $40.1 \text{ MJ/kg}$ , almost approaching to  $40.6 \text{ MJ/kg}$  of gasoline) (Gao et al., 2016). Li–air batteries have emerged as a potential replacement for Li-ion batteries in automotive applications. Research has been going on to develop novel material for core elements (porous carbon for air cathodes, catalysts, electrolytes, oxygen selective membranes, protected Li-metal) to make air-stable Li–air cells (Park et al., 2012). Efforts are also being made to develop bifunctional electrocatalysts to lower the overpotential of ORR and OER during the discharging and charging processes, which will help us to understand the full potential of this technology which is still arguably in its infancy (Vazhayil et al., 2021). A fuel cell is an electrochemical device that converts chemical energy to electrical energy. Among various available types of fuel cells, solid oxide and reversible fuel cells are more popular because of their ability of energy storage and fuel resurge, respectively. OER, being a part of the water electrolysis process, becomes important for developing these platforms. On the other hand, electrochemical water oxidation reaction also presents a feasible option to produce highly pure oxygens for medical and industrial purposes. According to WHO, during the ongoing COVID-19 pandemic, more than half a million COVID-19 patients in low and low middle-income countries estimated to need oxygen treatment every day (WHO, 2021). There are several methods commonly employed in medical oxygen productions (e.g., cryogenic distillation method, vacuum pressure swing adsorption, ceramic air separation technology, etc.), but all of them suffer from disadvantages such as its high cost, high energy consumption, contamination, or low production of pure oxygen. This makes electrochemical methods producing oxygen attractive because of their economical approach and eco-friendly nature. Pushkarev et al. reported an electrochemical oxygen pump (concentrator) with a solid polymer electrolyte which provides efficient *in situ* production of highly pure oxygen at a twice lower energy

consumption as compared to the water electrolyzer with a solid polymer electrolyte (Pushkarev et al., 2020).

We at Solaire with our product OM-REDOX (Oxygen Maker REDOX) have addressed the issue of portable oxygen supply at a very low cost (Figure 10). We have designed a device, which can produce oxygen by using water. The oxygen production rate is in the range of 3–5 L per minute (Lpm) and can be enhanced to 20–30 Lpm. Our patented product design and catalyst design (Patent file number: 202131020605) have been developed that can carry out water splitting under specially designed and fine-tuned patented condition. The process of biological water splitting bears resemblance to water splitting in which a chemical potential difference is used to split water. We have made several experiments to confirm with which catalyst the production of oxygen is the highest, and we have rigorously tested the quality of the catalyst and even ratified it with a hypoxia curing mouse model as well. The product uses electricity, which activates the catalyst in a sophisticated circuitry developed in-house by us. As we switch on the electricity oxygen is produced. The key process in our product lies in integration of mechanical, electrical, and chemical engineering with catalyst design science using easily sourced components and starting materials, rendering the product scalable and easy to manufacture in large scale. The simplest combination of circuitry and mechanical and chemical engineering principles used in this product reduces the production time and makes it easy to build and deliver to millions in need. The product OM REDOX is a direct demonstration of the translation of an academic result to a product in the market.

## CONCLUSION

The kinetics behind OER is quite sluggish, which makes water oxidation a difficult reaction to proceed. This necessitates the need for a catalyst and the optimal design of the electrode that can run the reaction at lower potential by overcoming the high activation energy barrier. In recent times, the electrocatalytic OER activity has been slightly improved due to the understanding of the scaling relation between  $\text{HO}^*$  and  $\text{HOO}^*$ . However, the targeted catalyst design should incorporate features of breaking the  $\text{HOO}^*$  and  $\text{HO}^*$  scaling and independently optimizing the adsorption energies of various intermediates (Kulkarni et al., 2018). Understanding the catalytic cycle with minute mechanistic details is very important to design efficient catalysts. It is very difficult to understand and control various competing redox mechanisms in OER. Hence, using various *in-situ* characterization techniques (e.g., femtosecond spectra, near-atmospheric X-ray photoelectron spectra (NAP-XPS), near-atmospheric scanning tunneling microscopy (NAP-STM), *in situ* X-ray absorption spectroscopy (XAS), and *in situ* diffuse reflectance infrared Fourier transform (DRIFT) spectra, corroborated with DFT computations, etc.) to capture a complete overview of the phase transformations, valence state changes, morphological variations, etc., under OER conditions is necessary (Suen et al., 2017). Search for non-

noble metal-based OER catalytic systems has also gained momentum because of high cost, unsatisfactory long-term stabilities, and limited compositions or morphologies of noble-metal-based systems. This has been discussed in detail in this review. Efforts to find efficient OER systems are not only focused on developing efficient catalytic materials, and it also finds its ways to efficient electrode and cell design strategies. Modifying the electrode surface by tuning the active catalytic sites, surface facets, interfaces has been in the forefront of electrode designs. However, uneven current and potential distributions have been the bottleneck problem to these approaches, which needs further attention. OER is used to make devices such as metal–air batteries and mainly production of hydrogen through water electrolysis. As for the process and application, sustainable energy utilization in OER is vital for its further applications, specifically using the cost-effective triboelectric nanogenerator. This advanced development can utilize sustainable mechanical energy such as wind, rain, etc., to obtain sustainable self-powered OER systems in the near future, and this self-powered approach is very perspective regarding the future goal of green energy generation. The water oxidation process takes place in nature on its own in plants photosystem II to provide protons and electrons for the photosynthesis process, and thus, oxygen gas is released in the atmosphere. Furthermore, water oxidation can be coupled with organic reactions, like  $\text{CO}_2$  reduction to formic acid and formaldehyde for synthesis purposes of important organic compounds. Therefore, water oxidation has immense importance as the green process for further futuristic aspects and improvement of the electrode design (geometry and electrocatalyst) will help to achieve more complex purposes in a sustainable way.

## AUTHOR CONTRIBUTIONS

SR designed the content of this review with PL and FV. RS, SD, AN, PM, and PK drafted different segments of the review. SR, FV, and PL supervised the work of PK in the matter of design of OM REDOX. RS, SD, AN, PM, and PK contributed equally to the work.

## FUNDING

This study received funding from IISER Kolkata and Solaire Initiative Pvt. Ltd. The funder was not involved in the study design, collection, analysis, interpretation of data, the writing of this article, or the decision to submit it for publication. All authors declare no other competing interests.

## ACKNOWLEDGMENTS

SD, AN, and PM acknowledge SRP-2021 for fellowships. PK acknowledges support from SOLAIRE. RS acknowledges DST-INSPIRE for a fellowship.



## REFERENCES

- Abe, R., Higashi, M., and Domen, K. (2010). Facile Fabrication of an Efficient Oxynitride TaON Photoanode for Overall Water Splitting into H<sub>2</sub> and O<sub>2</sub> under Visible Light Irradiation. *J. Am. Chem. Soc.* 132 (34), 11828–11829. doi:10.1021/ja1016552
- Alkire, R., and Gracon, B. (1975). Flow-Through Porous Electrodes. *J. Electrochem. Soc.* 122 (12), 1594–1601. doi:10.1149/1.2134076
- Alkire, R., and Ng, P. K. (1977). Studies on Flow-By Porous Electrodes Having Perpendicular Directions of Current and Electrolyte Flow. *J. Electrochem. Soc.* 124 (8), 1220–1227. doi:10.1149/1.2133531
- Allongue, P., Delamar, M., Desbat, B., Fagebaume, O., Hitmi, R., Pinson, J., et al. (1997). Covalent Modification of Carbon Surfaces by Aryl Radicals Generated from the Electrochemical Reduction of Diazonium Salts. *J. Am. Chem. Soc.* 119 (1), 201–207. doi:10.1021/ja963354s
- Arenas, L. F., Boardman, R. P., Ponce de León, C., and Walsh, F. C. (2018). X-ray Computed Micro-tomography of Reticulated Vitreous Carbon. *Carbon* 135, 85–94. doi:10.1016/j.carbon.2018.03.088
- Arenas, L. F., León, C. P. d., and Walsh, F. C. (2016). Mass Transport and Active Area of Porous Pt/Ti Electrodes for the Zn-Ce Redox Flow Battery Determined from Limiting Current Measurements. *Electrochimica Acta* 221, 154–166. doi:10.1016/j.electacta.2016.10.097
- Arenas, L. F., Ponce de León, C., and Walsh, F. C. (2019). Three-dimensional Porous Metal Electrodes: Fabrication, Characterisation and Use. *Curr. Opin. Electrochemistry* 16, 1–9. doi:10.1016/j.coelec.2019.02.002
- Arenas, L. F., Walsh, F. C., and de León, C. P. (2015). 3D-printing of Redox Flow Batteries for Energy Storage: a Rapid Prototype Laboratory Cell. *ECS J. Solid State. Sci. Technol.* 4 (4), P3080–P3085. doi:10.1149/2.0141504jss
- Baughman, R. H., Zakhidov, A. A., and De Heer, W. A. (2002). Carbon Nanotubes—The Route toward Applications. *Science* 297 (5582), 787–792. doi:10.1126/science.1060928
- Blakemore, J. D., Crabtree, R. H., and Brudvig, G. W. (2015). Molecular Catalysts for Water Oxidation. *Chem. Rev.* 115 (23), 12974–13005. doi:10.1021/acs.chemrev.5b00122
- Boujtita, M., Hart, J. P., and Pittson, R. (2000). Development of a Disposable Ethanol Biosensor Based on a Chemically Modified Screen-Printed Electrode Coated with Alcohol Oxidase for the Analysis of Beer. *Biosens. Bioelectron.* 15 (5–6), 257–263. doi:10.1016/s0956-5663(00)00075-0
- Busch, M., Halck, N. B., Kramm, U. I., Siahrostami, S., Krtill, P., and Rossmeisl, J. (2016). Beyond the Top of the Volcano? - A Unified Approach to Electrocatalytic Oxygen Reduction and Oxygen Evolution. *Nano Energy* 29, 126–135. doi:10.1016/j.nanoen.2016.04.011
- Campbell, S. A., Li, Y., Breakspear, S., Walsh, F. C., and Smith, J. R. (2007). Conducting Polymer Coatings in Electrochemical Technology Part 1 - Synthesis and Fundamental Aspects. *Trans. IMF* 85 (5), 237–244. doi:10.1179/174591907x229671
- Caro, C., Bedioui, F., and Zagal, J. H. (2002). Electrocatalytic Oxidation of Nitrite on a Vitreous Carbon Electrode Modified with Cobalt Phthalocyanine. *Electrochim. Acta* 47 (9), 1489–1494. doi:10.1016/s0013-4686(01)00875-1
- Castañeda, L. F., Walsh, F. C., Nava, J. L., and de León, C. P. (2017). Graphite Felt as a Versatile Electrode Material: Properties, Reaction Environment, Performance and Applications. *Electrochim. Acta* 258, 1115–1139.
- Chaki, N. K., and Vijayamohan, K. (2002). Self-assembled Monolayers as a Tunable Platform for Biosensor Applications. *Biosens. Bioelectron.* 17 (1–2), 1–12. doi:10.1016/s0956-5663(01)00277-9
- Chen, N., Qi, J., Du, X., Wang, Y., Zhang, W., Wang, Y., et al. (2016). Recycled LiCoO<sub>2</sub> in Spent Lithium-Ion Battery as an Oxygen Evolution Electrocatalyst. *RSC Adv.* 6 (105), 103541–103545. doi:10.1039/c6ra23483f
- Chen, S., Duan, J., Jaroniec, M., and Qiao, S.-Z. (2014). Nitrogen and Oxygen Dual-Doped Carbon Hydrogel Film as a Substrate-free Electrode for Highly Efficient Oxygen Evolution Reaction. *Adv. Mater.* 26 (18), 2925–2930. doi:10.1002/adma.201305608
- Critchley, R., Corni, I., Wharton, J. A., Walsh, F. C., Wood, R. J., and Stokes, K. R. (2013). The Preparation of Auxetic Foams by Three-Dimensional Printing and Their Characteristics. *Adv. Eng. Mater.* 15 (10), 980–985.
- Danilovic, N., Subbaraman, R., Chang, K.-C., Chang, S. H., Kang, Y. J., Snyder, J., et al. (2014). Activity-Stability Trends for the Oxygen Evolution Reaction on Monometallic Oxides in Acidic Environments. *J. Phys. Chem. Lett.* 5 (14), 2474–2478. doi:10.1021/jz501061n
- de León, P. C., Campbell, S., Smith, J., and Walsh, F. (2008). Conducting Polymer Coatings in Electrochemical Technology Part 2—Application Areas. *Trans. IMF* 86 (1), 34–40.
- Debe, M. K. (2012). Electrocatalyst Approaches and Challenges for Automotive Fuel Cells. *Nature* 486 (7401), 43–51. doi:10.1038/nature11115
- Dechakiatkrai, C., Lynam, C., Gilmore, K. J., Chen, J., Phanichphant, S., Bavykin, D. V., et al. (2009). Single-Walled Carbon Nanotube/Trititanate Nanotube Composite Fibers. *Adv. Eng. Mater.* 11 (7), B55–B60. doi:10.1002/adem.200800337
- Deinhammer, R. S., Ho, M., Anderegg, J. W., and Porter, M. D. (1994). Electrochemical Oxidation of Amine-Containing Compounds: a Route to the Surface Modification of Glassy Carbon Electrodes. *Langmuir* 10 (4), 1306–1313. doi:10.1021/la00016a054
- Dou, Y., Liao, T., Ma, Z., Tian, D., Liu, Q., Xiao, F., et al. (2016). Graphene-like Holey Co<sub>3</sub>O<sub>4</sub> Nanosheets as a Highly Efficient Catalyst for Oxygen Evolution Reaction. *Nano Energy* 30, 267–275. doi:10.1016/j.nanoen.2016.10.020
- Downard, A. J. (2000). Electrochemically Assisted Covalent Modification of Carbon Electrodes. *Electroanalysis* 12 (14), 1085–1096. doi:10.1002/1521-4109(200010)12:14<1085::aid-elant1085>3.0.co;2-a
- Du, C., Yang, X., Mayer, M. T., Hoyt, H., Xie, J., McMahon, G., et al. (2013). Hematite-Based Water Splitting with Low Turn-On Voltages. *Angew. Chem. Int. Ed.* 52 (48), 12692–12695. doi:10.1002/anie.201306263
- Du, Y., Khan, S., Zhang, X., Yu, G., Liu, R., Zheng, B., et al. (2019). In-situ Preparation of Porous Carbon Nanosheets Loaded with Metal Chalcogenides for a superior Oxygen Evolution Reaction. *Carbon* 149, 144–151. doi:10.1016/j.carbon.2019.04.048
- Duan, J., Chen, S., Vasileff, A., and Qiao, S. Z. (2016). Anion and Cation Modulation in Metal Compounds for Bifunctional Overall Water Splitting. *ACS Nano* 10 (9), 8738–8745. doi:10.1021/acsnano.6b04252
- Dunsch, L., Kavan, L., and Weber, J. (1990). Perfluoro Anion-Exchange Polymeric Films on Glassy Carbon Electrodes. *J. Electroanalytical Chem. Interfacial Electrochemistry* 280 (2), 313–325. doi:10.1016/0022-0728(90)87006-6
- Egorov, V., and O'Dwyer, C. (2020). Architected Porous Metals in Electrochemical Energy Storage. *Curr. Opin. Electrochemistry* 21, 201–208. doi:10.1016/j.coelec.2020.02.011
- Elakkiya, R., and Maduraiveeran, G. (2020). Two-dimensional Earth-Abundant Transition Metal Oxides Nanomaterials: Synthesis and Application in Electrochemical Oxygen Evolution Reaction. *Langmuir* 36 (17), 4728–4736. doi:10.1021/acs.langmuir.0c00714
- Fan, Z., Huang, X., Tan, C., and Zhang, H. (2015). Thin Metal Nanostructures: Synthesis, Properties and Applications. *Chem. Sci.* 6 (1), 95–111. doi:10.1039/c4sc02571g
- Fang, W., Huang, L., Zaman, S., Wang, Z., Han, Y., and Xia, B. Y. (2020). Recent Progress on Two-Dimensional Electrocatalysis. *Chem. Res. Chin. Univ.* 36 (4), 611–621. doi:10.1007/s40242-020-0182-3
- Fang, Z., Wang, Y., Liu, C., Chen, S., Sang, W., Wang, C., et al. (2015). Rational Design of Metal Nanoframes for Catalysis and Plasmonics. *Small* 11 (22), 2593–2605. doi:10.1002/smll.201402799
- Fleischmann, M., and Jansson, R. E. W. (1980). The Application of the Principles of Reaction Engineering to Electrochemical Cell Design. *J. Chem. Technol. Biotechnol.* 30 (1), 351–358.
- Gao, X., Zhang, H., Li, Q., Yu, X., Hong, Z., Zhang, X., et al. (2016). Hierarchical NiCo<sub>2</sub>O<sub>4</sub> Hollow Microcuboids as Bifunctional Electrocatalysts for Overall Water-Splitting. *Angew. Chem. Int. Ed.* 55 (21), 6290–6294. doi:10.1002/anie.201600525
- Goodridge, F., and Scott, K. (2013). *Electrochemical Process Engineering: A Guide to the Design of Electrolytic Plant*. Springer Science & Business Media.
- Gorlin, Y., and Jaramillo, T. F. (2010). A Bifunctional Nonprecious Metal Catalyst for Oxygen Reduction and Water Oxidation. *J. Am. Chem. Soc.* 132 (39), 13612–13614. doi:10.1021/ja104587v
- Górlin, M., Chernev, P., Ferreira de Araújo, J., Reier, T., Drespe, S. r., Paul, B., et al. (2016). Oxygen Evolution Reaction Dynamics, Faradaic Charge Efficiency, and the Active Metal Redox States of Ni-Fe Oxide Water Splitting Electrocatalysts. *J. Am. Chem. Soc.* 138 (17), 5603–5614.
- Haddon, R. C. (2002). Carbon Nanotubes. *Acc. Chem. Res.* 35 (12), 997. doi:10.1021/ar020259h

- Han, L., Dong, S., and Wang, E. (2016a). Transition-Metal (Co, Ni, and Fe)-Based Electrocatalysts for the Water Oxidation Reaction. *Adv. Mater.* 28 (42), 9266–9291. doi:10.1002/adma.201602270
- Han, L., Yu, X.-Y., and Lou, X. W. D. (2016b). Formation of Prussian-Blue-Analog Nanocages via a Direct Etching Method and Their Conversion into Ni-Co-Mixed Oxide for Enhanced Oxygen Evolution. *Adv. Mater.* 28 (23), 4601–4605. doi:10.1002/adma.201506315
- Hu, S., Lewis, N. S., Ager, J. W., Yang, J., McKone, J. R., and Strandwitz, N. C. (2015). Thin-film Materials for the protection of Semiconducting Photoelectrodes in Solar-Fuel Generators. *J. Phys. Chem. C* 119 (43), 24201–24228. doi:10.1021/acs.jpcc.5b05976
- Hu, S., Shaner, M. R., Beardslee, J. A., Lichterman, M., Brunschwig, B. S., and Lewis, N. S. (2014). Amorphous TiO<sub>2</sub> Coatings Stabilize Si, GaAs, and GaP Photoanodes for Efficient Water Oxidation. *Science* 344 (6187), 1005–1009. doi:10.1126/science.1251428
- Hubert, M. A., Patel, A. M., Gallo, A., Liu, Y., Valle, E., Ben-Naim, M., et al. (2020). Acidic Oxygen Evolution Reaction Activity-Stability Relationships in Ru-Based Pyrochlores. *ACS Catal.* 10 (20), 12182–12196. doi:10.1021/acscatal.0c02252
- Hwang, S. J., Kim, S.-K., Lee, J.-G., Lee, S.-C., Jang, J. H., Kim, P., et al. (2012). Role of Electronic Perturbation in Stability and Activity of Pt-Based alloy Nanocatalysts for Oxygen Reduction. *J. Am. Chem. Soc.* 134 (48), 19508–19511. doi:10.1021/ja307951y
- Jiao, Y., Zheng, Y., Jaroniec, M., and Qiao, S. Z. (2015). Design of Electrocatalysts for Oxygen- and Hydrogen-Involving Energy Conversion Reactions. *Chem. Soc. Rev.* 44 (8), 2060–2086. doi:10.1039/c4cs00470a
- Ju, H., and Shen, C. (2001). Electrocatalytic Reduction and Determination of Dissolved Oxygen at a Poly (Nile Blue) Modified Electrode. *Electroanalysis* 13 (8–9), 789–793. doi:10.1002/1521-4109(200105)13:8/9<789::aid-elan789>3.0.co;2-g
- Karyakin, A. A. (2001). Prussian Blue and its Analogues: Electrochemistry and Analytical Applications. *Electroanalysis* 13 (10), 813–819. doi:10.1002/1521-4109(200106)13:10<813::aid-elan813>3.0.co;2-z
- Kathiresan, M., and Velayutham, D. (2015). Ionic Liquids as an Electrolyte for the Electro Synthesis of Organic Compounds. *Chem. Commun.* 51 (99), 17499–17516. doi:10.1039/c5cc06961k
- Kong, J., Chapline, M. G., and Dai, H. (2001). Functionalized Carbon Nanotubes for Molecular Hydrogen Sensors. *Adv. Mater.* 13 (18), 1384–1386. doi:10.1002/1521-4095(200109)13:18<1384::aid-adma1384>3.0.co;2-8
- Kuang, Y., Yamada, T., and Domen, K. (2017). Surface and Interface Engineering for Photoelectrochemical Water Oxidation. *Joule* 1 (2), 290–305. doi:10.1016/j.joule.2017.08.004
- Kulkarni, A., Siahrostami, S., Patel, A., and Nørskov, J. K. (2018). Understanding Catalytic Activity Trends in the Oxygen Reduction Reaction. *Chem. Rev.* 118 (5), 2302–2312. doi:10.1021/acs.chemrev.7b00488
- Ledendecker, M., Geiger, S., Hengge, K. A., Lim, J., Cherevko, S., Mingers, A. M., et al. (2019). Towards Maximized Utilization of Iridium for the Acidic Oxygen Evolution Reaction. *Nano Res.* 12 (9), 1–6. doi:10.1007/s12274-019-2383-y
- Lertanantawong, B., O'Mullane, A. P., Surareungchai, W., Somasundrum, M., Burke, L. D., and Bond, A. M. (2008). Study of the Underlying Electrochemistry of Polycrystalline Gold Electrodes in Aqueous Solution and Electrocatalysis by Large Amplitude Fourier Transformed Alternating Current Voltammetry. *Langmuir* 24 (6), 2856–2868. doi:10.1021/la702454k
- Li, L., Wang, P., Shao, Q., and Huang, X. (2021). Recent Progress in Advanced Electrocatalyst Design for Acidic Oxygen Evolution Reaction. *Adv. Mater.* 33 (50), 2004243. doi:10.1002/adma.202004243
- Li, X., Pletcher, D., and Walsh, F. C. (2011). Electrodeposited lead Dioxide Coatings. *Chem. Soc. Rev.* 40 (7), 3879–3894. doi:10.1039/c0cs00213e
- Li, X., Zhao, L., Yu, J., Liu, X., Zhang, X., Liu, H., et al. (2020). Water Splitting: from Electrode to green Energy System. *Nano-Micro Lett.* 12 (1), 1–29. doi:10.1007/s40820-020-00469-3
- Lin, Y., Yang, L., Zhang, Y., Jiang, H., Xiao, Z., Wu, C., et al. (2018). Defective Carbon-CoP Nanoparticles Hybrids with Interfacial Charges Polarization for Efficient Bifunctional Oxygen Electrocatalysis. *Adv. Energ. Mater.* 8 (18), 1703623. doi:10.1002/aenm.201703623
- Low, C. T. J., Ponce-de-León, C., and Walsh, F. C. (2012). A Gold-Coated Titanium Oxide Nanotube Array for the Oxidation of Borohydride Ions. *Electrochemistry Commun.* 22, 166–169. doi:10.1016/j.elecom.2012.06.003
- Lu, L. (2019). Nanoporous Noble Metal-Based Alloys: A Review on Synthesis and Applications to Electrocatalysis and Electrochemical Sensing. *Mikrochim Acta* 186 (9), 1–21. doi:10.1007/s00604-019-3772-3
- Luo, M., Sun, Y., Zhang, X., Qin, Y., Li, M., Li, Y., et al. (2018). Stable High-Index Faceted Pt Skin on Zigzag-like PtFe Nanowires Enhances Oxygen Reduction Catalysis. *Adv. Mater.* 30 (10), 1705515. doi:10.1002/adma.201705515
- Lv, X., Zhu, Y., Jiang, H., Yang, X., Liu, Y., Su, Y., et al. (2015). Hollow Mesoporous NiCo<sub>2</sub>O<sub>4</sub> Nanocages as Efficient Electrocatalysts for Oxygen Evolution Reaction. *Dalton Trans.* 44 (9), 4148–4154. doi:10.1039/c4dt03803g
- Ma, L., Wang, C., Gong, M., Liao, L., Long, R., Wang, J., et al. (2012). Control over the Branched Structures of Platinum Nanocrystals for Electrocatalytic Applications. *ACS Nano* 6 (11), 9797–9806. doi:10.1021/nn304237u
- Ma, L., Wang, C., Xia, B. Y., Mao, K., He, J., Wu, X., et al. (2015). Platinum Multicubes Prepared by Ni<sup>2+</sup>-Mediated Shape Evolution Exhibit High Electrocatalytic Activity for Oxygen Reduction. *Angew. Chem. Int. Ed.* 54 (19), 5666–5671. doi:10.1002/anie.201500947
- Ma, T. Y., Dai, S., Jaroniec, M., and Qiao, S. Z. (2014a). Graphitic Carbon Nitride Nanosheet-Carbon Nanotube Three-Dimensional Porous Composites as High-Performance Oxygen Evolution Electrocatalysts. *Angew. Chem. Int. Ed.* 53 (28), 7281–7285. doi:10.1002/anie.201403946
- Ma, T. Y., Dai, S., Jaroniec, M., and Qiao, S. Z. (2014b). Metal-Organic Framework Derived Hybrid Co<sub>3</sub>O<sub>4</sub>-Carbon Porous Nanowire Arrays as Reversible Oxygen Evolution Electrodes. *J. Am. Chem. Soc.* 136 (39), 13925–13931. doi:10.1021/ja5082553
- Mao, S., Wen, Z., Huang, T., Hou, Y., and Chen, J. (2014). High-performance Bifunctional Electrocatalysts of 3D Crumpled Graphene-Cobalt Oxide Nanohybrids for Oxygen Reduction and Evolution Reactions. *Energy Environ. Sci.* 7 (2), 609–616. doi:10.1039/c3ee42696c
- Masa, J., Xia, W., Sinev, I., Zhao, A., Sun, Z., Grütze, S., et al. (2014). Mn<sub>x</sub>O<sub>y</sub>/NC and Co<sub>x</sub>O<sub>y</sub>/NC Nanoparticles Embedded in a Nitrogen-Doped Carbon Matrix for High-Performance Bifunctional Oxygen Electrodes. *Angew. Chem. Int. Ed.* 53 (32), 8508–8512. doi:10.1002/anie.201402710
- McCrory, C. C. L., Jung, S., Peters, J. C., and Jaramillo, T. F. (2013). Benchmarking Heterogeneous Electrocatalysts for the Oxygen Evolution Reaction. *J. Am. Chem. Soc.* 135 (45), 16977–16987. doi:10.1021/ja407115p
- Mei, B., Seger, B., Pedersen, T., Malizia, M., Hansen, O., Chorkendorff, I., et al. (2014). Protection of P+-N-Si Photoanodes by Sputter-Deposited Ir/IrO<sub>x</sub> Thin Films. *J. Phys. Chem. Lett.* 5 (11), 1948–1952. doi:10.1021/jz500865g
- Meng, Y., Song, W., Huang, H., Ren, Z., Chen, S.-Y., and Suib, S. L. (2014). Structure-Property Relationship of Bifunctional MnO<sub>2</sub> Nanostructures: Highly Efficient, Ultra-stable Electrochemical Water Oxidation and Oxygen Reduction Reaction Catalysts Identified in Alkaline Media. *J. Am. Chem. Soc.* 136 (32), 11452–11464. doi:10.1021/ja505186m
- Möhle, S., Zirbes, M., Rodrigo, E., Gieshoff, T., Wiebe, A., and Waldvogel, S. R. (2018). Modern Electrochemical Aspects for the Synthesis of Value-Added Organic Products. *Angew. Chem. Int. Ed. Engl.* 57 (21), 6018–6041. doi:10.1002/anie.201712732
- Morales-Guio, C. G., Liardet, L., and Hu, X. (2016). Oxidatively Electrodeposited Thin-Film Transition Metal (Oxy)hydroxides as Oxygen Evolution Catalysts. *J. Am. Chem. Soc.* 138 (28), 8946–8957. doi:10.1021/jacs.6b05196
- Munteanu, F. D., Kubota, L. T., and Gorton, L. (2001). Effect of pH on the Catalytic Electrooxidation of NADH Using Different Two-Electron Mediators Immobilised on Zirconium Phosphate. *J. Electroanalytical Chem.* 509 (1), 2–10. doi:10.1016/s0022-0728(01)00376-x
- Murray, R. W. (1980). Chemically Modified Electrodes. *Acc. Chem. Res.* 13 (5), 135–141. doi:10.1021/ar50149a002
- Murray, R. W., Ewing, A. G., and Durst, R. A. (1987). Chemically Modified Electrodes. Molecular Design for Electroanalysis. *Anal. Chem.* 59 (5), 379A–390A. doi:10.1021/ac00132a001
- Murray, R. W. (1992). Introduction to the Chemistry of Molecularly Designed Electrode Surfaces. *Mol. Des. Electrode Surf.* 22, 1–48.
- Mustafa, I., Susantyoko, R., Wu, C. H., Ahmed, F., Hashaikh, R., Almarzooqi, F., et al. (2019). Nanoscopic and Macro-Porous Carbon Nano-Foam Electrodes with Improved Mass Transport for Vanadium Redox Flow Batteries. *Sci. Rep.* 9 (1), 1–14. doi:10.1038/s41598-019-53491-w
- Nava, J., Oropeza, M., de León, C. P., González-García, J., and Frías-Ferrer, A. (2008). Determination of the Effective Thickness of a Porous Electrode in a Flow-Through Reactor; Effect of the Specific Surface Area of Stainless Steel

- Fibres, Used as a Porous Cathode, during the Deposition of Ag (I) Ions. *Hydrometallurgy* 91 (1–4), 98–103. doi:10.1016/j.hydromet.2007.12.001
- Nocera, D. G. (2012). The Artificial Leaf. *Acc. Chem. Res.* 45 (5), 767–776. doi:10.1021/ar2003013
- Oyama, N., and Anson, F. C. (1980). Catalysis of Electrode Processes by Multiply-Charged Metal Complexes Electrostatically Bound to Polyelectrolyte Coatings on Graphite Electrodes, and the Use of Polymer-Coated Rotating Disk Electrodes in Diagnosing Kinetic and Conduction Mechanisms. *Anal. Chem.* 52 (8), 1192–1198. doi:10.1021/ac50058a009
- Park, M., Sun, H., Lee, H., Lee, J., and Cho, J. (2012). Lithium-Air Batteries: Survey on the Current Status and Perspectives towards Automotive Applications from a Battery Industry Standpoint. *Adv. Energ. Mater.* 2 (7), 780–800. doi:10.1002/aenm.201200020
- Perry, S. C., and Denuault, G. (2015). Transient Study of the Oxygen Reduction Reaction on Reduced Pt and Pt Alloys Microelectrodes: Evidence for the Reduction of Pre-adsorbed Oxygen Species Linked to Dissolved Oxygen. *Phys. Chem. Chem. Phys.* 17 (44), 30005–30012. doi:10.1039/c5cp04667j
- Perry, S. C., Ponce de León, C., and Walsh, F. C. (2020). Review-The Design, Performance and Continuing Development of Electrochemical Reactors for Clean Electrosynthesis. *J. Electrochem. Soc.* 167 (15), 155525. doi:10.1149/1945-7111/abc58e
- Pi, Y., Zhang, N., Guo, S., Guo, J., and Huang, X. (2016). Ultrathin Laminar Ir Superstructure as Highly Efficient Oxygen Evolution Electrocatalyst in Broad pH Range. *Nano Lett.* 16 (7), 4424–4430. doi:10.1021/acs.nanolett.6b01554
- Pletcher, D. (2019). *A First Course in Electrode Processes*. Cambridge: Royal Society of Chemistry.
- Pushkarev, A. S., Pushkareva, I. V., Solov'yev, M. A., Butrim, S. I., and Grigoriev, S. A. (2020). The Study of the Solid Polymer Electrolyte Oxygen Concentrator with Nanostructural Catalysts Based on Hydrophobized Support. *Nanotechnol. Russ.* 15 (11), 785–792. doi:10.1134/S1995078020060154
- Ralph, T. R., Hitchman, M. L., Millington, J. P., and Walsh, F. C. (1999). Evaluation of a Reactor Model and Cathode Materials for Batch Electrolysis of L-Cystine Hydrochloride. *J. Electroanalytical Chem.* 462 (1), 97–110. doi:10.1016/s0022-0728(98)00393-3
- Ramesh, P., and Sampath, S. (2001). Electrochemical and Spectroscopic Characterization of Quinone Functionalized Exfoliated Graphite. *Analyst* 126 (11), 1872–1877. doi:10.1039/b106199m
- Risch, M., Ringleb, F., Kohlhoff, M., Bogdanoff, P., Chernev, P., Zaharieva, I., et al. (2015). Water Oxidation by Amorphous Cobalt-Based Oxides: *In Situ* Tracking of Redox Transitions and Mode of Catalysis. *Energ. Environ. Sci.* 8 (2), 661–674. doi:10.1039/c4ee03004d
- Sadakane, M., and Steckhan, E. (1998). Electrochemical Properties of Polyoxometalates as Electrocatalysts. *Chem. Rev.* 98 (1), 219–238. doi:10.1021/cr960403a
- Saleem, F., Zhang, Z., Xu, B., Xu, X., He, P., and Wang, X. (2013). Ultrathin Pt-Cu Nanosheets and Nanocones. *J. Am. Chem. Soc.* 135 (49), 18304–18307. doi:10.1021/ja4101968
- Santos, D. M. F., Sequeira, C. A. C., and Figueiredo, J. L. (2013). Hydrogen Production by Alkaline Water Electrolysis. *Quím. Nova* 36, 1176–1193. doi:10.1590/s0100-40422013000800017
- Sathre, R., Scown, C. D., Morrow, W. R., Stevens, J. C., Sharp, I. D., Ager, J. W., et al. (2014). Life-cycle Net Energy Assessment of Large-Scale Hydrogen Production via Photoelectrochemical Water Splitting. *Energ. Environ. Sci.* 7 (10), 3264–3278. doi:10.1039/c4ee01019a
- Seabold, J. A., and Choi, K.-S. (2012). Efficient and Stable Photo-Oxidation of Water by a Bismuth Vanadate Photoanode Coupled with an Iron Oxyhydroxide Oxygen Evolution Catalyst. *J. Am. Chem. Soc.* 134 (4), 2186–2192. doi:10.1021/ja209001d
- Seitz, L. C., Dickens, C. F., Nishio, K., Hikita, Y., Montoya, J., Doyle, A., et al. (2016). A Highly Active and Stable IrO<sub>x</sub>/SrIrO<sub>3</sub> Catalyst for the Oxygen Evolution Reaction. *Science* 353 (6303), 1011–1014. doi:10.1126/science.aaf5050
- Shao, Y., Zhang, S., Engelhard, M. H., Li, G., Shao, G., Wang, Y., et al. (2010). Nitrogen-doped Graphene and its Electrochemical Applications. *J. Mater. Chem.* 20 (35), 7491–7496. doi:10.1039/c0jm00782j
- Shen, M., Bennett, N., Ding, Y., and Scott, K. (2011). A Concise Model for Evaluating Water Electrolysis. *Int. J. Hydrogen Energ.* 36 (22), 14335–14341. doi:10.1016/j.ijhydene.2010.12.029
- Shi, G., Luo, M., Xue, J., Xu, F., Jin, L., and Jin, J. (2001). Study of an Au Colloid Self-Assembled Electrode and its Application to the Determination of Carbon Monoxide. *Fresenius' J. Anal. Chem.* 370 (7), 878–882. doi:10.1007/s002160100850
- Shi, Q., Zhu, C., Du, D., and Lin, Y. (2019). Robust noble Metal-Based Electrocatalysts for Oxygen Evolution Reaction. *Chem. Soc. Rev.* 48 (12), 3181–3192. doi:10.1039/c8cs00671g
- Shinagawa, T., and Takanabe, K. (2017). Towards Versatile and Sustainable Hydrogen Production through Electrocatalytic Water Splitting: Electrolyte Engineering. *ChemSusChem* 10 (7), 1318–1336. doi:10.1002/cssc.201601583
- Skádal, P., Morozova, N. O., and Reshetilov, A. N. (2002). Amperometric Biosensors for Detection of Phenol Using Chemically Modified Electrodes Containing Immobilized Bacteria. *Biosens. Bioelectron.* 17 (10), 867–873.
- Song, F., Bai, L., Moysiadou, A., Lee, S., Hu, C., Liardet, L., et al. (2018). Transition Metal Oxides as Electrocatalysts for the Oxygen Evolution Reaction in Alkaline Solutions: an Application-Inspired Renaissance. *J. Am. Chem. Soc.* 140 (25), 7748–7759. doi:10.1021/jacs.8b04546
- Song, F., Schenk, K., and Hu, X. (2016). A Nanoporous Oxygen Evolution Catalyst Synthesized by Selective Electrochemical Etching of Perovskite Hydroxide CoSn(OH)<sub>6</sub>nanocubes. *Energ. Environ. Sci.* 9 (2), 473–477. doi:10.1039/c5ee03453a
- Stern, L.-A., Feng, L., Song, F., and Hu, X. (2015). Ni<sub>2</sub>P as a Janus Catalyst for Water Splitting: the Oxygen Evolution Activity of Ni<sub>2</sub>P Nanoparticles. *Energ. Environ. Sci.* 8 (8), 2347–2351. doi:10.1039/c5ee01155h
- Strickler, A. L., Flores, R. A., King, L. A., Nørskov, J. K., Bajdich, M., and Jaramillo, T. F. (2019). Systematic Investigation of Iridium-Based Bimetallic Thin Film Catalysts for the Oxygen Evolution Reaction in Acidic media. *ACS Appl. Mater. Inter.* 11 (37), 34059–34066. doi:10.1021/acsami.9b13697
- Subbaraman, R., Tripkovic, D., Chang, K.-C., Strmcnik, D., Paulikas, A. P., Hirunsit, P., et al. (2012). Trends in Activity for the Water Electrolyser Reactions on 3d M(Ni,Co,Fe,Mn)Hydr(oxy)oxide Catalysts. *Nat. Mater.* 11 (6), 550–557. doi:10.1038/nmat3313
- Suen, N.-T., Hung, S.-F., Quan, Q., Zhang, N., Xu, Y.-J., and Chen, H. M. (2017). Electrocatalysis for the Oxygen Evolution Reaction: Recent Development and Future Perspectives. *Chem. Soc. Rev.* 46 (2), 337–365. doi:10.1039/c6cs00328a
- Suntivich, J., May, K. J., Gasteiger, H. A., Goodenough, J. B., and Shao-Horn, Y. (2011). A Perovskite Oxide Optimized for Oxygen Evolution Catalysis from Molecular Orbital Principles. *Science* 334 (6061), 1383–1385. doi:10.1126/science.1212858
- Surendranath, Y., Kanan, M. W., and Nocera, D. G. (2010). Mechanistic Studies of the Oxygen Evolution Reaction by a Cobalt-Phosphate Catalyst at Neutral pH. *J. Am. Chem. Soc.* 132 (46), 16501–16509. doi:10.1021/ja106102b
- Tahir, M., Mahmood, N., Pan, L., Huang, Z.-F., Lv, Z., Zhang, J., et al. (2016). Efficient Water Oxidation through Strongly Coupled Graphitic C<sub>3</sub>N<sub>4</sub> Coated Cobalt Hydroxide Nanowires. *J. Mater. Chem. A* 4 (33), 12940–12946. doi:10.1039/c6ta05088c
- Tahir, M., Pan, L., Idrees, F., Zhang, X., Wang, L., Zou, J.-J., et al. (2017). Electrocatalytic Oxygen Evolution Reaction for Energy Conversion and Storage: a Comprehensive Review. *Nano Energy* 37, 136–157. doi:10.1016/j.nanoen.2017.05.022
- Tammeveski, K., Kontturi, K., Nichols, R. J., Potter, R. J., and Schiffrin, D. J. (2001). Surface Redox Catalysis for O<sub>2</sub> Reduction on Quinone-Modified Glassy Carbon Electrodes. *J. Electroanal. Chem.* 515 (1–2), 101–112. doi:10.1016/s0022-0728(01)00633-7
- Tang, C., Wang, H.-F., and Zhang, Q. (2018). Multiscale Principles to Boost Reactivity in Gas-Involving Energy Electrocatalysis. *Acc. Chem. Res.* 51 (4), 881–889. doi:10.1021/acs.accounts.7b00616
- Tang, C., Wang, H.-S., Wang, H.-F., Zhang, Q., Tian, G.-L., Nie, J.-Q., et al. (2015). Spatially Confined Hybridization of Nanometer-Sized NiFe Hydroxides into Nitrogen-Doped Graphene Frameworks Leading to Superior Oxygen Evolution Reactivity. *Adv. Mater.* 27 (30), 4516–4522. doi:10.1002/adma.201501901
- Tang, C., Zheng, Y., Jaroniec, M., and Qiao, S. Z. (2021). Electrocatalytic Refinery for Sustainable Production of Fuels and Chemicals. *Angew. Chem. Int. Ed.* 60 (36), 19572–19590. doi:10.1002/anie.202101522
- Thorne, J. E., Jang, J.-W., Liu, E. Y., and Wang, D. (2016). Understanding the Origin of Photoelectrode Performance Enhancement by Probing Surface Kinetics. *Chem. Sci.* 7 (5), 3347–3354. doi:10.1039/c5sc04519c



- Tian, N., Zhou, Z.-Y., Sun, S.-G., Ding, Y., and Wang, Z. L. (2007). Synthesis of Tetrahexahedral Platinum Nanocrystals with High-index Facets and High Electro-Oxidation Activity. *Science* 316 (5825), 732–735. doi:10.1126/science.1140484
- Toyoshima, R., Yoshida, M., Monya, Y., Suzuki, K., Mun, B. S., Amemiya, K., et al. (2012). Active Surface Oxygen for Catalytic CO Oxidation on Pd(100) Proceeding under Near Ambient Pressure Conditions. *J. Phys. Chem. Lett.* 3 (21), 3182–3187. doi:10.1021/jz301404n
- Tsionsky, M., Gun, G., Glezer, V., and Lev, O. (1994). Sol-gel-derived Ceramic-Carbon Composite Electrodes: Introduction and Scope of Applications. *Anal. Chem.* 66 (10), 1747–1753. doi:10.1021/ac00082a024
- Vazhayil, A., Vazhayal, L., Thomas, J., Ashok C, S., and Thomas, N. (2021). A Comprehensive Review on the Recent Developments in Transition Metal-Based Electrocatalysts for Oxygen Evolution Reaction. *Appl. Surf. Sci. Adv.* 6, 100184. doi:10.1016/j.apsadv.2021.100184
- Viana, A. S., Kalaji, M., and Abrantes, L. M. (2002). Self-assembled Monolayers of Vitamin B12 Disulphide Derivatives on Gold. *Electrochimica Acta* 47 (10), 1587–1594. doi:10.1016/s0013-4686(01)00885-4
- Walcarus, A. (2001a). Electroanalysis with Pure, Chemically Modified and Sol-Gel-Derived Silica-Based Materials. *Electroanalysis* 13 (8-9), 701–718. doi:10.1002/1521-4109(200105)13:8/9<701::aid-elan701>3.0.co;2-6
- Walcarus, A. (2001b). Electrochemical Applications of Silica-Based Organic-Inorganic Hybrid Materials. *Chem. Mater.* 13 (10), 3351–3372. doi:10.1021/cm0110167
- Walsh, F. C., Arenas, L. F., and Ponce de León, C. (2018). Developments in Electrode Design: Structure, Decoration and Applications of Electrodes for Electrochemical Technology. *J. Chem. Technol. Biotechnol.* 93 (11), 3073–3090. doi:10.1002/jctb.5706
- Walsh, F. C., Bavykin, D. V., Torrente-Murciano, L., Lapkin, A. A., and Cressey, B. A. (2006). Synthesis of Novel Composite Materials via the Deposition of Precious Metals onto Protonated Titanate (TiO<sub>2</sub>) Nanotubes. *Trans. IMF* 84 (6), 293–299. doi:10.1179/174591906x149077
- Walsh, F. C. (2001). Electrochemical Technology for Environmental Treatment and Clean Energy Conversion. *Pure Appl. Chem.* 73 (12), 1819–1837. doi:10.1351/pac200173121819
- Walsh, F. C., and Low, C. T. J. (2016). A Review of Developments in the Electrodeposition of Tin. *Surf. Coat. Tech.* 288, 79–94. doi:10.1016/j.surfcoat.2015.12.081
- Walsh, F. C., Ponce de León, C., Bavykin, D. V., Low, C. T. J., Wang, S. C., and Larson, C. (2015). The Formation of Nanostructured Surfaces by Electrochemical Techniques: a Range of Emerging Surface Finishes. Part 2: Examples of Nanostructured Surfaces by Plating and Anodising with Their Applications. *Trans. IMF* 93 (5), 241–247. doi:10.1080/00202967.2015.1114724
- Walsh, F. C., and Ponce de León, C. (2018). Progress in Electrochemical Flow Reactors for Laboratory and Pilot Scale Processing. *Electrochimica Acta* 280, 121–148. doi:10.1016/j.electacta.2018.05.027
- Walsh, F. C., and Wills, R. G. A. (2010). The Continuing Development of Magnéli Phase Titanium Sub-oxides and Ebonex Electrodes. *Electrochimica Acta* 55 (22), 6342–6351. doi:10.1016/j.electacta.2010.05.011
- Walsh, F., and Reade, G. (1994a). Design and Performance of Electrochemical Reactors for Efficient Synthesis and Environmental Treatment. Part 1. Electrode Geometry and Figures of merit. *Analyst* 119 (5), 791–796. doi:10.1039/an9941900791
- Walsh, F., and Reade, G. (1994b). Design and Performance of Electrochemical Reactors for Efficient Synthesis and Environmental Treatment. Part 2. Typical Reactors and Their Performance. *Analyst* 119 (5), 797–803. doi:10.1039/an9941900797
- Wang, B., and Dong, S. (2000). Sol-gel-derived Amperometric Biosensor for Hydrogen Peroxide Based on Methylene green Incorporated in Nafion Film. *Talanta* 51 (3), 565–572. doi:10.1016/s0039-9140(99)00315-x
- Wang, B., Tang, C., Wang, H.-F., Chen, X., Cao, R., and Zhang, Q. (2019a). Core-branch CoNi Hydroxysulfides with Versatile Regulated Electronic and Surface Structures for superior Oxygen Evolution Electrocatalysis. *J. Energ. Chem.* 38, 8–14. doi:10.1016/j.jchem.2018.12.006
- Wang, C., Bai, Y., Wang, L., Long, R., Liu, D., Deng, M., et al. (2013a). Structural Effects of Palladium Nanocrystal Electrodes on Electrocatalytic Oxidation Reaction of Formic Acid. *Sci. Sin. Chim.* 43 (6), 744–753.
- Wang, J., Pamidi, P. V. A., and Park, D. S. (1997). Sol-gel-derived Metal-Dispersed Carbon Composite Amperometric Biosensors. *Electroanalysis* 9 (1), 52–55. doi:10.1002/elan.1140090112
- Wang, X. T., Ouyang, T., Wang, L., Zhong, J. H., Ma, T., and Liu, Z. Q. (2019b). Redox-Inert Fe 3+ Ions in Octahedral Sites of Co-Fe Spinel Oxides with Enhanced Oxygen Catalytic Activity for Rechargeable Zinc-Air Batteries. *Angew. Chem. Int. Ed.* 58 (38), 13291–13296. doi:10.1002/anie.201907595
- Wang, Y., Shao, Y., Matson, D. W., Li, J., and Lin, Y. (2010). Nitrogen-doped Graphene and its Application in Electrochemical Biosensing. *ACS Nano* 4 (4), 1790–1798. doi:10.1021/nn100315s
- Wang, Y., Zhang, Y.-Y., Tang, J., Wu, H., Xu, M., Peng, Z., et al. (2013b). Simultaneous Etching and Doping of TiO<sub>2</sub> Nanowire Arrays for Enhanced Photoelectrochemical Performance. *ACS Nano* 7 (10), 9375–9383. doi:10.1021/nm4040876
- Wang, Y., Zhou, T., Jiang, K., Da, P., Peng, Z., Tang, J., et al. (2014). Reduced Mesoporous Co<sub>3</sub>O<sub>4</sub> Nanowires as Efficient Water Oxidation Electrocatalysts and Supercapacitor Electrodes. *Adv. Energ. Mater.* 4 (16), 1400696. doi:10.1002/aenm.201400696
- WHO (2021). COVID-19 Oxygen Emergency Impacting More Than Half a Million People in Low- and Middle-Income Countries Every Day, as Demand Surges [Online]. who.int: World Health Organization. Available: [\(https://www.who.int/news/item/25-02-2021-covid-19-oxygen-emergency-impacting-more-than-half-a-million-people-in-low-and-middle-income-countries-every-day-as-demand-surges#:~:text=More%20than%20half%20a%20million%20COVID%2D19%20patients%20in%20LMICs,%2Dincome%20countries%20\(LMICs\)\)](https://www.who.int/news/item/25-02-2021-covid-19-oxygen-emergency-impacting-more-than-half-a-million-people-in-low-and-middle-income-countries-every-day-as-demand-surges#:~:text=More%20than%20half%20a%20million%20COVID%2D19%20patients%20in%20LMICs,%2Dincome%20countries%20(LMICs)) (Accessed 02 28, 2022 2022).
- Wiebe, A., Gieshoff, T., Möhle, S., Rodrigo, E., Zirbes, M., and Waldvogel, S. R. (2018). Electrifying Organic Synthesis. *Angew. Chem. Int. Ed.* 57 (20), 5594–5619. doi:10.1002/anie.201711060
- Wu, X., Niu, Y., Feng, B., Yu, Y., Huang, X., Zhong, C., et al. (2018). Mesoporous Hollow Nitrogen-Doped Carbon Nanospheres with Embedded MnFe<sub>2</sub>O<sub>4</sub>/Fe Hybrid Nanoparticles as Efficient Bifunctional Oxygen Electrocatalysts in Alkaline media. *ACS Appl. Mater. Inter.* 10 (24), 20440–20447. doi:10.1021/acsami.8b04012
- Xia, B. Y., Wu, H. B., Li, N., Yan, Y., Lou, X. W. D., and Wang, X. (2015). One-Pot Synthesis of Pt-Co Alloy Nanowire Assemblies with Tunable Composition and Enhanced Electrocatalytic Properties. *Angew. Chem. Int. Ed.* 54 (12), 3797–3801. doi:10.1002/anie.201411544
- Xia, Y., Gilroy, K. D., Peng, H.-C., and Xia, X. (2017). Seed-Mediated Growth of Colloidal Metal Nanocrystals. *Angew. Chem. Int. Ed.* 56 (1), 60–95. doi:10.1002/anie.201604731
- Xie, C., Yan, D., Chen, W., Zou, Y., Chen, R., Zang, S., et al. (2019). Insight into the Design of Defect Electrocatalysts: from Electronic Structure to Adsorption Energy. *Mater. Today* 31, 47–68. doi:10.1016/j.mattod.2019.05.021
- Xie, J., Zhang, H., Li, S., Wang, R., Sun, X., Zhou, M., et al. (2013). Defect-Rich MoS<sub>2</sub> Ultrathin Nanosheets with Additional Active Edge Sites for Enhanced Electrocatalytic Hydrogen Evolution. *Adv. Mater.* 25 (40), 5807–5813. doi:10.1002/adma.201302685
- Yang, Y., Fei, H., Ruan, G., and Tour, J. M. (2015). Porous Cobalt-Based Thin Film as a Bifunctional Catalyst for Hydrogen Generation and Oxygen Generation. *Adv. Mater.* 27 (20), 3175–3180. doi:10.1002/adma.201500894
- Yang, Y., Fei, H., Ruan, G., Xiang, C., and Tour, J. M. (2014). Efficient Electrocatalytic Oxygen Evolution on Amorphous Nickel-Cobalt Binary Oxide Nanoporous Layers. *ACS Nano* 8 (9), 9518–9523. doi:10.1021/nn503760c
- Yu, X.-Y., Feng, Y., Guan, B., Lou, X. W., and Paik, U. (2016a). Carbon Coated Porous Nickel Phosphides Nanoplates for Highly Efficient Oxygen Evolution Reaction. *Energ. Environ. Sci.* 9 (4), 1246–1250. doi:10.1039/c6ee00100a
- Yu, X., Zhang, M., Chen, J., Li, Y., and Shi, G. (2016b). Nitrogen and Sulfur Codoped Graphite Foam as a Self-Supported Metal-free Electrocatalytic Electrode for Water Oxidation. *Adv. Energ. Mater.* 6 (2), 1501492. doi:10.1002/aenm.201501492
- Yu, Y., Zhang, Q., Liu, B., and Lee, J. Y. (2010). Synthesis of Nanocrystals with Variable High-index Pd Facets through the Controlled Heteroepitaxial Growth of Trisectahedral Au Templates. *J. Am. Chem. Soc.* 132 (51), 18258–18265. doi:10.1021/ja107405x
- Yu, Z., Bai, Y., Tsekouras, G., and Cheng, Z. (2021). Recent Advances in Ni-Fe (Oxy) Hydroxide Electrocatalysts for the Oxygen Evolution Reaction in



- Alkaline Electrolyte Targeting Industrial Applications. *Nano Select.* doi:10.1002/nano.202100286
- Zen, J.-M., Chung, H.-H., and Kumar, A. S. (2000a). Flow Injection Analysis of Hydrogen Peroxide on Copper-Plated Screen-Printed Carbon Electrodes. *Analyst* 125 (9), 1633–1637. doi:10.1039/b004207m
- Zen, J.-M., Chung, H.-H., and Kumar, A. S. (2002a). Selective Detection of O-Diphenols on Copper-Plated Screen-Printed Electrodes. *Anal. Chem.* 74 (5), 1202–1206. doi:10.1021/ac011012l
- Zen, J.-M., Kumar, A. S., and Chen, H.-W. (2000b). Electrochemical Formation of Prussian Blue in Natural Iron-Intercalated Clay and Cinder Matrixes. *Electroanalysis* 12 (7), 542–545. doi:10.1002/(sici)1521-4109(200005)12:7<542::aid-elan542>3.0.co;2-5
- Zen, J.-M., Wang, H.-F., Senthil Kumar, A., Yang, H.-H., and Dharuman, V. (2002b). Preconcentration and Electroanalysis of Copper(II) in Ammoniacal Medium on Nontronite/Cellulose Acetate Modified Electrodes. *Electroanalysis* 14 (2), 99–105. doi:10.1002/1521-4109(200201)14:2<99::aid-elan99>3.0.co;2-w
- Zhang, B., Zheng, X., Voznyy, O., Comin, R., Bajdich, M., García-Melchor, M., et al. (2016a). Homogeneously Dispersed Multimetal Oxygen-Evolving Catalysts. *Science* 352 (6283), 333–337. doi:10.1126/science.aaf1525
- Zhang, G.-R., and Wöllner, S. (2018). Hollowed Structured PtNi Bifunctional Electrocatalyst with Record Low Total Overpotential for Oxygen Reduction and Oxygen Evolution Reactions. *Appl. Catal. B: Environ.* 222, 26–34. doi:10.1016/j.apcatb.2017.09.066
- Zhang, Y., Ouyang, B., Xu, J., Jia, G., Chen, S., Rawat, R. S., et al. (2016b). Rapid Synthesis of Cobalt Nitride Nanowires: Highly Efficient and Low-Cost Catalysts for Oxygen Evolution. *Angew. Chem. Int. Ed.* 55 (30), 8670–8674. doi:10.1002/anie.201604372
- Zhang, Y. Z., Zhao, H., and Yuan, Z. B. (2002). Electrodeposition of Rhein and its Electrocatalytic Activity toward Hemoglobin Reduction. *Electroanalysis* 14 (5), 382–386. doi:10.1002/1521-4109(200203)14:5<382::aid-elan382>3.0.co;2-y
- Zhao, X., Liu, X., Huang, B., Wang, P., and Pei, Y. (2019). Hydroxyl Group Modification Improves the Electrocatalytic ORR and OER Activity of Graphene Supported Single and Bi-metal Atomic Catalysts (Ni, Co, and Fe). *J. Mater. Chem. A* 7 (42), 24583–24593. doi:10.1039/c9ta08661g
- Zhao, X., Luo, B., Long, R., Wang, C., and Xiong, Y. (2015). Composition-dependent Activity of Cu-Pt alloy Nanocubes for Electrocatalytic CO<sub>2</sub> Reduction. *J. Mater. Chem. A* 3 (8), 4134–4138. doi:10.1039/c4ta06608a
- Zhao, Y., Nakamura, R., Kamiya, K., Nakanishi, S., and Hashimoto, K. (2013). Nitrogen-doped Carbon Nanomaterials as Non-metal Electrocatalysts for Water Oxidation. *Nat. Commun.* 4 (1), 2390–2397. doi:10.1038/ncomms3390
- Zhao, Y., Jia, X., Chen, G., Shang, L., Waterhouse, G. I. N., Wu, L.-Z., et al. (2016). Ultrafine NiO Nanosheets Stabilized by TiO<sub>2</sub> from Monolayer NiTi-LDH Precursors: an Active Water Oxidation Electrocatalyst. *J. Am. Chem. Soc.* 138 (20), 6517–6524. doi:10.1021/jacs.6b01606
- Zhu, Y.-P., Liu, Y.-P., Ren, T.-Z., and Yuan, Z.-Y. (2015). Self-Supported Cobalt Phosphide Mesoporous Nanorod Arrays: A Flexible and Bifunctional Electrode for Highly Active Electrocatalytic Water Reduction and Oxidation. *Adv. Funct. Mater.* 25 (47), 7337–7347. doi:10.1002/adfm.201503666
- Zhu, Y. P., Guo, C., Zheng, Y., and Qiao, S.-Z. (2017). Surface and Interface Engineering of noble-metal-free Electrocatalysts for Efficient Energy Conversion Processes. *Acc. Chem. Res.* 50 (4), 915–923. doi:10.1021/acs.accounts.6b00635
- Zhu, Y., Zhou, W., Sunarso, J., Zhong, Y., and Shao, Z. (2016). Phosphorus-Doped Perovskite Oxide as Highly Efficient Water Oxidation Electrocatalyst in Alkaline Solution. *Adv. Funct. Mater.* 26 (32), 5862–5872. doi:10.1002/adfm.201601902

**Conflict of Interest:** Author PK is employed by Solaire Initiative Pvt. Ltd.

The remaining authors declare that the research was conducted in the absence of any commercial or financial relationships that could be construed as a potential conflict of interest.

**Publisher's Note:** All claims expressed in this article are solely those of the authors and do not necessarily represent those of their affiliated organizations, or those of the publisher, the editors, and the reviewers. Any product that may be evaluated in this article, or claim that may be made by its manufacturer, is not guaranteed or endorsed by the publisher.

Copyright © 2022 Sen, Das, Nath, Maharana, Kar, Verpoort, Liang and Roy. This is an open-access article distributed under the terms of the Creative Commons Attribution License (CC BY). The use, distribution or reproduction in other forums is permitted, provided the original author(s) and the copyright owner(s) are credited and that the original publication in this journal is cited, in accordance with accepted academic practice. No use, distribution or reproduction is permitted which does not comply with these terms.



# Two-Photon Absorption: An Open Door to the NIR-II Biological Window?

Paige A. Shaw, Ewan Forsyth, Fizza Haseeb, Shufan Yang, Mark Bradley and Maxime Klausen\*

EaStCHEM School of Chemistry, University of Edinburgh, Edinburgh, United Kingdom

The way in which photons travel through biological tissues and subsequently become scattered or absorbed is a key limitation for traditional optical medical imaging techniques using visible light. In contrast, near-infrared wavelengths, in particular those above 1000 nm, penetrate deeper in tissues and undergo less scattering and cause less photo-damage, which describes the so-called “second biological transparency window”. Unfortunately, current dyes and imaging probes have severely limited absorption profiles at such long wavelengths, and molecular engineering of novel NIR-II dyes can be a tedious and unpredictable process, which limits access to this optical window and impedes further developments. Two-photon (2P) absorption not only provides convenient access to this window by doubling the absorption wavelength of dyes, but also increases the possible resolution. This review aims to provide an update on the available 2P instrumentation and 2P luminescent materials available for optical imaging in the NIR-II window.

**Keywords:** two-photon absorption, infrared dyes, fluorescent imaging, near-infrared II, two-photon microscopy, tissue penetration, pulsed lasers

## OPEN ACCESS

### Edited by:

Junsheng Chen,  
University of Copenhagen, Denmark

### Reviewed by:

Yuncong Chen,  
Nanjing University, China  
Fabiao Yu,  
Hainan Medical University, China

### \*Correspondence:

Maxime Klausen  
mklausen@ed.ac.uk

### Specialty section:

This article was submitted to  
Physical Chemistry and Chemical  
Physics,  
a section of the journal  
Frontiers in Chemistry

**Received:** 15 April 2022

**Accepted:** 04 May 2022

**Published:** 24 June 2022

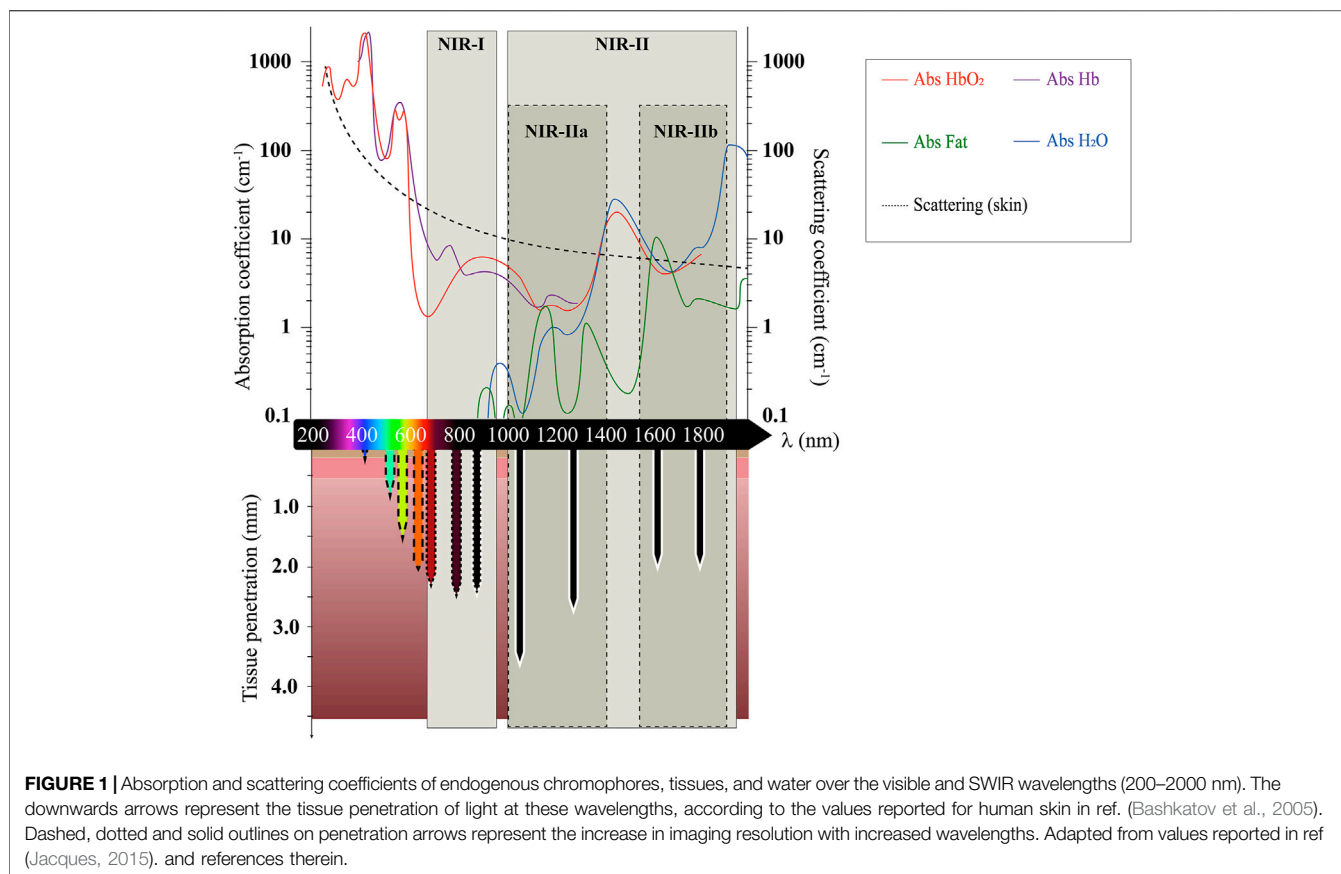
### Citation:

Shaw PA, Forsyth E, Haseeb F,  
Yang S, Bradley M and Klausen M  
(2022) Two-Photon Absorption: An  
Open Door to the NIR-II Biological  
Window?  
Front. Chem. 10:921354.  
doi: 10.3389/fchem.2022.921354

## 1 INTRODUCTION

Optical molecular imaging (OMI) technologies such as fluorescence imaging, Raman imaging, and optical coherence tomography, have emerged as safe and non-invasive tools to screen and monitor and diagnose disease in real-time, and follow treatment progress (Nicolson et al., 2021; Cao et al., 2019). Fluorescence-based OMI offers the ability to investigate biological systems with high spatio-temporal resolution and is now commonly applied to allow bio-molecular detection, drug distribution monitoring, image-guided surgery, and clinical diagnosis and therapy (Diao et al., 2015). The majority of *in vivo* fluorescence imaging approaches are performed using visible (400 nm–700 nm) and near-infrared I (NIR-I, 700 nm–900 nm) light due to the availability of light sources and detectors operating in this regime. However, the optical properties of tissues in this range of wavelengths intrinsically generate two challenges: a loss of signal due to poor penetration of light, and a low signal to background ratio (SBR) resulting from tissue auto-fluorescence (Zhang et al., 2016). The poor penetration of light *in vivo* arises due to the strong attenuation coefficients of tissue components, which causes photons to be scattered or absorbed by endogenous chromophores as they travel through tissues (Figure 1) (Keiser and Keiser, 2016). Tissue auto-fluorescence also represents a major limitation when imaging at shorter wavelengths. This loss in signal along with low SBR both contribute to the reduction in the resolution of the output image with increased depth, thereby limiting the optical imaging to micrometre depths.

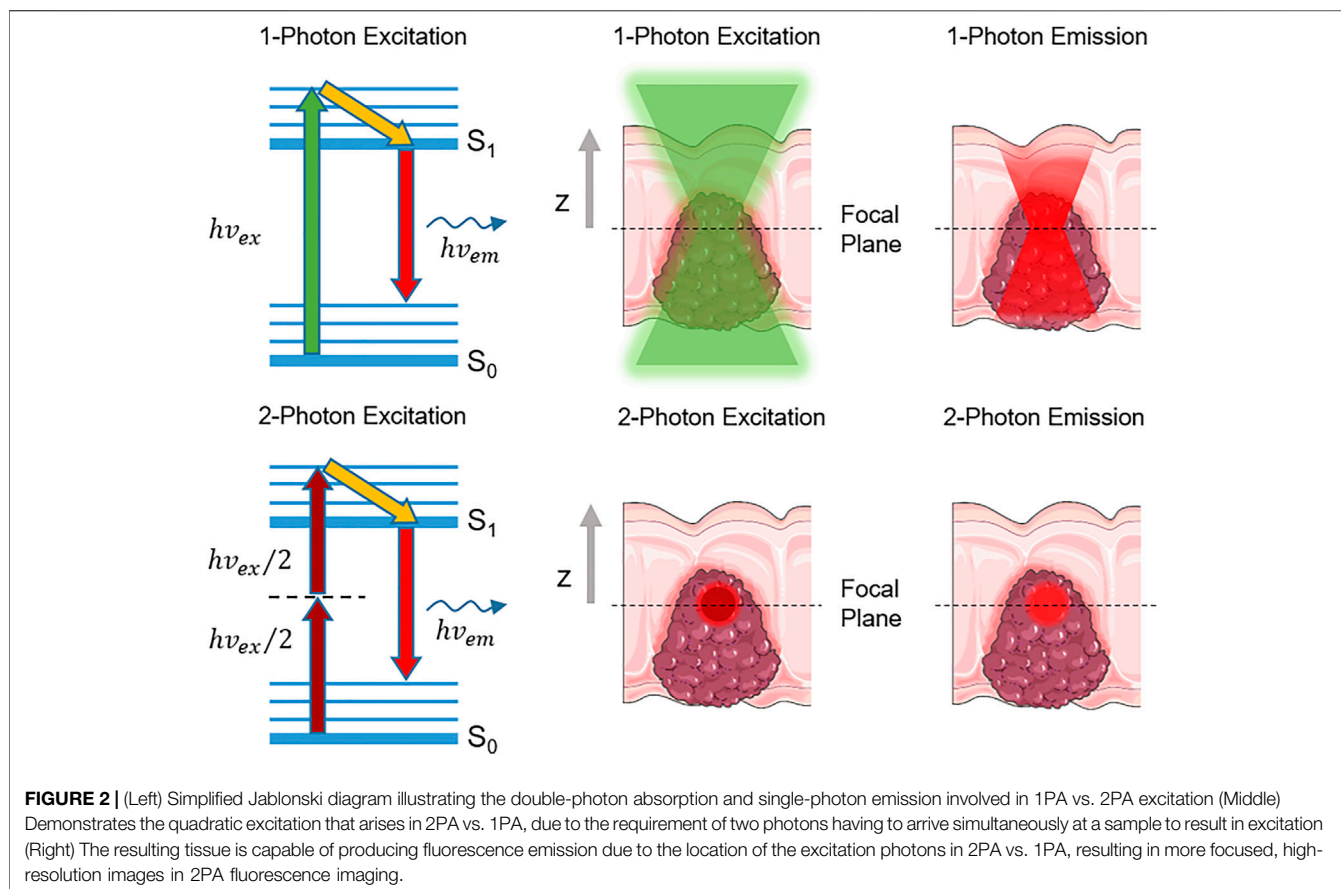
Favorably, the spectral properties of biological tissues are strongly wavelength-dependent, which opens two windows of “biological optical transparency” that enable higher resolution fluorescence



imaging (Nicolson et al., 2021; Cao et al., 2019; Sordillo et al., 2014a; Kenry et al., 2018; Chen et al., 2021; Hassan and Klaunberg, 2004; Li and Wang, 2018). Firstly, the absorption coefficients of tissue components such as whole blood (oxygenated HbO<sub>2</sub> or deoxygenated Hb), or fat (**Figure 1**) strongly decrease when reaching red/NIR wavelengths, which constitutes a first “NIR-I” transparency window (Bashkatov et al., 2005). Secondly, and more significantly, as the scattering coefficient of light is inversely proportional to the fourth power of its wavelength, photons of even longer wavelengths are more likely to continue on their intended linear trajectory rather than being scattered away due to their interactions within the tissue (Sordillo et al., 2014a; Wang et al., 2020a; Lockwood and Luo, 2016). For this reason, the use of low-energy light in the so-called “near-infrared II” (NIR-II) window (1000 nm–2000 nm), also known as the short-wave infrared region (SWIR), can not only help achieve higher penetration in biological tissue (**Figure 1**), but also aid in enhanced spatio-temporal resolution at fixed tissue depths, as well as reduce risks of photo-toxicity (Wang et al., 2020a; Ding et al., 2018). Moreover, tissue auto-fluorescence generated by endogenous molecules such as flavins, NADH, porphyrins, and collagens decreases significantly at longer wavelengths where these fluorophores do not absorb. Substantially diminished background auto-fluorescence is observed with NIR-II excitation, especially at wavelengths greater than 1500 nm;

with this reduction in auto-fluorescence contributing to enhanced spatio-temporal resolution and fidelity in 3D images (Li and Wang, 2018; Ding et al., 2018; Tian et al., 2020). The NIR-II window can be further sub-divided into two wavelength ranges spanning across a peak in water absorption at 1450 nm (**Figure 1**), i.e. the NIR-IIa (1000–1400 nm), and the NIR-IIb (1500–1800 nm) (Ma et al., 2021a; Feng et al., 2021). In spite of a higher endogenous absorption re-emerging at such wavelengths, several studies have revealed that the higher absorption coefficient of water can be beneficial in depleting the amount of scattered photons, thereby allowing “ballistic” photons to travel deeper into the tissue. This effect is known as “absorption-induced resolution enhancement” and can therefore produce clearer fluorescence images (Yoo et al., 1991; Sordillo et al., 2014b; Carr et al., 2018a; Feng et al., 2021).

The advancement from the NIR-I to the NIR-II optical window in fluorescence imaging has been facilitated by the development of NIR-II-absorbing probes suitable for biological imaging and by the increased availability of photodetectors sensitive enough in this spectral range (Hong et al., 2017). Currently, a variety of NIR-II imaging probes, including single-walled carbon nanotubes (SWCNTs), quantum dots (QDs), rare-earth doped nanoparticles (NPs), organic dyes, and semiconductor polymer NPs have been reported but these often have poor water solubility and limited physiological stability. Most significantly, as emitted photons are of lower



energy than standard single-photon (1P) excitation, NIR-II-emitting fluorophores usually suffer from poor emission quantum yields ( $\Phi_f$ ). Risks are also associated with the use of inorganic nano-systems including possible toxicity and lack of tissue specificity (Ding et al., 2018; Cao et al., 2019; Zhang et al., 2021a; Chen et al., 2021; Wang et al., 2021). The specific design of NIR-II-absorbing organic probes for bio-imaging has become a key challenge in the discipline, involving the multi-step synthesis of bulky water insoluble structures which often require complex purification (Sordillo et al., 2014a; Hong et al., 2017; Wanderi and Cui, 2022). On the other hand, a number of visible and NIR-I-absorbing fluorophores exhibiting high quantum yields are commercially available, and have the ability to target a wide range of biological substrates (Carr et al., 2018b). Such dyes are comparatively easy to synthesise and are routinely used for bio-imaging using one-photon absorption (1PA) (Escobedo et al., 2010). The use of two-photon (2P) fluorescence microscopy can facilitate the imaging in the NIR-II window by targeting 1P-absorbing visible/NIR-I dyes but with the added advantage of deep tissue penetration, exceptional feature clarity and high SBR (Carr et al., 2018b).

First predicted theoretically by Maria Göppert-Mayer in 1929 (Göppert, 1929; Göppert-Mayer, 1931), 2P absorption (2PA) is a third-order, resonant non-linear optical (NLO) process (Vivas et al., 2018; Ewart and Guenther, 2005) using the combined energy of two photons to generate an electronic transition from

the ground state ( $S_0$ ) to a singlet excited state ( $S_n$ ) (Figure 2, left) (He et al., 2008; Pawlicki et al., 2009; Klausen and Blanchard-Desce, 2021; Pascal et al., 2021). Contrary to 1P excitation (1PE), 2P excitation (2PE) therefore requires near-simultaneous absorption of two photons of the same frequency  $\nu$  (degenerate 2PA) or different frequencies  $\nu_1$  and  $\nu_2$  (non-degenerate 2PA). The excitation occurs as a two-step process, firstly involving a transition to a short-lived (sub-femtosecond) non-resonant excited state, called the “virtual state” (dashed line, Figure 2, left). Assuming that each chromophore is exposed to the same laser cross-section, photons must arrive on the attosecond timescale to further promote electron excitation to a singlet excited state. Furthermore, as with all non-linear processes, the relationship between the excitation light intensity and fluorescence intensity is non-linear (quadratic) and therefore excitation can only occur when the photon flux of the excitation light is in the range of  $10^{20}$ – $10^{30}$  photons/( $\text{cm}^2 \cdot \text{s}$ ) (Ewart and Guenther, 2005). This high energy density can be achieved by using an ultra-short ( $\sim 100$  fs) pulsed ( $\sim 80$  MHz) laser system (Ávila et al., 2019). In such non-linear conditions, the capacity of a dye to absorb 2P light differs from standard 1PE. The 2PA capacity of a dye is defined as its 2PA cross-section (e.g. the effective “photon-catching area” of the molecule), noted as  $\sigma_2$  and expressed in Göppert-Mayer unit ( $1 \text{ GM} = 10^{-50} \text{ cm}^4 \cdot \text{s} \cdot \text{photon}^{-1}$ ), as a tribute to Maria Göppert-Mayer’s work (He et al., 2008; Pawlicki et al., 2009; Klausen and Blanchard-Desce, 2021; Pascal et al., 2021).



After excitation and internal conversion, the electron relaxes to the lowest singlet excited state (Kasha's rule), from where all radiative and non-radiative decays occur, regardless of the type of excitation. With regards to biomedical imaging applications, this is essential, as the fluorescence generated (emission wavelength and efficiency) during radiative decay is the same after either 1PE or 2PE (Denk et al., 1990; Ewart and Guenther, 2005; Benninger and Piston, 2013). The efficiency of the radiative decay process is quantified by the fluorescence quantum yield  $\Phi_f$ , representing the number of photons emitted per photon absorbed. In microscopy applications, the overall brightness of a fluorescent imaging agent at a given wavelength is therefore defined as the product of its absorption capacity ( $\epsilon^{(\lambda)}$  in 1PA, or  $\sigma_2^{(\lambda)}$  in 2PA) and its emission quantum yield  $\Phi_f$ . In 2P applications, the 2P brightness  $\sigma_2\Phi_f$  thus allows direct comparison between fluorophores (Kim and Cho, 2015).

Further adding to the imaging benefits, as the quadratic nature of the 2P process confines the excitation to a femtoliter-sized volume where the light intensity is the highest, 2PE avoids photon absorption and fluorescence both above and below the focal point (Figure 2, middle and right). As the fluorescence only originates from the focal point without out-of-focus emission of light, 2P microscopy provides inherent "confocality", which allows high-resolution and high contrast imaging of thick living samples (Denk et al., 1990; Piston, 2005). This also prevents extensive photo-bleaching and photo-toxicity in live samples (Looney et al., 2011; Lu et al., 2020). Thanks to such unparalleled advantages over linear 1PE, 2PA has not only been extensively employed in bio-imaging and cell signal monitoring (Benninger and Piston, 2013; Kim and Cho, 2015; Kucikas et al., 2021; Helmchen and Denk, 2005; Ricard et al., 2018), but also in photodynamic therapy (PDT) (Sun et al., 2017a) and drug delivery (Klausen and Blanchard-Desce, 2021). In the context of NIR-II bio-imaging in particular, 2PE provides alternative solutions to the challenges met with standard 1PE. While the development of 1P-absorbing NIR-II-emitting OMI probes intrinsically leads to a high loss in brightness, 2PA directly exploits the emissive properties of 1P dyes at shorter wavelengths, which circumvents any loss of fluorescence quantum yield. The detection of fluorescence is also maximized with the use of common visible/NIR detectors with high sensitivities compared to their NIR-II counterparts, and by the increased distance between excitation and emission wavelengths preventing loss of signal due to spectral overlap. In addition, while standard single-photon confocal can only image samples of up to 200  $\mu\text{m}$  in thickness, 2P microscopy improves imaging penetration depth by at least 2-fold relative to confocal imaging (Wang et al., 2017; Rubart, 2004). Several studies have also shown improved biocompatibility of 2P imaging as compared to 1P confocal imaging (Wokosin et al., 1996a). Squirrel et al. demonstrated that 8h of confocal imaging at 514 nm resulted in the inhibition of hamster embryo development (Squirrel et al., 1999), even without staining. In contrast, embryo viability was maintained when imaged using a 1047 nm ultrashort pulsed laser with the same microscope system for a 24-hour period. Importantly, similar experiments have also demonstrated that even NIR-I femtosecond irradiation could impair cell division at low

power, and even lead to complete cell destruction (König et al., 1997). Therefore, the development of 2P microscopy in the NIR-II optical window represents an opportunity for higher-resolution and safer cellular imaging and would also facilitate a wider range of biological imaging applications such as image-guided surgery, diagnostics, gene expression monitoring, and chemical sensing (Figure 3). Such advanced applications have not yet been fully explored *in vivo* with NIR-II 2PA, but have shown great promise in *ex vivo* examples or utilizing shorter wavelengths for 2PE (Paoli et al., 2009; Grienberger and Konnerth, 2012; Cao et al., 2013; Fan et al., 2018).

In order to visualise, characterise and quantify biological entities, bright molecular imaging probes are needed (Yang et al., 2020a). To generate bright 2P microscopy images without causing considerable photo-damage to the sample at laser intensities required ( $1\text{ GW}\cdot\text{cm}^{-2}$  at the focal plane; or  $\sim 5\text{ mW}$  at the objective lens), it is estimated that the 2P brightness  $\sigma_2\Phi_f$  of the imaging agent should be more than 50 GM (Kim and Cho, 2015; Osmialowski et al., 2020). As such, breaking down the barriers to exploit NIR-II wavelengths in 2P bio-imaging involves three main challenges: (i) shifting the 2PA band of the imaging agent beyond 1000 nm, which typically involves 1PA above 500 nm; (ii) improving the 2PA cross-section  $\sigma_2$  above this wavelength, typically to values  $>50\text{--}100\text{ GM}$ ; and (iii) retaining a high enough fluorescence quantum yield  $\Phi_f$  to image tissues with high contrast. High water solubility, *in vivo*- and photo-stability, target specificity, and low toxicity are other general key criteria to develop ideal, clinically translatable OMI probes (Kim and Cho, 2015; Yang et al., 2020a; Rao et al., 2007; Yao and Belfield, 2012, 2012). Small organic fluorophores (Wang et al., 2020a; Wu et al., 2022), aggregation induced emission (AIE) dyes (Lu et al., 2020; Zhu et al., 2018), inorganic and hybrid nanomaterials (Yao et al., 2014) and fluorescent proteins (FPs) are key types of materials that have been used in the development of OMI probes to date, and have shown high potential in the field of 2P in the NIR-II region (Figure 3). NIR-II-absorbing 2P-responsive dyes find applications in several additional areas beyond the scope of this review, such as optical power limiting (Pascal et al., 2021), chemical and ion sensing (Ricard et al., 2018), or targeted photo-therapies (Sun et al., 2017a; Zhao et al., 2019). In this review, we aim to present the current state of available luminescent 2P probes in a biological imaging and microscopy context, and highlight the recent progress and tremendous potential in this field. In the first subsection, we present the different classes of materials available for such applications and summarise their key optical properties in Table 1. We then present the available pulsed excitation sources used for such applications and discuss examples of 2P *in vivo* imaging in this "second optical window" by exploring imaging and lasing systems (Table 2), and tissue penetration depths (Table 3).

## 2 NIR-II-ABSORBING LUMINESCENT MATERIALS FOR 2P BIO-IMAGING

### 2.1 Organic Fluorophores

Reaching the NIR-II window with 2P excitation typically involves using dyes with 1PA maxima ranging from orange to NIR-I wavelengths. The design of 2P-responsive organic fluorophores

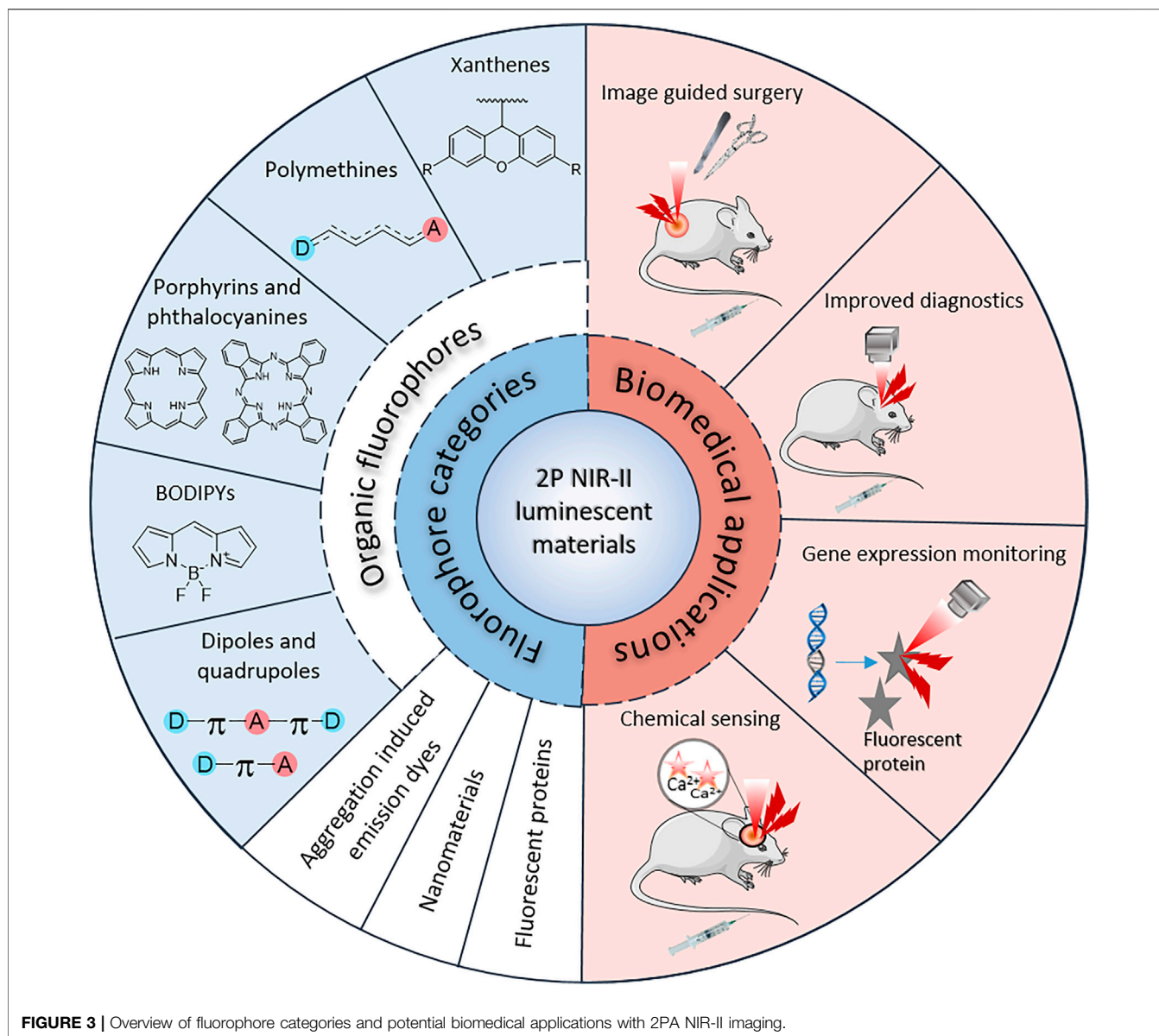


**FIGURE 3** | Overview of fluorophore categories and potential biomedical applications with 2PA NIR-II imaging.

has been covered extensively in several reviews and falls beyond the immediate scope of this review (He et al., 2008; Pawlicki et al., 2009; Klausen and Blanchard-Desce, 2021; Pascal et al., 2021; Kim and Cho, 2015). However, to achieve such results the following parameters must be taken into account. Even more so than in the context of standard 1PE, the size/length of the  $\pi$ -conjugated system and the magnitude of intramolecular charge transfer (ICT) are major driving forces for the 2PA capacity of a chromophore. Therefore, selecting strong electron-donating (ED) and electron-withdrawing (EW) moieties or extending the  $\pi$ -conjugated backbone in a push-pull compound are typical strategies to cause both ICT-induced bathochromic shifts in absorption wavelengths and increase in 2PA cross-sections. Nonetheless, to achieve NIR-II absorption, the selection rules of 2PA should be considered due to their direct effect on allowed electronic transitions within the molecule,

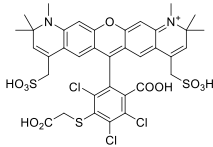
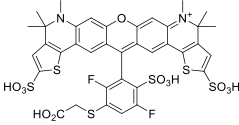
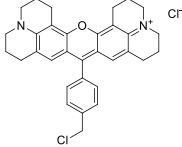
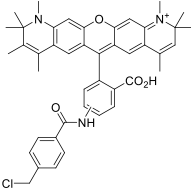
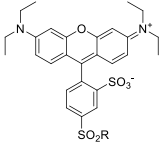
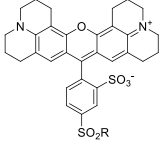
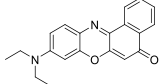
which in turn affects its maximum absorption wavelength. Symmetry-based selection rules state that 2P electronic transitions at  $2 \times \lambda_{1PA}^{max}$  wavelengths are forbidden in centrosymmetric chromophores. As a result, 2PA bands in symmetrical dyes are usually more intense, but shifted to higher energies, which can be a limitation in the design of NIR-II-absorbing dyes. Dipolar dyes present no such restriction as the transition to the first excited state is generally both 1P- and 2P-allowed. Therefore, 2P-absorbers with dipolar (D- $\pi$ -A) or symmetrical (quadrupolar D- $\pi$ -A- $\pi$ -D, A- $\pi$ -D- $\pi$ -A; or octupolar D-( $\pi$ -A)<sub>3</sub>, A-( $\pi$ -D)<sub>3</sub>) structures, sometimes belonging to well-known classes of dyes, have been investigated in recent years and will be reviewed below. With the development and increased accessibility of SWIR pulsed laser technologies (Section 3, Tables 2 and 3), several studies have shown that remarkable potential resides in the pool of current

**TABLE 1** | 1PA, 2PA and emission properties of NIR-II chromophores reported in literature. Solvent and method of 2P properties are also noted for comparison.

Probe	Chemical structure	Solvent	$\lambda_{1PA}^{max}$ (nm)	$\lambda_{em}^{max}$ (nm)	$\Phi_f$	$2\lambda_{1PA}^{max}$ (nm)	$\lambda_{2PA}$ (nm)	$\sigma_2^{(A)}$ (GM) <sup>a</sup>	$\sigma_2^{(A)}\Phi_f$ (GM) <sup>a</sup>	Ref.
Disodium fluorescein (1)		pH11	<b>Xanthenes</b>		0.90 <sup>c</sup>	994	1000	2.7	2.4 <sup>b</sup>	(Makarov et al., 2008; Mütze et al., 2012)
PhenGreen FL (diacetate, uncomplexed) (2)		PBS	492 <sup>c</sup>	517 <sup>c</sup>	0.80 <sup>c</sup>	984	1074	n.d.	n.d.	(Bestvater et al., 2002)
Rhodamine 6G (3)		MeOH	519 <sup>c</sup>	546 <sup>c</sup>	0.95 <sup>c</sup>	1038	1060	10	9.5 <sup>b</sup>	(Makarov et al., 2008)
Rhodamine B (4)		MeOH	553 <sup>c</sup>	627 <sup>c</sup>	0.70 <sup>c</sup>	1106	1040	39	27 <sup>b</sup>	Makarov et al., 2008
Rhodamine 101 (5)		EtOH	570 <sup>c</sup>	591 <sup>c</sup>	1.0 <sup>c</sup>	1140	1060	20	20 <sup>b</sup>	(Li and She, 2010; Mütze et al., 2012)
Rhodamine 123 (6)		PBS	507	529 <sup>c</sup>	0.90 <sup>c</sup> (EtOH)	1014	1090	n.d.	n.d.	(Bestvater et al., 2002)
Alexa Fluor 488 (7)		NaPhos	491	519 <sup>c</sup>	0.92 <sup>c</sup>	980	1000	21 <sup>b</sup>	19	(Bestvater et al., 2002; Anderson and Webb, 2011; Mütze et al., 2012)
Alexa Fluor 546 (8)		PBS	553	573 <sup>c</sup>	0.79 <sup>c</sup>	1112	1028	n.d.	n.d.	(Bestvater et al., 2002; Mütze et al., 2012)
Alexa Fluor 568 (9)		PBS	578 <sup>c</sup>	603 <sup>c</sup>	0.69 <sup>c</sup>	1156	1060	n.d.	n.d.	(Mütze et al., 2012)
Alexa Fluor 594 (10)		PBS	594 <sup>c</sup>	617 <sup>c</sup>	0.66 <sup>c</sup>	1180	1074	n.d.	n.d.	(Bestvater et al., 2002; Mütze et al., 2012)

(Continued on following page)

**TABLE 1 |** (Continued) 1PA, 2PA and emission properties of NIR-II chromophores reported in literature. Solvent and method of 2P properties are also noted for comparison.

Probe	Chemical structure	Solvent	$\lambda_{1PA}^{max}$ (nm)	$\lambda_{em}^{max}$ (nm)	$\Phi_f$	$2\lambda_{1PA}^{max}$ (nm)	$\lambda_{2PA}$ (nm)	$\sigma_2^{(A)}$ (GM) <sup>a</sup>	$\sigma_2^{(A)}\Phi_f$ (GM) <sup>a</sup>	Ref.
Alexa Fluor 610 <b>(11)</b>		PBS	612 <sup>c</sup>	628 <sup>c</sup>	–	1224	1010	n.d.	n.d.	(Mütze et al., 2012)
Alexa Fluor 633 <b>(12)</b>		H <sub>2</sub> O	632 <sup>c</sup>	647 <sup>c</sup>	–	1264	1260	n.d.	<5	(Kobat et al., 2009; Mütze et al., 2012)
MitoTracker Red <b>(13)</b>		PBS	579 <sup>c</sup>	599 <sup>c</sup>	0.15 [187]	1158	1133	n.d.	n.d.	(Bestvater et al., 2002)
CellTracker Red <b>(14)</b>		<i>In vitro</i>	585 <sup>c</sup>	602 <sup>c</sup>	n.d.	1170	1080	n.d.	n.d.	(Rakhymzhan et al., 2017)
Lissamine Rhodamine-IgG <b>(15)</b>		PBS	570 <sup>c</sup>	590 <sup>c</sup>	0.33 [188]	1140	1116	n.d.	n.d.	(Bestvater et al., 2002)
Texas Red-IgG <b>(16)</b>		PBS	596 <sup>c</sup>	615 <sup>c</sup>	0.90 <sup>c</sup>	1192	1150	n.d.	n.d.	(Bestvater et al., 2002)
ATTO 680 <b>(17)</b>		<i>In vitro</i>	681 <sup>c</sup>	698 <sup>c</sup>	0.30 <sup>c</sup>	1362	1260	n.d.	n.d.	(Rakhymzhan et al., 2017)
Nile Red <b>(18)</b>		MeOH	550	636	0.40	1100	1057	104	42	(Hornum et al., 2020)
<b>19</b>		MeOH	554	631	0.43	1108	1055	183	79	(Hornum et al., 2020)
<b>20</b>		MeOH	569	632	0.45	1065	1050	123	55	(Hornum et al., 2020)
<b>21</b>		MeOH	565	638	0.35	1130	1057	232	81	(Hornum et al., 2020)

(Continued on following page)



**TABLE 1 |** (Continued) 1PA, 2PA and emission properties of NIR-II chromophores reported in literature. Solvent and method of 2P properties are also noted for comparison.

Probe	Chemical structure	Solvent	$\lambda_{1PA}^{max}$ (nm)	$\lambda_{em}^{max}$ (nm)	$\Phi_f$	$2\lambda_{1PA}^{max}$ (nm)	$\lambda_{2PA}$ (nm)	$\sigma_2^{(A)}$ (GM) <sup>a</sup>	$\sigma_2^{(A)}\Phi_f$ (GM) <sup>a</sup>	Ref.
Cy3-IgG ( <b>22</b> )		PBS	<b>Polymethines</b>		0.1 <sup>c</sup>	1096	1032	n.d.	n.d.	(Bestvater et al., 2002)
Cy5 ( <b>23</b> )		H <sub>2</sub> O	646 <sup>c</sup>	662 <sup>c</sup>	0.28 <sup>c</sup>	1292	1220	143 <sup>b</sup>	≈40	(Kobat et al., 2009)
Cy5.5 ( <b>24</b> )		H <sub>2</sub> O	673 <sup>c</sup>	691 <sup>c</sup>	0.21 <sup>c</sup>	1346	1280	286 <sup>b</sup>	≈60	(Kobat et al., 2009)
Cy7 ( <b>25</b> )		H <sub>2</sub> O	750 <sup>c</sup>	773 <sup>c</sup>	0.30 <sup>c</sup>	1500	1320	200 <sup>b</sup>	≈60	(Kobat et al., 2009)
<b>26</b>		DMSO	753	780	0.17	1506	1552	240	41 <sup>b</sup>	(Berezin et al., 2011)
ICG ( <b>27</b> )		DMSO	794	817	0.12	1588	1552	590	71 <sup>b</sup>	(Berezin et al., 2011)
Cypate ( <b>28</b> )		DMSO	796	817	0.13	1592	1552	520	68 <sup>b</sup>	(Berezin et al., 2011)
<b>29</b>		DMSO	809	829	0.07	1618	1552	900	63 <sup>b</sup>	(Berezin et al., 2011)
DTTC ( <b>30</b> )		DMSO	771 <sup>c</sup>	800 <sup>c</sup>	0.80 <sup>c</sup>	1542	1552	160	128 <sup>b</sup>	(Berezin et al., 2011)
DODCI ( <b>31</b> )		EtOH	582 <sup>c</sup>	610 <sup>c</sup>	0.87 <sup>c</sup> (DMSO)	1164	1060	38	n.d.	(Li and She, 2010)
IR-140 ( <b>32</b> )		DMSO	825	≈840	0.06	1640	1552	950	57 <sup>b</sup>	(Berezin et al., 2011)
<b>33</b>		CH <sub>2</sub> Cl <sub>2</sub> CH <sub>3</sub> CN	1064 1043	≈1080 ≈1065	0.05 0.05	2128 2086	1800 1800	2250 1050	113 <sup>b</sup> 53 <sup>b</sup>	(Hu et al., 2013)
<b>34</b>		EtOH	650	665	n.d.	1300	1180	140	n.d.	(Fu et al., 2007)

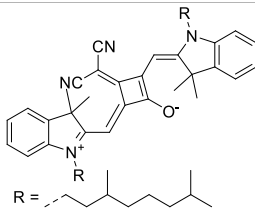
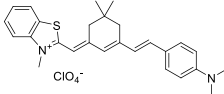
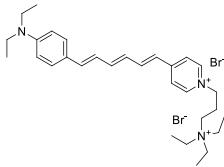
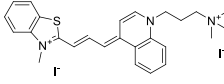
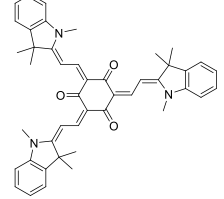
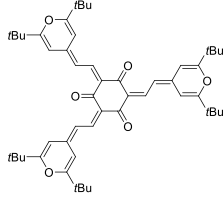
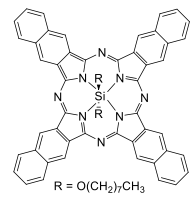
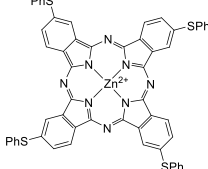
(Continued on following page)

**TABLE 1 |** (Continued) 1PA, 2PA and emission properties of NIR-II chromophores reported in literature. Solvent and method of 2P properties are also noted for comparison.

Probe	Chemical structure	Solvent	$\lambda_{1PA}^{max}$ (nm)	$\lambda_{em}^{max}$ (nm)	$\Phi_f$	$2\lambda_{1PA}^{max}$ (nm)	$\lambda_{2PA}$ (nm)	$\sigma_2^{(A)}$ (GM) <sup>a</sup>	$\sigma_2^{(A)}\Phi_f$ (GM) <sup>a</sup>	Ref.
<b>35</b>		EtOH	690	704	n.d.	1380	1260	150	n.d.	(Fu et al., 2007)
<b>36</b>		EtOH	770	n.d.	n.d.	1540	1340	60	n.d.	(Fu et al., 2007)
<b>37</b>		EtOH	824	n.d.	n.d.	1648	1480	600	n.d.	(Fu et al., 2007)
Alexa Fluor 647 ( <b>38</b> )		H <sub>2</sub> O	650 <sup>c</sup>	665 <sup>c</sup>	0.33 <sup>c</sup>	1300	1240	133 <sup>b</sup>	≈44	(Kobat et al., 2009; Mütze et al., 2012)
Alexa Fluor 680 ( <b>39</b> )		H <sub>2</sub> O	679 <sup>c</sup>	702 <sup>c</sup>	0.36 <sup>c</sup>	1358	1280	203 <sup>b</sup>	≈73	(Kobat et al., 2009)
Alexa Fluor 700 ( <b>40</b> )	— <sup>d</sup>	H <sub>2</sub> O	702 <sup>c</sup>	723 <sup>c</sup>	0.25 <sup>c</sup>	1404	1320	208 <sup>b</sup>	≈52	(Kobat et al., 2009)
Alexa Fluor 750 ( <b>41</b> )	— <sup>d</sup>	H <sub>2</sub> O	753 <sup>c</sup>	778 <sup>c</sup>	0.12 <sup>c</sup>	1506	1320	292 <sup>b</sup>	≈35	(Kobat et al., 2009)
<b>42</b>		MeOH	532	636	0.44	1064	1064 (900)	23 (570)	10 <sup>b</sup>	(Pascal et al., 2017)
<b>43</b>		MeOH	573	708	0.33	1146	1146	225	74 <sup>b</sup>	(Pascal et al., 2017)
<b>44</b>		MeOH	549	673	0.54	1098	1098	137	74 <sup>b</sup>	(Pascal et al., 2017)
<b>45</b>		Toluene	643	654	0.62	1286	1198	133	82 <sup>b</sup>	(Ceymann et al., 2016)

(Continued on following page)

**TABLE 1** | (Continued) 1PA, 2PA and emission properties of NIR-II chromophores reported in literature. Solvent and method of 2P properties are also noted for comparison.

Probe	Chemical structure	Solvent	$\lambda_{1PA}^{max}$	$\lambda_{em}^{max}$	$\Phi_f$	$2\lambda_{1PA}^{max}$	$\lambda_{2PA}$	$\sigma_2^{(A)}$	$\sigma_2^{(A)}\Phi_f$	Ref.	
			(nm)	(nm)		(nm)	(nm)	(GM) <sup>a</sup>	(GM) <sup>a</sup>		
46		Toluene	700	714	0.75	1400	1274	100	75 <sup>b</sup>	(Ceymann et al., 2016)	
Styryl 9M (47)		CHCl <sub>3</sub>	≈625	≈790	0.10 [189]	≈1250	1240	780	78	(Makarov et al., 2008)	
FM4-64 (48)		PBS CHCl <sub>3</sub> (López-Duarte et al., 2015)	471 564	691 761	n.d. 0.35	942 1128	1047	n.d.	n.d.	(Wokosin et al., 1996a; Nuriya et al., 2016)	
TO-PRO-3 (49)		H <sub>2</sub> O	641 <sup>c</sup>	657 <sup>c</sup>	n.d.	1284	1110	n.d.	n.d.	(Smith et al., 2012)	
50		THF	562	598	0.07	1124	1070	167	12 <sup>b</sup>	(Poronik et al., 2012)	
51		THF	615	655	0.02	1230	1150	214	4 <sup>b</sup>	(Poronik et al., 2012)	
52		CCl <sub>4</sub>	Porphyrins ≈770		≈780	n.d.	≈1540	1020 1270	470 48	n.d.	(Makarov et al., 2008)
53		CCl <sub>4</sub>	≈685	≈700	n.d.	≈1370	1270	13	n.d.	(Makarov et al., 2008)	

(Continued on following page)

**TABLE 1 |** (Continued) 1PA, 2PA and emission properties of NIR-II chromophores reported in literature. Solvent and method of 2P properties are also noted for comparison.

Probe	Chemical structure	Solvent	$\lambda_{1PA}^{max}$	$\lambda_{em}^{max}$	$\Phi_f$	$2\lambda_{1PA}^{max}$	$\lambda_{2PA}$	$\sigma_2^{(A)}$	$\sigma_2^{(A)}\Phi_f$	Ref.
			(nm)	(nm)		(nm)	(nm)	(GM) <sup>a</sup>	(GM) <sup>a</sup>	
54		CHCl <sub>3</sub>	≈525 ≈605 ≈680	710	n.d.	≈1050 ≈1210 ≈1360	≈1040 ≈1220 ≈1360	≈2000 ≈500 ≈200	n.d.	(Nowak-Król et al., 2013)
LysoTracker Red (55)		PBS	<b>BODIPYs</b> 577 <sup>c</sup> 590 <sup>c</sup>		0.07	1154	1100	n.d.	n.d.	(Bestvater et al., 2002)
BODIPY-TR (56)		MOPS	589 <sup>c</sup>	616 <sup>c</sup>	0.90 <sup>c</sup>	1178	1060	269 <sup>b</sup>	242	(Bestvater et al., 2002; Mütze et al., 2012)
IR-07 (57)		CH <sub>2</sub> Cl <sub>2</sub>	~700	750	0.30	~1400	1310	101	30 <sup>b</sup>	(Zheng et al., 2009)
58		THF	755	830	0.09	1560	1064	n.d.	n.d.	(Hu et al., 2020)
59		<b>Dipoles – Quadrupoles – Miscellaneous</b> NPs (Aq.)		480	678	0.17	960	1040	5.6 × 10 <sup>5</sup>	(Alifu et al., 2017)
60		H <sub>2</sub> O (0.1% DMSO)	530	740	n.d.	1060	1100	n.d.	n.d.	(Zhou et al., 2021)

(Continued on following page)

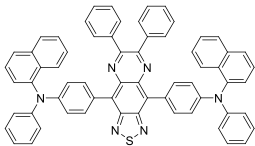
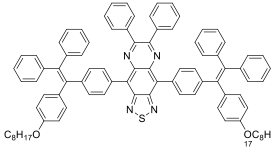
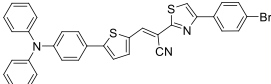
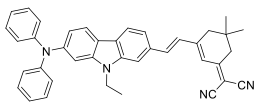
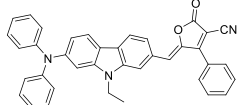
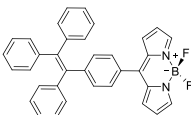


**TABLE 1 |** (Continued) 1PA, 2PA and emission properties of NIR-II chromophores reported in literature. Solvent and method of 2P properties are also noted for comparison.

Probe	Chemical structure	Solvent	$\lambda_{1PA}^{max}$ (nm)	$\lambda_{em}^{max}$ (nm)	$\Phi_f$	$2\lambda_{1PA}^{max}$ (nm)	$\lambda_{2PA}$ (nm)	$\sigma_2^{(N)}$ (GM) <sup>a</sup>	$\sigma_2^{(N)}\Phi_f$ (GM) <sup>a</sup>	Ref.
61		H <sub>2</sub> O	510	676	0.22	1020	1040	440	97 <sup>b</sup>	(Massin et al., 2013)
62		CH <sub>2</sub> Cl <sub>2</sub>	660	785	0.005	1320	1300	500	2.5 <sup>b</sup>	(Ricci et al., 2017)
63		CH <sub>2</sub> Cl <sub>2</sub>	678	782	0.0005	1356	1300	1400	0.7 <sup>b</sup>	(Ricci et al., 2017)
64		H <sub>2</sub> O	≈600	≈725	0.21	≈1200	1200	1.21 × 10 <sup>3</sup>	242 <sup>b</sup>	(Wang et al., 2019b)
65		CHCl <sub>3</sub>	634	704	0.16	1268	1250	920	147 <sup>b</sup>	(Li et al., 2012)
66		CHCl <sub>3</sub>	668	807	0.02	1336	1250	1200	24 <sup>b</sup>	(Li et al., 2012)
67		CHCl <sub>3</sub>	1088	1120	0.002	2176	2200	1300	2.6 <sup>b</sup>	(Ni et al., 2016)
68		CHCl <sub>3</sub>	1136	1193	0.0002	2272	2300	1500	0.3 <sup>b</sup>	(Ni et al., 2016)
Propidium iodide (69)		PBS	536 <sup>c</sup>	617 <sup>c</sup>	0.20 <sup>c</sup> (dsDNA bound)	1072	1015	n.d.	n.d.	(Bestvater et al., 2002)

(Continued on following page)

**TABLE 1 |** (Continued) 1PA, 2PA and emission properties of NIR-II chromophores reported in literature. Solvent and method of 2P properties are also noted for comparison.

Probe	Chemical structure	Solvent	$\lambda_{1PA}^{max}$ (nm)	$\lambda_{em}^{max}$ (nm)	$\Phi_f$	$2\lambda_{1PA}^{max}$ (nm)	$\lambda_{2PA}$ (nm)	$\sigma_2^{(A)}$ (GM) <sup>a</sup>	$\sigma_2^{(A)}\Phi_f$ (GM) <sup>a</sup>	Ref.
<b>AIEdots and AIEDots</b>										
<b>70</b>		NP (aq.)	613	790-810	0.14	1226	1040 1300	16100 1220	2240 <sup>b</sup> 170 <sup>b</sup>	(Qi et al., 2018; Liu et al., 2021)
<b>71</b>		NP (aq.) THF	454 ≈451	≈700 ≈699	0.19 n.d.	908	1200 n.d.	76300 n.d.	14500 <sup>b</sup> n.d.	(Wang et al., 2019c)
<b>72</b>		NP (aq.) H <sub>2</sub> O/ DMSO	≈479 ≈488	≈627 >627	0.06 n.d.	≈960	1040 n.d.	3200 n.d.	192 <sup>b</sup> n.d.	(Samanta et al., 2021)
<b>73</b>		NP (aq.) Toluene	510 491	709 ≈635	0.14 (solid state)	1020	1000 n.d.	≈520 n.d.	73 <sup>b</sup> n.d.	(Zheng et al., 2018)
<b>74</b>		NP (aq.) Toluene	538 528	755 ≈636	0.02 (solid state)	1076	1020 n.d.	887 n.d.	18 <sup>b</sup> n.d.	(Zheng et al., 2018)
<b>75</b>		NP (aq.) THF	522 511	620 532	0.05 n.d.	1044	1040 n.d.	2.9 × 10 <sup>5</sup> n.d.	1.5 × 10 <sup>5</sup> n.d.	(Wang et al., 2015)
<b>Carbon, hybrid and inorganic materials</b>										
<b>76</b>	SWCNT-based dopamine sensor	H <sub>2</sub> O	600–1000	1000–1265 <sup>a</sup>	0.0023	–	1560	216000	497 <sup>b</sup>	(Bonis-O'Donnell et al., 2017)
<b>77</b>	Aptamer-modified graphene oxide	H <sub>2</sub> O	440–720	500–650 <sup>f</sup>	0.34	–	1120	36000	12240 <sup>b</sup>	(Pramanik et al., 2014)
<b>78</b>	CDs prepared from urea and citric acid	H <sub>2</sub> O	540	624	0.06	1080	1200	n.d.	n.d.	(Li et al., 2018)
<b>79</b>	Carbon quantum dots prepared from tris(4-aminophenyl)amine	H <sub>2</sub> O	592	615	0.84	1184	1100	n.d.	n.d.	(Liu et al., 2020)
<b>80</b>	AuNP with SWCNT	H <sub>2</sub> O	500–1100	775	n.d.	–	1100	n.d.	n.d.	(Olesiak-Banska et al., 2019)
<b>81</b>	Au <sub>25</sub> cluster	H <sub>2</sub> O	675	830	<0.001	1350	1290	2700	n.d.	(Ramakrishna et al., 2008)
<b>82</b>	PEG-dithiolane AuNC	H <sub>2</sub> O	355, 670	820	0.08	1370	1100	300	24 <sup>b</sup>	(Oh et al., 2013)
<b>83</b>	Mn <sup>2+</sup> -ZnS QD	H <sub>2</sub> O	318	586	0.65	636	1180	265	172 <sup>b</sup>	(Subha et al., 2013)
<b>84</b>	PbS/CdS QD	H <sub>2</sub> O	665	1270	0.18	1330	1550	530	95 <sup>b</sup>	(Ni et al., 2022)
<b>QD605 (85)</b>	polymer-encapsulated CdSe-ZnS QD	H <sub>2</sub> O	350–475	605	0.71	–	1000	66200 <sup>b</sup>	47000	(Larson et al., 2003)
<b>Fluorescent proteins</b>										
tdTomato ( <b>86</b> )	–	H <sub>2</sub> O	554 <sup>g</sup>	581	0.72 <sup>b</sup>	1108	1050	278	200	(Drobizhev et al. 2011)
tdKatushka2 ( <b>87</b> )	–	H <sub>2</sub> O	588 <sup>g</sup>	633	0.44 <sup>b</sup>	1176	1100	143	63	(Drobizhev et al. 2011)
dsRed2 ( <b>88</b> )	–	H <sub>2</sub> O	561 <sup>g</sup>	587	0.71 <sup>b</sup>	1126	1050	103	73	(Drobizhev et al. 2011)
HcRFP ( <b>89</b> )	–	PBS	592 <sup>g</sup>	645 <sup>g</sup>	0.05 <sup>g</sup>	1184	1160	720 <sup>b</sup>	36	(Tsai et al., 2006)
mCherry ( <b>90</b> )	–	H <sub>2</sub> O	587 <sup>g</sup>	610	0.24 <sup>b</sup>	1174	1080	27	6.4	(Drobizhev et al. 2011)
mBanana ( <b>91</b> )	–	H <sub>2</sub> O	540 <sup>g</sup>	553	0.69 <sup>b</sup>	1080	1070	64	44	(Drobizhev et al. 2011)
mStrawberry ( <b>92</b> )	–	H <sub>2</sub> O	574 <sup>g</sup>	596	0.34 <sup>b</sup>	1148	1070	20	6.8	(Drobizhev et al. 2011)

(Continued on following page)

**TABLE 1 |** (Continued) 1PA, 2PA and emission properties of NIR-II chromophores reported in literature. Solvent and method of 2P properties are also noted for comparison.

Probe	Chemical structure	Solvent	$\lambda_{1PA}^{max}$ (nm)	$\lambda_{em}^{max}$ (nm)	$\Phi_f$	$2\lambda_{1PA}^{max}$ (nm)	$\lambda_{2PA}$ (nm)	$\sigma_2^{(A)}$ (GM) <sup>a</sup>	$\sigma_2^{(A)}\Phi_f$ (GM) <sup>a</sup>	Ref.
mRFP (93)	–	H <sub>2</sub> O	584 <sup>g</sup>	611	0.30 <sup>b</sup>	1168	1080	44	13	(Drobizhev et al. 2011)
TagRFP (94)	–	H <sub>2</sub> O	555 <sup>g</sup>	584	0.44 <sup>b</sup>	1110	1050	95	42	(Drobizhev et al. 2011)
mOrange (95)	–	H <sub>2</sub> O	548 <sup>g</sup>	565	0.70 <sup>b</sup>	1096	1080	67	47	(Drobizhev et al. 2011)
eqFP650 (96)	–	H <sub>2</sub> O	592 <sup>g</sup>	646	0.19 <sup>b</sup>	1184	1112	45	8.5	(Drobizhev et al. 2011)
Katushka (97)	–	H <sub>2</sub> O	588 <sup>g</sup>	635	0.35 <sup>b</sup>	1176	1080	66	23	(Drobizhev et al. 2011)
Katushka2 (98)	–	H <sub>2</sub> O	588 <sup>g</sup>	633	0.44 <sup>b</sup>	1176	1140	62	27	(Drobizhev et al. 2011)
mKate (99)	–	pH8	588 <sup>g</sup>	635	0.27 <sup>b</sup>	1176	1118	52	14	(Drobizhev et al. 2011)
mKate2 (100)	–	H <sub>2</sub> O	588 <sup>g</sup>	633	0.42 <sup>b</sup>	1176	1140	72	30	(Drobizhev et al. 2011)
mNeptune (101)	–	H <sub>2</sub> O	600 <sup>g</sup>	651	0.17 <sup>b</sup>	1200	1104	70	12	(Drobizhev et al. 2011)
mRaspberry (102)	–	H <sub>2</sub> O	598 <sup>g</sup>	625	0.19 <sup>b</sup>	1196	1118	31	5.8	(Drobizhev et al. 2011)
Neptune (103)	–	H <sub>2</sub> O	600 <sup>g</sup>	647	0.22 <sup>b</sup>	1200	1104	72	16	(Drobizhev et al. 2011)
tdRFP (104)	–	Aq. buffer	584 (Campbell et al., 2002)	579	0.68	1168	1110	20	13.7	(Drobizhev et al. 2011)

<sup>ab</sup>Two-photon absorption cross-section value taken at the excitation wavelength  $\lambda_{2PA}$  reported by the authors in the NIR-II window; note that this may differ from the maximum of the 2PA band. Value extrapolated from the data available and from the formula of the 2P brightness ( $= \sigma_2^{(A)} \times \Phi_f$ ).

<sup>c</sup>1P properties as reported by commercial suppliers, reported in water unless indicated otherwise.

<sup>d</sup>Chemical structures are propriety and undisclosed.

<sup>e</sup>Chirality-dependant.

<sup>f</sup>Excitation-dependant.

<sup>g</sup>Properties extracted from the fluorescent protein database (Available at <https://www.fpbases.org/>, Accessed on 11/04/2022).

biological stains and FDA approved fluorophores that offer such 1PA properties (Wokosin et al., 1996b; Bestvater et al., 2002; Fu et al., 2007; Makarov et al., 2008; Kobat et al., 2009) (Table 1).

### 2.1.1 Xanthene Derivatives

Thanks to their exceptional structural diversity, xanthene-type dyes are among the most widely used biological imaging agents. The highly versatile xanthene backbone allows for extensive structural modification, with the possibility to induce dramatic bathochromic shifts in absorption and emission through dye design. As a result, the 1PE bands of such fluorophores can range from green to NIR-II wavelengths (Liu and Scott, 2021), leading to the majority of current research being focused on the design of NIR-I to NIR-II 1P-absorbing xanthene dyes. To the best of our knowledge, only a small number of xanthene dyes have been specifically designed for 2PA in the NIR-II, but the vast number of commercially available probes in this family facilitates their use as a model for 2P measurements. This in turn has led to several seminal reports on their 2P properties at NIR-II wavelengths since the first examples in 1972 (Bradley et al., 1972).

The 2PA properties of several commercial fluorescein- and rhodamine-based probes have been studied thoroughly and are well reported (Bestvater et al., 2002; Makarov et al., 2008; Bradley et al., 1972; Li and She, 2010; Hermann and Ducuing, 1972). Fluoresceins, being the most blue-shifted xanthene dyes, possess almost no 2P response in the NIR-II window (Table 1), as evidenced by the negligible  $\sigma_2$  of disodium fluorescein (1) at

1060 nm (0.069 GM) (Makarov et al., 2008). However, the heavy metal indicator PhenGreen FL<sup>TM</sup> (2), a fluorescein derivative, was reported to show fluorescence when excited under 2PA at 1074 nm (Bestvater et al., 2002). Thanks to their higher internal charge transfer (ICT) and superior structural variety, Rhodamines possess a higher potential for 2PE in the NIR-II. Rhodamines 6G (3), B (4), 101 (5) and 123 (6) all present 2PA beyond 1000 nm (Table 1). Among them, Rhodamine B was reported with the highest 2PA cross-section in the early NIR-II window, with a second 2PA band at 1040 nm in MeOH (38 GM) (Makarov et al., 2008). Highly photo-stable Alexa Fluor<sup>TM</sup> dyes 488 to 633 (7–12) were also reported with 2PA bands between 985 nm and 1264 nm respectively (Bestvater et al., 2002; Kobat et al., 2009; Anderson and Webb, 2011; Mütze et al., 2012). Alexa Fluor<sup>TM</sup> 488 (7) responded moderately to 2PE at 1000 nm (Anderson and Webb, 2011), which corresponds to the tail of its absorption band. No quantification was performed on the other rhodamine-type Alexa Fluor<sup>TM</sup> dyes, however, several other accessible cell-labelling and bioconjugatable rhodamine derivatives were investigated, such as MitoTracker Red (13), or Lissamine Rhodamine (15) and TexasRed (16) conjugates (Bestvater et al., 2002).

Phenoxazines are nitrogen-containing xanthene derivatives that also demonstrated 2PA properties in the NIR-II. Rakhymzhan et al. demonstrated the use of extended phenoxazine ATTO680 (17) in live cells under 2PE at 1260 nm (Rakhymzhan et al., 2017). Nile Red (18) is another

well-known member of this class of dyes, and is commonly used as a reference for cross-section measurements using the 2P-excited fluorescence (2PEF) technique. In an effort to optimise the 2PA properties of Nile Red, Hornum *et al.* prepared and optically characterised a number of halo-substituted Nile Red derivatives (Hornum *et al.*, 2020). On this occasion, they measured a  $\sigma_2$  of 104 GM for Nile Red at 1057 nm. The  $\sigma_2$  of the reported derivatives were also measured between 1000 and 1200 nm, showing a substantial increase upon introduction of a trifluoromethyl group (compounds **19**, **20** and **21**). Interestingly, regio-isomer 2- (**21**) showed the highest gain in  $\sigma_2$  compared to isomers 3- and 4- (**19** and **20**). Nile Red derivatives are notably solvatochromic, which increased both their 2PA wavelengths and cross-sections by up to 313% with increasing polarity.

### 2.1.2 Polymethine Derivatives

Polymethine dyes consist of an alternating single and double-bond backbone, which connects two aromatic moieties. Cyanine (Cy) dyes are a member of this family of dyes, with the polymethine conjugated chain separating two nitrogen-containing heterocycles (i.e. indolenine, benzindole). These core structures can tolerate numerous structural changes including: i) lateral groups (i.e. sulfo, carboxyl) on the heterocycles to increase solubility; ii) cycloalkane-rings within longer polymethine chains (Cy7, Cy7.5, squarines) for structural rigidity and photo-property tuning; iii) flexible chains terminating in functional groups (i.e. carboxylic acid, alkyne, azide, NHS ester) for attachment to drug probes (Lee *et al.*, 2008; Pham *et al.*, 2008; Henary *et al.*, 2009; Sun *et al.*, 2019). The most recently reported NIR-II polymethines have been designed for 1P-excited fluorescence (1PEF), including BTC1070 which employed a pentamethine chain, benzothiopyrylium heterocycles and diethylamino ED moieties to achieve emission above 1000 nm (Wang *et al.*, 2019a). Selection rules will affect differently polymethines bearing identical or different substituents on each side of the poly-ene chain, which will therefore modify the nature of their dominant 2P transition. Largely blue-shifted transitions can be observed in certain environments in the case of symmetrical polymethines.

The polymethine family includes several commercially available and FDA-approved derivatives that have been evaluated under 2PE (Table 1). In 2002, Bestvater *et al.* reported the 2PA spectrum of Cy3 (**22**), showing a response at 1032 nm (Bestvater *et al.*, 2002), and modest 2P brightnesses were then measured by Fu *et al.* and Kobat *et al.* for the original Cy5 (**23**), Cy5.5 (**24**) and Cy7 (**25**) fluorophores in the 1200–1300 nm range (Fu *et al.*, 2007; Kobat *et al.*, 2009). While there is much reported about the structure-1P property relationships in custom-made polymethine dyes, even towards the NIR-I and -II regime, less is known about their 2P properties. Berezin *et al.* studied the 2P properties of several cyanine derivatives with comparable conjugation under 1552 nm excitation, by varying the central and hetero-aromatic moieties (Lee *et al.*, 2008; Berezin *et al.*, 2011). Strong absorption was reported at this wavelength for compound **26**, a direct Cy7 analogue (240 GM).

Replacing the indolenine units with  $\pi$ -extended benzindolenines causes an increase in ICT and oscillator

strength leading to red-shifted optical properties and higher  $\sigma_2$ . This is evidenced by the commercially available and FDA-approved dye indocyanine green (ICG, **27**) whose  $\sigma_2$  is more than doubled compared to **26**. Interestingly, ICG (**27**) was also used as a contrast agent for 2P fluorescence imaging at 790 nm (Kumari and Gupta, 2019), which leads to excitation in its blue-shifted  $S_0 \rightarrow S_2$  band. The fluorophore thus presented an Anti-Kasha fluorescence at 570 nm, emitting directly from the  $S_2$  excited state, which provided it with an excitation-dependent 2PEF. ICG is now used in a clinical context for diagnostic purposes (Schaafsma *et al.*, 2011; Hackethal *et al.*, 2018), and therefore possesses a strong potential to develop 2P imaging past 1500 nm. Cypate (**28**), a bio-conjugatable version of ICG replacing both side sulfonate groups with carboxylic acids was also prepared and characterised, leading to similar optical properties (Berezin *et al.*, 2011). Restriction of the polymethine chain with a phenylcyclohexene moiety (**29**) led to a 70% increase in cross-section but similar brightness. DTTC and DODCI (**30** and **31**), two benzothiazolyl and benzoxazolyl analogues of Cy7 and Cy5, were also used in studies at 1552 nm (Berezin *et al.*, 2011) and 1060 nm (Li and She, 2010) respectively. The reported cross-section for DODCI was measured at a wavelength significantly different from the  $2\lambda_{1PA}$  value, but was still considerably lower than for DTTC which contains an extra double bond in its  $\pi$ -conjugated system. Introducing aromatic units at the 4-position of the heptamethine chain led to increased cross-sections, but halved the quantum yield. IR-140 (**32**) therefore has the largest cross-section in this class of dyes thanks to a diphenylamine unit attached to the central cyclopentene-heptamethine chain; however, this does not yield a high brightness due to a poor  $\Phi_f$ . In this study, the best 2P brightness was calculated for DTTC, which was then selected for *ex vivo* 2PEF imaging of kidney tissue (Section 3) (Berezin *et al.*, 2011). Additionally, the 2P properties of 2-azaazulene polymethine dye **33** were extensively studied theoretically and experimentally to elucidate their symmetrical character (Hu *et al.*, 2013). By comparing the 2PA spectra of **33** in apolar dichloromethane and polar acetonitrile, the authors demonstrated a symmetry-breaking character in high polarity media leading to a restriction lifting of their forbidden transition at  $2\lambda_{1PA}^{max}$ , which is a crucial observation for the development of NIR-II responsive polymethines. A set of structure-property relationships was also constructed by Fu *et al.* in a seminal report on the 2PA properties of polymethine dyes (Fu *et al.*, 2007). Cross-sections ranging from 60 to 600 GM were measured in the NIR-II on different extended, locked and substituted cyanines (dyes **34–37**), which is consistent with other reports on similar dyes. This demonstrated similar effects of conjugation lengths and ICT on the 2PA spectra and cross-sections. A strong increase in  $\sigma_2$  was noted in particular for cyanine **37**, which presented the most constrained conformation. Alexa Fluor<sup>TM</sup> 647 and 680 (**38–39**) are other commercially available polymethine analogues reported with moderate 2P brightnesses (Kobat *et al.*, 2009; Mütze *et al.*, 2012).

Adding ketones to the central polymethine chain was found to produce fluorescent dyes **42–44** that show significant red-shifting and quantum yield increase in protic solvents (Pascal *et al.*, 2017). Because of their pseudo-quadrupolar character, these dyes exhibit



strong blue-shifted 2PA bands in the NIR-I, with  $\sigma_2$  values ranging from 570 to 1400 GM at 900–970 nm. However, their transition at  $2\lambda_{1PA}$  remains partially allowed, which leads to a second weaker 2PA peak in the 1100 nm region, reaching 250 GM in the case of bis-acceptor dye **44**. These dyes were modified to include hydrophilic, hydrophobic and water-solubilizing polymers, and were successfully used in 1P and 2P microscopy.

Squaraines are a particular example of keto-polymethine dyes combining two ED groups connected to a four strongly electron-deficient 4-membered ring system derived from squaric acid. This class of dyes is known for their potential to reach considerable 2PA cross-section values with relatively simple structures, which provides them with a high  $\sigma_2$  to molecular weight ratio (Chung et al., 2006; Sun et al., 2017b). Only a few examples of squaraine fluorophores were investigated in the NIR-II range; yet the simplest examples of squaraines, built from indolenine subunits, show intense 2PEF upon excitation past 1000 nm (Ceymann et al., 2016). Squaraine **45** and its malononitrile derivative **46** were described as bright red/NIR fluorophores ( $\lambda_{em}$  = 654 nm and 714 nm), with quantum yields of 0.62 and 0.75 respectively. Both dyes showed moderate 2P response ( $\sigma_2$  > 100 GM) around 1250 nm. Compound **45** was used for *in vitro* and *in vivo* for 2P imaging at 1200 nm (Yi et al., 2019). The authors demonstrated that the 2PEF of this small dye was enhanced 17.7 times in the presence of bovine serum albumin (BSA). Moreover, squaraine showed excellent photostability and low cytotoxicity. Interestingly, more advanced squaraine oligomers and branched structures were also investigated, showing high 2PA in the NIR-II (Scherer et al., 2002; Ceymann et al., 2016).

Other heptamethine cyanine dyes carrying different terminal heteroaromatic moieties (benzindolenine, thiazole, oxazoles, azaindoles, flavyliums) have been developed and widely used as 1P contrast agents. Dimethylamino flavylum polymethine dyes have been shown to exhibit significant bathochromic shifts compared to their analogous Cy dyes, thus taking their 1PE up to 1026 nm (Cosco et al., 2017). Funabiki et al. also showed the importance of the counter-ion in benzo [cd] indolenyl-substituted heptamethine cyanine dyes (Funabiki et al., 2019). Already reaching the NIR-II window for *in vivo* 1PEF microscopy, these would be excellent candidates to have their 2P properties investigated.

A common trait of cyanine-type dyes is their pseudo-centrosymmetric character that can make the 2PA transition at  $2\lambda_{1PA}$  partially forbidden (Hu et al., 2013), and therefore reduce their 2P brightness in the NIR-II. Non-symmetrical polymethines are another important sub-class of dyes that adopt a dipolar character and therefore overcome this feature. The 2PA spectrum of the commercially available dye Styryl 9M (**47**) was reported by Makarov et al., which highlighted a high 2PA cross-section (750 GM), in the 1150–1250 nm region (Makarov et al., 2008). Styryl 9M was notably used for the detection of lysozyme amyloid fibrils with 2PE (Udayan et al., 2020). The nonpolar and viscous environment generated by the hydrophobic channels of lysozyme fibrils led to a strong bathochromic shift in the absorption spectrum of the dye, accompanied by an increase in quantum yield. FM4-64 (**48**) (Wokosin et al., 1996a) and To-Pro-3 (**49**)

(Smith et al., 2012), two other non-symmetrical dipolar polymethines, were reportedly used in 2P imaging past 1064 nm. FM4-64 is also commonly used in second-harmonic generation experiments, which makes it a multi-modal imaging agent (Nuriya et al., 2016).

Merocyanines are a sub-group of dipolar polymethine chromophores constituted specifically of an amine (D) and a carbonyl (A) moiety, connected to each end of the poly-ene  $\pi$ -conjugated system. Merocyanines are typically sensitive to their local environment, with optical properties varying in contact with cell membranes, metal ions, or DNA; and 2PE was shown to be even more sensitive than 1PE to such variations in the local environment (Pascal et al., 2017). Fewer examples of 2P-responsive merocyanines have been reported in the NIR-II. However, in their investigation of keto-polymethines, Pascal et al. also reported a merocyanine-like dye **43** that showed a 2PA maximum at 1098 nm. Its moderate cross-section was compensated by a good  $\Phi_f$ , which led to a brightness value of 74 GM in MeOH. An interesting example of advanced merocyanine design was also achieved by incorporating the polymethine system onto a cyclohexanetrione moiety (Poronik et al., 2012). The resulting octupolar (D- $\pi$ )<sub>3</sub>-A structures **50** and **51** showed moderate 2PA response in the NIR-II transition ranging between 98 and 214 GM in THF.

### 2.1.3 Porphyrin and Phthalocyanine Derivatives

Porphyrins, phthalocyanines and other types of polypyrrole derivatives are commonly used as contrast agents or photosensitizers in biomedical applications (Josefsen and Boyle, 2012). The particular properties of such compounds make it possible to tune multiple parameters such as the lifetime of the excited state, and therefore their emissive character, by metalation. The 2PA properties of Zn-tetrakis-(phenylthio)-phthalocyanine (**52**) and Si-naphthalocyanine dioctyloxide (**53**), both commercially available, were investigated by Makarov et al. (Makarov et al., 2008). Both dyes showed 2PA bands at 1270 nm in CCl<sub>4</sub> with moderate cross-sections (Table 1). The silicon derivative however showed significant 2PA capacity in its higher energy band (470 GM at 1020 nm). In contrast, tetraphenylporphyrin showed virtually no absorption past 1000 nm, which is in accordance with the limited 1PA capacity associated with its red Q-band. Porphyrin derivatives can however exhibit large cross-sections, as fused-systems show an increase in both cross-section and  $\lambda_{ex2PA}$  with the increasing number of rings (Yoon et al., 2007), although this can lead to preferential non-radiative behaviour. Only a few examples of polypyrrole design have led to NIR-II responsive fluorescent dyes specifically for 2P imaging applications. *Meso* substitution is nonetheless a typical design strategy to amplify the 2P response of porphyrin dyes (Nowak-Król et al., 2012), and porphyrin dimers bridged by a diketopyrrolopyrrole unit at this position were prepared to form highly absorbing D- $\pi$ -A- $\pi$ -D dyes (Nowak-Król et al., 2013). Although no quantification was performed in this study, the authors claim that their porphyrin dimer (**54**) remained fluorescent at 710 nm. A band structure characteristic of porphyrin dyes was observed on the 2PA

spectrum, which leads to broad absorption between 1000 and 1450 nm. However, while these structures are of interest, their ability to be utilised in a bio-medical setting is limited due to poor solubility in aqueous environments, and the requirement of controlled self-assembly *in vitro*.

#### 2.1.4 BODIPY Derivatives

BODIPY dyes are often used as fluorescent trackers for imaging thanks to their high brightness, narrow fluorescence peaks and low sensitivity to changes in pH and polarity. BODIPY structures are highly tunable, and extensions of the  $\pi$ -conjugated system in positions 3- and 5- can lead to strong bathochromic shifts that can be exploited in 2PA. Several commercially available cell stains belong to this class of dyes, such as LysoTracker Red (**55**) which shows 2PA at 1032 nm (Bestvater et al., 2002). BODIPY TR (**56**) is a  $\pi$ -extended derivative with high photostability that was reported with superior 2P brightness ( $>200$  GM) at 1060 nm (Mütze et al., 2012). Extension at the 3- and 5- positions was also the strategy used by Zheng *et al.* to design the compound IR07 (**57**) in 2009 (Zheng et al., 2009). Albeit initially developed for optical power limiting applications, the dye still had a fluorescence quantum yield of 30% and a 2PA cross-section of 101 GM at 1310 nm in  $\text{CH}_2\text{Cl}_2$ , which makes it an interesting candidate for further developments in bio-imaging. Interestingly, Prasad and co-workers further extended this aminostyryl-BODIPY with phenylacetyles, and used compound **58** under 2PE at 1064 nm (Hu et al., 2020). As this dye had a relatively low fluorescence quantum yield of 9% (in THF), the authors investigated its application in 2P photo-acoustic imaging instead of traditional 2P fluorescence.

Theoretical reports have also shown the potential of BODIPY derivatives as 2P and 3P imaging agents (Zhang et al., 2015), which opens the way towards the rational design of NIR-II fluorophores. More advanced dye-design strategies have also been applied to optimise the 2PA properties of BODIPY fluorophores beyond 1000 nm (see Section 2.1.5).

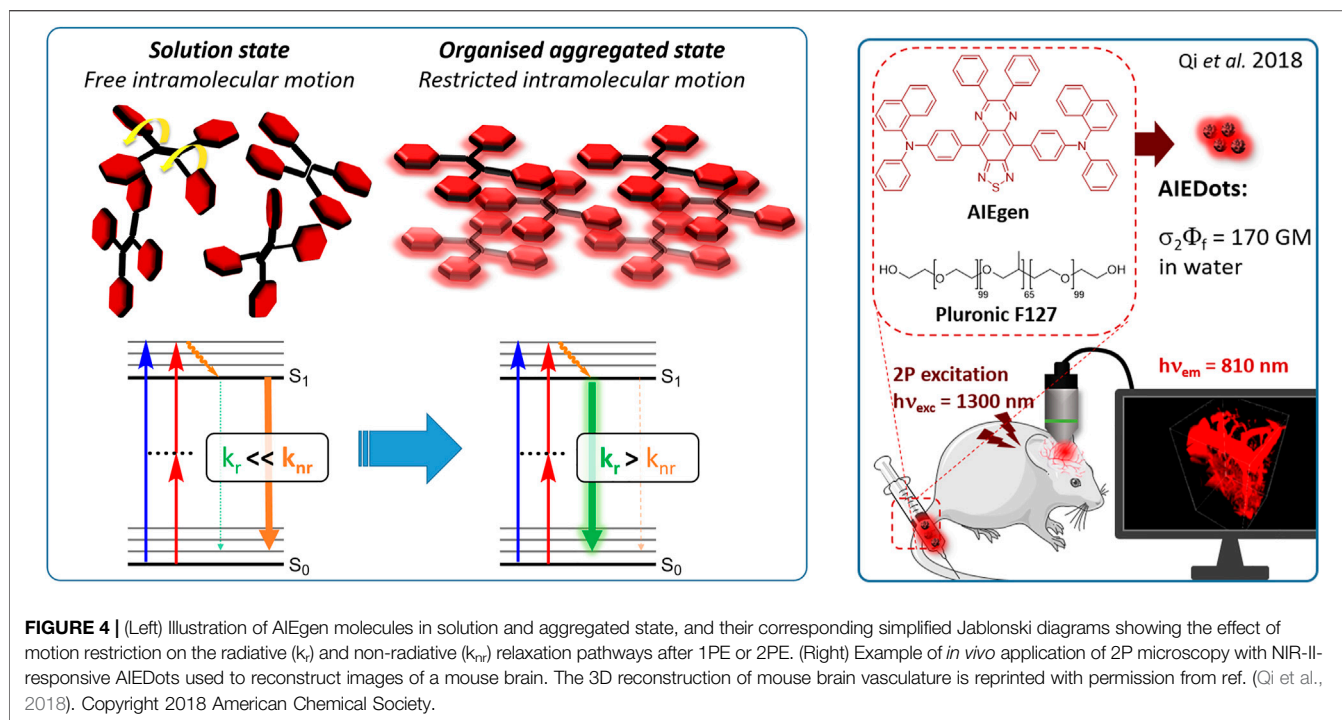
#### 2.1.5 Dipoles, Quadrupoles and Advanced Design Strategies

By taking advantage of strong ICT, relatively simple D- $\pi$ -A structures can sometimes lead to strongly red-shifted optical properties and important 2PA cross-sections. Importantly, in contrast to symmetrical dyes, their transitions at  $2\lambda_{1\text{PA}}^{\text{max}}$  are usually allowed, which is an important factor to reach the NIR-II window in 2PA. Triphenylamines are an important ED building block of 2P-responsive dipoles. Examples of triphenylamine dipoles include dye **59** that was incorporated within a poly (styrene-co-maleic anhydride) (PSMA) polymer, thus forming fluorescent nanoparticles (NPs) with high chemical and optical stability across a broad pH range (Alifu et al., 2017). The dipole emits in the NIR-I region, and interestingly shows a bathochromic shift of  $\lambda_{\text{em}}$  in the solid state. When excited at 1040 nm (2PA) the PSMA NPs of **59** emit over a wide range of wavelengths (500–950 nm) with a maximum at 678 nm. A large cross-section was measured for these NPs ( $5.6 \times 10^5$  GM), and the fluorescence quantum yield could be tuned from 1.7% to 16.9% by modifying the weight

ratio of dye to polymer. These NPs were used as contrast agents to facilitate the 2PA NIR-II imaging of mouse brain blood vessels at the deepest tissue penetration reported to date (Section 3.2, Table 3). Similar to **59**, a second NIR-II absorbing triphenylamine dipole **60** was also utilised for imaging *in vivo* (Section 3.2, Table 3) while acting as a lysosomal photosensitizer for PDT (Zhou et al., 2021). Tuning the EW moiety shifted the 1PA properties of this dipole to the red compared to **59**, allowing 2P imaging to be performed at 1100 nm, i.e. near the  $2\lambda_{1\text{PA}}$  value (530 nm).

Some other amino-substituted D- $\pi$ -A dyes have been shown to exhibit strong solvchromatic or fluorogenic behaviour (Klymchenko, 2017). A reported water-soluble dipolar fluorophore (**61**) exhibited a large 2PA cross-section value at 1040 nm (440 GM) (Massin et al., 2013). Strong solvato-fluorogenic properties were demonstrated for this dye, with a fluorescence quantum yield of 0.22 in water, and therefore a 2P brightness close to 100 GM. Similar relatively simple structures have led to highly red-shifted 2P active dyes, which constitutes efficient dye design examples. Using a dialkylamino ED group and a pyridinium acceptor in a D- $\pi$ -A structure led to dipole **62** that was reported with a  $\sigma_2$  of 500 GM at 1300 nm (Ricci et al., 2017). Interestingly, the corresponding D- $\pi$ -A- $\pi$ -D counterpart **63** was also prepared by the authors. With a  $C_{2v}$  symmetry leading to a “bis-dipolar” character, this compound showed an enhanced cross-section at 1300 nm compared to dipole **62**, but the emission quantum yield was reduced by an order of magnitude. With limited quantum yields, both dipole **62** and bis-dipole **63** showed limited 2P brightness. Benzothiadiazole (BTZ) and related derivatives are other typical moieties that have been used in the design of NIR-absorbing chromophores for 1P and 2P bio-imaging, in particular when incorporated as a strongly EW core in a D- $\pi$ -A- $\pi$ -D structure. This has led to a strong 2P response with the ability to extend beyond 1000 nm (Yao et al., 2016). However, these pseudo-centrosymmetrical chromophores, with forbidden transitions, can be counterproductive in NIR-II dye design. Moreover, water solubility can be a limitation for these molecules, and they tend to be used more commonly as AIE building blocks (Section 2.1.6), or incorporated in different types of NPs. For this purpose, Liu and co-workers prepared conjugated polymers from BTZ and thiophene derivatives (**64**) that proved highly NIR-emissive once incorporated in phospholipid-type NPs (Wang et al., 2019b). These polymer dots showed significant 2PA between 1000 and 1200 nm, with cross-sections in the 1000–2000 GM range. A 2P brightness of 242 GM was reported, along with impressive *in vivo* results (Section 3.2, Table 3).

Other advanced strategies have been applied to design NIR-II-absorbing 2P dyes with optimised 2PA cross-sections in the NIR-II, without focusing on emissive properties or imaging applications, which has been reviewed recently (Pascal et al., 2021). This includes the preparation of stable  $\pi$ -radical and diradical structures (Hisamune et al., 2015), macrocyclic dyes with controlled topology (Möbius dyes, *meso-meso*-linked porphyrin oligomers amongst others) (Tanaka et al., 2008), or multi-chromophoric systems with hybrid electronic transitions (Webster et al., 2009). During their investigation



of singlet biradical dyes, Li *et al.* reported the preparation of zethrene derivatives (**65** and **66**) with strong 2PA properties at 1250 nm (Li et al., 2012). The compounds retained fluorescent properties, however, measurements were only performed in chloroform because of their lipophilic nature. Ni *et al.* reported quinodimethane-bridged BODIPY dimers (**67** and **68**) that showed up to 26% diradical character, which provided strong 1PA at the beginning of the NIR-II window at 1100 nm (Ni et al., 2016). The corresponding 2PA band was, therefore, shifted beyond 2000 nm (up to 1500 GM at 2300 nm). Although no application in imaging was envisioned, the authors report that their BODIPY derivatives remain fluorescent in chloroform solutions, with up to a 0.2% quantum yield of infrared emission. This low  $\Phi_f$  value leads to very poor 2P brightness (up to 2.6 GM). The quinodimethane dimerization strategy was also used by Zeng *et al.* to prepare porphyrin dimers with intense 2PA cross-section at 1800 nm (Zeng et al., 2013). In this report, the Zinc and Magnesium porphyrin dimers showed emission bands in the 900 nm range ( $\text{CH}_2\text{Cl}_2$ ). Self-assembly of porphyrin-oligomers and 4,4'-bipyridine has also led to record cross-sections (up to  $2.3 \times 10^5$  GM) and strongly red-shifted 2PE (up to 1300 nm) by restricting rotation and enhancing electron transfer through the metal bridge (Drobizhev et al., 2006). Such strategies have led to  $\sigma_2$  of several thousands of GM above 1200 nm, but often lead to non-emissive compounds, typically because of preferential vibrational decay or very short excited state lifetimes (Cho et al., 2009). They are also susceptible to poor stability and lack of biocompatibility.

Other families of dyes have also been investigated with the goal of improving 2PA capacity in the NIR-II (Pascal et al., 2021), including for optical imaging applications. The classical dead cell

stain propidium iodide (**69**) shows 2PA response at 1015 nm (Bestvater et al., 2002). Polyaromatic fluorophores such as diketopyrrolopyrroles have also been proposed as potential multi-photon imaging agents in theoretical reports (Ye et al., 2017).

### 2.1.6 Aggregation Induced Emission Dyes and Dots

Dye design strategies for 2P-responsive NIR-II fluorophores can lead to highly lipophilic aromatic structures prone to forming irregular aggregates in aqueous environments. Fluorescence quantum yields can thus be dramatically reduced as a result of a reduction in the rate of radiative decay ( $k_r$ ), either by significant bathochromic shifts leading to favoured non-radiative vibrational decay ( $k_{nr}$ ) processes, by fluorescence quenching by water molecules, or by intermolecular  $\pi$ - $\pi$  stacking, which is known as “aggregation-caused quenching”. Counteracting this effect, certain lipophilic organic dyes generate an organised solid-state arrangement of chromophores with a local lipophilic environment within nano-aggregates. While the dye molecules move freely in diluted solution form, the restriction of intramolecular motions (i.e. vibrations, rotations etc.) in this organised aggregated state causes a strong decrease in the probability of non-radiative decay, and therefore a strong increase in fluorescence (Figure 4A, left). The concept of “aggregation-induced emission” (AIE) was first described in 2001 by Tang and co-workers (Luo et al., 2001), and has since become a popular approach to the design of 1P and 2P theranostic agents (Zhu et al., 2018; Yang et al., 2020b; Lu et al., 2020; Han et al., 2021) and circumvent the limitations of standard NIR-dye design strategies. In contrast to traditional organic fluorophores, AIE luminogens (AIEgens) typically exhibit low fluorescence in dilute solutions, but both high  $\Phi_f$  and photostability in the aggregated state, which are key requirements for high-resolution imaging.



In the context of 2P-imaging using NIR-II wavelengths, AIEgens provide a way to prepare highly NIR-shifted chromophores maintaining strong 2P brightness in water. The BTZ derivative **70** has been shown to exhibit AIE behaviour in two different studies, emitting NIR light after 2PE at 1200 nm (aqueous media) and 1300 nm (organic media) respectively (Qi et al., 2018; Liu et al., 2021). Significant cross-section values ( $1.6 \times 10^4$  GM at 1040 nm and 1220 GM at 1300 nm) were reported in the NIR-II for these AIEdots. The emission peak was measured at 810 nm with 14% quantum yield. This AIEgen was used to image mouse brain tissues with high resolution (Figure 4B, right), demonstrating the imaging benefits of NIR-II 2PA over NIR-I 1PA (Section 3.2, Table 3). The use of AIEgen dye **70** was then extended to 2P fluorescent lifetime imaging (2PFLIM) by the same research group (Liu et al., 2021). Replacing the arylamine EDG of this molecule with a propeller-shaped tetraphenylethene moiety (Wang et al., 2019c), a structure commonly used in the design of AIEgens, led to D- $\pi$ -A- $\pi$ -D dye **71** that was co-nanoprecipitated with a pegylated phospholipid. The 2PA spectrum of the resulting AIEdots showed a  $\sigma_2$  close to  $1 \times 10^5$  GM both at the maximum of the low energy band (1150 nm) and in the tail of the high-energy band (1000 nm). With a fluorescence quantum yield of 19% in aqueous media and high photo-stability, these AIE dots showed high potential for *in vivo* imaging, which was demonstrated in tumour tissues and blood vessels (Section 3.2 and Table 3).

Outside of the BTZ class of dyes, a 2PA fluorescent nanoprobe made of a triphenylamine-based brominated AIEgen (dye **72**) (Samanta et al., 2021), showing a similar structure to dipole **59** (Section 2.1.5), was reported. The triphenylamine ED group provides a good balance between strong twisted ICT in the molecule and unrestricted rotation to ensure possible AIE. These NPs showed large 2PA cross-section of  $3 \times 10^3$  GM at 1040 nm and a  $\Phi_f$  of 6%, which also allowed 2D and 3D imaging of brain vasculature (Section 3.2, Table 3). Similarly, four push-pull AIEgens based on a diphenylamine donor attached to different

EW moieties (Zheng et al., 2018) were prepared. All 2PA bands extended somewhat past 1000 nm, but the highest cross-sections were obtained with the isophorone and furanone dipoles **73** and **74** (887 GM at 1020 nm for the latter) which showed great promise in *ex vivo* cell and tissue studies. Finally, the tetraphenylethene propeller-shaped moiety was attached to a BODIPY dye to prepare AIEgen **75**. The NPs prepared from this dye showed a record absorption capacity past 1000 nm ( $2.9 \times 10^6$  GM at 1040 nm) (Wang et al., 2015), which is among the highest cross-section values in the NIR-II region all classes of materials combined. Therefore, AIEgens allow the combination of massive cross-sections, arising from the combined cross-section contribution of each dye in the NP, and of a fluorescence strongly switched-on in water. Both these factors combine to give unprecedented 2P brightness values ( $>10^4$  GM), which makes them high-potential materials for 2P imaging in the NIR-II (Section 3.2, Table 3).

## 2.2 Carbon, Hybrid and Inorganic Nanomaterials

Carbon and metal-containing nanomaterials have been investigated for decades as a source of 2P-reponsive imaging agents thanks to unique electronic, physical and morphological properties. Such materials also tend to show higher brightness and photo-stability than organic dyes, and thanks to their surface functionalisation, they provide huge versatility to expand into multimodal and theranostic applications. The potential toxicity of metal and carbon nanomaterials is arguably the main limitation to their use for *in vivo* imaging.

Carbon nanomaterials have been a key focus of research in bio-imaging over the past decade owing to their unique optical properties, large surface area, and robust photostability allowing long-term imaging. Carbon dots (CDs), single-wall carbon nanotubes (SWCNTs), graphene derivatives and nanodiamonds have all been reported as luminescent 2P-active

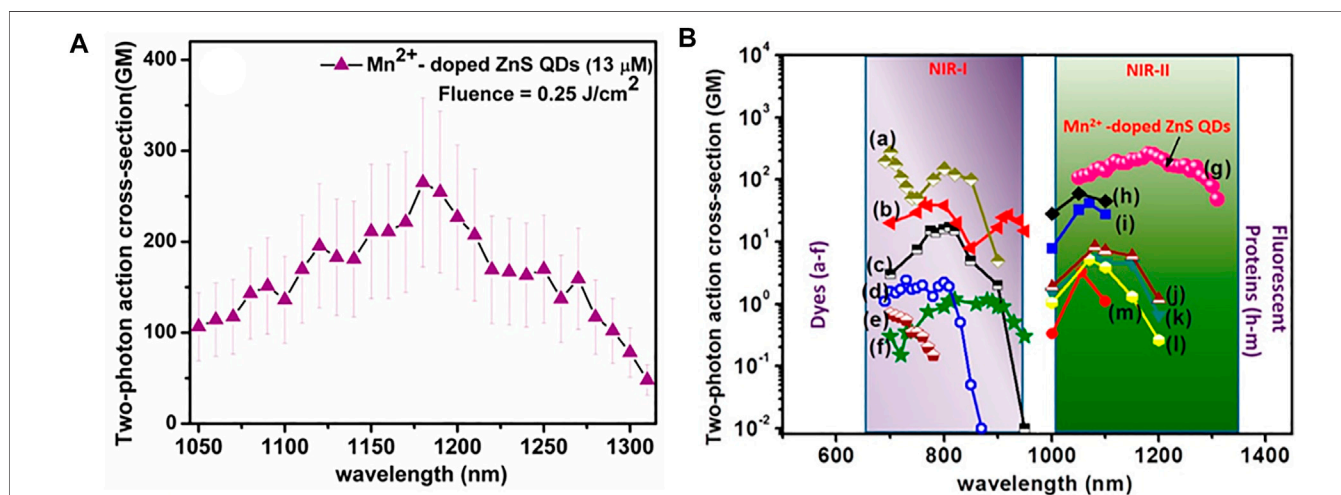


**FIGURE 5 | (A)** 2PA spectrum of Mn<sup>2+</sup>-doped ZnS QDs in the range from 1050 to 1300 nm reported by Subha et al. **(B)** Comparison of  $\sigma_2$  values in Mn<sup>2+</sup>-doped ZnS QDs (curve g) with other standard chromophores (curves a–f) and fluorescent proteins (curves h–m): (a) Rhodamine B, (b) Fluorescein, (c) Coumarin 307, (d) Cascade blue, (e) Dansyl and (f) Lucifer Yellow), and (h) tdTomato, (i) mBanana (j) mRFP (k) mCherry (l) mStrawberry (m) mTangerine). Reprinted with permission from ref. (Subha et al., 2013). Copyright 2013 American Chemical Society.



materials with imaging potential (Hong et al., 2015). In the NIR-II window, semiconducting SWCNTs have demonstrated strong potential, both because of their strong 2P response, and their NIR emission. In the context of optoneurology and neurotransmitter sensing, a dopamine-sensitive nanosensor was developed using SWCNT (**76**), and provided chirality-dependent fluorescent turn-on responses varying between 20% and 350% in the presence of the analyte (Bonis-O'Donnell et al., 2017). Sensing was performed at 1560 nm under 2PE with a  $\sigma_2$  estimated at  $2.16 \times 10^5$  GM, but the fluorescence quantum yield of **76** remained limited ( $\Phi_f = 0.0023$ ). These nanosensors were embedded 2 mm into strongly scattering tissue phantoms mimicking brain tissues, which demonstrated that the light scattering decreased from 42% to 4% using NIR-II 2PE compared to traditional 1PE. In 2014 an aptamer-modified graphene oxide material (**77**) was used to show excitation dependant luminescence outputs and develop multi-channel and multi-colour imaging of multi-drug resistant bacteria (Pramanik et al., 2014). In particular, 2PE of the material at 1120 nm led to bright red-light emission, which allowed imaging of methicillin-resistant *Staphylococcus Aureus* (MRSA) with a  $\sigma_2$  above  $3.6 \times 10^4$  GM in aqueous solution. Recently, nitrogen-doped graphene quantum dots were also reported with high luminescence and photosensitizing properties for antimicrobial applications (Kuo et al., 2022). Although the 2P properties of these graphene-based nano-objects were only measured up to 970 nm, they likely still possess 2P responses beyond 1000 nm. Finally, sulfoxide- and carbonyl-enriched CDs (**78**) were prepared by solvothermal treatment of readily available citric acid and urea. These CDs were brightly fluorescent at 760 nm under 1PE at 714 nm, with efficient NIR-II absorption upon 2P and three-photon (3P) excitation at 1200 and 1400 nm (Li et al., 2018). Carbon quantum dots prepared from tris(4-aminophenyl)amine (**79**) also led to ultra-narrow emission at 615 nm with high photoluminescence quantum yield (84%) (Liu et al., 2020). These CDs were used for *in vitro* for 2P imaging of tumor spheroids at 1100 nm, with a penetration depth reaching 200  $\mu$ m. Further 2P *in vivo* imaging was carried out in zebrafish larvae, in which a maximum penetration depth of 500  $\mu$ m was achieved (Section 3.2, Table 3).

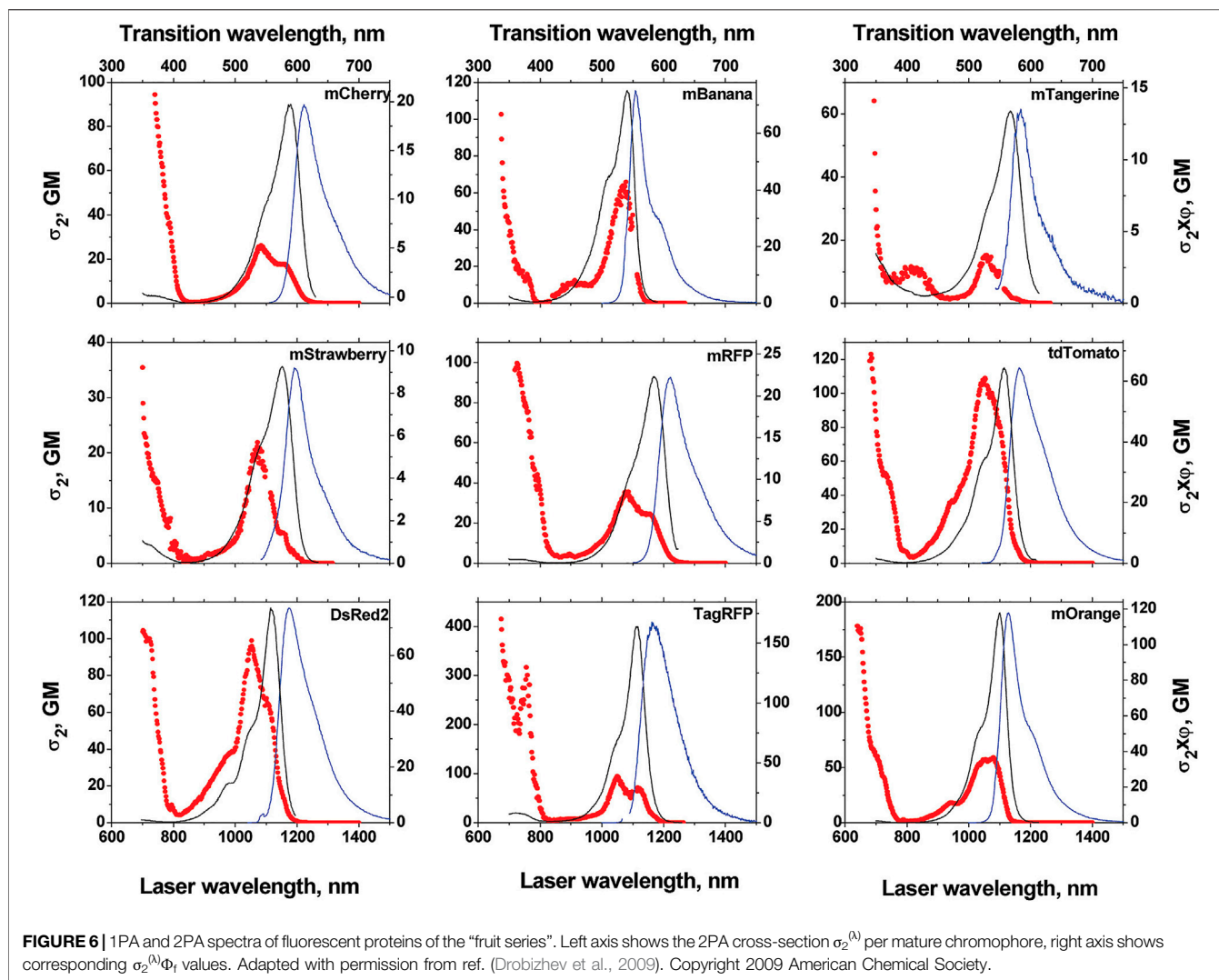
Noble metal nano-objects are known to interact strongly with high-intensity light pulses, which is the source of interesting NLO properties (Olesiak-Banska et al., 2019). In recent reports, gold nanoparticles (AuNPs) have been used to develop a hybrid theranostic platform (**80**) combining anti-GD2 antibodies and SWCNTs for selective 2P imaging and efficient photothermal therapy of human melanoma cancer cells at 1100 nm (Tchounwou et al., 2015). Although no  $\sigma_2$  or  $\Phi_f$  values were explicitly mentioned in the article, the authors measured the 2P-induced photoluminescence of the hybrid nanomaterial and evidenced that the strong plasmon-coupling generated by the gold increased the emission by 6 orders of magnitudes compared to the AuNPs or SWCNTs alone. The plasmon coupling also acted as a local nano-antenna to enhance the photothermal efficiency of this theranostic system. Recently, hybrid Au-Si NPs functionalised with a NIR-resonant cyanine dye were also exploited for tissue imaging with surface-enhanced resonance

hyper-Raman scattering (SERHRS) (Olson et al., 2022), a vibrational 2P spectroscopy technique.

Gold nano-clusters (AuNCs) are ultrasmall nano-materials constituted of as little as a dozen atoms of gold. Due to the proximity of their size to the de Broglie wavelength of an electron, they do not exhibit the typical plasmon resonance observed in larger AuNPs, but instead show strong quantum confinement effects, leading to molecule-like electronic transitions and fluorescence properties. AuNCs with a number of gold atoms varying from 25 to 2406 had their 2P fluorescence properties measured in the NIR-I and -II regions (Ramakrishna et al., 2008). In the NIR-I (800 nm), 2PA cross-sections ranging from  $5 \times 10^5$  to a  $3 \times 10^6$  GM were reported; but interestingly, the  $\sigma_2$  value per gold atom decreased drastically with the size of the AuNC, eventually showing saturation when transitioning to standard AuNP behaviour. In the NIR-II, the Au25 clusters (**81**) showed a cross-section of 2700 GM at 1290 nm with emission of light at 830 nm, however the quantum yield value of such systems is said to be in the  $10^{-7}$  range which limits their brightness. PEG-lipoic acid functionalised AuNCs (**82**) of 1.5 nm in size have also been discussed for cellular imaging (Oh et al., 2013). The 2PA cross-section of these AuNCs was above 300 GM at 1100 nm, and remained >100 GM at 1300 nm where the measurement ended. Fluorescence at 820 nm with a  $\Phi_f$  of 4–8% was reported depending on the surface functional group, and the objects were stable for months and generally non-toxic.

Quantum dots (QDs) are crystalline semiconductor materials that also display quantum confinement effects due to their nanometer size (Wegner and Hildebrandt, 2015; Barroso, 2011). The dependency of the confinement energy on the QD's diameter leads to size-dependent absorption and emission, with smaller NPs resulting in larger band gaps—and therefore blue-shifted emission, and larger NPs having more red-shifted emission. Their highly tunable size and properties, high stability, limited photobleaching, and reported 2PA cross-sections ( $>5.0 \times 10^4$  GM at  $\geq 1000$  nm) make them great candidates for OMI applications (Gui et al., 2017; Nyk et al., 2012). Due to their unique semiconducting energy profile, they also feature broad absorption bands which would make them ideal for 2PA NIR-II imaging where excitation wavelength can be laser-dependent (Section 3.1). The main drawbacks of QDs arise due to reports on potential toxicity related to their heavy metal components (Tsoi et al., 2013). Examples of 2P-responsive QDs in the NIR-II include Mn<sup>2+</sup>-doped ZnS QDs (**83**) reported in 2013 by Subha et al. (Subha et al., 2013), which presented 2P- and 3P-induced photoluminescence at 586 nm resulting from the electronic transitions of the manganese ions. A maximum 2PA cross-section of 265 GM was measured at 1180 nm, with an absorption band extending beyond 1250 nm (Figure 5A), which was higher than most standard dyes and fluorescent proteins (Section 2.3) reported at the time (Figure 5B). These QDs also possessed long photoluminescence lifetime (millisecond range).

Pioneering work combining 2P fluorescence and 2PFLIM using PbS/CdS QDs (**84**) as water-dispersible contrast agents was recently reported (Ni et al., 2022). These QDs allowed “NIR-to-NIR” imaging under 2PE at 1550 nm with a  $\sigma_2$  of 530 GM in water. Importantly, the QDs maintained bright fluorescence properties at



1270 nm, with a quantum yield of 18% in water, which is higher than most organic dyes at such long wavelengths. The high fluorescence lifetime ( $\tau = 501$  ns) of these QDs allowed the authors to implement a 2PFLIM system to complement 2P fluorescence imaging, and *in vivo* images of mouse brain blood vessels were obtained for the first time. As well as this, it is worth mentioning that Larson *et al.* reported polymer-encapsulated CdSe-ZnS QDs with 2P brightness of up to  $4.7 \times 10^4$  GM, which is orders of magnitude higher than organic fluorescent probes (Larson *et al.*, 2003). Although the measurements were only performed between 700 and 1000 nm at the time, brightness values proved relatively constant all over this range of wavelength thanks to their large absorption band; and QD605 (85), the brightest NP in their study, would likely still respond in the NIR-II regime.

## 2.3 Fluorescent Proteins

FPs are a class of proteins that contain chromophores that arise from specific amino-acid sequences in their polypeptide sequence undergoing a series of atypical transformations (Tsien, 1998; Shaner *et al.*, 2004). Unlike the aforementioned examples that

require injection or incubation with a contrast agent, FPs can be genetically encoded, and they can therefore generate luminescence with high target specificity. The 2P properties of NIR-II-responsive FPs have been well documented in the seminal work by Drobizhev *et al.* (2011). Several proteins absorbed efficiently above 1000 nm, and we limited our selection to the ones showing brightness values above 5 GM in Table 1 (compounds 86–104). Among them, the so-called “fruit proteins” have been reported with medium to strong 2P brightness in the 1000–1200 nm region (Figure 6) (Drobizhev *et al.*, 2011; Drobizhev *et al.*, 2009). With a maximum 2PA cross-section of 278 GM at 1050 nm, as well as an absorption band extending beyond 1200 nm, tdTomato (86) was reported as the brightest in the series (Shaner *et al.*, 2004; Drobizhev *et al.*, 2009). Proteins tdKatushka2 (87) and dsRed2 (88) follow with brightness values in the 50–100 GM range. As shown in Figure 6, the  $\sigma_2\Phi_f$  values per mature chromophore of FPs are comparable to those of organic fluorophores, and orders of magnitude lower than those of nanomaterials and AIEgens. Still, as highlighted by Drobizhev *et al.* (2011), these 2PA

**TABLE 2 |** Benefits associated with Fibre lasers over traditional solid-state and OPO lasers (adapted from ref (RPMC, 2020))

Solid-State/OPO-Based Lasers	Femtosecond Fibre Lasers
Large cumbersome design	Lightweight, up to 10x smaller
Expensive	Affordable
Less consistent pulse duration	Pulse duration always maintained
Lower power at long wavelengths (crystal-based amplifiers)	Maintains high power at long wavelengths (up to 4W at 920 nm)
Water-cooled	Air-cooled
High cost of ownership	Low maintenance and engineer fees (fast return on investment potential)

properties match well with current widespread NIR-II laser technologies such as Ti:Sapphire with optical parametric oscillators, neodymium (Nd)- and ytterbium (Yb)-doped fibre and glass lasers and chromium-forsterite (Cr-Mg<sub>2</sub>SiO<sub>4</sub>) lasers (Section 3.1) (Shaner et al., 2004; Drobizhev et al., 2009). FPs were therefore among the first luminescent trackers to be used successfully to perform 2P imaging of biological systems in the NIR-II window, and to develop new adapted multi-photon technologies. Gene expression in transgenic zebrafish embryo, tagged with a red FP (Hc-RFP, 89), was investigated by Tsai *et al.* using 2P imaging (Tsai et al., 2005; Tsai et al., 2006). Heart-specific regulatory elements of a zebrafish cardiac gene fused with the encoding element for Hc-RFP were injected into zebrafish embryos. This generated a zebrafish line that showed strong 2P red fluorescence in cardiac cells (Tsai et al., 2005). This red FP allowed imaging with a 1230 nm fs light source, providing superior imaging resolution compared with traditional green FP-based 2P microscopy. In addition, the properties of HcRFP were measured under 2PE by the same group, showing an excitation maximum around 1200 nm and an absorption cross-section of the same order as the green FP (GFP) (Tsai et al., 2006). The use of red FPs and mCherry (90) under OPO excitation has also been demonstrated (Herz et al.,

2010) and compared against NIR-I activated GFP. The authors report that, in the cortex of fluorescent-protein-expressing mice, a maximal imaging depth of 508  $\mu$ m was possible when imaging with tandem dimer RFP (TdRFP, 104) at 1110 nm, which represents an 80% enhancement compared to GFP-expressing mice imaged at 850 nm. The depth-dependent deterioration of the spatial resolution was also significantly lower at 1110 nm. Yang *et al.* induced the expression of the tdTomato protein in excitatory neurons of mice (Yang et al., 2013). The authors used this model to validate the development of their multi-colour OPO-based laser set up which was used successfully at 1070 nm for 2P imaging of the intact brain cortex (Section 3). Voigt *et al.* recently validated the design of a novel semiconductor-disk laser (SDL) by performing *in vivo* 2P imaging of FP-containing *Drosophila* larvae (Voigt et al., 2017).

### 3 IN VIVO 2P-NIR-II BIO-IMAGING: INSTRUMENTATION AND EXAMPLES

Two-photon absorption is a third-order NLO phenomenon. As such, 2PA can be observed in many types of materials provided

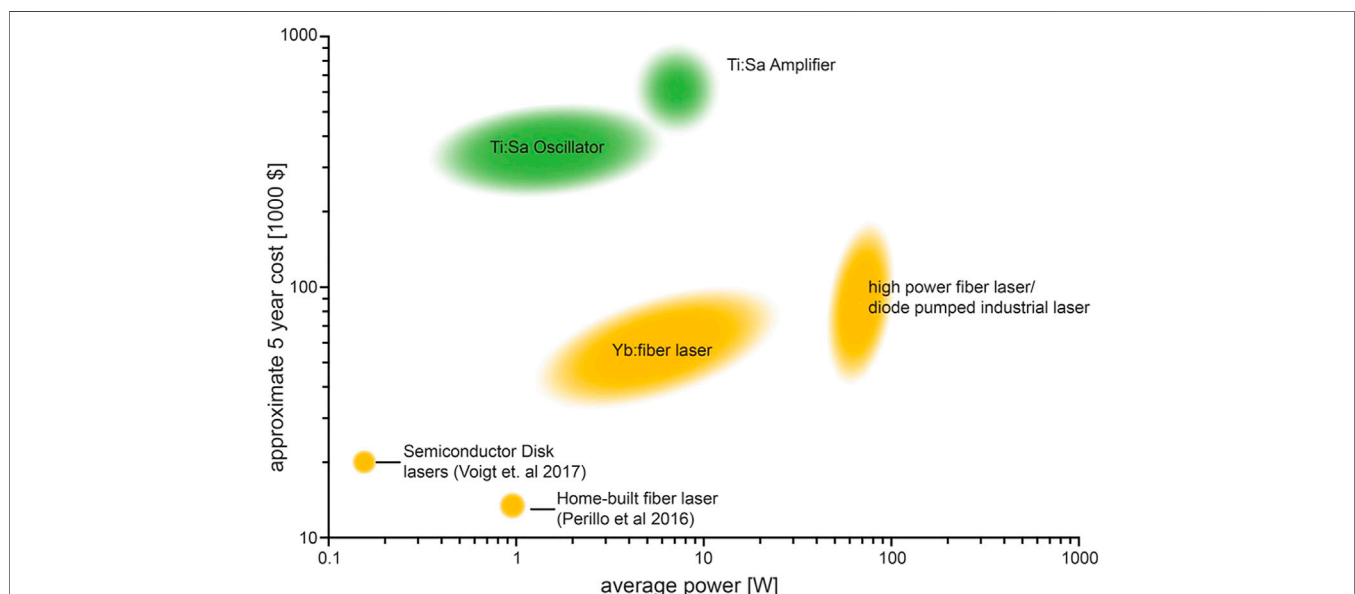


**FIGURE 7 |** The approximate 5-years costs of traditional tunable 2PA lasers (green) and alternative fixed wavelengths lasers (yellow), demonstrating the economical benefits of fixed wavelength fibre lasers. Reproduced from the supplementary material of ref (Mohr et al., 2020) with permission from the authors.

that the intensity of the electric field in the light source is strong enough to generate a non-linear polarisation in the material (He et al., 2008).

For 2PA imaging applications, high photon densities are required to ensure sufficient fluorophore excitation; requiring around one million times more photon flux compared to 1PA events (Le Bot, 2009). This involves the use of high intensity pulsed (mode-locked) lasers. Such systems provide brief but intense light pulses which results in high photon fluxes arriving at a sample to promote 2PE, while also keeping the average power low enough to prevent tissue damage. By reducing the average excitation power, the number of 1PA events are minimised, which is known to be the source of heating and resultant photo-damage. Laser requirements for 2P imaging are typically met with output powers of >1 W, pulse durations of <100 fs, repetition rates of typically between 80–100 MHz, and high peak powers (>100 kW). Lasers capable of producing pulses of light of durations shorter than picoseconds ( $10^{-12}$ ) do so using a method known as ‘mode locking’.

Recent years have shown an increase in successful 2PA NIR-II imaging with imaging depths of up to 1200  $\mu\text{m}$  into tissue being claimed (Alifu et al., 2017). However, most lasers explored in current literature have their output wavelengths in the NIR-IIa region, with most reports showing imaging performed at lasing wavelengths of <1300 nm (Section 3.2, Table 3). This is likely due to the limited capacities of current lasers struggling to reach the power, portability and flexibility requirements at such long wavelengths.

Traditional systems for 2P imaging involve the use of solid-state lasers (Drobizhev et al., 2011; Ustione and Piston, 2011). However, due to their drawbacks, such lasers have limited applications in the NIR-II window. As such, lasing systems involving the use of optical parametric oscillators (OPOs), optical parametric amplifiers (OPAs), and fibre lasers, are more commonly used for 2P NIR-II imaging.

## 3.1 NIR-II Laser Technologies

### 3.1.1 NIR-II Solid-State Pulsed Lasers

The first paper demonstrating 2P imaging applications was demonstrated by Denk et al. (1990) in which a 25 mW colliding pulse, mode-locked dye laser with an emission of 630 nm was used. Historically, dye lasers dominated the field of tuneable lasers but were then replaced by solid-state lasers (often based on Ti:Sapphire crystal) due to their bulky structures, complex liquid handling systems, and the involvement of toxic and volatile dyes (Ferguson et al., 1993).

Solid-state ‘mode-locked’ lasers compatible with 2P imaging produce high-power light pulses on a femtosecond time-scale. Solid-state lasers typically consist of a solid gain media typically doped with rare-earth ions, such as ytterbium, chromium, and neodymium, and optically pumped by a diode laser (Chénaïs and Forget, 2012; Arbuzov et al., 2013). Solid-state ‘mode-locked’ lasers have been historically used in imaging applications for their convenience, high potential output powers, and low cost. However, their applications in the NIR-II is restricted due to their shorter emission wavelengths or limited wavelength

tunability (Zhang et al., 2021b). Ti:Sapphire lasers have a range of advantages such as a wide tuning range, high output power, and femtosecond pulsing capability, however, they are not suited for 2P NIR-II imaging applications due to their emission wavelength (700–1000 nm) not reaching the NIR-II optical window.

Solid-state lasers based on crystals such as Cr:Forsterite are of particular interest as they can produce emission wavelengths between 1220 nm and 1270 nm and have been successfully applied in 2P NIR-II imaging applications with wavelengths of around 1230 nm (Shen et al., 2015; Tsai et al., 2005). Nd:YLF lasers are a common composition that produces a fixed lasing wavelength of 1047 nm (Squirrell et al., 1999; Wokosin et al., 1996b). As demonstrated in Section 2, the 2PE wavelength at 1047 nm overlaps with the absorption band of several bio-imaging dyes. However, both Cr:Forsterite and Nd:YLF mode-locked lasers lack a wide wavelength tuning range (Trägårdh et al., 2016), which implies that fluorescent probes must be carefully chosen in order to match the small bandwidths, therefore this tends to limit biological imaging to just one colour. An example of a solid-state laser being used for *in vivo* applications involve a Nd:YLF laser being used to perform 2P NIR-II imaging of a stained zebrafish embryo (Wokosin et al., 1996a) (Section 3.2, Table 3). To overcome the drawback of limited excitation wavelengths of such solid-state lasers, multi-colour 2P imaging can instead be achieved by using two tunable lasers in tandem, although this is a relatively high-cost solution. Other solutions have been found in utilising the second Stokes shift to extend output wavelengths in Ti:Sapphire laser systems, or in methods such as phase-shaping (Brenner et al., 2013; Trägårdh et al., 2016).

### 3.1.2 NIR-II OPO/OPA Systems

OPOs based on the second-order NLO interactions can convert the output wavelength of an input laser (pump) into two longer wavelengths with lower energy output waves, known as signal and idler (Trovatello et al., 2021). Both continuous wave (CW) and pulsed OPOs can be realised depending on requirements and applications (Sowade et al., 2013). In phase-matching conditions, parametric amplification occurs within a NLO crystal where all three waves are interacting (Trovatello et al., 2021). Wavelengths of the amplified signal can be tuned to access the near-, mid-, and far-infrared regions—which is often much harder to achieve in traditional laser systems. OPO systems have great potential in biological imaging applications as a wide range of wavelengths from a single laser allows multicolour imaging across the whole NIR spectrum, overcoming the limitations of standard solid-state systems. Such systems have only been commercially available within the last few decades, and have now extended lasing applications into the deep IR (up to 2500 nm) (Pascal et al., 2021), which has enabled the discovery of new 2P-absorbing organic molecules within this spectral range where other associated tools for optical investigation exist.

Traditional ‘mode-locked’ lasers in combination with OPO techniques now appear to be the laser system of choice for 2P NIR-II imaging applications (Table 3). Common 2P microscopes include a high-peak-power Ti:Sapphire laser used in combination with a compatible OPO, which can significantly extend the



wavelength range. For example, the Blaze laser from Radiantis offers a “one box” Ti:Sapphire/OPO system with three output ports (pump, signal and idler). The pump laser (Ti:Sapphire) provides a tunable wavelength range of 730–1020 nm, the signal output provides a tunable wavelength range of 1000–1550 nm, and the idler output provides a tunable range of 1620–4000 nm. Unfortunately, the output power of the tunable OPO laser decreases dramatically when tuned to longer wavelengths due to the lower conversion efficiency and higher intrinsic loss. Here, the power drops from 2.2 W to 250 mW with increasing wavelength, thus limiting its imaging applications. Due to the difficulties in developing long-wavelength lasers that also match the power requirements for 2P imaging, most current examples in the NIR-II window are demonstrated with wavelengths between 1000–1300 nm. An example of the benefits of OPOs was demonstrated by Herz *et al.* who showed the increased tissue penetration performance by using an OPO laser compared to a traditional Ti:Sapphire laser (Herz *et al.*, 2010). Recent advancement has led to the commercialisation of systems capable of 2P NIR-II imaging with the integration of OPO based lasers. The Olympus FVMPE-RS Multiphoton Microscope appears to be a popular system of choice for current 2P NIR-II *in vivo* imaging purposes, achieving impressive resolution and penetration depths (Section 3.2, Table 3) (Zhou *et al.*, 2021; Wang *et al.*, 2019b; Wang *et al.*, 2019c; Liu *et al.*, 2020). This microscope can image at wavelengths of up to 1300 nm and also contains detectors and other equipment required for plug-in bench top imaging. This is achieved by combining two lasers within the microscope, namely the MAi Tai DeepSee One Box ultra-fast laser (Ti:Sapphire-based for excitation up to 1040 nm), and an InSight® DS+™ OPO (up to 1348 nm). Also worth noting is the Leica TCS SP8 DIVE upright multiphoton/confocal microscope that claims to be the first multiphoton microscope with spectrally tunable detection. This microscope utilises an OPO laser source to realise a tunable output wavelength between 680–1300 nm and has also demonstrated 2P NIR-II imaging applications *in vivo* (Section 3.2, Table 3) (Liu *et al.*, 2020).

Limitations of OPO lasers arise due to the requirements of a pump source with high spatial coherence and optical intensity, often requiring a diode-pumped solid-state laser. Furthermore, complex procedures have to be undertaken that require variation in the crystal's temperature, orientation, and poling period in order to realise phase matching. Careful free-space alignment and temporal synchronisation are also required for the OPO cavity, which makes the system sensitive to external perturbation and hence a high-level of maintenance is needed. Power restraints, requirements of water cooling, bulkiness, high cost, and expensive maintenance requirements are further limitations for desirable “turn-key” 2P microscopy. To overcome these downfalls, other systems have been developed, such as OPAs. Although OPA systems have similar principles of converting the short-wavelength input pump to the output signal with wavelength in the NIR-II regime, they do not need cavity and temporal synchronisation which can result in a simpler structure and has a smaller footprint (Chen *et al.*, 2020).

Yang *et al.* demonstrated 2P NIR-II imaging by using a multi-colour ultrafast OPO source (Yang *et al.*, 2013), where brain tissues of a tdTomato-expressing mouse were imaged with 2PE at 1070 nm (Section 3.2, Table 3). Xu *et al.* have developed a periodically poled lithium niobate OPA system operating at 2-ps pulse duration (Xu *et al.*, 2021). In their work, imaging at a depth of 40  $\mu$ m was achieved in both label-free coherent anti-Stokes Raman scattering (CARS) and 2PE based imaging of mitochondrial flavin adenine dinucleotide autofluorescence in tissue samples.

### 3.1.3 Fibre Lasers

Fibre lasers were first demonstrated in the mid-1980s, followed by the development of high energy Q-switched fibre lasers and mode-locked fibre lasers (Rose, 2019). Fibre lasers consist of an optical fibre doped with rare-earth ions such as Erbium, Neodymium, or Ytterbium, similar to the elements used in their solid-state counterparts (Kim *et al.*, 2012; Mohr *et al.*, 2020). Light from a pump source is guided through this robust waveguide that provides a long gain medium length, resulting in a high optical gain (Rose, 2019).

Fibre lasers present unique optical and practical benefits for 2P NIR-II imaging by removing the requirement of bulk optics and free-space alignment, which offers the benefits of compactness, high stability, reduced initial and maintenance cost (Figure 7), and increased reliability compared to OPO lasers (Table 2). Simple air-cooling of fibre lasers is possible, due to the large surface-area of the fibre, compared to expensive and cumbersome water-cooling that traditional solid-state lasers require. This all results in greater flexibility for the end-user, with many in the near-future looking likely to replace the bulky and complex laser systems and provide a more ‘plug and play’ approach to 2P microscopy imaging.

Importantly, unlike solid-state lasers and OPO lasers that tend to decrease output power at longer wavelengths, fibre lasers can maintain high output powers at the wavelengths required for 2P imaging. This was demonstrated by Jung *et al.*, whose initial attempts of the 2PE of Chrimson-expressing neurons with a conventional femtosecond Ti:Sapphire laser did not result in reliable activation of the target neurons (Jung *et al.*, 2020). On the contrary, activation was observed upon 2P NIR-II excitation at 1070 nm (2W) by using a Yb-doped fibre laser which provided 5–10 times higher power output than the Ti:Sapphire laser. Another example of 2P NIR-II imaging was demonstrated by Kim *et al.*, showing tridimensional 2P imaging of *ex vivo* nerve cells at 1060 nm using a Yb-doped fiber lasers (Kim *et al.*, 2012).

The major challenge of developing high-power short-pulsed fibre lasers is to prevent the distortion of pulse shapes by nonlinear effects such as self-phase modulation and stimulated Raman scattering, which can consequently degrade peak power and 2PE efficiency (Liu and Yang, 2012). This could reduce the fluorescence signal and cause unwanted heating within the sample, and as such, certain technical approaches such as temporally stretching the pulse (Eisele, 2020) can be implemented to resolve this limitation. The tuning range of common fibre lasers for 2P imaging is below 100 nm due to the limited gain bandwidth. Current commercially available fibre lasers using common doping agents

**TABLE 3 |** Current examples of 2PA *in vivo* experiments performed using NIR-II absorbing fluorophores.

$\lambda_{2PA}$ (nm)	Imaging System	Laser used	$\lambda_{em}$ (nm)	Contrast media	Depth ( $\mu$ m)	Animal model	Biological media imaged	Administration Method	Toxic. Test <i>in vivo</i> (Y/N)	Year	Ref
1550	Home-built system	PolarOnyx Mercury <b>Fibre laser</b>	800	DTTC dye ( <b>30</b> )	180	Mouse	Resected kidney vasculature	Intravenous injection	N	2011	Berezin et al. (2011)
1200	Commercial Leica TCS SP8 MP	Laser with <b>OPO</b>	630	Squaraine <b>45</b>	40	Mouse	Ear vasculature	Ear blood vessel injection	N	2019	Yi et al. (2019)
1057	Home-built with BioRad MRC 600 confocal microscope	Nd:YLF <b>solid state laser</b>	~590	FM4-64 dye ( <b>48</b> )	45	Zebrafish embryo	Body	Pre-stained	N	1996	Wokosin et al. (1996a)
1040	Home built with Olympus, BX61 FV1200 microscope	Yb-doped photonic crystal <b>fibre laser</b>	~700	Triphenylamine dipole <b>59</b> encapsulated in PSMA NPs	1200	Mouse	Ear vasculature Brain vasculature Resected tumour vasculature	Tail vein injection	Y	2017	Alifu et al. (2017)
1100	Commercial Olympus FVMPE-RS	InSight® DS with <b>OPO</b>	740	PDT-imaging agent 60	210	Mouse	Resected tumour vasculature	Intravenous injection	Y	2021	Zhou et al. (2021)
1200	Commercial Olympus FVMPE-RS	InSight® DS with <b>OPO</b>	~700	BTZ SNPs ( <b>64</b> )	1010	Mouse	Brain vasculature	Rectoorbital injection	N	2019	Wang et al. (2019b)
1300	1. Home built with Olympus, BX61W1-FV1200 microscope 2. Home-Built system	1. PHAROS-10W with <b>OPA</b> 2. Laser from an <b>OPA</b>	810	AIEDots of BTZ dye <b>70</b> (~35 nm)	1065	Mouse	Ear vasculature Brain vasculature	Tail vein injection	Y	2018	Qi et al. (2018)
1040	Home built with Olympus, BX61 FV1200 microscope	Mira HP and Mira <b>OPA</b>	790	AIEDots of BTZ dye <b>70</b>	750	Mouse	Brain vasculature	Tail vein injection	N	2021	Liu et al. (2021)
1200	Commercial Olympus FVMPE-RS	InSight® DS with <b>OPO</b>	~700	AIEDots of BTZ dye <b>71</b>	800	Mouse	Brain/Ear tumour vasculature	Rectoorbital injection	Y	2019	Wang et al. (2019c)
1040	Nikon A1 Confocal Microscope	Laser with <b>OPO</b>	~650	AIEDots of triphenylamine dye <b>72</b>	800	Mouse	Brain vasculature	Retro orbital injection	Y	2021	Samanta et al. (2021)
1040	Home built with Olympus, BX61W1-FV1000	Yb-doped photonic crystal <b>fibre laser</b>	~620	AIEDots of BODIPY dye <b>75</b>	700	Mouse	Brain vasculature	Intravenous injection	Y	2015	Wang et al. (2015)
1100	Commercial Leica SP8 DIVE	Laser with <b>OPO</b>	615	Carbon quantum dots <b>79</b>	500	1. Zebrafish 2. Mouse	1. Zebrafish Body (2PA) 2. Mouse (1PA)	1. Dots added to media 2. Intravenous injection	1. N 2. Y	2020	Liu et al. (2020)
1550	Home built with Olympus, BX61 FV1200 microscope	FLCPA-01C Calmar <b>fibre laser</b>	1270	PbS/CdS quantum dots <b>84</b>	220		Brain vasculature	Intravenous injection	N	2022	Ni et al. (2022)
1070	Home built system	Ti:Sapphire laser with <b>OPO</b>	~580	Red Fluorescent Protein (tdTomato <b>86</b> )	300–500	Mouse	Brain neurons	Gene Expression (Six3 gene)	N	2013	Yang et al. (2013)

only provide distinct wavelengths of around 780 nm, 920 nm, 1050 nm, and 1550 nm (Eisele, 2020). Commonly used Yb-doped fibre lasers for 2P NIR-II imaging have a tunability range of around 1020–1080 nm (Liu and Yang, 2012). However, although difficult, methods for expanding the tunability range

of fibre lasers are being explored by implementing nonlinear effects as well as temperature and magnetic field control (Wei et al., 2021). Zhang *et al.* also recently developed a CW fibre laser with an output wavelength tunable from 1000 to 1900 nm by utilising a random distributed feedback Raman fibre laser.

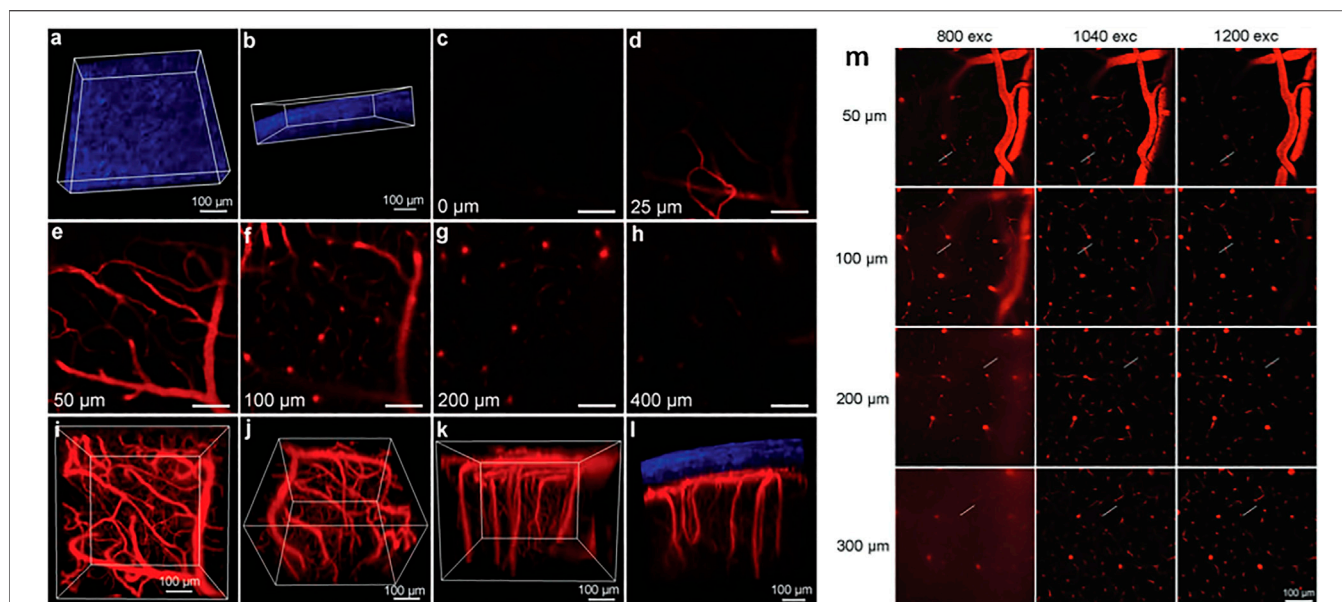


**FIGURE 8** | 2PA images of brain blood vessels in a mouse injected with CP dots. **(a,b)** 3D reconstructed second-harmonic generation images of mouse skull. **(c–h)** 2PA images at various vertical depths (0–400  $\mu\text{m}$ ) at 1200 nm excitation, 660–750 nm emission. **(i–l)** 3D reconstructed 2PA images of brain blood vessels. **(m)** comparison of 2PA images at excitation wavelengths of 800, 1040, and 1200 nm, of brain vasculature in a mouse injected with polymer dots. 2PA line intensity profiles with the different wavelengths across the blood vessels on the right were also acquired for the corresponding depths. Emission at 660–750 nm. Reprinted from ref (Wang et al., 2019b). with permission from John Wiley and Sons.

So far only a limited number of biological 2P NIR-II studies have been reported with fibre lasers despite their portability, ease-of-use, access to longer wavelengths, and high power features, possibly due to the lack of commercially available microscopes that integrates such lasers. However, *in vivo* studies using in-house built fibre lasers have demonstrated their high potential, both by performing 2P NIR-II imaging at 1550 nm—the longest wavelength so far reported (Berezin et al., 2011; Ni et al., 2022), and by reaching the deepest *in vivo* penetration (1040 nm) (Alifu et al., 2017) (Section 3.2, Table 3). In addition, the components of fibre lasers are much cheaper than OPO sources, as evidenced by Perillo *et al.* who developed a 2P NIR-II microscope using a mode-locked Yb-doped fibre laser for ~\$13000 and applied it to image FPs at 1060 nm with penetration depths of up to 900  $\mu\text{m}$  (Perillo et al., 2016). In contrast, the cost of a OPO-based imaging system commonly used for similar 2P NIR-II applications, such as the Olympus FVMPE-RS (Section 3.2, Table 3) can be up to 10–100 times higher. Modern solutions will hopefully arise in time with the development of affordable commercial benchtop fibre lasers suitable for 2P NIR-II clinical applications.

### 3.2 *In vivo* Examples of 2P NIR-II Imaging

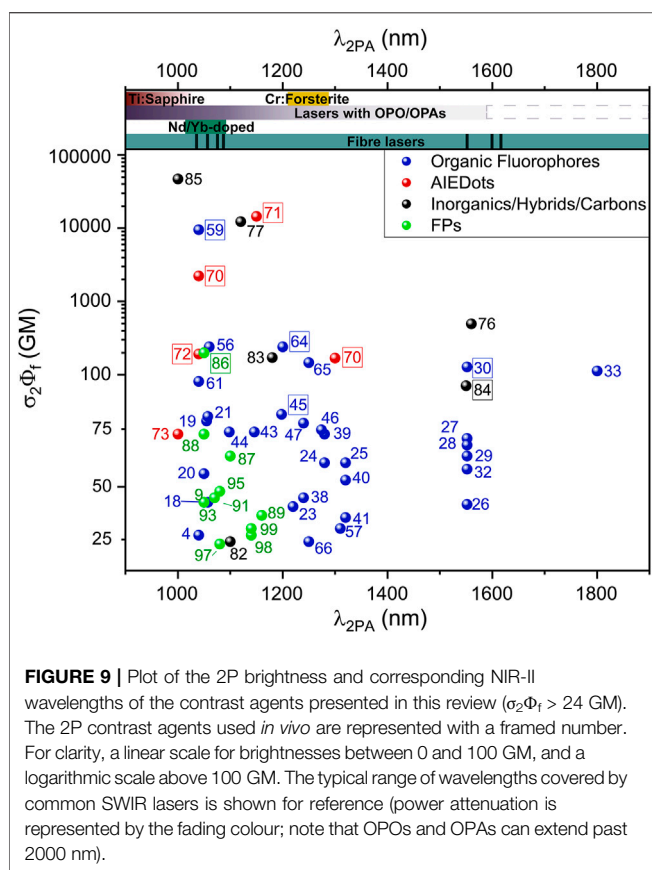
Clinically relevant examples of 2P NIR-II imaging have been reported using commercially available biological stains, FPs, and custom-made AIEgens. This section aims to discuss the probes presented in Section 2 in a photo-biological context, with a focus on *in vivo* examples.

The main aim of 2P NIR-II imaging is to improve resolution and depth perception when imaging. The latest examples of 2P NIR-II emitting materials being used *in vivo* (“*in vivo*” here indicating agents

being administered in a living creature; including examples of imaging post-resection) can be seen in Table 3. As well as having outstanding applications for bio-imaging, recent advances in NIR-II 2PE have led to developments in other biological applications such as PDT and photoacoustic imaging (Wang et al., 2020b; Hu et al., 2020; Ma et al., 2021b).

In 1996, Wokosin *et al.* demonstrated the improved 2P NIR-II imaging resolution at a penetration depth of 55  $\mu\text{m}$  into stained zebrafish embryos compared to traditional 1P confocal microscopy (Wokosin et al., 1996d). In this case, a traditional solid-state Nd:YLF mode-locked laser operating at 1057 nm was used to image safranin-stained embryos (a biological stain typically used for histology and cytology with an absorption and emission of ~500 nm and ~590 nm respectively) (Krumnschnabel et al., 2014). Zebrafish have a history of being used for biological imaging due to their transparency resulting in limited photon scattering. In the more recent work of Liu *et al.*, a penetration depth of 500  $\mu\text{m}$  was reached in zebrafish larvae using red-emitting CDs **79** excited at 1100 nm using a commercial microscope (Leica SP8 DIVE) fitted with an OPO system for 2PE (Liu et al., 2020). DTTC (**30**) is another example of a commercial stain used for 2P NIR-II imaging, where a fibre laser was used to achieve an imaging depth of up to 210  $\mu\text{m}$  at 1550 nm in a resected mouse kidney post-injection (Berezin et al., 2011).

Out of all *in vivo* studies reported in this range of wavelengths, AIEgen NPs and other NP-based systems appear to be the most popular choice to demonstrate superior penetration depth compared to other systems (Table 3). In the context of *in vivo* 2P imaging, NPs bypass the solubility limitation of organic dyes. They also show increased stability and cumulative size-related increase in



2PA cross-section; all of which make them promising imaging agents. The current record of tissue penetration was thus reported by Alifu *et al.* (Nowak-Król *et al.*, 2013) using triphenylamine dipole **59** incorporated within PSMA-based NPs, which led to 2P imaging at a depth of 1200  $\mu\text{m}$  into mouse brain vasculature. Using the BTZ-based AIEgen **70**, 2P imaging of mouse brain tissues was achieved with high resolution and showed significant improvements, reaching a depth of 1064  $\mu\text{m}$  at 1300 nm compared to 700  $\mu\text{m}$  under 1PA (Table 3) (Qi *et al.*, 2018). This highlights the sequential increased depth penetration of medical imaging using NIR-II wavelengths compared to shorter wavelengths, and the advantage of 2P over 1P microscopy. On a separate occasion, the same group used similar AIE NPs on a home built OPO laser-based system to demonstrate penetration depths of up to 750  $\mu\text{m}$  at a shorter 2P wavelength (1040 nm) (Table 3) (Liu *et al.*, 2021). Here, mouse brain vessels as small as 3.17  $\mu\text{m}$  were imaged. The AIEDots prepared from compound **72** by Samanta *et al.* also allowed 800  $\mu\text{m}$  brain tissue penetration under 2PE at 1040 nm (Table 3) (Samanta *et al.*, 2021). Interestingly, record absorption capacity and unprecedented 2P brightness values ( $>10^4$  GM) were measured for the tetraphenylethene-BODIPY (**75**) AIEDots made by Wang *et al.*, but the reported penetration depth was not higher than in more recent studies (700  $\mu\text{m}$  vs. 1200  $\mu\text{m}$ ) (Wang *et al.*, 2015). As this is one of the older reports from these studies (2015) it is worth noting that newer technologies with optimum imaging systems could assist in taking this value to similar levels. The potential development of non-invasive imaging techniques using 2P NIR-II excitation was

demonstrated by Wang *et al.* using polymer dots **64** as contrast agents (Wang *et al.*, 2019b). The imaging of mice brains was achieved at an impressive penetration depth of 400  $\mu\text{m}$  without craniotomy (intact skull) (Figure 8, a-l). The authors also showed the distinct resolution improvement using NIR-II light for 2P imaging when imaging at depths, when compared to light of shorter wavelengths (Figure 8, m). Among other classes of luminescent materials, *in vivo* 2P NIR-II imaging was shown for the first time using QDs as a contrast agent by Ni *et al.* with the PbS/CdS QDs **84** (Ni *et al.*, 2022). Imaging depths of 220  $\mu\text{m}$  were achieved in the mouse brain vasculature with a fibre laser operating at 1550 nm. Zhou *et al.* also demonstrated the potential of dual-functional dye **60** that combined 2PEF and ROS generation. 2P imaging of the probe was demonstrated using NIR-II irradiation and a white light laser was used to induce ROS generation in tumours of living mice, allowing for image-guided PDT (Zhou *et al.*, 2021). A triphenylamine dipole was thus used as a theranostic agent to combine 2P imaging and cancer treatment in mice (Table 3).

Unsurprisingly, commercially available OPO laser-based microscopes are popular systems for imaging experiments; with most examples performed in the early NIR-II range (1000–1300 nm) (Table 3) although imaging at wavelengths above 1200 nm could show the optimum optical benefits. This highlights the limitation of a lack of commercial imaging systems in the NIR-IIb range.

## 4 DISCUSSION AND PERSPECTIVES

The design of OMI probes usable in the “biological transparency windows” is arguably one of the most prevalent challenges in optobiology today. Shifting the 1PE band of dyes to the NIR-II is possible, but highly challenging as massive bathochromic shifts often come at the cost of fluorescence quantum yield and brightness. To circumvent this problem, 2P NIR-II imaging shows outstanding potential for expanding the applications of fluorescence-based medical imaging. By reducing auto-fluorescence and scattering while confining the excitation to a femtoliter-sized volume, this technique allows for dramatic resolution improvement and enhanced deep tissue imaging which would help the applications of image-guided surgery, point-by-point chemical detection, and image-based diagnostics reach their full potential. A wide range of probe design strategies have been implemented recently to achieve sufficient 2P brightness ( $>25$  GM) in this wavelength range (Figure 9). Organic fluorophores have the benefit of low toxicity and easy functionalisation to change their optical and biological properties. Among them, xanthene and polymethine dyes hold great potential for 2P NIR-II imaging due to their versatility allowing bathochromic shifts in their optical properties while retaining a highly emissive character. However, in designing such contrast agents, dye design rules and choice of fluorophore should be considered carefully as centrosymmetric molecules can easily fail to reach the NIR-II range because of selection rules. In contrast, significantly higher  $\sigma_2\Phi_f$  values are witnessed when 2P absorbers are integrated into nanoparticle structures, including AIE systems, achieving unprecedented 2P brightnesses of up to  $5.6 \times 10^5$  GM in the NIR-II. 2P NIR-II luminescent materials have the potential to



expand into image guided surgery, diagnostics and chemical sensing due to the high resolution and penetration depths that can be reached, which can also expand to controlled photo-release in therapy applications (Sun et al., 2017a; Zhao et al., 2019). For *in vivo* imaging, unsurprisingly, AIEgens have proven to be the 2P dyes of choice. Such nanosystems also show good biocompatibility and high brightnesses and facilitate mouse brain vascular imaging at depths of up to 1200  $\mu\text{m}$ , and even showed the potential for through-skull brain imaging. Nonetheless, such imaging agents require a certain amount of design and preparation, and more user-friendly solutions can be found in commercially available biological stains. Indeed, there is still to this day a significant gap in the availability and measurement of 2P properties of such dyes, even though many potential 2P dyes can be found in common cell stains (ICG, Alexa dyes etc.). Easily accessible and biologically compatible probes, and their custom-made derivatives, hold great potential in the development of 2P imaging in the NIR-II.

Such compounds, as well as synthetic fluorophores with higher NIR absorption capacities, have likely not yet been categorised due to the difficulty in taking such measurements in this optical window due to the lack of commercial 2P solutions. Nevertheless, more recently, commercially available OPO-based laser imaging systems have facilitated greater access to 2P NIR-II measurements and 2P imaging. These new systems have led to a dramatic rise in publications of *in vivo* studies emerging from 2015 and beyond, and will likely continue to be developed to push the field. Fibre lasers offer huge promise in this sense, by facilitating the necessary power requirements to encourage imaging at wavelengths above 1300 nm, and to give rise to a new generation of imaging agents and

biological applications. In this highly favourable context, we now hope that this review will serve as a motivation for researchers to explore the vast possibilities of multiphoton-excited luminescence in the NIR-II transparency windows.

## AUTHOR CONTRIBUTIONS

PS, EF, FH, SY, and MK; investigation, writing and original draft preparation. PS, MK; validation and formal analysis. PS, EF, MB, MK; review and editing. MB, MK, EF; supervision. MK; conceptualisation and project administration. All authors have read and agreed to the published version of the manuscript.

## FUNDING

We acknowledge the Engineering and Physical Sciences Research Council (EPSRC, United Kingdom) for funding of the programme grant EP/T020997, and for support of the Interdisciplinary Research Collaborations (EP/R018669/1 and EP/R005257) and of the CDT OPTIMA (EP/L016559).

## ACKNOWLEDGMENTS

The authors would like to thank Dr. Lin Xu (University of Southampton) for his input on laser systems and proofreading of **Section 3.1** of the manuscript.

## REFERENCES

- Alifu, N., Yan, L., Zhang, H., Zebibula, A., Zhu, Z., Xi, W., et al. (2017). Organic Dye Doped Nanoparticles with NIR Emission and Biocompatibility for Ultra-deep *In Vivo* Two-Photon Microscopy under 1040 Nm Femtosecond Excitation. *Dyes Pigments* 143, 76–85. doi:10.1016/j.dyepig.2017.04.017
- Anderson, V. L., and Webb, W. W. (2011). Transmission Electron Microscopy Characterization of Fluorescently Labelled Amyloid  $\beta$  1-40 and  $\alpha$ -synuclein Aggregates. *BMC Biotechnol.* 11, 125. doi:10.1186/1472-6750-11-125
- Arbuzov, V. I., and Nikonov, N. V. (2013). “Neodymium, Erbium and Ytterbium Laser Glasses,” in *Handbook of Solid-State Lasers*. Editors B. Denker and E. Shklovsky (Cambridge: Woodhead Publishing), 110–138. doi:10.1533/9780857097507.1.110
- Ávila, F. J., Gambin, A., Artal, P., and Bueno, J. M. (2019). *In Vivo* two-photon Microscopy of the Human Eye. *Sci. Rep.* 9, 10121.
- Barroso, M. M. (2011). Quantum Dots in Cell Biology. *J. Histochem Cytochem.* 59, 237–251. doi:10.1369/0022155411398487
- Bashkatov, A. N., Genina, E. A., Kochubey, V. I., and Tuchin, V. V. (2005). Optical Properties of Human Skin, Subcutaneous and Mucous Tissues in the Wavelength Range from 400 to 2000 Nm. *J. Phys. D. Appl. Phys.* 38, 2543–2555. doi:10.1088/0022-3727/38/15/004
- Benninger, R. K., and Piston, D. W. (2013). Two-photon Excitation Microscopy for the Study of Living Cells and Tissues. *Curr. Protoc. Cell Biol.* Chapter 4, Unit–24. doi:10.1002/0471143030.cb0411s59
- Berezin, M. Y., Zhan, C., Lee, H., Joo, C., Akers, W. J., Yazdanfar, S., et al. (2011). Two-Photon Optical Properties of Near-Infrared Dyes at 1.55  $\mu\text{m}$  Excitation. *J. Phys. Chem. B* 115, 11530–11535. doi:10.1021/jp207618e
- Bestvater, F., Spiess, E., Stobrawa, G., Hacker, M., Feurer, T., Porwol, T., et al. (2002). Two-photon Fluorescence Absorption and Emission Spectra of Dyes
- Relevant for Cell Imaging. *J. Microsc.* 208, 108–115. doi:10.1046/j.1365-2818.2002.01074.x
- Bonis-O'Donnell, J. T. D., Page, R. H., Beyene, A. G., Tindall, E. G., McFarlane, I. R., and Landry, M. P. (2017). Dual Near-Infrared Two-Photon Microscopy for Deep-Tissue Dopamine Nanosensor Imaging. *Adv. Funct. Mat.* 27, 1702112. doi:10.1002/adfm.201702112
- Bradley, D. J., Hutchinson, M. H. R., Koetser, H., and Tolansky, S. (1972). Interactions of Picosecond Laser Pulses with Organic Molecules II. Two-Photon Absorption Cross-Sections. *Proc. R. Soc. A Math. Phys. Eng. Sci.* 329, 105–119.
- Brenner, M. H., Cai, D., Swanson, J. A., and Ogilvie, J. P. (2013). Two-photon Imaging of Multiple Fluorescent Proteins by Phase-Shaping and Linear Unmixing with a Single Broadband Laser. *Opt. Express* 21, 17256–17264. doi:10.1364/oe.21.017256
- Campbell, R. E., Tour, O., Palmer, A. E., Steinbach, P. A., Baird, G. S., Zacharias, D. A., et al. (2002). A Monomeric Red Fluorescent Protein. *Proc. Natl. Acad. Sci. U.S.A.* 99, 7877–7882. doi:10.1073/pnas.082243699
- Cao, J., Zhu, B., Zheng, K., He, S., Meng, L., Song, J., et al. (2019). Recent Progress in NIR-II Contrast Agent for Biological Imaging. *Front. Bioeng. Biotechnol.* 7, 487. doi:10.3389/fbioe.2019.00487
- Cao, Y. Y., Ye, Y., Mastwal, S. S., Lovinger, D. M., Costa, R. M., and Wang, K. H. (2013). *In Vivo* two-photon Imaging of Experience-dependent Molecular Changes in Cortical Neurons. *J. Vis. Exp.* 71, 50148. doi:10.3791/50148
- Carr, J. A., Aellen, M., Franke, D., So, P. T. C., Bruns, O. T., and Bawendi, M. G. (2018). Absorption by Water Increases Fluorescence Image Contrast of Biological Tissue in the Shortwave Infrared. *Proc. Natl. Acad. Sci. U.S.A.* 115, 9080–9085. doi:10.1073/pnas.1803210115
- Carr, J. A., Franke, D., Caram, J. R., Perkinson, C. F., Saif, M., Askoxylakis, V., et al. (2018). Shortwave Infrared Fluorescence Imaging with the Clinically Approved Near-Infrared Dye Indocyanine Green. *Proc. Natl. Acad. Sci. U.S.A.* 115, 4465–4470. doi:10.1073/pnas.1718917115

- Ceymann, H., Rosspeintner, A., Schreck, M. H., Mützel, C., Stoy, A., Vauthey, E., et al. (2016). Cooperative Enhancement versus Additivity of Two-Photon-Absorption Cross Sections in Linear and Branched Squaraine Superchromophores. *Phys. Chem. Chem. Phys.* 18, 16404–16413. doi:10.1039/c6cp02312f
- Chen, B.-Y., Wu, S., Yu, Y.-J., Wu, C.-T., Wang, Y.-H., and Jin, G.-Y. (2020). 3.8  $\mu\text{m}$  Mid-infrared Optical Parametric Amplifier Based on MgO:PPLN Crystal. *Infrared Phys. Technol.* 111, 103448. doi:10.1016/j.infrared.2020.103448
- Chen, Y., Xue, L., Zhu, Q., Feng, Y., and Wu, M. (2021). Recent Advances in Second Near-Infrared Region (NIR-II) Fluorophores and Biomedical Applications. *Front. Chem.* 9, 750404. doi:10.3389/fchem.2021.750404
- Chénaïs, S., and Forget, S. (2012). Recent Advances in Solid-State Organic Lasers. *Polym. Int.* 61, 390–406.
- Cho, S., Lim, J. M., Hiroto, S., Kim, P., Shinokubo, H., Osuka, A., et al. (2009). Unusual Interchromophoric Interactions in  $\beta,\beta'$  Directly and Doubly Linked Corrole Dimers: Prohibited Electronic Communication and Abnormal Singlet Ground States. *J. Am. Chem. Soc.* 131, 6412–6420. doi:10.1021/ja900220y
- Chung, S.-J., Zheng, S., Odani, T., Beverina, L., Fu, J., Padilha, L. A., et al. (2006). Extended Squaraine Dyes with Large Two-Photon Absorption Cross-Sections. *J. Am. Chem. Soc.* 128, 14444–14445. doi:10.1021/ja065556m
- Cosco, E. D., Caram, J. R., Bruns, O. T., Franke, D., Day, R. A., Farr, E. P., et al. (2017). Flavilyium Polymethine Fluorophores for Near- and Shortwave Infrared Imaging. *Angew. Chem. Int. Ed.* 56, 13126–13129. doi:10.1002/anie.201706974
- Denk, W., Strickler, J. H., and Webb, W. W. (1990). Two-photon Laser Scanning Fluorescence Microscopy. *Science* 248, 73–76. doi:10.1126/science.2321027
- Diao, S., Blackburn, J. L., Hong, G., Antaris, A. L., Chang, J., Wu, J. Z., et al. (2015). Fluorescence Imaging *In Vivo* at Wavelengths beyond 1500 Nm. *Angew. Chem. Int. Ed.* 54, 14758–14762. doi:10.1002/anie.201507473
- Ding, F., Zhan, Y., Lu, X., and Sun, Y. (2018). Recent Advances in Near-Infrared II Fluorophores for Multifunctional Biomedical Imaging. *Chem. Sci.* 9, 4370–4380. doi:10.1039/c8sc01153b
- Drobizhev, M., Makarov, N. S., Tillo, S. E., Hughes, T. E., and Rebane, A. (2011). Two-photon Absorption Properties of Fluorescent Proteins. *Nat. Methods* 8, 393–399. doi:10.1038/nmeth.1596
- Drobizhev, M., Stepanenko, Y., Rebane, A., Wilson, C. J., Screen, T. E. O., and Anderson, H. L. (2006). Strong Cooperative Enhancement of Two-Photon Absorption in Double-Strand Conjugated Porphyrin Ladder Arrays. *J. Am. Chem. Soc.* 128, 12432–12433. doi:10.1021/ja0649623
- Drobizhev, M., Tillo, S., Makarov, N. S., Hughes, T. E., and Rebane, A. (2009). Absolute Two-Photon Absorption Spectra and Two-Photon Brightness of Orange and Red Fluorescent Proteins. *J. Phys. Chem. B* 113, 855–859. doi:10.1021/jp8087379
- Eisele, M. (2020). *Simplifying Two-Photon Microscopy*. Wiley Analytical Science.
- Escobedo, J. O., Rusin, O., Lim, S., and Strongin, R. M. (2010). NIR Dyes for Bioimaging Applications. *Curr. Opin. Chem. Biol.* 14, 64–70. doi:10.1016/j.cbpa.2009.10.022
- Ewart, P. (2005). "Spectroscopy | Nonlinear Laser Spectroscopy," in *Encyclopedia of Modern Optics*. Editor R.D. Guenther (Oxford: Elsevier), 109–119. doi:10.1016/b0-12-369395-0/00897-6
- Fan, Y., Sun, Y., Chang, W., Zhang, X., Tang, J., Zhang, L., et al. (2018). Bioluminescence Imaging and Two-Photon Microscopy Guided Laser Ablation of GBM Decreases Tumor Burden. *Theranostics* 8, 4072–4085. doi:10.7150/thno.25357
- Feng, Z., Tang, T., Wu, T., Yu, X., Zhang, Y., Wang, M., et al. (2021). Perfecting and Extending the Near-Infrared Imaging Window. *Light Sci. Appl.* 10, 197. doi:10.1038/s41377-021-00628-0
- Ferguson, A. I., and Malcolm, G. P. A. (1993). "Mode-Locked Solid State Lasers," in *Solid State Lasers: New Developments and Applications*. Editors M. Inguscio and R. Wallenstein (Boston, MA: Springer US), 29–44. doi:10.1007/978-1-4615-2998-9\_3
- Fu, J., Padilha, L. A., Hagan, D. J., Van Stryland, E. W., Przhonska, O. V., Bondar, M. V., et al. (2007). Molecular Structure-Two-Photon Absorption Property Relations in Polymethine Dyes. *J. Opt. Soc. Am. B* 24, 56–66. doi:10.1364/josab.24.000056
- Funabiki, K., Yanagawa, R., Kubota, Y., and Inuzuka, T. (2019). Thermo- and Photo-Stable Symmetrical Benzo[cd]indolenyl-Substituted Heptamethine Cyanine Dye Carrying a Tetrakis(pentafluorophenyl)borate that Absorbs Only Near-Infrared Light over 1000 Nm. *New J. Chem.* 43, 7491–7501. doi:10.1039/c9nj00867e
- Göppert, M. (1929). Über die Wahrscheinlichkeit des Zusammenwirkens zweier Lichtquanten in einem Elementarakt. *Sci. Nat.* 17, 932.
- Göppert-Mayer, M. (1931). Über Elementarakte mit zwei Quantensprüngen. *Ann. Phys.* 401, 273–294.
- Grienberger, C., and Konnerth, A. (2012). Imaging Calcium in Neurons. *Neuron* 73, 862–885. doi:10.1016/j.neuron.2012.02.011
- Gui, R., Jin, H., Wang, Z., and Tan, L. (2017). Recent Advances in Optical Properties and Applications of Colloidal Quantum Dots under Two-Photon Excitation. *Coord. Chem. Rev.* 338, 141–185. doi:10.1016/j.ccr.2017.02.007
- Hackethal, A., Hirschburger, M., Eicker, S., Mücke, T., Lindner, C., and Buchweitz, O. (2018). Role of Indocyanine Green in Fluorescence Imaging with Near-Infrared Light to Identify Sentinel Lymph Nodes, Lymphatic Vessels and Pathways Prior to Surgery - A Critical Evaluation of Options. *Geburtshilfe Frauenheilkd* 78, 54–62. doi:10.1055/s-0043-123937
- Han, X., Ge, F., Xu, J. L., and Bu, X. H. (2021). Aggregation-induced Emission Materials for Nonlinear Optics. *Aggregate* 2, e28. doi:10.1002/agt.228
- Hassan, M., and Klauenberg, B. A. (2004). Biomedical Applications of Fluorescence Imaging *In Vivo*. *Comp. Med.* 54, 635–644.
- He, G. S., Tan, L.-S., Zheng, Q., and Prasad, P. N. (2008). Multiphoton Absorbing Materials: Molecular Designs, Characterizations, and Applications. *Chem. Rev.* 108, 1245–1330. doi:10.1021/cr050054x
- Helmchen, F., and Denk, W. (2005). Deep Tissue Two-Photon Microscopy. *Nat. Methods* 2, 932–940. doi:10.1038/nmeth.818
- Henary, M., Mojzycz, M., Say, M., and Strekowski, L. (2009). Functionalization of Benzo[cd]indole System for the Synthesis of Visible and Near-Infrared Dyes. *J. Heterocycl. Chem.* 46, 84–87. doi:10.1002/jhet.39
- Hermann, J. P., and Ducuing, J. (1972). Dispersion of the Two-Photon Cross Section in Rhodamine Dyes. *Opt. Commun.* 6, 101–105. doi:10.1016/0030-4018(72)90204-0
- Herz, J., Siffrin, V., Hauser, A. E., Brandt, A. U., Leuenberger, T., Radbruch, H., et al. (2010). Expanding Two-Photon Intravital Microscopy to the Infrared by Means of Optical Parametric Oscillator. *Biophys. J.* 98, 715–723. doi:10.1016/j.bpj.2009.10.035
- Hisamune, Y., Nishimura, K., Isakari, K., Ishida, M., Mori, S., Karasawa, S., et al. (2015). Stable  $\pi$  Radical from a Contracted Doubly N-Confused Hexaphyrin by Double Palladium Metalation. *Angew. Chem. Int. Ed.* 54, 7323–7327. doi:10.1002/anie.201502285
- Hong, G., Diao, S., Antaris, A. L., and Dai, H. (2015). Carbon Nanomaterials for Biological Imaging and Nanomedicinal Therapy. *Chem. Rev.* 115, 10816–10906. doi:10.1021/acs.chemrev.5b00008
- Hong, G. S., Antaris, A. L., and Dai, H. J. (2017). Near-infrared Fluorophores for Biomedical Imaging. *Nat. Biomed. Eng.* 1, 0010. doi:10.1038/s41551-016-0010-0
- Hornum, M., Reinholdt, P., Zaręba, J. K., Jensen, B. B., Wüstner, D., Samoć, M., et al. (2020). One- and Two-Photon Solvatochromism of the Fluorescent Dye Nile Red and its CF<sub>3</sub>, F and Br-Substituted Analogues. *Photochem. Photobiol. Sci.* 19, 1382–1391. doi:10.1039/d0pp00076k
- Hu, H., Przhonska, O. V., Terenziani, F., Painelli, A., Fishman, D., Ensley, T. R., et al. (2013). Two-photon Absorption Spectra of a Near-Infrared 2-azaazulene Polymethine Dye: Solvation and Ground-State Symmetry Breaking. *Phys. Chem. Chem. Phys.* 15, 7666–7678. doi:10.1039/c3cp50811k
- Hu, W., Zhang, H., He, G. S., Baev, A., Xia, J., Huang, W., et al. (2020). Organic NIR-II Photoacoustic Agent Utilizing Combined Two-Photon and Excited State Absorption at 1064 Nm. *ACS Photonics* 7, 3161–3165. doi:10.1021/acsp Photonics.0c01227
- Jacques, S. L. (2015). Generic Tissue Optical Properties. Available at: [https://omlc.org/news/feb15/generic\\_optics/index.html](https://omlc.org/news/feb15/generic_optics/index.html).
- Josefsen, L. B., and Boyle, R. W. (2012). Unique Diagnostic and Therapeutic Roles of Porphyrins and Phthalocyanines in Photodynamic Therapy, Imaging and Theranostics. *Theranostics* 2, 916–966. doi:10.7150/thno.4571
- Jung, Y., Kennedy, A., Chiu, H., Mohammad, F., Claridge-Chang, A., and Anderson, D. J. (2020). Neurons that Function within an Integrator to Promote a Persistent Behavioral State in *Drosophila*. *Neuron* 105, 322–333. doi:10.1016/j.neuron.2019.10.028

- Keiser, G. (2016). "Light-Tissue Interactions," in *Biophotonics: Concepts to Applications*. Editor G. Keiser (Singapore: Springer Singapore), 147–196. doi:10.1007/978-981-10-0945-7\_6
- Kenry, Y., Duan, Y., and Liu, B. (2018). Recent Advances of Optical Imaging in the Second Near-Infrared Window. *Adv. Mat.* 30, e1802394. doi:10.1002/adma.201802394
- Kim, D. U., Song, H., Song, W., Kwon, H.-S., Sung, M., and Kim, D. Y. (2012). Two-photon Microscopy Using an Yb<sup>3+</sup>-Doped Fiber Laser with Variable Pulse Widths. *Opt. Express* 20, 12341–12349. doi:10.1364/oe.20.012341
- Kim, H. M., and Cho, B. R. (2015). Small-molecule Two-Photon Probes for Bioimaging Applications. *Chem. Rev.* 115, 5014–5055. doi:10.1021/cr5004425
- Klausen, M., and Blanchard-Desce, M. (2021). Two-photon Uncaging of Bioactive Compounds: Starter Guide to an Efficient IR Light Switch. *J. Photochem. Photobiol. C Photochem. Rev.* 48, 100423. doi:10.1016/j.jphotochemrev.2021.100423
- Klymchenko, A. S. (2017). Solvatochromic and Fluorogenic Dyes as Environment-Sensitive Probes: Design and Biological Applications. *Acc. Chem. Res.* 50, 366–375. doi:10.1021/acs.accounts.6b00517
- Kobat, D., Durst, M. E., Nishimura, N., Wong, A. W., Schaffer, C. B., and Xu, C. (2009). Deep Tissue Multiphoton Microscopy Using Longer Wavelength Excitation. *Opt. Express* 17, 13354–13364. doi:10.1364/oe.17.013354
- König, K., So, P. T. C., Mantulin, W. W., and Gratton, E. (1997). Cellular Response to Near-Infrared Femtosecond Laser Pulses in Two-Photon Microscopes. *Opt. Lett.* 22, 135–136. doi:10.1364/ol.22.000135
- Krumschnabel, G., Eigentler, A., Fasching, M., and Gnaiger, E. (2014). "Use of Safranin for the Assessment of Mitochondrial Membrane Potential by High-Resolution Respirometry and Fluorometry," in *Methods in Enzymology*. Editors L. Galluzzi and G. Kroemer (Academic Press), 163–181. doi:10.1016/b978-0-12-416618-9.00009-1
- Kucikas, V., Werner, M. P., Schmitz-Rode, T., Louradour, F., and van Zandvoort, M. (2021). Two-Photon Endoscopy: State of the Art and Perspectives. *Mol. Imaging Biol.* 2021, 1.
- Kumari, A., and Gupta, S. (2019). Two-photon Excitation and Direct Emission from S<sub>2</sub> State of U.S. Food and Drug Administration Approved Near-Infrared Dye: Application of Anti-kasha's Rule for Two-Photon Fluorescence Imaging. *J. Biophot.* 12, e201800086. doi:10.1002/jbio.201800086
- Kuo, W.-S., Wu, P.-C., Chang, C.-Y., Wang, J.-Y., Chen, P.-C., Hsieh, M.-H., et al. (2022). Graphene Near Infrared-I/II Probe in Two-Photon Excitation-wavelength-independent Photoluminescence and Photoinactivation. *Carbon* 193, 205–215. doi:10.1016/j.carbon.2022.03.019
- Larson, D. R., Zipfel, W. R., Williams, R. M., Clark, S. W., Bruchez, M. P., Wise, F. W., et al. (2003). Water-soluble Quantum Dots for Multiphoton Fluorescence Imaging *In Vivo*. *Science* 300, 1434–1436. doi:10.1126/science.1083780
- Le Bot, N. (2009). It Takes Two Photons to Tango. *Nat. Cell Biol.* 11, S17–S18. doi:10.1038/ncb1950
- Lee, H., Berezin, M. Y., Henary, M., Strekowski, L., and Achilefu, S. (2008). Fluorescence Lifetime Properties of Near-Infrared Cyanine Dyes in Relation to Their Structures. *J. Photochem. Photobiol. A Chem.* 200, 438–444. doi:10.1016/j.jphotochem.2008.09.008
- Li, C., and Wang, Q. (2018). Challenges and Opportunities for Intravital Near-Infrared Fluorescence Imaging Technology in the Second Transparency Window. *ACS Nano* 12, 9654–9659. doi:10.1021/acsnano.8b07536
- Li, D., Jing, P., Sun, L., An, Y., Shan, X., Lu, X., et al. (2018). Near-Infrared Excitation/Emission and Multiphoton-Induced Fluorescence of Carbon Dots. *Adv. Mat.* 30, e1705913. doi:10.1002/adma.201705913
- Li, S., and She, C. Y. (2010). Two-photon Absorption Cross-Section Measurements in Common Laser Dyes at 1-06  $\mu\text{m}$ . *Opt. Acta Int. J. Opt.* 29, 281–287. doi:10.1080/713820851
- Li, Y., Heng, W.-K., Lee, B. S., Aratani, N., Zafra, J. L., Bao, N., et al. (2012). Kinetically Blocked Stable Heptazethrene and Octazethrene: Closed-Shell or Open-Shell in the Ground State? *J. Am. Chem. Soc.* 134, 14913–14922. doi:10.1021/ja304618v
- Liu, C., and Scott, C. N. (2021). Design Strategies to Rhodamine Analogue Fluorophores for Near-Infrared II Biological Imaging Applications. *Dyes Pigments* 196, 109792. doi:10.1016/j.dyepig.2021.109792
- Liu, J., and Yang, L. (2012). *Femtosecond Fiber Lasers for Biomedical Solutions*. SPIE.
- Liu, W., Zhang, Y., Qi, J., Qian, J., and Tang, B. Z. (2021). NIR-II Excitation and NIR-I Emission Based Two-Photon Fluorescence Lifetime Microscopic Imaging Using Aggregation-Induced Emission Dots. *Chem. Res. Chin. Univ.* 37, 171–176. doi:10.1007/s40242-021-0405-2
- Liu, Y., Gou, H., Huang, X., Zhang, G., Xi, K., and Jia, X. (2020). Rational Synthesis of Highly Efficient Ultra-narrow Red-Emitting Carbon Quantum Dots for NIR-II Two-Photon Bioimaging. *Nanoscale* 12, 1589–1601. doi:10.1039/c9nr09524a
- Lockwood, D. J. (2016). "Rayleigh and Mie Scattering," in *Encyclopedia of Color Science and Technology*. Editor M. R. Luo (New York, NY: Springer New York), 1097–1107. doi:10.1007/978-1-4419-8071-7\_218
- Looney, M. R., Thornton, E. E., Sen, D., Lamm, W. J., Glenn, R. W., and Krummel, M. F. (2011). Stabilized Imaging of Immune Surveillance in the Mouse Lung. *Nat. Methods* 8, 91–96. doi:10.1038/nmeth.1543
- López-Duarte, I., Chairatana, P., Wu, Y., Pérez-Moreno, J., Bennett, P. M., Reeve, J. E., et al. (2015). Thiophene-based Dyes for Probing Membranes. *Org. Biomol. Chem.* 13, 3792–3802. doi:10.1039/c4ob02507e
- Lu, Q., Wu, C. J., Liu, Z., Niu, G., and Yu, X. (2020). Fluorescent AIE-Active Materials for Two-Photon Bioimaging Applications. *Front. Chem.* 8, 617463. doi:10.3389/fchem.2020.617463
- Luo, J., Xie, Z., Lam, J. W. Y., Cheng, L., Tang, B. Z., Chen, H., et al. (2001). Aggregation-induced Emission of 1-Methyl-1,2,3,4,5-Pentaphenylsilole. *Chem. Commun.* 2001, 1740–1741. doi:10.1039/b105159h
- Ma, H., Zhao, C., Meng, H., Li, R., Mao, L., Hu, D., et al. (2021). Multifunctional Organic Fluorescent Probe with Aggregation-Induced Emission Characteristics: Ultrafast Tumor Monitoring, Two-Photon Imaging, and Image-Guide Photodynamic Therapy. *ACS Appl. Mat. Interfaces* 13, 7987–7996. doi:10.1021/acsami.0c21309
- Ma, Z., Wang, F., Wang, W., Zhong, Y., and Dai, H. (2021). Deep Learning for *In Vivo* Near-Infrared Imaging. *Proc. Natl. Acad. Sci. U. S. A.* 118, e2021446118. doi:10.1073/pnas.2021446118
- Makarov, N. S., Drobizhev, M., and Rebane, A. (2008). Two-photon Absorption Standards in the 550–1600 nm Excitation Wavelength Range. *Opt. Express* 16, 4029–4047. doi:10.1364/oe.16.004029
- Massin, J., Charaf-Eddin, A., Appaix, F., Bretonnière, Y., Jacquemin, D., van der Sanden, B., et al. (2013). A Water Soluble Probe with Near Infrared Two-Photon Absorption and Polarity-Induced Fluorescence for Cerebral Vascular Imaging. *Chem. Sci.* 4, 2833–2843. doi:10.1039/c3sc22325f
- Meng, F., Liu, Y., Niu, J., and Lin, W. (2017). A Novel Fluorescent Probe with a Large Stokes Shift for Real-Time Imaging Mitochondria in Different Living Cell Lines. *Tetrahedron Lett.* 58, 3287–3293. doi:10.1016/j.tetlet.2017.07.030
- Mohr, M. A., Bushey, D., Aggarwal, A., Marvin, J. S., Kim, J. J., Marquez, E. J., et al. (2020). jYCaMP: an Optimized Calcium Indicator for Two-Photon Imaging at Fiber Laser Wavelengths. *Nat. Methods* 17, 694–697. doi:10.1038/s41592-020-0835-7
- Mütze, J., Iyer, V., Macklin, J. J., Colonell, J., Karsh, B., Petrášek, Z., et al. (2012). Excitation Spectra and Brightness Optimization of Two-Photon Excited Probes. *Biophysical J.* 102, 934–944. doi:10.1016/j.bpj.2011.12.056
- Ni, H., Wang, Y., Tang, T., Yu, W., Li, D., He, M., et al. (2022). Quantum Dots Assisted *In Vivo* Two-Photon Microscopy with NIR-II Emission. *Phot. Res.* 10, 189–196. doi:10.1364/prj.441471
- Ni, Y., Lee, S., Son, M., Aratani, N., Ishida, M., Samanta, A., et al. (2016). A Diradical Approach towards BODIPY-Based Dyes with Intense Near-Infrared Absorption Around  $\lambda = 1100\text{ nm}$ . *Angew. Chem. Int. Ed.* 55, 2815–2819. doi:10.1002/anie.201511151
- Nicolson, F., and Kircher, M. F. (2021). "Theranostics: Agents for Diagnosis and Therapy," in *Molecular Imaging*. Editors B. D. Ross and S. S. Gambhir (Academic Press), 655–677. doi:10.1016/b978-0-12-816386-3.00040-5
- Nowak-Król, A., Grzybowski, M., Romiszewski, J., Drobizhev, M., Wicks, G., Chotkowski, M., et al. (2013). Strong Two-Photon Absorption Enhancement in a Unique Bis-Porphyrin Bearing a Diketopyrrolopyrrole Unit. *Chem. Commun.* 49, 8368–8370. doi:10.1039/c3cc44728f
- Nowak-Król, A., Wilson, C. J., Drobizhev, M., Kondratuk, D. V., Rebane, A., Anderson, H. L., et al. (2012). Amplified Two-Photon Absorption in Trans-A2b2-Porphyrins Bearing Nitrophenylethynyl Substituents. *ChemPhysChem* 13, 3966–3972. doi:10.1002/cphc.201200507
- Nuriya, M., Fukushima, S., Momotake, A., Shinotsuka, T., Yasui, M., and Arai, T. (2016). Multimodal Two-Photon Imaging Using a Second Harmonic Generation-specific Dye. *Nat. Commun.* 7, 11557. doi:10.1038/ncomms11557



- Nyk, M., Wawrzynczyk, D., Szeremeta, J., and Samoc, M. (2012). Spectrally Resolved Size-dependent Third-Order Nonlinear Optical Properties of Colloidal CdSe Quantum Dots. *Appl. Phys. Lett.* 100, 041102. doi:10.1063/1.3679381
- Oh, E., Fatemi, F. K., Currie, M., Delehanty, J. B., Pons, T., Fragola, A., et al. (2013). PEGylated Luminescent Gold Nanoclusters: Synthesis, Characterization, Bioconjugation, and Application to One- and Two-Photon Cellular Imaging. *Part. Part. Syst. Charact.* 30, 453–466.
- Olesiak-Banska, J., Waszkielewicz, M., Obstarczyk, P., and Samoc, M. (2019). Two-photon Absorption and Photoluminescence of Colloidal Gold Nanoparticles and Nanoclusters. *Chem. Soc. Rev.* 48, 4087–4117. doi:10.1039/c8cs00849c
- Olson, J. E., Yu, J. H., Thimes, R. L., and Camden, J. P. (2022). Vibrational Two-Photon Microscopy for Tissue Imaging: Short-Wave Infrared Surface-Enhanced Resonance Hyper-Raman Scattering. *J. Biophoton.* 15, e202100158. doi:10.1002/jbio.202100158
- Osmialowski, B., Petrusevich, E. F., Antoniuk, M. A., Grela, I., Bin Jassar, M. A., Nyk, M., et al. (2020). Controlling Two-Photon Action Cross Section by Changing a Single Heteroatom Position in Fluorescent Dyes. *J. Phys. Chem. Lett.* 11, 5920–5925.
- Palit, D. K., Singh, A. K., Bhasikuttan, A. C., and Mittal, J. P. (2001). Relaxation Dynamics in the Excited States of LDS-821 in Solution. *J. Phys. Chem. A* 105, 6294–6304. doi:10.1021/jp004142r
- Paoli, J., Smedh, M., and Ericson, M. B. (2009). Multiphoton Laser Scanning Microscopy-A Novel Diagnostic Method for Superficial Skin Cancers. *Seminars Cutan. Med. Surg.* 28, 190–195. doi:10.1016/j.sder.2009.06.007
- Pascal, S., David, S., Andraud, C., and Maury, O. (2021). Near-infrared Dyes for Two-Photon Absorption in the Short-Wavelength Infrared: Strategies towards Optical Power Limiting. *Chem. Soc. Rev.* 50, 6613–6658. doi:10.1039/d0cs01221a
- Pascal, S., Denis-Quanquin, S., Appaix, F., Duperray, A., Grichine, A., Le Guennic, B., et al. (2017). Keto-polymethines: a Versatile Class of Dyes with Outstanding Spectroscopic Properties for in Cellulo and In Vivo Two-Photon Microscopy Imaging. *Chem. Sci.* 8, 381–394. doi:10.1039/c6cs02488b
- Pawlicki, M., Collins, H. A., Denning, R. G., and Anderson, H. L. (2009). Two-photon Absorption and the Design of Two-Photon Dyes. *Angew. Chem. Int. Ed.* 48, 3244–3266. doi:10.1002/anie.200805257
- Perillo, E. P., McCracken, J. E., Fernée, D. C., Goldak, J. R., Medina, F. A., Miller, D. R., et al. (2016). Deep In Vivo Two-Photon Microscopy with a Low Cost Custom Built Mode-Locked 1060 Nm Fiber Laser. *Biomed. Opt. Express* 7, 324–334. doi:10.1364/boe.7.000324
- Pham, W., Cassell, L., Gillman, A., Koktysh, D., and Gore, J. C. (2008). A Near-Infrared Dye for Multichannel Imaging. *Chem. Commun.* 2008, 1895–1897. doi:10.1039/b719028j
- Piston, D. W. (2005). When Two Is Better Than One: Elements of Intravital Microscopy. *PLoS Biol.* 3, e207. doi:10.1371/journal.pbio.0030207
- Poronik, Y. M., Hugues, V., Blanchard-Desce, M., and Gryko, D. T. (2012). Octupolar Merocyanine Dyes: a New Class of Nonlinear Optical Chromophores. *Chem. Eur. J.* 18, 9258–9266. doi:10.1002/chem.201200718
- Pramanik, A., Fan, Z., Chavva, S. R., Sinha, S. S., and Ray, P. C. (2014). Highly Efficient and Excitation Tunable Two-Photon Luminescence Platform for Targeted Multi-Color MDRB Imaging Using Graphene Oxide. *Sci. Rep.* 4, 6090. doi:10.1038/srep06090
- Qi, J., Sun, C., Li, D., Zhang, H., Yu, W., Zebibula, A., et al. (2018). Aggregation-Induced Emission Luminogen with Near-Infrared-II Excitation and Near-Infrared-I Emission for Ultradeep Intravital Two-Photon Microscopy. *ACS Nano* 12, 7936–7945. doi:10.1021/acs.nano.8b02452
- Rakhymzhan, A., Leben, R., Zimmermann, H., Günther, R., Mex, P., Reismann, D., et al. (2017). Synergistic Strategy for Multicolor Two-Photon Microscopy: Application to the Analysis of Germinal Center Reactions In Vivo. *Sci. Rep.* 7, 7101. doi:10.1038/s41598-017-07165-0
- Ramakrishna, G., Varnavski, O., Kim, J., Lee, D., and Goodson, T. (2008). Quantum-sized Gold Clusters as Efficient Two-Photon Absorbers. *J. Am. Chem. Soc.* 130, 5032–5033. doi:10.1021/ja800341v
- Rao, J., Dragulescu-Andrasi, A., and Yao, H. (2007). Fluorescence Imaging In Vivo: Recent Advances. *Curr. Opin. Biotechnol.* 18, 17–25. doi:10.1016/j.copbio.2007.01.003
- Ricard, C., Arroyo, E. D., He, C. X., Portera-Cailliau, C., Lepousez, G., Canepari, M., et al. (2018). Two-photon Probes for In Vivo Multicolor Microscopy of the Structure and Signals of Brain Cells. *Brain Struct. Funct.* 223, 3011–3043. doi:10.1007/s00429-018-1678-1
- Ricci, F., Carlotti, B., Keller, B., Bonaccorso, C., Fortuna, C. G., Goodson, T., et al. (2017). Enhancement of Two-Photon Absorption Parallels Intramolecular Charge-Transfer Efficiency in Quadrupolar versus Dipolar Cationic Chromophores. *J. Phys. Chem. C* 121, 3987–4001. doi:10.1021/acs.jpcc.6b10629
- Rose, M. H. H. (2019). *A History of the Laser: 1960 - 2019, Photonics Spectra*. Photonics Media.
- RPMC (2020). *Advantages of Two-Photon Microscopy Utilizing Femtosecond Fiber Lasers, Pulsed Lasers Blog Posts*. RPMC Lasers.
- Rubart, M. (2004). Two-photon Microscopy of Cells and Tissue. *Circulation Res.* 95, 1154–1166. doi:10.1161/01.res.0000150593.30324.42
- Samanta, S., Huang, M., Li, S., Yang, Z., He, Y., Gu, Z., et al. (2021). AIE-active Two-Photon Fluorescent Nanoprobe with NIR-II Light Excitability for Highly Efficient Deep Brain Vasculature Imaging. *Theranostics* 11, 2137–2148. doi:10.7150/thno.53780
- Schaafsma, B. E., Mieog, J. S. D., Hutteman, M., van der Vorst, J. R., Kuppen, P. J. K., Löwik, C. W. G. M., et al. (2011). The Clinical Use of Indocyanine Green as a Near-Infrared Fluorescent Contrast Agent for Image-Guided Oncologic Surgery. *J. Surg. Oncol.* 104, 323–332. doi:10.1002/jso.21943
- Scherer, D., Dörfler, R., Feldner, A., Vogtmann, T., Schwoerer, M., Lawrentz, U., et al. (2002). Two-photon States in Squaraine Monomers and Oligomers. *Chem. Phys.* 279, 179–207. doi:10.1016/s0301-0104(02)00384-1
- Shaner, N. C., Campbell, R. E., Steinbach, P. A., Giepmans, B. N. G., Palmer, A. E., and Tsien, R. Y. (2004). Improved Monomeric Red, Orange and Yellow Fluorescent Proteins Derived from Discosoma Sp. Red Fluorescent Protein. *Nat. Biotechnol.* 22, 1567–1572. doi:10.1038/nbt1037
- Shen, Y.-F., Tsai, M.-R., Chen, S.-C., Leung, Y.-S., Hsieh, C.-T., Chen, Y.-S., et al. (2015). Imaging Endogenous Bilirubins with Two-Photon Fluorescence of Bilirubin Dimers. *Anal. Chem.* 87, 7575–7582. doi:10.1021/acs.analchem.5b01903
- Smith, P. G., Baldacchini, T., Carter, J., and Zadayan, R. (2012). *Two-Photon Microscopy/Multimodal Imaging: Femtosecond Laser Developments Advance Two-Photon Imaging*. Spectra Physics: BioOptics World.
- Smith, S. N., and Steer, R. P. (2001). The Photophysics of Lissamine Rhodamine-B Sulphonyl Chloride in Aqueous Solution: Implications for Fluorescent Protein-Dye Conjugates. *J. Photochem. Photobiol. A Chem.* 139, 151–156. doi:10.1016/s1010-6030(01)00372-0
- Sordillo, L. A., Pratavieira, S., Pu, Y., Salas-Ramirez, K., Shi, L. Y., Zhang, L., et al. (2014). Third Therapeutic Spectral Window for Deep Tissue Imaging. *Opt. Biopsy Xii* 2014, 8940. doi:10.1117/12.2040604
- Sordillo, L. A., Pu, Y., Pratavieira, S., Budansky, Y., and Alfano, R. R. (2014). Deep Optical Imaging of Tissue Using the Second and Third Near-Infrared Spectral Windows. *J. Biomed. Opt.* 19, 056004. doi:10.1117/1.jbo.19.5.056004
- Sowade, R., Kiessling, J., and Breunig, I. (2013). *CW Laser Light Tunable from Blue to Red: OPOs Pave the Way*. Germany: Photonik International.
- Squirrell, J. M., Wokosin, D. L., White, J. G., and Bavister, B. D. (1999). Long-term Two-Photon Fluorescence Imaging of Mammalian Embryos without Compromising Viability. *Nat. Biotechnol.* 17, 763–767. doi:10.1038/11698
- Subha, R., Nalla, V., Yu, J. H., Jun, S. W., Shin, K., Hyeon, T., et al. (2013). Efficient Photoluminescence of Mn<sup>2+</sup>-Doped ZnS Quantum Dots Excited by Two-Photon Absorption in Near-Infrared Window II. *J. Phys. Chem. C* 117, 20905–20911. doi:10.1021/jp404124c
- Sun, C.-L., Lv, S.-K., Liu, Y.-P., Liao, Q., Zhang, H.-L., Fu, H., et al. (2017). Benzoindolic Squaraine Dyes with a Large Two-Photon Absorption Cross-Section. *J. Mat. Chem. C* 5, 1224–1230. doi:10.1039/c6tc04129a
- Sun, C., Li, B., Zhao, M., Wang, S., Lei, Z., Lu, L., et al. (2019). J-aggregates of Cyanine Dye for NIR-II In Vivo Dynamic Vascular Imaging beyond 1500 Nm. *J. Am. Chem. Soc.* 141, 19221–19225. doi:10.1021/jacs.9b10043
- Sun, Z., Zhang, L.-P., Wu, F., and Zhao, Y. (2017). Photosensitizers for Two-Photon Excited Photodynamic Therapy. *Adv. Funct. Mat.* 27, 1704079. doi:10.1002/adfm.201704079
- Tanaka, Y., Saito, S., Mori, S., Aratani, N., Shinokubo, H., Shibata, N., et al. (2008). Metalation of Expanded Porphyrins: A Chemical Trigger Used to Produce



- Molecular Twisting and Möbius Aromaticity. *Angew. Chem. Int. Ed.* 47, 681–684. doi:10.1002/anie.200704407
- Tchounwou, C., Sinha, S. S., Viraka Nellore, B. P., Pramanik, A., Kanchanapally, R., Jones, S., et al. (2015). Hybrid Theranostic Platform for Second Near-IR Window Light Triggered Selective Two-Photon Imaging and Photothermal Killing of Targeted Melanoma Cells. *ACS Appl. Mat. Interfaces* 7, 20649–20656. doi:10.1021/acsami.5b05225
- Tian, R., Ma, H., Zhu, S., Lau, J., Ma, R., Liu, Y., et al. (2020). Multiplexed NIR-II Probes for Lymph Node-Invaded Cancer Detection and Imaging-Guided Surgery. *Adv. Mat.* 32, e1907365. doi:10.1002/adma.201907365
- Trägårdh, J., Murtagh, M., Robb, G., Parsons, M., Lin, J., Spence, D. J., et al. (2016). Two-Color, Two-Photon Imaging at Long Excitation Wavelengths Using a Diamond Raman Laser. *Microsc. Microanal.* 22, 803–807. doi:10.1017/s143192761601151x
- Trovatello, C., Marini, A., Xu, X., Lee, C., Liu, F., Curreli, N., et al. (2021). Optical Parametric Amplification by Monolayer Transition Metal Dichalcogenides. *Nat. Photonics* 15, 6–10. doi:10.1038/s41566-020-00728-0
- Tsai, T.-H., Chen, S.-Y., Tai, S.-P., Lin, C.-Y., Tsai, H.-J., and Sun, C.-K. (2005). in *In Vivo Two-Photon Fluorescence Imaging with Cr: Forsterite Lasers Using Transgenic Lines Tagged by HcRed*. Editors A. Periasamy and P.T.C. So (Biomedical Optics), 265. doi:10.1117/12.585732
- Tsai, T.-H., Lin, C.-Y., Tsai, H.-J., Chen, S.-Y., Tai, S.-P., Lin, K.-H., et al. (2006). Biomolecular Imaging Based on Far-Red Fluorescent Protein with a High Two-Photon Excitation Action Cross Section. *Opt. Lett.* 31, 930–932. doi:10.1364/ol.31.000930
- Tsien, R. Y. (1998). The Green Fluorescent Protein. *Annu. Rev. Biochem.* 67, 509–544. doi:10.1146/annurev.biochem.67.1.509
- Tsoi, K. M., Dai, Q., Alman, B. A., and Chan, W. C. W. (2013). Are Quantum Dots Toxic? Exploring the Discrepancy between Cell Culture and Animal Studies. *Acc. Chem. Res.* 46, 662–671. doi:10.1021/ar300040z
- Udayan, S., Sherin, D. R., Vijaykumar, S., Manojkumar, T. K., Nampoori, V. P. N., and Thomas, S. (2020). Exploring the LDS 821 Dye as a Potential NIR Probe for the Two Photon Imaging of Amyloid Fibrils. *Biomater. Sci.* 8, 6082–6092. doi:10.1039/d0bm00548g
- Ustione, A., and Piston, D. W. (2011). A Simple Introduction to Multiphoton Microscopy. *J. Microsc.* 243, 221–226. doi:10.1111/j.1365-2818.2011.03532.x
- Vivas, M. G., De Boni, L., and Mendonça, C. R. (2018). “Two-Photon Spectroscopy of Organic Materials,” in *Molecular and Laser Spectroscopy*. Editor V.P. Gupta (Elsevier), 165–191.
- Voigt, F. F., Emaury, F., Bethge, P., Waldburger, D., Link, S. M., Carta, S., et al. (2017). Multiphoton *In Vivo* Imaging with a Femtosecond Semiconductor Disk Laser. *Biomed. Opt. Express* 8, 3213–3231. doi:10.1364/boe.8.003213
- Wanderi, K., and Cui, Z. (2022). Organic Fluorescent Nanoprobes with NIR-IIb Characteristics for Deep Learning. *Exploration* 2, 20210097. doi:10.1002/exp.20210097
- Wang, S., Liu, J., Goh, C. C., Ng, L. G., and Liu, B. (2019). NIR-II-Excited Intravital Two-Photon Microscopy Distinguishes Deep Cerebral and Tumor Vasculatures with an Ultrabright NIR-I AIE Luminogen. *Adv. Mat.* 31, e1904447. doi:10.1002/adma.201904447
- Wang, S., Chen, H., Liu, J., Chen, C., and Liu, B. (2020). NIR-II Light Activated Photosensitizer with Aggregation-Induced Emission for Precise and Efficient Two-Photon Photodynamic Cancer Cell Ablation. *Adv. Funct. Mat.* 30, 2002546. doi:10.1002/adfm.202002546
- Wang, S., Fan, Y., Li, D., Sun, C., Lei, Z., Lu, L., et al. (2019). Anti-quenching NIR-II Molecular Fluorophores for *In Vivo* High-Contrast Imaging and pH Sensing. *Nat. Commun.* 10, 1058. doi:10.1038/s41467-019-09043-x
- Wang, S., and Larina, I. V. (2017). “High-resolution Imaging Techniques in Tissue Engineering,” in *Monitoring and Evaluation of Biomaterials and Their Performance in Vivo*. Editor R. J. Narayan (Cambridge: Woodhead Publishing), 151–180. doi:10.1016/b978-0-08-100603-0.00008-0
- Wang, S., Li, B., and Zhang, F. (2020). Molecular Fluorophores for Deep-Tissue Bioimaging. *ACS Cent. Sci.* 6, 1302–1316. doi:10.1021/acscentsci.0c00544
- Wang, S., Liu, J., Feng, G., Ng, L. G., and Liu, B. (2019). NIR-II Excitable Conjugated Polymer Dots with Bright NIR-I Emission for Deep *In Vivo* Two-Photon Brain Imaging through Intact Skull. *Adv. Funct. Mat.* 29, 1808365. doi:10.1002/adfm.201808365
- Wang, Y., Hu, R., Xi, W., Cai, F., Wang, S., Zhu, Z., et al. (2015). Red Emissive AIE Nanodots with High Two-Photon Absorption Efficiency at 1040 Nm for Deep-Tissue *In Vivo* Imaging. *Biomed. Opt. Express* 6, 3783–3794. doi:10.1364/boe.6.003783
- Wang, Z., Wang, X., Wan, J. B., Xu, F., Zhao, N., and Chen, M. (2021). Optical Imaging in the Second Near Infrared Window for Vascular Bioimaging. *Small* 17, e2103780. doi:10.1002/smll.202103780
- Webster, S., Odom, S. A., Padilha, L. A., Przhonska, O. V., Peceli, D., Hu, H., et al. (2009). Linear and Nonlinear Spectroscopy of a Porphyrin–Squaraine–Porphyrin Conjugated System. *J. Phys. Chem. B* 113, 14854–14867. doi:10.1021/jp904460f
- Wegner, K. D., and Hildebrandt, N. (2015). Quantum Dots: Bright and Versatile *In Vitro* and *In Vivo* Fluorescence Imaging Biosensors. *Chem. Soc. Rev.* 44, 4792–4834. doi:10.1039/c4cs00532e
- Wei, Z., Chen, S., Ding, J., Sun, B., Qi, X., Lu, B., et al. (2021). Recent Advance in Tunable Single-Frequency Fiber Laser Based on Two-Dimensional Materials. *Front. Phys.* 8.
- Wokosin, D. L., Centonze, V. E., Crittenden, S., and White, J. (1996). Three-photon Excitation Fluorescence Imaging of Biological Specimens Using an All-Solid-State Laser. *Bioimaging* 4, 208–214. doi:10.1002/1361-6374(199609)4:3%3C208::AID-BIO11%3E3.0.CO;2-J
- Wokosin, D. L., Centonze, V. E., White, J. G., Hird, S. N., Sepsenwol, S., Malcolm, G. P., et al. (1996). “Multiple-photon Excitation Imaging with an All-Solid-State Laser,” in *Proceedings of SPIE - the International Society for Optical Engineering* (United States: SPIE), 38–49.
- Wokosin, D. L., Centonze, V., White, J. G., Armstrong, D., Robertson, G., and Ferguson, A. I. (1996). All-solid-state Ultrafast Lasers Facilitate Multiphoton Excitation Fluorescence Imaging. *IEEE J. Sel. Top. Quantum Electron.* 2 (4), 1051–1065. doi:10.1109/2944.577337
- Wu, J., Shi, Z., Zhu, L., Li, J., Han, X., Xu, M., et al. (2022). The Design and Bioimaging Applications of NIR Fluorescent Organic Dyes with High Brightness. *Adv. Opt. Mater.* 10, 2102514. doi:10.1002/adom.202102514
- Xu, D., Liang, S., Xu, L., Bourdakos, K. N., Johnson, P., Read, J., et al. (2021). Widely-tunable Synchronisation-free Picosecond Laser Source for Multimodal CARS, SHG, and Two-Photon Microscopy. *Biomed. Opt. Express* 12, 1010–1019. doi:10.1364/boe.411620
- Yang, J., Fang, M., and Li, Z. (2020). Organic Luminescent Materials: The Concentration on Aggregates from Aggregation-Induced Emission. *Aggregate* 1, 6–18. doi:10.1002/agt2.2
- Yang, S., Adhikari, S., Dobbala, M., Adusumilli, S., Rowley, J. D., Ganikhanov, F., et al. (2013). Multi-color Ultrafast Laser Platform for Nonlinear Optical Imaging Based on Independently Tunable Optical Parametric Oscillators. *Appl. Phys. B* 111, 617–625. doi:10.1007/s00340-013-5381-x
- Yang, X., Lovell, J. F., Murthy, N., and Zhang, Y. (2020). “Organic Fluorescent Probes for Diagnostics and Bio-Imaging,” in *Fluorescent Imaging in Medicinal Chemistry*. Editor Z. Cheng (Cham: Springer International Publishing), 33–53. doi:10.1007/7355\_2019\_88
- Yao, J., Yang, M., and Duan, Y. (2014). Chemistry, Biology, and Medicine of Fluorescent Nanomaterials and Related Systems: New Insights into Biosensing, Bioimaging, Genomics, Diagnostics, and Therapy. *Chem. Rev.* 114, 6130–6178. doi:10.1021/cr200359p
- Yao, S., and Belfield, K. D. (2012). Two-Photon Fluorescent Probes for Bioimaging. *Eur. J. Org. Chem.* 2012, 3199–3217. doi:10.1002/ejoc.201200281
- Yao, S., Kim, B., Yue, X., Colon Gomez, M. Y., Bondar, M. V., and Belfield, K. D. (2016). Synthesis of Near-Infrared Fluorescent Two-Photon-Absorbing Fluorenyl Benzothiadiazole and Benzoselenadiazole Derivatives. *ACS Omega* 1, 1149–1156. doi:10.1021/acsomega.6b00289
- Ye, C.-x., Zhang, J.-m., Lin, X.-d., Zhang, T., Wang, B., and He, T.-c. (2017). Multiphoton Absorption of Three Chiral Diketopyrrolopyrrole Derivatives in Near-Infrared Window I and II. *Opt. Mat. Express* 7, 3529–3537. doi:10.1364/ome.7.003529
- Yi, R., Das, P., Lin, F., Shen, B., Yang, Z., Zhao, Y., et al. (2019). Fluorescence Enhancement of Small Squaraine Dye and its Two-Photon Excited Fluorescence in Long-Term Near-Infrared I&II Bioimaging. *Opt. Express* 27, 12360–12372. doi:10.1364/oe.27.012360
- Yoo, K. M., Liu, F., and Alfano, R. R. (1991). Imaging through a Scattering Wall Using Absorption. *Opt. Lett.* 16, 1068–1070. doi:10.1364/ol.16.001068
- Yoon, M.-C., Noh, S. B., Tsuda, A., Nakamura, Y., Osuka, A., and Kim, D. (2007). Photophysics of Meso- $\beta$  Doubly Linked Ni(II) Porphyrin Arrays: Large Two-Photon Absorption Cross-Section and Fast Energy Relaxation Dynamics. *J. Am. Chem. Soc.* 129, 10080–10081. doi:10.1021/ja0735655

- Zeng, W., Ishida, M., Lee, S., Sung, Y. M., Zeng, Z., Ni, Y., et al. (2013). A P-Quinodimethane-Bridged Porphyrin Dimer. *Chem. Eur. J.* 19, 16814–16824. doi:10.1002/chem.201302023
- Zhang, H., Salo, D., Kim, D. M., Komarov, S., Tai, Y.-C., and Berezin, M. Y. (2016). Penetration Depth of Photons in Biological Tissues from Hyperspectral Imaging in Shortwave Infrared in Transmission and Reflection Geometries. *J. Biomed. Opt.* 21, 126006. doi:10.1117/1.jbo.21.12.126006
- Zhang, L., Zou, L.-Y., Guo, J.-F., Wang, D., and Ren, A.-M. (2015). A Theoretical Study of a Series of Novel Two-Photon Nitric Oxide (NO) Fluorescent Probes Based on BODIPY. *New J. Chem.* 39, 8342–8355. doi:10.1039/c5nj01023c
- Zhang, N.-n., Lu, C.-y., Chen, M.-j., Xu, X.-l., Shu, G.-f., Du, Y.-z., et al. (2021). Recent Advances in Near-Infrared II Imaging Technology for Biological Detection. *J. Nanobiotechnol.* 19, 132. doi:10.1186/s12951-021-00870-z
- Zhang, N.-N., Lu, C.-Y., Chen, M.-J., Xu, X.-L., Shu, G.-F., Du, Y.-Z., et al. (2021). Recent Advances in Near-Infrared II Imaging Technology for Biological Detection. *J. Nanobiotechnol.* 19, 132. doi:10.1186/s12951-021-00870-z
- Zhao, W., Zhao, Y., Wang, Q., Liu, T., Sun, J., and Zhang, R. (2019). Remote Light-Responsive Nanocarriers for Controlled Drug Delivery: Advances and Perspectives. *Small* 15, 1903060. doi:10.1002/smll.201903060
- Zheng, Q., He, G. S., and Prasad, P. N. (2009). A Novel Near IR Two-Photon Absorbing Chromophore: Optical Limiting and Stabilization Performances at an Optical Communication Wavelength. *Chem. Phys. Lett.* 475, 250–255. doi:10.1016/j.cplett.2009.05.040
- Zheng, Z., Zhang, T., Liu, H., Chen, Y., Kwok, R. T. K., Ma, C., et al. (2018). Bright Near-Infrared Aggregation-Induced Emission Luminogens with Strong Two-Photon Absorption, Excellent Organelle Specificity, and Efficient Photodynamic Therapy Potential. *ACS Nano* 12, 8145–8159. doi:10.1021/acsnano.8b03138
- Zhou, Y., Zhang, D., He, G., Liu, C., Tu, Y., Li, X., et al. (2021). A Lysosomal Targeted NIR Photosensitizer for Photodynamic Therapy and Two-Photon Fluorescence Imaging. *J. Mat. Chem. B* 9, 1009–1017. doi:10.1039/d0tb02692a
- Zhu, C., Kwok, R. T. K., Lam, J. W. Y., and Tang, B. Z. (2018). Aggregation-Induced Emission: A Trailblazing Journey to the Field of Biomedicine. *ACS Appl. Bio. Mat.* 1, 1768–1786. doi:10.1021/acsbm.8b00600

**Conflict of Interest:** The authors declare that the research was conducted in the absence of any commercial or financial relationships that could be construed as a potential conflict of interest.

**Publisher's Note:** All claims expressed in this article are solely those of the authors and do not necessarily represent those of their affiliated organizations, or those of the publisher, the editors and the reviewers. Any product that may be evaluated in this article, or claim that may be made by its manufacturer, is not guaranteed or endorsed by the publisher.

Copyright © 2022 Shaw, Forsyth, Haseeb, Yang, Bradley and Klausen. This is an open-access article distributed under the terms of the Creative Commons Attribution License (CC BY). The use, distribution or reproduction in other forums is permitted, provided the original author(s) and the copyright owner(s) are credited and that the original publication in this journal is cited, in accordance with accepted academic practice. No use, distribution or reproduction is permitted which does not comply with these terms.



# Key Considerations in Targeted Protein Degradation Drug Discovery and Development

Liena Qin<sup>1\*</sup>, Han Dai<sup>2\*</sup> and Junfeng Wang<sup>2,3,4\*</sup>

<sup>1</sup>Insilico Medicine Ltd., Shanghai, China, <sup>2</sup>High Magnetic Field Laboratory, CAS Key Laboratory of High Magnetic Field and Ion Beam Physical Biology, Hefei Institutes of Physical Science, Chinese Academy of Sciences, Hefei, China, <sup>3</sup>International Magnetobiology Frontier Research Center, Hefei, China, <sup>4</sup>Institute of Physical Science and Information Technology, Anhui University, Hefei, China

## OPEN ACCESS

### Edited by:

Hany S. Ibrahim,  
Martin Luther University of Halle-  
Wittenberg, Germany

### Reviewed by:

Tamer Elwaie,  
Cairo University, Egypt  
Emil Bulatov,  
Kazan Federal University, Russia  
Xavier Lucas,  
Roche, Switzerland

### \*Correspondence:

Liena Qin  
liena.qin@insilico.ai  
Han Dai  
daihan@hml.ac.cn  
Junfeng Wang  
junfeng@hml.ac.cn

### Specialty section:

This article was submitted to  
Chemical Biology,  
a section of the journal  
Frontiers in Chemistry

Received: 02 May 2022

Accepted: 08 June 2022

Published: 01 August 2022

### Citation:

Qin L, Dai H and Wang J (2022) Key  
Considerations in Targeted Protein  
Degradation Drug Discovery  
and Development.  
Front. Chem. 10:934337.  
doi: 10.3389/fchem.2022.934337

Targeting proteins' enzymatic functions with small molecule inhibitors, as well as functions of receptor proteins with small-molecule agonists and antagonists, were the major forms of small-molecule drug development. These small-molecule modulators are based on a conventional occupancy-driven pharmacological approach. For proteome space traditionally considered undruggable by small-molecule modulators, such as enzymes with scaffolding functions, transcription factors, and proteins that lack well-defined binding pockets for small molecules, targeted protein degraders offer the opportunity to drug the proteome with an event-driven pharmacological approach. A degrader molecule, either PROTAC or molecular glue, brings the protein of interest (POI) and E3 ubiquitin ligase in close proximity and engages the ubiquitin-proteasome system (UPS), the cellular waste disposal system for the degradation of the POI. For the development of targeted protein degraders to meet therapeutic needs, several aspects will be considered, namely, the selective degradation of disease-causing proteins, the oral bioavailability of degraders beyond Lipinski's rule of five (bRo5) scope, demands of new E3 ubiquitin ligases and molecular glue degraders, and drug resistance of the new drug modality. This review will illustrate several under-discussed key considerations in targeted protein degradation drug discovery and development: 1) the contributing factors for the selectivity of PROTAC molecules and the design of PROTACs to selectively degrade synergistic pathological proteins; 2) assay development in combination with a multi-omics approach for the identification of new E3 ligases and their corresponding ligands, as well as molecular glue degraders; 3) a molecular design to improve the oral bioavailability of bRo5 PROTACs, and 4) drug resistance of degraders.

**Keywords:** targeted protein degradation, PROTAC, molecular glue, chemically induced proximity, drug discovery and development

## INTRODUCTION

PROTAC (proteolysis-targeting chimera) (Sakamoto et al., 2001) is a type of small molecule capable of the engaging ubiquitin-proteasome system, the cellular waste disposal system (Salami and Crews 2017), to degrade disease-causing proteins, by recruiting E3 ubiquitin ligase and labeling the target protein with polyubiquitin for proteasomal recognition. Classical PROTAC molecules are heterobifunctional small molecules consisting of two ligands connected with a flexible or rigid

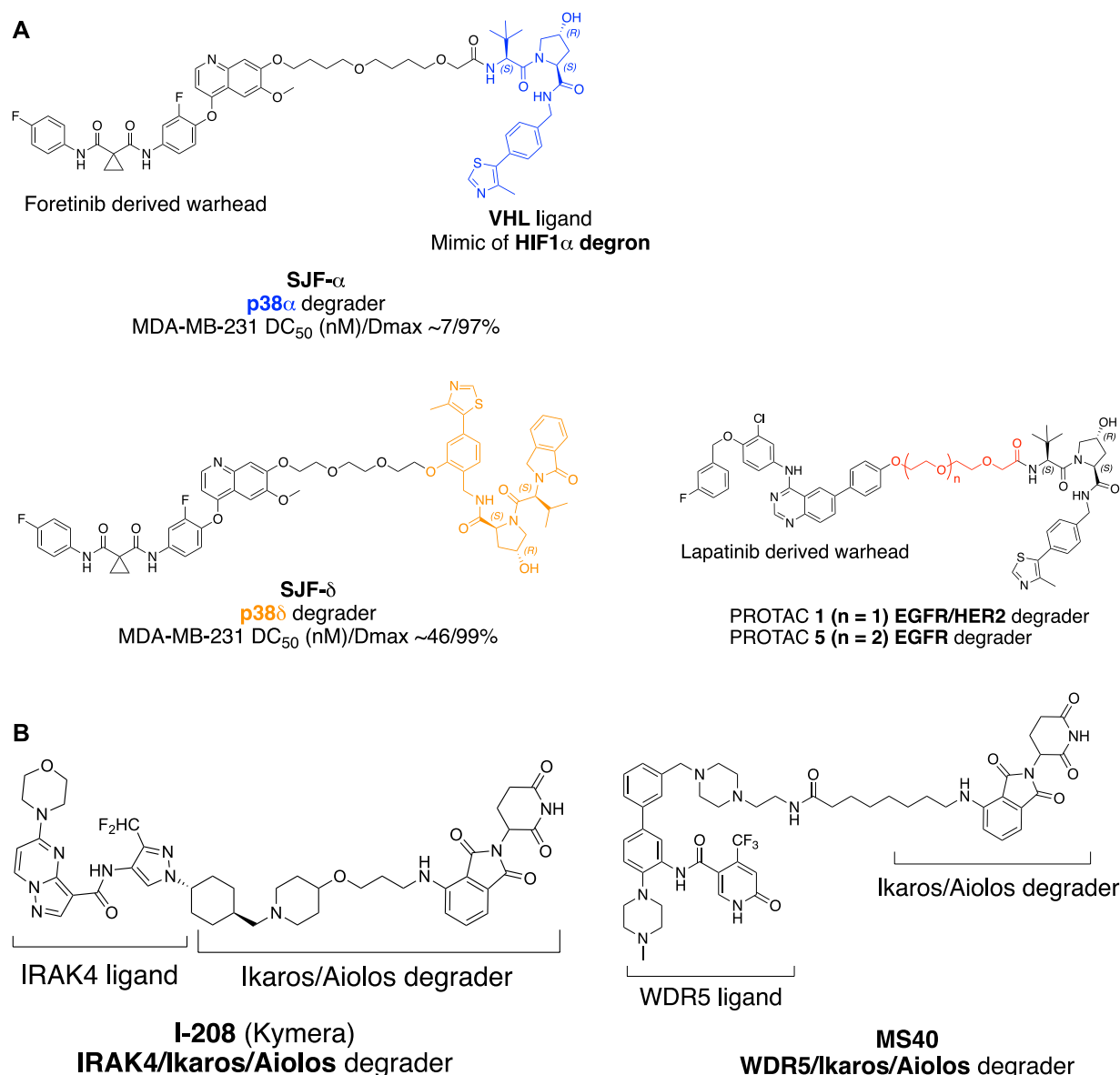


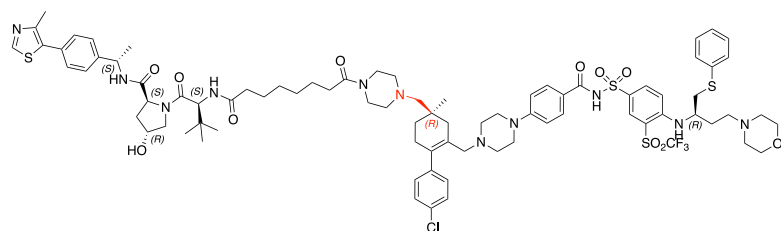
**FIGURE 1** | Factors influence the selectivity of degraders. **(A)** PROTAC with different linker attachment point to the VHL ligand selectively degrade p38 $\alpha$  and p38 $\beta$ . **(B)** Structure of IRAK/Ikaros/Aiolos multi-targets degrader **I-208** and WDR5/Ikaros/Aiolos multi-targets degrader **MS40**. **(C)** Bcl-2/Bcl-xL dual degradation by **753bR** achieved with different linker attachment points to warhead; and crystal structure of Navitoclax with BCL-2 (Souers et al., 2013) with four pockets indicated with an arrow. The crystal structure was processed with PyMOL. **(D)** Trivalent PROTAC with multi-protein or multi-domain binding warheads. **MZ1** with a preference for BRD4 degradation, **SIM1** with a preference for BRD2 degradation.

linker, with one ligand binding to POI, and the other binding to E3 ubiquitin ligase (Paiva and Crews 2019). The most prevalent E3 ligases used in pharmaceutical drug development are VHL (Von Hippel-Lindau) and CRBN (Cereblon) E3 ligases (Ishida and Ciulli 2021). Molecular glue degraders represented by immunomodulatory imide drugs (IMiDs) function similarly to PROTACs by engaging PPI (protein-protein interaction) between POI and E3 ligase, and directing the target protein for proteasomal degradation. Molecular glue (Schreiber 2021) degraders lack the typical linker seen in the PROTAC molecule. They are lower in molecular weight, and the binding affinity to each individual partner is lower or undetectable,

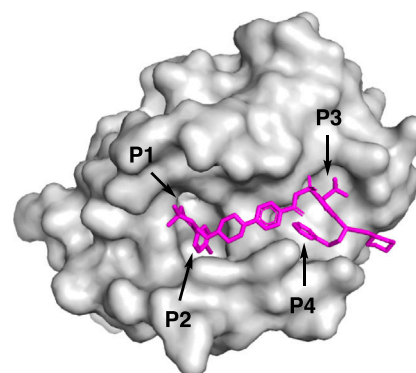
as shown in the case of sulfonamide with DCAF15 and RBM39 (Du et al., 2019). In some cases, a degrader molecule could harness features of both PROTAC and molecular glue to degrade multiple targets (**I-208**, **Figure 1B**). In this review, both PROTAC and molecular glue approaches will be treated as small molecule targeted protein degraders.

Targeted protein degraders have the potential to target conventionally undruggable proteome (Samarasinghe and Crews 2021; Schneider and Chris, 2021), either as chemical biology research tools (Burslem and Crews 2020) or as new therapeutic modalities (Cromm and Crews 2017; Lai and

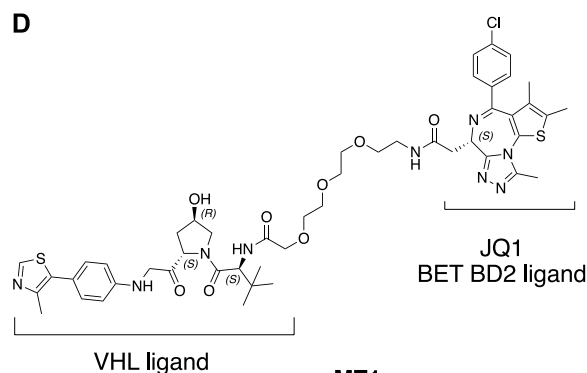


**C**

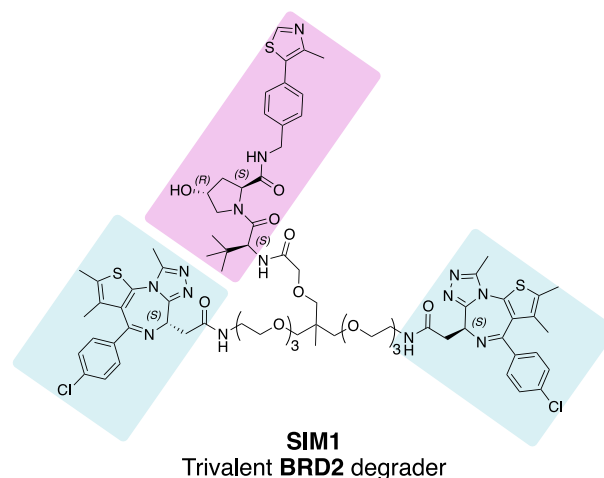
**753b (R)**  
BCL-2/BCL-xL dual degrader



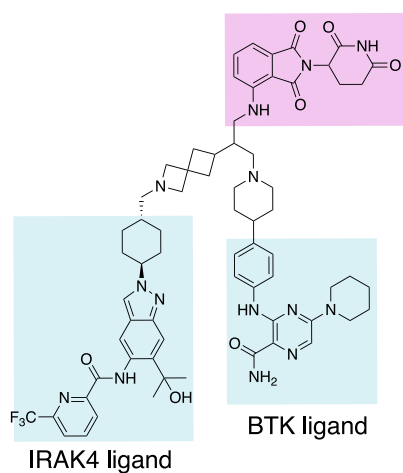
Navitoclax binds to BCL-2  
PDB 4LVT

**D**

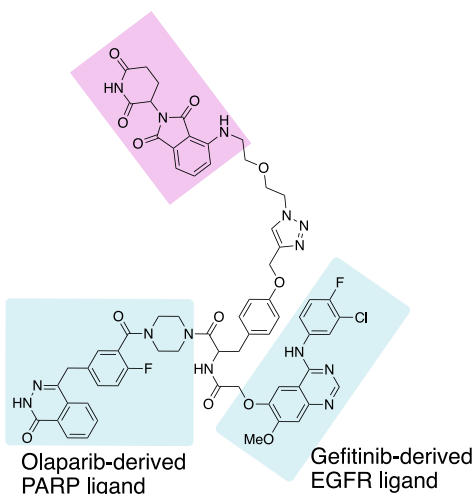
**MZ1**  
Bivalent BRD4 degrader



**SIM1**  
Trivalent BRD2 degrader



**I-8**  
Trivalent IRAK4/BTK/Ikros/Aiolos degrader



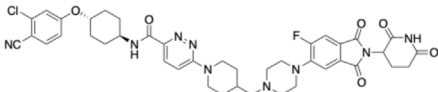
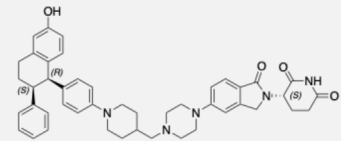
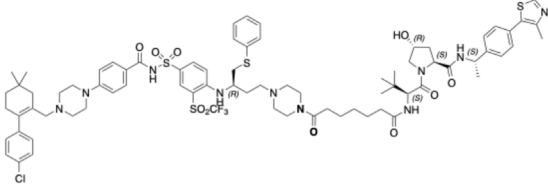
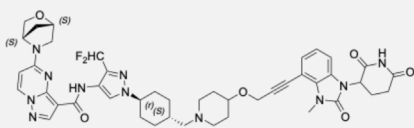
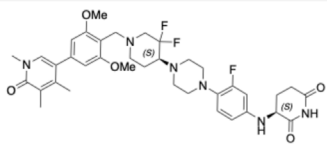
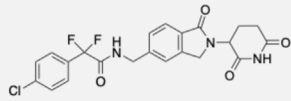
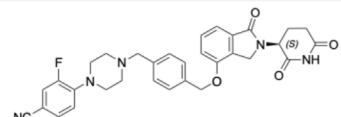
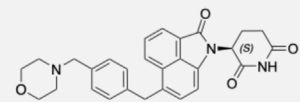
**DP-C-1**  
Trivalent PARP/EGFR degrader

**FIGURE 1 |** Continued.

Crews 2017; Nalawansha and Crews 2020), rapidly applied to cancer therapy (Dale et al., 2021), further applications include neurodegenerative disorders (Tomoshige and Ishikawa 2021).

Pioneered by the AR (Androgen receptor) degrader **ARV-110** (NCT03888612) and ER (Estrogen receptor) degrader **ARV-471** (NCT04072952), developed by Arvinas Inc. for the treatment of

**TABLE 1 |** Protein degraders approaching clinical trial (<https://clinicaltrials.gov/>) with structures disclosed.

Drug	Structure	MW	POI	E3 recruited	Administration
<b>ARV-110</b> (Arvinas) Prostate cancer/Phase II		812	Androgen receptor	CRBN	Oral tablet
<b>ARV-471</b> (Arvinas) Brest cancer/Phase II		724	Oestrogen receptor	CRBN	Oral
<b>DT2216</b> (Dialectic) Relapsed/Refractory Malignancies/Phase I		1542	BCL-xL	VHL	Intravenous infusion
<b>KT-474<sup>a</sup></b> (Kymera/Sanofi) Autoimmune/Phase I		866	IRAK4	CRBN	Oral tablet
<b>CFT8634</b> (C4 Therapeutics) Synovial sarcoma/IND		679	BRD9	CRBN	/
<b>CC-90009</b> (Bristol Myers Squibb) Acute Myeloid Leukaemia/Phase I		462	GSPT1	CRBN	Injection
<b>CC-92480</b> (Bristol Myers Squibb) Multiple myeloma/Phase I		568	Ikaros/Aiolos	CRBN	Oral
<b>CFT7455</b> (C4 Therapeutics) Multiple myeloma/Phase I		470	Ikaros/Aiolos	CRBN	Oral

<sup>a</sup>Chemical structure of KT-474 was speculated from reported patent (Mainolfi et al., 2020).

prostate cancer and breast cancer, respectively, the field has seen at least 15 degraders in a clinical trial (**Table 1**) (Mullard 2021).

Two aspects are key to fostering the development of targeted protein degraders in drug discovery and development, one is structure-guided design (Leissing, Luh, and Cromm 2020) of the heterobifunctional molecules, and the other is assay development driven by synthetic biology in combination with a multi-omics approach (Scholes et al., 2021) to systematically identify new E3 ubiquitin ligases and their corresponding ligands and molecular glue degraders. The design of selective PROTACs will be exemplified in the following context by the impact of linkerology on selective protein degradation, and the design of PROTACs to degrade multiple disease-causing proteins simultaneously. The impact of linkerology is also reflected in the physicochemical properties and oral bioavailability of PROTACs. Molecular design to improve oral bioavailability is important for bRo5 PROTAC drug development. The correlation of physicochemical features of PROTAC molecules with *in vivo* pharmacokinetics profile will be discussed. There are more than 600 E3 ubiquitin ligases encoded by the human genome, but only 2% of them have been applied in proximity-induced protein degradation. E3 ligases beyond VHL and CRBN for targeted protein degradation, for example, tissue-specific or disease-specific E3 ligases would considerably expand the application of targeted protein degradation for therapeutic purposes (Kannt and Đikić 2021; Guenette et al., 2022). Systematic searching for E3 ubiquitin ligases and their ligands is achieved using chemoproteomics methods applying cysteine reactive covalent small molecules to map the E3 ligase proteome. Assay development combined with multi-omics approaches is discussed. These benefit the targeted protein degradation field by providing the tools to systematically identify molecular glue degraders instead of being discovered by serendipity. At the end of the review, potential drug resistance mechanisms arising from targeted protein degradation will be briefly discussed. The design of degraders for therapeutic application discussed throughout the context reflects joint efforts from the chemistry and biology fronts to understand the molecular basis of disease pathways, as well as medicinal chemistry effort for the design of bioavailable molecules.

## SELECTIVITY OF PROTEIN DEGRADERS BY DESIGN

### Selective Degradation of Target Protein With Promiscuous Warhead

Turning a promiscuous small molecule inhibitor into a PROTAC, the selectivity could be rewired in the degradable proteome. A multi-kinase degrader generated by conjugating a highly promiscuous kinase inhibitor with CRBN-binding ligand was discovered to degrade a small set of kinases and CDK family proteins, using chemoproteomics method. In this study, Huang and coworkers demonstrated that target engagement is not sufficient for successful degradation (Huang et al., 2018). The selectivity of productive protein degradation is influenced by the

E3 ubiquitin ligase (Lai et al., 2016), linker attachment points to the warhead, linker attachment point to E3 ligase ligand, and linker length (termed 'linkerology'). The effect of E3 ubiquitin ligase selection and cell type on the degradation profile for PROTAC molecules will not be discussed here. This part will focus on the impact of linkerology on the selectivity of PROTAC molecules with promiscuous warheads.

The linker attachment point to a POI is usually selected at a solvent-exposed site of the warhead binding in a protein pocket. Linkers extended from a buried site may hinder the binding of a target protein and unsuccessful degradation. This can sometimes enhance the selectivity of a promiscuous warhead, as in the well-discussed case of enhancing the degradation of the cellular retinoic acid-binding protein (CRABP) over retinoic acid receptor (RAR) with the dual protein binder all-*trans* retinoic acid (ATRA) (Ishikawa et al., 2020).

Linker attachment point to E3 ligase ligand has the potential to influence the direction of assembly of the E3 ubiquitin complex. In a study evaluating protein degradation profile with promiscuous c-Met tyrosine kinase inhibitor Defactinib (Bondeson et al., 2018), p38 $\alpha$  was found to be degraded (DC<sub>50</sub> (nM)/D<sub>max</sub> 210/91%) with VHL recruiting E3 ligase in triple-negative breast cancer cell line MDA-MB-231, while the MAPK family homolog p38 $\delta$ , which shares 61% sequence identity with p38 $\alpha$ , was only slightly degraded (~30%). Later, a more potent selective p38 $\alpha$  degrader **SJF- $\alpha$**  (MDA-MB-231 DC<sub>50</sub> (nM)/D<sub>max</sub> ~7/97%) was developed (Smith et al., 2019). The linear linker and the VHL E3 ligase ligand were connected through the amide bond as depicted in **Figure 1A**. By changing the linker attachment point to the benzene ring of the VHL E3 ligase ligand through an ether bond, selective p38 $\delta$  degradation (MDA-MB-231 DC<sub>50</sub> (nM)/D<sub>max</sub> ~46/99%) was achieved. The distinct degradation selectivity of two PROTAC molecules between two homologous MAPK family proteins was illustrated by *in vitro* stable ternary complex formation of VHL-**SJF- $\alpha$** -p38 $\alpha$  and VHL-**SJF- $\delta$** -p38 $\delta$ , respectively. Molecular dynamic simulation of the ternary complexes indicates that the VHL/p38 $\alpha$  and VHL/p38 $\delta$  interface was altered. VHL protein was recruited in a different direction approaching the p38 $\alpha$ /p38 $\delta$  protein due to the distinct linker attachment points of the PROTAC molecules.

The impact of linker length on the selectivity of PROTACs is exemplified by epidermal growth factor receptor (EGFR) and human epidermal growth factor receptor 2 (HER2) degrader with receptor tyrosine kinase inhibitor Lapatinib derived warhead (Burslem et al., 2018). PROTAC **1** with two PEG (polyethylene glycol) linker degrades both EGFR and HER2, while PROTAC **5** with three PEG linkers selectively degrades EGFR (**Figure 1A**). This type of exquisite selectivity is also reported in the CDK4/6 case with a highly conserved kinase active site (Anderson et al., 2020).

### Design of PROTAC Synergistically Degrade Multiple Disease-Causing Proteins to Meet the Clinical Needs

Interleukin-1 receptor-associated kinase 4 (IRAK4) is a serine/threonine-protein kinase with scaffolding functions, involved in

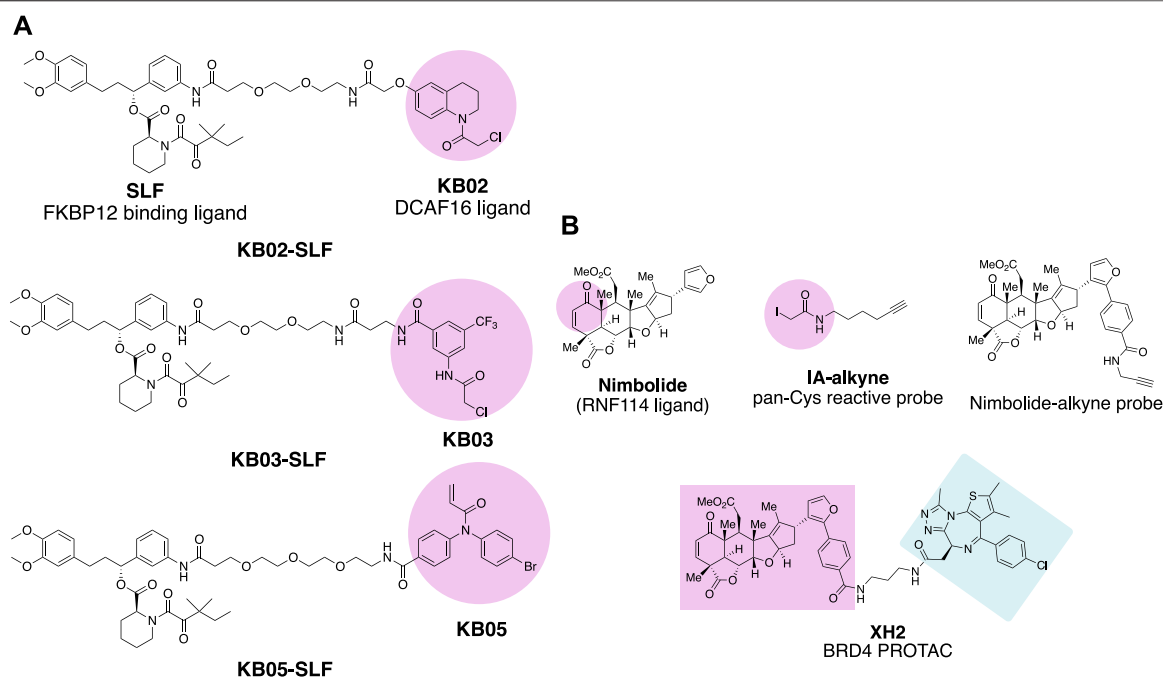


**FIGURE 2 |** Chemical probes for the identification of E3 ligases. **(A)** FKBP12 degrading molecules with “scout” fragment **KB02**, **KB03**, and **KB05** covalently react with Cysteine in the proteome. **(B)** Chemical probes for the identification of E3 ligase recruited by **Nimbolide**.

Toll-like receptor (TLR, except for TLR3) and Interleukin-1 receptor (IL-1R) signaling pathways (Hennessy et al., 2010; Picard et al., 2011). IRAK4 is a 51KD protein that consists of an N-terminal Death Domain (DD residues 1–125), a hinge domain (residues 140–150), and a C-terminal kinase domain (residues 150–460). Upon TLR activation, IRAK4 is rapidly recruited by MYD88 to the receptor-signaling complex to form the Myddosome complex, then phosphorylates initially IRAK1 via oligomerization of the N-terminal DD in each of these proteins, leading to NF- $\kappa$ B nuclear translocation and activation. The scaffolding function of the DD of IRAK4 is essential in IL-1 signaling, while the kinase function of IRAK4 is partially responsible (Kim et al., 2007; De Nardo et al., 2018). To target both scaffolding function and kinase activity of IRAK4, degradation is superior over of IRAK4 kinase inhibitor, similar to that reported on FAK (Law et al., 2021). On the other hand, Ikaros and Aiolos are the activators of the redundant NF- $\kappa$ B pathway and upstream type I INF regulator. A PROTAC molecule capable of degrading IRAK4/Ikaros/Aiolos simultaneously could meet the clinical needs in treating B cell malignancy (Yang et al., 2012).

The key question to address for an IRAK4 degrader with Ikaros/Aiolos degradation properties is the selectivity. By proteomic analysis in thalidomide-treated H9 human embryonic stem cells, C2H2 zinc finger transcription factor SALL4 was identified as a *bona fide* neo-substrate of the thalidomide-CRBN-DDB1-Cul4A E3 ligase complex. Loss of function of SALL4 was verified to be responsible for thalidomide-caused teratogenicity (Donovan et al., 2018). Despite the side effects of thalidomide, it was later approved

by FDA for the treatment of multiple myeloma under strict restrictions. Other thalidomide analogous immunomodulatory imide drugs (IMiDs), lenalidomide, and pomalidomide, have been developed for the treatment of cancer with fewer side effects and increased potency. Other than SALL4, IMiDs degrade a set of neo-substrates, most of which are C2H2 zinc finger proteins (Krönke et al., 2014; Donovan et al., 2018; Gao et al., 2020; Kozicka and Thomä, 2021) including Ikaros (IKZF1) and Aiolos (IKZF3). More selective Ikaros and Aiolos degraders are needed to reduce the safety concern as well as gain structural insights for the selectivity of degradation. **CC-92480** (Hansen et al., 2020) (NCT03989414) and **CFT7455** (Henderson et al., 2020) (**Table 1**) (NCT04756726) have been developed for the treatment of multiple myeloma and lymphoma by Bristol Myers Squibb and C4 Therapeutics independently, and are currently in phase I clinical trials. The selectivity of the IMiD degraders is achieved by introducing substitution to the phthalimide, therefore changing the approachable interface of CRBN by neo-substrates in the presence of IMiD (Leissing et al., 2020).

Kymera Therapeutics has designed a potent multi-targets IRAK4/Ikaros/Aiolos degrader **KT-413** for treating relapsed or refractory B-cell Non-Hodgkin's lymphoma, which is in phase I clinical trial (NCT05233033). Although the structure of **KT-413** has not been disclosed, the molecule **I-208** (Figure 1B) (Mainolfi et al., 2020) has been disclosed to be able to induce *in vivo* degradation of IRAK4/Ikaros/Aiolos in OCI-LY10 tumor xenograft, correlated with tumor regression.

A similar approach of designing the PROTAC **MS40** (Figure 1B) for the degradation of MDR5/Ikaros with a synergistic effect in mixed-lineage leukemia (MLL)-rearranged



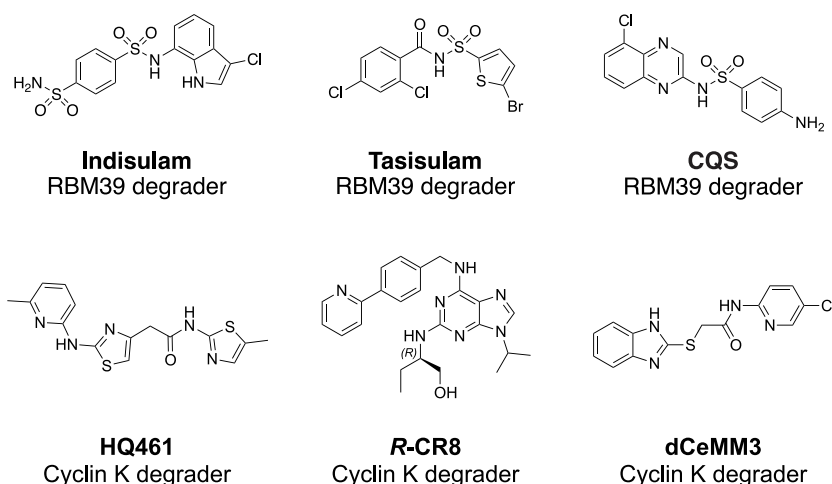


**FIGURE 3** | Structures of RBM39 degrading sulfonamides and CDK12 dependent Cyclin K degraders.

leukemias was reported most recently (D. Li et al., 2022). WD repeat domain 5 (WDR5) is an integral component of histone lysine methyltransferase complex and MLL complex. MLL-rearranged leukemias also exhibit high expression and dependency on Ikaros. **MS40** was shown to degrade WDR5/Ikaros/Aiolos in acute lymphoblastic leukemia (ALL) RS4; 11 cells, and WDR5/Ikaros in biphenotypic B myelomonocytic leukemia MV-4-11 cells at submicromolar range (MV-4-11 lack of expression of Aiolos). **MS40** has also shown modular *in vivo* tumor suppression activity in the subcutaneous MLL-AF9+AML PDX model, dosing at 100 mpk once daily for five days per week through intraperitoneal injection.

## Selective Degradation of Mono- or Bi-Target Protein With Dual Inhibitor

Navitoclax is a potent Bcl-xL and Bcl-2 dual inhibitor developed by AbbVie for the treatment of relapsed or refractory lymphoid malignancies. Navitoclax failed in the phase II clinical trial, due to on-target and dose-limiting thrombocytopenia (Mohamad Anuar et al., 2020). Platelets require Bcl-xL for survival. The VHL recruiting PROTAC **DT2216** (Table 1), utilizes Navitoclax as a warhead, achieved potent antitumor activity while less platelet toxicity *in vivo*, and is currently in Phase I clinical trial (NCT04886622). The reduced platelet toxicity was suggested to be due to the low expression level of VHL in platelet (He et al., 2019; Khan et al., 2019; He et al., 2020). The authors also validated that **DT2216** selectively degrades Bcl-xL in a Lys 87-dependent manner. Single Lys 87 mutation to arginine is sufficient to induce resistance to Bcl-xL degradation; if all the other lysines of Bcl-xL except Lys 87 were mutated, the degradation of Bcl-xL was retained.

The selective degradation of Bcl-xL over Bcl-2 could be explained by the linkerology of PROTAC molecule design. The linker of **DT2216** was designed by forming two amide bonds with VHL ligand and Navitoclax warhead respectively, one with the primary amine of the VHL ligand, and the other with

the secondary amine of piperazine, which was converted from morpholine of Navitoclax. Linker extension from the morpholine binding site of Bcl-xL exposed the Lys 87 for ubiquitination, while Bcl-2 lacks such an accessible lysine, which results in the selective degradation of Bcl-xL over Bcl-2. The result is consistent with the finding that a productive ternary complex formation is required for targeted protein degradation (Chung et al., 2020).

Furthermore, degradation of both BCL-xL and BCL-2 with improved anti-leukemic activity was achieved by changing the linker attachment point to the methyl group, which is solvent-exposed located at pocket 1 (**P1**) and pocket 2 (**P2**) intersection of Bcl-2 or Bcl-xL as indicated in Figure 1C, to generate **753b** (R enantiomer) (Figure 1C) (D. Lv et al., 2021, 2). By doing so, the Lys 17 of Bcl-2 was accessible for ubiquitination according to the computational modeling of the Bcl-2-**753b**-VHL E3 ligase. Meanwhile, Lys 87 and Lys 20 of Bcl-xL remain accessible for ubiquitination in the BCL-xL-**753b**-VHL E3 ligase composition.

## Trivalent PROTAC With Bivalent Warhead

Trivalent PROTAC contains a bivalent warhead, which binds to two domains of one protein or two proteins simultaneously. Degrading dual-target proteins in the complimentary pathological pathway or synthetic lethal pair could be interesting to generate a synergistic effect in drug development. However, simultaneous degrading of such protein pair by a trivalent PROTAC requires the two proteins to be present at the same time and space in a cellular context. The design of a trivalent PROTAC requires careful planning of the linkerology, which has been well illustrated by the structure-guided design of a trivalent PROTAC with a warhead binding to two domains of one protein (Imaide et al., 2021). Bromodomain-containing proteins BRD2/3/4 and BRDT are members of the bromodomain and extra terminal domain (BET) family of proteins, structurally featuring two bromodomains (BD1 and BD2), which recognize acetylated lysine during transcriptional regulation. The well-known BET BD inhibitor **JQ1** (Filippakopoulos et al., 2010) was converted to **MZ1** (Zengerle

et al., 2015) to give a VHL E3 ligase recruiting BET degrader. A more potent bivalent BD inhibitor **MT1**, which binds to the BD1 and BD2 of BET family proteins, was also reported with significant *in vivo* efficacy (Tanaka et al., 2016). Ciulli and coworkers validated the concept of developing a trivalent PROTAC **SIM1** (Figure 1D), guided by the chemical structure of **MZ1**, **MT1**, and the crystal structure of the BRD4 (BD2)-**MZ1**-VHL E3 ligase ternary complex (Gadd et al., 2017). The structure of BRD4 (BD2)-**MZ1**-VHL E3 ligase ternary complex suggests a three PEG point could be a branching point for another BD1 binding **JQ1** ligand. The eight PEG linker **SIM1** suggests sufficient length for linker attachment to the VHL ligand. The trivalent **SIM1** binds to both BD1 and BD2 domains of the BET protein and recruits VHL E3 ligase for targeted degradation of BET proteins. **SIM1** degrades BET family proteins with a preference for BRD2, which is different from **MZ1**'s preference for BRD4 degradation.

Trivalent PROTAC with a warhead targeting the synthetic lethal pair of EGFR and poly (ADP-ribose) polymerase (PARP) has been reported (Zheng et al., 2021). Based on the report that EGFR mutated lung cancer cells were sensitized to the treatment of PARP inhibitor Olaparib (Pfaffle et al., 2013), Zheng and coworkers designed a trivalent PROTAC with bivalent warhead derived from Olaparib and EGFR inhibitor Gefitinib (**DP-C-1**, Figure 1D). Both VHL and CRBN recruiting trivalent PROTACs were designed, and dose- and time-dependent degradation of EGFR and PARP was observed in non-small cell lung cancer cell line H1299 and pancreatic adenocarcinoma cell line SW1990 at  $\mu$ M range, respectively. Most recently, trivalent degraders targeting two synergistic protein targets, IRAK4 and BTK in B cell lymphoma, have been disclosed by Kymera Therapeutics (Weiss et al., 2022). The degraders represented by **I-8** (Figure 1D) also degrade Ikaros and Aiolos. Overall, these researches set a foundation for structure-guided design of PROTAC molecules for multidomain proteins, and potentially two protein targets synergistically for therapeutic benefits.

## SYSTEMATIC PROFILING OF E3 LIGASES, LIGANDS, AND MOLECULAR GLUE DEGRADERS

### Chemoproteomics Approach and Chemical Biology Assay Development for the Identification of New E3 Ligases and Ligands for Targeted Protein Degradation

The majority of PROTAC molecules in clinical trials recruit CRBN E3 ubiquitin ligase for targeted protein degradation (Table 1), including the AR degrader (**ARV-110**) (Crew et al., 2021), ER degrader (**ARV-471**) (Chen X. et al., 2021; Halford 2021), IRAK4 degrader (**KT-474**) (Mainolfi et al., 2020) (NCT04772885) and BRD9 degrader (**CFT8634**) (Nasveschuk et al., 2022) (NCT05355753). The Helios degrader, GSPT1 degrader (**CC-90009**) (Hansen et al., 2021) (NCT04336982), and Ikaros/Aiolos degraders are CRBN E3 recruiting molecular glue degraders. The only VHL E3 ligase recruiting PROTAC molecule currently in Phase I clinical trial is the Bcl-xL degrader (**DT2216**). Ligands of several E3 ubiquitin ligases including Nutlin-3a for MDM2 (Schneekloth

et al., 2008) and Bestatin for cIAP (Itoh et al., 2010), have been reported for targeted protein degradation, and their application in drug development is still limited. The systematic approach for the identification of E3 ligases DCAF16 and RNF114 could be inspirational for the discovery of other new E3 ligases and their corresponding ligands (Spradlin et al., 2019; Zhang X. et al., 2019).

Chloroacetamide and acrylamide containing "Scout" fragments are cysteine reactive electrophiles used by the pioneer of the Cravatt research team in activity-based protein profiling (Backus et al., 2016; Bar-PeledKemper et al., 2017). The 'Scout' fragments **KB02**, **KB03**, and **KB05** (Figure 2A) displayed broad cysteine reactivity in the human proteome, thus capable of capturing reactive cysteine residues of the E3 ubiquitin ligase pool once the scout fragments are turned into PROTAC molecules. Such PROTAC molecules are designed by linking FKBP12 binding protein-ligand SLF to the scout fragment. The molecules were tested in the HEK293 T cell line transduced with FLAG-tagged FKBP12 either with or without C-terminal NLS (nuclear localization sequence) KKKRKV. The compound **KB02-SLF** was found to promote the loss of nuclear FKBP12 in a Cullin E3 ligase and proteasome system-dependent manner. FLAG-mediated affinity enrichment was used to identify that the DCAF16 E3 ligase was associated with FKBP12\_NLS degradation in a KB02-SLF-dependent manner (Zhang X. et al., 2019).

Nimbolide is a natural product derived from the Neem tree and possesses anticancer activity (Elumalai and Arunakaran 2014). The chemical structure of Nimbolide features an  $\alpha,\beta$ -unsaturated ketone as Michael acceptor with the potential to act as an electrophile for the reactive cysteine residues of the target protein (Figure 2B). This enables isoTOP-ABPP (isotopic tandem orthogonal proteolysis-activity-based protein profiling) (Weerapana et al., 2010) to identify the direct protein targets of Nimbolide. The iodoacetamide-alkyne was used as the chemical probe in the experiment to react with those Cysteines spared by Nimbolide so that Nimbolide reactive cysteine-containing proteins will show differences in the quantitative mass spectrometry analysis. The E3 ligase RNF114 was identified to be the target of Nimbolide. The anticancer reactivity of Nimbolide arises from the inhibited ubiquitination and degradation of tumor suppressor p21 in the 231MFP breast cancer cell line by RNF114. The interaction of Nimbolide with RNF114 was further validated by pulldown of Flag-tagged RNF114 in 231MFP cells with the Nimbolide-alkyne probe (Figure 2B). The capability of E3 ligase RNF114 recruited by Nimbolide for targeted degradation was evaluated by the PROTAC molecule XH2 (Spradlin et al., 2019), to degrade BRD4 with the Bromodomain ligand **JQ1** as a warhead.

An indirect chemical biology method to evaluate the function of E3 ubiquitin ligases for targeted protein degradation is induced protein proximity by using a heterobifunctional small molecule (Ottis et al., 2017). E3 ubiquitin ligase and GFP were fused with HT7 (HaloTag7) and FKBP (FK506 binding protein) respectively, a heterobifunctional small molecule was designed with one side forming a covalent bond with Asp106 of HT7 while the other side binds to FKBP in a bump-hole mode. The E3 ubiquitin ligase and POI were induced close in space to evaluate the degradation signal. In the assay, GFP was used to give a fluorescent signal for

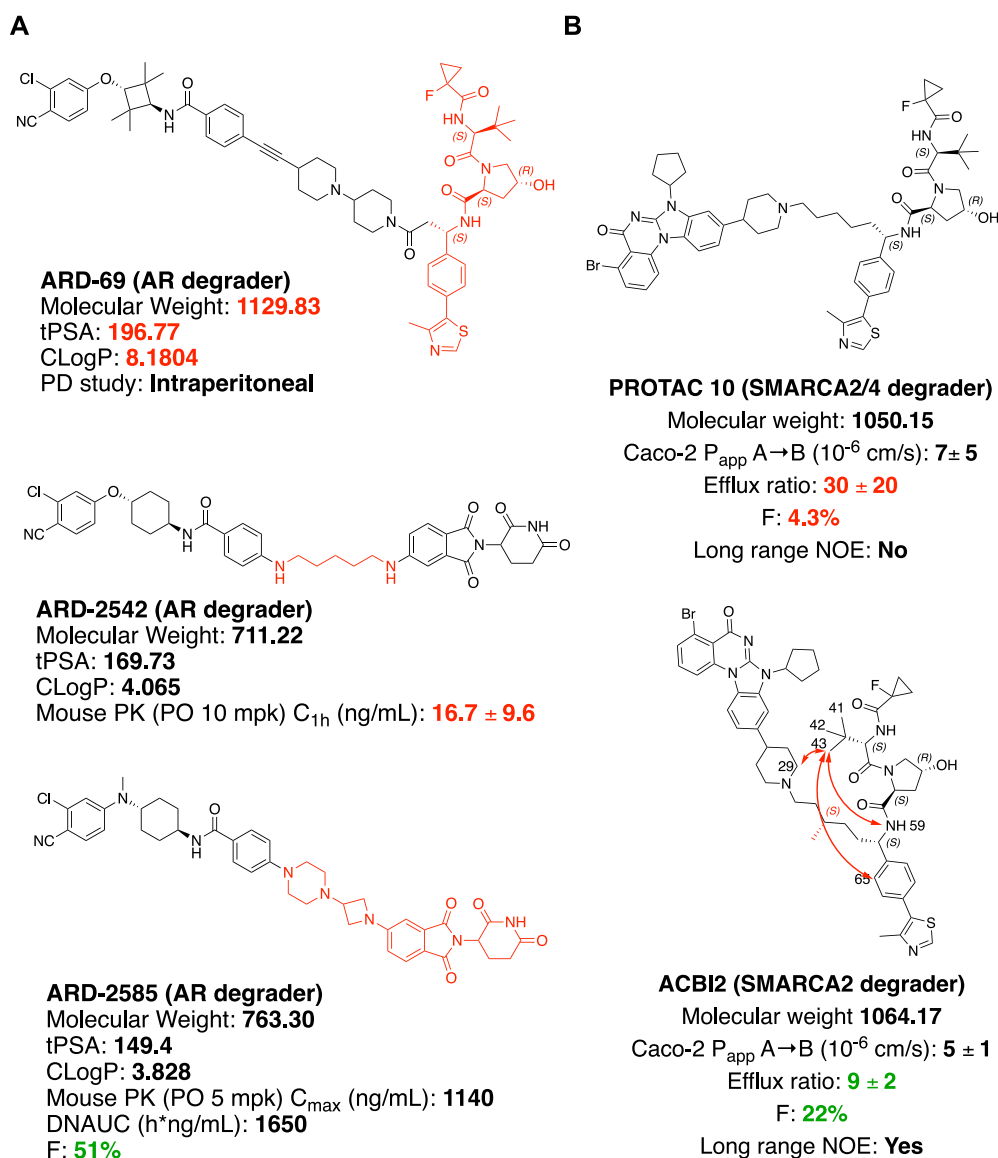


**FIGURE 4 |** Structure modification to improve oral bioavailability. **(A)** Structures of AR degraders, ARD-69 with VHL ligand, ARD-2542 with a flexible linear linker, ARD-2585 with the rigid linker. **(B)** Structures of SMARCA2/4 degraders. Red arrows indicate atoms with long range NOE.

monitoring the degradation event. More recently, the HiBit technology has been developed for measuring endogenous protein dynamics (Schwinn et al., 2020); and the NanoBRET assay (Riching et al., 2018) has also been developed to measure the kinetics of cellular degradation cascades. Those assays in combination provide methods to evaluate E3 ubiquitin ligases for targeted protein degradation in a high-throughput manner.

## Cell Biology Assay in Combination With Multi-Omics Methods for the Identification of Molecular Glue Degraders

In the past, molecular glue degraders were usually found by serendipity while searching for the mode of action of small

molecule drugs (Dong et al., 2021). Examples include thalidomide (Ito et al., 2010) and RBM39 (RNA binding motif protein 39) (T. Han et al., 2017) degrading sulfonamides (Figure 3) which were discovered to be molecular glue degraders. Thalidomide was used in the late 1950s and early 1960s for the treatment of morning sickness in pregnant women, which resulted in severe tragedies in causing thousands of miscarriages and birth defects. Via affinity-based protein profiling with a thalidomide-based probe in HeLa cell extracts, CRBN was found to bind to thalidomide, a substrate recognition subunit of DDB1-Cul4A Cullin RING E3 ubiquitin ligase. **Indisulam** was a small molecule compound with anticancer activity. The mode of action of indisulam was not revealed until recently by using a forward genetic method. Several

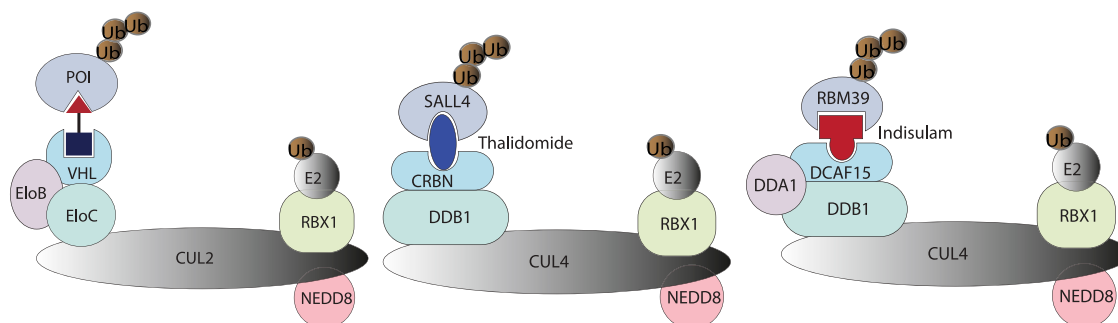


**FIGURE 5** | A PROTAC molecule is represented by a heterobifunctional molecule with a linker, which induces proximity between VHL and POI. Molecular glue degraders are represented by Thalidomide and Indisulam-induced protein-protein interaction between neosubstrate and substrate-binding subunit of E3 ubiquitin ligase (Bulatov and Ciulli 2015).

single amino acid mutations of Indisulam were found in common across the RBM39 resistant HCT-116 cell line. RBM39 was later found to be degraded by indisulam in a dose-dependent manner. Following co-immunoprecipitation and liquid chromatography and mass spectrometry analysis, DCAF15 E3 ligase was found to be engaged in the degradation of RBM39.

Small molecules targeting protein homeostasis specifically by engaging protein-E3 ligase interactions for targeted degradation might be more common than previously known. Cell biology assays in combination with multi-omics methods have been developed for systematically searching for small molecules with such capability (Mayor-Ruiz et al., 2020; Scholes et al., 2021). Phenotypic screening of 2,000 cytotoxic compounds was carried out in WT and UBE2M (E2 enzyme) mutated (hyponeddylated) myeloid leukemia cell line KBM-7 to identify correlations between the toxicity of small molecules with the neddylation level. Since the neddylation of cullin-RING E3 ligases (CRLs) is highly associated with the E3s' activity, the small molecules identified in the screen will be E3 ligase activity-dependent cytotoxic compounds. Four compounds (dCeMM1/2/3/4) were identified in the phenotypic screening. Quantitative expression proteomics revealed dCeMM1 to be RBM39 destabilizer and dCeMM2/3/4 to be a cyclin K degrader. CRISPR-Cas9 screening against all components of known CRLs revealed that cyclin K degradation is mediated by the CUL4B complex. Affinity-based protein profiling using a dCeMM3-derived chemical probe identified drug-mediated DDB1-CDK12-cyclin K complex formation. Drug sensitivity data for 4,518 clinical and pre-clinical compounds tested in 578 cancer cell lines were compared with the mRNA expression level of 499 E3 ligase components, and the cytotoxicity of the CDK inhibitor **R-CR8** (Figure 3) was found to correlate with the expression levels of CUL4 adaptor DDB1 (Ślabicki et al., 2020). In the counter-confirmation experiment, sgRNA targeting *DDB1* conferred resistance to **R-CR8**. In the proteome-wide analysis of protein abundance following **R-CR8** treatment, cyclin K was the only protein shown to be consistently decreased. In the *in vitro* pulldown experiment of CDK12 (AA713-1052 kinase domain) bound cyclin K in the presence

of **R-CR8**, DDB1 was significantly enriched versus in the absence of **R-CR8**. The crystal structure of CDK12<sup>713–1052</sup>-cyclin K<sup>1–267</sup> bound to **R-CR8** and DDB1<sup>ΔBPB</sup> was determined to illustrate the structural mechanism of **R-CR8** acting as a molecular glue degrader for cyclin K by strengthening the CDK12-DDB1 interaction.

At the same time, serendipitously, a screening effort for NRF2 inhibitors using NRF2 activity-based luciferase reporter assay, **HQ461** (Figure 3) was found to down-regulate NRF2 mRNA and expression levels (L. Lv et al., 2020). However, **HQ461**'s potent cytotoxicity in the A549 cell line was independent of NRF2 function. To explore the mechanism of function of the molecule, **HQ461** sensitive colorectal cancer cell line HCT-116 was treated with the compound to select resistant clones. Whole-exome sequencing against the **HQ461** resistant clones was performed to find the top-ranking variant was CDK12 G731E mutation. Both CDK12 and its interacting protein Cyclin K protein level were quantified, showing more than the 8-fold reduction of Cyclin K was observed after treatment with **HQ461** in the CDK12 wild-type cell line. The downregulation of Cyclin K was UPS-dependent. Pulldown using Flag-tagged CDK12 in the cell lysate treated with **HQ461** identified the interaction between CDK12 and DDB1. The **HQ461**-induced CDK12 (kinase domain)/CCNKAC/DDB1 complex was further evaluated by AlphaScreen assay and chemical cross-linking mass spectrometry. The assay results give evidence that **HQ461** function as a molecular glue between CDK12 and DDB1, which triggers UPS-dependent depletion of Cyclin K.

## IMPROVING THE ORAL BIOAVAILABILITY OF PROTAC MOLECULES

PROTAC molecules are usually beyond Lipinski's rule of five (Ro5) (Caron et al., 2021) for orally administered drugs, conventionally considered to indicate poor permeability and oral bioavailability. A classical PROTAC molecule harnesses a warhead which is the small molecule ligand of the target protein,



an E3 ligase ligand to recruit the VHL or CRBN subunit of Cullin ring E3 ligase, and a linker that brings the E3 ubiquitin ligase complex in close proximity to the target protein. Linkers of PROTAC molecules not only have a great influence on the degradation efficiency and selectivity of the target protein as previously reviewed (Cyrus et al., 2011; Zagidullin et al., 2020), but also had a profound impact on the *in vivo* PK profile of PROTACs, as shown in the cases of Androgen Receptor degraders and SMARCA2/4 degraders (Xiang et al., 2021; Kofink et al., 2022).

## Linker Rigidification to Improve the Oral Bioavailability of PROTAC

In castration-resistant prostate cancer (CRPC), the progression of the disease is uncontrolled despite the low testosterone level, due to AR (androgen receptor) amplification and hypersensitivity, AR mutations, and intra-tumoral androgen production (Chandrasekar et al., 2015). In resistance development, AR antagonists could also be switched to agonists after treatment with inhibitors (Culig et al., 1999). Degradation offers new opportunities to tackle these problems with the event-driven pharmacological mechanism (Salami and Crews 2017). **ARV-110**, an orally available AR PROTAC developed by Arvinas Inc., is currently a Phase II clinical trial for the treatment of metastatic castration-resistant prostate cancer. With the success of **ARV-110**, Wang and coworkers achieved an orally available AR PROTAC by linker rigidification with a CRBN E3 recruiting ligand. **ARD-69** (Figure 4A) is a potent AR PROTAC with an enzalutamide analog as an AR binder and a rigid linker connected with the optimized VHL ligand (X. Han et al., 2019). **ARD-69**, with molecular weight >1000, calculated TPSA (topological polar surface area) = 197 and ClogP = 8 respectively, was administered intraperitoneal in the *in vivo* PD study. By changing the E3 recruiting element to thalidomide, the molecule **ARD-2542** induced efficient *in vitro* degradation of AR, since both VHL and CRBN are expressed ubiquitously and could induce efficient degradation of AR. Although with significantly reduced molecular weight, calculated TPSA and ClogP, **ARD-2542** exhibited a low plasma concentration of about 17 ng/ml after 1 h of oral administration at 10 mpk in a mouse pharmacokinetics study. Changing the linear linker to rigid piperazine and azetidines, **ARD-2582** plasma concentration in mice was increased with C<sub>max</sub> at 1140 ng/ml after oral administration at 5 mpk. The oral bioavailability increased to 51% in mice (Xiang et al., 2021).

## Solution Conformation of PROTAC Impacts the Permeability

SMARCA2 and SMARCA4 are close homologs as a component of the SWI/SNF complex, involved in chromatin remodeling and repair (Mashtalir et al., 2018; Chetty and Serra 2020). In SMARCA4-deficient cancer, selectively targeting SMARCA2 would be a potential synthetic lethal therapeutic method to treat cancer (Hoffman et al., 2014). SMARCA2 and SMARCA4 share 73.6% of protein sequence identity by EMBOS Needle pairwise sequence

alignment (Madeira et al., 2019), containing both ATP-dependent helicase domain and bromodomain (BD) domain. Small molecule inhibitors of the bromodomain developed so far inhibit the bromodomain of both SMARCA2 and SMARCA4 (Theodoulou et al., 2016). Additionally, the ATP-dependent helicase function of SMARCA2 is not targeted by the bromodomain inhibitor. An orally available SMARCA2 selective degrader would have potential therapeutic value over small molecule inhibitors. **ACBI2** (Figure 4B) was reported by Kofink and coworkers to be SMARCA2 selective PROTAC with improved oral bioavailability over PROTAC **10** (Figure 4B) via a minor change of the linker (Kofink et al., 2022). The PROTAC **10**, with a five-carbon chain to link a SMARCA2/4 BD inhibitor and a VHL E3 ligase ligand, turned out to be a SMARCA2/4 degrader with only 4.3% oral bioavailability in mouse pharmacokinetic studies. The poor oral bioavailability was attributed to its poor permeability as indicated by the high efflux ratio from an *in vitro* Caco-2 permeability test. Introducing a methyl group to the full carbon chain to generate **ACBI2**, dramatically reduced the efflux ratio and thus increased the oral bioavailability to 22%. MD (Molecular Dynamics) simulation and NOE (Nuclear Overhauser effect) NMR spectroscopy were carried out to elucidate the link between conformational restraint and reduced efflux ratio. **ACBI2** was found to have reduced TPSA by MD simulation compared to PROTAC **10**. NOE is usually observed in NMR experiments between protons close in space. Long-range NOE observed in **ACBI2** but not PROTAC **10** indicates that **ACBI2** adopts a more constrained solution structure, which explains the reduced efflux ratio. For PROTAC with a constrained structure, macrocyclization could be a design strategy. In a case reported by Testa and coworkers, macrocyclization of **MZ1** leads to a 12-fold loss of binding to BRD4, however, the comparable cellular degradation activity to **MZ1** may indicate increased cell permeability (Testa et al., 2020). Because of the unique properties of bRo5 molecules, new descriptors such as EPSA and ChameLogD (Ermondi et al., 2020; Caron et al., 2021) have been introduced to take dynamic intramolecular hydrogen bond (dIMHB) into consideration for better correlation of the physicochemical properties of PROTACs with Caco-2 cell permeability profiles.

## DRUG RESISTANCE IN TARGETED PROTEIN DEGRADATION

One of the advantages of PROTAC is in overcoming some of the resistance mechanisms to traditional targeted therapies (Burke et al., 2022), represented by AR PROTAC ARV-110 to address metastatic castration-resistant prostate cancer (mCRPC) (Salami and Crews 2017; Halford, 2021; Mullard 2021). Acquired drug resistance quite often occurs during the use of clinical small molecule inhibitors or antagonists, such as T790M and C797S mutation of EGFR conferred drug resistance induced by EGFR inhibitors (Thress et al., 2015). Although the resistance could be addressed by developing third- or fourth generations of EGFR inhibitors, new drug resistance will emerge. PROTAC technology has shown certain advantages in overcoming drug resistance against cancer drug targets due to the degradation of target proteins with reduced evolutionary pressure of target mutations (Shibata et al., 2017; Burslem et al., 2018; Burslem

et al., 2019; Flanagan et al., 2019; Cheng et al., 2020; Robbins et al., 2020; Liu et al., 2021; Robbins et al., 2021). However, new mechanisms of drug resistance may occur (Zhang L. et al., 2019). Several research teams have revealed the vulnerabilities of UPS using siRNA-based loss-of-function screening (Ottis et al., 2019), resistance mutations by CRISPR-suppressor scanning (Gosavi et al., 2022), and potential acquired resistance mechanism against degraders by whole-exome sequencing in degrader selected cells lines (Zhang L. et al., 2019). The study of acquired resistance was carried out in SKM1, MV4; 11, LNCaP, and OVCAR8 cell lines. Resistance cell lines were selected after 4 months of treatment with BET PROTACs. The two AML cell lines (SKM-1 and MV4; 11) and the prostate cancer cell line (LNCaP) were much more sensitive to the compounds' treatment compared with the ovarian cancer cell line OVCAR8. No stable resistant clones were obtained from SKM-1, MV4; 11, and LNCaP cell lines. The resistant clones from the BET PROTAC insensitive OVCAR8 cell line were further validated. The genomic and transcriptional analysis indicated that resistance to VHL-based BET PROTAC was caused by CUL2 loss due to multiple genetic alterations at the CUL2 locus; the resistance to CRBN-based BET PROTAC was due to chromosomal CRBN gene deletion. PROTAC is usually applied to the cancer cell lines highly dependent on the UPS system for therapeutic purposes, therefore the probability of acquired resistance due to loss of function of E3 ubiquitin ligase is small. Although there is no reported PROTAC resistance in the clinic yet, with more degraders approaching clinical trial, it is important to look for new cancer cell line essential E3 ligases for precision medicine.

## Perspective

In cells, DNA, RNA, and proteins are the key elements at the foundation of biological complexity, forming the backbone of what Francis Crick in 1957 termed the "Central Dogma" of molecular biology. However, according to Stuart Schreiber, there is a missing link in the network of Central Dogma: small molecules. Small molecules have critical roles at all levels of biological complexity and yet remain orphans of the Central Dogma (Schreiber 2005). Small molecule perturbation of protein functions has contributed a profound part to modern small molecule drug discovery (Beck et al., 2022). In addition to individual protein targeting by small molecules, chemically-induced proximity by heterobifunctional small molecules could redirect the biological processes of protein homeostasis. Targeted protein degrader is the type of induced-proximity molecule which targets POI for the posttranslational modification (PTM) of ubiquitination and subsequent proteasomal degradation (Figure 5). Protein homeostasis is regulated by many other types of

PTMs (Uversky 2013), including but not limited to phosphorylation, acetylation, SUMOylation, hydroxylation, farnesylation, glycosylation, and ADP-ribosylation. These PTMs of proteins regulate protein life span, protein cellular location, and protein function. Small molecules targeting the protein homeostasis by inducing PTM beyond ubiquitination may impact small molecule drug development in the pharmaceutical industry. PROTAC will offer the opportunity to target traditionally undruggable targets by an event-driven pharmacological approach, opening new therapeutic modalities (Békés et al., 2022) to expand the druggable space. Inspired by PROTAC, induced-proximity drug modalities including LYTAC (Banik et al., 2020), AUTAC (Takahashi et al., 2019), ATTEC (Z. Li et al., 2020), PhosTAC (Yamazoe et al., 2020; Chen P.-H. et al., 2021), DUBTAC (Kanner et al., 2020; Henning et al., 2021) and RIBOTAC (Haniff et al., 2020; P.; Zhang et al., 2021), are of interest to the pharmaceutical industry, allowing targeting of disease-causing proteins and even RNAs. This has resulted in the emergence of new start-up companies in the targeted protein degradation area (<https://www.ventureradar.com/startup/Protein%20Degradation>). The developments within Cryo-EM and X-ray crystallography technology, CRISPR-Cas technology-based assay development, and increasing sequencing capability will additionally strengthen the structure-guided design and multi-omics approach to designing small molecule therapeutics with induced-proximity mechanisms.

## AUTHOR CONTRIBUTIONS

LQ, HD, and JW conceived the content, drafted the manuscript, and contributed to the final version of the manuscript.

## FUNDING

This work was primarily supported by the National Natural Science Foundation of China (Grant No. U1532269 to JW) and the Ministry of Science and Technology of China (Grant No. 2016YFA0400900 to JW). This work was also supported by the High Magnetic Field Laboratory of Anhui Province.

## ACKNOWLEDGMENTS

The authors thank Feng Ren for critically reading and editing the manuscript.

## REFERENCES

- Anderson, N. A., Cryan, J., Ahmed, A., Dai, H., McGonagle, G. A., Rozier, C., et al. (2020). Selective CDK6 Degradation Mediated by Cereblon, VHL, and Novel IAP-Recruiting PROTACs. *Bioorg. Med. Chem. Lett.* 30 (9), 127106. doi:10.1016/j.bmcl.2020.127106
- Backus, K. M., Correia, B. E., Lum, K. M., Forli, S., Horning, B. D., González-Páez, G. E., et al. (2016). Proteome-Wide Covalent Ligand Discovery in Native Biological Systems. *Nature* 534 (7608), 570–574. doi:10.1038/nature18002
- Banik, S. M., Pedram, K., Wisnovsky, S., Ahn, G., Riley, N. M., and Bertozzi, C. R. (2020). Lysosome-targeting Chimaeras for Degradation of Extracellular Proteins. *Nature* 584 (7820), 291–297. doi:10.1038/s41586-020-2545-9
- Bar-Peled, L., Kemper, E. K., Suciu, R. M., Vinogradova, E. V., Backus, K. M., Horning, B. D., et al. (2017). Chemical Proteomics Identifies Druggable Vulnerabilities in a Genetically Defined Cancer. *Cell* 171 (3), 696–709.e23. doi:10.1016/j.cell.2017.08.051
- Beck, H., Härter, M., Haß, B., Schmeck, C., and Baerfacker, L. (2022). Small Molecules and Their Impact in Drug Discovery: A Perspective on the Occasion of the 125th Anniversary of the Bayer Chemical Research Laboratory. *Drug Discov. Today* 27 (6), 1560–1574. doi:10.1016/j.drudis.2022.02.015

- Békés, M., Langley, D. R., and Crews, C. M. (2022). PROTAC Targeted Protein Degradation: The Past Is Prologue. *Nat. Rev. Drug Discov.* 21 (3), 181–200. doi:10.1038/s41573-021-00371-6
- Bondeson, D. P., Smith, B. E., Burslem, G. M., Buhimschi, A. D., Hines, J., Jaime-Figueroa, S., et al. (2018). Lessons in PROTAC Design from Selective Degradation with a Promiscuous Warhead. *Cell. Chem. Biol.* 25 (1), 78–87. e5. doi:10.1016/j.chembiol.2017.09.010
- Bulatov, E., and Ciulli, A. (2015). Targeting Cullin-RING E3 Ubiquitin Ligases for Drug Discovery: Structure, Assembly and Small-Molecule Modulation. *Biochem. J.* 467 (3), 365–386. doi:10.1042/BJ20141450
- Burke, M. R., Smith, A. R., and Zheng, G. (2022). Overcoming Cancer Drug Resistance Utilizing PROTAC Technology. *Front. Cell. Dev. Biol.* 10 (April), 872729. doi:10.3389/fcell.2022.872729
- Burslem, G. M., and Crews, C. M. (2020). Proteolysis-Targeting Chimeras as Therapeutics and Tools for Biological Discovery. *Cell.* 181 (1), 102–114. doi:10.1016/j.cell.2019.11.031
- Burslem, G. M., Schultz, A. R., Bondeson, D. P., Eide, C. A., Savage Stevens, S. L., Druker, B. J., et al. (2019). Targeting BCR-ABL1 in Chronic Myeloid Leukemia by PROTAC-Mediated Targeted Protein Degradation. *Cancer Res.* 79 (18), 4744–4753. doi:10.1158/0008-5472.CAN-19-1236
- Burslem, G. M., Smith, B. E., Lai, A. C., Jaime-Figueroa, S., McQuaid, D. C., Bondeson, D. P., et al. (2018). The Advantages of Targeted Protein Degradation over Inhibition: An RTK Case Study. *Cell. Chem. Biol.* 25 (1), 67–77. e3. doi:10.1016/j.chembiol.2017.09.009
- Caron, G., Kihlberg, J., Goetz, G., Ratkova, E., Poongavanam, V., and Ermondi, G. (2021). Steering New Drug Discovery Campaigns: Permeability, Solubility, and Physicochemical Properties in the BR05 Chemical Space. *ACS Med. Chem. Lett.* 12 (1), 13–23. doi:10.1021/acsmchemlett.0c00581
- Chandrasekar, T., Yang, J. C., Gao, A. C., and Evans, C. P. (2015). Mechanisms of Resistance in Castration-Resistant Prostate Cancer (CRPC). *Transl. Androl. Urol.* 4 (3), 365–380. doi:10.3978/j.issn.2223-4683.2015.05.02
- Chen, P.-H., Hu, Z., An, E., Okeke, I., Zheng, S., Luo, X., et al. (2021). Modulation of Phosphoprotein Activity by Phosphorylation Targeting Chimeras (PhosTACs). *ACS Chem. Biol.* 16 (12), 2808–2815. doi:10.1021/acscchembio.1c00693
- Chen, X., Crew, A., Flanagan, J., Sheryl, G., Royal, H., III, Marcia, M., et al. (2021). Methods of Treating Breast Cancer with Tetrahydronaphthalene Derivatives as Estrogen Receptor Degradation. United States Patent Application Publication US 2021/0060008 A1.
- Cheng, M., Yu, X., Lu, K., Xie, L., Wang, L., Meng, F., et al. (2020). Discovery of Potent and Selective Epidermal Growth Factor Receptor (EGFR) Bifunctional Small-Molecule Degradation. *J. Med. Chem.* 63 (3), 1216–1232. doi:10.1021/acs.jmedchem.9b01566
- Chetty, R., and Serra, S. (2020). SMARCA Family of Genes. *J. Clin. Pathol.* 73 (5), 257–260. doi:10.1136/jclinpath-2020-206451
- Chung, C.-w., Dai, H., Fernandez, E., Tinworth, C. P., Churcher, I., Cryan, J., et al. (2020). Structural Insights into PROTAC-Mediated Degradation of Bcl-XL. *ACS Chem. Biol.* 15 (9), 2316–2323. doi:10.1021/acscchembio.0c00266
- Crew, A., Snyder, L., Wang, J., Royal, H., III, and Marcia, M. (2021). Methods of Treating Prostate Cancer. United States Patent Application Publication US 2021/0113557 A1.
- Cromm, P. M., and Crews, C. M. (2017). Targeted Protein Degradation: From Chemical Biology to Drug Discovery. *Cell. Chem. Biol.* 24 (9), 1181–1190. doi:10.1016/j.chembiol.2017.05.024
- Culig, Z., Hoffmann, J. M., Erdel, M., Eder, I. E., Hobisch, A., Hittmair, A., et al. (1999). Switch from Antagonist to Agonist of the Androgen Receptor Blocker Bicalutamide Is Associated with Prostate Tumour Progression in a New Model System. *Br. J. Cancer* 81 (2), 242–251. doi:10.1038/sj.bjc.6690684
- Cyrus, K., Wehenkel, M., Choi, E.-Y., Han, H.-J., Lee, H., Swanson, H., et al. (2011). Impact of Linker Length on the Activity of PROTACs. *Mol. Biosyst.* 7 (2), 359–364. doi:10.1039/C0MB00074D
- Dale, B., Cheng, M., Park, K.-S., Kaniskan, H. Ü., Xiong, Y., and Jin, J. (2021). Advancing Targeted Protein Degradation for Cancer Therapy. *Nat. Rev. Cancer* 21 (10), 638–654. doi:10.1038/s41568-021-00365-x
- De Nardo, D., Balka, K. R., Cardona Gloria, Y., Rao, V. R., Latz, E., and Masters, S. L. (2018). Interleukin-1 Receptor-Associated Kinase 4 (IRAK4) Plays a Dual Role in Myddosome Formation and Toll-like Receptor Signaling. *J. Biol. Chem.* 293 (39), 15195–15207. doi:10.1074/jbc.RA118.003314
- Dong, G., Ding, Y., He, S., and Sheng, C. (2021). Molecular Glues for Targeted Protein Degradation: From Serendipity to Rational Discovery. *J. Med. Chem.* 64 (15), 10606–10620. doi:10.1021/acs.jmedchem.1c00895
- Donovan, K. A., An, J., Nowak, R. P., Yuan, J. C., Fink, E. C., Berry, B. C., et al. (2018). Thalidomide Promotes Degradation of SALL4, a Transcription Factor Implicated in Duane Radial Ray Syndrome. *ELife* 7 (August), e38430. doi:10.7554/eLife.38430
- Du, X., Volkov, O. A., Czerwinski, R. M., Tan, H., Huerta, C., Morton, E. R., et al. (2019). Structural Basis and Kinetic Pathway of RBM39 Recruitment to DCAF15 by a Sulfonamide Molecular Glue E7820. *Structure* 27 (11), 1625–1633. e3. doi:10.1016/j.str.2019.10.005
- Elumalai, P., and Arunakaran, J. (2014). Review on Molecular and Chemopreventive Potential of Nimboide in Cancer. *Genomics Inf.* 12 (4), 156. doi:10.5808/GI.2014.12.4.156
- Ermondi, G., Vallaro, M., Goetz, G., Shalaeva, M., and Caron, G. (2020). Updating the Portfolio of Physicochemical Descriptors Related to Permeability in the beyond the Rule of 5 Chemical Space. *Eur. J. Pharm. Sci.* 146 (April), 105274. doi:10.1016/j.ejps.2020.105274
- Filippakopoulos, P., Qi, J., Picaud, S., Shen, Y., Smith, W. B., Fedorov, O., et al. (2010). Selective Inhibition of BET Bromodomains. *Nature* 468 (7327), 1067–1073. doi:10.1038/nature09504
- Flanagan, J., Qian, Y., Gough, S., Andreoli, M., Bookbinder, M., Cadelina, G., et al. (2019). “Abstract P5-04-18: ARV-471, an Oral Estrogen Receptor PROTAC Degradation for Breast Cancer,” in Poster Session Abstracts, P5-04-18-P5-04-18 (American Association for Cancer Research). doi:10.1158/1538-7445.SABCS18-P5-04-18
- Gadd, M. S., Testa, A., Lucas, X., Chan, K.-H., Chen, W., Lamont, D. J., et al. (2017). Structural Basis of PROTAC Cooperative Recognition for Selective Protein Degradation. *Nat. Chem. Biol.* 13 (5), 514–521. doi:10.1038/nchembio.2329
- Gao, S., Wang, S., and Song, Y. (2020). Novel Immunomodulatory Drugs and Neo-Substrates. *Biomark. Res.* 8 (1), 2. doi:10.1186/s40364-020-0182-y
- Gosavi, P. M., Ngan, K. C., Yeo, M. J. R., Su, C., Li, J., Lue, N. Z., et al. (2022). Profiling the Landscape of Drug Resistance Mutations in Neosubstrates to Molecular Glue Degradation. *ACS Cent. Sci.* 8, 417–429. doi:10.1021/acscentsci.1c01603
- Guenette, R. G., Yang, S. W., Min, J., Pei, B., and Potts, P. R. (2022). Target and Tissue Selectivity of PROTAC Degradation. *Chem. Soc. Rev.* 51 (10), 101039, D2CS00200K. doi:10.1039/D2CS00200K
- Halford, B. (2021). Arvinas Unveils PROTAC Structures. *C&EN*, 5. doi:10.47287/cen-09914-scicon1
- Han, T., Gorski, M., Gaskill, N., Capota, E., Kim, J., Ting, T. C., et al. (2017). Anticancer Sulfonamides Target Splicing by Inducing RBM39 Degradation via Recruitment to DCAF15. *Science* 356 (6336), eaal3755. doi:10.1126/science.aal3755
- Han, X., Wang, C., Qin, C., Xiang, W., Fernandez-Salas, E., Yang, C.-Y., et al. (2019). Discovery of ARD-69 as a Highly Potent Proteolysis Targeting Chimera (PROTAC) Degradation of Androgen Receptor (AR) for the Treatment of Prostate Cancer. *J. Med. Chem.* 62 (2), 941–964. doi:10.1021/acs.jmedchem.8b01631
- Haniff, H. S., Tong, Y., Liu, X., Chen, J. L., Suresh, B. M., Andrews, R. J., et al. (2020). Targeting the SARS-CoV-2 RNA Genome with Small Molecule Binders and Ribonuclease Targeting Chimera (RIBOTAC) Degradation. *ACS Cent. Sci.* 6 (10), 1713–1721. doi:10.1021/acscentsci.0c00984
- Hansen, J. D., Correa, M., Alexander, M., Nagy, M., Huang, D., Sapienza, J., et al. (2021). CC-90009: A Cereblon E3 Ligase Modulating Drug that Promotes Selective Degradation of GSPT1 for the Treatment of Acute Myeloid Leukemia. *J. Med. Chem.* 64 (4), 1835–1843. doi:10.1021/acs.jmedchem.0c01489
- Hansen, J. D., Correa, M., Nagy, M. A., Alexander, M., Plantevin, V., Grant, V., et al. (2020). Discovery of CRBN E3 Ligase Modulator CC-92480 for the Treatment of Relapsed and Refractory Multiple Myeloma. *J. Med. Chem.* 63 (13), 6648–6676. doi:10.1021/acs.jmedchem.9b01928
- He, Y., Koch, R., Budamagunta, V., Lv, D., Khan, S., Zhang, X., et al. (2019). DT2216, a BCL-XL Proteolysis Targeting Chimera (PROTAC), Is a Potent Anti T-Cell Lymphoma Agent that Does Not Induce Significant Thrombocytopenia. *Blood* 134 (Suppl. ment\_1), 303. doi:10.1182/blood-2019-125820
- He, Y., Koch, R., Budamagunta, V., Zhang, P., Zhang, X., Khan, S., et al. (2020). DT2216, a Bcl-xL-specific Degradation Is Highly Active against Bcl-xL-dependent T Cell Lymphomas. *J. Hematol. Oncol.* 13 (1), 95. doi:10.1186/s13045-020-00928-9



- Henderson, J., He, M., Good, A., and Andrew, P. (2020). Tricyclic Degraders of Ikaros and Aiolos. *WO 2020/210630 A1*.
- Hennessy, E. J., Parker, A. E., and O'Neill, L. A. J. (2010). Targeting Toll-like Receptors: Emerging Therapeutics? *Nat. Rev. Drug Discov.* 9 (4), 293–307. doi:10.1038/nrd3203
- Henning, N. J., Boike, L., Spradlin, J. N., Ward, C. C., Belcher, B., Brittain, S. M., et al. (2021). Deubiquitinase-Targeting Chimeras for Targeted Protein Stabilization. *Prepr. Biochem.* doi:10.1101/2021.04.30.441959
- Hoffman, G. R., Rahal, R., Buxton, F., Xiang, K., McAllister, G., Frias, E., et al. (2014). Functional Epigenetics Approach Identifies BRM/SMARCA2 as a Critical Synthetic Lethal Target in BRG1-Deficient Cancers. *Proc. Natl. Acad. Sci. U.S.A.* 111 (8), 3128–3133. doi:10.1073/pnas.1316793111
- Huang, H.-T., Dobrovolsky, D., Paulk, J., Yang, G., Weisberg, E. L., Doctor, Z. M., et al. (2018). A Chemoproteomic Approach to Query the Degradable Kinome Using a Multi-Kinase Degradator. *Cell. Chem. Biol.* 25 (1), 88–99.e6. doi:10.1016/j.chembiol.2017.10.005
- Imaide, S., Riching, K. M., Makukhin, N., Vetma, V., Whitworth, C., Hughes, S. J., et al. (2021). Trivalent PROTACs Enhance Protein Degradation via Combined Avidity and Cooperativity. *Nat. Chem. Biol.* 17 (11), 1157–1167. doi:10.1038/s41589-021-00878-4
- Ishida, T., and Ciulli, A. (2021). E3 Ligase Ligands for PROTACs: How They Were Found and How to Discover New Ones. *SLAS Discov.* 26 (4), 484–502. doi:10.1177/2472555220965528
- Ishikawa, M., Tomoshige, S., Demizu, Y., and Naito, M. (2020). Selective Degradation of Target Proteins by Chimeric Small-Molecular Drugs, PROTACs and SNIPERs. *Pharmaceuticals* 13 (4), 74. doi:10.3390/ph13040074
- Ito, T., Ando, H., Suzuki, T., Ogura, T., Hotta, K., Imamura, Y., et al. (2010). Identification of a Primary Target of Thalidomide Teratogenicity. *Science* 327 (5971), 1345–1350. doi:10.1126/science.1177319
- Itoh, Y., Ishikawa, M., Naito, M., and Hashimoto, Y. (2010). Protein Knockdown Using Methyl Bestatin–Ligand Hybrid Molecules: Design and Synthesis of Inducers of Ubiquitination-Mediated Degradation of Cellular Retinoic Acid-Binding Proteins. *J. Am. Chem. Soc.* 132 (16), 5820–5826. doi:10.1021/ja100691p
- Kanner, S. A., Shuja, Z., Choudhury, P., Jain, A., and Colecraft, H. M. (2020). Targeted Deubiquitination Rescues Distinct Trafficking-Deficient Ion Channelopathies. *Nat. Methods* 17 (12), 1245–1253. doi:10.1038/s41592-020-00992-6
- Kannt, A., and Đikić, I. (2021). Expanding the Arsenal of E3 Ubiquitin Ligases for Proximity-Induced Protein Degradation. *Cell. Chem. Biol.* 28 (7), 1014–1031. doi:10.1016/j.chembiol.2021.04.007
- Khan, S., Zhang, X., Lv, D., Zhang, Q., He, Y., Zhang, P., et al. (2019). A Selective BCL-XL PROTAC Degradator Achieves Safe and Potent Antitumor Activity. *Nat. Med.* 25 (12), 1938–1947. doi:10.1038/s41591-019-0668-z
- Kim, T. W., Staschke, K., Bulek, K., Yao, J., Peters, K., Oh, K.-H., et al. (2007). A Critical Role for IRAK4 Kinase Activity in Toll-like Receptor-Mediated Innate Immunity. *J. Exp. Med.* 204 (5), 1025–1036. doi:10.1084/jem.20061825
- Kofink, C., Trainor, N., Mair, B., Wöhrle, S., Wurm, M., Mischerikow, N., et al. (2022). A Selective and Orally Bioavailable VHL-Recruiting PROTAC Achieves SMARCA2 Degradation *In Vivo*. *Prepr. Chem.* doi:10.26434/chemrxiv-2022-q63s3
- Kozicka, Z., and Thomä, N. H. (2021). Haven't Got a Glue: Protein Surface Variation for the Design of Molecular Glue Degradators. *Cell. Chem. Biol.* 28 (7), 1032–1047. doi:10.1016/j.chembiol.2021.04.009
- Krönke, J., Udeshi, N. D., Narla, A., Grauman, P., Hurst, S. N., McConkey, M., et al. (2014). Lenalidomide Causes Selective Degradation of IKZF1 and IKZF3 in Multiple Myeloma Cells. *Science* 343 (6168), 301–305. doi:10.1126/science.1244851
- Lai, A. C., and Crews, C. M. (2017). Induced Protein Degradation: An Emerging Drug Discovery Paradigm. *Nat. Rev. Drug Discov.* 16 (2), 101–114. doi:10.1038/nrd.2016.211
- Lai, A. C., Toure, M., Hellerschmied, D., Salami, J., Jaime-Figueroa, S., Ko, E., et al. (2016). Modular PROTAC Design for the Degradation of Oncogenic BCR-ABL. *Angew. Chem. Int. Ed.* 55 (2), 807–810. doi:10.1002/anie.201507634
- Law, R. P., Nunes, J., Chung, C. w., Bantscheff, M., Buda, K., Dai, H., et al. (2021). Discovery and Characterisation of Highly Cooperative FAK-Degrading PROTACs. *Angew. Chem. Int. Ed.* 60 (43), 23327–23334. doi:10.1002/anie.202109237
- Leissing, T. M., Luh, L. M., and Cromm, P. M. (2020). Structure Driven Compound Optimization in Targeted Protein Degradation. *Drug Discov. Today Technol.* 37 (December), 73–82. doi:10.1016/j.ddtec.2020.11.005
- Li, D., Yu, X., Kottur, J., Gong, W., Zhang, Z., Storey, A. J., et al. (2022). Discovery of a Dual WDR5 and Ikaros PROTAC Degradator as an Anti-cancer Therapeutic. *Oncogene*. doi:10.1038/s41388-022-02340-8
- Li, Z., Zhu, C., Ding, Y., Fei, Y., and Lu, B. (2020). ATTEC: A Potential New Approach to Target Proteinopathies. *Autophagy* 16 (1), 185–187. doi:10.1080/15548627.2019.1688556
- Liu, H., Ding, X., Liu, L., Mi, Q., Zhao, Q., Shao, Y., et al. (2021). Discovery of Novel BCR-ABL PROTACs Based on the Cereblon E3 Ligase Design, Synthesis, and Biological Evaluation. *Eur. J. Med. Chem.* 223 (November), 113645. doi:10.1016/j.ejmech.2021.113645
- Lv, D., Pal, P., Liu, X., Jia, Y., Thummuri, D., Zhang, P., et al. (2021). Development of a BCL-xL and BCL-2 Dual Degradator with Improved Anti-leukemic Activity. *Nat. Commun.* 12 (1), 6896. doi:10.1038/s41467-021-27210-x
- Lv, L., Chen, P., Cao, L., Li, Y., Zeng, Z., Cui, Y., et al. (2020). Discovery of a Molecular Glue Promoting CDK12-DBB1 Interaction to Trigger Cyclin K Degradation. *ELife* 9 (August), e59994. doi:10.7554/eLife.59994
- Madeira, F., Park, Y. M., Lee, J., Buso, N., Gur, T., Madhusoodanan, N., et al. (2019). The EMBL-EBI Search and Sequence Analysis Tools APIs in 2019. *Nucleic Acids Res.* 47 (W1), W636–W641. doi:10.1093/nar/gkz268
- Mainolfi, N., Nan, J., Arthur, K., Weiss, J., Zhang, Y., and Zheng, X. (2020). IRAK Degradators and Uses Thereof. World Intellectual Property Organization International Bureau WO 2020/113233 A1.
- Mashtalir, N., D'Avino, A. R., Michel, B. C., Luo, J., Pan, J., Otto, J. E., et al. (2018). Modular Organization and Assembly of SWI/SNF Family Chromatin Remodeling Complexes. *Cell* 175 (5), 1272–1288.e20. doi:10.1016/j.cell.2018.09.032
- Mayor-Ruiz, C., Bauer, S., Brand, M., Kozicka, Z., Siklos, M., Imrichova, H., et al. (2020). Rational Discovery of Molecular Glue Degradators via Scalable Chemical Profiling. *Nat. Chem. Biol.* 16 (11), 1199–1207. doi:10.1038/s41589-020-0594-x
- Mohamad Anuar, N. N., Nor Hisam, N. S., Liew, S. L., and Ugusman, A. (2020). Clinical Review: Navitoclax as a Pro-apoptotic and Anti-fibrotic Agent. *Front. Pharmacol.* 11 (November), 564108. doi:10.3389/fphar.2020.564108
- Mullard, A. (2021). Targeted Protein Degradators Crowd into the Clinic. *Nat. Rev. Drug Discov.* 20 (4), 247–250. doi:10.1038/d41573-021-00052-4
- Nalawansa, D. A., and Crews, C. M. (2020). PROTACs: An Emerging Therapeutic Modality in Precision Medicine. *Cell. Chem. Biol.* 27 (8), 998–1014. doi:10.1016/j.chembiol.2020.07.020
- Nasveschuk, C., Zeid, R., Yin, N., Jackson, K., Veits, G., and Moustakin, M. (2022). Compounds for Targeted Degradation of Brd9. United States Patent Application Publication US 2022/0098194 A1.
- Ottis, P., Palladino, C., Thienger, P., Britschgi, A., Heichinger, C., Berrera, M., et al. (2019). Cellular Resistance Mechanisms to Targeted Protein Degradation Converge toward Impairment of the Engaged Ubiquitin Transfer Pathway. *ACS Chem. Biol.* 9b00525. October, aacschembio. doi:10.1021/acschembio.9b00525
- Ottis, P., Toure, M., Cromm, P. M., Ko, E., Gustafson, J. L., and Crews, C. M. (2017). Assessing Different E3 Ligases for Small Molecule Induced Protein Ubiquitination and Degradation. *ACS Chem. Biol.* 12 (10), 2570–2578. doi:10.1021/acschembio.7b00485
- Paiva, S.-L., and Crews, C. M. (2019). Targeted Protein Degradation: Elements of PROTAC Design. *Curr. Opin. Chem. Biol.* 50 (June), 111–119. doi:10.1016/j.cbpa.2019.02.022
- Pfäffle, H. N., Wang, M., Gheorghiu, L., Ferraiolo, N., Greninger, P., Borgmann, K., et al. (2013). EGFR-activating Mutations Correlate with a Fanconi Anemia-like Cellular Phenotype that Includes PARP Inhibitor Sensitivity. *Cancer Res.* 73 (20), 6254–6263. doi:10.1158/0008-5472.CAN-13-0044
- Picard, C., Casanova, J.-L., and Puel, A. (2011). Infectious Diseases in Patients with IRAK-4, MyD88, NEMO, or IkBα Deficiency. *Clin. Microbiol. Rev.* 24 (3), 490–497. doi:10.1128/CMR.00001-11
- Riching, K. M., Mahan, S., Corona, C. R., McDougall, M., Vasta, J. D., Robers, M. B., et al. (2018). Quantitative Live-Cell Kinetic Degradation and Mechanistic Profiling of PROTAC Mode of Action. *ACS Chem. Biol.* 13 (9), 2758–2770. doi:10.1021/acschembio.8b00692
- Robbins, D. W., Kelly, A., Tan, M., McIntosh, J., Wu, J., Konst, Z., et al. (2020). Nx-2127, a Degradator of BTK and IMiD Neosubstrates, for the Treatment of



- B-Cell Malignancies. *Blood* 136 (Suppl. 1), 34. doi:10.1182/blood-2020-141461
- Robbins, D. W., Noviski, M., Rountree, R., Tan, M., Brathaban, N., Ingallinera, T., et al. (2021). Nx-5948, a Selective Degradator of BTK with Activity in Preclinical Models of Hematologic and Brain Malignancies. *Blood* 138 (Suppl. 1), 2251. doi:10.1182/blood-2021-147473
- Sakamoto, K. M., Kim, K. B., Kumagai, A., Mercurio, F., Crews, C. M., and Deshaies, R. J. (2001). Protacs: Chimeric Molecules that Target Proteins to the Skp1-Cullin-F Box Complex for Ubiquitination and Degradation. *Proc. Natl. Acad. Sci. U.S.A.* 98 (15), 8554–8559. doi:10.1073/pnas.141230798
- Salami, J., and Crews, C. M. (2017). Waste Disposal-An Attractive Strategy for Cancer Therapy. *Science* 355 (6330), 1163–1167. doi:10.1126/science.aam7340
- Samarasinghe, K. T. G., and Crews, C. M. (2021). Targeted Protein Degradation: A Promise for Undruggable Proteins. *Cell. Chem. Biol.* 28 (7), 934–951. doi:10.1016/j.chembiol.2021.04.011
- Schneekloth, A. R., Puchault, M., Seop, T., Tae, H. S., and Crews, C. M. (2008). Targeted Intracellular Protein Degradation Induced by a Small Molecule: En Route to Chemical Proteomics. *Bioorg. Med. Chem. Lett.* 18 (22), 5904–5908. doi:10.1016/j.bmcl.2008.07.114
- Schneider, M., Radoux, C. J., Hercules, A., Ochoa, D., Dunham, I., Zalmas, L.-P., et al. (2021). The PROTACtable Genome. *Nat. Rev. Drug Discov.* 20 (10), 789–797. doi:10.1038/s41573-021-00245-x
- Scholes, N. S., Mayor-Ruiz, C., and Winter, G. E. (2021). Identification and Selectivity Profiling of Small-Molecule Degradators via Multi-Omics Approaches. *Cell. Chem. Biol.* 28 (7), 1048–1060. doi:10.1016/j.chembiol.2021.03.007
- Schreiber, S. L. (2005). Small Molecules: The Missing Link in the Central Dogma. *Nat. Chem. Biol.* 1 (2), 64–66. doi:10.1038/nchembio0705-64
- Schreiber, S. L. (2021). The Rise of Molecular Glues. *Cell.* 184 (1), 3–9. doi:10.1016/j.cell.2020.12.020
- Schwinn, M. K., Steffen, L. S., Zimmerman, K., Wood, K. V., and Machleidt, T. (2020). A Simple and Scalable Strategy for Analysis of Endogenous Protein Dynamics. *Sci. Rep.* 10 (1), 8953. doi:10.1038/s41598-020-65832-1
- Shibata, N., Miyamoto, N., Nagai, K., Shimokawa, K., Sameshima, T., Ohoka, N., et al. (2017). Development of Protein Degradation Inducers of Oncogenic BCR - ABL Protein by Conjugation of ABL Kinase Inhibitors and IAP Ligands. *Cancer Sci.* 108 (8), 1657–1666. doi:10.1111/cas.13284
- Slabicki, M., Kozicka, Z., Petzold, G., Li, Y.-D., Manojkumar, M., Bunker, R. D., et al. (2020). The CDK Inhibitor CR8 Acts as a Molecular Glue Degradator that Depletes Cyclin K. *Nature* 585 (7824), 293–297. doi:10.1038/s41586-020-2374-x
- Smith, B. E., Wang, S. L., Jaime-Figueroa, S., Harbin, A., Wang, J., Hamman, B. D., et al. (2019). Differential PROTAC Substrate Specificity Dictated by Orientation of Recruited E3 Ligase. *Nat. Commun.* 10 (1), 131. doi:10.1038/s41467-018-08027-7
- Souers, A. J., Levenson, J. D., Boghaert, E. R., Ackler, S. L., Catron, N. D., Chen, J., et al. (2013). ABT-199, a Potent and Selective BCL-2 Inhibitor, Achieves Antitumor Activity while Sparing Platelets. *Nat. Med.* 19 (2), 202–208. doi:10.1038/nm.3048
- Spradlin, J. N., Hu, X., Ward, C. C., Brittain, S. M., Jones, M. D., Ou, L., et al. (2019). Harnessing the Anti-cancer Natural Product Nimbolide for Targeted Protein Degradation. *Nat. Chem. Biol.* 15 (7), 747–755. doi:10.1038/s41589-019-0304-8
- Takahashi, D., Moriyama, J., Nakamura, T., Miki, E., Takahashi, E., Sato, A., et al. (2019). AUTACs: Cargo-specific Degradators Using Selective Autophagy. *Mol. Cell.* 76 (5), 797–810.e10. doi:10.1016/j.molcel.2019.09.009
- Tanaka, M., Roberts, J. M., Seo, H.-S., Souza, A., Paulk, J., Scott, T. G., et al. (2016). Design and Characterization of Bivalent BET Inhibitors. *Nat. Chem. Biol.* 12 (12), 1089–1096. doi:10.1038/nchembio.2209
- Testa, A., Hughes, S. J., Lucas, X., Wright, J. E., and Ciulli, A. (2020). Structure-Based Design of a Macrocyclic PROTAC. *Angew. Chem. Int. Ed.* 59 (4), 1727–1734. doi:10.1002/anie.201914396
- Theodoulou, N. H., Tomkinson, N. C., Prinjha, R. K., and Humphreys, P. G. (2016). Clinical Progress and Pharmacology of Small Molecule Bromodomain Inhibitors. *Curr. Opin. Chem. Biol.* 33 (August), 58–66. doi:10.1016/j.cbpa.2016.05.028
- Thress, K. S., Pawletz, C. P., Felip, E., Cho, B. C., Stetson, D., Dougherty, B., et al. (2015). Acquired EGFR C797S Mutation Mediates Resistance to AZD9291 in Non-small Cell Lung Cancer Harboring EGFR T790M. *Nat. Med.* 21 (6), 560–562. doi:10.1038/nm.3854
- Tomoshige, S., and Ishikawa, M. (2021). PROTACs and Other Chemical Protein Degradation Technologies for the Treatment of Neurodegenerative Disorders. *Angew. Chem. Int. Ed.* 60 (7), 3346–3354. doi:10.1002/anie.202004746
- Uversky, V. N. (2013). “Posttranslational Modification,” in *Brenner's Encyclopedia of Genetics*. Editors K. Hughes and S. Maloy (Elsevier), 425–30, 425–430. doi:10.1016/B978-0-12-374984-0.01203-1
- Weiss, M., Zheng, X., and Xiao, Z. (2022)n.d. Double Degraders and Uses There of. World Intellectual Property Organization International Bureau WO/2022/087216.
- Weerapana, E., Wang, C., Simon, G. M., Richter, F., Khare, S., Dillon, M. B. D., et al. (2010). Quantitative Reactivity Profiling Predicts Functional Cysteines in Proteomes. *Nature* 468 (7325), 790–795. doi:10.1038/nature09472
- Xiang, W., Zhao, L., Han, X., Qin, C., Miao, B., McEachern, D., et al. (2021). Discovery of ARD-2585 as an Exceptionally Potent and Orally Active PROTAC Degradator of Androgen Receptor for the Treatment of Advanced Prostate Cancer. *J. Med. Chem.* 64 (18), 13487–13509. doi:10.1021/acs.jmedchem.1c00900
- Yamazoe, S., Tom, J., Fu, Y., Wu, W., Zeng, L., Sun, C., et al. (2020). Heterobifunctional Molecules Induce Dephosphorylation of Kinases-A Proof of Concept Study. *J. Med. Chem.* 63 (6), 2807–2813. doi:10.1021/acs.jmedchem.9b01167
- Yang, Y., Shaffer, A. L., Emre, N. C. T., Ceribelli, M., Zhang, M., Wright, G., et al. (2012). Exploiting Synthetic Lethality for the Therapy of ABC Diffuse Large B Cell Lymphoma. *Cancer Cell.* 21 (6), 723–737. doi:10.1016/j.ccr.2012.05.024
- Zagidullin, A., Milyukov, V., Rizvanov, A., and Bulatov, E. (2020). Novel Approaches for the Rational Design of PROTAC Linkers. *Explor. Target. Anti-Tumor Ther.* 1 (5), 381–390. doi:10.37349/etat.2020.00023
- Zengerle, M., Chan, K.-H., and Ciulli, A. (2015). Selective Small Molecule Induced Degradation of the BET Bromodomain Protein BRD4. *ACS Chem. Biol.* 10 (8), 1770–1777. doi:10.1021/acschembio.5b00216
- Zhang, L., Riley-Gillis, B., Vijay, P., and Shen, Y. (2019). Acquired Resistance to BET-PROTACs (Proteolysis-Targeting Chimeras) Caused by Genomic Alterations in Core Components of E3 Ligase Complexes. *Mol. Cancer Ther.* 18 (7), 1302–1311. doi:10.1158/1535-7163.MCT-18-1129
- Zhang, P., Liu, X., Abegg, D., Tanaka, T., Tong, Y., Benhamou, R. I., et al. (2021). Reprogramming of Protein-Targeted Small-Molecule Medicines to RNA by Ribonuclease Recruitment. *J. Am. Chem. Soc.* 143 (33), 13044–13055. doi:10.1021/jacs.1c02248
- Zhang, X., Crowley, V. M., Wucherpfennig, T. G., Dix, M. M., and Cravatt, B. F. (2019). Electrophilic PROTACs that Degrade Nuclear Proteins by Engaging DCAF16. *Nat. Chem. Biol.* 15 (7), 737–746. doi:10.1038/s41589-019-0279-5
- Zheng, M., Huo, J., Gu, X., Wang, Y., Wu, C., Zhang, Q., et al. (2021). Rational Design and Synthesis of Novel Dual PROTACs for Simultaneous Degradation of EGFR and PARP. *J. Med. Chem.* 64 (11), 7839–7852. doi:10.1021/acs.jmedchem.1c00649

**Conflict of Interest:** LQ is employed by Insilico Medicine Ltd.

The remaining authors declare that the research was conducted in the absence of any commercial or financial relationships that could be construed as a potential conflict of interest.

**Publisher's Note:** All claims expressed in this article are solely those of the authors and do not necessarily represent those of their affiliated organizations, or those of the publisher, the editors, and the reviewers. Any product that may be evaluated in this article, or claim that may be made by its manufacturer, is not guaranteed or endorsed by the publisher.

Copyright © 2022 Qin, Dai and Wang. This is an open-access article distributed under the terms of the Creative Commons Attribution License (CC BY). The use, distribution or reproduction in other forums is permitted, provided the original author(s) and the copyright owner(s) are credited and that the original publication in this journal is cited, in accordance with accepted academic practice. No use, distribution or reproduction is permitted which does not comply with these terms.



## OPEN ACCESS

## EDITED BY

Siddhartha Das,  
University of Maryland, College Park,  
United States

## REVIEWED BY

Zidan Zhang,  
University of Texas at Austin,  
United States  
Rajarshi Chakrabarti,  
Indian Institute of Technology Bombay,  
India

## \*CORRESPONDENCE

Stephen J. Paddison,  
spaddison@utk.edu

## SPECIALTY SECTION

This article was submitted to Theoretical  
and Computational Chemistry,  
a section of the journal  
Frontiers in Chemistry

RECEIVED 29 June 2022

ACCEPTED 14 July 2022

PUBLISHED 19 August 2022

## CITATION

Zhu Z and Paddison SJ (2022),  
Perspective: Morphology and ion  
transport in ion-containing polymers  
from multiscale modeling  
and simulations.  
*Front. Chem.* 10:981508.  
doi: 10.3389/fchem.2022.981508

## COPYRIGHT

© 2022 Zhu and Paddison. This is an  
open-access article distributed under  
the terms of the [Creative Commons  
Attribution License \(CC BY\)](#). The use,  
distribution or reproduction in other  
forums is permitted, provided the  
original author(s) and the copyright  
owner(s) are credited and that the  
original publication in this journal is  
cited, in accordance with accepted  
academic practice. No use, distribution  
or reproduction is permitted which does  
not comply with these terms.

# Perspective: Morphology and ion transport in ion-containing polymers from multiscale modeling and simulations

Zhengkao Zhu and Stephen J. Paddison\*

Department of Chemical and Biomolecular Engineering, University of Tennessee, Knoxville, TN, United States

Ion-containing polymers are soft materials composed of polymeric chains and mobile ions. Over the past several decades they have been the focus of considerable research and development for their use as the electrolyte in energy conversion and storage devices. Recent and significant results obtained from multiscale simulations and modeling for proton exchange membranes (PEMs), anion exchange membranes (AEMs), and polymerized ionic liquids (polyILs) are reviewed. The interplay of morphology and ion transport is emphasized. We discuss the influences of polymer architecture, tethered ionic groups, rigidity of the backbone, solvents, and additives on both morphology and ion transport in terms of specific interactions. Novel design strategies are highlighted including precisely controlling molecular conformations to design highly ordered morphologies; tuning the solvation structure of hydronium or hydroxide ions in hydrated ion exchange membranes; turning negative ion-ion correlations to positive correlations to improve ionic conductivity in polyILs; and balancing the strength of noncovalent interactions. The design of single-ion conductors, well-defined supramolecular architectures with enhanced one-dimensional ion transport, and the understanding of the hierarchy of the specific interactions continue as challenges but promising goals for future research.

## KEYWORDS

ion-containing polymers, specific interactions, morphology, ion transport, multiscale modeling, simulations

## Introduction

Ion-containing polymers are an emerging class of materials including ionic polymers with counter ions and nonionic/neutral polymers doping with ionic material of low molecular weight, combining the advantages of a polymer matrix with mobile ions. They exhibit versatile and attractive properties and have attracted considerable interest as solid electrolytes for a variety of applications. They selectively conduct ions but not electrons. They are broadly used in energy conversion and storage devices, electrodialysis for water treatment, and solar-driven desalination. Next-generation ion-conducting polymeric materials are being developed for fuel cells, lithium batteries, electrolyzers, and other

electrochemical devices. In fuel cells, a fuel such as: hydrogen, methane, or methanol is efficiently converted into electrical energy with the aid of catalysts with the typical byproduct being only water. This contrasts with solid-state Li-ion battery electrolytes where there must be no water present because of the reactive materials used in the electrodes. Thus, the presence of water is a crucial parameter in distinguishing the electrolytes suitable for fuel cells from those employed in some batteries. Differences in these materials including the coupled dynamics of the mobile ions and the chains naturally lead to different ion transport mechanisms and consequently design principles.

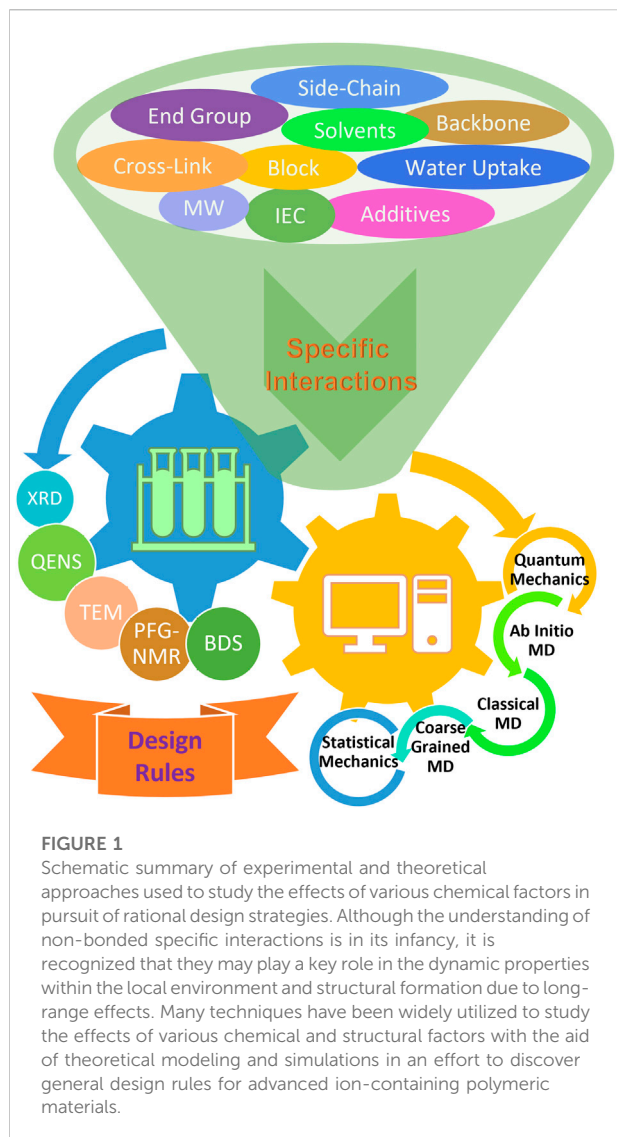
Over the past several decades, three main types of polymeric electrolytes: proton exchange membranes (PEMs), anion exchange membranes (AEMs), and polymerized ionic liquids (polyILs) have gained fundamental understanding and hence improvement from experimental work and theoretical studies (Kusoglu and Weber, 2017; Elabd, 2019; Wang and Park, 2020; Ma and Olvera de la Cruz, 2021; Shen et al., 2021). PEMs were commercialized to some extent because of their high proton conductivity and first use in the Gemini space program in the early 1960s (Kusoglu and Weber, 2017). However, the requirement of expensive noble metal catalysts impedes the application in the real world and provokes additional research into alternative PEMs. AEMs have also attracted significant attention as an alternative to PEMs in fuel cells due to the use of non-noble transition metals as electrocatalysts under the high OH<sup>-</sup> environment even though their conductivity is typically much lower (Dekel, 2018; Elabd, 2019). Thus, substantial effort has been expended to investigate the mechanisms underlying ion transport and improve the performance of AEMs. In view of the use of polymer electrolytes in batteries, polyILs, in which each repeating unit may be charged as opposed to ionomers that contain a relatively small percentage of charged units, are promising alternatives to organic liquid-based electrolytes that are toxic, flammable, and have a limited electrochemical stability window, due to their generally good mechanical stability, flexibility, improved safety, and durability. However, it remains challenging to enhance the ion conductivity of polyILs to a sufficient degree for electrochemical applications due to the sluggish local dynamics of the polymer chains, low dielectric constant, and small fraction of mobile ions in this class of materials (Bocharova and Sokolov, 2020; Son and Wang, 2020).

The performance of ion-containing materials is influenced by a variety of tunable factors, including: the functionalized end-groups; composition of block copolymers; polarity and rigidity of polymer backbones; molecular weight; conformational asymmetry; etc. Such factors provide an opportunity to tailor the structural and dynamical properties of the materials, although they bring challenges to identifying broadly applicable design rules. We hypothesize that the origins of how these factors affect the molecular packing and the dynamics of ions are mainly from the relatively weak specific

interactions in comparison to covalent bonds as they play a key role in block copolymers (Wang and Park, 2020). This provokes several important but as of yet unanswered questions: How do these specific interactions affect the properties of an ion-containing polymer? Do the specific interactions have synergistic or uncooperative effects? Which interactions are the most dominant or important? Hence, the development of more advanced ion-containing polymers depends on a better understanding of specific interactions of polymer/polymer, polymer/solvent, acidic or basic group/solvent, and fixed-/counter-ions. These interactions including hydrogen bonding, ion-dipole interactions, Coulombic, and acid-base interactions may govern molecular arrangements, selectivity of ion uptake and transport, and ion transference.

In determining the role of the specific interactions on the performance of a material, experimental techniques have been employed to study the structural and dynamical properties of ion-containing polymers at various length and time scales. For example, small angle x-ray scattering (SAXS), wide angle x-ray scattering (WAXS), small angle neutron scattering (SANS) have been widely applied to deduce hydrated morphology (Gebel and Diat, 2005), and quasi-elastic neutron scattering (QENS) (Perrin et al., 2007; Melchior and Jalarvo, 2019) and pulsed field gradient NMR (PFG-NMR) (Münchinger and Kreuer, 2019) to measure the self-diffusion coefficient of the ions and water molecules, and broadband dielectric spectroscopy (BDS) (Giffin et al., 2013) to compute the ion conductivity. Other techniques have been brought to bear including infrared (IR) spectroscopy (Zimudzi and Hickner, 2016), Raman spectroscopy (Meek et al., 2020), atomic force microscopy (AFM) (Economou et al., 2015), and transmission electron microscopy (TEM) (Allen et al., 2015; Zhang et al., 2021a), with which one can obtain a description of the molecular interactions, direct images of the surface and 3-D morphology.

Although advances in technology provide powerful and robust tools to elucidate important information on these materials, modeling and simulations are clearly necessary to complement experiment findings and guide further experimental directions with the purpose of enhancing our understanding of morphology formation and ion transport mechanisms as well as the development of improved materials for electrochemical applications. Given the complex morphological and dynamic behavior of ion-containing polymers, multiscale theoretical approaches are required to describe characteristics over a wide range of temporal and spatial scales. Quantum mechanical calculations and *ab initio* molecular dynamics (AIMD) simulations are regarded as highly accurate methods to gain information on the static and dynamic properties allowing for both the electronic and nuclear degrees of freedom, which are critical when studying proton/hydroxide ion diffusion since the associated proton transfer involves the breaking and forming of covalent bonds. However, the use of AIMD is limited to access small time and length scales. To



expand the systems up to the size of a hydrophilic pore or domain, multistate empirical valence bond (MS-EVB) (Chen et al., 2016) and reactive ReaxFF (Zhang and Van Duin, 2015) methodologies may be employed to study both vehicular diffusion and structural diffusion in hydrated ion exchange membranes, but it is still challenging to capture the solvation structures of proton/hydroxide ions and to transfer the force fields to different chemical structures. When dealing with nonreactive systems such as polyILs, classical molecular dynamics (MD) simulations are suitable in investigating the structure and ion transport at time scales up to microseconds. The deficiency is the difficulty in allowing for polarization effects, which is resolved by either developing a computationally expensive polarizable force field (Bedrov et al., 2019) or simply scaling the full charges by some fraction. The latter was recently proven to be capable of capturing polarizability

effects on both structural and dynamic properties of polyILs based on the comparison of the results obtained from the scaled partial charge force field and the Drude oscillator polarizable force field (Zhang et al., 2022). Although classical MD simulations are capable of predicting transport phenomena and structures within a small region, due to the limitations of time ( $<1 \mu\text{s}$ ) and length ( $<10 \text{ nm}$ ) scales, coarse-grained MD and dissipative particle dynamics (DPD) simulations are widely utilized in modeling phase separations within membranes that typically require large length scale of 10–200 nm (Zhu et al., 2022). To capitalize on both experimental and theoretical strategies, a tight feedback loop of modeling and simulations with a broad spectrum of experimental techniques will serve as a protocol for the rational design of functional materials with optimal properties (Figure 1).

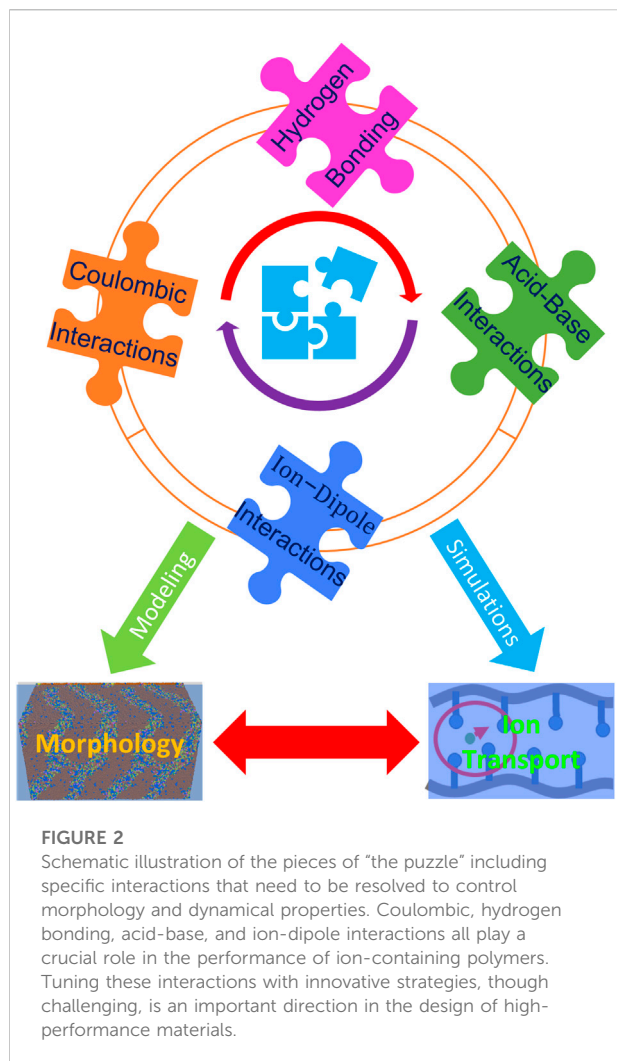
This Perspective describes recent and significant results regarding the specific interactions, morphology, and ion transport within ion-containing polymers. Emphasis is put on the interplay of morphology and ion transport. Specifically, we discuss the influences of polymer architecture, choice of the tethered ionic group, the rigidity of the polymer backbone, presence of a solvent, and additives on the morphology and ion transport. Finally, we highlight the challenges and prospects in advancing the performance of ion-containing materials, including the effects of specific interactions, the design of single-ion conductors, and well-defined supramolecular architectures with one dimensional enhanced ion transport channels.

## Specific interactions

Through decades of research into ion-containing polymers, important fundamental understanding of structure-property relationships has been elucidated. However, challenges remain, including addressing the following issues: how to retain water at high temperatures to improve water-mediated ion transport; how to synergistically achieve mechanical stability and fast ion transport; how to facilitate decoupling of the ion transport from segmental dynamics or viscosity; and how to organize tethered ionic groups to facilitate efficient transport of ions. To resolve these issues, the specific interactions have been thought to play a crucial role in governing the microstructure and dynamics of the ions in such materials, which is a promising perspective for future research and development.

These interactions include hydrogen bonding, acid-base interactions, Coulombic interactions, ionic interactions, and  $\pi$ - $\pi$  stacking (which may govern molecular arrangements). In view of the need to devise rational design rules, a hierarchy of intermolecular interactions should be fundamentally investigated through theoretical computations and simulations tightly coupled with advanced experimental strategies. This information should lead to insight into tailoring properties by





balancing the specific interactions between fragments or molecules. It is a challenging but promising target to resolve this “puzzle” of the various specific interactions within ion-containing polymers in order to guide the design of high-performance materials (Figure 2).

Hydrogen bonding is the most well known and thoroughly investigated interaction and has led to an adequate understanding of the nature of bonding and functionality. It plays a crucial role in determining the water uptake in ion exchange polymer systems and the miscibility of polymer chains. The combination of *in situ* FTIR spectroscopy, molecular dynamics simulations, and statistical thermodynamics methods has been employed to investigate the effects of these interactions on the local structures of a hydrated poly(ether imide)(PEI) system (De Nicola et al., 2017). The authors (De Nicola et al., 2017) concluded that water molecules tended to form “bridges” connecting two successive intrachain carbonyl groups of PEI through

hydrogen bonding and water-water interactions led to a “second shell” hydration layer.

The impact of acid-base interactions between sulfonic acid groups in a PEM and incorporated basic groups on the physicochemical properties of a membrane was investigated by synthesizing novel multi-block PEMs with three different basic groups (i.e. benzoxazolium, benzotriazolium, and propylamino groups) (Sui et al., 2019). The results reveal that a PEM with benzotriazolium (with an intermediate  $pK_a$ ) had the highest proton conductivity although the excessive water absorption and the membrane swelling were suppressed in all three membranes. It was reasoned that the moderate basicity forms a “protonation-deprotonation” loop between the hydrophobic and hydrophilic moieties reducing the proton transfer barrier. Strong basicity was thought to neutralize the membrane acidity thereby lowering the concentration of dissociated (i.e., mobile) protons.

Ionic interactions between fixed ionic groups and mobile ions have an influence on the ionomer’s local structure, hydration, ion transport within the ionic domain, and even the polymer chain segmental motion/dynamics. This type of interaction is strongly dependent on the hydration level since their effect is shielded and diminished as the water content is increased. The micromorphology of block copolymers was tailored by casting with various counter-cations (i.e.  $H^+$ ,  $Li^+$ ,  $K^+$ ,  $Cs^+$ ,  $TEA^+$ , and  $Ca^{2+}$ ), which acted as either a block compatibilizer or a block separator by tuning the ionic interactions (Nguyen et al., 2020). The choice of counter-cations can vary the phase-separated morphologies from disordered to highly ordered, and thereby the conductivity of the membrane. Shi et al. (Shi et al., 2020) studied the role of ionic interactions in the deformation and fracture behavior in model perfluorosulfonic acid (PFSA) membranes. They determined that the ionic crosslinks formed between the cations and the sulfonate anions of the polymer enhance the alignment and stretching of the polymer matrix and the effect decreases with the cation radius. Another theoretical study (Ghosh and Chakrabarti, 2016) showed that small sodium ions favorably reside around the sulfonate groups due to electrostatic interactions while bulky tetramethylammonium ions tend to stay near the hydrophobic backbones because of strong hydrophobic interactions in Nafion membranes.

Recently, these specific interactions between fixed-ions and counter-ions were also confirmed in Nafion, Aquivion, sulfonated polystyrene, sulfonated polyether ketone, sulfonated poly(phenylene sulfone), poly(acrylic acid) and ammonium functionalized poly(phenylene oxide) ionomers (Münchinger and Kreuer, 2019). The experimental observation of the different degrees of localizing  $Li^+$  and  $Cs^+$  by the dissolved ionomers suggests that the ion partitioning seems to be controlled by the acidity of the fixed ionic groups but not electrostatics. Explicitly, the ratio of  $[Li^+]/[Cs^+]$  decreases with increasing acidity, which ascribes to stronger stabilization of  $Cs^+$  in comparison to  $Li^+$ . The diffusivity of  $Cs^+$  decreases as the

acidity of the fixed ionic group increases, while the trend is inversed for  $\text{Li}^+$  before the onset of counter-ion binding, similar to the behavior of  $\text{H}^+$ . It was concluded that the strongest specific interaction exists between the most acidic fixed functional groups and cations with the highest polarizability and lowest electronegativity.

In summary, there exists several interactions between the various molecules and ions in these materials. It is worth noting that  $\pi$ - $\pi$  stacking interactions play a crucial role in promoting micro- or nano-phase separation and stabilizing porous structures. However, it is still at nascent stage especially in ion-containing materials since these interactions require delicate description of  $\pi$  systems allowing for electron density. It is crucial to elucidate how the interactions affect the morphology and dynamics, which are discussed in the following sections. To develop the desired properties, we have to balance the interactions *via* various approaches. For instance, the addition of nanoparticles into polymeric materials can reduce the hydrogen bonding between the cations and anions, improving the dissociation of ions by balancing the interaction of nanoparticles with cations and anions, which has been proven by the FTIR and the Raman spectroscopy (Pundir et al., 2018).

## Morphology

Understanding nanophase separation (i.e., characteristics of the hydrophobic domain in comparison to the ion conducting phase) in ion-containing polymeric systems is fundamentally important in the rational design of highly conducting electrolytes with mechanically and chemically stable integrity under diverse operating conditions. Generally, these polymers possess hydrophobic and hydrophilic components, which provoke phase separation of ionic domains from the polymeric matrix when exposed to polar solvents. Morphological differences are governed by various factors, such as the dissimilarity between pendant acidic or basic groups and the backbone, equivalent weight, side-chain chemistry, degree of hydration, *etc.* The underlying fundamentals of how these factors affect morphology are of significant interest.

## Hydrated PEM morphology

Phase separation upon hydration enhances the formation of pore networks that provide pathways for the movement of water and ions. The hydrophobic polymer matrix provides dimensional strength. The connectivity of the pore network is key to promoting long-range ion transport, which ultimately determines conductivity. An increase in hydration may improve phase separation by establishing percolating pore networks, but high-water content may also cause the swelling

of membranes resulting in the reduction of mechanical stability and constraint in the operating temperature below the boiling point of water. It is recognized that an increase in temperature enhances reaction kinetics and reduces the poisoning of the catalysts (Kusoglu and Weber, 2017). Therefore, it is desired, on one side, to form well-connected channels in membranes at low relative humidity; on the other side, to retain water in the ionic domains of membranes at higher operating temperatures. Nevertheless, there are various factors including polymeric architecture, degree of functionalization, pendant ionic groups, counterions, and hydration level, which play a complex role in the hydrated morphology of ion-containing membranes. It is impractical to conduct a case-by-case study to elucidate the interplay of the multitude of these factors. Moreover, the model-dependent interpretation of scattering data cannot provide precise geometries of the multiscale domains, which has been extensively discussed for perfluorosulfonic acid ionomers (Kusoglu and Weber, 2017).

Given these challenges of unambiguously determining the morphology, theoretical approaches have been resorted to providing insight into the quantification of morphology for ion-containing membranes. Coarse grained MD and DPD simulations are widely utilized in modeling phase separations within membranes that typically requires long-time relaxation and a large length scale of 10–200 nm (Dorenbos, 2017a; Dorenbos, 2017b; Sepehr et al., 2017; Liu et al., 2018a; Dong et al., 2018b; Liu et al., 2018b; Wang R. et al., 2019; Clark et al., 2019; Dorenbos, 2019; Lee, 2019; Luo and Paddison, 2019; Zhu et al., 2019; Chen C. et al., 2020; Luo et al., 2020a; Dorenbos, 2020; Lee, 2020; Sevinis Ozbulut et al., 2020; Zhu et al., 2022). To further quantify the morphology including the size, shape, and connectivity of the ionic domains, which cannot be extracted from the peaks obtained by scattering methods, cluster analysis including distance-based and density-based algorithms is a powerful tool to provide a plethora of information on water domain size, shape, and connectivity from the trajectory of a MD or DPD simulation, which will be described in this section. The latter is capable of characterizing the local regions of high density and isolating clusters that have some overlap (Clark et al., 2019; Sorte et al., 2019).

Nafion is the prototypical perfluorosulfonic acid (PFSA) ionomer and has been subject to extensive investigation (Yandrasits et al., 2019). Recently, Liu and coworkers examined the scaling behavior of the conformations and dynamics of mesoscopic models of hydrated Nafion membranes as well as a polymer melt. The authors compared the results obtained from five distinct DPD parameterizations of hydrated Nafion including one based on electronic structure calculations and others mapped from Flory-Huggins parameters along with varying harmonic spring bonded interactions (Liu et al., 2018b). The effect of the chain stiffness was also investigated in the dry and hydrated Nafion systems. The increase in chain stiffness gives rise to larger polymer end-to-

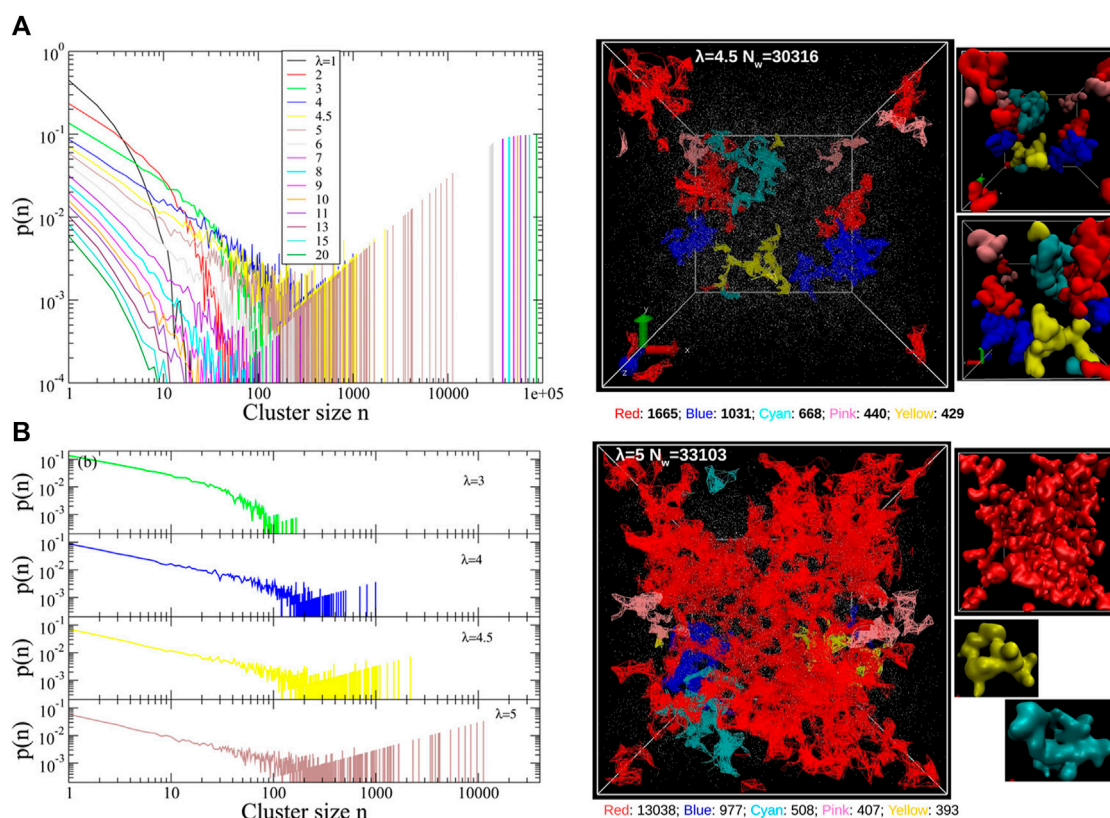


FIGURE 3

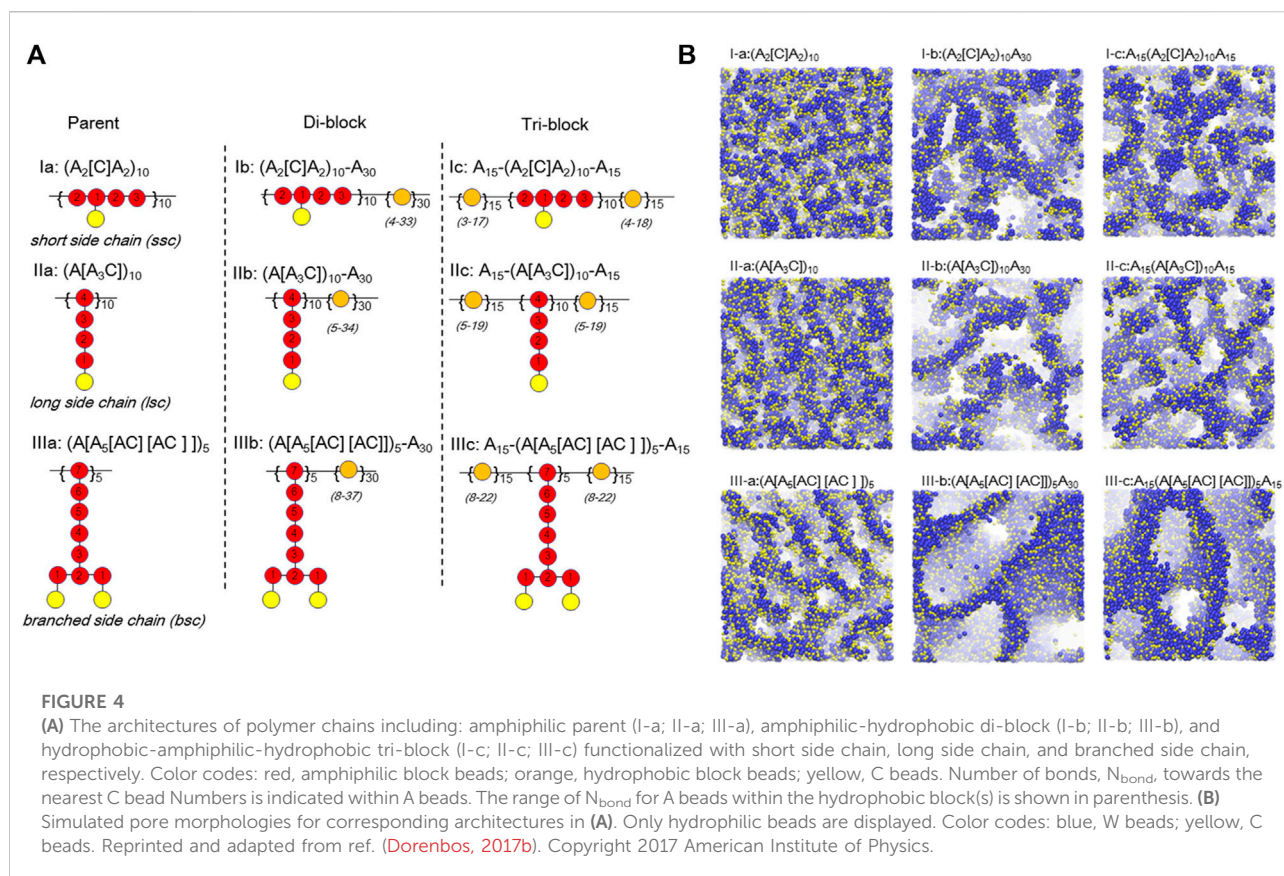
(A) Quantitative cluster size distribution from a distance-based cluster analysis algorithm for various hydration levels. (B) Cluster size distributions underlining the percolation threshold at  $\lambda = 5$ . Snapshots of water clusters for  $\lambda = 4.5$  (no percolating clusters) and  $\lambda = 5$  (percolating clusters) color-coded by the unique cluster IDs on the right panel. Reprinted and adapted with permission from ref. (Liu et al., 2018a). Copyright 2018 American Chemical Society.

end relaxation time along with slow segmental dynamics due to the stronger back scattering in the velocity autocorrelation function and larger residence time within the “cage” formed by the nearest neighbors. To demonstrate detailed information concerning the ionic aggregates, quantitative distance-based cluster analysis with realistic microscopic images colored by unique IDs was further developed to provide a wealth of information on water-filled ionic channel size, shape, and connectivity (Liu et al., 2018a). The water cluster size distribution suggests that all five DPD parameterizations of Nafion correctly show a percolating network after a certain degree of hydration (Liu et al., 2018b). The percolation threshold of the water domains in Nafion was determined to occur at a hydration level of 5  $\text{H}_2\text{O}/\text{SO}_3\text{H}$  through direct cluster analysis in contrast to a methodology that derived from radial distribution functions and the Connolly surface analysis (Liu et al., 2018a). Agglomerate of the small water domains is clearly demonstrated *via* this cluster analysis method (shown in Figure 3). These results further demonstrated the validity of a density functional theory (DFT) based parameterization (Sepehr

and Paddison, 2016) to compute the interaction parameters needed for the repulsion interaction in the simulations. This scheme addresses the challenge for the charged beads without reducing the efficiency of the DPD methodology by implicitly considering electrostatic interactions for the charged beads. A non-empirical fragment molecular orbital (FMO) method (Okuwaki et al., 2018a; Okuwaki et al., 2018b) was also developed as a novel scheme to consider polarization and charge transfer between beads. It is interesting to note that DPD is flexible for hydrated ion exchange membranes in terms of parameterization and coupling with smoothed particle hydrodynamics (SPH) (Jorn and Voth, 2012) or a dissociable Morse potential between the protons and the base and/or water beads (Lee et al., 2016; Vishnyakov et al., 2018).

Based on the successful application of DPD simulation on PFSA-type PEMs, there have been several attempts to control the architecture of the backbones and side-chains. Dorenbos (Dorenbos, 2017b) recently constructed three different parent architectures of a backbone by covalently bonding hydrophobic beads ([A]) to: short hydrophilic beads ([C]); long ([A<sub>3</sub>C]) beads;





or symmetrically branched  $A_5[AC][AC]$  side-chains. Subsequently, three di-block copolymers and three tri-block derivatives were modeled by connecting an  $A_{30}$  block (30 hydrophobic A beads) or an  $A_{15}$  block with three different parent architectures as shown in Figure 4A. The results demonstrated that the increase in side-chain length enlarges the pore size for polymers of similar ion exchange capacity (IEC) and that the largest pore size appears in the systems with branched side-chains (Figure 4B). Meanwhile, the author investigated the effects of doping  $(A_2[C])_{10}$  polymers with high IEC into a host polymer of  $A_{30}(A[A_5[AC][AC]])_5$  with a low IEC (Dorenbos, 2017a). These results show that the clearly distinguished pore networks disappear as the ratio of dopant is increased. This suggests that for a low dopant content the small amount of high IEC dopants is situated near well-connected pores formed by the low IEC host polymers, implying that one can increase the overall IEC of the blended membrane without sacrificing the percolated networks by adding a dopant. To further study the influence of designs with hydrophobic side-chains on the connectivity of the water containing domains, Dorenbos correlated the pore connectivity to the average number of bonds separating A from the nearest C ( $N_{bond}^{A-C}$ ) and between nearest C beads ( $N_{bond}^{C-C}$ ) (Dorenbos, 2019; Dorenbos, 2020). It was determined that the

connectivity of the water domains generally increases with increasing  $N_{bond}^{C-C}$  for the cases where  $N_{bond}^{C-C} > N_{bond}^{A-C}(\max)$  and fixed IEC, while the opposite trend occurs for the cases where  $N_{bond}^{C-C} < N_{bond}^{A-C}(\max)$ .

These results show a larger pore size for branched side-chain membranes than single side-chain membranes. Another potential strategy is to utilize multi-acid side-chains to improve the conductivity while retaining the good mechanical properties of the perfluorinated backbone, such as perfluorosulfonic imide side-chain perfluorinated polymers (PFIA) (Kusoglu et al., 2020) and perfluoroalkyl ionene chain-extended ionomers (PFICE) (Su et al., 2019). Compared with the PFSA material, the PFIA demonstrates higher proton conductivity at low hydrations due to both inter- and intra-side-chain interactions. The experimental and simulation results indicate highly ordered backbone configuration and better-dispersed smaller water clusters in PFIA than in PFSA (Kusoglu et al., 2020). Similarly, phase-separated morphology with enhanced local order was revealed by resonant X-ray scattering in both dry and hydrated PFICE ionomers, which improves proton dissociation at low hydration that can be discerned by the DFT-computed spectra of the PFICE side-chain (Su et al., 2019).



In addition to these modifications of the polymeric chemistry, the interactions between polymer segments and solvent molecules also have a strong influence on the aggregate structures. For instance, the aggregate structure of PFSA ionomers can be tuned with different solvents or mixtures of solvents (Welch et al., 2012; Doo et al., 2018). Fully atomistic MD simulations instead of coarse-grained approaches were used to study the effects of solvents (i.e., with dielectric constants,  $\epsilon_r = 2.38\text{--}109$ ) in PFSA ionomer dispersions (Tarokh et al., 2020). The authors introduced a new aggregation phase diagram for Nafion in the various solvents. The ionomer chains are physically cross-linked through strong electrostatic interaction between ionic clusters in low dielectric solvents (i.e.,  $\epsilon_r = 1.41\text{--}42.5$ ), self-assembled into lamella-like aggregates *via* weak hydrophobic interactions in the solvents with intermediate dielectric constant (i.e.,  $\epsilon_r = 42.5\text{--}78$ ), and formed elongated aggregates because of strong hydrophobic interactions in high dielectric solvents (i.e.,  $\epsilon_r \geq 78$ ). Simultaneously, the major deficiencies of a coarse-grained approach were revealed in that the aggregate structure in all solvents obtained from a coarse-grained model is unrealistic due to the fact that the solvent atoms are not explicitly modeled (Doo et al., 2018). More recently, experimental results show that the decrease in the polarity of the solvent increases the swelling of the fluoropolymer resulting in low proton mobility. Alkanes do not change the Nafion structure from its dry state due to the minimal interaction with fluoropolymer backbone and ionic groups (Katzenberg et al., 2021; Shi et al., 2021).

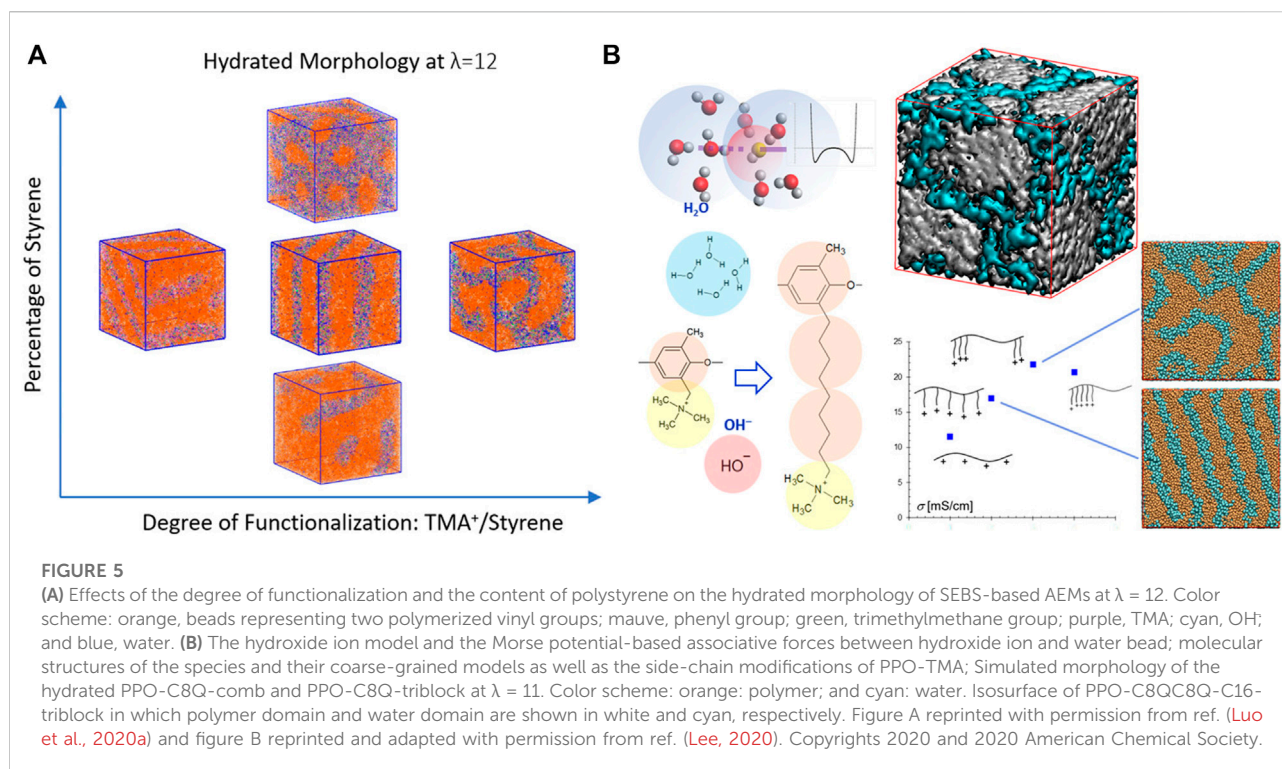
Compared to the pronounced hydrophobic/hydrophilic interactions in PFSA-based membranes, polymers with sulfonated aromatic rings have been explored as promising alternatives for fuel cell applications because they possess a wide variety of tunable chemical structures such as different degrees of sulfonation, various linkers between aromatic rings and fluorinated components of the macromolecules. Specifically, sulfonated Diels-Alder poly(phenylene) (SDAPP) (Abbott and Frischknecht, 2017; Clark et al., 2019; Sorte et al., 2019) and sulfonated poly(ether ether ketone) (sPEEK) (Chen S. et al., 2020) are the focus of many studies aiming at the elucidation of structure-property relationships. Frischknecht et al. (Abbott and Frischknecht, 2017; Clark et al., 2019; Sorte et al., 2019) undertook experimental and theoretical studies to investigate the influence of the degrees of sulfonation and hydration level as well as temperature on the morphology and the dynamic properties of water molecules and protons within SDAPP membranes (Sorte et al., 2019). The isolated hydrophilic clusters were observed at relatively low degrees of hydration and sulfonation and the increase of hydration and/or sulfonation improved the connectivity of the water (Clark et al., 2019). Besides the distance-based cluster analysis, the density-based clustering algorithm was applied to distinguish the local size and shape of the percolated water-containing clusters in particular for overlapped clusters. The clustering results obtained from these

two algorithms demonstrated that the densest clusters were bridged by narrow regions. Furthermore, the relative anisotropy of the shape in these clusters quantitatively showed that the clusters became more spherical with increasing degree of hydration and sulfonation (Abbott and Frischknecht, 2017; Clark et al., 2019).

MD simulations show that sPEEK membranes possess stronger electrostatic interactions between the sulfonate oxygen atoms and hydrated protons leading to much lower hydronium ion diffusivity and lower delocalization of free  $\text{H}_3\text{O}^+$  when compared to Nafion (Wang R. et al., 2019). The structure of hydrated hydronium ions deforms to adapt to the narrow regions of hydrophilic pores. The confinement effect on the diffusion of  $\text{H}_2\text{O}$  and  $\text{H}_3\text{O}^+$  is affected by the hydration level and the formation of conductive channels. It was concluded that weak nanophase separation and poor connected ionic domains in sPEEK membrane contribute to lower proton conductivity in comparison to Nafion. Okuwaki et al. (Okuwaki et al., 2018a) drew the same conclusion from FMO-DPD simulations of sPEEK and Nafion membranes.

As mentioned above, one conventional strategy is the blending of different types of polymers to enhance the chemical and physical properties of the materials. However, additional intermolecular interactions within the blends make the prediction of properties challenging. Recently, Ozbulut et al. studied the morphology of polymer blends of highly branched poly(arylene ether sulfone) (HBPAES) and linear poly(arylene ether sulfone) (LPAES) *via* both experiments and DPD simulations (Sevinis Ozbulut et al., 2020). The branched topology of HBPAES was tuned by changing the distance between the branch positions. The results revealed the miscibility of highly branched and linear polymers that was not influenced by the separation between the branch positions, which was further confirmed by the distribution of the radii of gyration for the pure polymers and the blend systems. It is also interesting to note that the increased strain at the break values is attributed to the anchoring regions rather than the strength of the non-bonded interactions in the blend.

Another promising route to advance the performance of non-PFSA membranes is to design highly ordered morphologies for efficient proton transport. This requires a fundamental understanding of how to balance the specific interactions within these materials. Recently, well-controlled chain folding has been achieved by Trigg and coworkers (Trigg et al., 2018) through precisely tethering sulfonic acid groups into the linear polyethylene backbone every twenty-first carbon atom to obtain highly ordered conductive layers for fast proton diffusion. The classical MD simulations further demonstrated that the diffusivities of water and hydronium ions were enhanced in the well-ordered water channels compared to that in the amorphous morphology. It was



suggested that this state-of-the-art strategy may be applied for cation/anion transport as well as anhydrous proton transport by modifying the chemistry of functional groups.

## Hydrated AEM morphology

In addition to PEMs, extensive investigations were performed on the hydrated morphology of polystyrene-*b*-poly(ethylene-co-butylene)-*b*-polystyrene (SEBS)-based AEMs (Sepehr et al., 2017; Luo and Paddison, 2019; Zhu et al., 2019; Luo et al., 2020a). The results indicated that the quaternary ammonium-functionalized SEBS AEMs phase separates into a functionalized polystyrene-rich phase and a hydrophobic phase. The water content clearly controls the morphology which evolves from perforated and interconnected lamella to perfect lamellae and then to disordered bicontinuous structures as the water content is increased (Sepehr et al., 2017). Reducing the functionalization and/or the percentage of styrene delays the formation of largely interconnected water networks (Figure 5A), but the increase in the styrene content facilitates the percolation to occur at a lower hydration level (Luo et al., 2020a). An alkyl spacer ( $C_4H_8$ ) grafted between the backbone and functional QA group as the linker, tail, and as both a linker and a tail strongly affect the morphology, the domain spacing of the hydrophilic phase, the distribution of the backbone-TMA<sup>+</sup> distance, and the water clusters. Specifically, additional spacers may postpone the

occurrence of a percolated water domain and thereby evenly distribute the water (Luo and Paddison, 2019). The choice of the functional group (trimethylammonium, methylimidazolium, or trimethylphosphonium) was found to have minimum effect on the backbone structures while moderately affecting water distribution. Compared to the cationic groups, the associated anion seemed to have a greater impact on the size of the exclusive water domains (Zhu et al., 2019).

The influences of alkyl chain length, side-chain structure, hydrophilic and hydrophobic spacers, and distribution and aggregation of the side-chains on the microstructure of polyphenylene oxide tetramethylammonium (PPO-TMA) as well as SEBS-based AEMs were systematically explored with DPD simulations by Lee and coworkers (Lee, 2019; Lee, 2020; Lee, 2021). The comparison of PPO-based and SEBS-based triblock copolymers shows that the latter possesses more hydrophobic and flexible backbones, in which nano-segregation occurs even without any side-chain modifications. The comb-like structure distribution of the side-chains contributed to the formation of a lamellar structure. Short side-chains acting as spacers helped to break the percolated water domain into smaller domains as the cationic groups were close to PPO backbones, indicating the larger impact of an alkyl spacer than an alkyl extender. A lamellar morphology may be transformed into an interconnected water network by tailoring the pendant length or composition of the side-chains as shown in Figure 5B (Lee, 2020). Adding hydrophobic alkyl

spacers was observed to enhance the phase separation and promote the formation of large water clusters. However, the strong hydrophobicity of the side-chains (either alkyl spacers or alkyl extenders) resulted in substantial protrusion into the water phase, which formed bottlenecks within the transport pathways retarding anion mobility. These results suggested that the less hydrophobic alkoxy spacers may help to form narrower but more connected channels (Lee, 2019). In contrast, adding hydrophilic spacers impedes the transport of hydroxide ions as well as water, ascribing to the stretched side-chains dispersing in the hydrophilic phase (Lee, 2021). This drawback may be resolved by altering multi-cation side-chain designs, which facilitate the formation of largely connected ion-conducting pathways. Coarse-grained MD simulations of two poly(ether ether ketone) (PEEK) membranes (Chen S. et al., 2020), in which the side-chains consist of either one or two quaternary ammonium (QA) groups, indicate that slightly smaller and better interconnected hydrophilic clusters occur in two QA than in single QA membranes and that the increase of grafting degree results in the decrease of cluster sizes for both membranes. In addition, the coordination number of OH<sup>-</sup> is greater in two QA systems than in single QA membranes, which probably improves the alkaline stability of two QA polymers (Chen S. et al., 2020). Furthermore, Li and coworkers (Li et al., 2021) found that both OH<sup>-</sup> conductivity and chemical/mechanical stability of the PPO-based AEM can be significantly improved by grafting a tri-cation side-chain with a long hydrophobic extender and an additional hydrophilic side-chain. These results further demonstrate the success of the strategy of multi-cations on each grafted functional group to balance the ionic conductivity and the chemical stability (Pan et al., 2013; Zhu et al., 2016; Li et al., 2021).

Alternatively, a delicate balance of hydrophilic and hydrophobic features in functional groups can mitigate the bottleneck issue (Zhang and Van Duin, 2015; Dong et al., 2018a; Dong et al., 2018c). Reactive force-field MD simulations were conducted on hydrated PPO-based homopolymers with five distinct quaternary ammonium cationic groups (R<sub>1</sub>: -CH<sub>3</sub>, R<sub>2</sub>: -C<sub>2</sub>H<sub>5</sub>, R<sub>3</sub>: -C<sub>3</sub>H<sub>7</sub>, R<sub>4</sub>: -C<sub>6</sub>H<sub>13</sub> and R<sub>5</sub>: -C<sub>4</sub>H<sub>8</sub>OCH<sub>3</sub>) (Dong et al., 2018a). The hydrated morphology indicated that the nanoscale water domains were connected by narrow channels and the size of the water channels increased dramatically with increasing water content. For the systems with symmetrically modified cation groups, long alkyl tails (i.e., 3R<sub>3</sub>) enhanced phase segregation, giving rise to the formation of large water clusters with fewer connections between those clusters. For the systems with asymmetric cationic groups, the distribution of pore sizes was narrower in the 2R<sub>1</sub>R<sub>4</sub> and 2R<sub>1</sub>R<sub>5</sub> than in 3R<sub>3</sub> at a hydration level of 5. Enhancement in the hydrophilicity for 2R<sub>1</sub>R<sub>5</sub> by introducing an ether group resulted in a more uniform distribution of the size of the water channels when compared with 2R<sub>1</sub>R<sub>4</sub>, indicating the formation of narrow connections between the water domains. These findings show

that the hydrophobicity of the functional groups should be strong enough to provide the desired nanophase segregation but not so strong as to provoke the formation of narrow bottlenecks between the water domains, e.g. 2R<sub>1</sub>R<sub>4</sub> (Dong et al., 2018a).

Although a high IEC improves the ionic conductivity of an AEM, it also causes swelling of the membrane giving rise to low dimensional stability. One potential approach is to utilize cross-linking to manage excess swelling in AEMs. Experimental results have shown that cross-linking significantly reduces the water uptake and swelling without sacrificing the anion conductivity and the interdomain spacing of the AEMs decreases with the degree of cross-linking for the poly(bromopropyl norbornene)-*b*-poly(butyl norbornene) copolymers (Chen et al., 2019) and the TMA-functionalized SEBS membranes (Jeon et al., 2019) both by using *N,N,N',N'*-tetramethyl-1,6-hexanediamine (TMHDA) as cross-linker, and the multiple quaternary ammonium-functionalized polysulfone AEMs modified with rigid  $\beta$ -cyclodextrin (Ma et al., 2020). However, few simulations have been undertaken to probe the influences of cross-linking on the morphology of AEMs despite the availability of the cross-link formation algorithm (Kacar et al., 2013).

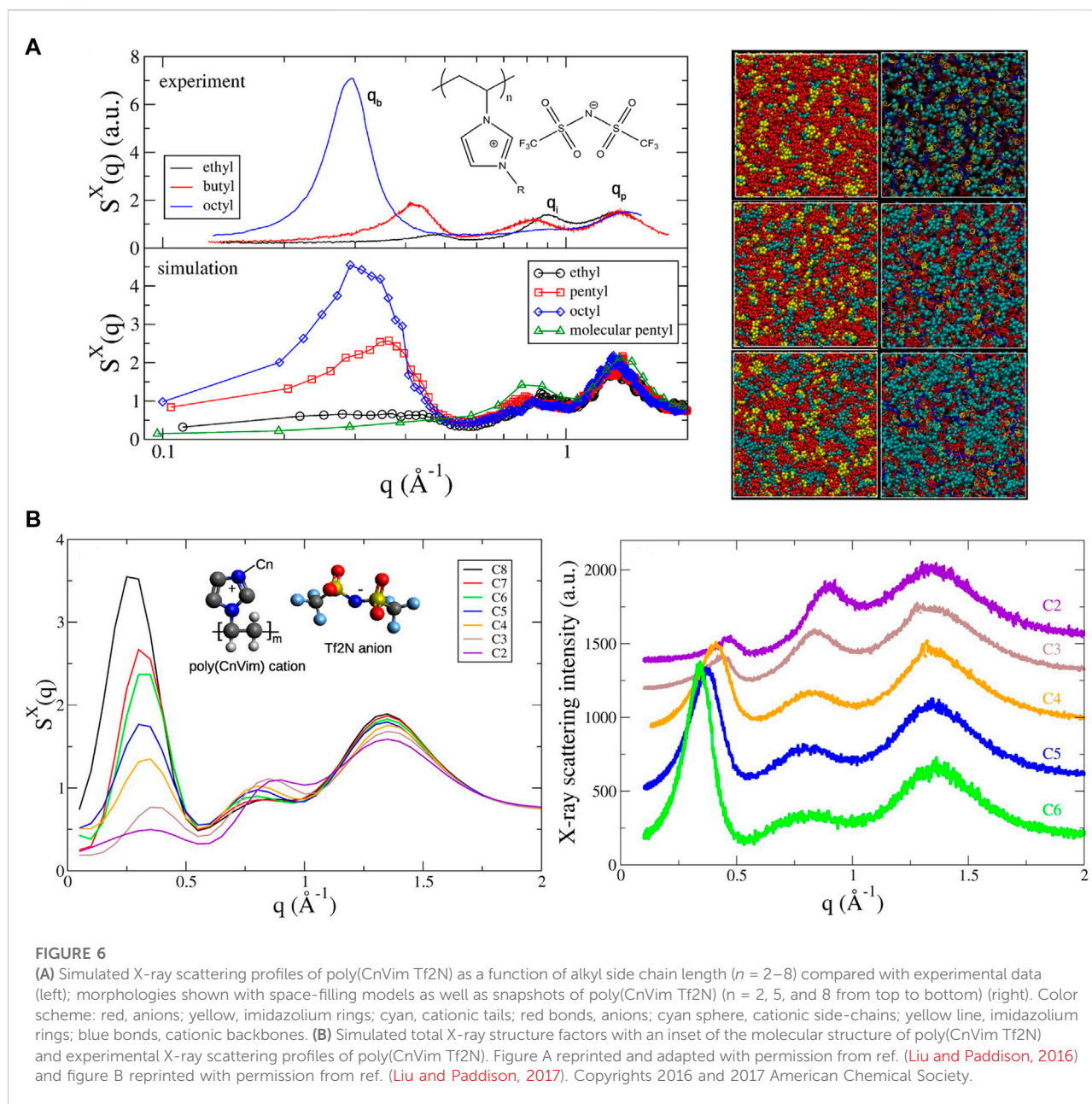
To date, a significant effort has been devoted to determining rational design rules. Nevertheless, general conclusions have not been obtained since there is a complex interplay of a number of factors. To this end, we suggest that machine learning may be a promising approach to resolving the complexity of effects on the hydrated morphology of ionomers.

## Anhydrous morphology

In anhydrous ion-containing polymers, ionic aggregates form due to specific interactions including strong electrostatic, metal/ion-dipole, etc. The influence of polymer architecture, the dielectric constant, and the specific mobile ions on the morphology of the ionic aggregates are of significant interest. Similar to hydrated ionomers, only percolating ionic domains may serve as ion conducting channels thereby providing high ionic conductivity. Although experiments can provide microscopic images of the ionomer such as those obtained from scanning transmission electron microscopy (STEM), and the approximate ionic aggregate size distribution from X-ray scattering, the details of the morphology such as the shape, size, and the percolation of the ionic domains are incompletely understood (Ketkar et al., 2019). Thus, MD simulations have been undertaken to resolve this problem.

Recently, Liu and Paddison performed atomistic MD simulations to study the structural properties of a homologous series of poly(n-alkyl-vinylimidazolium bistrifluoromethylsulfonylimide) (poly(nVim Tf2N)) ionic liquids (Liu and Paddison, 2016). The computed structure factors were observed to be in excellent agreement with X-ray scattering results in terms of peak position and shape. Three





distinct peaks were characterized as the low- $q$  peaks at  $0.2-0.6 \text{ \AA}^{-1}$  according to the backbone-to-backbone correlations ( $q_b$ ), the intermediated- $q$  peaks in the range of  $0.8-1.0 \text{ \AA}^{-1}$  corresponding to the ionic interactions ( $q_i$ ), and the high- $q$  peaks at  $1.0-2.0 \text{ \AA}^{-1}$  representing the pendant-to-pendant peak ( $q_p$ ) as shown in Figure 6A. The simulated nanostructures of poly(nVim Tf2N) ( $n = \text{ethyl, pentyl, and octyl}$ ) on the right side of Figure 6A illustrated the dramatic growth of the nonpolar aggregates with increasing the length of alkyl chain along with the homologous series and was quantified by the distribution of the nonpolar cluster size. It is worth noting

that the rational choice of the criterion for the connectivity in the distance-based cluster analysis algorithm is critical to correctly predicting the cluster size distribution. One strategy is to deconvolve the first peak of the radial distribution function by fitting it to a series of Gaussian functions and choosing the limit of the strongest Gaussian peak as the cutoff for the connectivity. Furthermore, a systematic increase in the alkyl chain length leads to the growth of nonpolar domain size (i.e., the backbone-to-backbone correlation length) and a slight increase in the ionic domains, despite a negligible shift of the pendant-to-pendant peak (Liu and Paddison, 2017). These results reveal a satisfactory



agreement between simulation and experiment as shown in Figure 6B. The complex interplay between morphology and ionic conductivity is discussed in the following section.

Analogous to the hydrated morphology, nanophase separation has been observed in block copolymers containing polyILs experimentally by Elabd and coworkers (Ye et al., 2012; Choi et al., 2013) and by Ganesan group with simulations (Zhang et al., 2019; Zhang et al., 2021b). The results show that the lamellar block copolymer has a similar anion concentration in the center to that of the homopolymers while the random copolymer displays the lowest local ion concentration. Moreover, the strength of cation-anion coordination is influenced by introducing nonconducting monomers, in which frustrated coordination behavior occurs in the interfacial area of the lamellar block copolymer and the bulk regions of the random copolymer. This was rationalized to be responsible for the low anion mobility in comparison to the homopolymer (Zhang et al., 2019). It should be noted that a multiscale simulation framework consisting of CG modeling and reverse mapping of the CG morphology was developed to extend the length and time scales of the simulated systems (Zhang et al., 2021b).

Ionomers are another essential type of single-ion conducting polymers, in which only the mobile ions contribute to the conductivity. Ion transport is governed by the morphology of the ionic aggregates. In an effort to reveal the distinct morphologies consisting of these ionic aggregates that are included in the single ionomer peaks of X-ray scattering, Frischknecht and Winey (Frischknecht and Winey, 2019) performed microsecond-long, all-atom classical MD simulations on a series of precise poly(ethylene-co-acrylic acid) ionomers with mobile lithium ions at 423 and 600 K. The spacer lengths between the backbone and acid groups were varied and tuned. The percolated ionic aggregates were found in three spacer length systems that were totally neutralized with lithium ions. For partially lithium neutralized systems, the acidic groups prefer to stay on the sides or ends of the lithium ion aggregates with some coexisting acid aggregates formed *via* hydrogen bonding. The evolution of the ionic domains revealed that the morphology reached steady state over hundreds of nanoseconds at a higher temperature while it cannot within the microsecond-long simulation at a lower temperature.

In contrast, Agrawal and coworkers (Agrawal et al., 2016) demonstrated that the ionic clusters formed in PSS melts with both  $\text{Na}^+$  and  $\text{Mg}^{2+}$  did not percolate across the sample according to the definition of the cluster that consists of  $\text{SO}_3^-$  groups that are within the distance criterion of 6 Å. Specifically, the majority of the clusters in a PSS/ $\text{Na}^+$  system are highly ordered and ladder-like in shape, while the clusters in PSS with  $\text{Mg}^{2+}$  are irregular and elongated. The cluster size distributions for both melts illustrate that charge-neutral clusters with an even number of  $\text{SO}_3^-$  groups are dominant over charged ones. Although both melts have a

broad distribution of cluster size, the PSS/ $\text{Mg}^{2+}$  has a larger average cluster size than that of PSS/ $\text{Na}^+$  even under shearing.

## Ion transport

Transport phenomena in ion-containing polymers comprise multiple mechanisms at different time and length scales. In hydrated ionomers, the rapid dynamical hydrogen bonding of the water facilitates the transport of ions in a vehicular (i.e., as a carrier) and/or in a structural way (i.e., typically in the case of proton transfer). Typically, ion diffusivity increases with hydration level, but a high degree of hydration generally causes swelling of the polymer matrix and may limit the operating conditions. In anhydrous polymeric systems, the ion conductivity is generally controlled by the slow segmental dynamics of the polymer. Thus, one strategy is to reduce the glass transition temperature ( $T_g$ ) or add liquid plasticizers, leading to the enhancement of the ion and segmental dynamics (Bocharova et al., 2017). In contrast, another method is to enhance the decoupling of ion transport from segmental dynamics (Wojnarowska et al., 2017), which would probably be achieved by the morphological confinement and/or tuning of specific interactions within ion-containing membranes.

## In hydrated systems

Hydrated membranes illustrate various hydrophilic ionic domains due to nanophase separation, in which various proton transport phenomena occur according to distinctions in the chemical structures of the ionomers. The formed hydrophilic ionic domains and in some cases, channels are composed of pendant functional groups, water molecules, and dissociated protons, giving rise to a complex confined environment for proton carrier transport.

Given the disparate range in the time and length scales of the phase-separated hydrated morphology and proton transport within a local environment, it is challenging with only a single model to properly describe proton transport (*via* structural diffusion) within a polymeric system and the conformation of a water network due to nanophase separation (Jorn et al., 2012). More importantly, the transport of  $\text{H}^+$  or  $\text{OH}^-$  occurs through the migration of a charged defect in the hydrogen bond network through a sequence of elementary proton transfer reactions/events, which requires a quantum mechanical description of covalent and hydrogen bond breaking and forming (Tuckerman et al., 1997; Tuckerman et al., 2010). Thus, significant effort has been devoted to addressing these challenges. There are two major directions: simulating the diffusion of ions and/or water in an equilibrium morphology

obtained from DPD simulations; and incorporating local interactions into coarse-grained MD/DPD simulations.

Dorenbos (Dorenbos, 2019; Dorenbos, 2020) performed grid-based Monte Carlo tracer diffusion calculations, which are capable of evaluating the diffusivity of water molecules based on equilibrium DPD morphologies but fails to describe proton transport behavior due to the lack of local interactions between the protons and the functional groups and solvent molecules. Another drawback is that the fixed pore networks cannot accurately represent the dynamical percolated water-containing domains (i.e., “channels”). A similar strategy was developed to simulate the transport of water in the fixed channels of the membrane (Johansson et al., 2015). The results obtained from both methods show that an increase in hydration improves the water diffusivity within the system (Johansson et al., 2015; Dorenbos, 2017a). It is interesting to note that the diffusivity of hydronium ions was also obtained from DPD simulations by modeling the hydronium ion bead with the proton associated with one to four water molecules (Xiao et al., 2018). The results indicate that the increase in the size of solvated hydronium complexes retards the hydronium transport.

Another approach is to map the coordinate of the coarse-grained water beads to the interpolation quasi-particles within the theory of SPH to describe proton transport in a mesoscopic structure of a PEM (tens of nanometers) (Jorn and Voth, 2012). This method combines the dynamic behavior of the protons from atomistic MD simulations and the mesoscopic structure of PEMs driven by the hydrophilic/hydrophobic interactions among the polymer matrix, functionalized side-chains, water, and protons. This scheme was applied to hydrated Nafion. To properly include double layer effects and the local strong interaction between the functional groups and protons, electrostatics and position dependent diffusivity were introduced. The computed conductivities showed good agreement with experimental data (Jorn and Voth, 2012). Moreover, proton transport behavior within various morphologies including lamellar, cylindrical, and cluster were also investigated using this SPH-based mesoscale method (Liu et al., 2015). The proton conductivity within the cluster morphology was found to be lower than that within the other two morphologies due to the higher porosity and tortuosity in the cluster morphology.

Apparently, these methods consider the proton/water transport indirectly based on the static equilibrated morphology. The dynamic dissociation and association of protons from the acidic groups cannot be simulated. An elegant way to incorporate protonation/deprotonation processes is to introduce a dissociative Morse potential into mesoscale DPD simulations. Neimark and coworkers (Lee et al., 2016; Vishnyakov et al., 2018) performed DPD simulations in synergy with dissociable Morse bonds between the protons and the conjugate bases and/or water beads to model proton hopping occurring in PEMs. This strategy successfully achieves the goal of simultaneously simulating the explicit

proton/water transport and the nanophase separation in hydrated PEMs. Model Nafion membranes were simulated using this method and the resulting proton diffusivities at moderate and high hydration levels agreed well with the diverse experimental data. Nevertheless, there was a significant discrepancy at low hydration, which was ascribed to the dynamic narrow bridges between water domains that required a higher fidelity in the simulations than achievable in DPD simulations (Vishnyakov et al., 2018). Importantly, the results showed a sharp increase around the percolation threshold. This phenomenon was directly observed using PFG-NMR by Vasenkov et al. (Berens et al., 2020). It is worth noting that the dynamic hydrophilic subphase connectivity plays a critical role in water diffusion, suggesting that it is still challenging to accurately estimate proton diffusivity at low hydration through coarse-grained modeling.

In an effort to mimic the structural diffusion of protons, various techniques have been implemented into classical MD simulations including multistate empirical valence bond models (e.g. MS-EVB) (Savage et al., 2014), bond order-based reactive force fields (e.g. ReaxFF) (Zhang and Van Duin, 2015), and quantum hopping (Q-HOP) (Devanathan et al., 2010). Recently, a combination of reactive and nonreactive polarizable MD simulations was used to study transport mechanisms of OH<sup>−</sup> in hydrated PPO-QA AEMs (Dong et al., 2018c). The morphology of these non-blocky AEMs at a hydration of 10 exhibited narrow percolating channels connecting the water domains. It was found that the vehicular mechanism made the dominant contribution to the conductivity in water-rich domains, while structural diffusion played a significant role in crossing the bottlenecks between large water domains under the confined environment of a channel (Dong et al., 2018a; Dong et al., 2018c). Their findings demonstrate that structural diffusion of OH<sup>−</sup> facilitates the diffusion through these bottlenecks without loss of anion hydration structure, while the vehicular diffusion of OH<sup>−</sup> through the bottlenecks requires a change in the hydration structure giving rise to a high kinetic barrier for such events. Notably, the decomposition of the total diffusivity into vehicular motion and discrete structural diffusion revealed that the structural diffusion is dominant and the structural diffusion is anticorrelated with the vehicular diffusion (Dong et al., 2018b).

To capture the delicate interplay of proton transfer and solvation structure, AIMD simulations are utilized, in which “on the fly” force fields obtained from DFT-based electronic structure calculations enable one to accurately simulate the breaking and formation of covalent bonds. However, the extremely high computational cost of AIMD simulations limits the accessible length and time scales. Thus, it is important to make careful selection in the simulated systems. Recent AIMD simulations of a model PEM functionalized with sulfonate end groups (SO<sub>3</sub><sup>−</sup>) using graphane bilayers were undertaken to study the hydronium ion diffusion mechanism (Zelovich et al., 2021; Zelovich and Tuckerman, 2021).

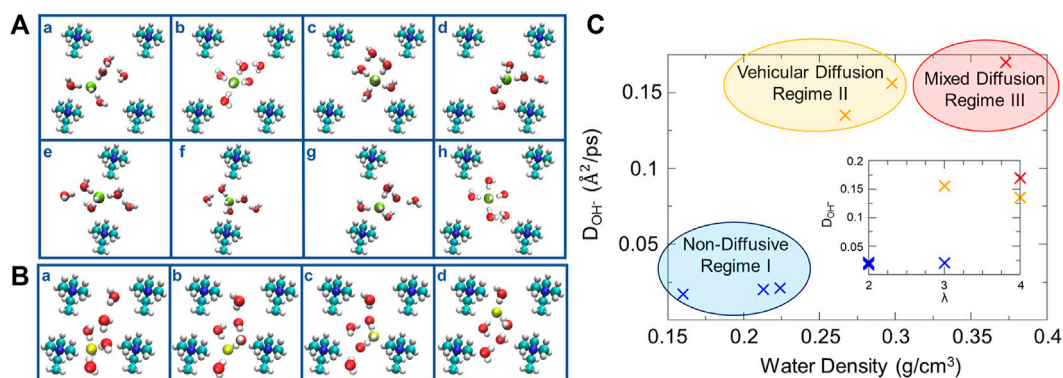


FIGURE 7

(A) Vehicular diffusion mechanism of  $\text{OH}^-$  in system a4 from a z-perspective. (B) Structural diffusion mechanism of  $\text{OH}^-$  in system b4 from a z-perspective. (C) Relationship between average diffusivity of  $\text{OH}^-$  and water density, inset:  $\text{OH}^-$  diffusivity vs. the hydration level. Reprinted and adapted with permission from ref. (Zelovich et al., 2019b). Copyright 2019 American Chemical Society.

Surprisingly, low coordination of the hydronium ions at a hydration level of  $3\text{H}_2\text{O}/\text{SO}_3\text{H}$  promotes the participation of the pendant  $\text{SO}_3^-$  groups in the structural diffusion process of the hydronium ions with the reaction:  $\text{SO}_3^- + \text{H}_3\text{O}^+ \leftrightarrow \text{SO}_3\text{H} + \text{H}_2\text{O}$ . It was reasoned that the non-uniform water distribution at a low hydration level facilitates the reaction between the hydronium ion and the anion group as the oxygen located next to  $\text{SO}_3^-$  obtains a coordination number of approximately one from surrounding  $\text{H}_2\text{O}$  and  $\text{H}_3\text{O}^+$  (Zelovich et al., 2021). Furthermore, the sulfonate functional group with the linker of  $(\text{CH}_2)_2$  possesses weaker acidity than with the linker of  $(\text{CF}_2)_2$ , resulting in more active participation in the  $\text{SO}_3^-/\text{H}_3\text{O}^+$  reaction and thereby improving instead of impeding the hydronium transport (Zelovich and Tuckerman, 2022).

Zelovich and coworkers (Zelovich et al., 2019a, Zelovich et al., 2019b) also employed graphane bilayers or carbon nanotubes with selected cationic groups attached with added water molecules and hydroxide ions to model the complex nanoconfined environment of an AEM. The effects of the hydration level, cation spacing, and cell geometry were studied to explore the mechanisms of  $\text{OH}^-$  transport. Structurally similar water layers exhibit a symmetrical distribution of oxygen atoms between the graphane layers while structurally dissimilar water layers enable the flow of water molecules. These exist in different systems under various structural confinement. The structural similarity in the water layers reduces the hydroxide ion diffusion, while structural dissimilarity improves the hydroxide ion transport. In regard to enhancing  $\text{OH}^-$  diffusion, various solvated  $\text{OH}^-$  structures were considered to be active/inactive complexes. The active 3-fold and inactive 4-fold structures (i.e., hydroxide ion coordinated by three or four water molecules) correlate with fast and slow time scale processes, respectively, based on the fitting of results from proton transfer correlation functions. In systems

of low hydration, the cation stabilizes the 3-fold complex acting as a fourth neighbor (shown in subplot a of Figure 7A), followed by the drift of this 3-fold complex toward the water molecules in the center of the cell forming a 4-fold planar structure (shown in subplot c of Figure 7A). This complex continues to move toward the nearby cation forming a stable 3-fold structure in the vicinity of the cation. An insufficient number of water molecules around the hydroxide ions leads to vehicular movement of the 3-fold complex between cationic groups. Increasing hydration helps build up a wire between the cation groups by rearranging the hydrogen bonds, which consequently invokes a series of proton transfer events *via* structural diffusion (shown in Figure 7B). Three distinct diffusion regimes were identified under low-hydration conditions: a non-diffusive regime at very low effective water density, a vehicular diffusion regime at intermediate water density, and a mixed diffusion regime with higher water density (Figure 7C). In contrast to PEMs, the cationic groups in AEMs form a bottleneck-like region for hydroxide ion transport at low water contents, consequently giving rise to the suppression of the diffusion of hydroxide ions (Zelovich et al., 2019a; Zelovich et al., 2019b; Zelovich and Tuckerman, 2021). Moreover, it is surprising to observe the non-monotonic temperature dependence of hydroxide diffusivity in both theoretical and experimental studies (Zelovich et al., 2022). This unexpected phenomenon was rationalized by examining the transport mechanisms of hydroxide ions at different hydration levels. Specifically, the vehicular diffusion is dominant at extremely low hydration ( $\lambda = 2$ ) and high temperature is required to break the hydrogen bonds of the stable solvated hydroxide clusters. At low hydration ( $2 < \lambda < 5$ ), moderate temperatures enhance trivial proton rattling but the hydroxide ions are still trapped in the cell center, which requires high temperatures to overcome the bottleneck between cations. Layered water structures occur at

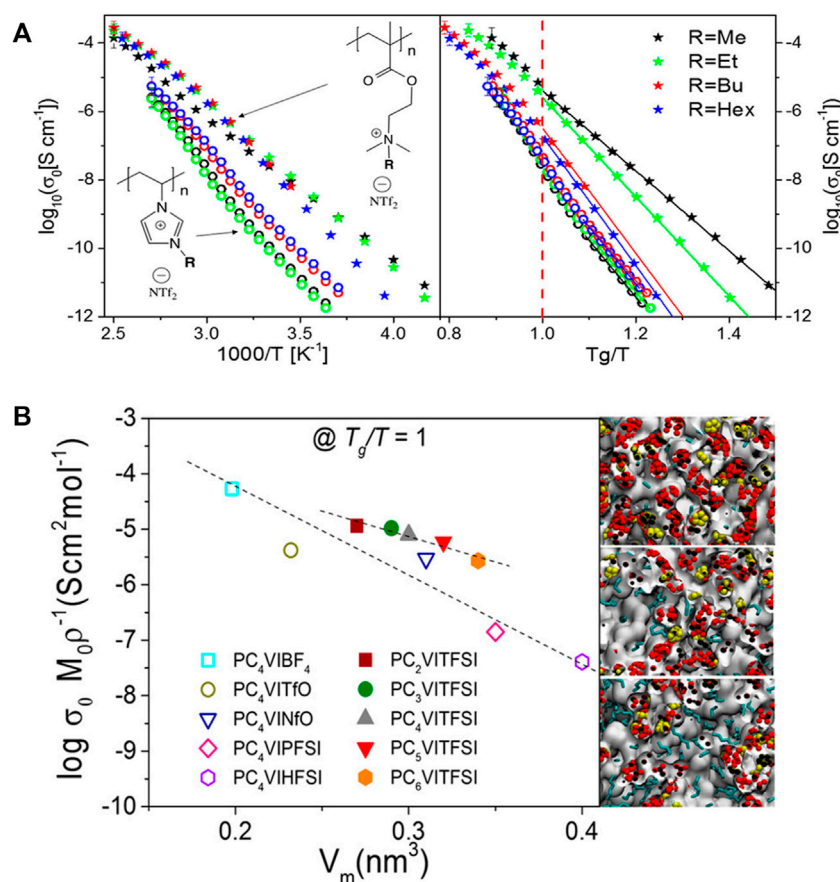


FIGURE 8

(A) Left: dc ionic conductivity vs. inverse temperature; right:  $T_g$ -independent ionic conductivity for ammonium (stars) and imidazolium (open circles) based polyILs. (B) Anion concentration-normalized dc conductivity at  $T_g/T = 1$  as a function of repeat unit molecular volume,  $V_m$ , (including the counterion) for imidazolium-based polyILs with different side chains and counterions. Figure A reprinted with permission from ref. (Heres et al., 2018) and figure B reprinted with permission from ref. (Iacob et al., 2017). Copyright 2018 and 2017 American Chemical Society.

high hydration ( $\lambda > 5$ ), leading to higher hydroxide diffusivity in the upper layer than in the cation-containing layer. Therefore, the temperature threshold for high hydroxide diffusivity occurs when the hydroxide ions can move to the upper layer where efficient structural diffusion is predominant (Zelovich et al., 2022). It may be concluded that the water distribution and the solvation structure of OH play a key role in determining the proton transport mechanisms. Obviously, the combination of water density, the space between cationic groups, and confinement conditions results in complex local environments.

Recognizing the important role of the solvation structure of OH under functionalized nanoconfined conditions, further study of the interplay of solvation patterns and diffusion mechanisms was undertaken by Zelovich and Tuckerman (Zelovich and Tuckerman, 2020). Five layers were defined and distinguished as outer water layers (i.e., the water in immediate proximity to the graphane bilayer L1 and L5), and inner water layers between the outer ones based on the

distribution of the oxygen atoms. Planar 3-fold and 4-fold solvation structures were observed in L1 and L5, respectively. This leads to a less preferable environment for enhancing hydroxide diffusion due to the relatively stable planar structures. The inner water layers exhibit the solvation characteristics similar to that in bulk aqueous hydroxide. Specifically, in the L2 water layer located on top of the cationic groups, a series of successive proton transfer events occur followed by a quiescent period, while the frequency of proton transfer in the L3 and L4 layers is higher than in the L2 layer. These interesting results show a novel avenue to design high-performance AEMs by engineering the water within a nanoconfined environment.

The transport mechanisms of hydroxide ions within poly(arylene ether sulfone ketone)s functionalized by quaternized ammonio-substituted fluorenyl groups (QPE) AEMs were investigated *via* classical and first-principles MD simulations (Takaba et al., 2017). The impact of the number of



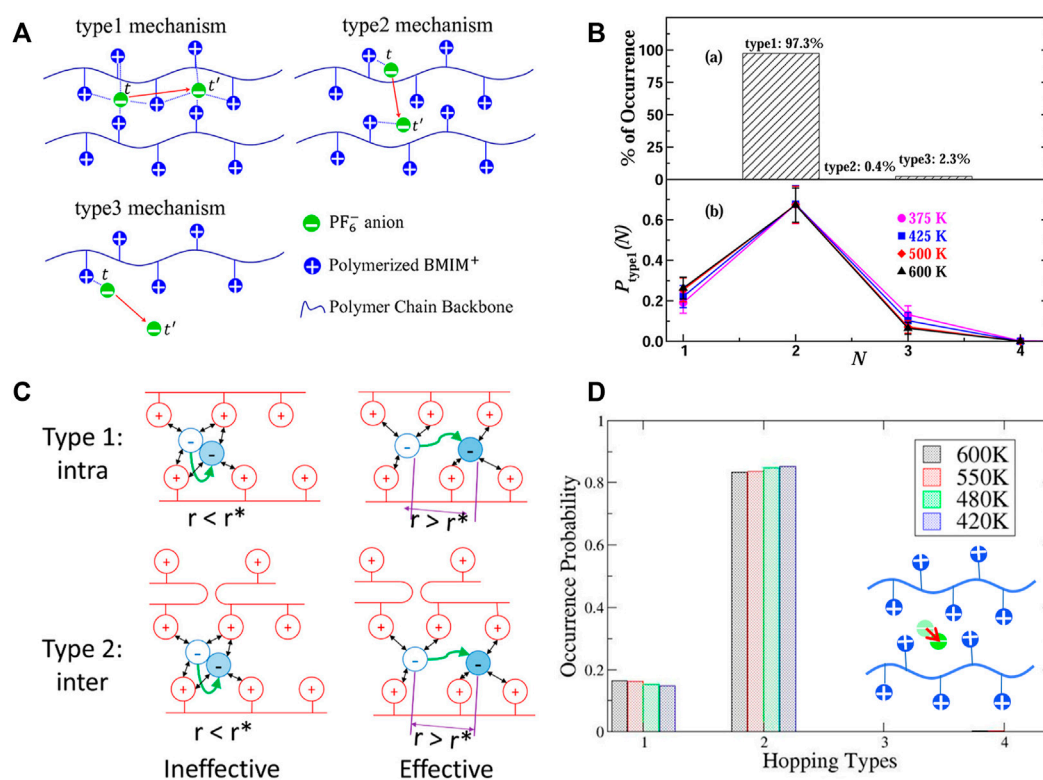


FIGURE 9

(A) Illustration of ion hopping types in polyIL electrolytes. (B) Percentage of hopping events in polyIL electrolytes (top); and decomposition of intrachain hopping events (type 1) assisted by  $N$  number of polymer chains (bottom). (C) Definition of effective hopping contributing to the long-range diffusion. (D) Probability of occurrence as a function of hopping type at four different temperatures when the ineffective ions were excluded. The inset is the definition of type 4: remaining intact (i.e. rattling). Figures A and B reprinted with permission from ref. (Mogurampelly et al., 2017) and Figures C and D reprinted and adapted with permission from ref. (Liu et al., 2021). Copyrights 2017 and 2021 American Chemical Society.

repeating units in QPE on the ion conductivity of OH is minimal and OH transport in hydrated QPE occurs through structural diffusion (i.e. hopping between the ammonium groups of QPE) accompanied by vehicular transport based on the classical MD results. The first principles MD simulations show that the transport of OH occurs through the formation of  $\text{H}_3\text{O}_2^-$  via the hydrogen bond network of the water molecules. AIMD simulations of the quaternary ammonium functionalized polystyrene-block-poly(ethylene-ran-butylene)-block-polystyrene (QSEBS) AEMs systems demonstrate that hydration increases structural diffusion, which contributes to OH conductivity, and hydroxide ions have the longest lifetime when the system is dry (Castañeda and Ribadeneira, 2020).

## In anhydrous systems

In addition to extensive investigations of proton transport in aqueous polymeric electrolytes, the mechanisms underlying ion transport in polyILs because of their application in batteries have attracted attention. Significant effort has been undertaken to

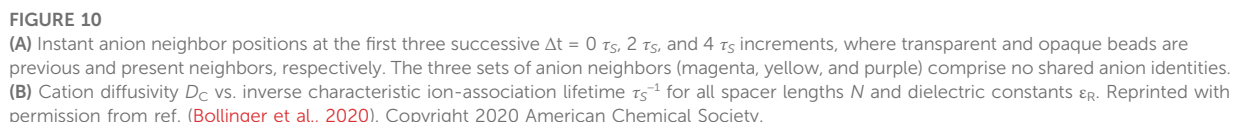
address the low conductivity in polyILs which may be promising materials due to their long lifetime and safety advantages. Thus far, many factors have been studied to promote a better understanding of ion transport mechanisms and formulate design rules for high-performance polyILs (Aziz et al., 2018; Bocharova and Sokolov, 2020; Son and Wang, 2020).

Early studies (Iacob et al., 2017; Heres et al., 2018) revealed that the length and rigidity of the side-chains play a crucial role in transporting ions along the polymer chains. It was found that ammonium-based polyILs show higher dc ionic conductivity than imidazolium systems at their respective glass transition temperatures based on the results from BDS, WAXS, and classical MD simulations (shown in the left panel of Figure 8A) (Heres et al., 2018). Additionally, the alkyl spacer length has a strong influence on the ionic conductivity at comparable time scales of the segmental dynamics for imidazolium polyILs (shown in the right panel of Figure 8A). Specifically, in the imidazolium polyILs, the  $T_g$ -independent ionic conductivity experiences one decade decrease as the alkyl side-chain length is systematically increased, which is correlated with an increase in the characteristic backbone-to-

backbone distance (Iacob et al., 2017). In contrast, the reduction of anion molecular volume leads to ~3 orders of magnitude increase in the  $T_g$ -independent ionic conductivity. Complemented by atomistic MD simulations, the morphologies were transformed from isolated apolar clusters within a continuous polar matrix for shorter alkyl groups to bicontinuous sponge-like morphologies for longer alkyl chains, which is shown in Figure 8B. Variation in the molecular structure results in greater effects on ion mobility than the effective number density of the mobile ions (Heres et al., 2018).

Ganesan et al. used atomistic MD simulations based on quantum-mechanically parametrized force fields to obtain a molecular-level understanding of the time scale and mechanisms underlying ion transport in model systems of poly(1-butyl-3-vinylimidazolium-hexafluorophosphate) polyILs (Mogurampelly et al., 2017). The intermittent and continuous correlation functions were used to probe the structural relaxation behavior of the association of anions and cations, and the average lifetime of the associations. The former was calculated with  $C(t) = h(t)h(0)/h$ , where  $h(t)$  is unity if one ion remains associated with another according to the first minima of the cation-anion radial distribution function at a given time  $t$ . The structural relaxation time was extracted by fitting the function to a stretched exponential. Alternatively, the structural relaxation processes can be captured from the intermediate scattering function at a characteristic wave vector, corresponding to the first peak of the anion-anion radial distribution function. Based on these detailed analyses, their results show that anion transport in polyILs is mainly governed by a mechanism involving intra- and inter-chain ion hopping that is facilitated through the breaking and formation of ion associations involving four polymerized cationic groups that belong to two polymer chains (see Figures 9A,B). This finding was confirmed by atomistic simulations that included polarizability effects (Zhang et al., 2022). More interestingly, the authors found that the mobile ions tend to associate with three polycations from two polymer chains when refining the ion hopping mechanism by excluding the rattling ions (Zhang et al., 2022). They determined that ion mobilities in these imidazolium-based polyILs are directly correlated to the average lifetimes of the ion associations while the ion mobilities in pure ILs are correlated to the structural relaxation time; indicating that anion hopping along the cation monomer chains underlies the transport of ions in polyILs (Mogurampelly et al., 2017). These results conclusively imply that anion transport is decoupled from the slow segmental relaxations in imidazolium-based polyILs, which is different from what has been observed in poly(ethylene oxide) and poly(propylene glycol) systems (Yoshida et al., 2011; Wang et al., 2014). The difference may be ascribed to the rigid polymer matrix that facilitates decoupling of ion transport from segmental dynamics.

However, it was subsequently argued that the breaking and forming of ion association probably do not contribute to long-range ion transport because most ions merely “rattle” amongst the polymerized cationic monomers within a cage (Xiao et al., 2020; Liu et al., 2021). No long-range transport may occur unless the ion escapes from its cage. Based on the MD simulations performed on both 1-butyl-3-methylimidazolium tetrafluoroborate ([BMIM]-[BF<sub>4</sub>]) IL and poly(1-butyl-3-vinylimidazolium-tetrafluoroborate) (poly([BVIM]-[BF<sub>4</sub>])) polyIL, the comparison between ion transport in ILs and that in polyILs confirmed that the anion diffusivity in polyIL is directly correlated with the anion hopping among cages formed by the cationic branch chains. Hence, the trap time in which an anion is trapped inside a cage determines the time scale of the anion transport rather than the ion association lifetime (Xiao et al., 2020). Nevertheless, the coupled motion of an anion and the surrounding ions governs the diffusivities of ions in the IL, i.e., the ion transport is correlated with the ion association lifetime. These phenomena were observed in additional all-atom MD simulations (Luo et al., 2020b; Liu et al., 2021), which improved the understanding of ion hopping mechanisms in polyILs. Specifically, the ion transport mechanism in polyIL poly(C2Vim)Tf<sub>2</sub>N was investigated by defining an additional ion transport mode, i.e., an intact type that corresponds to the rattling of an ion when trapped in a cage. As expected, there is a significant portion of intact anions (35–50%), implying that a considerable amount of mobile anions are trapped in the cages and do not contribute to long-range transport. Examination of the self-part of the van Hove function of the anions at the characteristic time of the greatest dynamical heterogeneity illustrates the occurrence of a secondary peak, which is a quantitative indication of diffusion *via* hopping (Liu et al., 2021). Note that the dynamical heterogeneity can be quantified with a non-Gaussian parameter ( $\alpha_2$ ) to indicate the deviation from purely Gaussian behavior and is required to be large enough ( $\alpha_2 > 1$ ) to distinguish the double peaks in the self-part of the van Hove function. If the effective mobile anions are distinguished from slow “immobile” ones according to the distance criterion of the local minimum between the two peaks in the self-part of the van Hove function of the anions, the categorization for only these effective mobile anions shows negligible intact anions and dominant inter-chain hopping over intra-chain events. This is in contrast to the classification with a short interval of sampling (Figures 9C,D). Indeed, these results conclusively show that the instant ion dissociation is necessary but not sufficient for effective hopping transport. Furthermore, the stringlike cooperative motion of the mobile ions was quantified according to the criterion:  $\min[|r_i(t) - r_j(0)|, |r_i(0) - r_j(t)|] < r_s$ , in which  $r_i(t)$  and  $r_j(t)$  are the coordinates of  $i$ th and  $j$ th anions at time  $t$ , and  $r_s$  is the cutoff distance for the string collection. The average string length for the polyILs is in the range of 1.6–2.2 anions, but close loops in the anion transport were not observed, which were



In view of the role of ionic aggregate morphology in the mechanisms of ion transport, coarse-grained MD simulations were performed on single-ion conducting polymers to obtain an understanding of how the nanoscale aggregation of the cations and anions covalently bonded to the polymer affect the rates and mechanism of cation transport (Bollinger et al., 2020). The authors suggested that cations diffused *via* stepping motions along with the ionic aggregates and correlated the diffusivity of cations to the lifetimes of continuous association between oppositely charged ions in percolated ionic aggregate formed systems (shown in Figure 10). It was emphasized that this correlation did not hold for systems with isolated ionic clusters. Additionally, a strategy was proposed to enhance ion transport based on the strength of the Coulombic interactions:

To achieve high lithium selectivity (indicated by transport number and transference number) in polymer electrolytes, one potential approach is to incorporate nanoparticles into ion-conducting solid polymers or liquids; although the mechanisms underlying ion transport in such materials

remain poorly understood (Diederichsen et al., 2017). Recently, coarse-grained multiscale simulations were performed on this type of polymer (Kadulkar et al., 2020). Their results suggest that the ionic conductivity is mainly due to  $\text{Li}^+$  transport along nanoparticle surfaces, in the vicinity of tethered anions. The increase in nanoparticle loading improves the connectivity of the cationic surface transport pathways at low nanoparticle concentrations. High nanoparticle loadings were observed to suppress ion mobility because of the strong cation-anion interaction and steric hindrance effects. It was further observed that high dielectric constant solvents facilitate the dissociation of cations, leading to higher ionic conductivity.

Another novel strategy is to develop locally ordered and rigid channels for ion transport with semicrystalline poly-zwitterionic (polyZI) materials, in which the  $\text{Li}^+$  transport number achieves up to 0.67 (Jones et al., 2022). This recent study demonstrated that formation of a nanoscale crystal phase occurs in the polyZI tethered with the zwitterion imidazolium-trifluoromethanesulfonamide (Im-TFSI), which is ascribed to the weak Coulombic interactions that prevent the pendant zwitterions from noncovalent cross-linking. The disparity in size between  $\text{Li}^+$  and the tethered anions promotes sufficient free volume for  $\text{Li}^+$  transport but not for the much larger TFSI, resulting in large selectivity for  $\text{Li}^+$  transport. These special confined conditions enable the decoupling of  $\text{Li}^+$  from the slow segmental relaxation in crystalline conductive pathways, although the transport of  $\text{Li}^+$  in the amorphous phase was also observed in these systems. Dating back to earlier studies, the influences of polyZI chemistry (Lind et al., 2016; Taylor et al., 2021) and ionic organization (Keith and Ganesan, 2020) on  $\text{Li}^+$  transport were investigated in theoretical and experimental studies. The experimental results showed improved room temperature ionic conductivities and elastic modulus. This was explained by the enhanced cation/anion dissociation and physical cross-linking within the polymers due to the strong interactions between zwitterions and the mobile ions (Lind et al., 2016; Taylor et al., 2021). Classical MD simulations of polyZIs with distinct organizations indicated that the counterion of the terminal moiety of the zwitterions possesses higher diffusivity than the counterion of the moiety adjacent to the backbone (Keith and Ganesan, 2020). Interestingly, the mobility of the former was found to be correlated with the ion-association behavior, while the latter transported coupling with a cage relaxation. These findings provide crucial insights into this emerging class of ion-containing materials.

In concluding this section, it is important to mention the origin of the difference between charge diffusivity computed from conductivity measurements and that determined by NMR. This is typically quantified with the Haven ratio,  $H = D_i/D_\sigma$ , in which  $D_i$  is the self-diffusivity measured by NMR without including all the ionic correlation terms, whereas  $D_\sigma$  the diffusivity derived from impedance spectroscopy using the Nernst-Einstein equation. The interested reader is referred to

the excellent perspective (Fong et al., 2021). In ionic liquids that are salts having a melting point below  $100^\circ\text{C}$ , an  $H > 1$  is explained by the movement of the cation-anion pairs that contribute to ion diffusion, but not to conductivity. However, this explanation was challenged by results from atomistic MD simulations (Kashyap et al., 2011). Further experimental studies of polyILs revealed that the major mechanism suppressing ionic conductivity is due to the strongly correlated movement of mobile ions with a like charge (Popov et al., 2020). Recently, simulations of ILs and polymerized ionic liquids with various degrees of polymerization ( $N$ ) revealed that the strong distinct correlations between neighboring cations in the backbone of polyILs lead to distinct cation-cation diffusivity that is larger than the self-diffusivity of cations in magnitude and independent of  $N$  at larger  $N$  (Zhang et al., 2020b). Hence, the inverse Haven ratio shows a maximum at  $N = 3$ . Moreover, the authors demonstrated that the ideal transference numbers decrease with increasing  $N$  for large  $N$  due to the cationic contribution to the conductivity, which challenges the notion that pure polyILs are single-ion conductors. Shen and Hall studied the effects of ion-polymer and ion-ion interactions on the correlation of anion and cation motions by modeling salt-doped homopolymers and block copolymers (Shen and Hall, 2020). The authors found that the increase of ion-monomer interactions gave rise to competing diffusion and ion correlation effects at low salt concentrations and progressively suppressed the conductivity with increasing salt concentration. The stronger ion-ion interactions reduce ion conductivity without being affected by ion concentration (Shen and Hall, 2020). It is worth noting that ion-ion correlations reduce the ionic conductivity in these systems, but enhance the conductivity in superionic ceramics. We would emphasize that one potential strategy is to turn negative ion-ion correlation into positive by tailoring the structure of ion channels and the specific interactions between the ions and lattice. For example, Kumar and coworkers developed one-dimensional ionic channels for anhydrous proton conduction by self-assembly of functionalized organic phosphonic acid and aromatic heterocyclic 1,2,4-triazole molecules (Kumar et al., 2019). The results demonstrate that the one-dimensional conductivity is improved compared with the 3-dimensional channels in Nafion.

## Summary and outlook

Recent significant findings are summarized including the morphology and the ion transport as well as underdeveloped specific interactions within the ion-containing membranes, emphasizing the interplay of morphology and ion transport. We discussed the influences of polymer architectures, tethered ionic groups, the rigidity of the backbone, the solvents, and the additives on the morphology and ion transport of the membranes from a multiscale perspective. Importantly, some novel design strategies were highlighted such as tuning the solvation structures



of hydronium/hydroxide ion in hydrated ion exchange membranes, turning negative ion-ion correlation to positive to improve the ionic conductivity in polyILs, etc. In addition, a variety of analytical approaches were reviewed including quantitative cluster analysis, categorization of hopping type, the definitions of dynamic heterogeneity, stringlike cooperative motion, *etc.*, for the purpose of gaining mechanistic insight. The remaining challenges include, but not limit to, the design of single-ion conductors, well-defined supramolecular architectures with one-dimensional enhanced ion transport channels, and the understanding of the specific interactions.

To further resolve fundamental issues in theoretically exploring the design rules for advancing the performance of ion-containing materials, we would like to propose several promising directions. First of all, the force field development for atomistic molecular dynamics and coarse-grained models would provide the possibility to gain accurate morphology and dynamical properties from simulations. Specifically, the novel machine learning technique could be extensively applied to the improvement of force fields considering the effects of multi-body interactions, polarizability, and delocalization of charge. New developed force fields for coarse-grained models such as the DFT-based parameterization method (Sepehr and Paddison, 2016), the fragment molecular orbital method (Okuwaki et al., 2018b), the MARTINI (Marrink et al., 2007), and the SPICA (Griffiths and Shinoda, 2019; Miyazaki et al., 2020) could be modified and extended to model ion-containing materials, especially the interfacial phenomena of bipolar membranes. Additionally, machine learning assisted backmapping coarse-grained models to atomistic represented models offers an opportunity to restore details at the atomistic level, leading to an increase in the spatial and temporal scales (Zhang et al., 2019; Li et al., 2020). In view of the temporal limitation of *ab initio* molecular dynamics simulations, it would be potentially promising to develop multi-timestep algorithms to investigate large time scale dynamic properties. To this end, the incorporation of proton transport behaviors into mesoscopic heterogeneity of phase-separated hydrated ionomers is still challenging. It would be promising to introduce various levels

of theory into the systems of interest, although the bridging between different levels of theory including coarse-grained approach has yet to be addressed. In addition, an energy decomposition analysis would be a powerful tool for a quantitative interpretation of the specific interactions between fragments/molecules to provide detailed insight into the interactions in terms of chemically meaningful components including: electrostatic, repulsive exchange, induction, and dispersion terms (Zhao et al., 2017).

## Author contributions

ZZ reviewed the literature and wrote the initial draft. SP proposed an article outline, revised the draft, and made editorial suggestions for the draft. Both ZZ and SP discussed the conceptual issues and themes for the review article.

## Funding

This work was supported by the U.S. Army Research Office under contracts W911NF-15-1-0501 and W911NF-16-1-0402.

## Conflict of interest

The authors declare that the research was conducted in the absence of any commercial or financial relationships that could be construed as a potential conflict of interest.

## Publisher's note

All claims expressed in this article are solely those of the authors and do not necessarily represent those of their affiliated organizations, or those of the publisher, the editors and the reviewers. Any product that may be evaluated in this article, or claim that may be made by its manufacturer, is not guaranteed or endorsed by the publisher.

## References

- Abbott, L. J., and Frischknecht, A. L. (2017). Nanoscale structure and morphology of sulfonated polyphenylenes via atomistic simulations. *Macromolecules* 50 (3), 1184–1192. doi:10.1021/acs.macromol.6b02232
- Agrawal, A., Perahia, D., and Grest, G. S. (2016). Cluster morphology-polymer dynamics correlations in sulfonated polystyrene melts: Computational study. *Phys. Rev. Lett.* 116 (15), 158001. doi:10.1103/PhysRevLett.116.158001
- Allen, F. I., Comolli, L. R., Kusoglu, A., Modestino, M. A., Minor, A. M., Weber, A. Z., et al. (2015). Morphology of hydrated as-cast nafion revealed through cryo electron tomography. *ACS Macro Lett.* 4 (1), 1–5. doi:10.1021/mz500606h
- Aziz, S. B., Woo, T. J., Kadir, M. F. Z., and Ahmed, H. M. (2018). A conceptual review on polymer electrolytes and ion transport models. *J. Sci. Adv. Mater. Devices* 3 (1), 1–17. doi:10.1016/j.jsamd.2018.01.002
- Bedrov, D., Piquemal, J.-P., Borodin, O., Mackerell, A. D., Roux, B., Schröder, C., et al. (2019). Molecular dynamics simulations of ionic liquids and electrolytes using polarizable force fields. *Chem. Rev.* 119 (13), 7940–7995. doi:10.1021/acs.chemrev.8b00763
- Berens, S. J., Yahya, A., Fang, J., Angelopoulos, A., Nickels, J. D., Vasenkov, S., et al. (2020). Transition between different diffusion regimes and its relationship with structural properties in nafion by high field diffusion NMR in combination with small-angle X-ray and neutron scattering. *J. Phys. Chem. B* 124 (40), 8943–8950. doi:10.1021/acs.jpcc.0c07249
- Bocharova, V., and Sokolov, A. P. (2020). Perspectives for polymer electrolytes: A view from fundamentals of ionic conductivity. *Macromolecules* 53 (11), 4141–4157. doi:10.1021/acs.macromol.9b02742

- Bocharova, V., Wojnarowska, Z., Cao, P.-F., Fu, Y., Kumar, R., Li, B., et al. (2017). Influence of chain rigidity and dielectric constant on the glass transition temperature in polymerized ionic liquids. *J. Phys. Chem. B* 121 (51), 11511–11519. doi:10.1021/acs.jpcc.7b09423
- Bollinger, J. A., Stevens, M. J., and Frischknecht, A. L. (2020). Quantifying single-ion transport in percolated ionic aggregates of polymer melts. *ACS Macro Lett.* 9 (4), 583–587. doi:10.1021/acsmacrolett.0c00139
- Castañeda, S., and Ribadeneira, R. (2020). Description of hydroxide ion structural diffusion in a quaternized SEBS anion exchange membrane using ab initio molecular dynamics. *J. Phys. Chem. C* 124 (18), 9834–9851. doi:10.1021/acs.jpcc.9b10018
- Chen, C., Arntsen, C., and Tse, Y.-L. S. (2020a). Simulation study of the effects of phase separation on hydroxide solvation and transport in anion exchange membranes. *J. Chem. Phys.* 152, 094903. doi:10.1063/1.5143168
- Chen, C., Tse, Y. L. S., Lindberg, G. E., Knight, C., and Voth, G. A. (2016). Hydroxide solvation and transport in anion exchange membranes. *J. Am. Chem. Soc.* 138 (3), 991–1000. doi:10.1021/jacs.5b11951
- Chen, S., Wang, H., Zhang, J., Lu, S., and Xiang, Y. (2020b). Effect of side chain on the electrochemical performance of poly (ether ether ketone) based anion-exchange membrane: A molecular dynamics study. *J. Memb. Sci.* 605, 118105. doi:10.1016/j.memsci.2020.118105
- Chen, W., Mandal, M., Huang, G., Wu, X., He, G., Kohl, P. A., et al. (2019). Highly conducting anion-exchange membranes based on cross-linked poly(norbornene): Ring opening metathesis polymerization. *ACS Appl. Energy Mat.* 2 (4), 2458–2468. doi:10.1021/acsapm.8b02052
- Choi, J.-H., Ye, Y., Elabd, Y. A., and Winey, K. I. (2013). Network structure and strong microphase separation for high ion conductivity in polymerized ionic liquid block copolymers. *Macromolecules* 46 (13), 5290–5300. doi:10.1021/ma400562a
- Clark, J. A., Santiso, E. E., and Frischknecht, A. L. (2019). Morphology and proton diffusion in a coarse-grained model of sulfonated poly(phenylenes). *J. Chem. Phys.* 151 (10), 104901. doi:10.1063/1.5116684
- De Nicola, A., Correa, A., Milano, G., La Manna, P., Musto, P., Mensitieri, G., et al. (2017). Local structure and dynamics of water absorbed in poly(ether imide): A hydrogen bonding anatomy. *J. Phys. Chem. B* 121 (14), 3162–3176. doi:10.1021/acs.jpcc.7b00992
- Dekel, D. R. (2018). Review of cell performance in anion exchange membrane fuel cells. *J. Power Sources* 375, 158–169. doi:10.1016/j.jpowsour.2017.07.117
- Devanathan, R., Venkatnathan, A., Rousseau, R., Dupuis, M., Frigato, T., Gu, W., et al. (2010). Atomistic simulation of water percolation and proton hopping in nafion fuel cell membrane. *J. Phys. Chem. B* 114 (43), 13681–13690. doi:10.1021/jp103398b
- Diederichsen, K. M., Mcshane, E. J., and McCloskey, B. D. (2017). Promising routes to a high Li<sup>+</sup> transference number electrolyte for lithium ion batteries. *ACS Energy Lett.* 2 (11), 2563–2575. doi:10.1021/acsenenergylett.7b00792
- Dong, D., Wei, X., Hooper, J. B., Pan, H., and Bedrov, D. (2018a). Role of cationic groups on structural and dynamical correlations in hydrated quaternary ammonium-functionalized poly(p-phenylene oxide)-based anion exchange membranes. *Phys. Chem. Chem. Phys.* 20 (29), 19350–19362. doi:10.1039/C8CP02211A
- Dong, D., Zhang, W., Barnett, A., Lu, J., Van Duin, A. C. T., Molinero, V., et al. (2018b). Multiscale modeling of structure, transport and reactivity in alkaline fuel cell membranes: Combined coarse-grained, atomistic and reactive molecular dynamics simulations. *Polymers* 10, 1289. doi:10.3390/polym10111289
- Dong, D., Zhang, W., Van Duin, A. C. T., and Bedrov, D. (2018c). Grotthuss versus vehicular transport of hydroxide in anion-exchange membranes: Insight from combined reactive and nonreactive molecular simulations. *J. Phys. Chem. Lett.* 9 (4), 825–829. doi:10.1021/acs.jpclett.8b00004
- Doo, G., Lee, J. H., Yuk, S., Choi, S., Lee, D.-H., Lee, D. W., et al. (2018). Tuning the ionomer distribution in the fuel cell catalyst layer with scaling the ionomer aggregate size in dispersion. *ACS Appl. Mat. Interfaces* 10 (21), 17835–17841. doi:10.1021/acsami.8b01751
- Dorenbos, G. (2020). How hydrophobic side chain design affects water cluster connectivity in model polymer electrolyte membranes: Linear versus Y-shaped side chains. *Int. J. Hydrogen Energy* 45 (58), 33906–33924. doi:10.1016/j.ijhydene.2020.09.010
- Dorenbos, G. (2019). Coarse-grained study of the effect of hydrophobic side chain length on cluster size distributions and water diffusion in (Amphiphilic-Hydrophobic) multi-block co-polymer membranes. *Polymer* 173, 43–57. doi:10.1016/j.polymer.2019.04.025
- Dorenbos, G. (2017a). Doping proton transport channels in poly-electrolyte membranes with high acidic site density polymers. *Eur. Polym. J.* 97, 14–25. doi:10.1016/j.eurpolymj.2017.09.040
- Dorenbos, G. (2017b). Improving proton conduction pathways in di- and triblock copolymer membranes: Branched versus linear side chains. *J. Chem. Phys.* 146, 244909. doi:10.1063/1.4989487
- Economou, N. J., Barnes, A. M., Wheat, A. J., Schaberg, M. S., Hamrock, S. J., Buratto, S. K., et al. (2015). Investigation of humidity dependent surface morphology and proton conduction in multi-acid side chain membranes by conductive probe atomic force microscopy. *J. Phys. Chem. B* 119 (44), 14280–14287. doi:10.1021/acs.jpcc.5b07255
- Elabd, Y. A. (2019). Ion transport in hydroxide conducting block copolymers. *Mol. Syst. Des. Eng.* 4 (3), 519–530. doi:10.1039/c9me00022d
- Fong, K. D., Self, J., McCloskey, B. D., and Persson, K. A. (2021). Ion correlations and their impact on transport in polymer-based electrolytes. *Macromolecules* 54 (6), 2575–2591. doi:10.1021/acs.macromol.0c02545
- Frischknecht, A. L., and Winey, K. I. (2019). The evolution of acidic and ionic aggregates in ionomers during microsecond simulations. *J. Chem. Phys.* 150 (6), 064901. doi:10.1063/1.5085069
- Gebel, G., and Diat, O. (2005). Neutron and X-ray scattering: Suitable tools for studying ionomer membranes. *Fuel Cells* 5 (2), 261–276. doi:10.1002/fuce.200400080
- Ghosh, S., and Chakrabarti, R. (2016). Molecular dynamics simulation elucidates the preferential binding affinity of sodium and tetramethylammonium ions for tetrameric nafion unit under aqueous conditions. *RSC Adv.* 6 (100), 97961–97968. doi:10.1039/C6RA21845H
- Giffin, G. A., Haugen, G. M., Hamrock, S. J., and Di Noto, V. (2013). Interplay between structure and relaxations in perfluorosulfonic acid proton conducting membranes. *J. Am. Chem. Soc.* 135 (2), 822–834. doi:10.1021/ja3099799
- Griffiths, M. Z., and Shinoda, W. (2019). tSPICA: Temperature- and pressure-dependent coarse-grained force field for organic molecules. *J. Chem. Inf. Model.* 59 (9), 3829–3838. doi:10.1021/acs.jcim.9b00480
- Haskins, J. B., Bennett, W. R., Wu, J. J., Hernández, D. M., Borodin, O., Monk, J. D., et al. (2014). Computational and experimental investigation of Li-doped ionic liquid electrolytes: [pyr14][TFSI], [pyr13][FSI], and [EMIM][BF4]. *J. Phys. Chem. B* 118 (38), 11295–11309. doi:10.1021/jp5061705
- Heres, M., Cosby, T., Mapesa, E. U., Liu, H., Berdzinski, S., Strehmel, V., et al. (2018). Ion transport in glassy polymerized ionic liquids: Unraveling the impact of the molecular structure. *Macromolecules* 52 (1), 88–95. doi:10.1021/acs.macromol.8b01273
- Jacob, C., Matsumoto, A., Brennan, M., Liu, H., Paddison, S. J., Urakawa, O., et al. (2017). Polymerized ionic liquids: Correlation of ionic conductivity with nanoscale morphology and counterion volume. *ACS Macro Lett.* 6 (9), 941–946. doi:10.1021/acsmacrolett.7b00335
- Jeon, J. Y., Park, S., Han, J., Maurya, S., Mohanty, A. D., Tian, D., et al. (2019). Synthesis of aromatic anion exchange membranes by friedel-crafts bromoalkylation and cross-linking of polystyrene block copolymers. *Macromolecules* 52 (5), 2139–2147. doi:10.1021/acs.macromol.8b02355
- Johansson, E. O., Yamada, T., Sundén, B., and Yuan, J. (2015). Dissipative particle dynamics approach for nano-scale membrane structure reconstruction and water diffusion coefficient estimation. *Int. J. Hydrogen Energy* 40 (4), 1800–1808. doi:10.1016/j.ijhydene.2014.11.030
- Jones, S. D., Nguyen, H., Richardson, P. M., Chen, Y.-Q., Wyckoff, K. E., Hawker, C. J., et al. (2022). Design of polymeric zwitterionic solid electrolytes with superionic lithium transport. *ACS Cent. Sci.* 8 (2), 169–175. doi:10.1021/acscentsci.1c01260
- Jorn, R., Savage, J., and Voth, G. A. (2012). Proton conduction in exchange membranes across multiple length scales. *Acc. Chem. Res.* 45 (11), 2002–2010. doi:10.1021/ar200323q
- Jorn, R., and Voth, G. A. (2012). Mesoscale simulation of proton transport in proton exchange membranes. *J. Phys. Chem. C* 116 (19), 10476–10489. doi:10.1021/jp300040w
- Kacar, G., Peters, E. A. J. F., and De With, G. (2013). Mesoscopic simulations for the molecular and network structure of a thermoset polymer. *Soft Matter* 9, 5785. doi:10.1039/c3sm50304f
- Kadulkar, S., Milliron, D. J., Truskett, T. M., and Ganesan, V. (2020). Transport mechanisms underlying ionic conductivity in nanoparticle-based single-ion electrolytes. *J. Phys. Chem. Lett.* 11 (17), 6970–6975. doi:10.1021/acs.jpclett.0c01937
- Kashyap, H. K., Annapureddy, H. V., Raineri, F. O., and Margulis, C. J. (2011). How is charge transport different in ionic liquids and electrolyte solutions? *J. Phys. Chem. B* 115 (45), 13212–13221. doi:10.1021/jp204182c
- Katzenberg, A., Angulo, A., Kusoglu, A., and Modestino, M. A. (2021). Impacts of organic sorbates on the ionic conductivity and nanostructure of perfluorinated sulfonic-acid ionomers. *Macromolecules* 54 (11), 5187–5195. doi:10.1021/acs.macromol.1c00494

- Keith, J. R., and Ganesan, V. (2020). Ion transport mechanisms in salt-doped polymerized zwitterionic electrolytes. *J. Polym. Sci.* 58 (4), 578–588. doi:10.1002/pol.20190099
- Ketkar, P. M., Shen, K.-H., Hall, L. M., and Epps, T. H. (2019). Charging toward improved lithium-ion polymer electrolytes: Exploiting synergistic experimental and computational approaches to facilitate materials design. *Mol. Syst. Des. Eng.* 4 (2), 223–238. doi:10.1039/c8me00105g
- Kumar, A., Pisula, W., and Mullen, K. (2019). One dimensional enhanced anhydrous proton conduction in well defined molecular columns induced by non-covalent interactions. *ChemPhysChem* 20 (5), 651–654. doi:10.1002/cphc.201801017
- Kusoglu, A., Vezzù, K., Hegde, G. A., Nawn, G., Motz, A. R., Sarode, H. N., et al. (2020). Transport and morphology of a proton exchange membrane based on a doubly functionalized perfluorosulfonic imide side chain perfluorinated polymer. *Chem. Mat.* 32 (1), 38–59. doi:10.1021/acs.chemmater.8b05012
- Kusoglu, A., and Weber, A. Z. (2017). New insights into perfluorinated sulfonic-acid ionomers. *Chem. Rev.* 117 (3), 987–1104. doi:10.1021/acs.chemrev.6b00159
- Lee, M.-T. (2020). Designing anion exchange membranes with enhanced hydroxide ion conductivity by mesoscale simulations. *J. Phys. Chem. C* 124 (8), 4470–4482. doi:10.1021/acs.jpcc.9b11566
- Lee, M.-T. (2019). Exploring side-chain designs for enhanced ion conductivity of anion-exchange membranes by mesoscale simulations. *J. Phys. Chem. C* 123 (17), 10802–10815. doi:10.1021/acs.jpcc.9b01815
- Lee, M. T. (2021). Designing highly conductive block copolymer-based anion exchange membranes by mesoscale simulations. *J. Phys. Chem. B* 125 (10), 2729–2740. doi:10.1021/acs.jpcc.0c10909
- Lee, M. T., Vishnyakov, A., and Neimark, A. V. (2016). Coarse-grained model of water diffusion and proton conductivity in hydrated polyelectrolyte membrane. *J. Chem. Phys.* 144, 014902. doi:10.1063/1.4938271
- Li, L., Wang, J.-A., Ma, L., Bai, L., Zhang, A., Qaisrani, N. A., et al. (2021). Dual-side-chain-grafted poly(phenylene oxide) anion exchange membranes for fuel-cell and electrodialysis applications. *ACS Sustain. Chem. Eng.* 9 (25), 8611–8622. doi:10.1021/acssuschemeng.1c02189
- Li, W., Burkhart, C., Polinska, P., Harmandaris, V., and Dostakis, M. (2020). Backmapping coarse-grained macromolecules: An efficient and versatile machine learning approach. *J. Chem. Phys.* 153 (4), 041101. doi:10.1063/5.0012320
- Lind, F., Rebolgar, L., Bengani-Lutz, P., Asatekin, A., and Panzer, M. J. (2016). Zwitterion-containing ionogel electrolytes. *Chem. Mat.* 28 (23), 8480–8483. doi:10.1021/acs.chemmater.6b04456
- Liu, H., Cavaliere, S., Jones, D. J., Rozière, J., and Paddison, S. J. (2018a). Morphology of hydrated nafion through a quantitative cluster Analysis: A case study based on dissipative particle dynamics simulations. *J. Phys. Chem. C* 122 (24), 13130–13139. doi:10.1021/acs.jpcc.8b01842
- Liu, H., Cavaliere, S., Jones, D. J., Rozière, J., and Paddison, S. J. (2018b). Scaling behavior of nafion with different model parameterizations in dissipative particle dynamics simulations. *Macromol. Theory Simul.* 27, 1800003. doi:10.1002/mats.201800003
- Liu, H., Luo, X., Sokolov, A. P., and Paddison, S. J. (2021). Quantitative evidence of mobile ion hopping in polymerized ionic liquids. *J. Phys. Chem. B* 125 (1), 372–381. doi:10.1021/acs.jpcc.0c06916
- Liu, H., and Paddison, S. J. (2017). Alkyl chain length dependence of backbone-to-backbone distance in polymerized ionic liquids: An atomistic simulation perspective on scattering. *Macromolecules* 50 (7), 2889–2895. doi:10.1021/acs.macromol.6b02708
- Liu, H., and Paddison, S. J. (2016). Direct comparison of atomistic molecular dynamics simulations and X-ray scattering of polymerized ionic liquids. *ACS Macro Lett.* 5 (4), 537–543. doi:10.1021/acsmacrolett.6b00061
- Liu, S., Savage, J., and Voth, G. A. (2015). Mesoscale study of proton transport in proton exchange membranes: Role of morphology. *J. Phys. Chem. C* 119 (4), 1753–1762. doi:10.1021/jp511830f
- Luo, X., Liu, H., Bae, C., Tuckerman, M. E., Hickner, M. A., Paddison, S. J., et al. (2020a). Mesoscale simulations of quaternary ammonium-tethered triblock copolymers: Effects of the degree of functionalization and styrene content. *J. Phys. Chem. C* 124, 16315–16323. doi:10.1021/acs.jpcc.0c03903
- Luo, X., Liu, H., and Paddison, S. J. (2020b). Molecular dynamics simulations of polymerized ionic liquids: Mechanism of ion transport with different anions. *ACS Appl. Polym. Mat.* 3 (1), 141–152. doi:10.1021/acscapm.0c00834
- Luo, X., and Paddison, S. J. (2019). DPD simulations of anion exchange membrane: The effect of an alkyl spacer on the hydrated morphology. *Solid State Ion.* 339, 115012. doi:10.1016/j.ssi.2019.115012
- Ma, B., and Olvera De La Cruz, M. (2021). A perspective on the design of ion-containing polymers for polymer electrolyte applications. *J. Phys. Chem. B* 125 (12), 3015–3022. doi:10.1021/acs.jpcc.0c08707
- Ma, L., Qaisrani, N. A., Hussain, M., Li, L., Jia, Y., Ma, S., et al. (2020). Cyclodextrin modified, multication cross-linked high performance anion exchange membranes for fuel cell application. *J. Memb. Sci.* 607, 118190. doi:10.1016/j.memsci.2020.118190
- Marrink, S. J., Risselada, H. J., Yefimov, S., Tieleman, D. P., and Vries, A. H. D. (2007). The MARTINI force field: Coarse grained model for biomolecular simulations. *J. Phys. Chem. B* 111, 7812–7824. doi:10.1021/jp071097f
- Meek, K. M., Reed, C. M., Pivovar, B., Kreuer, K.-D., Varcoe, J. R., Bance-Soualhi, R., et al. (2020). The alkali degradation of LDPE-based radiation-grafted anion-exchange membranes studied using different *ex situ* methods. *RSC Adv.* 10 (60), 36467–36477. doi:10.1039/d0ra06484j
- Melchior, J.-P., and Jalarvo, N. H. (2019). A quasielastic neutron scattering study of water diffusion in model anion exchange membranes over localized and extended volume increments. *J. Phys. Chem. C* 123 (23), 14195–14206. doi:10.1021/acs.jpcc.9b01873
- Miyazaki, Y., Okazaki, S., and Shinoda, W. (2020). pSPICA: A coarse-grained force field for lipid membranes based on a polar water model. *J. Chem. Theory Comput.* 16 (1), 782–793. doi:10.1021/acs.jctc.9b00946
- Mogurampelly, S., Keith, J. R., and Ganesan, V. (2017). Mechanisms underlying ion transport in polymerized ionic liquids. *J. Am. Chem. Soc.* 139 (28), 9511–9514. doi:10.1021/jacs.7b05579
- Münchinger, A., and Kreuer, K.-D. (2019). Selective ion transport through hydrated cation and anion exchange membranes I. The effect of specific interactions. *J. Memb. Sci.* 592, 117372. doi:10.1016/j.memsci.2019.117372
- Nguyen, H.-D., Nguyen, T. K. L., Planes, E., Jestin, J., Porcar, L., Lyonard, S., et al. (2020). Tailoring the proton conductivity and microstructure of block copolymers by counterion-selective membrane fabrication. *J. Phys. Chem. C* 124 (24), 13071–13081. doi:10.1021/acs.jpcc.0c04682
- Okuwaki, K., Mochizuki, Y., Doi, H., Kawada, S., Ozawa, T., Yasuoka, K., et al. (2018a). Theoretical analyses on water cluster structures in polymer electrolyte membrane by using dissipative particle dynamics simulations with fragment molecular orbital based effective parameters. *RSC Adv.* 8 (60), 34582–34595. doi:10.1039/c8ra07428c
- Okuwaki, K., Mochizuki, Y., Doi, H., and Ozawa, T. (2018b). Fragment molecular orbital based parametrization procedure for mesoscopic structure prediction of polymeric materials. *J. Phys. Chem. B* 122 (1), 338–347. doi:10.1021/acs.jpcc.7b08461
- Pan, J., Li, Y., Han, J., Li, G., Tan, L., Chen, C., et al. (2013). A strategy for disentangling the conductivity–stability dilemma in alkaline polymer electrolytes. *Energy Environ. Sci.* 6, 2912. doi:10.1039/c3ee41968a
- Perrin, J.-C., Lyonard, S., and Volino, F. (2007). Quasielastic neutron scattering study of water dynamics in hydrated nafion membranes. *J. Phys. Chem. C* 111 (8), 3393–3404. doi:10.1021/jp065039q
- Popov, I., Biernacka, K., Zhu, H., Nti, F., Porcarelli, L., Wang, X., et al. (2020). Strongly correlated ion dynamics in plastic ionic crystals and polymerized ionic liquids. *J. Phys. Chem. C* 124 (33), 17889–17896. doi:10.1021/acs.jpcc.0c03297
- Pundir, S. S., Mishra, K., and Rai, D. K. (2018). Ion transport studies in nanocomposite polymer electrolyte membrane of pva-[C4C1Im][HSO4]-SiO2. *J. Solid State Electrochem.* 22 (6), 1801–1815. doi:10.1007/s10008-018-3881-7
- Savage, J., Tse, Y.-L. S., and Voth, G. A. (2014). Proton transport mechanism of perfluorosulfonic acid membranes. *J. Phys. Chem. C* 118 (31), 17436–17445. doi:10.1021/jp504714d
- Seo, Y., Shen, K. H., Brown, J. R., and Hall, L. M. (2019). Role of solvation on diffusion of ions in diblock copolymers: Understanding the molecular weight effect through modeling. *J. Am. Chem. Soc.* 141 (46), 18455–18466. doi:10.1021/jacs.9b07227
- Sepehr, F., Liu, H., Luo, X., Bae, C., Tuckerman, M. E., Hickner, M. A., et al. (2017). Mesoscale simulations of anion exchange membranes based on quaternary ammonium tethered triblock copolymers. *Macromolecules* 50 (11), 4397–4405. doi:10.1021/acs.macromol.7b00082
- Sepehr, F., and Paddison, S. J. (2016). Dissipative particle dynamics interaction parameters from *ab initio* calculations. *Chem. Phys. Lett.* 645, 20–26. doi:10.1016/j.cplett.2015.12.032
- Sevinis Ozbulut, E. B., Seven, S., Bilge, K., Akkas, T., Tas, C. E., Yildiz, B., et al. (2020). Blends of highly branched and linear poly(arylene ether Sulfone)s: Multiscale effect of the degree of branching on the morphology and mechanical properties. *Polymer* 188, 122114. doi:10.1016/j.polymer.2019.122114

- Shen, K.-H., Fan, M., and Hall, L. M. (2021). Molecular dynamics simulations of ion-containing polymers using generic coarse-grained models. *Macromolecules* 54 (5), 2031–2052. doi:10.1021/acs.macromol.0c02557
- Shen, K.-H., and Hall, L. M. (2020). Ion conductivity and correlations in model salt-doped polymers: Effects of interaction strength and concentration. *Macromolecules* 53 (10), 3655–3668. doi:10.1021/acs.macromol.0c00216
- Shi, C., Liu, T., Chen, W., Cui, F., Liu, L., Cai, Y., et al. (2021). Interaction, structure and tensile property of swollen Nafion® membranes. *Polymer* 213, 123224. doi:10.1016/j.polymer.2020.123224
- Shi, S., Liu, Z., Lin, Q., Chen, X., and Kusoglu, A. (2020). Role of ionic interactions in the deformation and fracture behavior of perfluorosulfonic-acid membranes. *Soft Matter* 16 (6), 1653–1667. doi:10.1039/c9sm01964b
- Son, C. Y., and Wang, Z.-G. (2020). Ion transport in small-molecule and polymer electrolytes. *J. Chem. Phys.* 153 (10), 100903. doi:10.1063/5.0016163
- Sorte, E. G., Paren, B. A., Rodriguez, C. G., Fujimoto, C., Poirier, C., Abbott, L. J., et al. (2019). Impact of hydration and sulfonation on the morphology and ionic conductivity of sulfonated poly(phenylene) proton exchange membranes. *Macromolecules* 52 (3), 857–876. doi:10.1021/acs.macromol.8b02013
- Stacy, E. W., Gainaru, C. P., Gobet, M., Wojnarowska, Z., Bocharova, V., Greenbaum, S. G., et al. (2018). Fundamental limitations of ionic conductivity in polymerized ionic liquids. *Macromolecules* 51 (21), 8637–8645. doi:10.1021/acs.macromol.8b01221
- Su, G. M., Cordova, I. A., Yandrasits, M. A., Lindell, M., Feng, J., Wang, C., et al. (2019). Chemical and morphological origins of improved ion conductivity in perfluoro ionene chain extended ionomers. *J. Am. Chem. Soc.* 141 (34), 13547–13561. doi:10.1021/jacs.9b05322
- Sui, Y., Du, Y., Hu, H., Qian, J., and Zhang, X. (2019). Do acid-base interactions really improve the ion conduction in a proton exchange membrane? – a study on the effect of basic groups. *J. Mat. Chem. A* 7 (34), 19820–19830. doi:10.1039/c9ta06508c
- Takaba, H., Hisabe, T., Shimizu, T., and Alam, M. K. (2017). Molecular modeling of OH<sup>−</sup> transport in poly(arylene ether sulfone ketone)s containing quaternized ammonio-substituted fluorenyl groups as anion exchange membranes. *J. Memb. Sci.* 522, 237–244. doi:10.1016/j.memsci.2016.09.019
- Tarokh, A., Karan, K., and Ponnuram, S. (2020). Atomistic MD study of nafion dispersions: Role of solvent and counterion in the aggregate structure, ionic clustering, and acid dissociation. *Macromolecules* 53 (1), 288–301. doi:10.1021/acs.macromol.9b01663
- Taylor, M. E., Clarkson, D., Greenbaum, S. G., and Panzer, M. J. (2021). Examining the impact of polyelectrolyte chemistry on lithium ion transport in ionogel electrolytes. *ACS Appl. Polym. Mat.* 3 (5), 2635–2645. doi:10.1021/acsspm.1c00229
- Trigg, E. B., Gaines, T. W., Marechal, M., Moed, D. E., Rannou, P., Wagener, K. B., et al. (2018). Self-assembled highly ordered acid layers in precisely sulfonated polyethylene produce efficient proton transport. *Nat. Mat.* 17 (8), 725–731. doi:10.1038/s41563-018-0097-2
- Tuckerman, M. E., Chandra, A., and Marx, D. (2010). A statistical mechanical theory of proton transport kinetics in hydrogen-bonded networks based on population correlation functions with applications to acids and bases. *J. Chem. Phys.* 133, 124108. doi:10.1063/1.3474625
- Tuckerman, M. E., Marx, D., Klein, M. L., and Parrinello, M. (1997). On the quantum nature of the shared proton in hydrogen bonds. *Science* 275, 817–820. doi:10.1126/science.275.5301.817
- Vishnyakov, A., Mao, R., Lee, M.-T., and Neimark, A. V. (2018). Coarse-grained model of nanoscale segregation, water diffusion, and proton transport in nafion membranes. *J. Chem. Phys.* 148, 2024108. doi:10.1063/1.4997401
- Wang, R.-Y., and Park, M. J. (2020). Self-assembly of block copolymers with tailored functionality: From the perspective of intermolecular interactions. *Annu. Rev. Mat. Res.* 50 (1), 521–549. doi:10.1146/annurev-matsci-081519-020046
- Wang, R., Liu, S., Wang, L., Li, M., and Gao, C. (2019a). Understanding of nanophase separation and hydrophilic morphology in nafion and speek membranes: A combined experimental and theoretical studies. *Nanomater. (Basel)* 9, 869. doi:10.3390/nano9060869
- Wang, X., Chen, F., Girard, G. M. A., Zhu, H., Macfarlane, D. R., Mecerreyes, D., et al. (2019b). Poly(Ionic liquid)s-in-salt electrolytes with Co-Coordination-Assisted lithium-ion transport for safe batteries. *Joule* 3 (11), 2687–2702. doi:10.1016/j.joule.2019.07.008
- Wang, Y., Fan, F., Agapov, A. L., Yu, X., Hong, K., Mays, J., et al. (2014). Design of superionic polymers—new insights from walden plot analysis. *Solid State Ion.* 262, 782–784. doi:10.1016/j.ssi.2013.09.026
- Welch, C., Labouriau, A., Hjelm, R., Orler, B., Johnston, C., Kim, Y. S., et al. (2012). Nafion in dilute solvent systems: Dispersion or solution? *ACS Macro Lett.* 1 (12), 1403–1407. doi:10.1021/mz3005204
- Wojnarowska, Z., Feng, H., Fu, Y., Cheng, S., Carroll, B., Kumar, R., et al. (2017). Effect of chain rigidity on the decoupling of ion motion from segmental relaxation in polymerized ionic liquids: Ambient and elevated pressure studies. *Macromolecules* 50 (17), 6710–6721. doi:10.1021/acs.macromol.7b01217
- Xiao, J., Yan, D., Li, J., Li, Q., and Sun, H. (2018). Hydronium ions diffusion behavior in nafion membrane by mesoscopic simulation. *AIP Adv.* 8 (7), 075303. doi:10.1063/1.5035366
- Xiao, W., Yang, Q., and Zhu, S. (2020). Comparing ion transport in ionic liquids and polymerized ionic liquids. *Sci. Rep.* 10, 7825. doi:10.1038/s41598-020-64689-8
- Yandrasits, M. A., Lindell, M. J., and Hamrock, S. J. (2019). New directions in perfluoroalkyl sulfonic acid-based proton-exchange membranes. *Curr. Opin. Electrochem.* 18, 90–98. doi:10.1016/j.coelec.2019.10.012
- Ye, Y., Choi, J.-H., Winey, K. I., and Elabd, Y. A. (2012). Polymerized ionic liquid block and random copolymers: Effect of weak microphase separation on ion transport. *Macromolecules* 45 (17), 7027–7035. doi:10.1021/ma301036b
- Yoshida, K., Manabe, H., Takahashi, Y., and Furukawa, T. (2011). Correlation between ionic and molecular dynamics in the liquid state of polyethylene oxide/lithium perchlorate complexes. *Electrochim. Acta* 57, 139–146. doi:10.1016/j.electacta.2011.06.099
- Zelovich, T., Long, Z., Hickner, M., Paddison, S. J., Bae, C., Tuckerman, M. E., et al. (2019a). *Ab initio* molecular dynamics study of hydroxide diffusion mechanisms in nanoconfined structural mimics of anion exchange membranes. *J. Phys. Chem. C* 123 (8), 4638–4653. doi:10.1021/acs.jpcc.8b10298
- Zelovich, T., and Tuckerman, M. E. (2022). Controlling hydronium diffusivity in model proton exchange membranes. *J. Phys. Chem. Lett.* 13 (9), 2245–2253. doi:10.1021/acs.jpclett.1c04071
- Zelovich, T., and Tuckerman, M. E. (2021). OH<sup>−</sup> and H<sub>3</sub>O<sup>+</sup> diffusion in model AEMs and PEMs at low hydration: Insights from *ab initio* molecular dynamics. *Membr. (Basel)* 11, 355. doi:10.3390/membranes11050355
- Zelovich, T., and Tuckerman, M. E. (2020). Water layering affects hydroxide diffusion in functionalized nanoconfined environments. *J. Phys. Chem. Lett.* 11 (13), 5087–5091. doi:10.1021/acs.jpclett.0c01141
- Zelovich, T., Vogt-Maranto, L., Hickner, M. A., Paddison, S. J., Bae, C., Dekel, D. R., et al. (2019b). Hydroxide ion diffusion in anion-exchange membranes at low hydration: Insights from *ab initio* molecular dynamics. *Chem. Mat.* 31 (15), 5778–5787. doi:10.1021/acs.chemmater.9b01824
- Zelovich, T., Vogt-Maranto, L., Simari, C., Nicotera, I., Hickner, M. A., Paddison, S. J., et al. (2022). Non-monotonic temperature dependence of hydroxide ion diffusion in anion exchange membranes. *Chem. Mat.* 34 (5), 2133–2145. doi:10.1021/acs.chemmater.1c03594
- Zelovich, T., Winey, K. I., and Tuckerman, M. E. (2021). Hydronium ion diffusion in model proton exchange membranes at low hydration: Insights from *ab initio* molecular dynamics. *J. Mat. Chem. A* 9 (4), 2448–2458. doi:10.1039/d0ta10565a
- Zhang, W., and Van Duin, A. C. T. (2015). ReaxFF reactive molecular dynamics simulation of functionalized poly(phenylene oxide) anion exchange membrane. *J. Phys. Chem. C* 119 (49), 27727–27736. doi:10.1021/acs.jpcc.5b07271
- Zhang, Z., Cui, Y., Vila, R., Li, Y., Zhang, W., Zhou, W., et al. (2021a). Cryogenic electron microscopy for energy materials. *Acc. Chem. Res.* 54 (18), 3505–3517. doi:10.1021/acs.accounts.1c00183
- Zhang, Z., Krajniak, J., and Ganesan, V. (2021b). A multiscale simulation study of influence of morphology on ion transport in block copolymeric ionic liquids. *Macromolecules* 54 (11), 4997–5010. doi:10.1021/acs.macromol.1c00025
- Zhang, Z., Krajniak, J., Keith, J. R., and Ganesan, V. (2019). Mechanisms of ion transport in block copolymeric polymerized ionic liquids. *ACS Macro Lett.* 8 (9), 1096–1101. doi:10.1021/acsmacrolett.9b00478



- Zhang, Z., Nasrabadi, A. T., Aryal, D., and Ganesan, V. (2020a). Mechanisms of ion transport in lithium salt-doped polymeric ionic liquid electrolytes. *Macromolecules* 53 (16), 6995–7008. doi:10.1021/acs.macromol.0c01444
- Zhang, Z., Wheatle, B. K., Krajniak, J., Keith, J. R., and Ganesan, V. (2020b). Ion mobilities, transference numbers, and inverse haven ratios of polymeric ionic liquids. *ACS Macro Lett.* 9 (1), 84–89. doi:10.1021/acsmacrolett.9b00908
- Zhang, Z., Zofchak, E., Krajniak, J., and Ganesan, V. (2022). Influence of polarizability on the structure, dynamic characteristics, and ion-transport mechanisms in polymeric ionic liquids. *J. Phys. Chem. B* 126 (13), 2583–2592. doi:10.1021/acs.jpcb.1c10662
- Zhao, L., Von Hopffgarten, M., Andrada, D. M., and Frenking, G. (2017). Energy decomposition analysis. *WIREs Comput. Mol. Sci.* 8, 3. doi:10.1002/wcms.1345
- Zhu, L., Pan, J., Wang, Y., Han, J., Zhuang, L., Hickner, M. A., et al. (2016). Multication side chain anion exchange membranes. *Macromolecules* 49 (3), 815–824. doi:10.1021/acs.macromol.5b02671
- Zhu, Z., Luo, X., and Paddison, S. J. (2022). Coarse-grained modeling of ion-containing polymers. *Chem. Rev.* 122 (12), 10710–10745. doi:10.1021/acs.chemrev.1c00913
- Zhu, Z., Luo, X., and Paddison, S. J. (2019). DPD simulations of anion exchange membranes functionalized with various cationic groups and associated anions. *Solid State Ion.* 340, 115011. doi:10.1016/j.ssi.2019.115011
- Zimudzi, T. J., and Hickner, M. A. (2016). Signal enhanced FTIR analysis of alignment in NAFION thin films at SiO<sub>2</sub> and Au interfaces. *ACS Macro Lett.* 5 (1), 83–87. doi:10.1021/acsmacrolett.5b00800



## OPEN ACCESS

## EDITED BY

Ghasem Sargazi,  
Bam University of Medical Sciences and  
Health Services, Iran

## REVIEWED BY

Mohammadreza Moghaddam-manesh,  
Standard research institute of iran, Iran  
Daryoush,  
Graduate University of Advanced  
Technology, Iran  
Abdolali Golpayegani,  
Bam University of Medical Sciences and  
Health Services, Iran

## \*CORRESPONDENCE

Yan Li,  
Liyang6709@163.com

<sup>†</sup>These authors share first authorship

## SPECIALTY SECTION

This article was submitted to Chemical  
Biology,  
a section of the journal  
Frontiers in Chemistry

RECEIVED 07 July 2022

ACCEPTED 01 August 2022

PUBLISHED 26 August 2022

## CITATION

Li D, Yang R, Wu J, Zhong B and Li Y  
(2022), Comprehensive review of  $\alpha$ -  
carboline alkaloids: Natural products,  
updated synthesis, and  
biological activities.  
*Front. Chem.* 10:988327.  
doi: 10.3389/fchem.2022.988327

## COPYRIGHT

© 2022 Li, Yang, Wu, Zhong and Li. This  
is an open-access article distributed  
under the terms of the [Creative  
Commons Attribution License \(CC BY\)](#).  
The use, distribution or reproduction in  
other forums is permitted, provided the  
original author(s) and the copyright  
owner(s) are credited and that the  
original publication in this journal is  
cited, in accordance with accepted  
academic practice. No use, distribution  
or reproduction is permitted which does  
not comply with these terms.

# Comprehensive review of $\alpha$ -carboline alkaloids: Natural products, updated synthesis, and biological activities

Deping Li<sup>1,2</sup>, Renze Yang<sup>1†</sup>, Jun Wu<sup>1</sup>, Bin Zhong<sup>1,2</sup> and Yan Li<sup>1\*</sup>

<sup>1</sup>Department of Pharmacy, First Affiliated Hospital of Gannan Medical University, Ganzhou, China,

<sup>2</sup>Ganzhou Key Laboratory of Immunotherapeutic Drugs Developing for Childhood Leukemia, First Affiliated Hospital of Gannan Medical University, Ganzhou, China

$\alpha$ -carboline (9*H*-pyrido[2,3-*b*]indole), contains a pyridine ring fused with an indole backbone, is a promising scaffold for medicinal chemistry. In recent decades, accumulating evidence shows that  $\alpha$ -carboline natural products and their derivatives possess diverse bioactivities. However, hitherto, there is no comprehensive review to systematically summarize this important class of alkaloids. In this perspective, this paper represents the first review to provide a comprehensive description of  $\alpha$ -carbolines including natural products, updated literature of synthesis, and their diverse biological activities. Their biological activities including antitumor, anti-microbial, anti-Alzheimer's disease, anti-atherosclerosis, and antioxidant activities were highlighted. And the targets and the main structure activity relationships (SARs) will be presented. Finally, challenges and future directions of this class of compounds will be discussed. This review will be helpful in understanding and encouraging further exploration for this group of alkaloids.

## KEYWORDS

$\alpha$ -carboline, neocryptolepine, indolo[2,3-*b*]quinoline, biological activity, alkaloids

## 1 Introduction

Since the structural diversity and wide range of biological activities, carbolines are among the most attractive alkaloids. According to the position of the pyridine nitrogen atom relative to the indole ring, carbolines are classified as  $\alpha$ - (1),  $\beta$ - (2),  $\gamma$ - (3), or  $\delta$ -carbolines (4) (Figure 1) (Dai et al., 2018). Among them,  $\alpha$ -carboline (9*H*-pyrido[2,3-*b*]indole, 1), contains a pyridine ring fused with an indole backbone, has attracted renewed

**Abbreviations:** A $\beta$ , amyloid  $\beta$ -protein; AchE, acetylcholinesterase; AD, Alzheimer's disease; ALK, Anaplastic Lymphoma Kinase; BuChE, butyrylcholinesterase; ACTs, artemisinin-based combination therapies; Brk, breast tumor kinase; DiMIQ, 5,11-dimethy-5*H*-indolo[2,3-*b*]quinoline; DPPH, 2,2-Diphenyl-1-picrylhydrazyl; ED50, 50% effective dose; IC50, 50% inhibition concentration; ID50, 50% infective dose; LDL, low-density lipoprotein; MDR, Multidrug resistance; MIC, Minimum inhibitory concentration; MTP, microsomal triglyceride transfer protein; PARP, poly ADP ribose polymerase; RalA, ras-related protein; SAR, structure activity relationship; SI, select index; Top, topoisomerase; VLDL, very low-density lipoprotein; WHHL, Watanabe heritable hyperlipidemic.

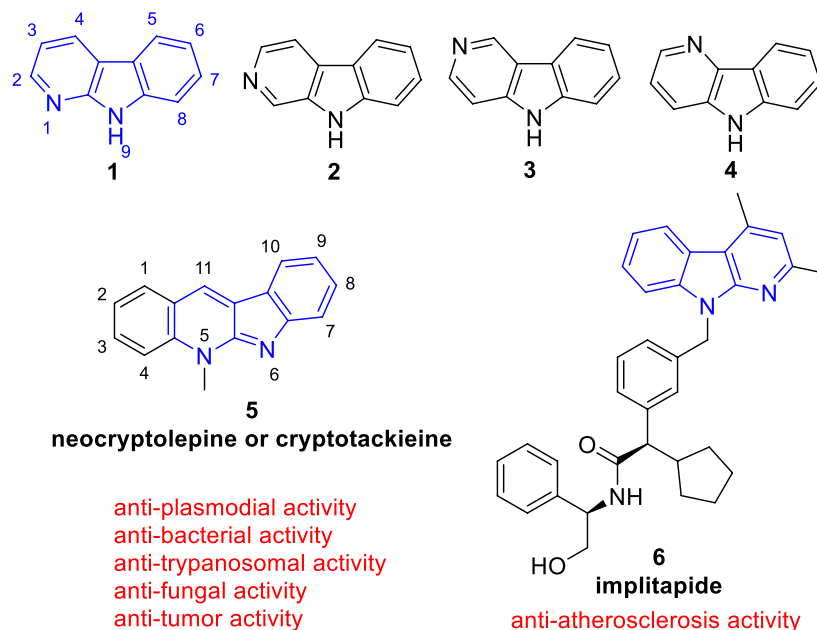


FIGURE 1

Core structure of simple  $\alpha$ - (1),  $\beta$ - (2),  $\gamma$ - (3), and  $\delta$ -carbolines (4). And the representative biological active  $\alpha$ -carboline based molecule (5) which exists in clinical used plants and (6) which reached clinical trails.

attention due to  $\alpha$ -carboline based molecules have been successively reported with diverse biological activities including anti-tumor (Pattey and Guyot, 1989), anti-plasmodial (Sharaf et al., 1996), anti-bacterial (Cimanga et al., 1998), anti-fungal (Cimanga et al., 1998), anti-trypanosomal (Jonckers et al., 2002), anti-Alzheimer's disease (Wang et al., 2017), anti-atherosclerosis (Ueshima et al., 2005), anti-inflammatory (Oda et al., 2009), and neuroprotection activity (Kim et al., 1997).

The classical use of  $\alpha$ -carboline alkaloids is that, the African medicinal plant *Cryptolepis sanguinolenta* (Lindl.) Schlechter (Periplocaceae), containing a biological active  $\alpha$ -carboline based molecule (neocryptolepine or cryptotackieine, 5), has long been used in the treatment of malaria, amoebiasis, fever, and other infectious diseases (Cimanga et al., 1996; Sharaf et al., 1996) (Figure 1). Nowadays, more and more studies have been conducted to modify the structure of  $\alpha$ -carboline natural products or the bare  $\alpha$ -carboline scaffold to obtain derivatives with better activity. Notably, implitapide (a molecule containing  $\alpha$ -carboline moiety, 6) has reached clinical trails as an microsomal triglyceride transfer protein (MTP) inhibitor to reduce the progression of atherosclerosis (Ueshima et al., 2005) (Figure 1). Growing bodies of evidence suggests that  $\alpha$ -carboline is a promising scaffold in medicinal chemistry for drug discovery.

However, to the best of our knowledge, there is no review on this important class of alkaloids except Wadsworth et al.

just reviewed their synthesis in 2015 (Wadsworth et al., 2015). In this perspective, this article aims to provide a comprehensive description of  $\alpha$ -carbolines including the natural products, the updated literature of synthesis, and the diverse biological activities of synthetic derivatives, which represents the first comprehensive review of this group of alkaloids. The main contents of this review are as follows: 1) In the first section,  $\alpha$ -carboline natural products and their biological activities will be described. 2) Since there was a review of synthesis reported in 2015, updated literature of synthesis will be briefly given in the second section according to the reaction type and the publication date. 3) In the third section, the wide range of biological activities of synthetic  $\alpha$ -carboline derivatives will be highlighted according to diseases, targets, research groups, and publication date. In order to better understand the context of the research, literature was first categorized by diseases/targets, then categorized by research groups. In each target/research group section, the logical sequence order was arranged by time. In case where adequate information is available, the structure activity relationships (SARs) of bioactivity will be presented. 4) Finally, challenges and future directions of this class of compounds will be discussed based on our expertise in this field (Liu et al., 2021; Li et al., 2022; Liu et al., 2022; Tian et al., 2022) and carefully analysis of related literature. This work will provide inspiration and encourage further exploration for this group of alkaloids.

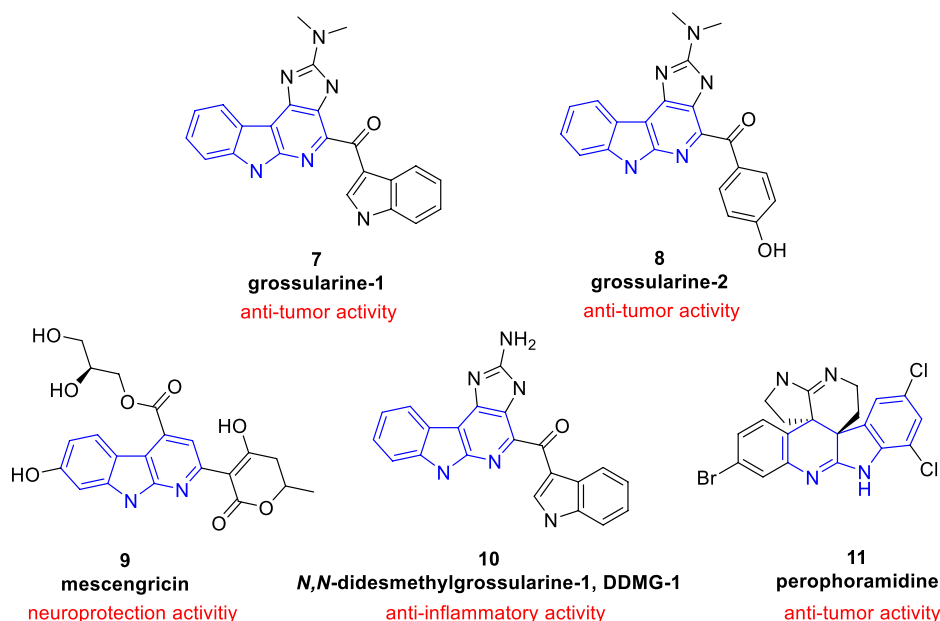


**FIGURE 2**  
Structures and biological activities of α-carboline based natural products.

## 2 Natural occurring α-carbolines

In comparison with other classes of carbolines (especially the renowned β-carbolines), α-carbolines are less presented in natural products. Only limited isolated natural products containing α-carboline skeleton were found (Figure 2).

Grossularine-1 (7) and grossularine-2 (8), isolated from the tunicate *sendrodoia grossularia*, were the first examples of naturally occurring α-carbolines. These two compounds were first found to exhibit striking cytotoxicity toward human and murine tumor cells (Pattey and Guyot, 1989).

Neocryptolepine (also known as Cryptotackieine, 5) possesses a linear indolo[2, 3-*b*]quinoline system or a chromophore of α-carboline fused with a benzene ring from another point of view, was isolated from the extract of root bark of African medicinal plant *Cryptolepis sanguinolenta* (Lindl.) Schlechter (Periplocaceae), which is a climbing liana from West and Central Africa used by traditional therapists in the treatment of malaria, amoebiasis, fever, and other infectious diseases (Cimanga et al., 1996; Sharaf et al., 1996). Further research showed 5 exhibited cytotoxicity and anti-plasmodial activity. Thus, as a promising natural product, literature about 5 and its derivatives is emerging (Lavrado et al., 2010; Wang et al., 2019; Nuthakki et al., 2022).

Mescengricin (9) was firstly isolated from *streptomyces griseoflavus* 2853-SVS4 as a neuronal cell protecting component (Kim et al., 1997). It possesses an α-

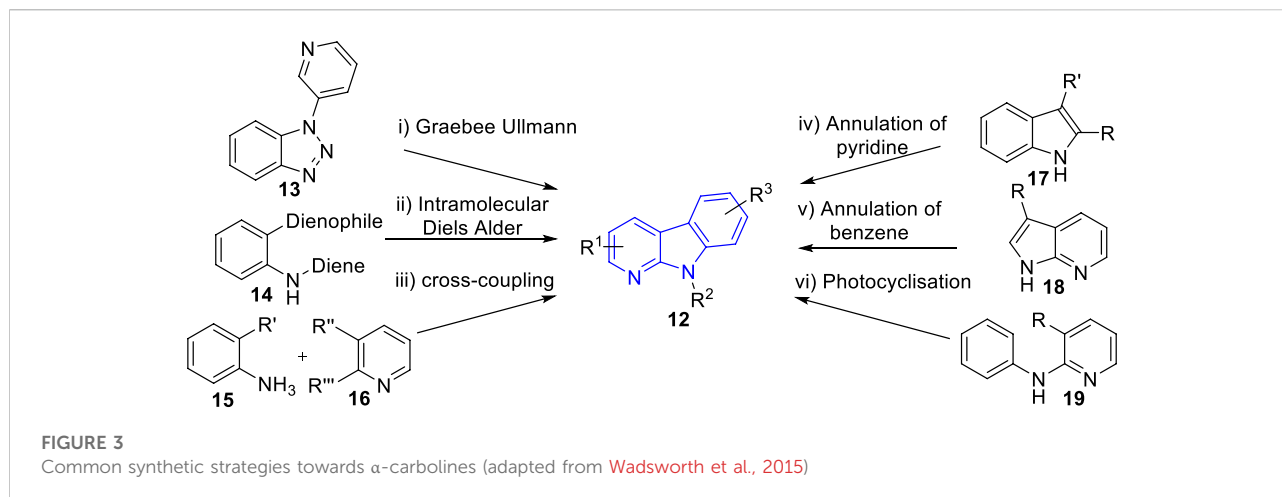
carboline skeleton substituted with a hydroxy, a glycerol-ester, and a hydroxydihydropyrone. In the process of screening neuronal cell protecting substances, it was found to protect chick primary mesencephalic neurons from L-glutamate toxicity with an EC<sub>50</sub> value of 6.0 nM (Shin et al., 2000).

*N,N*-Didesmethylgrossularine-1 (DDMG-1, 10) was isolated from *Polycarpa aurata* (an Indonesian ascidian). Pharmacological experiment showed that it inhibited the mRNA of TNF-α and IκB-α degradation and inhibited NF-κB binding to DNA site in LPS-stimulated RAW 264.7 cells. Moreover, it also inhibited the production of IL-8. These research suggested that 10 was a promising lead compound to treat chronic inflammatory diseases (Oda et al., 2009).

Perophoramidine (11), a polycyclic alkaloid containing an α-carboline moiety, was isolated from *Perophora namei* (a Philippine ascidian). It showed cytotoxicity against HCT116 cell line with an IC<sub>50</sub> value of 60 μM and induced cells apoptosis via poly ADP ribose polymerase (PARP) cleavage within 24 h (Verbitski et al., 2002).

Kapakahines (structures not shown), a large family of cyclic peptides containing an α-carboline skeleton, were isolated from *Cribrochalina olemda* (marine sponge) (Yeung et al., 1996; Nakao et al., 2003). They were often studied as fluorescently labeled chemical probes (Rocha et al., 2015; Kamihira and Nakao, 2021) or anti-malarial agents (Goto et al., 2021).





### 3 General synthetic strategies and advanced synthetic literature of $\alpha$ -carbolines

Due to the wide range of biological activities presented by  $\alpha$ -carboline natural products and their derivatives, interest in their synthesis has arisen. In 2015, Wadsworth et al. (Wadsworth et al., 2015) summarized the synthetic strategies towards  $\alpha$ -carbolines, which including modified Graebbe Ullmann method, Diels Alder method, transition metal catalysed of cross-coupling method, annulation of pyridine to indole derivatives method, annulation of benzene ring method, and photocyclisation of anilinopyridines method (Figure 3). As far as we know, there has been no novel strategy for  $\alpha$ -carbolines since then on. Here, we just summarized the representative literature on their synthesis since 2015.

#### 3.1 Cross-coupling strategy

Using a palladium-catalyzed Ullmann cross-coupling protocol, Yan et al. reported a unified approach to obtain the four isomeric carbolines **1**, **2**, **3**, **4** (Yan et al., 2017) (Supplementary Scheme S1). The pivotal steps associated with the unified approach were the palladium-catalyzed Ullmann cross-coupling of 2-iodocyclohex-2-en-1-one (**20**) with the pertinent halogenated nitropyridine (**21**, **24**, **27**, **30**) and the reductive cyclization of the consequential 2-pyridylcyclohex-2-en-1-one (**22**, **25**, **28**, **31**) to give the corresponding 6,7,8,9-tetrahydrocarboline (**23**, **26**, **29**, **32**). Oxidation of these tetrahydro compounds to their fully aromatic analogues (viz., the carbolines **1**, **2**, **3**, **4**) was easily achieved using 10 wt % palladium on carbon. And this unified approach not only could be used to synthesis core structures of **1**, **2**, **3**, **4**, but also their substituted derivatives, such as harman. While, this protocol was

limited by metal catalysis strategy and inflexibility with regard to substituents.

#### 3.2 Annulation strategy

Using a transition metal catalysis strategy, Medas and co-workers reported two new methods to afford annulated 2-aryl- $\alpha$ -carboline heterocycles (Medas et al., 2020). The first linear method was described that Rh(I) catalysis was used to form the  $\alpha$ -carboline skeleton by [2 + 2 + 2] cyclotrimerization. The second tandem catalytic method stated that using Pd(II) catalyst and mediating a Sonogashira reaction with a [2 + 2 + 2] cyclotrimerization in the same reaction flask to afford the same target molecules (Supplementary Scheme S2).

Through annulation of pyridine ring strategy, Debnath et al. reported an  $\alpha$ -carbolines synthesis method (Debnath et al., 2021) (Supplementary Scheme S3). Using 2-sulfonamidoindoles (**42**) reaction with acetoxy allenates (**43**) under phosphine catalysis to afford dihydro- $\alpha$ -carboline and  $\alpha$ -carboline scaffolds. At 25°C (room temperature), dihydro- $\alpha$ -carboline structures were achieved exclusively through key reactions of Michael addition, 1,4-proton shift, isomerization, 1,2-proton transfer, phosphine elimination, and aza-Michael addition. At 80°C (higher temperature),  $\alpha$ -carboline motifs were achieved via key steps of addition-elimination, aza-Claisen rearrangement, tosyl migration, and aromatization.

Although a broad array of strategies for the synthesis of  $\alpha$ -carbolines were described, many of them are limited by low yields, expensive reagents (such as metal catalysis strategy), starting materials which are difficult to obtain, or inflexibility with regard to substituents. Therefore, novel synthetic strategies of this class of compounds still needs to be explored.

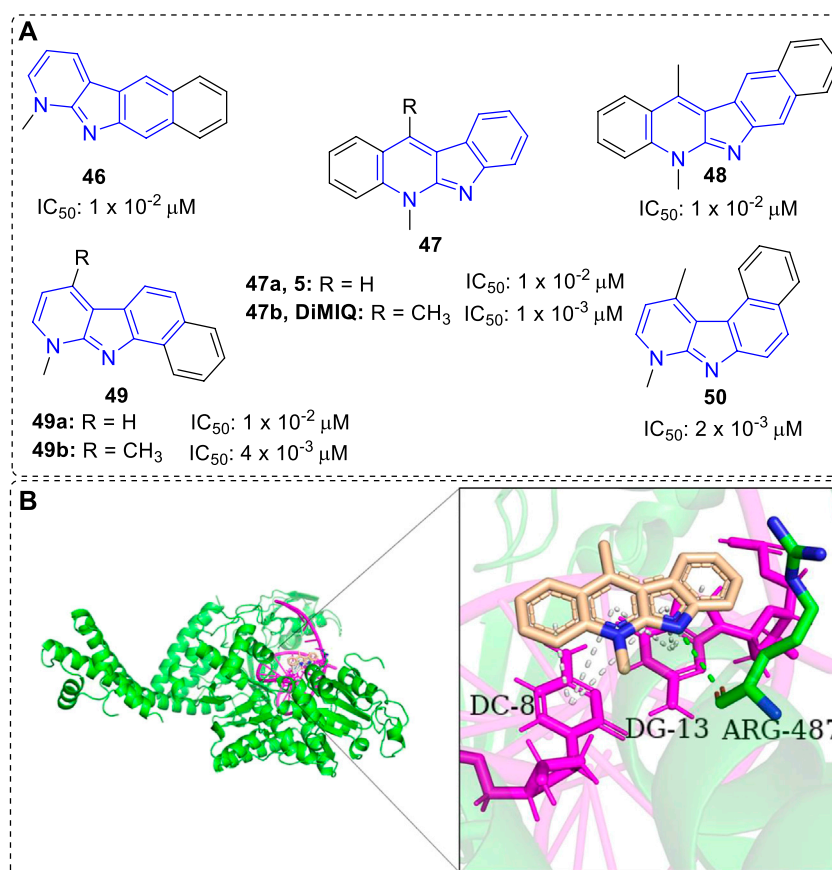


FIGURE 4

(A) Structures and bioactivity of compounds **46**–**50** with various shapes and sizes. IC<sub>50</sub> values were tested *in vitro* against KB cells. (B) DiMIQ (**47b**) in the active site of Top IIa complexed with DNA (PDB code: 5GWK). **47b** is represented in stick model, carbons in **47b** are colored wheat, DNA is colored magenta, ARG-487 residue of Top IIa is colored green and labeled. Hydrogen bond is presented as green dash line.  $\pi$ - $\pi$  interactions are presented as white dash lines.

## 4 Biological activities

### 4.1 Antitumor activity

According to the Global Cancer Statistics 2020, cancer is a leading cause of death and an big impediment to increase life expectancy in each country of the world. Worldwide, a predicted 19.3 million new cancer cases and approximated 10.0 million cancer deaths occurred in 2020 (Sung et al., 2021). Undoubtedly, it is imperative to design efficient drugs for the treatment of this disease. Based on its pathogenesis, many targets have been shown to be useful for tumor therapy, which include topoisomerase (Top) (Liang et al., 2019), aurora kinases (Pradhan et al., 2021), breast tumor kinase (Brk) (Tsui and Miller, 2015), microtubule (Kaur et al., 2014) and ras-related protein (Rala) (Fan et al., 2021), etc. Different structures of  $\alpha$ -carboline derivatives have been designed and synthesized to regulate these targets.

#### 4.1.1 DNA intercalators/top II inhibitors

Kaczmarek and co-workers have devoted themselves to the research of  $\alpha$ -carbolines since 1870s, but until 1992, they demonstrated 5,11-dimethy-5*H*-indolo[2,3-*b*]quinoline (DiMIQ, **47b**), a synthetic analog of **5**, was a DNA intercalator and Top II inhibitor (Figure 4). It was able to stabilize the Top II-DNA cleavable complex *in vitro* (Pognan et al., 1992). In addition, docking study vividly illustrated that **47b** was intercalated between the base pairs of DNA. There were hydrogen-bonding interaction formed between ARG-487 residue of Top II and indolic N-H of DiMIQ, and  $\pi$ - $\pi$  interactions formed between DC-8/DG-13 of DNA and aromatic rings of **47b** (Figure 4B). Therefore, indolo[2,3-*b*]quinolines, containing an  $\alpha$ -carboline moiety from another point of view, had been proved as a new family of the DNA intercalators and Top II inhibitors. In this regard, the studies of indolo[2,3-*b*]quinolines with anti-tumor activity before and after 1992 would be displayed in this section.

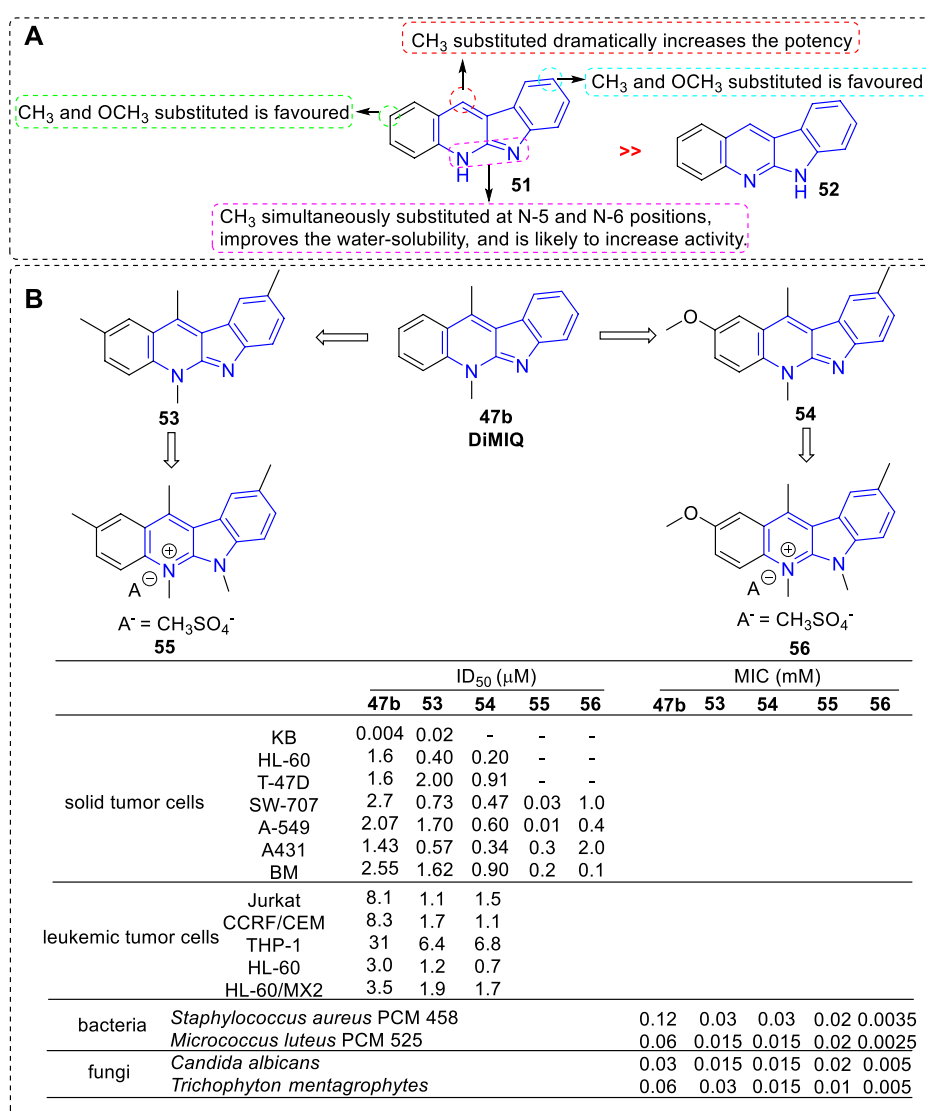


FIGURE 5

(A) SARs of 5*H*- and 6*H*-indolo[2,3-*b*]quinolines; (B) Structures and bioactivity of the representative compounds 53–56.

Early in 1988, certain tetra- or pentacyclic benzo-iso- $\alpha$ -carboline system of compounds were synthesized and their anti-tumor properties were evaluated by the research team of Kaczmarek (Kaczmarek et al., 1988a). The results clearly showed that the size and shape of the molecules (46–50) considerably influenced their bioactivity (Figure 4A). Among them, 47b, an analog of neocryptolepine (5), with a linear, tetracyclic moiety simultaneously bearing two methyl groups at N-5 and C-11 positions was the highest cytotoxicity compound. Further investigations showed it could significantly inhibit tumor growth *in vivo* against mice leukemias P388 and mice melanoma B16. Thus, modification of 47b has been a hot topic of research due to its anti-tumor activity.

In 1994, the biological activity of 5*H*- and 6*H*-indolo[2,3-*b*]quinolines were compared in the furtherance of SAR study (Czoch et al., 1994) (Figure 5). The results showed that all compounds belonging to the 5*H* series (e.g., 51), i.e., bearing a methyl on the pyridine nitrogen atom, displayed marked cytotoxicity against KB cells with IC<sub>50</sub> values in the range of  $2 \times 10^{-3}$  to  $9 \times 10^{-3}$   $\mu$ M. They stimulated the formation of Top II mediated DNA cleavage at concentration of 0.4–10  $\mu$ M. While, the compounds belonging to the 6*H* series (e.g., 52), i.e., lacking a methyl on the pyridine nitrogen atom, were less active in analogous tests compared with the 5*H* series. The reason may be that 5*H* series were partially protonated at pH value of 7.4 (physiological condition) and at low pH values these compounds

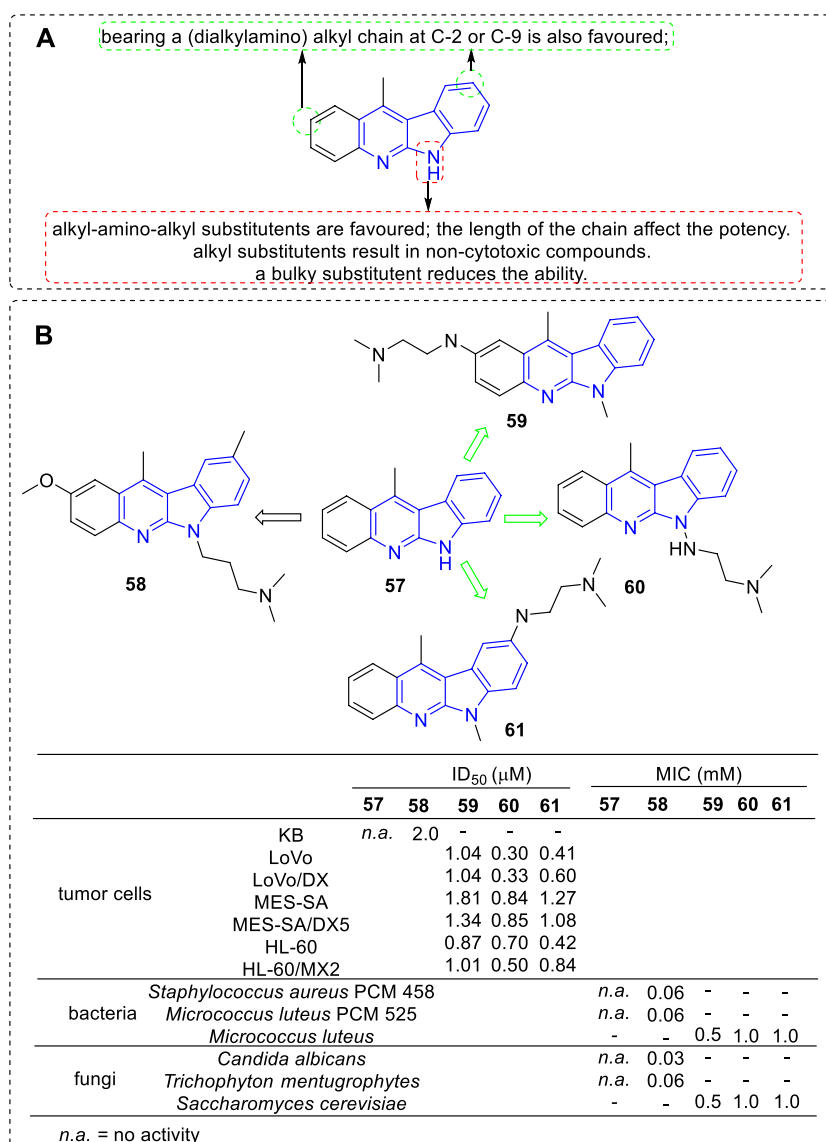


FIGURE 6

(A) SARs of 11-methylated 6H series compounds; (B) Structures and bioactivity of the representative compounds 57–61.

occurred in the form of salts, which result in a better water solubility. Among them, the most potent compound was **53** with two methyl groups substituted at C-2 and C-9 positions. Further, other analogs bearing methoxy groups at C-2 and/or C-9 positions were synthesized (Kaczmarek et al., 1999). The cytotoxicity were slightly improved in the compounds which bearing a methoxy group, or two methoxy groups at C-2 and C-9 positions compared with that of **47b**. The most potent compound was **54** bearing a methoxy substituted at C-2 position and a methyl substituted at C-9 position. Later, these compounds were tested for their cytotoxicity against a panel of leukemic cell lines, and a subline HL-60/MX2 with reduced expression of Top II

(Humeniuk et al., 2002). The results illustrated that all tested compounds possessed cytotoxicity toward these leukemic cell lines and their cytotoxicity relied on the substituents introduced to the indolo[2,3-*b*]quinoline core. Interestingly, THP-1 and HL-60/MX2 cell lines, resistant to etoposide (a reference Top II inhibitor), were susceptible to methoxy- and methyl-substituted derivatives, which suggested that Top II may not be the only target for this class of analogs. In 1998, in order to increase the water solubility, new members of indolo[2,3-*b*]quinoline simultaneously bearing methyl groups at N-5 and N-6 positions were prepared and their cytotoxicity were evaluated (Kaczmarek et al., 1998b). As a result, all obtained derivatives



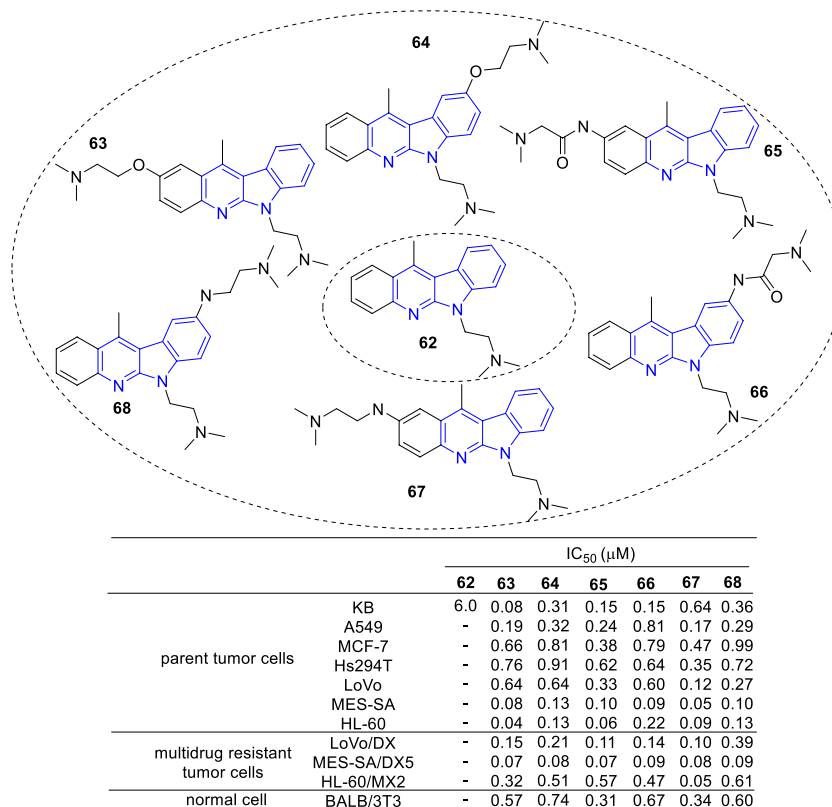


FIGURE 7

Structure and bioactivity of derivatives (62–68) which N-6 fixed an (dimethylamino) ethyl chain, C-2 or C-9 linked another (dimethylamino) ethyl chain by amide, ether or amine bond.

were easily soluble in water with a non-PH-dependent manner, and exhibited cytotoxicity against a panel of tumor cell lines with IC<sub>50</sub> values range from 0.01 to 0.3 μM. They also stimulated the formation of Top II mediated DNA cleavage at concentration of 0.4–0.5 μM. Compound 55, bearing a methoxy group at C-2 position and a methyl group at C-9 position, showed the most potent activity against A549 cell line.

Although 6H series (52) were less active than 5H series (51), further SAR study of 11-methylated 6H series (57) were still carried out and a panel of derivatives were synthesized in 2002 (Kaczmarek et al., 2002) (Figure 6). The substituents included alkyl-, (alkylamino) alkyl-, and 4-(3-chlorophenyl) piperazi-1-yl-propyl. According to the biological assay, only the introduction of an (alkylamino) alkyl chain into the core structure would be an advisable choice for Top II inhibition, cytotoxic and antimicrobial activity (e.g., 58). To further explore the effect of the introduction of (alkylamino) alkyl chains, novel derivatives bearing them at C-2 (e.g., 59), C-9 (e.g., 60) or N-6 (e.g., 61) position were synthesized (Godlewska et al., 2005). Their cytotoxic activity against a series of cancer cell lines as well as their drug-resistant sublines were evaluated. All the analogs exhibited DNA binding and Top II inhibiting activity *in vitro*, as

a result, showed cytotoxicity against the tested cancer cell lines and constrained the growth of Gram-positive bacteria and fungi. Notably, the results indicated a positive relationship between Top II inhibition and cytotoxicity. Certain compounds possess the ability to inhibit the growth of HL-60/MX2 cell line also suggested that Top II may not be the only target for 6H series, which was similar to that of 5H series mentioned above.

Then, novel derivatives which N-6 fixed an (dimethylamino) ethyl chain (62), C-2 or C-9 linked another (dimethylamino) ethyl chain by amide, amine or ether bond were synthesized and tested for their cytotoxic activity against a panel of cancer cell lines and multidrug resistant sublines (Luniewski et al., 2012) (Figure 7). Interestingly, all compounds (63–68) showed cytotoxic activity against the tested cell lines at a similar level.

Further, new derivatives substituted with aminoalkylamino groups at C-11 position were investigated (Wang et al., 2012; Shaban et al., 2017) (Figure 8). Their cytotoxic activity against a panel of cell lines and normal cells were evaluated. The main SARs could be summarized according to the antiproliferative assay: 1) 5-methylated derivatives were more potent than their related 6-methylated derivatives (69 vs. 70); 2) A halogen substituent at the 2-position influenced the antiproliferative

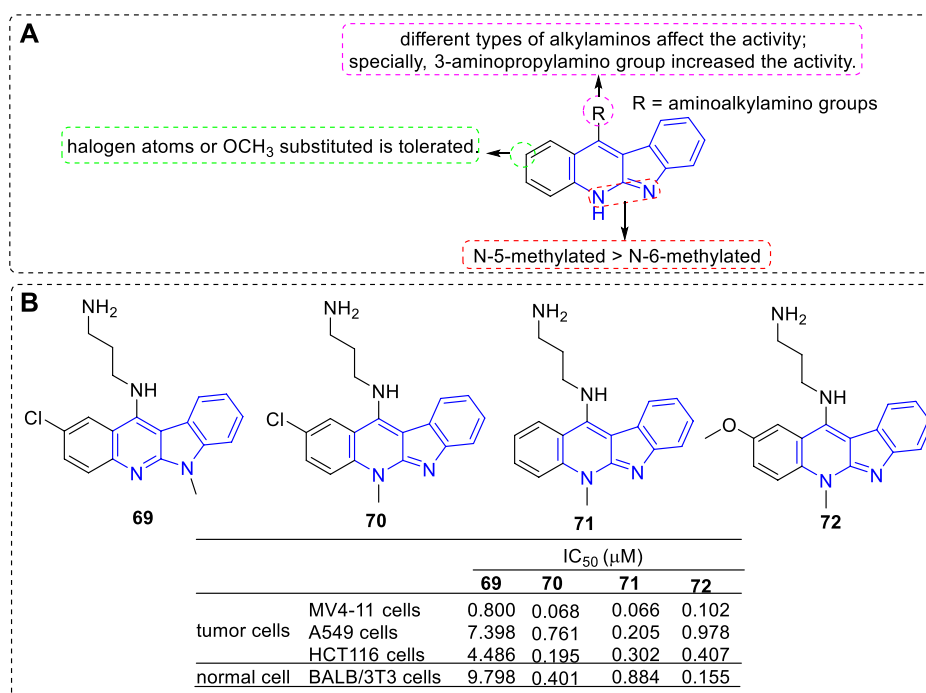


FIGURE 8

(A) SARs of derivatives substituted with aminoalkylamino groups at C-11 position; (B) Structures and bioactivity of the representative compounds 69–72.

activity (70 vs. 71); 3) An electron-donating group-OMe substituted at C-2 position is tolerated (71 vs. 72). 3) Proper alkylamino substituted at C-11 could favourably influence their activities and selectivities, especially the 3-aminopropylamino group (69–72).

To increase selectivity and solubility in water, a series of new analogues of 47b containing an amino acid or a dipeptide chain at C-2 or C-9 position were synthesized respectively (Sidoryk et al., 2012; Sidoryk et al., 2014) (Figure 9). As a result, all amino acid and peptide derivatives displayed moderate to good antiproliferative activity against A549, KB, MCF-7, and LoVo cell lines. The derivatives attaching a hydrophilic amino acid or a peptide chain to the hydrophobic core of 47b increased their hydrophilic properties and decreased their hemolytic activity compared to 47b itself, which was considered to correlate with the low toxicity *in vivo*. Although the author claimed that there were no significant cytotoxic differences between C-2 and C-9 substituted derivatives, we could obtain some key messages by a careful comparison: 1) The toxicity levels of C-2 substituted derivatives was higher than that of C-9 substituted derivatives, especially against A549, MCF-7, and LoVo cell lines (73 vs. 74); 2) C-9 substituted derivatives exhibited no significant differences in antiproliferative activity against cancer and normal cell lines; 3) C-2 substituted derivatives showed marked alterations in antiproliferative activity against cancer and normal cell lines,

which indicated the presence of a distinct mechanism of action towards these two types of cell lines.

In the continued efforts to improve their solubility properties and selectivity, derivatives containing guanidine or guanylamino acid substituents were manufactured and evaluated for their cytotoxic and anti-fungal activity (Sidoryk et al., 2015; Sidoryk et al., 2017) (Figure 10). As results, most of the tested compounds exhibited cytotoxic activity and compounds 75 and 77, which guanidine group directly linked to the core of 47b, exhibited a high selectivity between cancer and normal cells. Although cytotoxic activity was also observed in the *N*-guanylamino acid substituted derivatives (76 and 78), no significant selectivity of action was identified. On the contrary, 75 and 77 were inactive against *C. albicans* biofilms, while 76 possessed a potent anti-fungal activity against *C. albicans* biofilms with an IC<sub>50</sub> value of 4.2 μM. The results indicated that the existence and position of the guanyl moiety in the molecule was essential for cytotoxic activity and selectivity.

Artemisinin, a sesquiterpene lactone from *Artemisia annua*, is famous for its use in the treatment of malaria. Besides its anti-malarial activity, artemisinin and its derivatives are identified with anti-tumor potency (Efferth, 2006; Morrissey et al., 2010). With the aim to develop potent and selective antitumor agents, a series of artemisinin-47b hybrids were designed and synthesized (Wang et al., 2014). The hybrids 79 and 80 showed an increased

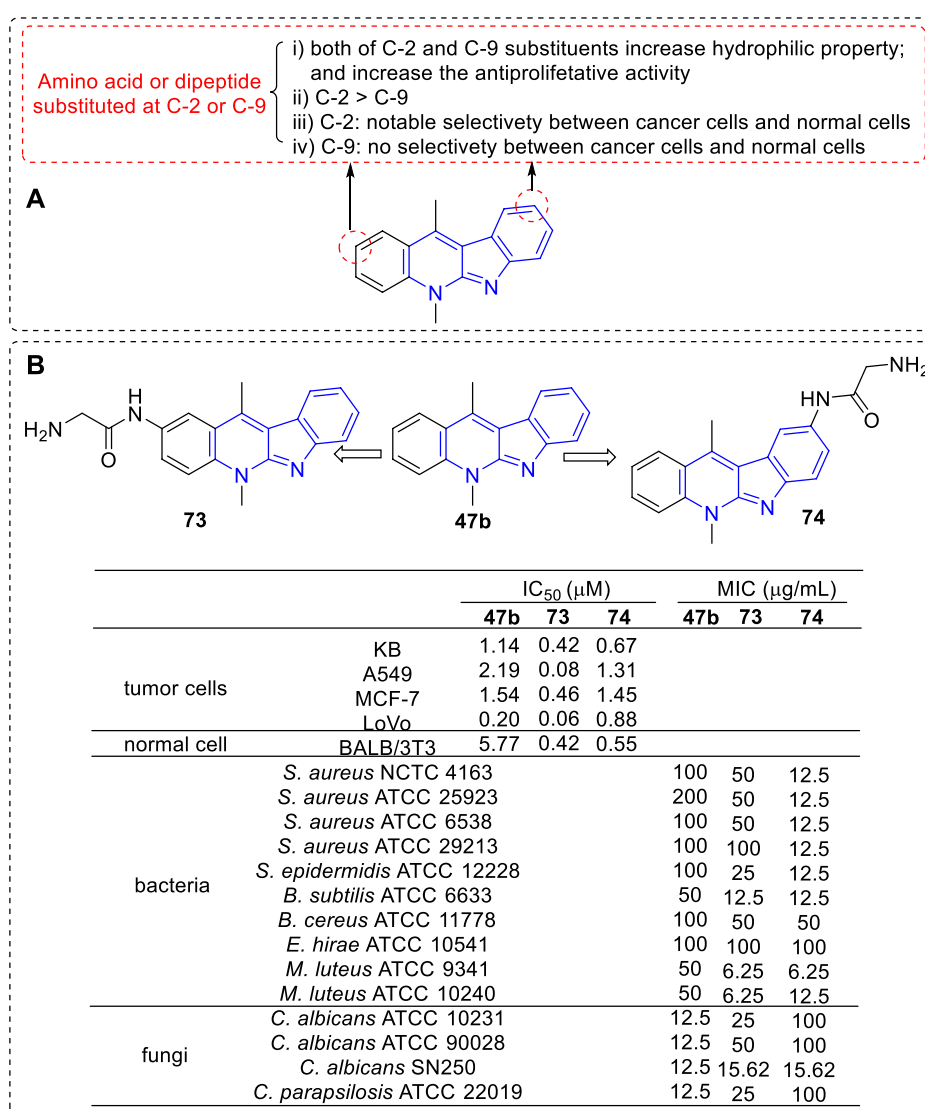


FIGURE 9

(A) SARs of derivatives containing an amino acid or a dipeptide chain at C-2 or C-9 position; (B) Structures and bioactivity of the representative compounds **73**–**74**.

antiproliferative activity against A549 and HCT-116 cell lines compared with dihydroartemisinin (DHA) (Figure 11).

Recently, novel *O*-aminoglycosides-**47b** hybrids were synthesized and evaluated against A549, MCF-7, Hs294T, HL-60, MES-SA, and LoVo cell lines (Figure 12). Hybrids of acosaminyl and **47b** (**81**) showed no selectivity between cancer and normal cells, while hybrids of daunosaminyl and **47b** (**82**) showed good selectivity between cancer and normal cells. Unexpectedly, certain MDR tumor cell lines including LoVo/DX, MES-SA/DX5 were also resistant to these analogs (Bednarek et al., 2006; Roslonek et al., 2016). This was surprising because the parent analogue **47b** displayed antiproliferative activity against all MDR cell lines examined.

Besides the group of Kaczmarek, there were other teams also focused on the research of **47b**. In the screening of novel compounds containing quinoline core as anti-tumor and anti-malarial agents, Akkachairin et al. inadvertently found a novel **47b** derivative **83** with moderate antiproliferative ability against a panel of cancer cell lines but alongside high selectivity toward normal cells (Akkachairin et al., 2020) (Supplementary Figure S1).

Altwayjry et al. synthesized four derivatives of **47b** (**84**–**87**) and evaluated their *in vitro* and *in vivo* effect versus Ehrlich ascites carcinoma (EAC). In addition, their antioxidant activity was also tested using the DPPH method. The results indicated that these naturally-based alkaloids

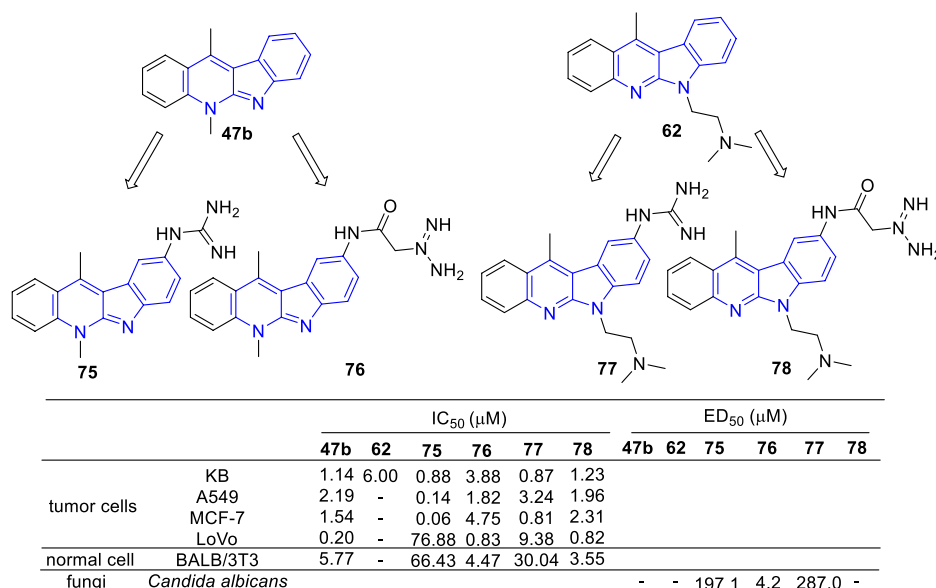


FIGURE 10

Structures and bioactivity of the representative derivatives (75–78) which C-9 substituted with guanidine, amino acid or guanylamino acid.

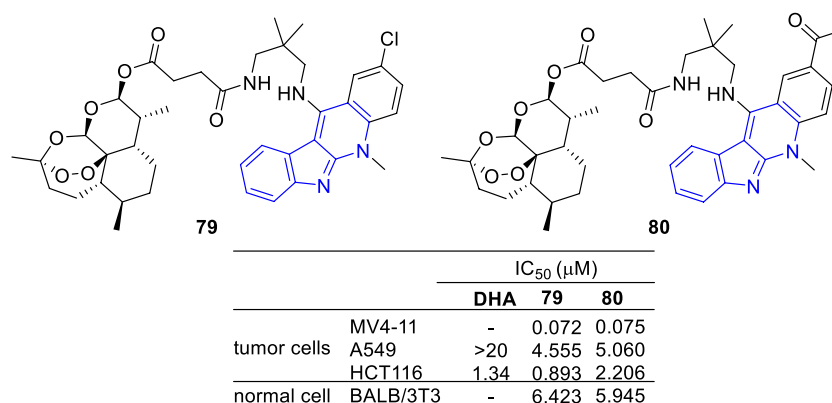


FIGURE 11

Structures and bioactivity of the representative artemisinin-indoloquinoline hybrids 79 and 80.

exhibited antioxidant activity, notable anti-tumor activity and represented an important class of leads as natural-based antitumor drugs (Altwayry et al., 2021) (Supplementary Figure S2).

#### 4.1.2 Aurora B kinase inhibitors

Aurora kinases are essential mitotic cell-cycle regulators and play key roles in cell mitosis and division. Among them, Aurora B is a chromosome passenger protein essential for phosphorylation of histone H3, chromosome segregation, and cytokinesis. Aurora B is frequently elevated in cancer, and represents an attractive

target for cancer therapy (Carmena and Earnshaw, 2003; Fu et al., 2007; Carmena et al., 2009).

Farrell et al. reported an Aurora B kinase inhibitor TAK-901 (88) (Farrell et al., 2013), which inhibited AurB/INCENP with an IC<sub>50</sub> value of 15 nM and inhibited various human cancer cell lines with IC<sub>50</sub> values ranging from 40 to 500 nM. Docking study illustrated that 88 occupied the ATP-binding pocket. Hydrogen-bonding interactions formed between LYS-87, LYS-106 as well as ASN-205 residues and 88, and  $\pi$ - $\pi$  interactions formed between PHE-88 residue and  $\alpha$ -carboline ring of 88. Since synthetic difficulty hampered its further clinical evaluation. The team



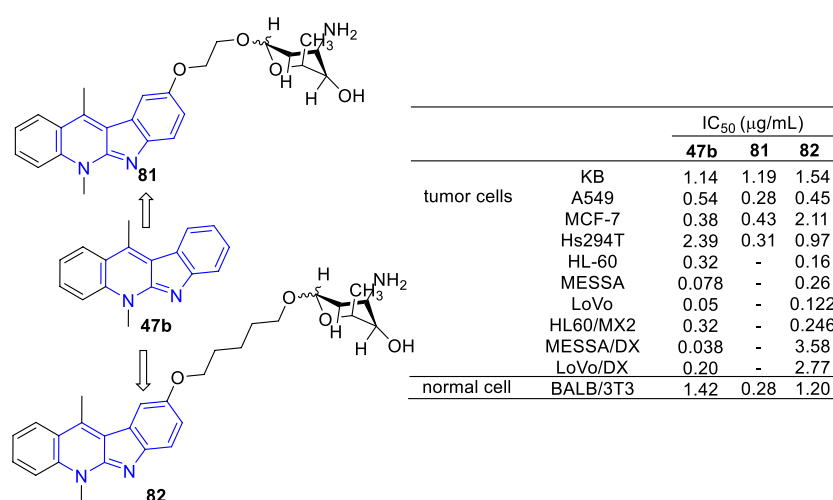


**FIGURE 12**  
Structures and bioactivity of the representative *O*-aminoglycosides-47b hybrids **81** and **82**.

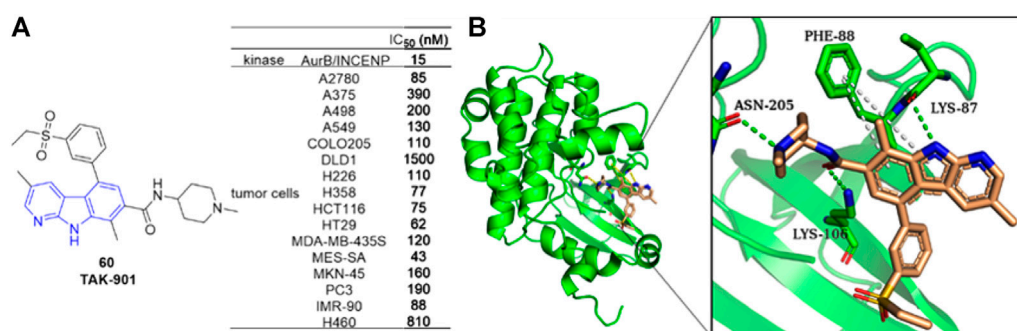


**FIGURE 13**  
(A) Structure and bioactivity of **88** as an Aurora B inhibitor; (B) Binding mode of **88** docked into Aurora B kinase (green ribbon representation, PDB code: 4AF3). **88** is represented in stick model, carbons in ligand are colored wheat. Hydrogen bond is presented as green dash lines.  $\pi$ - $\pi$  interactions are presented as white dash lines.

later reported a practical and efficient synthetic process for **88** using an integrated Pd-catalyzed crosscoupling strategy (Mineno et al., 2015) (Figure 13).

#### 4.1.3 Brk inhibitors

Breast tumor kinase (Brk), which was originally found expressed in a metastatic breast tumor, plays an essential role in both cell dysregulation and metastasis. Brk has become an ideal cellular target for tumor therapy because it occurs in a majority of breast tumors but low or undetectable amounts of Brk occurs in normal tissues (Mitchell et al., 1994; Barker et al., 1997; Brauer and Tyner, 2010).

Mahmoud et al. discovered a series of 4-anilino  $\alpha$ -carbolines as a new class of potent Brk inhibitors (Mahmoud et al., 2014). The type and position of the aniline substituents determined the Brk inhibitory activity, which led to  $IC_{50}$  values varying from nanomolar to inactive. The main SARs were summarized (Figure 14A): 1) Substituents introduced at 3'-position of the aniline residue seemed more promising compared with substituents introduced at sole 2'-position; 2) At the 3'-position of the aniline residue: A lipophilic thioether function was unfavourable; The bulky and hydrophobic trifluoromethyl substituent showed a slight decrease in Brk inhibition; A chloro substituent and hydroxy substituent with less space showed a strong increase for Brk inhibition; 3) Combined substituent

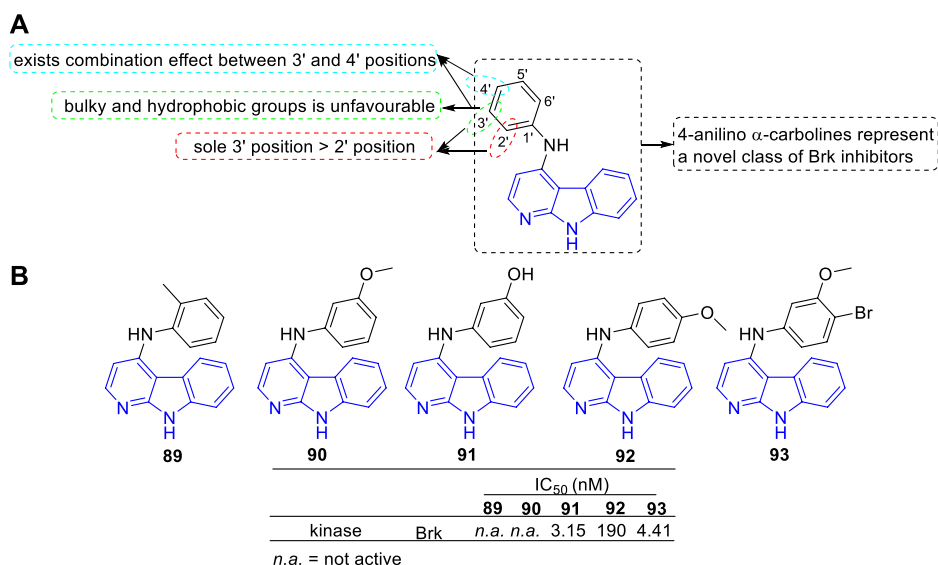


**FIGURE 14**  
 (A) SARs of 4-anilino  $\alpha$ -carbolines as Brk inhibitors; (B) Structures and bioactivity of the representative compounds **89–93**.

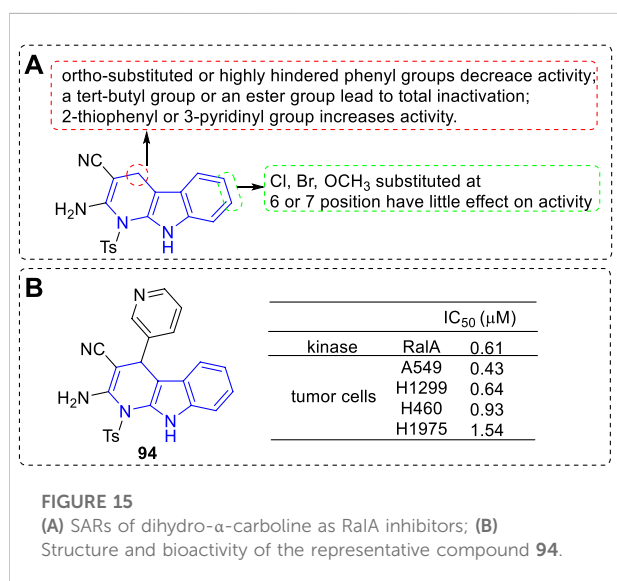


**FIGURE 15**  
 (A) SARs of dihydro- $\alpha$ -carboline as RalA inhibitors; (B) Structure and bioactivity of the representative compound **94**.

effects showed that 3'-methoxy and 4'-bromo substituents increased the activity compared to sole 3'-methoxy substituent which was found to be inactive (**93** vs. **90**). Structures and bioactivity of the representative compounds (**89–93**) were shown in Figure 14B. Later, the team reported two 4-anilino  $\alpha$ -carboline derivatives (structures not shown) possessed the ability to induce nonadhesive breast cancer cells death through inhibiting Brk activity (Oelze et al., 2015).

#### 4.1.4 RalA inhibitors

RalA, a member of the Ras small GTPases superfamily, is critical for Ras-mediated human cancer cells proliferation (Hunter et al., 2015; Yan and Theodorescu, 2018). It has been proved that RalA plays an essential role in regulating cancer initiation, invasion, migration, and metastasis, which makes it an interesting tumor therapeutic target (Bum-Erdene et al., 2020; Chen et al., 2020).

Leng et al. designed and synthesized a series of dihydro- $\alpha$ -carboline derivatives and some of them could inhibit RalA and proliferative of a panel of cancer cell lines (Leng et al., 2020). The main SARs could be summarized (Figure 15A): 1) C-4 position: 1) The ortho-substituted or highly hindered phenyl residue would lead to lower activity; 2) Introduction of a tert-butyl or an ester group to the phenyl residue would result in total inactivation; 3) 2-thiophenyl or 3-pyridinyl moiety exhibited higher activity; 2) C-6 or C-7 position: The kind and position of the substituents had little effect on the bioactivity. The most potent derivative (**94**) inhibited RalA with an IC<sub>50</sub> value of 0.61  $\mu$ M and proliferative of A549 cell lines with an IC<sub>50</sub> value of 0.43  $\mu$ M (Figure 15B).

#### 4.1.5 Microtubule and Top II dual inhibitors

Microtubule consists of microtubulins, participates in the mitotic spindle assembly (Kavallaris, 2010). Top II, a nuclear enzyme, is essential for resolving DNA entanglement and for segregating chromosomes in mitosis (Chen et al., 2013). Both of them are standout anti-tumor targets and their related inhibitors

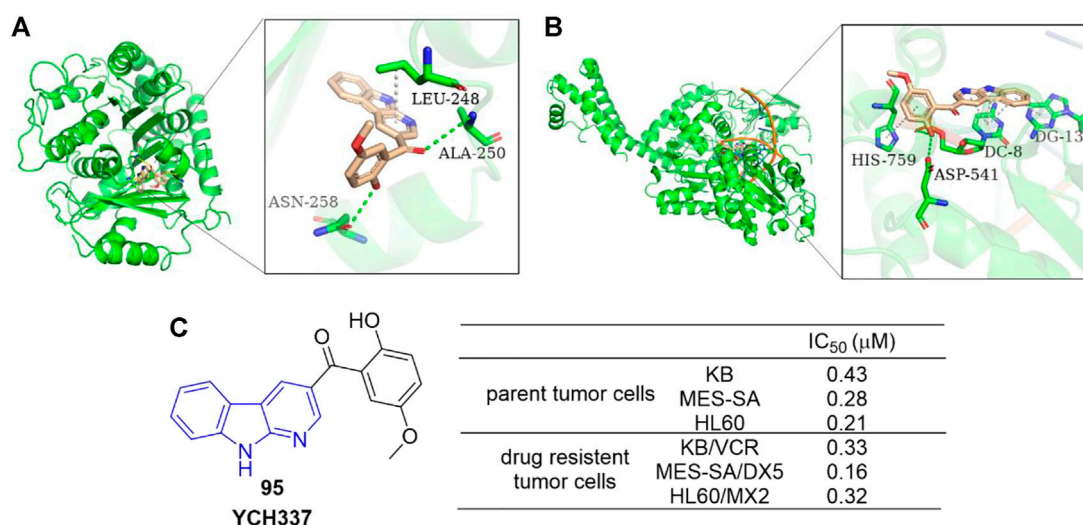


FIGURE 16

**(A)** Binding mode of **95** docked into microtubule (green ribbon representation, PDB code: 1SA0). **95** is represented in stick model, carbons in **95** are colored wheat. Hydrogen bonds are presented as green dash lines.  $\pi$ -sigma interaction is presented as a white dash line. **(B)** Binding mode of **95** docked into Top II $\alpha$  (green ribbon representation, PDB code: 5 gwk). **95** is represented in stick model, carbons in **95** are colored wheat. Hydrogen bonds are presented as green dash lines.  $\pi$ - $\pi$  interactions are presented as white dash lines. **(C)** The structure and bioactivity of the representative compound **95** as microtubule and Top II dual inhibitor.

have been extensively used in the treatment of cancer therapy (Jackson et al., 2007; Nitiss, 2009).

Yi et al. reported an  $\alpha$ -carboline derivative YCH337 (**95**), which targeted both microtubule and Top II (Yi et al., 2015). It suppressed microtubule polymerization *via* binding to the colchicine site and subsequently resulted in mitotic arrest. Docking study showed that there were hydrogen-bonding interactions formed between ALA-250 as well as ASN-258 residues of microtubule and **95**, and  $\pi$ -sigma interaction formed between LEU-248 residue and aromatic rings of **95** (Figure 16A). It also inhibited Top II and caused DNA double-strand breaks. Docking study illustrated that there were hydrogen-bonding interactions formed between ASP-541 as well as HIS-759 residues of Top II and **95**, and  $\pi$ - $\pi$  interactions formed between DC-8/DG-13 of DNA and aromatic rings of **95** (Figure 16B). Its disruption of microtubule was more potent than Top II. Notably, **95** nearly equally inhibited proliferation of MDR tumor cells and their corresponding parent cells (Figure 16C).

#### 4.1.6 ALK inhibitor

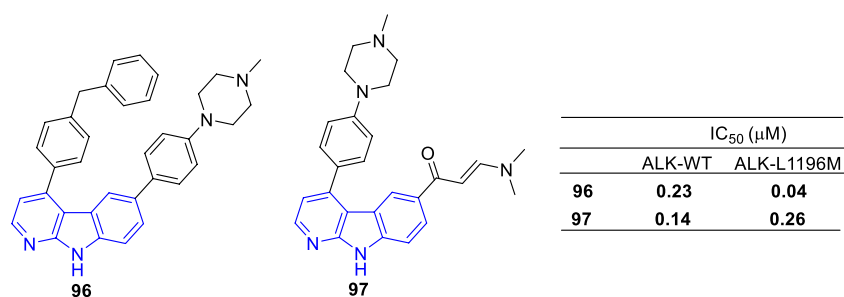
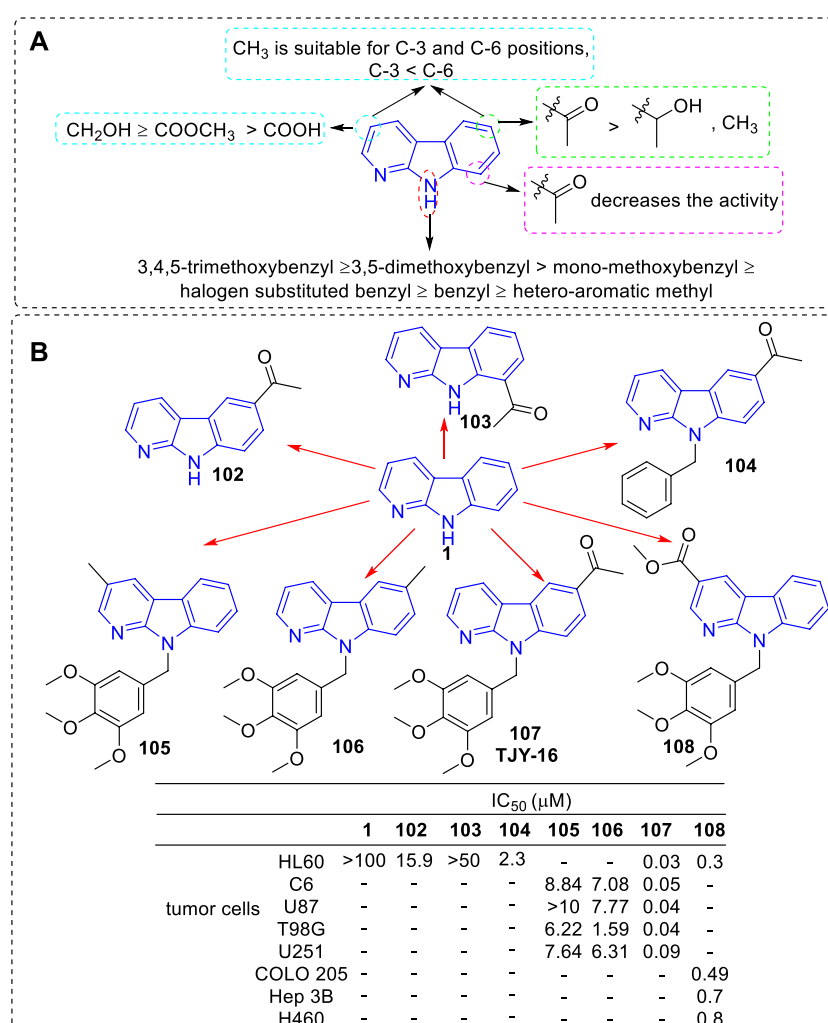
The Anaplastic Lymphoma Kinase (ALK) is aberrantly is rearranged or mutated in several tumors including inflammatory myofibroblastic tumor (IMT), anaplastic large-cell lymphoma (ALCL), neuroblastoma, inflammatory myofibroblastic tumor and nonsmall cell lung cancer (NSCLC) patients. (Mologni et al., 2022a). Thus, ALK has become a therapeutic target for personalized medicine in some selected cancers.

Mologni and coworkers designed and developed some novel ALK inhibitors based on a 4,6-substituted  $\alpha$ -carboline scaffold. Compound **96** showed potent non-ATP-competitive inhibition of wild-type and mutant ALK in biochemical and cellular assays, as well as in xenograft mouse models (Mologni et al., 2022b). Compound **97** showed selective inhibition of native and mutant drug-refractory ALK kinase *in vitro* as well as in human ALK<sup>+</sup> lymphoma and in a Ba/F3 model cells (Mologni et al., 2022a; Mologni et al., 2022b) (Figure 17).

#### 4.1.7 Targets indetermination

Early in 1978, Namirski synthesized some 2-position substituted  $\alpha$ -carboline. Among them, compound **98** showed cytostatic activity (Nantka and Kaczmarek, 1978). At 50 mg/kg dose level, it inhibited tumor growth of transplanted Ehrlich ascites carcinoma and Nemeth-Kellner lymphoma with inhibition of 59 and 66% respectively. Later in 1986, the team synthesized a series of new  $\alpha$ -carboline and evaluated their anti-tumor activity against L1210 (lymphoid leukemia), P388 (lymphocytic leukemia), and Sarcoma180 (Wieczorek et al., 1986). The results showed that  $\alpha$ -carboline derivatives substituted at C-4 position with a methyl group (**99**) or C-6 position with a fluorine (**100**) or chlorine (**101**) atoms caused moderate inhibition of the Sarcoma 180 growth but not other kinds of tumor (Supplementary Figure S3).

In 2010 and 2016, the team of Li successively reported a series of 3, 6, 8, or 9-substituted  $\alpha$ -carboline and tested their

**FIGURE 17**Structure and bioactivity of the representative compounds **96** and **97**.**FIGURE 18**(A) SARs of 3, 6, 8, or 9-substituted α-carbolines for their antitumor activity; (B) Structures and bioactivity of the representative compounds **102–108**.



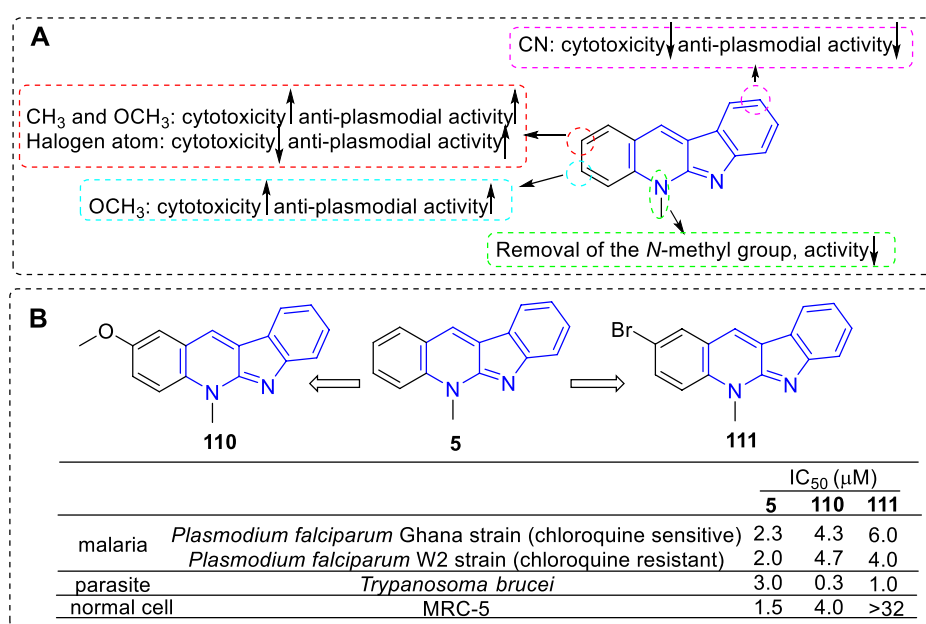


FIGURE 19

(A) SARs of **5** derivatives for their anti-plasmodial activity; (B) Structures and bioactivity of the representative compounds **110** and **111**.

antitumor activity (Tsai et al., 2010; Huang et al., 2016; Lin et al., 2016). Based on the results of activity, the main SARs could be summarized (Figure 18A): 1) The nonsubstituted  $\alpha$ -carboline (**1**) had almost no cytotoxicity; 2) An N-9 methylaryl moiety was a critical functional moiety for maintaining the potency. The following rank order was found: 3,4,5-trimethoxybenzyl  $\geq$  3,5-dimethoxybenzyl > mono-methoxybenzyl  $\geq$  halogen substituted benzyl  $\geq$  benzyl  $\geq$  hetero-aromatic methyl. 3) Based on the C-3 substituents, the following rank order was found: CH<sub>2</sub>OH  $\geq$  COOCH<sub>3</sub>  $\geq$  COOH. 4) Introduction of an acetyl group at C-6 but not C-8 position increased the inhibitory activity; 5) Substituents of C-3, C-6, and C-9 showed synergistic effects. The structures of the representative compounds **102–108** and their activity were shown in Figure 18B.

Besides, Zhang et al. achieved some 2 or 2,4-substituted  $\alpha$ -carbolines with moderate anti-tumor activities via an effective and convenient method (Zhang et al., 2014). Since a few of these compounds were selected to determine their anti-tumor activity, the SAR could not be obtained. The most potent compound **109** exhibited antiproliferative of BEL-7402 cells with an IC<sub>50</sub> value of 0.58  $\mu$ M (Supplementary Figure S4). Emam et al. obtained several Copper (II) complexes with aminoalkylaminoneocryptolepine as anticancer agents (Emam et al., 2015). The most potent compound (structures not shown) exhibited antiproliferative activity of HT-29 cells with an IC<sub>50</sub> value of 0.58  $\mu$ M.

## 4.2 Anti-microbial activity

### 4.2.1 Anti-plasmodial activity

Due to the introduction of the artemisinin-based combination therapies (ACTs), a great success has been achieved globally in the treatment of malaria over the period 2000 to 2019, but there were still an estimated 229 million malaria cases in 2019 (<https://www.who.int/teams/global-malaria-programme>). Therefore, the development of novel drugs to treat malaria is still needed. Natural products isolated from plants are an important resource for the discovery of new drugs. Compound **5**, isolated from the root bark of African plants *Cryptolepis sanguinolenta*, is one of the representative natural products with anti-plasmodial activity besides artemisinin. Compound **5** and its derivatives have achieved great attention for their ability against malaria.

Pieters and coworkers have devoted themselves to the research of compound **5** and its derivatives against malaria since the 1990s (Cimanga et al., 1997; Cimanga et al., 1998). But until in 2002, they reported a set of synthetic analogs and evaluated their anti-plasmodial activity against chloroquine-sensitive and chloroquine-resistant *Plasmodium falciparum* strains (Jonckers et al., 2002; Van et al., 2004). Interestingly, for all compounds, the chloroquine-resistant strain were more sensitive than the chloroquine-sensitive strain. From the results, the main SARs could be summarized (Figure 19): 1) C-1 substitution led to a loss of anti-plasmodial activity; 2) Many of the 2-substituted derivatives displayed higher activity against

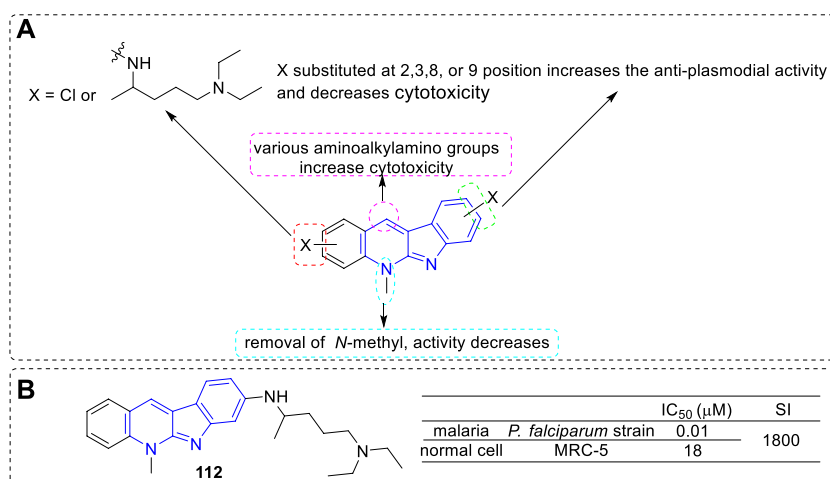


FIGURE 20

(A) SARs of **5** derivatives with basic (aminoalkylamino) side chains; (B) Structure and bioactivity of the representative compound **112**.

plasmodia than that of **5** itself but were also more cytotoxic (e.g., **110**). However, the 2-halo-substituted derivatives were more active against *P. falciparum* than that of **5** and less cytotoxic (e.g., **111**); 3) C-3 substituted derivatives possessed about the same or more anti-plasmodial activity against chloroquine-resistant strain, but they were more cytotoxic; 4) C-9 cyano substitution led to a reduction of cytotoxicity but also a loss of the anti-plasmodial activity. Although some **5** derivatives displayed a higher anti-plasmodial activity than **111**, these compounds also showed a more pronounced cytotoxicity. Therefore, compound **111** was considered as the most promising lead for anti-malarial agents in this regard. The mechanism research showed that **111** displayed a low affinity for DNA and no inhibition of human Top II, and this explained the reason for its low cytotoxicity. Further research illustrated this selective anti-plasmodial activity may be associated with the inhibition of  $\beta$ -hematin formation.

On further exploration of the anti-malarial potential of **5** derivatives, they introduced halo-substituents as in **111** to reduce the cytotoxicity of the parent compound. In addition, they introduced basic (aminoalkylamino) side chains with the aim to improve the biological activity, as a basic side chain was required for the accumulation of components into the food vacuole, and required for inhibition of hemozoin formation, which was an important character for the activity of chloroquine (El et al., 2009). Hence, a series of **5** derivatives with an *N*<sup>1</sup>,*N*<sup>1</sup>-diethylpentane-1,4-diamine chain (the basic side chain of chloroquine), or other aminoalkylamino chains, chloro-substituents, and a combination of both in various positions were prepared. Then, all the analogues were evaluated for their anti-plasmodial activity against a chloroquine-sensitive *P. falciparum* strain and for cytotoxicity against MRC5 cell line. Most of the compounds showed anti-plasmodial activity in the nanomolar

range. According to the activity data, the main SARs were summarized (Figure 20): 1) Most halo-substituted analogs were indeed less cytotoxic than their parent compounds, but also showed lower anti-plasmodial activity; 2) Substituted with the basic *N*<sup>1</sup>,*N*<sup>1</sup>-diethylpentane-1,4-diamine side chain led to a substantial increase of the anti-plasmodial activity, and the compound with basic chain substituted at C-8 position (**112**) appeared the most potent; 3) Compounds removal of the 5-methyl group only resulted in a 1–3 fold loss in potency (still potency), which indicated not the *N*-methyl moiety, but rather the existence of a basic nitrogen atom, was critical for biological activity; 4) Compounds substituted other various aminoalkylaminogroups at C-11 position led to a remarkable increase in cytotoxicity.

Another research group, the team of Inokuchi, has also been committed to modifying **5** in order to improve its anti-plasmodial activity. In 2012, they obtained a series of derivatives by introducing various functional groups at C-11 position (Mei et al., 2013). These functional groups included thiazolidin-4-one (a biologically privileged skeleton which is well tolerated in human subjects), sulfonamide, thiophene-2-carboxamide, and urea/thiourea (aim to improve the solubility properties and the anti-parasitic activity *in vitro*). All of the derivatives were tested for their anti-plasmodial activities toward CQS (NF54) and CQR (K1) of *Plasmodium falciparum* and for cytotoxicity against mammalian L6 cells. The results revealed that urea derivatives highly contributed to anti-plasmodial activity and selectivity. In 2013, the research group continually carried out modifications by fixing a urea/thiourea unit at C-11 position and introducing ester groups at the C2 and/or C9 positions on the core structure of **5** (Lu et al., 2013; Wang et al., 2013). The results illustrated that the ester substituted

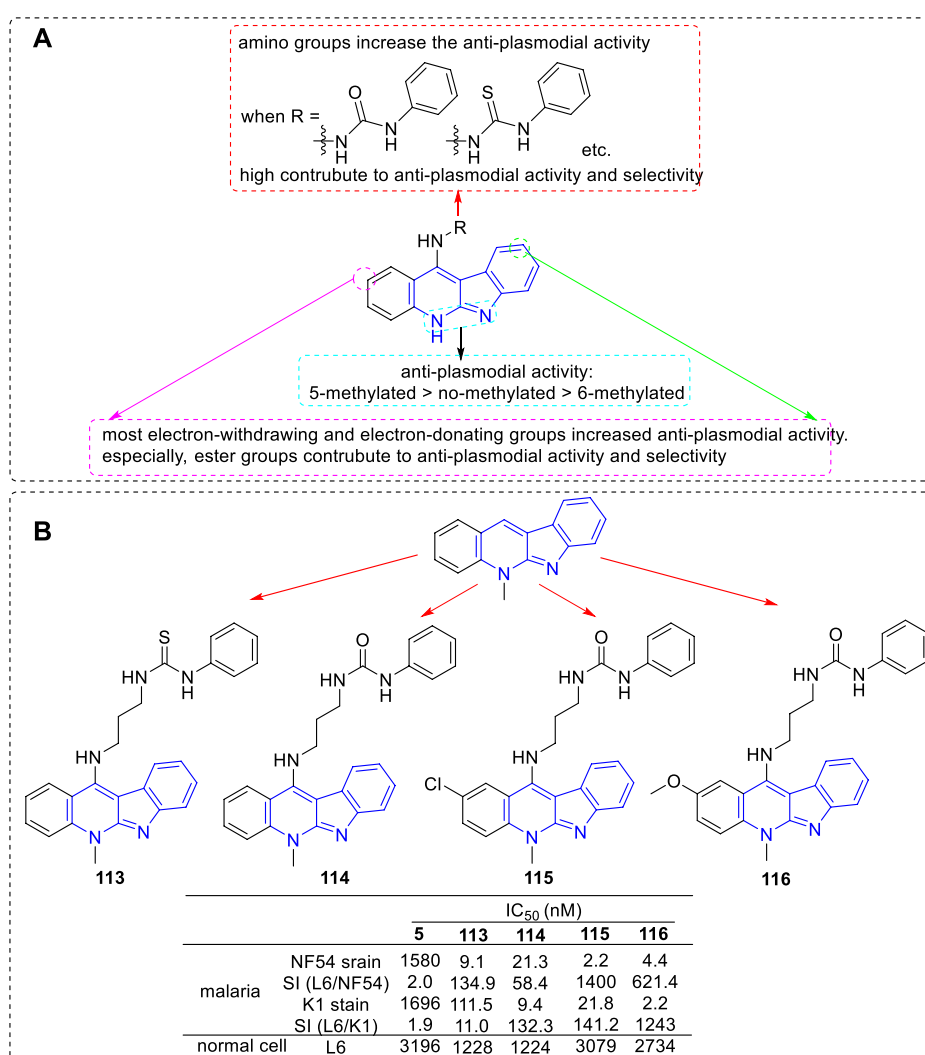
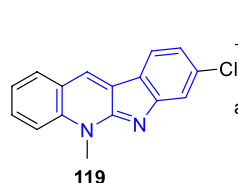


FIGURE 21

(A) SARs of **5** derivatives with various functional groups at C-11 position; (B) Structures and bioactivity of the representative compounds **113–116**.

derivatives not only possessed higher anti-plasmodial activity against both strains, but also a low cytotoxic activity against L6 cells. In the same year, they reported a set of 6-methyl-5*H*-indolo[2,3-*b*]quinoline (congener of **5**) derivatives. These derivatives also were substituted with various alkylamino or  $\omega$ -aminoalkylamino groups at C-11 position. The results suggested that the activity of 6-methylated derivatives were less potent than that of the corresponding 5-methylated derivatives. Based on the sequential reports, the main SARs could be summarized (Figure 21A): 1) The introduction of an amino group at the C-11 position could significantly increase the anti-plasmodial activity compared with the nonsubstituted analogs; 2) Protected nonbasic nitrogen at the terminal of amino group substantially affected the anti-plasmodial

activity. These derivatives with nonbasic groups possessed higher select index (SI) data compared with that of the derivatives with free terminal amine substituents. Especially, a urea/thiourea unit highly contributed to anti-plasmodial activity and selectivity; 3) Both electron-withdrawing and electron-donating groups introduced at C-2 and/or C-9 positions increased anti-plasmodial activity. But some of them also increased cytotoxicity. Especially, ester groups were favourable for anti-plasmodial activity and selectivity; 4) The anti-plasmodial activity with or without N-methyl group was assigned in the order of 5-methylated > no-methylated > 6-methylated. Several representative compounds (**113–116**) and their activity are shown in Figure 21B. Among these compounds, **113–115** were selected for further study against *Plasmodium*



	EC <sub>50</sub> (μg/ml)
<i>Sclerotinia sclerotiorum</i>	2.80
<i>Rhizoctonia solani</i>	4.93
<i>Botrytis cinerea</i>	0.07
<i>Fusarium graminearum</i>	1.92
<i>Magnaporthe oryzae</i>	2.82
<i>Mycosphaerella melonis</i>	0.11

**FIGURE 22**  
Structure and anti-fungal activity of the representative compound **119**.

*berghei* in Swiss mice. After intraperitoneal for four consecutive days at the dose of 50 mg/kg, compounds **113** and **114** showed some reduction of 15.4 and 22.1% in parasitaemia on day 4, respectively. Unfortunately, compound **115** showed no activity and all mice lost weight.

In the discovery of novel compounds containing quinoline core fused five-membered ring structures as anti-tumor and anti-plasmodial agents, Akkachairin *et al.* inadvertently found a novel derivative of compound **5** (**117**) with moderate anti-plasmodial activity but high selectivity (Akkachairin *et al.*, 2020) (Supplementary Figure S5).

#### 4.2.2 Anti-bacterial activity

The team of Kaczmarek not only explored the anti-tumor activity but also the anti-microbial activity of  $\alpha$ -carboline. Early in 1986, they reported certain iso- $\alpha$ -carboline (e.g., **118**) exhibited anti-bacterial (Gram-positive *Micrococcus luteus* and *Kitasatosporia setae* strains) in the concentration of 0.5  $\mu$ M/ml (Czoch *et al.*, 1986) (Supplementary Figure S6).

Other  $\alpha$ -carboline derivatives with anti-bacterial activity were seen in Section 4.1.1 (Figures 5, 6, 9).

#### 4.2.3 Anti-fungal activity

Certain  $\alpha$ -carboline derivatives with anti-fungal activity were seen in Section 4.1.1 and Section 4.2.2 (Figures 5, 6, 9, 10; Supplementary Figure S6).

Besides the anti-pathogenic fungi of  $\alpha$ -carboline derivatives mentioned above, the anti-agriculturally fungi activity was also reported by Zhu *et al.* (Zhu *et al.*, 2020). They designed and synthesized a series of 5 derivatives and screened their anti-fungal activity against six agriculturally important fungi, including *Rhizoctonia solani*, *Botrytis cinerea* (*B. cinerea*), *Fusarium graminearum*, *Mycosphaerella melonis*, *Sclerotinia sclerotiorum*, and *Magnaporthe oryzae*. Many of these analogs presented remarkable anti-fungal activity with EC<sub>50</sub> values lower than 1  $\mu$ g/ml. Notably, compound **119** exhibited the most effective inhibitory potency against *B. cinerea* with an EC<sub>50</sub> value of 0.07  $\mu$ g/ml (Figure 22). Subsequently, they carried out its mechanism research through integrating proteomics and transcriptomics (Shang *et al.*, 2021). And the results indicated

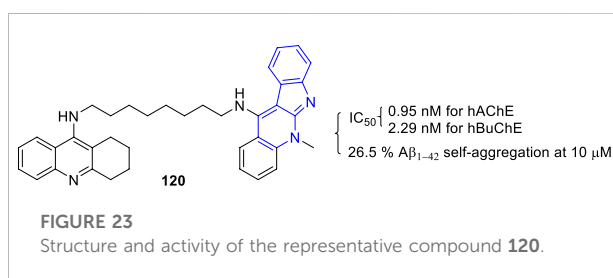


**FIGURE 23**  
Structure and activity of the representative compound **120**.

that it caused the death of *R. solani* mycelia by binding UQCRFS1 and blocking the ion transfer.

#### 4.2.4 Anti-trypanosomal activity

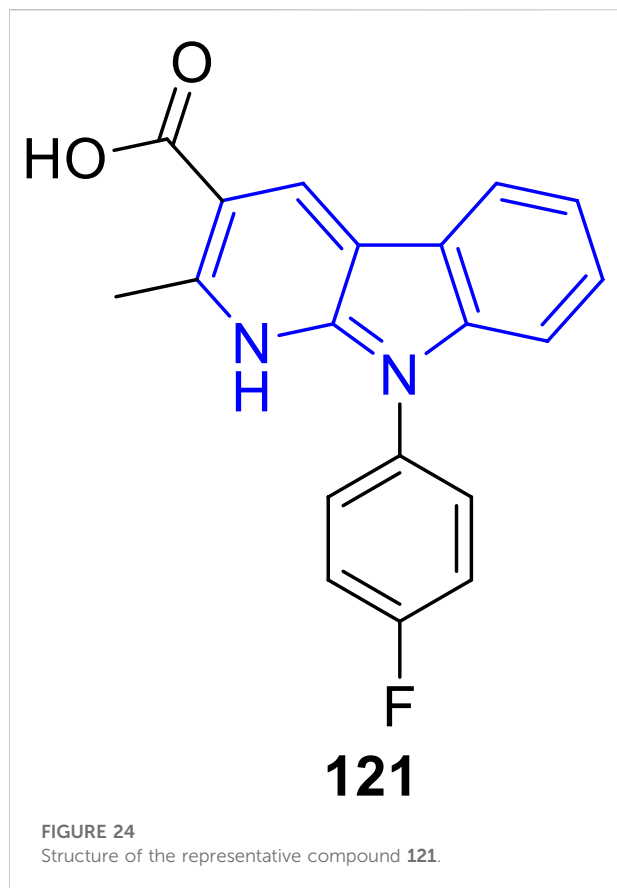
Some indolo[2,3-*b*]quinoline analogs prepared by the research team of Pieters also exhibited anti-trypanosomal activity against *T. cruzi* and *Trypanosoma brucei* in the micromolar range and no obvious cytotoxicity was observed (Jonckers *et al.*, 2002) (Section 4.2.1; Figure 19).

### 4.3 Anti-alzheimer's disease activity

Alzheimer's disease (AD) is a progressive neurodegenerative disease resulting in memory loss, disorientation, speech failure and behavioral changes (Selkoe, 2001; Querfurth and LaFerla, 2010), leading to a significant burden to public health systems worldwide (Bosboom *et al.*, 2012). Amyloid  $\beta$ -protein (A $\beta$ ) as well as acetylcholinesterase (AChE) and butyrylcholinesterase (BuChE) enzymes are associated with pathology of AD (Adlard *et al.*, 2009; Craig *et al.*, 2011).

The team of Inokuchi synthesized novel tacrine-5 heterodimers and evaluated their activity towards A $\beta$  as well as AChE and BuChE (Wang *et al.*, 2017). The most potent compound **120** showing a moderate inhibition of the A $\beta$ <sub>1-42</sub> self-aggregation (26.5% at 10  $\mu$ M), and a high inhibition of AChE and BuChE with IC<sub>50</sub> values of 0.95 and 2.29 nM, respectively (Figure 23).



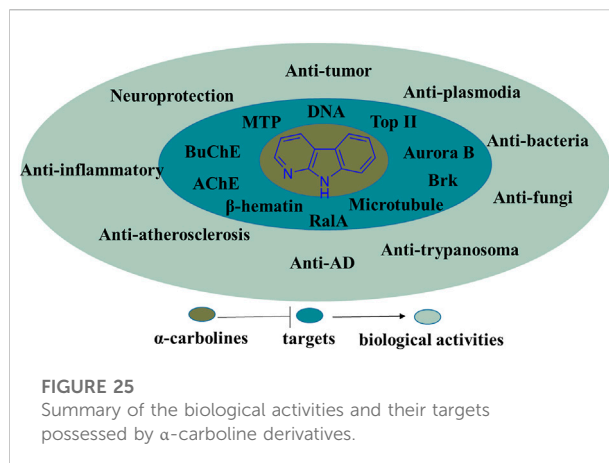


#### 4.4 Anti-atherosclerosis activity

Implitapide (**6**), a microsomal triglyceride transfer protein (MTP) inhibitor, had been shown to reduce progression of atherosclerosis (MartinL et al., 2000; Ueshima et al., 2005). At the dose of 12 mg/kg to low-density lipoprotein (LDL)-receptor-deficient Watanabe heritable hyperlipidemic (WHHL) rabbits, the plasma cholesterol level, triglyceride level, and the very low-density lipoprotein VLDL secretion rate were decreased by 70, 45, and 80%, respectively.

#### 4.5 Antioxidant activity

Recently, Zhang and coworkers (Zhang et al., 2022) designed and synthesized a series of α-carboline derivatives to improve the damage of cardiomyocyte caused by oxidative stress. The biological studies showed that most of the α-carbolines exhibited obvious protective activities against H<sub>2</sub>O<sub>2</sub>-induced cardiomyocyte injury. Particularly, compound **121** significantly increased the cell viability in H<sub>2</sub>O<sub>2</sub>-induced oxidative stress in H9c2 cardiomyoblasts with a concentration-dependent manner. Other biological results including measurement of the activities of MDA, SOD, and GSH-Px, flow cytometry analysis, and



Western blot analysis also revealed the potential of **121** as a promising cardioprotective agent against H<sub>2</sub>O<sub>2</sub>-induced oxidative injury (Figure 24).

Therefore, these analogs may be used to treat many oxidation related diseases such as cancer, cardiovascular, and inflammation caused by oxidative stress (Altwaitjry et al., 2021).

#### 4.6 Miscellaneous

Besides the activities mentioned above, α-carboline derivatives also showed other biological activities. Amino-α-carboline, which was formed during the cooking of meat or fish, could be used as mutagens due to its genotoxicity (Yoshida et al., 1979; Zhang et al., 1996). Mescengricin (**9**), was first found in the process of screening for neuronal cell protecting components, showed protection of chick primary mesencephalic neurons from L-glutamate toxicity, suggesting this class of α-carbolines possess a potential of neuroprotective activity (Shin et al., 2000). DDMG-1 (**10**) could inhibit the mRNA degradation of IκB-α, mTNF-α, and influence other inflammation related factors including NF-κB, IL-8, etc., indicating this class of analogs should be further researched for the treatment of chronic inflammatory diseases (Oda et al., 2009). Some α-carbolines were used to develop organic semiconductors (Han et al., 2015) and host materials (Hwang et al., 2020) due to their highly planar, rigid, polycyclic chromophore structure and sufficiently large triplet energy.

### 5 Conclusion and future directions

In summary, the α-carboline natural products, recent literature of synthesis and information of the biological activities possessed by α-carboline alkaloids have been presented in the review. In the section of biological activities, some SARs and activity mechanisms had been described.

Undoubtedly,  $\alpha$ -carboline derivatives exert diverse biological activities, suggesting this class of alkaloids have great potential in medicinal chemistry (Figure 25). Although there are no  $\alpha$ -carboline-based drugs on the market currently, some  $\alpha$ -carboline-based compounds have reached clinical trials (implitapide, **85** for example). The research of  $\alpha$ -carbolines as drugs should be going.

Still, there will be a long way to go before  $\alpha$ -carbolines become drugs, and incontrovertibly many challenges will be faced. The first challenge is their synthesis. Although a broad array of strategies have been reported for their synthesis, it is surprising that few literature reported the total synthesis of  $\alpha$ -carboline natural products. Many of the synthetic methods of  $\alpha$ -carbolines described are limited by low yields, starting materials difficult to obtain, expensive reagents, or inflexibility with regard to substituents and substitution patterns. The second challenge is their activity. It can be found from literature that many novel  $\alpha$ -carbolines have been synthesized, but their activity is poor or mediocre. The third challenge is their clinical research. Although some teams have studied  $\alpha$ -carbolines for decades, and some compounds possessed good activity, there are still no compounds reached clinical trials.

Nevertheless, some future directions of  $\alpha$ -carboline-based medicinal chemistry could be summarized as follows: 1) Efficient and facile synthesis methods still need to develop; 2) The structural modification of active  $\alpha$ -carbolines still needs to be carried out. On the one hand, to improve their physicochemical properties or selectivity, on the other hand, to broaden the scope of compounds for diverse biological activity; 3) Recent biological activity research of  $\alpha$ -carbolines mainly focuses on anti-tumor activity, research on other biological activities should be reinforced; 4) The mechanisms of their biological activities should be elucidated, especially their target should be clear; 5) Due to their polycyclic chromophore structure, making  $\alpha$ -carbolines into medical materials is also an important direction.

## References

- Adlard, P., James, S., Bush, A., and Masters, C. (2009). beta-Amyloid as a molecular therapeutic target in Alzheimer's disease. *Drugs Today (Barc)* 45, 293–304. doi:10.1358/dot.2009.45.4.1353853
- Akkachairin, B., Rodphon, W., Reamtong, O., Mungthin, M., Tummatorn, J., Thongsornkleeb, C., et al. (2020). Synthesis of neocryptolepines and carbocycle-fused quinolines and evaluation of their anticancer and antiparasmodial activities. *Bioorg. Chem.* 98, 103732. doi:10.1016/j.bioorg.2020.103732
- Altwayjry, N., El-Ghlban, S., El Sayed, I. E., El-Bahnsawye, M., Bayomi, A. I., Samaka, R. M., et al. (2021). *In vitro* and *in vivo* antitumor activity of indolo[2,3-b]quinolines, natural product analogs from neocryptolepine alkaloid. *Molecules* 26, 754–775. doi:10.3390/molecules26030754
- Barker, K., Jackson, L., and Crompton, M. (1997). BRK tyrosine kinase expression in a high proportion of human breast carcinomas. *Oncogene* 15, 799–805. doi:10.1038/sj.onc.1201241
- Bednarek, E., Bocian, W., Sitkowski, J., Ulkowska, A., Kaczmarek, L., Badowska-Roslonek, K., et al. (2006). <sup>1</sup>H and <sup>13</sup>C NMR data for indolo[2,3-b]quinoline-

## Author contributions

All authors contributed to the review concept, design, and bibliographic research. DL, RY, JW, and YL prepared the first version of the manuscript. DL, RY, and BZ prepared the schemes and figures. DL, RY, and YL critically reviewed the final version.

## Funding

Financial supported by doctoral research start-up funds for doctors in First Affiliated Hospital of Gannan Medical University (Grant No. QD202219).

## Conflict of interest

The authors declare that the research was conducted in the absence of any commercial or financial relationships that could be construed as a potential conflict of interest.

## Publisher's note

All claims expressed in this article are solely those of the authors and do not necessarily represent those of their affiliated organizations, or those of the publisher, the editors and the reviewers. Any product that may be evaluated in this article, or claim that may be made by its manufacturer, is not guaranteed or endorsed by the publisher.

## Supplementary Material

The Supplementary Material for this article can be found online at: <https://www.frontiersin.org/articles/10.3389/fchem.2022.988327/full#supplementary-material>

aminoglycoside hybrids, a novel potent anticancer drug family. *Magn. Reson. Chem.* 44, 459–462. doi:10.1002/mrc.1737

Bosboom, P., Alfonso, H., Eaton, J., and Almeida, O. (2012). Quality of life in Alzheimer's disease: Different factors associated with complementary ratings by patients and family carers. *Int. Psychogeriatr.* 24, 708–721. doi:10.1017/S1041610211002493

Brauer, P., and Tyner, A. (2010). Building a better understanding of the intracellular tyrosine kinase PTK6 - BRK by BRK. *Biochimica Biophysica Acta - Rev. Cancer* 1806, 66–73. doi:10.1016/j.bbcan.2010.02.003

Bum-Erdene, K., Liu, D., Gonzalez-Gutierrez, G., Ghosayel, M., Xu, D., and Meroueh, S. (2020). Small-molecule covalent bond formation at tyrosine creates a binding site and inhibits activation of Ral GTPases. *Proc. Natl. Acad. Sci. U. S. A.* 117, 7131–7139. doi:10.1073/pnas.1913654117

Carmena, M., and Earnshaw, W. (2003). The cellular geography of aurora kinases. *Nat. Rev. Mol. Cell Biol.* 4, 842–854. doi:10.1038/nrm1245

- Carmena, M., Ruchaud, S., and Earnshaw, W. (2009). Making the auroras glow: Regulation of aurora A and B kinase function by interacting proteins. *Curr. Opin. Cell Biol.* 21, 796–805. doi:10.1016/j.ccb.2009.09.008
- Chen, F., Li, X., Zhu, H., and Huang, W. (2020). Regulation of the ras-related signaling pathway by small molecules containing an indole core scaffold: A potential antitumor therapy. *Front. Pharmacol.* 11, 280. doi:10.3389/fphar.2020.00280
- Chen, S., Chan, N., and Hsieh, T. (2013). New mechanistic and functional insights into DNA topoisomerases. *Annu. Rev. Biochem.* 82, 139–170. doi:10.1146/annurev-biochem-061809-100002
- Cimanga, K., Bruyne, T. D., Pieters, L., Claeys, M., and Vlietinck, A. (1996). New alkaloids from *Cryptolepis sanguinolenta*. *Tetrahedron Lett.* 37, 1703–1706. doi:10.1016/0040-4039(96)00112-8
- Cimanga, K., Bruyne, T. D., Pieters, L., Vlietinck, A. J., and Turger, C. A. (1997). *In vitro* and *in vivo* antiparasitic activity of cryptolepine and related alkaloids from *cryptolepis sanguinolenta*. *J. Nat. Prod.* 60, 688–691. doi:10.1021/np9605246
- Cimanga, K., De Bruyne, T., Pieters, L., Totte, J., Tona, L., Kambu, K., et al. (1998). Antibacterial and antifungal activities of neocryptolepine, biscryptolepine and cryptolepine, alkaloids isolated from *Cryptolepis sanguinolenta*. *Phytomedicine* 5, 209–214. doi:10.1016/S0944-7113(98)80030-5
- Craig, L., Hong, N., and McDonald, R. (2011). Revisiting the cholinergic hypothesis in the development of Alzheimer's disease. *Neurosci. Biobehav. Rev.* 35, 1397–1409. doi:10.1016/j.neubiorev.2011.03.001
- Czoch, W. P., Mordarski, M., Kaczmarek, L., and Namirski, P. N. (1986). Structure-activity relationship studies on selected iso- $\alpha$ -carboline. *Arch. Immunol. Ther. Exp.* 34, 327–331.
- Czoch, W. P., Pognan, F., Kaczmarek, L., and Boratyński, J. (1994). Synthesis and structure-activity relationship of methyl-substituted indolo[2, 3-b]quinolines: Novel cytotoxic, DNA topoisomerase II inhibitors. *J. Med. Chem.* 37, 3503–3510. doi:10.1021/jm00047a008
- Dai, J., Dan, W., Zhang, Y., and Wang, J. (2018). Recent developments on synthesis and biological activities of gamma-carboline. *Eur. J. Med. Chem.* 157, 447–461. doi:10.1016/j.ejmech.2018.08.015
- Debnath, S., Kumar, A. S., Chauhan, S., and Kumara Swamy, K. C. (2021). Divergent reactivity of delta- and beta'-acetoxy allenates with 2-sulfonamidoindoles via phosphine catalysis: Entry to dihydro- $\alpha$ -carboline,  $\alpha$ -carboline, and spiro-cyclopentene motifs. *J. Org. Chem.* 86, 11583–11598. doi:10.1021/acs.joc.1c01137
- Efferth, T. (2006). Molecular pharmacology and pharmacogenomics of artemisinin and its derivatives in cancer cells. *Curr. drug targets* 7, 407–421. doi:10.2174/138945006776359412
- El, S. I., Van der Veken, P., Steert, K., Dhooghe, L., Hostyn, S., Van Baelen, G., et al. (2009). Synthesis and antiparasitic activity of aminoalkylamino-substituted neocryptolepine derivatives. *J. Med. Chem.* 52, 2979–2988. doi:10.1021/jm801490z
- Emam, S. M., El Sayed Iel, T., and Nassar, N. (2015). Transition metal complexes of neocryptolepine analogues. Part I: Synthesis, spectroscopic characterization, and *in vitro* anticancer activity of copper(II) complexes. *Spectrochimica Acta Part A Mol. Biomol. Spectrosc.* 138, 942–953. doi:10.1016/j.saa.2014.03.114
- Fan, G., Lou, L., Song, Z., Zhang, X., and Xiong, X. (2021). Targeting mutated GTPase KRAS in tumor therapies. *Eur. J. Med. Chem.* 226, 113816. doi:10.1016/j.ejmech.2021.113816
- Farrell, P., Shi, L., Matuszkiewicz, J., Balakrishna, D., Hoshino, T., Zhang, L., et al. (2013). Biological characterization of TAK-901, an investigational, novel, multitargeted Aurora B kinase inhibitor. *Mol. Cancer Ther.* 12, 460–470. doi:10.1158/1535-7163.MCT-12-0657
- Fu, J., Bian, M., Jiang, Q., and Zhang, C. (2007). Roles of Aurora kinases in mitosis and tumorigenesis. *Mol. cancer Res.* 5, 1–10. doi:10.1158/1541-7786.MCR-06-0208
- Godlewska, J., Luniewski, W., Zagrodzki, B., Kaczmarek, L., Pohl, A. B., Dus, D., et al. (2005). Biological evaluation of omega-(dialkylamino)alkyl derivatives of 6H-indolo[2, 3-b]quinoline--novel cytotoxic DNA topoisomerase II inhibitors. *Anticancer Res.* 25, 2857–2868.
- Goto, Y., Kamihira, R., Nakao, Y., Nonaka, M., Takano, R., Xuan, X., et al. (2021). The efficacy of marine natural products against *Plasmodium falciparum*. *J. Parasitol.* 107, 284–288. doi:10.1645/20-93
- Han, J., Thirupathiah, B., Kwon, G., Kim, C., and Seo, S. (2015). Synthesis and characterization of carbazole- and  $\alpha$ -carboline-based thiophene derivatives as organic semiconductors for organic thin-film transistors. *Dyes Pigm.* 114, 78–84. doi:10.1016/j.dyepig.2014.10.024
- Huang, H. C., Liu, W. T., Hua, K. S., Hung, H. C., Tsai, J. Y., Kuo, S. C., et al. (2016).  $\alpha$ -Carboline derivative TJY-16 inhibits tumor growth by inducing G2/M cell cycle arrest in glioma cells. *J. Biomed. Sci.* 23, 10–21. doi:10.1186/s12929-016-0222-y
- Humeniuk, R., Kaczmarek, L., Peczyńska-Czoch, W., and Marcinkowska, E. (2002). Cytotoxicity and cell cycle effects of novel indolo[2, 3-b]quinoline derivatives. *Oncol. Res.* 13, 269–277. doi:10.3727/096504003108748320
- Hunter, J., Manandhar, A., Carrasco, M., Gurbani, D., Gondi, S., and Westover, K. (2015). Biochemical and structural analysis of common cancer-associated KRAS mutations. *Mol. Cancer Res.* 13, 1325–1335. doi:10.1158/1541-7786.MCR-15-0203
- Hwang, J., Lee, C., Jeong, J. E., Kim, C. Y., Woo, H. Y., Park, S., et al. (2020). Rational design of carbazole- and carboline-based polymeric host materials for realizing high-efficiency solution-processed thermally activated delayed fluorescence organic light-emitting diode. *ACS Appl. Mat. Interfaces* 12, 8485–8494. doi:10.1021/acsami.9b20279
- Jackson, J., Patrick, D., Dar, M., and Huang, P. (2007). Targeted anti-mitotic therapies: Can we improve on tubulin agents? *Nat. Rev. Cancer* 7, 107–117. doi:10.1038/nrc2049
- Jonckers, T. H. M., Miert, S. V., Cimanga, K., Bailly, C., Colson, P., Pauw-Gillet, M. C. D., et al. (2002). Synthesis, cytotoxicity, and antiparasitic activity of new neocryptolepine derivatives. *J. Med. Chem.* 45, 3497–3508. doi:10.1021/jm011102i
- Kaczmarek, L., Balicki, R., Namirski, P. N., Peczyńska-Czoch, W., and Mordarski, M. (1988a). Cancerostatics, VI. Synthesis and antineoplastic properties of some benzo-iso- $\alpha$ -carboline. *Arch. Pharm.* 321, 463–467. doi:10.1002/ardp.19883210807
- Kaczmarek, L., Czoch, W. P., Opolski, A., Wietrzyk, J., Marciniowska, E., Boratyński, J., et al. (1998b). Methoxy- and methyl-methoxy-5, 6, 11-trimethyl-6H-indolo[2, 3-b]quinolinium derivatives as novel cytotoxic agents and DNA topoisomerase II inhibitors. *Anticancer Res.* 18, 3133–3138.
- Kaczmarek, L., Czoch, W. P., Osadacz, J., Mordarski, M., Sokalski, W. A., Boratyński, J., et al. (1999). Synthesis, and cytotoxic activity of some novel indolo[2, 3-b]quinoline derivatives DNA topoisomerase II inhibitors. *Bioorg. Med. Chem.* 7, 2457–2464. doi:10.1016/s0968-0896(99)00200-x
- Kaczmarek, L., Luniewski, W., Zagrodzki, B., Godlewska, J., Osadacz, J., Wietrzyk, J., et al. (2002). Synthesis of 6-substituted 6H-indolo[2, 3-b]quinolines as novel cytotoxic agents and topoisomerase II inhibitors. *Acta Pol. Pharm.* 59, 199–207.
- Kamihira, R., and Nakao, Y. (2021). Small-scale preparation of fluorescently labeled chemical probes from marine cyclic peptides, kapakahines A and F. *Mar. Drugs* 19, 76–87. doi:10.3390/md19020076
- Kaur, R., Kaur, G., Gill, R., Soni, R., and Bariwal, J. (2014). Recent developments in tubulin polymerization inhibitors: An overview. *Eur. J. Med. Chem.* 87, 89–124. doi:10.1016/j.ejmech.2014.09.051
- Kavallaris, M. (2010). Microtubules and resistance to tubulin-binding agents. *Nat. Rev. Cancer* 10, 194–204. doi:10.1038/nrc2803
- Kim, J.-S., Shin-ya, K., Hayakawa, Y., and Seto, H. (1997). Structure of mesengricin, A novel neuronal cell protecting substance produced by streptococcus griseoflavus. *Tetrahedron Lett.* 38, 3431–3434. doi:10.1080/10286020008039901
- Lavrado, J., Moreira, R., and Paulo, A. (2010). Indoloquinolines as scaffolds for drug discovery. *Curr. Med. Chem.* 17, 2348–2370. doi:10.2174/092986710791698521
- Leng, H. J., Wang, Y. T., He, X. H., Xia, H. L., Xu, P. S., Xiang, P., et al. (2020). Design and efficient synthesis of RalA inhibitors containing the dihydro- $\alpha$ -carboline scaffold. *ChemMedChem* 16, 851–859. doi:10.1002/cmdc.202000722
- Li, D., Liu, W., Huang, Y., Liu, M., Tian, C., Lu, H., et al. (2022). Facile synthesis of C1-substituted beta-carbolines as CDK4 inhibitors for the treatment of cancer. *Bioorg. Chem.* 121, 105659. doi:10.1016/j.bioorg.2022.105659
- Liang, X., Wu, Q., Luan, S., Yin, Z., He, C., Yin, L., et al. (2019). A comprehensive review of topoisomerase inhibitors as anticancer agents in the past decade. *Eur. J. Med. Chem.* 171, 129–168. doi:10.1016/j.ejmech.2019.03.034
- Lin, Y. C., Chen, Y. F., Tseng, L. S., Lee, Y. H., Morris-Natschke, S. L., Kuo, S. C., et al. (2016). Synthesis and structure-activity relationship studies of novel 3, 9-substituted  $\alpha$ -carboline derivatives with high cytotoxic activity against colorectal cancer cells. *Eur. J. Med. Chem.* 110, 98–114. doi:10.1016/j.ejmech.2016.01.004
- Liu, W., Liu, X., Liu, W., Gao, Y., Wu, L., Huang, Y., et al. (2022). Discovery of novel  $\beta$ -carboline derivatives as selective AChE inhibitors with GSK-3 $\beta$  inhibitory property for the treatment of Alzheimer's disease. *Eur. J. Med. Chem.* 229, 114095. doi:10.1016/j.ejmech.2021.114095
- Liu, W., Liu, X., Tian, L., Gao, Y., Liu, W., Chen, H., et al. (2021). Design, synthesis and biological evaluation of harmine derivatives as potent GSK-3 $\beta$ /DYRK1A dual inhibitors for the treatment of Alzheimer's disease. *Eur. J. Med. Chem.* 222, 113554. doi:10.1016/j.ejmech.2021.113554

- Lu, W. J., Wicht, K. J., Wang, L., Imai, K., Mei, Z. W., Kaiser, M., et al. (2013). Synthesis and antimalarial testing of neocryptolepine analogues: Addition of ester function in SAR study of 2, 11-disubstituted indolo[2, 3-b]quinolines. *Eur. J. Med. Chem.* 64, 498–511. doi:10.1016/j.ejmech.2013.03.072
- Luniewski, W., Wietrzyk, J., Godlewska, J., Switalska, M., Piskozub, M., Peczyńska-Czoch, W., et al. (2012). New derivatives of 11-methyl-6-[2-(dimethylamino)ethyl]-6H-indolo[2, 3-b]quinoline as cytotoxic DNA topoisomerase II inhibitors. *Bioorg. Med. Chem. Lett.* 22, 6103–6107. doi:10.1016/j.bmcl.2012.08.032
- Mahmoud, K. A., Wersig, T., Slynko, I., Schachtele, C., Totzke, F., et al. (2014). Discovery of 4-anilino alpha-carbolines as novel Brk inhibitors. *Bioorg. Med. Chem. Lett.* 24, 1948–1951. doi:10.1016/j.bmcl.2014.03.002
- Martin, L., Sorbera, A., Silvestre, J., and Castañer, J. (2000). Implitapide. Hypolipidemic, Treatment of atherosclerosis, MTP inhibitor, ApoB secretion inhibitor. *Drugs Future* 25, 1138–1144.
- Medas, K. M., Lesch, R. W., Edima, F. B., Wrenn, S. P., Ndahayo, V., and Mulcahy, S. P. (2020). Metal-catalyzed cyclotrimerization reactions of cyanamides: Synthesis of 2-Aryl-alpha-carbolines. *Org. Lett.* 22, 3135–3139. doi:10.1021/acs.orglett.0c00891
- Mei, Z. W., Wang, L., Lu, W. J., Pang, C. Q., Maeda, T., Peng, W., et al. (2013). Synthesis and *in vitro* antimalarial testing of neocryptolepines: SAR study for improved activity by introduction and modifications of side chains at C2 and C11 on indolo[2, 3-b]quinolines. *J. Med. Chem.* 56, 1431–1442. doi:10.1021/jm300887b
- Mineno, M., Sera, M., Ueda, T., Mizufune, H., Zanka, A., O'Bryan, C., et al. (2015). Integrated cross-coupling strategy for an alpha-carboline-based Aurora B kinase inhibitor. *J. Org. Chem.* 80, 1564–1568. doi:10.1021/jo502489x
- Mitchell, P., Barker, K., Martindale, J., Kamalati, T., Lowe, P., Page, M., et al. (1994). Cloning and characterisation of cDNAs encoding a novel non-receptor tyrosine kinase, brk, expressed in human breast tumours. *Oncogene* 9, 2383–2390.
- Mologni, L., Orsato, A., Zambon, A., Tardy, S., Bisson, W. H., Schneider, C., et al. (2022a). Identification of non-ATP-competitive  $\alpha$ -carboline inhibitors of the anaplastic lymphoma kinase. *Eur. J. Med. Chem.* 238, 114488. doi:10.1016/j.ejmech.2022.114488
- Mologni, L., Tardy, S., Zambon, A., Orsato, A., Bisson, W., Ceccon, M., et al. (2022b). Discovery of novel  $\alpha$ -carboline inhibitors of the anaplastic lymphoma kinase. *ACS Omega* 7, 17083–17097. doi:10.1021/acsomega.2c00507
- Morrissey, C., Gallis, B., Solazzi, J., Kim, B., Gulati, R., Vakar-Lopez, F., et al. (2010). Effect of artemisinin derivatives on apoptosis and cell cycle in prostate cancer cells. *Anticancer. Drugs* 21, 423–432. doi:10.1097/CAD.0b013e328336f57b
- Nakao, Y., Kuo, J., Yoshida, W. Y., Kelly, M., and Scheuer, P. J. (2003). More kapakahines from the marine sponge *Cribrochalina olemda*. *Org. Lett.* 5, 1387–1390. doi:10.1021/ol026830u
- Nantka, N. P., and Kaczmarek, Ł. (1978). Synthesis and preliminary cytostatic screening of some alpha-carboline derivatives. *Pol. J. Pharmacol. Pharm.* 30, 569–572.
- Nitiss, J. (2009). Targeting DNA topoisomerase II in cancer chemotherapy. *Nat. Rev. Cancer* 9, 338–350. doi:10.1038/nrc2607
- Nuthakki, V. K., Mudududda, R., and Bharate, S. B. (2022). Role of basic aminoalkyl chains in the lead optimization of Indoloquinoline alkaloids. *Eur. J. Med. Chem.* 227, 113938. doi:10.1016/j.ejmech.2021.113938
- Oda, T., Lee, J. S., Sato, Y., Kabe, Y., Sakamoto, S., Handa, H., et al. (2009). Inhibitory effect of N, N-didesmethylgrossularine-1 on inflammatory cytokine production in lipopolysaccharide-stimulated RAW 264.7 cells. *Mar. Drugs* 7, 589–599. doi:10.3390/md7040589
- Oelze, M., Mahmoud, K. A., Sippl, W., Wersig, T., Hilgeroth, A., and Ritter, C. A. (2015). Novel 4-anilino-alpha-carboline derivatives induce cell death in nonadhesive breast cancer cells through inhibition of Brk activity. *Int. J. Clin. Pharmacol. Ther.* 53, 1052–1055. doi:10.5414/CPXCES14EA07
- Pattey, C. M., and Guyot, M. (1989). Grossularine-1 and grossularine-2, cytotoxic  $\alpha$ -carbolines from the tunicate: *Dendrodoa grossularia*. *Tetrahedron* 45, 3445–3450. doi:10.1016/s0040-4020(01)81023-1
- Pognan, F., Saucier, J.-M., Paoletti, C., Kaczmarek, L., Namirski, P. N., Mordarski, M., et al. (1992). A carboline derivative as a novel mammalian DNA topoisomerase II targeting agent. *Biochem. Pharmacol.* 44, 2149–2155. doi:10.1016/0006-2952(92)90341-f
- Pradhan, T., Gupta, O., Singh, G., and Monga, V. (2021). Aurora kinase inhibitors as potential anticancer agents: Recent advances. *Eur. J. Med. Chem.* 221, 113495. doi:10.1016/j.ejmech.2021.113495
- Querfurth, H. W., and LaFerla, F. M. (2010). Alzheimer's disease. *N. Engl. J. Med.* 362, 329–344. doi:10.1056/nejmra0909142
- Rocha, D. D., Espejo, V. R., Rainier, J. D., La Clair, J. J., and Costa-Lotufo, L. V. (2015). Fluorescent kapakahines serve as non-toxic probes for live cell Golgi imaging. *Life Sci.* 136, 163–167. doi:10.1016/j.lfs.2015.06.014
- Roslonek, K. B., Ciesielska, A., Świtalska, M., Piskozub, M., P.-Czoch W. Wietrzyk, J., et al. (2016). Syntheses and cytotoxic activity of new 5H-indolo[2, 3-b]quinoline O-aminoglycosides. *Acta Pol. Pharm.* 73, 683–692.
- Selkoe, D. (2001). Alzheimer's disease: Genes, proteins, and therapy. *Physiol. Rev.* 81, 741–766. doi:10.1152/physrev.2001.81.2.741
- Shaban, E., Switalska, M., Wang, L., Wang, N., Xiu, F., Hayashi, I., et al. (2017). Synthesis and *in vitro* antiproliferative activity of 11-substituted neocryptolepines with a branched omega-aminoalkylamino chain. *Molecules* 22, 1954. doi:10.3390/molecules22111954
- Shang, X. F., Dai, L. X., Zhang, Z. J., Yang, C. J., Du, S. S., Wu, T. L., et al. (2021). Integrated proteomics and transcriptomics analyses reveals the possible antifungal mechanism of an indoloquinoline alkaloid neocryptolepine against *Rhizoctonia solani*. *J. Agric. Food Chem.* 69, 6455–6464. doi:10.1021/acs.jafc.1c01385
- Sharaf, H. M., Schiff, P. L., Tackie, A. N., Phoebe, C. H., and Martin, G. E. (1996). Two new indoloquinoline alkaloids from *cryptolepis sanguinolenta*: Cryptosanguinolentine and cryptotackieine. *J. Heterocycl. Chem.* 33, 239–243. doi:10.1002/jhet.5570330204
- Shin, Y. K., Kim, J. S., Furihata, K., Hayakawa, Y., and Seto, H. (2000). A novel neuronal cell protecting substance mescengricin produced by *Streptomyces griseoflavus*. *J. Asian Nat. Prod. Res.* 2, 121–132. doi:10.1080/10286020008039901
- Sidoryk, K., Jaromin, A., Edward, J. A., Switalska, M., Stefanska, J., Cmoch, P., et al. (2014). Searching for new derivatives of neocryptolepine: Synthesis, antiproliferative, antimicrobial and antifungal activities. *Eur. J. Med. Chem.* 78, 304–313. doi:10.1016/j.ejmech.2014.03.060
- Sidoryk, K., Switalska, M., Rozga, P., Wietrzyk, J., Bujak, I., Zerek, B., et al. (2017). An efficient synthesis of indolo[2, 3-b]quinoline guanidine derivatives with their *in vitro* and *in vivo* study. *Med. Chem. Res.* 26, 3354–3366. doi:10.1007/s00044-017-2028-1
- Sidoryk, K., Switalska, M., Jaromin, A., Cmoch, P., Bujak, I., Kaczmarska, M., et al. (2015). The synthesis of indolo[2, 3-b]quinoline derivatives with a guanidine group: Highly selective cytotoxic agents. *Eur. J. Med. Chem.* 105, 208–219. doi:10.1016/j.ejmech.2015.10.022
- Sidoryk, K., Switalska, M., Wietrzyk, J., Jaromin, A., Pietka-Ottlik, M., Cmoch, P., et al. (2012). Synthesis and biological evaluation of new amino acid and dipeptide derivatives of neocryptolepine as anticancer agents. *J. Med. Chem.* 55, 5077–5087. doi:10.1021/jm3000468t
- Sung, H., Ferlay, J., Siegel, R. L., Laversanne, M., Soerjomataram, I., Jemal, A., et al. (2021). Global cancer Statistics 2020: GLOBOCAN estimates of incidence and mortality worldwide for 36 cancers in 185 countries. *Ca. A Cancer J. Clin.* 71, 209–249. doi:10.3322/caac.21660
- Tian, C., Huang, S., Xu, Z., Liu, W., Li, D., Liu, M., et al. (2022). Design, synthesis, and biological evaluation of beta-carboline 1, 3, 4-oxadiazole based hybrids as HDAC inhibitors with potential antitumor effects. *Bioorg. Med. Chem. Lett.* 64, 128663. doi:10.1016/j.bmcl.2022.128663
- Tsai, J.-Y., Lin, Y.-C., Hsu, M.-H., Kuo, S.-C., and Huang, L.-J. (2010). Synthesis and cytotoxicity of 1, 6, 8, 9-substituted  $\alpha$ -carboline derivatives. *Kaohsiung J. Med. Sci.* 26, 593–602. doi:10.1016/s1607-551x(10)70091-7
- Tsui, T., and Miller, W. (2015). Cancer-associated mutations in breast tumor kinase/PTK6 differentially affect enzyme activity and substrate recognition. *Biochemistry* 54, 3173–3182. doi:10.1021/acs.biochem.5b00303
- Ueshima, K., Umeno, H. A., Nagayoshi, K., Takakuar, S., Matsuo, M., and Mutoh, S. (2005). Implitapide, a microsomal triglyceride transfer protein inhibitor, reduces progression of atherosclerosis in apolipoprotein E knockout mice fed a western-type diet: Involvement of the inhibition of postprandial triglyceride elevation. *Biol. Pharm. Bull.* 28, 247–252. doi:10.1248/bpb.28.247
- Van, M. S., Jonckers, T., Cimanga, K., Maes, L., Maes, B., Lemiere, G., et al. (2004). *In vitro* inhibition of beta-haematin formation, DNA interactions, antiparasitodal activity, and cytotoxicity of synthetic neocryptolepine derivatives. *Exp. Parasitol.* 108, 163–168. doi:10.1016/j.exppara.2004.08.006
- Verbitski, S. M., Mayne, C. L., Davis, R. A., Concepcion, G. P., and Ireland, C. M. (2002). Isolation, structure determination, and biological activity of a novel alkaloid, perophoramidine, from the philippine ascidian perophoramei. *J. Org. Chem.* 67, 7124–7126. doi:10.1021/jo026012f
- Wadsworth, A. D., Naysmith, B. J., and Brimble, M. A. (2015). A review of the synthesis of alpha-carbolines. *Eur. J. Med. Chem.* 97, 816–829. doi:10.1016/j.ejmech.2014.11.038
- Wang, L., Moraleda, I., Iriepa, I., Romero, A., Lopez-Munoz, F., Chioua, M., et al. (2017). 5-Methyl-N-(8-(5, 6, 7, 8-tetrahydroacridin-9-ylamino)octyl)-5H-indolo[2, 3-b]quinolin-11-amine: A highly potent human cholinesterase inhibitor. *Medchemcomm* 8, 1307–1317. doi:10.1039/c7md00143f



- Wang, L., Switalska, M., Mei, Z. W., Lu, W. J., Takahara, Y., Feng, X. W., et al. (2012). Synthesis and *in vitro* antiproliferative activity of new 11-aminoalkylamino-substituted 5H- and 6H-indolo[2, 3-b]quinolines; structure-activity relationships of neocryptolepines and 6-methyl congeners. *Bioorg. Med. Chem.* 20, 4820–4829. doi:10.1016/j.bmc.2012.05.054
- Wang, L., Switalska, M., Wang, N., Du, Z. J., Fukumoto, Y., Diep, N. K., et al. (2014). Design, synthesis, and biological evaluation of artemisinin-indoloquinoline hybrids as potent antiproliferative agents. *Molecules* 19, 19021–19035. doi:10.3390/molecules191119021
- Wang, N., Switalska, M., Wang, L., Shaban, E., Hossain, M. I., Sayed, I. E. T. E., et al. (2019). Structural modifications of nature-inspired indoloquinolines: A mini review of their potential antiproliferative activity. *Molecules* 24, 24112121. doi:10.3390/molecules24112121
- Wang, N., Wicht, K. J., Wang, L., Lu, W. J., Misumi, R., Wang, M. Q., et al. (2013). Synthesis and *in vitro* testing of antimalarial activity of non-natural Type neocryptolepines: Structure-activity relationship study of 2, 11 and 9, 11-disubstituted 6-methylindolo[2, 3-b]quinolines. *Chem. Pharm. Bull.* 61, 1282–1290. doi:10.1248/cpb.c13-00639
- Wieczorek, J., Czych, W. P., Mordarski, M., Kaczmarek, Ł., and Namirski, P. N. (1986). Antineoplastic activity of azacarbazoles. I. Synthesis and antitumor properties of alpha-carboline and its selected derivatives. *Arch. Immunol. Ther. Exp.* 34, 315–321.
- Yan, C., and Theodorescu, D. (2018). RAL GTPases: Biology and potential as therapeutic targets in cancer. *Pharmacol. Rev.* 70, 1–11. doi:10.1124/pr.117.014415
- Yan, Q., Gin, E., Banwell, M. G., Willis, A. C., and Carr, P. D. (2017). A unified approach to the isomeric  $\alpha$ - $\beta$ - and  $\delta$ -carbolines via their 6, 7, 8, 9-tetrahydro counterparts. *J. Org. Chem.* 82, 4328–4335. doi:10.1021/acs.joc.7b00323
- Yeung, B. K., Nakao, Y., Kinnel, R. B., Carney, J. R., Yoshida, W. Y., Scheuer, P. J., et al. (1996). The kapakahines, cyclic peptides from the marine sponge *Cribrochalina olemda*. *J. Org. Chem.* 61, 7168–7173. doi:10.1021/jo960725e
- Yi, J. M., Zhang, X. F., Huan, X. J., Song, S. S., Wang, W., Tian, Q. T., et al. (2015). Dual targeting of microtubule and topoisomerase II by  $\alpha$ -carboline derivative YCH337 for tumor proliferation and growth inhibition. *Oncotarget* 6, 8960–8973. doi:10.18632/oncotarget.3264
- Yoshida, D., Matsumoto, T., and Okamoto, H. (1979). Interaction between amino-alpha-carboline and amino-gamma-carboline on mutagenicity in *Salmonella typhimurium*. *Mutat. Research/Genetic Toxicol.* 68, 175–178. doi:10.1016/0165-1218(79)90146-0
- Zhang, R. H., Yang, D., Liao, X. M., Zhang, H., Chen, G. Q., Zhang, W. L., et al. (2022). Design, synthesis, and *in vitro* protective effect evaluation of  $\alpha$ -carboline derivatives against H<sub>2</sub>O<sub>2</sub>-induced cardiomyocyte injury. *Eur. J. Med. Chem.* 238, 114469. doi:10.1016/j.ejmech.2022.114469
- Zhang, X. B., Felton, J. S., Tucker, J. D., Orlando, C., and Heddle, J. A. (1996). Intestinal mutagenicity of two carcinogenic food mutagens in transgenic mice: 2-amino-1-methyl-6-phenylimidazo[4, 5-b]pyridine and amino( $\alpha$ )carboline. *Carcinogenesis* 17, 2259–2265. doi:10.1093/carcin/17.10.2259
- Zhang, X., He, Q., Xiang, H., Song, S., Miao, Z., and Yang, C. (2014). Rapid access to  $\alpha$ -carbolines via a one-pot tandem reaction of  $\alpha$ ,  $\beta$ -unsaturated ketones with 2-nitrophenylacetonitrile and the anti-proliferative activities of the products. *Org. Biomol. Chem.* 12, 355–361. doi:10.1039/c3ob41921e
- Zhu, J. K., Gao, J. M., Yang, C. J., Shang, X. F., Zhao, Z. M., Lawoe, R. K., et al. (2020). Design, synthesis, and antifungal evaluation of neocryptolepine derivatives against phytopathogenic fungi. *J. Agric. Food Chem.* 68, 2306–2315. doi:10.1021/acs.jafc.9b06793



## OPEN ACCESS

## EDITED BY

Ghasem Sargazi,  
Bam University of Medical Sciences and  
Health Services, Iran

## REVIEWED BY

Alireza Rezvani,  
University of Sistan and Baluchestan, Iran  
Mohammadreza Moghaddam-manesh,  
Standard Research Institute of Iran, Iran

## \*CORRESPONDENCE

Ezekiel Adebiji,  
✉ [ezekiel.adebiyi@covenantuniversity.edu.ng](mailto:ezekiel.adebiyi@covenantuniversity.edu.ng)

## SPECIALTY SECTION

This article was submitted to Medicinal and  
Pharmaceutical Chemistry,  
a section of the journal  
Frontiers in Chemistry

RECEIVED 19 October 2022

ACCEPTED 20 December 2022

PUBLISHED 06 January 2023

## CITATION

Elebiju OF, Ajani OO, Oduselu GO,  
Ogunnupebi TA and Adebiji E (2023),  
Recent advances in functionalized  
quinoline scaffolds and  
hybrids—Exceptional pharmacophore in  
therapeutic medicine.  
*Front. Chem.* 10:1074331.  
doi: 10.3389/fchem.2022.1074331

## COPYRIGHT

© 2023 Elebiju, Ajani, Oduselu,  
Ogunnupebi and Adebiji. This is an open-  
access article distributed under the terms  
of the [Creative Commons Attribution  
License \(CC BY\)](https://creativecommons.org/licenses/by/4.0/). The use, distribution or  
reproduction in other forums is permitted,  
provided the original author(s) and the  
copyright owner(s) are credited and that  
the original publication in this journal is  
cited, in accordance with accepted  
academic practice. No use, distribution or  
reproduction is permitted which does not  
comply with these terms.

# Recent advances in functionalized quinoline scaffolds and hybrids—Exceptional pharmacophore in therapeutic medicine

Oluwadunni F. Elebiju<sup>1,2</sup>, Olayinka O. Ajani<sup>1,2</sup>,  
Gbolahan O. Oduselu<sup>1,2</sup>, Temitope A. Ogunnupebi<sup>1,2</sup> and  
Ezekiel Adebiji<sup>1,3,4\*</sup>

<sup>1</sup>Covenant University Bioinformatics Research (CUBRe), Covenant University, Ota, Nigeria, <sup>2</sup>Department of Chemistry, College of Science and Technology, Covenant University, Ota, Nigeria, <sup>3</sup>Department of Computer and Information Science, Covenant University, Ota, Nigeria, <sup>4</sup>Division of Applied Bioinformatics, German Cancer Research Center (DKFZ), Heidelberg, Germany

Quinoline is one of the most common nitrogen-containing heterocycles owing to its fascinating pharmacological properties and synthetic value in organic and pharmaceutical chemistry. Functionalization of this moiety at different positions has allowed for varying pharmacological activities of its derivative. Several publications over the last few decades have specified various methods of synthesis. This includes classical methods of synthesizing the primary quinoline derivatives and efficient methods that reduce reaction time with increased yield employing procedures that fulfill one of the twelve green chemistry principles, “safer solvent”. The metal nanoparticle-catalyzed reaction also serves as a potent and effective technique for the synthesis of quinoline with excellent atom efficiency. The primary focus of this review is to highlight the routes to synthesizing functionalized quinoline derivatives, including hybrids that have moieties with predetermined activities bound to the quinoline moiety which are of interest in synthesizing drug candidates with dual modes of action, overcoming toxicity, and resistance amongst others. This was achieved using updated literature, stating the biological activities and mechanisms through which these compounds administer relief. The ADMET studies and Structure-Activity Relationship (SAR) of novel derivatives were also highlighted to explore the drug-likeness of the quinoline-hybrids and the influence of substituent characteristics and position on the biological activity of the compounds.

## KEYWORDS

admet, drug design, hybrid, pharmacological activity, quinoline, synthesis

## 1 Introduction

Heterocyclic compounds are cyclic compounds with atoms different from carbon within the ring. These atoms are referred to as heteroatoms, they include oxygen, nitrogen, sulfur, etc. The presence of heteroatoms allows for functionalities and activities, making them of critical importance for medicinal chemists (Hossain, 2018). The most prominent bioactive chemical compounds are nitrogen-containing heterocycles, which are found in natural products (as alkaloids in a range of plants), physiologically active synthetic chemicals, medications, and other products (Teja and Khan, 2020).

Quinoline is a nitrogen-containing fused bicyclic heterocycle with the chemical formula  $C_9H_7N$  (Figure 1). It is also known as benzo [b] pyridine. Its derivatives have been used in many fields, including medicine (Desai et al., 2021). Figure 2 shows some commercially available drugs with quinoline moiety. Quinoline is a multifunctional scaffold in medicinal chemistry that forms a salt with acids and undergoes electrophilic and nucleophilic substitution reactions (Yadav and Shah, 2021). This property allows for functionalization at numerous ring positions and its use as an intriguing synthetic building block in the design of drugs and their synthesis. The substituent characteristics and position are important to note as they play a significant role in the functionality of synthesized compounds, allowing for a wide range of applications and biological activities (Abdelbaset et al., 2018).

Quinoline and its derivatives have been of interest to scientists, with many chemists seeking to find more effective synthetic methods by improving on existing synthesis *via* reaction optimization (Yadav and Shah, 2021). The growing resistance of disease-causing organisms to commercially available drugs and increasing toxicity exhibited as side effects have allowed for the synthesis of potential drug candidates involving a combination of two biologically active molecules into one single hybrid entity. Quinoline hybrids have been synthesized in recent years and reported to have improved activity when compared to standard drugs used. Examples shown in Figure 3 are the Quinoline-

coumarin hybrid (Taheri et al., 2019), the Quinoline-benzothiadiazole hybrid (Medeiros et al., 2021), the Quinoline-thiazole hybrid (Eissa et al., 2021), Quinoline-triazine hybrid (Ghanim et al., 2022), amongst others. This review focuses on the synthesis, pharmacological activity, Structure-Activity Relationship (SAR), and ADMET studies of quinoline derivatives including quinoline hybrids to uncover their drug-likeness and the activities responsible for the novel pharmacological activity.

## 2 Chemistry of quinoline

### 2.1 Synthesis of quinoline derivatives

Quinoline and its various derivatives have been demonstrated to be quite easy to produce by, utilizing various synthetic approaches to obtain pharmacologically active derivatives (Yadav and Shah, 2021). Some of the synthesis techniques are.

#### 2.1.1 Classical synthesis of quinoline

The quinoline motif can be synthesized using a variety of classical synthetic methods. These classical methods have been employed in recent years in the synthesis of functionalized quinoline derivatives. Popular synthetic pathways that include aniline as reactants are shown in Figure 4. Substituted aniline is also used as a reactant to achieve

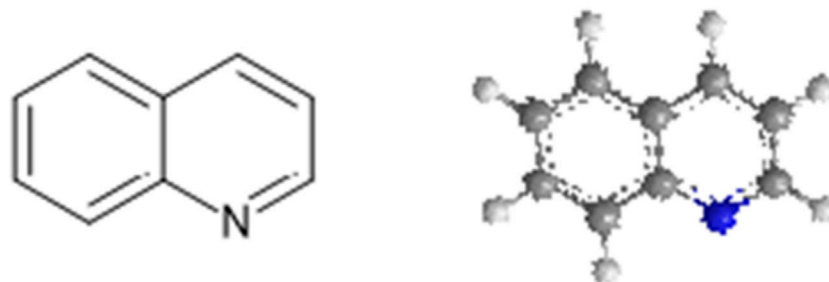


FIGURE 1  
Chemical and 3D structure of quinoline.

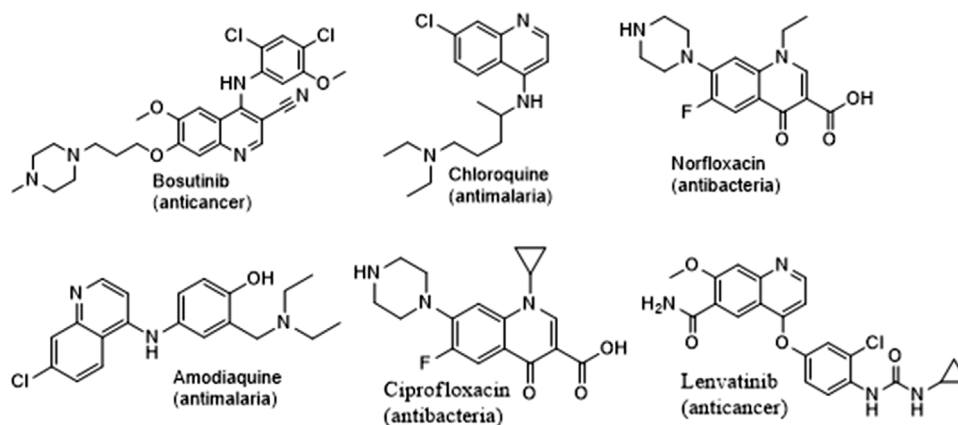


FIGURE 2  
Structures of some commercially available quinoline containing drugs.

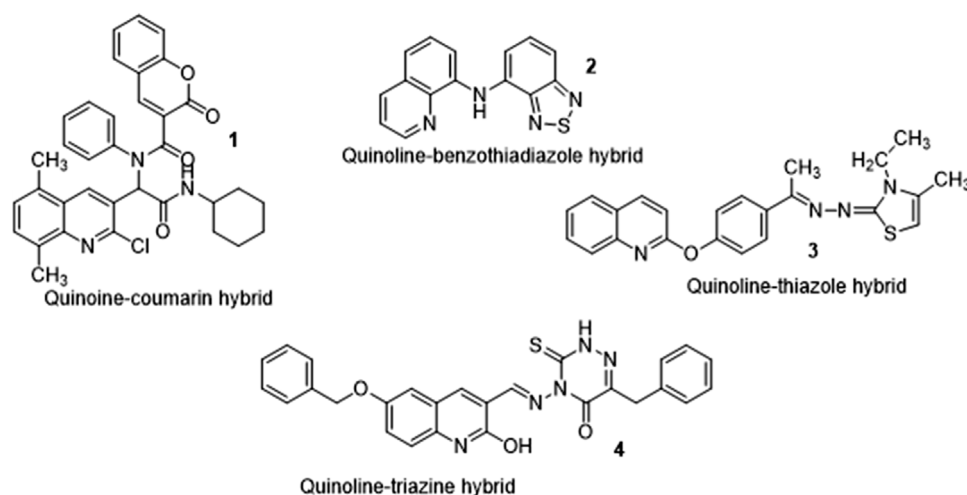


FIGURE 3  
Structures of reported quinoline hybrids.

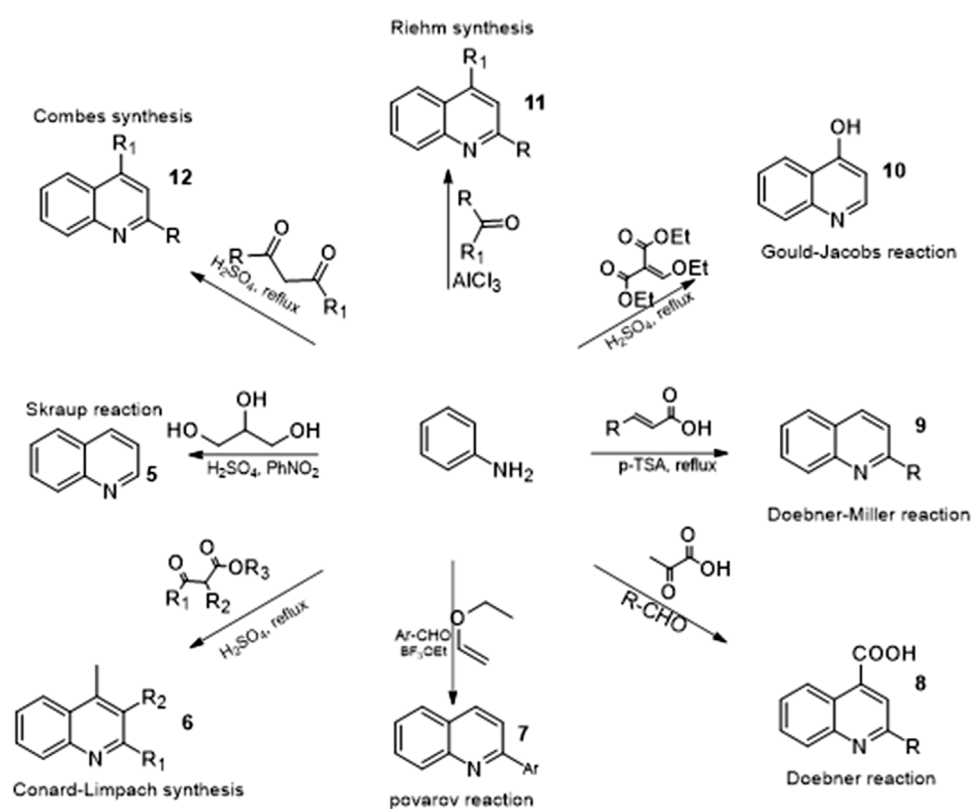


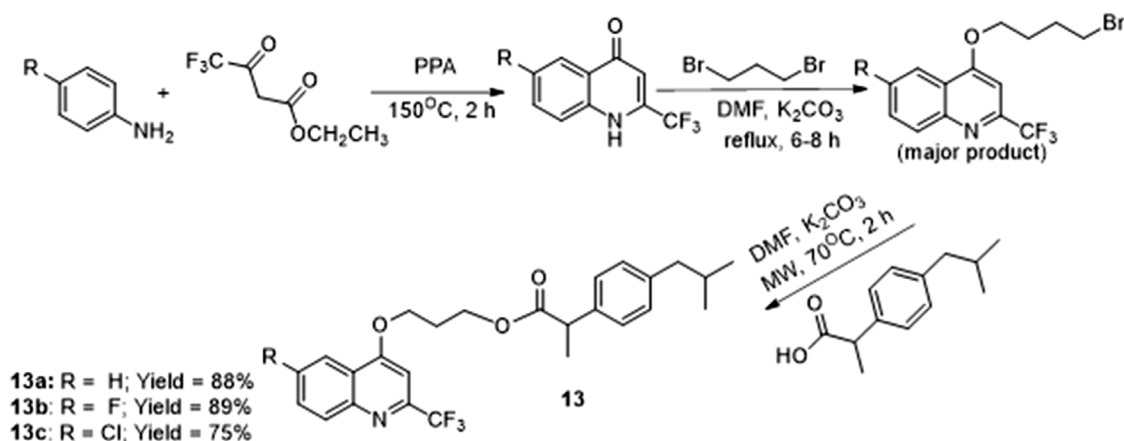
FIGURE 4  
Classical synthetic route of quinoline.

derivatives that can be further functionalized at strategic positions (Nainwal et al., 2019).

Ghanim et al. used the Conrad-Limpach cyclo condensation approach as in (Scheme 1) to react *p*-substituted aniline and ethyl 4,4,4-trifluoro-3-oxobutanoate to synthesize a di-substituted quinoline

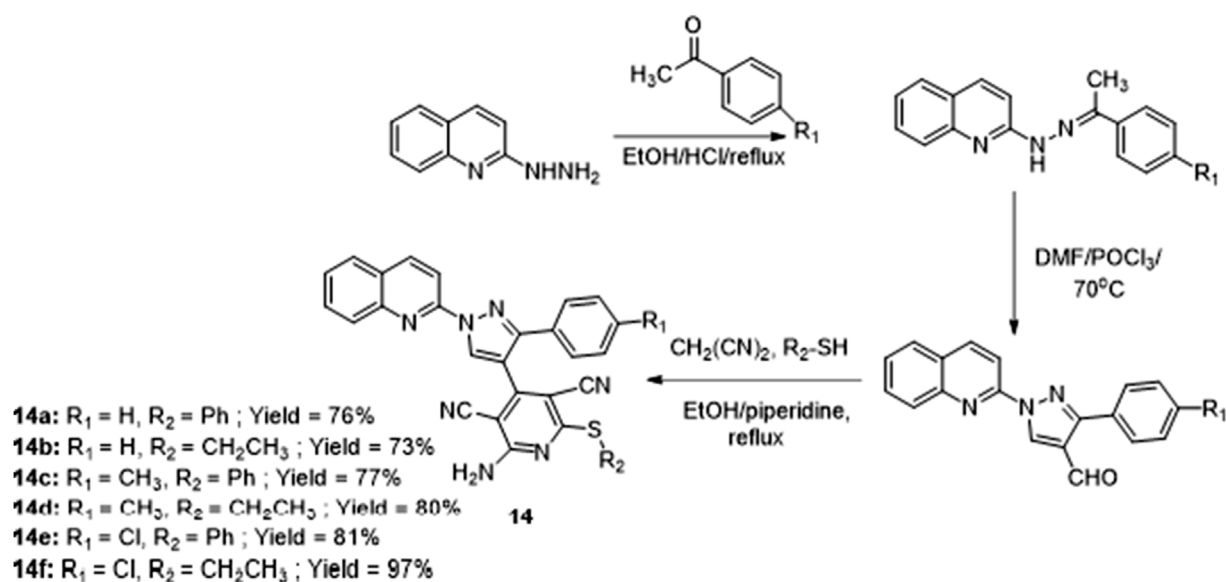
which was an intermediate in the preparation of ibuprofen-quinoline hybrids. Compounds **13a**, **13b**, and **13c** had the most promising anti-inflammatory activities. The color of the hybrids ranged from colorless oil to white microcrystals and the melting points of the solid crystals fell between (60–70)°C (Ghanim et al., 2022).





SCHEME 1

Conrad-Limpach cyclo condensation for the synthesis of ibuprofen-quinoline hybrid.



SCHEME 2

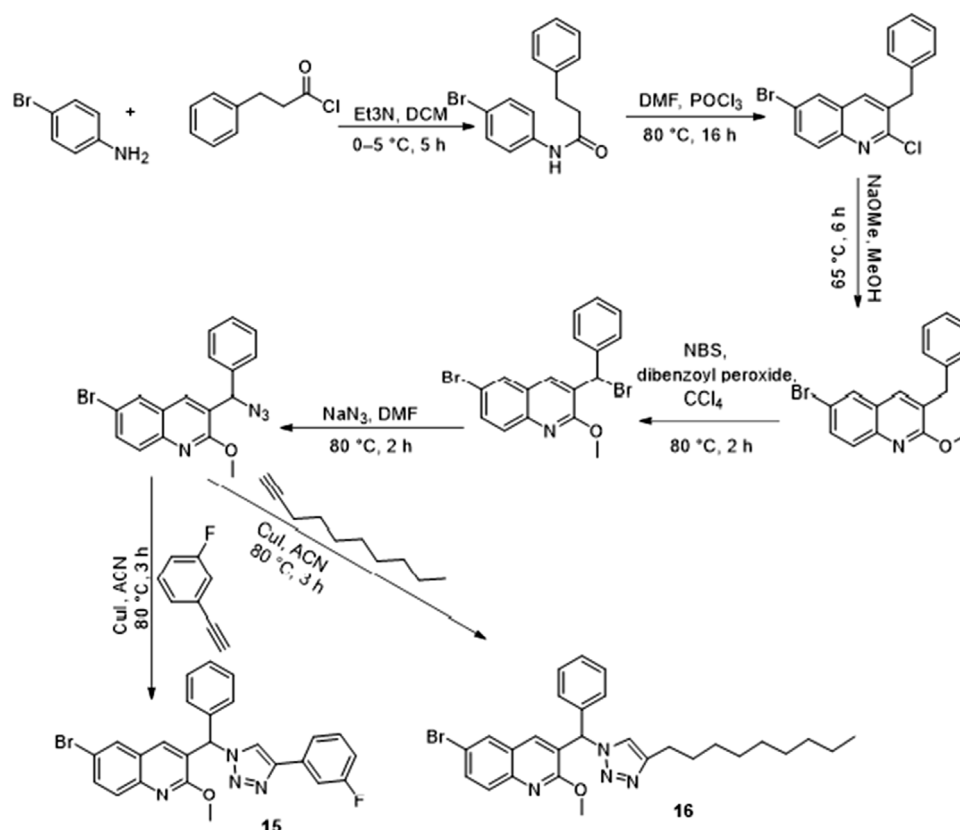
Vilsmeier-Haack synthesis of pyrazole and pyridine-quinoline hybrids.

Amer et al. employed the Vilsmeier-Haack procedure to synthesize pyrazole-pyridine-based quinoline hybrids (Scheme 2), via the formylation of quinoline hydrazones to form the 4-formyl pyrazole derivatives. In a one-pot synthesis, 4-formyl pyrazole derivatives were combined with malononitrile and thiophenol to produce 2-substituted quinoline derivatives. All derivatives **14a-f** were reported to exhibit broader antimicrobial activities when compared to standards. The hybrids were yellow in color with melting points between (160–200)°C and others greater than 250°C (Mahgoub, 2018).

Ramprasad et al. (Scheme 3), reacted bromo-substituted aniline with phenylpropanoid chloride and triethylamine in DCM, which was formylated and subsequently cyclized through the Vilsmeier-Haack reaction. This was followed by a substitution reaction of the chloro group with a methoxy group. The intermediate was then treated with

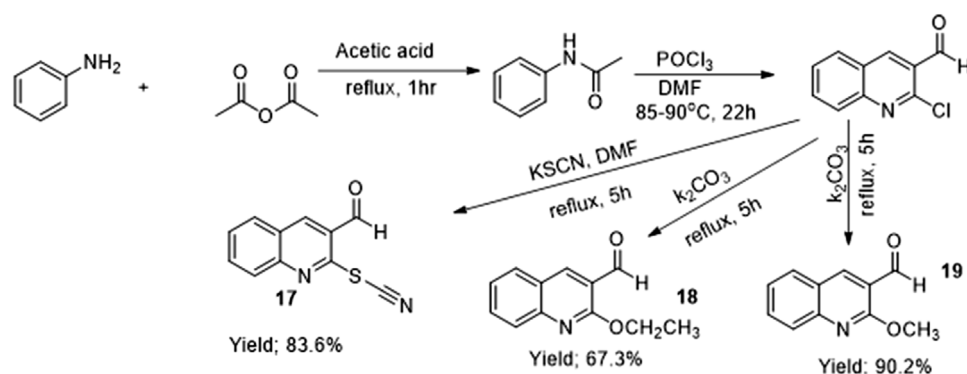
*n*-bromosuccinamide (NBS), and tetrachloromethane (CCl<sub>4</sub>) to give a derivative that was then transformed into a substituted azide compound. This intermediate was then transformed into a substituted azide compound. This intermediate was then reacted with substituted alkynes in acetonitrile under reflux conditions to give the corresponding quinoline-triazole hybrids with melting points ranging from (73–220)°C. Derivatives including compounds 15 and 16 which were reported to be the most active among the series against *Mycobacterium bovis* (Ramprasad et al., 2019).

Zelege et al. used the Vilsmeier-Haack reaction to synthesize quinoline-carbaldehyde derivatives (Scheme 4) from acetamide derivatives which were previously prepared by acetylation of aniline. Under different reaction conditions, substitution via an aromatic nucleophilic approach was done to introduce alternative nucleophiles resulting in the formation of new derivatives.



SCHEME 3

Vilsmeier-Haack synthesis of quinoline-triazole hybrids.



SCHEME 4

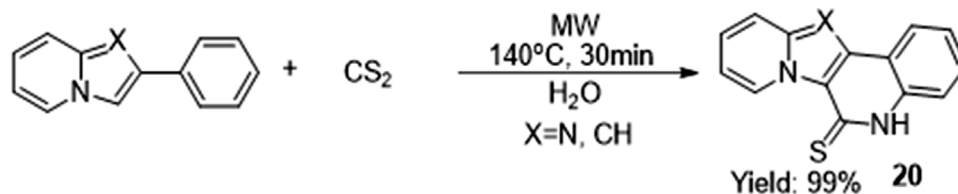
Vilsmeier-Haack synthesis of quinoline-carbaldehyde derivatives.

Compounds 17, 18 and 19 were some of the reported derivatives. The color of derivatives ranged from white to grey, to orange and yellow, with melting points between 90–180) °C (Zelege et al., 2020).

### 2.1.2 Microwave-assisted synthesis

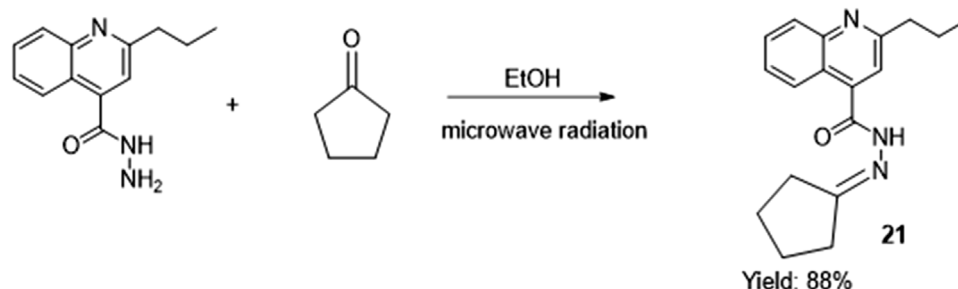
Environmental concerns have risen in chemical research, prompting the development of a variety of concepts to

eliminate and reduce waste production. A microwave uses dipole rotation and ionic conduction to transport energy directly to reactive species. Microwaves generate electric and magnetic fields, but the electric field alone is used to heat a material, allowing a cut down on both the amount of energy used and the time it takes for a reaction to happen (Nainwal et al., 2019). It is an environmentally friendly reaction as it takes place in enclosed chambers.



SCHEME 5

Microwave-assisted synthesis of fused quinoline-thiones.



SCHEME 6

Microwave-assisted condensation of hydrazide-hydrazone quinoline derivatives.

Li et al. synthesized derivatives of quinoline-thiones fused with poly-heterocyclic by reacting pyridine-imidazole derivative with carbon disulfide in different bases *via* a microwave annulation process through 6 $\pi$ electrocyclization to create scaffolds. The solvent used and time were varied while the temperature was kept constant. Reaction conditions reported in [Scheme 5](#) gave the best yield of 99% using water as solvent. It was reported that microwave-assisted heating generally improved reaction efficiency ([Li et al., 2020](#)).

Ajani et al. synthesized hydrazide-hydrazone derivatives ([Scheme 6](#)) *via* microwave-assisted condensation reaction of the NH<sub>2</sub> free end of carbohydrazide derivative with various aliphatic and alicyclic ketones carbonyl centers that are sp<sup>2</sup> hybridized in ethanol. The reaction took between 1 and 3 min to complete due to its exposure to microwave radiation, and the melting points of most of the derivatives were greater than 300°C. Compound **21** was one of the reported compounds ([Ajani et al., 2018](#)).

### 2.1.3 Ultrasound-assisted synthesis

Ultrasound-assisted multicomponent reactions in water are good instruments for generating bioactive chemicals. This is because they provide higher yields than other approaches. They have been used in the synthesis of a range of heterocyclic compounds.

Diaconu et al. used ultrasound irradiation to produce the quinoline-imidazolium hybrids by *N*-alkylation of the acidic nitrogen in benzimidazole with substituted  $\omega$ -halogen acetophenones ([Scheme 7](#)). All derivatives including compounds **22**

and **23** were reported to have improved yield when compared with conventional heating methods ([Diaconu et al., 2021](#)).

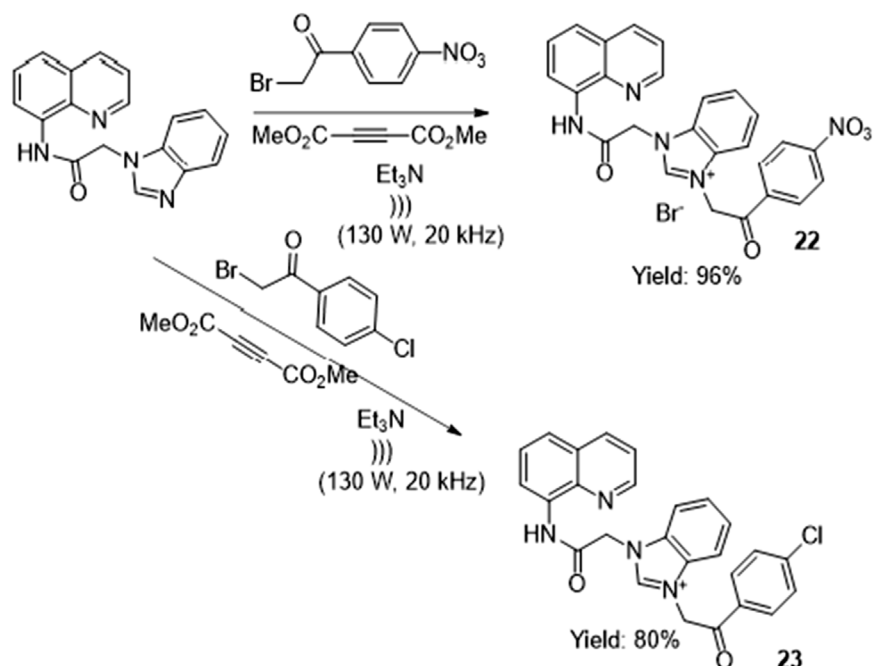
Upadhyay et al. synthesized and investigated 2-substituted quinoline derivatives ([Scheme 8](#)), one of which is **24** by one-pot three-component fusion of methyl 3,3-diethoxypropionate, varying aniline derivatives, and aldehyde at 60°C under ultrasonic circumstances utilizing SnCl<sub>2</sub>·2H<sub>2</sub>O as a catalyst and water as solvent ([Upadhyay et al., 2018](#)).

### 2.1.4 Transition metal nanoparticles mediated synthesis

Angajala et al. used the Knoevenagel condensation of quinoline-carbaldehyde and cyclohexanone-fuse derivatives to produce quinoline-acridine hybrids ([Scheme 9](#)). They used copper nanoparticles as a catalyst, stirring for 2 h at room temperature in DMF. Compound **25** represents the hybrids where the position and identity of 'R' are dependent on the carbaldehyde derivative used. The synthesized derivatives were confirmed using NMR (<sup>1</sup>H and <sup>13</sup>C) which confirmed the number of proton and carbon atoms with their respective chemical shift ([Angajala et al., 2020](#)).

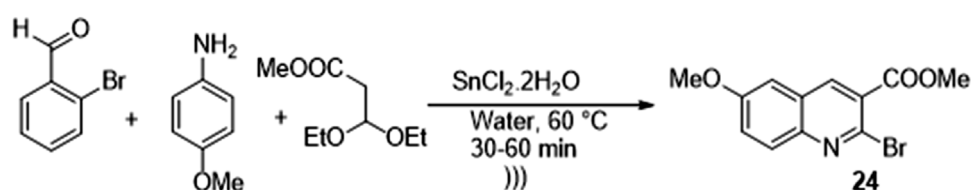
### 2.1.5 Click chemistry-supported synthesis

Upadhyay et al. designed and synthesized a series of quinoline derivatives using molecular hybridization approach supported by click chemistry ([Scheme 10](#)). Most of the derivatives were white solids with melting points above 100°C, compound **26** was one of the derivatives ([Upadhyay et al., 2018](#)).



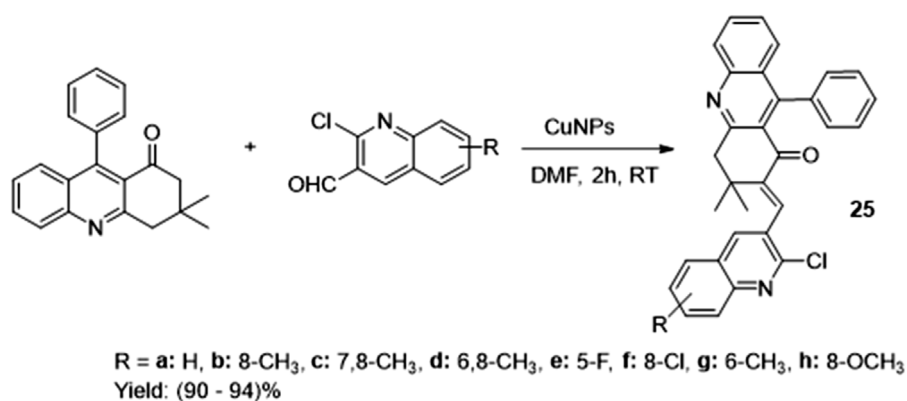
SCHEME 7

Ultrasound-assisted quinoline imidazolium salts synthesis.



SCHEME 8

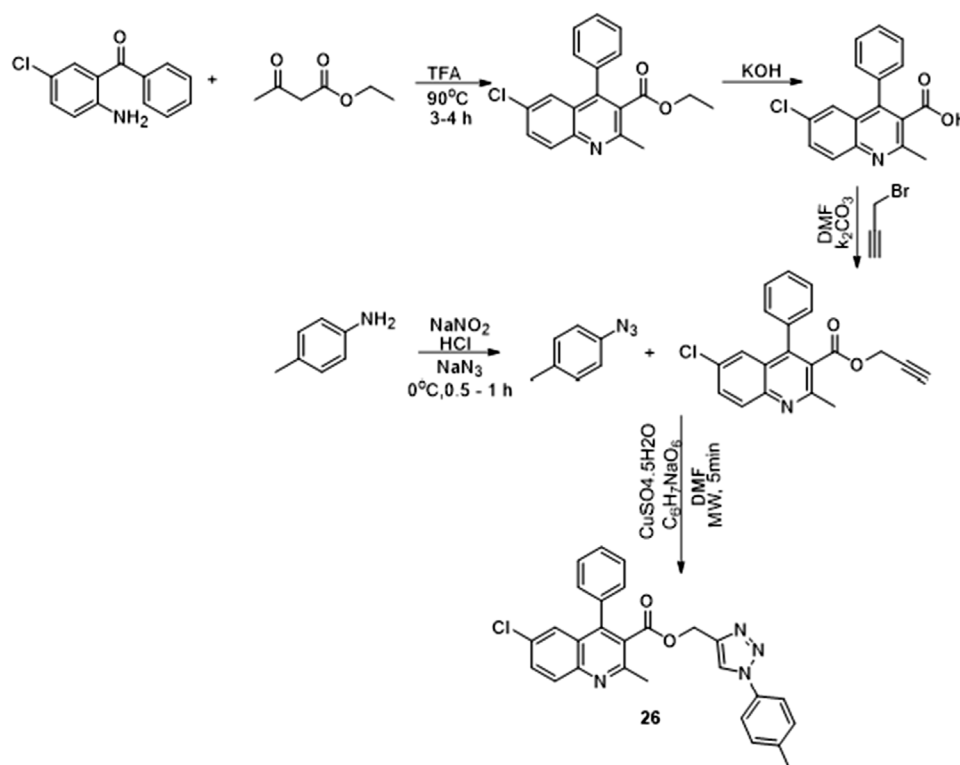
Ultrasound-assisted synthesis of 2-substituted quinolones.



SCHEME 9

CuNPs mediated Knoevenagel condensation.





SCHEME 10

Synthesis of quinoline hybrid via click chemistry.

## 3 Activities of some quinoline motifs

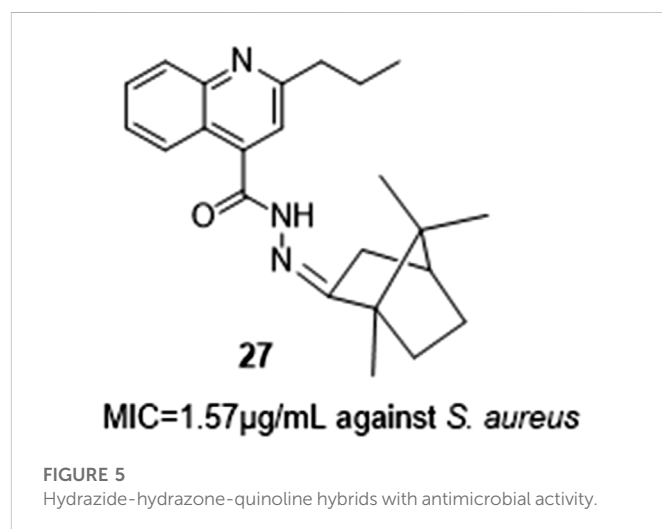
### 3.1 Pharmacological activities

In a bid to investigate their pharmacological activities, reacting quinoline scaffolds with moieties having pharmacophore characteristics have been explored. This has led to the production of hybrids, some of which have been reported to possess higher pharmacological activity when compared to commercially available quinoline-based medicines indicating a synergistic effect of moieties introduced.

#### 3.1.1 Antimicrobial activities

Amer et al. *via in vitro* analysis tested pyrazole- and pyridine-based quinoline hybrids for both antibacterial and antifungal activities. Antifungal analysis was conducted against *Candida albicans* using Ketoconazole as standard at a concentration of 100 µg/mL while antibacterial screening against two Gram-positive bacteria (*Staphylococcus aureus* and *Bacillus subtilis*), and two Gram-negative bacteria (*Salmonella typhimurium* and *Escherichia coli*) was carried out using Ciprofloxacin as standard. Some of the synthesized derivatives, such as 15, displayed far broader antibacterial activity than Ciprofloxacin, while others demonstrated good to moderate antimicrobial performance against the pathogens examined. These compounds were found to have antibacterial activity against a variety of bacteria (Mahgoub, 2018).

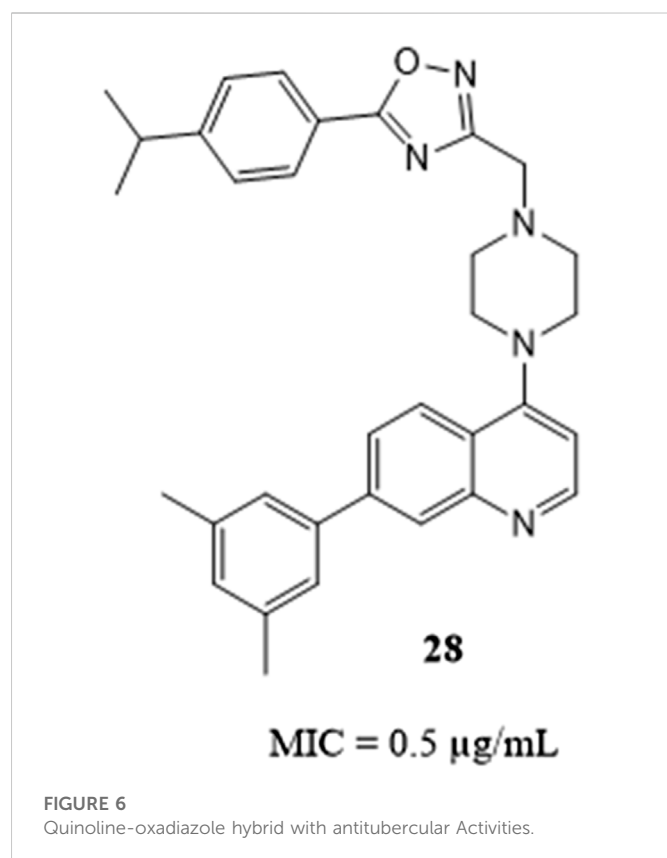
Ajani et al. synthesized a series of hydrazide-hydrazone-quinoline hybrids using microwave irradiation (Figure 5). When compared to gentamicin, most of the novel quinoline hydrazide-hydrazones were



reported to have higher inhibitory power, the most active being 27 having MIC values from 1.59 to .39 µg/mL against *Staphylococcus aureus*, *Bacillus licheniformis*, *Micrococcus varians*, *Escherichia coli*, and *Proteus vulgar* (Ajani et al., 2018).

#### 3.1.2 Antitubercular activities

Multidrug-resistant tuberculosis (MDR-TB) has been a significant obstacle in the fight against tuberculosis around the world. The quinoline-oxadiazole hybrids were synthesized by Shruthi et al. as a novel family of TB-specific compounds. Compound 28 with a MIC



value of .5 µg/mL was reported to have the highest activity against Mtb WT H<sub>37</sub>Rv (Figure 6). Pharmacokinetics (PK) studies demonstrated that it is orally bioavailable having blood levels above the MIC of 2.5 µg/mL. The compounds produced were found to be metabolically stable, bioavailable, non-toxic, and exhibited good PK values, making them suitable for further research in a TB infection on an animal model (Shruthi et al., 2020).

Ramprasad et al. developed target quinoline-triazole hybrids and evaluated them against the growth of *Mycobacterium bovis*. The test compounds strongly reduced *Mycobacterium bovis* growth in antitubercular screening tests, with two of the derivatives **15** and **16**, having MIC values of 31.5 and 34.8 µM respectively. The findings of the compounds that demonstrate promising activity stress the importance of future research and the development of new antitubercular medications (Ramprasad et al., 2019).

### 3.1.3 Antiproliferative activity

Nitric oxide release and induction of apoptosis are some of the mechanisms nitrones and oximes use to exhibit antiproliferative properties. Activation of caspase (a group of key apoptosis mediators) occurs when reactive nitrogen species (RNS) including NO<sub>2</sub> and N<sub>2</sub>O<sub>3</sub> targets P53. Caspase-3 which is the most important one can activate death protease and cleave some important cellular proteins (Porter and Jänicke, 1999).

Abdelbaset et al. synthesized quinolone nitrones and quinoline oxime derivatives and determined the NO release of derivatives. They reported that nitrones release more NO than oximes on average and this contributed to them exhibiting increased antiproliferative activity than the oxime derivatives. Compounds **29**, **30**, **31**, and **32** which are quinoline-nitrones derivatives had a high percentage of inhibition of

growth and antiproliferative action as opposed to the quinoline oximes derivatives which were ineffective (Figure 7). The nitrone derivatives with IC<sub>50</sub> values ranging from .45–.91 µM against RPMI-8226 leukemia cell line were found to be more potent than the standard medicine doxorubicin. IC<sub>50</sub> values ranging from .98–2.98 µM was recorded against HCT-116 colon cancer cell lines which were equivalent to that of the standard drug. A considerable rise in the level of caspase-3 protein in RPMI-8226 was observed when derivatives were evaluated as caspase-3 activators (Abdelbaset et al., 2018).

Quinoline derivatives with enhanced water solubility and antiproliferative action were synthesized by Li et al. via the introduction of a flexible alkylamino side chain at position-4 and an alkoxy group at position-7 of the quinoline nucleus. The derivatives were evaluated as potential antiproliferative drugs based on the chemical structure of the lead derivative. Preliminary SAR analysis suggested that big and bulky substituents at position-7 facilitated antiproliferative activity and the presence of amino side-chain substituents enhanced this activity. The length of the alkylamino side chain moiety also influenced antiproliferative potency, especially for derivatives with two CH<sub>2</sub> units. Compound **34** was found to be the most effective among the derivatives (Li et al., 2019).

### 3.1.4 Antileishmanial activity

Macrophages play an important role in the cellular immune response and are activated as the first line of defense by host against *Leishmania sp.* Activation lead to increase in intracellular calcium levels and nitric oxide production which plays a role in parasite death (Muálem de Moraes Alves et al., 2021). Upadhyay et al. discovered that imidazo-quinoline hybrids via macrophage activation exhibited antileishmanial activity, hence synthesized series of quinoline-triazole hybrids which were evaluated as possible antileishmanial agents on cutaneous leishmaniasis as adjunct to antimonial using experimental models and clinical studies (Figure 8). Among all the derivatives, therapeutic *in vitro* action was observed for compounds **35**, **36**, **37**, and **38** against intracellular amastigotes of *Leishmania donovani*. Using the golden hamster model, *in vivo* antileishmanial activity of *L. donovani* was investigated for these four derivatives and compound **37** demonstrated promising leishmanicidal activity (Upadhyay et al., 2018).

Costa et al. synthesized and evaluated the anticancer and antileishmanial properties of several 4-substituted quinolones, compound **39** and **40** were reported to have the best anti-melanoma and anti-leukemia activity with the lowest EC<sub>50</sub> values for decreased cell viability. Apoptosis dependent on caspases, the activity of cysteine protease, and mitochondrial permeabilization were reported to have been observed according to the mechanistic investigation. Another derivative, **41** had the best inhibitory activity against *L. mexicana* cysteine proteases type B. These findings suggest that 4-substituted quinolines could be useful as anticancer and antileishmanial drugs (Costa et al., 2020).

### 3.1.5 α-glucosidase inhibitory activity

Urease, beta-glucuronidase, thymidine phosphorylase, and α-amylase are all inhibited by nitrogen-containing heterocyclic moieties. Taha et al. developed quinoline-Schiff base hybrids as a potent family of *in vitro* α-glucosidase (an enzyme that hydrolyzes polysaccharides and disaccharides, the main cause of diabetes mellitus) inhibitors (Figure 9). All derivatives inhibited α-glucosidase activity *in vitro* at doses ranging from 6.20 to 48.50 µM

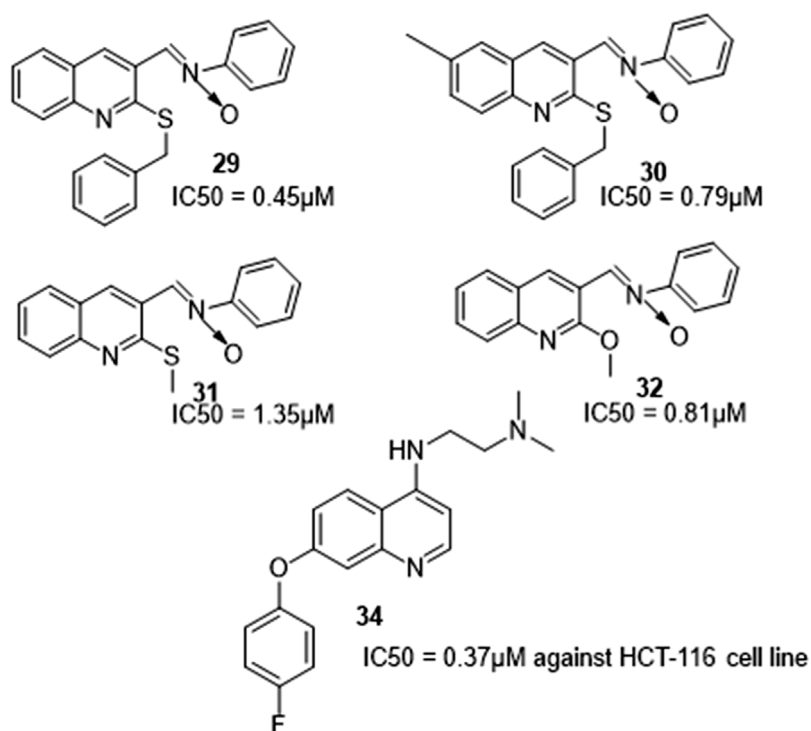


**FIGURE 7**  
Quinolone derivatives with antiproliferative activity.

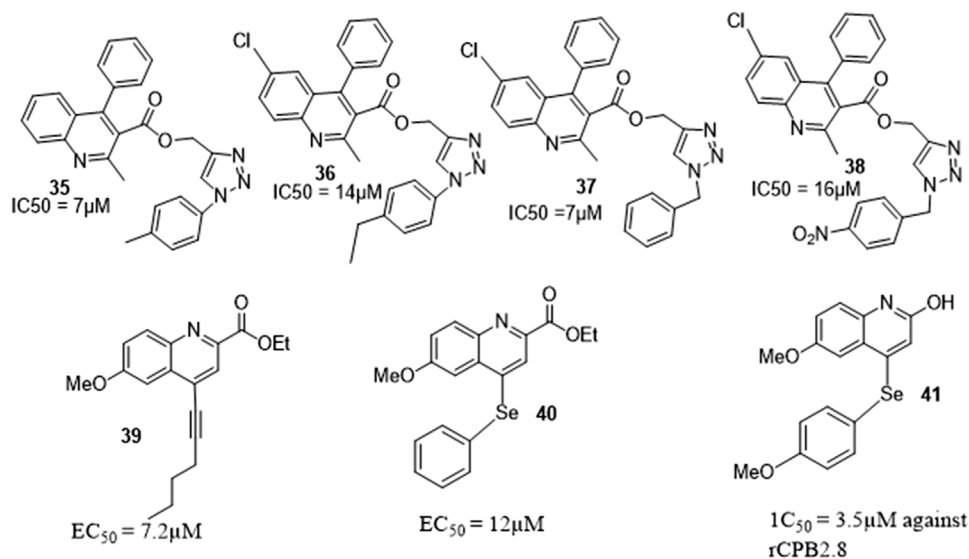


**FIGURE 8**  
Quinoline hybrids with antileishmanial activity.

with acarbose as the reference drug. Derivatives with two OH groups, **42**, and a fluoro group, **43** were the most effective in the series (Taha et al., 2019).

Nikookar et al. synthesized dihydropyran-quinoline derivatives and investigated the *in vitro* inhibitory effects against  $\alpha$ -glucosidase. The most

potent derivatives were **44** ( $IC_{50} = 10.3 \mu M$ ) with chloro substitution on position 4 on the phenyl ring and **45** ( $IC_{50}$  value of  $15.7 \mu M$ ) with fluoro substitution on position 4 on the phenyl ring. A modification of the fluoro group from position 4 to 3 on the phenyl ring lowered the inhibitory action as in **46** ( $IC_{50} = 95.7 \mu M$ ) (Nikookar et al., 2018).

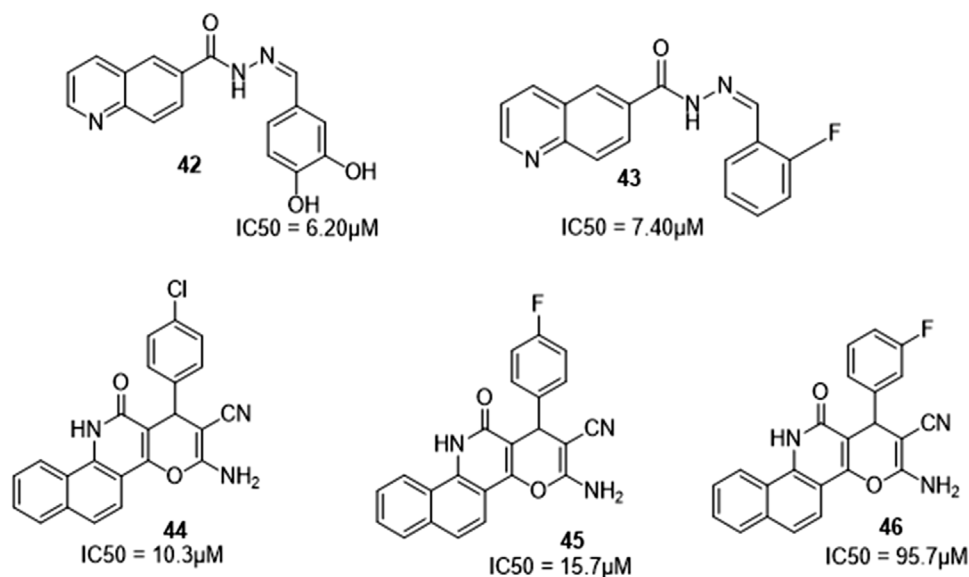
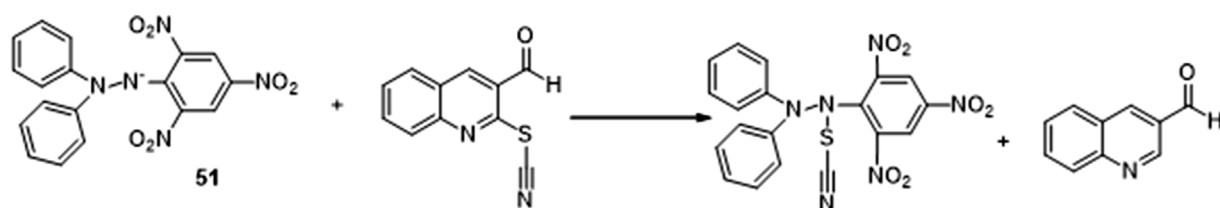


**FIGURE 9**  
Quinoline hybrids with  $\alpha$ -glucosidase inhibitory activity.



**SCHEME 11**  
Mechanism of compound 51 scavenging activity.

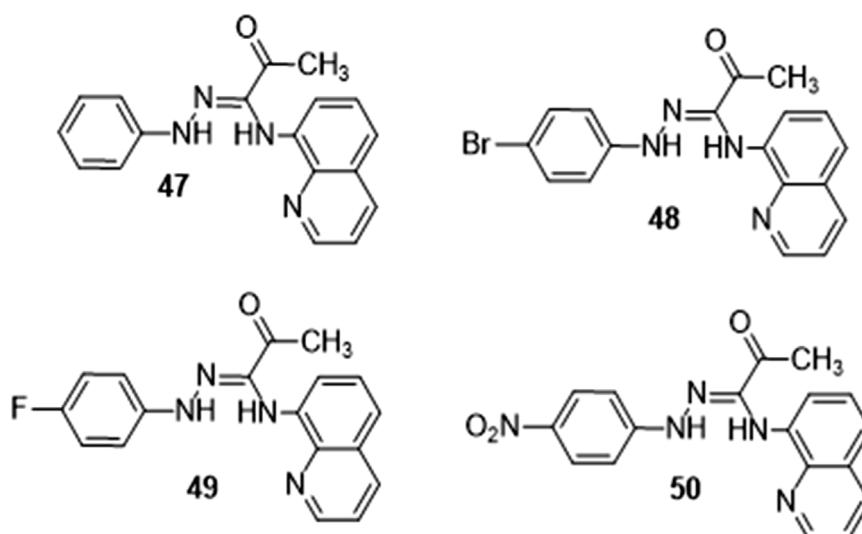


**FIGURE 10**  
Derivatives with anti-inflammatory activity.



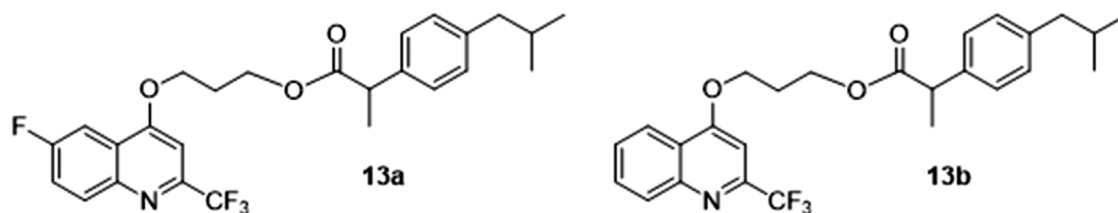


**FIGURE 11**  
Ibuprofen-quinoline hybrids with anti-inflammatory activity.

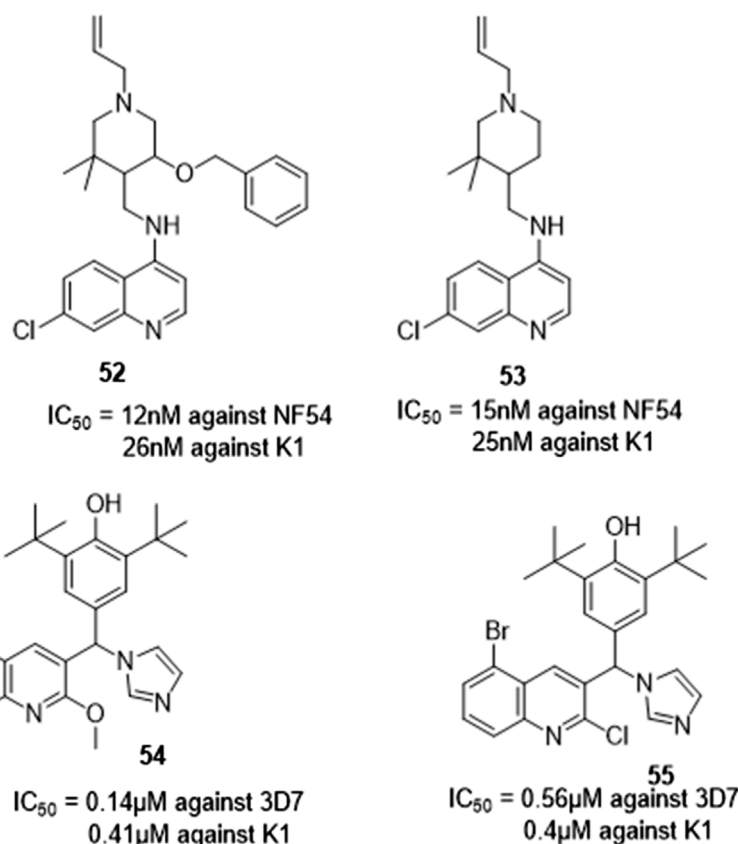


**FIGURE 12**  
quinoline derivatives with antimalaria activity.

### 3.1.6 Antioxidant activity

Investigation of the antioxidant capabilities of azoimine-quinoline hybrids by Douadi et al. was achieved by assessing the 1,1-diphenyl-2-picrylhydrazyl (DPPH) free radical scavenging activity of derivatives. The DPPH test was utilized to determine their reactivity. When the stable free radical DPPH is scavenged, it takes on a purple color and turns yellow ( $\lambda_{\text{max}} = 517\text{ nm}$ ). Antioxidants react with DPPH to generate DPPH-H, which is a non-radical form. The concentration and absorbance at 517 nm of DPPH will decrease as a result. Various dosages of derivatives were used to assess a compound's scavenging capacity of DPPH free

radical. The results using these derivatives demonstrate that the DPPH radical's absorbance reduced as the concentration was increased. At very low concentrations, the derivatives were reported to show greater antioxidant potential than ascorbic acid (Douadi et al., 2020).

The antioxidant activity of the quinoline derivatives synthesized by Zeleke et al. was determined using DPPH. All derivatives had moderate activity, with compound 51 having the highest activity (radical scavenging activity of 67% at a concentration of 100 g/mL). Compound 51 has no easily transferable hydrogen, it was proposed that the sulfur in the thiocyanate functional group donates an electron

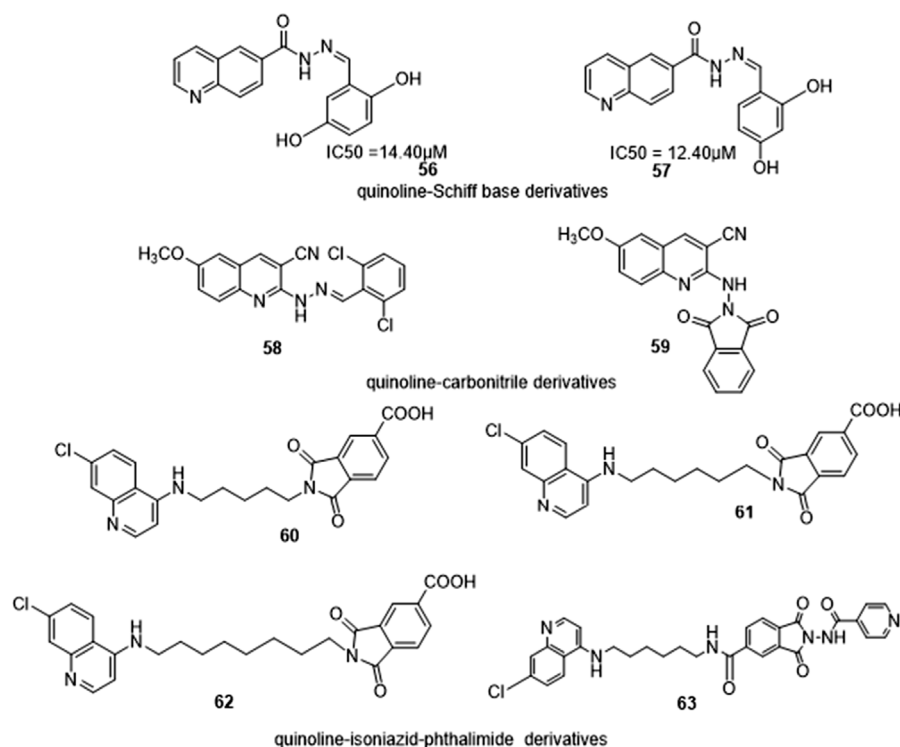


**FIGURE 13**  
Some quinoline derivatives with reported SAR.

to the lone pair of the nitrogen atom's electron, making a connection with sulfur as shown in [Scheme 11](#) ([Zelege et al., 2020](#)).

### 3.1.7 Anti-inflammatory activity

Douadi et al. investigated quinoline-azoimine hybrids' anti-inflammatory capabilities *in vitro* by comparing their suppression of albumin denaturation to that of the gold standard, diclofenac sodium ([Figure 10](#)). Compounds **48** and **49** have anti-inflammatory characteristics similar to diclofenac, according to the research. Compounds **47** and **50** were found to decrease inflammation by 70.32% and 54.22% respectively at a concentration of 100 mg/mL. These figures are lower than those for diclofenac. Compound **49** showed the highest anti-inflammatory activity when compared to the others ([Douadi et al., 2020](#)).

Ghanim et al. evaluated ibuprofen-quinoline hybrids ([Figure 11](#)) and their anti-inflammatory properties to see if they were comparable to their progenitor (ibuprofen, a clinically authorized anti-inflammatory medicine that reveals its peak anti-inflammatory action at 3 h). It was reported that their anti-inflammatory effects were comparable to ibuprofen's with the mean edema thickness of the control group staying nearly constant until it dropped at 24 h. The anti-inflammatory activity of most potent derivatives was low and mild at 1 h and 2 h respectively and then potency increased with time at 3 h and 4 h, indicating their promising activity at 3 h compared to the commonly used drugs ([Ghanim et al., 2022](#)).

### 3.1.8 Antimalarial activity

Van de Walle et al. synthesized quinoline-piperidine derivatives to test their antimalarial potential. Almost all derivatives showed promise

against NF54 and K1 a chloroquine sensitive and a chloroquine-resistant *Plasmodium falciparum* strain respectively ([Figure 12](#)). *In vitro* evaluation of the compounds was reported to have demonstrated outstanding anti-plasmodium activity, with compounds **52** and **53** showing the greatest results with  $IC_{50}$  values of 12 nM and 15 nM against NF54 and 26 nM and 25 nM against K1 parasite strains respectively. Additionally, no cytotoxicity issues were discovered during biological testing in Chinese hamster ovary (CHO) cells. The derivatives were presented as promising structures for more effective antimalarial optimization treatments, given the critical need for novel antimalarial medications to fight the developing resistance of the parasite to artemisinins ([Van de Walle et al., 2020](#)).

Roy et al. synthesized quinoline imidazole hybrids and used an SYBR green-based fluorescence assay to assess antimalarial activity. Compounds **54** and **55** were reported to be the most active with  $IC_{50}$  values lower than the other derivatives. The activity of the other compounds were also reported to be moderately active against the CQ-sensitive strain falling within the range of 1.0–3.8  $\mu M$   $IC_{50}$  values.

Parasite inhibition as a function of stereochemistry was also investigated *via* enantiomeric separation of the racemic mixture of compounds. Asymmetric synthesis of one stereoisomer of compound **54** with negligible cytotoxicity and good selectivity index (SI) was investigated. A complete biological profile was recommended as well due to the reported observed increased activity when compared to the other stereoisomer. This will allow investigation of the biological activities of each enantiomer, assisting in the rationalization of the balance between antiparasitic activity, cytotoxicity, and resistance concerns ([Roy et al., 2022](#)).

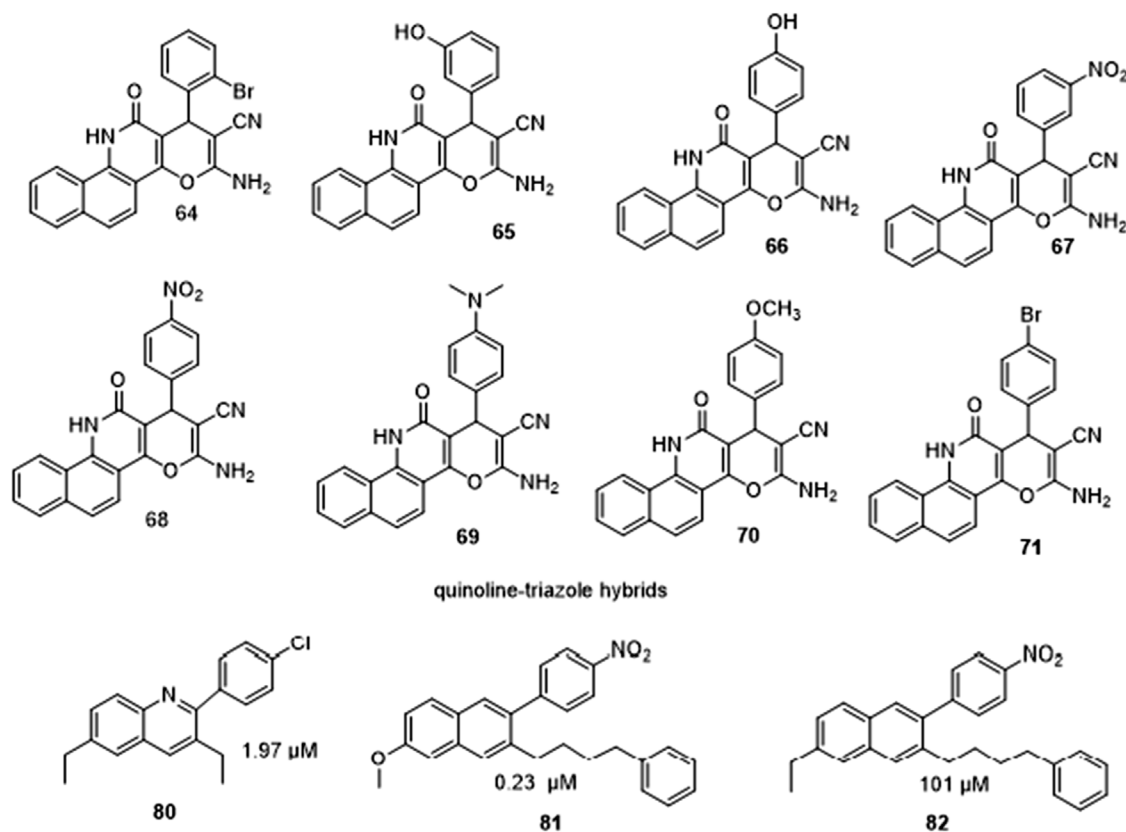


**FIGURE 14**  
SAR studies showing change in potency of quinoline derivatives as substituent changes.

### 3.2 Structural activity relationship (SAR) of some quinoline hybrids

Quinoline-Schiff bases were synthesized by Almandil et al. and their inhibitory action was tested against  $\alpha$ -glucosidase *in vitro* in the presence of the reference drug acarbose. It was reported that changing the position of hydroxyl on the phenyl ring reduced inhibitory activity, with derivatives containing two OH groups on the phenyl ring exhibiting excellent inhibitory activity (Figure 13). The SAR investigation showed that derivative 42, a dihydroxy on positions 3 and 4 ( $IC_{50}$  = 6.20  $\mu$ M) had the best anti- $\alpha$ -glucosidase activity. Derivatives 56 and 57 ( $IC_{50}$  = 12.40 and 14.10  $\mu$ M) were discovered to have less inhibitory potential than 42 due to changes in the position of OH- groups from positions 3 and 4 (Almandil et al., 2019).

El-Gamal et al. synthesized quinoline-carbonitrile derivatives and found them to be promising antibacterial lead compounds by varying the substitutions at position 6, indicating the biological preference of the methoxy group over methyl or without any substitution. Different substitutions on the quinoline molecule were investigated and SAR analyses of derivatives as possible antibacterial drugs. Compared to derivatives with methyl groups, it was reported that compounds 58 and 59 with methoxy group had increased inhibition zone (El-Gamal et al., 2018).

Rani et al. investigated the antiparasmodial activity of synthesized quinoline-isoniazid-phthalimide triads on *Plasmodium falciparum* CQR-W2 strain and accessed cytotoxicity on the Vero cell line of mammalian. The antiparasmodial and cytotoxic activities of

synthesized triads were investigated with the reference drug being chloroquine (CQ). The antiparasmodial activity of the 4-aminoquinoline-phthalimides derivatives differs as the spacer length changes, as seen by  $IC_{50}$  values of 50.8, 30.2, and 43.2 nM for 60, 61, and 62 respectively. The triads were made by substituting the quinolone with isoniazid (INH) around the phthalimide core giving rise to the most promising derivative in series 63 with an  $IC_{50}$  value of 11 nM (Rani et al., 2021).

Ramprasad et al. synthesized target quinoline-triazole hybrids (Figure 14) and found that the hybrids with fluoro on position 3 of the triazole, 16 and 17 with the n-octyl group were reported to be the most promising leads. The type of substituents on the 1,2,3-triazole affected the compounds' activity. Meta substitution of Fluorine on the phenyl ring increased activity, however, fluorine on ortho- and para-position of the phenyl did not. When  $IC_{50}$  values of 66 and 68 which are 4-substituted derivatives were compared to 65 and 67 the 3-substituted derivatives the results demonstrated that the 4-position is more effective. Furthermore, the 4-Bromo derivative 51 outperformed the 2-Bromo derivative 64 in terms of activity. This revealed that the activity is influenced by the character of substituent on the 4-position of the phenyl. Furthermore, compounds 69 and 70 were reported to inhibit  $\alpha$ -glucosidase in virtually identical ways even though their substituents on the 4-position of the phenyl ring differ in electron affinity; hence, in these groups of compounds, the inhibitory action was dependent on the substituent position (Ramprasad et al., 2019).

Ghanim et al. observed SAR in manufactured ibuprofen-quinolinyl hybrids and reported that the bio-properties exhibited

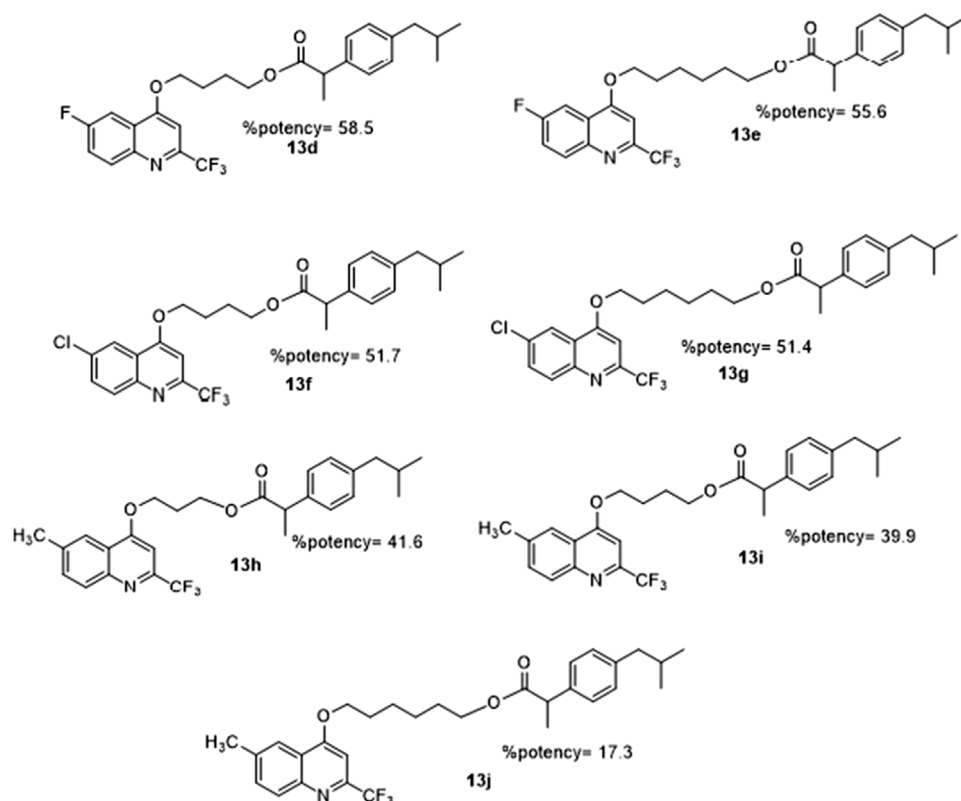


**FIGURE 15**  
SAR activity of Ibuprofen-quinolinyl hybrids.

are dependent on the substituent of the quinolinyl heterocycle as shown in (Figure 15). Compounds **13c**, **13f**, and **13g** (the Cl substituted derivatives), **13b**, **13d**, and **13e** (the F substituted derivatives), and **13h**, **13i**, and **13j** (methyl-substituted) show that the fluorine substituent out-performs chlorine and methyl in terms of percent potency. The alkyl chain that connects ibuprofen to the quinolinyl heterocycle influences bioactivity as its length differs. The substituent with 3 carbon alkyl linker was reported to be more suited for exhibiting higher anti-inflammatory activity than those with 4 and 6-carbon (Ghanim et al., 2022).

The Quinoline-Indole-Schiff base derivative synthesized by B. Li et al. was reported to have excellent antiproliferative activities and did not exhibit any cell toxicity in all the tested tumor cell lines (Figure 16). IC<sub>50</sub> values of derivatives **71**, **72**, **73**, **74**, **75**, and **76** range from 1.24 to 4.95  $\mu$ M and showed a  $\pi$ - $\pi$  interaction between Nur77-LBD and the naphthalene ring. The substitution of naphthalene at the N'-methylene site with indole, as in **77**, and other bicyclic aromatic rings as in **78** and **79** reduced antiproliferative activity with IC<sub>50</sub> values greater than 20  $\mu$ M, indicating that the bicyclic ring attached to N'-methylene affects activity (Li et al., 2021).

Hayat et al. synthesized a variety of substituted quinoline derivatives and tested their inhibitory activity against h-NTPDase, the derivatives were reported to inhibit h-NTPDase1 to varying degrees, with IC<sub>50</sub> ranging from .23 to 101.0  $\mu$ M. The standard used was Suramin with an IC<sub>50</sub> of 16.1  $\mu$ M. Derivatives with an alkyl or benzyloxy propyl group in the quinoline ring were reported to be the most potent with IC<sub>50</sub> values ranging from 1.97 to 19.3  $\mu$ M.

Inhibitory activity of derivatives with an alkyl group was reported to be good to moderate whereas compound **80** with a simple methyl group had an IC<sub>50</sub> value of 1.97  $\mu$ M and showed strong inhibition of h-NTPDase1. Compound **81** having a NO<sub>2</sub> group and an OCH<sub>3</sub> group with an IC<sub>50</sub> value of .23  $\mu$ M was reported to be the most effective inhibitor of h-NTPDase1 in this series. Although the methoxy group is an electron donor, however in this compound is reported to withdraw electrons inductively, hence the stronger inhibitory effect was attributed to the combination of two groups withdrawing electrons, as the NO<sub>2</sub> group is also an electron-withdrawing group. The decrease in h-NTPDase1 inhibition when the OCH<sub>3</sub> group was substituted with an electron-giving substituent like CH<sub>3</sub> in **82** led to this conclusion (Hayat et al., 2019).

### 3.3 ADMET prediction of some selected derivatives

ADMET properties combine drug pharmacokinetic properties including absorption, distribution, metabolism and excretion, and drug pharmacodynamics properties including drug efficacy and toxicity. These properties help in optimization and facilitate the selection of drug candidates with the best safety and pharmacological profile while understanding the mechanisms behind their activity. They influence the bioavailability of drugs orally, absorption in the bio-membrane, and metabolism (Kalita et al., 2019).



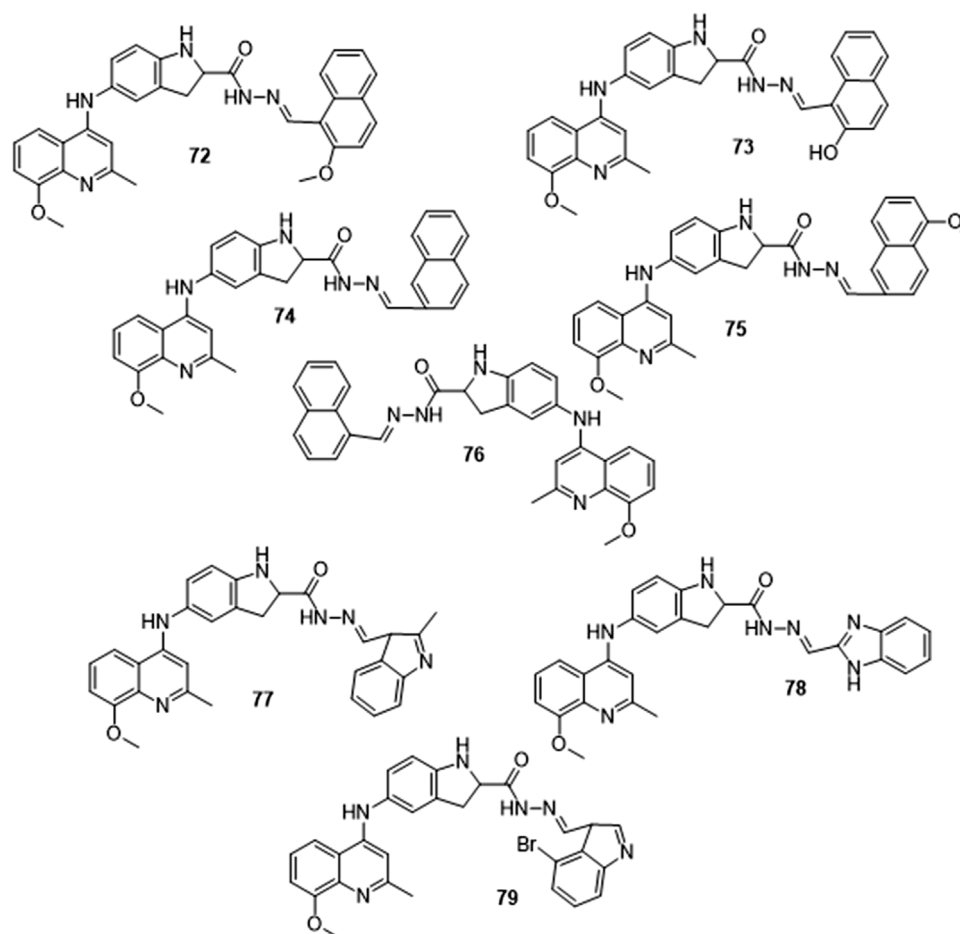


**FIGURE 16**  
Quinoline-Indole-Schiff base derivative.

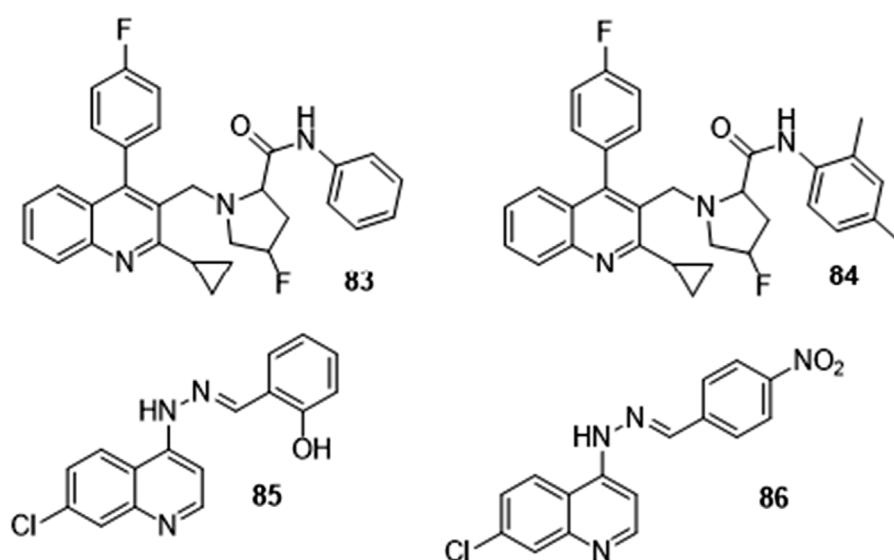


**FIGURE 17**  
Quinoline-fluoroproline amide and quinoline-imine hybrids with reported insilico ADMET.

Various quinoline derivatives (Figure 17) have been reported with their ADMET properties indicating their drug-likeness, some of which are stated below.

Ganesan et al. synthesized a series of quinoline-fluoroproline amide hybrids including **83** and **84** and predicted their ADMET parameter *insilico* and stated that the derivatives obeyed the Lipinski rule of five and exhibited low skin permeability. They were reported to inhibit P-Glycoprotein I and II with a very low volume of distribution, Central Nervous System (CNS), and Blood Brain Barrier (BBB) permeability. The hybrids were also reported to be CYP2D6, and CYP3A4 inhibitors and have no inhibitory activity against the CYP1A2, CYP2C9, and CYP2C19 enzymes of the cytochrome P450 which many drugs rely on for metabolism. Toxicity tests of anticipated chemicals proved that they were non-toxic and non-Mutagenic (Ganesan et al., 2020).

Kalita et al. carried out an *in silico* ADMET study on a series of quinoline-imine derivatives and reported that derivatives had excellent intestinal absorption and are soluble in water, they were non-inhibitors of cytochrome CYP2D6 and had mild to moderate BBB penetration (as they are intended for use in the treatment of cerebral malaria). They also differed in the level to which they bound with protein. Compounds **85** and **86** were reported to be the most potent of this series of derivatives (Kalita et al., 2019).

## 4 Conclusion and recommendation

Quinoline derivatives including their hybrids are important structural scaffolds in therapeutically effective molecules in medicinal chemistry research. Their pharmacological activities necessitate a review of its chemistry and biodiversity hence their biological applications including their excellent paths to bind to biomolecular targets have been examined in this study. This further confirms their usefulness as drug design precursors and for the development of novel therapeutic prospects. Identification of moieties that have the potential for improved activities when coupled with quinoline to form hybrids is

important. In synthesizing derivatives that are therapeutic candidates for the treatment of diverse infectious diseases. These hybrids can have better selectivity and dual mode of action in a bid to overcome drug resistance. They can then be characterized, validated, optimized, screened, and tested to confirm treatment efficacy. Once proven to be of use, the drug development process before clinical trials can begin.

## Author contributions

OE wrote and prepared the main text, OA and GO reviewed, improved the text and revised the draft, TO and EA proofread. All authors have approved the final version of this review.

## Funding

This work was supported by the Fogarty National Institutes of Health Common Fund (Grant No: U2RTW010679).

## Conflict of interest

The authors declare that the research was conducted in the absence of any commercial or financial relationships that could be construed as a potential conflict of interest.

## Publisher's note

All claims expressed in this article are solely those of the authors and do not necessarily represent those of their affiliated organizations, or those of the publisher, the editors and the reviewers. Any product that may be evaluated in this article, or claim that may be made by its manufacturer, is not guaranteed or endorsed by the publisher.

## References

- Abdelbaset, M. S., Abdel-Aziz, M., Abuo-Rahma, G. E. D. A., Abdelrahman, M. H., Ramadan, M., and Youssif, B. G. M. (2018). Novel quinoline derivatives carrying nitrones/oximes nitric oxide donors: Design, synthesis, antiproliferative and caspase-3 activation activities. *Arch. Pharm.* 352 (1), 1800270. doi:10.1002/ardp.201800270
- Ajani, O. O., Iyaye, K. T., Audu, O. Y., Olorunshola, S. J., Kuye, A. O., and Olanrewaju, I. O. (2018). Microwave assisted synthesis and antimicrobial potential of quinoline-based 4-hydrazide-hydrazone derivatives. *J. Heterocycl. Chem.* 55 (1), 302–312. doi:10.1002/jhet.3050
- Almandil, N. B., Taha, M., Rahim, F., Wadood, A., Imran, S., Alqahtani, M. A., et al. (2019). Synthesis of novel quinoline-based thiazole, evaluation of their antileishmanial potential and molecular docking studies. *Bioorg. Chem.* 85, 109–116. doi:10.1016/j.bioorg.2018.12.025
- Angajala, G., Aruna, V., and Subashini, R. (2020). An efficient nano-copper catalyzed base-free Knoevenagel condensation: A facile synthesis, molecular modelling simulations, SAR and hypoglycemic studies of new quinoline tethered acridine analogues as PPAR $\gamma$  agonists. *J. Mol. Struct.* 1220, 128601. doi:10.1016/j.molstruc.2020.128601
- Costa, C. A., Lopes, R. M., Ferraz, L. S., Esteves, G. N., Di Iorio, J. F., Souza, A. A., et al. (2020). Cytotoxicity of 4-substituted quinoline derivatives: Anticancer and antileishmanial potential. *Bioorg. Med. Chem.* 28 (11), 115511. doi:10.1016/j.bmc.2020.115511
- Desai, N. C., Kotadiya, G. M., Jadeja, K. A., Shah, K. N., Malani, A. H., Manga, V., et al. (2021). Synthesis, antitubercular, antimicrobial activities and molecular docking study of quinoline bearing dihydropyrimidines. *Bioorg. Chem.* 115, 105173. doi:10.1016/j.bioorg.2021.105173
- Diaconu, D., Amariucui-Mantu, D., Mangalagiu, V., Antoci, V., Zbancioc, G., and Mangalagiu, I. I. (2021). Ultrasound assisted synthesis of hybrid quinoline-imidazole derivatives: A green synthetic approach. *RSC Adv.* 11 (60), 38297–38301. doi:10.1039/D1RA07484A
- Douadi, K., Chafaa, S., Douadi, T., Al-Noaimi, M., and Kaabi, I. (2020). Azoimine quinoline derivatives: Synthesis, classical and electrochemical evaluation of antioxidant, anti-inflammatory, antimicrobial activities and the DNA/BSA binding. *J. Mol. Struct.* 1217, 128305. doi:10.1016/j.molstruc.2020.128305
- Eissa, S. I., Farrag, A. M., Abbas, S. Y., El Shehry, M. F., Ragab, A., Fayed, E. A., et al. (2021). Novel structural hybrids of quinoline and thiazole moieties: Synthesis and evaluation of antibacterial and antifungal activities with molecular modeling studies. *Bioorg. Chem.* 110, 104803. doi:10.1016/j.bioorg.2021.104803
- El-Gamal, K. M., El-Morsy, A. M., Saad, A. M., Eissa, I. H., and Alswah, M. (2018). Synthesis, docking, QSAR, ADMET and antimicrobial evaluation of new quinoline-3-carbonitrile derivatives as potential DNA-gyrase inhibitors. *J. Mol. Struct.* 1166, 15–33. doi:10.1016/j.molstruc.2018.04.010
- Ganesan, M. S., Raja, K. K., Murugesan, S., Kumar, B. K., Rajagopal, G., and Thirunavukkarasu, S. (2020). Synthesis, biological evaluation, molecular docking, molecular dynamics and DFT studies of quinoline-fluoroproline amide hybrids. *J. Mol. Struct.* 1217, 128360. doi:10.1016/j.molstruc.2020.128360
- Ghanim, A. M., Girgis, A. S., Kariuki, B. M., Samir, N., Said, M. F., Abdelnaser, A., et al. (2022). Design and synthesis of ibuprofen-quinoline conjugates as potential anti-inflammatory and analgesic drug candidates. *Bioorg. Chem.* 119, 105557. doi:10.1016/j.bioorg.2021.105557
- Hayat, K., Afzal, S., Saeed, A., Murtaza, A., Ur Rahman, S., Khan, K. M., et al. (2019). Investigation of new quinoline derivatives as promising inhibitors of NTPDases: Synthesis, SAR analysis and molecular docking studies. *Bioorg. Chem.* 87, 218–226. doi:10.1016/j.bioorg.2019.03.019
- Hossain, M. (2018). A review on heterocyclic: Synthesis and their application in medicinal chemistry of imidazole moiety. *Sci. J. Chem.* 6 (5), 83. doi:10.11648/j.sjc.20180605.12

- Kalita, J., Chetia, D., and Rudrapal, M. (2019). Design, synthesis, antimalarial activity and docking study of 7-chloro-4- (2-(substituted benzylidene)hydrazineyl)quinolines. *J. Med. Chem. Drug Des.* 2 (1), 928–937. doi:10.2174/1573406415666190806154722
- Li, B., Yao, J., He, F., Liu, J., Lin, Z., Liu, S., et al. (2021). Synthesis, SAR study, and bioactivity evaluation of a series of Quinoline-Indole-Schiff base derivatives: Compound 10E as a new Nur77 exporter and autophagic death inducer. *Bioorg. Chem.* 113, 105008. doi:10.1016/j.bioorg.2021.105008
- Li, S., Hu, L., Li, J., Zhu, J., Zeng, F., Huang, Q., et al. (2019). Design, synthesis, Structure-Activity Relationships and mechanism of action of new quinoline derivatives as potential antitumor agents. *Eur. J. Med. Chem.* 162, 666–678. doi:10.1016/j.ejmech.2018.11.048
- Li, X.-Y., Liu, Y., Chen, X. L., Lu, X. Y., Liang, X. X., Zhu, S. S., et al. (2020). 6 $\pi$ -Electrocyclization in water: Microwave-assisted synthesis of polyheterocyclic-fused quinoline-2-thiones. *Green Chem.* 22 (14), 4445–4449. doi:10.1039/C9GC04445K
- Mahgoub, S. (2018). Synthesis, characterization and antimicrobial activity of some novel quinoline derivatives bearing pyrazole and pyridine moieties. *Egypt. J. Chem.* 61, 0. doi:10.21608/ejchem.2018.3941.1345
- Medeiros, G. A., Correa, J. R., de Andrade, L. P., Lopes, T. O., de Oliveira, H. C., Diniz, A. B., et al. (2021). A benzothiadiazole-quinoline hybrid sensor for specific bioimaging and surgery procedures in mice. *Sensors Actuators B Chem.* 328, 128998. doi:10.1016/j.snb.2020.128998
- Muálem de Moraes Alves, M., Arcanjo, D. D. R., Carvalho, R. C. V. d., Amorim, L. V., Santos, I. L. d., Santos, R. R. L., et al. (2021). Methods of macrophages activation and their modulation for the prospection of new antileishmania drugs: A review. *Biosci. J.* 37, e37077. doi:10.14393/Bj-v37n0a2021-53770
- Nainwal, L. M., Tasneem, S., Akhtar, W., Verma, G., Khan, M. F., Parvez, S., et al. (2019). Green recipes to quinoline: A review. *Eur. J. Med. Chem.* 164, 121–170. doi:10.1016/j.ejmech.2018.11.026
- Nikookar, H., Mohammadi-Khanaposhtani, M., Imanparast, S., Faramarzi, M. A., Ranjbar, P. R., Mahdavi, M., et al. (2018). Design, synthesis and *in vitro*  $\alpha$ -glucosidase inhibition of novel dihydropyrano[3, 2-c]quinoline derivatives as potential anti-diabetic agents. *Bioorg. Chem.* 77, 280–286. doi:10.1016/j.bioorg.2018.01.025
- Porter, A. G., and Jänicke, R. U. (1999). Emerging roles of caspase-3 in apoptosis. *Cell Death Differ.* 6 (2), 99–104. doi:10.1038/sj.cdd.4400476
- Ramprasad, J., Kumar Sthalam, V., Linga Murthy Thampunuri, R., Bhukya, S., Ummanni, R., Balasubramanian, S., et al. (2019). Synthesis and evaluation of a novel quinoline-triazole analogs for antitubercular properties via molecular hybridization approach. *Bioorg. Med. Chem. Lett.* 29 (20), 126671. doi:10.1016/j.bmcl.2019.126671
- Rani, A., Sharma, A., Legac, J., Rosenthal, P. J., Singh, P., and Kumar, V. (2021). A trio of quinoline-isoniazid-phthalimide with promising antiplasmodial potential: Synthesis, *in-vitro* evaluation and heme-polymerization inhibition studies. *Bioorg. Med. Chem.* 39, 116159. doi:10.1016/j.bmc.2021.116159
- Roy, D., Anas, M., Manhas, A., Saha, S., Kumar, N., and Panda, G. (2022). Synthesis, biological evaluation, Structure-Activity Relationship studies of quinoline-imidazole derivatives as potent antimalarial agents. *Bioorg. Chem.* 121, 105671. doi:10.1016/j.bioorg.2022.105671
- Shruthi, T. G., Subramanian, S., and Eswaran, S. (2020). Design, synthesis and study of antibacterial and antitubercular activity of quinoline hydrazone hybrids. *Heterocycl. Commun.* 26 (1), 137–147. doi:10.1515/hc-2020-0109
- Taha, M., Sultan, S., Imran, S., Rahim, F., Zaman, K., Wadood, A., et al. (2019). Synthesis of quinoline derivatives as diabetic II inhibitors and molecular docking studies. *Bioorg. Med. Chem.* 27 (18), 4081–4088. doi:10.1016/j.bmc.2019.07.035
- Taheri, S., Nazifi, M., Mansourian, M., Hosseinzadeh, L., and Shokoohinia, Y. (2019). Ugi efficient synthesis, biological evaluation and molecular docking of coumarin-quinoline hybrids as apoptotic agents through mitochondria-related pathways. *Bioorg. Chem.* 91, 103147. doi:10.1016/j.bioorg.2019.103147
- Teja, C., and Khan, F. R. N. (2020). Radical transformations towards the synthesis of quinoline: A review. *Chem. – Asian J.* 15 (24), 4153–4167. doi:10.1002/asia.202001156
- Upadhyay, A., Kushwaha, P., Gupta, S., Dodda, R. P., Ramalingam, K., Kant, R., et al. (2018). Synthesis and evaluation of novel triazolyl quinoline derivatives as potential antileishmanial agents. *Eur. J. Med. Chem.* 154, 172–181. doi:10.1016/j.ejmech.2018.05.014
- Van de Walle, T., Boone, M., Van Puyvelde, J., Combrinck, J., Smith, P. J., Chibale, K., et al. (2020). Synthesis and biological evaluation of novel quinoline-piperidine scaffolds as antiparasitoid agents. *Eur. J. Med. Chem.* 198, 112330. doi:10.1016/j.ejmech.2020.112330
- Yadav, P., and Shah, K. (2021). Quinolines, a perpetual, multipurpose scaffold in medicinal chemistry. *Bioorg. Chem.* 109, 104639. doi:10.1016/j.bioorg.2021.104639
- Zeke, D., Eswaramoorthy, R., Belay, Z., and Melaku, Y. (2020). Synthesis and antibacterial, antioxidant, and molecular docking analysis of some novel quinoline derivatives. *J. Chem.* 2020, 1–16. doi:10.1155/2020/1324096



## OPEN ACCESS

## EDITED BY

Tingchao He,  
Shenzhen University, China

## REVIEWED BY

Hongbin Yang,  
China University of Petroleum, Huadong,  
China  
Ajaya Bhattarai,  
Tribhuvan University, Nepal

## \*CORRESPONDENCE

Guang Zhao,  
✉ zhaoguang@upc.edu.cn  
Caili Dai,  
✉ daicl@upc.edu.cn

## SPECIALTY SECTION

This article was submitted to  
Polymer Chemistry,  
a section of the journal  
Frontiers in Chemistry

RECEIVED 11 October 2022

ACCEPTED 02 January 2023

PUBLISHED 12 January 2023

## CITATION

Lu S, Bo Q, Zhao G, Shaikh A and Dai C  
(2023), Recent advances in enhanced  
polymer gels for profile control and water  
shutoff: A review.  
*Front. Chem.* 11:1067094.  
doi: 10.3389/fchem.2023.1067094

## COPYRIGHT

© 2023 Lu, Bo, Zhao, Shaikh and Dai. This is  
an open-access article distributed under  
the terms of the [Creative Commons  
Attribution License \(CC BY\)](#). The use,  
distribution or reproduction in other  
forums is permitted, provided the original  
author(s) and the copyright owner(s) are  
credited and that the original publication in  
this journal is cited, in accordance with  
accepted academic practice. No use,  
distribution or reproduction is permitted  
which does not comply with these terms.

# Recent advances in enhanced polymer gels for profile control and water shutoff: A review

Siyu Lu<sup>1</sup>, Qiwei Bo<sup>2</sup>, Guang Zhao<sup>1\*</sup>, Azizullah Shaikh<sup>3</sup> and Caili Dai<sup>1\*</sup>

<sup>1</sup>School of Petroleum Engineering, China University of Petroleum (East China), Qingdao, Shandong, China,

<sup>2</sup>Sinopec International Petroleum Exploration and Production Corporation, Beijing, China, <sup>3</sup>Balochistan University of Information Technology, Engineering and Management Sciences Quetta, Balochistan, Pakistan

Polymer gels have been effectively employed as a water management material for profile control and water shutoff treatments in low-middle temperature and low-middle salinity reservoirs. However, most polymer gel systems have limitations under high temperature and salinity reservoir conditions, such as short gelation time, poor strength, and long-term instability. Therefore, several researchers have developed enhanced polymer gels to satisfy the water control requirements in high temperature and salinity reservoirs. This work reviews the five main types of enhanced polymer gels that have been developed so far: nano silica-enhanced gel systems, cellulose-enhanced gel systems, graphite-enhanced gel systems, oily sludge-enhanced gel systems, and foam-enhanced polymer gel systems. Further, this article investigates the fundamental properties, strengthening and crosslinking mechanisms, reservoir application conditions, and field applications of several enhanced polymer systems. In this paper, it is found that the addition of strengthening materials can increase the bound water content in the gel network and significantly improve the temperature and salt resistance of polymer gel, so as to cope with the application of profile control and water plugging in high temperature and high salt reservoirs. Moreover, it also offers references and future research directions for enhanced polymer gel systems.

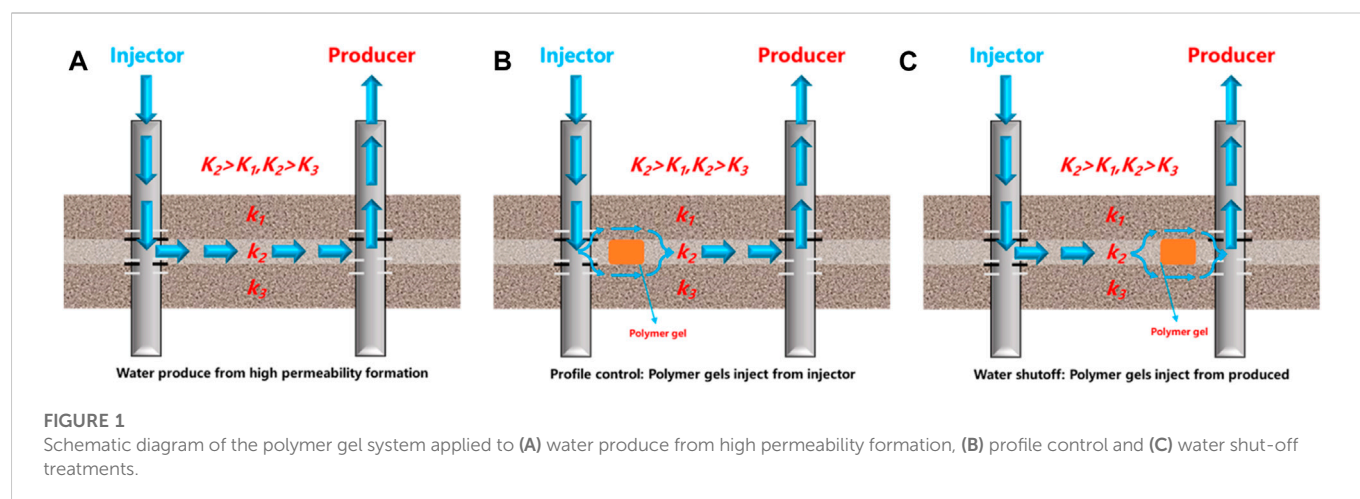
## KEYWORDS

enhanced polymer gels, crosslinking mechanism, enhanced mechanism, profile control, water shutoff

## 1 Introduction

Presently, oilfields have developed various profile control and water shutoff techniques to address issues including excessive water production and serious reservoir heterogeneity (Majid et al., 2018). Polymer gel systems have become the most popular and promising water management material (Sydansk and Seright, 2007), due to the benefits of controllable gelation time, gel strength, and low cost, as shown in Figure 1. When the gelation solution is injected into the reservoir formation, the solution is converted to highly viscoelastic polymer gel. Thus the polymer gel systems can plug the high permeability layers, reduce the heterogeneity of the reservoir, and increase the sweep coefficient (Cheraghian and Hendraningrat, 2016). Thus, the residual oil can be easily driven out after water injection into the low and middle permeability layers. Generally, the conventional gel systems based on phenolic resin or chromium crosslinkers have been successfully applied to the reservoirs with temperatures ( $\leq 80^{\circ}\text{C}$ ) and salinities ( $\leq 50,000\text{ mg/L}$ ) (Al-Muntasheri et al., 2010). The increasing application of high temperature and salinity reservoirs has emerged as a new hotspot with the continued development of conventional reservoirs (Ziegler, 2017). Yet, even after extensive water flooding, the high temperature and salinity reservoirs still face high produced water-cut. In these reservoirs, the profile control and water shutoff treatments are





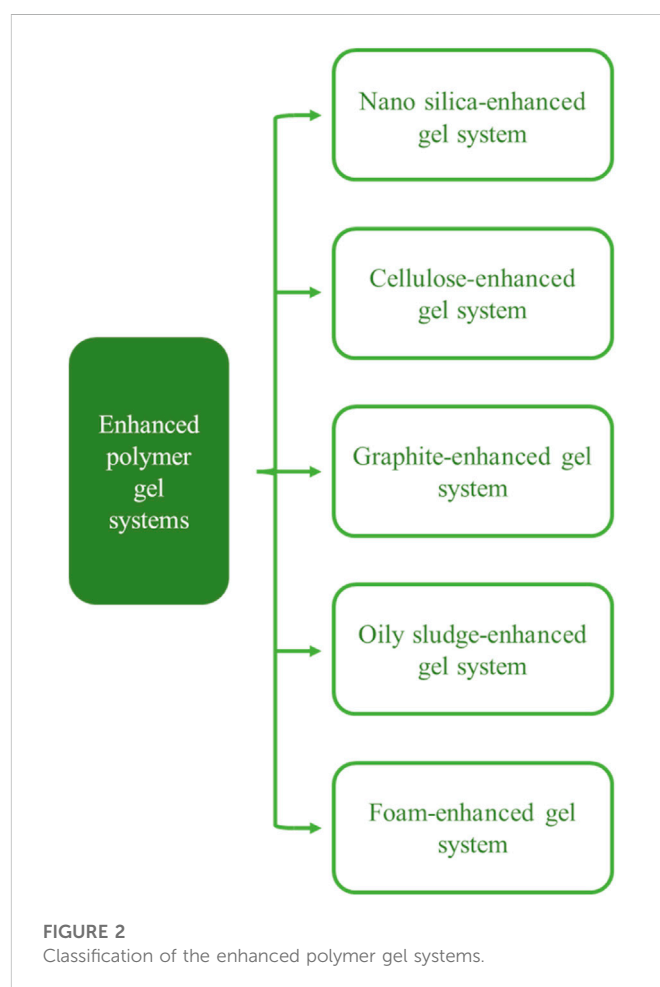
urgently being carried out (Zhao et al., 2006). However, conventional polymer gel systems have drawbacks of short gelation time, low strength, and long-term instability under high temperature and salinity reservoir conditions, leading to degraded gel systems, failure profile control, and water shutoff treatments (Bryant et al., 1997; Zhu et al., 2017).

Previous studies have compiled three reasons that make polymers unsuitable for application in high temperature and salinity reservoirs (Abdulbaki et al., 2014; Bai et al., 2015). Higher temperatures result in more rapid thermal motion of the molecules, which accelerates collisions between polymer and crosslinking agent molecules. This leads to the anomaly that the gelation time of the polymer gel systems is faster. However, the reduced gel formation time results in the polymer gel's inability to penetrate the deep formation and a limited ability for water control. When the temperature rises, the chemical bonds between the polymer monomers are readily disrupted, resulting in polymer cracking. This makes the polymer gels weak and unable to plug the high permeability zones.

Prior studies have made excellent achievements in improving the temperature and salinity resistance of polymers and crosslinking agents in order to address the application issues of polymer gels in high temperature and salinity reservoirs in recent years. Additionally, to improve the temperature and salinity resistance of the polymer gels, some researchers have proposed adding some improved particles into the gel-forming fluid, such as nano-silica, cellulose, graphite, oily sludge, and foam; as shown in Figure 2. However, to the best of our knowledge, few papers have reviewed polymer-enhanced gel systems for water treatment in high-temperature and high-salt reservoirs, although more and more studies are being carried out. This study will evaluate an enhanced polymer gel system from the perspectives of chemistry and petroleum engineering in order to provide direction and discuss the potential for future applications in high temperature and salinity reservoirs.

## 2 Nano silica-enhanced gel system

Because of the gradual complexity of the reservoir conditions, conventional polymer gels like polyacrylamide (PAM) polymer gel systems and xanthan gum quickly break down or precipitate (Samuelson and Constien, 1996) when the reservoir temperature is more than 80°C and the salinity is more than 50,000 mg/L



(Caulfield et al., 2002; Zhao et al., 2013). Moreover, the gelation time is shortened due to the limited crosslinking ability of the inorganic crosslinking agent, resulting in the instability of the gel system to migrate in the formation's depth. Subsequently, nano silica particles are prepared and added to form nano silica-enhanced gel systems to increase strength and long-term stability, as shown in Table 1.

Zareie et al. (2019) prepared an enhanced gel system by partially hydrolyzed polyacrylamide (HPAM), chromium acetate crosslinking

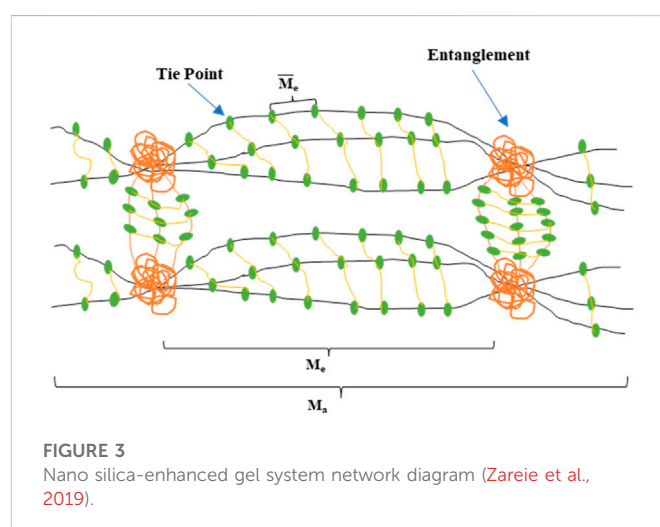
TABLE 1 Progress of nano silica-enhanced gel systems.

Nano silica-enhanced gel system				
Gelant formulation	Gelation temperature	Gelation time	Gel strength	References
Partially hydrolyzing polyacrylamide, Chromium acetate, Nano-silica	90°C	Not given	H-grade	Zareie et al. (2019)
Polyacrylamide, polyethyleneimine, Thiourea, Nano-silica	105°C	14 h	I-grade	Suleymanov and Shovgenov, (2021)
Partially hydrolyzing polyacrylamide, Chromium acetate, Nano-silica	Not given	9 h	H-grade	Fadil et al. (2020)
Nano-silica, Inorganic chloride	80°C	18 h	Not given	Huang et al. (2017)
Polyacrylamide, hydroquinone, hexamethylenetetramine, Nano-silica	Not given	16 h	Not given	Liu et al. (2017)

agent, and nano-silica particles. The gel strength reaches H-grade at 90°C with an elastic modulus of more than 26,000 Pa when 9% of nano-silica is added to the gelation solution. The gelation solution of this enhanced gel system has the characteristic of low viscosity at the initial gelation stage, which enables entering the in-depth formation. Also, the gel system could maintain a nano-silica network and its original characteristics without breaking when a strain of 100%–300% was applied, which justifies the high shearing stability of the fluid system.

Moreover, the expansion rate of the system in distilled water can be increased rapidly within the first 30 min (Cassagnau, 2013). The gelation time increases due to the cage-like structure of nano-silica particles. These characteristics may bring good profile control and water shut-off effects. However, the study also found that the gelation time decreased when the concentration of nano silica was added to the gel by more than 12%. The reasons may be due to excessive crosslinking or agglomeration synergism of nano-silica in the gelation solution. The network structure and nano-silica particles act as a physical crosslinking agent and minimize the molecular weight between the two nodes in the network structure when compared to conventional HPAM gel systems. The molecular weight of this nano silica-enhanced gel system decreased from 726 g/mol to 257 g/mol, and the number of nodes increased by 55%, as shown in Figure 3. Accordingly, the nano silica-enhanced gel system significantly improves the temperature and salinity resistance.

Suleymanov and Shovgenov (2021) prepared an enhanced polymer gel system using PAM, polyethyleneimine (PEI), thiourea, and nano-silica at 211,688 mg/L salinity, as shown in Figure 4. When the nano-silica particles with an average particle size of 152.1 nm were added to the gelation solution, the gelation time and the gel strength at 105°C were 14 h, and I-grade, respectively. Generally, the lower bound water content and the easier dehydration of the gel system in high temperature and salinity reservoir conditions result in gel instability. The bound water content of the gel system increased by 19.532% after adding nano-silica particles. In addition, the system's relative response factor (RRF) is still high after 30 days at 105°C through his research. As a result, the stability of enhanced gel systems brings a stronger plugging capability in porous media of formation. His paper summarizes the strengthening mechanisms of silica particles for two reasons. First, the hydrophilic nano-silica can act as a



crosslinking agent, which generates silanol groups and increases the crosslink chance and density in the enhanced gel system. Second, the generated silanol groups interacting with the polymer free radicals through hydrogen bonds can significantly reduce the dehydration of the polymer gel system.

The studies also found that the system's performance is degraded when the concentration of nano-silica particles exceeds 1%. The reason may be that the gel system's strength is weakened by the over-crosslinking or self-aggregation of nano-silica particles. The concentration of nano-silica particles has a great influence on the stability of the gel. Therefore, while utilizing the nano-silica enhanced gel for profile control or water shutoff treatments, the concentration of nano-silica particles must be set at an appropriate value.

Liu et al. (2017) prepared an enhanced polymer gel system with polyacrylamide (PAM), hydroquinone (HQ), hexamethylenetetramine (HMTA), and nano-silica at high temperature and salinity conditions. The study found that adding nano-silica can significantly shorten the gelation time and improve the gel strength, elasticity, and viscosity of the enhanced gel system. Compared with the gel system without nano-silica, the maximum temperature tolerance of the enhanced gel system increased from 137.8°C to 155.5°C. When

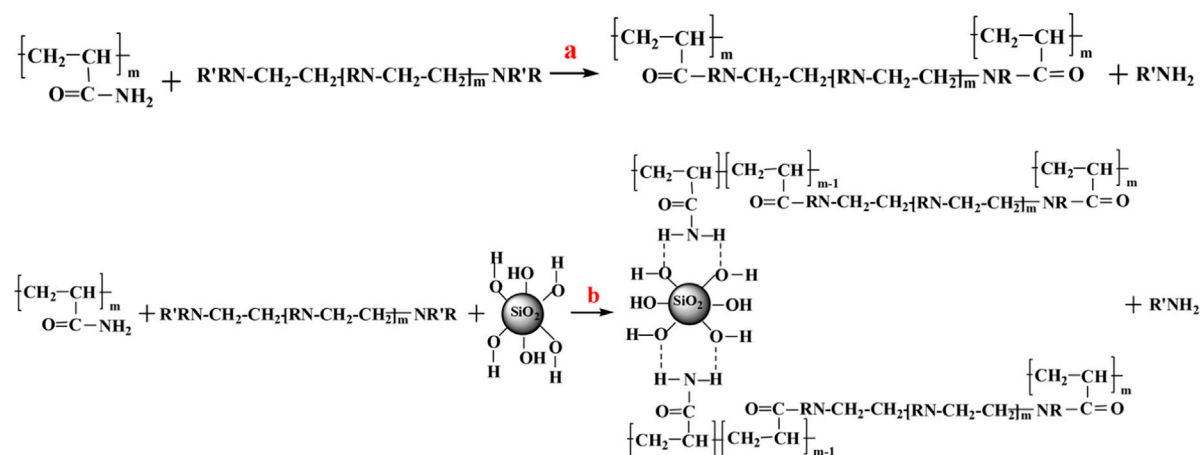


FIGURE 4

Schematic diagram of the enhanced gel system synthesis (Cassagnau, 2013).

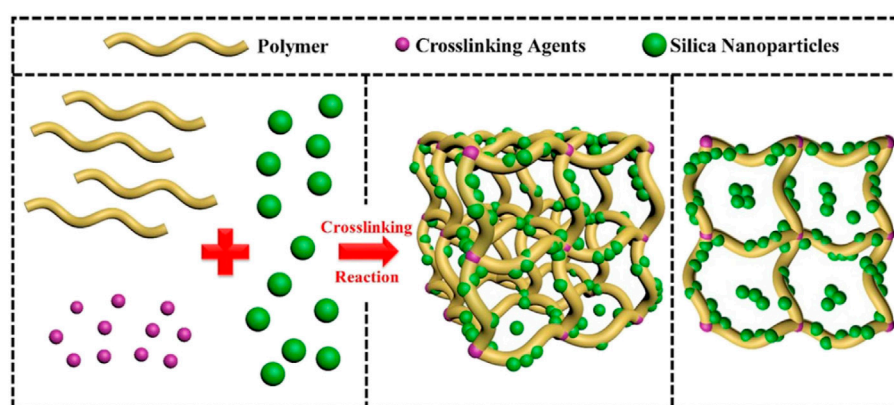


FIGURE 5

Strengthening mechanism of nano-silica particles to gel strength (Liu et al., 2017).

the nano-silica was added, the concentration of bound water in this nano silica-enhanced gel system increased from 22.5% to 39.9%. The nano silica-enhanced gel system forms a uniformly distributed three-dimensional network structure. The nano-silica significantly improves the network structure of this gel system to enhance the gel strength. Accordingly, the aggregation and arrangement of nano-silica particles can also be found in the polymer, chain bundles, and the network structure of the gel structure, as shown in Figure 5. In addition, the bound water content was significantly increased after adding nano-silica, which was beneficial to the hydrophilicity and thermal stability of the polymer gel.

Environmental scanning electron microscopy (ESEM) analysis revealed that the three-dimensional network structure was uniformly distributed throughout the gel system, as shown in Figure 6. The aggregation and arrangement of nano-silica particles can be found in gel's polymer chain bundle and network structure. It helps to stabilize the gel system in high temperature and salinity reservoir conditions.

Fadil et al. (2020) used partially hydrolyzed polyacrylamide (HPAM), chromium acetate, and nano-silica particles to make an HPAM/Cr<sup>3+</sup> nano silica-enhanced gel system. The study found that the gelation time was shortened with the increased concentration of nano-silica particles. When the concentration of the nano-silica was .3%, the gelation time and gel strength were respectively 9 h and H-grade, but the gel strength decreased from H-grade to G-grade after 25 h. However, the gelation time is shortened with the increase in nano-silica concentration. The short gelation time may not be conducive to transport in the formation's porous media. The study found that the addition of nano-silica particles particularly increased the gel system's strength and reduced its loss of strength. The reason may be that the presence of nano-silica particles in the polymer gel system promoted the crystal structure of the matrix so that the nano silica-enhanced gel system had good rigidity. Usually, the instability of the gel system is often related to its own thickening phenomenon (Pham and Hatzignatiou, 2016). Moreover, adding nano-silica particles to the gel system bring a

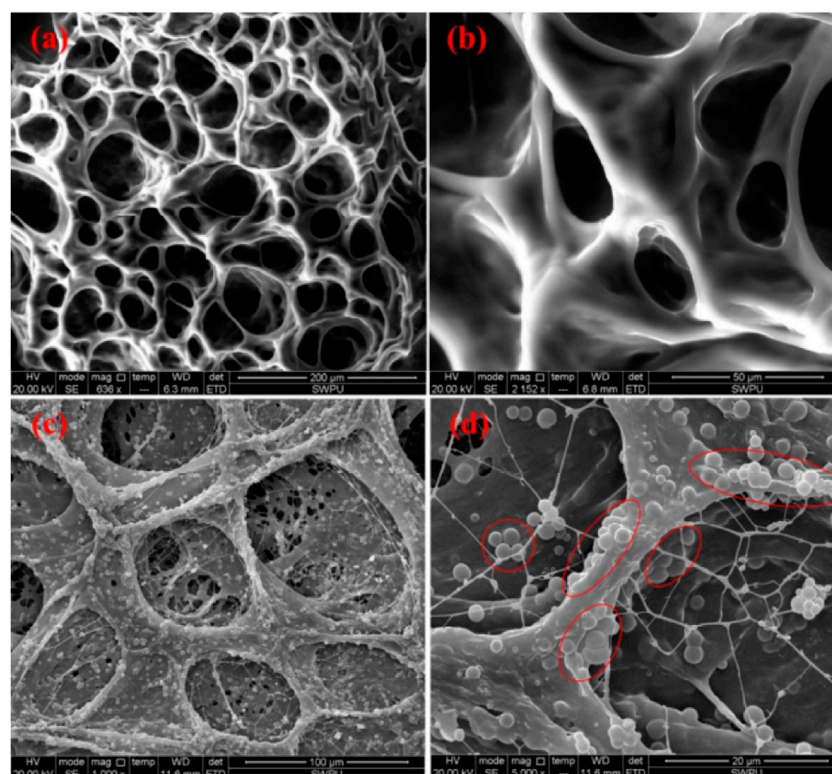


**FIGURE 6**  
ESEM micrographs of gel samples prepared with different concentrations of nano-silica particles. (A), (B) Without nano-silica particles. (C), (D) .2 wt% (Liu et al., 2017).

denser gel network structure with a higher thickening effect, reducing free water and increasing bound water in the enhanced gel system, which also results in the enhancement of the stability.

Huang et al. (2017) constructed a nano silica-enhanced gel system at 150°C using nano-silica (particles ranging in size from 3 to 17 nm) and initiators. In this type of gel system, the higher concentration with the smaller nano-silica particles usually brings a faster-crosslinking speed. The study found that colloidal nanoparticles can remain stable in an alkaline solution, and the stability of the polymer gel system decreases with increasing temperature. The gelation time reached 18 h at 80°C, but the gelation time was affected by pH conditions. The lower the pH is, the shorter the gelation time. When the pH value was less than 7, the nano silica-enhanced gel system was unstable and easily aggregated. So, the gel solution must be prepared at an appropriate pH level when using this gel system for profile control and water shutoff treatments.

### 3 Cellulose-enhanced gel system

As a natural and renewable polymer material, cellulose has been widely used to prepare polymer gel systems (Chang et al., 2010). Also, some modified celluloses have high salinity and temperature resistance advantages (Dai et al., 2014). These materials provide the potential for preparing high temperature and salinity resistance gel systems. Compared with natural cellulose, cellulose nano-crystals (CNCs) are one-dimensional nano-materials (diameter 2–20 nm, length

50–300 nm), which not only have the renewable nature of natural cellulose but also have unique high crystallization (Hu et al., 2015), high surface ratio, low density, and excellent mechanical properties (Maiti et al., 2013). Different from conventional polymer materials, CNCs can be used as matrix enhancement to strengthen the crosslinking structure and can also be used as an interfacial adsorbent to improve the stability of the dispersion system. Therefore, adding CNCs can improve conventional polymer gel systems' thermal stability and salinity resistance. Presently, many researchers have introduced CNCs into polymer gel systems to improve further thermal stability, salinity resistance, and mechanical strength (Goetz et al., 2009; Sampath et al., 2017). Adewole and Muritala (2019) previously summarized the application of several natural polymers in oilfields. From the application aspect of petroleum engineering in the future, this section highlights the fundamental performance, strengthening mechanism, and microstructure of cellulose-enhanced gel systems, as shown in Table 2.

Zhang et al. (2016) prepared a cellulose-enhanced gel system using ultrafine cellulose, acrylamide graft copolymer, cationic polyacrylamide (C-PAM), phenolic resin crosslinker, and ammonium chloride. The viscosity of the cellulose-enhanced gel system can be up to 35,000 mPa s when gelled at 80°C and 100,000 mg/L. This gel system also has a good shear resistance. For example, the viscosity of this gelation solution holds over 60% of the initial viscosity when continuous shearing at 100 s<sup>-1</sup>. After gelation, the viscosity of the cellulose-enhanced gel system still remains at more



TABLE 2 Progress of cellulose-enhanced gel systems.

Cellulose-enhanced gel systems				
Gelant formulation	Gelation temperature	Gelation time	Gel strength	References
C-PAM, phenolic resin crosslinker PF, ammonium chloride	80°C	Not given	Not given	Zhang et al. (2016)
TCNF, citric acid	Not given	Not given	Not given	Petroudy et al. (2018)

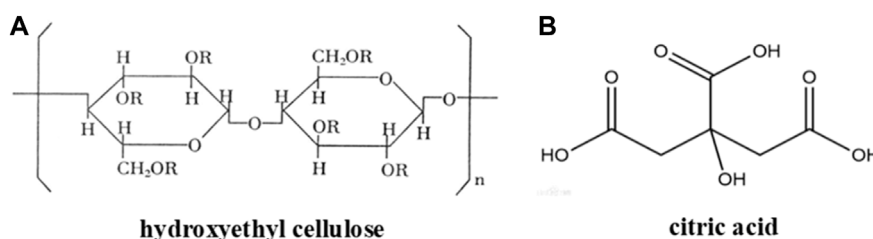


FIGURE 7

Chemical structures of (A) hydroxyethyl cellulose and (B) citric acid.

than 80%. The high shear resistance of this gel system could keep a strong plugging capacity when transporting in porous media.

Petroudy et al. (2018) prepared a high water-absorption cellulose-enhanced gel system using sodium carboxymethyl cellulose and hydroxyethyl cellulose, also as well as tempo-oxidized cellulose nanofibers (TCNFs) and citric acid as crosslinking agents; as shown in Figure 7. The research showed that the gel system had a high swelling time, up to 200 g/g. The gel system had biodegradation and non-toxicity characteristics, while the ion sensitivity of the system decreased with increasing TCNF content. The strengthening mechanism is mainly based on multifunctional carboxylic acid that can react with cellulose. The multifunctional carboxylic acid is linked to the esterification reaction with the cellulose hydroxyl group, which further reacts with another cellulose hydroxyl group through the esterification reaction so that the cellulose plays a role in crosslinking (Zhou et al., 2013). Finally, this reaction resulted in the formation of a stable cellulose-enhanced gel system.

## 4 Graphite-enhanced gel system

Graphite particles have excellent characteristics, such as high-temperature tolerance, softness, self-lubrication, thermal stability, and

easy modification (Du et al., 2018). These characteristics make it possible to prepare a graphite-enhanced gel system (Asghar et al., 2014). The high-temperature tolerance and high-salinity resistance were obviously improved when the graphite particles were embedded on the polymer branches or involved in the crosslinking reaction in the gel system (Yakovlev et al., 2006; Sengupta et al., 2011). In this paper, several of the basic properties of graphite-enhanced gel systems are summarized from the perspective of petroleum engineering, such as crosslinking mechanism, strengthening mechanism, and microscopic morphology, as shown in Table 3.

PAM-CG or PAM-GO graphite-enhanced gel systems were created by Michael et al. (2020) using polyacrylamide (PAM), hydroquinone (HQ), hexamethylenetetramine (HMTA), and graphite or graphite oxide (GO). The chemical structures of hydroquinone (HQ) and hexamethylenetetramine (HMTA) are shown in Figure 8. When .01% of CG particles are added, the elastic modulus and viscous modulus of the PAM-CG gel system reach 2,290 Pa and 415 Pa. Whereas, when .01% of GO particles are added, the elastic modulus and viscous modulus of the PAM-GO gel system reached 925 Pa and 158 Pa, respectively. The PAM-CG gel system has a stronger elastic and viscous modulus than the PAM-GO gel system. It may be related to the gel system's various crosslinking modalities or crosslinking densities of graphene particles. Both these

TABLE 3 Progress of graphite-enhanced gel systems.

Graphite-enhanced gel systems				
Gelant formulation	Gelation temperature	Gelation time	Gel strength	References
Polyacrylamide, hydroquinone, hexamethylenetetramine, graphene	150°C	Not given	Not given	Michael et al. (2020)
Polyacrylamide, hydroquinone, hexamethylenetetramine, graphene oxide	150°C	Not given	Not given	Michael et al. (2020)
NH-1, crosslinking agent I, crosslinking agent II, Graphite, CMC	160°C	Not given	Not given	Wang et al. (2020)
Polyacrylamide, nano-graphite, modified phenolic resin	130°C	Not given	Not given	Lv et al. (2020)

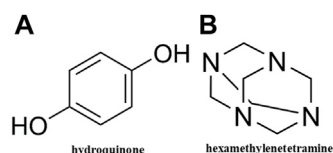


**FIGURE 8**  
Chemical structures of (A) hydroquinone and (B) hexamethylenetetramine.

gel systems have excellent elasticity, and their water absorption capacity reached 27% and 25%. Furthermore, the degradation enthalpies of both gel systems reached 2153 J/g and 1350 J/g, respectively. This indicates that under high temperature and salinity reservoir conditions, both gel systems are long-term stable. The sand-pack flowing experiment showed that when both gel systems were formed in the porous media, the plugging rate could be above 80%. The study has proven that both graphite-enhanced gel systems had the advantages of good thermomechanical, water expansion, and self-healing properties.

The scanning electron microscope (SEM) micrograph images demonstrate that both gel systems contain porous features, as shown in Figure 9. It can be observed that the PAM-CG gel system has a two-dimensional sheet-like structure with tiny hexagonal pores as a result of the presence of CG particles. However, the hexagonal pores were not observed in the microstructure of the PAM-GO gel system, which may be related to the hydrophilicity of GO particles.

Wang et al. (2020) prepared a graphite-enhanced gel system with polymer NH-1, crosslinking agents I and II, graphite particles, and suspension concentrate carboxymethyl cellulose (CMC); however, the precise crosslinker formula was not provided. The viscosity of the graphite-enhanced gel system reached 430,000 mPa s at 200°C. The graphite-enhanced gel system can be applied to reservoirs with temperatures from 160°C to 280°C and mineralization degrees from 8,000 mg/L to 10,000 mg/L. So, this gel system has great application potential for steam channel control in a heavy oil reservoir.

Lv et al. (2020) prepared a high temperature and salinity resistant graphite-enhanced gel system with polyacrylamide (PAM), modified phenolic resin, and modified nano-graphite. This gel system can be crosslinked and have long-term stability under 130°C and 200,000 mg/

L. This graphite-enhanced gel system performs well in terms of shear resistance and injection. Also, it has strong erosion resistance and plugging ability in different permeability formations. Additionally, the graphite-enhanced gel technology may avoid dehydration since it has more hydrophilicity than the conventional polymer system. The gelation mechanism is due to the crosslinking reaction between hydroxymethyl in phenolic resin and amide groups, forming a three-dimensional network gel; the crosslinking mechanism is shown in Figure 10.

The modified nano-graphite can improve the stability of the grid structure in the enhanced gel system and improve its water locking ability. The addition of modified nano graphite mainly strengthened the elastic modulus of the enhanced system, and the viscoelasticity of the enhanced gel system is more stable at high temperature. Compared with conventional PAM gel, the degradation rate of polymer in enhanced gel system is slower, the mass ratio of bound water is higher, and the gel is more hydrophilic. The modified nano-graphite mainly enhances the temperature resistance, salt resistance and shear resistance of the enhanced polymer through the characteristics of the inorganic particles, thereby significantly improving the stability of the enhanced gel system.

The SEM micrograph images of the PAM polymer gel system and nano-graphite enhanced gel system are shown in Figure 11. It can be observed that the enhanced gel system has a three-dimensional network structure of porous media with high crosslink density and close arrangement. In contrast, the network structures of the PAM gel system are relatively loose and have small pores. The special network structures of the enhanced gel system may bring high thermal stability under high temperature and salinity reservoir conditions.

## 5 Oily sludge-enhanced gel system

Oily sludge is a solid waste produced in an oilfield development process and crude oil transportation and storage (Hu et al., 2013). If not managed appropriately, oily sludge will seriously impact the environment and human health (Caili et al., 2010). The use of oily sludge as a strengthening agent in gel systems has been studied with the development of profile control and water shutoff technologies, as shown in Table 4. Changqing Oilfield (Chen et al., 2019) produced an oily sludge-enhanced gel system using oily sludge, secondary alkyl sodium sulfonate (SAS-

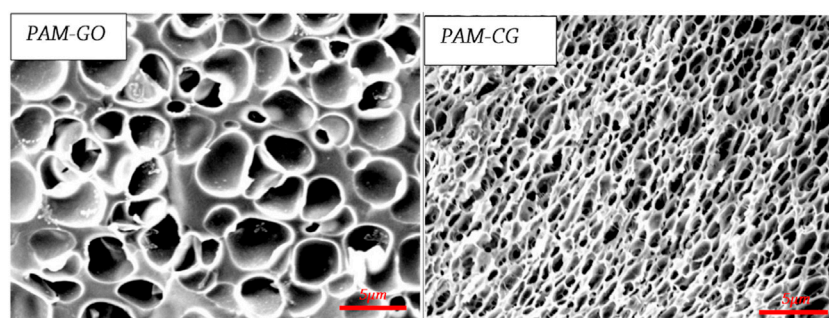


**FIGURE 9**  
SEM images of PAM-CG and PAM-GO (Michael et al., 2020).

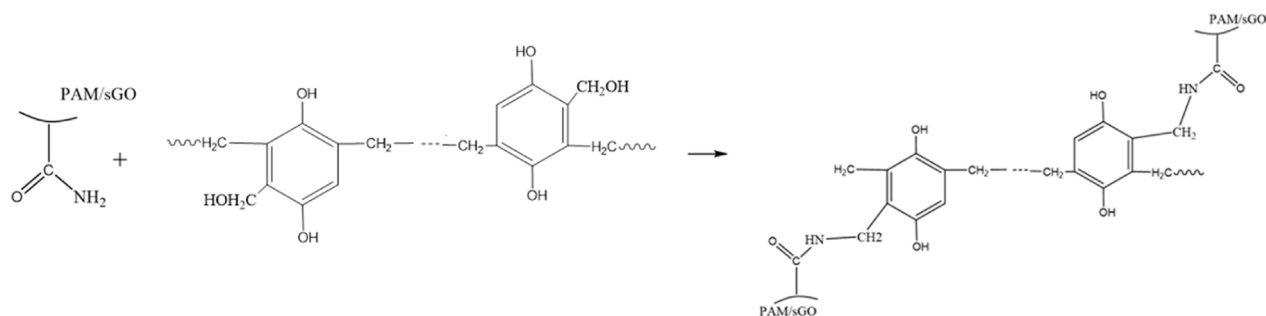


FIGURE 10

The gelation mechanism of the graphite-enhanced gel system (Lv et al., 2020).

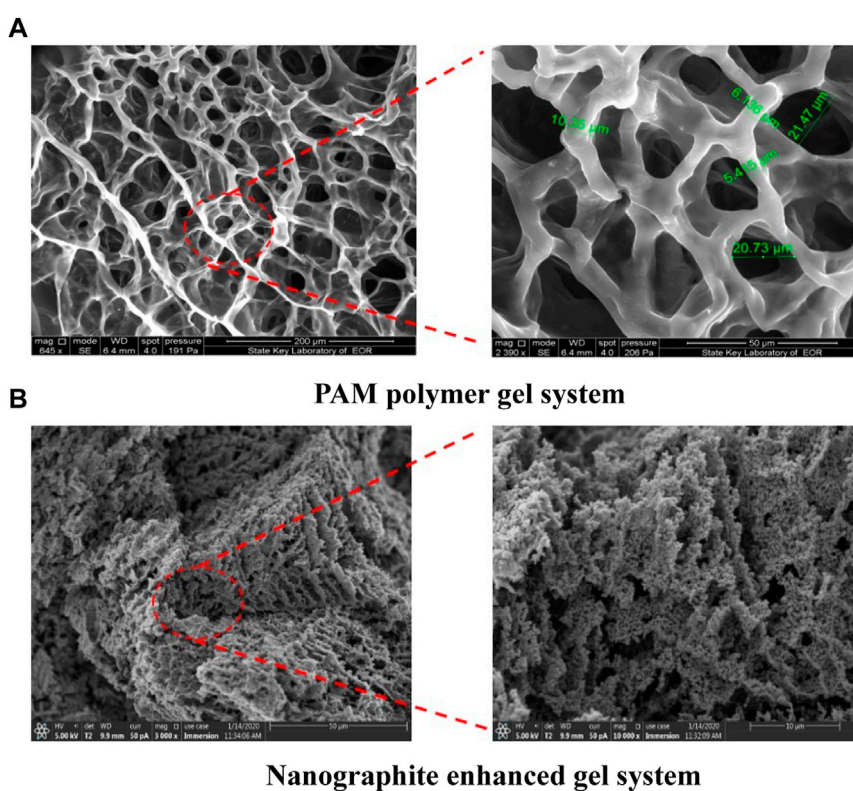


FIGURE 11

SEM images of the (A) PAM gel system and (B) nano-graphite enhanced gel system (Lv et al., 2020).

TABLE 4 Progress of oily sludge enhanced gel systems.

Oily sludge-enhanced gel systems				
Gelant formulation	Gelation Temperature	Gelation time	Gel strength	References
Secondary alkyl sodium sulfonate, polyether, zirconium crosslinking agent, oily sludge	Not given	Not given	2.7 MPa	Chen et al. (2019)
Polyacrylamide, oily sludge, suspending agent, crosslinking agent	80°C	22 h–28 h	Not given	Zhu et al. (2020)

60), polyether (F-68), and fluorinated hydrophobically associating polyacrylamide (FPAM). The synthesis route of FPAM is shown in Figure 12. Based on this, a zirconium crosslinking agent was added to form an oily sludge-enhanced gel system. Due to the exit of amphiphilic hydrophobic association polymer, the suspended amount of oily sludge can be up to 40%. This gel system has been successfully used for profile control treatment in the oilfield. According to the production curve, the injection pressure rapidly increased by approximately 2.7 MPa during the injection period and then stabilized at 10.8 MPa. The water cut rate decreased by 11.5%, while the daily oil well production increased by .6 m<sup>3</sup>/d.

Gudong Oilfield (Zhu et al., 2020) obtained an oily sludge enhanced gel system using polyacrylamide (PAM), suspending agent, oily sludge, and a crosslinking agent by adjusting the gelation time from 22 to 28 h. The gel system can maintain a high strength with a viscosity retention rate of more than 91% after aging for 180 days at 80°C. The sand-pack plugging experiment shows that the plugging rate and the breakthrough pressure can reach 94% and 6.2 MPa, respectively. The experimental data indicate that the enhanced gel system has strong anti-aging effectiveness, better cost management, and potential application prospects.

## 6 Foam-enhanced gel system

The conventional and enhanced gel systems have been successfully used for profile control and water shutoff treatments (Kabir, 2001). Due to the gel system's capability to efficiently plug high permeability zones, the injected water will turn to intermediate and low permeability zones, followed by the

increased swept volume (Sengupta et al., 2012). However, these gel systems cannot reduce the oil-water interfacial tension. While the foam systems have selectively plugging capability and oil-water interfacial tension reduction capacity (Miller and Fogler, 1995). However, the conventional foam is instability when flowing in porous media of reservoir formation. Considering the advantages and disadvantages of gel and foam systems, previous researchers have done many works on the progress of foam-enhanced gel systems (Wassmuth et al., 2000). The foam-enhanced gel systems are usually composed of polymer, crosslinker, foaming agent, and gas (Sydansk, 1994; Coskuner et al., 2015). When foam-enhanced gel systems form in the reservoir formation (Liu et al., 2006), the gel systems reduce the oil-water interfacial tension (Zhong et al., 2017), while the foam systems considerably increase the stability (Zhu et al., 2014; Chaudhary et al., 2021). Compared with conventional gel systems, foam-enhanced gels have higher temperature and salt resistance stability. Because the foam-enhanced gels have a long half-life and a large plugging radius, so the foam-enhanced gels can long-term stable plugging high permeability layer, so as to achieve more effective profile control and water plugging, as shown in Table 5.

Zhao et al. (2015) successfully prepared a long-term stable foam-enhanced gel system with comb polymer, phenolic resin crosslinker, betaine surfactant, and nitrogen gas. The system can be crosslinked at 100°C with the gelation time adjusting from 5 to 30 h. The foam-enhanced gel system has a longer half-life than the conventional aqueous foam. The half-life and foaming volume of the foam-enhanced gel system is increased by 10 times and 1.5 times, respectively. In addition, the half-life and volume of the foam-enhanced gel system remain almost unchanged after 28 h of gel formation. The viscosity of the foam-enhanced gel system was significantly increased due to the crosslinking reaction. While

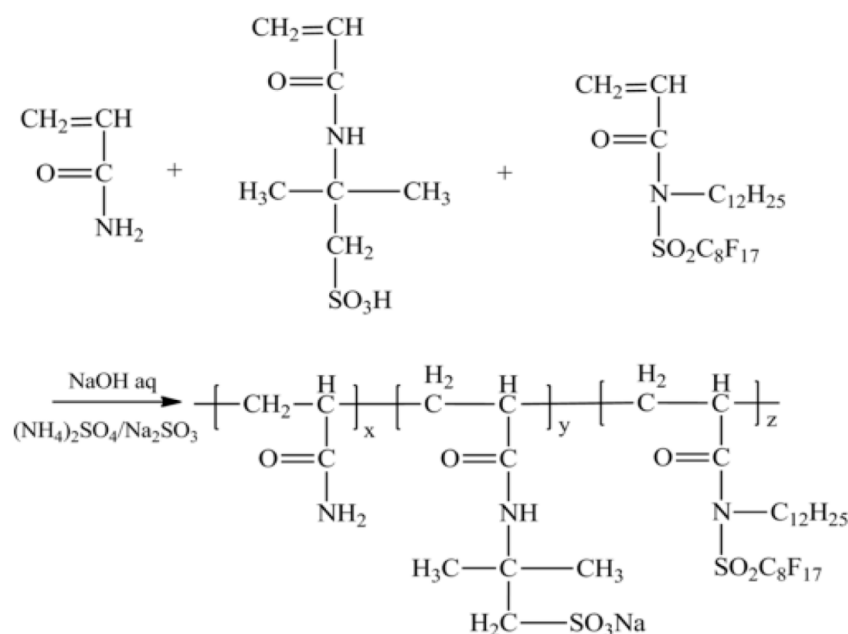


FIGURE 12  
Synthesis route of FPAM (Chen et al., 2019).



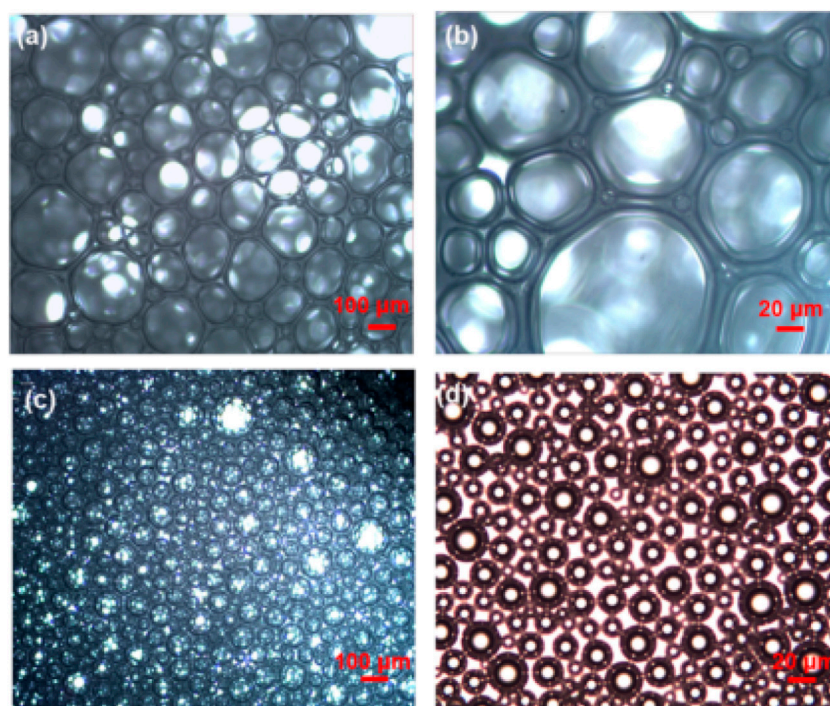


FIGURE 13

Morphology of conventional aqueous foam and foam-enhanced gel. (A) and (B) Conventional aqueous foam with only .3% surfactant; (C) and (D) foam gel (.3% surfactant + .3% comb polymer + .6% phenolic resin cross-linker) (Zhao et al., 2015).

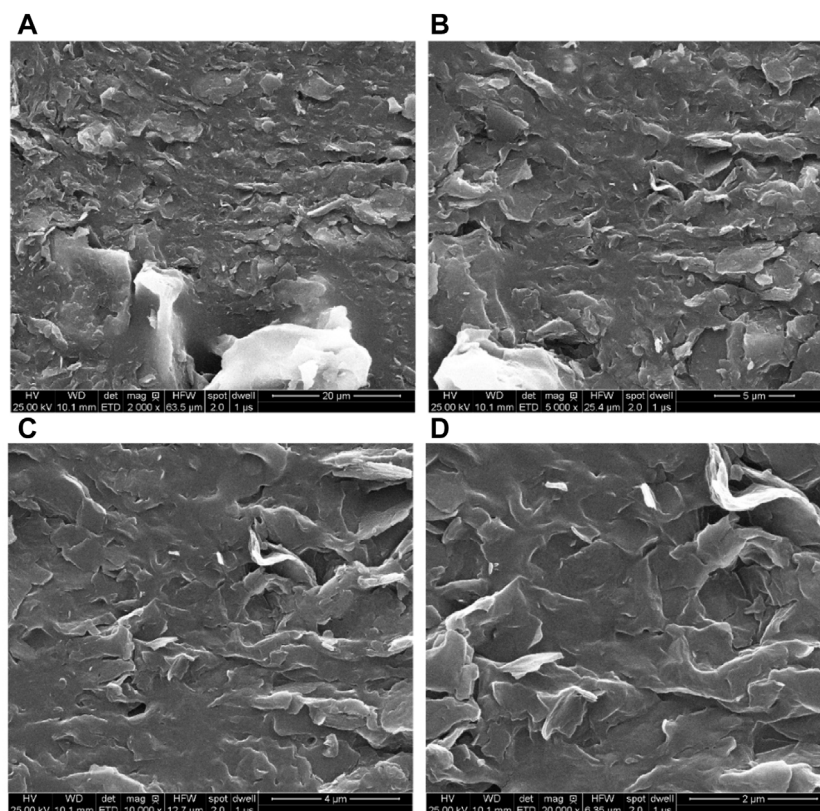
TABLE 5 Progress of foam-enhanced gel systems.

Foam-enhanced gel systems				
Gelant formulation	Gelation Temperature	Gelation time	Gel strength	References
Comb polymer, phenolic resin, N <sub>2</sub>	100°C	14 h	Not given	Zhao et al. (2015)
Partially hydrolyzing polyacrylamide, Cr <sup>3+</sup> , sodium sulfite, N <sub>2</sub>	Not given	Not given	Not given	Qing et al. (2009)
Polyacrylonitrile, phenolic resin, alkali lignin	175°C	3.5 h	G-grade	Li et al. (2022)

the interfacial tension was also reduced, resulting in a decrease in the foam volume. The foam-enhanced gel system has a denser and more consistent structure when compared to the conventional foam system, as shown in Figure 13. However, due to the increase in viscosity, the thickness and strength of the foam film are also increased, which enhances the stability and plugging ability of the foam in the porous medium.

For profile control treatments, the foam-enhanced gel technology has been successfully applied in 6 water injection wells in the Henan Oilfield. The injection pressure and oil production from these wells showed a sharp decline up to December 2011. The well-test data shows that the formation heterogeneity is very serious, and the reservoir temperature is as high as 100°C. After the foam-enhanced gel system treatments, an increase in five parameters (injection pressure, water injection, pressure index, full degree, and injectivity index) (Zhao et al., 2006; Zhao, 2011) was observed, which proves that the foam-enhanced gel system has a good in-depth profile control ability.

Qing et al. (2009) prepared a foam-enhanced gel system with HPAM, sodium dichromate, sodium sulfite, and nitrogen. The foam-enhanced gel system was successfully applied to the Well H1304 of the Huoshaoshan fractured oilfield. After injection of 9,413 m<sup>3</sup> foam-enhanced gel system, the oil production increased by 7,800 m<sup>3</sup>, and the input-output ratio was around 1:3. Li et al. (2022) prepared a high temperature and salinity resistance foam-enhanced gel system with polyacrylonitrile, phenolic resin, alkali lignin, foaming agent, and nitrogen. This foam-enhanced gel system is useful in reservoirs with high-temperature (175°C) and high-salinity (200,000 mg/L). Through the sand-pack flowing experiments, the foam-enhanced gel system has a stronger plugging capacity than the conventional foam gel systems. From SEM images (Figure 14), a dense and compact network structure may be produced when the foam-enhanced gel system is developed. The structure improves the liquid foam film's viscoelasticity, which slows the escape of gas from inside the foam and promotes foam stability.

**FIGURE 14**

SEM image of the mature gel. The magnification of (A), (B), (C) and (D) are 2000, 5,000, 10,000, and 20,000 respectively (Li et al., 2022).

## 7 Conclusion

This paper reviews the progress of several enhanced polymer gel systems for profile control and water shutoff treatments. The most recent advancements in the present enhanced polymer gel systems comprise nano silica-enhanced gel systems, cellulose-enhanced gel systems, graphite-enhanced gel systems, oily sludge-enhanced gel systems, and foam-enhanced gel systems.

According to the present research level and the existing reservoir development scenario, an enhanced polymer gel system is an essential development direction for high water production control in high temperature and salinity reservoirs. Nano silica, graphite, cellulose, oily sludge and other strengthening materials can be used to strengthen the gel to deal with high temperature and high salt reservoir conditions. Nano-silica can reduce the bound water content and participate in the construction of the three-dimensional structure of the gel system, and can also improve the hydrophilicity of the gel systems. The addition of nano-cellulose enables the gel to crosslink between the cellulose chains to increase the strength. Due to its good plasticity and its lamellar structure, nano-graphite can also improve the temperature and salt resistance of the gel systems. Previous researchers have made many works on the enhanced gel system's composition, crosslink and enhanced mechanisms, on-site applications, and so on. For prospective researchers, these findings serve as an excellent reference and source of development ideas. It has

the enormous potential to produce more perceptive research findings for enhanced polymer gel systems.

## Author contributions

SL: Writing- Original draft preparation. QB Writing- Reviewing and Editing. GZ: Writing- Reviewing and Editing. AS: Writing- Reviewing and Editing. CD: Supervision.

## Funding

This work was supported by the National Key R&D Program of China (2018YFA0702400) and National Natural Science Foundation of China (5207040347).

## Conflict of interest

Author QB was employed by Sinopec International Petroleum Exploration and Production Corporation.

The remaining authors declare that the research was conducted in the absence of any commercial or financial relationships that could be construed as a potential conflict of interest.

## Publisher's note

All claims expressed in this article are solely those of the authors and do not necessarily represent those of their affiliated

## References

- Abdulbaki, M., Huh, C., Sepehrnoori, K., Delshad, M., and Varavei, A. (2014). A critical review on use of polymer microgels for conformance control purposes. *J. Pet. Sci. Eng.* 122, 741–753. doi:10.1016/j.petrol.2014.06.034
- Adewole, J. K., and Muritala, K. B. (2019). Some applications of natural polymeric materials in oilfield operations: A review. *J. Pet. Explor. Prod. Technol.* 9 (3), 2297–2307. doi:10.1007/s13202-019-0626-9
- Al-Muntasheri, G. A., Sierra, L., Garzon, F., Lynn, J. D., and Izquierdo, G. (2010). "Water shut-off with polymer gels in a high temperature horizontal gas well: A success story," in Paper SPE 129848-MS Presented at the SPE Improved Oil Recovery Symposium, Tulsa, Oklahoma, USA, 24 April 2010. doi:10.2118/129848-MS
- Asghar, H., Hussain, S., Sattar, H., Brown, N., and Roberts, E. (2014). Environmentally friendly preparation of exfoliated graphite. *J. Ind. Eng. Chem.* 20 (4), 1936–1941. doi:10.1016/j.jiec.2013.09.014
- Bai, B., Zhou, J., and Yin, M. (2015). A comprehensive review of polyacrylamide polymer gels for conformance control. *Pet. Explor. Dev.* 42 (4), 525–532. doi:10.1016/S1876-3804(15)30045-8
- Bryant, S. L., Bartosek, M., Lockhart, T. P., and Giacca, D. L. (1997). Polymer gels for high temperature water shutoff applications. *SPE J.* 2 (04), 447–454. doi:10.2118/36911-PA
- Caili, D., Qing, Y., and Fulin, Z. (2010). In-depth profile control technologies in China—A review of the state of the art. *Pet. Sci. Technol.* 28 (13), 1307–1315. doi:10.1080/10916460903419164
- Cassagnau, P. (2013). Linear viscoelasticity and dynamics of suspensions and molten polymers filled with nanoparticles of different aspect ratios. *Polymer* 54 (18), 4762–4775. doi:10.1016/j.polymer.2013.06.012
- Caulfield, M. J., Qiao, G. G., and Solomon, D. H. (2002). Some aspects of the properties and degradation of polyacrylamides. *Chem. Rev.* 102 (9), 3067–3084. doi:10.1021/cr010439p
- Chang, C., Duan, B., Cai, J., and Zhang, L. (2010). Superabsorbent hydrogels based on cellulose for smart swelling and controllable delivery. *Eur. Polym. J.* 46 (1), 92–100. doi:10.1016/j.eurpolymj.2009.04.033
- Chaudhary, N. K., Guragain, B., Rai, S., Chaudhary, N., Chaudhary, R., Sachin, K. M., et al. (2021). Alcohol-based sanitizers: An effective means for preventing the spread of contagious viral diseases including COVID-19. *Tenside. Surfact. Det.* 58 (6), 416–426. doi:10.1515/tsd-2020-2314
- Chen, S., Su, G., Chen, Z., Hu, J., Yang, H., Luo, Y., et al. (2019). Research and application of gel oily sludge profile control system in Changqing Oilfield. *Sci. Technol. Eng.* 19 (33), 170–178.
- Cheraghian, G., and Hendraningrat, L. (2016). A review on applications of nanotechnology in the enhanced oil recovery part A: Effects of nanoparticles on interfacial tension. *Int. Nano Lett.* 6 (2), 129–138. doi:10.1007/s40089-015-0173-4
- Coskuner, G., Naderi, K., and Babadagli, T. (2015). An enhanced oil recovery technology as a follow up to cold heavy oil production with sand. *J. Pet. Sci. Eng.* 133, 475–482. doi:10.1016/j.petrol.2015.06.030
- Dai, C., Zhao, G., You, Q., and Zhao, M. (2014). A study on environment-friendly polymer gel for water shut-off treatments in low-temperature reservoirs. *J. Appl. Polym. Sci.* 131 (8). doi:10.1002/app.40154
- Du, Y., Li, D., Liu, L., and Gai, G. (2018). Recent achievements of self-healing graphene/polymer composites. *Polymers* 10 (2), 114. doi:10.3390/polym10020114
- Fadil, N. A., Irawan, S., Mohd Isa, N. A., and Shafian, S. R. (2020). Gelation behavior of polyacrylamide reinforced with nano-silica for water shutoff treatment in oil field. *Solid State Phenom.* 307, 252–257. doi:10.4028/www.scientific.net/SSP.307.252
- Goetz, L., Mathew, A., Oksman, K., Gatenholm, P., and Ragauskas, A. J. (2009). A novel nanocomposite film prepared from crosslinked cellulosic whiskers. *Carbohydr. Polym.* 75 (1), 85–89. doi:10.1016/j.carbpol.2008.06.017
- Hu, G., Li, J., and Zeng, G. (2013). Recent development in the treatment of oily sludge from petroleum industry: A review. *J. Hazard. Mat.* 261, 470–490. doi:10.1016/j.jhazmat.2013.07.069
- Hu, Z., Patten, T., Pelton, R., and Cranston, D. (2015). Synergistic stabilization of emulsions and emulsion gels with water-soluble polymers and cellulose nanocrystals. *ACS Sustain. Chem. Eng.* 3 (5), 1023–1031. doi:10.1021/acsschemeng.5b00194
- Huang, J., Al-Mohsin, A., Bataweel, M., Karadkar, P., Li, W., and Shaikh, A. (2017). "Systematic approach to develop a colloidal silica based gel system for water shut-off," in Paper SPE 183942-MS Presented at the SPE Middle East Oil & Gas Show and Conference, Manama, Kingdom of Bahrain, 6 March 2017. doi:10.2118/183942-MS
- Kabir, A. (2001). "Chemical water & gas shutoff technology-an overview," in Paper SPE 72119-MS Presented at the SPE Asia Pacific Improved Oil Recovery Conference, Kuala Lumpur, Malaysia, 8 October 2001. doi:10.2118/72119-MS
- Li, S., Wang, L., Sun, L., Li, Z., and Ren, G. (2022). Formulation evaluation of an innovative composite foamed gel with high temperature and salinity compatibility in heavy oil reservoirs. *J. Pet. Sci. Eng.* 210, 110007. doi:10.1016/j.petrol.2021.110007
- Liu, Y., Bai, B., and Shuler, P. J. (2006). "Application and development of chemical-based conformance control treatments in China oilfields," in Paper SPE 99641-MS Presented at the SPE/DOE Symposium on Improved Oil Recovery, Tulsa, Oklahoma, USA, 22 April 2006. doi:10.2118/99641-MS
- Liu, Y., Dai, C., Wang, K., Zou, C., Gao, M., Fang, Y., et al. (2017). Study on a novel cross-linked polymer gel strengthened with silica nanoparticles. *Energy fuels.* 31 (9), 9152–9161. doi:10.1021/acs.energyfuels.7b01432
- Lv, Y., Dai, C., and Zhao, G. (2020). *Preparation and stability mechanism of temperature and salt resistant modified-graphite hybrid polymer gel*. Dongying, China: China University of Petroleum Press.
- Maiti, S., Jayaramudu, J., Das, K., Reddy, S. M., Sadiku, R., Ray, S. S., et al. (2013). Preparation and characterization of nano-cellulose with new shape from different precursor. *Carbohydr. Polym.* 98 (1), 562–567. doi:10.1016/j.carbpol.2013.06.029
- Majid, A. L., Masoud, H., Mohsen, V. S., Mahsa, B. S., and Aghdas, H. (2018). Experimental study of swelling and rheological behavior of preformed particle gel used in water shutoff treatment. *J. Pet. Sci. Eng.* 169, 739–747. doi:10.1016/j.petrol.2018.06.029
- Michael, F. M., Krishnan, M. R., AlSoughayer, S., Busaleh, A., Almohsin, A., and Alsharaeh, E. H. (2020). Thermo-elastic and self-healing polyacrylamide-2D nanofiller composite hydrogels for water shutoff treatment. *J. Pet. Sci. Eng.* 193, 107391. doi:10.1016/j.petrol.2020.107391
- Miller, M. J., and Fogler, H. S. (1995). A mechanistic investigation of waterflood diversion using foamed gels. *SPE Prod. Fac.* 10 (01), 62–70. doi:10.2118/24662-PA
- Petroudy, S. R. D., Ranjbar, J., and Garmaroodi, E. R. (2018). Eco-friendly superabsorbent polymers based on carboxymethyl cellulose strengthened by TEMPO-mediated oxidation wheat straw cellulose nanofiber. *Carbohydr. Polym.* 197, 565–575. doi:10.1016/j.carbpol.2018.06.008
- Pham, L. T., and Hatzignatiou, D. G. (2016). Rheological evaluation of a sodium silicate gel system for water management in mature, naturally-fractured oilfields. *J. Pet. Sci. Eng.* 138, 218–233. doi:10.1016/j.petrol.2015.11.039
- Qing, Y., Yefei, W., Wei, Z., Ziyuan, Q., and Fulin, Z. (2009). Study and application of gelled foam for in-depth water shutoff in a fractured oil reservoir. *J. Can. Pet. Technol.* 48 (12), 51–55. doi:10.2118/132162-PA
- Sampath, U., Ching, Y. C., Chuah, C. H., Singh, R., and Lin, P. C. (2017). Preparation and characterization of nanocellulose reinforced semi-interpenetrating polymer network of chitosan hydrogel. *Cellulose* 24 (5), 2215–2228. doi:10.1007/s10570-017-1251-8
- Samuelson, M., and Constien, V. (1996). "Effects of high temperature on polymer degradation and cleanup," in Paper SPE 36495-MS Presented at the SPE Annual Technical Conference and Exhibition, Denver, Colorado, 6 October 1996. doi:10.2118/36495-MS
- Sengupta, B., Sharma, V., and Udayabhanu, G. (2012). A study of the effect of the concentration of constituents on the characteristics of a cross-linked polyacrylamide gel. *Pet. Sci. Technol.* 30 (18), 1865–1881. doi:10.1080/10916466.2010.493907
- Sengupta, R., Bhattacharya, M., Bandyopadhyay, S., and Bhowmick, A. K. (2011). A review on the mechanical and electrical properties of graphite and modified graphite reinforced polymer composites. *Prog. Polym. Sci.* 36 (5), 638–670. doi:10.1016/j.progpolymsci.2010.11.003
- Suleymanov, A. B., and Shovgenov, A. D. (2021). "Nano composite polymer composition for water shutoff treatment at high formation temperature," in Paper SPE 207066-MS Presented at the SPE Annual Caspian Technical Conference, Virtual, October 5–7, 2021. doi:10.2118/207066-MS
- Sydansk, R. D. (1994). Polymer-enhanced foams part 1: Laboratory development and evaluation. *SPE Adv. Technol. Ser.* 2 (02), 150–159. doi:10.2118/25168-PA
- Sydansk, R. D., and Seright, R. S. (2007). When and where relative permeability modification water-shutoff treatments can be successfully applied. *SPE Prod. Oper.* 22 (2), 236–247. doi:10.2118/99371-PA
- Wang, C., Zhang, L., Ju, G., and Sun, Q. (2020). Development and performance evaluation of a high-temperature profile control system. *ACS Omega* 5 (28), 17828–17838. doi:10.1021/acsomega.0c02642
- Wassmuth, F., Hodgins, L., Schramm, L., and Kutay, S. (2000). "Screening and coreflood testing of gel foams to control excessive gas production in oil wells," in Paper SPE 59283-MS Presented at the SPE/DOE Improved Oil Recovery Symposium, Tulsa, Oklahoma, 3 April 2000. doi:10.2118/59283-MS
- Yakovlev, A., Finaenov, A., Zabud'Kov, S., and Yakovleva, E. (2006). Thermally expanded graphite: Synthesis, properties, and prospects for use. *Russ. J. Appl. Chem.* 79 (11), 1741–1751. doi:10.1134/S1070427206110012



- Zareie, C., Bahramian, A. R., Sefti, M. V., and Salehi, M. B. (2019). Network-gel strength relationship and performance improvement of polyacrylamide hydrogel using nano-silica; with regards to application in oil wells conditions. *J. Mol. Liq.* 278, 512–520. doi:10.1016/j.molliq.2019.01.089
- Zhang, L., Pu, C., Zheng, L., and Gu, X. (2016). Synthesis and performance evaluation of a new kind of gel used as water shutoff agent. *J. Pet. Explor. Prod. Technol.* 6 (3), 433–440. doi:10.1007/s13202-015-0194-6
- Zhao, F., Dai, C., Wang, Y., Feng, D., and Chen, K. (2006). Comprehension of water shutoff in oil wells and its technical keys. *Acta petro. Sin.* 27 (5), 71–74. doi:10.7623/syxb200605013
- Zhao, F. (2011). Pressure index decision-making technique and its application progresses. *J. China Univ. Pet.* 35 (1), 82–88. doi:10.3969/j.issn.1673-5005
- Zhao, F. (2006). *Principle of EOR*. Dongying: China University of Petroleum Press.
- Zhao, G., Dai, C., You, Q., Zhao, M., and Zhao, J. (2013). Study on formation of gels formed by polymer and zirconium acetate. *J. Sol-Gel Sci. Technol.* 65 (3), 392–398. doi:10.1007/s10971-012-2951-z
- Zhao, G., Dai, C., Zhang, Y., Chen, A., Yan, Z., and Zhao, M. (2015). Enhanced foam stability by adding comb polymer gel for in-depth profile control in high temperature reservoirs. *Colloids Surf. A* 482, 115–124. doi:10.1016/j.colsurfa.2015.04.041
- Zhong, H., Zhang, W., Fu, J., Lu, J., and Yin, H. (2017). The performance of polymer flooding in heterogeneous type II reservoirs—an experimental and field investigation. *Energies* 10 (4), 454. doi:10.3390/en10040454
- Zhou, Y., Fu, S., Zhang, L., and Zhan, H. (2013). Superabsorbent nanocomposite hydrogels made of carboxylated cellulose nanofibrils and CMC-gp (AA-co-AM). *Carbohydr. Polym.* 97 (2), 429–435. doi:10.1016/j.carbpol.2013.04.088
- Zhu, D., Hou, J., Wei, Q., Wu, X., and Bai, B. (2017). Terpolymer gel system formed by resorcinol-hexamethylenetetramine for water management in extremely high-temperature reservoirs. *Energy fuels.* 31 (2), 1519–1528. doi:10.1021/acs.energyfuels.6b03188
- Zhu, D., Wei, L., Wang, B., and Feng, Y. (2014). Aqueous hybrids of silica nanoparticles and hydrophobically associating hydrolyzed polyacrylamide used for EOR in high-temperature and high-salinity reservoirs. *Energies* 7 (6), 3858–3871. doi:10.3390/en7063858
- Zhu, Y., Liang, X., Zhu, R., Tian, Y., Feng, X., and Wang, Z. (2020). Preparation and evaluation of plugging control system based on oily sludge from Shengli Gudong Oilfield. *Chem. Ind. Eng.* 37 (05), 14–21. doi:10.13353/j.issn.1004.9533.20191931
- Ziegler, R. (2017). Technology focus: High-Pressure/High-Temperature challenges (april 2017). *J. Pet. Technol.* 69 (04), 79. doi:10.2118/0417-0079-JPT



# Frontiers in Chemistry

Explores all fields of chemical science across the periodic table

Advances our understanding of how atoms, ions, and molecules come together and come apart.

It explores the role of chemistry in our everyday lives - from electronic devices to health and wellbeing.

## Discover the latest Research Topics

[See more →](#)

### Frontiers

Avenue du Tribunal-Fédéral 34  
1005 Lausanne, Switzerland  
[frontiersin.org](https://frontiersin.org)

### Contact us

+41 (0)21 510 17 00  
[frontiersin.org/about/contact](https://frontiersin.org/about/contact)



### Frontiers in Chemistry

